

Junbo Jia

Modern Earthquake Engineering

Offshore and Land-based Structures



Springer

Modern Earthquake Engineering

Junbo Jia

Modern Earthquake Engineering

Offshore and Land-based Structures



Springer

Junbo Jia
Aker Solutions
Bergen
Norway

ISBN 978-3-642-31853-5
DOI 10.1007/978-3-642-31854-2

ISBN 978-3-642-31854-2 (eBook)

Library of Congress Control Number: 2016949602

© Springer-Verlag GmbH Germany 2017

This work is subject to copyright. All rights are reserved by the Publisher, whether the whole or part of the material is concerned, specifically the rights of translation, reprinting, reuse of illustrations, recitation, broadcasting, reproduction on microfilms or in any other physical way, and transmission or information storage and retrieval, electronic adaptation, computer software, or by similar or dissimilar methodology now known or hereafter developed.

The use of general descriptive names, registered names, trademarks, service marks, etc. in this publication does not imply, even in the absence of a specific statement, that such names are exempt from the relevant protective laws and regulations and therefore free for general use.

The publisher, the authors and the editors are safe to assume that the advice and information in this book are believed to be true and accurate at the date of publication. Neither the publisher nor the authors or the editors give a warranty, express or implied, with respect to the material contained herein or for any errors or omissions that may have been made.

Printed on acid-free paper

This Springer imprint is published by Springer Nature
The registered company is Springer-Verlag GmbH Germany
The registered company address is: Heidelberger Platz 3, 14197 Berlin, Germany

*To those who live with me every day, and who
brought me into existence*

Preface

Earthquakes are among the most destructive natural disasters on our planet. Over history, enormous engineering and research efforts have been devoted to the study of causes and consequences of earthquakes, the prediction and forecasting of future earthquakes, the determination of ground motion intensities in a particular site, and the seismic response assessment and the mitigation measures for various types of structures and foundations. All these efforts have been intended simply to keep structures and their contents from falling down and causing damage and to keep people safe during earthquakes.

During the last century, through a synergy of various pieces of know-how associated with the contents above, a unique scientific topic, earthquake engineering, has finally been formed. It is essentially focused on finding solutions to problems posed by seismic hazards. During its development, earthquake engineering has borrowed much from other engineering disciplines in its understanding of seismic wave propagations and ground motion characteristics, in considering nonlinear soil and structural responses and engineering dynamics, and in developing probability-based design approaches. Although earthquake engineering as a scientific topic is by no means fully understood (and perhaps never will be), the great amount of activity in this field has made it possible to form a practical subject in a fairly systematic, coherent, and quantitative manner.

The development of modern earthquake engineering has been closely linked to advances in computer technology, allowing engineers to solve problems of increasing complexity in two aspects: First, it allows for the calculation of results based on classical solutions but with numerical evaluation of certain terms that cannot be expressed in a closed form; second, it also allows for the modeling of complex systems (structures, foundations, soils, or faults) using approximation methods such as finite element method and to perform numerical calculations to obtain the system's response. However, even though engineers and researchers are using computers to solve many seismic problems with great complexity, many of them lack an actual understanding of the essential principles in earthquake engineering, and their capability to properly evaluate seismic ground motions and structural responses is thus limited and even weaker than that of those working

on this subject decades ago. This is also partly because the complexity of the analyzed seismic problems has dramatically increased in recent decades, which is more case-dependent, and therefore, less general conclusions can be drawn. Eventually, this has led to many engineers and researchers losing the “big picture” and intuition toward original problems and principles. Moreover, the division of responsibilities between seismologists and civil engineers has become more “clear,” thus *“eliminating the previously critical need for engineers to get involved ‘up front’ in the seismic input characterization for a project”* (CA Cornell). In many cases, professional structural and geotechnical engineers are not able to qualify the seismic input ground motions with respect to their seismological features, and seismologists and geotechnical and structural engineers often understand each other only poorly. Furthermore, students who study earthquake engineering are given canned class exercises and deterministic projects, which are often far different from the real-world seismic engineering problems that have a great diversity in various aspects. Therefore, in spite of increased knowledge on earthquake engineering, the problems of seismic design are in many cases handled without success despite large expenditures of investment. This leads to an insurmountable barrier to efficiently manage the risk of structures and to further improve the design, potentially posing a significant safety hazard, and may also result in significant economic loss. Such considerations motivated me to write this book.

The objective of this book is to offer a methodical presentation of essentials of earthquake engineering, based on “understandable” mathematics and mechanics with an emphasis on engineering application aspects; to present the most useful methods for determining seismic ground motions and loading on structures; to apply both the well-accepted and emerging methods to perform seismic design and analysis for real-world engineering structures; and to implement various types of mitigation measures to increase the seismic resistance of structures. Instead of being generic, the book is filled with concrete explanations from real-world engineering practices.

The background assumed for reading this book includes a basic knowledge of matrix algebra, differential and integral calculus, structural dynamics or engineering vibrations, structural mechanics, strength of materials, and a working knowledge of probability theory.

Chapter 1 provides a review of and introduction to historical earthquakes and consequences; the cause of earthquakes, with a special focus on tectonic-related earthquakes and fault rupture mechanism; earthquake prediction and forecasting; and the relevance of earthquake engineering with offshore structures. Chapter 3 presents the seismic wave propagation, earthquake magnitude and intensity measures, measurements and characterizations of seismic motions, etc. These two chapters together introduce readers to basic knowledge of engineering seismology necessary for civil engineers.

Note that previous earthquake engineering efforts have mainly focused on land-based structures. More offshore structures with large capital investment are being placed in areas with active seismicity, and many existing offshore structures are regarded as having inadequate seismic resistance due to increased/updated

knowledge on seismic hazard and assessment methods, as well as due to original deficiencies and damages that took place during manufacturing, construction, and operation of structures. Therefore, Chap. 2 is dedicated to introducing different types of offshore structures, their dynamic characteristics, and their similarities with and differences from land-based structures. This serves as an introduction for further exploring their seismic responses and resistance discussed in later chapters.

Since the determination of ground motions is of great importance for both geotechnical and structural engineers to assess a particular design to be installed at a specific site/location, Chaps. 4 through 7 present the representation and the determination of earthquake ground motions for civil engineering applications.

As the ground motions at two locations more than hundreds of meters apart can differ to certain extent, thus potentially magnifying the response of extended structures with multiple supports or structures sensitive to torsional vibrations, Chap. 8 discusses the characterization, determination, and influence of spatial varied ground motions.

Based on the knowledge of engineering seismology and ground motion determination and representation presented in previous chapters, Chap. 9 presents the determination of seismic hazard and risk, of which the former is an essential part for seismic design, and the latter describes the social, economic, and environmental consequences of earthquakes.

As seismic analysis and design for offshore structures are important topics in this book, Chap. 10 presents relevant knowledge of hydrodynamic load effects and ice loading effects on offshore structures, which may occur simultaneously and be combined with seismic loading applied on structures. This is followed by a brief introduction to shock wave due to seaquakes and its effects on floating offshore structures as discussed in Chap. 11. In Chap. 12, causes, calculation, characterization, and mitigations of tsunami waves are presented.

Note that the contents presented from Chap. 3 through Chap. 12 are mainly focused on the ground motion and loading generated or triggered by earthquakes, Chap. 13 discusses damages of structures and foundations due to ground motions. In addition, the human safety and motion-induced interruptions are also briefly discussed in this chapter.

Chapter 14 presents the essential design philosophy and its realization in prescriptive codes and performance-based design. The former, prescriptive codes have gained a great deal of popularity by placing a strong focus on characterizing uncertainties associated with both load and resistance; the latter, performance-based design, is promoted by many professionals as a tool for future structural and geotechnical design.

From Chap. 15, the contents of the book move into various topics on seismic structural analysis and design, as well as mitigation measures. Chapter 15 presents traditional and recent seismic analysis methods, among which the traditional methods mainly aim for pursuing accuracy of calculated seismic responses, while the recently developed methods place more focus on the compatibility between the structural response calculation and the evaluation of detailed performance demand, on revealing a structure's intrinsic seismic response and essential performance

characteristics and on improving the robustness of seismic load estimation and analysis results.

The majority of the contents in the first 15 chapters provide readers a “big picture” to determine the seismic motions and to evaluate their effects on engineering structures, in the aspects of fault rupture, wave propagation (path effects), local geotechnical site effects, soil structure interactions, and structural dynamics.

Chapter 16 describes the response assessment methods of offshore structures due to potential sudden subsidence accidents. In Chap. 17, available methods to assess hydrodynamic impacts of liquid inside tanks and their influence on the structural integrity are presented.

As inexpensive digital computers and user-friendly geotechnical and structural engineering software have extensively been used in the practice of civil engineering, Chap. 18 presents a selection of computer systems for improving numerical analysis efficiencies. It also details how to manage computation precision during either analytical or numerical analysis, the later of which is often ignored by researchers and engineers.

Chapters 19 through 29 discuss various mitigation measures and strategies to decrease the negative influence of earthquakes. These include the avoidance of significant dynamic amplifications, ductility design, increasing damping by using either structural damping or direct damping devices, base and hanging isolation system, dynamic absorber, load- and energy-sharing mechanism, structural health monitoring, resistance of non-structural elements, and seismic rehabilitation.

While the book does not seek to promote any specific “school of thought,” it inevitably reflects this author’s “best practice” and “own interpretations.” This is particularly apparent in the topics selected and level of detail devoted to each of them, their sequences, and the choices of many mathematical treatments and symbol notations, etc. The author hopes that this does not deter the readers from seeking to find their own “best practice” and dive into the vast knowledge basin of modern earthquake engineering, which is extremely enjoyable as readers go deeper and wider. Moreover, the book is densely referenced to allow readers to explore more detailed information on each topic presented.

Seismic design comprises a combination of decisions made from an environment of partial truth, partial knowledge, and partial uncertainties. In this process, both academic know-how and professional experience play equally important roles. By incorporating more advanced (but not necessarily more complicated) knowledge of earthquake engineering into the experiences accumulated from engineering applications, there is a margin to further reduce uncertainties. As a result, more cost-effective and safer designs can then be achieved. Moreover, engineering applications for designing earthquake-resistant structures are, in many ways, more of an art than a science. Even though seismic designs must be thoroughly checked in a rigorous scientific manner, intuition, imagination, and a synthesis of experience and knowledge play essential roles in the process of design.

It must be admitted that the development of earthquake engineering is far from mature. To further develop this subject, researchers and engineers are motivated to

propose more dedicated and new theories and apply them to mitigate the associated risks due to earthquakes.

In preparing such a text, it is rather difficult to acknowledge all the help given to the author. First, I am indebted to the earthquake, offshore, and civil engineering communities who have undertaken extensive research and development that has led to accumulated knowledge, methods, and engineering applications in this field, on which this book is based. I would also like to thank individuals who have stimulated my interests through technical discussions and those who reviewed parts of or the entire manuscript. These include (in alphabetical order) the following: Atilla Ansal (European Association for Earthquake Engineering), Kuvvet Atakan (University of Bergen), Gunnar Bremer (Aker Solutions), Jacopo Buongiorno (Massachusetts Institute of Technology), Wai-Fah Chen (University of Hawaii), Donald W. Davies (Magnusson Klemencic Associates), Odd Magnus Faltinsen (Norwegian University of Science and Technology), Ove Tobias Gudmestad (University of Stavanger), Muneo Hori (University of Tokyo), Amir M. Kaynia (Norwegian Geotechnical Institute), Steven L. Kramer (University of Washington), Conrad Lindholm (NORSAR), Lance Manuel (University of Texas At Austin), Preben Terndrup Pedersen (Technical University of Denmark), John Michael Rotter (University of Edinburgh and Imperial College), Valentin Shustov (California State University), Richard Snell (Oxford University), Didier Sornette (Swiss Federal Institute of Technology, Zurich), Douglas Stock (Digital Structures, Inc. Berkeley), Christopher Stubbs (Colebrand International Limited, London), and Armin Winkler (GERB Schwingungisolierungen GmbH & Co.KG). Furthermore, I would like to thank Statoil, BP and Norwegian Geotechnical Institute for their close cooperation on relevant engineering projects. Moreover, there are numerous others not named to whom I extend my sincere thanks.

This book has an extensive list of references reflecting both the historical and recent developments of the subject. I would like to thank all the authors referenced for their contribution to the area. However, the literatures listed at the end of each chapter can only be indicative. It is impossible for me to acknowledge all the individual contributions.

Finally, I dedicate this book to Jing and Danning, for their support and patience. I conclude this preface with an expression of deep gratitude to them.

Bergen, Norway

Junbo Jia

About this Book

This book addresses applications of earthquake engineering for both offshore and land-based structures. It is self-contained as a reference work and covers a wide range of topics, including topics related to engineering seismology, geotechnical earthquake engineering, structural engineering, as well as special contents dedicated to design philosophy, determination of ground motions, shock waves, tsunamis, earthquake damage, seismic response of offshore and arctic structures, spatial varied ground motions, simplified and advanced seismic analysis methods, sudden subsidence of offshore platforms, tank liquid impacts during earthquakes, seismic resistance of non-structural elements, and various types of mitigation measures, etc. The target readership includes professionals in offshore and civil engineering, officials and regulators, as well as researchers and students in this field.

Contents

1	Introduction	1
1.1	Historical Earthquake Events	1
1.2	Consequences of Earthquakes	5
1.3	Benefits of Earthquakes	18
1.4	Causes of Earthquakes	19
1.4.1	Tectonic-Related Earthquakes and the Elastic Rebound Theory	20
1.4.2	Volcanic Earthquakes	25
1.4.3	Human Induced/Triggered Earthquakes	27
1.4.4	Ice Induced Earthquakes	33
1.5	Faults	34
1.6	Tectonic Plate Boundaries and Fault Zones	40
1.6.1	Spreading Zones	41
1.6.2	Subduction Zones	44
1.6.3	Transform Fault Zones	48
1.6.4	Intraplates	49
1.6.5	Relation of Plate Boundaries with Earthquake Occurrences	51
1.7	Earthquake Mitigation Measures and Modern Earthquake Engineering	52
1.8	Earthquake Prediction and Forecast	56
1.8.1	Earthquake Prediction	56
1.8.2	Earthquake Forecast	59
1.8.3	The Social and Economic Impact of Earthquake Predictions	59
1.9	Motivations of Offshore Earthquake Engineering	61
1.10	Closing Remarks	68
	References	68

2 Offshore Structures Versus Land-Based Structures	73
2.1 Introduction to Offshore Structures	73
2.1.1 Offshore Platforms.	73
2.1.2 Offshore Wind Turbine Substructures and Foundations	81
2.2 Accounting of Dynamics in the Concept Design of Structures	87
2.2.1 Dynamics Versus Statics	87
2.2.2 Characteristics of Dynamic Responses.	92
2.2.3 Frequency Range of Dynamic Loading	97
2.3 Difference Between Offshore and Land-Based Structures	102
References.	106
3 Characterize Ground Motions	107
3.1 Definition of Earthquake Locations.	107
3.2 Seismic Waves	107
3.2.1 Body Waves	108
3.2.2 Surface Waves.	113
3.2.3 Guided Waves.	117
3.3 Measuring Seismic Motions Using Seismogram	119
3.3.1 Measurement Using Seismograph	119
3.3.2 Torsional Seismic Motions	124
3.4 Magnitude and Intensity	124
3.4.1 Magnitude	125
3.4.2 Intensity Categories	134
3.5 Non-stationary and Peak Ground Motions	137
3.5.1 Peak Ground Motions and Its Relationship with Magnitude and Intensity	137
3.5.2 Contribution of Body and Surface Wave to Ground Motions	140
3.5.3 Moving Resonance	141
3.6 Attenuation Relationship and Uncertainties.	142
3.7 Duration of Ground Motions	152
3.7.1 Effects of Ground Motion Durations	152
3.7.2 Definition of Ground Motion Duration	154
3.7.3 Approximation of Ground Motion Duration	157
3.8 Source of Ground Motion Recording Data	162
References.	162
4 Determination of Site Specific Earthquake Ground Motions	169
4.1 From Fault Rupture to Seismic Design.	169
4.2 Site Period	175
4.2.1 General	175
4.2.2 Influence of Soil Depth on the Site Period	179

4.3	Site Response and Soil–Structure Interactions	182
4.3.1	General	182
4.3.2	Kinematic Interaction	185
4.3.3	Subgrade Impedances and Damping	186
4.3.4	Inertial Interaction	186
4.3.5	Effects of Soil–Structure Interaction	187
4.3.6	Characteristics of Site Responses.	188
4.3.7	Effects of Topographic and Subsurface Irregularities	190
4.3.8	Applicability of One-, Two-, and Three-Dimensional Site Response Analysis	194
4.3.9	Linear, Equivalent Linear or Non-linear Soil Modeling	195
4.3.10	Location to Input Seismic Motions for a Site Response Analysis.	197
4.4	Water Column Effects on Vertical Ground Excitations.	197
	References	198
5	Representation of Earthquake Ground Motions	203
5.1	General.	203
5.2	Earthquake Excitations Versus Dynamic Ocean Wave, Wind, and Ice Loading	204
5.3	Power Spectrum of Seismic Ground Motions	207
5.3.1	Introduction to Fourier and Power Spectrum.	207
5.3.2	Power Spectrum of Seismic Ground Motions	215
5.4	Response Spectrum.	218
5.4.1	Background	218
5.4.2	Elastic Response and Design Spectrum.	220
5.4.3	Ductility-Modified (Inelastic) Design Spectrum Method	239
5.4.4	Vertical Response Spectrum	245
5.5	Time History Method	249
5.5.1	General Method.	249
5.5.2	Drift Phenomenon and Its Correction	250
5.6	Wavelet Transform Method	254
	References	261
6	Determining Response Spectra by Design Codes	267
6.1	General.	267
6.2	Code Based Simplified Method for Calculating the Response Spectrum.	268
6.2.1	Construction of Design Spectrum in Eurocode 8 for Land-Based Structure.	269

6.2.2	Construction of Design Spectrum in ISO 19901 and Norsok for Offshore Structures	272
References		280
7	Record Selection for Performing Site Specific Response Analysis	281
7.1	General	281
7.2	Selections of Motion Recordings	282
7.3	Modification of the Recordings to Fit into the Design Rock Spectrum	283
7.3.1	Direct Scaling	283
7.3.2	Spectrum/Spectral Matching	283
7.3.3	Pros and Cons of Direct Scaling and Spectrum Matching	287
7.4	Performing the Site Response Analysis Using Modified/Matched Recordings	288
References		290
8	Spatial Varied (Asynchronous) Ground Motion	293
8.1	General	293
8.2	Cross-Covariance, Cross-Spectra Density Function and Coherence Function	297
8.2.1	Cross-Covariance in Time Domain	297
8.2.2	Cross-Spectra Density in the Frequency Domain	298
8.2.3	Coherence Function in the Frequency Domain	298
8.3	Simulation of SVEGM	300
8.4	Effects of SVEGM	304
References		308
9	Seismic Hazard and Risk Assessment	311
9.1	Seismic Hazard Analysis	311
9.1.1	Introduction	311
9.1.2	Deterministic Seismic Hazard Analysis (DSHA)	313
9.1.3	Probabilistic Seismic Hazard Analysis (PSHA)	315
9.1.4	Deaggregation (Disaggregation) in PSHA for Multiple Sources	332
9.1.5	Logic Tree Method	336
9.2	Seismic Hazard Map	338
9.3	Apply PSHA for Engineering Design	342
9.4	Conditional Mean Spectrum	346
9.5	Forecasting “Unpredictable” Extremes—Dragon-Kings	351
9.6	Assessing Earthquake Disaster Assisted by Satellite Remote Sensing	353
9.7	Seismic Risk	354
References		356

10 Influence of Hydrodynamic Forces and Ice During Earthquakes	361
10.1 Hydrodynamic Forces	361
10.1.1 Introduction to Hydrodynamic Force Calculation	361
10.1.2 Effects of Drag Forces	366
10.1.3 Effects and Determination of Added Mass	367
10.1.4 Effects of Buoyancy	369
10.1.5 Effects and Modeling of Marine Growth	369
10.2 Effects of Ice	372
10.2.1 General	372
10.2.2 Effects of Ice–Structure Interaction on the Seismic Response of Structures	375
10.2.3 Icing and Its Effects	376
References	377
11 Shock Wave Due to Seaquakes	379
11.1 Introduction	379
11.2 Simplified Model for Simulating Seaquakes	380
11.3 Case Study by Kiyokawa	381
References	385
12 Introduction to Tsunamis	387
12.1 Cause of Tsunamis	387
12.2 History and Consequences of Tsunamis	391
12.3 Characterizing Tsunami Size	393
12.4 Calculation of Tsunami Waves	395
12.4.1 Tsunami Generation at Source	396
12.4.2 Tsunami Propagation in Ocean	399
12.4.3 Tsunami Run-up (Shoaling) at Coastal Areas and Sloped Beach	400
12.4.4 Shallow Water Wave Theory	402
12.5 Tsunami Induced Load on Structures Located in Shallow Water and Coastal Areas	404
12.6 Structural Resistance Due to Tsunami	407
12.7 Mitigation of Tsunami Hazard	408
References	411
13 Earthquake Damages	413
13.1 General	413
13.2 Structural and Foundation Damage	413
13.3 Soil Liquefaction	416
13.3.1 General	416
13.3.2 Assessment of Liquefaction	419
13.3.3 Mitigation Measures of Soil Liquefaction	421

13.4	Landslides	421
13.4.1	General	421
13.4.2	Assessment of Regional Landslide Potential by Arias Intensity	423
13.5	Human Body Safety and Motion Induced Interruptions	424
13.5.1	General	424
13.5.2	Remedial Measures with Regard to Human Body Safety	425
13.5.3	Motion Induced Interruptions	426
13.6	Structural Damage Measures	427
13.6.1	Basic Parameters for Damage Measures	427
13.6.2	Damage Indices	428
	References	429
14	Design Philosophy	433
14.1	General	433
14.2	Prescriptive Code Design	436
14.2.1	Introduction	436
14.2.2	Limit States Design	437
14.2.3	Allowable Stress Design	439
14.2.4	Plastic Design	441
14.2.5	Load and Resistance Factor Design	442
14.2.6	Levels of Reliability Method	457
14.2.7	ASD Versus LRFD	458
14.2.8	Development of Seismic Design Codes	459
14.2.9	Hierarchy of Codes and Standards	460
14.3	Introduction to Performance-Based Design	462
14.3.1	Limitations of Traditional Prescriptive Code Design	462
14.3.2	Introduction to Performance-Based Design	463
14.3.3	Performance-Based Design for Structures	466
14.3.4	Introduction to Practical Methods for PBD	467
	References	468
15	Seismic Analysis and Response of Structures	471
15.1	General	471
15.2	Traditional Seismic Analysis Methods	472
15.2.1	Introduction	472
15.2.2	Simplified Static Seismic Coefficient Method	476
15.2.3	Random Vibration Analysis	478
15.2.4	Response Spectrum Analysis	478
15.2.5	Non-linear Static Pushover Analysis	487
15.2.6	Non-linear Dynamic Time Domain Analysis	495
15.2.7	Case Studies	497

15.2.8	Response Difference Between Response Spectrum and Non-linear Dynamic Time Domain Analysis	510
15.3	Selection of Principal Directions in Seismic Analysis.	510
15.4	Recently Developed Methods	511
15.4.1	Incremental Dynamic Analysis	511
15.4.2	Endurance Time Analysis	514
15.4.3	Critical Excitation Method.	519
15.5	Characteristics of Seismic Responses	521
15.6	Seismic Transient Excited Vibrations	523
15.7	Whipping Effect	525
15.7.1	Introduction	525
15.7.2	Investigation of the Whipping Effect for a Jacket and Topside Structure	526
15.7.3	Investigation of the Whipping Effect for a GBS and Topside Structure	531
15.7.4	Investigation of the Whipping Effect for a Tower-Podium System	532
15.7.5	Documented Observations of Whipping Responses	534
15.7.6	Mitigation of Whipping Response	537
15.8	Influences from Structures' Orientations	538
15.9	Remarks on Modeling of Material Properties for Seismic Analysis	539
	References	541
16	Sudden Subsidence and Its Assessment	547
16.1	General	547
16.2	Structural Assessment	548
16.2.1	Simplified Static Approach	548
16.2.2	Dynamic Time History Approach	548
16.3	Case Studies	550
16.3.1	Case Study 1: Response of Topside Bridges and Modules Due to Sudden Subsidence.	550
16.3.2	Case Study 2: Response of a Topside Flare Boom Due to Sudden Subsidence	553
17	Tank Liquid Impact	555
17.1	General	555
17.2	Tank Damages Due to Earthquakes	557
17.3	Calculation of Hydrodynamic Forces Due to Tank Impact	561
17.3.1	Fluid–Tank Interaction in Horizontal Direction	562
17.3.2	Effects of Flexibility of Tank Walls	579
17.3.3	Fluid–Tank Interaction in the Vertical Direction	581
17.3.4	Implementation of Fluid Modeling in Finite Element Analysis.	581

17.4	Soil-Tank Interaction	584
17.5	Codes and Standards for Seismic Tank Design.	584
	References	585
18	Selection of Computer System and Computation Precision	589
18.1	General.	589
18.2	Computer System for Improving Numerical Analysis Efficiency	589
18.3	Computation Precision	593
	References	594
19	Avoid Dynamic Amplifications	595
19.1	Seismic Design Principles.	595
19.2	Stiffness and Mass Distribution.	598
19.3	Elevation Control	599
19.4	Dynamic Magnification Due to Torsional Effects	605
19.4.1	Introduction	605
19.4.2	Mitigation Measures	606
19.4.3	Accounting for Torsional Effects	609
	References	610
20	Ductility Through Structural Configuration and Local Detailing	613
20.1	Steel Brace Frames.	613
20.2	Buckling-Restrained Brace Frame.	621
20.3	Moment Resisting Frame	623
20.4	Shear Walls	625
20.5	Eccentrically Braced Frame	627
20.6	Local Structural Detailing.	628
	References	631
21	Damping.	633
21.1	General.	633
21.2	Damping Apparatus	635
21.3	Equivalent Viscous Damping	636
21.4	Relationship Among Various Expressions of Damping.	637
21.5	Practical Damping Modeling for Dynamic Analysis	638
21.5.1	Modal Damping	638
21.5.2	Rayleigh Damping.	639
21.5.3	Caughey Damping.	640
21.5.4	Non-proportional Damping	641
21.6	Damping Levels for Engineering Structures	642
21.6.1	Material Damping	642
21.6.2	Structural/Slip Damping	643
21.6.3	System Damping	644

21.6.4	Hydro- and Aerodynamic Damping	644
21.6.5	Typical Damping Levels	644
	References	646
22	Direct Damping Apparatus	647
22.1	Introduction	647
22.2	Viscous Damper	650
22.2.1	Introduction	650
22.2.2	Advantages and Drawbacks of Viscous Dampers	653
22.2.3	Engineering Applications of Viscous Dampers	654
22.3	Viscous Damping Walls	657
22.4	Cyclic Responses Among Structural Members Made of Elastic, Viscous and Hysteretic (Viscoelastic) Materials	659
22.5	Viscoelastic Damper	661
22.5.1	General	661
22.5.2	Design of Viscoelastic Dampers	663
22.5.3	Engineering Applications of Viscoelastic Dampers	666
22.6	Friction Damper	666
22.6.1	Introduction to Friction Dampers	666
22.6.2	Pall Friction Damper	667
22.6.3	Other Types of Friction Dampers	670
22.6.4	Pros and Cons of Friction Dampers	676
22.6.5	Modeling of Friction Dampers	678
22.6.6	Design of Friction Dampers	678
22.6.7	Engineering Applications of Friction Dampers	681
22.7	Yielding Damper	682
22.7.1	General	682
22.7.2	Types of Yielding Dampers	682
22.7.3	Engineering Applications of Yielding Dampers	690
22.8	Lead Dampers	692
22.9	Shape Memory Alloy Dampers	693
22.10	Comparison of Structural Behavior Among Conventional Structures and Structures with Different Damping Apparatus Installed	696
	References	698
23	Base and Hanging Isolation System	703
23.1	General	703
23.2	Dynamic Analysis of Base Isolation System	705
23.3	Elastomeric Bearings	707
23.3.1	General	707
23.3.2	Simplified Calculation of Rubber Bearings' Properties	711
23.3.3	Compression and Tension Capacity of Rubber Bearings	714

23.3.4	Determination of Damping in Rubber Bearings	714
23.3.5	Design of Elastomeric Bearings	715
23.3.6	Advantages and Drawbacks	717
23.3.7	Engineering Applications	718
23.3.8	Performance of Elastomeric Bearings During Real Earthquake Events	722
23.4	Sliding Isolation Systems	724
23.4.1	General	724
23.4.2	Determination of Basic Properties for Sliding Isolation Systems	726
23.4.3	Design of Sliding Isolation Systems	728
23.4.4	Advantages and Drawbacks of Sliding Isolation Systems	729
23.4.5	Engineering Applications	730
23.5	Testing of Base Isolation System	733
23.6	Selection and System Comparison Among Conventional Design, Base Isolation and Damping Apparatus	734
23.7	Hanging Isolation System	736
	References	738
24	Dynamic Absorber	743
24.1	General	743
24.2	Dynamic Responses Due to the Installation of Dynamic Absorbers	746
24.3	Design Procedure for an Optimized Dynamic Absorber	748
24.4	Practical Considerations for Designing a Dynamic Absorber	750
24.5	Tuned Mass Damper (TMD)	750
24.5.1	General	750
24.5.2	Advantages and Drawbacks of TMDs	753
24.5.3	Engineering Applications	753
24.5.4	Research of TMD Systems	758
24.6	Tuned Liquid Damper (TLD)	759
24.6.1	General	759
24.6.2	Calculation of Structural Response with TSDs Installed	761
24.6.3	Research Progress of TLDs	763
24.6.4	Advantages and Drawbacks of TLDs	767
24.6.5	Engineering Applications of TLDs	769
24.7	Multifrequency Dynamic Absorber	772
24.8	Impact Dampers	774
24.8.1	General	774
24.8.2	Advantages and Drawbacks of Impact Dampers	776
24.8.3	Engineering Applications of Impact Dampers	776
	References	779

25 Load and Energy Sharing Mechanism	783
25.1 General	783
25.2 Connecting to Adjacent Structures	783
25.3 Lock-up and Shock Transmission Unit	785
References	788
26 Resistance of Non-structural Components	789
References	793
27 Structural Health Monitoring and Earthquake Insurance	795
27.1 Introduction	795
27.2 Vibration-Based SHM	797
27.3 Drone Based Structural Inspections	799
27.4 Inspections by Remotely Unmanned Underwater Vehicles	803
27.5 Earthquake Insurance	805
References	806
28 Control Techniques for External Damping Devices	809
28.1 Introduction	809
28.2 Passive Control Devices	809
28.3 Semi-active and Active Control Devices	811
28.4 Hybrid Control Devices	812
References	812
29 Seismic Rehabilitation for Structures	815
29.1 General	815
29.2 Seismic Rehabilitation Measures	815
29.3 Strengthening of Structures	816
29.4 Reinforcement of Structural Members	822
29.4.1 Local Joint Reinforcement for Tubular Structures	822
29.4.2 Sticking Steel Reinforcement	824
29.4.3 Adding Members, Enlarging Cross Sections and Shortening Spans	824
29.4.4 Retrofitting Using Fiber-Reinforced-Polymer (FRP)	826
29.4.5 Load Sequence Effects Due to the Reinforcement	832
29.4.6 External Pre-stressing Using FRP	833
References	835
Appendix	837
Index	839

Chapter 1

Introduction

An earthquake achieves what the law promises but does not in practice maintain—the equality of all men.

Ignazio Silone (1900–1978, Italian author and politician)

1.1 Historical Earthquake Events

No places on Earth are entirely free of the risk of earthquakes. Earthquakes are among the most destructive natural phenomena on the planet, having substantial social and economic consequences. Within 40 s, high amplitude earthquakes can almost completely destroy the infrastructures of a region, leaving people reeling in their wake, in some cases for a period of up to decades later.

The earliest written records of earthquakes date back to 1177 BC in China. However, Chinese legends mention other earthquakes dating back to 2221 BC. Earthquakes in Europe were mentioned in 580 BC, but the earliest record with descriptive information occurred in the mid-sixteenth century. The earliest known earthquakes in America were in Mexico in the late fourteenth century and in Peru in 1471, but their descriptions were not well documented. However, by the seventeenth century, descriptions of the effects of earthquakes were already published worldwide—although they were often exaggerated or distorted [1].

In ancient times, earthquakes were things of myth and legend. They are referred to substantially on seven occasions in the Bible, from Exodus to Tribulations, and are mentioned many more times in biblical times. The End Times are described as “famines and earthquakes in various places” (Matthew 24: 6–8). In some countries such as China, they were also believed to represent the supernatural wrath of God, which meant they could therefore not be resisted by human beings. For example, after the magnitude 8 earthquake of Sanhe-Pinggu (Beijing) that occurred on the 2nd of September 1679, the Qing Emperor Kangxi (Fig. 1.1) issued a bulletin to the public to apologize for his inappropriate conduct of his daily work, and admitted that the earthquake was God’s punishment due to his lack of respect to God and his people. This opinion was actually cherished by the emperors and people of almost every dynasty in China for more than 2000 years, as being a consequence of not respecting and being harmonized with people, nature, and God. In Japan, people cherished the view that large quakes were caused by underground movements of catfish. Therefore, after damaging quakes, they tried to punish catfish in order to avoid future nightmares, as shown in Fig. 1.2. Nowadays, scientists think that



Fig. 1.1 Qing Emperor Kangxi



Fig. 1.2 After the 1855 Ansei earthquake in Tokyo, people punished catfish in order to prevent future earthquakes



Fig. 1.3 “The Last Day of Pompeii” by Karl Briullov, a painting depicting the ruins of the city of Pompeii due to an earthquake and the volcanic eruption of Vesuvius that occurred in AD 79

catfish can sense minute changes in electrical currents generated underground before a quake. This could account for their sudden bursts of activity at the water surface.

Ancient earthquakes caused abundant losses of human lives and damage to infrastructures, with an example shown in Fig. 1.3. It is particularly noteworthy

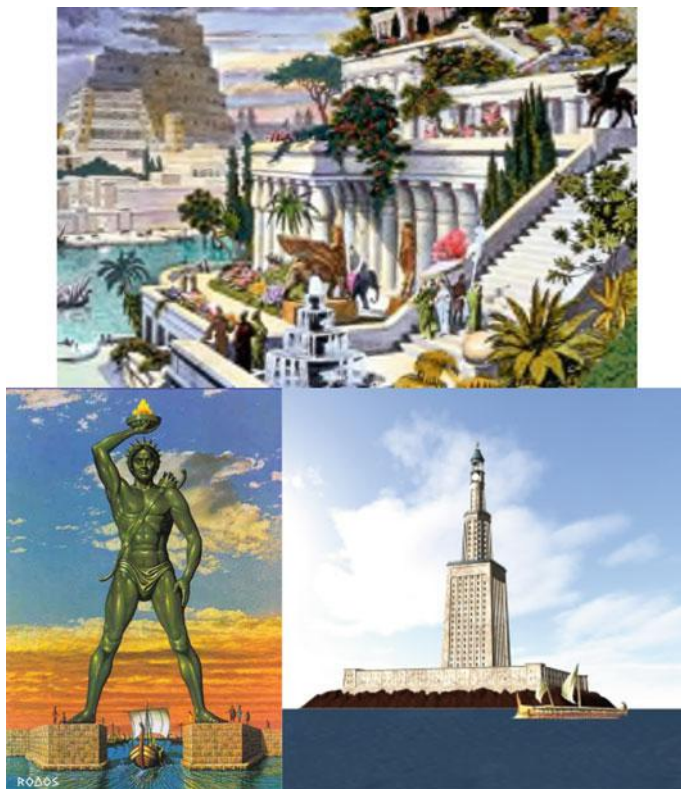


Fig. 1.4 Hanging Gardens of Babylon (*upper*), Colossus of Rhodes (*lower left*), and Lighthouse of Alexandria (*lower right*, painting by Emad Victor Shenouda) among the “Seven Ancient Wonders”

that, among the six collapsed “Seven Ancient Wonders”, three were destroyed by earthquakes: the Hanging Gardens of Babylon (356 BC) in the Middle East, the Colossus of Rhodes (226 BC) in Greece, and the Lighthouse of Alexandria (AD 1303) in Egypt, as shown in Fig. 1.4. In addition, the Mausoleum at Halicarnassus, or Tomb of Mausolus (353 BC) shown in Fig. 1.5 is also thought to have been destroyed by an earthquake. The earthquake causing the highest loss of human lives in history occurred in 1556 AD in Shanxi, China, with a magnitude of 8.0: since this earthquake occurred in a densely populated area, it killed around 830,000 people.



Fig. 1.5 A scaled model of the Tomb of Mausolus (photo by Nevit Dilmen)

1.2 Consequences of Earthquakes

During the last century, earthquakes caused around 1,260,000 fatalities and more than 10 million serious injuries. The most significant earthquakes in terms of loss of lives were the Tangshan earthquake (1976, China) with 300,000 fatalities, the Haiti earthquake (Haiti, 2010, Fig. 1.6) with 92,000 fatalities, and the Wenchuan earthquake (2008, China, Fig. 1.7) with 80,000 fatalities. In addition, the damaging tsunami caused by the sudden uplift of the sea floor due to deep ocean earthquake on 26th of December 2004 also led to a loss of 230,000 lives (Fig. 1.8). In terms of economic losses, the most significant earthquakes were the Sendai earthquake and tsunami (2011, Japan) causing a loss of US\$ 200 billion, followed by the Kobe earthquake (1995, Japan, Figs. 1.9 and 1.10), with US\$ 57–200 billion, the Wenchuan earthquake (2008, China) with US\$ 75 billion, and the Northridge earthquake (1994, USA, Fig. 1.11) with US\$ 44 billion. The direct financial and human losses during a devastating earthquake, as shown in Table 1.1, can cost as much as 40 % of the gross national product (GNP) of a country [2, 3]. The damage of infrastructures may potentially pose a further threat to life and property safety,



Fig. 1.6 Collapse of Haitian national palace during the magnitude 7.0 Haiti earthquake 2010 (photo from Logan Abassi, UNDP Global)

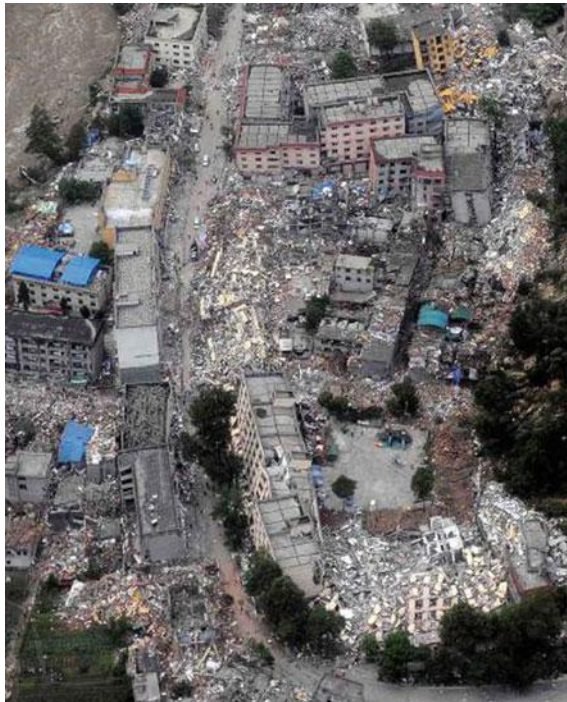


Fig. 1.7 Building collapse during the magnitude 7.9 Wenchuan earthquake of 2008



Fig. 1.8 A village near the coast of Sumatra lies in ruin after the tsunami that struck South East Asia in December 2004 (photo courtesy of US Navy)

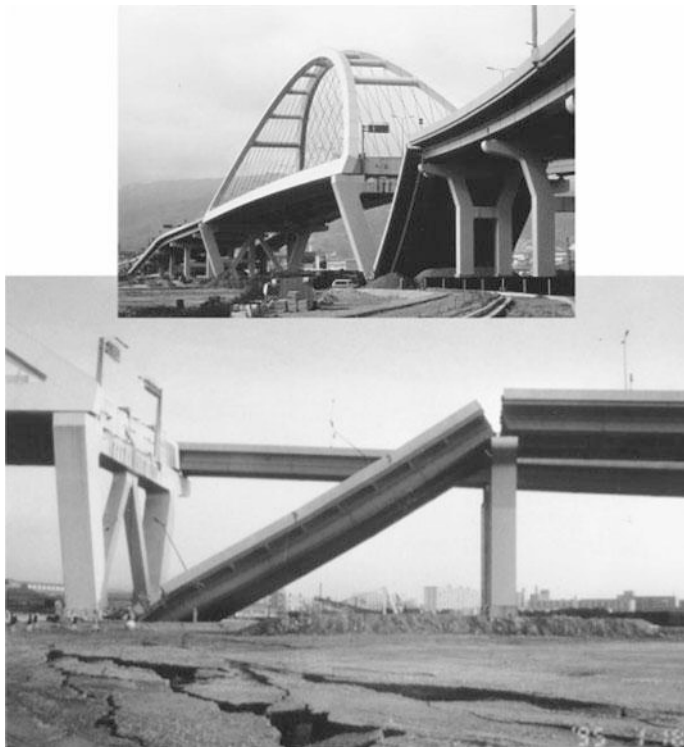


Fig. 1.9 Nishinomiya-ko Bridge approach span collapse during the 1995 magnitude 7.2 Kobe earthquake (photo courtesy of Kobe Collection, EERC Library, University of California, Berkeley)

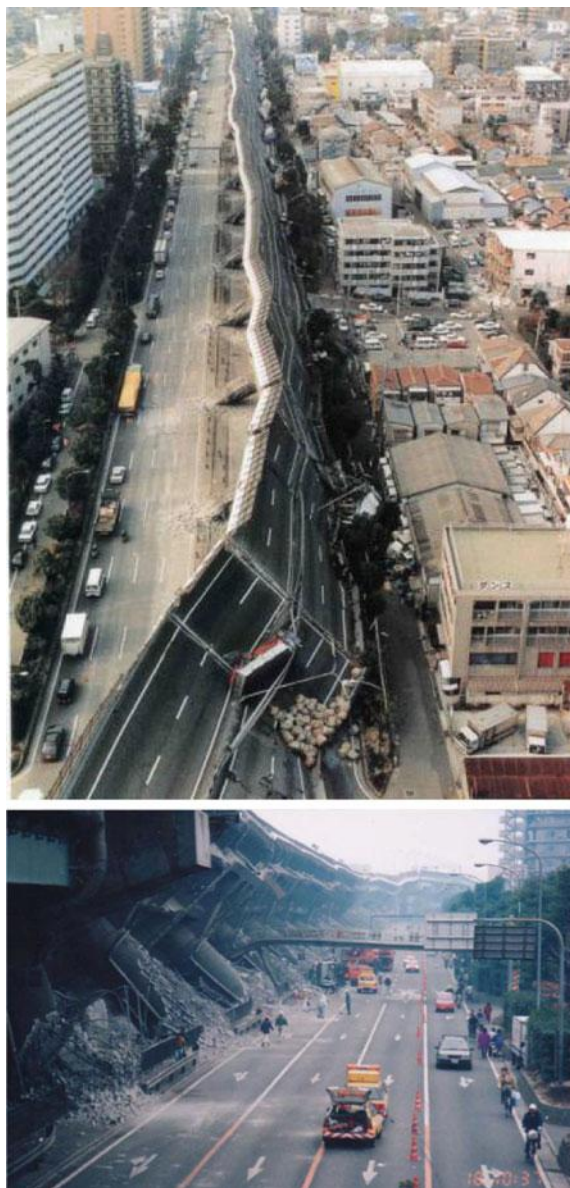


Fig. 1.10 Collapse of elevated 18-span Fukae Viaduct during the 1995 magnitude 7.2 Kobe earthquake [4]. The RC columns, which were 9.9–12.4 m high with diameters of 3.1–3.3 m, were damaged by severe flexural and diagonal cracks that developed around 2–3 m above the footing. This was where one-third of the longitudinal reinforcement bars terminated



Fig. 1.11 Damaged bridge and highways due to the 1994 magnitude 6.7 Northridge earthquake (photo from Robert A. Eplett, FEMA)

Table 1.1 Financial losses of important earthquakes occurring from 1970 to 2011^a

Country	Earthquake location	Year	Loss (\$ billion)	Loss (% GNP)
Nicaragua	Managua	1972	2.0	40.0
Guatemala	Guatemala city	1976	1.1	18.0
Romania	Bucharest	1977	0.8	3.0
Yugoslavia	Montenegro	1979	2.2	10.0
Italy	Campania	1980	45.0	6.8
Mexico	Mexico city	1985	5.0	3.0
Greece	Kalamata	1986	0.8	2.0
EI Salvador	San Salvador	1986	1.5	31.0
USSR	Armenia	1988	17.0	3.0
Iran	Manjil	1990	7.2	7.2
Japan	Kobe	1995	100	~2.0
China	Wenchuan	2008	60	1.8
New Zealand	Canterbury	2010	6	5.3
Haiti	Port-au-Prince	2010	8	121
Chile	Santiago	2010	30	19
New Zealand	Christchurch	2011	15	10
Japan	Sendai	2011	210–300	3.8–5.4

^aThe Great Kanto earthquake, which occurred in 1923 with a fatality of 142,000, was not listed in this table as it occurred before 1970

such as collapse of water dams, as shown in Fig. 1.12. In many devastating earthquakes, not only does massive structural and foundation damage occur, but non-structural and fire damages also contribute to financial losses, and losses of

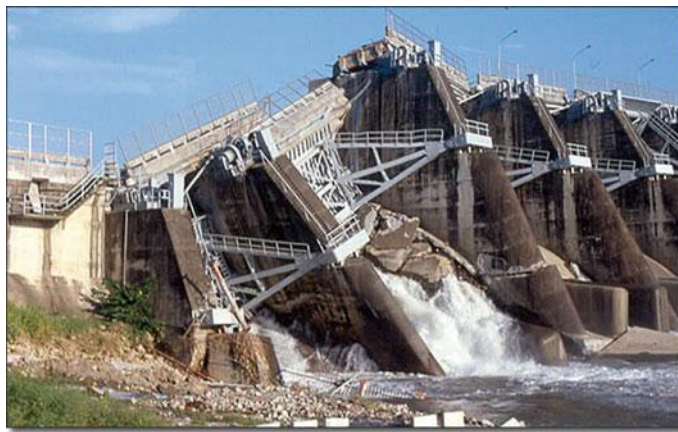


Fig. 1.12 Total collapse of a dam after the 1999 magnitude 7.3 Taiwan 921 earthquake (courtesy of Washington State Department of Ecology)



Fig. 1.13 Fire spread in the urban area immediately after the 1995 magnitude 7.2 Kobe earthquake [4]

human life. For example, due to broken electrical lines and gas mains during the Kobe earthquake (1995), more than 7000 houses and buildings were destroyed by fire (Fig. 1.13). The extent of fire damage was almost proportional to the amount of infrastructural damage [4].

The earthquakes also apply disturbances on soils, causing changes in ground-water flows and damage to water well systems, which in turn can cause abrupt changes in the level of the water table and a sudden drying up of surface springs [5]. For example, during the magnitude 5.8 Virginia earthquake that occurred on 23

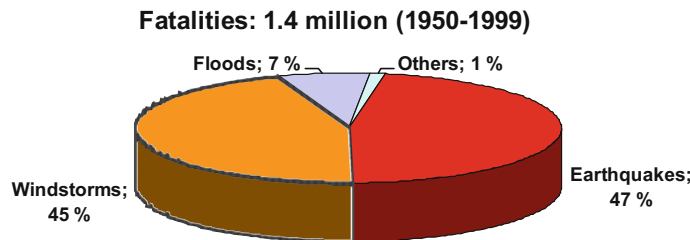


Fig. 1.14 Distribution of fatalities for different types of natural hazards

Fig. 1.15 Distribution of economic losses for different types of natural hazards

Economic losses: US\$ 960 billions (1950-1999)

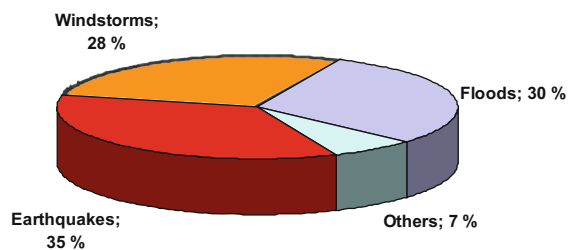


Table 1.2 Global occurrence of earthquakes (data from USGS)

Size	Magnitude	Annual average number
Great	>8.0	1
Major	7.0–7.9	15
Strong	6.0–6.9	134
Moderate	5.0–5.9	1319
Light	4.0–4.9	13,000 (estimated)
Minor	3.0–3.9	130,000 (estimated)
Rather minor	2.0–2.9	1,300,000 (estimated)

August, 2011, the maximum recorded water level change was around 0.6 m in a well in Pennsylvania.

From 1950 to 1999, among all natural disasters, 234 are categorized as great natural catastrophes. Based on the survey of those 234 great natural catastrophes [6], Figs. 1.14 and 1.15 show the distributions of consequence for different types of natural hazards. Earthquakes are apparently the most important natural hazards in terms of both fatalities and economic losses, followed by windstorms and floods.

Table 1.2 lists the number of annual earthquake occurrences globally based on their size. Among them, more than 100,000 earthquakes that can be felt by people occurred world-wide [7]. It is estimated that about 800 earthquakes occur per year, with destructive effects if they take place in a populated area. Fortunately, the majority of these destructive earthquakes were centered in unpopulated regions or

in oceans. Moreover, mainly due to the fact that more and more seismographs are being installed, statistically, the number of earthquakes occurring annually worldwide has an increasing trend. However, the number of large earthquakes (magnitude 6.0 and greater) has remained relatively constant.

As 2/3 of the Earth's crust is seismically active and the majority of world large cities are located in earthquake prone areas, today, more than 1 billion people still live under a significant risk to their lives and property due to earthquakes and their unpredictability. Rather than a problem unique to specific countries, the earthquakes are a global phenomenon that poses great threat to many people in many parts of the world [8]. Moreover, with the rapid urbanization especially in developing countries, an increasing number of people and an increasing value of infrastructures, more facilities are and will be located in an earthquake prone area. This implies an even higher importance to understand the earthquake hazard and to take proper mitigation measures. However, as a study of seismic losses (economic and fatalities) in recent decades, as shown in Fig. 1.16, makes clear, the mitigation measures to reduce seismic risk need to differ between developing and developed countries. For developing countries, fatalities are much more significant than economic losses, while for developed countries, the opposite trend can be identified. An example of this is the 1995 Kobe earthquake, which killed 5420 people while causing an economic loss of 100 billion US\$. Therefore, the seismic problems in developed countries are related to an increase in urban system and population, whereas in developing countries the main source of increasing seismic risk can be attributed to the overcrowding of cities with non-engineered buildings, inadequate infrastructures and services, together with environmental degradation [9].

Figure 1.17 shows seismic vulnerability and losses considering both physical and socio-economic aspects in a risk analysis. Note that the risk is determined by both probabilities of occurrence for a specific hazard and the associated

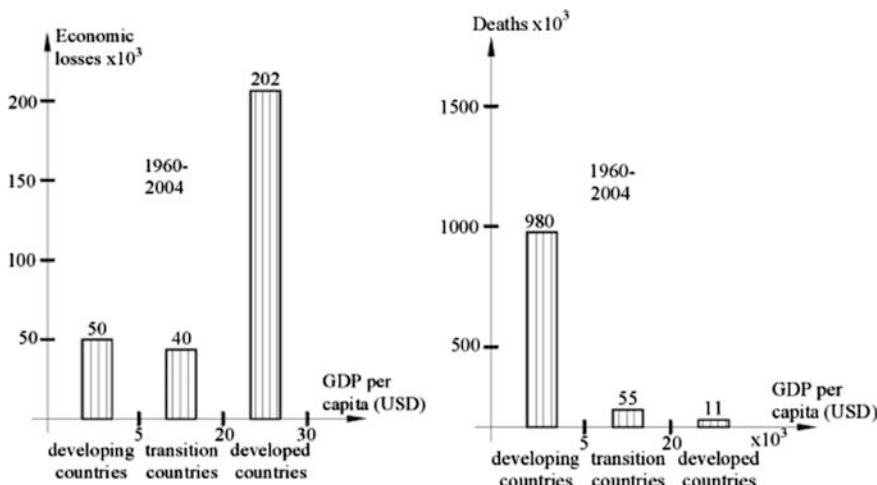


Fig. 1.16 Seismic losses in economic terms (*left*) and fatalities (*right*) versus GDP per capita [9]

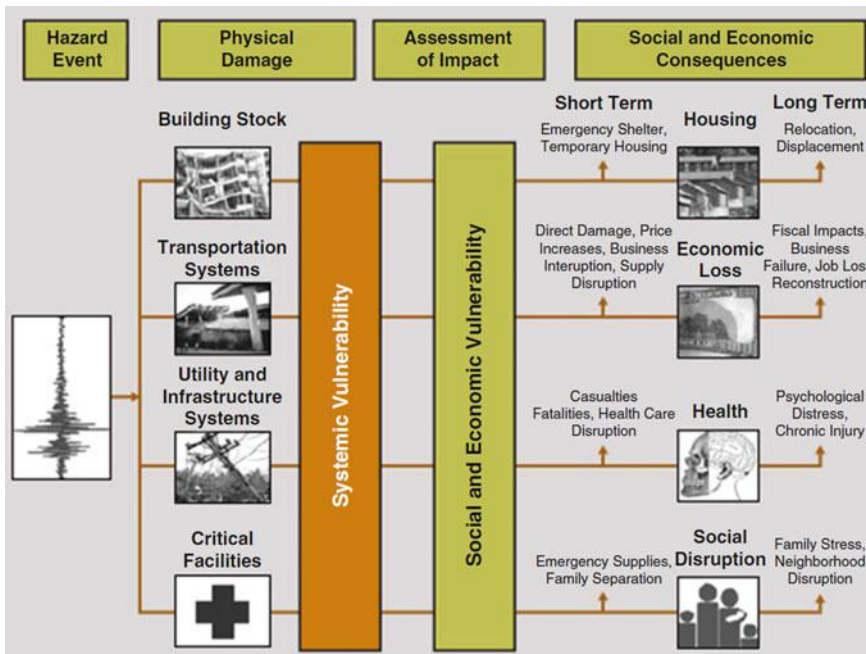


Fig. 1.17 Seismic vulnerability and losses in both physical and socio-economic aspects (courtesy of European Collaborative Research Project SYNER-G: <http://www.vce.at/SYNER-G/files/project/proj-overview.html>)

consequence (exposed value and vulnerability of an infrastructure), and it relates not only to loss of life and injury, but also to the damage to properties and losses associated with damage repair and business interruptions. Even if the hazard at a given site can normally not be changed, the seismic risk can be continuously increasing due to the added value of infrastructures and increased costs of business interruptions. Examples of this are offshore platforms with significant upgrading or newly installed high value equipment; or an existing building being enlarged or upgraded with more functions and facilities. Furthermore, different from an extreme storm causing strong wind and wave load on structures, a damaging earthquake cannot be predicted in advance, as will be discussed in Sect. 1.8. Therefore, mitigation measures for avoiding earthquake induced damages can only be taken without any assumption of evacuation and preparation in advance with forecasted data. In addition, it is common sense that risk due to earthquake is only concentrated in areas of high seismicity. However, due to the lack of preventative measures in low seismicity regions, the structures designed for low seismicity regions may be even more vulnerable than those for a high seismicity region, especially for structures that are improperly designed. And this may finally lead to a high risk for some infrastructures in low seismicity regions [10]. Figure 1.18 shows the collapse of a wheat silo that occurred during a minor earthquake in a rather low seismicity

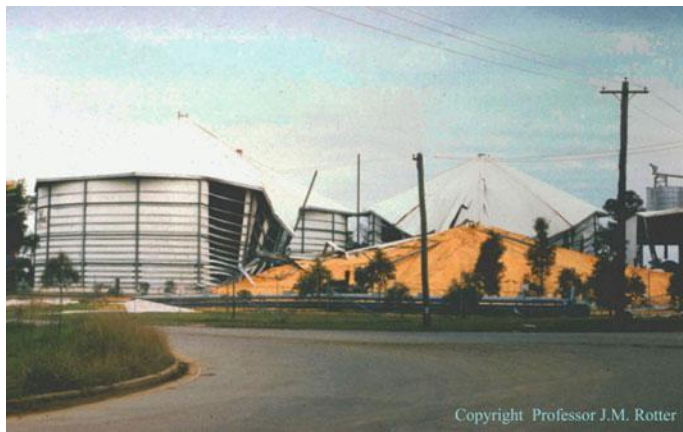


Fig. 1.18 Collapse of a wheat silo in Australia (courtesy of John Michael Rotter, University of Edinburgh)

area west of the city of Sydney, Australia. A forensic investigation indicates that the most likely cause of this accident is that the minor earthquake triggered the top part of the silo content (wheat) to impact the upper wall of the silo, which finally resulted in the loss of the silo's integrity.

In addition to the damage due to earthquakes, earthquake induced tsunamis also directly caused extensive damage on coastal structures, in the form of structural and non-structural damage, foundation damage, underwater and shoreline landslides etc. Along with the huge loss of life and property, complete ecosystems have been stripped away in low lying areas such that restoration and re-establishment of livelihoods can take decades to achieve [11].

In contrast to tsunamis that are giant sea waves created by the sudden uplift of the sea floor, during a strong earthquake, the seismic wave can also excite waters in an enclosed body of water (such as swimming pools, lakes, reservoirs, ponds etc.) or semi-enclosed sea, causing the water to slosh back and forth from one end to the other [12], known as seiches, as shown in Fig. 1.19. On occasion, seiches can also be induced by tsunamis as a result of local geographic peculiarities, meaning that tsunami damage is often worse in harbors and bays than it is along straight coastlines. For instance, the tsunami that hit Hawaii in 1946 had a 15-min interval between wave fronts. The natural resonant period of Hilo Bay is about 30 min, indicating that every second wave was in phase with the motion of water in Hilo Bay, thus creating a seiche in the bay. As a result, Hilo suffered worse damage than any other place in Hawaii, with the tsunami/seiche reaching a height of around 11 m along the Hilo Bayfront, causing a loss of 96 lives in the city alone and extensive damage of infrastructures in the area, as shown in Fig. 1.19. It is worthy of mention that seiche waves may continue for several days after a tsunami. The period of this back and forth oscillation strongly depends on the geometry of the enclosed lake and semi-enclosed sea (Fig. 1.20).

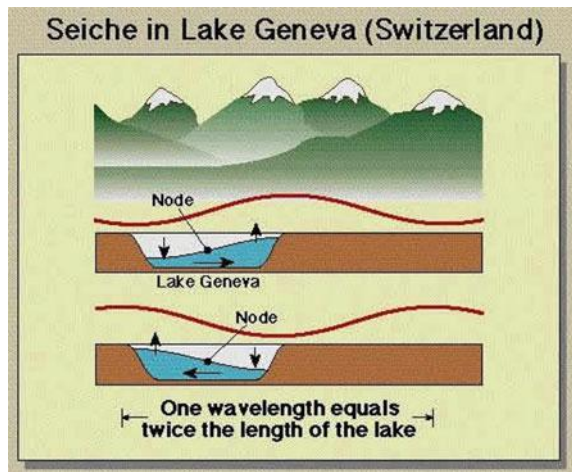


Fig. 1.19 Illustration of seiche in Lake Geneva (courtesy of Brennan, Geneseo State University of New York)



Fig. 1.20 Damaging wave due to seiche in Hilo Harbor, Hawaii induced by tsunami on 1 April 1946 (courtesy of National Oceanic and Atmospheric Administration)

Earthquakes not only cause economic losses and loss of human life, but also have serious psychological effects on people who are experiencing them and affected by them. Fear and helplessness are the most common emotional reactions. In the first few days after a major earthquake, the affected communities will focus on rescuing those who have been trapped under rubble, caring for injured, assessing the extent of the damage, and planning the management of the problems caused by the earthquake. The regular activities of the affected communities may be greatly



Fig. 1.21 The destruction in Yokohama during the magnitude 7.9 great Kanto earthquake of 1923 (courtesy of Yokohama City Central Library)

disordered, fearful anticipation of further earthquake is prevalent, acute stress disorder and depression are common. Ongoing aftershocks may cause additional traumatic stress. In the year that follows a major earthquake, survivors face the difficult tasks related to bereavement, injury, material loss, homelessness, disruption of activities, relocation and other related stressors [13]. The psychological effects can also cause relevant social disorders, which can sometimes even contribute to wars. For example, after the Great Kanto earthquake in 1923 (Fig. 1.21) which killed 142,000 people, a pernicious rumor was dispersed among panic-stricken survivors: Koreans were taking advantage of disasters, committing arson and robbery, and were in possession of bombs. This caused mass murder of Koreans by brutal mobs in Tokyo and Yokohama. The Great Kanto earthquake together with the worldwide depression from 1929 led to Japan's economic depression, which was believed by many historians to be an essential reason for the expansion of Japanese military force and its subsequent deployment during the Second World War. Another example is that within 3 months of the Sendai earthquake on 11 March 2011, the number of suicide activities in Japan increased dramatically over the previous months, an occurrence that is believed to be linked to the Sendai earthquake disaster.

There are thus far no recorded structural or non-structural damages on offshore structures, primarily because few platforms and other types of offshore infrastructures have been exposed to significant earthquakes. However, offshore oil and gas activities are also being carried out in areas with high seismic activities such as China, California, Alaska, the Caspian Sea, Japan, Peru and Russia etc. It is clear that in those areas, earthquakes pose a serious threat to offshore structures' integrity, oil production, equipment and above all the safety of the people working on the



Fig. 1.22 The Sakhalin LUN-A GBS structure located off Sakhalin Island—an area with high seismicity (courtesy of Aker Solutions)

platforms and other offshore structures. Figure 1.22 shows the installation of Sakhalin LUN-A Gravity Based Structure (GBS) located at an area with significant seismicity, which is an important part of the Sakhalin II project, the world's largest offshore engineering project to date. Furthermore, even if some platforms have experienced a major earthquake, this does not mean that those platforms are "earthquake proof": another earthquake might produce significantly higher levels of shaking on the platforms [14].

However, earthquake damage to subsea pipelines, equipment and communication cables have been reported during, for example, the 1964 Alaska earthquake, 1971 San Fernando earthquake, 1995 Kobe earthquake, 2003 Algeria earthquake, 2011 Sendai earthquake, etc. This caused significant financial loss, including secondary losses resulting in service interruption, fires, explosions, and environmental contamination [15].

In addition, sudden subsidence of offshore platforms, which can be induced or triggered by minor earthquakes or offshore activities, is more and more being realized to be a serious threat to the integrity of offshore infrastructures, and may also have substantial consequences regarding reservoir safety. One example of sudden subsidence is the one that occurred in the vicinity of the Ekofisk oilfield (Fig. 1.23) in the North Sea, on 7 May 2001, which led to an immediate drop of the platforms by 80 mm.

The elaboration above of historical earthquakes and their consequences provides a clue as to how we can take proper mitigation measures for the future. However, they do not provide iron laws as to what exactly we must see and do for the future [16]. For example, some characteristics of ground motions recorded during the Mexico Michoacan earthquake (1985) and Kobe earthquake (1995) cannot be explained by the past knowledge of earthquake engineers. In this respect, our creativity, judgement and even intuition are vital, and they are essential during the development of modern earthquake engineering.



Fig. 1.23 Platforms at Ekofisk oilfield in the North Sea, where sudden subsidence occurred on 7 May 2001 (courtesy of Aker Solutions)

1.3 Benefits of Earthquakes

Despite the devastating impact of earthquakes, some side benefits coexist. However, they cannot match up to the destructive effects of earthquakes.

The seismograph picture recorded during earthquakes can help scientists to learn about the interior of the earth. The measurements of seismic wave velocity can be used to compute the mechanical properties of rocks, and this also gives information about the fracture system underground. It has been proven to be helpful for designing programs to drill oil and gas wells, and for providing essential geotechnical data to design dams, foundations and many other large construction projects. By measuring period of Earth's local motions and free oscillation of a global scale due to a strong earthquake, it is possible to obtain essential information regarding the characteristics of the deep internal structure of the Earth. Some earthquakes can even elevate old land to the soil surface for scientists to study.

Earthquakes can form new landmarks, which can be used by human beings for construction or scenery purposes [17].

In addition, earthquakes can also loosen the soil, allowing nutrients and minerals to be deposited evenly, creating a more fertile soil.

An important area relevant to earthquakes and crust activities is the utilization of geothermal energy stored in the Earth's crust, which originates from the original formation of the planet and from radioactive decay of materials. It has a great potential as a clean and renewable energy source. Today, geothermal energy is mainly extracted from shallow geothermal resources with a total capacity of 11.4 GW and electricity generated from geothermal energy is around 80 TWh per year. For example, 25 % of the total electricity demand in Iceland, which is a high seismicity country, is provided by geothermal power. Figure 1.24 shows a geothermal power plant in Iceland. However, the really significant potential of



Fig. 1.24 Steam rising from the Nesjavellir Geothermal Power Station in Iceland

geothermal energy is in the deeper crust at depths between 3 and 5 km where temperatures are 100 °C or higher. Extracting this energy is, however, at present only operational in experimental facilities and presents significant research and application challenges [18].

Unlike earthquakes, volcanoes can form new, fertile soils. Under the right conditions, the internal heat associated with young volcanic systems will be harnessed to produce geothermal energy. Abundant metallic mineral deposits in the world are associated with hydrothermal activity near volcanoes. People also use volcanic products as building materials, as abrasive and cleaning agents, and as raw materials for many chemical and industrial uses. It is now widely recognized by scientists that the short term hazards posed by volcanoes are balanced by benefits of volcanism and related processes over geologic time [19].

1.4 Causes of Earthquakes

There are four types of earthquake categories, distinguished by their causes:

- Tectonic-related earthquakes
- Volcano-induced earthquakes
- Human induced/triggered earthquakes
- Ice induced earthquakes

Among these, tectonic-related earthquakes cause the most significant damage to human lives and properties.

1.4.1 Tectonic-Related Earthquakes and the Elastic Rebound Theory

In 1912 Alfred Wegener proposed that a large super-continent Pangaea (meaning “all lands” in Greek) was split into smaller fragments about 225–200 million years ago. These then drifted apart to form the present arrangement of continents, and the entire process of the continental drift is illustrated in Fig. 1.25. He gave as the simple

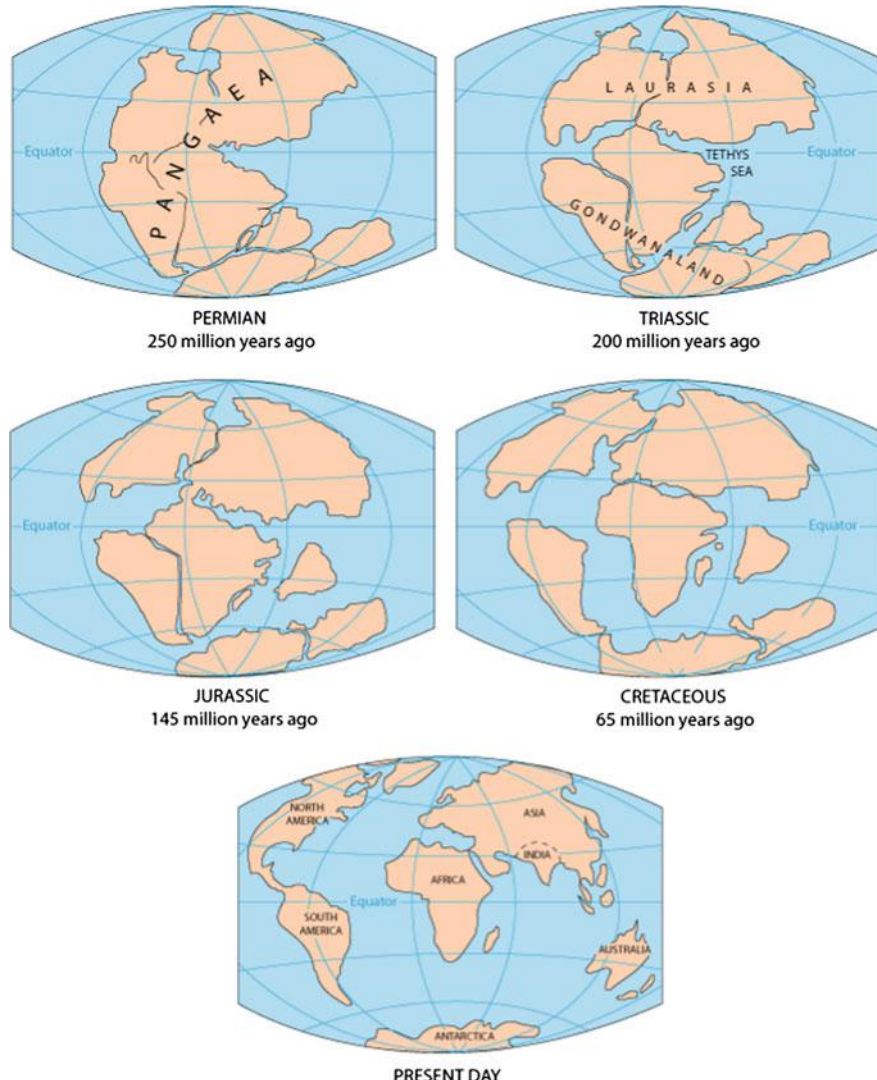


Fig. 1.25 Process of continental drift during the past 225–200 years (courtesy of USGS)

mechanism for this drifting the less dense continents floating and drifting over denser oceanic crust, like icebergs in the ocean. At the time this theory was subject to great skepticism by the majority of geologists, as Wegener failed to provide a convincing physical explanation of plate drift. But the paleomagnetic evidence found later on appeared to strongly support Wegener theory of continental drift.

Based on the theory of continental drift and extensive geological research later on, it is now widely accepted that over tens of millions of years of Earth's evolution, the surface of the lithosphere (a rigid 10–150 km thick plate composed of crust and upper mantle) ruptured into a number of pieces called tectonic plates as shown in Fig. 1.26, which shows that the Earth's crust is divided into seven continental sized plates (Asian, Eurasian, African, American, Antarctic, Australia-Indian, and Pacific) and eight sub-continental (secondary) sized tectonic plates (e.g., Nazca, Philippine, Cocos, Arabian, Caribbean, etc.), plus dozens of tertiary microplates. These tectonic plates are themselves relatively rigid, relatively cool slabs that form the crust and upper mantle of the Earth with a thickness of up to 250 km. They move relative to one another at a speed of between 2 and 10 cm/year. However, when the tectonic plates move against and collide with each other, the lithosphere buckles, warps, and is torn apart. This sudden slip (namely elastic rebound) disrupts the balance and position of the tectonic plates and induces a sudden release of energy arising from the stresses built up during the deformation processes of the Earth's crust, finally causing the Earth's surface to shake with noticeable magnitude and tremendous force. This is when an earthquake occurs. Due to the stress redistribution of the fault, a major earthquake may also trigger

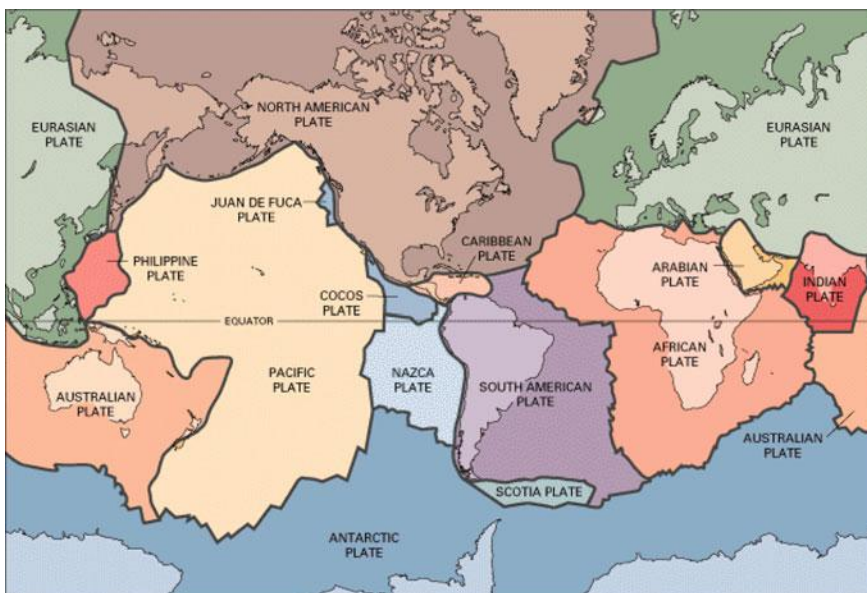


Fig. 1.26 The division of tectonic plates, with the so-called “Ring of Fire” (courtesy of USGS)

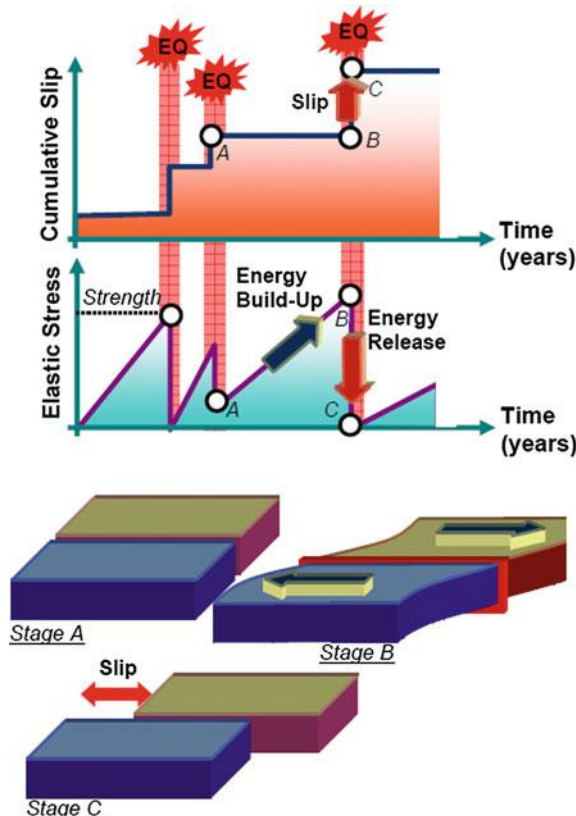


Fig. 1.27 The process of strain build-up and release as described by the elastic bound theory [22]

local aftershocks within days, but this stress redistribution is rather local and limited to distances from the epicenter no more than two or three times the length ruptured by the primary earthquake. Therefore, it is widely accepted that even megaquakes cannot trigger large quakes more than a couple of 1000 km away [20], even though recent research shows that they may trigger smaller earthquakes at a remote distance where the faults are critically stressed, as will be discussed in Sect. 1.4.3. After an earthquake, the strain begins to build again at the modified tectonic plate interface as illustrated in Fig. 1.27. Since the deformation of the plates occurs predominantly at the boundaries between the plates, most earthquakes occur on the boundaries of the tectonic plates as shown in Fig. 1.28, which also provides a strong support for the theory of plate tectonics. The process described above is the idea of elastic rebound theory, which was first presented by Reid [21] by studying the displacement of the ground surface around the San Andreas Fault following the San Francisco earthquake of 1906. Today, the theory still represents state-of-the-art of all studies of fault rupture. According to this theory, two major earthquakes associated with the rupture of a portion of a fault will have a certain time interval

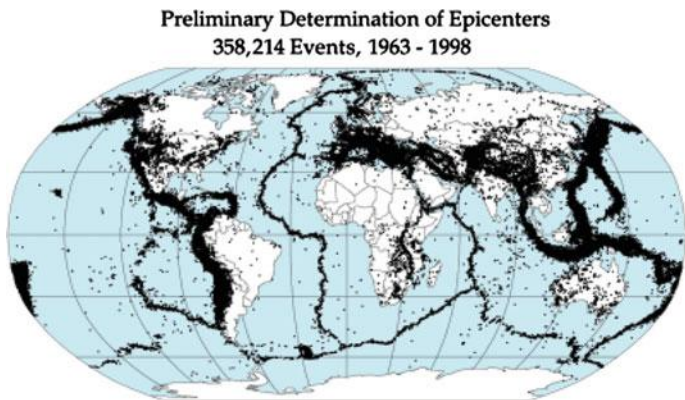


Fig. 1.28 The distribution of epicenters of 358,214 earthquake events (courtesy of NASA)

for the stress on that fault to build up again and cause an earthquake, which is referred to as the seismic gap. This hypothesis has been partially proved by scientist by identifying the time gap between two subsequent earthquakes associated with the rupture of the same portion of a fault. For example, the 1989 Loma Prieta earthquake with a moment magnitude of 6.9 occurred associated with a portion of the San Andreas Fault has been identified as a seismic gap. And it is also widely accepted that the larger the magnitude of an earthquake, the larger is its recurrence interval (time between earthquakes) and the greater the amount of fault movement that will occur during the earthquake. However, the research to study the seismic gap has only been carried out for a few well-studied fault zones such as the San Andreas Fault. By contrast, little is known about recurrence intervals or strain rates for many areas where large intraplate earthquakes (earthquakes within tectonic plates) have occurred. Moreover, the rates of strain build-up could change over time, which would also modify the recurrence intervals. In addition, strain is sometimes distributed along several parallel faults, making it more difficult to ascertain how much strain has built up on any particular fault segment [22].

It is well accepted that under the influence of global warming, the level of the oceans will in general increase. Interestingly, a hypothesis based on the continental drift theory but currently much debated is that, based on the theory of the continents drifting and sea floor spreading (Sect. 1.6), the speed of tectonic plate drift will increase with the elevated sea levels, causing stronger tectonic plate collisions that will ultimately lead to more frequent earthquake occurrence and volcanic activities.

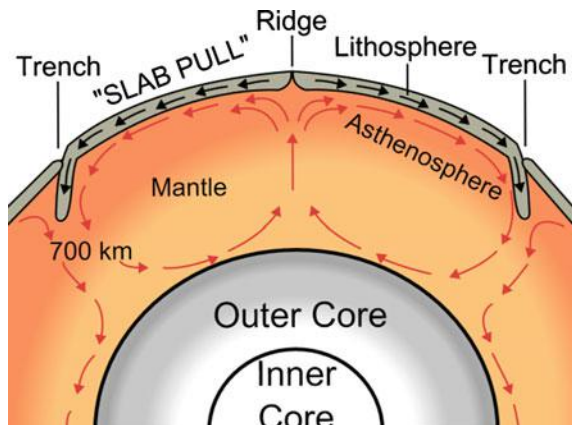
The theory of plate tectonics and the elastic rebound theory help to explain the location and mechanism of earthquake occurrences. When a fault has formed at a plate boundary, the shearing resistance for the continued movement of the fault is less than the shearing resistance required to fracture new intact rock [23]. This indicates that the faults at the boundaries that have generated earthquakes in the past are likely to produce future earthquakes. This paves the way for the development of seismic hazard analysis, as will be introduced in a later chapter.

Many people misunderstand the fault rupture mechanism and believe that, since the pressure developed at tectonic plate edges (Fig. 1.26) and the stress on a fault will be released by earthquakes, such that frequent small magnitude earthquakes can avoid the occurrence of a major one, this also forms one of the motivations of human engineered earthquakes, as will be described in Sect. 1.7. In fact, the energy released by low magnitude earthquakes is almost negligible compare to a major earthquake. Therefore, small quakes can only sometimes be precursors or “foreshocks” (small earthquakes before a major earthquake) to a major earthquake, rather than a mitigator of a major earthquake.

Readers may notice that the presentation of causes of the tectonic-related earthquake above only describes the characteristics of plate movement without explaining what causes the movement of the plates, i.e. it is a kinematic theory rather than a dynamic theory. There is still no confirmative conclusion regarding the sources driving the plate movement, while the most widely accepted one links the plate movement with convection between the upper cooler and lower warmer mantle (semi-molten rock), which is the slow creeping motion of Earth’s solid silicate mantle caused by convection currents carrying heat from the interior of the Earth to the surface. As the cooler material (denser) sinks and warmer (light) material rises, as shown in Fig. 1.29, shear stress is induced at the bottom of the crust plates, leading to the relative movement between plates. Typical mantle convection speed is 20 mm/year near the crust but can vary significantly.

To understand the mechanism of the tectonic-related earthquakes, it is necessary to obtain physical properties and seismological stress conditions (such as dynamic friction) of the target fault zones (Sect. 1.5). This may require a direct access to the fault zone by drilling. For example, a recent project for performing such a task is the Japan Trench Fast Drilling Project (JFAST), which is to determine the fault zone mechanism of the 2011 Sendai earthquake. The target drilling sites were located about 1000 m below the seafloor at a water depth of 7000 m.

Fig. 1.29 The convection of mantle (courtesy of USGS)



1.4.2 Volcanic Earthquakes

The eruption of volcanoes, as shown in Figs. 1.30, 1.31 and 1.32, not only directly send pumice, ash and poisonous gases into the air, spew lava that races down mountainsides and destroy nearly everything in their path, but may also lead to a disturbance of the tectonic plates, causing earthquakes, which are typically much



Fig. 1.30 The explosive eruption of Mount St. Helens, on 21 March 1982, sent pumice and ash 15 km into the air and resulted in a lahar (the *dark deposit* on the snow) flowing from the crater into the valley (courtesy of USGS)



Fig. 1.31 The eruption of Iceland's most active Volcano Grímsvötn, in May 2011, sent pumice and ash 20 km into the air (courtesy of NASA Goddard Space Flight Center)



Fig. 1.32 The eruption of Etna, Italy, 12 May 2011 (photo courtesy of CRI online)

smaller than earthquakes caused by non-volcanic sources. Two types of volcanically generated earthquakes are volcano-tectonic earthquakes and long period earthquakes. An example of this volcanoes induced earthquakes is the one induced by the volcanic eruption of Vesuvius that occurred in AD 79, as shown in Fig. 1.3, with a death toll of at least 1250 based on the number of dead bodies found in excavations of Pompeii. The largest known volcano in the world is the Tamu Massif, located in a remote part of the north-western Pacific Ocean 1600 km east of Japan. Because the summit of Tamu Massif (Fig. 1.33) is at a depth of more than 2000 m below sea level, the remote location and great depth made it very difficult to collect information about this volcano. The base of the Tamu Massif extends to a depth of about 6.4 km, with a height of 4460 m. Interestingly, for decades, researchers knew more about the large volcanoes on Mars than they did about Tamu Massif—until 5 September 2013, when geologists confirmed it was a single volcano, which, if corroborated, would make Tamu Massif the largest known volcano on Earth.

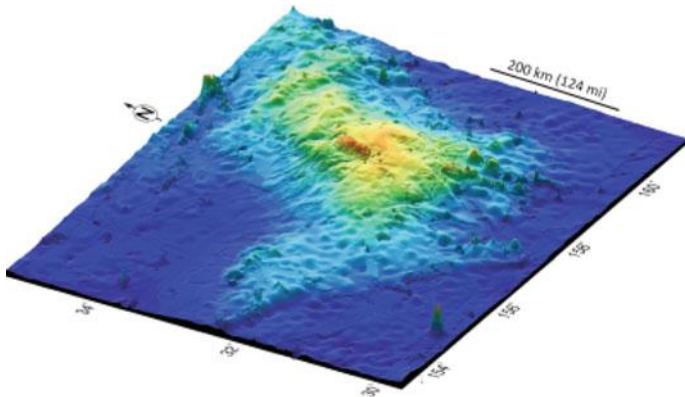


Fig. 1.33 A 3D map of Tamu Massif submarine volcano, the largest known volcano on Earth (courtesy of IODP)

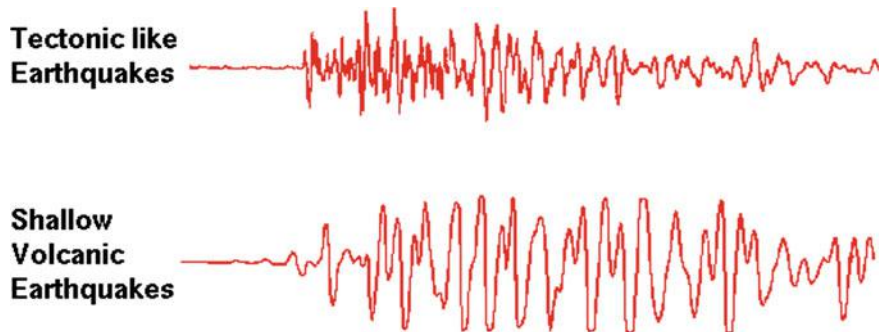


Fig. 1.34 Record of ground motions for tectonic like earthquakes and shallow volcanic earthquakes recorded at Mount St. Helens (courtesy of USGS)

Earthquakes and volcanic activities are interactive. From a satellite-derived heat flux inventory for global volcanism between 2000 and 2006, researchers [24] showed that 37 volcanic responses were related to regional earthquakes. For example, in the Cook Inlet region of Alaska, a magnitude 7.1 earthquake occurred on 31 December 1901, which was generated by a volcanic eruption that also caused several tsunamis. Whether a volcano responds or not depends on earthquake magnitude, distance to the epicenter (point on the Earth's surface directly above the focus, which is the point where an earthquake originates), and orientation of the earthquake focal mechanism in respect to the volcano. Under certain circumstances, a significant earthquake can also trigger subsequent volcanic eruptions over a wide range of distances and times [25]. For example, on 29 November 1975, an eruption at the summit of Kilauea in Hawaii began half hour after the magnitude 7.5 Kalapana earthquake that occurred beneath the south flank of the volcano. Similarly, the Cordon Caulle volcano in central Chile erupted 2 days after the great earthquake, with a moment magnitude of 9.5 on 22 May 1960 off the coast of Chile [25].

Apart from the relatively low levels of energy released during a volcanic earthquake compared to those of a significant tectonic-related earthquake, the frequency content of measured seismic motions during the two types of earthquakes is also different. Figure 1.34 shows typical real-time seismic motions recorded at Mount St. Helens, including both tectonic-related and volcanic earthquakes. By observing this figure, it can be seen that tectonic deep earthquakes (and those located away from volcanoes) produce high frequency seismic motions with sharp arrivals, while shallow volcanic earthquakes (located less than 3 km under the dome) produce medium to low frequency seismic arrivals.

1.4.3 Human Induced/Triggered Earthquakes

Human beings are quite capable of generating disasters, and these show signs of becoming bigger and more deadly as the scale of technology increases [11]. For

example, extensive exploration, such as constructing a large water reservoir, mining, extraction of fossil fuels, disposal of hydraulic fracturing waste, or blasting rocks etc., can all lead to small or medium-sized earthquake events.

Among them, the most common human induced or triggered earthquakes are due to the filling of a water reservoir. Water reservoirs are often built in valleys, below which active erosion of faults has often occurred in history. Extra water pore pressure, which is created in the micro-cracks and fissures in the ground under and near a reservoir, can act to lubricate the faults that are already under tectonic strain, thus decreasing the effective strength of the rock. In addition, the weight of water blocked by the reservoir also has the trend of changing the stress in the faults. If the area is already under considerable tectonic stress, both mechanisms can trigger earthquakes. The energy released in a reservoir triggered earthquake is normally the tectonic strain energy that has been prematurely released because of the reservoir. Therefore, reservoirs can increase the frequency of earthquakes in areas of high seismic activity, and can cause earthquakes to occur in areas that were thought to be seismically inactive. They normally occur immediately on or a few years after the filling of the reservoir. Figure 1.35 shows the correlation between number of earthquake events per 10 days and reservoir water depth for the rock and earth filled Nurek dam, which is the largest reservoir in Tajikistan, at 315 m high and 70 km long. It is obvious that earthquakes occur more frequently when or immediately after the variation rate of water level increases in the reservoir. In addition, researchers also reported that the number of earthquakes increased when the maximum water level was reached and for the duration for which high levels were maintained [26, 27]. Reservoir triggered earthquakes normally occur in the form of shallow depth earthquakes within a few kilometers of the ground. Globally, there are more than 100 identified sites of earthquakes triggered by the filling of water reservoirs, causing the loss of more than 200 lives, 1500 injuries, and the homelessness of thousands. Examples of these are the magnitude 6.2 Xinfengjiang earthquake that occurred in 1962 in China, and the magnitude 6.3 Koyna earthquake that occurred in 1967 in India. Within 10 years of the construction of the Hoover Dam in Nevada blocking the Colorado River to produce Lake Mead, over 600 earthquakes occurred, which include one magnitude 5 and two magnitude 4 earthquakes [28]. More and more scientists [29–31] are increasingly considering the

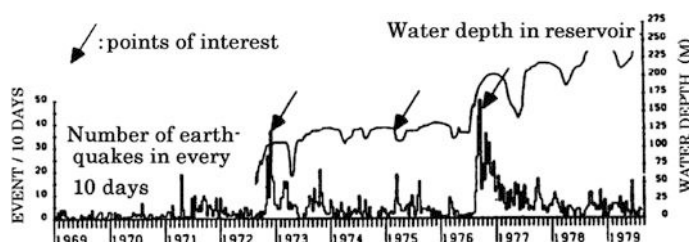


Fig. 1.35 Relationship between the number of earthquakes every 10 days and reservoir water depth at Nurek dam [32]

possibility that the magnitude 7.9 Wenchuan earthquake that occurred in 2008 in China, which left 80,000 dead, could also have been triggered by the Zipingpu Dam (Fig. 1.36), which was filled to a weight of 315 million metric tons of water in 2004 and is just 500 m from the fault that failed during the Wenchuan earthquake and 5.5 km from the quake's epicenter. As aforementioned, one of the most dangerous times, in respect of dam triggered earthquakes, is when the water level is dramatically falling, which was exactly what happened at the dam one week before the Wenchuan earthquake. Note that the construction of a water reservoir may increase the likelihood of larger earthquakes in the surrounding regions. The earthquake resistance of infrastructures built before or even after the construction of the reservoir normally cannot account for this increased earthquake likelihood, which can pose an elevated risk in the affected region.

Deep well injection is also an important cause of earthquakes. It generally weakens the strength of a fault by pressurizing the fluid in the fault, thus reducing its friction resistance and the fault blocks slip, leading to seismic events. Other processes involved in the triggering of seismic activity may include a transfer of stress to a weaker fault, hydraulic fracture, contraction of rocks due to the extraction of fluids, subsidence due to the saturation of a rock formation, mineral precipitation along a fault, and density-driven stress loading [33]. The process of well injection triggered seismic activity is illustrated in Fig. 1.37. The first seismic activity believed to be caused by well injection is near Denver, Colorado in 1962, which was originally a seismic quiet area while was injected with toxic waste into hazardous waste disposal wells. The focal depths of the relevant earthquakes ranged between 4 and 8 km, just below the 3.8 km deep wells [28]. A more recent well-known accident is the Castor Project, which aimed to store gas in a depleted



Fig. 1.36 Zipingpu Dam

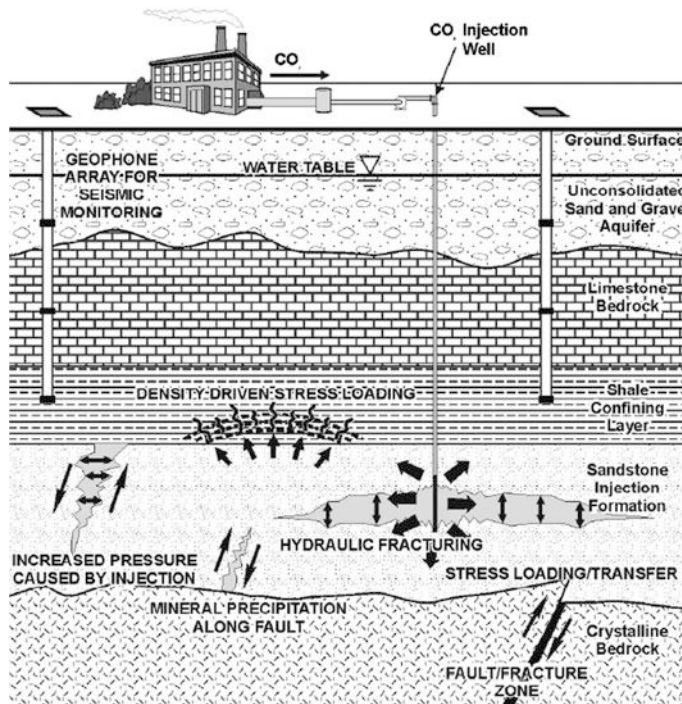


Fig. 1.37 The process involved in seismic activity triggered by underground injection wells (courtesy of National Energy Technology Laboratory and Battelle Memorial Institute)

oil reservoir 1.7 km under the Mediterranean Sea in the Gulf of Valencia and send it via a pipeline to Spain's national grid. It was the largest investment of the Spanish gas system ever, with the potential to store 1.3 billion m³ of gas to guarantee supply and price stability for the future. However, due to vast gas injection, more than 220 minor earthquakes were detected in the area, with some of them being as strong as 4.2 on the Richter scale, and the project was finally halted in September 2013 by the Spanish government by paying 1.35 billion Euros to the operator and owner in compensation.

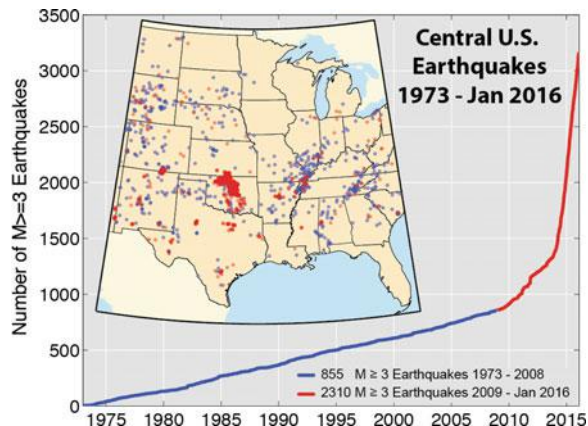
Horizontal drilling together with hydraulic fracturing makes the extraction of tightly bound natural gas from shale formations economically feasible [34], resulting in the expansion of shale oil and gas drilling activities in recent years. However, they can also induce earthquakes with a magnitude up to 5.0, due to both hydraulic fracturing and fluid injection containing water, sand and chemicals with high pressure into deep disposal wells at a typical depth of a few kilometers, as shown in Fig. 1.38. This process creates fractures in deeply buried rocks to allow for the extraction of oil and natural gas as well as geothermal energy, while also adding stress to existing faults and destabilizing and lubricating natural faults, and can potentially trigger shallow earthquakes. Although enhanced oil recovery and



Fig. 1.38 Oilfield waste arrives by tanker truck at a wastewater disposal facility near Platteville, USA, after the removal of solids and oil, the wastewater is injected into a deep well for permanent storage underground (courtesy of USGS)

hydraulic fracturing have been implicated in some recent seismicity, studies [35] indicate that the majority of the increase in seismicity is induced by the deep disposal of fluids produced by oil and gas production. Research [36] suggested that the magnitude of this type of earthquake may be correlated to the volume of injected fluid, while the frequency of earthquake occurrence is influenced by the injection rate. Recent studies [35, 37] also illustrate that the average number of magnitude 3 or larger earthquake occurrences per year has steadily increased in the United States, as shown in Fig. 1.39, starting in 2001—the beginning of the shale

Fig. 1.39 Cumulative number of earthquakes with a magnitude of 3.0 or larger in the central and eastern United States, 1970–January 2016. An increase in the rate of earthquakes can be identified starting around 2009 (courtesy of USGS)



gas boom—and culminating in a six-fold increase by 2011 over twentieth century levels. States experiencing higher levels of seismic activity compared to the pre-2005 average include Arkansas, Colorado, Texas, New Mexico, Ohio, Oklahoma, and Virginia. As an example, within the central and eastern United States, more than 300 earthquakes above a magnitude 3.0 occurred in the 3 years from 2010 to 2012, compared with an average rate of 21 events per year observed from 1967 to 2000. In 2014 alone, there were 659 magnitude 3.0 and larger earthquakes. However, researchers at the US Geological Survey (USGS) believe that among 40,000 waste fluid disposal wells for oil and gas operations in the United States, only a small fraction of these wells have induced earthquakes that are large enough from engineering point of view. As presented in Sect. 1.4.1, it is well accepted that even megaquakes cannot trigger large earthquakes more than a couple of 1000 km away [17]. However, a more recent study [38] argues that large earthquakes in Japan and Chile may potentially unsettled injection waste disposal sites in Oklahoma, Texas and Colorado in the U.S., creating smaller earthquakes, even if this argument has not been fully confirmed by researchers. Other drilling activities can also cause earthquakes, such as the magnitude 3.6 earthquake that occurred in St. Gallen, Switzerland, on 20 July 2013, which was related to the test measurements and simulations for the drilling of geothermal power plant project.

Recently, conspiracy theorists have also claimed that strong earthquake can be induced by triggering a cascade of electrons that could flip the Earth's magnetic poles; they specifically link this theory to the American military's "High Frequency Active Auroral Research Program" (HAARP), as shown in Fig. 1.40 [39]. This operates a 3.6 MW signal station, in the 2.8–10 MHz region of the high frequency



Fig. 1.40 HAARP antenna array

band, into the ionosphere, to analyze the ionosphere and investigate the potential for developing ionospheric enhancement technology for radio communications and surveillance purposes [40]. However, there is as yet no solid evidence to verify these conspiracy theories.

1.4.4 Ice Induced Earthquakes

Ice sheets can also produce earthquakes by shearing the Earth's crust [41]. Recent research indicates that the melting ice sheet and deglaciation in the Polar Regions may release an enormous amount pressure that has built up in the Earth's crust and trigger a massive earthquake [42]. This is the case as, because the thick ice sheets crush the crust, an upward trend is formed ahead of the ice with the crust depressed beneath the ice. This caused the rising of the mainland of Norway since the retreat of the last ice sheets about 9000 years ago [43]. When the ice load is fully or partially released, earthquakes are likely to occur. Therefore, similar to tectonic earthquakes, global warming may have the potential to cause more ice induced earthquakes in the future.

Moreover, during the melting of glacial ice, due to the possible liquid water trapped underneath the glacial ice, which works as a thin lubrication layer due to the hydraulic pressure of the water at the glacier's base, the whole ice mass may then slip by as much as 10 m with a duration ranging from seconds or half minutes (typical) to an hour (note that a tectonic earthquake normally last less than a minute), with the accompanying scraping of ice mass against rocky ground having the potential to generate low frequency elastic waves, leading to an occurrence of earthquake known as ice-quake or glacial earthquakes [44]. The quake can be sufficiently substantial to shake the ground as much as a magnitude 6 earthquake. Based on the analysis of the seismic record of Greenland from 1993 to 2005, Ekström et al. [45] reported that 6–15 ice-quakes occurred every year in Greenland, but this number jumped to 20 in 2003, 23 in 2004 and 32 in 2005. The rates of occurrence correlate with the increase in temperature in Greenland due to global warming.

In addition, when frozen soil or rock saturated with water or ice experiences a drop in temperature, it eventually freezes and expands under colder temperatures, putting stress on its surroundings. This stress builds up gradually until it is relieved in a sudden cracking action in the originally frozen soil, which is referred to as a cryoseism, also known as a frost-quake and another type of ice-quake. The condition for a cryoseism to occur varies, which means that, in reality, accurate predictions are not entirely possible and may constitute a factor in structural design and engineering when constructing in an area historically known for such events [46]. Cryoseisms may be mistaken for minor earthquakes since they appear similar an earthquake, with tremors, vibrations, ground cracking and related noises [32], while cryoseisms often exhibit high intensity in a very localized area [32], in the immediate proximity of the epicenter [47], as compared to the widespread effects of

an earthquake. The relation between global warming and the frequency of cryoseisms has also been speculated upon [32].

1.5 Faults

As presented in Sect. 1.4, the most important earthquakes are tectonic-related earthquakes because they cause the most significant damage to human lives and properties. Therefore, as a starting point to understand the knowledge in the aspects of earthquake measurement, hazard, and assessment, and mitigation measures, etc., as will be discussed in later chapters, it is important to understand fault mechanism (Sect. 1.5) and associated tectonic boundaries (Sect. 1.6).

As presented in Sect. 1.4.1, during earthquakes, zones of fracture between two blocks of rock form, allowing the blocks to move relative to each other. These zones are called faults, as shown in Fig. 1.41, and the slip generated at the fault during earthquakes normally occurs in both vertical (dip-slip) and lateral (strike-slip) directions, but with one of these directions being predominant. Generally three types of faults (Fig. 1.41) can be defined based on the relative movements between the two adjacent plates: normal, reverse, and strike-slip (lateral) faults. The former two are also classified as the dip-slip fault. In addition, faults can also be an oblique-slip type as shown in Fig. 1.42, which is a combination of significant strike-slip and dip-slip.

Normal fault (Figs. 1.43 and 1.44) occurs in response to pulling or tension. The overlying block (hanging wall) moves down relative to the underlying block (footwall), and most of the normal faults have dip angles (the angle between the

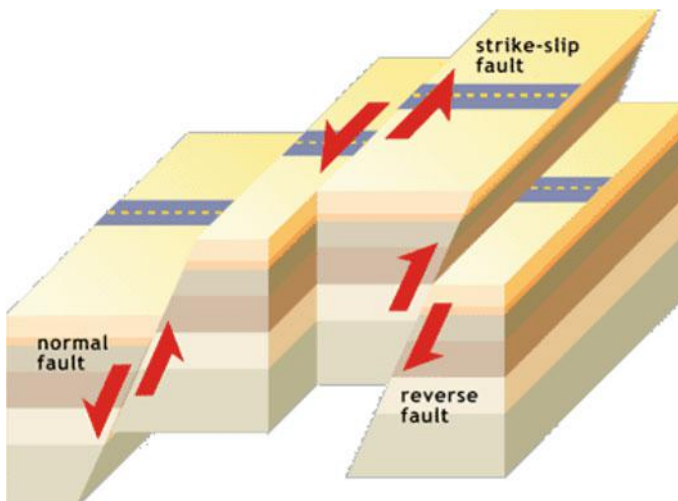
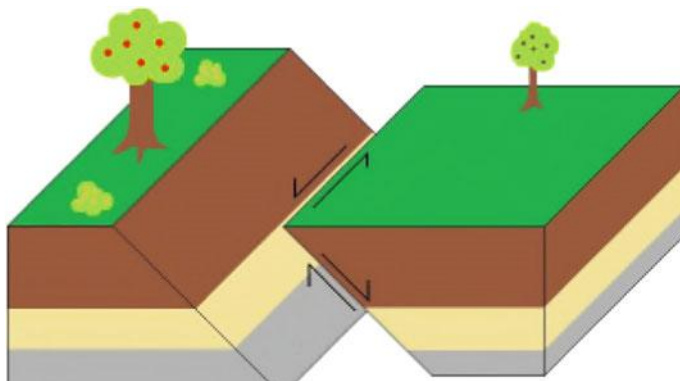


Fig. 1.41 Three types of basic fault type (courtesy of NASA Exploratorium Earthquake Science)



Oblique-slip fault: Arrows represent relative movement.

Fig. 1.42 Oblique-slip fault is a combination of strike-slip and dip-slip

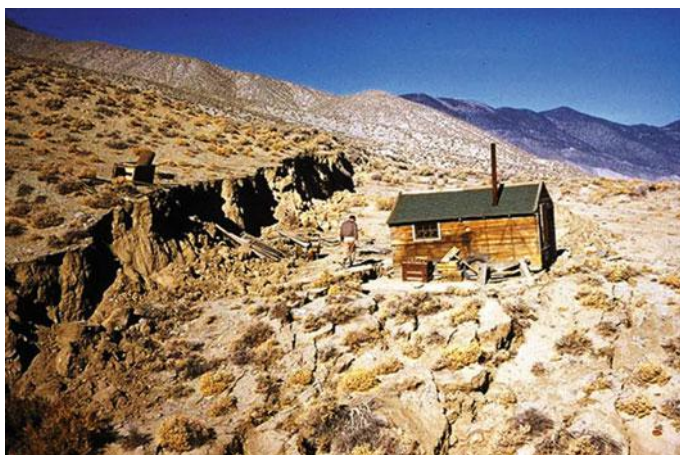


Fig. 1.43 Appearance of normal faults on the ground formed during the magnitude 7.1 Nevada earthquakes at Dixie-Valley-Fairview Peaks, 1954 (photo from the Steinbrugge Collection, Earthquake Engineering Research Center, UC Berkeley)

horizontal plane and the fault plane) ranging from 40 to 60° . These dips often flatten out with depth. As shown in Figs. 1.43 and 1.44, the movement of normal faults is mainly in the vertical direction, with a small amount of horizontal movement. Due to the slide down of overlying block, normal faults are typically associated with tensile stresses in the crust and result in a horizontal stretching of the crust. Some normal faults dip at angles as low as 10° or less. These low-angle normal faults pose special interesting problems for structural geologists.

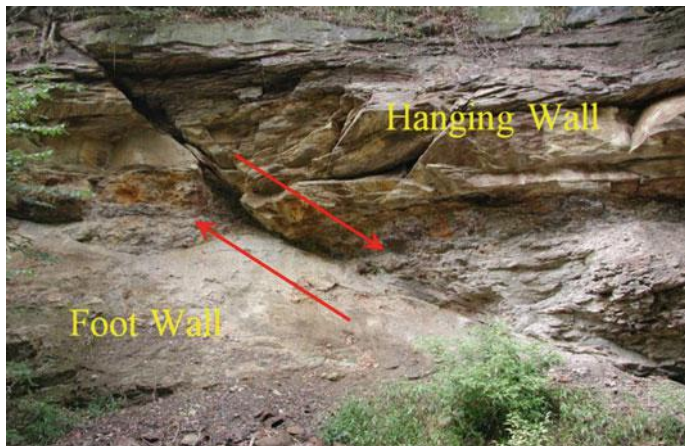


Fig. 1.44 Appearance of normal faults [48]

Reverse fault (Fig. 1.45) occurs in response to squeezing or compression. The overlying block (hanging wall) moves up relative to the underlying block (foot-wall). Reverse fault is associated with horizontal compressive stresses in the crust and therefore causes horizontal shortening of the crust. Most of the reverse faults have dips larger than 45° . A reverse fault having a small dip between about 10° and 40° is called a thrust fault, as shown in Fig. 1.46. Even though most reverse faults are small and only cause local deformations, thrust faults occur in all scales. Some of them can be quite large, such as the thrust faults in the Swiss Alps, the northern



Fig. 1.45 Appearance of reverse faults (courtesy of USGS)



Fig. 1.46 Appearance of thrust faults, which is a special type of reverse fault having low dip angles (figure under license CC BY-SA 4.0, by Mikenorton)

Rockies, Himalayas, and Appalachians, where thrust faults have a scale of up to 50 km [49].

Strike-slip (lateral) fault occurs in response to either type of stress and is associated with shearing. The blocks move horizontally and are parallel to one another. Strike-slip is divided into two lateral senses: left-lateral (sinistral) and right-lateral (dextral). The lateral faults normally produce a very long trace line and a parallel fracture zone as shown in Fig. 1.47. The crushed and broken rocks during the lateral faulting are more easily eroded. Therefore, lateral faults are typically indicated by linear valleys or troughs. Figure 1.48 shows a lateral fault associated with volcano and earthquake activities near the coast of Iceland. A special class of strike-slip fault is the transform fault as will be discussed in Sect. 1.6.3, which can form a plate boundary. Figure 1.49 shows the aerial view of the large scale San Andreas transform fault, named after San Andreas Lake, a small body of water that was formed in a valley between two plates. The fault was first identified in North California in 1895 by Andrew Lawson, a professor from University of California, Berkeley. During the San Francisco earthquake in 1906 with a moment magnitude of 7.8, this fault stretched southward into South California.

As mentioned previously, a fault showing a combination of both dip-slip and strike-slip is called an oblique-slip fault, as shown in Figs. 1.42 and 1.50. Actually, nearly all faults will have some components of both dip-slip and strike-slip, but with one of these directions being predominant. Therefore, to define a fault as oblique requires both dip and strike components to be measurable and significant.

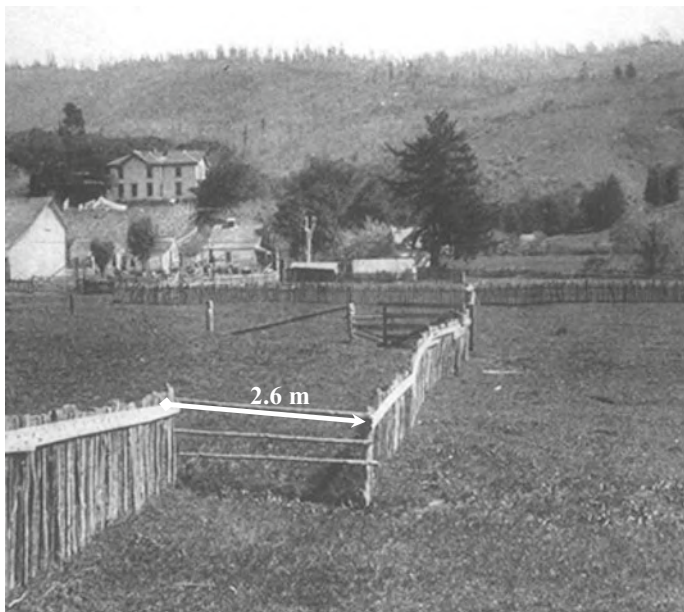
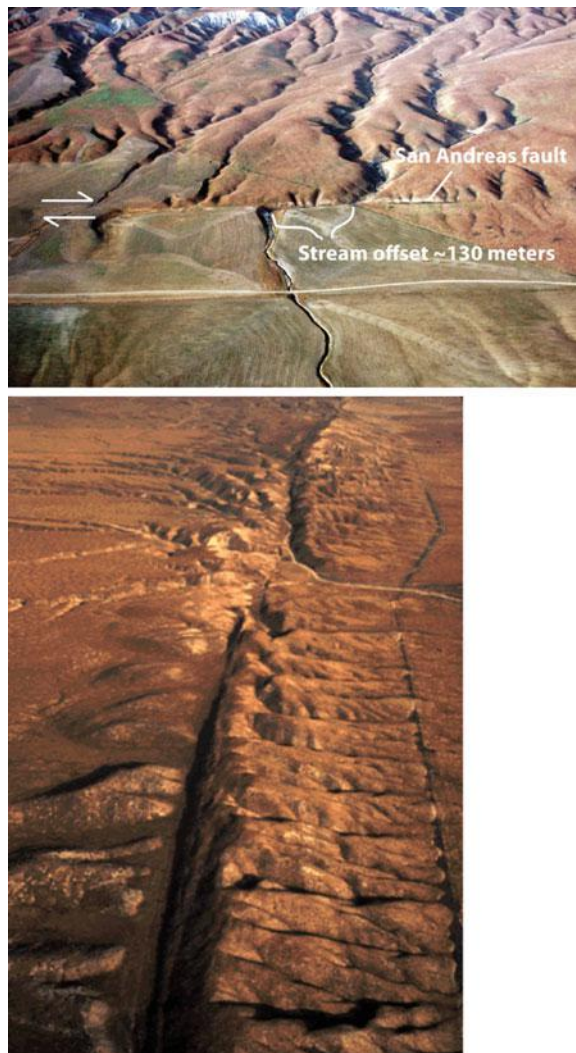


Fig. 1.47 An indication of a lateral fault formed during the moment magnitude 7.8 of San Francisco earthquake, 1906

Fig. 1.48 A lateral fault in Thingvellir Lake, Iceland, at the boundary between the Eurasian and North American tectonic plates. The undersea mountain ranges are formed by numerous eruptions of basalt lava along their length powered by magma rising and falling in the mantle



Fig. 1.49 Part of the San Andreas Fault in California (courtesy of USGS)



In addition, there are also other types of faults, such as listric faults, which are similar to normal faults but the fault plane curves, with the dip being steeper near the surface, and shallower with increased depth, reaching a horizontal (flattened) slip at certain depths, as shown in Fig. 1.51; ring faults, which are faults that occur within collapsed volcanic calderas and the sites of bolide strikes; and synthetic and antithetic faults, which are minor faults, with the synthetic faults dip in the same direction as the major faults while the antithetic faults dip in the opposite direction.



Fig. 1.50 Appearance of an oblique-slip fault produced during the Richter magnitude 7.1 Nevada earthquake of 1915, the strike-slip component is shown by the offset of the fence

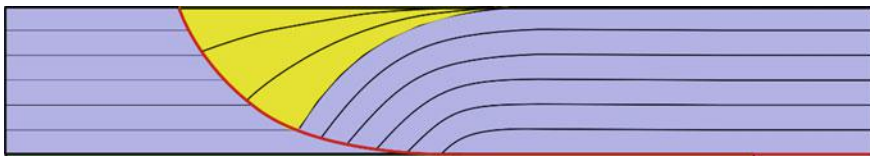


Fig. 1.51 An illustration of Listric faults

1.6 Tectonic Plate Boundaries and Fault Zones

Large faults within the Earth's crust result from the action of plate tectonic forces. Energy release associated with rapid movement on active faults is the cause of most earthquakes. Since faults do not usually consist of a single, clean fracture, geologists use the term 'fault zone' when referring to the zone of complex deformation associated with the fault plane. On the global view, there are three main types of fault zones used to identify tectonic plate boundaries, namely spreading zone or divergent boundary, subduction zone or convergent boundary, and transform fault

zone/boundary. The largest earthquakes occurrence and the highest energy release are associated with seismic activities related to subduction zones.

1.6.1 Spreading Zones

Due to mantle convection, as presented previously, in certain areas two tectonic plates move away from each other, creating an opening, and hot magma from the mantle rises up through the opening, causing both volcanoes and earthquakes. Such areas are known as spreading zones. The boundaries between two plates that are moving apart are called divergent boundary, spreading ridge, or spreading rift. The majority of faults along spreading zones are normal (Figs. 1.43 and 1.44). The speed of spreading ranges from 2 to 18 cm per year, with the highest speed found in the Pacific Ocean ridges and the lowest one found along the Mid-Atlantic ridge [8]. Most of the spreading zones are centered in the ocean, with the best-known one being the mid-ocean ridge shown in Fig. 1.52, discovered in the 1950s, which is an underwater mountain system that consists of various mountain ranges (chains), typically having a valley known as a rift running along its spine (Fig. 1.53), formed by plate tectonics. It is worth mentioning that many of the volcanic activities occurring on the sea floor are located at spreading zones. Spreading ridges can also be extended above the sea surface. An example of this are the 150 active volcanoes on the island of Iceland, which are located at the divergent boundary between the North American Plate and Eurasian Plate, as shown in Figs. 1.54 and 1.55, making

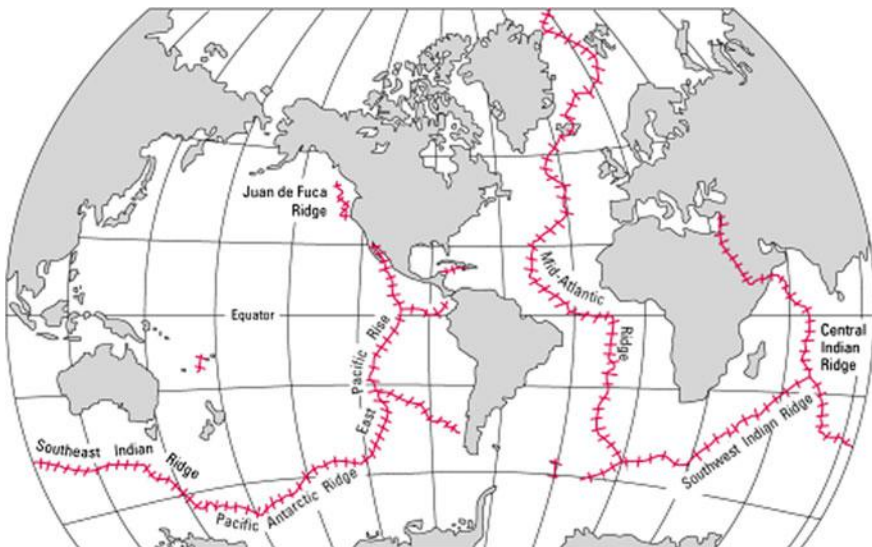


Fig. 1.52 World distribution of mid-ocean ridges (courtesy of USGS)

Fig. 1.53 Mid-oceanic ridges at seabed in Atlantic Ocean clearly showing the characteristics of spreading zones

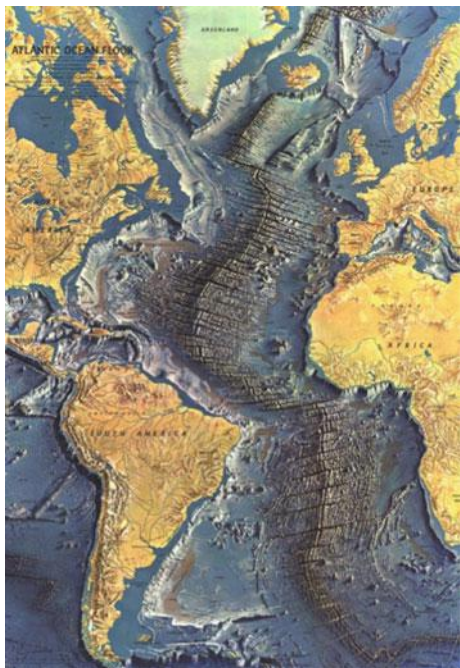


Fig. 1.54 Volcanoes (*solid triangles*) located at the Mid-Atlantic Ridge located along the boundary between the North American Plate and Eurasian Plate (courtesy of USGS)

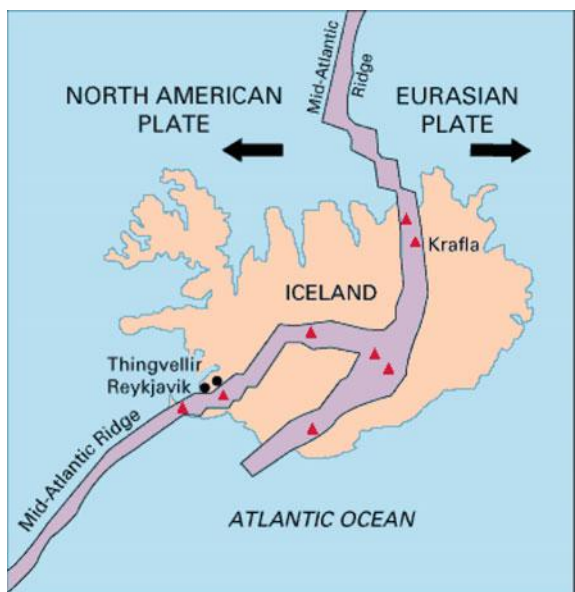




Fig. 1.55 Faults located along the Mid-Atlantic Ridge in Iceland

Iceland a place where a mid-ocean ridge can be seen on land (Fig. 1.55) and in shallow waters (Fig. 1.48). New crust is created by hot magma rising up from the mantle and constantly filling the gap created by the diverging plates, as shown in Fig. 1.56. It was the discovery of this worldwide mid-ocean ridge system that led to the theory of seafloor spreading and general acceptance of Wegener's theory of continental drift (Sect. 1.4.1) and expansion as plate tectonics [50, 51].

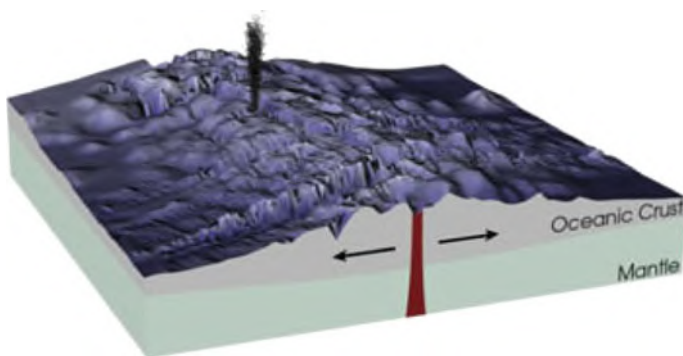


Fig. 1.56 Rising magma located along a mid-ocean ridge, forming a new ocean plate that spreads away from the spreading ridge (courtesy of NASA)

1.6.2 Subduction Zones

1.6.2.1 Introduction to Subduction Zones

After presenting the concept of spreading zone, a question may arise: as the volume of earthquakes remains constant, if new oceanic crust is continuously being created along the spreading zones, it cannot be balanced by the consumption of the plate material at other locations, the Earth would then be expanding. In reality, the old oceanic crust, more than 200 million years old, is “re-cycled” back into the mantle at deep ocean trenches under its own weight beneath the lighter crust (typically continental crust), as shown in Fig. 1.57. This occurs at subduction zones where two tectonic plates move towards one another and one slides under the other, generating both earthquakes (in the sloping zone at the interface between the subducting and overriding plates) and volcanoes, and the faults at subduction zones are often reverse. Most subduction zones are found in the Pacific Ocean near the edge of continents, indicating that the Pacific Ocean is shrinking while the Atlantic Ocean is expanding.

1.6.2.2 Convergent Boundary

The boundary between two tectonic plates that move towards one another is called a convergent boundary, which can be divided into three types: oceanic-continent subduction zone, ocean-oceanic subduction zones, and continent-continent collision zone.

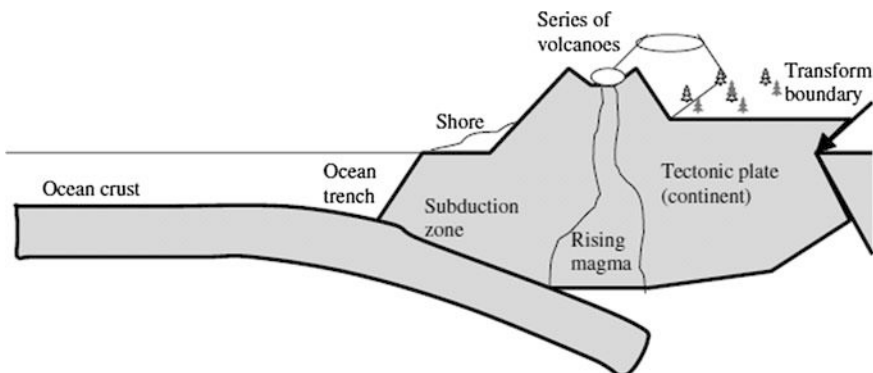


Fig. 1.57 Cross section through a subduction zone (with ocean trench), transform boundary and a tectonic plate (continent) [52]

In the ocean-continental subduction zone, usually the denser oceanic plates (with a typical density of 3.0 g/cm^3) will subduct beneath the less dense continental plate (with a typical density of 2.8 g/cm^3), resulting in a deep ocean trench as shown in Fig. 1.57. During this process, even though the oceanic plates become ductile and cannot generate earthquakes at a rather deep location, the melting plates can produce magma that rises and forms a line of volcanoes parallel to the subduction zone on the overriding plate, as shown in Fig. 1.57. The deepest recorded earthquake thus far was around 700 km at the subduction zone, which is a proof of this mechanism. One example of an ocean-continental subduction zone is the Peru–Chile trench (also called the Atacama Trench), which lies off the coast of South America, shown in Fig. 1.58, where the oceanic Nazca Plate is being subducted under the continental South American Plate. It has a length of 5900 km, with the deepest location being 8069 m below the sea surface. The continental South American Plate is crumpled and forced up, creating the Andes mountain range. Earthquakes are common in this region: sometimes violent and linked to a sudden uplift of the land, occasionally by as much as several meters. Earthquakes along the trench also produced nine significant tsunamis during the last century, resulting in

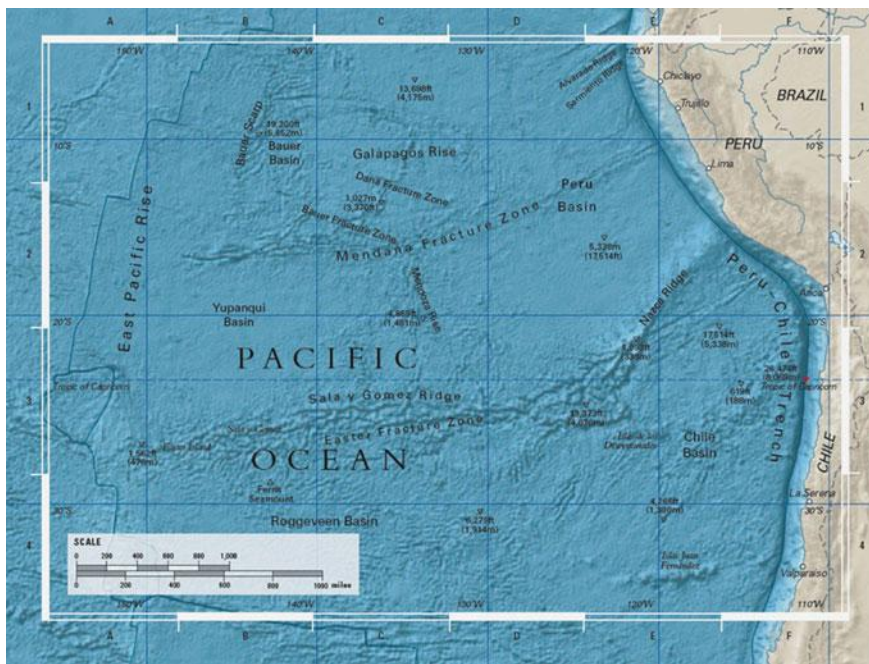


Fig. 1.58 The Peru–Chile Trench is located at an ocean-continental subduction zone (courtesy of Oceana)

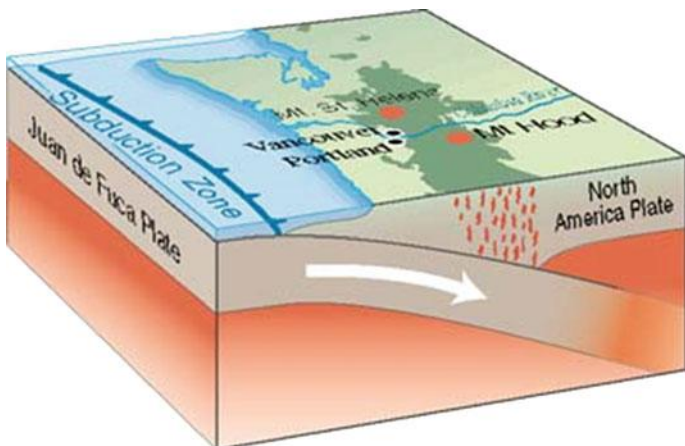


Fig. 1.59 The Juan de Fuca Plate subducting under the northerly portion of the western side of the North American Plate

more than 2000 fatalities. Moreover, the melting of the rocks around the subducting plate has led to volcanism in that many of the Andes' tallest peaks are volcanoes. The Cascadia subduction zone (Fig. 1.59) and Japan Trench are two other well-known ocean-continental subduction zones.

In oceanic-oceanic subduction zones, two oceanic plates converge. Similar to an oceanic-continental subduction zone, one plate is usually subducted under the other, forming a deep trench on the seabed. As the subducting oceanic crust meets with the asthenosphere, magma rises to the surface and forms volcanoes. Given enough time (millions of years), the submarine volcanoes grow high enough to rise above sea level and form a chain of islands, known as island arcs. An example of the oceanic-oceanic subduction zone is the formation of the well-known Marianas Trench that runs parallel to the Mariana Islands, as shown in Figs. 1.60 and 1.61, where the relatively fast-moving Pacific Plate converges with the less speedy Philippine Plate. At nearly 11,000 m below sea level, the Challenger Deep (Fig. 1.60), at the southern end of the Marianas Trench, is the deepest trench identified so far. Tonga Trench in the South Pacific Ocean is another well-known ocean-oceanic subduction zone, with a convergence rate of approximately 15–24 cm per year, which is the fastest plate velocity recorded on the planet, making this region the Earth's most active zone of mantle seismicity.

At a continent-continental collision zone, two continental plates meet each other, and neither is subducted because the continental rocks are relatively light and resist

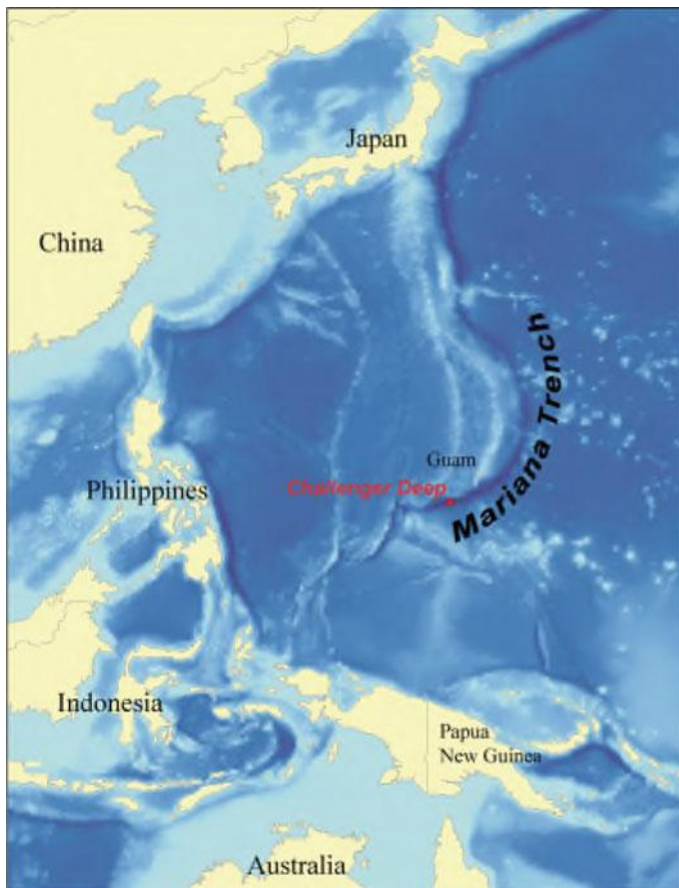


Fig. 1.60 The Marianas Trench (courtesy of NOAA) located at an oceanic-oceanic subduction zone

downward movement, squeezing and folding the sediments between them and pushing upward or sideways, finally producing mountain ranges. This is the explanation for high mountain range formation such as the Himalayas (shown in Fig. 1.62) and Alps: the former is formed by the collision between the Indian plate and the Eurasian plate in early tertiary time, and the latter is due to the collision between the Eurasian and African plates.

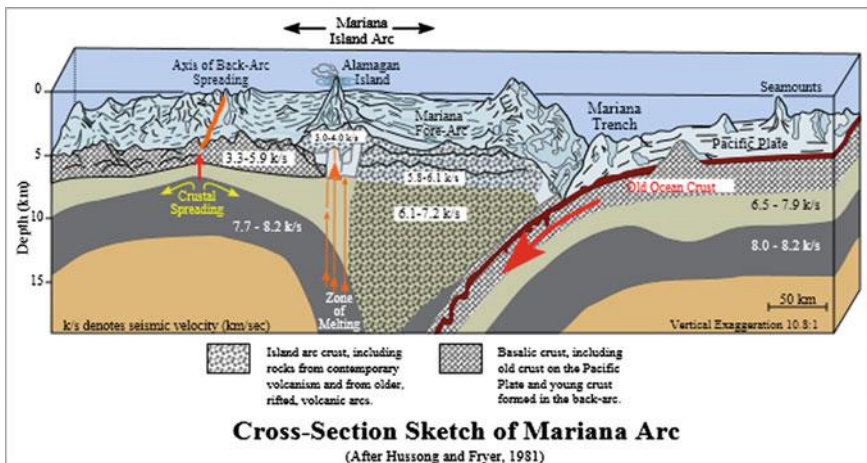


Fig. 1.61 The formation of Marianas Trench [53]

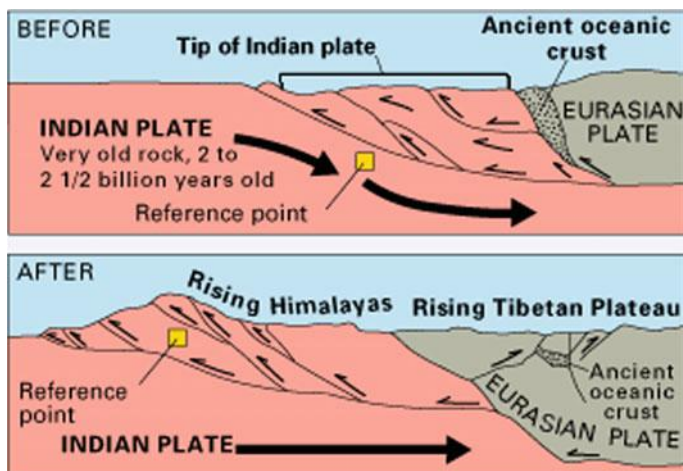
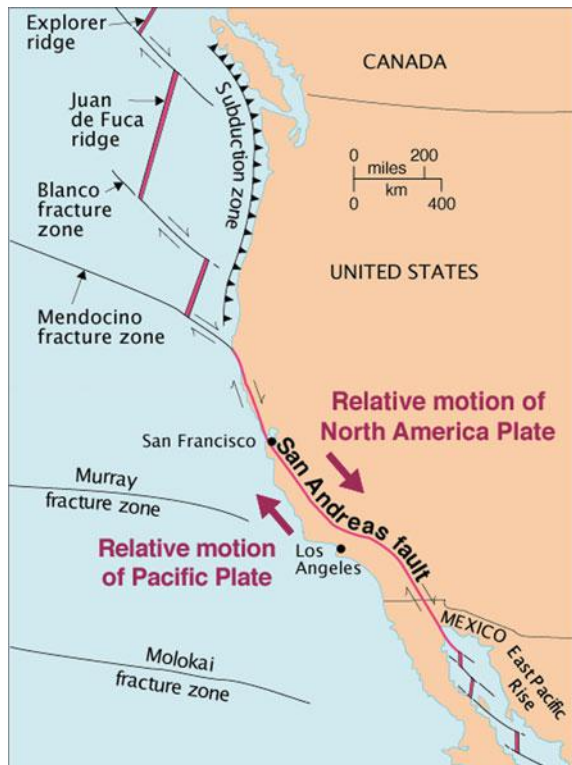


Fig. 1.62 The collision between the Indian and Eurasian plates has pushed up the Himalayas and the Tibetan Plateau at a continent-continental collision zone (courtesy of USGS)

1.6.3 Transform Fault Zones

Along transform faults or transform boundaries, two plates slide past one another, predominantly horizontally, in either a sinistral or dextral direction, and neither plate is destroyed in this process at the boundary, causing the only earthquakes that normally occur with shallow focal depth and large amplitude. Transform faults are also referred to as conservative plate boundaries, as lithosphere is neither created

Fig. 1.63 Map of San Andreas Fault in California (courtesy of USGS)



nor destroyed. Obviously, the faults are lateral, such as the San Andreas Fault shown in Fig. 1.63, which is a right-lateral strike-slip faulting and links the Juan de Fuca ridge and the East Pacific ridge (Fig. 1.52). As a result, numerous earthquakes occurring in California are related to this strike-slip faulting, as shown in Fig. 1.64, such as the San Francisco earthquake (1906) with a moment magnitude of 7.8, and the Loma Prieta earthquake (1989) with a moment magnitude of 6.9. Transform faults are usually found in the ocean basin and connect offsets in the mid-ocean ridges (forming an inter-connecting fault system), with a smaller number of them connecting mid-ocean ridges and subduction zones [54]. The mid-ocean ridge aforementioned is actually offset (or segmented) by many transform faults.

1.6.4 Intraplates

Within each tectonic plate, there are many sub-segments that also occasionally move and collide with each other. This may cause weaker but nevertheless still damaging earthquakes in any part of our planet, referred to as intraplate earthquakes. However, if the externally applied boundary stresses due to the internal

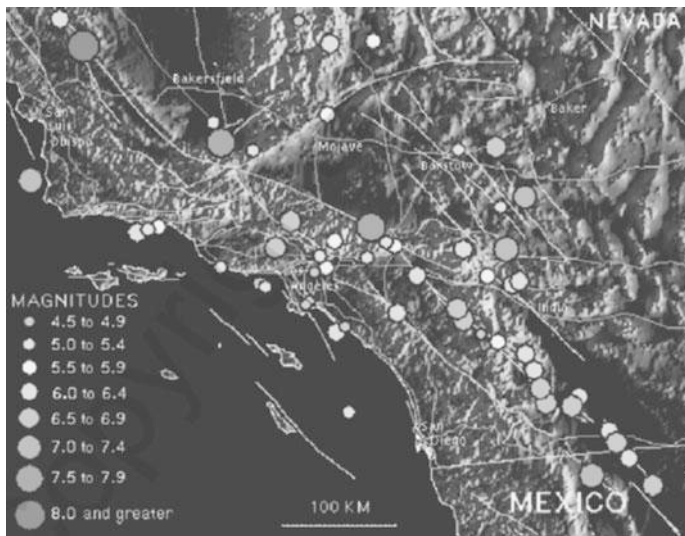


Fig. 1.64 Epicenters of historic earthquakes (1812–1996) with a magnitude of more than 4.5 occurring close to San Andreas Fault and traces of faults. The magnitude indicated is normally moment magnitude for earthquakes above magnitude 6 or Richter magnitude for earthquakes below magnitude 6 (courtesy of USGS)

plate distortion are significant, large earthquakes can also occur inside tectonic plates, such as the Richter magnitude 7.8 of Tangshan earthquake (1976) in the east of China, the magnitude 8.0 of New Madrid earthquake (1811) in the south of the United States (three large magnitude earthquakes that occurred in New Madrid Zone ranked on the top list of largest earthquake events in North America during the past 200 years) [23], the moment magnitude 6.7 of Northridge earthquake (1994), moment magnitude 7.7 of Gujarat earthquake (2001), and moment magnitude 8.2 of Indian Ocean earthquake (2012). In general, the seismic gap (time period between the fault ruptures, see Sect. 1.4.1) is shorter at the boundary of tectonic plates than that at internals of a plate.

Even though many urbanized areas are close to areas along faults in the normally stable intraplates, compared to earthquakes near tectonic plate boundaries, intraplate earthquakes are not well understood. In many cases, the causative fault is deeply buried, and sometimes cannot even be found. Under these circumstances it is difficult to calculate the exact seismic hazard for an area, especially if there has been only one earthquake in historical times, and the hazards associated with them may be difficult to quantify. The best measure to better understand the intraplate earthquakes so far is to perform detailed micro-seismic monitoring, involving dense arrays of seismometers. In this manner, minor earthquakes associated with a causative fault can be located with required accuracy. However, since the majority of intraplate earthquakes are of minor magnitude, some of them are mistaken for cryoseisms, as presented in Sect. 1.4.4.

1.6.5 Relation of Plate Boundaries with Earthquake Occurrences

Figure 1.65 shows the main types of plate boundaries. The faults associated with subduction zone can have significantly larger widths than that of the transform faults, on which strain on crustal or tectonic plate can build up. This process can take hundreds, thousands or even more years, before a sudden and significant slippage of one plate over another, with the combined large fault area and more slippage (the large dimensions of faults give rise to more significant slip) eventually resulting in higher energy releases. This is why the largest earthquakes in the world occur at regions associated with subduction zones rather than areas associated with transform faults. Further, earthquakes associated with the fault ruptures at subduction zones generally occur at greater hypocentral depths than quakes that occur on transform zones. For example, one of the few large earthquakes associated with transform faults is the 1906 San Francisco earthquake (which will be discussed in a later chapter) with a moment magnitude of 7.8, while the largest earthquakes around subduction zones were the 1960 Chilean earthquake and 1964 Alaska earthquake, with moment magnitudes of 9.5 and 9.1, respectively.

In terms of seismic energy, approximately 98 % is released at plate boundaries, of which 80 % originates from subduction zones, 15 % from continent-continent collisions and up to 5 % from mid-ocean ridges [55]. In terms of earthquake frequency of occurrence, the subduction zones (with ocean trenches) and transform boundaries between major tectonic plates as well as intraplate faults are the most frequent and strongest sources of earthquakes. The sites near such earthquake sources are likely to experience increased seismic hazard [52]. For example, Japan

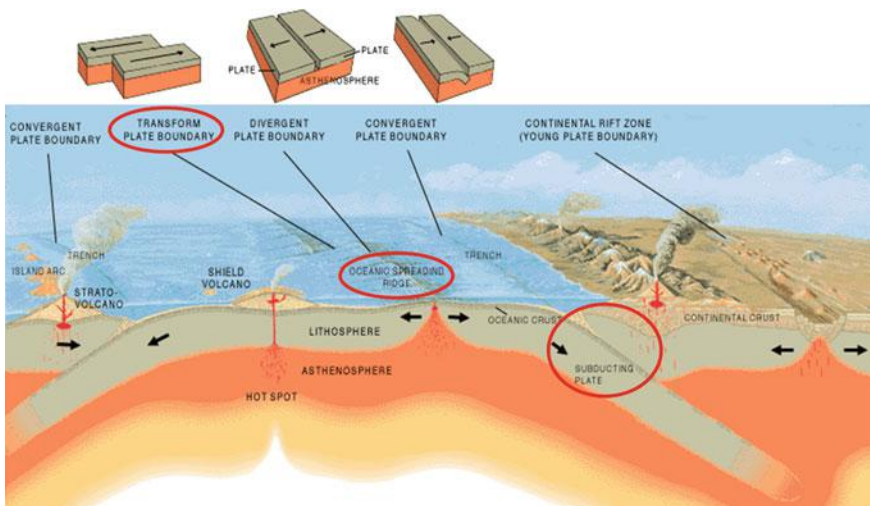


Fig. 1.65 Main types of plate boundaries (courtesy of USGS)

is continuously experiencing significant earthquakes because it is sitting on the junction between Eurasian and Philippine tectonic plates. Similarly, California lies on the San Andreas Fault at the boundary between North American and Pacific plates, as aforementioned, which is a continental transform fault that extends roughly 1300 km as shown in Fig. 1.63, and its motion is right-lateral strike-slip horizontally. This fault is divided into three segments, each with different characteristics, and a different degree of earthquake risk. Although the most significant (southern) segment only dates back about 5 million years, the oldest sections were formed by the subduction of a spreading ridge about 30 million years ago.

1.7 Earthquake Mitigation Measures and Modern Earthquake Engineering

During the last century, researchers and engineers have made tremendous efforts to mitigate the dangers created by earthquakes in three ways: prediction of future earthquakes, human engineered earthquake, and earthquake engineering.

Earthquake prediction (short term) and forecasting (long term) aim to predict as accurately as possible location and time of a future strong earthquake. It has been one of the most cherished goals of seismologists for more than 100 years. As will be described in Sect. 1.8, instead of wide applications of earthquake forecasting in the seismic hazard estimation (which will be discussed in a later chapter), due to limited knowledge and the complexity of the mechanisms involved in an earthquake, a reliable earthquake prediction is so far unattainable.

Human engineered earthquakes aim to trigger an earthquake that would otherwise have occurred in a populated area such that it instead takes place where the population is sparse and there are few infrastructures, or in the deep sea. In some instances, it is even possible to make what would have been a large, destructive earthquake occur in a series of small earthquakes. By doing so, the energy accumulated in seismic faults that have the potential to cause extensive damage in terms of lives and the economy will be dissipated and extremely destructive earthquakes can be prevented. However, as discussed in Sect. 1.4.1, the energy released by low magnitude earthquakes is almost negligible compared to a major earthquake. For example, it would take 32 magnitude 5's, 1000 magnitude 4's, or 32,000 magnitude 3's to equal the released energy of one magnitude 6 earthquake event. Therefore, small earthquakes can sometimes simply be precursors or “foreshocks” to a major earthquake rather than a mitigator of a major earthquake. On the other hand, human induced earthquakes can be observed through methods such as underground fluid injection, evacuation or nuclear explosion. There is evidence that injection of fluids into deep wells, the filling of large reservoirs, and mining activity can cause earthquakes that do have damaging effects as presented in Sect. 1.4.3. However, other evidences also point to the ineffectiveness of attempts to induce or trigger earthquakes. For example, the largest underground nuclear test ever to be conducted

in the United States, which occurred on 6 November 1971 in Amchitka, did not induce any earthquakes in the seismically active Aleutian Islands. Another thermonuclear test in January 1968, conducted in central Nevada, caused a fresh fault rupture of a length of about only 1200 m. In these attempts, the energy contained in seismic waves produced by the fault movement was insignificant when compared with the energy released by the nuclear explosion. However, it is claimed that the test induced aftershocks with magnitudes of up to 5.0 [28].

As of yet human beings have not been able either to prevent or certainly predict earthquakes. However, the risk induced by a strong earthquake can be significantly mitigated or even managed by designing and constructing infrastructures in such a way that they can resist strong ground motions. This can be achieved by characterizing the hazard and analyzing the structural responses (e.g., identifying earthquake faults, unconsolidated sediment likely to amplify earthquake waves, and unstable land prone to sliding or liquefying during strong shaking, calculating the structural and foundation response, etc.), assessing the structural performance, preparing in advance by taking preventative measures, and taking proper actions during and after a damaging earthquake. These are the pillars of modern earthquake engineering, and the content of the current book. In addition to concentration on earthquake engineering for land-based structures, special focus will be placed on the application of earthquake engineering knowledge for offshore structures.

Earthquake engineering is an interdisciplinary scientific area, it identifies and solves problems associated with occurrence of earthquakes, with the goal of reducing seismic risks to socio-economically acceptable levels, it requires as it does knowledge and development from geology, seismology, geotechnical, marine and structural engineering, and even architecture and insurance. However, the role of the other parties tends to be poorly understood by various disciplines, and there is also a big gap between state-of-the-art earthquake engineering and the knowledge of practicing engineers. As an example, for buildings, around 70 % of the earthquake losses are due to damage to non-structural elements such as building contents and cladding, rather than the collapse of buildings [56]. On the other hand, those non-structural elements receive minimum engineering designs and there is a lack of understanding of engineer's anticipated building movement by the architect and the contractor on site. Therefore, it is of great importance to enhance the considerations of seismic design in different disciplines and parties.

From seismology's point of view, it is important to understand the mechanism and sources of ground motions, to assess the seismic hazard for each specific location, area, and region, and to present required inputs to civil engineers, risk analysts, authorities and other relevant parties to assess the risk associated with human lives, economy and infrastructure safety, etc.

For civil engineers, it is important to find solutions for structures and foundations to withstand seismic excitations. Three approaches are typically used in a combined manner. The first one involves an interpretation of the hazard assessment results provided by seismologists, and use it in a smart manner, so that an economical while reliably safe solution can be reached. To reach this objective, interaction and mutual understanding between seismologists and civil engineers are essential. The

second approach is to design a structure with sufficient strength, stiffness, ductility, redundancy, and damping to withstand seismic ground motion. In this aspect, the choice of structural form, material properties, foundation type used in construction, the assumption of damage scenarios, and selection of a decent seismic response calculation method are important factors influencing the seismic design. Sometimes, it is essential to find an optimized structural design with respect to those parameters so that the seismic response can be mitigated to a great extent. Because this approach relies on inherent strength and system damping (typically less than a few percent) to dissipate the seismic energy, a certain level of inelastic deformation and associated damage has to be accepted [57]. The third approach involves the design of external damping devices to dissipate seismic energy or isolation devices to cut the transmission path between the seismic ground motions and structures. The objective is to mitigate seismic response of structures and forces acting on structures. Depending on whether power is required or not, the control of those devices can be a type of passive, semi-active, active, or hybrid. The relevant topics above will be discussed throughout this book.

Upon the presentations above, it is known that the core contents of earthquake engineering are related to seismological, geotechnical, structural and risk assessment aspects, which include assessment of site-specific earthquake loading (seismic hazard analysis), structural and foundation analysis, and loss analysis etc. Among them, the mitigation measures on structures and non-structural elements such as equipment for resisting earthquake loading also play an important role in modern earthquake engineering. Moreover, the concerns regarding the earthquake resistance should be fully integrated into the architectural design, which requires a harmony between structural engineers and architects. And all these aspects require dedicated efforts and an active collaboration among engineers from different disciplines.

It is noticed that, during the last 30 years, due to the wide spread of strong motion accelerographs and computer techniques, earthquake engineering has rapidly developed in all relevant areas. It has also been greatly influenced by large engineering projects for constructing high cost infrastructures, such as offshore platforms, nuclear power plants, large dams, high rise buildings, long-span bridges, and LNG storage tanks etc., for which a higher safety level is required than for ordinary structures [58]. On the other hand, many existing and new-build infrastructures are still under high risk due to earthquakes, especially for those that were built according to past design codes that have been found to be inadequate. There are always other urgent issues which push back the resolution of the problems, this is especially the case in many developing countries. For example, even though earth-made constructions are quite fragile with regard to seismic resistance as shown in Fig. 1.66 [59], until the end of the last century around 30 % of the world's population still lived in this type of constructions, with approximately 50 % of them located in developing countries due to cultural, climatic and economic reasons [59, 60].



Fig. 1.66 Destruction of adobe houses during the moment magnitude 8.0 Pisco earthquake on 15 August 2007, Peru [59]

Moreover, Adobe constructions are very common in some of the world's most seismic hazard-prone regions, as shown in Fig. 1.67 [61]. In respect of this matter, “time is a critical factor; every day without action is a day lost in the effort to prevent collapses and save lives” [62]. As an example, the 2010 magnitude 7.0 Haiti earthquake mentioned in Sect. 1.1 caused a loss 92,000 lives and massive destruction. In contrast, the death toll of a larger earthquake that occurred in Chile in 2010 with a magnitude of 8.8 was 520. Among other reasons, the implementation and enforcement of earthquake resistance building codes in Chile has been shown to significantly reduce infrastructure damages and to save lives. However, as seismic design is typically more expensive and requires more expertise for infrastructures built in seismically active areas, in many parts of developing countries, infrastructures are still built that do not adhere to local design codes and standards.

Past earthquakes have also shown that many infrastructures in poorly maintained conditions performed well during major earthquakes. Local site conditions, focusing effects, construction quality, and building shape and size etc. have all been suggested as possible explanations. These experiences also show that no building is automatically immune from damage because of its style of construction [63].

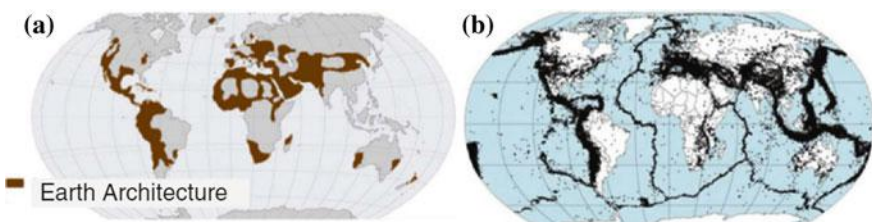


Fig. 1.67 Distribution of earth-made constructions (left) [61] around the world and earthquake epicenters between 1963 and 1998 (right) (courtesy of NASA)

1.8 Earthquake Prediction and Forecast

Compared to earthquakes, many other natural hazards are more predictable, or at least give more obvious pre-warnings. This is due to the complexity of the mechanism inducing an earthquake and the limitation of our knowledge and investigation methods toward earthquake research. For instance, hurricanes take days or weeks to form and only occur at certain times of the year, giving ample time for communities in the potential path to prepare and evacuate [64]; on the other hand, in order to understand the layers and nature of the Earth's crust, including seismic discontinuities, Russia has carried out the deepest drilling ever done by mankind on the Kola Peninsula. At a depth of 12,262 m (the original goal was 15,000 m) below ground level, given that the diameter of the Earth is 6371 km, this remains simply a fraction.

1.8.1 Earthquake Prediction

Because of the remarkably destructive effects of earthquakes, many scientists, especially seismologists, continuously try to find ways and rules to predict the location, time of occurrence, and the significance of ground shaking of future earthquakes.

Even though there is no solid scientific ground for predicting forthcoming earthquake events, experiences from the major earthquakes showed that before a strong earthquake occurs, some unusual physical phenomena occur, such as a rapid tilting of the ground and more frequent smaller earthquakes, dramatic changes of water levels in wells [65], radon or hydrogen gas emissions from the Earth [66, 67], changes in seismic wave velocities [68], large scale changes in soil temperature, changes in electromagnetic fields and ion concentration of the ionosphere, etc.

It is particularly interesting to mention that before a significant earthquake, peculiar animal behavior can sometimes be observed. The earliest reference to unusual animal behavior prior to a significant earthquake is from Greece in 373 BC. Rats, toads, weasels, snakes, and centipedes reportedly left their homes and headed for safety several days before a destructive earthquake [69, 70]. Anecdotes abound of animals, fish, birds, reptiles, and insects exhibiting strange behavior anywhere from weeks to seconds before an earthquake, as reported during many earthquakes such as the 1975 Haicheng earthquake, 1989 Loma Prieta earthquake, 1995 Kobe earthquake, 2008 Wenchuan earthquake, 2009 L'Aquila earthquake, 2015 Nepal earthquake, etc.

It is noticed that some animals can sense low frequency electromagnetic signals and behave unusually. This low frequency sign can be created by the fracturing of the crystalline rock along faults. Therefore, some people have suggested a measure to predict an earthquake simply by counting missing pet advertisements and correlating this relationship to lunar-tide cycles.

Foreshocks may also be precursors of earthquakes. For example, before the magnitude 9.0 Sendai earthquake that occurred in 2011, four major foreshocks occurred with a magnitude ranging from 6.0 to 7.2.

The prediction of the earthquake in Haicheng (which had a population of about 1 million at that time) that occurred in China in 1975 is one of several well-known successful short term earthquake predictions: an evacuation warning was issued the day before a strong earthquake with a magnitude of 7.3. In the preceding months many unusual phenomena occurred: changes in land elevation and in ground water levels, widespread reports of peculiar animal behavior, and many foreshocks. It was an increase in foreshock activities that finally triggered the evacuation warning [71]. Haicheng earthquake finally caused 2014 fatalities, and it was estimated that the number of fatalities and injuries would have exceeded 150,000 if no earthquake prediction and evacuation had been made. However, most damaging earthquakes have not been successfully predicted before they occurred.

With respect to short term prediction, other information has also been collected and used to study the possibility of earthquake prediction, such as statistical information, seismic gap of previous earthquakes based on the elastic rebound theory (Sect. 1.4.1), characteristics of foreshock and aftershocks based on the seismic wave measurements and their correlation with a potential future earthquake, physical measurements of changes in distance, ground elevation or physical properties of rocks to monitor the movement along faults and the build-up of strain, and geological evidence in an area combined with previous earthquake records, etc.

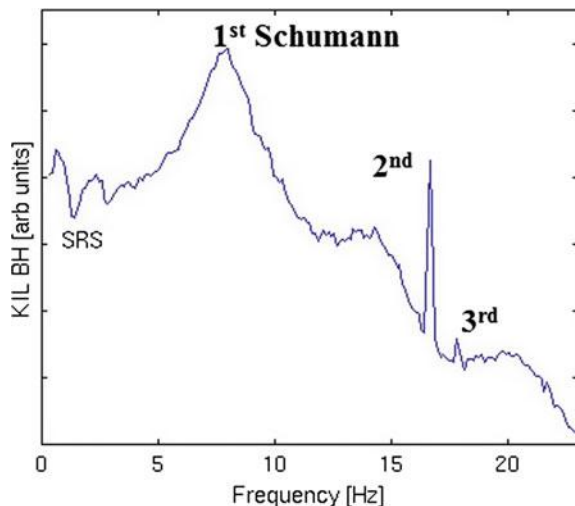
Recent research has recognized that earthquakes are linked: an earthquake on one fault can trigger or mitigate seismic activities on other nearby faults. This can be carried out by comparing the satellite radar images of Earth deformation at different times to link regional earthquake events. Based on these research activities, two methods for predicting future earthquakes are under development: statistical analysis or geophysical precursors of earthquakes [72, 73]. The former is based on the occurrence history of earthquakes in a region and it provides a clue to the recurrence of an earthquake with a given magnitude. However, it does not have a solid physical background and therefore is a method only because there are no better alternatives. Contrary to the statistical method, the geophysical precursors investigate the physical state of earthquakes that are precursory to earthquakes. It gives hints on possible earthquakes in medium or short term notice, and works on the basis of the monitoring of physical properties or signals, such as underground water level, ground uplift and tilt, electrical resistivity of rocks, P-wave changes etc. In recent years, scientists have developed and deployed increasingly sophisticated instruments to capture signals from the Earth, including not only earthquake waves but also warping of the crust. Data has been recorded since prior to a number of recent moderate, magnitude 6–7 earthquakes in California, but no sign of precursory signals has been revealed from the recorded data yet [74]. It is possible that the combination of the two methods aforementioned may increase the reliability of the prediction.

The VAN method [75], which is perhaps the best-known earthquake prediction method, proposed by researchers from the National and Capodistrian University of Athens, stated that by measuring geolectric voltages (referred to as “seismic electric signals (SES) in the VAN method”), earthquakes larger than magnitude 5, within 100 km of the epicentral location, within 0.7 units of magnitude, could be predicted in a 2-h to 11-day time window. Subsequent papers claimed a series of successful predictions [76, 77]. However, by using this method, a large number of false alarms were generated in the 1980s, which received intense public criticism at that time. In 1996, a special issue [78] of *Geophysical Research Letters*, 161 pages in length, was dedicated to the discussion on the VAN method. By studying the statistical significance of the VAN method, some researchers found that the method was flawed, and the claims of successful predictions were statistically insignificant. In 2001, the VAN method was modified to include time series analysis [79].

In recent years, a new field of research interest for earthquake prediction has been to analyze the Schumann resonance phenomena in Earth’s electromagnetic field, and to relate anomalous spectrum in the Schumann resonance band (generally below 50 Hz) to short term earthquake prediction [80–82]. The Schumann resonance is caused by lightning discharges in the cavity formed by the Earth surface and the ionosphere, showing a set of spectrum peaks in the extremely low frequency portion of the Earth’s electromagnetic field spectrum, as shown in Fig. 1.68. However, the physical mechanisms involved in this method are not clear and the observations are not fully conclusive.

Despite of various earthquake prediction methods presented above, since the prediction of earthquakes is far above the concurrent human knowledge and technology, most scientists still believe that human beings cannot predict

Fig. 1.68 The spectrum peaks of the Earth’s electromagnetic field showing different orders of Schumann resonances



earthquakes with any certainty. Scientifically, this is because when the strain energy is built up on a fault, the fault normally becomes unstable; with the great complexity of the fault rupturing mechanism, any small background earthquake may or may not continue rupturing and turning into a large earthquake [71]. Therefore, only mitigation measures not including evacuation can be taken to avoid earthquake induced damage.

1.8.2 Earthquake Forecast

It is important to distinguish earthquake forecasting from earthquake prediction. The former is a probabilistic assessment of general earthquake hazard, including the frequency and the magnitude of damaging earthquakes, in a given area over periods of years or decades [83]. The latter one is basically similar to a weather forecast, and aims to predict a certain earthquake. Prediction needs to fulfil certain criteria: it must be precise enough to warrant the cost of increased precautions, including the disruption of ordinary activities and commerce; timely enough so that preparations can be made; and reliable, as false alarms and canceled alarms are economically costly [84] and undermine confidence in the alarms, thereby degrading the effectiveness of any kind of warnings [85].

Regarding earthquake forecasting, scientists worldwide have made great efforts to narrow down the regions that are at high probability of earthquake occurrences and infrastructure damages. Based on the knowledge of previous earthquakes and geological records etc., and by implementing them into various probability distribution models, they provide long term (measured by for example 10–10,000 years of return period) forecasting of earthquakes in various output formats, such as earthquake hazard map etc. This will be elaborated in Chap. 9.

1.8.3 The Social and Economic Impact of Earthquake Predictions

The social and economic impact of earthquake predictions or relevant activities depends on the accuracy of the prediction, population size, economy in the region, severity of the predicted earthquake, length of the time, and—the most uncertain thing—how people react. From a physiological point of view, when under panic, human beings are more likely to be misled by incorrect information. A failed prediction can cause significant economic loss of a region. For example, in 1978,

two American Mexicans wrote a letter to the president of Mexico at that time that a strong earthquake and subsequent tsunami would occur in Oaxaca on 23 April 1978. This rumor was propagated and also appeared in the local newspapers, causing people to panic. Even though the rumor was criticized by the local government immediately, the associated economic loss in the area was equivalent to the loss that would have occurred in the case of a strong earthquake with magnitude 7.0. In another example, in the summer of 1982, based on the region's rising tempo of earthquake occurrences, volcanic history, shifting hot spring patterns and 10-in. uplift on the floor of an ancient volcanic caldera, the United States Geological Survey (USGS) issued a volcanic hazard notice for the eastern Sierra Nevada. This is estimated to have led to a 40 % decline in business in the resort town of Mammoth Lakes, California, in the summer of 1982. On the other hand, just 6 days before the deadly magnitude 6.3 L'Aquila earthquake (Fig. 1.69) occurred in central Italy on 6 April 2009, a group of geologists and volcanologists held an emergency meeting in L'Aquila to assess the potential risk posed by hundreds of seismic tremors of small magnitude, known as a swarm, that had been shaking the town and the surrounding area during the previous 3 months. The expert group finally concluded that it was impossible to determine whether the tremors would be followed by a devastating earthquake, which provided the local residents with a false sense of security. The earthquake that finally occurred led to 308 deaths, and half of the homes in the regional capital L'Aquila were destroyed, making this the deadliest earthquake to hit Italy since 1980. Seven experts involved in downplaying the risk during their assessment were given a six-year prison sentence in October 2012 (Fig. 1.70).



Fig. 1.69 Building damage and collapse during the magnitude 6.3 L'Aquila earthquake, 2009 (photo from [empasedecentrale](#))

COURT OF L'AQUILA**OPERATIVE PART OF THE JUDGEMENT**

ITALIAN REPUBLIC
IN THE NAME OF THE ITALIAN PEOPLE

Judge Dr. Marco Billi, on October 22nd 2012, delivered and published by reading the operative part of the judgement, the following

SENTENCE

Having considered articles 533 and 535 of the code of penal procedure, the defendants **BARBERI Franco, DE BERNARDINIS Bernardo, BOSCHI Enzo, SELVAGGI Giulio, CALVI Gian Michele, EVA Claudio and DOLCE Mauro** are declared guilty of the crime ascribed to them (articles. 113, 589 and 590 of the penal code) regarding the death of:

1. Bernardini Giovanna;

2. Giugno Francesco;

...

And, granted to all defendants extenuating circumstances, condemns them to six years in prison each.

Having considered article 535 of the code of penal procedure, imposes on all defendants, jointly, the payment of the process costs.

Having considered articles 29 paragraph 1 and 32 paragraph 3 of the penal code, declares the defendants **BARBERI Franco, DE BERNARDINIS Bernardo, BOSCHI Enzo, SELVAGGI**

Fig. 1.70 Excerpt from Italy's Major Risk Committee conviction sentence

1.9 Motivations of Offshore Earthquake Engineering

Offshore structures represent large capital investments. Structures are being placed in offshore areas worldwide and are being designed to withstand forces resulting from various types of environmental loads such as hurricanes, arctic storms, tidal currents, earthquakes, ice floes and icebergs. Moreover, offshore platforms are currently being placed in deeper waters and, therefore, have become larger, more complex, and more expensive.

As 70 % of the Earth's surface is covered by water, presently there are more than 10,000 fixed offshore platforms, 5000 subsea wells and 20,000 km of offshore pipelines installed worldwide [86], contributing to over 30 % of global oil and gas production. Even though breakeven oil price offshore (around 45–80 US\$/boe) is higher than its onshore counterpart, the contribution of offshore energy is expected to further increase. Moreover, offshore energy exploration is expanding to deep and ultra-deep waters worldwide.

A large number of earthquakes occur along the west of North and South America, in Southern Europe, the North Atlantic, North Africa, and South, North and East Asia. A large number of offshore installations are also located in those regions. Earthquakes potentially pose a great threat to offshore installations: to structures, equipment attached to structures, and to foundations. Recent geological studies have also identified the potential for significant or increased seismic activities in regions once regarded to be far removed from seismic hazard. In the event of major submarine earthquakes, in addition to the strong ground motion, high tsunami waves also pose a threat to coastal structures, even though only the largest of earthquakes that occur far from shore will be felt by people on land [87]. The macro-seismic data for offshore regions and knowledge about submarine earthquakes is at present insubstantial. For example, even using cutting-edge technology, the description of ocean deformation and damage due to offshore earthquakes is still a challenging and difficult task. In recent years the recognition of distinctive palaeotsunami deposits has been used to improve our understanding of former offshore earthquakes [88]. However, due to our limited knowledge of tsunami deposits and the connection of these to earthquakes, most of the effects of offshore earthquakes are still not known.

Even if the presently available knowledge of the effects of earthquakes on land provides valuable knowledge for the study of earthquakes offshore, the fact that both the supporting structures and the ground excitations are located at sea means that the earthquake engineering for offshore structures cherishes unique characteristics that will distinguish them from their onshore counterparts, which will be discussed briefly in Sect. 2.3. However, the current offshore structural design codes and practices devote far more efforts to structural assessments due to wave and wind effects than those due to earthquakes, even though the latter may be the predominant challenge for some structures and in certain regions. This is partially because the majority of offshore structures have been built in earthquake-quiet areas (with only around 100 offshore template-type platforms installed in seismically active regions [89, 90]). However, seismicity studies of the Earth show that many areas of the ocean are seismically active, and a high percentage of all earthquakes occur in the circum-Pacific belt including many on or near the continental shelf [91]. There are also numerous other earthquakes recorded having occurred under the continental shelf, in marginal seas and deep ocean areas [92]. Moreover, the increasing energy crunch and impending future shortage have spurred an upsurge in interest in developing the potential oil reserves in strong earthquake prone areas, such as Sakhalin area.

If the seismicity in the relevant area is upgraded due to inadequate consideration of ground motions at the time when an offshore structure is designed, or the occurrence of damage, corrosion or fatigue, this may lead to a reduced capacity for aging platforms. Existing offshore structures may then have inadequate capacity with regard to seismic resistance. In order to design and maintain offshore structures and non-structural components with sufficient reliability and low enough levels of uncertainty, the evaluation of loads and structural performance in the event of offshore earthquakes is important. On the other hand, the engineering applications

for designing earthquake resistant structures are, in many ways, more of an art than a science, and both academic knowhow and professional experience play an important role. By incorporating the more advanced knowledge of earthquake engineering into the experiences accumulated from engineering applications, there is a margin to further reduce the uncertainty. As a result of this, more cost-effective and safer designs can then be achieved.

Furthermore, the business interruption losses due to the damage of offshore facilities may be enormous. This has been witnessed in offshore facility failures due to other natural disasters. For example, after Hurricane Ivan in 2004, business interruption represented almost two-thirds of the ultimate paid loss for the offshore energy market.

For fixed marine structures, structural integrity due to earthquake loading is obviously an important factor to evaluate. Furthermore, as the marine risers (pipes used to deliver fluid, gas, electrical signals or power from the seabed and upward) made of steel have very low structural strength against lateral loading unless they are tensioned, it is therefore important to maintain the upper end tension at a certain level under all loading conditions, irrespective of platform motions, dynamic riser response and internal flow parameters. The tensioner system will therefore act as a heave compensating system with an adequate stroke capacity and ability to maintain a near constant tension. If the relative platform/riser motion exceeds the stroke capacity, unwanted loss or increase of tension will occur. Such situations may result in excessive bending stresses in the riser, excessive rotations of the ball joint or excessive riser tension, potentially causing damage to the well template or the riser tensioning system, and an enhancement of the mechanical interaction between neighboring risers or between the riser and the platform in a negative manner [93]. Therefore, consequences of such events due to seismic ground motions should be considered during the design of the risers.

In situations where floating structures are moored at a quay wall utilizing a tight mooring system such as tension leg platforms (TLPs) do, there is a possibility that the structure will suffer from the effects of seismic motions at the seabed mainly in the horizontal directions [94], even though TLPs may show a favorable response subject to earthquake loading combined with wave loading [95]. Riser stroke, tether rotation angle and similar geometric allowances shall be sufficient. Moreover, the foundation for mooring anchors of floating structures, such as an anchor pile as shown in Fig. 1.71, can also be subject to kinematic loading [96], which further challenges the reliability of the mooring solution.

Even if floating structures are considered to be isolated from the horizontal seismic motions, earthquake induced shocks have been reported but rarely with associated damage. The longitudinal (compressive) P-wave generated vertical seismic motions at seabed/riverbed/lakebed can propagate through waters and result in vertical shocks (hydrodynamic pressure) applied on ships, submerged structures, submarines, and other floating offshore structures. These are often referred to as seaquakes. Phenomena due to seaquakes have been described by ship crews as, “The ship struck an unknown shoal or rocks,” “A sunken vessel re-floated and collided against the ship,” “We saw an underwater eruption” and so on [97].

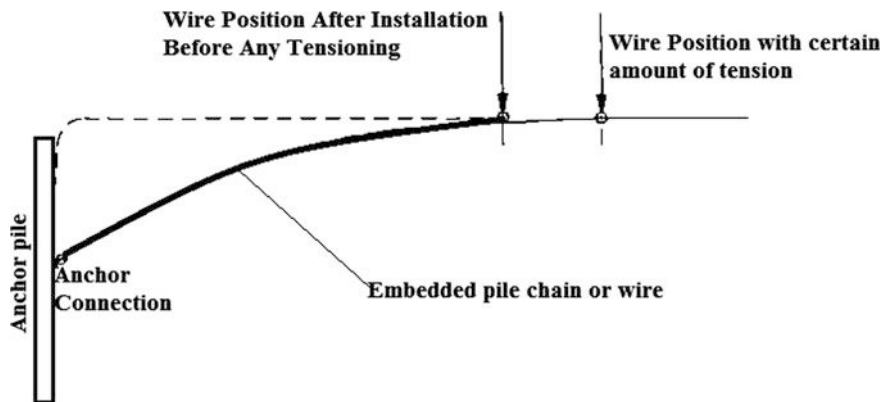


Fig. 1.71 An example of a typical anchor pile with pile chain or wire. The anchor pile can potentially be subject to seismic loading

Thousands of seaquake occurrences are known and occasionally listed in the casualty reports of Lloyd's List and other sources. For example, on 28 February 1969, a 32,000 ton Norwegian motor tanker 'Ida Knudsen' sailed in ballast from Lisbon to the Persian Gulf. She experienced "violent vertical shock" lasting for around 10 s off the coast of Portugal, even though the wave height and wind speed at that time were rather mild. The vertical shock led to serious damage to her structure and function in the hull, superstructure, machinery and other equipment [98]. The ship was condemned as a total loss, sold "as is" for only US\$ 730,000, and rebuilt as *Petros Hajikyriakos* (Fig. 1.72). This accident was found to be caused by a surface wave magnitude 7.8 earthquake with an epicenter offshore from Gibraltar, which is only 20 km from where the ship was damaged. Therefore, it is obvious that the ship damage was related to the seaquake. The response of floating



Fig. 1.72 MS Petros Hajikyriakos (photo by Frost Walter Edwin)

structures to seaquakes depends on the frequency of seismic waves and the depth of water. In water with a shallow depth and a flat seabed of an open sea area, a floating structure makes almost the same movements as that of the seabed motions. In deep waters or where the seismic motions are dominated by high frequency in relation to the compressibility of the water, the response of a floating structure due to seaquake is quite different from the seismic motion at seabed. Furthermore, the seaquake response of TLPs (Fig. 2.1) is higher than that without the tension leg system [99]. For submerged floating tunnels (Fig. 1.73) with moorings secured at anchor bars at seabed, the effects of seaquake (water transfers the seabed motion to the tunnel structure with hydrodynamic pressures on it) can be more significant than that of the seabed seismic motions (vertical mooring transfer seabed motions to the tunnel structure) [100]. In offshore regions with high seismicity, extreme displacements and shock waves due to seaquakes are often of primary interest in the design of a taut mooring system, which arrives at the seabed with an angle, indicating that in a taut leg mooring the anchor point at seabed has to be capable of resisting both horizontal and vertical forces.

For offshore installations near coasts and coastal infrastructures, not only severe seismic ground motion but also high tsunami waves may threaten the safety of the structures. Tsunami waves, which are generated by the abrupt deformation of the sea floor and especially the vertical displacement of the overlying water, may cause damage to both fixed and floating structures [101]. Even though the height of tsunami waves is generally not greater than that of a storm wave, they have much greater power to damage structures. They can move entire structures off their foundations and carry them inland, damage buildings through impact with vessels carried from offshore and other debris accumulated as the wave advances inland, undercut foundations and pilings with erosion caused by receding waves, overturn structures by suction of receding or thrust of advancing waves, and cause the impact

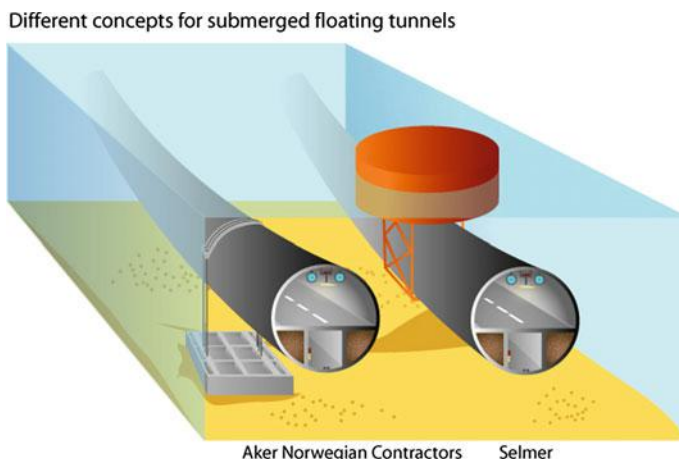


Fig. 1.73 Submerged floating tunnels with a vertical mooring (*left*) or floating (*right*) solution

of large ships with docks during oil or cargo transfer operations, often leading to fires. Tsunami also poses a great threat to human life and infrastructure. For example, the 10th strongest tsunami of the 1990s took more than 4000 lives [102]. On 26 December 2004, a great earthquake with a magnitude of 9.3 occurred 150 km off the west coast of the Indonesian island of Sumatra. The quake generated the most destructive tsunami (Fig. 1.74) ever in Southeast Asia, causing a loss of 225,000 lives and US\$ 13 billion in damage, affecting 11 countries bordering the Indian Ocean. In regions with high seismicity such as Sakhalin in Russia and Alaska in the USA, where more and more offshore infrastructures are being constructed, the potential risk from tsunami and earthquakes is also significant. For example, the powerful earthquake and tsunami in North Kurilsk of Sakhalin in 1952 damaged the region and caused a great number of fatalities. More recently, a magnitude 9.0 earthquake hit the offshore area near Sendai, north-east Japan on 11 March, 2011, triggering a tsunami with a maximum height of more than 15 m that caused a loss of more than 20,000 lives and US\$ 200 billion.

For submarine systems, earthquakes also pose a potential threat in the form of strong ground motions, soil liquefaction, and the dynamic impact from soil sliding due to nearby slope instability.

Along with fixed and floating offshore structures used in oil and gas industries, offshore bridges (Fig. 1.75) have seen significant development over the last 70 years. In recent decades, more sophisticated concepts have been developed, such as immersed tube, undersea tunnel and submerged floating tunnel, as shown in Fig. 1.76. However, various levels of damage to offshore bridges during earthquakes have been reported, with an example shown in Fig. 1.77. In addition, compared to the bridges on land, such as river bridges, offshore bridges have their

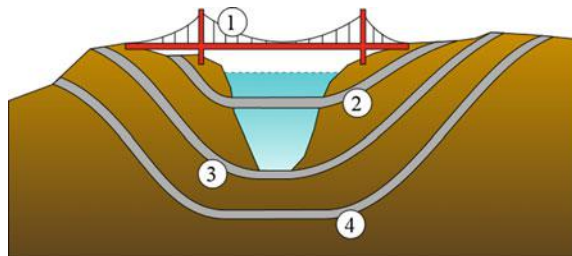


Fig. 1.74 Tsunami at Ao Nang, Thailand during the 2004 Indian Ocean earthquake and tsunami (photo courtesy of David Rydevik)



Fig. 1.75 Examples of offshore bridges

Fig. 1.76 Water-spanning structures: 1 Suspension bridge 2 Submerged floating tunnel 3 Immersed tube 4 Undersea tunnel



unique characteristics in the aspects of design and construction complexity, environmental loading, geotechnical conditions, corrosion protection measures, maintenance, and the consequences in case a bridge collapses. Therefore, it is of great importance to make a dedicated evaluation due to all action effects including seismic loading.

Since earthquakes, seaquakes and tsunamis have great potential to cause damage to offshore infrastructures, it is important to develop technology for earthquake detection, description and evaluation for the sake of eventually obtaining earthquake resistant forms and techniques of construction for offshore platforms, offshore bridges, and oil and gas exploration projects, and to provide basic material and theoretical support for further improvement of specifications and standards.



Fig. 1.77 Collapse of deck of old San Francisco Bay Bridge during the moment magnitude 6.9 Loma Prieta earthquake of 1989 (courtesy of USGS)

1.10 Closing Remarks

With the continuing expansion of cities and construction of infrastructures over areas (both on land and offshore) at risk from earthquakes, volcanic eruptions, and tsunamis [103], earthquake engineering is ever more challenged to find ways to enhance the protection of the populations and properties at risk through more robust and resilient infrastructure design, more effective warning systems, and more realistic evacuation or shelter-in-place plans.

On the other hand, as a scientific topic, earthquake engineering is by no means fully understood (and perhaps never will be). As it deals with issues on the basis purely of the evidence and phenomena that have occurred, and it is analyzed and presented within our capability of relevant knowledge accumulation, understanding, and intelligence, it is important to be humble when carrying out research and engineering associated with earthquake engineering. To manage or even change things that are beyond our knowledge is rather risky.

In conclusion, it is obvious that strong earthquakes will continue to occur and cause disasters. Assessing earthquake risk and improving the engineering designs may be the only way for human beings to mitigate future disasters. Earthquakes by themselves do not kill people; unsafe structures do.

References

1. US Geological Survey (USGS) (1997) Earthquakes in history
2. Coburn A, Spence R (1992) Earthquake protection. Wiley, New York

3. Elnashai AS (2002) A very brief history of earthquake engineering with emphasis on developments in and from the British Isles. *Chaos Solitons Fractals* 13:967–972
4. Kitagawa Y, Hiraishi H (2004) Overview of the 1995 Hyogoken Nanbu earthquake and proposals for earthquake mitigation measures. *J Jpn Assoc Earthq Eng* 4(3) (Special Issue):1–29
5. Earthquakes, Volcanoes, and Tsunamis, Resources for Environmental Literacy (2007) National Science Teachers Association. NTA Press, Houston
6. Munich Re Group (1999) Topics 2000: natural catastrophes—the current position. Münchener Rückversicherungs-Gesellschaft, München
7. FEMA P-749 (2010) Earthquake-resistant design concepts. Washington, DC
8. Kramer S (1996) Geotechnical earthquake engineering. Prentice Hall, London
9. Gioncu V, Mazzolani F (2010) Earthquake engineering for structural design. CRC Press, Boca Raton
10. Bachmann H (2003) Seismic conceptual design of buildings—basic principles for engineers, architects, building owners, and authorities, Swiss Federal Office for Water and Geology and Swiss Agency for Development and Cooperation. BWG, Bern
11. Lincoln SF (2006) Challenged earth: an overview of humanity's stewardship of earth. World Scientific Publishing Co., New Jersey
12. Jia J (2014) Essentials of applied dynamic analysis. Springer, Heidelberg
13. Fink G (2010) Stress of war, conflict and disaster. Elsevier Academic Press, Amsterdam
14. FEMA (2012) Course presentation, earthquake basics: science, risk, and mitigation. FEMA, Emmitsburg, 19 July 2012
15. Bai Y, Bai Q (2005) Subsea pipelines and risers, 2nd edn. Elsevier Science, Amsterdam
16. Reitherman R (2008) International aspects of the history of earthquake engineering. Earthquake Engineering Research Institute
17. USGS (2008) The “plus side” of volcanoes
18. University of Bergen (2009) Geoviten-Ekstern, Department of Earth Science, University of Bergen, vol 3, 2009
19. Tilling RI (1985) Volcanoes: USGS General Interest Publication
20. Perkins S (2011) Are larger earthquakes a sign of the times? Nat News
21. Reid HF (1910) The mechanics of the earthquake, the California earthquake of April 18, 1906, report of the State Investigation Commission, vol 2. Carnegie Institution of Washington, Washington
22. Murty CVR (2001) Earthquake tip. Indian Institute of Technology, Kanpur, India
23. Towhata I (2008) Geotechnical earthquake engineering. Springer, Berlin
24. Donne DD, Harris AJL, Ripepel M, Wright R (2010) Earthquake-induced thermal anomalies at active volcanoes. *Geology* 38(9):771–774
25. Hill DP, Pollitz F, Newhall C (2002) Earthquake-volcano interactions. *Phys Today* 55(11): 41–47. American Institute of Physics
26. Rastogi BK, Gupta HK (1975) Dams and earthquake. Elsevier, Amsterdam
27. Gupta HK (1983) Induced seismicity hazard mitigation through water level manipulation: a suggestion. *Bull Seismol Soc Am* 73:679–682
28. Nelson SA (2011) Earthquake prediction, control and mitigation (lecture notes). Tulane University, Sep 2011
29. Kerr RA, Stone R (2009) A human trigger for the great quake of Sichuan? *Science* 323 (5912):322
30. Moore M (2009) Chinese earthquake may have been man-made, say scientists. *The Telegraph*, 2 Feb 2009
31. Franiere SL (2009) Possible link between dam and China quake. *The New York Times*, 5 Feb 2009
32. Cryoseisms in Maine (2005) Maine Geological Survey, the State of Maine, Oct 2005
33. Sminchak J, Gupta N, Byrer C, Bergman P (2001) Issues related to seismic activity induced by the injection of CO₂ in deep saline aquifers. In: Proceedings of first national conference on carbon sequestration, Washington

34. Vidic RD, Brantley SE, Vandenbossche JM, Joxtheimer D, Abad JD (2013) Impact of shale gas development on regional water quality. *Science* 340(6134):826–836
35. Rubinstein JL, Mahani AB (2015) Myths and facts on wastewater injection, hydraulic fracturing, enhanced oil recovery, and induced seismicity. *Seismol Res Lett* 86(4):1060–1067
36. Silverstein K (2014) Shale oil and gas: potential for earthquakes could cause sector to lose footing. *Forbes Business*, 5 June 2014
37. Ellsworth WL, Hickman SH, Lleons AL, McGarr A, Michael AJ, Rubinstein JL (2012) Are seismicity rate changes in the midcontinent natural or manmade? Session: the M5.8 Central Virginia and the M5.6 Oklahoma earthquakes of 2011. Annual meeting of Seismological Society of America, San Diego, CA, 17–19 Apr 2012
38. Nikiforuk A (2014) Swarms of earthquakes shake up shale gas fields. *The Tyee*, 31 Jan 2014
39. Shachman N (2009) Strange new air force facility energizes ionosphere, fans conspiracy flames. *Wired Magazine*, 20 July 2009
40. HAARP (2009) Purpose and Objectives of the HAARP Program. <http://www.haarp.alaska.edu>
41. Hunt AG, Malin PE (1998) Possible triggering of Heinrich events by ice-load-induced earthquakes. *Nature* 393:155–158
42. Inman M (2008) Melting ice sheets can cause earthquakes, study finds. *National Geographic News*, 14 Mar 2008
43. Morner NA (1978) Faulting, fracturing, and seismicity as functions of glacio-isostasy in Fennoscandia. *Geology* 6(1):41–45
44. Irvine T (2006) Ice quakes. *Vibration Data Newsletter*, 2006
45. Ekström G, Nettles M, Tsai VC (2006) Seasonality and increasing frequency of Greenland glacial earthquakes. *Science* 311(5768):1756–1758
46. Lacroix AV (1980) A short note on cryoseisms. *Earthquake Notes*
47. Ebel JE, Bedell R, Uruzua A (1995) A report on the seismic vulnerability of the State of Vermont, *Geology of Mineral Resources*, Vermont Geological Survey, July 1995
48. <http://ww.geology.ptt.edu>
49. Network (2011) Earth science (lecture notes), <http://www.sleepingdogstudios.com>
50. Spaulding NE, Namowitz SN (2005) Earth science. McDougal Littell, Boston
51. McIntyre M, Eilers HP, Mairs J (1991) Physical geography. Wiley, New York
52. Srbulov M (2008) Geotechnical earthquake engineering: simplified analyses with case studies and examples. Springer, Heidelberg
53. Fryer P, Hussong DM (1981) Seafloor spreading in the Mariana Trough: results of Leg 60 drill site selection surveys. In: Hussong DM, Uyeda S et al (eds) *Proceedings of the Deep Sea Drilling Project*, pp 45–55
54. USGS (1997) How earthquakes happen
55. www.norsar.no
56. Klemencic R, Davies D, Johansson O, Beaman D (2012) Embodied carbon and the case for longevity. Ninth CTBUH World Congress, Shanghai
57. Beer M, Kougioumtzoglou IA, Patelli E, Au IS-K (eds) (2015) *Encyclopedia of earthquake engineering*, 1st edn. Springer, Heidelberg
58. Lee WHK, Jennings P, Kisslinger C, Kanamori H (2002) International handbook of earthquake and engineering seismology, part A: international geophysics. Academic Press, London
59. Anibal C, Miranda GJ, Humberto V (2014) Structural rehabilitation of old buildings. Springer, Heidelberg
60. Houben H, Guillard H (1994) Earth construction: a comprehensive guide. Practical Action, London
61. De Sensi B (2003) Terracruda, la diffusione dell'architettura di terra, www.terracruda.com/architetturadiffusione.htm
62. Ilki A, Karadogan F, Pala S, Yuksel E (2009) Seismic risk assessment and retrofitting: with special emphasis on existing low rise structures (Geotechnical, Geological and Earthquake Engineering), 1st edn. Springer, Heidelberg

63. Sahin C (2014) Seismic retrofitting of existing structures. Portland State University
64. National Earthquake Technical Assistance Program (2012) New earthquake basics training course (lecture notes), emergency management institute, the federal emergency management agency (FEMA). FEMA, Emmitsburg
65. Roeloffs E, Quilty E (1997) Water level and strain changes preceding and following the August 4, 1985 Kettleman Hills, California, earthquake. *Pure Appl Geophys* 149:21–60
66. Tsunogai U, Wakita H (1995) Precursory chemical changes in ground water: Kobe earthquake, Japan. *Science* 269(5220):61–63
67. Wakita H (1996) Earthquake chemistry II, collected papers, 2nd ed. Laboratory for Earthquake Chemistry, Faculty of Science, University of Tokyo, Tokyo
68. Talwani P (1971) Prediction of an earthquake at Blue Mountain Lake
69. Kirschvink JL (2000) Earthquake prediction by animals: evolution and sensory perception. *Bull Seism I Soc Am* 90:312–323
70. Grant RA, Halliday T, Balderer WP, Leuenberger F, Newcomer M, Cyr G, Freund FT (2011) Ground water chemistry changes before major earthquakes and possible effects on animals. *Int J Environ Res Public Health* 8:1936–1956
71. Ludwin R (2004) Earthquake prediction. The Pacific Northwest Seismic Network, 2004
72. Gray C (1996) Review of two methods of predicting earthquakes, UER 1996. Technical communication. University of Wisconsin-Madison
73. Toshi A (1982) Earthquake prediction techniques: their application in Japan. University of Tokyo Press, Tokyo
74. Hough S (2009) Predicting the unpredictable: the tumultuous science of earthquake prediction. Princeton University Press, Princeton
75. Varotsos P, Alexopoulos K, Nomicos K (1981) Seven-hour precursors to earthquakes determined from telluric currents. *Praktika Acad Athens* 56:417–433
76. Varotsos P, Alexopoulos K, Nomicos K, Lazaridou M (1986) Earthquake prediction and electric signals. *Nature* 322(6075):120
77. Mulargia F, Gasperini P (1992) Evaluating the statistical validity beyond chance of “VAN” earthquake precursors. *Geophys J Int* 111:32–44
78. Geller RJ (1996) Debate on evaluation of the VAN method: Editor’s introduction. *Geophys Res Lett* 23(11):1291–1293
79. Varotsos P, Sarlis N, Skordas E (2011) Natural time analysis: the new view of time; precursory seismic electric signals, earthquakes and other complex time series. Springer, Heidelberg
80. Hayakawa M, Ohta K, Nickolaenko AP, Ando Y (2005) Anomalous effect in Schumann resonance phenomena observed in Japan, possibly associated with the Chi-chi earthquake in Taiwan. *Ann Geophys* 23:1335–1346
81. Hayakawa M, Ohta K, Sorokin VM, Yaschenko AK, Izutsu J, Hobara Y, Nickolaenko AP (2010) Interpretation in terms of gyrotropic waves of Schumann-resonance-like line emissions observed at Nakatsugawa in possible association with nearby Japanese earthquakes. *J Atmos Solar Terr Phys* 72:1292–1298
82. Fraser-Smith AC (2009) The ultralow-frequency magnetic fields associated with and preceding earthquakes. In: Hayakawa M (ed) Electromagnetic phenomena associated with earthquakes. Transworld Research Network, Trivandrum, pp 1–20
83. Kanamori H (2003) Earthquake prediction: an overview. *Int Handbook Earthq Eng Seismol Int Geophys* 616:1205–1216
84. Thomas LM (1983) Economic impacts of earthquake prediction. In: Proceedings of the seminar on earthquake prediction case histories, Geneva, 12–15 Oct 1982, UNDPRO, pp 179–185
85. Atwood LE, Marie AM (1998) Exploring the “cry wolf” hypothesis. *Int J Mass Emerg Disasters* 16(3):279–302
86. Quick Stats (2015) Offshore Engineer, 24 Jan 2015
87. Marrow PC (1992) Seismic monitoring of the north sea—prepared by global seismology for the health and safety executive. *Health Saf Executive OTH* 90:323

88. Dawson AG (1999) Linking tsunami deposits, submarine slides and offshore earthquakes. *Quat Int* 60(1):119–126
89. Tabeshpour MR, Komachi Y, Golafshani AA (2012) Assessment and rehabilitation of jacket platforms. In: Moustafa A (ed) *Earthquake-resistant structures—design, assessment and rehabilitation*. Intech, Rijeka
90. Komachi Y, Tabeshpour MR, Golafshani AA, Mualla I (2011) Retrofit of Ressalat jacket platform (Persian Gulf) using friction damper device. *J Zhejiang Univ SCI A* 12(9):680–691
91. Chandrasekaran AR, Krishna J (1976) Elements of earthquake engineering. Sarita Prakashan, India
92. Puri VK, Prakash S (1991) Proceedings of the second international conference on recent advances in geotechnical earthquake engineering and soil dynamics, St. Louis, Missouri
93. Larsen CM (1993) Analysis of tensioner system stroke for marine risers. Technical report STF70 F93011, SINTEF structures and concrete
94. Hamamura K (1987) Can earthquake excitations be escape on free surface? Investigation of seaquake, *Fune-No-Kagaku* vol 40, pp 58–61
95. Chandrasekaran S, Gaurav (2008) Offshore triangular tension leg platform earthquake motion analysis under distinctly high sea waves. *J Ships Offshore Struct* 3(3):173–184
96. Jia J, Dynamics S, Modeling F (2016) Off-shore and earthquake engineering. Springer, Heidelberg
97. Okamoto K, Sakuta M (1993) Effects of seaquakes on floating structures. In: Narendra K (ed) *Recent advances in marine science and technology*, Saxena. Pacon International, Honolulu, Hawaii
98. Ambraseys N (1985) A damaging seaquakes. *Earthq Eng Struct Dyn* 13:421–424
99. Yoneyama H, Nozu A (1996) Experimental study on seaquake response characteristics of floating structures. In: 11th world conference on earthquake engineering, paper no. 763, Acapulco, Mexico, 23–28 June 1996
100. Perotti F, Shi C, Domaneschi M, Martinelli L (2013) The non-linear dynamic response of submerged floating tunnels to earthquake and seaquake excitation. *Strait Crossings*, Bergen Norway, 16–19 June 2013
101. Söding H, Blok JJ, Chen HH, Hagiwara K, Isaacson M, Jankowski J, Jefferys ER, Mathisen J, Rask I, Richer JP, Römelin JU, Varsta P (1990) Environmental forces of offshore structures: a state-of-the-art review. *Mar Struct* 3(1):59–81
102. FEMA, Guidelines for design of structures for vertical evacuation from Tsunamis. Federal Emergency Management Agency (FEMA), USA, 2008
103. United Nations Educational, Scientific and Cultural Organization (UNESCO) (2010) Engineering: issues, challenges and opportunities for development

Chapter 2

Offshore Structures Versus Land-Based Structures

2.1 Introduction to Offshore Structures

2.1.1 Offshore Platforms

Offshore structures (Fig. 2.1) with their facilities are used to drill wells, to extract and process oil and natural gas, or to temporarily store product until it can be brought to shore for refining and marketing. In many cases, an offshore platform also contains facilities (e.g., living quarters) to house the work-force as well. They are defined by either their functions or their circumstances and configurations [1]. A brief review of the different types of platforms with their structural forms and uses, and the developments, are presented in a few literatures [2–4].

The functions of an offshore structure may be one of the following (even though multiple functions may be possible for a structure):

- Exploratory Drilling Structures: a Mobile Offshore Drilling Unit (MODU) configuration is largely determined by the variable deck payload and transit speed requirements.
- Production Structures: a production unit can have several functions, e.g., processing, drilling, workover, accommodation, oil storage and riser support.
- Storage Structures: used for storing the crude oil temporarily at the offshore site before its transportation to the shore for processing.

Depending on the circumstances and configuration, offshore platforms may be fixed to the ocean floor, which is typically referred to as fixed offshore platforms, including the conventional fixed jacket platforms (shown in Fig. 2.1) for a water depth of less than 400 m, jackups (shown in Fig. 2.34) being placed in relatively shallow waters (less than 150 m), compliant piled tower (shown in Fig. 2.1) that can be used for water depths up to 900 m, and an artificial island (Fig. 2.2). Offshore platforms may also be floating structures, including buoyant (e.g., semi-submersibles shown in Fig. 2.3, FPSO, and spars shown in Fig. 2.1) and

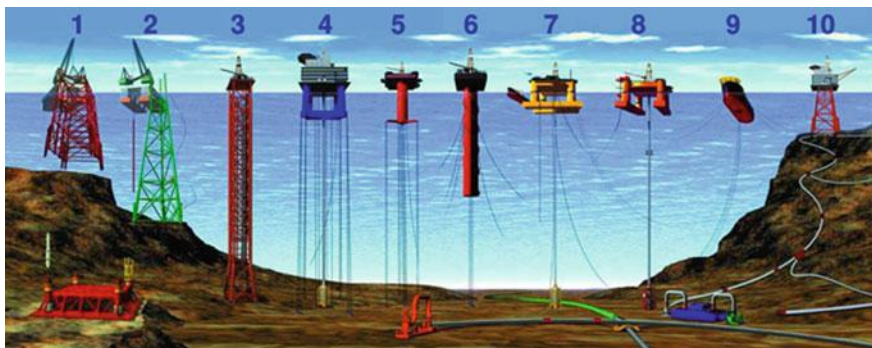


Fig. 2.1 Various types of offshore structures. 1 and 2 conventional fixed jacket platforms; 3 compliant piled tower; 4 and 5 vertically moored tension leg and mini-tension leg platform (TLP); 6 Single point anchor reservoir platform (SPAR); 7 and 8 semi-submersibles; 9 floating production, storage, and offloading facility (FPSO); 10 subsea completion and tie-back to host facility (courtesy of US National Oceanic and Atmospheric Administration)

Fig. 2.2 An artificial island (Northstar Island) for oil drilling in the Beaufort Sea



positively buoyant (e.g., tension leg platforms shown in Fig. 2.1). In addition, remote subsea wells, as shown in Fig. 2.4, may also be connected to a platform by flow lines and by umbilical connections. These subsea solutions may consist of one or more subsea wells, or of one or more manifold centers for multiple wells. It is noted that the function, water depth, and environmental loading are essential factors to influence the structural design concepts for offshore platforms.

For fixed offshore structures, they can be piled (Fig. 2.8) or gravity based (GBS, as shown in Fig. 2.9), or a compliant (number 3 in Fig. 2.1) or articulated structure. A significant advantage of fixed platforms is that they use conventional well systems that developed along with platforms, leading to an economical design until water depths increase to the point where the cost of the structure outweighs the savings from the well system. These platforms use the minimum possible amount of



Fig. 2.3 A floating drilling platform Aker H6e (courtesy of Aker Solutions)

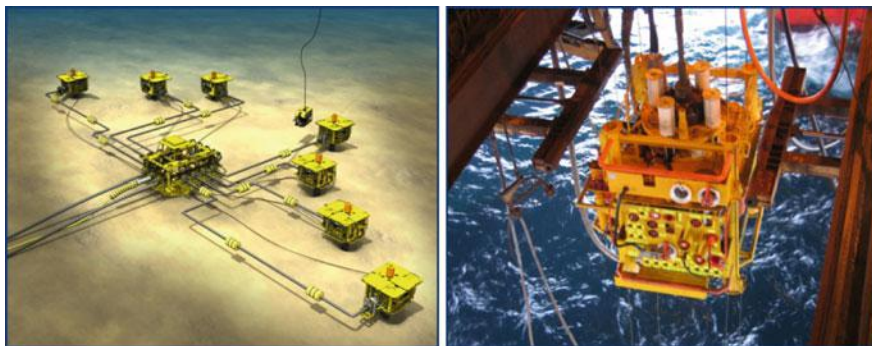


Fig. 2.4 Subsea wells (courtesy of Aker Solutions)

material and expose the least possible area to environmental loads. The most widely used fixed offshore structures are jacket structures as shown in Fig. 2.8. They are especially advantageous when operated at offshore sites with soft soil condition. The pile foundations supporting the jacket structures are put in place and connected to each leg to support the jacket. This leads to a transformation of the moment loading at mudline caused by lateral loading due to earthquake, or ocean wave and wind loading applied at superstructure, into axial forces in the jacket piles [5], as illustrated in Fig. 2.5. Therefore, jacket piles are usually insensitive to the lateral loads. Jacket piles can support a significant amount of load from substructure. Moreover, jacket structures can be constructed in sections and transported, making it more efficient for construction. Gravity based structures, which rely on the weight of the structure itself to resist the environmental loading, are also adopted, particularly in the North Sea. They are frequently installed at sites where driving piles

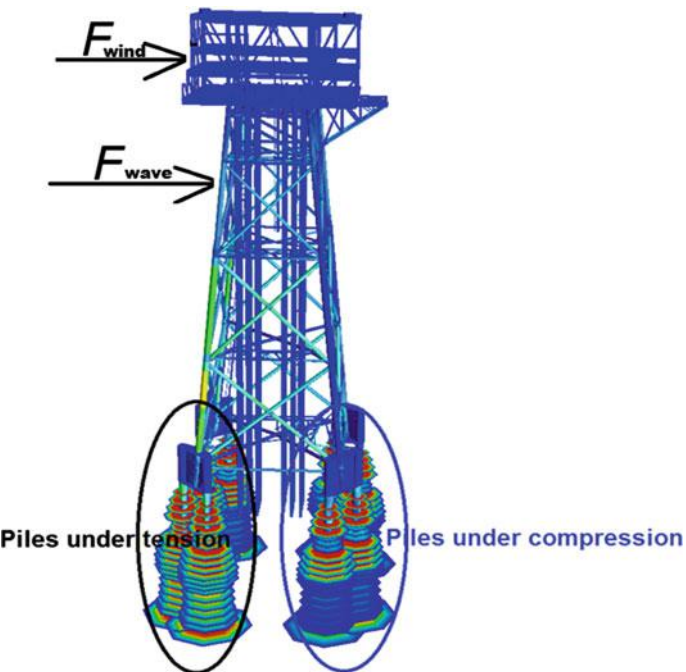


Fig. 2.5 Piles subjected to tensile and compressive axial loading due to the lateral wind and wave loading transferred from the *upper part* of the structure

becomes difficult. These structures have foundation elements that contribute significantly to the required weight and spread over a large area of the sea floor to prevent failure due to overturning moments caused by lateral loads. They are capable of supporting large topside loads during towing out, thus minimizing the hook-up work during installation. Moreover, their merits also include (1) construction onshore for transport; (2) towing to the site of installation; (3) quick installation by flooding; and (4) use of traditional methods and labor for installation [6]. GBS is typically constructed with reinforced concrete and consists of a large cellular base surrounding several unbraced columns that extend upward from the base to support the deck and equipment above the water surface. Gravity based platforms consist of production risers as well as oil supply and discharge lines contained in one of the columns; the corresponding piping system for exchange of water is installed in another column, and drilling takes place through the third column [6]. This particular type is referred to as a CONDEEP (concrete deep water) structure. Gravity based structures are particularly suitable to resist enormous horizontal loading such as ice loading, in which a jacket or a jackup structure would not offer the required global capacity to resist ice or ice ridge loading or is forced to limit operations (in case of a mobile jackup structure) to a short summer season, which may damage legs and/or unprotected conductors/risers (conductors/risers are

typically installed inside the concrete shaft in a GBS). It should also be noted that the gravity based platform can also be constructed with steel instead of concrete, such as the Maureen Alpha steel gravity platform in the United Kingdom. Table 2.1 lists the water depths of typical GBS platforms operated in the North Sea, with the highest one being Troll A platform (Fig. 2.6) with a total height of 481 m. It is operated at a water depth of 330 m, and has a bottom dimension of 160 m × 60 m and a natural period of 4 s. Troll A is also the tallest structure that has ever been moved on Earth.

As the water depth increases, bottom supported compliant structures are more economical. As this type of structure is rather flexible, they move with the dynamic environmental loads such as winds, waves and currents to a limited extent, rather than resisting them as a GBS or a jacket structure does. Therefore, the compliant platforms resist lateral environmental loading by their relative movements instead of their weight as a GBS structure does. These types of structures are attached to the seabed by means of tension legs, guy lines, flexible members or articulated joints. The buoyancy force or the force of elasticity of the axially stressed legs generates the restoring forces. As the system is not soft, the fundamental natural frequency remains low. The designs are technically and economically feasible as they increase

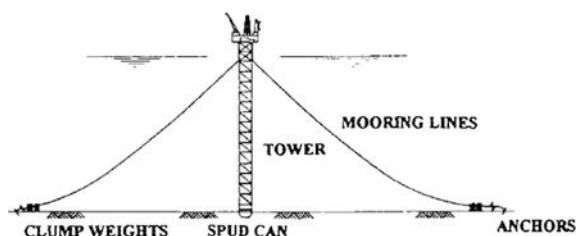
Table 2.1 Water depths of representative gravity based platforms installed in the North Sea

Platform	Water depth (m)
Troll A	330
Gulfaks A	133
Gulfaks B	133
Gulfaks C	214
Oseberg North	100
Oseberg A	100
Ekofisk 1	70
Draugen	251
Heidrun	350
Statfjord A	145
Statfjord B	145
Statfjord C	145
Frigg TP 1	104
Frigg TP 2	103
Frigg MCP01	94
Frigg CDP1	98
Frigg TCP2	104
Brent B	140
Brent C	141
Brent D	142
Cormorant A	149
Dunlin A	153
Beryl A	118

Fig. 2.6 Troll A platform

the natural periods of the structure to such an extent that typical storm wave periods are far below the natural periods of the structures. Examples of bottom supported compliant platforms are compliant towers (3 in Fig. 2.1), guyed towers (Fig. 2.7), buoyant towers, flexible towers, articulated towers, and hybrid compliant platforms. Given the discussion above, it would be assumed that the load distribution and transfer mechanism is quite different between the fixed and the compliant structures [7]: in a fixed structure the static and dynamic forces are almost all transmitted to the seafloor; while for the compliant structures, the horizontal dynamic loads are counteracted by the inertia forces. This reduces the internal forces in the structure as well as the support reactions. The vertical dynamic loads are transferred to the seafloor, much as with a fixed offshore structure (Figs. 2.8 and 2.9).

As the water depth further increases and the sites are sometimes located far off the continental shelf, floating structures are more used because they are economically attractive for deep water sites with a reduced structural weight compared to conventional fixed and bottom supported platforms. Floating structures resist loads by undergoing large excursions when subjected to environmental loads and thereby reducing the forces on the structures. However, as large motions are expected, geometric nonlinearity is an

Fig. 2.7 Illustration of a guyed tower

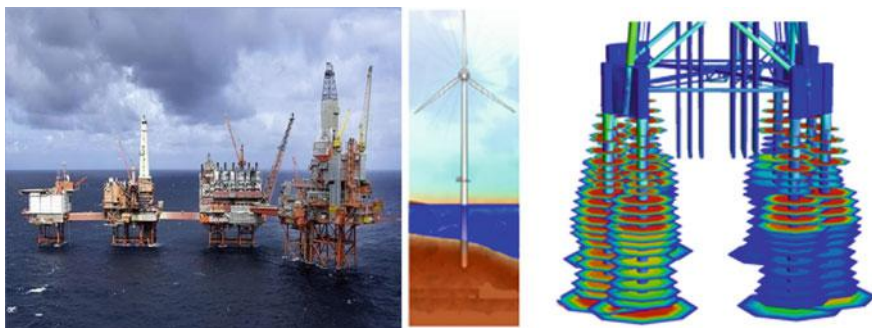
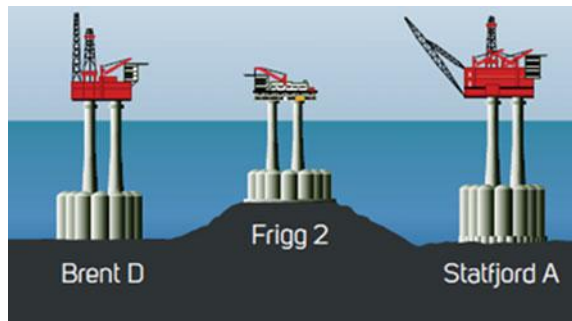


Fig. 2.8 Fixed jacket structures (*left*), pile foundations of a fixed monopile (*middle*) and of a jacket structure (*right*)

Fig. 2.9 Fixed GBS offshore structures with gravity based foundation design (courtesy of Aker Solutions)



important consideration in the analysis of floating structures. Floating structures are required to be moored in place. Subject to the environment loading, the floater remains within a specified circle of operation from a desired mean location, which is generally achieved by mooring lines or a dynamic positioning system [8]. Typical floating offshore structures include the semi-submersibles shown in Fig. 2.3, FPSO, and spars shown in Fig. 2.1, tension leg platforms (which are vertically restrained while horizontally compliant, permitting surge, sway and yaw motions) shown in Fig. 2.10 and tension buoyant towers. The selection process for the floater type generally depends on the following factors: well pattern, export methodology, service life and geographical region, gas to oil ratio, topside weight, well count and water depth. As floating structures have low stiffness, their natural periods of motions are higher than that of the wave loading, thus avoiding the resonance with wave loading. For example, typical natural periods of motions for a TLP are more than 100 s for surge and sway, more than 80 s for yaw, and 3–5 s for heave, pitch and roll.

For platforms operating in deep waters, since the distance between platforms and ports increases, deck spaces of the topside need to be designed with variable load capacities. For example, for drilling platforms, deck space is very important because more space is required for third-party equipment for well completion and

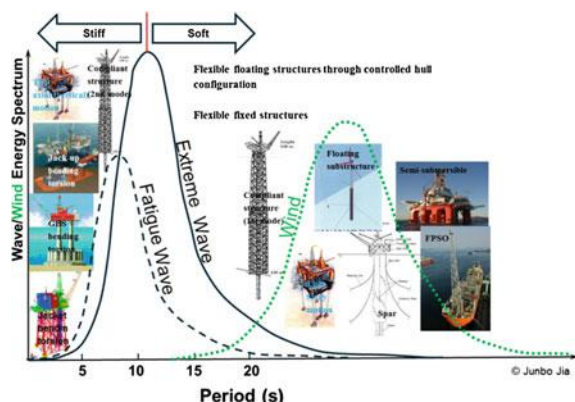
Fig. 2.10 A tension leg drilling platform (*left*) and a semi-submersible platform (*right*) (courtesy of Aker Solutions)



well testing activities, in addition to the space for drilling equipment. This typically requires that the topside be designed with variable load capacities between 10,000 and 20,000 t [6].

In addition to functionality, environmental loading and water depth, dynamic behavior and performance of each type of offshore structures also strongly influence the selection of structural form and design concept. As shown in Fig. 2.11, the natural periods corresponding to the global bending and global torsional vibrations for fixed offshore structures and the period of axial leg tension vibrations of TLPs should be below the period of ocean wave and wind loading, thus avoiding resonance conditions, which would otherwise cause excessive dynamic responses. On

Fig. 2.11 Accounting of dynamics in the design of offshore structures (from a lecture “Dynamic Analysis and Design of Offshore Structures” by the author at OMAE 2016, Pusan)



the other hand, to avoid resonance motion responses of floating structures due to wave loading (normally the dominating loads for offshore structural designs), they generally have natural periods of motions higher than the period of ocean wave loadings, even though they may potentially reach a resonance condition due to dynamic loading caused by wind turbulence.

Typically, the design of fixed offshore structures has to consider the impact from earthquakes. The design of TLP also needs to consider the influence from the seismic loading transferred to tension leg(s) and the response of connected floating structures.

2.1.2 Offshore Wind Turbine Substructures and Foundations

Offshore sites provide a reliable source of strong winds due to the cooling and heating effect of water and land. Moreover, wind turbulence offshore is generally lower than that of inland sites. Therefore, due to the higher wind speed and lower wind turbulence offshore than over adjoining land, in recent years, offshore wind farms have rapidly developed across the world, dominated by developers in Europe and East Asia. In the meantime, the United States is also catching up by completing its first offshore wind farm with five steel jacket substructures (each carry a 6 MW wind turbine), installed at the Block Island Wind Farm site in December 2015. So far, more than 80 % of the operated and currently planned offshore wind farms are located in Europe.

A wind turbine-supporting structure system includes both rotor-nacelle assembly and support structure. The former includes rotor (blades and hub) and nacelle assembly (all components above tower except the rotor, including driven train, bed plate, yaw system, and nacelle enclosure, etc.). The latter include a tower (connecting the substructure to rotor-nacelle assembly), substructure (for fixed substructure, it extends upwards from the seabed and connects the foundation to the tower; for floating substructure, it is the part below the tower), and foundation (transferring various types of load acting on the structure into the seabed soil).

The substructures and foundations for offshore wind turbines (OWTs), as shown in Fig. 2.12, can be either fixed to the seabed, bottom supported compliant structures, or floating structures.

The types of fixed offshore structures can be gravity foundation, monopile, tripod-pile, tripile, jacket(braced frame)-pile, and suction bucket, as shown in Fig. 2.13. The basic types of floating structure concepts used for offshore wind turbines are TLP (Fig. 2.14), spar (Fig. 2.15), and semi-submersibles (Fig. 2.16). The world's first floating wind farm Hywind Scotland is planned to be completed by 2017. It lies 25 km off the northeast coast of Scotland near Peterhead and consists of five 6 MW spar type floating turbines operating in water depths of between 95 and 120 m. The concept designs using bottom supported compliant



Fig. 2.12 Wind turbines with their substructures and electrical substation located in the North Sea (license under CC BY-SA 3.0, by StekruBe)

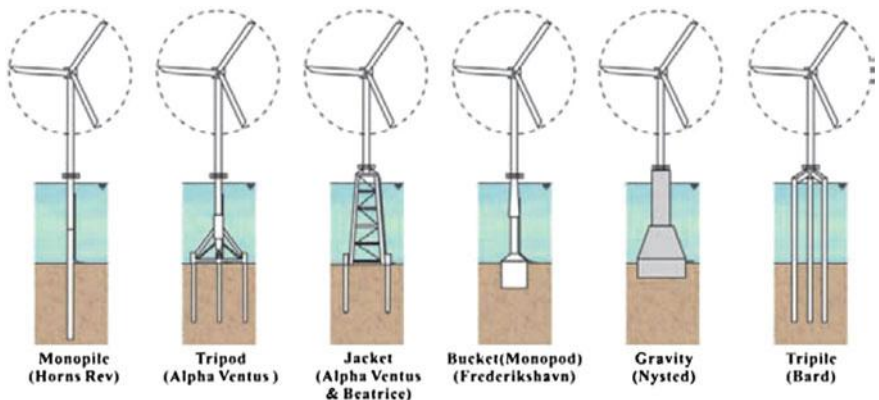


Fig. 2.13 The types of existing substructures and foundations for fixed offshore wind turbines [16]

Fig. 2.14 Schematic illustration of a TLP used for an OWT substructure

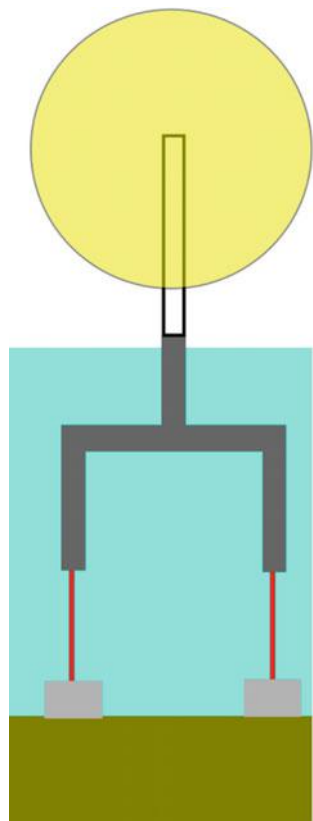


Fig. 2.15 Schematic illustration of a single floating cylindrical spar buoy moored by catenary cables

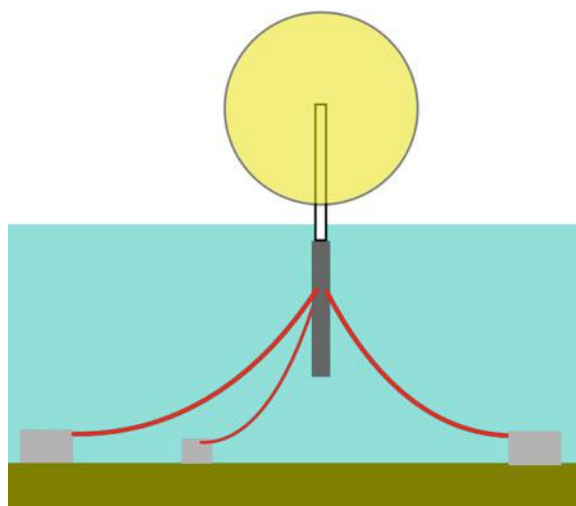


Fig. 2.16 WindFloat, which is a semi-submersible structure for an OWT operating at a rated capacity of 2 MW approximately 5 km offshore of Aguçadoura, Portugal (under license CC BY-SA 3.0 by untrakkdrover)



structures for OWTs have not received much popularity, because the low frequency wind turbulence may interfere with the natural frequency of the compliant structure, potentially causing resonance. Moreover, the interaction between a compliant structure and the wind turbine can exert significant forces on the top of the relatively flexible structure, leading to significant deflections of the compliant structure.

Monopile currently represents the most common substructure application for OWT in shallow waters. It is a relatively simple design in which the tower to supporting turbines, made up of steel pipe, is supported by the monopole, either directly or through a transition piece. The vertical loads are transferred to the seabed by shaft friction and tip resistance. The vertical bearing capacity is therefore largely determined by the diameter of the mono pile (typically between 2 and 6 m), which attracts the lateral hydrodynamic loads due to wind, waves and current. These horizontal loads dominated by bending moments will be further transferred to the soil. Monopile is so far a cost competitive solution and suitable for shallow waters up to 30 m. One critical issue for the design of monopiles is the consideration of cyclic behavior of piles with large diameter. Investigations have shown that the horizontal deflections of large diameter monopiles are underestimated for extreme loads [5]. On the other hand, experiences from operating offshore wind farms supported by monopiles indicate that the foundation stiffness for small operational loads is significantly underestimated. The installation method involves lifting or floating the structure into position using equipment such as floating crane vessels, drilling jack-up units, and specially constructed installation vessels before driving the piles into the seabed.

Jacket designs are more and more utilized in the applications of OWT. As an example, jacket structures were chosen as substructures by the Moray Offshore Wind Farm project (1500 MW total) in the UK, with up to 8 MW for each offshore wind turbine. The obvious benefits (compare to a monopile) are the reduction in hydrodynamic loading and weight, and suitability for increased water depth (30 m+). Jacket structures are less dependent on soil conditions compared to monopile and tripod, and are more suitable for sites with soft soil conditions.

Fig. 2.17 A close look at a tripod used as a substructure for OWT (courtesy of Aker Solutions)



They are easily capable of supporting OWT with 6 MW or more. The smaller diameter of the piles (typically less than 2.5 m) also means a reduction in required driving power and less noise during piling. In addition, better precision for pile orientation and positioning can be ensured. By considering the financial limits, OWT using jacket works well for water depths up to 60 m.

The main part of the tripod, shown in Fig. 2.17, consists of a tubular pole, but the lower part consists of braces and legs. The tubular steel foundation piles are driven through the sleeves in the three legs. As a tripod has a large base surface, it performs well in resistance to overturning moments. Moreover, it also has more redundancy due to three installed piles rather than one (monopile) [9].

Gravity based foundations consist of a slender steel or concrete substructure mounted onto a single large reinforced concrete or a ballast-filled steel shell. To maintain stability, tensile loads between the bottom of the support structure and the seabed are resisted by self-weight of the foundation. The gravity based foundations require a flat base and scour protection. A significant advantage of gravity based foundations is associated with their transportation, as they can be fabricated and partially assembled in local yards, transported and completely installed at sea, depending on the fabrication yard capacity, the available draft during their transportation, and the availability of ballast materials.

Bucket foundations consist of a sub-structure column connected to an inverted steel bucket through flange-reinforced shear panels. The length of the skirt is normally in the same order as the bucket diameter, where the volume of soil inside the foundation may act as a permanent gravity base foundation. Bucket foundation is therefore similar to gravity base foundations in shape and size but differ in the method of installation and primary mode of stability. The installation of a bucket foundation is typically through pushing due to the weight of the foundation and its associated mass and/or creating a negative pressure inside the foundation to generate a downward pressure. These operations enable the foundation to penetrate

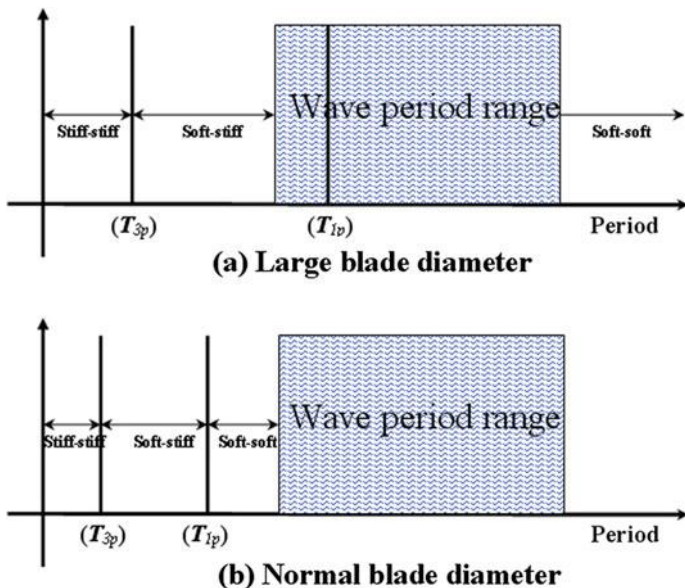


Fig. 2.18 Period interval for stiff-stiff, soft-stiff and soft-soft design of OWT substructures

into the seabed and to finally reach a desirable penetration depth. To create the negative pressure, water and air inside the foundation are pumped out through top of bucket when the rim of bucket seals with the seabed.

The dynamic characteristics of offshore wind turbine structures are slightly different from those of traditional offshore platform structures. An offshore wind turbine system comprises five physical components: rotor, transmission, generator, support structure, and control system. Each of these influences the dynamic behavior of the complete turbine system. It is noticed that the two most significant excitations are due to the rotation of blades and wave induced forces. In order to avoid resonance due to the excitations from wind turbine blade rotation and wave loadings, the support structure should be designed with a natural period as far as possible from the periods of both blade and wave excitations. This gives three possible natural period ranges for designing the support structure as shown in Fig. 2.18: a natural period larger than the first blade excitation period T_{1p} (soft-soft design), the one between the first (T_{1p}) and the second blade excitation period T_{3p} (soft-stiff design), and the one below the second blade excitation period T_{3p} (stiff-stiff design).

Traditionally, the soft-soft design is preferred because this usually leads to an economical design due to the need for less material and construction cost. In the offshore wind energy industry, the general trend is that the scale of turbines is becoming larger and larger. This would result in an increase of the blade's diameter, e.g., a 170 m diameter for a 7 MW wind turbine. The first and second excitation periods are also significantly increased for those large OWTs. This motivates the engineer to shift from a soft-soft to a soft-stiff or even to a stiff-stiff design. Moreover,

the variable tip speed of the turbine also becomes a design alternative, which adds additional restrictions on the natural period range of the structures. In addition, it is also possible to convert the existing/abandoned offshore rigs into substructures for OWT systems, which can avoid/delay enormous decommissioning costs for energy companies as well as avoid cost and pollution for constructing new substructures for OWTs. Most of the existing fixed offshore platform structures have natural periods below 3.5 s; after removing part of the heavy topside modules at the top of the platforms, the natural periods will further decrease. This period range is then relevant to the soft-stiff or even soft-soft design. For developing this concept, one also needs to account for the cost with respect to maintenance and power grid integration.

Except artificial damping devices, an optimized control system and the associated control algorithm for both generator torque and pitch angle of wind turbine blades (either for a collective pitch control for all blades or an individual pitch control for each blade) can also mitigate dynamic loadings applied on an OWT tower. Such a control supplies additional damping to generally lightly-damped tower, and may even help to minimize both wind and wave induced platform motions. It normally involves a modeling of an extra pitch demand responsible for counter-balancing the vibrations and motions of the tower. This load reduction will allow for a more cost-effective structural design.

2.2 Accounting of Dynamics in the Concept Design of Structures

2.2.1 *Dynamics Versus Statics*

Over history, the safety and serviceability of structures have basically been measured on the basis of their static behavior, which required adequate stiffness and strength. This was perhaps because the necessary knowledge of dynamics was less accessible to engineers than their static counterpart. Nowadays, it is common knowledge that all bodies possessing stiffness and mass are capable of exhibiting dynamic behavior.

The major difference between dynamic and static responses is that dynamics involves the inertia forces associated with the accelerations at different parts of a structure throughout its motion. If one ignores the inertia force, the predicted responses can be erroneous. As an example, let's consider a bottom fixed cantilevered tower subjected to sea wave loadings as shown in Fig. 2.19 [10]. In addition to the static bending moment due to wave loadings applied on the structure, as shown in Fig. 2.19b, the stiffness and mass of the structure will react to the wave loadings and generate internal forces on both the top mass block (Q_i) and the tower (q_i), shown in Fig. 2.19c. Rather than a single function of mass, the amplitudes of the inertia forces are related to a ratio between stiffness and mass (eigenfrequency), mass, as well as damping, thus resulting in additional dynamic bending action (Fig. 2.19d).

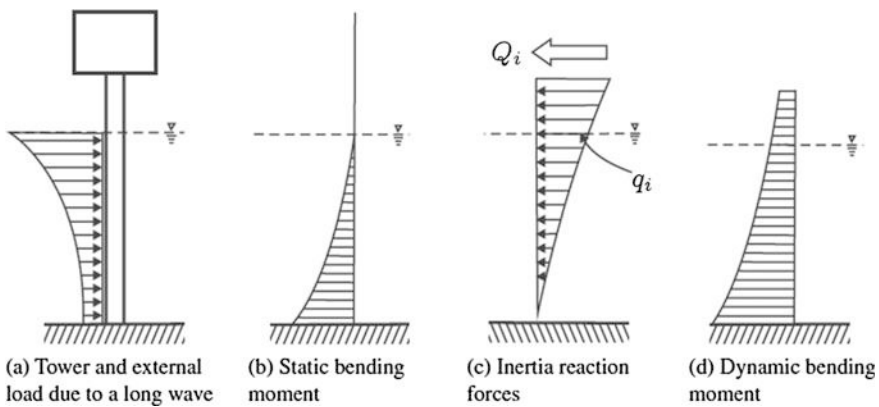
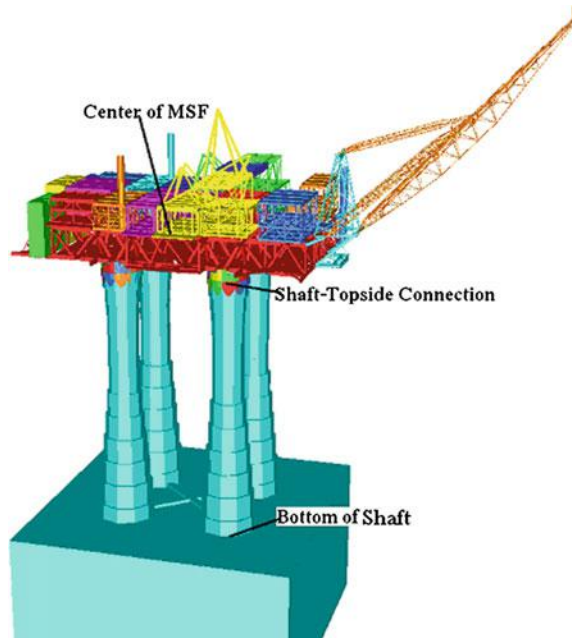


Fig. 2.19 Wave induced static versus instantaneous dynamic forces and moments in a bottom-fixed cantilevered tower [10]

Fig. 2.20 A GBS with a heavy topside supported by four concrete shafts (legs)



As another example, consider a gravity-based structure (GBS), shown in Fig. 2.20, that is subjected to the ground motions recorded during El Centro earthquake, which have a high energy content at the vibration period above 0.2 s (below 5 Hz in Fourier amplitude shown in Fig. 2.21, which will be explained in Sect. 5.3.1). The dynamic responses of the platform are investigated by varying the thickness of four shafts from half of the reference thickness, to the reference

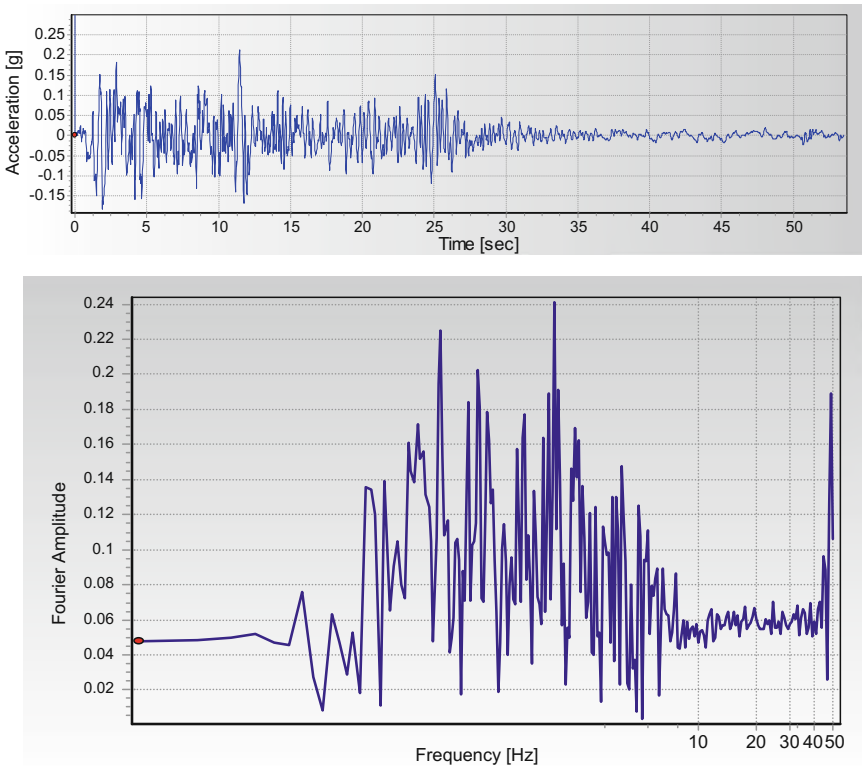
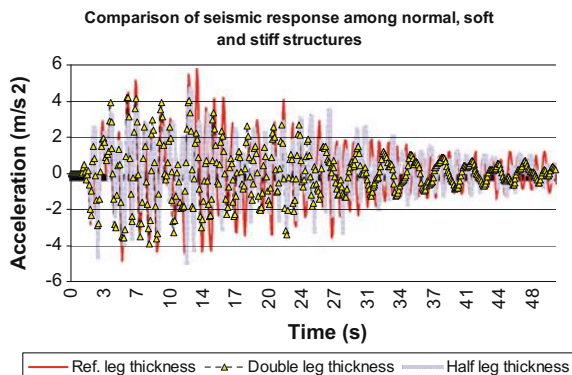


Fig. 2.21 Ground motions EW component (*upper*) recorded during El Centro earthquake and its Fourier amplitude (*lower*)

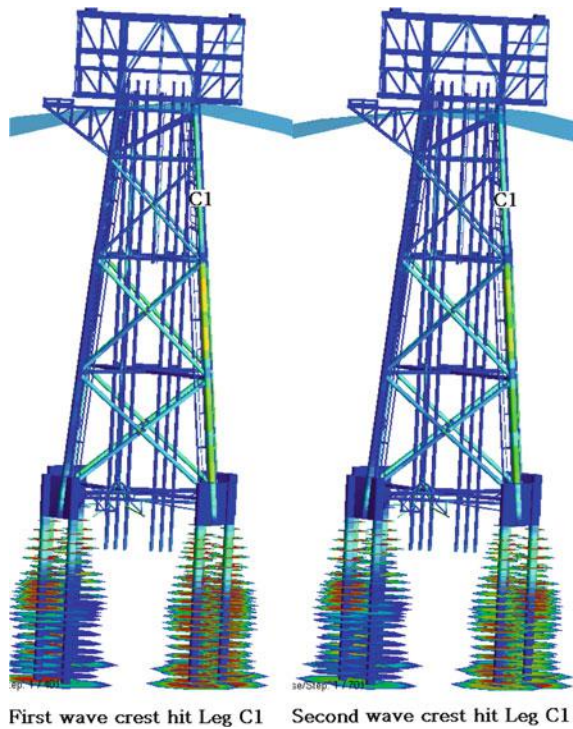
Fig. 2.22 Acceleration at the shaft-topside connection with various leg/shaft stiffness (peak acceleration: 4.7 m/s^2 for double leg thickness, 5.8 m/s^2 for reference leg thickness, 4.2 m/s^2 for half leg thickness)



thickness, to twice the reference thickness. It is obvious that the GBS becomes stiff by increasing the shafts' thickness. If a static analysis is performed, under the same seismic excitations the stiffer structure would have lower responses. However, the seismic responses involving dynamic effects may not obey this rule. Figure 2.22 shows the acceleration at the shaft-topside connection. It is clearly shown that the peak acceleration for the reference shaft thickness case is higher than that of the half-thickness case. However, the trend of peak acceleration response variation with the change of stiffness cannot be identified, as the peak acceleration for the double shaft thickness (the stiffest one) is lower than that for other cases with lower stiffness. This indicates the effects of inertia, which are more complex than their static counterpart. As will be discussed in Chap. 5 and Sect. 15.5, the response variation trend can be identified by relating the seismic responses to the dynamic characteristics of both structures and excitations.

Even for dynamic insensitive structures with low periods of resonance compared to that of the dynamic loading, dynamics does include the inertia effects due to loading that varies with time, even if this load variation may be quite slow. The inertia effects could lead to the fatigue failure of the materials at stress conditions well below the breaking strength of the materials. They may also be responsible for the discomfort of human beings. Figure 2.23 shows an offshore jacket structure subjected to two consequent sea waves; the jacket has a resonance period of 2.5 s.

Fig. 2.23 An offshore jacket structure subjected to a wave with a wave height of 31.5 m and a wave peak period 15.6 s (courtesy of Aker Solutions)



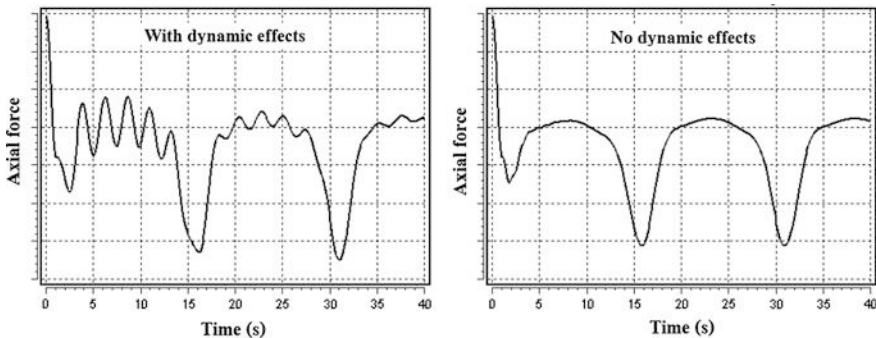


Fig. 2.24 Axial force time history on the *lower part* of leg C1 of the offshore jacket with and without dynamic inertia effects (the exact magnitude of axial forces are omitted to protect the interests of the relevant parties)

Figure 2.24 compares the calculated axial force time history at a leg C1 with and without accounting for the dynamic inertia effects. When the dynamic effects are ignored (right figure), the axial forces history entirely follows the variation of the wave and has a period of wave loading (15.6 s) well above the structure's resonance period (2.5 s). However, when the dynamic effects are accounted for, fluctuations (left figure) of the axial force can be clearly observed as a background noise with the resonance period of the structure (2.5 s). Depending on the magnitude of this background noise, it may influence the integrity of the structure with regard to fatigue damage.

From another angle, the dynamic loading often has a different orientation than the static one. For example, the static loading of a structure under the gravity of the Earth is strictly toward the Earth. However, when the structure is subjected to dynamic loading due to, for example, wind, earthquake or sea waves, the direction of resultant loadings change from downward to the one that is more toward a horizontal orientation, this can result in an entirely different pattern regarding the load level and load path, and this obviously influences the structural design. Therefore, structural engineers are required to have a complete picture of load path and level, and structures designed must have corresponding load resisting systems that form a continuous load path between different parts of the structures and the foundation. The structure shown in Fig. 2.23 represents a typical configuration of the jacket structure and a clear path for load transferring, i.e., the gravity and acceleration loads from topside, the wave load applied on the upper part of the jacket, and the jacket gravity and acceleration loads are all transferred through legs and braces down to the pile foundation at the bottom.

Before concluding this section, it is of great importance to emphasize that dynamics is a rather more complex process than its static counterpart. The natural frequency of a structure can change when a change in its stiffness, mass or damping occurs. What makes dynamics even more complicated is that, strictly speaking, regular harmonic loadings and responses, with a sine or cosine form at a single

frequency, do not represent environmental loadings (such as earthquake loadings) and the associated responses in the real world, even if they can be a good simplification when the dynamics at a single frequency is dominating. This implies that one should always assess whether the vibrations in various frequencies need to be accounted for or not.

2.2.2 Characteristics of Dynamic Responses

If we take an SDOF spring-mass-damper system under forced excitation as an example, which is illustrated in Fig. 2.25, the equation of motions for the system is expressed as:

$$m\ddot{x}(t) + c\dot{x}(t) + kx(t) = F(t) \quad (2.1)$$

By exerting an external harmonic force ($F(t) = F_0 \sin(\Omega t)$) with an amplitude of F_0 and an angular frequency of Ω shown in Fig. 2.25, or displacement excitations in a harmonic form on the spring-mass-damper system, an SDOF spring-mass-damper system under forced harmonic excitation is constructed. The governing linear differential equation of motions for this system in case of harmonic force excitations can then be written as:

$$m\ddot{x}(t) + c\dot{x}(t) + kx(t) = F_0 \sin(\Omega t) \quad (2.2)$$

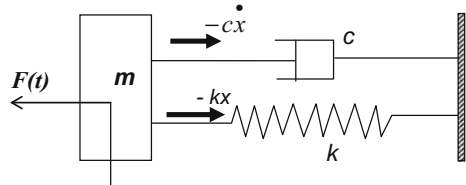
Dividing both sides of the equation above by m , this equation is rewritten as:

$$\ddot{x}(t) + \frac{c}{m}\dot{x}(t) + \omega_n^2 x(t) = (F_0/m) \sin(\Omega t) \quad (2.3)$$

It is noted that the viscous damping is very important in an oscillating system because it helps to efficiently limit the excursion of the system in a resonance situation. As a reference, we first define the critical damping c_c , which is the lowest damping value that gives no oscillation responses, i.e., the system does not vibrate at all and decays to the equilibrium position within the shortest time. This represents the dividing line between oscillatory and non-oscillatory motions:

$$c_c = 2\sqrt{km} = 2m\omega_n \quad (2.4)$$

Fig. 2.25 An SDOF spring-mass-damper system under an external force $F(t)$



The actual damping ratio can be specified as a percentage of critical damping:

$$\zeta = \frac{c}{c_c} \quad (2.5)$$

By realizing that $c = 2\omega_n m \zeta$, the equation of motions for the system finally gives:

$$\ddot{x}(t) + 2\omega_n \zeta \dot{x}(t) + \omega_n^2 x(t) = (F_0/m) \sin(\Omega t) \quad (2.6)$$

As the equation above is a second-order non-homogeneous equation, the general solution for it is the sum of the two parts: the complementary solution $x_c(t)$ to the homogeneous (free vibrations) equation and the particular solution $x_p(t)$ to the non-homogeneous equation:

$$x(t) = x_c(t) + x_p(t) \quad (2.7)$$

The complementary solution exhibits transient vibrations at the system's natural frequency and only depends on the initial condition and the system's natural frequency, i.e., it represents free vibrations and does not contain any enforced responses:

$$x_c(t) = X e^{-\zeta \omega_n t} \sin\left(\sqrt{1 - \zeta^2} \omega_n t + \phi\right) \quad (2.8)$$

It is noticed that this aspect of the vibration dies out due to the presence of damping, leaving only the particular solution exhibiting steady-state harmonic oscillation at excitation frequency Ω . This particular solution is also called the steady-state solution that depends on the excitation amplitude F_0 , the excitation frequency Ω as well as the natural frequency of the system, and it persists motions for ever:

$$x_p(t) = E \sin(\Omega t) + F \cos(\Omega t) \quad (2.9)$$

By substituting the equation above and its first and second derivatives into Eq. (2.6), one obtains the coefficients E and F as:

$$E = \frac{F_0}{k} \frac{1 - (\Omega/\omega_n)^2}{\left[1 - (\Omega/\omega_n)^2\right]^2 + [2\zeta(\Omega/\omega_n)]^2} \quad (2.10)$$

$$F = \frac{F_0}{k} \frac{-2\zeta\Omega/\omega_n}{\left[1 - (\Omega/\omega_n)^2\right]^2 + [2\zeta(\Omega/\omega_n)]^2} \quad (2.11)$$

By inserting the expression for coefficient E and F into Eq. (2.9) and rearranging it, one can rewrite the steady-state solution as:

$$x_p(t) = \frac{F_0}{km} \frac{\sin(\Omega t - \varphi)}{\sqrt{\left[1 - (\Omega/\omega_n)^2\right]^2 + [2\zeta(\Omega/\omega_n)]^2}} \quad (2.12)$$

where φ is the phase between the external input force and the response output, with the most noticeable feature being a shift (particularly for underdamped systems) at resonance. It can be calculated as:

$$\varphi = \tan^{-1} \left(\frac{2\zeta(\Omega/\omega_n)}{1 - (\Omega/\omega_n)^2} \right) \quad (2.13)$$

It is clearly shown that the steady-state solutions are mainly associated with the excitation force and the natural frequency. Figure 2.26 shows an example of the dynamic responses due to the contribution from both transient and steady-state responses, with a Ω/ω_n ratio of 0.8, a damping value of 0.05 ($\varphi = 0.21$), and $\phi = 0.1$. Phases between the two types of response can be clearly observed.

When mass m in Fig. 2.25 is subjected to harmonic excitations, the magnitude and phase of the displacement responses strongly depend on the frequency of the excitations, resulting in three types of steady-state responses, namely quasi-static, resonance, and inertia dominant responses, which are illustrated in Fig. 2.27.

When the frequencies of excitations Ω are well below the natural frequencies of the structure ω_n , both the inertia and damping term are small, and the responses are controlled by the stiffness. The displacement of the mass follows the time varying force almost instantaneously. Subject to environmental loading such as wind or ocean wave loading, the majority of land-based structures and fixed offshore structures are designed to reach this condition, as shown in Fig. 2.28. However, earthquake loading is likely to have a dominant frequency higher than the natural frequency of structures.

When the excitation frequencies are close to the natural frequency of the system, the inertia term becomes larger. More importantly, the external forces are almost overcome (controlled) by the viscous damping forces. Resonance then occurs by

Fig. 2.26 Transient and steady-state responses due to external harmonic force excitations applied on a system with $\omega_n = 1.0$, $\Omega = 0.8$, $\zeta = 0.05$, and $\phi = 0.1$

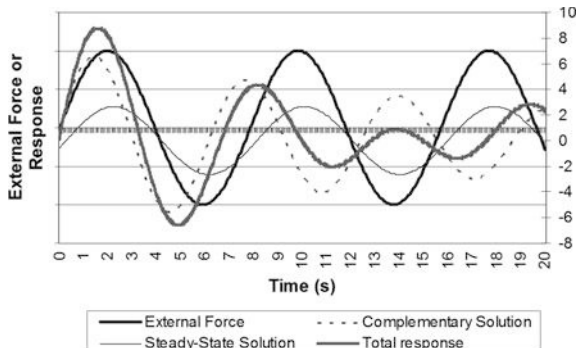
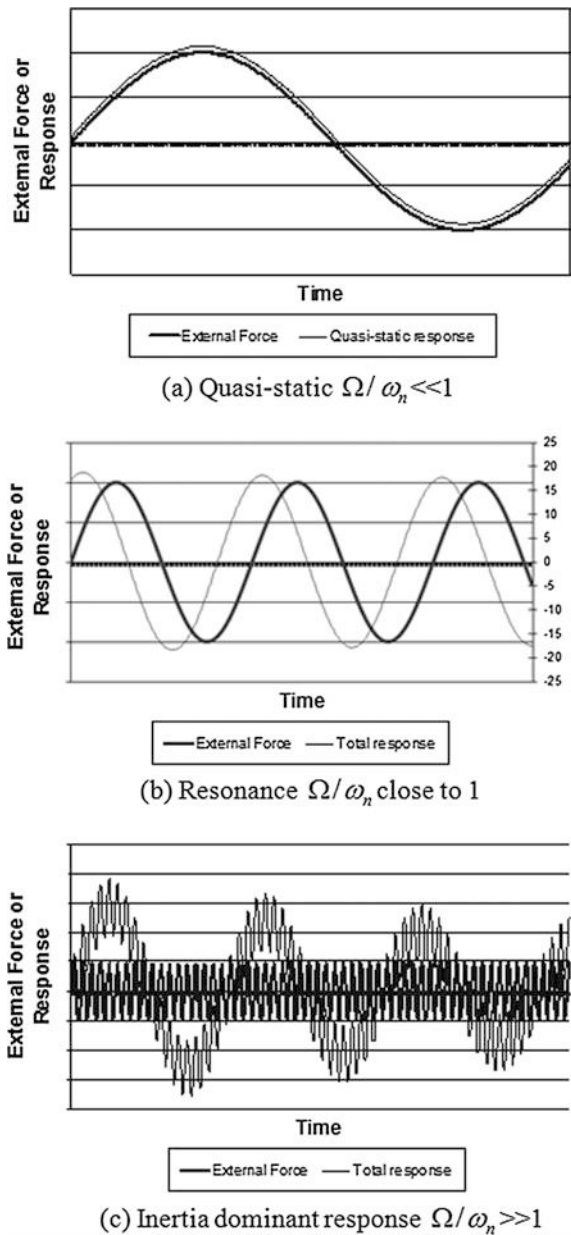
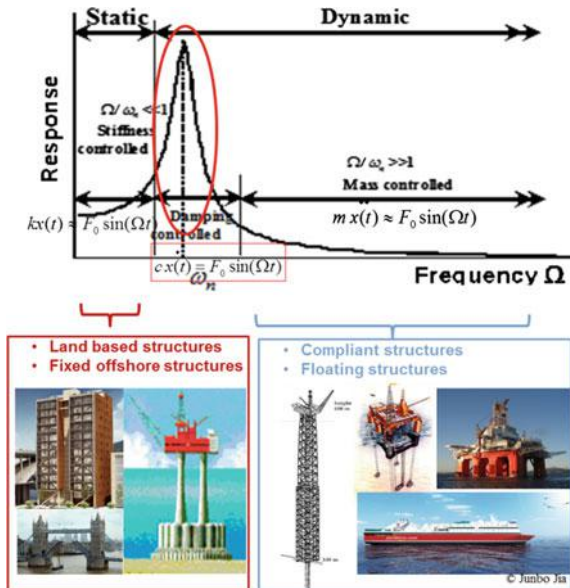


Fig. 2.27 Damped responses due to harmonic excitations with the characteristics of **a** quasi-static ($\Omega/\omega_n \ll 1$); **b** resonance (Ω/ω_n close to 1); and **c** inertia dominant responses ($\Omega/\omega_n \gg 1$), for a system with $\omega_n = 1.0$ and viscous damping ratio $\zeta = 0.03$ [11]



producing responses that are much larger than those from quasi-static responses, as shown in the circle in the upper figure of Fig. 2.28, and there is a dramatic change of phase angle, i.e., by neglecting the damping, the displacement is 90° out of phase with the force, while the velocity is in phase with the excitation force. In a typical

Fig. 2.28 Response of various types of offshore and land-based structures in three frequency ranges subjected to external environmental loading with a frequency of Ω , the natural frequency of the structure is denoted as ω_n (from an oral presentation by the author at the 11th International Conference on Recent Advances in Structural Dynamics, Pisa, 2013)



situation in which the damping is well below 1.0, the responses are much larger than their quasi-static counterparts. From an energy point of view, when the frequency of excitations is equal to the natural frequency, the maximum kinetic energy is equal to the maximum potential energy. Almost all engineering structures are designed to avoid this resonance condition. Possible scenarios of resonance conditions are: when the resonance period (site period) of soil layers at sites due to shear wave transmission is close to the natural period of the structure; when the resonance period of the surface wave is close to the natural period of the structure; or when significant plasticity develops on structural members during a strong earthquake, leading to a decreased natural frequency of the structure, which may track the decreasing predominant frequency of the ground motions, causing resonance with ground motions (moving resonance), etc. These possible resonance conditions will be discussed in Chap. 3.

When the excitation frequencies are well above the natural frequency of the system, the external forces are expected to be almost entirely overcome by the inertia force, the excitations are so frequent that the mass cannot immediately follow the excitations. The transient vibrations are normally more significant than steady-state oscillations. The responses of the mass are therefore small and almost out-of-phase (phase angle approaches 180°) with the excitation forces, as illustrated in Fig. 2.28. From an energy point of view, this reflects the condition in which the maximum kinetic energy is larger than the maximum potential energy [11]. Offshore compliant structures and floating structures are normally designed to behave “softly” in their motion responses, and therefore have natural frequencies of motion ω_n well below the external wave loading frequency. This condition is also a

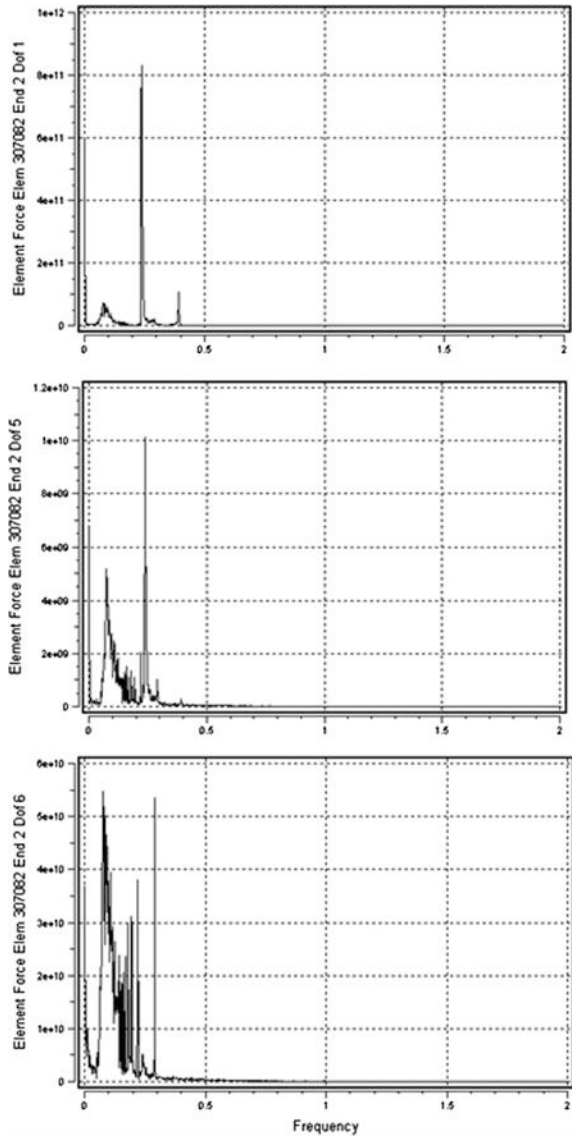
most usual scenario encountered during an earthquake event. It is noted that for most of the engineering structures and typical site conditions, the long period of seismic ground excitations are usually small, except for the ground motions caused by the seismic surface (Rayleigh) waves, which can have dominating long period components of ground motions, which will be presented in Chap. 3. Therefore, subject to seismic ground excitations, a large amount of offshore and land-based structures are likely to reach this condition.

As a structure typically has—or more precisely, has to be represented-modeled by—a large number of degrees-of-freedom, in addition to the natural frequency, which is typically the first eigenfrequency of the structure, it has more numbers/orders of eigenfrequencies, and the total number of eigenfrequencies is equal to the number of degrees-of-freedom of the structure. However, the first few eigenfrequencies, especially the natural frequency, normally dominate the majority of the total modal mass participating in structural vibrations, and are therefore the most important ones contributing to the dynamic response of the structure [11]. From a modal response point of view, the lower order eigenfrequencies of the structure are normally separated well apart. In this frequency range, with small damping, the modal response will generally be dominated by a single mode with frequency close to the loading frequency and a single mode with natural frequency of the structure. And if the loading frequency is lower than the 1st eigenfrequency of the structure, then the structural response will show two peaks at the loading frequency corresponding to quasi-static response and the natural frequency of the structure contributing to dynamic response of the structure. As an example, Fig. 2.29 shows ocean wave induced frequency responses of a welded joint on an offshore jacket structure (Fig. 2.30) in the North Sea. Generally, two peaks in this frequency response graph can be identified: one corresponds to the wave modal frequency (0.08 Hz); the other corresponds to the structure's natural frequency (0.24 Hz). On the other hand, the higher order eigenfrequencies are more closely spaced and modal mass participation of each mode vibration is much less than that of the first few eigen-modes. This is more obvious for highly redundant structures. With a dynamic loading in this frequency region, multiple eigen-modes contribute in a similar extent to the modal response, and vibration modes above the loading frequency will be out-of-phase with those below the loading frequency, the net vibration is likely to be less than any of the single mode vibrations in this frequency range (dynamic cancelation).

2.2.3 Frequency Range of Dynamic Loading

If relevant, subjected to environmental loading, such as wind, earthquakes, ocean waves, current, and ice, etc., all engineering structures should be designed by accounting for their dynamics with a special consideration on resonance, which can be relevant to structural performances associated with ultimate strength, fatigue strength and serviceability limits. Each type of loading has different dominant

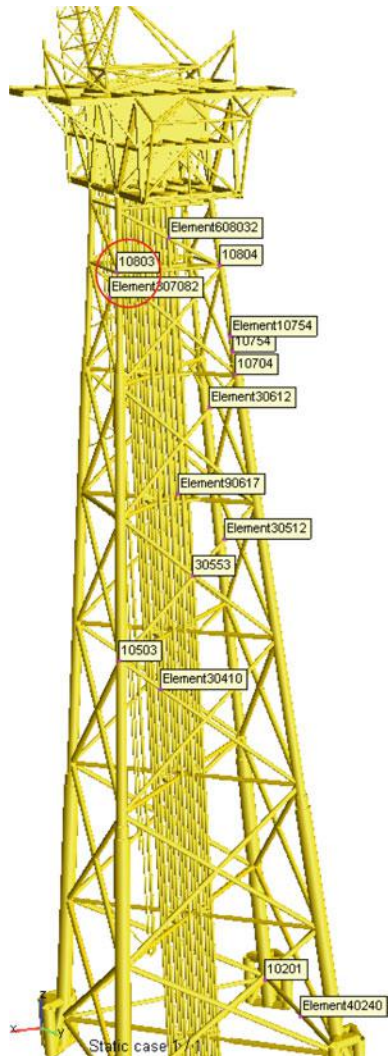
Fig. 2.29 Frequency responses of the axial force (Dof 1) [N], in-plane bending moments (Dof 5) [Nm] and out-of-plane bending moments (Dof 6) [Nm] for a weld joint 10803 (Fig. 2.30) at the top of a jacket, and the jacket is subject to wave loading corresponding to a sea state with a significant wave height $H_s = 8.8$ m, and a modal wave period $T_p = 13.2$ s (0.08 Hz) [17]



ranges of loading frequency as shown in Fig. 2.31. In addition, other types of dynamic loading induced by explosion, machinery vibrations, vehicle- or human induced excitations may also require a dedicated consideration on solving relevant dynamic problems in the design.

It is noted that the dominant frequency of seismic ground motions is not only dependent on the frequency of seismic waves generated at the source due to fault

Fig. 2.30 The location of the welded joint 10803 on the jacket



fractures, but also even more influenced by site conditions associated with soil layers and ground topology. Therefore, their peak period has a large range of up to 4 s.

Furthermore, Fig. 2.31 also indicates that the difference of dominant frequency range for different types of environmental loading is significant. This can pose a challenge in designing an optimized structure to resist the different types of dynamic loading. For example, for fixed offshore structure or land-based structures, to avoid significant dynamic amplification and/or excessive vibrations, it is usually desirable to design a stiff structure to resist wind and ocean wave loading, so that the natural period of the structure is far below the dominant period range of wind and wave loading, thus avoiding resonance and limiting excessive vibrations. On

Typical Short Term Environmental Loading Frequency

- **Seismic strong ground motions**
 - Peak period below 4 s
 - Typical dominated period between 0.2 s to 0.5 s
 - Majority of motion energy between 0.3 s and 30 s
- **Wind**
 - Slowing varying mean wind speed: period in order of hours
 - Rapid fluctuating instantaneous wind speed peak period: period 15 s – a few minutes
 - Most of the energy of fluctuating instantaneous wind speed: above 1 s
- **Wave**
 - Slowing varying wave: period in order of hours, e.g., significant wave height and characteristic wave period
 - Rapid fluctuating individual waves: period 3-26 s
- **Current**
 - Varying slowly with time, can be assumed as constant (long period)
- **Ice (level ice) loads**
 - Vertical structures: wide banded
 - Conical structures: narrow banded, above 0.2 s

Fig. 2.31 Typical short term environmental loading frequency/period (from an oral presentation by the author at the 11th International Conference on Recent Advances in Structural Dynamics, Pisa, 2013)

the other hand, the low dominant period of seismic loading requires a “softer” structure design that cherishes a higher natural period. This contradiction has been encountered in various structural design projects. Sometimes a “balance” between the two needs to be sought, such as the design of Taipei 101. It has a natural period of around 7 s, which is obviously above the dominant period of earthquake loading. Even though this natural period of 7 s is also far below the period of loading due to wind turbulence (fluctuating part of wind), it can induce significant peak acceleration at the top of Taipei 101, causing both human discomfort and structural metal fatigue. To solve this problem, a large tuned mass damper (TMD) weighing 660 t (Fig. 2.32), as will be discussed in Chap. 24, was introduced to mitigate sway motion of the building, particularly in major typhoons or earthquakes where movement of the top floor can exceed 1.5 m. The TMD will reduce peak acceleration of the top occupied floor from 7.9 to 5.0 mg due to wind storm with a return period of half year. For a 1000–2500 year return period of strong earthquake, the TMD will be rather effective to mitigate the dynamic response of the structure, and

Fig. 2.32 A tuned mass damper (*upper*) suspended from the 92nd to the 87th floor at Taipei 101 (*lower*) (under licenses of CC BY-SA 3.0 by Guillom and Peeldden)



to remain in place and intact after strong seismic ground motions cease and the vibration of the structure terminates. In addition, another two small TMDs are designed to mitigate vibration at two tip vibration modes at periods of around 1 s.

Slender light weight structures such as guyed steel stacks, chimneys, slender tips of flare booms or other elevated structures, with two examples shown in Figs. 2.32 and 2.33, the structural design is governed by the wind loading rather than the seismic loading because the structure has a high natural period (compared with the dominant period of earthquake loading) and the wind loading increases with the height from the ground surface. However, due to the tips of those slender structures normally being much softer (with much lower stiffness) than the structural parts below the tips, during earthquakes, they can exhibit significant vibrations, which is referred to as a whipping effect, as will be discussed in Sect. 15.7. Therefore, the design of the slender tips of structures may be governed by seismic loading and therefore requires a dedicated consideration of their seismic resistance.



Fig. 2.33 A flare boom with a slender tip (courtesy of Aker Solutions)

2.3 Difference Between Offshore and Land-Based Structures

The major difference between offshore structures and their land-based counterparts is reflected in the aspects regarding cost and consequence, possibility of evacuation, the availability of seismic ground motion records, structural dynamic behavior and geometry characteristics, structural and hydrodynamic damping, other accompanied environmental and operational loads, as well as special geotechnical issues such as site conditions and sudden subsidence. Therefore, the assessment and design experience adopted for land-based structures must be borrowed with care before applying them for offshore structures.

Compared to that of an infrastructure on land, evacuation during a strong earthquake at a site offshore is almost impossible and can have very serious consequences. This also leads to a higher safety requirement for structural and non-structural elements for offshore structures than structures onshore.

The cost and consequence of structural failure or collapse of offshore structures are normally much more significant than a typical land-based structure such as a building. Therefore, seismic performance assessment for offshore structures is generally associated with a higher required reliability and assessment accuracy. This may limit the applicability of some simplified analysis methods and simplification in the structural modeling that are typically adopted for structural analysis for typical land-based structures.

Offshore structures generally have a much wider range of natural period (1–120 s, depending on the types) than typical onshore building structures (below 9 s). This may sometimes significantly alter the dynamic response subject to earthquake loading and other types of environmental loading.

Due to the significant environmental loading mainly induced by ocean waves, offshore structures are generally much larger in plan than most buildings but do not have a common foundation form to resist the overturning moment generated by the wave and other environmental loads. Hence, subjected to seismic or ocean wave loading, offshore structures are more likely to exhibit a combined torsion and bending (translation) response [12].

An offshore platform generally has a heavy topside at the top of the supporting structure as shown in Fig. 2.9. For example, for a typical jacket (Fig. 2.8) or a jackup (Fig. 2.34) platform, the weight of the topside is normally up to a few times higher than the weight of the supporting structure. Elevation control (as will be discussed in Sect. 19.3) is applied for onshore buildings or tower (Fig. 2.35) structures to avoid a global resonance associated with one or two vibration modes due to earthquake and other dynamic loadings. This requires that a structure should generally be designed with a pyramid shape (with a gradually decreased stiffness and mass per unit height with the increase in its height) to prevent the resonance amplification. This is difficult to achieve in offshore structural design, because a significant mass (in many cases the major mass) is located at the top of the supporting structure. This makes the modal mass participation corresponding to the most important global bending or torsional vibration mode rather high, so that when the resonance occurs due to the vibration participation of the topside, a significant inertia force will be generated and applied on the supporting structure, leading to a large vibration response.

The presence of heavy offshore foundations together with the weight of the platform may change the soil properties, which influences both the foundation impedance (stiffness and damping) and the foundation capacity control.

Compared to that of onshore structures, the space in an offshore platform is generally limited, making it more difficult to place dampers and other mitigation equipment to attain an effective reduction in dynamic response.

Fig. 2.34 Two jackups with supporting structures made of tubular legs (*left*) or trusses (*right*). The jackups are towed to the site and legs are jacked down, engaging the seafloor raising the platforms (courtesy of Dong Energy)



Fig. 2.35 The 320 m high Eiffel tower with an elevation control design, comprising more than 15,000 wrought-iron structural members joined by 2.5 million rivets. The structural weight is 7300 t (photo courtesy of Jing Dong)

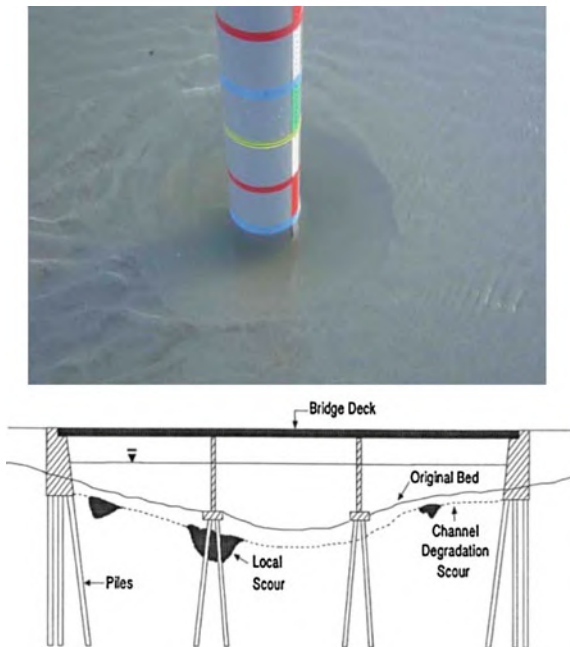


The presence of sea water induces additional loads due to added mass, hard marine growth and hydrodynamic damping. Marine growth also adds weight on supporting structures. Therefore, in addition to inertia forces due to ground accelerations transferred to structures, for offshore structures, the relative motions between the submerged structural members and their surrounding fluids also create hydrodynamic damping forces. Furthermore, the surrounding fluids will also enhance the inertia effects of the submerged structural members, which are referred to as the effects of added mass. Both the added mass and the hard marine growth can introduce significant inertia effect to the structure, leading to an increase in natural periods.

The hydrodynamic damping induced by fluid–structure interaction will generally slightly decrease the dynamic response, even though this effect is rather limited and can normally be neglected in mild sea states. When a strong earthquake occurs together with a significant storm (i.e., large wave height), the hydrodynamic damping forces applied on offshore structures can be dramatically increased. Note that the joint probability of occurrence of both events (significant earthquakes and extreme storm waves) is practically extremely low, and is therefore not considered by typical offshore structural design codes.

Due to the abrasion of soil surface by the passing of current, wave and flood, the shear stress generated from the flowing water may exceed the threshold value of the soil erosion resistance, removing the sediment such as sand and rocks from around the foundation (such as piles, bridge abutments or piers). A hole is then formed at the upper soil surface, which is called scour as shown in Fig. 2.36. Scour leads to a reduction in capacity for both the upper structure and the foundation. It particularly reduces the stability of the foundation and increases the maximum design moments in the pile, which requires a larger pile penetration depth and pile cross section area.

Fig. 2.36 Steep-sided local scour pits around a single pile (upper figure), and an illustration of scour at the bottom of a bridge foundation (lower figure)



For a small diameter subjected to monotonic horizontal load, the maximum pile bending stress increases almost linearly with the scour depth [13]. Due to the degrading of the foundation stiffness, the presence of scour hole also decreases natural frequency of the structure system. In case the change in natural frequency is significant, it can dramatically alter (decrease or increase) the seismic spectral acceleration value corresponding to the natural frequency, thus significantly changing the seismic force and responses in the foundation and superstructure. In addition, geometrical variation of the mudline leads to more complicated design requirements for the pipeline and cables at seabed.

In addition, due to the effects of water column, depending on the water depth, vertical ground motion acceleration at seabed will be decreased by the effects of finite water column at some frequency ranges while being amplified at other frequency ranges. However, in general, the peak vertical acceleration at seafloor can be reduced by as much as 50 % [14, 15]

The variation of fluid tank levels on offshore structures also changes the mass of the structure. This alternates the dynamic response, and presents potential challenges to perform vibration-based structural health monitoring [11], which is to detect structural damages through the observation of changes in measured eigenfrequencies and corresponding vibration mode shapes.

Compared to land-based structures, offshore structures are generally designed to resist more significant lateral environmental loads due to the presence of wave, current and/or ice crushing loading. Therefore, even though the action points of

those loadings on structures may be far from that of the earthquake induced ground excitations, the seismic performance of offshore structures are normally better than their land-based counterparts.

Finally, but not the least consideration, as a consequence of a special type of earthquake, the sudden subsidence of offshore platforms, as will be elaborated in Chap. 16, has been realized to be a serious risk by more and more energy companies as well as authority bodies, which needs consideration during the design.

References

1. Chakrabarti S (ed) (2005) Handbook of offshore structures. Elsevier, Oxford
2. Gerwick BCJ (1986) Construction of offshore structures. Wiley, New York
3. Reddy DV, Arockiasamy M (1991) Offshore structures. Krieger Publishing Company, Malabar
4. Clauss G et al (1992) Offshore structures. Conceptual design and hydromechanics (translated by MJ Shields), vol 1. Springer, Berlin
5. Jia J (2016) Soil dynamics and foundation modeling: offshore and earthquake engineering. Springer, Heidelberg
6. Chandrasekaran S (2015) Advanced marine structures. CRC Press, Boca Raton
7. Pike J (2011) Compliant tower. <http://www.globalsecurity.org/military/systems/ship/platform-compliant-tower.htm>
8. Chakrabarti S (2008) Challenges for a total system analysis on deepwater floating systems. Open Mech J 2:28–46
9. van Wijngaarden M (2013) Concept design of steel bottom founded support structures for offshore wind turbines. Delft University of Technology
10. Naess A, Moan T (2012) Stochastic dynamics of marine structures. Cambridge University Press, Cambridge
11. Jia J (2014) Essentials of applied dynamic analysis. Springer, Heidelberg
12. Sharpe RL, Newmark NM (1977) Extending seismic design provisions for buildings to the design of offshore structures. Offshore technology conference, Houston, Texas, May 1977
13. Diamantidis D, Arnesen K (1986) Scour effects in piled structures: a sensitivity analysis. Ocean Eng 13:497–502
14. Smith CE (1997) Dynamic response of steel-jacket platform subject to measured seafloor earthquake ground motions. In: Proceedings 8th international conference on the behaviour of offshore structures, BOSS'97, vol 3. Delft: Pergamon, Elsevier Science Ltd., Oxford, England
15. Sleess GE (1990) The long-term measurement of strong-motion earthquakes offshore South California. In: Proceedings of OTC 1990, society of petroleum engineers, Richardson, Texas
16. Kuo YS, Abdel Rahman K, Wu KT, Huang TY, Achmus M (2014) Suitability of a pile group foundation for an offshore wind turbine. In: Proceedings of the 24th international ocean and polar engineering conference, Busan
17. Jia J (2016) The effect of gravity on the dynamic characteristics and fatigue life assessment of offshore structures. J Constr Steel Res 118(1):1–21

Chapter 3

Characterize Ground Motions

We learn geology the morning after the earthquake
Ralph Waldo Emerson, *The Conduct of Life*, 1860.

3.1 Definition of Earthquake Locations

To determine the location of an earthquake occurrence, two geometric notations, namely hypocenter and epicenter, will be introduced first. Because the majority of earthquakes are caused by the rupture of the rock along a fault or multiple faults, and thousands of square kilometers of fault plane surface may be involved in this rupture, while it is important to define a location in a fault where the rupture initiates, this location is normally referred to as hypocenter or focus as shown in Fig. 3.1. From the hypocenter, the rupture spreads across the fault at velocities ranging from 2 to 3 km/s [1]. The projected point on the ground's surface above the hypocenter is called the epicenter. Obviously the hypocenter is located at a distance below the epicenter; this distance is called the focal depth or hypocentral depth. Similarly, the distance between the focus and a place of interest (observer or site) is called the hypocentral distance or focal distance.

3.2 Seismic Waves

When an earthquake occurs, the energy released due to fault rupture radiates over a broad spectrum of frequencies through the Earth, generating both body waves and surface waves. They propagate away from the earthquake source, and travel to ground surface/seabed through soil media, causing ground movement. This process is illustrated in Fig. 3.2. The body wave travels through the Earth's interior, while the surface wave is generated due to the interaction between the body waves and the materials close to the Earth surface. It therefore only travels close to the ground

Fig. 3.1 Illustration of focus (hypocenter), epicenter, epicentral distance, and hypocentral distance [2]

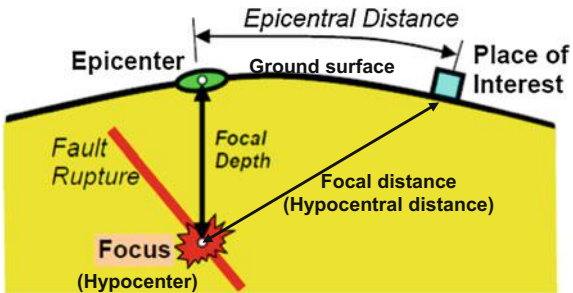
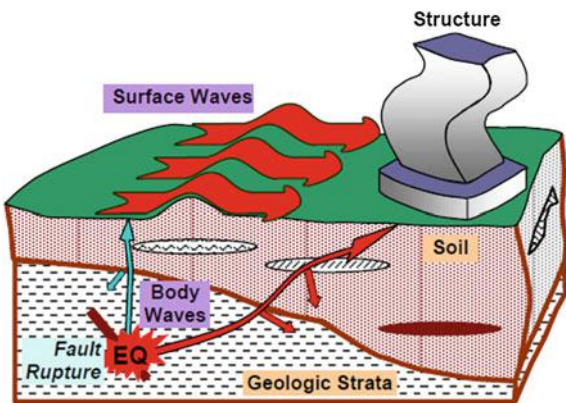


Fig. 3.2 Arrival of body and surface waves [2]



surface. In addition, a third type of wave called guided wave is particularly significant for a channel or a layer between two discontinuities. All three types of waves above will be presented in this Sect. 3.2.

3.2.1 Body Waves

The body waves comprise two types: P-wave or S-wave.

3.2.1.1 P-Wave

P-wave, also known as primary (P) wave, compressional wave or longitudinal wave, is, during an earthquake event, the fastest wave to arrive at a site. P-waves have typical speeds ranging from 200 to 1400 m/s in soil, and can reach 5000 m/s for hard rock and around 1500 m/s in water soils. Since for soils saturated with water, the modulus of compressibility of water is larger than that of the soft soil skeleton, the measured P-wave velocity is actually the velocity of the sound

propagating in water media without reflecting the engineering nature of soil. Similar to sound waves, it transmits the energy through push and pull motion, which causes compressions and extensions (dilations) of the materials as shown in Fig. 3.3, leading to a variation of pressure and volume change. It can travel through solids, liquids and even gases (sound wave is a typical type of P-wave).

The velocity of P-wave can be calculated as:

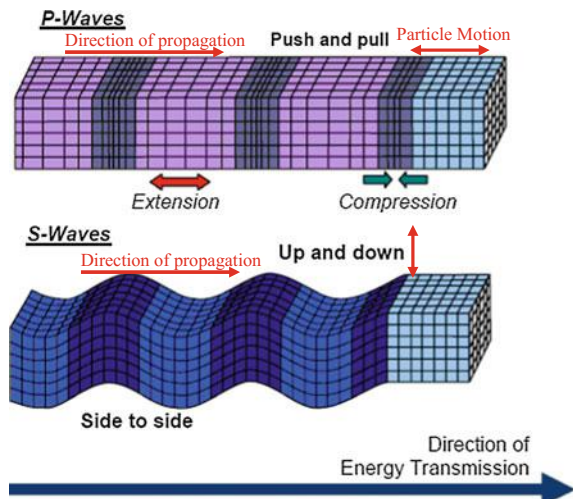
$$v_p = \sqrt{\frac{G(2 - 2\nu)}{\rho(1 - 2\nu)}} \quad (3.1)$$

where G , ν , and ρ are the shear modulus, Poisson's ratio, and density of the soil, respectively.

From the equation above, it is noticed that when the soil becomes incompressible, i.e., Poisson's ratio is close to 0.5, the velocity of P-wave approaches infinity.

The traveling speed depends on incompressibility, rigidity and density of the materials through which the P-wave travels. Therefore, during an earthquake event, P-wave provides an advance warning as it travels faster than the normally more destructive waves (mainly S-wave, and sometimes surface wave as well). However, how efficient the advance warning is depends on an accurate detection of P-wave and the time interval between the arrival of P-wave and other destructive waves. Depending on the depth, distance from the epicenter and magnitude of the earthquake, this time interval (between P- and S-wave arriving) is normally in the order of a few seconds up to around a minute. Since the rock and soil are rather resistant to the compression-dilation effects, the P-wave has only a minor influence on the ground motion. However, P-wave can also generate significant ground motions especially at sites close to fault ruptures. Moreover, as mentioned in Chap. 1, the

Fig. 3.3 Motions caused by harmonic body waves (the direction of propagation is the direction wave energy travel) propagating in a homogeneous isotropic medium [2, 3]



P-wave generates vertical seismic motions at seabed/riverbed/lakebed, which can propagate through waters and result in vertical shocks (hydrodynamic pressure) applied on ships, submerged structures, submarines, and other floating offshore structures, known as seaquake wave or shock wave, which will be discussed in Chap. 11.

3.2.1.2 S-Wave

S-wave, also known as secondary (S-) wave, shear wave, or transverse wave, has the most significant impact on the ground motion because the soil generally has rather weak shear resistance. It transmits the energy through shear action at a right angle to the direction of motion, which causes shear deformation of the materials (Fig. 3.3). Note that as liquids such as sea water have no shear resistance and S-wave can only travel in solids such as rock and soil, the seabed will therefore essentially behave as a free surface as the ground on land. Figure 3.4 shows the transmission pattern of shear wave from the earthquake source to the ground. S-wave travels more slowly than P-wave in rock and soil due to the fact that shear resistance in soil and rock are relatively low compared to those of the compression-dilation resistance. Compared to P-wave, S-wave normally cherishes a higher amplitude and period with a lower wave speed ranging from 100 m/s (very soft soil) to 800 m/s (very stiff soils) for soils and around 3000 m/s for hard rocks.

The velocity of S-wave can be calculated as:

$$v_s = \sqrt{\frac{G}{\rho}} \quad (3.2)$$

where G and ρ are the shear modulus and density of the soil, respectively.

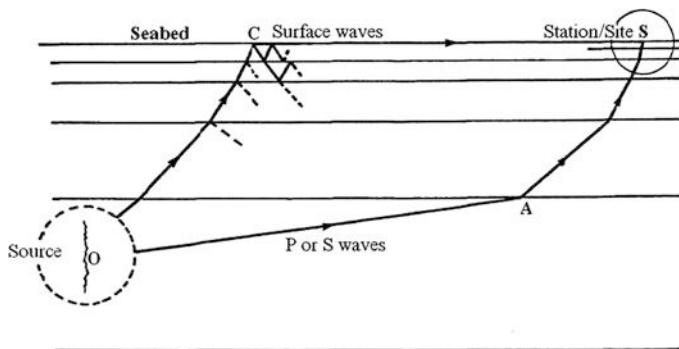


Fig. 3.4 The transmission path of body (OAS) and surface (OCS) wave from an earthquake source (O) to station/site (S) [4]

From the equation above, it is noticed that a material with a high stiffness-to-density ratio has a high wave propagation velocity.

Figure 3.5 shows the time history measurement of P-wave and S-wave at different distances from the epicenter.

S-wave is the one that generally causes strong ground motions that can have damaging effects on structures, because the horizontal peak ground acceleration is mostly influenced by the S-waves, and only in some cases by surface waves (Sect. 3.2.2), i.e., if the distance between the earthquake source and a site is larger than twice of the Earth crust thickness, instead of body wave, the surface wave is likely to produce the peak ground motions. One of the important tasks in the site response analysis (Chap. 4), which is a typical task to obtain the ground motions as will be elaborated in Chap. 4, is to calculate the horizontal ground motions due to the propagation of S-wave through soil media.

The ratio of the transmission velocity between the P-wave and S-wave is:

$$\frac{v_p}{v_s} = \sqrt{\frac{2 - 2v}{1 - 2v}} \quad (3.3)$$

Obviously, P-wave is faster than S-wave, and the significance of the velocity difference between the two types of waves depends on the Poisson's ratio (indicating soil's compressibility). For typical soils with $v = 0.3$, the ratio of the velocity between the P-wave and S-wave is 1.87.

By identifying the direction of particle movement, S-wave can be divided into SH (horizontal plane particle movement) and SV (vertical plane particle movement) wave, which are shown in Figs. 3.6 and 3.7. It should be noted that the SV and the P-wave interact with each other during their propagation as shown in Figs. 3.8 and 3.9. This is because the particle motion associated with SV wave is in parallel to the wave propagation direction: when it arrives at a boundary between two soil layers, it generates both P-wave and SV wave in refracted and reflected phases [6].

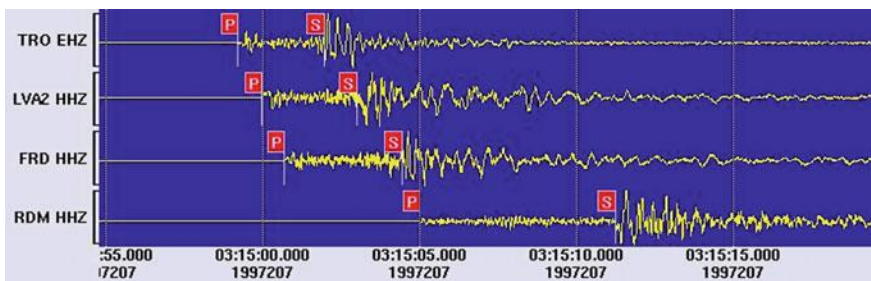


Fig. 3.5 The measured records of P- and S-waves at different distances from the epicenter [5] (courtesy of Robert John Mellors)

Fig. 3.6 Refraction and reflection of SH wave in one dimension

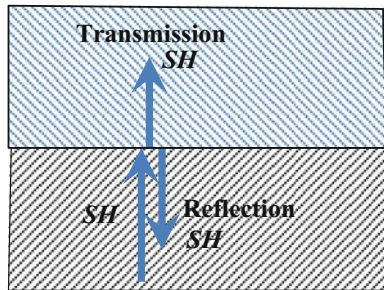


Fig. 3.7 Refraction and reflection of SV wave

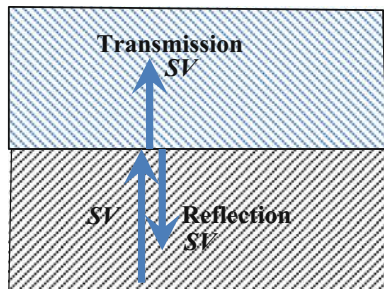


Fig. 3.8 Refraction and reflection of SV wave

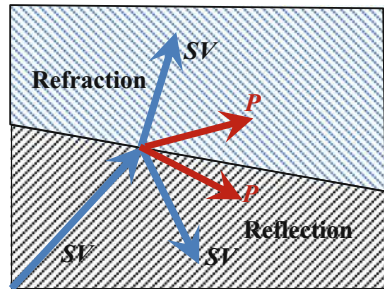
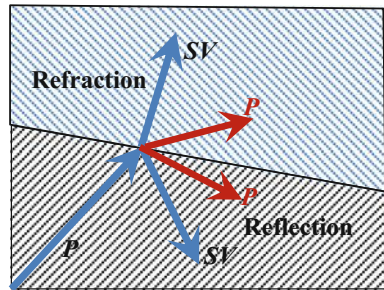


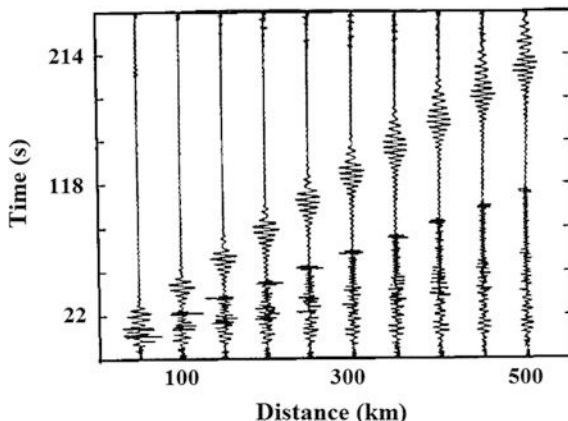
Fig. 3.9 Refraction and reflection of P-wave



3.2.2 Surface Waves

Different from body wave, surface wave travels along paths parallel to the surface of the Earth. It is generated by an interaction of body waves with the ground surface. At a distance from the earthquake source or if the ground motion is measured by peak ground velocity (PGV) or peak ground displacement (PGD), surface wave can be responsible for peak ground motions as shown in Fig. 3.28. Compared to body wave, surface wave has a longer period with a relatively slower decay with time. Figure 3.4 shows the typical transmission path of body and surface waves [4]. At a distance larger than a few times the thickness of the Earth's crust (30–50 km), surface wave is more predominant than body wave to produce the peak ground motions as shown in Fig. 3.10, even if it propagates at a lower frequency range than that of the body wave. Surface wave arises from the interaction of elastic waves with the free surface, and is a result of a linear combination of P-wave and S-wave. Its amplitude decays with depth within a medium. The surface wave comprises of Love wave and Rayleigh wave as shown in Fig. 3.11. While Love wave requires some kinds of a wave guide formed by a velocity increase with depth (gradient-wise or layer-wise), Rayleigh wave exists at any free surface. As a result of geometric spreading in 2-D (radiation), the energy carried by surface wave decays with source-to-site distance R from the source as $1/R$, in contrast to $1/R^2$ for body wave, i.e., a decrease in ground motion amplitude associated with surface wave (mainly Rayleigh wave) is inversely proportionally to \sqrt{R} , while for body wave induced ground motion amplitude, this decrease is inversely proportional to R . Due to surface wave's slower rate of decay than that of body wave, it can circle the globe many times following a large earthquake.

Fig. 3.10 Variation in ground shaking varied with the distance from the earthquake source, with short period body wave followed by the longer period surface wave [7]



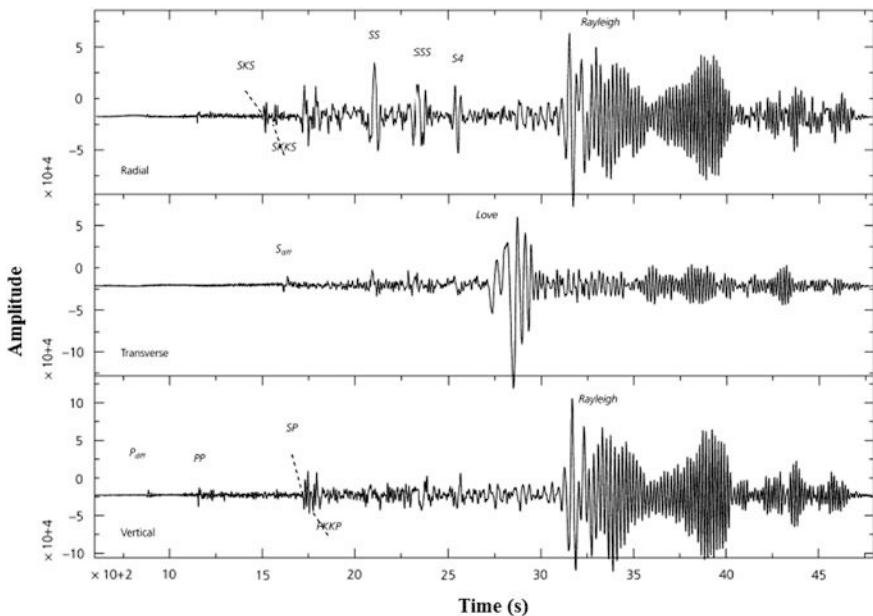


Fig. 3.11 Amplitude histories showing Rayleigh and Love wave

3.2.2.1 Love Wave (LQ or G)

Love wave (LQ or G), also known as Q-wave (Quer: lateral in German), named after the British mathematician AEH Love, is produced from SH wave with a soft surficial layer and has a vertical component of particle motion. Unlike Rayleigh wave, which has coupled P-SV type displacement, Love wave contains only SH-motion. This wave occurs when an elastic halfspace is overlain by a softer surface layer. Love wave is analogous to S-wave because it transmits the energy through shear action close to the ground surface, causing the horizontal shifting of the Earth. The upper figure in Fig. 3.12 illustrates the wave propagation and the particle motions caused by the Love wave. Because the particle motion occurs in the horizontal plane, the Love wave is essentially a type of sideways shear wave. Being a type of SH wave, Love wave does not have a volume change and it only exists in layered media.

3.2.2.2 Rayleigh Wave (LR or R)

Rayleigh wave (LR or R) is a rolling wave produced by the interaction of P and/or SV waves with the Earth's surface as shown in Fig. 3.13. It involves both the vertical and horizontal particle motions similar to ocean waves. The lower figure in Fig. 3.12 illustrates the particle motions caused by the Rayleigh waves. The

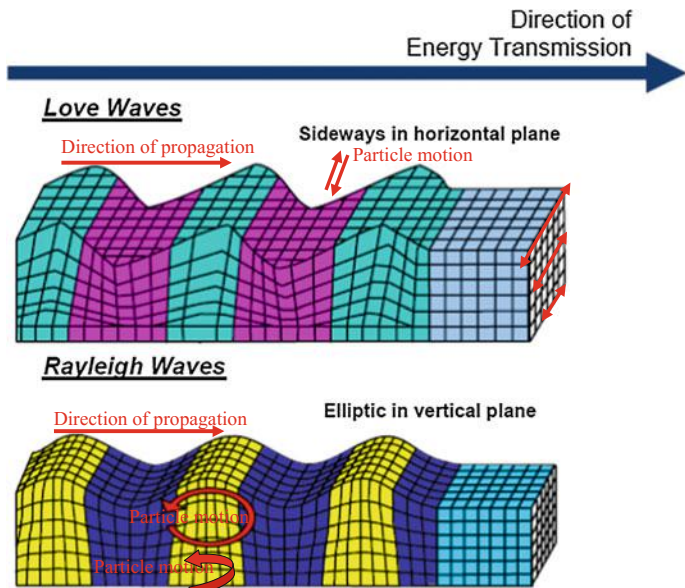
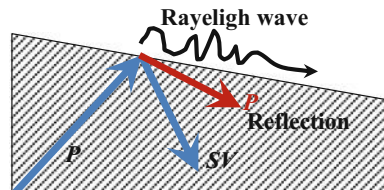


Fig. 3.12 The displacements of the fundamental mode (motions) caused by surface waves [2, 3]

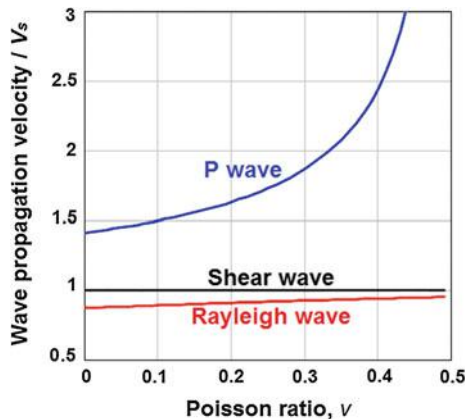
Fig. 3.13 Rayleigh wave is a combination of P-wave and SV wave that can exist at the top of homogeneous halfspace



direction of the particle movement is below some depths reversed, such that it becomes clockwise. While an important difference between Rayleigh wave and ocean wave is that, theoretically, in ocean wave all water particles travel in clockwise circles, in a Rayleigh surface wave, particles at the surface trace out counter-clockwise ellipses, while particles at a depth of more than 1/5 of a wavelength trace out clockwise ellipses. Rayleigh wave is a type of surface acoustic wave with low frequency (less than 20 Hz, and can be detected by animals, but not human beings), causing surface ripples (deformations in both vertical and horizontal directions) through the vertical oscillation.

Figure 3.14 compares the relative velocity among shear wave, P-wave and Rayleigh wave. Obviously, the relative velocity among three waves depends on the Poisson ratio. P-wave is the fastest traveling wave among the three and its velocity is most sensitive to a variation in Poisson's ratio of the transmission media, while the velocity of Rayleigh wave is slightly lower than the shear wave velocity. In

Fig. 3.14 Wave propagation velocity



addition, Love wave is faster than Rayleigh wave. Therefore, as the waves radiate outwards from an earthquake source, the different types of waves separate out from one to another in a predictable pattern. It is worth mentioning that Rayleigh wave is a major component of ground vibrations caused by traffic and construction works (e.g., pile driving).

Readers may bear in mind that, for a predefined wave propagating through the same media, the wave frequency f and velocity v do not change. Therefore, the wave length λ is also constant as it can be determined by its relation with frequency and velocity:

$$v = \lambda f \quad (3.4)$$

However, if the same wave propagates through different media, the velocity changes, as does the wave length according to the equation above. Moreover, for the same type of wave (e.g., S-wave or Rayleigh wave) with different frequencies, as long as that type of wave propagates in the same media, the velocity is always the same. However, because the frequencies are different, the wave lengths are therefore different.

The relative contribution of the body and surface wave to the ground motion and the corresponding arrival time depend on the distance between sites and epicenter, the focal depth of the earthquake source, and the reflection and refraction of the waves along their paths. Given the significant decay of surface wave amplitudes with depth, earthquakes with focal depths deeper than the recorded wave lengths will produce dramatically reduced or insignificant surface waves. Therefore, the amplitude ratio between body and surface waves in broad band records is a convenient tool to distinguish shallow and deep earthquakes.

Surface wave generally only affects large span structures, since the focal depth of the majority of earthquakes is below 10 km, and only relatively high period surface wave is generated for those earthquakes, with an example shown in Fig. 3.28. Surface waves can be very damaging to pipelines and long-span structures since

they can produce relative motions (at low frequency range) between supports. While in the case of basin-induced surface waves, their frequency content is dependent on the site period of soil in the basin, one may also record lower period surface waves, to which small span structures can be sensitive as well.

As shown in Fig. 3.10, the ground motion associated with surface wave (especially Rayleigh wave) is normally dominant for sites a large distance from the earthquake source. This figure also shows that the surface wave generally has a longer period than the body wave and duration of ground motion increases with the distance from the earthquake source. Therefore, while body wave (especially S-wave) is typically associated with the structural damage close to the source, surface wave (especially Rayleigh wave) is often the most important wave responsible for structural damage some distance from the source.

3.2.3 Guided Waves

Guided wave or channel wave is originally a type of body wave that travels through layered media and its properties change only vertically and not horizontally. Guided wave is particularly significant for a channel or a layer between two discontinuities, such as coal seam (low velocity layer) adjacent to upper and lower soil layers (with higher rigidity), or low velocity zone inside the mantle wedge, so that a low velocity channel/layer is formed through which body wave can travel as guided wave or channel wave, and sometimes combined with surface wave [8]. Quite often, surface wave affected by a low velocity soil layer situated within a few wave lengths below the ground surface is also called channel wave [9].

Guided waves include L_g wave, R_g wave and T -wave:

L_g wave is essentially high frequency Love wave at a regional distance of thick continental crust. It travels along the continental path with relatively little energy loss, but is cut off abruptly when the path has even a small oceanic segment. It is normally recorded at epicentral distance of around 5° or higher, which is very useful for finding the boundary of a continental structure. The L_g wave travels by multiple reflections within the crust with a typical velocity of around 3.5 km/s, and it dominates the seismograms of the horizontal channels.

R_g wave is generated near ground surfaces due to seismic events such as rock or mine-bursts, industrial or underground nuclear explosions. It is essentially a high frequency Rayleigh wave, and shows normal dispersion and has relatively large amplitudes on vertical components. This type of wave is especially useful to detect man-made seismic sources near the surface and within 200 km from the source, as most of the natural earthquakes have a focus depth of at least a few kilometers for crustal earthquakes or even deeper for intermediate or deep earthquakes in subduction zones. Because the R_g wave is more strongly attenuated than the L_g wave, its amplitude is decreased to an insignificant level at a location more than 600 km from the source. R_g wave travels through continental crust with a velocity of around 3 km/s.

T-wave (Tertiary wave) is also called third wave, and is observed at coastal seismic stations that record sub-ocean earthquakes at regional distances. It propagates much slower (at least a few minutes later) than body waves (P-wave and S-wave). *T*-wave generally propagates through deep parts of the ocean termed a Sound Fixing and Ranging (SOFAR) channel as shown in Fig. 3.15, which is a low velocity layer where sound wave is focused, with a minimum sound velocity of about 1.5 km/s. The physics behind the SOFAR channel is that the speed of sound is greatly affected by the temperature in the upper part of the ocean and by the pressure in the deeper part of ocean: as the speed of sound decreases as temperature decreases, while the speed of sound increases as the pressure (depth) increases, the “channeling” of sound occurs because there is a minimum sound speed along the depth due to the combined effects of temperature and pressure. Depending on the salinity and temperature of sea water, this channel is often located between 700 and 1300 m below the sea surface, and below this depth, the sound velocity increases again, as illustrated in Fig. 3.16. *T*-wave can travel thousands of kilometers within the SOFAR channel. Different from that of P-wave, there is no sharp onset for *T*-wave group. Ewing et al. [10] showed that *T*-wave propagates as sound wave through the water and as body wave travel over the land path.

In engineering applications, guided wave transmitted in pipelines can be used for detecting corrosion in pipelines as a non-destructive testing method.

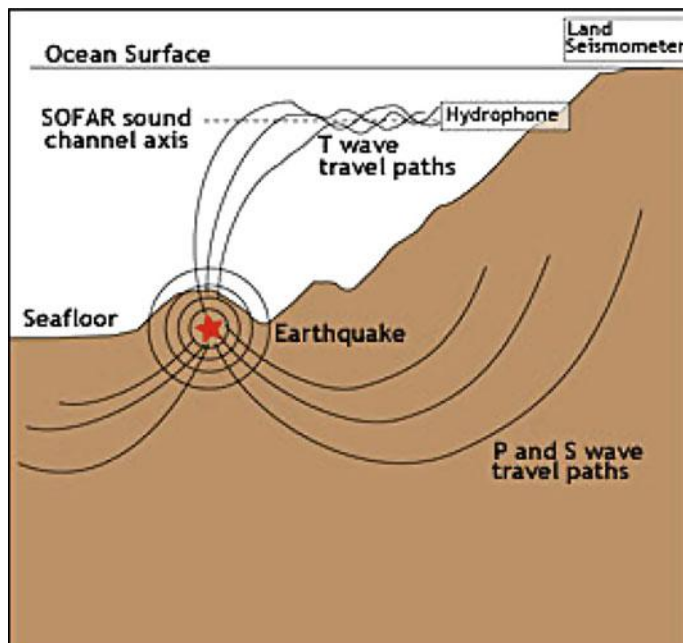
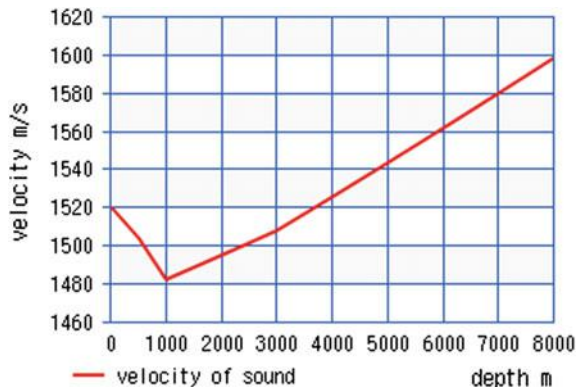


Fig. 3.15 T-waves traveling through Sound Fixing and Ranging channel [11]

Fig. 3.16 Typical sound velocity distribution along the depth of sea water according to UNESCO algorithm (the salinity is assumed to be 3.4 %, the temperature of sea water is assumed to be 4 °C at a depth of 1000 m, and 2 °C at a depth of 3000 m) [12]



3.3 Measuring Seismic Motions Using Seismogram

3.3.1 Measurement Using Seismograph

The first seismogram was invented by a Chinese scientist Heng Zhang in AD 132, and was called Houfeng Didong Yi (literally, “instrument for measuring the seasonal winds and the movements of the Earth”) as shown in Fig. 3.17. It was a large bronze vessel around 2 meters in diameter; at eight points around the vessel were dragon’s heads holding bronze balls. When there was an earthquake, one of the mouths would open and drop its ball into a bronze toad at the base, making a sound and supposedly showing the direction of the earthquake. The available text says that inside the vessel was a central column that could move along eight tracks; this is thought to refer to a pendulum, though it is not known exactly how this was linked to a mechanism that would open only one dragon’s mouth. On at least one occasion, probably at the time of a large earthquake in Gansu China in AD 143, the seismoscope indicated an earthquake even though it was not felt by the majority of the people.

In the modern world, two types of seismogram are used to monitor seismic wave fields. The first type is the standard inertial seismometers measuring three components of translational ground motion (displacement, velocity, acceleration), forming the basis for monitoring seismic activity and ground motions. The second type aims at measuring the deformation (strains) of the Earth.

The current book only illustrates inertial seismometers, which are also called seismographs. A prototype of the seismograph, shown in Fig. 3.18, is a heavy mass lifted by a wire. The wire is connected to a bar, which is connected to a drum with paper on it. The drum and bar are rigidly connected to the ground. When an earthquake occurs, due to the pendulum effects, everything moves except the heavy mass and the pen. If the paper moves straight at a constant speed, the heavy mass will press the pen to draw a “time series” of ground motion in displacement.



Fig. 3.17 The first seismogram (Houfeng Didong Yi) invented by Chinese scientist Heng Zhang in AD 132

As will be presented in Sect. 3.4.1, to measure the earthquake magnitude in Richter scale, the Wood-Anderson seismograph shown in Fig. 3.22, which is sensitive to horizontal motions, is used to measure the seismic wave induced ground motions. It is important to know that this instrument has a particular natural period of 0.8 s, a critical damping ratio of 0.8 and a magnification of 2800.

The seismograph measures and documents the ground motions in all required period range by using digital technology. The right figure of Fig. 3.18 shows a FBA-3 force balance accelerometer seismogram. It is a mass-spring-damper device, packaged in a cast aluminum base and cover, sealed to prevent the entrance of dirt

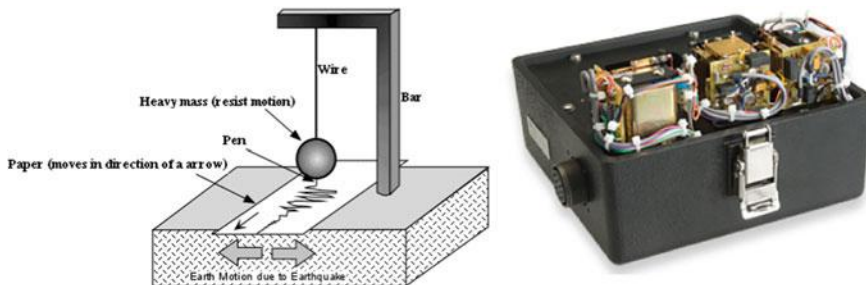


Fig. 3.18 Illustration of basic seismogram mechanism on the left (courtesy of Prof. Stephen A. Nelson, Tulane University) and a digital seismogram (*right*) of FBA-3 in the right, with full scale range of $\pm g$, undamped natural frequency of 50 Hz and damping 70 % of critical (courtesy of Kinemetrics, Inc.)

and moisture. The three accelerometers are orthogonally mounted on an internal deck plate. The transducer element is characterized by a natural frequency of 50 Hz and a viscous damping ratio of 70 %. These two parameters enable the digital instrument to record, without excessive distortion, acceleration time functions containing from very low to high frequencies (e.g. 30 Hz), and the analog instrument is accurate over a narrower frequency range [13, 14]. It is worth mentioning that since the occurrence of earthquakes is rare, many strong motion accelerometers do not record continuously, but are triggered by the P-wave that transmits fastest during an earthquake. Furthermore, with the aid of GPS satellite clocks, the recorded time histories can be marked with the absolute time, allowing the possible correlation of the analog records measured from various sites during an earthquake.

As shown in Fig. 3.19, as P-wave travels faster than S-wave, it will appear in the seismogram first but normally smaller in amplitude than. If S-wave does not appear on the seismogram, it probably indicates that the earthquake occurred on the other side of the planet, because S-waves cannot travel through the liquid layers of the planet.

The epicentral distance between the epicenter and the seismogram can be calculated based on time interval between the arrival of P-wave and S-wave. As a rule of thumb, the time interval in seconds multiplied by 8 is the distance between the epicenter and seismogram in kilometers. Or one can use a time-distance chart to determine the distance as shown in Fig. 3.23. In order to locate the epicenter, at least three seismographic stations at different distances from the epicenter are needed. The essential procedure is to draw a circle around one of the seismographic stations on a map, in which the radius of the circle equals the distance to the epicenter; then draw circles around the other two seismic stations. The point at which the three circles meet is the epicenter. This procedure is illustrated in Fig. 3.20. It should be noted that this procedure can only determine the epicenter,

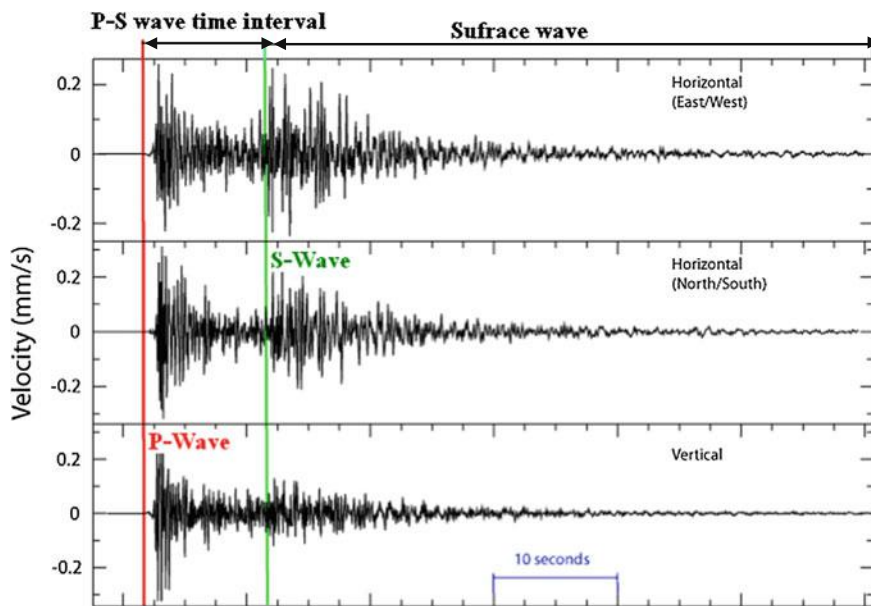


Fig. 3.19 The seismogram showing P-wave and S-wave in three perpendicular directions

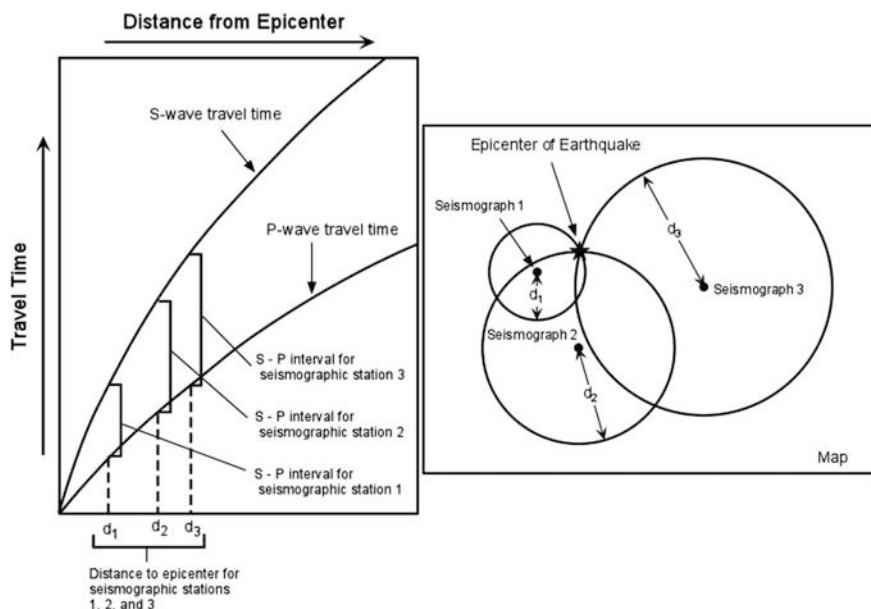


Fig. 3.20 Illustration of the method for locating epicenter (courtesy of Stephen Nelson, Tulane University)

which is the surface location of the earthquake source. A more comprehensive tool is needed to locate the depth of the earthquake source.

Immediately following the S-wave, the surface wave will appear and often with an even larger amplitude and period than S-wave if measured in velocity or displacement, which is illustrated in Fig. 3.28. For shallow earthquakes, the surface wave may be the most significant wave recorded by a seismograph. It is usually the only wave recorded a long distance (Fig. 3.1) from medium sized earthquakes [15] due to the slower decay of surface waves with distance than that of the body waves (Sect. 3.2.2).

Nowadays, strong motion recording and prediction (both empirically and theoretically) have become of primarily the task of seismologists and geophysicists, relieving geotechnical and structural engineers of that responsibility [16]. However, an understanding of this matter is still rather important for engineers in performing seismic design and analysis, and to be able to interact with seismologists and geophysicists in evaluating seismic risk and developing seismic design codes.

Monitoring stations with installed seismograms can also be used to measure seismic wave signals generated by other types of significant energy release (e.g. large explosion or nuclear test) at any parts of the world. For example, Fig. 3.21 shows recordings from one of the Norwegian seismic monitoring stations (the ARCES array in Karasjok), which is located a distance of 6260 km from the nuclear explosion test site, and the seismic pressure waves were recorded at this station 9 min and 43 s after the explosion took place.

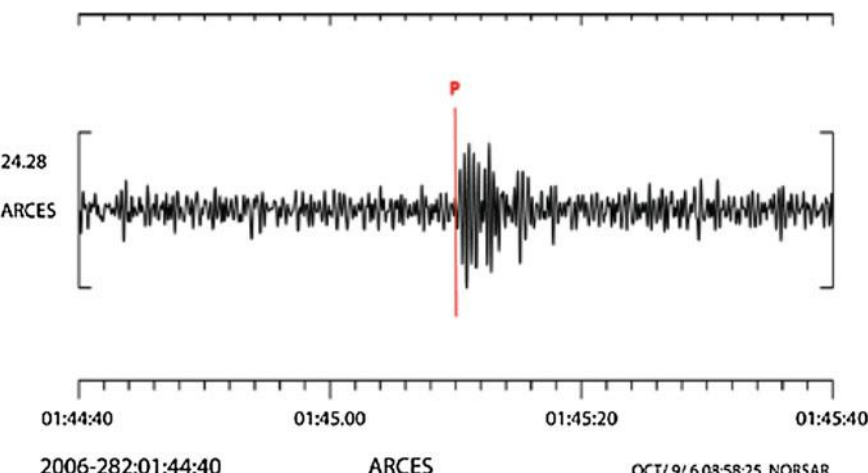


Fig. 3.21 Recording of the explosion by the ARCES seismic array located in northern Norway; the onset of the seismic pressure wave is marked with P, the time corresponds to Greenwich Mean Time (courtesy of NORSAR)

3.3.2 *Torsional Seismic Motions*

It is noticed that translational components during a seismic event are accompanied by rotational components because of the traveling wave effects. Tilting of the recorder's base can severely contaminate its response. Thereby, the recorded data may become a mixture of translational and rotational motions, and may be far from representing the true ground motion in the direction of recording [17].

Since the rotational ground motions (rocking and torsion) are likely to be caused due to the incidence of SV wave and surface wave, they are generally assumed to be small compared to their horizontal and vertical translational counterparts [18], and also due to the difficulties in the measurement operation (the wide frequency band and distance range are above capacity of sensitivity for measurement devices), the three rotational degrees-of-freedom motions are normally not important and can be omitted. Based on the difference in the tilt sensitivity of the horizontal and vertical pendulums, Graizer [19, 20] presented a method to calculate the rotational ground motion components from the recorded translational components.

It was only recently, with the adoption of the ring laser technology, that an accurate measurement of rotational degree-of-freedom motions was achieved. The measurements revealed that the rotational ground motions had been previously underestimated by people and may reach a few degrees for sites near faults. Various recorded structural damage may be potentially caused by rotational ground motions or a combination of translational and rotational ground motions [17]. For instance, torsional response of tall buildings in Los Angeles during the 1971 San Fernando earthquake could be attributed to the torsional ground motions [21], while a combination of rotational and longitudinal differential motions may have caused the collapse of bridges during the San Fernando (1971) and Miyagi-ken-Oki (1978) earthquakes [22], and during the Northridge 1994 earthquake [23]. Earthquake damage to pipelines, which is not associated with faulting or landslides and is due to large differential motions and strains in the soil, reflects the consequences of the propagating seismic waves and of the associated large rotations and twisting of soil blocks, which are caused by lateral spreads and early stages of liquefaction [17, 24, 25].

3.4 Magnitude and Intensity

Among others, the two most widely used measures to characterize earthquakes are magnitude and intensity. They are important parameters both for scientific purposes and hazard assessment.

3.4.1 *Magnitude*

To characterize the energy release due to the fault rupture during an earthquake, based on instrumental measurements of emanating wave amplitude, earthquake magnitude can be determined. Therefore, a general form of magnitude can be expressed as:

$$M = \log_{10}(A/T) + F(h, \Delta) + C \quad (3.5)$$

where A is the amplitude of the signal; T is its dominant period; F is a correction for the variation of amplitude with the earthquake's depth h and angular distance (the epicentral distance in degrees) Δ from the seismometer; and C is a regional scaling factor.

From the equation above, it is noticed that A and T do not have the same unit, therefore, the definition of earthquake magnitude is obviously dimensionally wrong. However, this does not impede its usefulness as an empirical formula to measure the earthquake size.

It is also noticed that since the magnitude scale is logarithmic, an increase in one unit, e.g. from 4 to 5, indicates a tenfold increase in seismic wave amplitude. Moreover, magnitudes can be negative for very small displacements.

The advantages of using magnitude as a measure of earthquake size are that the magnitude is directly measured from seismograms without sophisticated signal processing, and the estimate is intuitively meaningful, e.g., magnitude 2 is small, magnitude 6 is relatively strong.

There are various definitions of earthquake magnitude, such as Richter, surface wave, body wave, and moment magnitude, which will be introduced in the subsequent sections.

3.4.1.1 Richter (Local) Magnitude

Named after CF Richter, who first defined the earthquake magnitude, the Richter magnitude (M_L) [26], also known as local magnitude, was the first widely used instrumental magnitude scale, and was originally used as a means of describing sizes of local earthquakes in Southern California. As stated by Richter (1958): “Magnitude was originally defined as the logarithm of the maximum amplitude on a seismogram written by an instrument of specific standard type at a distance of 100 km. ... Tables were constructed empirically to deduce from any given distance to 100 km. ... The zero of the scale is fixed arbitrarily to fit the smallest recorded earthquakes.” As the magnitude was intended to represent a measure of the energy released by an earthquake and is independent of the locations of observation, it is defined mathematically as a logarithmic scale:

$$M_L = \log_{10} A - \log_{10} A_0 + S \quad (3.6)$$

where A is the maximum trace amplitude (deflection from zero to peak in mm) for a given earthquake at a given distance recorded on the horizontal component of a standard Wood-Anderson torsion seismometer as shown in Fig. 3.22, consisting of a small copper cylinder attached to a vertical metal fiber, and the restoring force is supplied by tension in the fiber. The Wood-Anderson seismograph is sensitive to horizontal motions, which are detected via light reflected from a small mirror in the cylinder. It is important to know that this instrument has a particular natural period of 0.8 s, critical damping ratio of 0.8 and a magnification of 2800; S is a station correction term. The empirical function $-\log_{10}A_0$ depends only on the distance of the instrument's hypocentral distance R in kilometers:

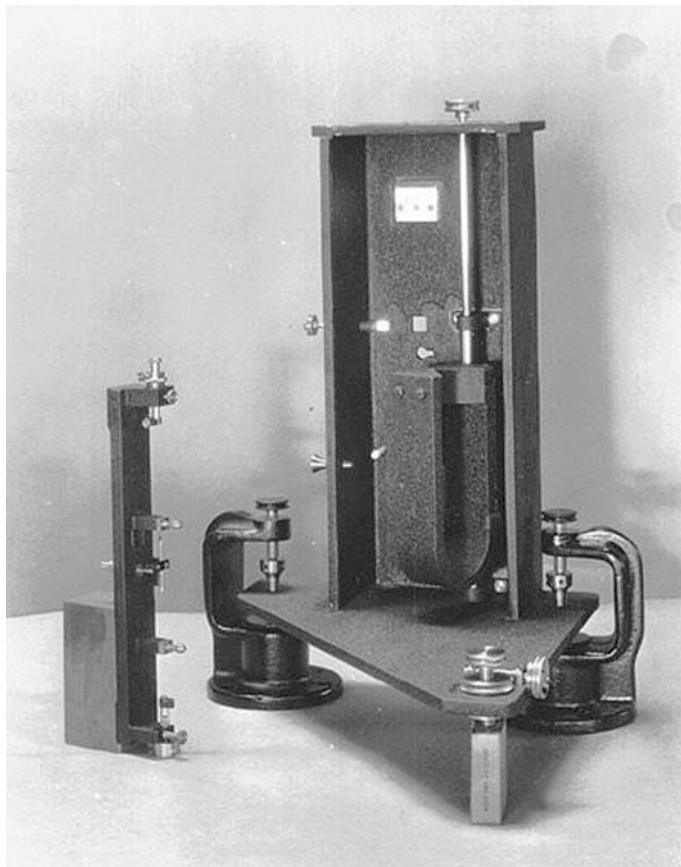


Fig. 3.22 Wood-Anderson seismograph (courtesy of JB Macelwane Archives, Saint Louis University)

$$-\log_{10}A_0 = a \cdot \log_{10}(R/100) + b \cdot (R - 100) + 3.0 \quad (3.7)$$

where a and b are coefficients for geometrical spreading and anelastic attenuation, respectively.

From the two equations above, it is noticed that, without station correction term S , the two equations above imply that an earthquake of 0 Richter magnitude is defined as a maximum amplitude of 0.001 mm at a distance of 100 km. Due to the logarithmic scale, each whole number increase of magnitude indicates a tenfold increase in measured amplitude and a 31.6 times increase of released energy. Thus, a maximum seismogram amplitude (at a distance of 100 km) of 0.01 mm represents Richter amplitude of 1.0, 0.1 mm equals M_L 2.0, 1 mm equals 3.0, and so on.

In practice, readings from all observing stations are averaged after adjustment with station-specific corrections to obtain the value of magnitude.

Instead of using the equations above, one can determine the Richter magnitude of the earthquake based on the measurement at any given distance based on the chart shown in Fig. 3.23: first draw a line between the point of the epicenter distance (presented in Sect. 3.3) in the left graph and point in the rightmost chart that corresponds to the maximum measured displacement amplitude of the strongest wave in the seismograph; the cross point at the middle graph (magnitude) indicates the Richter magnitude.

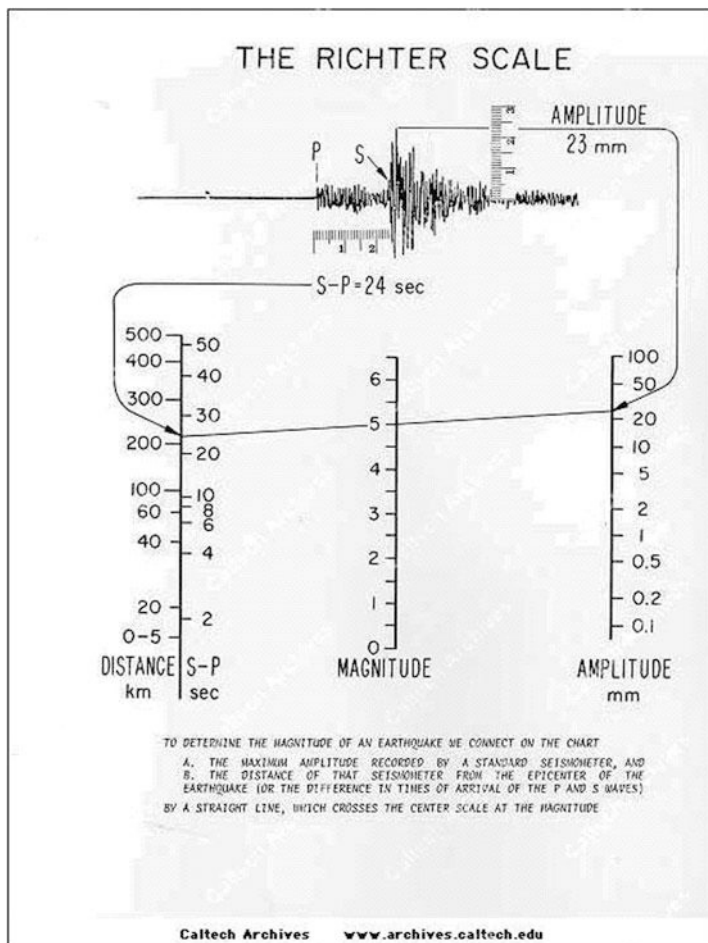
The Richter magnitude is normally measured from dominating S-wave and Lg wave, in which the latter includes a mixture of higher frequency modes surface waves.

Today, Richter magnitude is still used as a measure of earthquake size for earthquakes with magnitudes up to 6.5 and with epicentral distances less than 600 km (the reason why it is called “local” magnitude). For earthquakes with magnitude larger than 6.5, this measure is believed to be “saturated” due to instrument characteristics and reliance on measuring only a single, short period peak, which will be discussed in Sect. 3.4.1.5.

Nowadays, Wood-Anderson seismograph is rarely used for recording the seismic wave field. However, as mentioned before, Richter magnitudes are sometimes still reported, this may be due to the fact that many infrastructures have a natural period close to 1 s, which is close to that of a Wood-Anderson seismograph (0.8 s). Therefore, M_L is often a good indicator of structural damage potential.

3.4.1.2 Surface Wave Magnitude

Richter magnitude is based on a measurement that does not distinguish the motions contributed by body and surface waves. However, with an increase in epicentral distance, the body wave induced ground motions decrease significantly. And at a large epicentral distance of more than 1000 km, the higher frequency vibrations are



The procedure may be interpreted to give a definition of the magnitude scale number being used, as follows: *The magnitude of any shock is taken as the logarithm of the maximum trace amplitude, expressed in microns, with which the standard short-period torsion seismometer ($T_0 = 0.8 \text{ sec.}$, $V = 2800$, $h = 0.8$) would register that shock at an epicentral distance of 100 kilometers.*

This definition is in part arbitrary; an absolute scale, in which the numbers referred directly to shock energy or intensity measured in physical units, would be preferable. At present the data for correlating the arbitrary scale with an absolute scale are so inadequate that it appears better to preserve the arbitrary scale for its practical convenience. Since the scale is logarithmic, any future reduction to an absolute scale can be accomplished by adding a constant to the scale numbers.

Fig. 3.23 The time-distance (left) with amplitude (right) and magnitude (middle) chart (courtesy of California Institute of Technology Archives)

attenuated and seismic surface waves are dominated by waves with a long period of 20 s (corresponding to a wavelength of about 60 km). To solve this “saturation” problem, for significant shallow earthquakes with focal depth less than 70 km, with a large epicentral distance more than 1000 km [32], surface wave magnitude M_s is the most commonly used measure of earthquake sizes, which was developed by Gutenberg [27]:

$$M_s = \log_{10}A + 1.656\log_{10}\Delta + 1.818 \quad (3.8)$$

where A is the maximum horizontal ground displacement amplitude (zero to peak) in micrometers rather than the trace amplitude recorded on a standard Wood-Anderson seismograph. This means that the effects of the seismometer on the ground motion measurement must be removed; Δ is the epicentral distance in degrees, with 360° corresponding to the circumference of the Earth.

If the amplitude of Rayleigh waves with a period of about 20 s is used, the surface wave amplitude is defined as:

$$M_s = \log_{10}A + 1.66 \cdot \log_{10}\Delta + 2.0 \quad (3.9)$$

In China, the surface wave amplitude is determined by [28]:

$$M_s = \log_{10}A - \log_{10}T + 1.661 \cdot \log_{10}\Delta + 3.5 \quad (3.10)$$

where T is the period of surface wave. In case the wave periods along two perpendicular directions in the horizontal plane are different, a weighting procedure is needed to obtain the resultant period.

3.4.1.3 Body Wave Magnitude

Note the fact that the amplitude of the first few cycles of P-wave is not strongly affected by the hypocentral depth (focal depth) [1], while the amplitude of the surface wave is so insignificant as a reliable measure of deep focus earthquakes, the body wave magnitude is often used for characterizing deep focus earthquakes based on the records of early portion of the body wave train associated with P-wave:

$$m_b = \log_{10}A - \log_{10}T + Q(h, \Delta) \quad (3.11)$$

where A and T is the displacement amplitude in micrometers and period of P-wave; Q is an empirical term that is a function of focal depth h and angular distance (the epicentral distance in degrees) Δ , which can be derived as a global average or for a specific region.

In the measurement of m_b , seismometers used for measurements and the portion of the wave train measured vary worldwide. For example, in US, it is a common practice to use the first 5 s of the record, and periods less than 3 s (usually about 1 s), on instruments with a peak response of about 1 s.

$$m_b = \log_{10} A - \log_{10} T + 0.01\Delta + 5.9 \quad (3.12)$$

Until now, we have learned the definition of Richter, body and surface wave magnitude. Figure 3.24 shows the period ranges of various measures of earthquake magnitude associated with different types of propagating waves and physical phenomena, indicating the bias of each definition of magnitude.

3.4.1.4 Moment Magnitude

It is noticed that the magnitude is often measured a few hundred kilometers away from the epicenter. The maximum measurable Richter magnitude and body wave magnitude are around of 6–7, and the maximum measurable surface wave magnitude is about 8. For stronger earthquakes, the measured ground shaking becomes less sensitive to the size of the earthquake than smaller earthquakes, which is often referred to as the phenomenon of saturation, as will be discussed in the Sect. 3.4.1.5. Moreover, for measurement taken more than about 600 km away from the epicenter, the Richter magnitude gives unreliable results (according to USGS Earthquake Magnitude Policy). To overcome this drawback while maintaining consistency, based on an estimation of the seismic moment during the rupture of faults rather than the measurement of ground shaking levels, the strongest earthquake can be measured by the moment magnitude M_w (subscript w means mechanical work) [31], which is the only magnitude scale that does not have an upper limit of applicability:

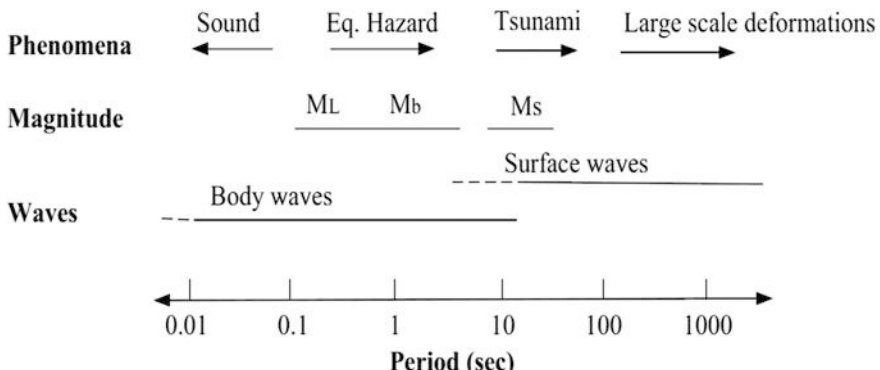


Fig. 3.24 Period ranges of various measures of earthquake magnitude associated with different types of propagating waves and physical phenomena [29, 30]

$$M_W = \frac{2}{3} \log_{10} M_0 - 10.73 \quad (3.13)$$

where M_0 is the seismic moment due to fault rupture in dyne-cm (1 dyn = 10^{-5} N). It is directly related to the elastic rebound theory as presented in Chap. 1. It can be estimated from geological records of historical earthquakes [32], or from the long period components of a seismogram [33].

If the seismic moment is measured in Nm, the equation above can be converted into:

$$M_W = \frac{2}{3} \log_{10} M_0 - 6.06 \quad (3.14)$$

$$M_0 = GA\delta \quad (3.15)$$

where G is the shear modulus of the fault material (normally rock) in dyne/cm², it indicates the hardness of the rock; A is the area of fault plane rupture in cm², i.e. the depth times the length of the fault (the geometry of the fault controls the distance between the fault and the site and is used in estimating the magnitude; usually the faults are idealized as plane rectangles); and δ is the mean relative slip (dislocation) or movement between the two sides of the fault in cm, or slip rate times the time interval of the earthquake recurrence. The reason for taking the mean value is because the fault dimensions and dislocations can vary significantly along the fault; the slip rate is estimated by dividing the amount of cumulative displacement, measured from displaced geologic or geomorphic features, by the estimated age of the geological material or feature. It is an average value over a short geologic time period, and is reliable to the extent that the strain accumulation and the subsequent release over this time period has been uniform and corresponding to the same tectonic stress environment. Table 3.1 shows the slip rates of a few representative faults, from which one can conclude that the slip rates vary considerably, with the highest value among prominent and highly active faults (Fairweather and San Andreas faults), and even for the same fault, significant uncertainties of the slip rate

Table 3.1 Slip rates of selected faults [34]

Fault name	Slip rate (mm/year)
Fairweather, Alaska	38–74
San Andreas, California	20–53
Hayward Fault, Northern California	7–11
Wasatch, Utah	0.9–1.8
Newport-Inglewood, Southern California	0.1–1.2
Atlantic Coast faults	0.0002

can be observed, which pertains to various segments as well as to a specific segment of a fault [34].

From the three equations above, it is obvious that the longer and deeper a fault is, and the harder the fault rock is, the stronger an earthquake can be generated by the fault. The seismic moment provides a basic link between the physical parameters that characterize the faults and the seismic waves radiated due to rupturing along the fault. It is therefore a more useful measure of the earthquake size.

There are several interpolation models to evaluate the relationship between fault length L in km and moment magnitude M_w , with a typical form as follows:

$$\log_{10}^L = AM_w + B \quad (3.16)$$

where A and B are two constants, which are highly sensitive because of a \log_{10} relationship between the fault length and the value of the right hand side of the equation.

Ambrasseys and Jackson [35] proposed that $A = 0.82$ and $B = -4.09$.

By distinguishing the energy release among different fault types (Chap. 1), Wells and Coppersmith [36] proposed that the relationship can be calculated as:

$$\log_{10}L = -3.55 + 0.74M_w \quad \text{for strike-slip faults} \quad (3.17)$$

$$\log_{10}L = -2.86 + 0.63M_w \quad \text{for reverse faults} \quad (3.18)$$

$$\log_{10}L = -3.22 + 0.69M_w \quad \text{for all other fault types} \quad (3.19)$$

Figure 3.25 compares the seismic moment release for the largest earthquakes from 1906 to 2005 compared to all other earthquakes for the same period. It is obvious that the three largest earthquakes (Sumatra, Alaska and Chile) comprise almost half of the total moment release of all earthquakes under consideration during the 100 year period.

In the past 30 or so years, the use of seismic moment has provided a physically more meaningful measure. Therefore, present practice appears to be moving toward the use of M_w in preference to other magnitudes [37]. Even if moment magnitude is applicable and unbiased over the whole range of released energy, it is normally recommended to characterize only large magnitudes of earthquakes (e.g. $M_w = 3.5\text{--}5.0$ or higher). For smaller magnitudes of earthquakes, the value of moment magnitude is comparable to Richter magnitude.

3.4.1.5 Saturation of Magnitude Measures

Table 3.2 shows the characterization of earthquake size for six earthquakes measured by moment, body wave and surface wave magnitude. It is noticed from this table that all earthquakes greater than the San Fernando earthquake have a body wave magnitude of 6.2. Similarly, all earthquakes larger than the San Francisco

Global Seismic Moment Release January 1906 - December 2005

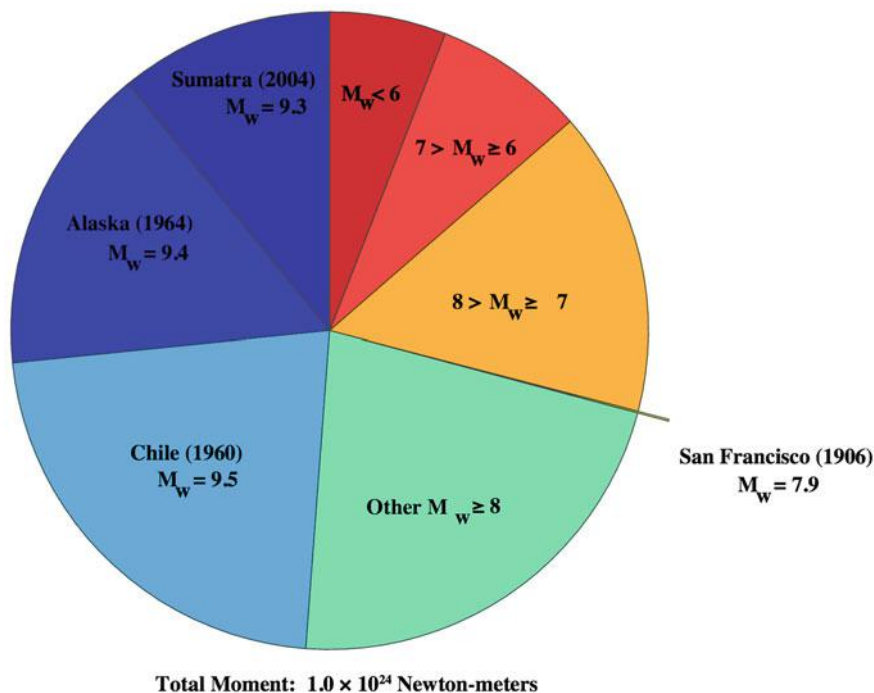


Fig. 3.25 Pie chart showing how the total seismic moment released by earthquakes over the period 1906–2005 was distributed, with the largest individual earthquakes (*left side*) and groups of earthquakes (*right side*). The thin sliver of the 1906 San Francisco Earthquake is also depicted for comparison purposes. M_w designates moment magnitude

Table 3.2 Determination of earthquake size based on different measures of amplitude

Earthquake	Fault area (km ²) (length · width)	Average relative slip (m)	Seismic moment (dyn-com) M_0	Moment magnitude M_w	Body wave magnitude m_b	Surface wave magnitude M_s
Truckee, 1966	10×10	0.3	8.3×10^{24}	5.9	5.4	5.9
San Fernando, 1971	20×14	1.4	1.2×10^{26}	6.7	6.2	6.6
Loma Prieta, 1989	40×15	1.7	3.0×10^{26}	6.9	6.2	7.1
San Francisco, 1906	450×10	4	5.4×10^{27}	7.8		7.8
Alaska, 1964	500×300	7	5.2×10^{29}	9.1	6.2	8.4
Chile, 1960	800×200	21	2.4×10^{30}	9.5		8.3

earthquake have a surface wave magnitude of 8.3–8.4, even if the seismic moment increases significantly for those stronger earthquakes. This phenomenon is normally referred to as magnitude saturation. It may be mentioned that the San Francisco earthquake, which had moment magnitude of 7.8, represents approximately the maximum size of continental transform (fault) earthquakes, such as the earthquakes that occurred in California associated with the San Andreas Fault (Chap. 1). The Alaska and Chile earthquakes had moment magnitudes of more than 9.0 because the rupture areas were much larger than the rest of the earthquakes in the table, and they occurred on shallow dipping subduction thrust interfaces as described in Chap. 1. By investigating the relationship between moment magnitude and other magnitude measures as shown Fig. 3.26, the flattening at higher amplitude due to the saturation effects can be clearly identified. Table 3.3 summarizes the applicability of various measures of earthquake magnitude.

It is worth mentioning that, in the last two decades, research efforts have been extended to pursue the moment magnitude scale accuracy for high frequencies, which are important in localizing small earthquakes. Earthquakes below magnitude 3 scale are poorly estimated because the Earth attenuates high frequency waves near the surface, making it difficult to resolve quakes smaller than 100 m. By use of seismographs in deep wells this type of attenuation can be minimized [38].

3.4.2 Intensity Categories

With the magnitude representing the energy released in the earthquake, intensity is categorized by the size related to damage in an area caused by an earthquake in that

Fig. 3.26 Comparison among different types of magnitude definitions showing the magnitude saturation (M_s surface wave magnitude; m_B long period body wave magnitude; M_L Richter (local) magnitude; m_b short period body wave magnitude) [34]

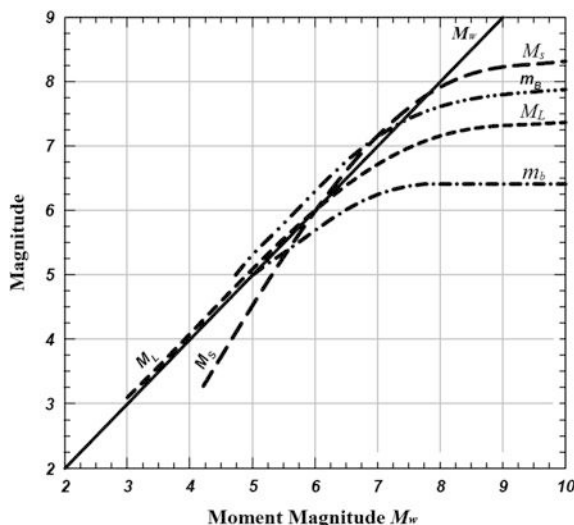


Table 3.3 Applicability of various measures of earthquake magnitude

Item	Richter (local) magnitude	Body wave magnitude	Surface wave magnitude	Moment magnitude
Measured wave type	S and L_g waves and higher order surface waves	P-wave	Rayleigh wave	Physical modeling of faults rather than measuring ground motions
Applicable earthquake focal depth	Normally shallow, but can be deep	Deep	<70 km	Shallow and deep
Applicable epicentral distance	<600 km	NA	>1000 km	NA
Measurable magnitude	<6.5	<7.5	<6–8	Basically no restrictions, practically used for earthquake with $M_w > 3.5$
Measured wave amplitude period	0.8 s	1–5 s	3–20 s	NA

area. It is normally estimated based on the reported effects of human beings' response, structural and non-structural element damage, and the natural environment, which are established under the common consensus of seismologists and engineers. Even though it is a qualitative measurement of ground motions level, the bias in the estimation of the intensity category is minimal. The most widely used intensity category measure [39] globally is modified Mercalli intensity (MMI). And there are other measures adopted in local regions such as Medvedev-Sponheur-Karnik (MSK), Rossi-Forel (R-F), Chinese Intensity Scale (corresponding approximately to MMI), and the Japan Meteorological Agency (JMA) scales etc.

The MMI is divided into 12 categories as follows (USGS):

- I. Not felt except by a very few under especially favorable conditions.
- II. Felt only by a few persons at rest, especially on upper floors of buildings.
- III. Felt quite noticeably by persons indoors, especially on upper floors of buildings. Many people do not recognize it as an earthquake. Standing motor cars may rock slightly. Vibrations similar to the passing of a truck. Duration estimated.
- IV. Felt indoors by many, outdoors by few during the day. At night, some awakened. Dishes, windows, doors disturbed; walls make cracking sound. Sensation like heavy truck striking building. Standing motor cars rocked noticeably. The PGA associated with this intensity level is typically around 0.02 g.
- V. Felt by nearly everyone; many awakened. Some dishes, windows broken. Unstable objects overturned. Pendulum clocks may stop. The PGA associated with this intensity level is typically around 0.04 g.

- VI. Felt by all, many frightened. Some heavy furniture moved; a few instances of fallen plaster. Damage slight. The PGA associated with this intensity level is typically around 0.07 g.
- VII. Damage negligible in buildings of good design and construction; slight to moderate in well-built ordinary structures; considerable damage in poorly built or badly designed structures; some chimneys broken. The PGA associated with this intensity level is typically around 0.15 g.
- VIII. Damage slight in specially designed structures; considerable damage in ordinary substantial buildings with partial collapse. Damage great in poorly built structures. Fall of chimneys, factory stacks, columns, monuments, walls. Heavy furniture overturned. The PGA associated with this intensity level is typically around 0.30 g.
- IX. Damage considerable in specially designed structures; well-designed frame structures thrown out of plumb. Damage great in substantial buildings, with partial collapse. Buildings shifted off foundations. The PGA associated with this intensity level is typically around 0.5 g.
- X. Some well-built wooden structures destroyed; most masonry and frame structures destroyed with foundations. Rails bent. The PGA associated with this intensity level is typically around 0.6 g.
- XI. Few, if any (masonry) structures remain standing. Bridges destroyed. Rails bent greatly.
- XII. Total damage. Lines of sight and level are distorted. Objects thrown into the air.

Note that the magnitude is an objective and rigorous description of the released energy, i.e., one particular earthquake only has a definite magnitude, while the intensity scale is a subjective measure of the shaking level at a specific location, i.e., for the same earthquake, the intensity at different locations can be different. Therefore, it is difficult to determine a reliable relationship between the two measures. Table 3.4 gives intensities that are typically observed at locations near epicenters of earthquakes of different magnitudes.

Table 3.4 MMI and its typical corresponding magnitudes (USGS)

Magnitude	Typical maximum modified mercalli intensity
1.0–3.0	I
3.0–3.9	II–III
4.0–4.9	IV–V
5.0–5.9	VI–VII
6.0–6.9	VII–IX
7.0 and higher	VIII or higher

3.5 Non-stationary and Peak Ground Motions

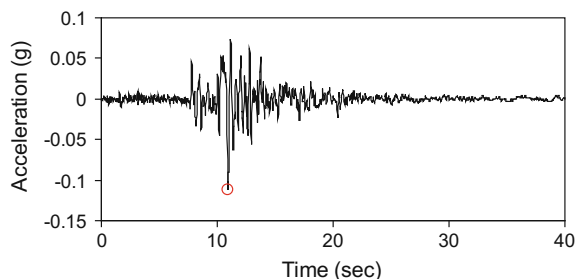
3.5.1 Peak Ground Motions and Its Relationship with Magnitude and Intensity

Compared to magnitude and intensity, peak ground acceleration (PGA) does provide more direct information for geotechnical and structural engineers, and is especially useful for constructing the design spectrum for structural analysis, as will be elaborated in Sect. 5.4. It is defined as the peak of the ground motion acceleration, as shown in Fig. 3.27. The PGA is normally below 0.5 g (g is the acceleration of gravity) for even a destructive earthquake. However, PGA of more than 1.0 g has also been reported in many earthquakes, such as the 1994 Northridge earthquake.

Generally, the horizontal PGA motions are higher than their vertical counterparts. However, at sites near the epicenter, the vertical PGA motions can be close to the horizontal ones, as will be discussed in Sect. 5.4.4. For example, the accelerogram readings at the Pacoima Dam during the 1971 Richter magnitude 6.6 San Fernando earthquake reached 1 g in both horizontal and vertical direction, and the one recorded at Cedar Hills Nursery (near the epicenter) in Tarzana, California during the Richter magnitude 6.9 Northridge earthquake of 1994 also reported a similar phenomenon: both the horizontal and vertical ground acceleration components approach 2 g, being the strongest ground movement recorded in the Northridge earthquake, and most of the sites with high ratios of vertical to horizontal PGA were deep soil sites, often in alluvial basins. In particular, of the nine sites with the ratios of vertical to horizontal PGA more than unity, only one was located on a rock site [40], which is believed to have been caused by S-to-P-wave conversion and wave scattering at the basin-bedrock interface, supplying energy to vertical components of strong ground motions. In addition, this fact is also responsible for the observed frequency content differences of the vertical and horizontal components of the ground motions.

The conversion between the intensity level *MMI* and the horizontal peak ground acceleration (PGA) a in cm/s^2 may be expressed as follows [26]:

Fig. 3.27 Recorded horizontal ground motions at a site (the cycle shows that the PGA is -0.11 g)



$$\log_{10} a = \frac{MMI}{3} - 0.5 \quad (3.20)$$

The equation above indicates that, if other conditions are the same, the PGA at a magnitude 8 earthquake is around 100 times of that of a magnitude 6 earthquake.

It should be noted that, although PGA can provide a reliable measure for the relative intensity of ground motions, it does not give any information regarding the frequency content that influences the amplification of a structure's dynamic response subject to ground motions. On the other hand, the frequency content of ground motions can be illustrated by using earthquake time histories, power spectrum or design spectrum etc., as will be elaborated in Chap. 5.

Furthermore, by observing Fig. 3.28, which shows the recorded horizontal ground motion at a site expressed in acceleration, velocity and displacement, it can be concluded that the PGA is associated with high frequency motions, the peak ground velocity (PGV) is associated with the intermediate frequency (lower than the high frequency but higher than a low frequency range) components of motions, while the peak ground displacement (PGD) is associated with the low frequency motions. This can be explained by the relationship among time histories measured by acceleration, velocity and displacement: a time derivate of the displacement

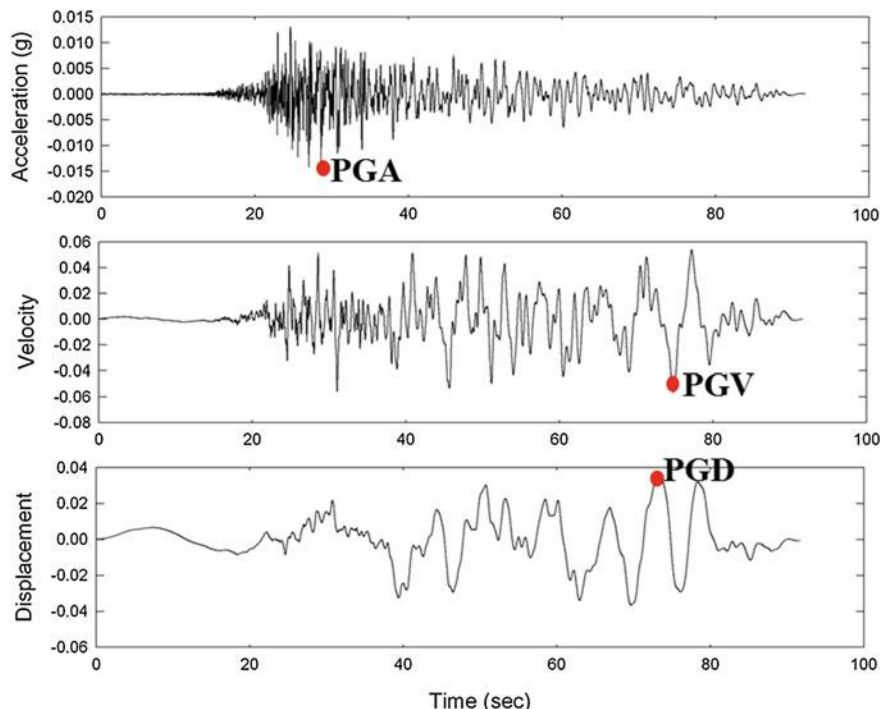


Fig. 3.28 Recorded horizontal ground motion at a site in acceleration, velocity and displacement

history gives velocity history, and a time derivate of velocity history is the acceleration history. In the opposite way, the acceleration history integrated with time is the velocity history, and the velocity history integrated with time is the displacement history. This means that, if one defines the angular frequency of the motion as ω , the amplitude of the acceleration record is ω^2 times of the displacement. As this ω^2 ratio increases with an increase in frequency, an acceleration record intensifies high frequency components, while low frequency components of motion are more visible in a derived or recorded displacement time history.

Furthermore, from Fig. 3.28, it is also found that the PGA is related to motions due to the shear wave at high frequency range and it occurs much earlier than the PGV and PGD. In this case the PGV and PGD is mainly associated with the surface wave propagation in the intermediate and low frequency range. Even if the PGV and PGD sometimes occur at around the same time as the PGA, the three measures still reflect the peak responses at different frequency ranges, as mentioned above.

In case the ground movement and deformation are of interest, the PGV is a better measure for the ground motion intensity. For example, for the assessment of capacity of buried structures such as pipe networks subjected to substantial ground motions, design codes often employ PGV rather than PGA when correlating ground motion intensity and damage to pipe networks. PGV is also much less sensitive to the high frequency content variability in ground motions, which is highly variable even on small length scales due to wave scattering, and hence it has a smaller spatial variability than the PGA. PGD is often quite difficult to determine in an accurate manner due to signal processing errors and long period noise, and is less used than PGA and PGV.

Table 3.5 shows peak values of near-source ground motion recordings for five significant earthquakes that occurred from 1978 to 1989. It is worth mentioning that

Table 3.5 Peak near-source ground motions from five significant earthquakes [41]

Earthquake		Distance (km)	Acceleration (g)	Velocity (cm/s)	Displacement (cm)
Tabas (1978 Tabas, Iran, M_w 7.4)		3	0.92	125	106
El Centro (1979 Imperial Valley, USA, M_w 6.5)	Array 6	1	1.74	110	55
	Array 7	1	0.65	110	41
1987 Superstition, USA, M_w 6.6	Parachute Test Site	0	0.53	138	60
	Superstition Mountain	0	0.91	44	16
1989 Loma Prieta, USA, M_w 6.9	Los Gutos Presentation Center	0	0.62	102	40
	Lexington Dam	5	0.44	120	40
1988, Langcang, Yunnan, China, M_s = 6.7	Zhutang	1	0.44	46.1	13.1

some of these peak ground motions shown in this table are higher than what is required in relevant seismic design codes.

The discussion above clarifies that the peak velocities and peak accelerations are typically associated with motions at different frequencies as mentioned above. In order to determine the significance of seismic responses and the potential damage, the seismic excitations can be categorized based on the ratio between the peak ground accelerations and peak ground velocities, namely a/v ratio [42]. This ratio is interpreted as the angular frequency of the equivalent harmonic motions. It provides a rough indication of which frequency contents of ground motions are most significant, and reflects the characteristics of sources, travel path, site conditions, duration of seismic motions, and structural responses. A low a/v ratio smaller than 0.8 g/ms^{-1} indicates that significant responses are contained in a few long duration ground motion acceleration pulses, which are likely to occur at a soft soil site. Such ground motions can amplify responses of flexible structures with high natural period. A high a/v ratio greater than 1.2 g/ms^{-1} indicates that the ground motions contain many high frequency oscillations with large amplitude, which are likely to occur at a rock and rather stiff soil site. A stiff structure is sensitive to oscillations within this frequency range. Ground motions with an a/v ratio between 0.8 and 1.2 g/ms^{-1} have significant energy content for a wide range of frequencies [43], and a/v ratio also has a significant effect on maximum inelastic response and hysteretic energy dissipation of structures.

3.5.2 Contribution of Body and Surface Wave to Ground Motions

By further observing Fig. 3.28 we see that, in general, the records are non-stationary in both amplitude and frequency content. The non-stationary amplitude is characterized by the initial build-up of the ground acceleration after the arrival of the first seismic waves, a period of strong motion at a roughly constant amplitude (stationary stage), and a gradual decay. The non-stationary in frequency content is reflected by a change in time of the frequency content of the ground motions, i.e., the relative amplitudes of the various frequency components of the ground acceleration change with time, and the frequency contents depend on the source mechanism, source-to-site distance and site conditions, etc.

Typically, the high frequency content arrives sooner, leading to a tendency for the ground motion frequency content to shift towards lower frequencies as time elapses, partially due to seismic wave dispersion, i.e., the P-wave, S-wave and surface wave travel at different speeds, arriving at a given site at different time instants, and most of the surface wave energy (dispersive energy) with low frequency arrives after the body wave (non-dispersive energy wave) has subsided (since high frequency energy is more rapidly attenuated). In other cases, the effect

of decreasing dominant frequencies in ground motions has been attributed to site resonance.

The relative significance of body and surface wave forms depends on various factors such as source mechanism, source-to-site distance, direction to the source, topography and sediment geometry.

3.5.3 *Moving Resonance*

The frequency non-stationarity is sometimes responsible for collapses of structures with natural period lower than the dominant period of ground motions. Under the excitations due to initial build-up of ground motions, those structures only exhibit partial damages due to plasticity development of structural members or damages of secondary structures (such as windows or doors), while the partial damages will lead to degradation in the global stiffness of the structures, causing an increase in natural period of the structures. The increased natural period may track the decreasing predominant frequency of the ground motion (most likely due to the arrival of surface wave with lower dominant frequency than the initial body wave, and sometimes also due to the soil liquefaction that decreases the natural frequency of soil columns), leading the structures to respond in resonance. This phenomenon is called moving resonance, which is discussed by Conte [44]. More broadly, moving resonance is defined as a type of resonance of structures subject to excitations, due to changes in structures' natural period and/or changes in dominant period/frequency of non-stationary ground excitations with time. From a case study, Conte [44] stated that, for initially stiff structures, moving resonance can lead to a significant increase of maximum ductile response of structures by up to 60 %. Paradimitriou and Beck [45] found that the variation in both frequency content and amplitude with time may significantly affect the response of both linear and softening non-linear structural systems. By studying the influence of non-linear structural response under two non-stationary seismic excitations, Wang and Zhou [46] found that the structural response during the build-up of ground motion (initial 25 s) stage under two excitations are essentially similar, while significant differences appear during the decay stage; and structural collapse and significant damages, if they happened, often occurred during this decay stage. By carrying out a systematic study of seismic response using wavelet transform (Sect. 5.6), Naga [47] concluded that a significant effect of moving resonance is observed for ground motions with energy that was concentrated in a narrow period band, but the motions spread out in time, such as the seismic motions recorded during the 1994 Northridge earthquake at Canyon County and 1995 Kobe earthquake at Nishi-Asaki, and the 1940 Imperial Valley earthquake. Even pulse like ground motions such as the ones that occurred during the 1999 Chi-chi earthquake have a propensity to moving resonance.

3.6 Attenuation Relationship and Uncertainties

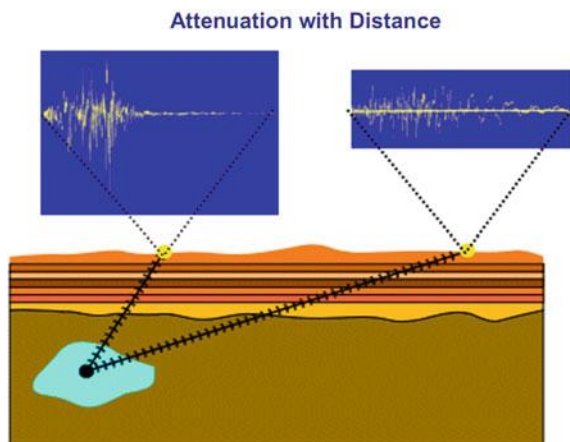
It is well known that any kind of flux transmitted through a medium or media will have a gradual loss in intensity, which is called attenuation. This is the case for the transmission of seismic waves in that the intensity of ground shaking generally decreases as the distance increases from the seismic fault rupture where the earthquake shaking is generated.

The major source for the attenuation is radiation damping, i.e., spreading of seismic waves as they propagate through Earth's interior. A secondary cause of ground attenuation is material damping, i.e., transfer of wave energy into heat by soil particle friction caused by wave movement [37].

After every earthquake, seismologists collect the recordings of accelerations versus distance of sites to fault ruptures or the epicenter due to attenuation effects as shown Fig. 3.29. By relating this to the magnitude of the corresponding earthquake, the most fundamental attenuation relationship can be drawn as curves shown in Fig. 3.30, which essentially indicate a relationship/equation among the intensity of ground motions such as peak ground acceleration (PGA) as presented in Sect. 3.5.1 or spectral pseudo-acceleration as will be presented in Sect. 5.4.2, as a function of earthquake magnitude, the distance between the seismic source and the site and other essential seismic parameters. This relationship is normally called attenuation relations or ground motion prediction equations (GMPEs). It is one of the most important components in seismic hazard analysis because the ground motion intensity could vary significantly depending on attenuation models to be used.

Here readers need to bear in mind that in history, the name “attenuation models” was used in accounting for only the source-to-site distance and magnitude effects. More recently, the name has gradually been replaced by “ground motion prediction equations/models” because more parameters than the magnitude and the source-to-site distance are accounted for in the prediction of earthquake intensities. However, in various literatures, both names are used to indicate the same issue.

Fig. 3.29 Illustration of the attenuation with distance from the fault rupture to two sites at surface [48]



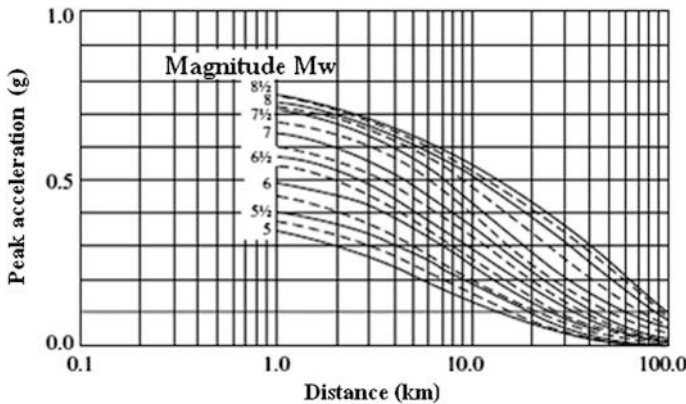


Fig. 3.30 Attenuation curves: relationship between the PGA and distance from a fault in different magnitude earthquakes [49]

When utilizing the GMPE, readers need to understand the exact definition of source-to-site distance, which varies depending on the required input for the subsequent ground motion prediction model. As shown in Fig. 3.31, the distance can be site-to-epicenter (R_{epi}) and site-to-hypocenter (R_{hyp}), which are the easiest distances to determine after an earthquake and need only consider the location of the rupture initiation, but they are inappropriate to use if the length of fault rupture is a significant fraction of the distance between the fault and the site. Furthermore, because the peak ground motion is likely to be produced by the rupture of high-stressed fault zone, the distance between the site to the high-stressed zone (R_{hsz}) is feasible in the ground motion prediction models, but this zone is rather difficult to locate after an earthquake occurrence and is almost impossible to

Fig. 3.31 Schematic definition of source-to-site distance

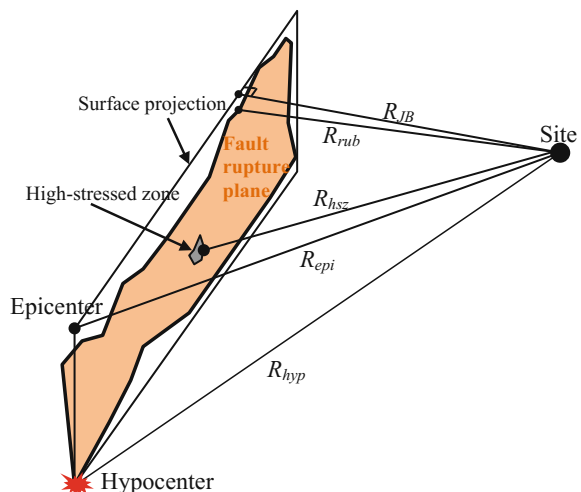
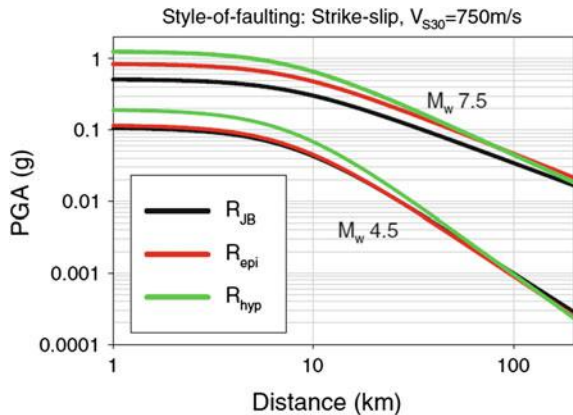


Fig. 3.32 GMPE curves based on different source-to-site distance definitions [50]



determine before an earthquake. Therefore, the most extensively used source-to-site distance in various GMPEs is the closest point on the rupture surface (R_{rub} , not including sediments overlying basement rock) or the closest point on the surface projection of the fault rupture (R_{JB} , which is also called Joyner-Boore distance), which are illustrated in Fig. 3.31. Figure 3.32 shows an example of GMPE curves based on different source-to-site distance definitions.

By accounting for path effects on the wave propagation to a specific site and possibly its local soil dynamic behavior, the GMPEs are usually selected to reflect the mechanics of ground motion process as closely as possible, which minimize the number of empirical coefficients. Mathematically, this can be performed by fitting the strong motion records data into a lognormal distribution, using for example regression analysis.

Kramer [32] summarized that common forms of the GMPEs are based on the following findings obtained from measurements during numerous earthquakes:

1. The logarithms of the peak values of strong motion parameters roughly follow Gaussian (normal) distribution. This is why most of the GMPEs are obtained based on the regression analysis using the logarithm of a ground motion variable rather than the ground motion variable itself.
2. The logarithm of a ground motion variable is roughly proportional to the earthquake magnitude.
3. Due to seismic wave radiation, a decrease in ground motion amplitude associated with body wave is inversely proportional to the source-to-site distance R , while for surface wave (mainly Rayleigh wave) amplitude, this decrease is inversely proportional to \sqrt{R} .
4. Due to material damping, the ground motion amplitude decreases exponentially with R .
5. As a fault ruptures in an area instead of a point, during an earthquake, seismic waves arrive at a site from different source-to-site distance, with the one producing the relatively strong motion at a distance R , while the effective distance is

larger than R by an amount that increases with increasing fault rupture area (directly influenced by the earthquake energy release or magnitude).

6. The ground motion variables may also be influenced by the plate boundary source type (e.g. crustal active tectonic region, crustal stable continental region, and subduction region), fault type (strike-slip, normal, or reverse faulting), or site characteristics (e.g. alluvium, hard rock, soft rock, etc.).

To account for all the observations above, a typical empirically derived GMPE is established using statistical regression based on observations from a large amount of ground motion observation data collected from past earthquakes. The model describes a relationship between a ground motion parameter Y (i.e., PGA, PGV, modified Mercalli intensity (*MMI*), peak spectral acceleration at different periods, cumulative absolute velocity, or Arias Intensity, etc.) and the predictor variables (earthquake magnitude M , source-to-site distance R , and uncertainty E , sometimes also including θ accounting for rupture mechanism, local soil conditions, as well as directivity parameters). The predicted ground motion is typically quantified in terms of a median (in case of non-log of ground motion parameter) or mean value (in case of natural-log of ground motion parameter $\ln Y$) $f(M, R, \theta)$ of the ground motion parameter plus its uncertainty function E (the scatter around the $f(M, R, \theta)$):

$$\ln Y = f(M, R, \theta) + E(M, R, \theta) \quad (3.21)$$

where $\ln Y$ is the natural-log of the ground motion intensity Y .

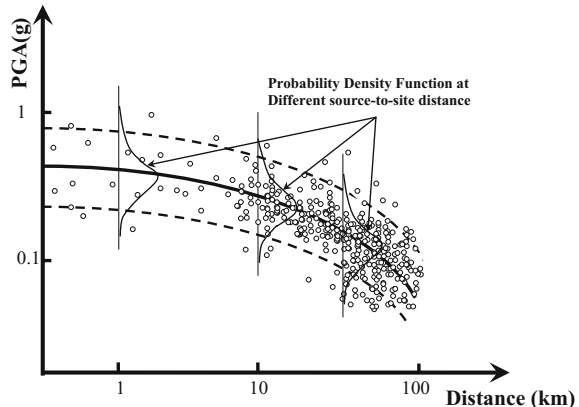
The uncertainty E can normally be assumed to follow a normal distribution with a zero mean and a standard deviation of $\sigma_{\ln Y}$ [51–53]. Thus, the uncertainty of ground motion follows a lognormal distribution:

$$E = \varepsilon \sigma_{\ln Y(M, R, \theta)} \quad (3.22)$$

where $\sigma_{\ln Y}$ is the standard deviation of natural-log of the ground motion intensity Y , which describes uncertainty regarding the value of the ground motion variable, and it normally follows a normal distribution; $\sigma_{\ln Y}$ was originally assumed to be a constant, while in the last 30 years, it has been found that $\sigma_{\ln Y}$ changes with the variation of earthquake magnitude; ε is a constant number of standard deviations ($\sigma_{\ln Y}$) measured as the difference relative to the mean predicted ground motion $f(M, R, \theta)$ and represents the observed variability in $\ln Y$. It is sometimes called normalized residual ε (e.g., $\varepsilon = -2.0$ would be 2.0 standard deviations smaller than the mean value of $\ln Y$), which also follows a normal distribution with a mean value of 0 and a constant standard deviation of 1.

Figure 3.33 illustrates the mean value and standard deviation of ground motions $\ln Y$ varied with the source-to-site distance measured during a single earthquake event. It can be seen that there is a large scatter around the mean value curve. Under the assumption that the PGA varied with distance follows a normal distribution, the mean \pm standard deviation should enclose about 2/3 of the observed values, as shown in this figure. It is important to account for the probability distribution of ground motion

Fig. 3.33 An illustration of observed PGA at various sites during an earthquake event with a measured magnitude; the solid line indicates the mean value of $\ln Y$ (Y is the observed PGA), and the two dashed lines indicate $\ln Y \pm \sigma_{\ln Y}$. Each round dot indicates the PGA obtained from a recorded ground motion



intensities because the probabilistic seismic hazard analysis (Sect. 9.1), which is to calculate the ground motion intensities with various levels of return periods, must account for the uncertainties in the probability distribution of ground motion intensities rather than just taking the predicted mean intensity. Here, the return period is an average time in years between exceeding an event of specified magnitude of loading, which is determined based on the acceptable level of risk for relevant parties, as will be presented in Sect. 9.1.3.

Over history, various types of GMPEs have been developed. Most of them can be generalized in a form expressed as follows:

$$\ln Y = c_1 + c_2 M + c_3 M^{c_4} + c_5 \ln[R + c_6 \exp(c_7 M)] + c_8 R + f(\text{source}) + f(\text{site}) + \varepsilon \sigma_{\ln Y} \quad (3.23)$$

where c_1 to c_8 are constants associated with each term; R is measured either as the closest distance to the surface projection of the rupture surface (R_{JB} in Fig. 3.31, defined as the closest distance to the surface projection of the fault, which is approximately equal to the epicentral distance for events with $M < 6$) or the closest distance to the rupture surface (R_{rub} in Fig. 3.31); $\sigma_{\ln Y}$ is dependent of M and R ; in practice, ε can be assumed to be independent of M and R [54].

It is noted that the general equation of GMPEs expressed above lists all terms associated with c_1 to c_8 . However, in many cases, only some terms need to be included. For example, the GMPE used in Norway as defined in the 1998 version of NORSAR [30] uses only four terms as below:

$$\ln Y = C_1 + C_2 M_i + C_3 \ln R_j + C_4 R_j + \varepsilon \sigma_{\ln Y} \quad (3.24)$$

where Y is the ground motion variable, M_i and R_j are magnitude and source-to-site distance of during an earthquake event; and C_1 , C_2 , C_3 and C_4 are empirically determined constants.

Cornell et al. [55] presented a simple GMPE for mean and log peak ground accelerations (in g) with a standard deviation of 0.57 for $\ln PGA$ for all magnitudes and source-to-site distance (R in km):

$$\overline{\ln PGA} = -0.152 + 0.859M - 1.803 \ln(R + 25) \quad (3.25)$$

Recently, Boore and Atkinson [56] presented an attenuation relationship model, which contains ground-motion prediction equations (GMPEs) for average horizontal component ground motions as a function of earthquake magnitude, source-to-site distance, local average shear wave velocity, and fault type. These equations are defined in terms of peak ground acceleration (PGA), peak ground velocity (PGV), and 5 %-damped pseudo-absolute-acceleration spectra (PSA) at periods between 0.01 and 10 s. For periods less than 1 s, the analysis used 1574 records from 58 main shocks with distances ranging from 0 to 400 km (the number of available data decreased as period increased):

$$\ln Y = F_M(M) + F_D(R_{JB}, M) + F_S(V_{S30}, R_{JB}, M) + \varepsilon\sigma_T \quad (3.26)$$

where Y is the spectral acceleration (Sect. 5.4.2), F_M , F_D and F_S represent the magnitude scaling, distance function, and site amplification, respectively; M is moment magnitude; R_{JB} is the Joyner-Boore distance; and the velocity V_{S30} is the time-averaged shear wave velocity from the surface to a depth of 30 m. The predictive variables are M , R_{JB} and V_{S30} ; the fault type is an optional predictive variable that enters into the magnitude scaling term; as mentioned above, ε is the fractional number of standard deviations of a single predicted value of $\ln Y$ away from the mean value of $\ln Y$.

All terms in the equation above, also including the coefficient σ_T , are period dependent.

The attenuation model presented by Boore and Atkinson above is applicable for moment magnitude ranging from 5 to 8, R_{JB} smaller than 200 km and $V_{S30} = 180\text{--}1300$ m/s.

Idriss [57] presented an empirical model for estimating the horizontal pseudo-absolute spectral accelerations (PSA) generated by shallow crustal earthquakes. The model parameters are presented for sites with an average shear wave velocity in the upper 30 m of soil layers, $V_{S30} > 900$ m/s, and for sites with $450 \text{ m/s} < V_{S30} < 900 \text{ m/s}$. Site specific dynamic response calculations are recommended to calculate spectral ordinates for sites with $V_{S30} < 180$ m/s. In this model, the median values of peak horizontal ground acceleration (PGA) and PSA for short periods are in the order of 15–20 % lower for strike-slip events and 30–40 % lower for reverse events than those calculated using relationships before the NGA (Pacific Earthquake Engineering Research Center's Next Generation Attenuation) [58] database was available. The differences decrease significantly at longer periods:

$$\ln[PAA(T)] = \alpha_1(T) + \alpha_2(T)M - [\beta_1(T) + \beta_2(T)M]\ln(R_{rup} + 10) + \gamma(T)R_{rup} + \varphi(T)F \quad (3.27)$$

where $PAA(T)$ is the pseudo-absolute acceleration measured in g for period T , at a spectral damping ratio of 5 %; M is moment magnitude; R_{rup} is closest distance to the rupture surface in kilometers (Fig. 3.31); $\gamma(T)$ is a “distance” adjustment factor (partially accounts for anelastic attenuation); $\varphi(T)$ is a source mechanism (or style of faulting) factor; F refers to source mechanism designator with $F = 0$ for “strike-slip” events and $F = 1$ for “reverse” events; $\alpha_1(T)$, $\alpha_2(T)$, $\beta_1(T)$ and $\beta_2(T)$ are parameters obtained from the regression process.

It is noticed that both the Boore and Atkinson model and Idriss model are derived using empirical regression from an extensive strong motion database compiled by the “PEER NGA” project (Pacific Earthquake Engineering Research Center’s Next Generation Attenuation).

Table 3.6 lists various types of attenuation relationship for both shallow crustal and subduction earthquakes, and the associated record properties of each type of the relationship. Most of them are established based on the regression analysis. Most relationships for active tectonic regions use records at a distance less than 200 km from the sites, whereas models for stable continental regions use records at source-to-site distance of less than 500 km. The models for subduction earthquakes use records at longer distance. These limiting distances represent the applicable ranges of distance where the models provide reliable estimates of ground motions and different attenuation models would not provide significantly different estimates. Figure 3.34 shows an example of PGA estimated by attenuation models for active tectonic regions compared to actual records on rock sites.

Based on an evaluation of the magnitude scaling rate (MSR) for five modern ground-motion prediction equations for large shallow crustal earthquakes, Zhao and Lu [80] found that four NGA models, namely Abrahamson and Silva 2008 [81], Boore and Atkinson 2008 [56], Campbell and Bozorgnia 2008 [65] and Chiou and Youngs 2008 [63] varied significantly. They also showed that a model without a magnitude term fits the response spectra from 12 of the 13 large crustal earthquakes with M_W over 7.0 well, indicating an insignificant influence of the magnitude on the attenuation relationship. They attributed zero magnitude scaling to the rapid increase in fault length and duration of strong shaking with increasing magnitude and to the reduced energy ratio (the energy contributed to the response spectra over the total energy of a strong motion record) for records from large earthquakes. For large subduction interface earthquakes with M_W over 7.0, an increase in magnitude may similarly lead to an increase in duration but may not necessarily lead to a significant increase in ground-motion amplitude. For subduction zone earthquakes, the MSR can be more significant than that of the shallow crustal earthquakes, but still lower than the existing attenuation relationship equations [82].

On the basis of the discussion in this section, it is noticed that traditional attenuation relationships are measured in terms of ground motions in the baserock underlying surface soil, which excludes the amplification or de-amplification of the

Table 3.6 Various types of attenuation relationships (mainly based on [59])

Earthquake source	Attenuation relationship	Source-to-site distance range (km)	Magnitude range
Shallow crustal active tectonic region	Boore and Atkinson [56]	0–400	5.0–8.0
	Boore et al. [60]	0–118	5.2–7.7
	Ambraseys et al. [61]	0–100	5.0–7.6
	Abrahamson and Silva [62]	0–220	4.4–7.4
	Chiou & Youngs [63]	0–200	4.0–8.5 (strike-slip faulting) 4.0–8.0 (normal or reverse faulting)
	Campbell [64]	3–60	4.7–8.0
	Campbell and Bozorgnia [65]	0–200	4.0–8.5 (strike-slip faulting) 4.0–8.0 (reverse faulting) 4.0–7.5 (normal faulting)
	Esteva and Villaverde [66]	15–150	
	Idriss [67]	1–100	4.6–7.4
	Idriss [57]	0–200	4.6–7.4
Shallow crustal stable continental region	Sadigh et al. [68]	0–100	4.0–8.0
	Spudich et al. [69]	0–70	5.0–7.7
	Sabetta and Pugliese [70]	1.5–180	4.6–6.8
	Atkinson and Boore [71]	10–500	4.0–7.5
	Dahle et al. [72]	6–490	3.0–8.0
Subduction Zone	Hwang and Huo [73]	5–200	5.0–7.5
	Toro 2002 [74]	1–500	5.0–8.0
	Atkinson and Boore [75]	10–400	4.0–8.0
	Crouse [76]	8–850	4.8–8.2
	Fukushima and Tanaka [77]	10–300	4.5–8.2
	Megawati et al. [78]	198–1422	4.5–8.0
	Petersen et al. [79]	10–500	5.0–8.2

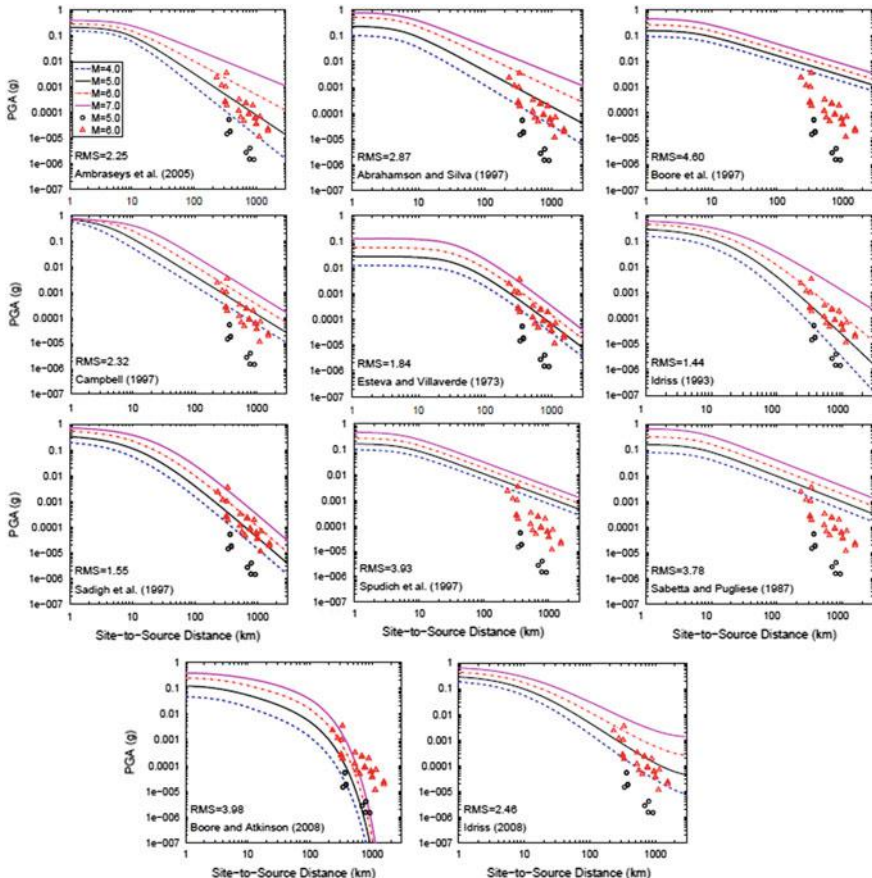


Fig. 3.34 Comparison of attenuation curves for shallow crustal active tectonic regions and recorded PGA on rock sites in Thailand from shallow crustal earthquakes [59]

soil. The more recent attenuation relationships are further developed to account for the soil type at sites and type of causative tectonic fault. They often provide not only average peak or spectral values but also standard deviation from the average values, i.e., likely scatter of individual data, which can be quite considerable. A large number of attenuation relationships exist because they are derived based on limited data and/or they consider limited factors affecting ground motions [37]. For a summary of these relationships, see Table 3.6 and Refs. [83] and [84].

In earthquake engineering, the attenuation relationship is most often used to predict the peak ground acceleration or response spectrum acceleration (Sect. 5.4) at rock in a specified site, which can then be implemented in design codes and regulatory requirements. The ground acceleration on the site can be determined by accounting for the local site conditions by, for example, site response analysis (Chap. 4). The attenuation model can be applied to predict both horizontal and

vertical components of ground motions. However, in many cases, the vertical component of the ground motions is derived based on the established relationships for the ratio of vertical to horizontal spectral accelerations, as will be presented in Sect. 5.4.4.

With the increased number of measured earthquake records, the attenuation relationships are also being updated. They are typically updated in the relevant literatures every 3–6 years or shortly after the occurrence of large earthquakes in regions with well recorded seismic data. Therefore, it is recommended to check if there is a more recent one to use for seismic hazard analysis as will be discussed in Sect. 9.1.

It is noted that, compared to the attenuation models developed for seismically active regions, the models developed for stable continental regions is much rarer mainly due to a lack of recording data. To solve this problem, by assuming a source and attenuation model with limited recorded data, stochastic simulations are often employed to develop predictive ground motion equations that describe the ground motion expected from large earthquakes in the stable continental regions.

Instead of using PGA, spectral acceleration, or spectral velocity as intensity measures in GMPEs, which are a type of strength based parameter, a few researchers [85–87] presented ground motion prediction models using seismic energy-based intensity measures. The motivation for using energy-based parameters is that they account for influences from both the seismic motion amplitude and numbers of seismic loading cycles experienced by a structure, and can correlate equally well or even better with structural and non-structural damage than the conventional strength based parameters [88]. A number of energy-measures [89–93] have been proposed for the relevant studies, which are essentially intended to define equivalent measures representing the seismic input energy on a structure and the energy absorbed by the structure. For more details regarding the energy-based intensity measures used in GMPEs, readers may read references cited above.

It must be emphasized that even if abundant research and practice have been carried out on establishing reliable GMPEs in each region, they still suffer from a shortage of data for large seismic events at short distances and only account for wave propagation effects, such as amplification in sedimentary basins [94]. On the other hand, simulations of fault ruptures using physics based models and the resulting ground motion have the potential to overcome the lack of measured data and to properly model wave propagation in basins. Therefore, seismologists are increasingly turning to such physics based methods [95] for ground motion prediction.

Recent studies [94, 96, 97] also indicate that by a careful time series analysis of ambient seismic field (seismic noise) at various measurement stations using the surface wave Green's functions, the ground motion prediction associated with the long period seismic motions, which are dominated by surface wave fundamental modes at the period band of 5–20 s, can be established. This could be an alternative to obtain the ground motion prediction relationships for which less recorded data are available to perform regression analysis.

Finally, it should be emphasized that, even if the ground motion prediction models presented in this section reflect current developments within this topic, they are far from matured. As they are relatively simple mathematical expressions with various assumptions and limitations, they can by no means accurately reflect the complexity of the earthquake generation and seismic wave propagation. Furthermore, all ground motion prediction models are based on the ground motion data recorded over only less than a century but are used to predict the ground motion intensities for a return period of up to thousands of years, which further increases the uncertainties of the prediction models. Therefore, all those uncertainties are taken as an inherent variability in the current seismic hazard assessment practice [98], which will be presented in Sect. 9.1.

For a more detailed elaboration of attenuation models, Bozorgnia and Bertero [99] is a recommended read. Reference [100] also presents a rather comprehensive coverage of the attenuation models developed until 2010, which can be downloaded from the website of PEER report [101].

3.7 Duration of Ground Motions

3.7.1 *Effects of Ground Motion Durations*

However, most seismic design codes are based on maximum amplification parameters such as peak and spectral acceleration. Those parameters may neither exhibit a straight correlation with loss and damage nor explicitly consider damage due to hysteretic behavior. The duration of seismic motions directly affects the structural or foundation behavior when the accumulated cyclic effects of motions are of concern, especially when the problem regarding strength or stiffness degradation is encountered. The number of inelastic cycles and cumulative damage measures are closely related to strong motion duration. For example, bedrock motions with a long duration induce a large number of cyclic loadings, which may cause a degradation in soil stiffness and strength and a significant increase of pore water pressure, leading to the liquefaction of saturated and partially saturated soil due to the loss of cohesion [6, 102]. The stiffness and strength degradation due to the plastic deformation of structural members under cyclic earthquake loadings is also influenced by the duration of ground motions.

Note that although the influence of duration on the seismic response of soils is well acknowledged and several methods for the assessment of liquefaction potential accounting for the duration have been successfully applied, there is, by contrast, no such unanimous view regarding the influence of duration on inelastic structural response [103]. Over the last decades, several studies have investigated the effects of duration on various structural parameters. By choosing v/a ratio (ratio of peak ground velocity to peak ground acceleration) and effective duration as two basic intensity parameters of ground motion, Sucuoğlu and his co-workers [104]

investigated the influence of these parameters on the damage potential of ground motions. They found that SDOF systems with intermediate period are more vulnerable to damage due to ground motions with either high v/a ratio larger than 0.10, with effective duration longer than 10 s, or with both. Ruiz-García [105] evaluated the influence of duration on the residual displacement demands of both SDOF and MDOF systems. He found that neglecting short duration effects on the SDOF systems with periods between 1.0 and 2.0 s can lead to an overestimation of the residual displacement demands. In addition, he observed that neglecting the long duration records can lead to an underestimation and an overestimation respectively of residual displacement demands for structures with natural period $T > 1.0$ s and $1.0 < T < 2.0$ s. Finally, he found that the long duration records can produce larger residual displacement demands than short duration records in MDOF systems.

In addition, the seismic ground motion duration also affects the operational reliability of equipment during earthquakes and landslides (Sect. 13.4), etc.

However, due to the variability of individual earthquake characteristics, the durations of two earthquake events can be significantly different. This is illustrated in Fig. 3.35, which shows the ground motion records from four different earthquake events. To cope with this situation, various researchers proposed different types of definitions of ground motion durations. The main purpose of these definitions is often to isolate a range of the motion that is particular relevant to certain types of engineering assessment. In general, the proposed definitions can be classified as bracketed duration, significant duration, uniform duration, and structural response duration [106]. Note that the structural response duration can often be examined by applying bracketed, significant or uniform definitions to the response of a particular SDOF oscillator. Therefore, Sect. 3.7.2 will present the definitions of bracketed, significant or uniform duration.

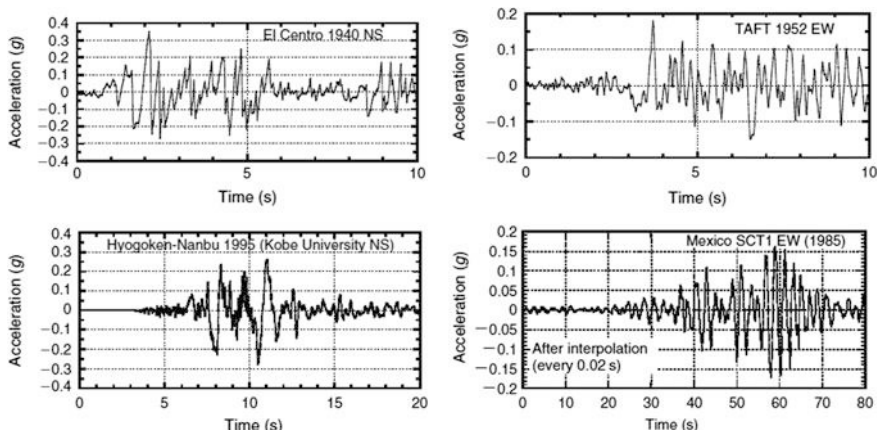


Fig. 3.35 Ground motion records from El Centro NS 1940, Taft EW 1952, Hyogoken-Nanbu, Kobe University NS 1995 and Mexico Michoacan SCT1 EW 1985 [107]

3.7.2 Definition of Ground Motion Duration

By reviewing 30 different definitions of strong ground motion duration, Bommer and Martinez-Pereira [108] classified ground motion parameters into three genetic categories: bracketed, uniform and significant duration.

Both relative and absolute durations can be used to define these three categories of durations. If peak ground acceleration is used to characterize the seismic motions, relative duration measures rather than absolute ones are recommended for use [109].

3.7.2.1 Bracketed Duration

Bracketed duration [110] is defined as the time between the first and last exceedance of a specified threshold acceleration (with a typical value of 0.05 g) [111], as shown in Fig. 3.36. It stresses the importance of frequency dependence and threshold level.

The absolute bracketed duration can be expressed as:

$$D_{ab} = \max(t) - \min(t) \quad (3.28)$$

where t is the solution of:

$$H(|a(t)| - a_0) = 1 \quad (3.29)$$

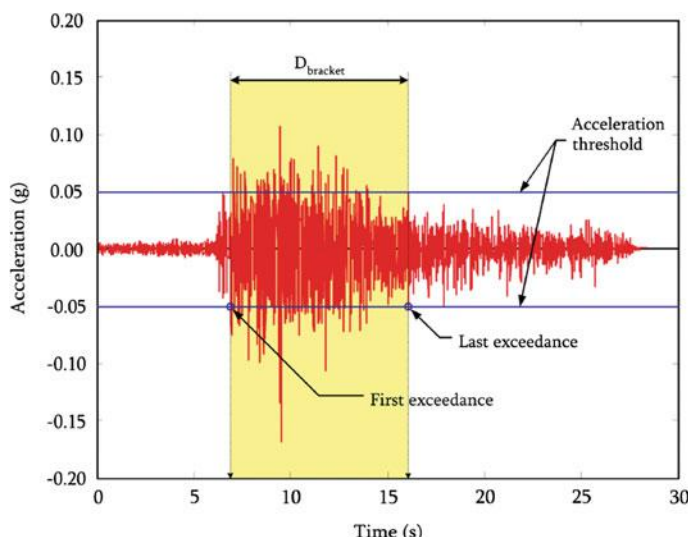


Fig. 3.36 The absolute bracketed duration (D_{bracket} in the figure) with a threshold value of 0.05 g for a time history recorded from the 1988 Saguenay 1125S17L accelerogram (magnitude: 5.9, source-to-site distance: 70.3 km) [112]

where $H(\cdot)$ is the heaviside step function (unit step function), which is a discontinuous function whose value is zero for negative argument and one for positive argument; $a(t)$ is the recorded acceleration component as a function of time t ; a_0 is the threshold acceleration often taken as 0.05 g as mentioned above.

Similarly, the relative bracketed duration can be expressed as:

$$D_{rb} = \max(t) - \min(t) \quad (3.30)$$

where t is the solution of:

$$H(|a(t)| - a_0 \text{PGA}) = 1 \quad (3.31)$$

where a_0 is a fraction and is often taken as 0.05.

3.7.2.2 Significant Duration

By contrast, the significant duration is computed from the seismic energy evolution represented by the simple integral of the square of ground motion histories, which is the time in which a specified amount of energy is dissipated, typically between time instants at which 5 and 95 % (or 5 and 75 %) of the total energy has been recorded [113], where the energy is characterized by the Arias Intensity, as will be presented below.

Significant duration is a well accepted measure of the strength of a ground motion [114]. It determines the intensity of shaking by measuring the acceleration of transient seismic waves, and has been found to be a reliable parameter to describe earthquake shaking necessary to trigger geotechnical aspects of failure such as landslides (Sect. 13.4). It was originally proposed by Chilean engineer Arturo Arias [115], who defined Arias Intensity as the time integral of the square of the transient ground acceleration:

$$I_A(t) = \frac{\pi}{2g} \int_0^{T_d} a^2(t) dt \text{ (m/s)} \quad (3.32)$$

where g is the acceleration due to gravity; T_d is the record length of signal above the threshold.

The absolute significant duration, sometimes also referred to as effective duration, was originally named by Bommer and Martinez-Pereira [108] and defined as the length of the time interval between the two time points when the Arias Intensity exceeds two separate fixed threshold values, which can be expressed as:

$$D_{abs} = \int_0^{\infty} \{H(I_A(t) - AI_1) - H(I_A(t) - AI_2)\} dt \quad (3.33)$$

where $H(\cdot)$ is the heaviside step function; AI_1 is the first threshold usually taken as 0.01 m/s; and AI_2 is the second threshold usually taken as 0.125 m/s.

The relative significant duration is defined as the length of the time interval between when the normalized Arias Intensity exceeds two separate fixed threshold values, which can be expressed as:

$$D_{rs} = \int_0^{\infty} \{H(A(t) - A_1) - H(A(t) - A_2)\} dt \quad (3.34)$$

where $A(t) = I_A(t)/\max[I_A(t)]$ is the normalized Arias Intensity; A_1 and A_2 are the first and second thresholds, respectively, which are usually taken as 0.05 and 0.95 [116]. This gives the relative significant duration as the time span when 90 % (or a user defined fraction) of the seismic wave energy is released at a given location.

In cases in which many ground motions are associated with different tectonic environments and spectral intensities, the Arias energy is more applicable than the intensity driven energy measure of the bracketed and uniform duration estimate [103]. Therefore, significant duration has been widely adopted for both geotechnical and structural assessment. For example, it has been considered by several researchers to construct the duration-dependent seismic design spectra [117], to study the effects of ground motion duration on the residual displacement demands [105], and on the analysis of structural collapse [118, 119], and many other relevant studies [120, 121]. Significant duration is also a relatively robust definition with respect to the definitions of the beginning and ending thresholds [108] and well correlated to the amount of dissipated energy and damage potential of earthquakes.

3.7.2.3 Uniform Duration

The absolute uniform duration is specified as the length of time for which the ground acceleration exceeds a fixed threshold value [122]. It is essentially the sum of all time intervals in which the ground motion acceleration exceeds a specified threshold acceleration a_0 , as can be expressed as:

$$D_{abu} = \int_0^{\infty} H(|a(t)| - a_0) dt \quad (3.35)$$

where $H(\cdot)$ is the heaviside step function; $a(t)$ is the recorded acceleration component as a function of time t .

From the definition above, it can be concluded that the absolute bracketed duration is not less than the absolute uniform duration for a given acceleration component and any given threshold:

$$D_{abs} \geq D_{abu} \quad (3.36)$$

The relative uniform duration is specified as the length of time for which the ground acceleration exceeds a threshold value, given as a fraction of the peak ground acceleration, which can be expressed as:

$$D_{ru} = \int_0^{\infty} H(|a(t)| - a_0 PGA) dt \quad (3.37)$$

where a_0 is the threshold fraction value of the PGA that is often taken as 0.05.

Similarly, the relative bracketed duration is not less than the relative uniform duration for a given acceleration component and any given threshold:

$$D_{rb} \geq D_{ru} \quad (3.38)$$

3.7.3 Approximation of Ground Motion Duration

3.7.3.1 Factors Affecting the Ground Motion Duration

Generally, the duration of ground motions is influenced by the earthquake magnitude, source-to-site distance and local site conditions.

Depending on the time required to release accumulated strain energy, the duration of ground motion is correlated to the length or area of fault ruptures. Therefore, with an increased magnitude of an earthquake, meaning an increased rupture size, the duration of the resulting ground motion also increases. Table 3.7 shows the duration of ground motion corresponding to various levels of earthquake magnitude [123]. As an example, during the magnitude 9.0 Sendai earthquake of 2011, the reported duration of strong shaking continued for three to five minutes [124].

To evaluate the liquefaction potential, duration can also be expressed by the equivalent number of cycles of the ground motions [137, 138]. Table 3.8 shows the equivalent number of uniform stress cycles varying with the earthquake magnitude. The utilization of this results in conjunction with the assessment of liquefaction potential [6]. With the increase of earthquake magnitudes, the duration of ground

Table 3.7 The duration of ground motion corresponding to various levels of earthquake magnitude

Richter magnitude	Ground motion duration (second)
8–8.9	30–180
7–7.9	20–130
6–6.9	10–30
5–5.9	2–15
4–4.9	0–5

Table 3.8 Equivalent number of stress cycles presented by Seed and Idriss [139]

Anticipated earthquake magnitude in Richter scale	Approximate equivalent number of stress cycles
5.25	2–3
6	5–6
6.75	10
7.5	15
8.5	26

shaking and hence the equivalent number of uniform stress cycles also increase. Consequently, cyclic shear strain will increase. For a presentation of assessment liquefaction potential, readers may read references [6, 32].

The increase in source-to-site distance also decreases the duration, and above certain distance, the ground motion will drop below the threshold acceleration and the bracket duration will be zero.

Based on data of 648 horizontal earthquake motions from western North America and 620 horizontal motions for central and eastern North America, Lee and Russell [112] developed a predictive model to estimate the bracket durations. By comparing the bracketed durations for central and eastern North America motions with those from active shallow crustal regions (e.g. western North America), the ground motions in central and eastern North America were found to have longer bracketed durations than those in western North America. This is particularly the case for larger magnitudes at far distances, in which the bracketed durations in central and eastern North America tend to be significantly longer than those in western North America.

Esteva and Rosenblueth [126] described the duration in terms of the earthquake magnitude and source-to-site/station distance. Dobry et al. [127] obtained a linear regression with respect to magnitude and discussed the variation of duration for different soils. Trifunac and Brady [116] obtained a linear regression with respect to site classification, earthquake magnitude and epicentral distance. Trifunac and Westermo [109] obtained regressions in the frequency domain of duration in terms of magnitude, epicentral distance and site characteristics at the station.

Besides the earthquake magnitude and site-to-source distance, local site conditions also influence the duration of the ground shaking, with rock sites having a generally shorter duration. This has been identified by, among others, Chang and Krinitzky [125], who presented bracketed durations with a threshold acceleration of 0.05 g for both rock and soil (other than rock) sites with epicenter distances less than 10 km as shown in Table 3.9. This information is derived from a limited ground motion dataset of 201 horizontal ground motions from 25 historical earthquakes occurred in western United States, mostly from the 1971 San Fernando earthquake with a moment magnitude of 6.6. However, they did not provide an approach on how they performed the regression analyses, and they linearly extrapolated and/or interpolated the relationship developed from magnitude and

Table 3.9 Typical bracketed durations with a threshold acceleration of 0.05 g for rock and soil site [125]

Magnitude	Duration (s)	
	Rock sites	Soil sites
5.0	4	8
5.5	6	12
6.0	8	16
6.5	11	23
7.0	16	32
7.5	22	45
8.0	31	62
8.5	43	86

distance ranges where data was available to ranges for which little-to-no data was available.

3.7.3.2 Estimation of Ground Motion Duration

A simple strong motion duration model was proposed by Herrmann [128] in terms of source duration and the epicentral distance:

$$T = 1/f_0 + 0.05 \cdot D \quad (3.39)$$

where f_0 is the corner frequency (which is the lower boundary frequency of largest acceleration portion in a smooth Fourier spectrum of ground motion, see Sect. 5.3.1) in Hz and D is the distance of the epicenter in km.

The formula above has frequently been used in strong motion attenuation studies for eastern North America. However, for design applications for many other countries such as Norway, since the duration may reach well above 5 s (typically ranges from 3–4 to 15 s), the formula above can be un-conservative.

Bommer and Martinez-Pereira [108] presented the shaking duration for a particular rock site as a regression function of earthquake magnitude:

$$\lg D_{abs} = 0.69M_w - 3.70 \quad (3.40)$$

where D_{abs} is the effective duration (absolute significant duration); M_w is the moment magnitude.

A more general formulation to correlate the relative significant duration D_{rs} to both earthquake moment magnitude M_w and distance to the closest point on the surface projection of the fault rupture R_{JB} (Fig. 3.31) with four regression coefficients b_1 , b_2 , b_3 and b_4 can be expressed as follows:

$$\lg D_{rs} = b_1 + b_2 M_w + b_3 \sqrt{b_4^2 + R_{JB}^2} \quad (3.41)$$

where b_4 is a depth parameter to prevent the singularity for $R_{JB} = 0$.

Based on the equation above, Fig. 3.37 shows an example of relative significant duration as a function of source-to-site distance and earthquake magnitude, based on the ground motion data from shallow strike-slip earthquakes from Armenia, Greece, Iceland, Italy, Slovenia and Turkey given by ISEDS [129]. It is clearly shown that the relative duration increases with the increase in source-to-site distance and magnitude. Even though the near-source sites generally have a short duration of less than 10 s, the uncertainties are significant and can be as much as 50 % if one standard deviation is adopted to the mean values reflected in Fig. 3.37 [103]. However, this trend can vary depending on which type of duration definition is adopted for study. For example, the absolute duration for a fixed threshold value in general tends even to decrease with increasing source-to-site distance.

Yaghmaei-Sabegh and his co-workers [130] proposed a model for the prediction of ground-motion significant duration D_{rs} based on regression analysis as a function of moment magnitude (M_w), distance to the closest point on the surface projection of the fault rupture R_{JB} , and site condition or soil type (S):

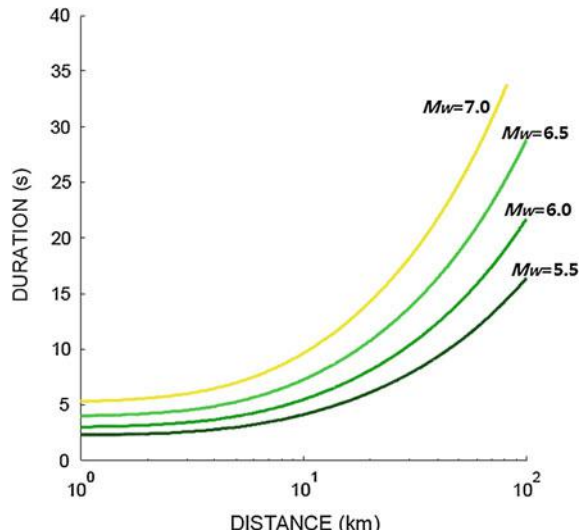
$$\lg D_{rs} = f_1(R_{JB}) + f_1(M_w) + f_3(S) \quad (3.42)$$

where soil type $S = 0, 1, 2, 3$ corresponds to sites with soft soil, stiff soil, very dense soil or soft rock, and rock.

The equation above can be written with regression parameters $a_1, a_2, a_3, a_4, \alpha$, and β determined by regression analysis based on available data:

$$\lg D_{rs} = [a_1 + a_2 \cdot \lg(R_{JB})]^{\alpha} + a_3(M_w)^{\beta} + a_4 S \eta_i \varepsilon_{ij} \quad (3.43)$$

Fig. 3.37 Relative significant duration D_{rs} of shallow strike-slip earthquakes with near vertical fault plane [103]



where the inter-event term η_i is the event term for the earthquake event i and the intra-event term ε_{ij} is residual for record j in event i . These two error terms are assumed to be independent and normally distributed with variance τ^2 and σ^2 , respectively. Accordingly, the total standard error for mixed effects is then $\sqrt{\sigma^2 + \tau^2}$.

Based on prediction models proposed by various researchers, Fig. 3.38 shows a comparison of the predicted D_{rs} with a fixed site-to-source distance of 30 km on a rock site as a function of magnitude. The prediction models included in this figure are Trifunac and Brady (1975) [116], Dobry and Idriss (1978) [127], McGuire and Barnhard (1979) [131], Kamiyama (1984) [132], Abrahamson and Silva (1996) [133], Bruno and Fabrice (2000) [134], Kempton and Stewart (2006) [135], Bommer et al. (2009) [136] and Yaghmaei-Sabegh (2014) [130]. It is shown that, in general, the models agree with each other to a certain extent. However, large differences between the models of Kamiyama (1984), Trifunac and Brady (1975) and Dobry and Idriss (1978) developed in the 1970s and 1980s can be identified, which is possibly due to a lack of correlation among the data recorded during a given event in these studies [130].

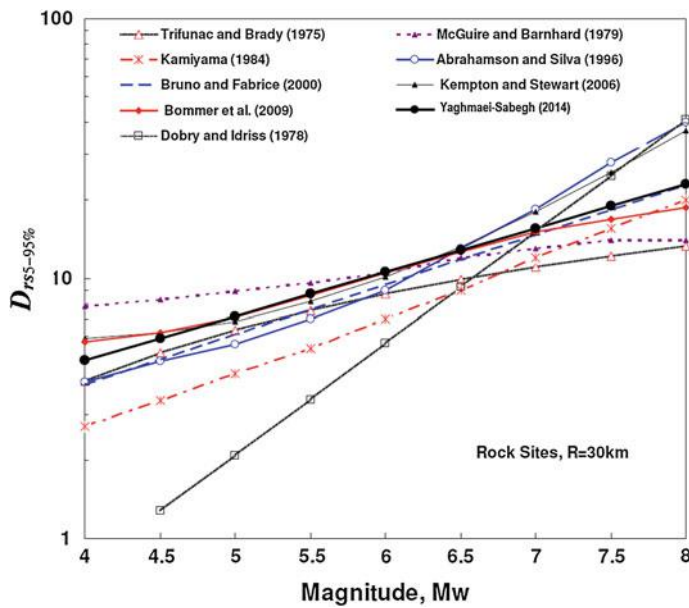


Fig. 3.38 Comparison of predicted values of D_{rs} from various proposed models with a fixed site-to-source distance of 30 km on a rock site as a function of magnitude [130]

Eurocode 8 [140] specifies that the duration of the accelerogram shall be consistent with the magnitude and the other relevant features of the seismic event underlying the establishment of the design ground accelerations. When site specific data are not available, the minimum duration of the stationary part of the accelerograms (highest ground motion portion as shown in Fig. 3.27) should be equal to 10 s.

3.8 Source of Ground Motion Recording Data

Records of seismic ground motions are essential for the development of earthquake engineering, such as to study the attenuation relationship, to calculate the site specific ground motions, and to develop the seismic hazard map, etc. Fortunately, several databases of ground motion records are made available accompanied by a number of earthquake and site parameters, such as earthquake magnitude, source-to-site distance, and ground type at the recording station. The best-known ones are listed below:

- The Pacific Earthquake Engineering Research Center, PEER (<http://peer.berkeley.edu/smacat/>)
- US Geological Survey (USGS) (<http://nsmp.wr.usgs.gov> for time histories of ground motion and <http://earthquake.usgs.gov/eqcenter/> for earthquake data)
- European Earthquake Data Base (<http://www.ised.cv.ic.ac.uk/>)
- The National Geophysical Data Center, NGDC (<http://www.ngdc.noaa.gov/nndc/struts/form?t=101650&s=1&d=1>)
- The China Earthquake Data Centre (www.smsd-iem.net.cn)
- The Broadband Seismograph Network of Japan (www.fnet.bosai.go.jp)
- Kyoshin Network K-NET (at <http://www.k-net.bosai.go.jp/>).

The time history records in the databases above are normally corrected by the standard processing techniques that remove low and high frequency noise from them. This is because raw records may contain also non-standard errors and therefore uncorrected records should not be used for the analyses [37]. The non-standard errors include insufficient digitizer resolution, transversal wave trigger, insufficient sampling rate, multiple baselines, spikes, multiple shocks, early termination during recording and clipping [141].

References

1. Bolt BA (1989) The nature of earthquake ground motion. In: Naeim F (ed) The seismic design handbook. Van Nostrand Reinhold, New York
2. Murty CVR (2001) Earthquake tip. Indian Institute of Technology, Kanpur, India
3. FEMA 99, Non-technical explanation of the NEHRP recommended provisions, 1999

4. Tsai N-C (1969) Influence of local geology on earthquake ground motion. Ph.D. thesis, California Institute of Technology
5. <http://www-rohan.sdsu.edu/~rmellors/index.html>
6. Jia J (2016) Soil dynamics and foundation modeling: offshore and earthquake engineering. Springer, Heidelberg
7. Bungum H, Selnes PB (1988) Earthquake loading on the Norwegian continental shelf. Norwegian Geotechnical Institute, Oslo
8. Evison FF (1955) A coal seam as a guide for seismic energy. *Nature* 176:1224–1225
9. Gutenberg B (1955) Channel waves in the Earth's crust. *Geophysics* 20(2):283–294
10. Ewing M, Press MF, Worzel JL (1952) Further study of T phase. *Bull Seismol Soc Am* 42:37–51
11. Irvine T (2006) Vibration data. Newsletter, June, 2006
12. Chen CT, Millero FJ (1977) Speed of sound in seawater at high pressures. *J Acoust Soc Am* 62(5):1129–1135
13. Chopra AK (2000) Dynamics of structures: theory and application to earthquake engineering, 2nd edn. Prentice Hall, New Jersey
14. Chen WF, Lui EM (2006) Earthquake engineering for structural design, 1st edn. CRC Press, London
15. UPSeis. www.geo.mtu.edu
16. Allin Cornell C (1988) Presidential address to seismological society of America
17. Kalkan E, Graizer V (2007) Multi-component ground motion response spectra for coupled horizontal, vertical, angular accelerations and Tilt. Paper no. 485. ISET J Earthq Technol 44 (1):259–284
18. Bouchon M, Aki K (1982) Strain, tilt, and rotation associated with strong ground motion in the vicinity of earthquake faults. *Bull Seismol Soc Am* 72:1717–1738
19. Graizer VM (1989) Bearing on the problem of inertial seismometry, Izvestiya. Phys Solid Earth 25(1):26–29
20. Graizer VM (1991) Inertial seismometry methods, Izvestiya. Phys Solid Earth 27(1):51–61
21. Hart GC, Lew M, Dijulio RM (1975) Torsional response of high-rise buildings. *J Struct Div Proc ASCE* 101(ST2):397–414
22. Bycroft GN (1980) Soil–foundation interaction and differential ground motions. *Earthq Eng Struct Dyn* 8(5):397–404
23. Trifunac MD, Todorovska MI, Ivanović SS (1996) Peak velocities and peak surface strains during Northridge, California, earthquake of 17 January 1994. *Soil Dyn Earthq Eng* 15 (5):301–310
24. Ariman T, Muleski GE (1981) A review of the response of buried pipelines under seismic excitation. *Earthq Eng Struct Dyn* 9(2):133–152
25. Trifunac MD, Todorovska MI (1998) Nonlinear soil response as a natural passive isolation mechanism—the 1994 Northridge, California, earthquake. *Soil Dyn Earthq Eng* 17(1):41–51
26. Richter CF (1935) An instrumental earthquake scale. *Bull Seismol Soc Am* 25:1–32
27. Gutenberg B, Richter CF (1956) Earthquake magnitude, intensity, energy and acceleration. *Seismol Soc Am* 46(2):105–145
28. China Earthquake Administration, GB 17740–1999, General Ruler for Earthquake Magnitude, 1999
29. Lay T, Wallace TC (1955) Modern global seismology. Academic Press, Amsterdam, p 521
30. Norwegian Seismic Array (NORSAR) (1998) Seismic zonation for Norway, prepared for Norwegian Council for Building Standardization by NORSAR and Norwegian Geotechnical Institute, 1998
31. Hanks TC, Kanamori H (1979) A moment magnitude scale. *J Geophys Res* 84(B5):2348–2350
32. Kramer SL (1996) Geotechnical earthquake engineering. Prentice Hall, Upper Saddle River, NJ
33. Bullen KE, Bolt BA (1985) An introduction to the theory of seismology. Cambridge University Press, Cambridge

34. Idriss IM, Archuleta RJ (2007) Evaluation of earthquake ground motions. Federal Energy Regulatory Commission, Wahington, DC
35. Ambrasseys NN, Jackson JA (1998) Faulting associated with historical and recent earthquake in Eastern Mediterranean region. *Geophys J Int* 133:390–406
36. Wells DL, Coppersmith KJ (1994) New empirical relationships among magnitude, rupture length, rupture width and surface displacement. *Bull Seismol Soc Am* 84:974–1002
37. Srbulov M (2008) Geotechnical earthquake engineering: simplified analyses with case studies and examples. Springer, Heidelberg
38. Abercrombie RE (1995) Earthquake source scaling relationships from −1 to 5 ML using seismograms recorded at a 2.5 km depth. *J Geophys Res* 100:B12
39. Chen W-F, Scawthorn C (2003) Earthquake engineering handbook. CRC Press, London
40. Bozorgnia Y, Bertero VV (eds) (2004) Earthquake engineering: from engineering seismology to performance-based engineering. CRC Press, Boca Raton
41. Zhou XY, Hu YX (2001) An overview and preview of China-US joint research on earthquake engineering. In: Spencer BF Jr, Hu YX (eds) Earthquake engineering frontiers in the new millennium. Swets & Zeitinger BV, Lisse
42. Riks E (1972) The application of Newton's method to the problem of elastic stability. *J Appl Mech* 39:1060–1065
43. Papadakakis M, Lagaros ND, Fragiadakis M (2006) Seismic design procedures in the framework of evolutionary based structural optimization, computational mechanics? Solids, structures and coupled problems. Springer, Netherlands
44. Conte JP (1992) Effects of earthquake frequency nonstationary on inelastic structural response. In: Proceedings of the 10th world conference on earthquake engineering, Madrid, Spain, pp 3645–3651
45. Paradimitriou K, Beck JL (1992) Stochastic characterization of ground motion and applications to structural response. In: Proceedings of the 10th world conference on earthquake engineering, Madrid, Spain, pp 835–844
46. Wang J, Zhou J (1997) The influence of non-stationarity of seismic motions on the nonlinear response of structures. *Earthq Eng Eng Vib* 17(2):16–20
47. Naga P (2011) Analyzing the effect of moving resonance on seismic response of structures using wavelet transforms. Virginia Polytechnic Institute and State University
48. Bobby Motwani, Are we Ready for ... “EI Centro”? www.bobbyness.net, 2010
49. Mualchin L, Jones AL (1992) Peak acceleration from maximum credible earthquakes in California (rock and stiff soil sites). California Department of Conservation, Division of Mines and Geology, Open-File Report 92–1
50. Akkar S, Sandikci MA, Bommer JJ (2014) Empirical ground-motion models for point- and extended-source crustal earthquake scenarios in Europe and Middle East. *Bull Earthq Eng* 12(1):359–387
51. Campbell KW (2003) Prediction of strong ground motion using the hybrid empirical method and its use in the development of ground-motion (attenuation) relations in eastern North America. *Bull Seismol Soc Am* 93:1012–1033
52. Joyner WB, Boore DM (1981) Peak horizontal acceleration and velocity from strong motion records including records from the 1979 Imperial Valley, California earthquake. *Bull Seismol Soc Am* 71:2011–2038
53. Atkinson GM, Boore DM (2006) Earthquake ground-motion predictions for eastern North America. *Bull Seismol Soc Am* 96:2181–2205
54. Bazzurro P, Cornell CA (1999) Disaggregation of seismic hazard. *Bull Seismol Soc Am* 89:501–520
55. Cornell CA, Banon H, Shakal AF (1979) Seismic motion and response prediction alternatives. *Earthq Eng Struct Dyn* 7(4):295–315
56. Boore D, Atkinson G (2008) Ground-motion prediction equations for the average horizontal component of PGA, PGV, and 5 %-damped PSA at spectral periods between 0.01 s and 10.0 s. *Earthq Spectra* 24:99–138

57. Idriss IM (2008) An NGA empirical model for estimating the horizontal spectral values generated by shallow crustal earthquakes. *Earthq Spectra* 24(1):217–242
58. Chiou BSJ, Darragh R, Silva W (2008) An overview of the NGA database. *Earthq Spectra* 24:23–44
59. Chintanapakdee C, Naguit ME, Charoenyuth M (2008) Suitable attenuation model for Thailand. In: The 14th world conference on earthquake engineering, Beijing
60. Boore DM, Joyner W, Fumal T (1997) Equations for estimating horizontal response spectra and peak acceleration from western North America earthquakes: a summary of recent work. *Seismol Res Lett* 68(1):128–153
61. Ambraseys N, Douglas J, Sarma S, Smit P (2005) Equations for the estimation of strong ground motions from shallow crustal earthquakes using data from Europe and the Middle East: horizontal peak ground acceleration and spectral acceleration. *Bull Earthq Eng* 3:1–53
62. Abrahamson NA, Silva WJ (1997) Empirical response spectral attenuation relations for shallow crustal earthquakes. *Seismol Res Lett* 68(1):94–109
63. Chiou BSJ, Youngs RR (2008) An NGA model for the average of horizontal component of peak ground motion and response spectra. *Earthq Spectra* 24(1):173–216
64. Campbell KW (1997) Empirical near-source attenuation relationships for horizontal and vertical components of peak ground acceleration, peak ground velocity and pseudo-absolute acceleration response spectra. *Seismol Res Lett* 68(1):154–179
65. Campbell KW, Bozorgnia Y (2008) NGA ground motion model for the geometric mean horizontal component of PGA, PGV, PGD and 5 % damped linear elastic response spectra for periods ranging from 0.01 to 10 s. *Earthq Spectra* 24(1):139–171
66. Esteva L, Villaverde R (1973) Seismic risk, design spectra and structural reliability. In: Proceedings of the Fifth world conference on earthquake engineering, Rome
67. Idriss IM (1993) Procedures for selecting earthquake ground motions at rock sites. Report to National Institute of Standards and Technology, Gaithersburg, Maryland, Center for Geotechnical Modeling, Department of Civil and Environmental Engineering, University of California at Davis, Report No. NIST GCR, pp 93–625
68. Sadigh K, Chang C, Egan J, Makdisi F, Youngs R (1997) Attenuation relationships for shallow crustal earthquakes based on California strong motion data. *Seismol Res Lett* 68 (1):180–189
69. Spudich P, Fletcher J, Hellweg M, Boatwright J, Sullivan C, Joyner W, Hanks T, Boore D, McGarr A, Baker L, Lindh A (1997) SEA96-A new predictive relation for earthquake ground motions in extensional tectonic regimes. *Seismol Res Lett* 68(1):190–198
70. Sabetta F, Pugliese A (1987) Attenuation of peak horizontal acceleration and velocity from Italian strong motion records. *Bull Seismol Soc Am* 77:1491–1513
71. Atkinson GM, Boore DM (1997) Some comparisons between recent ground motion relations. *Seismol Res Lett* 68(1):24–40
72. Dahle A, Climent A, Taylor W, Bungum H, Santos P, Ciudad Real M, Lindholm C, Strauch W, Segura F (1995) New spectral strong motion attenuation models for Central America. In: Proceedings of the fifth international conference on seismic zonation, Oct 17–19, Nice, France
73. Hwang H, Huo J (1997) Attenuation relations of ground motions for rock and soil sites in eastern united states. *Soil Dyn Earthq Eng* 16:363–372
74. Toro GR (2002) Modification of the Toro et al. (1997) attenuation equations for large magnitudes and short distances. *Risk Eng* 4:1–4–10
75. Atkinson GM, Boore DM (1997) Stochastic point-source modeling of ground motions in Cascadia Region. *Seismol Res Lett* 68(1):74–85
76. Crouse CB (1991) Ground motion attenuation equation for earthquakes on Cascadia subduction zones. *Earthq Spectra* 7(2):201–236
77. Fukushima Y, Tanaka T (1991) A new attenuation relation for peak horizontal acceleration of strong earthquake ground motion in Japan. *Shimizu Tech Res Bull* 1(10):1–11

78. Megawati K, Pan T, Koketsu K (2005) Response spectral attenuation relationships for sumatran-subduction earthquakes and the seismic hazard implications to Singapore and Kuala Lumpur. *Soil Dyn Earthq Eng* 25(1):11–25
79. Petersen MD, Mueller C, Harmsen S, Frankel AD, Rukstales K, Dewey J, Hartzell S (2004) Probabilistic seismic hazard analysis for Sumatra, Indonesia and across the southern Malaysian Peninsula. *Tectonophysics* 390:141–158
80. Zhao JX, Lu M (2011) Magnitude-scaling rate in ground-motion prediction equations for response spectra from large, shallow crustal earthquakes. *Bull Seismol Soc Am* 101(6):2643–2661
81. Abrahamson NA, Silva WJ (2008) Summary of the Abrahamson & Silva NGA ground-motion relations. *Earthq Spectra* 24(1):67–97
82. Zhao JX (2011) Magnitude scaling in ground motion prediction equations for response spectra from large subduction interface earthquakes from Japan. In: Fourth IASPEI/IAEE international symposium on effects of surface geology on seismic motion, University of California Santa Barbara, Aug 23–26
83. Douglas J (2004) Ground motion estimation equations 1964–2003. Reissue of ESEE Report 01-1: a comprehensive worldwide summary of strong motion attenuation relationships for peak ground acceleration and spectral ordinates (1969 to 2000), Department of Civil & Environmental Engineering, Soil Mechanics Section, Report 04-001-SM, Imperial College, London, UK
84. Douglas J (2006) Errata of and additions to: ground motion estimation equations 1964–3003, Intermediary Report BRGM/RP-54603-FR
85. Housner GW (1956) Limit design of structures to resist earthquakes. In: First conference on earthquake engineering, EERI, Berkeley
86. Akiyama H (1985) Earthquake-resistant limit-state design for buildings. University of Tokyo Press, Japan
87. Cheng Y, Lucchini A, Mollaioli F (2014) Correlation of elastic input energy equivalent velocity spectral values. *Earthq Struct Int J* 7(4):485–510
88. Sari A (2003) Energy considerations in ground motion attenuation and probabilistic seismic hazard studies site. Ph.D. thesis, University of Texas, Austin
89. Uang CM, Bertero VV (1988) Use of energy as a design criterion in earthquake-resistant design. Report No: UCB/EERC-88/18, Earthquake Engineering Research Center, College of Engineering, University of California at Berkeley
90. Kuwamura H, Galambos TV (1989) Earthquake load for structural reliability. *J Struct Eng ASCE* 115(6):1446–1462
91. Chapman MC (1999) On the use of elastic input energy for seismic hazard analysis. *Earthq Spectra* 15(4):607–635
92. Chou CC, Uang CM (2000) An evaluation of seismic energy demand: an attenuation approach. PEER Report 2000/04, Pacific Earthquake Engineering Research Center
93. Leelataviwat S, Goel SC, Stojadinovic B (2002) Energy-based seismic design of structures using yield mechanism and target drift. *J Struct Eng* 128(8):1046–1054
94. Denolle MA, Dunham EM, Prieto GA, Beroza GC (2013) Ground motion prediction of realistic earthquake sources using the ambient seismic field. *J Geophys Res Solid Earth* 118:1–17
95. Olsen KB, Day SM, Minster JB, Cui Y, Chourasia A, Faerman M, Moore R, Maechling P, Jordan T (2006) Strong shaking in Los Angeles expected from southern San Andreas earthquakes. *Geophys Res Lett* 33:7
96. Tanimoto T, Alvizuri C (2006) Inversion of the HZ ratio of microseisms for S-wave velocity in the crust. *Geophys J Int* 165:323–335
97. Koper KD, Seats K, Benz H (2011) On the composition of Earth's short-period seismic noise field. *Bull Seismol Soc Am* 100(2):606–617
98. Baker JW (2008) An introduction to probabilistic seismic hazard analysis (PSHA). US Nuclear Regulatory Commission

99. Bozorgnia Y, Bertero VV (eds) (2004) Earthquake engineering: from engineering seismology to performance-based engineering. CRC Press, Boca Raton
100. Douglas J (2011) Ground-motion prediction equations 1964–2010. Pacific Earthquake Engineering Research Center, California
101. http://peer.berkeley.edu/publications/peer_reports.html
102. Elnashai AS, Di Sarno L (2008) Fundamentals of earthquake engineering. Wiley, UK
103. Snaebjornsson JT, Sigbjörnsson R (2008) The duration characteristics of earthquake ground motions. In: The 14th world conference on earthquake engineering, Beijing
104. Sucuoğlu H, Yücenem S, Gezer A, Erberik A (1998) Statistical evaluation of the damage potential of earthquake ground motions. *Struct Saf* 20(4):357–378
105. Ruiz García J (2010) On the influence of strong-ground motion duration on residual displacement demands. *Earthq Struct* 1:327–344
106. Bommer JJ, Martinez-Pereira A (1996) The prediction of strong motion duration for engineering design. In: Proceedings of the 11th world conference on earthquake engineering, Mexico, Acapulco, paper no. 84, 1996
107. Izuru T (2007) Critical excitation methods in earthquake engineering, 1st edn. Elsevier Science Ltd., Oxford
108. Bommer JJ, Martinez-Pereira A (1999) The effective duration of earthquake strong motion. *J Earthq Eng* 3(2):127–172
109. Trifunac MD, Westermo BD (1982) Duration of strong earthquake shaking. *Soil Dyn Earthq Eng* 1(3):117–121
110. Bolt BA (1969) Duration of strong motion. In: Proceedings of the fourth conference on earthquake engineering, Santiago, Chile, pp 1304–1315
111. Bolt B (1973) Duration of strong motion. In: Proceedings of the fifth world conference on earthquake engineering, Rome, Italy, 6D, paper no. 292
112. Lee J, Green RA (2012) An empirical bracketed duration relation for stable continental regions of North America. *Earthq Struct* 3(1):1–15
113. Trifunac MD, Brady AG (1975) A Study of the duration of strong earthquake ground motion. *Bull Seismol Soc Am* 65:581–626
114. Stafford PJ, Berrill JB, Pettinga JR (2009) New predictive equations for Arias Intensity from crustal earthquakes in New Zealand. *J Seismol* 13(1):31–52
115. Arias A (1970) A measure of earthquake intensity. In: Hanson RJ (ed) Seismic design for nuclear power plants. MIT Press, Cambridge, MA, pp 438–489
116. Trifunac MD, Brady AG (1975) A study on the duration of earthquake strong motion. *Bull Seismol Soc Am* 65:581–626
117. Chai YH, Fajfar P, Romstad KM (1998) Formulation of duration-dependent inelastic seismic design spectrum. *J Struct Eng ASCE* 124(8):913–921
118. Raghunandan M, Liel B (2013) Effect of ground motion duration on earthquake-induced structural collapse. *Struct Saf* 41:119–133
119. Chandramohan R, Baker JW, Deierlein GG (2015) Quantifying the influence of ground motion duration on structural collapse capacity using spectrally equivalent records. *Earthq Spectra*. doi:[10.1193/122813EQS298MR2](https://doi.org/10.1193/122813EQS298MR2)
120. Tiwari AK, Gupta VK (2000) Scaling of ductility and damage-based strength reduction factors for horizontal motions. *Earthq Eng Struct Dyn* 29(7):969–987
121. Hou H, Qu B (2015) Duration effect of spectrally matched ground motions on seismic demands of elastic perfectly plastic SDOFs. *Eng Struct* 90:48–60
122. Sarma SK, Casey BJ (1990) Duration of strong motion in earthquakes. In: Proceedings of the ninth European conference on earthquake engineering, Moscow, USSR, vol 10A, pp 174–183
123. Nelson SA (2011) Earthquake prediction, control and mitigation (lecture notes). Tulane University, Sept, 2011
124. Diep F (2011) Fast facts about the Japan earthquake and tsunami. *Scientific American*, March, 2011

125. Chang FK, Krinitzsky EL (1977) Duration, spectral content, and predominant period of strong motion earthquake records from western United States. Miscellaneous paper 5-73-1, US Army Corps of Engineers Waterways Experiment Station, Vicksburg, Mississippi
126. Esteva L, Rosenblueth E (1964) Espectros de temblores a distancias moderadas y grandes. Bol SMIS Mexico 2(1):1–18
127. Dobry R, Idriss IM, Ng E (1978) Duration characteristic of horizontal components of strong motion earthquake records. Bull Seismol Soc Am 68(5):1487–1520
128. Herrmann RB (1985) An extension of random vibration theory estimates of strong ground motion to large distances. Bull Seismol Soc Am 75:1447–1453
129. Ambraseys NN, Smit PM, Douglas J, Margaris B, Sigbjörnsson R, Ólafsson S (2004) Internet site for European strong motion data. B Geofis Teor Appl 45(3):113–129
130. Yaghmaei-Sabegh S, Shoghian Z, Sheikh MN (2014) A new model for the prediction of earthquake ground-motion duration in Iran. Nat Hazards 70(1):69–92
131. McGuire RK, Barnhard TP (1979) The usefulness of ground motion duration in prediction of severity shaking. In: Proceedings of the second national conference on earthquake engineering, Stanford, CA, pp 713–722
132. Kamiyama M (1984) Effect of subsoil conditions and other factors on the duration of earthquake ground shaking. In: Proceedings of the eighth world conference on earthquake engineering, San Francisco, vol 2, pp 793–800
133. Abrahamson NA, Silva WJ (1996) Empirical ground motion models. Report to Brookhaven National Laboratory
134. Bruno H, Fabrice C (2000) Empirical determination of ground shaking duration due to an earthquake using strong motion accelerograms for engineering applications. In: Proceedings of the 14th world conference on earthquake engineering, Beijing, China, 12–18 Oct, paper no. 2254
135. Kempton JJ, Stewart PJ (2000) Prediction equations for significant duration of earthquake ground motions consideration site and near-source effects. Earthq Spectra 22:958–1013
136. Bommer JJ, Stafford PJ, Alarcón JA (2009) Empirical equations for the prediction of the significant, bracketed, and uniform duration of earthquake ground motion. Bull Seismol Soc Am 99(6):3217–3233
137. Godinho J (2007) Probabilistic seismic hazard analysis. University of Patras, Greece
138. Stewart JP, Chiou S, Bray JD, Graves RW, Somerville PG, Abrahamson NA (2001) Ground Motion evaluation procedures for performance based design. PEER report 2001/09, PEER Center, College of Engineering, UC Berkley
139. Seed HB, Idriss IM (1982) Ground motions and soil liquefaction during earthquakes. Earthquake Engineering Research Institute, Oakland, p 134
140. Eurocode 8 (2004) Design of structures for earthquake resistance—Part 1: general rules, seismic actions and rules for buildings, 2004
141. Douglas J (2003) What is a poor quality strong motion record? Bull Earthq Eng 1(1):141–156

Chapter 4

Determination of Site Specific Earthquake Ground Motions

Essentially, all models are wrong, but some are more useful than others.

George Edward Pelham Box, Statistician, 1987.

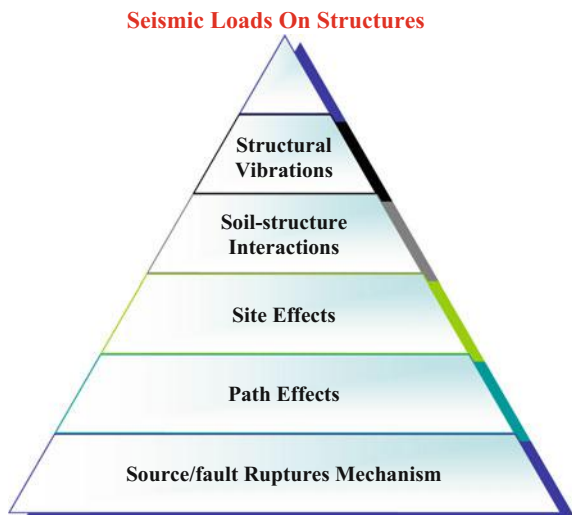
4.1 From Fault Rupture to Seismic Design

Different from the loads generated by the wind, wave/current and ice, which are due to the external forces applied on structures, earthquake loads are purely induced by the ground accelerations transferred to the foundation of the structures. Therefore, the determination of the earthquake ground motion is an essential part of earthquake engineering.

The rupture of faults generates the seismic wave as the source of earthquakes. The wave is then transmitted and modified by wave scattering, anelastic attenuation and geometric spreading, known as path effects, and is further transmitted through soil layers before it reaches the ground surface, known as site effects. However, as the rate and duration of energy released from earthquake sources (source effects) is relatively random, and the path effects are complex, it is not possible to obtain the exact excitation to which the foundation of the structure will be subjected. Therefore, extrapolating the effects of the energy released from sites of potential seismic activity to the location of structure under investigation is a rather complex process.

As shown in Fig. 4.1, four major characterizations enable the determination of earthquake ground excitation (seismic input): the seismic sources, i.e. the rupture mechanism at source; the transmission of the excitation from the sources to the sites, i.e. wave propagations; local geotechnical effects on the motions of the soil; and soil–structure interactions (SSI) during the earthquake events. Therefore, the level of ground shaking is mainly influenced by the fault rupture mechanism (characteristics), source-to-site distance, and local soil effects. Moreover, seismic loading applied on structures is strongly influenced by dynamic/vibration

Fig. 4.1 The “journey” of seismic wave transmission from fault ruptures to seismic loading applied on structures



characteristics of the structures, primarily due to the interaction between the stiffness and the inertia of the structures interferences by the seismic wave transmission. This effect can typically be characterized by the eigenpairs (eigenfrequencies and the corresponding mode shapes) of the most important eigenmodes with high modal mass participations.

The fault rupture mechanism is rather complicated to predict and is still a topic under further development. It generates waves in a wide-band frequency range with both high and low frequency contents. The high frequency seismic waves have high intensity but damp out rather quickly during seismic wave propagation. The low frequency seismic waves possess low acceleration but large displacement properties, and they damp out much more slowly.

When the seismic waves travel away from the fault rupture as shown in Fig. 3.4, they spread out (radiation damping) and are also partially absorbed by the media they travel through (material damping). Therefore, the seismic energy will be reduced with an increase in source-to-site distance. With the assumption of isotropically elastic characteristics of the transmission media, the effects of nature and length of the intermediate path from the fault to a site at bedrock or rock outcrop can be estimated by the attenuation relationship presented in Sect. 3.6, which is established using statistical regression analysis based on observations from a large amount of ground motion observation data collected from past earthquakes.

After arriving at bedrock or rock outcrop, the seismic wave will continue to transmit through soil media before arriving at ground surface or structural foundations, which is illustrated in Fig. 4.2. The soil media work as a filter to tune the seismic wave in both energy and frequency content. This tuning process usually eliminates the high frequency motion and filters the motion into a narrow frequency motion at seabed, with an amplification at and around site period (Sect. 4.2). This is illustrated in Fig. 4.3. Here the bedrock is defined as consolidated rocks underlying

Fig. 4.2 Illustrations of seismic wave transmission from the bedrock (2) to the ground surface/seabed (3) (courtesy of NORSAR)

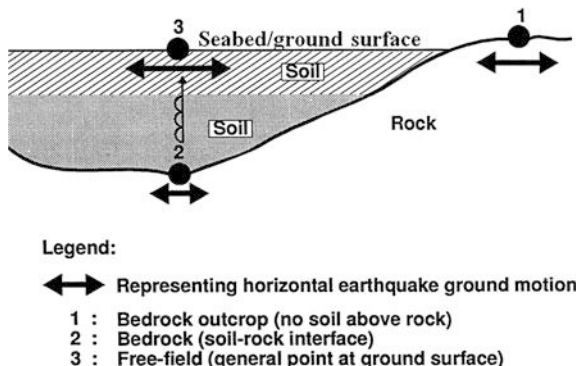
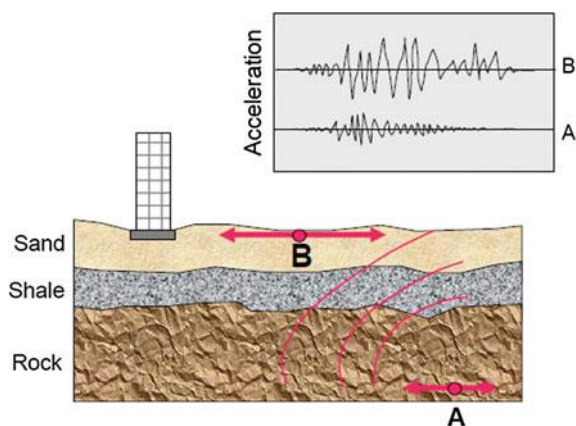


Fig. 4.3 Transmission of seismic wave through soil layers with a tunation of seismic wave in both energy (represented by motion amplitude) and frequency content (courtesy of FEMA)



the surface of a terrestrial planet, usually the Earth, as shown in Fig. 4.4, and an area of broken and weathered unconsolidated rock in the basal subsoil is often lying above the bedrock. The rock outcrop is a visible exposure of bedrock or ancient superficial deposits on the surface of the Earth [1], which can be viewed as a continuation of bedrock at the ground surface as shown in Fig. 4.5. Readers need to distinguish the rock outcrop from the cliffs: outcrops have a continuous line around each area of bare rock, while cliffs have a continuous line along the top edge with lines protruding down.

In engineering practice, due to the complexity of fault rupture and seismic wave transmission from fault rupture to the bedrocks, their influence can normally be assessed through a seismic hazard analysis by also accounting for various types of uncertainties, which will be presented in Sect. 9.1. After the seismic motion at bedrocks is obtained, the site effects can be assessed by either using the simple relationship between the ground motion and the site characteristics such as soil type or site topology (typically given in either design codes or relevant handbooks, see Sect. 6.2), or performing a site response analysis (Sect. 4.3).

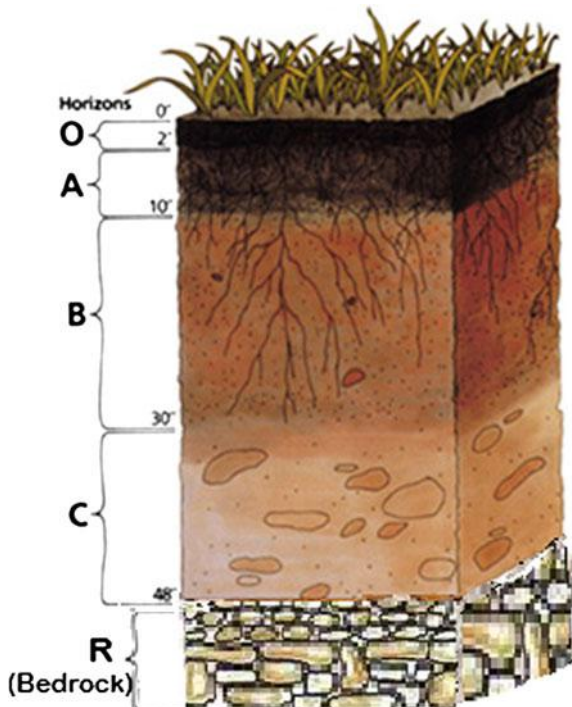


Fig. 4.4 Bedrock underneath broken and weathered unconsolidated rocks in the basal subsoil



Fig. 4.5 Appearance of rock outcrop

The amplitude, frequency content and duration of bedrock/rock outcrop motions are important factors influencing the soil response and the subsequent seismic motions at ground surface. High amplitude of bedrock motion tends to cause inelasticity in the soil, i.e. the soil will absorb a certain amount of seismic wave

energy, and the ground motions are not amplified proportionally to the bedrock motions. Compared to the case in which the soil is elastic, this will in general decrease the ground acceleration while increasing the displacement, placing higher demand on structures with medium and long natural period of vibrations. The process of transmission of seismic wave from bedrock/rock outcrop through soil media to the ground surface is typically referred to as kinematic interaction, which is an important task in a site response analysis. The results of a site specific response are design ground motions, provided that the seismic motion input in the analysis is consistent with the bedrock or rock outcrop motion predicted from a seismic hazard analysis (Chap. 9). Alternatively, design ground motions can also be obtained based on the relevant seismic design code provisions (Chap. 6), in which sites are roughly grouped into a few classes, each representing similar soil profiles rather than the exact soil profile as a site response analysis does. Therefore, the design ground motion determined from codes and standards is usually more conservative than the one developed from a site response analysis. This difference between the site specific response analysis and the code based design ground motions provides an economic incentive that implicitly encourages the development of site specific design ground motions [23] as will be presented in Sect. 4.3.

Moreover, the soil properties for the soil surrounding the foundation may change due to seismic excitations, which also influence the stiffness and damping of the foundation, thus affecting structural responses. The foundation stiffness and damping are typically referred to as subgrade impedances.

By obtaining the seismic ground motion and the foundation stiffness and damping, a seismic structural analysis can then be performed, which is usually referred to as inertial interaction, as will be introduced in Sect. 4.3.4 and elaborated in Chap. 15.

In many cases, by establishing a modeling (typically using finite element method) comprising soil media (for seismic wave transmissions), foundations, and structures as an integrated system, it is possible to include the kinematic interaction, subgrade impedance and inertial interaction in one analysis. The solution is obtained typically in the time domain by direct numerical integration. This is referred to as the direct analysis approach.

On the other hand, for improving the computational efficiency, various types of frequency domain methods are adopted to address the influence from the soil, even though it cannot explicitly account for the non-linear effects of soil–structure interactions. This method is often referred to as the substructure approach, in which the soil–foundation–structure system is partitioned into distinct parts as soil, foundation, and superstructure: their responses are first obtained independently, and then combined to satisfy compatibility of forces and displacements to formulate the complete solution.

During the transmission of seismic wave, the geometric properties of sites due to topographic irregularity (such as sloping or irregular ground surface) and subsurface irregularity (such as sloping layer boundaries, irregular boundaries or basins) may significantly affect the seismic wave propagation. When their effects are significant, special considerations of modeling, such as two-dimensional or even

three-dimensional modeling, may be required in relevant analysis. The two-dimensional or three-dimensional modeling can also capture different types of seismic wave (body and surface wave) propagation. For a discussion of this topic, the reader may refer to [2].

It should be noted that a future earthquake at given site can never be predicted with great confidence [3, 4], even though the strong motion accelerograms that are available and properly interpreted may be the closest thing to the scientific truth in earthquake engineering [5]. Therefore, it is essential to determine a set of ground motions. These do not need to be an accurate representation of real ground motions at a target site in future earthquakes, but can induce responses, damages and other impacts on the target infrastructure in a representative manner and level of severity, so that a decent implication of risk and conservatism can be ensured. This also requires an explicit requirement of significance of ground shaking associated with a certain level of probability of exceedance. Because a structure required to have little or no damage during any earthquakes may result in an unacceptable engineering design with regard to cost, there must be trade-offs between short-term cost of providing an earthquake resistant design and long-term cost (for the majority of structure this will never be realized) of earthquake induced damage.

Once the ground excitations of the structure have been determined (Chap. 4), depending on the seismic analysis demand with respect to characteristics of excitation and structures, and also with the analysis purpose and accuracy requirement, the ground motions will be represented in certain formats (Chap. 5), i.e. in time domain, expressed as a response spectrum, or being converted into frequency domain, with either deterministic or stochastic implication. They can then be applied to a structure model representing both the superstructure together with the foundation and the effects of surrounding environment (water and/or ice). Depending on the level of excitations accounted for, many of the properties during structural modeling may be non-linear in nature, such as a degradation of foundation stiffness, yielding and large deformations of the structural members, and fluid–structure interactions. These can lead to considerable demand of efforts on modeling and calculation. By fulfilling these requirements, the structural response can be calculated with sufficient representativeness of accuracy, and a reliable demand modeling can be established.

After the demand modeling is established, the capacity control (Sect. 13.6) can then be performed. If the structural responses are still in the elastic range, demand can be expressed as force and the capacity control in terms of strength. If the structural members reach yielding, demand can normally be expressed with displacement, and the capacity control is then strain based. As the strain based control may need to reflect cyclic degradation and strain rate effects, dynamic testing may therefore be required to set appropriate limits. In addition to the strength and strain capacity, the stability check should also be included in the capacity control.

The criteria of capacity control is typically provided by prescriptive design codes based on a limit state concept (Sect. 14.2). However, since the prescriptive codes include a great number of provisions, which are designed to ensure life safety and damage control (safety check) required by regulatory authorities, they cannot

explicitly provide acceptable levels of life-cycle performance, which is an important concern for infrastructure owners and operators as well as other relevant parties such as insurance companies. To solve this limitation, performance-based design can be used, which is to introduce design checks at more limit states (than the ones specified by prescriptive design codes) to the probability that the seismic action can reach the intensity required to induce the corresponding failure modes, as will be introduced in Sect. 14.2.9.

4.2 Site Period

4.2.1 General

Besides the characteristics of structures and the ground motions, the characteristics of soil between the bedrock and the structural foundations further complicate the problem of carrying out seismic assessment. The soil media act as a filter to bedrock/rock outcrop motions and influence both the frequency content and magnitude of the ground motions.

If the soil is stiff, e.g. the foundation is founded on rock, the ground motions will generally be short period, and vice versa. If the natural period of soil is close to the predominant period of bedrock motions, the ground motions will be amplified compared with the bedrock motions. Furthermore, such amplification may be further enhanced on structural response if the natural period of the structures at the site is close to the dominant period of ground motions. To avoid double resonances (resonance of seismic wave in soil with bedrock motions and then resonance of ground motions with the natural period of structures), in a preliminary design stage of a structure, engineers should design a structure with the natural period far from (normally above) the natural period of ground motions, which is also called the site period. A number of analytical studies confirm that the amplification of soil is more or less independent of soil thickness [6]. Based on wave propagation energy models, the site amplification is a function of the wave velocity (or the impedance) of the shallow soil rather than of the thickness of the soil deposit [7, 8]. Moreover, the stiffness of the soil layers deeper than 30 m is often well correlated with the wave velocity in the top 30 m [9], even if there are some exceptions as will be discussed in Sect. 4.2.2. Therefore, by assuming the soil is elastic and the bedrock displaces dominated by shear motions, the eigenperiod of soils layers can be calculated based on the average shear wave velocity down to certain depths along the soil profile, normally taken as 30 m by the majority of seismic design codes:

$$T_{\text{site}} = 4H/v_s(1 + n/2) \quad n = 0, 1, 2, \dots \quad (4.1)$$

where H (in meters) is the depth of soil layers.

Normally the most important eigenperiod of soil deposits is the first one corresponding to $n = 0$ in the equation above, which is used as an estimation of site

period. Physically, this period is the longest time that a seismic wave can travel within one wave length, as shown in Fig. 4.9. As an example, for a rough estimation, the shear wave velocity in soil media may be approximated as 300 m/s. Therefore, for a soil with thickness of 30 m, the site period is 0.4 s ($= (4 \times 30) / 300$ m/s). At this period, the ground surface will vibrate at an amplitude much greater than the bedrock motions. This can be clearly shown by reading the response spectrum as will be presented in Sect. 5.4. However, for rather loose and soft soil, the shear wave velocity can be as low as 60–80 m/s, in which case the above example gives a site period of only 1.5–2.0 s, which is in a possible range of the natural vibration period for an offshore platform.

By modeling a soft soil site consisting of 27 soil layers and performing a site response analysis, Fig. 4.6 shows a comparison of the peak ground acceleration at the bedrock and ground surface (seabed) with a site period of 2.4 s. By observing the response spectrum (which will be presented in Sect. 5.4) shown in this figure, it is noticed that the soil layers de-amplify the acceleration response at lower period range (related to the peak ground acceleration) while amplifying the response at medium and high period range. It is shown that the motions at ground surface are slightly lower than those at bedrock. On the other hand, Fig. 4.7 shows the significant magnification of site response of the ground surface compare with the seismic excitations at the bedrock at a relatively stiff soil site. The site is modeled with 17 soil layers with a calculated site period of 0.48 s. Furthermore, even at the same site, the amplitude of seismic motions at the bottom of the soil layers can influence the amplification or de-amplification of the site response characteristics, primarily due to the presence of soil nonlinearity.

Site amplification can be the cause of abundant structural damages during large earthquake events. An example of this was the massive damage in downtown Mexico City during the 8.1 magnitude Mexico City earthquake of 1985. Although the downtown of Mexico City is located 390 km away from the fault rupture area, it is built above the soil from an ancient 37–60 m thick soft layer of lake deposits under the Mexico City Basin, which used to be a big lake and was buried naturally and artificially over a long period of time. The soil has an average shear wave velocity of around 75 m/s, as shown in Fig. 4.8. This gives a site period of 2.0–3.0 s [10, 11]. A total of 412 buildings collapsed and another 324 were seriously damaged in Mexico City. A large percentage of the buildings that were damaged were between 8 and 18 stories high, indicating possible resonance effects around 2–3 s. The site amplifications during the 1994 Northridge earthquake also caused several structural collapses [12].

Several methods are available to make a hand calculation of site period:

1. Based on the weighted average of shear wave velocity:

$$v_s = \left(\sum_{i=1}^{i=n} v_{si} H_i \right) / H \quad (4.2)$$

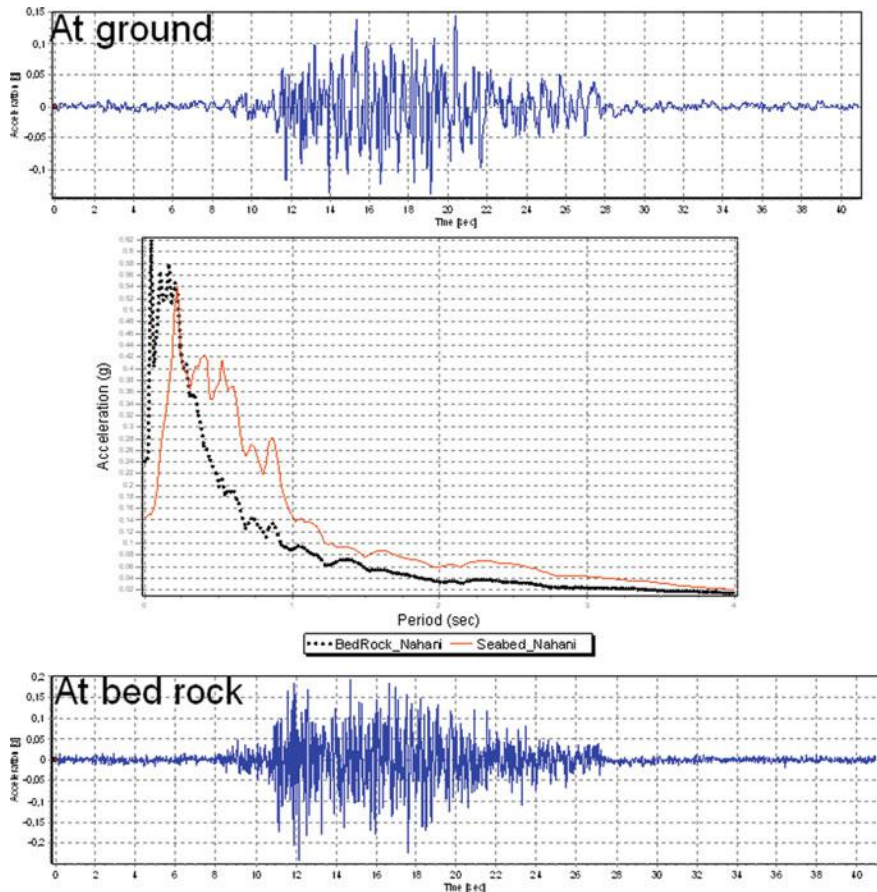


Fig. 4.6 Acceleration time histories of seismic excitations at bedrock (*lower*) and site responses at ground surface (*upper*) and their acceleration response spectra at a site modeled with 27 soil layers with a site period of 2.4 s. The site response analysis is performed based on the equivalent linear soil model (Sect. 4.3.9)

where v_{si} and H_i are shear wave velocity and depth of the soil layer i , n is the total number of soil layers, $H = \sum H_i$.

Then the site period can be calculated as:

$$T_{\text{site}} = 4H/v_s \quad (4.3)$$

2. Based on the weighted average of the soil's shear modulus and density:

$$T_{\text{site}} = 4H \left/ \left[\left(\sum_{i=1}^{i=n} \mu_i H_i \right) \right/ \left(\sum_{i=1}^{i=n} \rho_i H_i \right) \right] \quad (4.4)$$

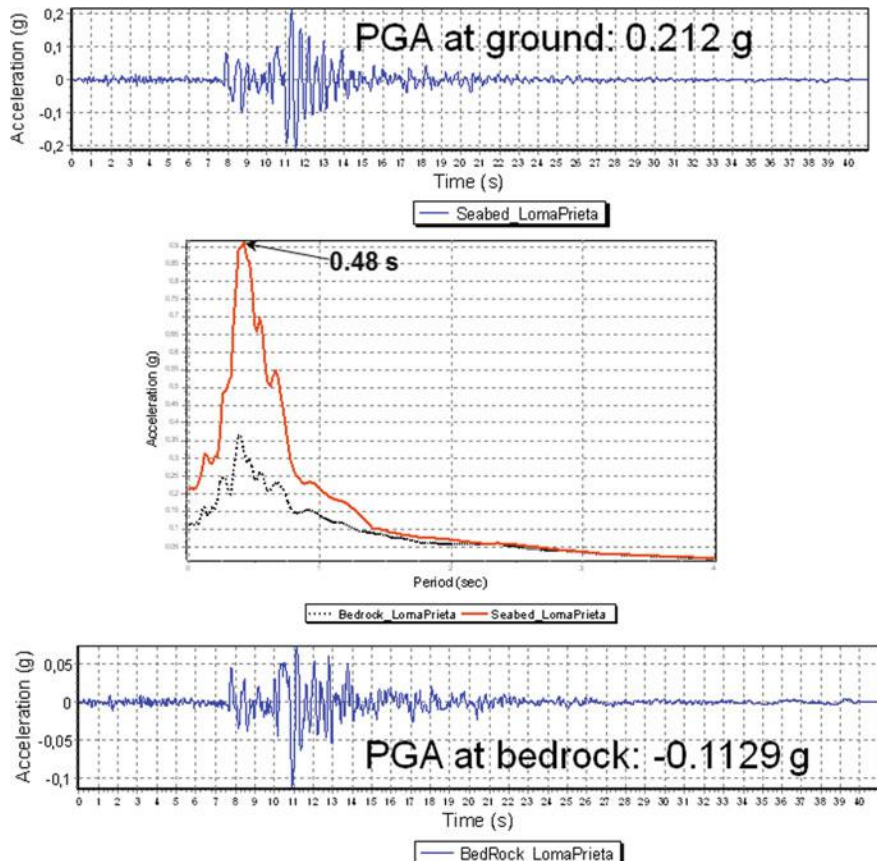


Fig. 4.7 Time history of seismic excitations at bedrock (*lower*) and site responses at soil surface (*upper*) and their acceleration response spectra with a site modeled by 17 soil layers with a site period of 0.48 s (relatively stiff soil). The site response analysis is performed based on the equivalent linear soil model to model both shear modulus and damping

where μ_i , ρ_i and H_i are shear modulus, density and depth of the soil layer i , n is the total layer of the soil, $H = \sum H_i$.

3. Based on the sum of site period for each layer:

$$T_{\text{site}} = \sum_{i=1}^n (4H_i/v_{si}) \quad (4.5)$$

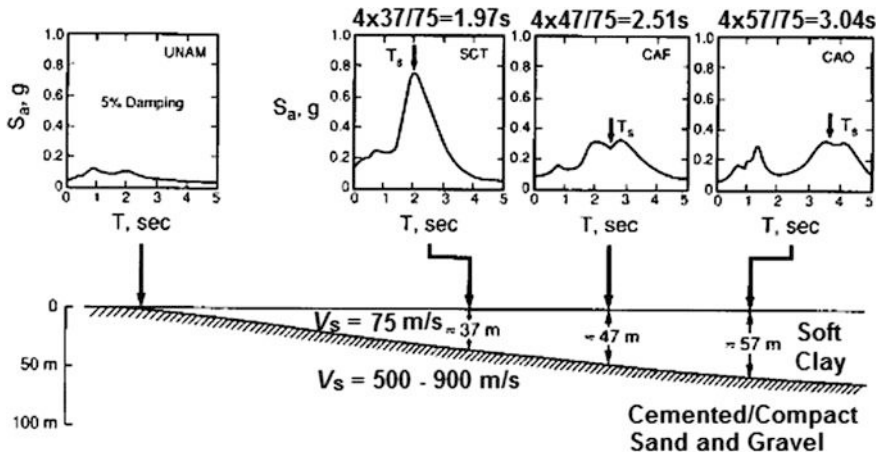


Fig. 4.8 Acceleration spectra from recorded time histories at several stations in Mexico City during the magnitude 8.1 Mexico City earthquake of 1985 [13, 14]

4. Based on a linear approximation of fundamental mode shape

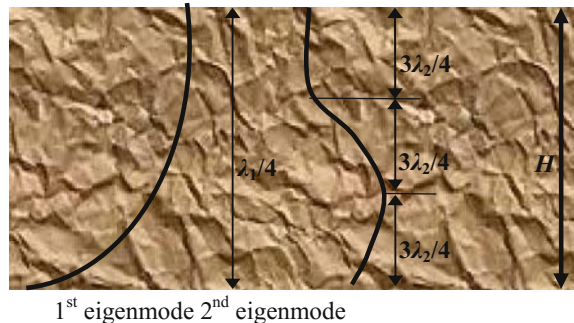
$$T_{\text{site}} = 2\pi / \sqrt{3 \sum_{i=1}^{i=n} (v_i^2 H_i) / H^3} \quad (4.6)$$

For seismic design of offshore and land-based structures, based on the soil properties in the uppermost 30 m of the soil, various seismic design codes, such as ISO 19901-2 [15] and Eurocode 8 [16], provide the estimation value of v_s ; see Sects. 6.2.1 and 6.2.2 for details.

4.2.2 Influence of Soil Depth on the Site Period

The consideration of the top 30 m thickness of soil layers in the majority of seismic design codes, or 20 m of thickness in the China building code [17] to calculate the average shear velocity, is most appropriate for rather short period content of the bedrock motions. For seismic wave with longer periods the wave lengths are much longer than 30 or 20 m, and the site response is likely to be affected by soil characteristics at much greater depths. Moreover, the consideration of the top 30 or 20 m depth often assumes that the soil layers extend to a few hundred meters depth before reaching the bedrock. The calculation may not be suitable for regions where a soil-bedrock interface is found at even a few meters below the soil surface.

Fig. 4.9 The relationship between the first and second eigenmode due to horizontal shaking



Even for sites having deep soil but with the stiffness of the deeper soils that are well correlated with the shear wave velocity at the top 30 m, Boore et al. [9] found that the depth over which average shear wave velocity should be averaged is one-quarter of the wavelength associated with the period of interest, which can be greater than 30 m. Significant soil amplifications can be produced due to high impedance contrasts and associated seismic wave reflections at depths much greater than 30 m, which have almost no correlation with the soil properties of the top 30 m. Therefore, averaging the soil deposit characteristics over depth may result in inaccurate predictions of actual site amplification. A better estimate can generally be obtained by performing a site response analysis (Sect. 4.3) including a more dedicated soil layering modeling of the deposit.

Example Calculate the first and second eigenperiod of a homogeneous soil layer due to the horizontal shaking. The soil layer has a height $H = 26$ m and a shear wave velocity $v_s = 250$ m/s.

Solution The wave lengths corresponding to the first eigenperiod (T_1) and second eigenperiod (T_2) are λ_1 and λ_2 , respectively. Their relationship with the soil layer height H is shown in Fig. 4.9 and can be expressed as:

$$\lambda_1 = 4H = v_s T_1 \quad (4.7)$$

$$\lambda_2 = 4H/3 = v_s T_2 \quad (4.8)$$

Therefore:

$$T_1 = 4H/v_s = 4 \times 26/250 = 0.416 \text{ s}$$

$$T_2 = 4H/(3v_s) = 4 \times 26/(3 \times 250) = 0.139 \text{ s}$$

Table 4.1 Soil's shear wave velocity distribution along the soil depth

Layer number i	Thickness H_i	Shear wave velocity v_{si}
1	4.0	360
2	5.0	575
3	11.0	1050
4	26.0	2060
5	>60.0	2400

Example The shear wave velocity distribution for a site with shallow soil layers is shown in Table 4.1. Calculate the site period and the average shear wave velocity.

Solution The site period based on the average shear wave velocity of the uppermost 30 m soil is often used to classify the type of site and estimate the site period. Therefore, the site period for the uppermost 30 m soil can be calculated as:

$$T_{\text{site}} = \sum_{i=1}^n (4H_i/v_{si}) = \frac{4 \times 4 \text{ m}}{360 \text{ m/s}} + \frac{4 \times 5 \text{ m}}{575 \text{ m/s}} + \frac{4 \times 11 \text{ m}}{1050 \text{ m/s}} + \frac{4 \times 10 \text{ m}}{2060 \text{ m/s}} \\ = 0.14 \text{ s}$$

The shear wave velocity for the uppermost 30 m soil is calculated as:

$$v_{si,30} = \sum_{i=1}^n H_i \left/ \sum_{i=1}^n (H_i/v_{si}) \right. = \frac{30}{\frac{4}{360} + \frac{5}{575} + \frac{11}{1050} + \frac{10}{2060}} = 854 \text{ m/s}$$

However, it is noticed from Table 4.1 that the site consists of a shallow sedimentary soil, and the soil stiffness dramatically increases below the bottom of soil layer 2, indicating that the impedance contrast between soil layer 2 and soil layer 3 is rather high. Therefore, in reality, soil dynamic response will be dominated by the response of soil on the upper two layers (uppermost 9 m) rather than the uppermost 30 m. The realistic site period for the uppermost 9 m soil can be calculated as:

$$T_{\text{site}} = \sum_{i=1}^n (4H_i/v_{si}) = \frac{4 \times 4 \text{ m}}{360 \text{ m/s}} + \frac{4 \times 5 \text{ m}}{575 \text{ m/s}} = 0.08 \text{ s}$$

The realistic shear wave velocity for the uppermost 9 m soil is calculated as:

$$v_{si,9} = \sum_{i=1}^n H_i \left/ \sum_{i=1}^n (H_i/v_{si}) \right. = \frac{9}{\frac{4}{360} + \frac{5}{575}} = 454 \text{ m/s}$$

A significant difference can be observed between the realistic estimations based on the uppermost 9 m (below the bottom of soil layer 2 the soil stiffness significantly increases) and the estimation based on the uppermost 30 m soil.

4.3 Site Response and Soil–Structure Interactions

4.3.1 General

The response of a structure under seismic excitations is affected by interactions between three connected parts: the structure, the foundation, and the soil underlying and surrounding the foundation [18]. A soil–structure interaction (SSI) analysis estimates the collective response of the entire soil–foundation–structure system to specified ground motions by determining the effects of kinematic interaction (normally by site response analysis), soil–foundation flexibility (foundation impedance) and inertia interaction (seismic analysis).

The motion of soil is different from what it would have been in the presence of the foundation of structures and vice versa. Therefore, two obvious facts promote the importance of the SSI. Firstly, the structural response due to earthquake for a structure on deformable soils can be significantly different from that of a structure that would be supported on a rigid foundation. Secondly, the ground motion at the base of a structure and its vicinity can also be different from that if there has been no structure standing above. Even for relatively rigid structure supported on hard soils, SSI can still be important in that the relative stiffness between the structure and foundations can significantly influence the energy and force transferring from the foundation to the structure. The effects of SSI generally increase the natural period of the upper structure and modify the damping ratio and seabed/ground motion with respect to amplitude, frequency content and duration, therefore affecting the structure's response. A successful implementation of SSI analysis requires collaboration between structural and geotechnical engineers.

Originally motivated by the design of large scale infrastructures that have high risk, such as nuclear power plants, which require high safety measures for the infrastructures and equipment, SSI analysis is now widely used for various types of infrastructures both onland and offshore.

In the SSI analysis, two different mechanical problems need to be dealt with: the structures including foundations and the surrounding soil media. In general, it is rather challenging or impossible to obtain an analytical or even semi-analytical solution. Therefore, computational models are normally used for solving the problem. Practically, two types of analysis approaches are available: direct analysis approach (Sect. 4.3.1.1) and substructure approach (Sect. 4.3.1.2).

4.3.1.1 Direct Analysis Approach

The direct analysis approach involves directly modeling a structure, foundations and surrounding soils (represented as a continuum) as an integrated system and to compute the response at various parts. For a complex foundation-soil system, the direct analysis is often performed using finite element analysis. The solution is typically obtained in the time domain by direct numerical integration. The approach can consider non-linear behavior of the soil and superstructure, but requires a special consideration on the external fictitious boundary of the soil model to eliminate wave reflections and to introduce seismic excitation. It is obvious that the required computational cost associated with direct analysis approach is high, especially when the system is geometrically complex or contains significant non-linearities in the soil or structural materials.

4.3.1.2 Substructure Approach

For improving the computational efficiency, various types of frequency domain methods using substructure approach can be adopted to address the influence from the soil, even though it cannot explicitly account for the non-linear effects of soil–structure interactions. In the substructure approach, the SSI problem is partitioned into distinct parts as soil, foundation, and superstructure, and their responses are first obtained independently, and are then combined to satisfy compatibility of forces and displacements and to formulate the complete solution. Soil motions at free-field are calculated. Due to the soil nonlinearities, the corresponding soil material properties are then determined based on the strain level calculated for the free-field condition. This is followed by an evaluation of transfer functions to convert free-field motions to foundation input motions, after which the foundation impedance, dealing with the coupling of soil to the lumped mass model to represent the stiffness and damping at the soil-foundation interface, can be implemented to calculate a response under combined structure-impedance subjected to the foundation input motions. It is obvious that the substructure approach is normally limited to linear behavior and results in frequency dependent equations that are solved by use of Fourier synthesis. In this approach, the interaction effects are typically accounted for by adding to the fixed base structural model a number of frequency dependent springs and dashpots representing the flexibility of the soil and the radiation of energy away from the foundation.

From the discussion above, it will be inferred that the obvious advantages of the substructure approach are the convenience regarding both modeling and computation, the approach requires little modifications to the fixed base structural model and hence allows for the possibility of using well-established techniques to derive the solution. However, a certain number of approximations (perhaps inaccuracies) appear in the aspects of foundation modeling (geometry, stiffness) and the soil behavior (elasticity, linearity), etc. [19].

Compared to the bedrock/rock outcrop motion, the seabed/ground surface motion is in many cases higher due to the interaction between the bedrock motion and soil column, while the interaction usually eliminates the high frequency motion and filters the motion to a narrow frequency motion. Furthermore, the soil properties surrounding the foundation will also influence the stiffness of the foundation, which directly affect the structural response. In addition, the overall stability of the offshore installations may be dominated by the strength of the local soil.

One-dimensional site response analysis is normally performed due to its computation efficiency, and strictly speaking, it is only valid if soil layers are horizontal and extend infinitely in the horizontal direction. Even if this assumption is not strictly satisfied, in most cases, it is sufficiently valid for engineering purposes. The analysis can be performed by vertically propagating shear waves in the soil layers. Two- or three-dimensional site response analysis does not require the assumption required for the one-dimensional analysis. However, this analysis is normally performed by finite element analysis. Section 4.3.8 will briefly discuss the applicabilities of one-, two- and three-dimensional site response analysis.

By partitioning the soil–structure system into a simpler set of soil and upper structure, Fig. 4.10 illustrates a standard three-step method in a substructure approach [21] for soil–structure interaction analysis. It includes both the geotechnical analysis (kinematic interaction and subgrade impedances) and structural analysis (intertia interaction), as will be presented in Sects. 4.3.2–4.3.4.

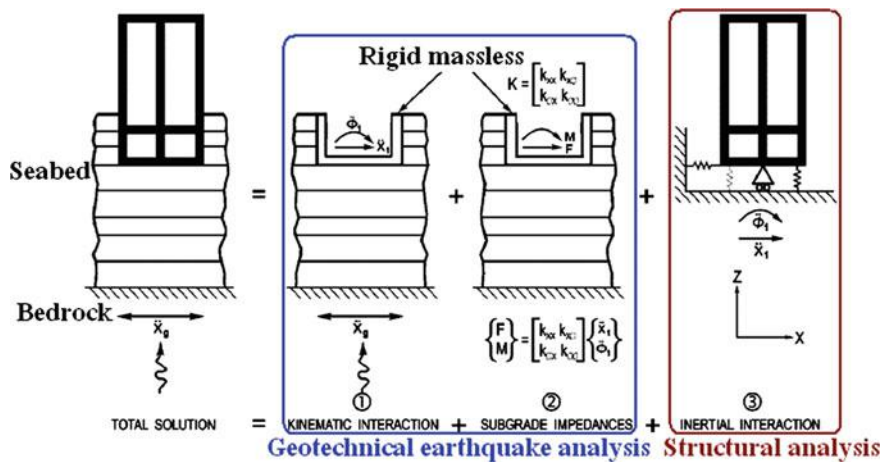


Fig. 4.10 Schematic illustration of three-step method in engineering practice to represent the actual soil–foundation–structure interactions [20]

For linear and equivalent linear analyses (Sect. 4.3.9), the effects of kinematic interaction and inertia effects can be separated. This means that one can first obtain the kinematic interaction and use it as input for structural analysis. By combining the results from both analyses, the overall response can be obtained.

It should be noted that the SSI analysis is not only applied in earthquake engineering, but also in conditions in which vibrations or impulses are transmitted to soils and induce wave propagation through the ground that can result in vibrations of structures nearby. An example of these conditions is transmissions of soil vibrations (due to, for example, construction activities) to the upper structure, which influence inhabitants' comfort or even the safety of structures.

4.3.2 Kinematic Interaction

The purpose of the kinematic interaction is to compute the motions (\ddot{x}_1 and $\ddot{\phi}_1$) at soil surface or a designated location in soil for given bedrock motions \ddot{x}_g . This is often referred to as site response analysis or ground response analysis.

The ground motion induces soil deformation known as free-field motion. However, the foundation embedded into the soil will not follow the free-field motion. This inability of the foundation to match the free-field motion leads to kinematic interaction. Practically, it calculates the motion of a rigid massless foundation at seabed/ground surface subject to the same bedrock seismic excitation \ddot{x}_g as the original structure and soil, and the modeled foundation has the identical shape as the actual foundation. Typically, the conventional method based on one-dimensional horizontal shear wave propagation model and quasi-linear solution can be used. If relevant, it is recommended to account for soil nonlinearities by inputting the soil stiffness and damping dependent on strain. This is performed through either an equivalent linear analysis or a non-linear analysis [23] as will be discussed in Sect. 4.3.9. Quite often, in a kinematic interaction analysis, the influence of foundation on the soil properties (especially on shear modulus) is neglected, making the calculated motions from the kinematic interaction identical to those of the free-field motions.

To perform the calculation of kinematic interaction, the earthquake input motion should be known, either at a specific point (e.g., ground surface, bedrock, rock outcrop) or in the form of incident waves (e.g., oblique shear waves) propagating up from a reference depth. For a validation of the analysis, a comparison of frequency contents between the calculated and measured one, in the form of Fourier amplitude spectrum, may be used. This is because a single comparison of peak ground responses between the calculated and measured one may not sufficiently reflect all aspects of differences. For more details of kinematic interaction, Ref. [23] is recommended reading.

4.3.3 Subgrade Impedances and Damping

The purpose of this step is to calculate the frequency dependent impedance representing the foundation stiffness and dashpots of the soil medium surrounding the foundation, taking the embedment and soil layer into account. For more details, see Refs. [2, 23].

4.3.4 Inertial Interaction

Inertial interaction is intended to calculate the dynamic response of a structure supported on a foundation impedance, and subjected (at the base) to the excitation time histories (\ddot{x}_1 and $\ddot{\phi}_1$), obtained in kinematic interaction analysis (Sect. 4.3.2).

While kinematic interaction and subgrade impedances are related to the geotechnical earthquake analysis, inertia interaction analysis is essentially a structural analysis.

The three-step method shown in Fig. 4.10 is practically exact from the mathematical point of view, i.e. the response of the upper structure is not significantly influenced by the simplification in the substructure approach (partitioning the soil–structure system into soil and upper structure). On the other hand, as the kinematic interaction is estimated based on a massless foundation mass modeling, the method gives unreliable results for a soft soil condition where non-linear soil behavior is significant.

Since the impedance functions are a frequency domain approach, when performing the seismic analysis in time domain, the frequency domain solutions for soil must be converted to an equivalent soil model in time domain, the detailed description of the method is given in Refs. [2, 11, 23].

From a vibration point of view, SSI increases the damping while decreasing the dominant frequency of dynamic responses. The damping involved in an SSI is generally beneficial to reduce dynamic responses of the upper structure. In addition, soft soil-foundation increases the flexibility of the structure, and generally reduces the response at the upper structure. However, the influence of SSI is not beneficial if the lower order of eigenfrequencies of an upper structure is close to the dominant frequency of the ground shaking. It is therefore very important to include the effects of SSI in the analysis if the upper structure is heavy and the soil is soft [22].

For structures supported on soft soil, one-dimensional site response analyses is necessary for SSI analysis purposes. For important structural elements, such as the base of a shear wall, massless elastic springs can often be used to estimate the foundation stiffness. For massive structures, such as large and heavy offshore GBS

structures or gravity dams, a part of the foundation may be modeled by three-dimensional solid elements.

In Chap. 15, various types of seismic analysis methods will be presented.

4.3.5 Effects of Soil–Structure Interaction

In general, the soil–structure interaction can be rather significant for stiff structures resting on soft soil sites, while it may not be that significant for soft (flexible) structures founded on stiff soil deposits. The natural period of a soil–structure system is longer than that of a fixed base structure. The ground motions due to SSI may be amplified or de-amplified, which is important for attaining a dedicated seismic design of structures.

The main effects of SSI on structural response are softening a structure's foundation, thus lengthening the natural period of the structure, and increasing the damping of the foundation-structure system.

The SSI is traditionally considered to have dominating beneficial effects because it was believed to reduce dynamic forces (e.g. bending force and shear force) applied on structures, and therefore to increase the safety. This is mainly due to an increase of the structure's natural period and increased damping associated with soil deformability. By absorbing the smooth design acceleration spectra, which have an essentially constant acceleration branch and a declining acceleration branch, an increase in natural periods of structures generally leads to a decrease of accelerations in structures and foundations. This had been realized by many design codes suggesting conservative simplification through neglecting the SSI effects in a seismic analysis. However, this conservative simplification is only applied to a certain class of structures and soil conditions, such as light structures in relatively stiff soil.

On the other hand, neglecting SSI may lead to an unsafe design for both the superstructure and the foundation. From a geotechnical earthquake engineering point of view, soft soil sediments can significantly increase the period of seismic waves. This is reflected in design acceleration spectra (Fig. 5.19) with a higher period range of constant acceleration plateau up to 1 s for soft soil than a lower period range for stiff soil. This effect has been recognized by the study of the spectra of ground motion record of earthquakes in Brancea 1977, Michoacan 1985 and Kobe 1995 [24]. From a seismological rather than geotechnical perspective, the fault rupture propagation toward a site, referred to as forward fault rupture directivity, causes most of the seismic rupture energy to arrive in the form of long periods pulse of motion, increasing the spectral values of the horizontal component normal to the fault strike at periods longer than about 0.5 s [25]. From the structural engineering point of view, with the presence of SSI effects, the natural period of a

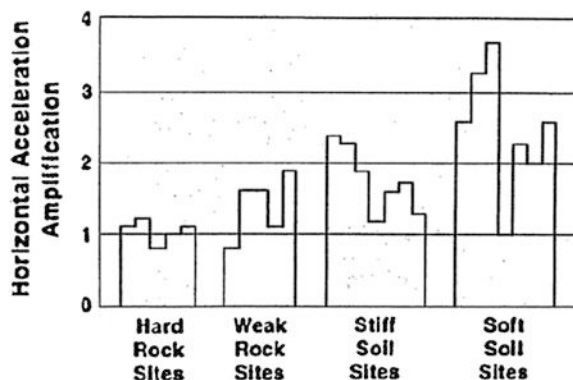
structure is decreased, this may induce the resonance of the structure subjected to longer period of ground motions due to SSI. Therefore, as a result of geotechnical, seismological and structural factors, the effects of SSI increase the fundamental period for both soils and structures, and may therefore increase the structural response.

4.3.6 Characteristics of Site Responses

4.3.6.1 Horizontal Ground Motions

The horizontal amplification factor F_a , defined as the ratio between peak horizontal ground acceleration at seabed/ground surface and that at bedrock or rock outcrop, is influenced by both the local soil conditions, ground topology, and the intensity and frequency content of earthquake motions [2, 26, 27]. The soil condition is important to determine the ground motions. Figure 4.11 illustrates an example of horizontal acceleration amplification in various soil conditions. Even though the variation trend of amplification depends on the combination of various factors such as site conditions and seismic ground motions at bedrock or rock outcrop, the figure shows that soils can amplify or de-amplify the ground motions. In general, loose unconsolidated soil may amplify ground motion compared to the bedrock motion. Based on a parametric study of site response analysis at three offshore sites on the Norwegian continental shelf [28], it is found that the local soil may have a rather pronounced effect on both the level and the distribution of energy of ground motions and may be an important factor in hazard studies. The variation in amplification for different soil conditions is large. Within certain frequency ranges, soil can amplify the rock

Fig. 4.11 An example of horizontal acceleration amplification at various soil sites (courtesy of FEMA)



outcrop motion by a factor up to 6 for low load levels (probability of exceedances of 10^{-2}) and by a factor up to 5 for high load levels (probability of exceedances of 10^{-4}). At short periods ranging from 0.1 to 0.3 s and with soft soil conditions, the amplification factor is rather high; while for rocky conditions, the amplification is low. Note that a typical fixed offshore structure cherishes a natural period (global vibration mode) above 1.0 s, the short period range of seismic ground motions does not have significant influence on the amplification of its lateral/horizontal structural response. However, the influence of the vertical ground motion at the short period range would be potentially important on responses of various types of structures, such as heavily loaded deck structures with large cantilevers or horizontal cantilever structures (e.g., cantilever beams at module support frame or a stiff flare boom), which have rather high longitudinal stiffness.

In addition, the increase in sediment depth (depth of control motions) may also lead to significant changes in response, which is the case for several offshore regions such as the Norwegian continental shelf, where very deep unconsolidated sediments underlain by a few kilometers of sedimentary rock are typical.

4.3.6.2 Vertical Ground Motions

Vertical ground motions are mainly contributed to by P-waves, and partially contributed to by horizontal shear waves. Because the pressure wave velocities of the soil and the underlying rock have little difference, i.e. high vertical stiffness, the ground motions at seabed/ground surface are essentially quite similar and can in some cases be assumed to be identical to the seismic motions at bedrock. Therefore, different from that of the horizontal response, the amplification of vertical ground motions due to the local soil is normally insignificant.

The vertical peak ground acceleration is generally 10–50 % lower than the horizontal peak ground acceleration. The relationship between vertical and horizontal components of the seismic action mainly depends on the period, the distance between sites to relevant faults, the local site conditions, and earthquake magnitude, while the ratio is relatively insensitive to earthquake mechanism and sediment depth [29].

It is well accepted that one can derive the vertical ground motion spectrum by scaling the horizontal motion response spectrum by either a factor or different factors at different frequency range. For designs of important structures such as nuclear power plants, dedicated vertical ground motion spectra may be directly given. The vertical to horizontal spectral ratio V/H is generally less than 2/3 at mid to long periods but significantly higher at short periods, and at short period the V/H spectral ratio is sensitive to the site-to-source distance. It is higher on soil sites than on rock sites, and is higher on soft soil sites than on stiff soil sites. A recent study by Bozorgnia and Campbell [30] presents that V/H spectral ratio for soil sites is relatively less sensitive to magnitude than the site-to-source distance. The V/H spectral ratio will be further discussed in Sect. 5.4.4.

4.3.7 Effects of Topographic and Subsurface Irregularities

4.3.7.1 General

The ground motions are not only influenced by the properties and thickness of soil layers at a site due to the filter effects of soil profile on the seismic wave propagations, but are also affected by the surface topology of the site and the subsurface's irregular interfaces of soil materials and rock. The irregular shape of surface and subsurface topography is often attributed responsibility for the focusing and defocusing of seismic energy as seismic waves propagate within the irregularity as well as for the generation of surface waves due to diffraction phenomena at the lateral discontinuities that interfere with body waves and lead to complex compositions of seismic wave field and thus irregular distribution of damage [31–33, 61].

Typical examples of surface irregularities are sloping or irregular ground surface; and typical examples of subsurface irregularities are sloping layer boundaries and irregular boundaries or basins. The effects from both types of irregularities can be significant. Evidence of amplification effects, produced from both weak and strong motion events, are available worldwide.

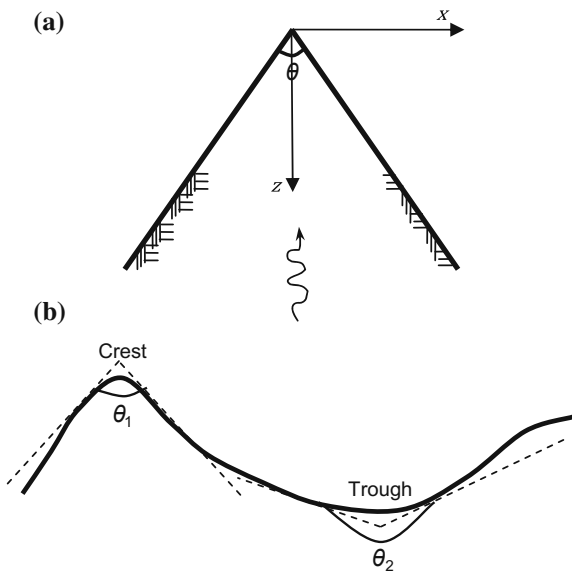
The relevant site response analysis to account for the surface and subsurface effects requires two- or even three-dimensional analyses (Sect. 4.3.8), usually using finite element analysis, which may involve significant analysis efforts. On the other hand, a preliminary evaluation of those effects is sometimes possible based on simple hand calculation.

4.3.7.2 Effects of Irregular Surface Topology

It has long been recognized that infrastructures constructed at the tops of hills, ridges, and canyons suffer more intensive damage than those situated at the bases of hills or on level surfaces, as have been reported in past earthquakes such as the 1909 Lambesc earthquake in France [34], the 1976 Friuli earthquake in Italy [35], the 1980 Irpinia earthquake in Italy [36], the 1985 Chile earthquake [37], the 1989 Loma Prieta earthquake [38], the 1999 Chi-chi earthquake [39], and the 1999 Athens earthquake [40]. As an example, apparent topographic effects were observed on the abutment of Pacoima Dam in San Fernando during the 1971 earthquake [41], where an unexpected high acceleration of 1.25 g was also recorded at the crest of a narrow rocky ridge adjacent to the dam in Tarzana station during the Northridge 1994 earthquake [23]. In Europe, seismic motion measurements reported similar observations of large amplifications, with a ratio of almost 10, in a narrow frequency band around 5 Hz [42, 43].

These effects are related mainly to three physical phenomena: (1) the sensitivity of surface motion to the incidence angle around the critical, especially for SV waves; (2) the focusing and de-focusing of seismic waves along the topographic relief; and (3) the diffraction of body and surface waves that propagate downwards

Fig. 4.12 Simple ground surface topology irregularities (solid line) for: **a** an infinite wedge subject to plane seismic waves in the direction of its axis; **b** approximation of actual ground surface at crest and trough by wedges [44]



and outwards from the topographic features and lead to interference patterns between direct and diffracted waves [33].

Aki [44] has examined the effects of elementary irregular surface topology with simple exact solutions. For an idealized wedge topology subject to vertical propagating SH wave excitation, the frequency-independent amplification ratio of $2\pi/\theta$ can be applied at the vertex of a wedge with angle θ , as illustrated in the upper figure in Fig. 4.12. By using this relationship, one can calculate the amplification of a real topographic profile such as a ridge-valley terrain, as shown in the lower portion figure of Fig. 4.12. Provided that the crest and the trough are sufficiently far apart, the ratio of amplification between the crest and trough shown in the lower figure of Fig. 4.12 can be approximated as θ_2/θ_1 . He also stated that the amplification in simple irregularities due to incident P-SV waves, although somewhat larger in the average than for SH waves, is roughly of the same magnitude. Castellani [45] and Bard [46] also presented that the amplifications for incoming SV waves are slightly larger than those of the SH wave.

Surface topographic effects have been considered in various seismic design codes. For example, in Eurocode 8 [16], a correction factor for both ridge and cliff-type topographies as a function of the height and the slope angle is used. The so-called aggravation factor gives an extra amplification of 20–40 % compared with the one determined based on the one-dimensional site response estimation. The Italian Building Code [47] introduces an amplification factor to modify the ordinates of the acceleration response spectra referred to soil category A and horizontal topographic surface for dynamic design. Such factors depend on the contributions of both soil layer and irregular surface topology. However, neither code explicitly

specifies the contribution of seismic motion amplification due to subsurface geometric irregularities of bedrock and contacts between soil strata.

4.3.7.3 Effects of Subsurface Irregularity

Note that many urban areas are located on or near alluvial valleys. It is hence important to evaluate the seismic motions influenced by curvature of basins, in which softer alluvial soils have been deposited, where the lateral variation along the horizontal direction can trap body waves and cause some incident body waves to propagate through the alluvium and generate the local surface waves [48]. The edge-generated Rayleigh wave induced by conversion from the S-wave incidence at the basin edge dominates the ground motions inside the basin after the arrival of body waves [49]. When the impedance contrast is large, the surface waves are reflected at the basin edges and propagate repeatedly between the edges. This can eventually lead to increased amplifications and longer duration of ground motions compared with those obtained from conventional one-dimensional site response analysis that only considers vertically propagating shear wave [23].

The effect of subsurface irregularity on earthquake ground motions has been discussed by several researchers [50–52, 62]. For example, studies showed that the lateral discontinuities at shallow sedimentary valley at a site located in northern Greece generate locally diffracted surface waves that affect the frequency content and the amplification of seismic motion as well as duration of observed ground motion [53, 54].

In the case of deep valleys, the amplification functions from one-dimensional and two-dimensional numerical simulations are different both at the center and at the edges. Bard and Bouchon [55] proposed an empirical criterion, which can be applied to sine-shaped valleys in order to identify the significance of two-dimensional effects:

$$\frac{h}{l} \begin{cases} \geq \frac{0.65}{\sqrt{C_v - 1}}, & \text{two-dimensional resonance} \\ < \frac{0.65}{\sqrt{C_v - 1}}, & \text{one-dimensional resonance + lateral propagation} \end{cases} \quad (4.9)$$

where h is the thickness of the soil deposit; l is the half width of the valley; C_v is the soil-bedrock velocity contrast.

It should be noted that the equation above can be interpreted as an empirical boundary between truly two-dimensional valley effects (when $\frac{h}{l} \geq \frac{0.65}{\sqrt{C_v - 1}}$) and side effects that are focused at the valley edges which are coupled to one-dimensional behavior (when $\frac{h}{l} < \frac{0.65}{\sqrt{C_v - 1}}$). However, it is worth mentioning that the equation has been derived from numerical simulations of propagation of P- and S-waves under simplified hypotheses on soil behavior and valley geometry; being in reality much more complex, boundaries between the two effects shall be regarded with respect to each case studied [56].

Table 4.2 Effects of surface and subsurface irregularities on seismic ground motions [23, 57]

Structure	Conditions	Effects	Significance	Most suitable quantitative predictions
Surface irregularity	Sensitive to shape ratio, very significant for frequencies corresponding to wavelengths equal to the mountain width	Amplification at the crest, de-amplification or amplification at base, rapid changes in amplitude phase along slopes	Amplification up to a factor of 30, with a typical value ranging from 2 to 10	Poor, generally underpredict the amplification, may be due to ridge–ridge interaction and three-dimensional effects
Sediment-filled valleys	Local changes in shallow sediment thickness	Increased duration	Duration of significant motion can be doubled	Fair
	Generation of long period surface waves from body waves at shallow incidence angle	Increased amplification and duration due to trapped surface waves	Duration and amplification of significant motions may be increased over one-dimensional projections	Good at periods above 1 s
Shallow and wide soil filled valley (depth/width: <0.25)	Effects most pronounced near edges; largely vertically propagating shear waves away from edges	Wide range frequency amplification near edges due to generation of surface waves	One-dimensional models may underpredict at higher frequencies by about 2 near edges	Away from edge, one-dimensional site response analysis is good; near edges higher dimensional site response analysis is recommended
Deep and narrow soil filled valley (depth/width >0.25)	Effects throughout valley width	Broad range frequency amplification across the valley due to whole valley modes	One-dimensional model may underpredict for a wide range frequency range by about 2–4; resonant frequencies shifted from one dimension	Fair; given detailed description of vertical and lateral changes in soil properties

Silva et al. [57] summarized the effects of surface and subsurface irregularities with comments on their quantitative predictability, which are presented in Table 4.2.

Even though a certain amount of studies have been performed that present the importance of the effects of subsurface topology on the ground motions, they have not been fully recognized by engineering communities, mainly due to a lack of measurement data that can help provide a better understanding of the effects in a simplified manner, and also due to its complexity in the two- or three-dimensional modeling.

4.3.8 Applicability of One-, Two-, and Three-Dimensional Site Response Analysis

For simplification, it is usually reasonable to assume that the soil layers are horizontally extended to infinity with a level ground, and the incident earthquake motions are spatially-uniform, horizontally-polarized shear waves and only propagate vertically. These assumptions can be justified by the fact that soil properties normally vary more rapidly in the vertical direction than in the horizontal direction. The stress waves from the source propagate almost vertically when they arrive at the ground surface, and waves' velocity normally decreases from the source towards the ground. The stress waves from the source are therefore bent by successive refractions into an almost vertical path. Even though the waves within firm ground propagate in a shallow inclined direction, they propagate nearly vertically between the soil and the firm ground by refraction [58]. With the assumptions above, the one-dimensional wave propagation analysis can be performed, based on either the solution to the wave equation or on a lumped mass simulation. It generally results in a conservative evaluation for site responses, and many structures designed based on one-dimensional analysis sustained the loading during the major earthquake events. One-dimensional wave propagation analysis can be carried out by a number of commercial software programs such as SHAKE [66].

However, more recent research has characterized two-dimensional site effects on ground motions [31, 59–61]. Compared to one-dimensional effects, the differences of two-dimensional effects are related to the propagation of locally generated surface waves and possible two-dimensional resonance [62–65]. By considering the sedimentary basin effects and neglecting the topographic site effects, Chávez-Garcia and Faccioli [62] investigated the possibility of including some kinds of provision for the two-dimensional complex effects in a seismic design code. Their study indicates that, compared to one-dimensional effects, two-dimensional site effects can significantly increase (by a factor of more than 2 on the response spectra) the ground motion amplitude in a wide period range. Owing to the additional lateral restriction to motions of sediments, two-dimensional amplification becomes significant for lower periods than one-dimensional amplification. They also showed that the most significant parameter controlling the two-dimensional basin amplification factor is the velocity contrast between sediments and bedrock. Therefore, not only top soil layers (used for one-dimensional site effects), but also bedrock properties should be modeled to perform a two-dimensional site effects analysis.

Theoretical three-dimensional site response analysis is only quantitatively different from its two-dimensional counterpart. The third dimension increases ground motion amplification somewhat, and the additional lateral restriction shifts peak frequencies to higher values.

As a general rule for more irregular ground topology and subsurface soil deposits as discussed in Sect. 4.3.7, two-dimensional or even three-dimensional effects may need to be accounted for. Therefore, to capture different types of seismic wave propagation, and/or to account for site geometric properties that may

affect the seismic wave propagation, two-dimensional and three-dimensional site response analysis is required, which is usually performed by finite element analysis. For more details, readers may refer to [2].

4.3.9 Linear, Equivalent Linear or Non-linear Soil Modeling

For small to medium sized ground motions, the soil can be modeled as a linear elastic or visco-elastic material. This is applied to the regions with lower seismicity. However, for sites with potentially large ground shaking, the soil can exhibit strong nonlinearity, and a non-linear soil modeling should then be adopted. To minimize the computation efforts, some commercial codes such as SHAKE [66] use the equivalent linear analysis [23] method to treat the nonlinearity of the soil.

In a typical soil dynamic analysis with equivalent linear model, the equivalent linear model (shear modulus and damping are assumed to be constant) is combined with a harmonic base motion to calculate the dynamic response of soils. The seismic excitation time histories at a location/depth of soils will be divided (de-convoluted) into harmonic components through Fourier series expansion. This is followed by the computation of each individual response to each divided harmonic component. These individual responses are finally combined together to obtain the responses at various depths in the soil. Even though the shear modulus and damping level varies with the variation of strain during an entire seismic event, for mild earthquakes, this variation of strain is limited, and it would thus be convenient to assume a constant soil strain level at each soil layer, so that a constant shear modulus and damping level will be used to compute the dynamic response throughout the entire time duration of the seismic excitations. This is often performed by assuming an initial strain to estimate the shear modulus and damping level, which are used to compute the dynamic soil response, from which the effective shear strain $\gamma_{\text{eff},i}$ at soil layer i can be obtained by reducing the maximum shear strain response $\gamma_{\text{max},i}$ (peak shear strain) in the computed soil response with a reduction factor R_γ :

$$\gamma_{\text{eff},i} = R_\gamma \cdot \gamma_{\text{max},i} \quad (4.10)$$

Empirically, for the transient motion of soil during an actual earthquake, the factor R_γ is usually taken as 0.65, this is an approximation by comparing measured transient shear strain time histories during previous earthquake events with the harmonic ones (obtained from typical laboratory tests, which normally represent more significant loading conditions than the transient ones) that have the same peak cyclic shear strain. Obviously, the way to determine the factor R_γ lack a solid theoretical background.

By using the equivalent linear soil model, an iterative procedure has to be implemented, as it is not possible to determine the maximum level of strain in each

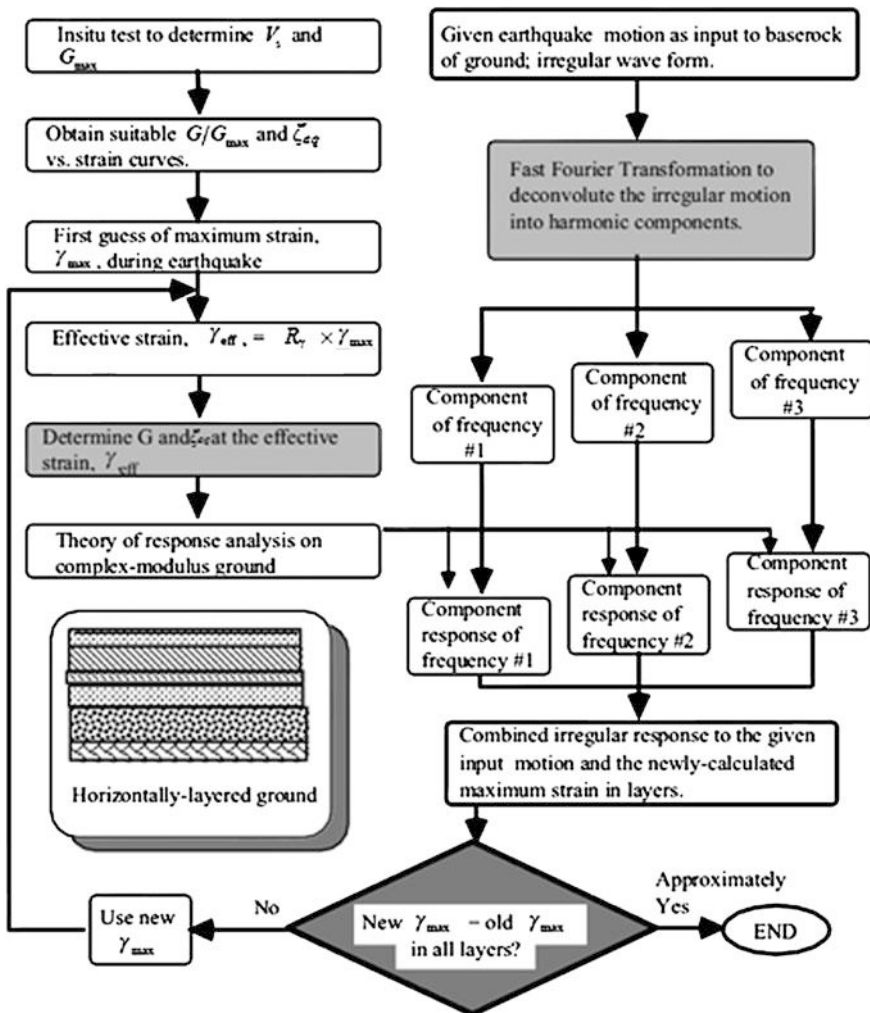


Fig. 4.13 The procedure of dynamic site response analysis using equivalent linear soil modelling [11]

layer of the soil profile before the analysis is completed, i.e., firstly, one needs to predefine the initial value of shear modulus and damping properties for each layer and then to perform a shear wave propagation analysis. From the calculated maximum shear strain response $\gamma_{max,i}$, the effective strain $\gamma_{eff,i}$ can be determined by the equation above. Thereafter, the shear modulus and damping for layer i will be recalculated and used to compute the dynamic responses again in the next iteration, which is used to estimate the effective strain further. This iteration will be repeated until the differences between the effective strain in two successive iterations is smaller than a specified tolerance. The procedure of equivalent linear analysis is

illustrated in the flow chart shown in Fig. 4.13. Its merits are reflected in the aspects of computational cost, robustness, simplicity, and convenience.

From the discussion above, it can be seen that equivalent linear analysis is sufficient for most analysis. However, it cannot calculate the residual deformation under dynamic repeated loading of the soil and may wrongly predict resonance events. For details of soil modeling in a site response analysis, readers may refer to [2, 11, 23].

4.3.10 *Location to Input Seismic Motions for a Site Response Analysis*

The seismic motion records to be used in a site response analysis for a site should generally be compatible with the geologic conditions at the bottom of the site profile being simulated. If bedrock is reasonably shallow and its depth is known, the profile should extend into rock, and seismic motion input should be defined for the rock condition. If the site consists of deep soils that cannot reasonably be simulated in their entirety, the soil profile may then be extended to a firm soil horizon with a strong impedance contrast with the soil layers above the firm soil. In this case, one may adopt input motions at the rock outcrop or the firm soil [67].

4.4 Water Column Effects on Vertical Ground Excitations

By studying the ground motion measurement offshore and comparing it with the nearby onshore record with comparable epicentral distance (85 and 98 km) at Santa Barbara Island during September 1981, Smith [68] and Sleefe [69] presented that, due to the presence of the water column, the vertical seismic ground motions at the seafloor were much lower than those based on the measurements onshore. This is especially important for mat supported structures, because they receive most of the motion from the soils near the seabed. This statement is also confirmed by other researchers [70, 71], who developed an analysis that includes the effects from the finite water column. They indicated that, depending on the water depth, some frequencies can be reinforced and amplified by the water column effects, while others can be cancelled. The peak vertical accelerations at the seabed can be reduced by as much as 50 %.

By studying eight offshore seismic records with magnitudes between 4.7 and 6.1 during a 20 year period, and comparing them with onshore records with comparable epicentral distance (ranging from 49.4 to 309 km) and site characteristics, Boore and Smith [72] concluded that offshore earthquake ground motion is in general the same as its onshore counterpart. However, similar to what was found by Smith [68] and Sleefe [69] previously, Boore and Smith also presented that the sediment layer and the water volume over the site damped the vertical component

of the ground motions. As a result, the V/H ratios (vertical to horizontal component of motion) for offshore locations are smaller than those with comparable site characteristics at onshore locations. In addition, as the amount of damping is proportional to the period of the ground motions, the difference between the vertical component of the ground motions onshore and the offshore motions decreases as the periods become longer and increases as the periods become shorter [73].

References

1. Howell JV (1960) Glossary of geology and related sciences. American Geological Institute, Washington, pp 207–208
2. Jia J (2016) Soil dynamics and foundation modeling: offshore and earthquake engineering. Springer, Heidelberg
3. Anderson JC, Bertero VV (1987) Uncertainties in establishing design earthquakes. *J Struct Eng ASCE* 113(8):1709–1724
4. PEER Center (2000) ATC, Japan Ministry of Education, science, sports and culture, US-NSF, Effects of near-field earthquake shaking. In: Proceedings of the US–Japan workshop, San Francisco, March, pp 20–21
5. Duek CM, Luco JE, Carriveau AR, Hradilek PJ, Lastrico R, Ostrom D (1970) Strong earthquake motion and site conditions, Hollywoook. *Bull Seismol Soc Am* 60(4):1271–1289
6. Dobry R, Martin GM, Parra E, Bhattacharyya A (1992) Development of site-dependent ratios of elastic response spectra (RRS) and site categories for building seismic codes. In: Martin GM (ed) Proceedings of the 1992 NCEER/SEAOC/BSSC workshop on site response during earthquakes and seismic code provisions. National Center for Earthquake Engineering Research Special Publication NCEER-94-SP01 (Buffalo, NY), University of Southern California, Los Angeles, Nov 18–20, 1992
7. Joyner WB, Warrick R, Fumal T (1981) The effect of Quaternary alluvium on strong ground motion in the Coyote Lake, California earthquake of 1979. *Bull Seismol Soc Am* 71:1333–1349
8. Aki K (1988) Local site effects on strong ground motion. In: Von Thun L (ed) Proceeding of the specialty conference on earthquake engineering and soil dynamics II: recent advances in ground-motion evaluation. ASCE Geotechnical Special Publication No. 20, Park City, Utah, 27–30 Jun, 1988, pp 103–155
9. Boore DM, Joyner WB, Fumal TE (1997) Equations for estimating horizontal response spectra and peak acceleration from western North American earthquakes: a summary of recent work. *Seismol Res Lett* 68(1):128–153
10. Elnashai AS, Di Sarno L (2008) Fundamentals of earthquake engineering. Wiley, New York
11. Towhata I (2008) Geotechnical earthquake engineering. Springer, Heidelberg
12. Broderick BM, Elnashai AS, Ambraseys NN, Barr JM, Goodfellow RG, Higazy EM (1994) The Northridge (California) earthquake of 17 January 1994: observations, strong motion and correlative response analysis. *Engineering seismology and earthquake engineering, research report no. ESEE 94/4*, Imperial College, London
13. Dobry R, Iai S (2000) Recent developments in the understanding of earthquake site response and associated seismic code implementation, GeoEng2000, Melbourne
14. Seed HB, Romo MP, Sun JI, Jaime A, Lysmer J (1988) The Mexico earthquake of September 19, 1985: relationships between soil conditions and earthquake ground motions. *Earthq Spectra* 4(4):687–729
15. ISO19901-2 (2004) Petroleum and natural gas industries—specific requirements for offshore structures—Part 2: Seismic design procedures and criteria

16. Eurocode 8 (2004) Design of structures for earthquake resistance—part 1: general rules, seismic actions and rules for buildings
17. China Net for Engineering Construction Standardization (2010) Code for seismic design of buildings, GB 50011-2010. China Building Industry Press, Beijing
18. FEMA, NEHRP Recommended Seismic Provisions for New Buildings and Other Structures, FEMA P-750/2009 Edition, prepared by the Building Seismic Safety Council of the National Institute of Building Sciences for the Federal Emergency Management Agency, Washington, DC, 2009
19. Lanzi A (2011) Approximate analysis of dynamic soil–structure interaction. University of California, San Diego
20. Kaynia A (2009) Seismic analyses of Statfjord B, 16th of April, Norwegian Geotechnical Institute
21. Idriss IM et al (1979) Analyses for soil–structure interaction effects for nuclear power plants, Report of the Structural Division, ASCE, New York
22. Safak E (2006) Time domain representation of frequency-dependent foundation impedance functions. *Soil Dyn Earthq Eng* 26:65–70
23. Kramer SL (1996) Geotechnical earthquake engineering. Prentice Hall, Upper Saddle River, NJ
24. Gazetas G (2006) Seismic design of foundations and soil–structure interaction. In: First European conference on earthquake engineering and seismology, Geneva
25. Somerville PG (1998) The amplitude and duration effects of rupture directivity in near fault ground motions. In: Dakoulas P, Yegian MK, Holtz RD (eds) Geotechnical earthquake engineering and soil dynamics III, ASCE
26. Martin GR, Dobry R (1994) Earthquake site response and seismic code provisions. National Center for Earthquake Engineering Research Bulletin, 8(4)
27. Crouse CB, McGuire JW (1997) Site response studies for purpose of revising NEHRP seismic provisions. Dames and Moore Consultants, Seattle, Washington
28. NGI, NORSAR, PRINCIPIA (1988) Earthquake loading on the Norwegian Continental Shelf, Oslo
29. Bozorgnia Y, Campbell KW (2004) The vertical-to-horizontal response spectral ratio and tentative procedures for developing simplified V/H and vertical design spectra. *J Earthq Eng* 8:175–207
30. Bozorgnia Y, Campbell K (2015) NGA-West2 vertical-to-horizontal (V/H) ground motion model. *Earthq Spectra* 31:2
31. Faccioli E (1991) Seismic amplification in the presence of geological and topographic irregularities. In: Prakash S (ed) Proceedings of the second international conference on recent advances in geotechnical earthquake engineering and soil dynamics, 11–15 March, St. Louis, Missouri, Univ. of Missouri-Rolle, vol 2, pp 1779–1797
32. Chávez-García FJ, Sanchez LR, Hatzfeld D (1996) Topographic site effects and HVSR. A comparison between observations and theory. *Bull Seismol Soc Am* 86:1559–1575
33. Pitilakis K, Raptakis D, Makara K, Ktenidou O-H, Pandi K, Manakou M, Pitilakis D, Diagouras D (2004) Effects of surface and subsurface topography on strong ground motion at the City of Aigion, Greece. In: 13th World conference on earthquake engineering, Vancouver
34. Angot A (1910) Le tremblement de terre du 11 juin 1909 dans le Sud-Est de la France, I, Enquête du Bureau Central Météorologique. *Ann Géogr* 103:8–15
35. Brambati A, Faccioli E, Carulli GB, Cucchi F, Onofri R, Stefanini S, Ulcigrai F (1980) Studio de microzonazione sismica dell'area di Tarcento (Friuli), Regione Autonomia Friuli-Venezia Giulia e Università degli Studi di Trieste con la collaborazione del Politecnico di Milano, Trieste
36. Siro L (1982) Southern Italy November 23 1980 earthquake. In: Proceedings of the seventh European conference on earthquake engineering, Athens, Greece, Sept, 1982
37. Çelebi M, Hanks T (1986) Unique site response conditions of two major earthquakes of 1985: Chile and Mexico. In: Proceedings of the international symposium of engineering geology problems in seismic areas, vol 4, Bari, Italy, Apr 1986

38. Hartzell SH, Carver DL, King KW (1994) Initial investigation of site and topographic effects at Robinwood Ridge, California. *Bull Seismol Soc Am* 84:1336–1349
39. Huang BS (2000) Two-dimensional reconstruction of the surface ground motion of an earthquake: the September 21, 1999, Chi-chi, Taiwan earthquake. *Geophys Res Lett* 27:3025–3028
40. Assimaki D, Gazetas G, Kausel E (2005) Effects of local soil conditions on the topographic aggravation of seismic motion: parametric investigation and recorded field evidence from the 1999 Athens earthquake. *Bull Seismol Soc Am* 95:1059–1089
41. Boore DM (1972) A note on the effect of simple topography on seismic SH waves. *Bull Seismol Soc Am* 62:275–284
42. Chavez-García FJ, Rodriguez M, Field EH, Hatzfeld D (1997) Topographic site effects: a comparison of two non-reference methods. *Bull Seismol Soc Am* 87:1667–1673
43. Neichtschein S, Bard PY, Gariel JC, Meneroud JP, Dervin P, Cushing M, Gaubert B, Vidal S, Duval AM (1995) A topographic effect study in the Nice region. In: Proceedings of the fifth international conference on seismic zonation, 17–19 Oct, Nice, France, Ouest Edition Nantes, II, pp 1067–1074
44. Aki K (1988) Local site effects on strong ground motion. In VonThun JL (ed) *Earthquake engineering and soil dynamics II: recent advances in ground motion evaluation*, Jun 27–30, Park City, Utah, pp 103–155
45. Castellani A, Peano A, Sardella L (1982) On analytical numerical techniques for seismic analysis of topographic irregularities. In: Proceedings of the seventh European conference on earthquake engineering, Athens, Greece, 20–25 Sept, 1982
46. Bard PY (1982) Diffracted waves and displacement field over two-dimensional elevated topographies. *Geophys J R Astron Soc* 71:111–120
47. DM 14 GENNAIO 2008. Norme Tecniche per le Costruzioni, GU n. 29 del 4 febbraio 2008
48. Vidale JE, Helmberger DV (1988) Elastic finite difference of the 1971 San Fernando Earthquake. *Bull Seismol Soc Am* 78(1):122–141
49. Hisada Y, Yamamoto S (1996) One-, two-, and three-dimensional site effects in sediment-filled basins. In: Proceedings of the 11th world conference on earthquake engineering, No. 2040, Acapulco, Mexico
50. Makra K, Raptakis D, Chávez-García FJ, Pitilakis K (2001) Site effects and design provisions: the case of EUROSEISTEST. *Pure Appl Geophys* 158(12):2349–2367
51. Frankel A, Vidale J (1992) A three-dimensional simulation of seismic waves in the Santa Clara Valley, California, from a Loma Prieta aftershock. *Bull Seismol Soc Am* 82:2045–2074
52. Olsen KB, Archuleta RJ, Matarese JR (1995) Three-dimensional simulation of a magnitude 7.75 earthquake on the San Andreas fault. *Science* 270:1628–1632
53. Raptakis D, Chávez-García FJ, Makra K, Pitilakis K (2000) Site effects at EUROSEISTEST-I, Determination of the valley structure and confrontation of observations with 1D analysis. *Soil Dyn Earthq Eng* 19(1):1–22
54. Chávez-García FJ, Raptakis D, Makra K, Pitilakis K (2000) Site effects at EUROSEISTEST-II, results from 2D numerical modeling and comparison with observations. *Soil Dyn Earthq Eng* 19(1):23–39
55. Bard PY, Bouchon M (1985) The two-dimensional resonance of sediment-filled valleys. *Bull Seismol Soc Am* 75(2):519–541
56. Vessia G, Russo S, Presti DL (2011) A new proposal for the evaluation of the amplification coefficient due to valley effects in the simplified local seismic response analyses. *Riv Ital Geotec* 4:51–77
57. Silva WJ, Turcotte T, Moriwaki Y (1988) Soil response to earthquake ground motion, EPRI report NP-5747. Electric Power Research Institute, Palo Alto, CA
58. GovindaRaju L, Ramana GV, HanumanthaRao C, Sitharam TG (2004) Site-specific ground response analysis. *Curr Sci* 87(10):1354–1362
59. Faccioli E (1996) On the use of engineering seismology tools in ground shaking scenarios. In: Proceedings of the 11th world conference on earthquake engineering, Acapulco, No. 2007

60. Aki K (1993) Local site effects on weak and strong ground motion. *Tectonophysics* 218:93–111
61. Bard PY (1994) Effects of surface geology on ground motion: recent results and remaining issues. In: Proceedings of the 10th European conference on earthquake engineering, Vienna 1, pp 305–323
62. Chávez-García FJ, Faccioli E (2000) Complex site effects and building codes: making the leap. *J Seismol* 4:23–40
63. Bard PY, Bouchon M (1980) The seismic response of sediment-filled valleys, Part 1. The case of incident SH waves. *Bull Seismol Soc Am* 70:1263–1286
64. Bard PY, Bouchon M (1980) The seismic response of sediment-filled valleys, Part 2. The case of incident P and SV waves. *Bull Seismol Soc Am* 70:1921–1941
65. Bard PY, Bouchon M (1985) The two-dimensional resonance of sediment filled valleys. *Bull Seismol Soc Am* 75:519–554
66. Schnabel PB, Lysmer J, Seed HB (1972) SHAKE, A computer program for earthquake response analysis of horizontally layered sites, No. EERC 72-12, Earthquake Engineering Research Center, College of Engineering, University of California, Berkeley
67. Pacific Earthquake Engineering Research Center (PEER), Guidelines for performance-based seismic design of tall buildings, Version 1.0, California, Nov, 2010
68. Smith CE (1997) Dynamic response of steel-jacket platform subject to measured seafloor earthquake ground motions. In: Proceedings of the eight international conference on the behavior of offshore structures, vol 3. Pergamon, Elsevier Science Ltd., Oxford
69. Sleefe GE (1990) The long-term measurement of strong-motion earthquakes offshore South California. In: Proceedings of OTC 1990, Society of Petroleum Engineers, Richardson, Texas
70. Crouse CB, Quilter J (1991) Seismic hazard analyses and development of design spectra for Maui A Platform. In: Proceedings of the Pacific conference on earthquake engineering, Auckland, New Zealand
71. Dolan DKM, Crouse CB, Quilter JM (1992) Seismic reassessment of Maui A. In: Proceedings of the offshore technology conference, OTC 1992, Society of Petroleum Engineers, Richardson, Texas
72. Boore DM, Smith CE (1999) Analysis of earthquake recordings obtained from the seafloor earthquake measurement system (SEMS) instruments deployed off the coast of Southern California. *Bull Seismol Soc Am* 89(1):260–274
73. Brown LA (2003) Assessment of seismic risk for subsea production systems in the Gulf of Mexico. M.Sc. thesis, Texas A&M University, USA, Dec 2003

Chapter 5

Representation of Earthquake Ground Motions

Things should be made as simple as possible but not a bit simpler than that.

Albert Einstein (1879–1955)

5.1 General

It is noted that the most important parameters of an earthquake ground motions are its maximum motion, predominant period and effective durations [1]. However, different from other loadings, earthquake induced loading and ground motion cherish high uncertainties in these aspects, as well as, more broadly, on its occurrence, magnitude, frequency content and duration. The uncertainties come from many sources: the energy suddenly released during an earthquake is built up rather slowly through tectonic movements; historical records over a time span of a couple of hundred years do not provide a complete picture of the seismic hazard. Moreover, the rupture and faulting process during an earthquake is extremely complex and affected by many parameters that are difficult to predict [2].

In the frequency domain, three types of spectra can be applied to describe the ground motion, namely Fourier spectrum (Sect. 5.3.1), and its closely related power spectrum (Sect. 5.3.2), and response spectrum (Sect. 5.4). The two former ones are stochastic methods while the latter one is categorized as a deterministic one due to the response spectra being generated from deterministic time history responses. As will be elaborated in Sect. 5.4, the Fourier spectrum or power spectrum combined with the phase information (through phase spectrum) can completely describe a ground motion (provided that the ground motion is stationary) while the response spectrum cannot. On the other hand, the use of Fourier spectrum and power spectrum normally requires that the seismic excitation is close to a stationary process, which is likely to be the case for only the central (strong motion) part of an earthquake record. The response spectrum method does not have this restriction. Moreover, from a engineering point of view, the response spectrum is a more

convenient and valuable tool to represent the ground motions, and it is especially suitable for a direct assessment of the effects of ground motions on structural response. Section 5.3 will present the power spectrum to represent the ground motions and how non-stationary characteristics of seismic motions can be approximated in this method.

Time history method (Sect. 5.5) enables the application of non-linear dynamic structural analysis (Chap. 15), which has the unique advantage of reducing the computational and modeling uncertainties, accompanied by an increase in computational efforts (compared to power spectrum and response spectrum method).

Before the advent of computer techniques in daily engineering work, to avoid intensive computation cost, the response spectrum was the most widely adopted approach for defining the earthquake ground motion input regardless of types of structural analysis (i.e. equivalent static analysis or response spectrum analysis, see Chap. 15), which will be discussed in Sect. 5.4. From the late of 20th century, with the rapid development of computer techniques and subsequent dramatic reduction in computation cost, time history analysis became more and more popular since it can reduce more uncertainties in the seismic loading and response calculations. However, spectrum method is still the most widely used not only in seismic structural analysis, but also within the context of (spectrum compatible) accelerograms generation (Chap. 7) and time history analysis, even though this method has been questioned by many researchers including one of its original promoters [3].

Since earthquake ground motion is in general non-stationary, as mentioned above, analysis in the frequency domain loses the time-located information. To solve this problem and also to more efficiently analyse the ground motions in the time–frequency domain, recent researches promote the application of wavelet transform method, which will be introduced in Sect. 5.6.

5.2 Earthquake Excitations Versus Dynamic Ocean Wave, Wind, and Ice Loading

Compared to other random environmental loading such as ocean wave, wind, and ice loading, seismic loading has both similar and different characteristics with respect to frequency, duration, action locations, linearity of loading and response, as well as stationarity, which is illustrated in Table 5.1.

The characteristics above are essential to determine the relevant design philosophy, analysis and design methods, load representation, as well as required engineering skills. For example, ocean wave, wind and ice loading can sometimes be approximated as a stationary process and, being linear, the loading can be represented by power spectra, in case the structures subject to those loading are also linear or nearly linear (response is proportional to the magnitude of loading), the response can be obtained based on stochastic dynamics and be calculated in frequency domain rather than in time domain. This will significantly reduce the computational efforts.

However, seismic loading is non-stationary in both amplitude and frequency content as discussed in Sect. 3.5. Therefore, it may be challenging to directly represent the entire process of seismic loading with power spectra. On the other hand, power spectra can be used to represent the strong/central motion part of the seismic loading, and by scaling the seismic loading with different factors at different time range, the non-stationary properties can also be approximated, as will be discussed in Sects. 5.3 and 8.3. As another example, the applied loading due to seismic and ocean wave loading can normally be defined at a single location/point or a few locations/points, while the load data for the dynamic gust wind loading has to be defined on many points/locations in a structure, and their correlations become stronger for closer locations [4]. Similar issues have to be addressed for extended structures subject to earthquake loading, in which the relative motion between structural supports or various locations cannot be ignored, which will be discussed in Chap. 8.

Table 5.1 Essential characteristics of various types of environmental loading

Item	Earthquake	Ocean wave	Wind	Ice
Loading period	Narrow or wide banded, 0.3–30 s	Approximately narrow banded, 3 (small wave)–26 s (storm wave)	Approximately narrow banded, 15 s—a few minutes	Wide-banded for vertical structures; narrow banded and above 0.2 s for conical structures, see Fig. 5.1
Durations (s)	A few second to 3 min	Hours	Hours	Varies significantly depending on the ice condition
Single point load data	Single point for shallow foundation; various points for pile foundations; multiple excitations for extended structures	Single point	Multiple points over the entire structure exposed to wind	Single point or a small area during ice–structure interaction
Linearity regarding loading	Yes	Theoretically non-linear mainly due to the fluid–structure interaction and wave nonlinearity; can be linearized for small amplitude of waves	Theoretically non-linear mainly due to the fluid–structure interaction; can normally be linearized	Yes

(continued)

Table 5.1 (continued)

Item	Earthquake	Ocean wave	Wind	Ice
Linearity regarding response	Linear for small amplitude of loading while non-linear for significantly high amplitude of loading or loading causing structural resonance	The same as to the left	The same as to the left	The same as to the left
Stationary or not	Non-stationary, but with a period of strong motion being stationary	Approximately stationary	Approximately stationary	Stationary for homogenous level ice sheet continuously crushing at a sufficiently high drift speed; non-stationary for non-homogeneous ice sheets, pressure ridges, open leads and low drift speeds



a. without cone (winter 2007/2008)

**Fig. 5.1** A monopod structure with vertical leg structure (*left*) during the first winter, later modified with an ice-breaking cone (*right*) installed during the second winter [5]

5.3 Power Spectrum of Seismic Ground Motions

The concept of spectrum can be attributed to Isaac Newton, who, with the aid of a prism, discovered that sunlight can be decomposed into a spectrum of colors from red to violet in about 1700. This indicates that any light comprises numerous components of light of various colors (wave lengths). The earliest function most closely resembling the spectral density function was developed by Arthur Schuster, who investigated the presence of periodicities in meteorological [6], magnetic [7], and optical [8] phenomena. The spectrum provides a measure of the light's intensity varied with respect to its wavelength. This concept has been generalized to represent many physical phenomena by decomposing them into their individual components.

5.3.1 Introduction to Fourier and Power Spectrum

5.3.1.1 Fourier Spectrum

Invented by Baron Jean Baptiste-Joseph Fourier in 1807, but the subject of great skepticism from his contemporaries at that time, the Fourier transform has now become a major analysis method in the frequency domain across a wide range of engineering applications. It states that any periodical function $\delta(t)$ in the time domain, not necessarily harmonic, has an equivalent counterpart in the frequency domain, which can be represented by a convergent series of independent harmonic functions as a Fourier series:

$$\delta(t) = c_0 + \sum_{i=1}^N c_i \sin(\omega_i t + \gamma_i) \quad (5.1)$$

where

c_0 is the average value of $\delta(t)$, $c_0 = \frac{1}{T_0} \int_0^{T_0} \delta(t) dt$

T_0 is the duration of the motions

c_i is the amplitude of the n th harmonic of Fourier series, $c_i = \sqrt{a_i^2 + b_i^2}$

$a_i = \frac{2}{T_0} \int_0^{T_0} \delta(t) \cos(\omega_i t) dt$ is the amplitude of cosinsoidal excitations

$b_i = \frac{2}{T_0} \int_0^{T_0} \delta(t) \sin(\omega_i t) dt$ is the amplitude of sinuasoidal excitations

ω_i is the n th frequency of component, with the lowest one being $\omega_0 = \frac{2\pi}{T_0}$

γ_i is the phase angle, $\gamma_i = \tan^{-1}\left(\frac{a_i}{b_i}\right)$, which defines the stagger related to time origin, and controls the times at which the peaks of harmonic motions/loading/responses occur, and influences the variation of $\delta(t)$ with time

Physically, the equation above is a representation of irregular records by the sum of an N sine waves of amplitudes c_i and frequency ω_i .

The Fourier series gives a complete description of motions since the motions can be recovered by the inverse Fourier transform.

For most motion records, such as sea wave elevations, by judicious choice of the datum level of the measurements, its average value (c_0) can be assumed to be zero. Equation (5.1) can then be reduced to:

$$\delta(t) = \sum_{i=1}^N c_i \sin(\omega_i t + \gamma_i) \quad (5.2)$$

Total energy is proportional to the average of the squares $\delta(t)$, which is the sum of the energy contents for each individual component at each frequency ω_i (Parseval theorem).

A plot of c_i versus ω_i from Eq. (5.2) is called a Fourier amplitude spectrum (normally referred to as a Fourier spectrum). To further explain the application of this concept, let's take the analysis of earthquake ground motions as an example. For a given earthquake and site, in order to obtain a complete picture of the strength of seismic ground motions (upper figure in Fig. 5.2) in each individual frequency or period, the Fourier spectrum is introduced as the Fourier amplitude (c_i) that varies with frequency or period, as shown in Fig. 5.2. From Fourier analysis of abundant strong ground motion time histories, it is found that the periods (inverse of frequency) of major motion contents range from 0.3 to 30 s.

Readers may bear in mind that narrow-banded time series have a dominant frequency, and it is typically the result of resonance or near-resonance responses, while a broad/wide-banded motions or excitations have a noticeable variety of frequencies. Since the mean values of the time series are constant and do not contribute to the Fourier amplitude in the frequency domain, the narrow- and broad-banded time series can be illustrated in the frequency domain using the Fourier amplitude spectrum as shown in Fig. 5.3.

Figure 5.4 shows the Fourier amplitude spectrum of the ground acceleration histories (Fig. 5.5) for four earthquake events of El Centro NS (Imperial Valley 1940), Kobe University NS (Hyogoken-Nanbu 1995), SCT1 EW (Mexico Michoacan 1985), JMA Kobe NS (Hyogoken-Nanbu 1995). It is clearly shown that, within the period range longer than 0.25 s, where the majority of seismic motion energy is concentrated, spectrum peaks appear at different frequencies. The Fourier amplitude spectrum for Mexico SCT1 EW record is comparatively narrow banded, with the majority of energy concentrated at a period of around 2.4 s. For the JMA Kobe NS record, the energy content is spread at a wide range of frequencies.

The ups and downs in a Fourier spectrum, for example for an earthquake ground motion record, can be smoothed and plotted in a logarithmic scale. The smoothed spectrum shown in Fig. 5.6 has a standard shape with the largest acceleration over an immediate range of frequency. This immediate range of frequency is defined by

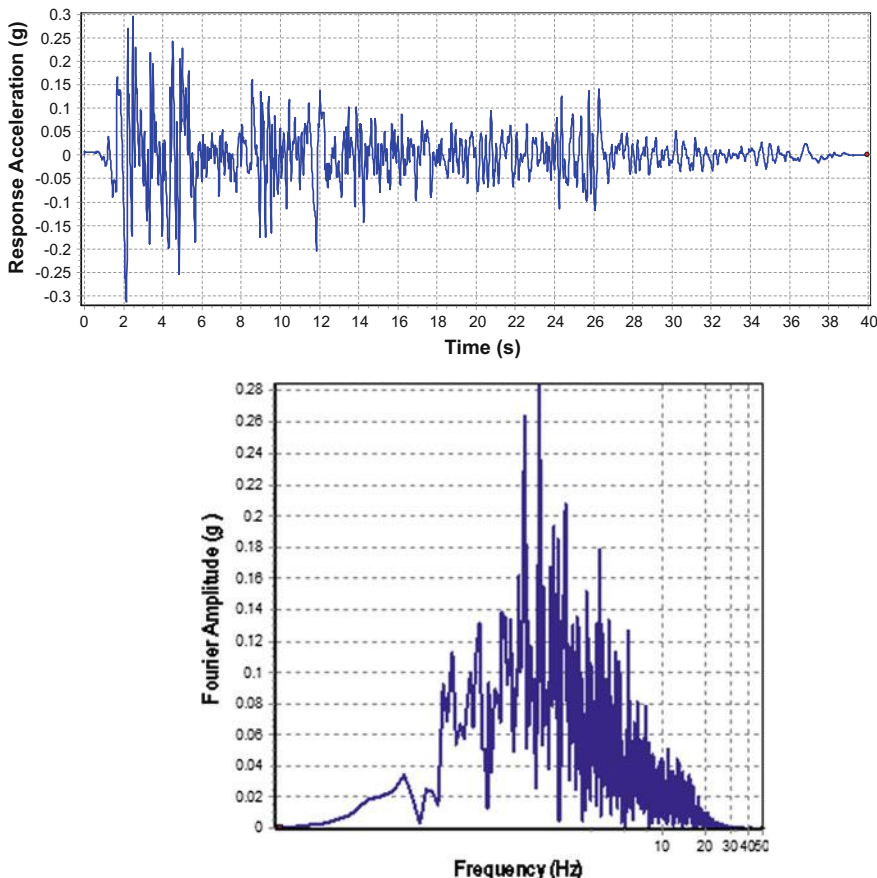
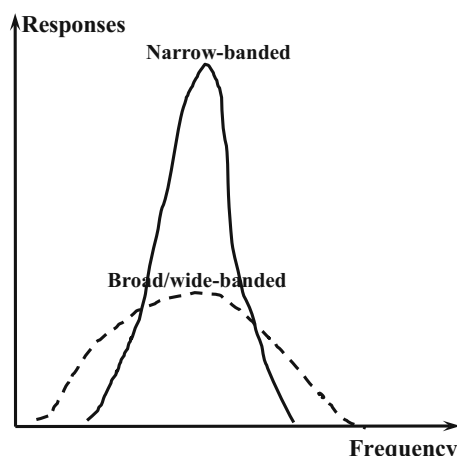


Fig. 5.2 Fourier amplitude spectrum (*lower*) of the strong ground motions (*upper*) recorded at Imperial Valley, California

Fig. 5.3 Fourier amplitude spectrum for a narrow-banded and a broad-banded random process with both of their origins of ordinate at the mean value of each time series



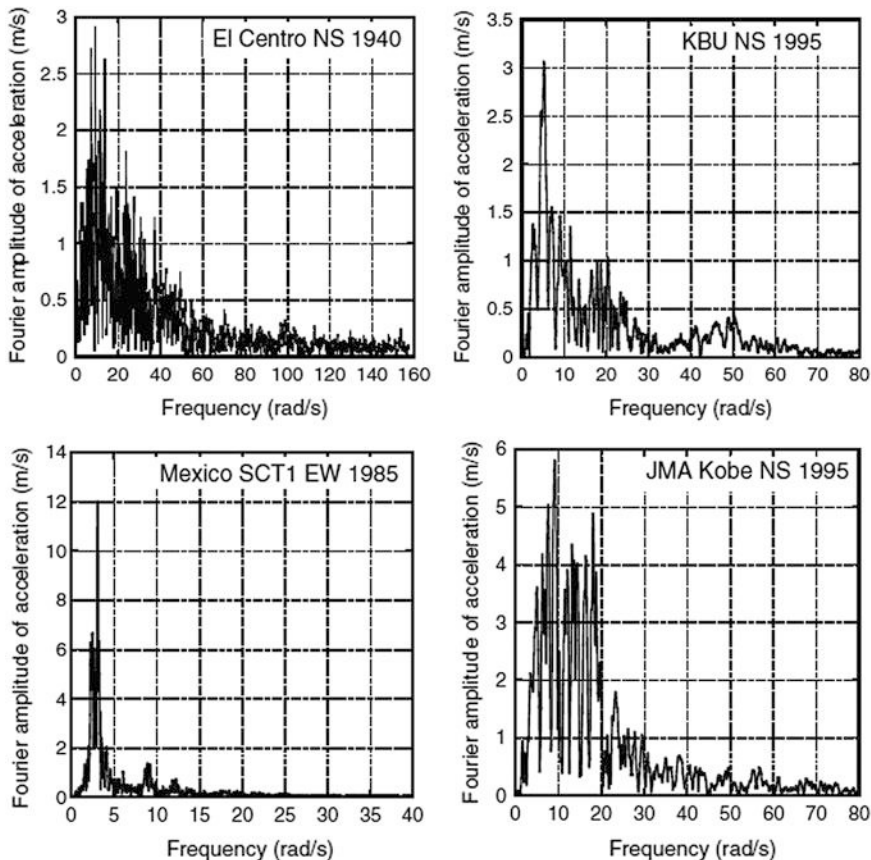


Fig. 5.4 Fourier amplitude spectrum of strong ground motions recorded at four different earthquake events [9]

its upper boundary frequency (cutoff frequency) f_{cutoff} , and the lower boundary frequency (corner frequency) f_{corner} as shown in Fig. 5.6.

In earthquake engineering, if a Fourier amplitude spectrum is used to represent ground motions, f_{corner} is the one above, in which earthquake radiation spectra are inversely proportional to the cube root of the seismic moment [10, 11]. The ground motions at corner frequency are higher for large earthquakes than that for small ones. Below f_{corner} , the spectra are proportional to the seismic moment. However, the characteristics of cutoff frequency are unfortunately much less clearly understood. Hanks [12] and Papageorgiou and Aki [13] indicated that the cutoff frequency relates to the near-site effects and source effects and can be regarded as constant for a given geographic region.

A plot of γ_i versus ω_i from Eq. (5.2) is called a Fourier phase spectrum. Different from the Fourier amplitude spectrum, the Fourier phase spectra from actual earthquake records do not have any standard shape [17].

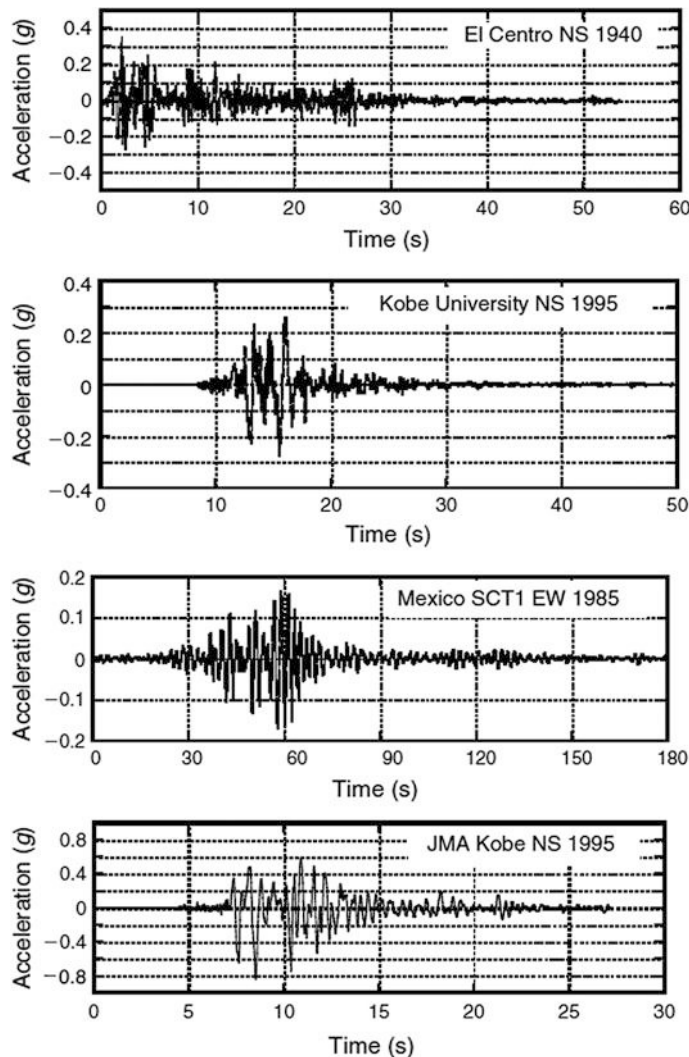
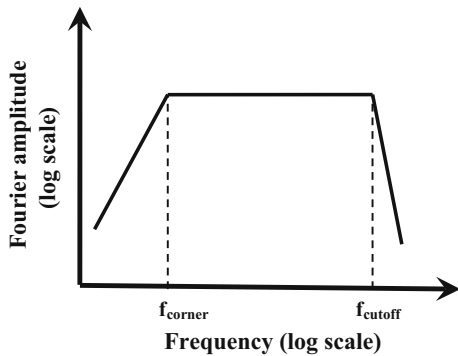


Fig. 5.5 Time history of strong ground accelerations recorded during the four different earthquake events [9]

5.3.1.2 Power Spectrum Density

In most cases, engineers are only interested in the absolute value of the Fourier amplitude instead of whether it is part of the sine or cosine series. This is because the absolute value provides the total amount of information contained at a given frequency. Since the square of the absolute value is considered to be the power of

Fig. 5.6 Smoothed Fourier amplitude spectrum with corner and cutoff frequency logarithmic space [17]



the signal, instead of the Fourier spectrum the motions can then be expressed in terms of power $P(\omega_i)$, defined as:

$$P(\omega_i) = \frac{1}{2} c_i^2 \quad (5.3)$$

where c_i is the amplitude of the i th harmonic of the Fourier series.

Imagining that $\zeta(t)$ is voltage, the power dissipated across a 1 Ω resistor is then $[\zeta(t)]^2$, and the total power dissipated across the resistor is $\int_0^{T_0} [\zeta(t)]^2 dt$. By assuming that the total power of motions calculated from the sum of each individual frequency component (Parseval's theorem) equals that of the time domain, one reaches:

$$\sum_{n=1}^{+\infty} P(\omega_i) = \int_0^{T_0} [\zeta(t)]^2 dt = \frac{1}{\pi} \int_0^{\omega_N} c_i^2 d\omega = \frac{1}{\pi} \sum_{i=1}^N c_i^2 \Delta\omega_i \quad (5.4)$$

where $\omega_N = \frac{\pi}{\text{sample time interval } \Delta t \text{ over the time history}}$ is the highest frequency in the Fourier series, or Nyquist frequency, i.e., the frequency range beyond which the motion content cannot be accurately represented. In such a condition, a distorted Fourier spectrum called aliasing will be introduced. $\Delta\omega_i$ is half of the spacing between two adjacent harmonics ω_{i+1} and ω_{i-1} .

For an efficient (optimal) signal sampling, in order to extract valid frequency information, one must bear in mind that the sampling of the motion/loading/response signals must occur at a certain rate: (1) for a time record with the duration of T seconds, the lowest frequency component measurable is $\Delta\omega_{\min} = \frac{2\pi}{T}$ or $\Delta f_{\min} = \frac{1}{T}$. (2) The maximum observable frequency is inversely proportional to the time step, i.e., $\omega_{obs} = \frac{2\pi}{\text{sample time interval } \Delta t \text{ over the time history}}$, and the sampling rate must be at least twice the desired frequency (ω_{\max} or f_{\max}) to be measured, i.e., $\omega_{obs} > 2\omega_{\max} = 2\omega_N$, where ω_N is the Nyquist frequency. With the two properties (1) and (2) above, the sampling parameters can be expressed as:

$$\omega_{\max} = \omega_N = \frac{\pi}{\Delta t} \quad \text{or} \quad f_{\max} = \frac{1}{2\Delta t} \quad (5.5)$$

$$\Delta t = \frac{\pi}{\omega_{\max}} = \frac{\pi}{\omega_N} \quad \text{or} \quad \Delta t = \frac{1}{2f_{\max}} \quad (5.6)$$

The description above is often referred to as the Shannon or Nyquist sampling theorem.

By dividing the total power in the equation above with the duration T_0 , one gets the average power intensity λ_0 :

$$\lambda_0 = \frac{1}{T_0} \int_0^{T_0} [\zeta(t)]^2 dt = \frac{1}{\pi T_0} \int_0^{\omega_N} c_i^2 d\omega = \frac{1}{\pi T_0} \sum_{i=1}^N c_i^2 \Delta\omega_i \quad (5.7)$$

By observing this equation, it is also noticed that the average power intensity λ_0 is equal to the mean squared motion record (σ_{ζ}^2).

The power spectral density $S(\omega)$ is therefore defined such that the following equation can be fulfilled:

$$\lambda_0 = \int_0^{\omega_N} S(\omega) d\omega \quad (5.8)$$

It is obvious that:

$$S(\omega_i) = \frac{1}{\pi T_0} c_i^2 \quad (5.9)$$

The expression above also shows the relationship between the power spectral density $S(\omega)$ and the Fourier amplitude c_i .

The benefits of using power spectral density lie in the fact that it can characterize many different motion records and identify their similarities, and can be used for further computation to obtain the responses. This is especially the case for characterizing stationary Gaussian type motions. For example, for sea wave elevation or wind velocity, even though a one-to-one wave elevation or wind velocity does not generally exist, all records that result in identical spectral density do have the same statistical properties, i.e., the details of records that vary greatly may have identical spectral density.

The calculation of power spectrum can be used to estimate the statistical properties of many records, such as wave elevations, wind velocities, ground surface roughness, seismic ground motions, etc., and these can then be further used to compute stochastic responses using random vibration techniques. It also has the

merit of executing the computation much faster than the Fast Fourier Transformation (FFT), because the computation is performed in place without allocating memory to accommodate complex results. However, since phase information is lost and cannot be reconstructed from the power spectrum's output sequence, power spectrum cannot be utilized if phase information is desired.

When using the power spectrum, various terminologies that are slightly different from each other exist in different fields or different purposes of applications. For example, the ordinate of the wave spectral density can be based on an amplitude spectrum $\left(\frac{S}{2}\right)^2$, an amplitude half-spectrum $\left(\frac{S}{2}\right)^2/2$, a height spectrum (ζ^2) , or a height double spectrum $2\zeta^2$ etc. [15]. The abscissa can be chosen as angular frequency, cyclic frequency or period.

Figure 5.7 shows an example of the power spectrum density of strong ground motions (Fig. 5.2) recorded at Imperial Valley.

In some applications, the power spectral density $S(\omega)$ is normalized by its area (λ_0), which gives:

$$S_\zeta(\omega) = \frac{1}{\lambda_0} S(\omega) \quad (5.10)$$

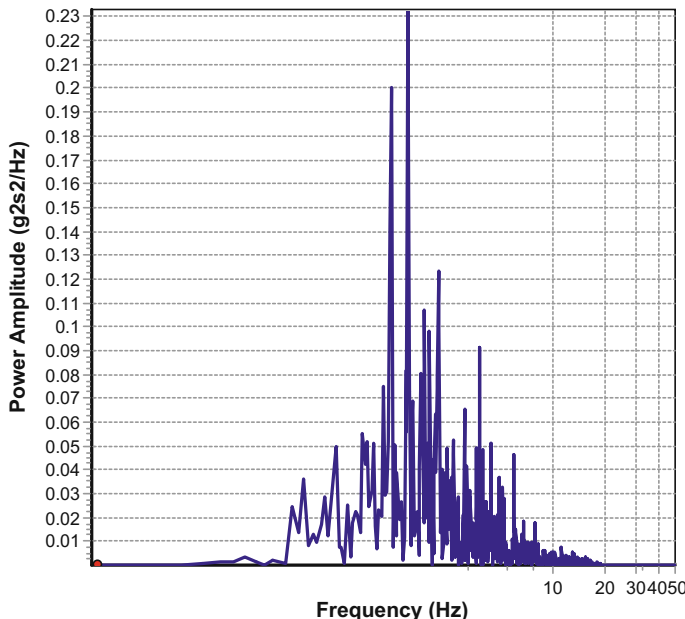


Fig. 5.7 Power of the strong ground motion (Fig. 5.2) recorded at Imperial Valley; g represents the acceleration of Earth's gravity

Example To characterize the global vibrations of a high-rise building and identify the local vibrations and acoustic performance on certain floors in this building, measurements of acceleration are planned. The lowest frequency Δf_{\min} component measurable and the maximum desired frequency (f_{\max}) are designed as 0.2 and 100 Hz, respectively. Determine a suitable time duration, the number of sampling points and the sample time interval for the measurement.

Solution One can determine the time duration for measurement using the lowest frequency or the highest period measurable as: $T = \frac{1}{\Delta f_{\min}} = 5$ s.

$$\text{The number of sampling points is: } N = \frac{f_{\text{obs}}}{\Delta f_{\min}} = \frac{2f_{\max}}{\Delta f_{\min}} = \frac{2 \times 100 \text{ Hz}}{0.2 \text{ Hz}} = 1000,$$

$$\text{and the sample time interval over the time history is: } \Delta t = \frac{T}{N} = \frac{5 \text{ s}}{1000} = 0.005 \text{ s} \quad (\text{or } \Delta t = \frac{1}{2f_{\max}} = \frac{1}{2 \times 100} = 0.005 \text{ s}).$$

Readers may bear in mind that only processes with finite variance can be represented by spectra. Fortunately, even if theoretically the variance of a process can be infinite, almost every process in the engineering world has a finite variance.

Although using the Fourier transformation is the most common way of generating a power spectrum, other techniques such as the maximum entropy method can also be used [14].

5.3.2 Power Spectrum of Seismic Ground Motions

Even though many excitations are nearly periodical and stationary, such as wave and wind loadings on structures, ships' propeller excitation forces, etc. [16], earthquakes' ground motions are neither periodical (e.g., strong ground motions have not repeated themselves during any earthquake event), nor stationary, i.e., the intensity builds up to a maximum value in the early part of the motions, then remains constant for a period of time, and finally decreases near the end of the motions [17].

However, as a modification of the traditional power spectrum density function, Kanai [18] and Tajimi [19] presented that, for both engineering and research purposes, one may still assume that strong ground accelerations are a stationary stochastic process by passing a white noise process through a filter, i.e., the actual excitations are regarded as a function of output from a series of filters (usually a linear second-order system) subjected to white noise input S_0 . In terms of acceleration amplitude, the Kanai-Tajimi model can be expressed as:

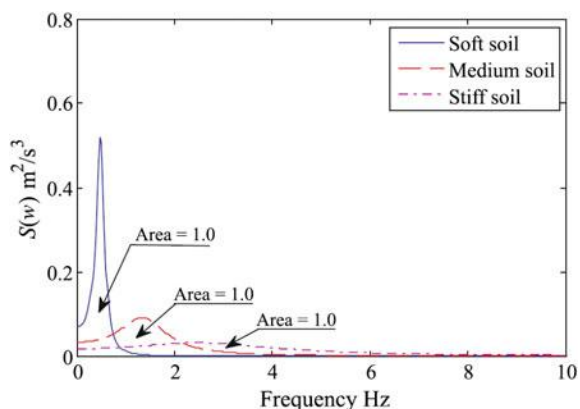
$$S_g(\omega) = \frac{\omega_g^4 + 4\xi_g^2\omega_g^2\omega^2}{\left(\omega_g^2 - \omega^2\right)^2 + 4\xi_g^2\omega_g^2\omega^2} S_0 \quad (5.11)$$

where ω_g and ξ_g are characteristic ground frequency and damping ratio, respectively, they are filter parameters representing the natural frequency and damping of the soil layer, respectively; S_0 is a scaling factor to define the white noise intensity level depicting earthquake amplitude; The power spectral density is often filtered twice in order to remove the singularities at $\omega = 0$, i.e., the non-zero power spectrum density occurs for zero frequency.

The spectral density has its maximum value when $\omega = \omega_g$. By a proper selection of ω_g and ξ_g , the equation above can be used to represent different spectral density shapes. Kanai [18] and Tajimi [19] reported that ξ_g varies from 0.2 (relatively narrow banded) for soft soil to 0.6 (relatively wide banded) for hard rock sites. While many researchers and engineers tend to use $\xi_g = 0.6$, from a geotechnical engineering point of view, it is reasonable to assume that the power spectra of the horizontal ground motions have a similar shape, while the vertical motion component is more wide banded. Based on this assumption, Kubo and Penzien [20] simulated the 1971 San Fernando earthquake ($M_w = 6.5$) with $\xi_g = 0.2$ and $\xi_g = 0.3$ for two horizontal ground motion components and $\xi_g = 0.6$ for the vertical component. Figure 5.8 illustrates the Kanai-Tajimi power spectral density functions for soft, medium and stiff soil conditions. It is obvious that the spectrum under soft soil conditions is more narrow banded than that of the stiff soil conditions. Therefore, resonance of structures is more likely to occur under soft soil conditions than under stiff soil conditions.

Compared to the selection of ξ_g , the determination of ω_g is more important. This is because even if the wide-band power spectral density tends to overestimate the

Fig. 5.8 The Kanai-Tajimi power spectral density functions for different types of soil (ξ_g is assumed to be 0.2 for soft soil, 0.4 for medium soil and 0.6 for stiff soil) [21]



contribution from high frequencies, this normally does not result in a significant change of ground motions. However, the ω_g determines the dominant frequency of ground motion input. When the dominant frequency is close to the natural frequency of a structure subjected to ground motions, resonance of structural responses would occur. A typical value of $\omega_g = 5\pi$ can be assigned for rock sites.

A few previously adopted values of ξ_g and ω_g are listed as follows [22]: for EI Centro 1940 N-S component, $\omega_g = 12$ and $\xi_g = 0.6$; for Kobe 1995 N-S component, $\omega_g = 12$ and $\xi_g = 0.3$; for Uemachi, the simulated ground motion using the fault rupture model gives $\omega_g = 3$ and $\xi_g = 0.3$. Those selections of values are widely used in the research of tuned mass dampers [23, 24].

Clough and Penzien [25] modified the Kanai-Tajimi model by introducing a second filter to assure a finite power for the ground displacement:

$$S_g(\omega) = \left[\frac{\omega_g^4 + 4\xi_g^2\omega_g^2\omega^2}{(\omega_g^2 - \omega^2)^2 + 4\xi_g^2\omega_g^2\omega^2} \right] \left[\frac{\omega^2}{(\omega_f^2 - \omega^2)^2 + 4\xi_f^2\omega_f^2\omega^2} \right] S_0 \quad (5.12)$$

where ω_f and ξ_f are the parameters of a second filter, for medium stiffness soil, $\omega_g = 10.0$ rad/s, $\xi_g = 0.4$, $\omega_f = 1.0$ rad/s, and $\xi_f = 0.6$ [26].

In order to represent the non-stationary characteristics of ground motions, based on the power spectra, the time series of ground motion can be generated first, and then further modified by a shape function $\delta(t)$ varying with time to reflect the non-stationary characteristics of ground motions (Sect. 3.5.2). This procedure will be presented in Sect. 8.3.

It should be noted that models expressed with the power spectral density presented above can only provide the excitation information phenomenally. They give no information on how spectra amplitudes are scaled with earthquake source and distance (the attenuation effects). This drawback may be eliminated by calibrating the model to the measured ground motions or target response spectra. In cases when no such data is available, an alternative is to fit them into physical power spectra density models based on seismological description of source and wave propagation [27]. Interested readers may read Hanks and McGuire [28], Boore [29] and Herman [30].

Before leaving this section, readers need to make a clear distinction between the power spectrum and response spectrum (Sect. 5.4) in earthquake engineering applications. Even if both of them are expressed in terms of frequency and indicate the amplification of seismic response varying with frequency: the former is of a stochastic nature while the latter is based on a calculation of maximum responses under ground motion history, i.e., the response spectrum is essentially a deterministic type.

5.4 Response Spectrum

5.4.1 Background

Since earthquake ground motion is by nature of short duration, non-stationary, transient and non-periodic, and is also broad-banded in frequency content, it can never reach steady-state vibrations. This means that even if the structure has a zero damping, the motion amplitude is limited to a finite value. Therefore, the stochastic based root of mean square response utilized by the power spectrum method is in many cases not appropriate to represent the earthquake ground motions, and a deterministic time history analysis is therefore desired to estimate the response. However, a dynamic time history analysis is computationally demanding. Moreover, to reach a design in a conservative manner, often only the maximum amplitude of the response time history is needed for carrying out the seismic analysis, which needs a special consideration when combining each individual component of the response.

To solve the dilemma above, a response spectrum [31, 32], originally calculated from the accelerograms [33, 34], is now widely used to represent the earthquake loading for seismic analysis. A typical response spectrum is defined as a plot of maximum responses in terms of displacement, velocity or acceleration of an ensemble of linear, single degree-of-freedom oscillators having various natural periods, but the same value of internal damping ratio (typically 5 %) to a specified input time history of seismic motions, which is illustrated in Fig. 5.9.

The elastic response spectrum method for calculating seismic response was first proposed in the 1940s [32], which provides a convenient means for representing the elastic behavior of simple structures, as will be discussed in Sect. 5.4.2.

However, it was followed by a recognition of the fact that the forces predicted by such spectra far exceed normal design requirements [35] in case rare and significant seismic loading associated with a high return period (Sect. 9.1.3) is applied. Because structures having much less strength than prescribed by the elastic spectral values were observed to have performed well in rather severe earthquakes, it became apparent that the elastic response spectrum is not a direct and realistic measure of behaviors of many structures during significant earthquake events, and even moderate earthquakes may be expected to produce inelastic deformations in typical building structures. Therefore, response spectrum was later extended to evaluate the inelastic forces and deformation [41], leading to a ductility-modified spectrum, as will be discussed in Sect. 5.4.3.

Before going into technical details of response spectrum, it should be emphasized that the response analysis using seismic response spectrum only calculates the maximum responses (typically measured by displacement) and member forces in

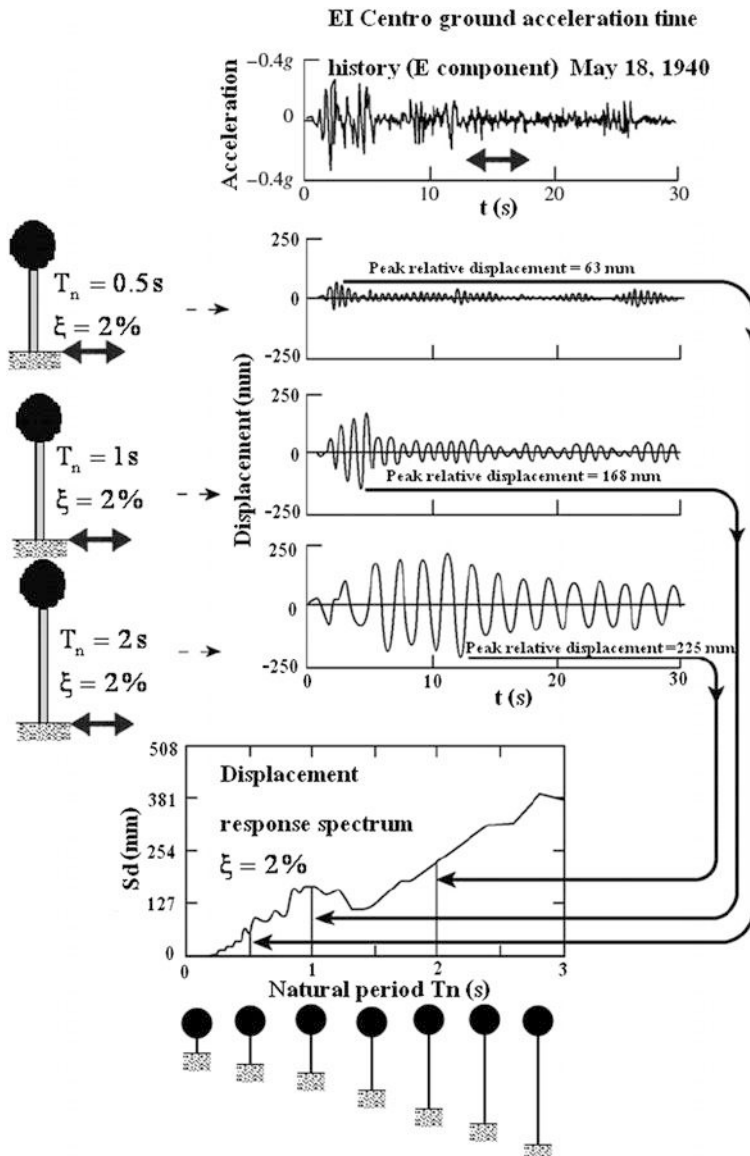


Fig. 5.9 Schematic illustration of constructing ground motion response spectrum ($S_d - T_n$) for EI Centro earthquake ($M_w = 6.9$) [42]

each vibration mode of structures without sign information. However, in reality, the members will not necessarily be designed for this maximum peak value. Therefore, the response spectrum analysis may lead to an over-conservative design.

5.4.2 Elastic Response and Design Spectrum

5.4.2.1 Elastic Response Spectrum

In practice, a single degree-of-freedom (SDOF) system with a constant damping ratio of a few percent, representing target structures, is subjected to a prescribed ground excitation time history as shown in Fig. 5.9. As the ground motion typically excites a large number of vibration modes of the structures, by varying the natural period of the SDOF in a range of engineering interest for the structure's eigenperiod (e.g. 0.02–10 s), and using numerical time integration methods such as Newmark's method etc., the maximum calculated relative displacement magnitude of the SDOF at each natural period is then plotted on a response spectrum graph. This spectrum is often referred to as the deformation/displacement response spectrum. Figure 5.9 illustrates a schematic flow chart for constructing a ground motion displacement response spectrum S_d varied with natural period T_n , that can be expressed as:

$$S_d = \max(u(t|T_n)) \quad (5.13)$$

From the equation above, it is obvious that the most important task to establish the displacement response spectrum is to calculate the responses of the SDOFs with varied natural periods. To perform this task, let us consider an SDOF system excited by suddenly applied excitations $F(t)$ (shown in Fig. 5.10) that are neither harmonic nor periodical. The general form of the governing equation of motions is:

$$m\ddot{x}(t) + c\dot{x}(t) + kx(t) = F(t) \quad (5.14)$$

By dividing the equation above with m and rearranging it, one obtains:

$$\ddot{x}(t) + 2\zeta\omega_n\dot{x}(t) + \omega_n^2x(t) = \frac{1}{m}F(t) \quad (5.15)$$

where ω_n and ζ are the natural angular frequency and ratio of critical damping for the system, respectively.

For developing a formula for evaluating response to a general dynamic loading, the unit impulse response procedure [4] for approximating the response of a structure to arbitrary excitations may be used as the basis. We then consider a system subjected to a force with a short duration as shown in Fig. 5.11. For a

Fig. 5.10 An SDOF spring-mass-damper system under an external force $F(t)$

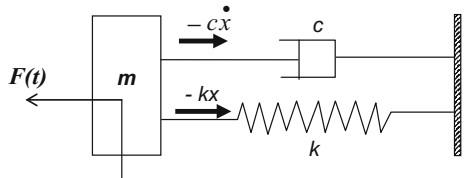
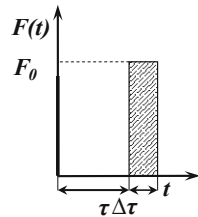


Fig. 5.11 Impulsive force excitations



general close-form solution of the equation above, the convolution integral method can be used to obtain the responses. This method is derived using the equilibrium of momentum:

$$\int_{t_1}^{t_2} F(t) dt = m[x(t_2) - x(t_1)] \quad (5.16)$$

The time integral of force is designated by the symbol $\hat{\hat{F}}$:

$$\hat{\hat{F}} = \int_{\tau}^{\tau + \Delta\tau} F_0 dt \quad (5.17)$$

We hereby define an impulsive force with the amplitude of $\hat{\hat{F}}/\Delta\tau$ and the time duration of $\Delta\tau$. When $\hat{\hat{F}}$ is equal to unity, the force in the limiting case $\Delta\tau \rightarrow 0$ is called the unit impulse or Dirac delta function ($\delta(t - \tau)$), which has the following properties:

$$\int_0^{+\infty} \delta(t - \tau) d\tau = 1 \quad (5.18)$$

$$\delta(t - \tau) = 0 \quad \text{for } t \neq \tau \quad (5.19)$$

Therefore, the impulsive force applied at time τ is:

$$F(t) = F_0 \delta(t - \tau) \quad (5.20)$$

The responses to a unit impulse applied at $t = 0$ with initial conditions equal to zero are called impulsive responses and are denoted by $h(t)$. For any time later than τ , the impulsive responses $h(t - \tau)$ can be obtained by shifting $h(t)$ to the right along the scale by $t = \tau$.

Thereafter, at $t = 0$, a radical change in the system motions takes place when the short duration and high amplitude forces excite an initial motion of the system, followed by free vibrations. For a unit impulse at $t = 0$, i.e., $F_0 = 1$, the velocity

and displacement of the mass immediately after the initial impulse at $t = 0^+$ are therefore:

$$h(0^+) = \frac{1}{m} \quad (5.21)$$

$$h(0^+) = 0 \quad (5.22)$$

The velocity and displacement due to an applied step force $F(0)$ are:

$$x(0^+) = \frac{1}{m} \quad (5.23)$$

$$x(0^+) = 0 \quad (5.24)$$

By realizing the initial condition $h(0) = 0$, one can derive the impulsive of the undamped system:

$$h(t) = \begin{cases} \frac{1}{m\omega_n} \sin(\omega_n t) & \text{for } t > 0 \\ 0 & \text{for } t < 0 \end{cases} \quad (5.25)$$

Or:

$$x(t) = \begin{cases} \frac{F_0}{m\omega_n} \sin(\omega_n t) = \frac{F_0}{k} [1 - \cos(\omega_n t)] & \text{for } t > 0 \\ 0 & \text{for } t < 0 \end{cases} \quad (5.26)$$

From the equation above it is noticed that the maximum displacement of the system due to the step excitations is twice the quasi-static displacement ($\frac{F_0}{k}$).

The responses of the damped system are:

$$h(t) = \begin{cases} \frac{1}{m\omega_d} e^{-\zeta\omega_n t} \sin(\omega_d t) & \text{for } t > 0 \\ 0 & \text{for } t < 0 \end{cases} \quad (5.27)$$

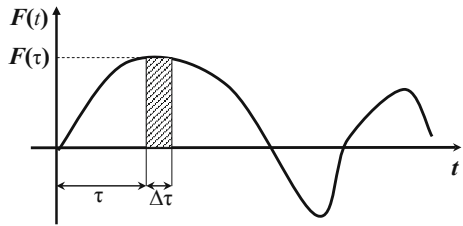
Or

$$x(t) = \begin{cases} \frac{F_0}{m\omega_d} e^{-\zeta\omega_n t} \sin(\omega_d t) & \text{for } t > 0 \\ 0 & \text{for } t < 0 \end{cases} \quad (5.28)$$

Note that the entire excitation history may be considered to consist of a succession of short impulses. The derivation above can then be extended to calculate the responses under arbitrary excitation histories as shown in Fig. 5.12. The excitations $F(t)$ can be regarded as a series of impulses with different amplitudes. We here examine one impulse starting at time τ . Again, in the limiting case $\Delta\tau \rightarrow 0$, its contribution to the total responses at time t is:

$$\Delta x(t, \tau) = F(\tau) \Delta\tau h(t - \tau) \quad (5.29)$$

Fig. 5.12 Arbitrary force histories applied on a system



For a linear system, the principle of superposition is applicable. Therefore, the response at time t is the sum of responses due to a sequence of individual impulses, this is known as convolution integral:

$$x(t) = \int_0^t F(\tau)h(t - \tau)d\tau \quad (5.30)$$

Or

$$x(t) = \sum F(\tau)h(t - \tau)\Delta\tau \quad (5.31)$$

$h(t - \tau)$ is obtained from Eq. (5.27) by replacing t by $t - \tau$. Therefore, the damped responses in Eq. (5.28) can be rewritten as:

$$\begin{aligned} x(t) &= \frac{1}{m\omega_d} \int_0^t F(\tau)e^{-\zeta\omega_n(t-\tau)} \sin[\omega_d(t-\tau)]d\tau \\ &= \frac{1}{\omega_n\sqrt{1-\zeta^2}} \int_0^t a(\tau)e^{-\zeta\omega_n(t-\tau)} \sin\left[\omega_n\sqrt{1-\zeta^2}(t-\tau)\right]d\tau \end{aligned} \quad (5.32)$$

The equation above is referred to as Duhamel's integral, which is often adopted to calculate the responses of SDOFs with varied natural periods in order to calculate the spectral displacement responses.

The integral of the equation above is the velocity response function $V(t)$, so that the earthquake displacement response becomes:

$$x(t) = \frac{V(t)}{\omega} \quad (5.33)$$

And the effective earthquake force, or base shear, applied on a target structure can then be approximated as:

$$Q(t) = m\omega V(t) \quad (5.34)$$

The two equations above actually describe the earthquake response at any time t for an SDOF structure, with solutions depending upon how Eq. (5.27) is evaluated.

As mentioned before, for design purpose, it is usually sufficient to evaluate only the maximum responses, instead of the entire history of forces and displacements. For each SDOF system with a designated natural period T_n ($= 2\pi/\omega_n$), the maximum value of response velocity function $V(t)$ is called the spectral velocity:

$$S_V = \{V(t)\}_{\max} \quad (5.35)$$

It is noted that the three equations above are based on the assumption that the displacement vibrations are harmonic (in reality the seismic ground motion displacement cannot be harmonic) at each undamped natural period T_n , the corresponding maximum velocity response is also called pseudo-velocity values since it is not exactly the maximum velocity of a damped system. By following this assumption, the pseudo-relative-velocity spectrum (or pseudo-velocity spectrum), denoted as PSV, and the pseudo-acceleration spectrum, denoted as PSA, can be defined by two equations below:

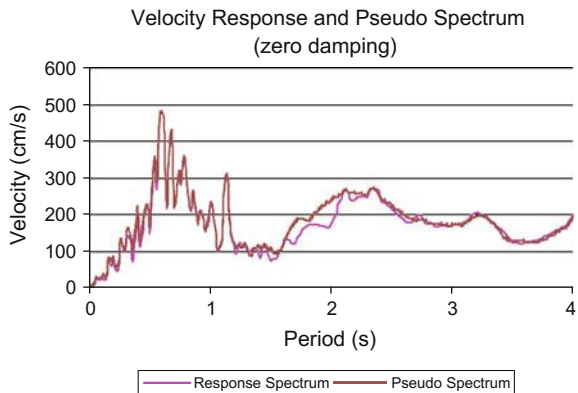
$$\text{PSV} = \omega S_d = \left(\frac{2\pi}{T_n}\right) S_d \quad (5.36)$$

$$\text{PSA} = \omega^2 S_d = \left(\frac{2\pi}{T_n}\right)^2 S_d = \omega \cdot \text{PSV} \quad (5.37)$$

From the three equations above, it is obvious that, if the relative spectral displacement is known, the pseudo-velocity and the pseudo-acceleration can be calculated. In addition, readers may bear in mind that spectrum measured by acceleration intensifies high frequency (higher than the natural frequency of the SDOF system) components, and the spectrum measured by velocity intensifies vibration components around the natural frequency of the SDOF system, while low frequency components are more clearly identified by a response spectrum measured with displacement.

Special attention should be paid to the construction of the velocity and acceleration spectrum: as discussed above, they are derived from the “true” displacement response spectrum instead of the maximum value of velocity and acceleration time history directly calculated from a dynamic analysis of an SDOF system. In general, the maximum value of velocity and acceleration time history at each natural period T_n are not equal to the value of velocity and acceleration spectrum derived from the displacement response spectrum. This is illustrated in Fig. 5.13 with a comparison between the “true” response spectrum and pseudo-spectrum under the same ground motions. Generally, for short period system, the pseudo-velocity is higher than the “true” velocity response. This trend is more significant when the natural period of the system becomes shorter. On the other hand, for long period system, the pseudo-velocity is less than the “true” velocity response. The differences between

Fig. 5.13 Velocity response and pseudo-velocity spectrum subject to the ground motion documented from Chi-chi earthquake, 21 September, 1999



the two types of velocity spectra is smallest for undamped systems and increases with an increase in damping. Similarly, the pseudo-acceleration spectra and “true” response spectra are identical when the damping of the system is zero. Even with damping, the difference between the two acceleration spectra is rather small for short period systems and is of some significance only for long period systems with large values of damping [16]. Therefore, under earthquake excitations, within the frequency and damping ranges that are of engineering interest, the maximum value of velocity and accelerations can be assumed to be equal to their pseudo-counterparts, with the acceleration equivalence being closer to the “true” one than the velocity equivalence. Moreover, since only the displacement response is needed to calculate exact values of seismic forces applied on a structure, displacement spectra (the basis to derive the pseudo-velocity and pseudo-acceleration spectra) provide sufficient information, there is little motivation to study the “true” response spectra because they are not required to determine the peak deformations and forces in a system. For a clear mathematical explanation of this difference, reference [16] is recommended.

It should also be noted that the acceleration spectrum indicates accelerations due to ground motions, without accounting for a constant acceleration of gravity g . Moreover, by reviewing the concept of acceleration, velocity and displacement, it should be further emphasized that the spectral acceleration is an absolute acceleration of a structure in space, since the force causing the acceleration itself is determined by the relative compression/extension of the spring with respect to the ground motion, while the spectral velocity and spectral displacement are relative values with respect to the moving ground.

As mentioned above, different from the power spectrum or Fourier spectrum (Sect. 5.3), which are stochastic representations of motions in frequency domain, the response spectrum is a deterministic method in frequency domain, i.e. a time domain quantity. This is because, for each frequency, it represents the response of a structure from the passing of an entire seismic excitation time history, the unit of the ordinate for response spectrum should therefore cherish the same unit as the name of the spectrum stands for, i.e. the same unit as acceleration, velocity, and

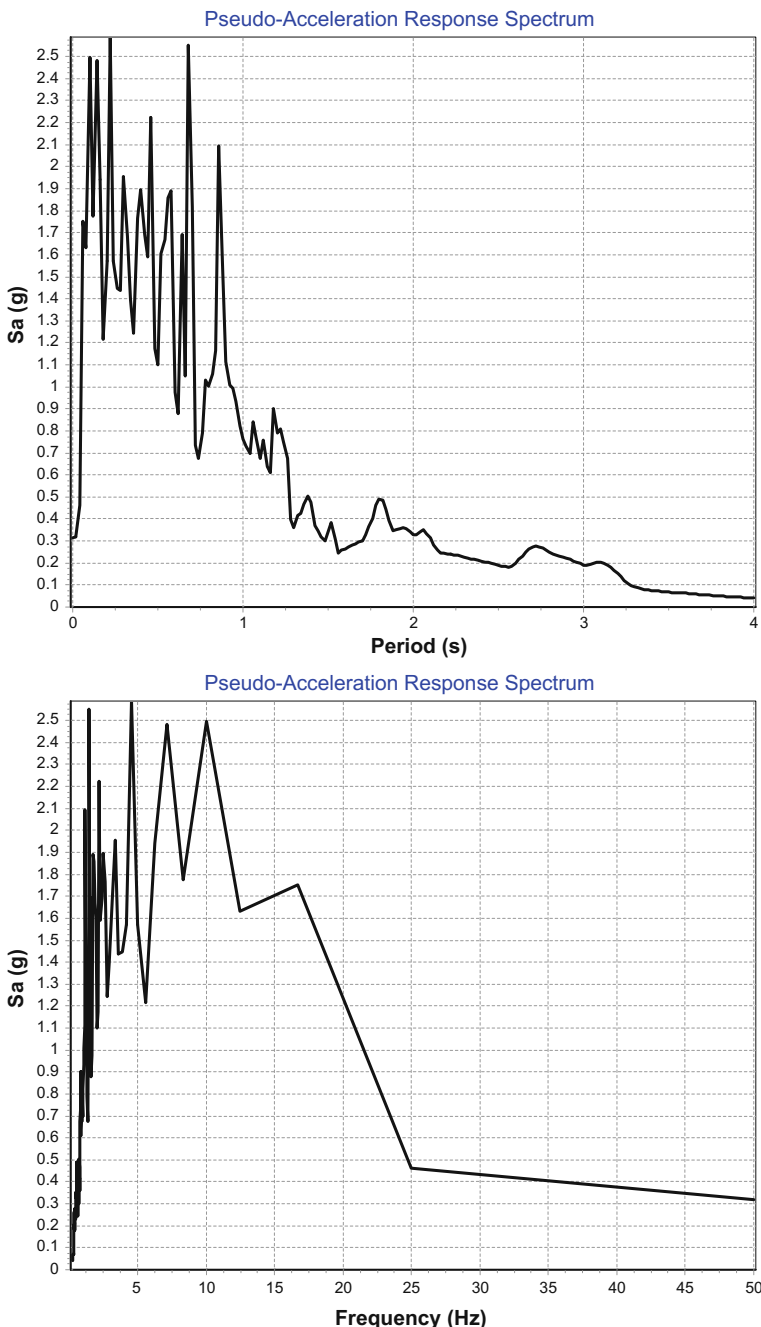


Fig. 5.14 Pseudo-acceleration response spectrum (zero damping) with either a period or frequency horizontal axis. The ground motion was documented from Imperial Valley earthquake

displacement for acceleration, velocity and displacement response spectrum, respectively. The horizontal axis may be expressed either in period or frequency (Fig. 5.14). In the pseudo-acceleration response spectrum measured with frequency shown in Fig. 5.14, it is noticed that the curve covers a large range of frequency, but the frequency content below 5 Hz has many ups and down. In order to reduce a wide range to a more manageable size, one can use a logarithmic scale plot as shown in Fig. 5.15.

Not only the value of the spectrum and but also the spectral shape strongly influences the structural responses. If scaled ground motions have the same or very similar spectral shapes as the target ground motions, the resulting structural responses from scaled ground motions are statistically similar to responses from unscaled ground motions. Earthquake magnitude, source-to-site distance, and local site condition can affect the spectral shape of records. The ground motion parameter ε presented in Sect. 3.6 is also an important parameter to influence the spectral shape [43, 44]. Large positive ε values at a given period are typically associated with a peak in the response spectrum at that period, because the ε value indicates an extreme/rare spectral value at that period while other spectral values at other periods are not necessarily so extreme.

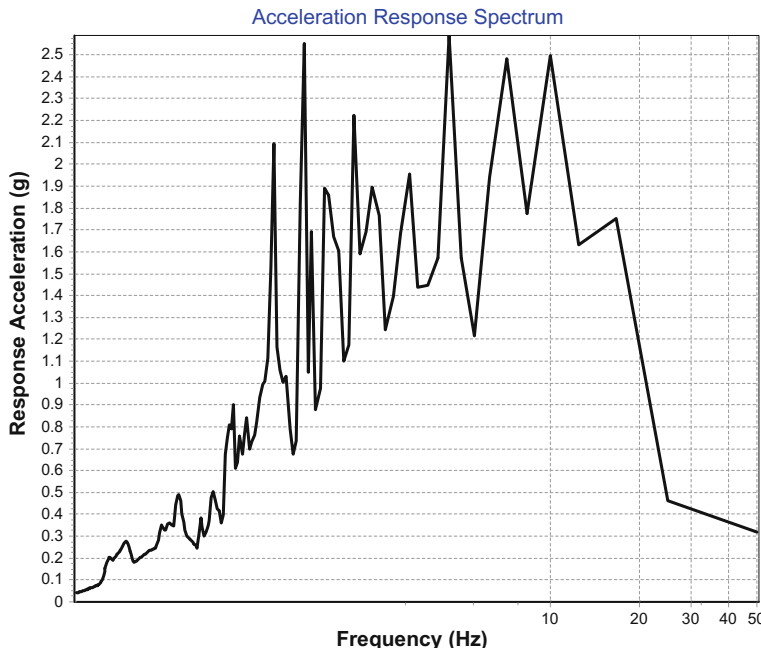


Fig. 5.15 Response spectrum (zero damping) of ground motion at Imperial Valley measured with logarithmic scale

Because all structures have some degrees of damping, the peaks in the response spectra are of limited significance and are therefore smoothed out by introducing damping for structures (in the current example shown in Fig. 5.9 the damping ratio is 2 %). This also indicates that the damping is already included and is assumed in a design response spectrum. It is therefore important not to remodel this damping in an structural modeling when performing the seismic response spectrum analysis. Moreover, since the design response spectrum is usually generated based on a constant damping ratio of 5 %, for many structures, a transformation between a spectrum with the target damping level and the one with that of the 5 % damping is needed. This is usually performed by applying a damping correction factor relative to a reference value of 1.0 (for 5 % damping ratio), such as the one presented in ISO 19901-2 [45] and Eurocode 8 [46], as will be presented in Sect. 5.4.2.3. Moreover, the generation of response spectrum with zero damping is not only physically unrealistic, but also numerically problematic because a significant amplification of response will appear when no damping is presented.

For stiff structures, PGA is preferably used since the acceleration has a large portion of frequency content in high frequency range. For less stiff structures, PGV, which cherishes a significant portion of frequency content in the intermediate frequency range, is more in favor for calculating structural response. It is not usual to use PGD for seismic design.

Readers also need to bear in mind that, in a probabilistic seismic hazard analysis as will be presented in Sect. 9.1, the spectra acceleration at different periods are associated with different earthquake events. At the longer period, it normally represents the peak response accelerations of high magnitude of earthquake(s), whereas the spectral accelerations at lower period range typically correspond to peak response accelerations of relatively small magnitude earthquakes.

Figure 5.16 shows the ground acceleration time history for both rigid and flexible structures with 0 and 20 % of critical damping values. It shows that flexible structures can work as a filter to dramatically reduce the acceleration and therefore forces. With zero damping, the rigid structure follows the acceleration of the ground motion. However, the flexible structure shows a sort of harmonic vibration without significant influences from the ground motions. The more flexible a structure is, the closer the structure's response is to the harmonic vibrations.

The unique relationships among the spectral displacement, pseudo-velocity and pseudo-acceleration make it possible to present response spectral values in a tripartite plot as shown in Fig. 5.17, where displacement, velocity and acceleration can be read on separate axes from the same curve.

Attention should also be paid to the response spectrum recorded on soft soil. As response spectra of motions recorded on soft soil attain their maxima at different, well-separated periods, averaging them can eliminate their peaks causing this effect, resulting in a flat shape of spectrum (analogous to that used in current seismic design codes) as shown in Fig. 5.18. It is therefore more rational to use response spectra plotted against the normalized periods, T/T_g (T_g is the period of spectral velocity) [48]:

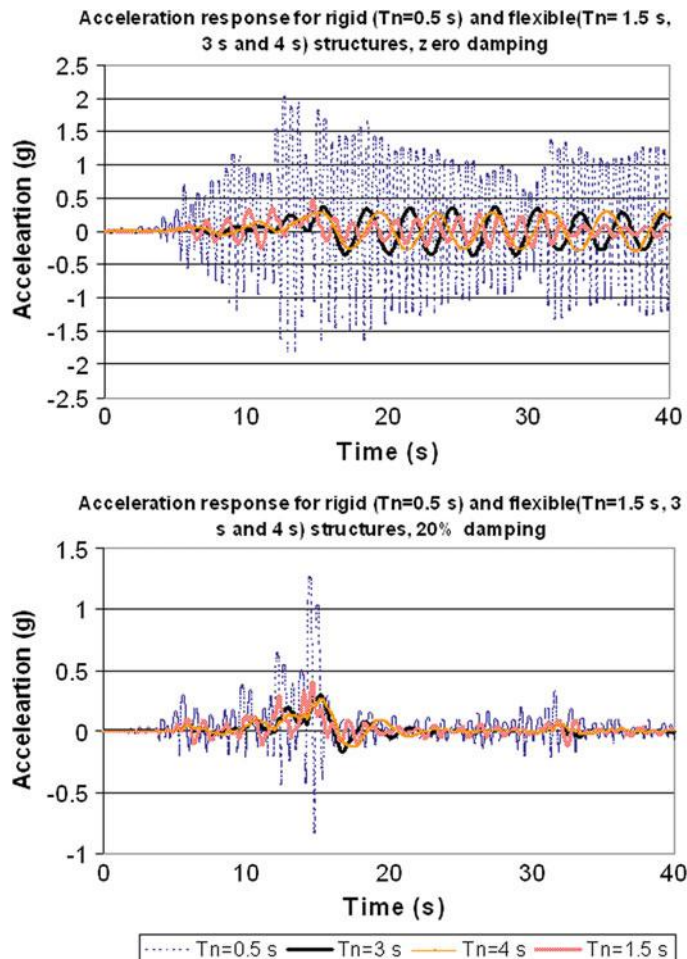


Fig. 5.16 Acceleration response time history with a variation in undamped structural natural periods ($T_n = 0.5$ s and $T_n = 3.0$ s) and damping (zero damping and 20 % of critical damping), subject to the ground motion documented from Chi-chi earthquake on 21 September, 1999

$$S_a = S_a(T/T_g) \quad (11)$$

5.4.2.2 Elastic Design Spectrum

The actual response spectrum curve shown in Fig. 5.9 only represents one single excitation and exhibits many fluctuations with peaks and valleys. For the design and safety assessment of infrastructures, the spectrum needs to account for every possible future earthquake likely to occur in a given zone (with a certain probability of

Fig. 5.17 Single degree-of-freedom response spectra (upper figure) plotted in a “tripartite” fashion for levels of damping 0, 2, 5, 10, 20 % of critical (top to bottom) subject to the seismic acceleration recordings of the surface wave magnitude 6.0 Whittier Narrows Dam earthquake in Los Angeles, 1 October, 1987 [47]

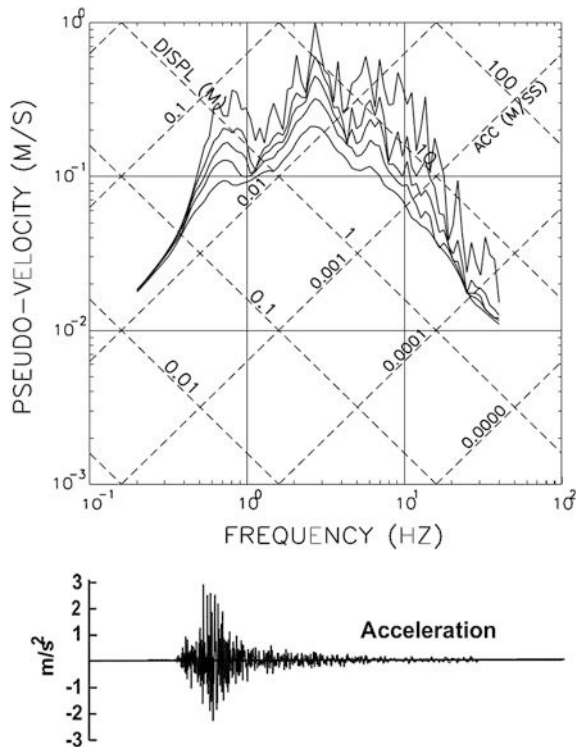
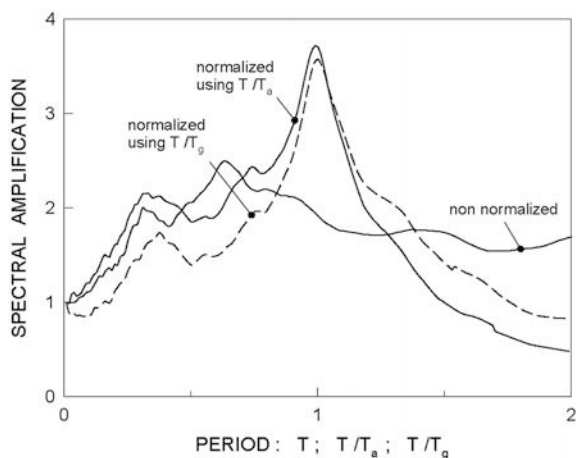


Fig. 5.18 Average acceleration spectra based on 24 actual motions recorded on soft soil; the periods are normalized before averaging with: **a** period of peak spectral acceleration (T_a); **b** period of peak spectral velocity (T_g); the assumed damping is 5 % [49]



occurrence as will be discussed in Sect. 9.1. This can be fulfilled by including information to represent ground motion characteristics of various past earthquakes at the same site, or if this is not possible, from other sites under similar conditions.

Here, similar conditions mean similar magnitude of the earthquake, local soil conditions, distance of site from the causative fault, fault mechanism, and geology of the travel path of seismic waves from the source to the sites [16]. However, Iervolino and Cornell [50] argue that magnitude and fault seem not to be important criteria to select the seismic motions.

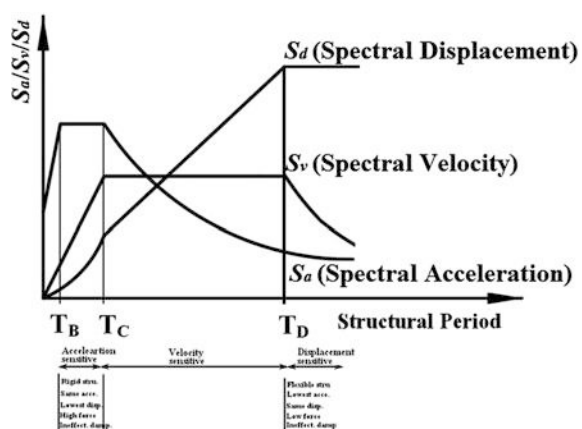
Even though the jaggedness (peaks and valleys) indicates the sensitivity of the response of structures to a slight variation of structures' natural period, in engineering practice, design specification should not be too sensitive to a slight variation of structures' natural period. Therefore, the fluctuations in the actual response spectrum must be smoothed using curve fitting techniques to reach a design spectrum with an idealized spectrum shape, which is called design response spectrum or design spectrum.

Based on the calculation of response spectrum for each individual ground motion, as presented in Sect. 5.4.2.1, statistical analysis shall be carried out to obtain the mean, standard deviation of the ordinate at each period of the response spectrum. By averaging several spectra from past earthquakes, the mean or median response spectrum can be obtained. In addition, the mean (or median) plus one or two standard deviations (sigma) is also of interest for engineering applications with a reliability based design. Both spectra are much smoother than the response spectrum of an individual ground motions. Below, the general method to obtain design spectrum for practical seismic design will be presented. For a more detailed presentation of background knowledge and procedure to obtain seismic design spectrum by seismic hazard analysis, see Chap. 9.

A design acceleration response spectrum generally has a trapezoidal shape as shown in Fig. 5.19. Even though the idealized trapezoidal shape spectrum is not a close approximation to the actual spectrum, it is helpful in constructing a design spectrum representing many ground motions [16].

As an example, we hereby characterize the design spectrum by defining three regions with the assumed boundary periods of $T_A = 0.03$ s, $T_B = 0.125$ s,

Fig. 5.19 Earthquake design spectrum measured by acceleration, velocity and displacement



$T_C \approx 0.5$ s and $T_D \approx 3.0$ s shown in Fig. 5.19. Note that for a specific ground motion, the control periods for constructing the design spectrum, i.e. T_B , T_C and T_D vary with damping. The values of them depend on the soil type and earthquake magnitude. Various design codes such as Eurocode 8 [46] specify the values for these periods.

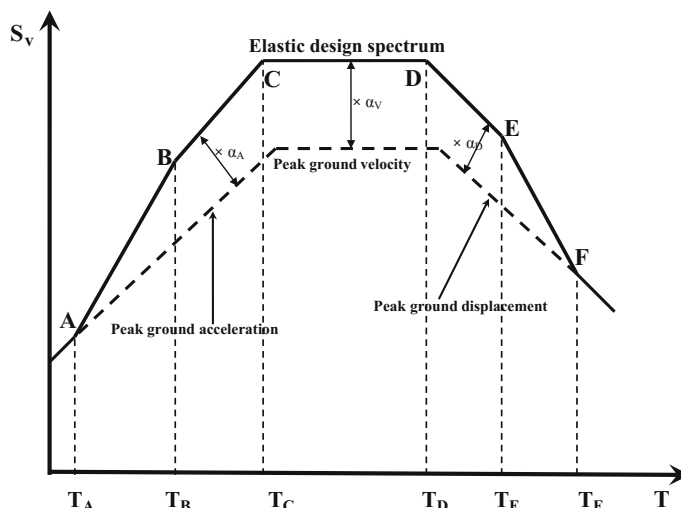
1. At short period range between T_B and T_C as shown in Fig. 5.19, the spectrum generally has a constant acceleration. Stiff structures' natural periods may be within this region. Their responses are governed by the ground acceleration motions and the structure moves like a rigid body with significant inertia forces due to the large acceleration. Even though the structural accelerations are rather close to the ground accelerations, the displacements are relatively small. In addition, the viscous damping has little effects on the response behavior of a stiff/rigid structure. Actually, in the right portion of this period range toward T_C , the structures' accelerations are larger than ground accelerations, with the amplification depending on the structures' natural periods and viscous damping values. For simplicity, the structures' accelerations can still be assumed to be constant with amplification depending on damping value.
2. At rather higher periods than T_D , the spectrum has a constant displacement. In a sense its maximum deformation is controlled by the characteristics of ground motion displacement, and is insensitive to the characteristics of associated ground velocity and acceleration. Soft structures' natural periods are likely to be in this regime. Their responses are governed by the ground displacement motions and the structure moves like a flexible body with rather small inertia forces due to small or zero acceleration. The structural displacement rather than acceleration is rather close to the ground motions, i.e., the absolute displacement is close to zero. In addition, the viscous damping has little influence on the response behavior of a flexible structure. As will be presented later in this book, this phenomenon is actually the basis for the utilization of base isolated structures. Actually, in the left portion of this period range towards T_D , the structures' displacements are larger than ground motions, with the amplification depending on the structures' natural periods and viscous damping values. However, for simplicity, the structures' displacements can still be assumed to be constant, with amplification depending on damping value.
3. In the intermediate period between T_C and T_D , strictly speaking, the structures' velocity should be higher than ground motion velocities, while for simplicity, the spectrum can be idealized as having a constant velocity. The responses of structures with natural periods lying within this period range will be governed by the ground motion velocities. In addition, viscous damping has a strong influence to mitigate dynamic structural responses for structures with natural periods lying within this period range.

The procedure of constructing a design spectrum, based on the amplification of peak ground motions in different period range, can be summarized as follows:

- Calculate the peak ground acceleration, peak ground velocity and peak ground displacement. The relationship between these three items can normally be based on a statistical study of previous earthquake ground motion records, such as the one recommended by Newmark et al. [51] as illustrated in Table 5.2. For example, a horizontal peak ground acceleration of 0.4 g in alluvium gives a horizontal peak ground velocity of 0.48 m/s (0.4×1.2 m/s) and gives a horizontal peak ground displacement of 0.364 m (0.4×0.91 m).
- Define the boundary of each period range of the spectrum, the following values are recommended by Chopra [16]: $T_A = 0.03$ s, $T_B = 0.125$ s, $T_C \approx 0.5$ s, $T_D \approx 3.0$ s, $T_E = 10.0$ s and $T_F = 33$ s as shown in Figs. 5.20, 5.21 and 5.22. The spectrum can be defined completely by peak ground motions (PGA, PGV but rarely PGA) and the amplification factor at T_A , T_B , T_C , T_D , T_E and T_F . Among which T_A , T_B , T_E and T_F are fixed values, while T_C and T_D vary with damping. Without further details, they can be determined by the intersection points of the constant acceleration, constant velocity and constant displacement branches of the spectrum. In various design codes, the value of T_B is also specified depending on the soil type and earthquake amplitude.

Table 5.2 Spectral bounds for alluvium and crystalline rock

	Horizontal ground motion		Vertical ground motion	
	Crystalline rock	Alluvium	Crystalline rock	Alluvium
Peak ground acceleration	1 g		2/3 g	
Peak ground velocity (m/s)	0.71	1.2	0.43	0.74
Peak ground displacement (m)	0.3	0.91	0.28	0.84

**Fig. 5.20** Construction of elastic pseudo-velocity design spectrum

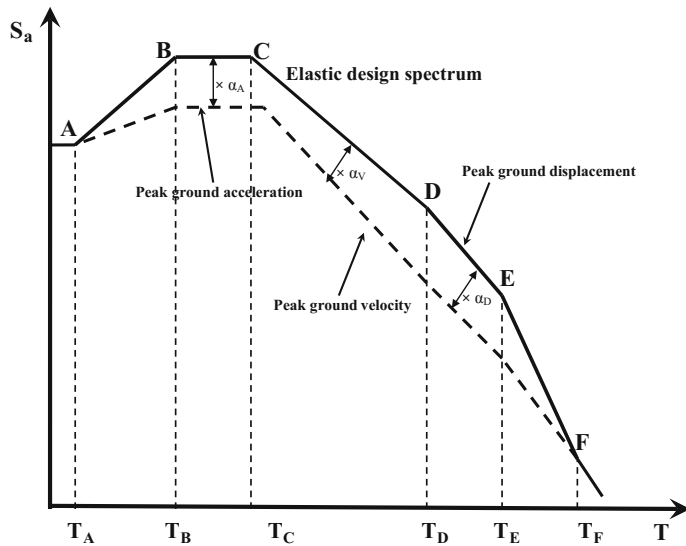


Fig. 5.21 Construction of elastic pseudo-acceleration design spectrum

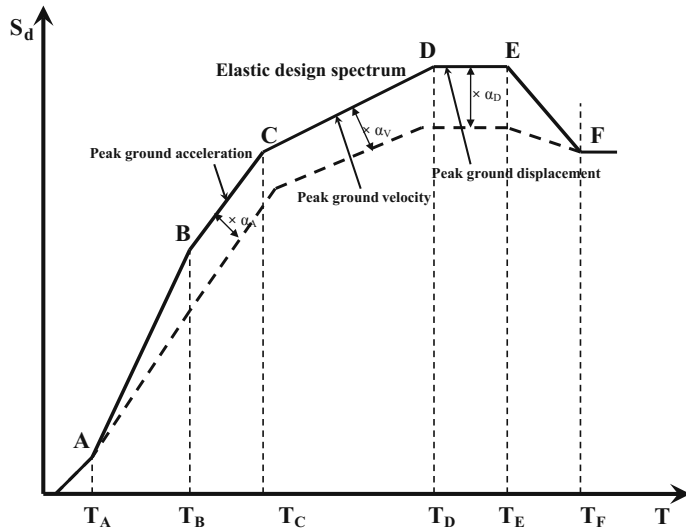


Fig. 5.22 Construction of elastic displacement design spectrum

3. Plot three dashed lines corresponding to the peak ground acceleration (between T_B and T_C), peak ground velocity (between T_C and T_D) and peak ground displacement (between T_D and T_E) as shown in Fig. 5.20 (for elastic

pseudo-velocity design spectrum), Fig. 5.21 (for elastic pseudo-acceleration design spectrum) and Fig. 5.22 (for elastic displacement design spectrum).

4. Estimate the spectral amplification factors for three period regions of the spectrum: α_A for peak/constant acceleration region, α_V for peak/constant velocity region, α_D for peak/constant displacement region. The amplification factors depend on both the cumulative probability level considered, e.g. mean (50 %) or mean plus one sigma (84.1 %), and the damping. Table 5.3 shows an example of recommended amplification factors by Newmark and his coworkers [51] for elastic design spectra. It is based on the statistical studies of a large number of ground motion records on firm ground (rock and competent sediments) with different damping levels from 0.5 to 20 %. The damping value is defined as the total structural (system) and soil damping in the form of some percentages of critical damping. It should be noted that the amplification factor listed in Table 5.3 only applies to firm ground. In engineering practice, various types of soil need to be considered. Therefore, most of the seismic design codes give the soil type dependent amplification factor in the form of soil factor together with a correction factor. In addition, various damping values are accounted for in the design codes by a damping correction factor. See Sect. 6.2 for details.
5. Multiply the ordinate for peak ground acceleration at the BC branch with the factor of α_A . Multiply the ordinate for peak ground velocity at the CD branch with the factor of α_V . Multiply the ordinate for peak displacement at the DE branch with the factor of α_D .
6. Draw a line $S_v = \frac{S_a}{\omega} = \left(\frac{T_n}{2\pi}\right) S_a$ for periods shorter than T_A . Draw a line $S_v = \omega S_d = \left(\frac{2\pi}{T_n}\right) S_d$ at periods longer than T_F .
7. Use a straight line to connect A and B as well as E and F.
8. Based on the elastic pseudo-velocity design spectrum shown in Fig. 5.20, the construction of elastic pseudo-acceleration (Fig. 5.21) and elastic displacement (Fig. 5.22) design spectrum can be performed using the relationships among the pseudo-acceleration, pseudo-velocity and displacement.

Table 5.3 Amplification factors for elastic design spectra with different damping ratio and non-exceedance probabilities of 84.1 and 50 %, respectively

Damping ζ (%)	Mean plus one sigma (84.1 %)			Median (50 %)		
	α_A	α_V	α_D	α_A	α_V	α_D
0.5	5.10	3.84	3.04	3.65	2.59	2.01
1	4.38	3.38	2.73	3.21	2.31	1.82
2	3.66	2.92	2.42	2.74	2.03	1.63
3	3.24	2.64	2.24	2.46	1.86	1.52
5	2.71	2.30	2.01	2.12	1.65	1.39
7	2.36	2.08	1.85	1.89	1.51	1.29
10	1.99	1.84	1.69	1.64	1.37	1.20
20	1.26	1.37	1.38	1.17	1.08	1.01

Example Determine the design spectrum with a peak ground acceleration of 0.27 g, peak ground velocity of 0.29 m/s and peak ground displacement of 0.24 m. The damping of the structure is assumed to be 2 and 5 % respectively.

Solution the procedure is illustrated in Fig. 5.23 (2 % damping) and Fig. 5.24 (5 % damping). By considering Table 5.3, it is clear that the ordinates (corresponding to mean plus one sigma) for constant acceleration, velocity and displacement with 2 % damping are 35, 27 and 20 % higher than that with 5 % damping. It should be noted that, by scaling the spectrum to match the peak ground acceleration estimated for the site, the resulting spectrum shape can be generalized in engineering practice [16]. For example, if the peak ground acceleration is 0.54 g, then the ordinate of spectrum in Fig. 5.24 multiplied by 2 (0.54 g/0.27 g) gives the design spectrum for a site with PGA of 0.54 g.

At this stage, readers should have a general picture of how to construct a response and design spectrum and understand the differences between them.

5.4.2.3 Effects of Damping

When a structure is stiff with a low natural period below 0.5 s, it is more sensitive to acceleration than displacement, and the structure tends to move in the same acceleration amplitude as the ground. Viscous damping has little influence on the

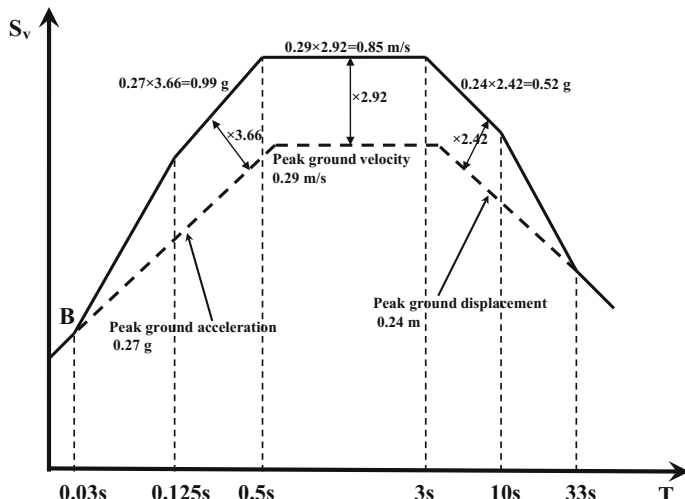


Fig. 5.23 Construction of elastic pseudo-velocity design spectrum in log scale with PGA of 0.27 g, PGV of 0.29 m/s, PGD of 0.24 m, and the damping ratio of 2 %

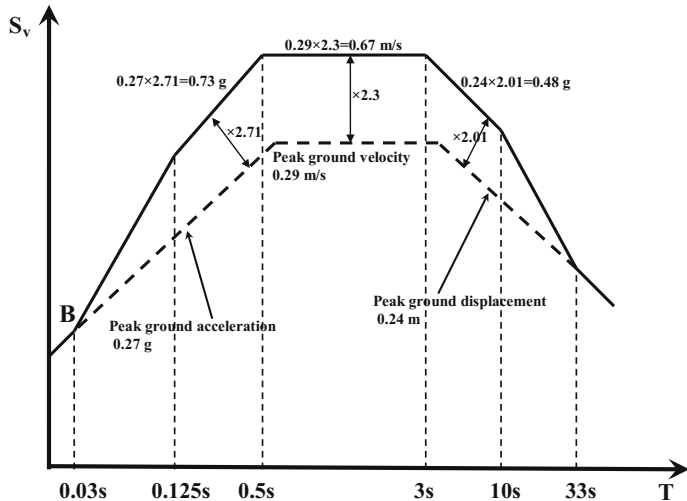


Fig. 5.24 Construction of elastic pseudo-velocity design spectrum in log scale with PGA of 0.27 g, PGV of 0.29 m/s, PGD of 0.24 m, and the damping ratio of 5 %

structural response. When a structure is flexible with a rather high period, the structural masses tend to remain motionless, and do not generate any significant loading. The viscous damping has little influence on the structural responses too. However, when a structure is in between the very high and the very low period above, i.e., at velocity sensitive region, the damping has the greatest effects. Furthermore, if a structure's natural period is close to the period of earthquake ground motions, the energy is effectively fed into the structure and the structural responses are amplified, leading to a resonance or a close-to-resonance condition. However, in this condition, the viscous damping in the structure will efficiently absorb the energy from the structural response and dissipate it, thus mitigating the build-up of the resonant responses and reducing the response amplitudes. It is also noted that the damping effects are greater for small damping values than that for high damping values, i.e., when the damping ratio is increased from zero to 5 %, the reduction in response is much more significant than that due to a damping increase from 15 to 30 %. Because the inherent damping for the majority of structures is low, it can be realized that in order to reduce the dynamic response, one can either increase damping by adding for example dampers, or increase the structures' natural period by using for example a base isolation system, which will be discussed later in this book.

Design response spectra in design codes are normally given based on an inherent system damping of 5 %. If spectral values for other damping ratios are required, then the spectral accelerations can adjusted using a scaling factor (correction coefficient). For example, in Norsok [52], with a damping of $\zeta\%$ ($\zeta\%$ should be between 2 and 10 %), η can be calculated as:

$$\eta = -\ln(\zeta/100)/\ln(20) \quad (5.38)$$

NORSAR [47] recommends to use:

$$\eta = 1.48 - 0.30 \ln(\zeta) \quad (5.39)$$

Section 6.2 introduces the formula to calculate the correction coefficient η used in ISO 19901-2 and Eurocode 8.

5.4.2.4 Shear Wave Velocity Estimation with Shallow Soil Depth or Soils and Rock Below 30 m

In the classification of soils, the average shear wave velocity ($v_{s,30}$) is determined based on the characteristics of the top 30 m [53] (or 20 m [54]) thickness of soil layers, which is the travel time of seismic shear wave from soil surface to 30 or 20 m deep divided by 30 or 20 m. However, this is based on the assumption that the sites have very deep soil layers much higher than 30 m of thickness, such as the recommendations made by ICC [55] and NEHRP [56], in which regression analyses of recorded seismic ground motions in the United States are available for sites with soil layers extended up to a few hundred meters downward before reaching the bedrock, and the stiffness of the soil layers deeper than 30 m is often well correlated with the wave velocity in the top 30 m.

However, as shallow bedrocks are very common in high seismicity regions, this classification method is under significant research scrutiny [57–61] and may not be suitable for regions where a soil-bedrock interface is found at even a few meters below the soil surface. Studies [62] of a large number of records at sites with soil layers at depths from a few meters to 180 m in China, Australia and India have shown that, when engineering rock (with shear wave velocities larger than 700 ± 60 m/s) depths are shallow, the site classification approaches adopted in the design codes give a higher shear wave velocity (stiffer soil column) than reality. Site response [59] also indicates that a simplified site amplification analysis by seismic codes may be on the un-conservative side.

Therefore, for sites having depths of less than 30 m, a detailed site specific response analysis (Chap. 4) is recommended to estimate the shear wave velocity and amplification characteristics.

In case the shear wave velocity or site class for any particular site is not important, statistical data from many earthquake records in various stations can be used to estimate the average shear wave velocity for sites with shallow soil depths. Based this assumption, Boore [63] and Atkinson and Boore [64] proposed methods for extrapolating the velocities between site depth and 30 m of depth.

As discussed in Sect. 4.2.2, the estimation of site period and shear wave velocity based on the top 30 or 20 m of soil layers is most appropriate for rather short period content of the bedrock motions. For longer periods, seismic wave lengths are much longer, the site response is then likely to be affected by soil characteristics at much

greater depths. Furthermore, even for deep soil with stiffness of the deeper soils that is well correlated with the shear wave velocity at the top 30 m, Boore et al. [65] found that the depth over which average shear wave velocity should be averaged is one-quarter of the wavelength associated with the period of interest, which can be greater than 30 m. Moreover, significant soil amplifications can be produced due to high impedance contrasts and associated seismic wave reflections at depths much greater than 30 m, which have almost no correlation with the soil properties at the top 30 m. The soil amplification estimation based on the top 30 or 20 m of soil layers may then be on the non-conservative side, especially for long site period soil columns having deep and low damping deposits of soil on very hard rock [66]. This is suspected to have been the cause of destructive site amplification in the magnitude 6.5 Caracas, Venezuela earthquake of 1967 [67, 68], the Loma Prieta earthquake in 1989 [69], and the Kobe earthquake of 1995 [70].

5.4.3 Ductility-Modified (Inelastic) Design Spectrum Method

5.4.3.1 Ductility for Elastic-Perfect-Plastic Structures

Subject to extremely strong ground motions, for an economical design, most of the structures are expected to deform into their inelastic range through structures' plasticity development, as will be discussed in Sect. 14.1. Note that the elastic design spectrum assumes that structures exhibit linear elastic behavior under ground motion. This can be justified if ground motion is mild and the structures do not exhibit plastic deformation. However, under strong earthquake motions, due to the fact that the ductile material such as steel or aluminum has a significant amount of ductility to develop above their yield strength, structural ductility promotes the following effects:

- After yielding accelerations are limited and therefore the forces on structures are also limited
- Damping due to ductility/plasticity can dissipate a certain amount of energy
- Yielding increases the natural period, i.e. reduced acceleration in the response spectrum
- Plastic hinges form in one direction but close in the other

To avoid explicit inelastic structural analysis in design, the capacity of the structure to dissipate energy, through mainly ductile behavior of its elements and/or other mechanisms, is taken into account by performing an elastic analysis based on a modified response spectrum reduced with respect to the elastic one [46]. This modified spectrum is called the ductility-modified (inelastic) design spectrum. It should be noted that the modified spectrum does not account for the change of

natural period, while this can be addressed using a dynamic time history analysis as will be addressed later in this book.

For a local structural member such as a steel beam or column subject to bending, one may define the ductile characteristics as the ratio of maximum displacement (δ_u) over the displacement (δ_y) at the initial yielding of the member:

$$\mu = \frac{\delta_u}{\delta_y} \quad (5.40)$$

For a global ductile structure such as an offshore steel structure or a steel frame building, this is indicated by a significant amount of plastic deformation over elastic range. However, after the plasticity has been developed in each individual member of a structural system, unlike that in the elastic range, the relationship between the global load level and the deformation of each individual member may be different among each member, i.e. the member deformation is not proportional to global loads. In addition, due to the formation of plastic hinge, an increase in global load may even decrease the member forces in certain members. This raises difficulties of determining a unified ductility coefficient for a structural system that can be applied to every member in the system. On the other hand, investigations show that the maximum structural displacement amplitudes produced by a given ground motion tend to be reasonably independent of the yield strength of the structure, i.e., the maximum displacement in a typical engineering structure was found to be about the same whether it remains elastic or yields [86–88]. For engineering purposes, by assuming that all inelastic deformation is caused by the formation of plastic hinges, and the plastic hinges in a structure occur simultaneously [89, 90], one can express the ductile characteristics of a structure system with ductility coefficient or ductility factor [91]:

$$\mu = \frac{\Delta_p}{\Delta_y} \quad (5.41)$$

where Δ_p is maximum horizontal displacement of a structure with inelastic behavior; Δ_y is maximum horizontal displacement of the structure when it just reaches yielding.

Based on the relationship between elastic and inelastic response as shown in Figs. 5.25 and 5.26, the unit shape factor analysis can be used to determine the ductility of a structure.

For structures with relatively high natural period corresponding to Fig. 5.25, the velocity ($T_C < T < T_D$) or displacement ($T > T_D$) in the linear elastic spectrum (Fig. 5.19) is constant, and the difference between the elastic (Δ_e) and inelastic displacement (Δ_p) is rather small. Therefore, the “equal maximum displacement” assumption is valid as an approximation:

Fig. 5.25 Global base shear (BS_e is the horizontal elastic inertia force and BS_y is the horizontal yield force) and displacement (Δ) relationship for elastic and inelastic response of structural system at relatively *high* natural period of the structure (i.e. velocity is constant in the linear elastic spectrum)

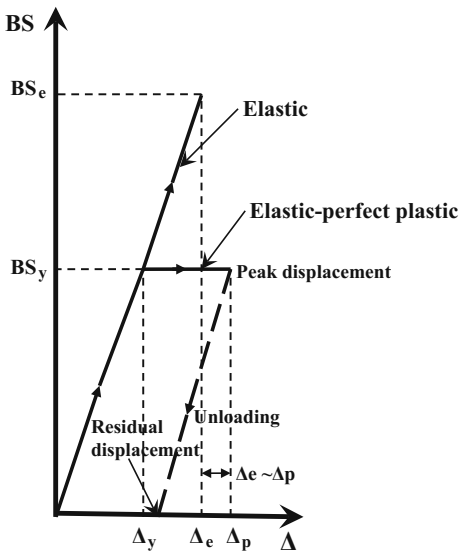
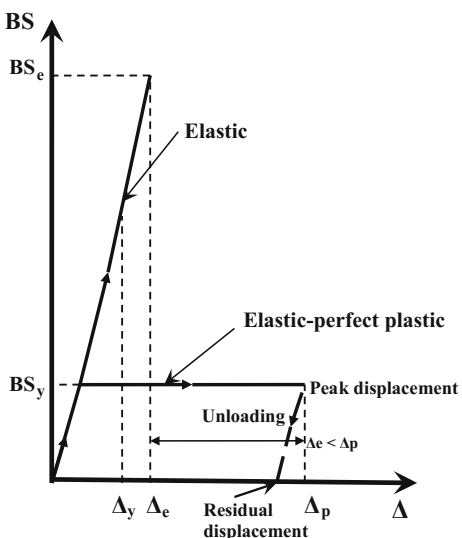


Fig. 5.26 Global base shear (BS_e is the horizontal elastic inertia force and BS_y is the horizontal yield force) and displacement (Δ) relationship for elastic and inelastic response of structural system at relatively *low* natural period of the structure (i.e. acceleration is constant in the linear elastic spectrum)



$$\Delta_e = \Delta_p \quad (5.42)$$

By adopting the rule of similarity of triangles, one has:

$$\frac{(BS_e - BS_y)}{(\Delta_e - \Delta_y)} = \frac{BS_e}{\Delta_p} \quad (5.43)$$

where BS_e is the horizontal elastic inertia force; BS_y is the horizontal yield force.

By rearranging the equation above, one obtains:

$$\frac{BS_e}{BS_y} = \frac{\Delta_p}{\Delta_y} = \mu \quad (5.44)$$

At low natural period of a structure corresponding to Fig. 5.26, the acceleration in the linear elastic spectrum (Fig. 5.19) is constant, and the difference between the elastic (Δ_e) and inelastic displacement (Δ_p) is rather significant. Therefore, the “equal maximum energy” can be assumed to be:

$$E_e = E_p \quad (5.45)$$

The absorbed energy due to the elastic response E_e and the absorbed energy due to the inelastic response E_p can be expressed by two equations as follows:

$$E_e = \frac{1}{2} BS_e \cdot \Delta_e \quad (5.46)$$

$$E_p = \frac{1}{2} BS_y \cdot \Delta_y + BS_y(\Delta_p - \Delta_y) \quad (5.47)$$

By inputting the two equations above into Eq. (5.45), one obtains:

$$\frac{BS_e}{BS_y} = \sqrt{\frac{2\Delta_p}{\Delta_y} - 1} = \sqrt{2\mu - 1} \quad (5.48)$$

The ratio of base shear $\frac{BS_e}{BS_y}$ above is known as behavior factor (R) in structural design codes for both offshore and land-based structures.

For structures with relatively high natural period, it is obvious that $R = \mu$. For structures with low natural period, $R = \sqrt{2\mu - 1}$.

From a comparison between Eqs. (5.44) and (5.48), it is noted that structures with high natural period can more effectively resist the earthquake excitations than structures with low natural period do, provided that the structure has sufficient ductility.

Readers should note that an important assumption in using ductility-modified spectrum is that, whether a structure responds elastically or yields significantly, the deformations of a structure produced by a given ground motion are essentially the same, which is often referred to as the equal displacement rule. However, currently, there is not enough research to examine the validity of the equal displacement rule.

The introduction of the ductility factor makes it possible to account for inelastic effects of structures in a linear analysis by means of specific response modification coefficients and deflection amplification factors that are dependent on the structural and ductility class/level, which are related to both the force reduction factor (FRF)

and the deflection amplification factor (DAF). Note that US recommendations [36, 37] propose two different dedicated factors for force and deflections; Eurocode 8 [46] uses the equal displacement rule in most cases, implicitly assuming that DAF and FRF are equal to the behavior factor. This Eurocode 8 procedure was used to obtain a set of ductility-modified (inelastic) design spectra, as will be presented in Sect. 5.4.3.2. In addition, it is also noted that the deflection amplification factors proposed in US provisions are in general either equal to or lower than the corresponding force reduction factor, depending on the structural system and its level of inelasticity [38, 39]. As a result, the US provisions are less conservative when compared to Eurocode 8, since the latter approach considers the DAF-to-FRF ratio as unity [40].

Despite the benefits of using a ductility-modified spectrum, it has many limitations, which deter its general promotion. For example, the plastic deformations may not be distributed similarly to the elastic deformation. Furthermore, for more complex (redundant) structures, in which several modes of vibration may be excited significantly due to a ground excitation history, even elastic behavior cannot be predicted precisely by elastic response spectrum method [92]. Moreover, yielding pattern may appear as a general or an extremely localized phenomenon, and may then eliminate the vibration mode characteristics based on the elastic assumption, which is the basis for the validation of superposition techniques used for modal response combination in a response spectrum analysis, as will be discussed later in this book, and the relationship between the total inelastic energy absorption and the maximum local yield amplitudes can be extremely complex [41].

5.4.3.2 Construction Ductility-Modified (Inelastic) Design Spectrum Method

In Sect. 5.4.2, the construction of elastic design spectrum has been elaborated. By recognizing boundary periods (T_B , T_C and T_D) of the displacement-, velocity- and acceleration-constant regions in Fig. 5.19, the ductility-modified design spectrum can be obtained by dividing the elastic design spectrum with the behavior factor R varying with period/frequency, as described in Sect. 5.4.3.1:

$$R = \begin{cases} 1 & \text{for } T < T_B \\ \sqrt{2\mu - 1} & \text{for } T_B < T < T_C \\ \mu & \text{for } T_C < T < T_D \end{cases} \quad (5.49)$$

It should be emphasized that the operation of dividing spectrum applies to different ordinates of the spectrum: at acceleration-constant region ($T_B < T < T_C$), the acceleration design spectrum is divided by a factor of $\sqrt{2\mu - 1}$; and at velocity-constant region ($T_C < T < T_D$), the velocity design spectrum is divided by a factor of μ ; at displacement-constant region ($T_D < T < 10$ s), the displacement

design spectrum is divided by a factor of μ . Furthermore, at the lower bound of the spectrum (e.g. $T = 0.03$ s), one may set the ordinate of either displacement-, velocity- or acceleration design spectrum for inelastic spectrum as the same value as that of the elastic one, then join this value with the ordinate of inelastic design spectrum at T_B with a straight line. At the upper bound of the spectrum (e.g. $T = 33$ s), divide ordinate of elastic displacement design spectrum by the value of μ , then join this value with the ordinate of inelastic displacement design spectrum at $T = 10$ s with a straight line. During this construction process, attention should always be paid to the transformation between displacement-, velocity- or acceleration design spectrum using the equations in Sect. 5.4.2.1. Figure 5.27 shows an inelastic design spectrum. It should be noted that the value of T_c is not fixed and depends on the damping [16].

Figure 5.28 shows a comparison of inelastic spectrum according to Eurocode 8 [46] with various ductility factors. The peak ground acceleration is 0.6 g, with soil type 1 and subsoil class B. It should be noted that the ductility factors for a structure may be different along different horizontal directions, although the ductility classification is the same for all directions.

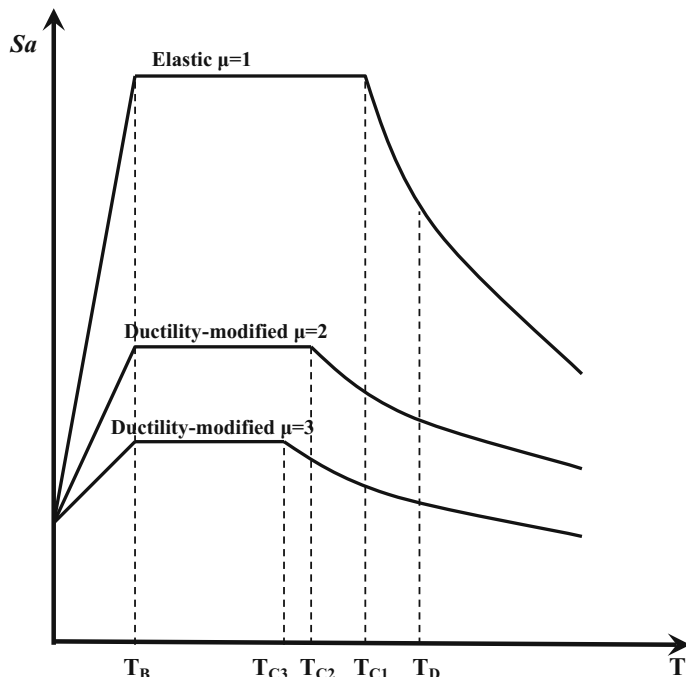
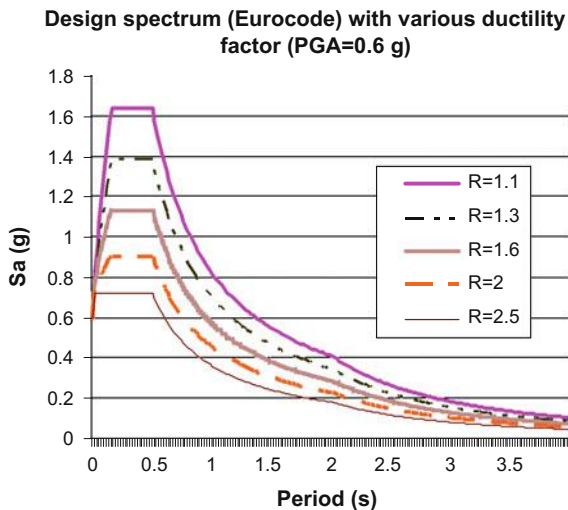


Fig. 5.27 Inelastic pseudo-acceleration design spectrum (linear scale)

Fig. 5.28 Inelastic (pseudo-acceleration) design spectrum with various values of ductility factor R



5.4.4 Vertical Response Spectrum

Both structural and non-structural components may be sensitive to the vertical input motion because they are normally stiff in the vertical direction and their eigenperiods corresponding to vertical global vibrations are generally short [71]. In the neighborhood of the epicenter the vertical component of motion is even larger than the horizontal components [72]. Moreover, as alluvial basin enables the S-to-P-wave conversion and wave scattering at the basin-bedrock interface, supplying energy to vertical components of strong ground motions, this also increases the ratios of vertical to horizontal PGA. Field evidence collected in the Kalamata (Greece, 1986), Northridge (USA, 1994) and Kobe (Japan, 1995) earthquakes indicates that damage and collapse of concrete and steel buildings and several bridges can be attributed to high vertical ground motions [73]. The available data shows that the peak vertical acceleration (PVA) amplification mainly occurs within the top 20 m of soil. At the ground surface, PVA can be amplified by a factor of 2–3 [74].

The vertical ground motions are mainly caused by P-waves, and partially contributed to by SV waves. Because the pressure wave velocities of the soil and the underlying rock have little differences, i.e. high vertical stiffness, the ground motions at seabed/ground surface are essentially quite similar or can in many cases be assumed to be identical to the vertical seismic motions at bedrock. Therefore, different from that of the horizontal response, the amplification of vertical ground motions due to the local soil condition is often insignificant.

Because of the distinct characteristics of frequency contents between vertical and horizontal ground motions, a simple scaling of horizontal motions to represent the vertical seismic motions should be avoided. Therefore, the estimation of vertical

ground motions makes use of the magnitude and distance data from the deaggregation (Sect. 9.1.4) of the seismic hazard (Sect. 9.1.3) and an appropriate ground motion prediction equation (GMPE), see Sect. (3.6) to develop a period dependent V/H (vertical to horizontal) ground motion spectrum ratio, which can then be applied to the horizontal design spectrum to generate a target vertical spectrum for design with an associated return period. Special attention should be paid to characteristics of short period range of V/H spectra, as will be discussed below.

In many situations an appropriate GMPE for vertical ground motions may not exist. Therefore, the vertical peak ground acceleration is generally taken to be 10–50 % lower than the horizontal peak ground acceleration. The relationship between vertical and horizontal components of the seismic action mainly depends on the period, the site-to-source distance, the local site conditions, and the earthquake magnitude, while the ratio is relatively insensitive to earthquake mechanism and sediment depth [75]. The closer a site is to the epicenter, the larger the vertical peak ground acceleration that can be measured. The V/H spectra are generally less than 2/3 at mid to long periods but significantly higher at short periods, and at short periods the V/H spectral ratio is sensitive to the source-to-site distance: higher on soil sites than on rock sites, and higher on soft soil sites than on stiff soil sites. A recent study by Bozorgnia and Campbell [76] also shows that V/H spectral ratio for soil sites is sensitive to the source-to-site distance, but relatively less sensitive to magnitude. Figure 5.29 shows V/H ratios plotted against moment magnitude (left) and peak vertical acceleration for recordings measured within 30 km of the closest faults, which include 240 components of ground motions recorded at 80 stations from earthquakes worldwide extracted from the NGA database. The median V/H ratio is equal to 0.9, being much higher than the commonly accepted value of 2/3 [77]. The maximum V/H ratio in the subset is close to 4.0, which was measured during the 1979 Imperial Valley earthquake ($M_w = 6.5$) and to the El Centro Array

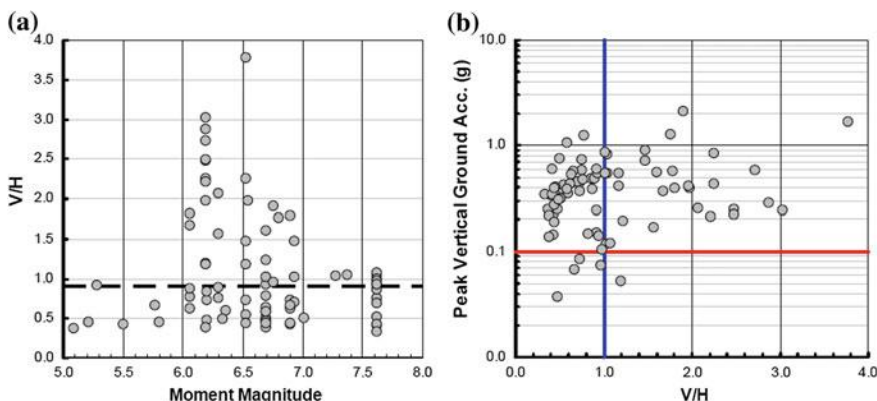


Fig. 5.29 Ratios of peak vertical to horizontal acceleration (V/H) plotted against moment magnitude (left, dashed lines indicate the sample median) and peak vertical acceleration (right) [77]

#6 station, which recorded a peak vertical ground acceleration of more than 1.6 g. By observing the right figure of Fig. 5.29, it is found that higher vertical acceleration tends to create larger V/H ratio.

As mentioned before, the vertical bedrock responses are often established in conjunction with probabilistic seismic hazard analysis (PSHA), presented in Sect. 9.1.3 to develop vertical spectra by scaling the PSHA results for the horizontal ground motion (see examples presented by Akkar et al. [78], Gülerce and Abrahamson [79] and Bommer et al. [80]).

Two methods are available to develop V/H spectral ratio. The first method is to develop vertical and horizontal GMPEs and consequently compute the median values of the V/H ratio [81]. The advantage of this approach is that the full characteristics of both the horizontal and vertical ground motions are preserved [76]. The second approach is to develop a GMPE directly for the V/H spectral ratios using the V/H empirical data [80]. The apparent advantage of this approach is that it allows a direct calculation of between-event and within-event residuals and standard deviations of the V/H spectral ratio [76].

Practically, it is well accepted to derive the vertical ground motion spectrum by scaling the horizontal motion spectrum by either a factor or different factors at different frequency range. Traditionally, based on the assumption that the shape of response spectrum between the vertical and horizontal seismic motions are rather similar, only one constant factor (typically with a value between 1/2 and 2/3) is applied on the entire frequency/period range, such as the one recommended by the original version of ISO 19901-2 released in 2004 [45], which uses a constant V/H ratio of 0.5 for all period range. Similarly, the code for seismic design of buildings in China [54] adopts a constant factor of 0.65.

By realizing that the shape between the vertical and horizontal seismic motions is to a certain extent different, many codes adopt V/H ratios varied with frequency. For example, in Eurocode 8 [46], V/H ratios depend on the surface wave magnitude and the period range. Table 5.4 shows the recommended V/H ratios between vertical and horizontal spectra proposed by NORSAR [47] only used for sites in Norway. Similar format of V/H ratios based on the frequency range is available in many seismic design codes and guidelines such as BSSC [56].

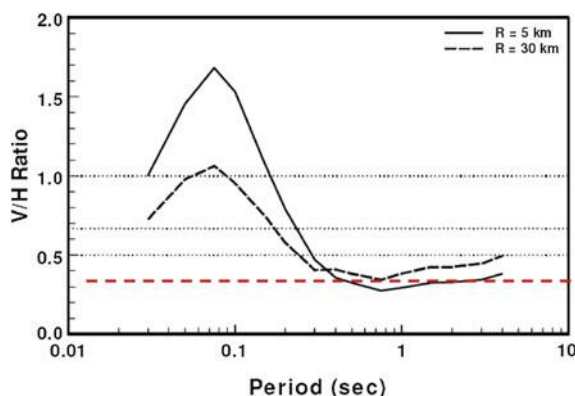
In a more dedicated way than V/H spectra, vertical spectra are directly specified. An example is the one adopted in the seismic design code of nuclear power plants in China [83], in which the vertical spectra are given for both rock and stiff soil sites with various damping ratios, which clearly show that the shape between the vertical and horizontal seismic motions are different. This is more obvious for stiff soil sites than that of the rock site.

Table 5.4 Recommended V/H ratios between vertical and horizontal spectra proposed by NORSAR [47, 82]

Frequency f (Hz)	Ratio between vertical and horizontal spectra (V/H)
$f < 1$ Hz	0.9
$1 \text{ Hz} \leq f \leq 3$ Hz	$0.9 - 0.42 \log_{10} f$
$f > 1$ Hz	0.7

However, there is no solid scientific basis for assuming that the vertical component of seismic motion is smaller than its horizontal counterpart. As shown in Fig. 5.30, for near-source regions, the vertical to horizontal spectral ratio has a distinct peak at short periods that generally exceeds 2/3 and the ratio is less than 2/3 at long period range. Therefore, the use of the traditional vertical to horizontal spectral ratio of 2/3 can result in either an underestimation (over short period range) or an overestimation (over long period range) of the expected vertical ground motions. Based on the recent study by Bozorgnia and Campbell [76], an updated V/H model is recommended that supersedes the previous V/H model [75] proposed by the same authors. This updated model is applicable for shallow crustal earthquakes occurring worldwide in active tectonic domains for magnitudes ranging from 3.3 to as large as 8.5, depending on the style of faulting, and distances as far as 300 km from the source. Based on the arguments above, the second edition of ISO offshore standard for seismic design ISO 19901-2 [84] recommends a modification of V/H ratio (Fig. 5.31) compared with its previous version released in 2004 [45], which uses a unified 0.5 ratio for all period range as mentioned before. This can pose a higher demand for topside structures, subsea structures, and equipment on the topside as the increase in vertical spectral acceleration in the low period range of the design spectrum can cause an accountable increase of vertical seabed motions. This is because the supporting structures of the fixed offshore platforms are generally stiff in the vertical direction, and the vertical accelerations are likely to be transferred to the topside through the supporting structures without significant modification in both magnitude and frequency content (note the opposite trend may be found for horizontal accelerations). Moreover, since the topside structures generally have rather low natural periods, the low period part of acceleration components transferred to the topside structures can then cause a response amplification. Similarly, the guidelines for Seismic Design of High Bridges in China [85] released in 2008 also specify that the V/H spectrum can be established depending on the site conditions:

Fig. 5.30 V/H spectral ratio at short distances (R) proposed by Bozorgnia and Campbell in 2004 [75]



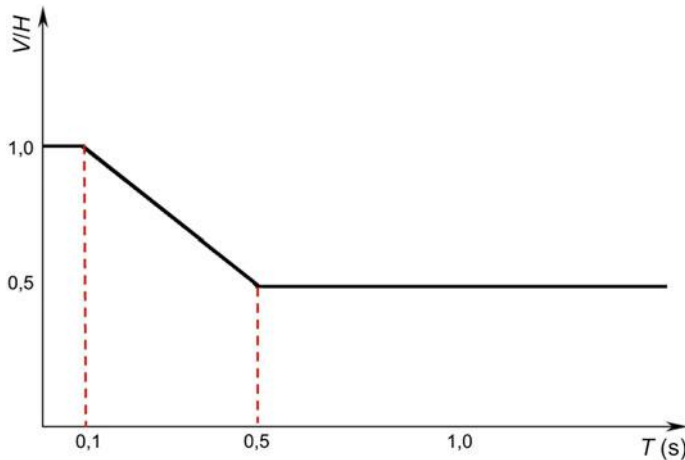


Fig. 5.31 V/H spectral ratio recommended by the 2nd edition of ISO [84]

$$V/H = 0.65 \text{ for rock site} \quad (5.50)$$

$$V/H = \begin{cases} 1.0 & \text{for } T < 0.1 \text{ s} \\ 1.0 - 2.5(T - 0.1) & \text{for } 0.1 \text{ s} \leq T \leq 0.3 \text{ s for sites with other soil conditions} \\ 0.5 & \text{for } T \geq 0.3 \text{ s} \end{cases} \quad (5.51)$$

where T is the vibration period of target structures.

5.5 Time History Method

5.5.1 General Method

The time history method requires a set of deterministic excitation time histories to be used as input, which account for the uncertainties and differences in frequency characteristics, duration and severity. Each time history takes the non-stationary characteristics of ground motions into account. The information regarding the phase lag of the ground motion among three translational directions and signs (compression or tension) of the structural member forces are also explicitly included in the analysis. Moreover, the duration of the time history should be sufficiently long to capture the load sequence and hysteretic effects on the responses for structures, foundations, and soil.

The required number of time histories varies among various seismic design codes, with a minimum of three. For example, ISO 19901-2 [45] requires at least four time histories, while Eurocode 8 [46] requires at least three.

Note that a set of recorded accelerograms in detail are only available in very few sites of the world, simulated (usually by performing site specific response analyses, see Chap. 4) and artificial accelerograms are often used for the dynamic analysis. These accelerograms should be consistent with a design spectrum, i.e., their corresponding response spectrum will be approximately equal to a prescribed or target spectrum, see Sect. 7.3.

In the application of the time history method for assessing structural response, there is a debate on whether the characteristic strength or the mean strength of structural materials should be used to assess the structural response: modeling the structural system using characteristic material strength could lead to unrealistic behavior, but on the other hand, modeling to mean values may not always be representative of reality, for example the contractor may over-specify material strength [93].

In Chap. 15, this method will be further discussed with details.

5.5.2 Drift Phenomenon and Its Correction

Velocity and displacement time series are derived from correponding accelerograms by single- and double-integrations of the acceleration record as shown in Figs. 5.32 and 5.33. However, by observing these two figures, noticeable drifts (gray lines) can be identified especially for displacement time series: while the velocities oscillate around zero near and after the end of the strong ground motions, the displacement time series reach essentially constant residual values.

This phenomenon is obviously unphysical and can lead to erroneous estimates of peak ground displacement and structural response at long period spectral range. A correctly derived long period ground motion can be used in understanding the source- and path-related specific features of far- and near-fault ground motions [94]. Long period motions are also important for a reliable estimation of deformation-demand for structures, particularly with an increasing interest in displacement-based design and non-linear seismic response. Furthermore, the drift also often affects a robust estimate of large scale soil–structure interaction response, especially for structures having large horizontal dimensions where the traveling wave effects become significant [95].

The drift related noise is embedded in records from both analog and digital accelerographs, although the characteristics of the noise are usually different for the two types of records. And it is not necessarily distributed in a stationary manner throughout the record, but can be confined to a certain short portion of time series [96].

The source of the long period noise seems to be variations in the acceleration baseline. These variations could be due to true ground motion (tilting and rotation produced by wave propagation, as well as local permanent ground failures),

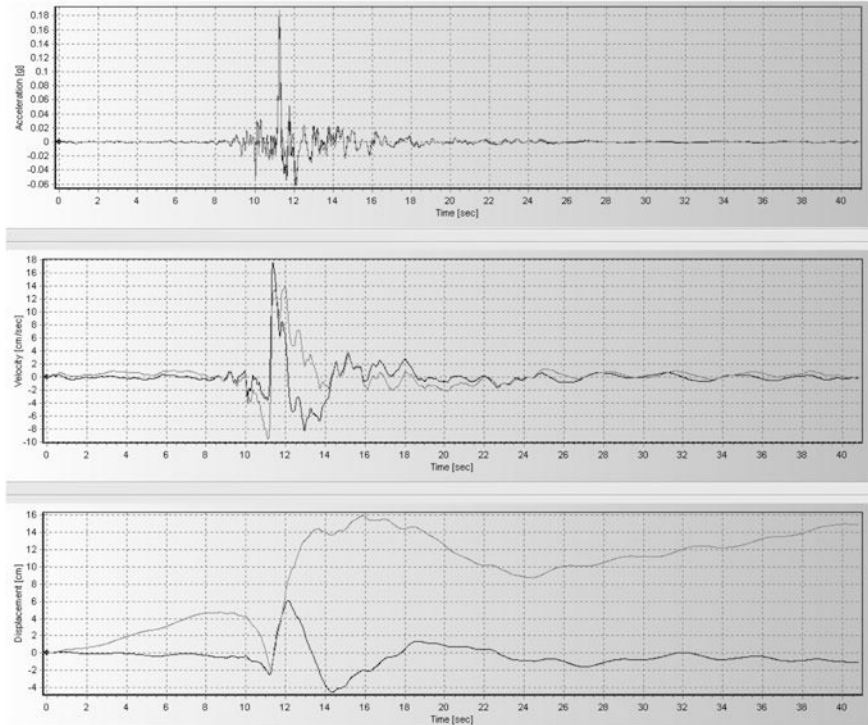


Fig. 5.32 Horizontal acceleration (*upper*) recorded during Friuli earthquake in Italy, and its corresponding velocity (*middle*) and displacement (*lower*) time series derived from single- and double-integrations of the acceleration record using SeismoSignal; the *black* and *gray* line indicate the time series with and without baseline-correction, respectively

instrumental effects (amplitude-dependent mechanical or electrical hysteresis in the sensor), analog-to-digital conversion [97], and the accumulation of random noise in time series also result from the single- and double-integration.

Various methods are proposed to solve the problems of baseline-offsets, even though there is no universal correction method for any kind of ground motion records [98].

As mentioned before, since the unrealistic drift to be removed can be different at different portions of time series, one popular baseline-correction method, as implemented in SeismoSignal [99], consists of (1) determining, through regression analysis (e.g. least-squares-fit method), the polynomial curve (typically is of a type among linear, quadratic or cubic) that best fits the acceleration time series; (2) subtracting from the actual acceleration values by their corresponding counterparts obtained with the regression-derived equation. By performing the two steps above, spurious baseline trends, usually well noticeable in the displacement time history obtained from double time integration of uncorrected acceleration records, can normally be removed from the input motion.

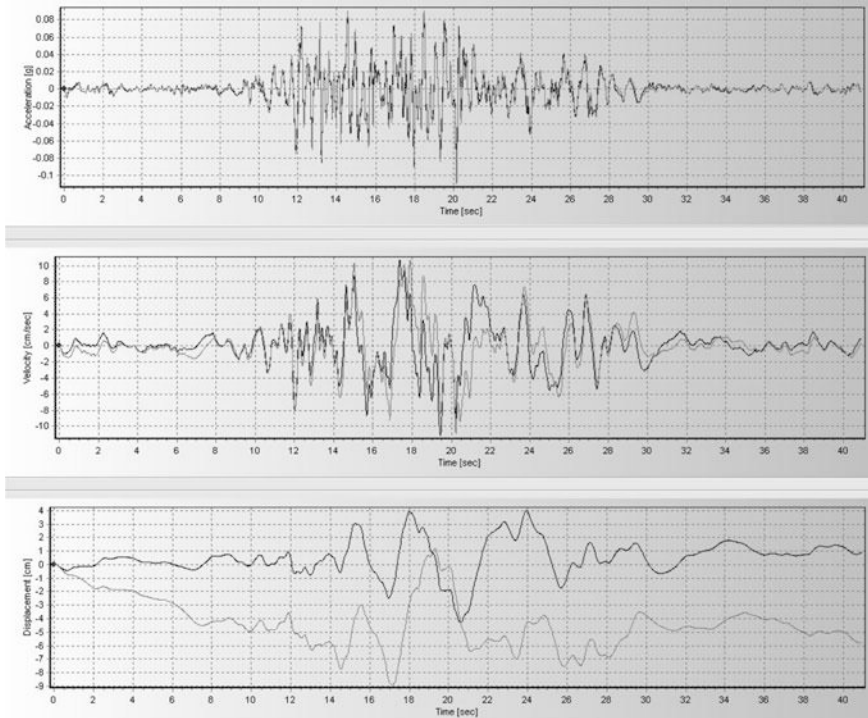


Fig. 5.33 Horizontal acceleration (*upper*) recorded during Nahanni earthquake in Canada, and its corresponding velocity (*middle*) and displacement (*lower*) time series derived from integrations of the acceleration record using SeismoSignal; the *black* and *gray* line indicate the time series with and without baseline-correction, respectively

In step (1) above, the polynomial curve $\ddot{x}(t)$ to fit the acceleration can normally be assumed to be linear, quadratic and cubic:

$$\ddot{x}(t) = a_0 + a_1 t \text{ for linear curve} \quad (5.52)$$

$$\ddot{x}(t) = a_0 + a_1 t + a_2 t^2 \text{ for quadratic order curve} \quad (5.53)$$

$$\ddot{x}(t) = a_0 + a_1 t + a_2 t^2 + a_3 t^3 \text{ for cubic order curve} \quad (5.54)$$

where a_1 , a_2 , a_3 , and a_4 are four constants to be determined during the curve fitting; t is time.

The curve fitting to acceleration time series can be obtained by, for example, minimizing the mean square acceleration:

$$\min \left\{ \sum_{t=0}^{N\Delta t} \left[\ddot{x}(t) - \ddot{\bar{x}}(t) \right]^2 \right\} \quad (5.55)$$

where N is the total number of time steps for the baseline-correction of time series, with each time step being Δt .

Based on the fact that the baseline of the acceleration record has random shifts during the interval of strong shaking and the shifts could be represented by an average baseline-correction over this interval, Iwan et al. [100] proposed that two baselines should be removed at two portions of time series: a_m between times t_1 and t_2 , and a_f from time t_2 to the end of the record. The value a_m is an average shift in baseline that could occur during strong shaking. Strictly speaking, t_2 can be any time instant between t_1 and the end of the acceleration record, which satisfies the constraint that the average of the corrected velocity is zero near the end of the record. Note that the degree of drift strongly depends on the value of t_2 [98]. Iwan et al. [100] proposed two specific options for determining t_2 : (1) t_2 is the time after which the acceleration never exceeds 0.5 m/s^2 ; (2) t_2 is chosen to minimize the final displacement. As a third alternative, t_2 can also be chosen as a time instant at which the line fitting to velocity series becomes zero [98]. The black lines in Figs. 5.32 and 5.33 show the baseline-corrected time series. It is clearly shown that the drift in derived displacement time series is essentially eliminated.

In cases where undesirable long period fluctuations still appear in the baseline-corrected time series, a windowed filter process in frequency domain can be carried out by applying a high-pass filter to the baseline-corrected acceleration data, with an example equation expressed as below and shown in Fig. 5.34 [101]:

$$\beta(T) = \begin{cases} 1 & 0 \leq T \leq T_0 \\ e^{-(T-T_0)/\alpha} & T \geq T_0 \end{cases} \quad (5.56)$$

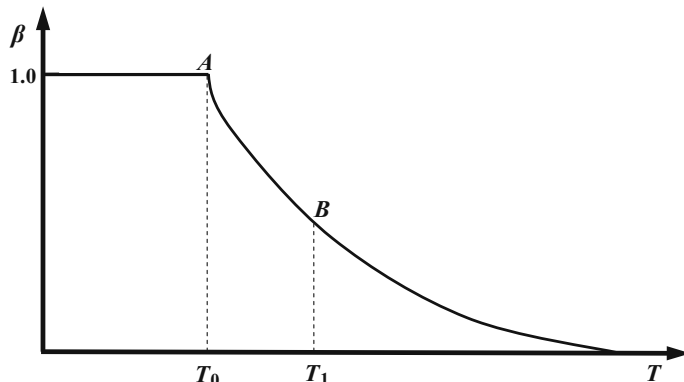


Fig. 5.34 An example of a windowed filter

where T is period in seconds, a and T_0 are two parameters that can be determined by using two key points A and B shown in Fig. 5.34.

Based on the data from laboratory tests, Zhou et al. [102] suggested that after the baseline-corrected acceleration series have been obtained, the velocity series calculated by integrating the baseline-corrected acceleration series may be further put through a similar baseline-correction process. By integrating the updated baseline-corrected velocity time series, the displacement time histories can be obtained. These obtained displacement time histories can go through a high-pass filter to further remove the long period oscillations.

In case a response spectrum analysis using design spectra is performed, the drift of time history for generating the design spectra can normally be omitted as the influence of baseline-correction on the variation of design spectrum is normally very marginal. Similarly, the baseline-correction has minor effects on the frequency content in case a power spectrum or a Fourier spectrum is used in the calculation of seismic responses.

However, it should be noted that the process of drift correction also eliminates the permanent ground deformation, which can degrade the reliability of the assessment results in case permanent ground displacement is of engineering concern.

5.6 Wavelet Transform Method

In Sect. 3.5, it is presented that seismic ground motions are in general non-stationary, i.e. they change significantly with time. However, power spectrum only gives a representation of average energy distribution by decomposing the signal into infinitely long and independent sine and cosine series, through which all time-located information is lost, i.e. it provides the information on how much but not when the particular frequency components exist [103]. Even though this provides a sufficient modeling for representing the stationary process, its application for non-stationary processes cannot be justified. When seismic waves start to break, the frequency content of the signal changes rapidly in time. This is particularly the case when a moving resonance (Sect. 3.5.3) occurs, which is a situation in which the increased eigenperiod of a structure (due to a degradation in its stiffness) approaches the decreasing predominant frequency of the ground motion due to ground motion components contributed by low frequency surface waves or soil failure (e.g. liquefaction), leading to a resonance during the decay stage of the ground motions. Moving resonance has sometimes been responsible for collapses of structures during past earthquakes, as mentioned in Sect. 3.5.3.

To analyze the non-stationary problem above, the traditional Fourier transformation only provides information on the frequency content, but the information on the frequency localization in time in a non-stationary process is essentially lost. However, the problem can be solved if one has the flexibility to allow for a resolution in both time and frequency to vary in the time–frequency plane, so that a

multi-resolution representation of the process can be reached. This leads to the application of wavelet transform method.

As a starting point to learn wavelet transform method, one may adopt the Short Time Fourier Transform (STFT) by analyzing only a small portion of the signal at a time. In this process, a window function is selected to window the signal, and the width of this window should be selected so that the signal within each window is stationary. Figure 5.35 illustrates an example of STFT, where a window function “w” is chosen as a square wave window. The result of each square box is represented by a coefficient, the width along the horizontal axis indicates its time resolution and the height along its vertical axis represents its frequency resolution. Because a single fixed width window is used for all frequencies in the STFT, the resolution of the analysis is the same at all locations in the time–frequency plane. An important drawback of using a fixed window width is that the STFT cannot capture both high and low frequency content simultaneously. To solve this problem, a more flexible approach by varying the window size is required, leading to the wavelet transform, i.e. STFT gives a fixed resolution at all times, whereas wavelet transform gives a variable resolution.

Therefore, in order to trace the time-located information, the localized decomposition is performed using the wavelet transform, which is a mathematical expression to identify different frequency components of a time history at discrete windows of time using a variable resolution matched to the frequency under consideration. It allows the use of long time intervals where more precise low frequency information is needed, and shorter regions where high frequency information is needed.

Wavelets were actually developed independently in the fields of mathematics, quantum physics, electrical engineering, and seismic geology. Interchanges between these fields have led to many new wavelet applications such as image compression, turbulence, human vision and radar. They were introduced in 1980 for processing seismic signals [104], which is a waveform of effectively limited duration that has an average value of zero. In other words, a wavelet is a wave-like oscillation with amplitude that starts at zero, increases, and then decreases back to zero as shown in Fig. 5.36. Wavelets are the basis of wavelet transform just as sine waves are the basis of Fourier transformation, while sinusoids do not have limited duration and they extend from minus to plus infinity, whereas wavelets last for very

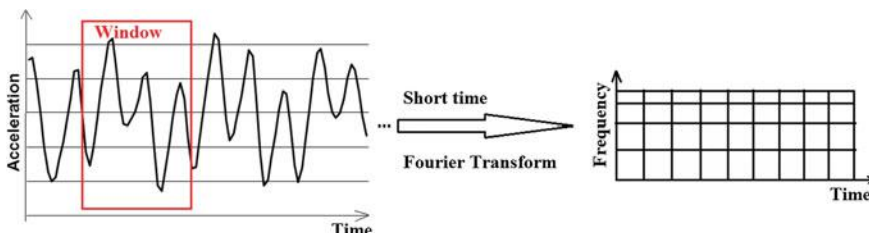


Fig. 5.35 Illustration of STFT

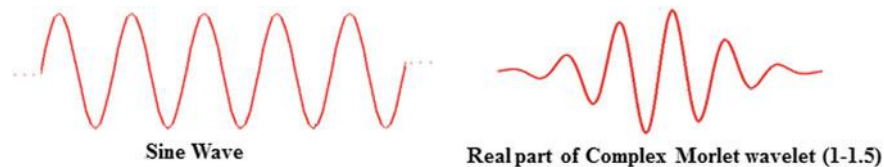


Fig. 5.36 A wavelet (right figure, which has 1.5 oscillations in 1 s) is the basis of wavelet transform just as sine waves (left figure) are the basis of Fourier transformation [105]

limited duration. Furthermore, sinusoids are smooth and predictable, but wavelets can be irregular and asymmetric. Moreover, Fourier analysis is a method of breaking up a signal into a series of sine and cosine waves with different frequencies, wavelet analysis breaks a time signal into shifted and scaled wavelets of the original (mother) wavelet (time-scale domain), which is a prototype for generating other wavelet functions [106].

As mentioned before, wavelet transformation has advantages over the traditional Fourier transformation in analyzing physical situations where the signal contains discontinuities and sharp spikes (non-stationary process). Figure 5.37 illustrates the differences between different types of transforms [107]. The right figure in Fig. 5.37 shows that wavelet analysis consists of decomposing a signal/motion into a hierarchical set of approximations and details. The levels in the hierarchy often correspond to those in a dyadic scale.

If the ground motion $a(t)$ is non-stationary, i.e. its average is significantly different from that at a time instant, one may use a transformation through a suitably positioned frequency window. The window is a function that tapers in both positive and negative directions, and is centered over the time instant of interests. A series of spectra are then obtained, each of which is related to a time index, and a corresponding time-frequency representation of function is also obtained.

Based on the interested frequency band, by tuning the width of the window, an efficient representation of wavelet function can be expressed as follows, known as continuous wavelet transform (CWT):

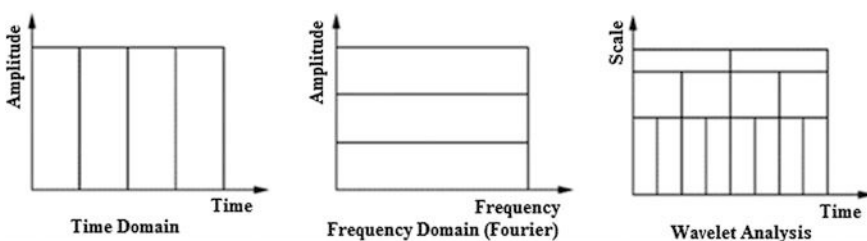


Fig. 5.37 Comparison of different transformations [107]

$$W_\psi(\alpha, \beta) = \frac{1}{\sqrt{\alpha}} \int_{-\infty}^{\infty} a(t) \psi^* \left(\frac{t - \beta}{\alpha} \right) dt \quad (5.57)$$

where $\psi(t)$ is the mother wavelet function or wavelet basis, i.e. a decaying oscillatory function; $*$ denotes the complex conjugate; α is a scale parameter, which is to characterize the frequency of the signal, it either dilates or compresses a signal (i.e., high scale values correspond to dilated (or stretched out) signals that can give information of slowly changing features of the signal at low frequencies, as shown in the left figure of Fig. 5.38, and low scale values correspond to compressed signals, which are capable of capturing rapidly changing features of the signal cherishing higher frequencies, as shown in the right figure of Fig. 5.38. The variation in width for different frequency bands can be achieved by different values of α : it is inversely proportional to the frequency, representing the periodic or harmonic nature of the signal); the term $\frac{1}{\sqrt{\alpha}}$ is the normalizing term and is used to maintain the same energy before and after the transformation process; β is a translation/shifting parameter, shifting a wavelet simply means delaying (or hastening) its onset, which is used to describe the location of the window in time, at $t = \beta$ and its neighborhood; $a(t)$ is localized or centered, and α changes the frequency content of $a(t)$; $W_\psi(\alpha, \beta)$ is the resulting coefficient, which shows local information with respect to $a(t)$, and is a measurement of the similitude between the dilated/shifted parent wavelet and the signal at time t and scale α . The normalization by the root of scale ensures that the integral energy given by the wavelet is independent of the dilation. The relations between the scale α and the frequency f can be obtained by:

$$f = f_c / (\alpha \cdot \Delta t) \quad (5.58)$$

where Δt is the sampling period; f_c is the center frequency of a wavelet in Hz; and f is the pseudo-frequency corresponding to the scale α .

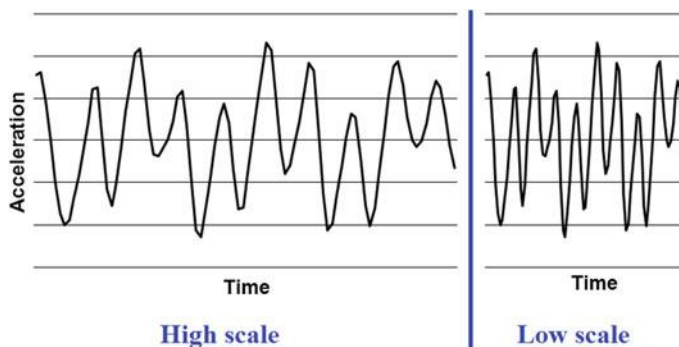


Fig. 5.38 The appearance of signals with high and low value of scale parameter α

The mother wavelet function $\psi(t)$ can be expressed through various formulations. One of the popular functions is the Mexican hat wavelet defined by:

$$\psi(t) = (1 - t^2)e^{-0.5 \cdot t^2} \quad (5.59)$$

The ground motion $a(t)$ can be reconstructed from its wavelet transform $W_\psi a(\alpha, \beta)$ as expressed by:

$$a(t) = \frac{1}{2\pi C_\psi} \int_{-\infty}^{\infty} \int_{-\infty}^{\infty} \frac{1}{\alpha^2} W_\psi a(\alpha, \beta) \psi\left(\frac{t - \beta}{\alpha}\right) d\alpha d\beta \quad (5.60)$$

where the admissibility constant $C_\psi = \int_{-\infty}^{\infty} \frac{|\hat{\psi}(\omega)|^2}{|\omega|} d\omega$, $\hat{\psi}(\omega)$ is the Fourier transform of mother wavelet function $\psi(t)$; the mother wavelet function $\psi(t)$ is a band-pass filter with non-zero frequency and finite energy, C_ψ is therefore also finite.

From the discussion above, it is known that the idea of the continuous wavelet transform is to decompose the function $a(t)$ into the wavelet coefficients $W_\psi(\alpha, \beta)$, using the basis of wavelet functions $\psi(t)$.

For numerical computation performed by computers, α and β cannot be continuous variables such as what the Mexican hat wavelet model expresses above. The Discrete Wavelet Transform (DWT) is therefore introduced by taking only discrete values of α and β : $\alpha = a_0^m$ and $\beta = nb_0 \cdot a_0^m$. Usually, $a_0 = 2$, and b_0 is taken as the minimum sampling rate from the Nyquist criterion [4] for the band-pass filter represented by the mother wavelet.

The resolution of the wavelet coefficients of both CWT and DWT is determined based on the principle of multi-resolution analysis, which gives a decent time resolution at high frequencies and appropriate frequency resolution at low frequencies, as illustrated in Fig. 5.39. In this figure, each box corresponds to a wavelet coefficient and the width of the box along x-axis represents its time resolution, and the height along the y axis represents its frequency resolution. The top row in the figure contains many rectangular boxes with small width along the time axis and large width along the frequency axis, meaning more information in time is included and hence higher frequencies can be resolved better in time. In contrast, the bottom row of the figure corresponds to lower frequencies, and contains resolution boxes having small width along frequency axis, meaning more information in frequency is included, hence lower frequencies can be resolved better in frequency.

From the discussion above, it is obvious that, compared to the Fourier transform, the wavelet transform allows exceptional localization, both in time domain by translating t of the wavelet, and in frequency domain via changing scale α from minimum to maximum. Since the wavelet transform can give a full time–frequency representation of seismic ground motions, it has been extensively researched in respect of representing and characterizing seismic ground motions [108, 109],

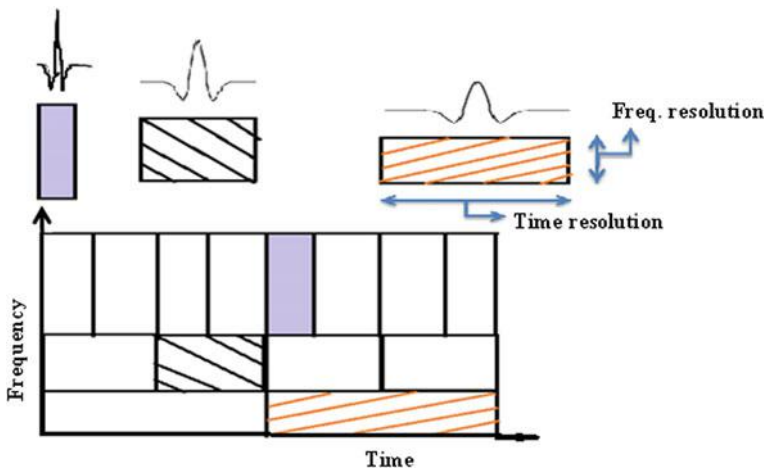


Fig. 5.39 The resolution of the wavelet coefficients [105]

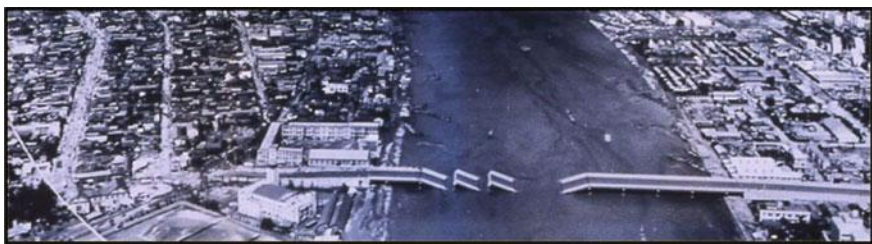


Fig. 5.40 Collapse of the Showa Bridge during the Niigata earthquake 1964

spectrum matching [110], and studying the moving resonance and effect of spectral non-stationarity on structural response [111, 112]. Interested readers may read [113] for details.

As an example of real accident due to moving resonance as mentioned at the beginning of this section, Fig. 5.40 shows the collapse of the Showa Bridge during the magnitude 7.4 Niigata earthquake of 1964. This collapse is suspected to have been induced by soil liquefaction tuned with the period of the liquefied sites: the increased natural period of the bridge due to the elongation of unsupported length of the pile is close to 6 about 70 s after the onset of the ground shaking, and this coincides with the period of ground motions at liquefied soil at about 70 s, which can be observed by converting the ground motion time histories into wavelet energy spectrum using the wavelet transformation, as shown in Fig. 5.41. This tuning effect (resonance) caused excessive deflection at the pile head, resulting in unseating of the bridge deck from the supporting pier and thereby initiating the collapse of the bridge [114].

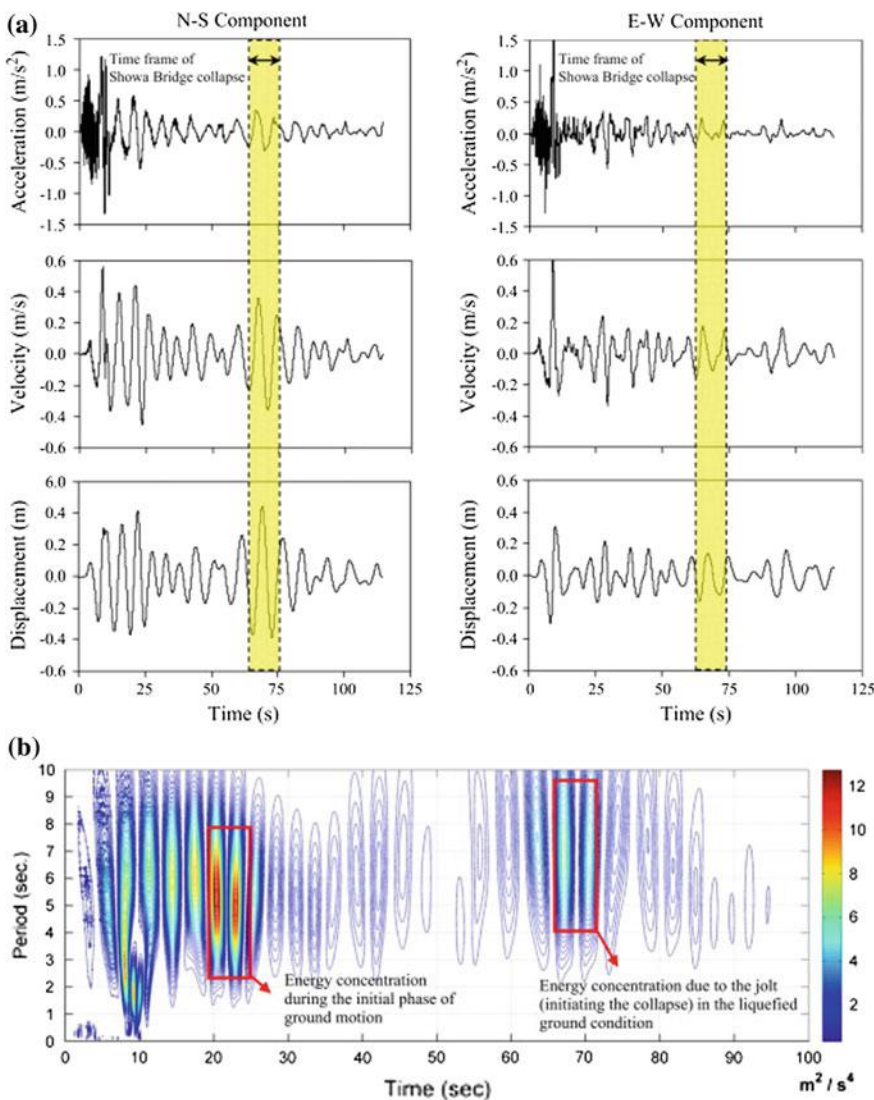


Fig. 5.41 **a** Recorded acceleration record and its corresponding velocity and displacement time histories [115]. **b** Wavelet energy spectrum of NS component of the ground motion [116]

Various researchers [117–121] have developed methods to generate earthquake accelerograms using wavelet analysis. For more details, readers may read the references cited above.

In the past few decades, wavelet mathematics has attracted extensive research efforts. In civil engineering, they have the potential not only to analyze seismic signals and ground motions, but also on a more efficient and thorough understanding of structural responses due to environmental loadings. For example, by using the wavelet transform, the responses of offshore floating structures due to both high frequency wave slamming loads and low frequency hydrodynamic wave loads can be detected in a wavelet energy spectrum. The improved understanding of the method renders wavelet transform a convenient and efficient time-scale decomposition method for handling non-stationary problems. It even has the potential to be used as a tool to assist an efficient structural health monitoring task. However, despite extensive research efforts, the techniques associated with this method are only slowly moving from the realm of mathematics/research into engineering applications.

References

1. Schnabel PB, Lysmer J, Seed HB (1972) SHAKE, a computer program for earthquake response analysis of horizontally layered sites. No. EERC 72-12, Earthquake Engineering Research Center, College of Engineering, University of California, Berkeley
2. Schüller GI (1991) Structural dynamics, recent advances. Springer, Berlin
3. Wilson Ed (2015) Termination of the response spectrum method (RSM), July 13, 2015
4. Jia Junbo (2014) Essentials of applied dynamic analysis. Springer, Heidelberg
5. Yue QJ, Qu Y, Bi XJ, Kärnä T (2007) Ice force spectrum on narrow conical structures. *Cold Reg Sci Technol* 49(2):161–169
6. Schuster Arthur (1898) On the investigation of hidden periodicities with application to a supposed 26 day period of meteorological phenomena. *Terrestr. Magnet.* 3:13–41
7. Schuster Arthur (1900) The periodogram of magnetic declination as obtained from the records of Greenwich Observatory during the years 1871–1895. *Trans Camb Philos Soc* 18:107–135
8. Schuster Arthur (1906) The periodogram and its optical analogy. *Proc R Soc Lond Ser A* 77:136–140
9. Izuru Takewaki (2007) Critical excitation methods in earthquake engineering, 1st edn. Elsevier Science, Oxford
10. Brune JN (1970) Tectonic stress and the spectra of seismic shear waves from earthquakes. *J Geophys Res* 75:4997–5009
11. Brune JN (1971) Correction. *J Geophys Res* 76:5002
12. Hanks TC (1982) f_{\max} . *Bull Seismol Soc Am* 72:1867–1879
13. Papageorgiou AS, Aki K (1983) A specific barrier for the quantitative description of inhomogeneous faulting and the prediction of strong ground motion. II. Applications of the model. *Bull Seismol Soc Am* 73:953–978
14. Weisstein EW (2011) Maximum entropy method, MathWorld—a Wolfram web resource
15. Wilson JF (2003) Dynamics of offshore structures. Wiley, New Jersey
16. Chopra AK (2000) Dynamics of structures: theory and application to earthquake engineering, 2nd edn. Prentice Hall, Upper Saddle River
17. Kramer SL (1996) Geotechnical earthquake engineering. Prentice Hall, Upper Saddle River
18. Kanai K (1967) Semi-empirical formula for the seismic characteristics of the ground. *Bull Earthq Res Inst Univ Tokyo* 35:309–325

19. Tajimi H (1960) A statistical method of determining the maximum response of a building structure during an earthquake. In: Proceedings of the second world conference on earthquake engineering, vol 2, pp 781–798
20. Kubo T, Penzien J (1979) Simulation of three-dimensional strong ground motions along principal axes. *San Fernando Earthq Eng Struct Dyn* 7:265–278
21. Moustafa Abbas (2010) Identification of resonant earth-quake ground motion. *Sādhanā* (Indian Academy of Science) 5(3):355–371
22. Kanaji H, Hamada N, Naganuma T (2005) Seismic retrofit of a cantilever truss bridge in the Hanshin expressway. In: Proceedings of the international symposium on earthquake engineering
23. Chen G, Wu J (2001) Optimal placement of multiple tuned mass dampers for seismic structures. *J Struct Eng ASCE* 127(9):1054–1062
24. Li C, Liu Y (2004) Ground motion dominant frequency effect on the design of multiple tuned mass dampers. *J Earthq Eng* 8(1):89–105
25. Clough RW, Penzien J (1993) Dynamics of structures, 2nd edn. McGraw-Hill, New York
26. Der Kiureghian A, Neuenhofer A (1992) Response spectrum method for multi-support seismic excitations. *Earthq Eng Struct Dyn* 21:713–740
27. Bessason B (1992) Assessment of earthquake loading and response of seismically isolated bridges. PhD thesis, MTA-rapport 1991: 88, Norges Tekniske Høgskole, Trondheim
28. Hanks TC, McGuire RK (1986) The character of high frequency strong ground motion in space and time. *Eng Mech* 112:154–174
29. Boore DM (1983) Stochastic simulation of high frequency ground motions based on seismological models of the radiated spectra. *Bull Seismol Soc Am* 73(6):1865–1894
30. Herman RB (1985) Letter to the editor? An extension of random vibration theory estimates of strong ground motion to large distances. *Bull Seismol Soc Am* 75(5):1447–1453
31. Biot MA (1932) Transient oscillations in elastic systems. PhD thesis No. 259, Aeronautics Department, California Institute of Technology, Pasadena, USA
32. Biot MA (1943) Analytical and experimental methods in engineering seismology. *Trans ASCE* 108(1):365–385
33. Suyehiro K (1926) A seismic vibration analyzer and the records obtained therewith, vol 1. Bulletin of the Earthquake Research Institute, Tokyo
34. Housner GW (1941) An investigation of the effects of earthquakes on buildings. PhD thesis, California Institute of Technology
35. Housner GW, Martel RR, Alford JL (1953) Spectrum analysis of strong motion earthquake. *Bull Seismol Soc Am* 43(2):97–119
36. NEHRP (2009) NEHRP Recommended provisions for new buildings and other structures (FEMA P-750), 2009 ed. Building Seismic Safety Council, National Institute of Building Sciences, Washington, DC
37. ASCE 7-05 (2006) Minimum design loads for buildings and others structures. American Society of Civil Engineers, Reston, VA
38. Kumar M, Stafford PJ, Elghazouli AY (2013) Influence of ground motion characteristics on drift demands in steel moment frames designed to Eurocode 8. *Eng Struct* 52:502–517
39. Kumar M, Stafford PJ, Elghazouli AY (2013) Seismic shear demands in multi-storey steel frames designed to Eurocode 8. *Eng Struct* 52:69–87
40. Brunesi E, Nascimbene R, Casagrande L (2016) Seismic analysis of high-rise mega-braced frame-core buildings. *Eng Struct* 115:1–17
41. Clough RW, Benuska KL, Wilson EI (1965) Inelastic earthquake response of tall buildings. In: Third world conference on earthquake engineering, New Zealand
42. Chen WF, Lui EM (2006) Earthquake engineering for structural design, 1st edn. CRC Press, London
43. Baker JW, Cornell CA (2005) A vector-valued ground motion intensity measure consisting of spectral acceleration and epsilon. *Earthq Eng Struct Dyn* 34(10):1193–1217
44. Baker JW, Cornell CA (2006) Spectral shape, epsilon and record selection. *Earthq Eng Struct Dyn* 35(9):1077–1095

45. ISO19901-2 (2004) Petroleum and natural gas industries—specific requirements for offshore structures—part 2: seismic design procedures and criteria
46. Eurocode 8 (2004) Design of structures for earthquake resistance—part 1: general rules, seismic actions and rules for buildings
47. NORSAR (1998) Seismic zonation for Norway, prepared for Norwegian Council for Building Standardization by NORSAR and Norwegian Geotechnical Institute
48. Gazetas G (2006) Seismic design of foundations and soil–structure interaction. In: First European conference on earthquake engineering and seismology, Geneva
49. Mylonakis G, Gazetas G, Nikolaou A, Michaelides O (2000) The role of soil on the collapse of 18 piers of the elevated Hanshin Expressway in the Kobe earthquake. In: Proceedings of the 12th world conference on earthquake engineering, New Zealand
50. Iervolino I, Cornell CA (2005) Record selection for nonlinear seismic analysis of structures. *Earthq Spectra* 3:685–713
51. Newmark NM, Blume JA, Kapur KK (1973) Seismic design spectra for nuclear power plants. *J Power Div* 99(2):287–303
52. NORSO Standard N-003 (2004) Actions and action effects, Rev. 2, Oct 2004
53. ICC (2007) Standards Australia, structural design actions—earthquake actions in Australia, AS 1170.4-2007, Sydney, Australia
54. China Net for Engineering Construction Standardization (2010) Code for Seismic Design of Buildings, GB 50011-2010. China Building Industry Press, Beijing
55. International Code Council (ICC) (2006) International building code, 5th edn. ICC, Falls Church, VA
56. Building Seismic Safety Council (BSSC) (2009) NEHRP recommended seismic provisions for new buildings and other structures. Rep. FEMA P-750, FEMA, Washington, DC
57. Rodriguez-Marek AR, Bray JD, Abrahamson NA (2001) An empirical geotechnical seismic site response procedure. *Earthq Spectra* 17(1):65–87
58. Anbazhagan P, Parihar A, Rashmi HN (2011) Amplification based on shear wave velocity for seismic zonation: comparison of empirical relations and site response results for shallow engineering bedrock sites. *Geomech Eng* 3(3):189–206
59. Anbazhagan P, Sheikh N, Parihar A (2013) Influence of rock depth on seismic site classification for shallow bedrock regions. *Nat Hazards Rev* 14(2):108–121
60. Lee VW, Trifunac MD, Todorovska M, Novikova EI (1995) Empirical equations describing attenuation of peaks of strong ground motion, in terms of magnitude, distance, path effects and site conditions. Rep. No. CE 95-02, Dept. of Civil Engineering, Univ. of Southern California, Los Angeles
61. Kokusho T, Sato K (2008) Surface-to-base amplification evaluated from KiK-net vertical array strong motion records. *Soil Dyn Earthq Eng* 28(9):707–716
62. Anbazhagan P, Sheikh MN, Tsang HH (2010) Seismic site classification practice in Australia, China and India, suitability. In: Abraham R, Latheswary S, Unnikrishnan N (eds) International conference on materials mechanics and management, New Delhi, pp 189–197
63. Boore DM (2004) Estimating V_s (30) (or NEHRP site classes) from shallow velocity models. *Bull Seismol Soc Am* 94(2):591–597
64. Atkinson GM, Boore DM (2003) Empirical ground-motion relations for subduction-zone earthquakes and their application to Cascadia and other regions. *Bull Seismol Soc Am* 93:1703–1729
65. Boore DM, Joyner WB, Fumal TE (1997) Equations for estimating horizontal response spectra and peak acceleration from western North American earthquakes: a summary of recent work. *Seismol Res Lett* 68(1):128–153
66. Dobry R, Iai S (2000) Recent developments in the understanding of earthquake site response and associated seismic code implementation. In: Proceedings of GeoEng2000, international conference on geotechnical & geological engineering, Melbourne, Australia, pp 186–129
67. Dobry R, Ramos R, Power MS (1997) Site factors and site categories in seismic codes: a perspective. In: Power MS, Mayes RL (eds) Proceedings of the NCEER Workshop on the

- national representation of seismic ground motion for new and existing highway facilities, Report NCEER-97-0010, May 29–30, San Francisco, pp 137–170
- 68. Papageorgiou AS, Kim J (1991) Study of the propagation and amplification of seismic waves in Caracas Valley with reference to the 29 July 1967 earthquake: SH waves. *Bull Seismol Soc Am* 81(6):2214–2233
 - 69. Chang SW, Bray JD (1995) Seismic response of deep, stiff soil deposits in the Oakland, California area during the Loma Prieta earthquake. Report. No. UCB/GT/95-06, Geotechnical Engineering, Dept. of Civil and Environmental Engineering, Univ. of California, Berkeley, California
 - 70. Motosaka M, Nagano M (1997) Analysis of amplification characteristics of ground motions in the heavily damaged belt zone during the 1995 Hyogo-ken Nanbu earthquake. *Earthq Eng Struct Dyn* 26(3):377–393
 - 71. Bozorgnia Y, Mahin SA, Brady AG (1998) Vertical response of 12 structures recorded during the Northridge earthquake. *Earthq Spectra* 14:411–432
 - 72. Richter CF (1958) Elementary seismology. WH Freeman and Company, San Francisco
 - 73. Papazoglou AJ, Elnashai AS (1996) Analytical and field evidence of the damaging effect of vertical earthquake ground motion. *J Earthq Eng Struct Dyn* 25(10):1109–1137
 - 74. Elgamal AW, Liangcai H (2004) Vertical earthquake motions records: an overview. *J Earthq Eng* 8(5):663–697
 - 75. Bozorgnia Y, Campbell KW (2004) The vertical to horizontal response spectral ratio and tentative procedures for developing simplified V/H and vertical design spectra. *J Earthq Eng* 8:175–207
 - 76. Bozorgnia Y, Campbell K (2016) Ground motion model for the vertical-to-horizontal (V/H) ratios of PGA, PGV, and response spectra
 - 77. Kalkan Erol, Graizer Vladimir (2007) Multi-component ground motion response spectra for coupled horizontal, vertical, angular accelerations and tilt. *ISET J Earthq Technol* 44 (1):259–284 (Paper No. 485)
 - 78. Akkar S, Sandikkaya MA, Ay BO (2014) Compatible ground-motion prediction equations for damping scaling factors and vertical to horizontal spectral amplitude ratios for the broader European region. *Bull Earthq Eng* 12:517–547
 - 79. Gülerce Z, Abrahamson NA (2011) Site specific design spectra for vertical ground motion. *Earthq Spectra* 27:1023–1047
 - 80. Bommer JJ, Akkar S, Kale Ö (2011) Model for vertical to horizontal response spectral ratios for Europe and the Middle East. *Bull Seismol Soc Am* 101(4):1783–1806
 - 81. Bozorgnia Y, Campbell K (2004) Vertical to horizontal response spectra ratio and tentative procedures for developing simplified V/H and vertical design spectra. *J Earthq Eng* 8 (2):175–207
 - 82. NORSAR, Risk Engineering, Inc. (1991) Ground motions from earthquake on Norwegian continental shelf. Summary report, Report for Operatørkomite Nord (OKN), Stavanger, Norway
 - 83. GB 50267-97 (1998) Code for seismic design of nuclear power plants. Ministry of Construction of People's Republic of China
 - 84. ISO19901-2 (2016) Petroleum and natural gas industries—specific requirements for offshore structures—part 2: seismic design procedures and criteria, 2nd edn
 - 85. JTG/T B02-01-2008 (2008) Guidelines for seismic design of high bridges. Ministry of Transport of the People's Republic of China
 - 86. Belstos AS, Newmark NM (1960) Effect of inelastic behaviour on the response of simple systems to earthquake motions. In: Proceedings of the second world conference on earthquake engineering, Tokyo, pp 895–912
 - 87. Penzien J (1960) Elasto-plastic response of idealized multi-story structures subjected to a strong motion earthquake. In: Proceedings of the second world conference on earthquake engineering
 - 88. Berg GV, Thomaides SS (1960) Energy consumption by structures in strong motion earthquakes. In: Proceedings of the second world conference on earthquake engineering

89. Naeim F (2001) The seismic design handbook, 2nd edn. Kluwer Academic Publisher, USA
90. Wakabayashi M (1980) Design of earthquake resistant buildings. McGraw-Hill, New York
91. Blume JA, Newmark NM, Corning L (1961) Design of multistory reinforced concrete buildings for earthquake motions. Portland Cement Association, Chicago
92. Clough RW (1955) On the importance of higher modes of vibration in the earthquake response of a tall building. *Bull Seismol Soc Am* 45(4):289–301
93. International Association of Oil and Gas Producers (2014) Reliability of offshore structures —current design and potential inconsistencies. OGP Report No. 486
94. Spudich P, Chiou BSJ (2008) Directivity in NGA earthquake ground motions: analysis using isochrone theory. *Earthq Spectra* 24:279–298
95. Lin YK, Zhang R, Yong Y (1990) Multiply supported pipeline under seismic wave excitations. *J Eng Mech ASCE* 116:1094–1108
96. Boore DM, Bommer JJ (2005) Processing of strong motion accelerograms: needs, options and consequences. *Soil Dyn Earthq Eng* 25:93–115
97. Akkar Sinan, Boore DM (2009) On baseline corrections and uncertainty in response spectra for baseline variations commonly encountered in digital accelerograph records. *Bull Seismol Soc Am* 99(3):1671–1690
98. Boore DM (2001) Effect of baseline corrections on displacements and response spectra for several recordings of the 1999 Chi-Chi, Taiwan, earthquake. *Bull Seismol Soc Am* 91:1199–1211
99. www.seismosoft.com
100. Iwan WD, Moser MA, Peng CY (1985) Some observations on strongmotion earthquake measurement using a digital accelerograph. *Bull Seismol Soc Am* 75:1225–1246
101. Yang J, Li JB, Lin G (2006) A simple approach to integration of acceleration data for dynamic soil–structure interaction analysis. *Soil Dyn Earthq Eng* 26:725–734
102. Zhou Y, Zhang W, Yu H (1997) Analysis of long-period error for accelerograms recorded by digital seismographs. *Earthq Eng Eng Vib* 17(2):1–9 (in Chinese)
103. Gupta VK (2009) Wavelet-based random vibrations in earthquake engineering (lecture). IIT Kanpur, India
104. Gauppillaud P, Grossmann A, Morlet J (1984) Cycle-octave and related transforms in seismic signal analysis. *Geo-exploration* 23:85–102
105. Pradeep N (2011) Analyzing the effect of moving resonance on seismic response of structures using wavelet transforms. Virginia Polytechnic Institute and State University
106. Heidari A, Salajegheh E (2008) Wavelet analysis for processing of earthquake. *Asian J Civil Eng (Build Hous)* 9(5):513–524
107. Li Hongnan, Yi Tinghua, Ming Gu, Huo Linsheng (2009) Evaluation of earthquake-induced structural damages by wavelet transform. *Prog Nat Sci* 19(4):461–470
108. Chanerley AA, Alexander NA (2010) Obtaining estimates of the low-frequency “fling”, instrument tilts and displacement timeseries using wavelet decomposition. *Bull Earthq Eng* 8 (2):231–255
109. Zhou T, Li Z, Jia J, Jia Z (2003) Dynamic response analysis of isolated seismic foundation structure under earthquake motion using wavelet transformation. *Ind Constr* 33(6):21–23
110. Atik L, Abrahamson N (2010) An improved method for nonstationary spectral matching. *Earthq Spectra* 26(3):601–607
111. Koduru SD (2010) Influence of spectral nonstationarity on structural damage. In: Proceedings of the ninth US National and 10th Canadian conference on earthquake engineering, vol 8
112. Cao H, Friswell M (2009) The effect of energy concentration of earthquake ground motions on the nonlinear response of RC structures. *Soil Dyn Earthq Eng* 29(2):292–299
113. Albert B, Francis JN (2009) A first course in wavelet with Fourier analysis. Wiley, New York
114. Bhattacharya S, Tokimatsu K, Goda K, Sarkar R, Shadlou M, Rouholamin M (2014) Collapse of Showa Bridge during 1964 Niigata earthquake: a quantitative reappraisal on the failure mechanisms. *Soil Dyn Earthq Eng* 65:55–71

115. Kudo K, Uetake T, Kanno T (2008) Re-evaluation of nonlinear site response during the 1964 Niigata earthquake using the strong motion records at Kawagishi-cho, Niigata city. In: Proceedings of the 12th world conference on earthquake engineering
116. Yoshida N, Tazoh T, Wakamatsu K, Yasuda S, Towhata I, Nakazawa H, Kiku H (2007) Causes of Showa Bridge collapse in the 1964 Niigata earthquake based on eyewitness testimony. *Soils Found* 47(6):1075–1087
117. Iyama J, Kuwamura H (1999) Application of wavelet to analysis and simulation of earthquake motions. *Earthq Eng Struct Dyn* 28:255–272
118. Mukherjee S, Gupta K (2002) Wavelet-based characterization of design ground motions. *Earthq Eng Struct Dyn* 31:1137–1190
119. Zhou Z, Adeli H (2003) Wavelet energy spectrum for time–frequency localization of earthquake energy. *Comput Aided Civil Infrastruct Eng* 13:133–140
120. Suárez LE, Montejo LA (2005) Generation of artificial earthquakes via the wavelet transform. *Int J Solids Struct* 42(21–22):5905–5919
121. Chordati Amiri G, Asadi A (2008) New method for simulation earthquake records by using adapted wavelet. In: The 14th world conference on earthquake engineering, Beijing

Chapter 6

Determining Response Spectra by Design Codes

6.1 General

Ideally, if one uses abundant ground motion records or converts those motions into many corresponding individual response spectra, and takes these records or response spectra as earthquake loads input for a structure, the response and strength evaluation for the structure can be relatively reliable. However, in reality, this is not feasible. Therefore, decent approaches have to be adopted to compromise with the reality for engineering practice.

Generally, there are two major practical methods for obtaining the ground motions: code based simplified method, as will be presented in this chapter, and site specific response analysis method, presented in Sect. 4.3.

The former is a convenient means to estimate the free-field ground motions by approximating the site effects with a few site/soil classes based on the characteristics of seismic wave propagation at the site. By inputting these data and other relevant information into a standardized response spectrum shape, the resultant design spectrum can be obtained. The code based simplified method only requires the information from the geotechnical report and simple spreadsheet or even hand calculation, and the outputs for the simplified method are a design spectrum representing the design ground motions. This may be applicable for most typical land-based building structures.

However, for offshore structures and other important infrastructures such as nuclear power plants, dams, irregular structures, and for structures sitting on soft soil sites, detailed site response analysis is recommended. The outputs for the detailed methods are either a design response spectrum or ground motion time histories. The site response analysis can often be performed based on the assumption that the soil layer extends horizontally and infinitely, in which a one-dimensional analysis is applicable. More sophisticated analysis such as two-dimensional or three-dimensional analysis may be required under certain conditions to account for the surface wave propagation and geometric irregularity, see Sect. 4.3.8 for a

discussion. In addition, the ground motions may also be strongly influenced by the presence of foundations [1].

It is obvious that the seismic loading determined from codes and standards is usually more conservative than one developed from a site specific response analysis. This difference continuously encouraged engineering communities more and more to choose site specific response analyses for determining design ground motions.

Sections 6.2, 4.3, and Chap. 7 provide practical guidance on how to obtain the seismic ground motion intensity based on the two methods mentioned above.

6.2 Code Based Simplified Method for Calculating the Response Spectrum

Major seismic design codes provide simplified methods for engineers to determine the ground motion. A few important ones for seismic design of either land-based or offshore structures are listed below:

- ISO19901-2, Petroleum and Natural Gas Industries—Specific Requirements for Offshore Structures—Part 2: Seismic Design Procedures and Criteria, 2nd ed., 2016
- Eurocode 8: Design of Structures for Earthquake Resistance, Part 1: General Rules, Seismic Actions and Rules For Buildings, 2004
- Uniform Building Code, Volume 2: Structural Engineering Design Provisions, 1997
- International Building Code, 2006
- Code for Seismic Design of Buildings, GB 50011-2010 (China), 2010
- Building Center of Japan: The Seismic Code: Guidelines for Structural Calculations

The construction of the code based response spectrum is mainly based on the amplification due to the local soil/site condition at different damping levels. However, if possible, it is recommended to perform a dynamic site response analysis (Sect. 4.3) to obtain the ground motion and the response spectrum. This is especially important for soft soil conditions, as mentioned before.

It is noticed that the ground type in the majority of the design codes is determined by the average shear wave velocity $v_{s,30}$ in the uppermost 30 m of the soil. However, in case the the site consists of a shallow sedimentary soil, or the impedance contrast between two adjacent soil layers is significant, a lower soil column depth rather than the uppermost 30 m actually determines the average shear wave velocity, which is discussed in Sect. 4.2.2. If this is the case, it is recommended to consult relevant specialists to determine a correct ground type or more preferably to perform a site response analysis to determine design ground motions.

6.2.1 Construction of Design Spectrum in Eurocode 8 for Land-Based Structure

For typical land-based structures, Eurocode 8 [2] gives systematic guidance on how to construct the design spectrum.

The general procedure can be summarized as follows:

1. Specify the seismic action types: if the earthquakes that contribute most to the seismic hazard (Sect. 9.1) defined for the site for the purpose of probabilistic hazard assessment have a surface wave magnitude, M_s , not greater than 5.5, it is recommended that the Type 2 spectrum be adopted.
2. Soil classification: identify soil classes by the average shear wave velocity $v_{s,30}$ in the uppermost 30 m of the soil. See Table 6.1 for details. The average shear velocity $v_{s,30}$ is calculated by:

Table 6.1 Category of soil classes A–E in Eurocode 8 [2]

Ground type	Description of stratigraphic profile	Parameters		
		$v_{s,30}$ (m/s)	N_{SPT} (blows/30 cm)	c_u (kPa)
A	Rock or other rock-like geological formation, including at most 5 m of weaker material at the surface	>800	–	–
B	Deposits of very dense sand, gravel, or very stiff clay, at least several tens of meters in thickness, characterized by a gradual increase of mechanical properties with depth	360–800	>50	>250
C	Deep deposits of dense or medium dense sand, gravel or stiff clay with thickness from several tens to many hundreds of meters	180–360	15–50	70–250
D	Deposits of loose-to-medium cohesionless soil (with or without some soft cohesive layers), or of predominantly soft to firm cohesive soil	<180	<15	<70
E	A soil profile consisting of a surface alluvium layer with v_s values of type C or D and thickness varying between about 5 m and 20 m, underlain by stiffer material with v_s versus > 800 m/s			
S ₁	Deposits consisting of or containing a layer at least 10 m thick, of soft clays/silts with a high plasticity index (PI > 40) and high water content	<100 (indicative)	–	10–20
S ₂	Deposits of liquefiable soils, of sensitive clays, or any other soil profile not included in types A–E or S ₁			

$$v_{s,30} = \frac{30}{\sum_{i=1,N} \frac{h_i}{v_i}} \quad (6.1)$$

where h_i and v_i are the thickness (in meters) and shear wave velocity (at a shear strain level of 10^{-5} or less) of the i th formation or layer, in a total of N , existing in the top 30 m.

Eurocode 8 [2] defines five different soil types from A to E as shown in Table 6.1. The main difference between each class is the average shear velocity $v_{s,30}$, that exists in the upper 30 m of the soil layers. In the situation in which the average shear wave velocity is not available, the standard penetration test (SPT) blow-count N_{SPT} can be used for soil classification. In Table 6.1, c_u is the undrained shear strength. Attention needs to be paid to soil class S_1 and S_2 , under which both the ground motions and soil–structure interaction can be anomalous, and for which special studies for the definition of the seismic action are required. Particularly for S_2 , the possibility of soil failure under the seismic action shall be taken into account. For soil class S_1 , the soils at the site typically have very low values of $v_{s,30}$, low internal damping and an abnormally extended range of linear behavior and can therefore produce anomalous seismic site amplification and soil–structure interaction effects; special study to define the seismic action should be carried out in order to establish the dependence of the response spectrum on the thickness and $v_{s,30}$ value of the soft clay/silt layer and on the stiffness contrast between this layer and the underlying materials (see the example given in Sect. 4.2.2).

3. Establish horizontal and vertical elastic response spectra

- Horizontal response spectrum

The horizontal components of the seismic action can be constructed in a similar but more convenient way than what is described in Sect. 5.4.2.2. As indicated in Fig. 6.1, T_B , T_C , T_D and 4 s in the abscissa of the figure define the range of constant ground acceleration, velocity and displacement region. Instead of checking the amplification factor as described in Sect. 5.4.2.2 and Table 5.3, the ordinate of the spectrum can be calculated as:

$$S_e(T) = \begin{cases} a_g \cdot S \cdot \left[1 + \frac{T}{T_B} \cdot (2.5 \cdot \eta - 1) \right] & \text{at } 0 \leq T \leq T_B \\ 2.5 \cdot a_g \cdot S \cdot \eta & \text{at } T_B \leq T \leq T_C \\ 2.5 \cdot a_g \cdot S \cdot \eta \cdot \left[\frac{T_C}{T} \right] & \text{at } T_C \leq T \leq T_D \\ 2.5 \cdot a_g \cdot S \cdot \eta \cdot \left[\frac{T_C T_D}{T^2} \right] & \text{at } T_D \leq T \leq 4 \text{ s} \end{cases} \quad (6.2)$$

where $S_e(T)$ is the horizontal elastic response spectrum; T is the undamped vibration period of a linear single-degree-of-freedom system; a_g is the design ground acceleration on type A ground ($a_g = \gamma_I \cdot a_{gR}$); γ_I is the importance factor, which varies from 0.8 (important class I, minor important) to 1.4 (important class IV, vital

important); a_{gR} is the reference peak ground acceleration on type A ground, which is decided by each national authority for each seismic zone and can be derived from zonation maps in the national annex. It normally corresponds to a reference probability of exceedance for the non-collapse requirement (or equivalently the reference probability of exceedance in 50 years); as given in Tables 6.2 and 6.3, T_B is the lower limit of the period of the constant spectral acceleration branch, T_C is the upper limit of the period of the constant spectral acceleration branch, T_D is the value defining the beginning of the constant displacement response range of the spectrum; S is the soil factor, which represents the ground motion amplification due to the presence of (soft) subsoil layers in relation to geological bedrock (halfspace); η is the damping correction factor with a reference value of $\eta = 1$ for 5 % viscous damping, if another damping value of $\xi\%$ different from 5 % is used, it can be determined as $\eta = \sqrt{\frac{10}{5+\xi}} \geq 0.55$.

It is worth mentioning that, through investigations for characterizing long period ground motions for seismic design of structures, various studies [8–10] state that significant long period values can be expected, thus a T_D of more than 2 s for the 5 % damped target spectra is suggested, i.e., spectral displacement demands increase linearly up to T_D .

Fig. 6.1 Description of elastic acceleration design spectrum according to Eurocode 8 [2]

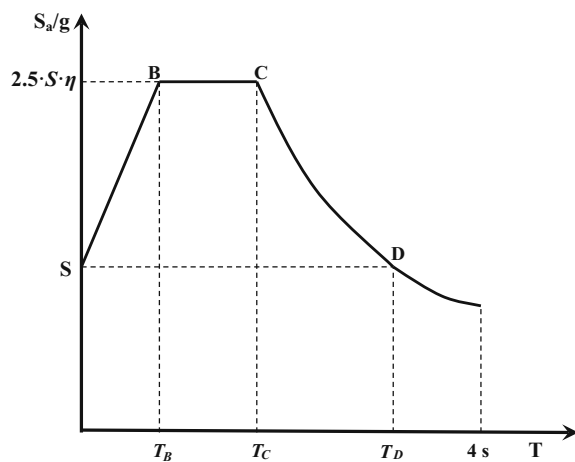


Table 6.2 The values of S and T_B , T_C and T_D recommended for Type 1 (the earthquake has a surface wave magnitude M_s greater than 5.5) elastic response spectra^a [2]

Ground type	S	T_B	T_C	T_D
A	1.0	0.15	0.4	2.0
B	1.2	0.15	0.5	2.0
C	1.15	0.20	0.6	2.0
D	1.35	0.20	0.8	2.0
E	1.4	0.15	0.5	2.0

Table 6.3 The values of S and T_B , T_C and T_D recommended for Type 2 (the earthquake has a surface magnitude M_s not greater than 5.5) elastic response spectra^a [2]

Ground type	S	T_B	T_C	T_D
A	1.0	0.05	0.25	1.2
B	1.35	0.05	0.25	1.2
C	1.5	0.10	0.25	1.2
D	1.8	0.10	0.30	1.2
E	1.6	0.05	0.25	1.2

^aFor ground types S_1 and S_2 , special studies should provide the corresponding values of S , T_B , T_C and T_D

- Vertical response spectrum

As described in Sect. 5.4.4, the PGA and local soil amplification for vertical response spectrum is different from that of the horizontal response spectrum. Therefore, the design vertical ground acceleration a_{vg} should be smaller than its horizontal counterpart a_g , and the soil factor S should always be 1.0. T_B , T_C , T_D and 4 s in the abscissa of Fig. 6.1 can still be used to define the range of constant ground acceleration, velocity and displacement region for the vertical response spectrum. The ordinate of the spectrum can then be calculated as:

$$S_{ve}(T) = \begin{cases} a_{vg} \cdot \left[1 + \frac{T}{T_B} \cdot (3.0 \cdot \eta - 1) \right] & \text{at } 0 \leq T \leq T_B \\ 3.0 \cdot a_{vg} \cdot \eta & \text{at } T_B \leq T \leq T_C \\ 3.0 \cdot a_{vg} \cdot \eta \cdot \left[\frac{T_C}{T} \right] & \text{at } T_C \leq T \leq T_D \\ 3.0 \cdot a_{vg} \cdot \eta \cdot \left[\frac{T_C \cdot T_D}{T^2} \right] & \text{at } T_D \leq T \leq 4 \text{ s} \end{cases} \quad (6.3)$$

where $S_{ve}(T)$ is the vertical elastic response spectrum; T is the undamped vibration period of a linear single-degree-of-freedom system; a_{vg} is the design vertical ground acceleration, $a_{vg} = \begin{cases} 0.9a_g \text{ for Type 1} \\ 0.45a_g \text{ for Type 2} \end{cases}$; T_B is the lower limit of the period of the constant spectral acceleration branch, $T_B = 0.05$ s for both Type 1 and Type 2 spectrum; T_C is the upper limit of the period of the constant spectral acceleration branch, $T_C = 0.15$ s for both Type 1 and Type 2 spectrum; T_D is the value defining the beginning of the constant displacement response range of the spectrum, $T_D = 1.0$ s for both Type 1 and Type 2 spectrum; η is defined the same as that of the horizontal response spectrum.

6.2.2 Construction of Design Spectrum in ISO 19901 and Norsok for Offshore Structures

For offshore structures, a number of codes such as ISO 19901-2 [3] and Norsok [4] provide instructions on how to construct the design spectrum.

6.2.2.1 Design Spectrum by ISO 19901

ISO 19901 [3] gives step by step guidance on how to construct the design spectrum.

The following steps illustrate the procedure for calculating both the horizontal and vertical response spectrum based on ISO 19901-2 [3, 5]:

1. Locate the sites for investigation in the seismic zonation maps in either ISO 19901-2 [3] or relevant national annex, which shows the rock outcrop spectral accelerations at vibration period of 1 and 0.2 s with 1000 year return period (Sect. 9.1.3). Then obtain the site spectrum accelerations $S_{a,\text{map}}$ ($T = 1$ s) and $S_{a,\text{map}}$ ($T = 0.2$ s).
2. Soil classification: identify soil classes by the average shear wave velocity $v_{s,30}$ in the uppermost 30 m of the soil:

$$v_{s,30} = \frac{30}{\sum_{i=1,N} \frac{h_i}{v_i}} \quad (6.4)$$

where h_i and v_i are the thickness (in meters) and shear wave velocity of the i th formation or layer, in a total of N , existing in the top 30 m of effective seabed.

ISO 19901-2 [3] defines five different soil classes from A/B to F as shown in Table 6.4. The main difference between each class is the average shear velocity $v_{s,30}$ that exists in the upper 30 m of the seabed. In case the average shear velocity is not available, the average of normalized cone penetration resistance (\bar{q}_{cl}) for sand or undrained shear strength c_u for clay in the upper 30 m of the seabed can be used for soil classification according to the equation above, where v_s is replaced by \bar{q}_{cl} and c_u ; and \bar{q}_{cl} can be calculated as:

$$\bar{q}_{cl} = \left(\frac{q_c}{p_a} \right) \cdot \left(\frac{p_a}{\sigma'_{v0}} \right)^{\frac{1}{2}} \quad (6.5)$$

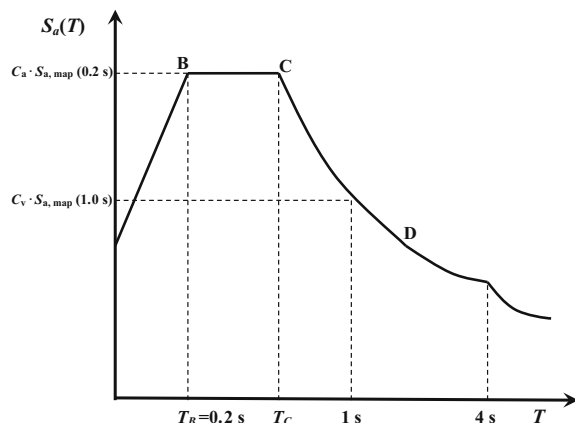
where q_c is the cone penetration resistance; $p_a = 100$ kPa is the atmospheric pressure; σ'_{v0} is the vertical effective stress.

3. Construct horizontal and vertical elastic response spectra with 1000 years' return period
 - Horizontal response spectrum with a return period of 1000 years

As illustrated in Fig. 6.2, 0.2, 1, and 4 s in the abscissa of the figure define the boundary where different curves applied. Instead of checking the amplification factor described in Sect. 5.4.2.2 and Table 5.3, the ordinate of the spectrum can be calculated as:

Table 6.4 Category of soil classes A–E in ISO 19901-2 [3]

Ground type	Description of stratigraphic profile	Parameters		
		$v_{s,30}$ (m/s)	Sand: \bar{q}_{cl}	Clay: c_u (kPa)
A/B	Hard rock/rock, thickness of soft sediments <5 m	>750	—	—
C	Very dense hard soil and soft rock	350–750	≥ 200	≥ 200
D	Stiff to very stiff soil	180–350	80–200	80–200
E	Soft to firm soil	120–180	<80	<80
F	—	Any profile, including those otherwise classified as A to E, containing soils having one or more of the following characteristics: <ul style="list-style-type: none"> • $v_{s,30} \leq 120$ m/s • Soils vulnerable to potential failure or collapse under seismic actions such as liquefiable soils, highly sensitive clays, collapsible weakly cemented soils • Ooze (clay containing more than 30 % calcareous or siliceous material of biogenic origin) with a thickness of more than 10 m • Soil layers with high gas content or ambient excess pore pressure greater than 30 % of in situ effective overburden; layers greater than 2 m thick with sharp contrast in shear wave velocity (greater than $\pm 30\%$) and/or undrained shear strength (greater than $\pm 50\%$) compared to adjacent layers 		

Fig. 6.2 Description of elastic acceleration design spectrum according to ISO 19901-2 [3]

$$S_{a,\text{site}}(T) = \begin{cases} (3T + 0.4) \cdot \eta \cdot C_a \cdot S_{a,\text{map}}(T = 0.2 \text{ s}) & \text{at } 0 \leq T \leq 0.2 \text{ s} \\ C_v \cdot \eta \cdot S_{a,\text{map}}(T = 1.0 \text{ s})/T & \text{at } 0.2 < T \leq 4 \text{ s} \\ 4 \cdot C_v \cdot \eta \cdot S_{a,\text{map}}(T = 1.0 \text{ s})/T^2 & \text{at } T > 4 \text{ s} \end{cases} \quad (6.6)$$

where $S_{a,\text{site}}(T)$ is the horizontal acceleration response spectrum at site with a return period of 1000 years; T is the undamped vibration period of a linear single-degree-of-freedom system; $S_{a,\text{map}}(T)$ is the rock outcrop spectral accelerations at vibration period of T with 1000 years of return period; η is the damping correction factor with a reference value of $\eta = 1$ for 5 % viscous damping, for other damping levels of $\xi\%$, it can be determined as $\eta = \frac{\ln(100/\xi)}{\ln(20)}$. C_a is the site correction factor applied to the acceleration part of a response spectrum, shown in Tables 6.5 and 6.7 for shallow and pile foundation, respectively; $C_v(T)$ is the site correction factor applied to the velocity part of a response spectrum, as shown in Tables 6.6 and 6.7 for shallow and pile foundation, respectively.

- Vertical response spectrum

ISO 19901-2 2004 [3], it requires that 50 % of the corresponding horizontal spectral acceleration be taken as the site vertical spectral acceleration at a period T . The vertical spectrum shall not be further reduced due to water column effects (Sect. 4.4). However, the second edition of ISO 19901-2 [5] released in 2016

Table 6.5 Values of C_a recommended for constructing design response spectra for shallow foundations and 0.2 s period spectral acceleration [3]

Ground type	$S_{a,\text{map}}(T = 0.2 \text{ s})$				
	$\leq 0.25 \text{ g}$	$(0.25 \text{ g}, 0.5 \text{ g}]$	$(0.5 \text{ g}, 0.75 \text{ g}]$	$(0.75 \text{ g}, 1.0 \text{ g})$	$\geq 1.25 \text{ g}$
A/B	1.0	1.0	1.0	1.0	1.0
C	1.2	1.2	1.1	1.0	1.0
D	1.6	1.4	1.2	1.1	1.0
E	2.5	1.7	1.2	0.9	0.9
F	A site specific geotechnical investigation and dynamic site response analyses shall be performed				

Table 6.6 Values of C_v recommended for constructing design response spectra for shallow foundations and 1.0 s period spectral acceleration [3]

Ground type	$S_{a,\text{map}}(T = 1.0 \text{ s})$				
	$\leq 0.1 \text{ g}$	$(0.1 \text{ g}, 0.2 \text{ g}]$	$(0.2 \text{ g}, 0.3 \text{ g}]$	$(0.3 \text{ g}, 0.4 \text{ g})$	$\geq 0.5 \text{ g}$
A/B	1.0	1.0	1.0	1.0	1.0
C	1.7	1.6	1.5	1.4	1.3
D	2.4	2.0	1.8	1.6	1.5
E	3.5	3.2	2.8	2.4	2.4
F	A site specific geotechnical investigation and dynamic site response analyses shall be performed				

Table 6.7 Values of C_a and C_v recommended for constructing design response spectra for deep pile foundations [3]

Ground type	C_a	C_v
A/B	1.0	0.8
C	1.0	1.0
D	1.0	1.2
E	1.0	1.8
F	A site specific geotechnical investigation and dynamic site response analyses shall be performed	

recommends a modification of V/H ratio (Fig. 5.31) compared with its previous edition released in 2004 [3]. This change is particularly apparent at a low period range lower than 0.1 s, in which a V/H ratio of 1.0 is specified at this period range. This could potentially set a higher requirement for the seismic resistance of topside structures. For more information, see Sect. 5.4.4.

4. Seismic action procedure

The ALE (abnormal severity under the action of which a structure should not suffer complete loss of integrity) spectral acceleration ($S_{a,ALE}(T)$) is obtained based on values of the 1000 year spectral acceleration at the site:

$$S_{a,ALE}(T) = N_{ALE} \cdot S_{a,site}(T) \quad (6.7)$$

where the scaling factor N_{ALE} is equal to 1.6 for L1 type (target annual probability of failure of 4×10^{-4}) structures; 1.15 for L2 type (target annual probability of failure of 1×10^{-3}) structures; and 0.85 for L3 type (target annual probability of failure of 2.5×10^{-3}) structures.

Different from the utilization of behavior factor described in Sect. 5.4.3.2, by dividing the ALE (abnormal severity under the action of which a structure should not suffer complete loss of integrity) spectral acceleration $S_{a,ALE}(T)$ with a reserve capacity factor C_r (regardless of variation of period), the spectra acceleration for ELE (earthquake with a severity under which the structure should sustain without major damage), $S_{a,ELE}(T)$ condition can be obtained.

For fixed steel offshore structures, the number of legs is an essential parameter for assessing the reserve strength and energy dissipation. ISO 19902 [3, 5] recommends a minimum reserve capacity factor (C_r) of 1.1 for a general fixed offshore steel structure, and 1.4 for a platform with three or more legs. To avoid the situation in which the return periods for the ELE condition are too short, the reserve capacity factor shall in no case exceed 2.8 for L1 type structures, 2.4 for L2 structures, and 2.0 for L3 structures.

$$S_{a,ELE}(T) = \frac{S_{a,site}(T)}{C_r} \quad (6.8)$$

The seismic reserve capacity factor C_r considers the static reserve strength and the ability to sustain large non-linear deformations of each structure type (e.g. steel versus reinforced concrete). It represents the ratio of spectral acceleration causing catastrophic system failure of the structure, to the ELE spectral acceleration [3, 5].

For any specified return period, the seismic action can be calculated based on site specific seismic hazard curve (Sect. 9.1.3). Readers may refer to Sects. 9.1.3 and 9.3 for a presentation of this method.

6.2.2.2 Design Spectrum by Norsok N-003

As specified by Norsok N-003 [4], currently required for determining action and action effects for offshore installations in Norway, Fig. 6.3 shows the bedrock spectral displacement, velocity and acceleration (normalized to 10 m/s^2 acceleration at 40 Hz for the horizontal main motion component) varied with the frequency. Furthermore, it gives the local soil amplification factor varied with period. The soil/site is only categorized by two classes of soils (soft and stiff/hard) compared with the 5 classes of soils (Table 6.4) given by ISO 19901-2 [3] [5]. Note that both the bedrock spectra and the amplification factor are divided into the probability of exceedance of 10^{-2} (represents a seismic event that may reasonably be expected to occur during operation life of an offshore platform) and 10^{-4} (represents a seismic event that has little likelihood of occurring during operation life of the platform). This figure can be used together with the accelerations given in seismic zonation maps. In terms of seismic hazard described by PGA contour lines, Fig. 6.4 shows an example of a seismic zonation map for the North Sea with both 100 year (probability of exceedance of 10^{-2}) and 10,000 year (probability of exceedance of 10^{-4}) return period of earthquake events [6]. For example, according to this map, the horizontal bedrock peak ground acceleration at the site of Statfjord oil field (latitude 61.2, longitude 1.83) is 2.7 m/s^2 for a 10,000 year and 0.33 m/s^2 for a 100 year return period of earthquake. The spectrum with an annual probability of exceedance of 10^{-4} and 10^{-2} are then multiplied by the normalized spectrum in Fig. 6.3 with a factor of 0.27 and 0.033. Figure 6.5 shows the bedrock response spectra for events with 100 year and 10,000 year return period of earthquake.

Based on the assumption that the ratio between vertical response spectrum to horizontal response spectrum is equal to 0.7 for frequencies greater than 3 Hz, equal to 0.9 for frequencies less than 1 Hz and between 0.9 to 0.7 for frequencies between 1 and 3 Hz, the vertical response spectrum can be constructed as shown in Fig. 6.6.

Note that the spectrum shown in Fig. 6.3 is based on a damping level of 5 % of critical damping. If the damping has a value other than 5 %, the spectrum can be scaled with regard to the expected acceleration level at 50 Hz or to the expected

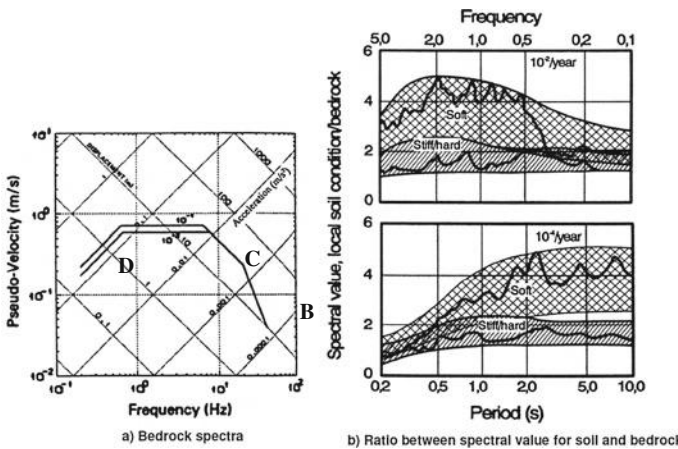


Fig. 6.3 Design response spectra (normalized to 10 m/s^2 acceleration at 40 Hz) with 5 % damping [4]

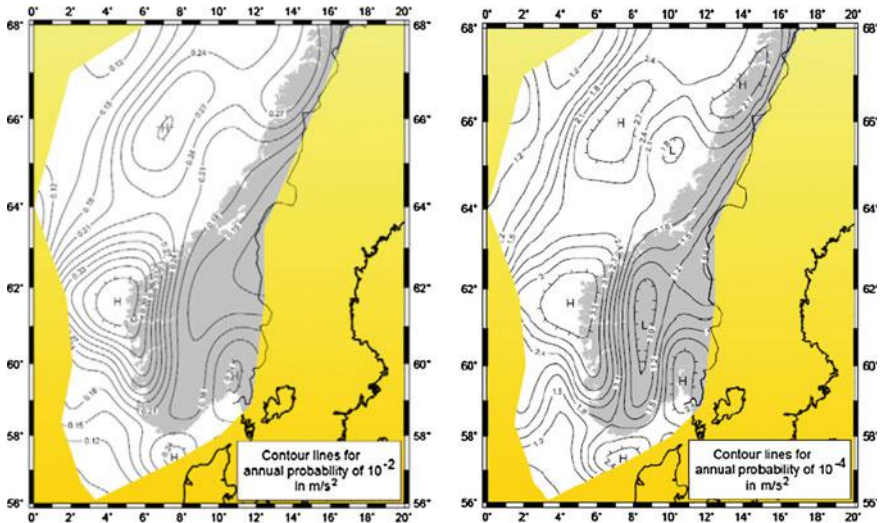


Fig. 6.4 Seismic zonation maps for 100 and 10,000 year return period of earthquake events in terms of PGA contour lines [6]

velocity at 1 Hz. The scaling factor η with a damping of $\zeta\%$ ($\zeta\%$ should be between 2 and 10 %) can be calculated as:

$$\eta = -\ln(\zeta/100)/\ln(20) \quad (6.9)$$

Fig. 6.5 Horizontal bedrock pseudo-response spectra with 5 % damping for 100 and 10,000 year return period of earthquake at a field in Norwegian continental shelf

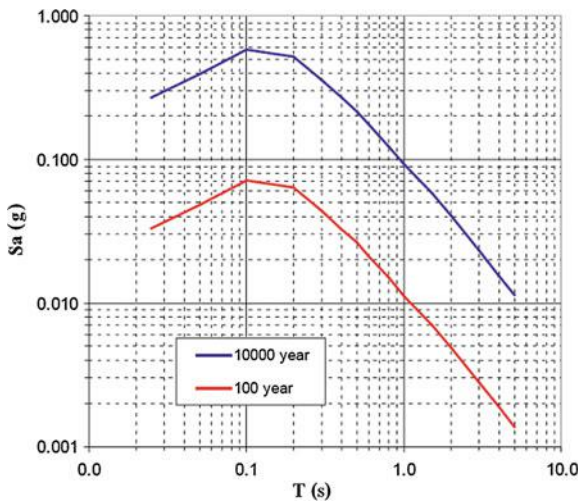
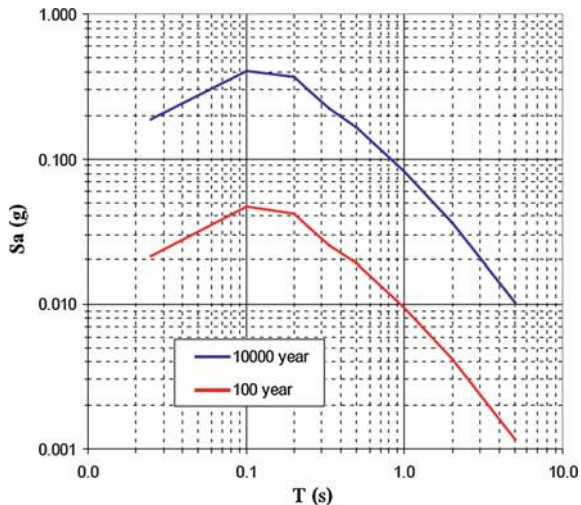


Fig. 6.6 Vertical bedrock pseudo-response spectra with 5 % damping for 100 and 10,000 year return period of earthquake at a field in Norwegian continental shelf



To reduce uncertainties, NORSO [4] also recommends carrying out a site specific soil response analysis (Sect. 4.3) for soft soils condition for 10,000 ;year return period of earthquake.

It is worth mentioning that the seismic zonation map shown in Fig. 6.4 is based on historical studies from before 1996 [6]. Based on recent developments in seismic hazard analysis in North Europe and other parts of the world, currently, Standard Norway [7] is initiating a project to generate a new seismic zonation map based on updated attenuation models (Sect. 3.6), PGA (change from original PGA at 40 Hz into the PGA at zero period), logic tree (Sect. 9.1.5), zonation method, etc. Furthermore, it is recommended by earthquake engineering experts in Europe that

every seismic assessment for offshore structures in Norwegian waters perform a site specific seismic hazard analysis (Sect. 9.1) to obtain the design ground motion intensity at bedrock.

References

1. Jia J (2017) Soil dynamics and foundation modeling: offshore and earthquake engineering. Springer, Heidelberg
2. Eurocode 8 (2004) Design of structures for earthquake resistance—part 1: general rules, seismic actions and rules for buildings
3. ISO19901-2 (2004) Petroleum and natural gas industries—specific requirements for offshore structures—part 2: seismic design procedures and criteria
4. NORSOK standard N-003 (2004) Actions and action effects, Rev. 2, Oct. 2004
5. ISO19901-2 (2016) Petroleum and natural gas industries—specific requirements for offshore structures—part 2: seismic design procedures and criteria, 2nd edn
6. NORSAR (1998) Seismic zonation for Norway. Report prepared for Norwegian Council for Building Standardization by NORSAR and Norwegian Geotechnical Institute
7. Standard Norway (2014) Earthquake loading for Norway and adjacent shelf regions and the Svalbard Archipelago, Technical Proposal, Oslo, October
8. Faccioli E, Paolucci R, Rey J (2004) Displacement spectra for long periods. *Earthq Spectra* 20 (2):347–376
9. Faccioli E, Villani M (2009) Seismic hazard mapping for Italy in terms of broadband displacement response spectra. *Earthq Spectra* 25(3):515–539
10. ASCE 7-05 (2006) Minimum design loads for buildings and others structures. American Society of Civil Engineers, Reston, VA

Chapter 7

Record Selection for Performing Site Specific Response Analysis

7.1 General

Compared to the coded based simplified method (Sect. 6.2), site specific response analysis (Sect. 4.3) is a more refined method to determine ground motions. As presented in Sect. 3.2.1, even though the P-waves arrive first and cause the vertical shaking of the ground, it is normally the shear waves that cause strong horizontal ground motions and possible subsequent structural damage. Therefore, apart from the shear waves transmitted vertically through soil (from bedrock to ground), which normally show little amplification or de-amplification, a site response analysis places special focus on the estimation of the horizontal ground and soil motions due to the transmission of horizontal shear (SH) waves propagated vertically. In addition, to capture different types of seismic waves (body and surface waves) propagations, and also to account for the irregular geometric properties of the sites (Sect. 4.3.7) that may affect the seismic wave propagation, a two-dimensional or three-dimensional site response analysis (Sect. 4.3.8), usually with the aid of finite element analysis, may need to be performed [1].

In a site response analysis, it is normally required to use a minimum of three to seven accelerogram sets for response history analysis. Each accelerogram set selected must consist of at least two horizontal components, and in many cases, the vertical component may also be included. It is important to select records that are generally compatible with the earthquake magnitude and source-to-site distance found from deaggregation (Sect. 9.1.4). If multiple magnitude-distance combinations contribute significantly to the hazard, then one should select records from each contributing earthquake as part of the total number of records. When the hazard is controlled by faults producing moderate to large magnitude earthquakes at close distances to the site, an appropriate number of ground motion records should be selected to include near-fault and directivity effects, such as velocity pulses producing relatively large spectral ordinates at long periods [2].

Obviously, the selection of time history records is essential in a site response analysis to calculate the design ground motions. Ideally, recorded accelerograms with response spectra equal to the design spectra should be used in site response analyses. However, this is almost impossible because the design spectra are based on the medians of numerous response spectra, each with varying frequency content. The resulting design spectra are therefore smoother or more uniform than any individual spectrum derived from recorded time histories of earthquake motions. Moreover, the equal-probability-of-exceedance design spectra (also called uniform hazard spectrum as will be discussed in Sect. 9.1) can be the results of contributions from various earthquakes with difference sources and magnitudes at different spectra periods, with the larger magnitude seismic events contributing more to the higher period.

Therefore, artificial accelerograms have to be generated to best approximate the design response spectrum at bedrock. This requires selections of motion recordings, and a modification of the recordings to fit into the design spectrum at bedrock. The obtained artificial accelerograms at the bedrock are used to perform site response analyses in order to calculate the ground motion time histories at the selected locations (depth), which are used to best estimate the ground motion response spectra at the selected locations to reach a design response spectrum. The entire procedure above is presented in Sects. 7.2, 7.3 and 7.4.

It is noted that selecting, scaling and matching ground motions to obtain a compatible set of records plays a key role in seismic assessment with an acceptable level of confidence. No unanimous consensus has been yet achieved on this subject. The current book briefly introduces a few popular while general methods on how to select and modify ground motions recordings in order to perform a site response analysis. For more elaborated information on this topic, Ref. [3], which was developed as part of the PEER Transportation Research Program, is recommended reading.

Readers may bear in mind that the general rules for selecting, scaling and matching ground motions discussed in this chapter can also be applied for obtaining artificial ground motion histories that are compatible with the design spectra at ground surface of a site, which may also be used for seismic time history analyses, even if the site effects are roughly accounted for when using a code based design spectrum presented in Chap. 6.

7.2 Selections of Motion Recordings

The ground motion suite must include a wide range of intensity measures representative of seismic hazard at the area of interest. Ideally, the response spectra of the selected recordings (obtained from measured recordings at different stations) should approximately fit or reasonably envelop the ground motion design spectra (typically given by seismic design codes) at the bedrock or rock outcrop. However, if this is

not attainable, a modification of selected recordings or generation of artificial bedrock seismic motions has to be performed to fulfill the requirements above, which will be discussed in Sect. 7.3.

7.3 Modification of the Recordings to Fit into the Design Rock Spectrum

As mentioned in Sect. 7.2, in order to generate time histories to best approximate the design response spectrum at bedrock, it is important to match the motion recordings to the target design spectrum, and this process to obtain the matched time histories is typically carried out by trial and error. Note that there is no consensus worldwide on the best practice for the scaling/modification of the ground motion records; it is still a subject of significant study and the results vary with the degree of inelastic response of structure for the chosen level of seismic hazard [4]. Generally, two methods are available for performing the matching, namely direct scaling and spectrum matching, as will be discussed in Sects. 7.3.1 and 7.3.2.

7.3.1 Direct Scaling

Direct scaling involves applying one constant factor to individual pairs of ground motions to make their response more closely match the target design spectrum over a certain range of periods [5]. Because elastic response spectra correspond to linear response of SDOF systems, the same scale factor applies to spectral accelerations at all periods.

7.3.2 Spectrum/Spectral Matching

Spectrum/spectral matching, also called response spectrum compatibilization, is intended to manipulate each individual ground motion record in the time domain by addition of wave packets, i.e. the recordings are scaled with different factors in different frequency range, using for example wavelets algorithm [6, 7], such that the response spectra would approximate target design spectra at the bedrock or rock outcrop.

A slightly different method is to scale each ground motion record so that the average response spectrum over the periods of interests is equal to the average of the target spectrum over the same periods.

By modifying the spectral shape of each individual ground motion record, spectral matching essentially adjusts the frequency content of accelerograms until the response spectrum is within user-specified limits of a target response

over a defined period range [8, 9]. One way to determine the scaling factor β is, for example, to minimize the errors with respect to a target acceleration spectrum at a number (N_r) of eigenperiods typically below 4 s:

$$\text{error} = \min \left(\sum_{i=1}^{N_r} \left(1 - \frac{\beta \cdot S_a(T_i)^{\text{record}}}{S_a(T_i)^{\text{target}}} \right) \right) \quad (7.1)$$

where $S_a(T_i)^{\text{target}}$ and $S_a(T_i)^{\text{record}}$ are the spectral accelerations for the i th eigen-period from the target spectrum and the response spectrum of the original selected record, respectively.

Figure 7.1 shows that three original selected recordings (Kobe earthquake, 17 Janauary 1995; Imperial Valley of EI Centro Site earthquake 18 May 1940; Trinidad earthquake, March 1988) are matched to the target design spectrum with respect to both amplitude and frequency content, and the three matched spectra are transferred back to the time histories as shown in Fig. 7.2.

Therefore, spectral matching generally reduces spectral variability among a suite of records, and increases the pool of available ground motions with a certain shape. It is the former point that has made this process especially alluring to practicing engineers [10]. Moreover, the reduction in spectral variability due to spectrum matching generally leads to a reduction in non-linear structural response variability [13], which essentially implies that fewer ground motions are required to obtain an estimate of a particular response quantity [14].

Another widely adopted spectrum scaling method is based on the 5 % damped first mode spectral acceleration, which can minimize the bias of damage estimation statistically [15]. This is because the response spectra for time histories matched with the first mode spectral acceleration is generally less “broad band” than that matched with uniform hazard spectra at entire periods or over a large range of periods, even though uniform hazard spectra usually envelope the first mode spectral acceleration. However, one may realize that for many structures, the higher order of vibration modes also make an important contribution to seismic responses. For example, shear forces at upper-story of a building or floor accelerations can be more sensitive to higher order mode excitation than that of the first eigenmode vibrations, even if the displacement response is more dependent on the fundamental global vibration mode response. Therefore, a scale factor that covers a larger period range should then be adopted.

The seismic records can be obtained from several public ground motion record databases, which are often accompanied by a number of earthquake and site parameters, such as earthquake magnitude, source-to-site distance, and ground type at the corresponding recording stations. Section 3.8 provides links to access the database of a few ground motion recordings.

The target spectra can be obtained using one of the two following options: (1) the design response spectra calculated from the relevant seismic design code procedures, which correspond roughly to uniform hazard spectra (Sect. 9.1) for the site; or (2) site specific scenario spectra that preserve realistic spectral shapes for

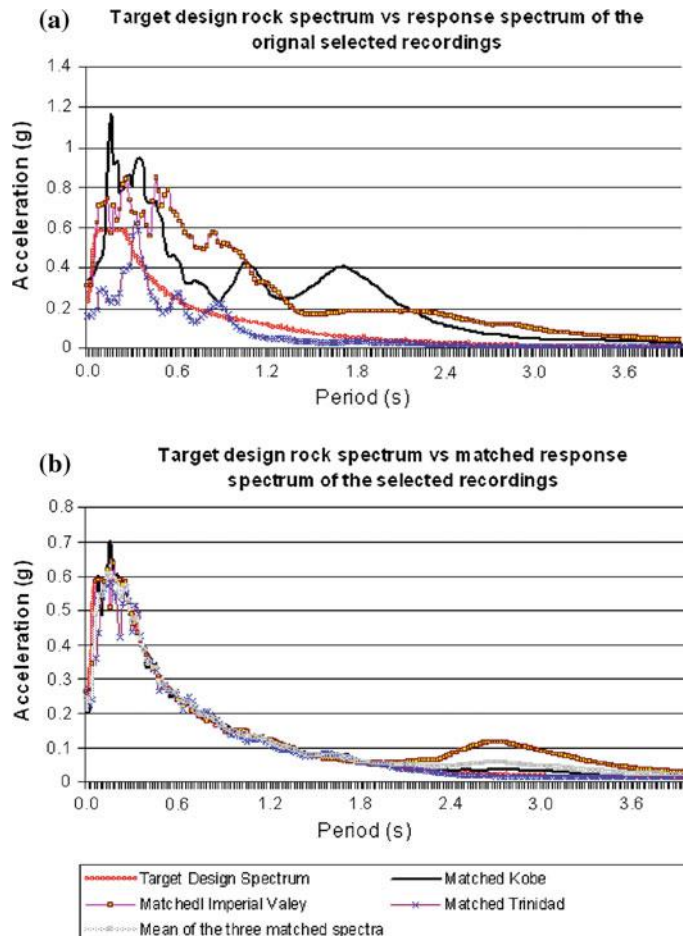
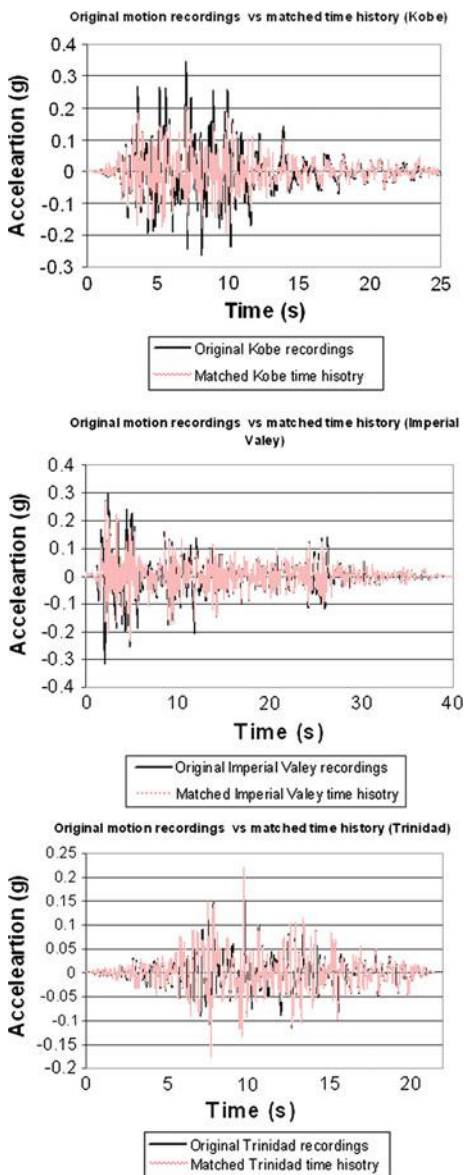


Fig. 7.1 The comparison between the target design rock spectrum and the response spectrum for 5 % damping of **a** the three selected recordings (*upper*) and **b** the matched spectra and their average (*lower*)

controlling earthquakes and match the design spectral ordinate at different periods of interest, also known as conditional mean spectra (CMS), as will be presented in Sect. 9.4.

The process of spectrum matching can be carried out by several commercial codes, such as SeismoMatch [11] or RspMatchEDT [12], through which the response spectrum of individual motion record can be modified to match the target design spectrum.

Fig. 7.2 The comparison between the original motion recordings and the time history calculated from the matched spectra (Fig. 7.1) with 5 % damping



7.3.3 Pros and Cons of Direct Scaling and Spectrum Matching

Both direct scaling and spectrum matching have merits and drawbacks.

Both methods are inconsistent with the physical conditions and can result in different characteristics from the ground motion recordings [16, 17], except for cases in which time histories are matched to a conditional mean spectrum (Sect. 9.4).

Direct scaling in certain senses retains the original ground motion characteristics, including peaks and valleys in the response spectrum. But it is questionable, since scaling a ground motion does not account for variations in ground motion characteristics (e.g. frequency content), which change with intensity [18], i.e., extreme intensity ground motions have different frequency contents than low intensity ground motions. This is more obvious for long period ground motions. Moreover, natural periods for many structures are high, while ground motion records may not have such a long period; this hence requires a large scaling factor, which may result in unrealistic structural responses.

The drawbacks of simple scaling can be overcome by the spectrum matching method, which usually presents a larger number of cycles than the recorded ground motions, indicating a stronger ground motion for a wider range of structural periods, which implies a more conservative loading scenario [19]. However, since the spectrum matching method changes the frequency content of the original records, it may eliminate the inherent record-to-record spectral shape variability and the variability of the structural response. This drawback of spectrum matching has been realized by many researchers, and recent research [16, 20–24] shows a non-conservative bias in the median non-linear displacement of structural models analyzed by a suite of matched ground motions compared to a suite of unmatched ground motions representing an equivalent scenario. Note that a time domain analysis requires only a few ground motions to be analyzed. This may eliminate the variability of a structure's dynamic response if those ground motions are obtained from spectrum matching [25]. This bias appears to result partially from the scaled ground motions having inappropriate values of spectral shape or the parameter ε (Sects. 3.6 or 9.4), which is an indirect measure of spectral shape [26]. This bias is more apparent for uniform hazard spectra, which often represent unrealistic seismic motions as it combines the statistical variability of several earthquakes rather than a single one. Therefore, in a number of seismic design codes, this method is not recommended to use, or is only permitted to use with great care by fulfilling a list of strict criteria, or is allowed to be used only if several site response analyses are performed, with the majority of the seismic motion time histories obtained from the real records and the rest (the minority) from the calculation by the spectrum matching method, as recommended by the code for seismic design of buildings in China [27]. As mentioned before, a recent method to eliminate the bias due to the inappropriate values of spectral shape or the parameter ε is to adopt a few conditional mean spectra conditioned at a number of periods of interests, which will be presented in Sect. 9.4.

Moreover, the duration of strong ground motion is dependent on magnitude and is not explicitly represented in a spectral shape [28], though peak displacement amplitude does tend to increase with time based on random vibration theory. Therefore, demand parameter depending on degradation (e.g. collapse capacity) may be biased if the duration is not included in the ground motion selection criteria.

7.4 Performing the Site Response Analysis Using Modified/Matched Recordings

After selecting the ground motion recordings, a modification or matching of those recordings may be performed to fit them into the design response spectrum at bedrock/rock outcrop, which has been presented in Sects. 7.2 and 7.3. By inputting the modified/matched motion histories at the bedrock/rock outcrop and carrying out site response analysis (Sect. 4.3), response time histories and response spectra at seabed can then be calculated. As mentioned before, most of the codes and standards, such as Eurocode 8 [29], Norsok N-003 [30] and China's building code [27], require using at least three bedrock motion histories to compute the ground motion time histories and the response spectra. ISO 19901-2 [31] requires a minimum of four and recommends that seven time history analyses be used to capture the randomness in a seismic event. The recordings are preferably assigned at a hypothetical bedrock outcrop (point 1 in Fig. 4.2) rather than the base of the soil profile (point 2 in Fig. 4.2). This is because the rock is generally not perfectly rigid, the motions at the base of the soil profile (rock) are not identical to that of the rock outcrop, while the stations for measuring recordings are generally located at the rock outcrop (or even at soil layers) rather than the bedrock [32]. Moreover, it is noticed that, historically, seismic records are measured on a variety of soil conditions, ranging from rock outcrop to very soft soil, but rarely at bedrock due to technical challenges. More recently, researchers have become more careful to select the locations for installing the accelerometers, and tried their best to place the accelerometers on rock outcrop or very stiff soil.

It is recommended to perform a sensitivity analysis. By accounting for the variation of soil properties from lower bound, average (best-estimate) to upper bound value, this may detect some significant impact of soil properties on the ground motions. If the ground motions are not sensitive to the variation of soil properties, typically, the best-estimate value of soil properties can be used to compute the ground motion time histories. Thereafter, a site response analysis can be carried out typically by either equivalent linear analysis (Sect. 4.3.9) or by non-linear analysis [1]. Various computation codes are available to perform this task, such as SHAKE 2000 or D-MOD2000.

The set of time histories of ground motions computed through a site response analysis can then be directly used for calculating structural responses in time

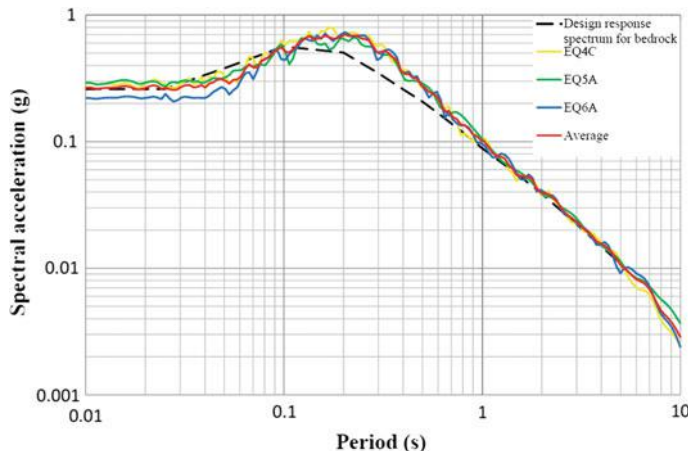


Fig. 7.3 Computed seabed acceleration response spectrum (Average) based on three bedrock horizontal ground motions (EQ4C, EQ5A and EQ6A) matched to a target bedrock design response spectrum (courtesy of Aker Solutions)

domain. Alternatively, the set of response spectra obtained from the time histories of ground motions may be interpreted in some manners (e.g. by taking the mean value of the all response spectra) and smoothed to develop one design response spectra at seabed/ground surface, which can account for the contribution from all individual ground motion histories of the set of time histories, and be applied for calculating structural responses using response spectrum analysis as will be presented in Chap. 15. Figure 7.3 shows an example of response spectra of three computed horizontal acceleration time histories on the seabed/ground surface for

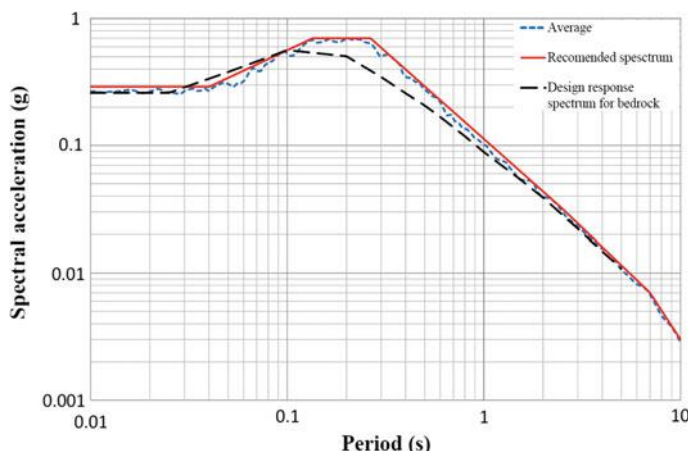


Fig. 7.4 Recommended horizontal design spectrum on seabed (courtesy of Aker Solutions)

earthquake events with a return period (Sect. 9.1.3) of 10,000 years. Using the average values of the three computed spectra, a design response spectrum can be obtained as shown in Fig. 7.4.

References

1. Jia J (2016) Soil dynamics and foundation modeling: offshore and earthquake engineering. Springer, Heidelberg
2. Pacific Earthquake Engineering Research Center (PEER) (2010) Guidelines for Performance-Based Seismic Design of Tall Buildings, Version 1.0, California, Nov 2010
3. Baker JW, Shahi SK, Jayaram N (2011) New ground motion selection procedures and selected motions for the PEER Transportation Research Program, Pacific Earthquake Engineering Research Center, University of California, Berkeley, CA, PEER Report 2011/03
4. Willford M, Whittaker A, Klemencic R (2008) Recommendations for the seismic design of high-rise buildings. Council on Tall Buildings and Urban Habitat
5. ASCE 7-05 (2005) Minimum design loads for buildings and other structures. American Society of Civil Engineers
6. Amiri GC, Ashrafi P, Rahami H (2006) New development of artificial record generation by wavelet theory. Struct Eng Mech 22:185–195
7. Amiri GC, Asadi A (2008) New method for simulation of earthquake records by using adapted wavelet. In: The 14th world conference on earthquake engineering, Beijing
8. Abrahamson NA (1992) Non-stationary spectral matching. Seismol Res Lett 63(1):30
9. Hancock J, Watson-Lamprey J, Abrahamson NA, Bommer JJ, Markatis A, McCoy E, Mendis R (2006) An improved method of matching response spectra of recorded earthquake ground motion using wavelets. J Earthq Eng 10:67–89
10. Seifried AE (2013) Response compatibilization and impact on structural response assessment, PhD thesis, Stanford University
11. <http://www.seismosoft.com>
12. <http://www.shake2000.com>
13. Shome N, Cornell CA, Bazzurro P, Carballo JE (1998) Earthquakes, records and nonlinear responses. Earthq Spectra 14(3):469–500
14. Hancock J, Bommer JJ, Stafford PJ (2008) Numbers of scaled and matched accelerograms required for inelastic dynamic analyses. Earthq Eng Struct Dynam 37(14):1585–1607
15. Shome N, Cornell CA, Bazzurro P, Carballo JE (1998) Earthquakes, records, and nonlinear responses. Earthq Spectra 14:469–500
16. Bazzurro P, Luco N (2006) Do scaled and spectrum-matched near-source records produce biased nonlinear structural responses? In: Conference, National Engineering, Earthquake Engineering
17. Luco N, Bazzurro P (2007) Does amplitude scaling of ground motion records result in biased nonlinear structural drift responses? Earthq Eng Struct Dyn 36:1813–1835
18. Han SW, Wen YK (1994) Method of reliability-based calibration of seismic structural parameters. University of Illinois and Urbana-Champaign. UIUC-ENG-94 2016, Structural Research Series No. 595, Champaign, IL, 170pp
19. Papadakakis M, Lagaros ND, Fragiadakis M (2006) Seismic design procedures in the framework of evolutionary based structural optimization, computational mechanics: solids, structures and coupled problems. Springer, Dordrecht
20. Carballo JE, Cornell CA (2000) Probabilistic seismic demand analysis: spectrum matching and design, Report No. RMS-41, Department of Civil and Environmental Engineering, Reliability of Marine Structures Program, Stanford University, Stanford

21. Watson-Lamprey J, Abrahamson N (2006) Bias caused by use of spectrum compatible motions. In: Eighth US national conference on earthquake engineering, San Francisco, CA
22. Iervolino I, De Luca F, Cosenza E (2010) Spectral shape-based assessment of SDOF nonlinear response to real, adjusted and artificial accelerograms. Eng Struct 32(9):2776–2792
23. Heo Y, Kunnath S, Abrahamson N (2011) Amplitude-scaled versus spectrum-matched ground motions for seismic performance assessment. J Struct Eng 137(3):278–288
24. Grant DN, Diaferia R (2013) Assessing adequacy of spectrum-matched ground motions for response history analysis. Earthq Eng Struct Dyn 42(9):1265–1280
25. Moehle JP (2008) Performance-based seismic design of tall buildings in the US. In: 14th world conference on earthquake engineering, Beijing
26. Baker JW, Cornell CA (2005) A vector-valued ground motion intensity measure consisting of spectral acceleration and epsilon. Earthq Eng Struct Dyn 34(10):1193–1217
27. China Net for Engineering Construction Standardization (2010) Code for seismic design of buildings, GB 50011-2010. China Building Industry Press, Beijing
28. Bommer JJ, Acevedo AB (2004) The use of real earthquake accelerograms as input to dynamic analysis. J Earthq Eng 8:43–91
29. Eurocode 8 (2004) Design of structures for earthquake resistance—part 1: general rules, seismic actions and rules for buildings
30. NORSO standard N-003 (2004) Actions and action effects, rev. 2, Oct 2004
31. ISO19901–2 (2004) Petroleum and natural gas industries—specific requirements for offshore structures—part 2: seismic design procedures and criteria, 2004
32. EM 1110-2-6050 (1999) Engineering and design—response spectra and seismic analysis for concrete hydraulic structures, US Army Corps of Engineers

Chapter 8

Spatial Varied (Asynchronous) Ground Motion

8.1 General

The spatial varied ground motions are categorized as either large scale (regional) or local scale seismic motion. The former refers to the attenuation relationship with a scale of 10 km, which describes the relationship between accelerations and site-to-source distance, as elaborated in Sect. 3.6. The latter is related to the local spatial variation with a scale of a few hundred meters, which leads to a variation of seismic ground motion in magnitude, phase and frequency content at different locations. The current chapter will discuss the local spatial variation.

In the traditional engineering practice and design codes' requirements, it is assumed that earthquake ground motions are uniform at all supports of a structure and they are associated with an infinite value of seismic wave velocity, so that the seismic waves arrive at different locations on the seabed at the same time, i.e., there is no phase information between different supports. However, for extended-in-plan structure systems (both above ground and buried ones) covering a large area such as bridges with multiple supports [1] (Fig. 8.1), structural systems comprising several connected structures (Fig. 8.2), pipelines [2, 3] (Fig. 8.3), tunnels and dams [4, 5], and dikes [6], etc., the seismic waves may arrive at different support locations at different times. During this arrival time period, the amplitude, frequency content and the phase (arriving time) of the seismic motions are likely to change mainly depending on the distance between the support points and the local soil conditions, local seismic motions may be enhanced with out-of-phase displacements at various locations, and different parts of the structural system may respond asynchronously with large displacement responses. This phenomenon is called spatial variation of earthquake motion (SVEGM).

Figure 8.4 illustrates the recorded accelerograms at two locations 200 m apart [7, 8]. It shows that at many time instants, the accelerations at the two locations are different in both amplitude and phase. In an extreme case, the difference in motion



Fig. 8.1 Collaspe of a Nishinomiya bridge approach span during the magnitude 7.2 Kobe earthquake of 1995 due to the damage to unseating prevention devices (a plate-type restrainer) (courtesy of Kobe Collection, EERC Library, University of California, Berkeley)



Fig. 8.2 Several offshore jacket structures connected by bridges at Valhall fields in the North Sea (courtesy of Aker Solutions)

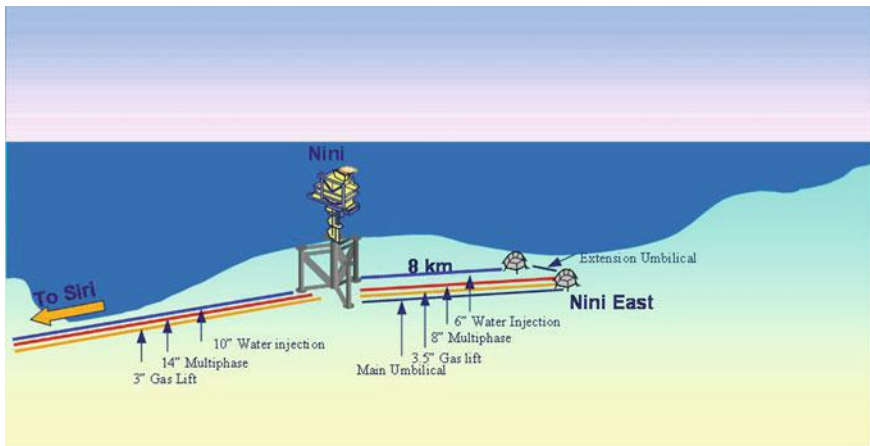


Fig. 8.3 Illustration of a layout for subsea pipelines (courtesy of Dong Energy, Denmark)

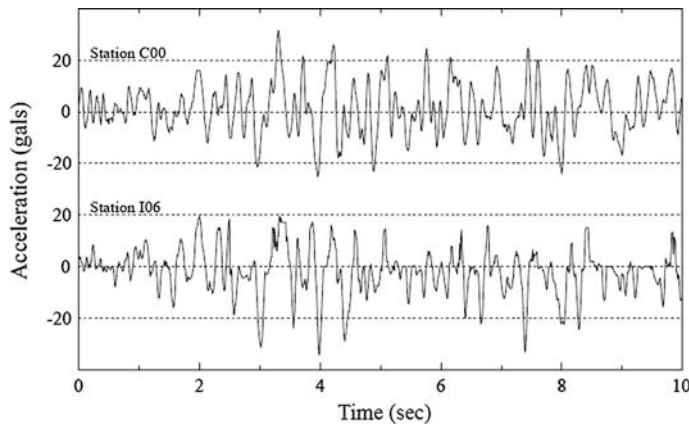


Fig. 8.4 Recorded seismic ground motion at two locations 200 m apart

amplitudes due to the SVEGM is comparable with the input ground motion amplitudes [9].

The significance of SVEGM has been recognized since the 1980s, when the records from extended seismic arrays like SMART-1 became available [10]. Moreover, numerous damages of extended land-based structures have been observed as a possible consequence of SVEGM, such as the falling off of Gavin Canyon Bridge's under-crossing and the span unseating in the 1994 Northridge earthquake [11], the unseating of deck and spans falling off (due to large longitudinal displacements between piers) at elevated highway bridges (Fig. 8.1) during the Kobe earthquake 1995 [12], etc.

It is noted that, due to the effects of SVEGM, both horizontal and vertical motions may not only induce the bending of structures, but also exert large torsional moments between the principal structural planes. If one of the relevant ground motion frequencies is close to the structures' natural frequency or other eigenfrequencies corresponding to dominant vibration modes, resonance will occur with a magnification of structures' responses.

Four effects cause SVEGM:

- (1) Wave passage effects: these are due to the non-vertical wave propagation (waves travel at finite velocity) time delay. This effect can be roughly modeled by applying a time shift to each structure's support excitation time history, based on a lower bound of the range of measured seismic wave velocity (may be taken as 2.5 km/s). This effect is only considered in the design for structures at least 400 m long.
- (2) Extended source effects: involving loss of coherence in terms of statistical dependence, this is due to the different manner of superpositions of seismic waves arriving from an extended source and are scattered by irregularities and inhomogeneities along the path and at the site, causing a loss of coherency, while the time lag generates different motions at different locations. This effect is sometimes referred to as complex wave scattering effect and is observed empirically in the recorded data from closely spaced strong motion instruments.
- (3) Local soil/site effects: the upper soil condition at different locations may be different, making the amplitude and frequency content of the seismic ground motion different at the different locations. This may be the most significant source of spatially varying input motions for most extended structures. Variations in local soil conditions are generally accounted for by conducting one-dimensional site response analyses for representative soil columns at each support location of structures. The base of each column is subjected to the free-field design ground motions and the difference in soil response at the top of the soil columns is assumed to represent the variation in ground motions due to local soil conditions. Structures of almost any length can be susceptible to the effect of soil variability from one end to the other.
- (4) Foundation filter effects: due to the flexibility of the foundation, it filters the seismic motion during the transmission of seismic waves (kinematic interaction, as described in Sect. 4.3.2) and interacts with the inertial force generated by the upper structures' vibrations (inertial interaction, as presented in Sect. 4.3.4).

Excepting the local soil effects that are most important and should be addressed in a separate site response analysis, to include for the effects of SVEGM, it is normally sufficient to account for the effects of (1) seismic wave passage and (2) the loss of coherence presented above, which will be discussed in Sect. 8.3.

Nowadays, time history analysis is the predominant method used to assess the response of significantly extended structures due to SVEGM. It can be carried out

with various degrees of sophistication. A simple way is to apply spatially varying excitations on various locations (e.g., multiple supports) of a structure, while a more complicated way is to model structures, foundations and their soil media as an integrated system and perform a dynamic analysis, so that a simulation of both seismic wave propagation and structural responses can be performed in the same analysis. Moreover, for structures with multiple supports, such as a bridge, the spatial differential motion can be applied on the structures' supports. For continuous and extended structures such as pipelines, dams and dikes, continuous variation of the ground motions occurs along the structures, which needs to be treated in a dedicated and rational way. For more details, readers may read references [3, 13–15].

Other analysis methods using a modified response spectrum approach were also researched, such as the one proposed by Loh et al. [16] in the early 1980s, which were further developed by various researchers [17–21], some of which include a stochastic description [19–21]. However, they are not yet widely accepted as a recommended engineering practice.

8.2 Cross-Covariance, Cross-Spectra Density Function and Coherence Function

8.2.1 Cross-Covariance in Time Domain

Incoherence function Sect. 5.3.1.2, it is noted that the power spectra density (mean square response spectrum) of the responses does not contain any information regarding phase between the response and the loading. This information can be conveniently included by introducing cross-covariance or cross-correlation function:

$$C_{XY}(\tau) = E[X(t)Y(t + \tau)] \quad (8.1)$$

where τ is the time lag; $E(\cdot)$ stands for the mean (expected) value; $X(t)$ and $Y(t)$ are two stationary processes.

The time lag τ at which the maximum occurs often has physical significance [22].

It is possible to reverse the order of the subscripts in the equation above, so that the following relationship also holds:

$$C_{YX}(\tau) = E[Y(t)X(t + \tau)] \quad (8.2)$$

The cross-covariance possesses the property of symmetry, i.e., the two equations above are reflections of one another about the origin:

$$C_{XY}(\tau) = C_{YX}(-\tau) \quad (8.3)$$

The cross-covariance has an upper and lower bound:

$$-\sigma_X \sigma_Y + \mu_X \mu_Y \leq C_{XY}(\tau) \leq \sigma_X \sigma_Y + \mu_X \mu_Y \quad (8.4)$$

Cross-covariance has its limitations when studying dispersive propagation problems in which the time delay is frequency dependent, such as the propagation of seismic wave from bedrock to ground, which travels faster and farther at low frequencies than at high frequencies [22]. In this case, the cross-spectra density, as will be introduced in Sect. 8.2.2, need to be used.

8.2.2 Cross-Spectra Density in the Frequency Domain

The cross-spectra density function is defined as the Fourier transform of the cross-covariance:

$$S_{XY}(\omega) = \frac{1}{2\pi} \int_{-\infty}^{\infty} C_{XY}(\tau) e^{-i\omega\tau} d\tau \quad (8.5)$$

$$S_{YX}(\omega) = \frac{1}{2\pi} \int_{-\infty}^{\infty} C_{YX}(\tau) e^{-i\omega\tau} d\tau \quad (8.6)$$

Different from the power spectra density (auto-spectra density), which includes only one process and is real valued, the cross-spectra density function includes two processes, and is therefore complex so that the information regarding the phase shift between the two processes is accounted for.

Similar to cross-covariance, symmetry also holds for the cross-spectra density function, i.e., $S_{XY}(\omega)$ and $S_{YX}(\omega)$ are complex conjugates of each other:

$$S_{XY}(\omega) = S_{YX}(-\omega) = S_{YX}^*(\omega) \quad (8.7)$$

Note that the area under spectrum density function $S_X(\omega)$ is the mean-square (variance) of the process $X(t)$, the integral of the cross-spectral density is equal to the expected value of the product $X(t) Y(t)$, which is their covariance.

8.2.3 Coherence Function in the Frequency Domain

As will be presented in Sect. 8.3, the linear dependence of two processes (ground motions) at two locations $X(t)$ and $Y(t)$ can be expressed with non-dimensional coherence function:

$$Coh_{XY}(\omega) = \gamma_{XY}^2(\omega) = \frac{|S_{XY}(\omega)|^2}{S_X(\omega)S_Y(\omega)} = \frac{S_{XY}(\omega)S_{XY}^*(\omega)}{S_X(\omega)S_Y(\omega)} \quad (8.8)$$

Since $|S_{XY}(\omega)|^2 \leq S_X(\omega)S_Y(\omega)$, the coherence function is bounded by:

$$0 \leq \gamma_{XY}^2(\omega) \leq 1 \quad (8.9)$$

$\gamma_{XY}^2(\omega) = 1$ indicates a purely linear dependence between $X(t)$ and $Y(t)$. On the other hand, $\gamma_{XY}^2(\omega) = 0$ shows that there is no linear relationship between $X(t)$ and $Y(t)$ at all. However, the value of coherence function normally lies between these two extreme cases, indicating that systems are either not perfectly linear or unconsidered simultaneous loads/noises other than $F(t)$ exist to corrupt the measurements.

In modal testing to obtain the eigenfrequencies and mode shapes, engineering environments always involve measurement noise, which comes from many sources, such as the environment (non-source related vibrations), quantization noise and electrical components etc. The obtained coherence function can be seen as a signal-to-noise ratio of the measurements. A coherence function equal to 1 indicates zero noise in the measurement, while when the value of the coherence function is 0, a pure noise situation is indicated.

Figure 8.5 shows coherence functions from a modal testing of a ship deck. It is clearly shown that, at the eigenfrequencies that are of interest (5–20 Hz) for structural engineers, the coherence function is close to 1 for almost all measurement positions (2–6). This indicates that the proportion of noise energy in the measured

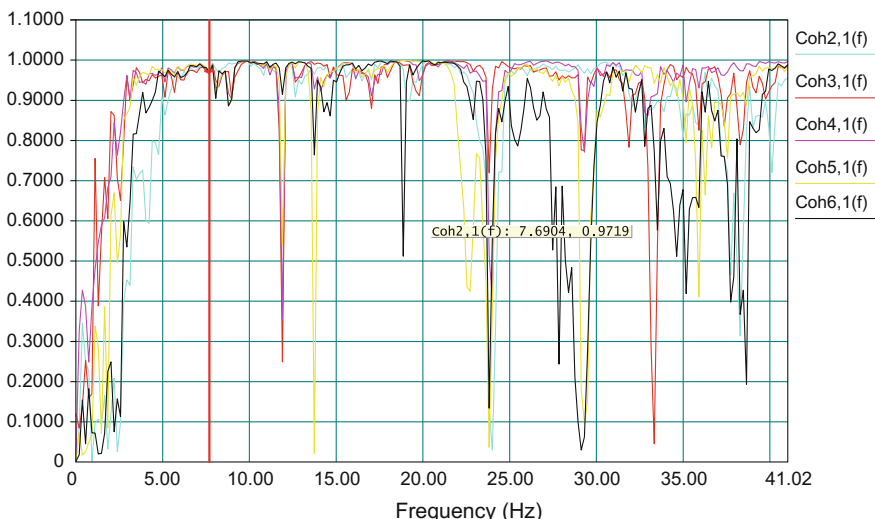


Fig. 8.5 Coherence functions at various locations on a ship deck during a modal testing

signal is in the order of a few percent. In general, the best signal-to-noise ratio was obtained at those measurement positions close to the excitation position.

8.3 Simulation of SVEGM

Several techniques [23–26] to simulate the spatially variable seismic ground motions have been proposed, with the most widely used ones being covariance matrix decomposition method [23] and spectral representation method [24].

To simulate SVEGM in a stochastic manner, three components are required: (1) target power spectrum as described in Sect. 5.3; (2) coherence function to describe the motion relationship between two location points as will be presented in this section; (3) shape function to simulate non-stationary characteristics of ground motions, as will also be presented in this section.

In general, the spatial variation of seismic motions can be described mathematically either by auto-covariance and cross-covariance (in time domain), or by coherence functions (in frequency domain). In engineering practice, the ground motions at different locations can normally be defined by a homogeneous and isotropic Gaussian stochastic model, with its spatial variability expressed by its coherency spectrum, or coherence function. By introducing multiple-support excitations in a structural modeling, provided an appropriate representation of the influence of the foundation is available, the response due to the SVEGM effects can be calculated.

By accounting for only the wave passage effect, the seismic safety of a nuclear reactor and the responses of a large bridges in California has been assessed [27]. Moreover, it has been shown that there is a high degree of transferability of this coherence between various geological sites [28].

The general form of complex coherence function between two location points A and B at frequency ω can be defined as:

$$\gamma_{AB}(\omega) = |\gamma_{AB}| e^{i\Theta_{AB}} = S_{AB}(\omega) / [S_A(\omega)S_B(\omega)]^{1/2} \quad (8.10)$$

where $|\gamma_{AB}|$ is the modulus of the coherence function; $|\gamma_{AB}(\omega)|$ is referred to as the loss of coherency or lagged coherency; i is the imaginary unit; Θ_{AB} represents the phase of the coherence function; $S_{AB}(\omega)$ is the cross-spectral matrix of ground motions between points A and B ; $S_A(\omega)$ and $S_B(\omega)$ are power spectral densities of ground motions along the same direction at points A and B , respectively;

In the equation above, it is noted that the loss of coherency $|\gamma_{AB}|$ is a measure of the similarity of ground motions at points A and B , excluding the effect of traveling seismic waves, which is accounted for in the phase of the coherence function Θ_{AB} . Moreover, quite often, the real value of coherency $\text{Re}[\gamma_{AB}(\omega)]$,

referred to as unlagged coherency, is used for analysis, the equation above can then be rewritten as:

$$S_{AB}(\omega) = \gamma_{AB}(\omega)[S_A(\omega)S_B(\omega)]^{1/2} \quad (8.11)$$

The equation above clearly indicates the dependence between the input spectral densities $S_A(\omega)$ and $S_B(\omega)$, their coherence function $\gamma_{AB}(\omega)$, and the output cross-spectral density function $S_{AB}(\omega)$ [21].

Der Kiureghian [29] proposed a more complicated coherence function to account for the influences due to the wave passage effects, loss of coherency, and the local soil/site effects, in which the cross-spectral density of accelerations can be expressed as:

$$\gamma_{AB}(\omega) = \gamma_{AB}^{(l)}(\omega)\gamma_{AB}^{(w)}(\omega)\gamma_{AB}^{(s)}(\omega) = \gamma_{AB}^{(l)}(\omega) \exp\left[i\left(\Theta_{AB}^{(w)}(\omega) + \Theta_{AB}^{(s)}(\omega)\right)\right] \quad (8.12)$$

where $\gamma_{AB}^{(l)}(\omega)$ represents the loss of coherency between points A and B; $\gamma_{AB}^{(w)}(\omega)$ represents the phase delay due to the wave propagation; and $\gamma_{AB}^{(s)}(\omega)$ represents local soil/site effects.

From the equation above, it is noticed that the loss of coherency is represented by a real function: the wave passage and site effects result in the phase changes $\Theta_{AB}^{(w)}(\omega)$ and $\Theta_{AB}^{(s)}(\omega)$ of the complex coherency.

Elnashai and Di Sarno [30] presented that the coherency of two ground motions is a measure of correlation of amplitudes and phase angles at different frequencies. Incoherence (or loss of coherence) is strongly frequency dependent. For frequencies lower than 1.0–2.0 Hz, the coherence factor is close to 1.0, i.e. the loss of coherence can normally be neglected. Coherence decreases significantly at higher frequencies: for frequencies higher than 5 Hz, the reduction of coherence factor is more than 50 %. On the other hand, Der Kiureghian and Neuenhofer [18] stated that the modulus of coherency is rather sensitive to spatial separation, even for relatively low frequencies. Moreover, experimental evidence collected during significant earthquakes indicates that the peak values of ground motion do not change substantially over rather long distances [31]. Therefore, direct observations of the moduli of coherency can be misleading about important peak response measures of the seismic ground motion [21].

Note that local soil effects (most likely the most important contributor to SVEGM) can also be addressed in a separate site response analysis, to simulate the SVEGM, it is normally sufficient to account for the effects of seismic wave passage and the loss of coherence by establishing the coherence functions as mentioned before in Sect. 8.1; the function depends on the frequency and separation distance. A widely used model to represent the spatial variation of ground motions is based on the Luco and Wong coherency function [32], which establishes the coherence of any pairs of locations, which can be expressed as:

$$\gamma(\xi, \omega_n) = e^{-\left(\frac{\omega_n \xi}{v_s}\right)^2} \cdot e^{\left[\frac{\omega_n \xi L}{v_{app}}\right]} \quad (8.13)$$

where α indicates the mechanical characteristics of the soil; a low value of α (e.g. 2×10^{-4}) represents a slow exponential decay in the coherency as the frequency ω_n and separation distance ξ increase. On the other hand, a high value of α (e.g. 10^{-3}) represents a sharp exponential decay in the coherency as frequency and separation distance increase.

The first term in the right hand side of the equation above shows an exponential decay of coherence due to the variation in separation distance ξ between two locations, shear wave velocity v_s and frequency ω_n . This item controls the geometric incoherence of ground motions, which decreases as soil becomes stiffer. The second term represents the seismic wave passage effect. It gives a longer signal arrival delay when the projected horizontal distance ξ^L and the frequency ω_n increase, and when the apparent velocity v_{app} decreases. The coherence level is mainly governed by shear wave velocity and apparent surface wave velocity. When the surface wave travels at infinite speed ($v_{app} = \infty$), the second term equals to 1, i.e., the seismic waves arrive at all locations simultaneously, and the loss of coherence is only due to the geometric incoherence (the first term). The shear wave velocity v_s is generally much lower than the apparent wave velocity. For soft soil, v_s is in a range of 200–300 m/s [33].

Several other models are available to simulate the coherence of asynchronous ground motion, such as the Harichandran-Vanmarcke model [34], Loh-Yeh model [35], Feng-Hu model [36], Oliveira-Hao-Penzien model [37] and Qu-Wang-Wang model [38], etc. For more details of those models, readers may read the references cited above.

One way to implement the coherency function into a power spectrum of seismic ground motions is to subdivide the frequency range into N segments ($n = 1, 2, \dots, N$) and the space into M points in space grids, by using the general form of complex coherency function, an M by M cross-spectral density matrix can then be expressed for each sample frequency and each component by:

$$S_{j,k}\{\omega_n\} = \begin{bmatrix} 1 & \gamma_{12}(\omega_n) & \dots & \gamma_{1M}(\omega_n) \\ \gamma_{21}(\omega_n) & 1 & \dots & \gamma_{2M}(\omega_n) \\ \dots & \dots & \dots & \dots \\ \gamma_{M1}(\omega_n) & \gamma_{M2}(\omega_n) & \dots & 1 \end{bmatrix} \cdot [S_j(\omega_n)S_k(\omega_n)]^{0.5} \quad (8.14)$$

where $S_j(\omega_n)$ and $S_k(\omega_n)$ are power spectral densities (at frequency ω_n) of ground motions along the same direction at points j and k , respectively.

A Cholesky decomposition [39] can be performed on the matrix above so that it can be rewritten as the product of lower triangular matrix $H(\omega_n)$ and its transposed complex conjugate:

$$S_{j,k}(\omega_n) = H_{j,k}\{\omega_n\} \cdot H_{j,k}^{*T}\{\omega_n\} \quad (8.15)$$

where:

$$H\{\omega_n\} = \begin{bmatrix} H_{11}(\omega_n) & 0 & \dots & 0 \\ H_{21}(\omega_n) & H_{22}(\omega_n) & \dots & 0 \\ \dots & \dots & \dots & \dots \\ H_{M1}(\omega_n) & H_{M2}(\omega_n) & \dots & H_{MM}(\omega_n) \end{bmatrix}$$

Based on the assumption of Gaussian process, the simulated excitation acceleration $a_m(t)$ in space (at point m) at time t can be expressed as:

$$a_m(t) = 2 \sum_{k=1}^m \sum_{n=1}^{N-1} |H_{mk}(\omega_n)| \cdot \sqrt{\Delta\omega} \cdot \cos[\omega_n t + \psi_{mk}(\omega_n) + \theta_{kn}] \quad (8.16)$$

where $\Delta\omega = \frac{\omega}{N}$ is the sample density in the frequency domain ($0 - \omega_n$); $\psi_{mk}\{\omega_n\} = \arctan\left(\frac{\text{Im}[H_{mk}\{\omega_n\}]}{\text{Re}[H_{mk}\{\omega_n\}]}\right)$ is the phase angle between two points in space; θ_{kn} is a random phase angle uniformly distributed between 0 and 2π .

In order to optimize the computer storage and increase the computation speed, the equation above can be rewritten using an exponential format:

$$a_m(t) = 2 \sum_{k=1}^m \sum_{n=1}^{N-1} \left(|H_{mk}(\omega_n)| \cdot \sqrt{\Delta\omega} \cdot e^{[i(\psi_{mk}\{\omega_n\} + \theta_{kn})]} \right) \cdot e^{i\omega_n t} \quad (8.17)$$

By using the equation above, a series of spatially correlated ground motion time histories at various locations can be obtained. The non-stationary ground motions can then be calculated by multiplying these time histories with a shape function $\delta(t)$ varying with time. Figure 8.6 shows a shape function proposed by Monti et al. [40], which can be expressed as:

Fig. 8.6 A shape function proposed by Monti et al. [40]

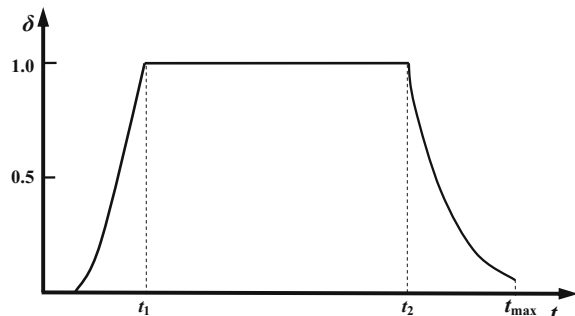


Table 8.1 An example of parameter values of shape function (proposed by Monti et al.) used to simulate the SVEGM [41]

Acceleration component	t_1 (s)	t_2 (s)	t_{\max} (s)	β
Longitudinal and transverse	3	33	44	0.02
Vertical	3	27	44	0.02

$$\delta(t) = \begin{cases} \left(\frac{t}{t_1}\right), & 0 \leq t \leq t_1 \\ 1, & t_1 \leq t \leq t_2 \\ \exp\left(\frac{t-t_2}{t_{\max}-t_2} \ln \beta\right), & t_2 \leq t \leq t_{\max} \end{cases} \quad (8.18)$$

where t_1 and t_2 are the ramp duration and decay starting time, respectively; t_{\max} is the time history duration; and β is the ratio of the envelope amplitude at t_{\max} to the amplitude during the stationary phase ($t_1 \leq t \leq t_2$). Table 8.1 shows an example of those parameter values used to simulate the SVEGM for submarine pipelines. Figure 8.7 shows an example generated multi-support earthquake ground displacement excitations. The difference of ground motions can be clearly identified.

It is noted that adopting the coherence function to describe the spatial variability of ground motions has several drawbacks. An important drawback is that the incoherence effect, the wave passage effect and the local soil/site effect are described separately by statistical spectral models that are stationary in time and homogeneous in space [9], which implies the need to resort to convolutive methods with a low reliability [42–44].

Rather than using coherency functions, various commercial finite element analysis softwares can account for the effects of wave passage, local soil/site, and the loss of coherence, which are directly modeled in a soil–structure interaction analysis to compute the asynchronous ground motions.

For those interested in delving deeper, reference [45] is recommended reading.

8.4 Effects of SVEGM

For structures with short span or dimensions, the effects of SVEGM can normally be neglected, while for large dimension and rather stiff structures, it should be taken into account. The effects due to SVEGM may lead to either a conservative or un-conservative assessment, which cannot be predicted by intuition based on experience. Generally, the spatial variation due to local soil/site and wave passage effect is the most important factor to affect the seismic response, and the incoherence effect is less significant. Therefore, for less important structures, the incoherence effect may be neglected for the practical design. Furthermore, if the seismic wave

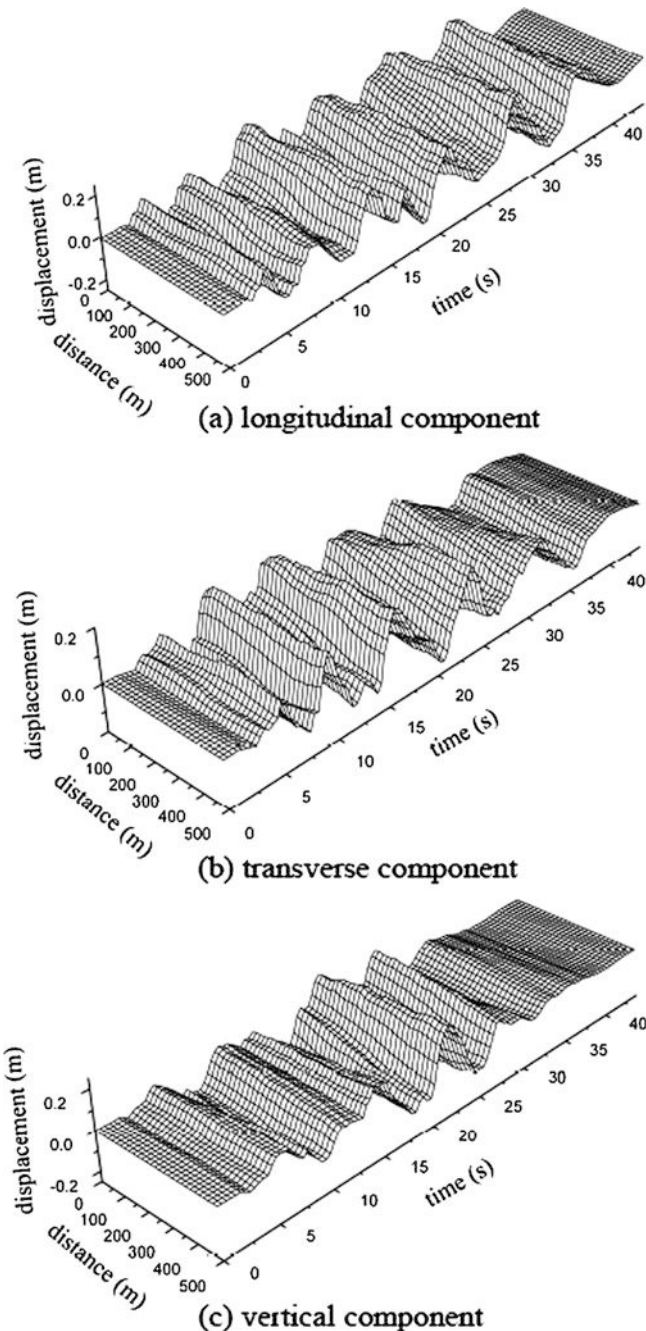


Fig. 8.7 An example of spatially generated displacement time history fields showing the SVEGM [41]

speed is unknown, a few possible speeds can be selected to calculate the seismic response, with the most unfavorable results being used in a practical design [46].

From the historic observed damages due to earthquakes as presented in Sect. 8.1, SVEGM has been identified as a major source of large response for extended structures [47]. SVEGM may significantly increase response amplification due to the possibility of local amplification of the ground motion as a consequence of topographical irregularities and local soil condition. If a structure has dimensions greater than the main wavelengths of the ground motion, different parts of its foundations can vibrate out-of-phase due to the asynchronous seismic motion input. The presence of relevant differential motion may make the structure move in an incoherent way with respect to the surrounding ground. It is sufficient to generate the incoherent motion on a scale length in the order of 100 m [9].

Fig. 8.8 An offshore jackup structure modeling showing significant torsional vibration in its fundamental eigenmode

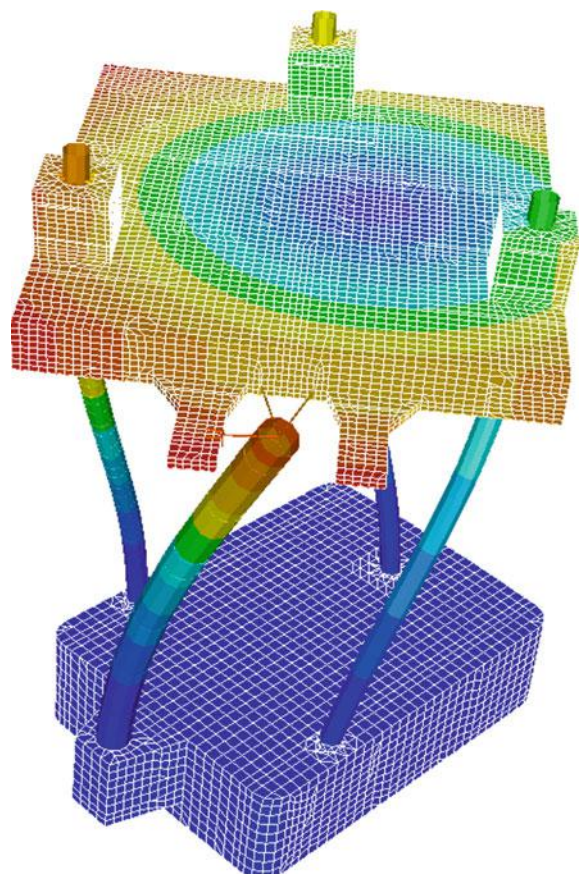




Fig. 8.9 A 25 story L shape office building (courtesy of GSA and Schematic Design & Planning)

From the investigation of dynamic response of bridges under SVEGM, Tzanetos et al. [11], Lupoi et al. [48] and Sextons et al. [49–51] have concluded that the SVEGM can excite the higher order of vibration modes, potentially causing response amplification.

For structures with significant torsional eccentricity, i.e., structures with low torsional stiffness, such as the jackup structure shown in Fig. 8.8, which exhibits significant torsional vibration in its fundamental eigenmode, or an L shape building structure as shown in Fig. 8.9, the effects of SVEGM can also be significant. Figure 8.10 shows the transfer function of the horizontal displacement at a flexible roof corner of an L-shaped building. The building is a typical concrete-steel composite industrial structure sitting on soft soil with a shear wave velocity of 305 m/s, and the foundation consists of isolated foundations under the wall and columns. The incoherent seismic motion at the foundation level was idealized by a homogeneous stochastic field with an isotropic and anisotropic correlation structure. Luco and Wong's coherency function [32] was adopted to model the motion incoherency. The EI Centro NS accelerations were used as the input motion, and the wave passage effects were introduced by time lags on different foundation locations. Due to the torsional eccentricity, the spectrum peak of the transfer function at the flexible corner with incoherent ground motion (i.e. with SVEGM) is 60 % higher than that with coherent ground motion input.

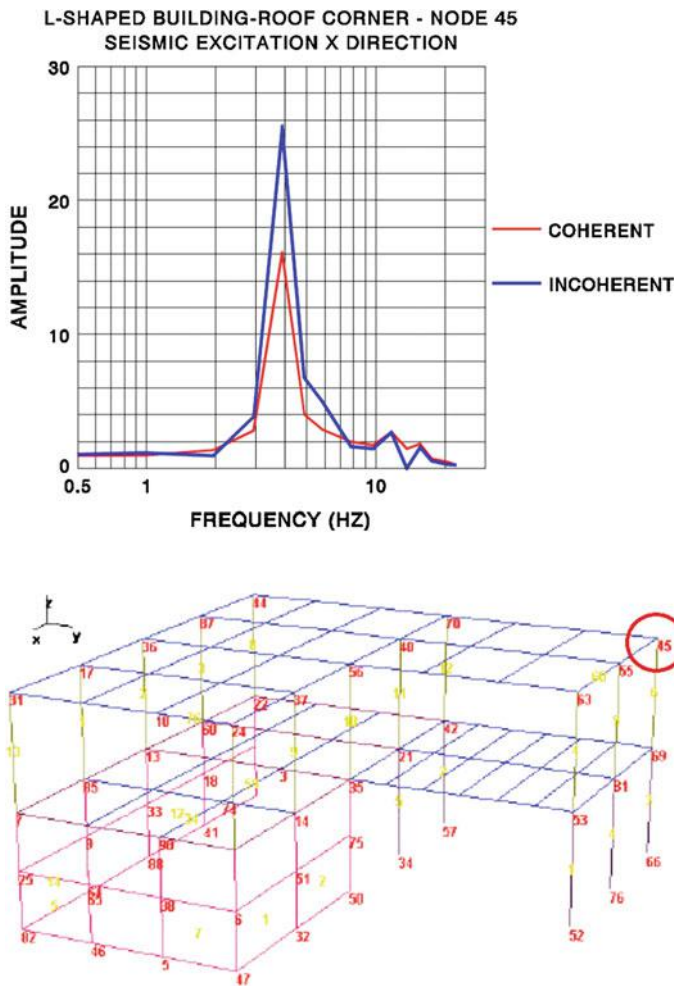


Fig. 8.10 Frequency response (*upper*) of the horizontal displacement with and without consideration of SVEGM at a flexible roof corner (*lower*) of a L shape building [52]

References

1. Gupta ID, Trifunac MD (1998) Defining equivalent stationary psdf to account for nonstationarity of earthquake ground motion. *Soil Dyn Earthq Eng* 17(2):89–99
2. Hindy A, Novak M (1980) Pipeline response to random ground motion. *Proc ASCE J Eng Mech Div* 106(EM2):339–360
3. Datta TK (1999) Seismic response of buried pipelines: a state-of-the-art review. *Nucl Eng Des* 192(2–3):271–284
4. Kojic S, Trifunac MD (1991) Earthquake stresses in arch dams. I: theory and antiplane excitation. *J Eng Mech ASCE* 117(3):532–552

5. Kojic S, Trifunac MD (1991) Earthquake stresses in arch dams. II: excitation by SV, P and Rayleigh waves. *J Eng Mech ASCE* 117(3):553–574
6. Todorovska MI, Hayir A, Trifunac MD (2001) Antiplane response of a dike with flexible structure-soil interface to incident SH-waves. *Soil Dyn Earthq Eng* 21(7):603–613
7. Harichandran RS (1999) Spatial variation of earthquake ground motion. Department of Civil and Environmental Engineering, Michigan State University
8. Lupoi A, Franchin P, Pinto PE, Monti G (2005) Seismic design of bridges accounting for spatial variability of ground motion. *Earthq Eng Struct Dyn* 34(4–5):327–348
9. Romanelli F, Panza GF, Vaccari F (2004) Realistic modeling of the effects of asynchronous motion at the base of bridge piers. *J Seismol Earthq Eng* 6(2):19–28
10. Abrahamson NA, Bolt BA, Darragh RB, Penzien J, Tsai YB (1987) The SMART 1 accelerograph array (1980–1987): a review. *Earthq Spectra* 3(2):263–287
11. Tzanatos N, Elnashai AS, Hamdan FH, Antoniou S (2000) Inelastic dynamic response of RC bridges subjected to spatial non-synchronous earthquake motion. *Adv Struct Eng* 3 (3):191–214
12. Burdette NJ, Elnashai AS, Lupoi A, Sextos AG (2008) Effect of asynchronous earthquake motion on complex bridges. I: methodology and input motion. *J Bridge Eng* 13(2):166–172
13. Novak M (1990) Spatial correlation effects in random vibration of structures. In: Proceedings of the European conference on structural dynamics, EURODYN'90, Bochum, vol 2, pp 631–636
14. Todorovska MI, Trifunac MD (1990) Note on excitation of long structures by ground waves. *J Eng Mech ASCE* 116(4):952–964
15. Zerva A, Shinozuka M (1991) Stochastic differential ground motion. *Struct Saf* 10 (1–3):129–143
16. Loh CH, Penzien J, Tsai YB (1982) Engineering analyses of SMART 1 array accelerograms. *Earthq Eng Struct Dyn* 10(4):575–591
17. Abrahamson NA, Bolt BA (1985) The spatial variation of the phasing of seismic strong ground motion. *Bull Seismol Soc Am* 75(5):1247–1264
18. Der Kiureghian A, Neuenhofer A (1992) Response spectrum method for multi-support seismic excitations. *Earthq Eng Struct Dyn* 21:713–740
19. Zembaty Z, Krenk S (1993) Spatial seismic excitations and response spectra. *J Eng Mech ASCE* 119(12):2449–2460
20. Zembaty Z, Rutenberg A (2002) Spatial response spectra and site amplification effects. *Eng Struct* 24(11):1485–1496
21. Zembaty Zbigniew (2007) Spatial seismic excitation and response spectra. *ISET J Earthq Technol* 44(1):225–233
22. Wirsching PH, Paez TL, Ortiz K (1995) Random vibrations—theory and practice. Wiley, New York
23. Hao H, Oliveira CS, Penzien J (1989) Multiple-station ground motion processing and simulation based on SMART-1 array data. *Nucl Eng Des* 111:293–310
24. Zerva A (1992) Seismic ground motion simulations from a class of spatial variability model. *Earthq Eng Struct Dynam* 21(4):351–361
25. Conte JP, Pister KS, Mahin SA (1992) Nonstationary ARMA modeling of seismic ground motions. *Soil Dyn Earthq Eng* 11:411–426
26. Ramadan O, Novak M (1993) Simulation of spatially incoherent random ground motions. *J Eng Mech* 119(5):997–1016
27. Bozorgnia Y, Bertero VV (eds) (2004) Earthquake engineering: from engineering seismology to performance-based engineering. CRC Press, Boca Raton
28. Schneider JF, Stepp JC, Abrahamson NA (1992) The spatial variation of earthquake ground motion and effects of local site conditions. In: Proceedings of the 10th world conference earthquake engineering, Madrid, pp 967–972
29. Der Kiureghian A (1996) A coherency model for spatially varying ground motions. *Earthq Eng Struct Dynam* 25(1):99–111
30. Elnashai AS, Di Sarno L (2008) Fundamentals of earthquake engineering. Wiley, New York

31. Todorovska MI, Trifunac MD (1997) Amplitudes, polarity and time of peaks of strong ground motion during the 1994 Northridge, California. *Earthq Soil Dyn Earthq Eng* 16(4):235–258
32. Luco JE, Wong HL (1986) Response of a rigid foundation to a spatially random ground motion. *J Earthq Eng Struct Dyn* 14:891–908
33. Wilson JC, Jennings PC (1985) Spatial variation of ground motion determined from accelerograms recorded on a highway bridge. *Bull Seismol Soc Am* 75(6):1515–1533
34. Harichandran RS, Vanmarcke EH (1986) Stochastic variation of earthquake ground motion in space and time. *J Eng Mech ASCE* 112:154–175
35. Loh CH, Yeh YT (1988) Spatial variation and stochastic modeling of seismic differential ground movement. *Earthq Eng Struct Dyn* 16:583–596
36. Feng QM, Hu YX (1981) Mathematical model of spatial correlative ground motion. *Earthq Eng Eng Vib* 1:1–8 (in Chinese)
37. Oliveira CS, Hao H, Penzien J (1991) Ground motion modeling for multiple-input structural analysis. *Struct Saf* 10:79–93
38. Qu TJ, Wang JJ, Wang QX (1996) A practical power spectrum model for spatially varying seismic motion. *J Seismolog* 18:55–62
39. Dai M, Guo W (2004) Multivariate spectral analysis using Cholesky decomposition. *Biometrika* 91:629–643
40. Monti G, Nuti C, Pintio E (1996) Nonlinear response of bridges under multisupport excitation. *J Struct Eng* 122(5):476–484
41. Zhou J, Li X, Feng X, Dong R (2008) Nonlinear seismic analysis of free spanning submarine pipelines under spatially varying earthquake ground motions. In: Proceedings of the eighth international offshore and polar engineering conference, Vancouver
42. Romanelli F, Vaccari F (1999) Site response estimation and ground motion spectral scenario in the Catania area. *J Seismolog* 3:311–326
43. Field EH (2000) The SCEC phase III working group, accounting for site effects in probabilistic seismic hazard analyses of Southern California: overview of the SCEC Phase III Report. *Bull Seismol Soc Am* 90(6B):S1–S31
44. Panza GF, Romanelli F, Vaccari F (2001) Seismic wave propagation in laterally heterogeneous anelastic media: theory and applications to the seismic zonation. *Adv Geophys* 43:1–95
45. Zerva A (2008) Spatial variation of seismic ground motion-modeling and engineering applications. CRC Press, Boca Raton
46. Lin J, Zhang Y (2005) Seismic random vibration of long-span structures, vibration and shock handbook. Taylor & Francis, New York
47. Burdette NJ, Elhashai AS, Lupoi A, Sextos AG (2008) Effect of asynchronous earthquake motion on complex bridges. I: methodology and input motion. *J Bridge Eng* 13(2):158–165
48. Lupoi A, Franchin P, Pinto PE, Monit G (2005) Seismic design of bridges accounting for spatial variability of ground motion. *Earthq Eng Struct Dyn* 34:327–348
49. Sextos AG, Kappos AJ, Mergos P (2004) Effect of soil–structure interaction and spatial variability of ground motion on irregular bridges: the case of the Krystallopigi bridge. In: Proceedings of the 13th world conference on earthquake engineering, Paper No 2298
50. Sextos AG, Pitilakis KD, Kappos AJ (2003) Inelastic dynamic analysis of RC bridges accounting for spatial variability of ground motion, site effects and soil–structure interaction phenomena. Part 1: methodology and analytical tools. *Earthq Eng Struct Dyn* 32:607–627
51. Sextos AG, Pitilakis KD, Kappos AJ (2003) Inelastic dynamic analysis of RC bridges accounting for spatial variability of ground motion, site effects and soil–structure interaction phenomena. Part 2: parametric study. *Earthq Eng Struct Dyn* 32:629–652
52. Ghioce DM (2001) Seismic soil–structure interaction including non-synchronous motion effects for structures with torsional eccentricities. In: The second UJNR workshop on soil–structure interaction (SSI), 2001

Chapter 9

Seismic Hazard and Risk Assessment

There is always going to be an element of doubt, as one is extrapolating into areas one doesn't know about.

Richard Smith

9.1 Seismic Hazard Analysis

The evolution of engineering practice away from ‘worst case’ design criteria and the now widespread use by professional earth science firms of probabilistic seismic hazard analysis (with its resulting continuous spectrum of ground motion levels and probabilities) eliminate the previously critical need for engineers to get involved ‘up front’ in the seismic input characterization for a project...

Carl Allin Cornell (1938–2007)

9.1.1 Introduction

Hazard is defined as inherent physical characteristics that pose potential threats to people, property, or the environment. Within the context of seismic hazard, the main purpose of hazard analysis is to quantitatively assess ground shaking level at a site, through either deterministic analysis (as when a specific earthquake scenario is assumed, as will be introduced in Sect. 9.1.2); or probabilistic analysis, in which various earthquake scenarios and uncertainties are explicitly accounted for [1], as will be presented in Sect. 9.1.3. The effects of local soil on the seismic wave transmission are often assessed separately by a site specific response analysis, as discussed in Chap. 4.

A seismic hazard analysis normally comprises the following two tasks:

1. Identify earthquake sources: this is to identify all the possible earthquake sources and the fault geometry associated with a specific region or site. It is normally performed by studying the geologic evidence, tectonic evidence, historical seismicity and recent instrumental seismicity records. Based on this information, the potential for future earthquakes can be evaluated. In this task, it is important to determine the occurrence rate of earthquake activities and the associated range of magnitude. For more detailed information on identification and characterizing earthquake sources, readers may read reference [1].
2. Determine the ground motions or ground motion parameters: based on selected attenuation relations (Sect. 3.6), this is normally performed by carrying out either deterministic (DSHA) or probabilistic (PSHA) seismic hazard analysis, of which the former is based on a single earthquake scenario (a predefined earthquake source) with a selected magnitude and single source-to-site distance; and the latter is based on various scenarios (earthquakes on different sources); it also accounts for the uncertainties associated with earthquake size, location, and time of earthquake occurrence etc. For the PSHA, the median of the ground motion parameter or the mean of the natural-log of ground motion parameter value and standard deviation of earthquake spectral ordinates for different levels of given magnitudes, source-to-site distance, and site conditions etc., should be established. The resulting ground motion selection provides a necessary link between seismic hazard and structural response [2].

A dedicated seismic hazard analysis can help not only to increase the reliability of structural design, but also greatly reduce the uncertainties without degrading a required safety level, leading to a more economical design. For example, Diablo Canyon nuclear power plant (Fig. 9.1) at the edge of the Pacific Ocean in San Luis Obispo, California was constructed in 1968. The original design was based on a deterministic seismic hazard analysis to determine the ground motion from an earthquake associated with a particular fault in the region, based on historical records and geological evidence, then by using this information to perform the capacity control of structures, systems and components at the facility to ensure they could withstand seismic ground shaking [3]. Since then, different new faults have been identified that almost circle the plant, with the closest one, the Shoreline Fault found in 2008, coming within only 600 m of the reactors, and Hosgri fault, found in 1971, lying 5 km away. However, with a dedicated PSHA, recently, seismologists could even show a lower ground motion intensity demand than what was required in the original design using DSHA [4, 5].

Most of the seismic design codes rely on both DSHA and PSHA for seismic hazard analyses.

Sometimes, analysis with real-time recorded ground-motion time series at the locations of seismic (strong motion) stations can also be performed to assess the seismic hazard. While a major problem involved in this method is that the locations for which ground-motion data are available are not likely to comply with the sites of



Fig. 9.1 The Diablo Canyon Power Plant, north of Avila Beach, in San Luis Obispo County, California (courtesy of ML Baird)

interests, this problem can be partially solved by seeking the available records at stations nearby (typically less than 30 km) the sites of interest. As most of the ground-motion data available are realistic ground-motion data recorded at the ground surface, the soil amplification effects are already included in the analysis with real-time data.

9.1.2 Deterministic Seismic Hazard Analysis (DSHA)

Prior to PSHA, DSHA was prevalent. In DSHA, by identifying the potential earthquake sources (faults), individual earthquake scenarios in terms of magnitude and location are developed for each relevant seismic source and a predefined ground motion probability level.

After identifying the earthquake source location(s), the source-to-site distance (Fig. 3.31) can be computed, see Sect. 9.1.3.1 for details. Given the magnitude, the distance, and the number of standard deviations for the ground motion, the ground motion is then computed for each earthquake scenario using a ground motion model (attenuation relation presented in Sect. 3.6) that is based on either empirical ground motion model or numerical simulations. The largest ground motion from any of the considered scenarios is used for the design ground motion. The approach is “deterministic” in that single values of parameters (magnitude, source-to-site distance,

and number of standard deviations for the ground motion) are selected for each scenario [6].

It should be noted that even if deterministic estimates of ground motion extremes at a site are basically obtained by considering a single event of a specified magnitude and source-to-site distance, in case a site has several known active faults in its proximity, a maximum magnitude is normally defined for each fault.

Practically, a DSHA can be performed by the following four steps [1]:

1. Identify all earthquake sources (e.g. known faults) capable of producing non-negligible ground motions at a site, determine their locations relative to the site, and specify the source models by defining source zones and the largest amplitude (earthquake potential) that each source is capable of producing.

The source models at the target region are basically derived from the earthquake catalogs of historical and instrumental seismicity. This statistic is inevitably obtained within geologically short periods. Therefore, it may be supplemented by additional data, such as the results from seismic monitoring, geodetic monitoring, deep geologic investigation etc.

The maximum magnitude is normally a function of the fault length and historical knowledge of past earthquakes on that particular source, and is therefore not strictly associated with a defined return period (Sect. 9.1.3). In this step, the probability of occurrence for potential source rupture is implicitly assumed to be unity, as will be discussed in Sect. 9.1.3.1, this probability can be taken into account in a PSHA.

Determining the earthquake potential (magnitude) is a rather subjective choice. The results may be very sensitive to the background and objectives of the decision maker. An event chosen in this manner was historically described as a maximum credible earthquake (MCE), which is the largest earthquake that is capable of occurring under the known tectonic framework for a specific fault or seismic source, as based on geologic and seismologic data. There may be several MCEs for one site, each from a different fault or seismic source.

2. For each source zone, select source-to-site distance. Typically, the shortest distance is selected. This actually implicitly assumes that, in each source zone, the probability of occurrence is 100 % at the points closest to the site, and zero elsewhere.
3. Specify the controlling earthquake that produces the largest ground shaking among all ground shakings and relationship that describes the attenuation of ground motion with distance identified, i.e., it is based on the source potential determined in step 1 and source-to-site distance obtained in step 2.
4. Determine the ground motion by the controlling earthquake.

Again, readers need to bear in mind that, by its nature, a DSHA does not explicitly account for the likelihood of a particular earthquake scenario occurrence, and it is not associated with a specific return period, although the particular earthquake event used can have a return period associated with it. The return period for the maximum event on a given fault can vary from several hundred to several

thousand years, depending on the activity rate of the fault. Therefore, deterministic results cannot be used for a quantitative assessment of the overall risk of an infrastructure.

Although DSHA has the merit of being simple, the relevant conceptual problems arise quickly and are difficult to solve. It is commonly misunderstood by engineers that the hazard determined from the four steps above is the “worst case,” because the largest amplitude and shortest source-to-site distance are usually used to calculate the design ground motions [7]. However, this may not be the case because the limitations due to the deterministic method itself, i.e., the variability/scatter of the design event and ground motion intensity. It provides no information on the likelihood of occurrence of the controlling earthquake and the effects of uncertainties in the various steps required to calculate the ground motion characteristics. Therefore, nowadays, DSHA may only be used to complement the PSHA, as will be discussed in Sect. 9.1.3. For example, a deterministic seismic hazard analysis sometimes specifies a mean plus one standard deviation response spectrum as shown in Fig. 3.33 (the mean value of $\ln Y \pm \sigma_{\ln Y}$), but even this response spectrum will be exceeded 16 % of the time. Because the scatter is normally distributed, there is no theoretical upper bound on the amplitude of ground motion that might be produced at a given magnitude and distance. Obviously, there is a true physical upper bound on ground motion intensity caused by an inability of the earth to carry more intense seismic waves without shattering or otherwise failing. Even though this limit can provide information to determine extremely high ground motions used for design of rather important structures such as nuclear waste repositories, it has almost no engineering sense on the majority of structures such as buildings or bridges, which are analyzed for ground motion intensities that are exceeded once every few thousand years. Thus, the theoretical upper bound of ground motions has no practical sense for most seismic designs [8].

As mentioned before, historically, the result obtained from a DSHA is often referred to as Maximum Credible (or Capable) Earthquake (MCE). More recently, however, the acronym has been retained but taken to indicate Maximum Considered Earthquake as the most severe earthquake effects considered, in recognition of the fact that larger earthquakes (and larger ground motion intensities) than those shown by MCE can happen. The Maximum Considered Earthquake is often quantified by MCE maps based on a combination of the results of deterministic and probabilistic estimates of ground motions.

9.1.3 Probabilistic Seismic Hazard Analysis (PSHA)

Different from DSHA that only calculates a so-called “worst case” ground motion parameters, PSHA is a more rational seismic hazard method that considers all (hopefully) possible earthquake scenarios to calculate the ground motion parameters with their associated probabilities of occurrence. This is also the primary advantage of PSHA over DSHA.

It is obvious that a great number of uncertainties pose challenges to quantify future earthquakes. Those uncertainties mainly relate to the earthquake location, the magnitude, source-to-site distance, resulting shaking intensity for the given magnitude, site condition, and time of occurrence of future earthquakes, etc. All or most of these parameters can only be characterized by probability distributions with randomness. Moreover, the source-to-site distance is a computed parameter that depends on the earthquake location and rupture dimension, which in turn have randomness [6].

To quantify these uncertainties, and combine them to produce a description of the distribution of future seismic motions that may occur at a site, Cornell [9] first explicitly described the procedure to perform a PSHA, which is essentially to consider many scenarios (earthquakes on various sources) and account for the uncertainties mentioned above, and to calculate the annual rate of exceedance of different levels of selected ground motion parameters. The uncertainties typically include: (1) aleatory uncertainties associated with random variability and characterized by probability distributions, which can be integrated in a PSHA procedure described in the current section; (2) epistemic uncertainties due to lack of knowledge with respect to earthquake source processes and wave propagation, which can be reduced by additional data characterized by a probability distribution; the identification, quantification and incorporation of epistemic uncertainty require a dedicated judgment from a number of experts, and can be accounted for using logic trees, as will be introduced in Sect. 9.1.5.

In a PSHA, when a site is selected, all the zones within a certain radius from the site are being taken into account. For the probabilistic analysis, all scenarios from deterministic analysis are therefore included, forming a full set of scenarios and with all possible magnitude and location combinations for the site. For each earthquake scenario, all possible ground motions are computed for each possible value of standard deviations above or below the median (or mean) ground motion [6].

Practically, a PSHA also involves four steps that are similar to that of DSHA. The major difference between the two methods is that, in each step of a PSHA, the uncertainties mentioned above are taken into account through probability descriptions (typically using probability distribution functions), as shown in Fig. 9.2. As many of the major potential pitfalls in executing a successful PSHA are procedural rather than technical, a significant amount of research efforts during the past decades have been directed to procedural guidance. They will be introduced in the subsequent sections.

9.1.3.1 Define Earthquake Source and Geometry

The first step in a PSHA is to define source seismicity, geometry and probability distribution of magnitude and source-to-site distance, including: (1) identify all earthquake sources; (2) characterize the probability distribution of earthquake magnitudes; and (3) characterize the probability of source-to-site distances associated with potential earthquakes.

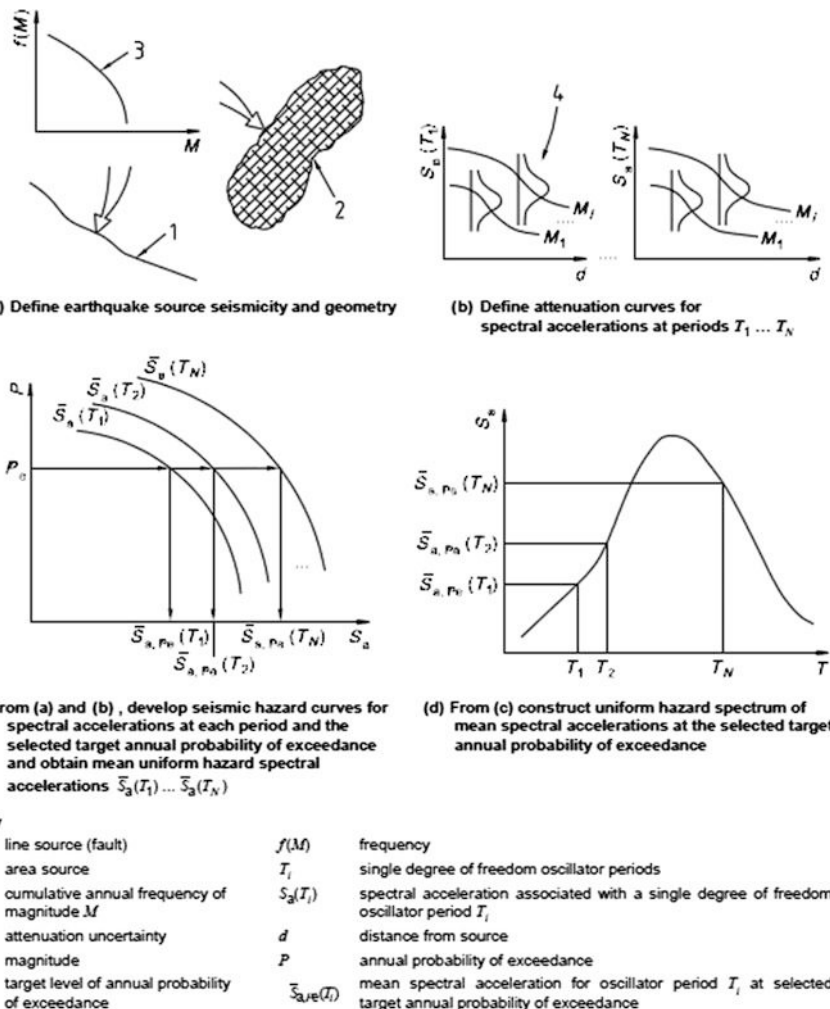


Fig. 9.2 Four steps for performing a PSHA [10]

This is similar to that of DSHA, the only difference being that the probability of various magnitudes on all potential sources affecting the site should be considered. Here the potential earthquake sources can be either faults or area sources of diffused seismicity not directly attributable to a known fault. Also, a maximum magnitude is assigned to each source [10]. In many cases, the probability distribution of source-to-site distance also needs to be characterized, as will be presented in step (3).

1. Identify all earthquake sources:

The source zones can be categorized as point, linear or three-dimensional sources. Earthquakes induced by volcanic activities or short fault ruptures can generally be

assumed to be point sources as the zones are small. For shallow fault zones that have well defined planes in which the changes in hypocentral depth distance have insignificant influence on hypocentral distance, the linear (areal) source is the most suitable one to adopt. However, for areas where the fault mechanism (especially the fault geometry) is poorly understood or defined, which typically corresponds to dispersed seismic activity and that not directly associated with known faults, one has to use three-dimensional volumetric sources. In the calculation of source-to-site distances and the associated uncertainties, the linear source and volumetric source are sometimes simplified as a line source and area source, respectively, as will be discussed in step (3).

2. Characterize the probability distribution of earthquake magnitudes:

The probability of source rupture is generally assumed to be uniformly/homogeneously distributed within each seismogenic/source zone, implying that earthquakes are equally likely to occur at any location within each seismogenic zone. This assumption may be revised if detailed seismological studies on the local area deviate from the homogenous zone model. By combining with source geometry, the probability distribution of the corresponding source-to-site distance can be calculated. It should be noted that a uniform fault rupture distribution in space may not result in a uniform distribution of source-to-site distance.

It is necessary to establish an annual frequency of earthquake occurrence for each source as a function of earthquake magnitude, by specifying the average rate at which an earthquake with a certain magnitude will be exceeded. Globally, the earthquake occurrence varying with magnitude is usually expressed in terms of the Gutenberg-Richter relationship (also called Gutenberg-Richter recurrence law) [11] as shown in Fig. 9.25, which defines that the magnitude M is exponentially distributed:

$$\log_{10}N_c = a - bm \quad (9.1)$$

where N_c is the cumulative number of earthquakes with the magnitude larger than m occurring on a seismic source per unit time, it is also referred to as the rate of the earthquake with magnitudes greater than m ; a and b are region constant, which is estimated through curve fitting using statistical analysis of historical earthquake observations, with additional constraining data provided by other types of geological evidence; a is the activity rate parameter indicating the overall rate of earthquakes in a region, it is a function of sample size and is therefore liable to vary substantially from one seismic source to another, the total number of earthquakes with magnitude larger than or equal to zero is $10a$; b describes the relative number of small and large earthquakes in the region, worldwide it is around 1.0 with a deviation of ± 0.3 . For the North Sea, by using curve fitted linear regression with a correlation coefficient of 0.99 complied with the instrumentally determined earthquake through 1980–1989 [12], it is obtained that $a = 4.42$ and $b = 0.84$. This indicates that the number earthquakes above magnitude 4.0 that occurred annually in the North Sea is around 2.

Note that earthquakes with smaller magnitude are not of interest for structural designs. The Gutenberg-Richter relationship described above is normally used to calculate the cumulative distribution function (CDF) for earthquakes within a range of magnitude larger than m_{min} (m_{min} must be smaller than m):

$$\begin{aligned} F_M(m) &= P(M \leq m | M > m_{min}) \\ &= \frac{10^{1-bm_{min}} - 10^{a-bm}}{10^{a-bm_{min}}} = 1 - 10^{-b(m-m_{min})} \end{aligned} \quad (9.2)$$

By taking the derivative of the CDF above, one obtains the probability density function (PDF) for M :

$$f_M(m) = \frac{d}{dm} F_M(m) = b \ln(10) 10^{-b(m-m_{min})} \quad (9.3)$$

However, since the energy that can be released by relevant fault ruptures is limited based on the fault size, the maximum magnitude of earthquake that can occur over that particular region is limited as well. Physically, there is an upper limit m_{max} of earthquake magnitude that each source can produce. In such a case, the linear Gutenberg-Richter relationship can still be applied but with an upper limit of earthquake magnitude, which is normally modeled by a truncated (bounded) Gutenberg-Richter relationship, with the corresponding CDF rewritten as:

$$F_M(m) = \frac{1 - 10^{-b(m-m_{min})}}{1 - 10^{-b(m_{max}-m_{min})}} \quad (9.4)$$

And the corresponding PDF is then rewritten as:

$$f_M(m) = \frac{b \ln(10) 10^{-b(m-m_{min})}}{1 - 10^{-b(m_{max}-m_{min})}} \quad (9.5)$$

For numerical or hand calculations, the continuous distribution of the magnitude has to be rewritten as a discrete set of magnitudes, and the probability of occurrence between magnitude m_i and m_{i+1} ($m_{i+1} > m_i$) is:

$$P(M \in (m_i, m_{i+1})) = F_M(m_{i+1}) - F_M(m_i) \quad (9.6)$$

The Gutenberg-Richter relationship is essentially a power law typical for fractal sets that implies scale invariance and self-similarity. As will be discussed in Sect. 9.5, it may not be capable of predicting earthquakes with very large magnitudes.

More realistic than what the Gutenberg-Richter relationship can predict, statistics and geologic evidence show that annual probability of occurrence of ruptures for specific faults have repeated occurrences with a reasonably consistent magnitude [13]. The relationship based on this observation is normally referred to as the

characteristic earthquake model and requires a minor modification of the probability density function [14].

3. Characterize the probability distribution of source-to-site distances associated with potential earthquakes:

It is normally assumed that the probability distribution of earthquakes within a source zone is uniformly distributed, i.e., earthquakes will occur with equal probability of occurrence at any location on the relevant fault. However, sometimes non-uniform distribution is also possible. As the definition of source point can vary significantly as shown in Fig. 3.31, a uniform distribution of the source zone does not often result in a uniform distribution of source-to-site distances as mentioned before. The uncertainty in source-to-site distance can be characterized by a PDF or CDF.

For a point source, the PDF is equal to 1 when the distance is equal to the site-to-point source distance and otherwise it is equal to 0.

To model the faults on the boundary of two tectonic plates, a line fault source model with a total length of $2l$ km is normally adopted as shown in Fig. 9.3. By assuming that earthquake epicenters are equally likely at all locations, the probability of observing a distance R less than r km is equal to the fraction of the fault located within a radius of r , the corresponding CDF is then calculated as:

$$F_R(r) = \begin{cases} 0 & \text{for } r < s \\ P(R \leq r) = \frac{2\sqrt{r^2 - s^2}}{2l} & \text{for } s \leq r < l + 1 \\ 1 & \text{for } r \geq l + 1 \end{cases} \quad (9.7)$$

With the corresponding PDF expressed as:

$$f_R(r) = \frac{d}{dr} F_R(r) = \begin{cases} \frac{r}{l\sqrt{r^2 - s^2}} & \text{for } s \leq r < l + 1 \\ 0 & \text{for } r \geq l + 1 \text{ or } r < s \end{cases} \quad (9.8)$$

Note that the two equations above are based on the assumption that the fault can be represented as a line source. By following a similar procedure, the CDF and PDF corresponding to a plane source can be developed, which is more typical in a seismic hazard analysis.

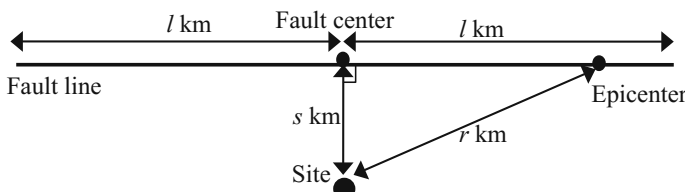
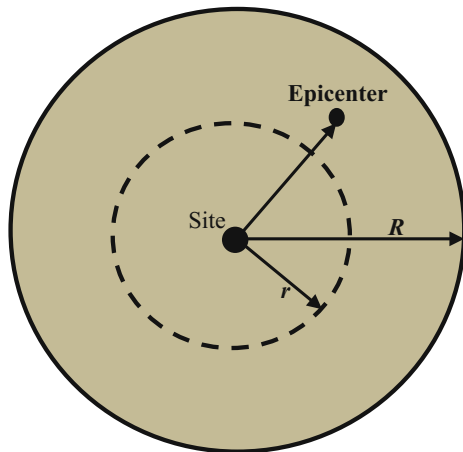


Fig. 9.3 An illustration of line source

Fig. 9.4 An illustration of a circular shape area source with a radius of R



For earthquakes that are not produced by specific faults, a circular shape area source (Fig. 9.4) with a radius of R (say 100 km) can be adopted. By assuming a uniform probability distribution of earthquake epicenter within the area, the corresponding CDF of an epicenter that is located within a distance of less than r from the site is equal to the ratio of the area of a circle with the radius r and the area of the circle with the radius R :

$$F_R(r) = \begin{cases} 0 & \text{if } r = 0 \\ P(R \leq r) = \frac{\pi r^2}{\pi R^2} = \frac{r^2}{R^2} & \text{for } 0 \leq r < R \\ 1 & \text{for } r \geq 100 \end{cases} \quad (9.9)$$

The corresponding PDF is:

$$f_R(r) = \frac{d}{dr} F_R(r) = \begin{cases} \frac{2r}{R^2} & \text{for } 0 \leq r < R \\ 0 & \text{otherwise} \end{cases} \quad (9.10)$$

9.1.3.2 Establish Attenuation Relationship

The second step in a PSHA is to calculate the ground motion intensity by specifying the ground motion attenuation relationships as a function of earthquake magnitude and source-to-site distance etc., with a consideration of its randomness. This requires a probability distribution of magnitude and source-to-site distance, as mentioned above in the previous step, to represent the uncertainty of the predicted ground motion at a site. The attenuation relationships are normally developed based on statistical analyses of ground motion records from past earthquakes occurring in similar geological and tectonic conditions, as previously presented in Sect. 3.6.

In this step, it is assumed that the fault rupture energy is released at the hypocenter. However, for major earthquakes, as the area of fault rupture is so large that parts may be much closer to the site than the hypocenter, the effects may potentially lead to a situation in which the resultant location measured by released energy can be closer to the site than the hypocentral distance. This is especially the case for large earthquakes with a distant hypocenter [15].

As presented in Sect. 3.6, in the modeling of ground motion attenuation relationship, the ground motion parameter Y (i.e., PGA, PGV, modified Mercalli intensity (MMI), or peak spectral acceleration at different periods) is normally modeled as a function of earthquake magnitude M , source-to-site distance R (sometimes also includes θ to account for rupture mechanism, local soil conditions, as well as directivity parameters), and uncertainty E , which can be expressed as follows:

$$\ln Y = f(M, R) + E \quad (9.11)$$

9.1.3.3 Develop Seismic Hazard Curve

The third step in PSHA is to perform probabilistic calculation to obtain the exceedance probability for a given ground motion (y), $P[Y \geq y]$ from the ground-motion attenuation relationship selected in the previous step, i.e., to calculate the probability that a ground motion will be exceeded during a specified time period/duration. This is carried out by accounting for the various uncertainties in earthquake size, location and ground motion intensity as mentioned above, and a summation over individual probabilities from all sources. This finally provides the total annual probability of exceedance for a given level of ground motions.

Note that the uncertainty E can normally be assumed to follow a normal distribution with a zero mean and a standard deviation $\sigma_{\ln Y}$, i.e., $E = \varepsilon \sigma_{\ln Y}$, where ε is a constant number of standard deviations ($\sigma_{\ln Y}$) measured as the difference relative to the median or mean ground motion $f(M, R)$. One can then compute the probability of exceeding any y level of ground motion intensity level:

$$P(Y > y | m, r) = 1 - \Phi\left(\frac{\ln y - \bar{\ln Y}}{\sigma_{\ln Y}}\right) \quad (9.12)$$

where $\Phi()$ is the standard normal cumulative distribution function, which can be checked from various mathematical handbooks; $\bar{\ln Y}$ and $\sigma_{\ln Y}$ can be calculated from the statistical calculation of observed data (with an example shown in Fig. 3.33) from the historical earthquakes.

The equation above can be expressed by incorporating the probability density function $f_Y(u)$ of the ground motion parameter Y (given m and r) without checking the $\Phi()$ value, i.e., $f_Y(u)$ can be written out analytically [8]. An integral form of expression can then be used and be calculated either analytically or numerically:

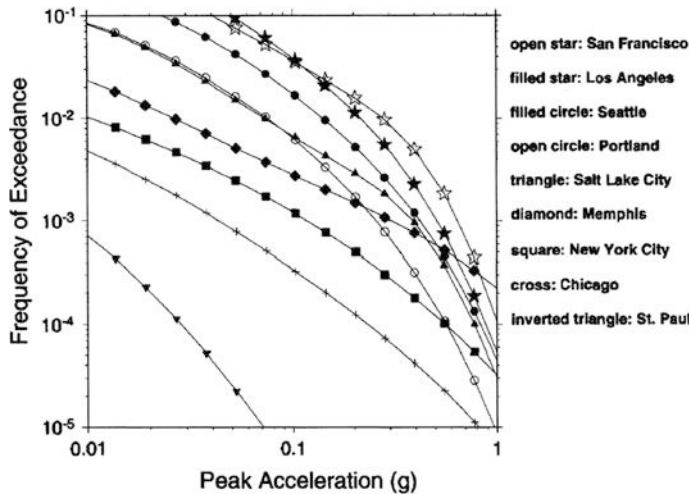


Fig. 9.5 Seismic hazard curve showing the peak ground acceleration versus annual probability of exceedance for various sites in the United States (courtesy of USGS)

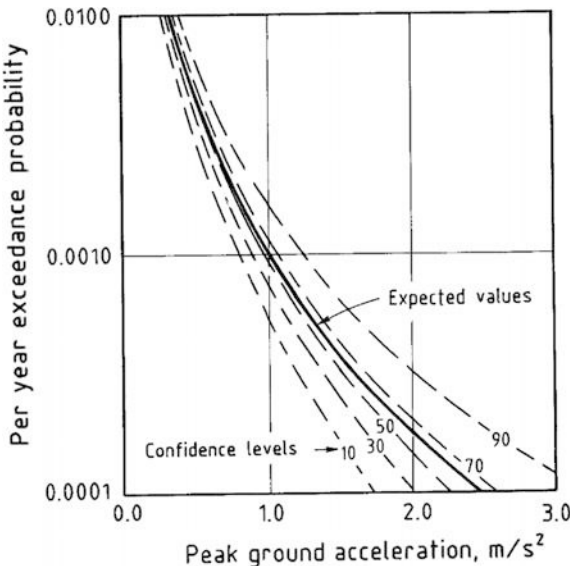
$$P(Y > y | m, r) = \int_y^{\infty} \frac{1}{\sqrt{2\pi}\sigma_{\ln Y}} e^{-\frac{1}{2}\left(\frac{\ln u - \bar{\ln Y}}{\sigma_{\ln Y}}\right)^2} du \quad (9.13)$$

Based on the equation above, which can be evaluated numerically using a PSHA software, Fig. 9.5 shows the peak ground acceleration versus annual probability of exceedance for various sites in United States. This type of curve is often referred to as a seismic hazard curve.

The majority of design codes use design spectrum to characterize the ground motion intensity. For each spectral period (dominant period) T_i and the selected target probability of exceedance P_e , one can plot a site specific hazard curve with a \log_{10} - \log_{10} basis. This shows the probability distribution of the spectral parameters (such as spectral acceleration $S_{a,P_e}(T_i)$). Figure 9.6 shows the peak ground acceleration ($T_i = 0$ s) versus annual probability of exceedance for an offshore site on the Norwegian continental shelf. It is noticed that the slope of the curve is steep, the peak ground acceleration with a return period of 10,000 years (with an annual probability of exceedance of 0.0001) is around 2.5 times of that for a return period of 1000 years (with an annual probability of exceedance of 0.001).

It is worth mentioning that, as an alternative to PSHA, one may directly utilize the ground-motion attenuation and earthquake occurrence frequency relationships to derive a hazard curve that can be used for seismic risk assessment. In this method, M is expressed as a function of R , $\ln Y$ and E . This approach is referred to as seismic hazard assessment (SHA). For more details, readers may read Wang [17, 18].

Fig. 9.6 Seismic hazard curve showing the peak ground acceleration for different levels of confidence versus annual probability of exceedance for a site on the Norwegian Continental Shelf [16]



For each target annual probability of exceedance P_e , it is required to construct a uniform hazard spectrum (UHS) such that at each period, the spectral acceleration at that period corresponds to the target annual probability of exceedance. UHS is not only the PSHA-based design spectrum [19], but also the state-of-the-practice and the basis for the definition of design seismic actions on structures in the most advanced seismic codes.

Since in PSHA the probabilities associated with ground motion values are calculated by combining the probabilities of ground motion from various sources, the ground motion probabilities are not associated with a specific fault or event. In fact, while it seems conservative to use the expected ground motion from the largest possible earthquake occurring at the closest location on the nearest fault, those values can be significantly smaller than ground motions calculated from a probabilistic method. This possible outcome is particularly true if the largest earthquake on the nearest fault is associated with a shorter return period than being considered in a probabilistic method, or if the site is affected by several faults, each contributing to the overall probability of exceedance. The opposite outcome is also possible when the return period of the largest earthquake on the nearest fault is much greater than the desired return period of the ground motion [10]. This can be studied through deaggregation analyses, as will be presented in Sect. 9.1.4.

To find a probability of exceedance, one needs to know the distribution of earthquakes in time. By assuming that the earthquake occurrence in time has a constant rate, and time to the next earthquake is independent of time to the last earthquake, the relationship between the average return period (or inverse of the average recurrence rate) and the target annual probability of exceedance can be described by the Poisson model, which defines the probability of at least one

exceedance ($N \geq 1$) of an earthquake with a specific ground motion level in a period of t years:

$$P_e[N \geq 1] = 1 - e^{-\lambda t} \quad (9.14)$$

where λ is the average recurrence rate (also called the average rate of annual occurrence, annual rate of exceedance, or annual frequency of exceedance) of the event with considered earthquake magnitude. This model is adopted by the majority of current seismic design codes.

In case the average recurrence rate is small, say less than 0.05, there is a convenient approximation of the exceedance probability for small probability:

$$1 - e^{-\lambda \cdot t} \approx \lambda t \quad (9.15)$$

If one sets time period of interest $t = 1$ year, the annual probability of exceedance can be calculated as:

$$q = 1 - e^{-\lambda \cdot 1} = 1 - e^{-\frac{1}{R}} \quad (9.16)$$

where R is called return period, or recurrence interval, which is defined as the average time between the design conditions being exceeded.

It should be emphasized that the adoption of return period is the average time span between shaking intensity that is equal to or greater than a specified value. It does not mean that a certain event associated with a return period must occur in the return period time, it is only used as an estimate of the likelihood of an event. For example, a 100 year earthquake may not regularly happen every 100 years. Therefore, PSHA presents earthquake occurrence only implicitly.

Readers need to bear in mind that Poisson process is a memoryless model, in that it is independent of elapsed time. In addition, it is also independent of size or location of any previous events. Therefore, this model is only applicable for a large area with many tectonic faults [20].

Example Based on Poisson process, calculate the average rate of annual occurrence λ and return period of at least one event that has 10 % probability of being exceeded in the next 50 years (time span).

Solution with $P_e[N \geq 1] = 10\%$, $t = 50$, one then has: $10\% = 1 - e^{-\lambda \cdot 50}$, and the average rate of annual occurrence λ is 0.0021; and the return period $R = 1/\lambda = 475$ years.

Obviously, a structure and/or its foundation shall be designed and constructed to withstand a seismic action having a lower probability of occurrence than the design seismic action. However, if it is required to sustain unrealistically/impossibly high seismic loading within its service life without damage and the associated limitations of use, the costs of which would be extraordinarily high. Therefore, the seismic

Table 9.1 Typical values and relationships of reference probabilities of exceedance and corresponding return periods

Probability of exceedance (%)	Time span (years)	Return period (years)
50	50	72
50	100	144
20	10	45
10	10	95
20	50	224
10	50	475
5	50	975
10	100	949
5	100	1950
2	50	2475
1	50	4975

action to be considered for a “damage limitation requirement” at component level and a “non-collapse limitation level” at the system level should have reasonable probability of exceedances, as will be discussed in Chap. 14. Therefore, for the design of critical structures, such as nuclear power plants, offshore platforms, dams, bridges etc., smaller values of the reference probability of exceedance, or longer reference return periods would be selected. Table 9.1 shows the inter-relation of these two parameters.

Sometimes, it is more desirable to use a certain ground motion having a P_f probability of exceedance in T_f years, to determine the probability P_Q , which is the same ground motion that is exceeded at least once in Q years. Since the level of ground motion (defined by its annual exceedance rate or return period) remains constant, working with the above equations, it can easily be derived that the sought probability is:

$$P_Q = 1 - (1 - P_f)^{Q/T_f} \quad (9.17)$$

Based on the equation above, Table 9.2 shows relationships among typical exceedance probabilities and associated time spans for a certain level of ground motion. If we take the peak ground acceleration (event) that has 10 % probability of being exceeded in the next 50 years as a reference, it is noticed that the probability of exceeding this reference peak ground acceleration is reduced to 1/5 for a 10 year span, while the probability for a 1000 year span becomes almost 9 times that of the reference.

By combining the Gutenberg/Richter occurrence model with Poisson distribution, Ritsema [21] applied the theory of extremes from the Gumbel model [22] to calculate the extreme value of earthquake magnitude for the whole North Sea region, which is presented in Table 9.3. One fact that needs to be mentioned is that the largest North Sea earthquake during the last century was the Oslofjord

Table 9.2 Relationships among typical exceedance probabilities and associated time spans for a certain level of ground motion

If a ground motion has a probability of exceedance in 50 years	In 10 years this ground motion will have a probability of exceedance (%)	In 100 years this ground motion will have a probability of exceedance (%)	In 1000 years this ground motion will have a probability of exceedance (%)	In 3000 years this ground motion will have a probability of exceedance (%)	In 10,000 years this ground motion will have a probability of exceedance (%)
20 %	4	36	99	100	100
10 % (corresponding to a return period of 475 years)	2	19	88	100	100
5 %	1	10	64	95	100
2 %	0.4	4	33	70	98

Table 9.3 Extreme value of earthquake magnitudes with various levels of return period in the whole North Sea

Return period (years)	Magnitude	Uncertainty in magnitude
5	4.6	±0.4
10	5.1	±0.2
15	5.4	±0.2
25	5.6	±0.2
50	5.9	±0.2
75	6.0	±0.3
100	6.1	±0.4
200	6.3	±0.6
500	6.5	±0.9
1000	6.6	±1.1
5000	6.7	±1.6
7000	6.7	±1.7
10,000	6.8	±1.8

earthquake of 1904, with a magnitude M_s of around 5.4. Further, it is also noticed that the seismicity in the Norwegian part of the North Sea is in general greater than that in the UK part [23]. Figure 9.7 shows that the probability for at least one earthquake of more than magnitude 6.7 to occur in the United States between 2003 to 2032 is 62 %.

It should be mentioned that more complicated models for calculating earthquake occurrence have been developed over recent decades, including time-dependent models [24], renewal models [25, 26], and time-predictable models [27]. For example, time-dependent models were used for the estimation of seismic hazard for

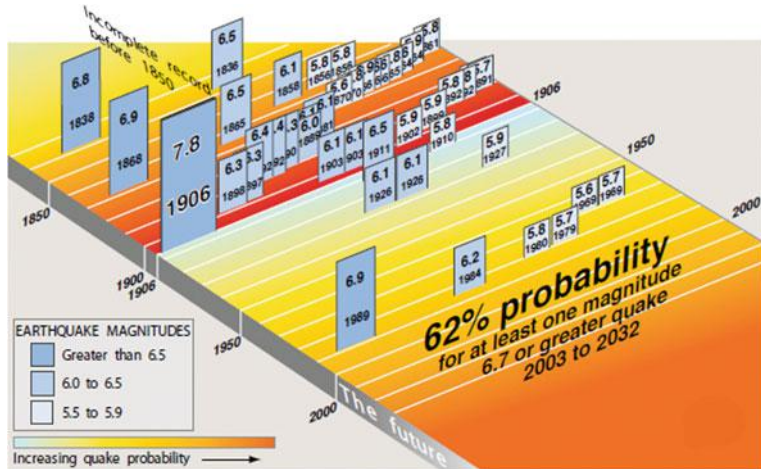


Fig. 9.7 The history and probability of earthquakes in the United States (courtesy of USGS)

San Francisco Bay Area by the US Geological Survey, provided that sufficient data are available [28].

So far, we have learned the knowledge on how to calculate the probability distribution of earthquake magnitude (Gutenberg-Richter relationship) and source-to-site-distance, denoted as $f_M(m)$ and $f_R(r)$, respectively. We have also learned how to compute the probability of exceeding any y level of ground motion intensity level $P(Y > y|m, r)$. Each of the parameters above can be determined through scientific studies of historical earthquakes and processing of observed data. In addition, by understanding how to correlate the average rate of annual occurrence λ with the annual probability of exceedance P , one can then assess the annual occurrence rate $\lambda(Y > y)$ for ground intensity level $Y > y$. By assuming that for each source the probability of occurrence for magnitude and source-to-site-distance is independent, the annual occurrence rate for all n sources is equal to the sum of annual occurrence rate $\lambda(M_i > m_{\min})$ for each individual source i :

$$\lambda(Y > y) = \sum_{i=1}^n \lambda(M_i > m_{\min}) \int_{m_{\min}}^{m_{\max}} \int_0^{r_{\max}} P(Y > y | m, r) f_{M_i}(m) f_{R_i}(r) dr dm \quad (9.18)$$

where $\lambda(M > m_{\min})$ is the rate of occurrence of earthquakes greater than m_{\min} from the source.

Strictly speaking, magnitude and source-to-site-distance are dependent on each other with a joint distribution. One may thus use a joint distribution for magnitude and source-to-site-distance $f_{M,R}(m,r)$, but the independence assumption above allows a simplification of the expression to a great extent.

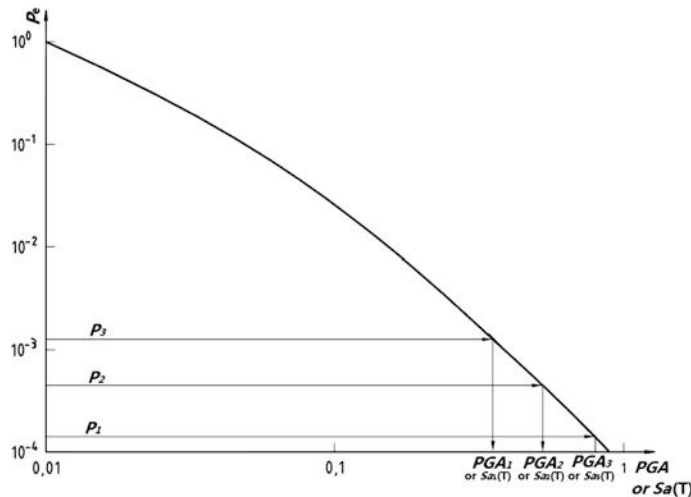


Fig. 9.8 Seismic hazard curve showing the relationship between various levels of the ground motion intensity [peak ground acceleration PGA or spectrum acceleration at a period T: $S_a(T)$] and the corresponding annual probability of exceedances (P_e)

For numerical calculation, the integral in the equation above has to be converted into discrete summation of occurrence rate with n_M and n_R intervals (for a range of possible M_i and R_i combinations):

$$\lambda(Y > y) = \sum_{i=1}^n \lambda(M_i > m_{\min}) \sum_{j=1}^{n_M} \sum_{k=1}^{n_R} P(Y > y | m_j, r_k) P(M_i = m_j) P(R_i = r_k) \quad (9.19)$$

The above results can easily be converted into a seismic hazard curve as illustrated in Figs. 9.5, 9.6 and 9.8, which show the annual occurrence rate ($P_e[N \geq 1] = 1 - e^{-\lambda t}$) versus the ground motion intensities.

For uncertainties that are not reflected in the seismic hazard curve, a correction factor C_c above unity may then be adopted to account for those uncertainties, as implemented in ISO 19901-2 [30]. And the value of C_c is strongly dependent on the slope of the seismic hazard curve. For regions with low seismic ground motion levels, correction factors are normally close to unity.

9.1.3.4 Construction of Spectra Acceleration at Discreted Periods

As mentioned above, several ground motion parameters can be accounted for, such as PGA, PGV, PGD, spectral accelerations at various periods etc., with the methodology of PSHA remaining essentially the same for all cases [31]. For

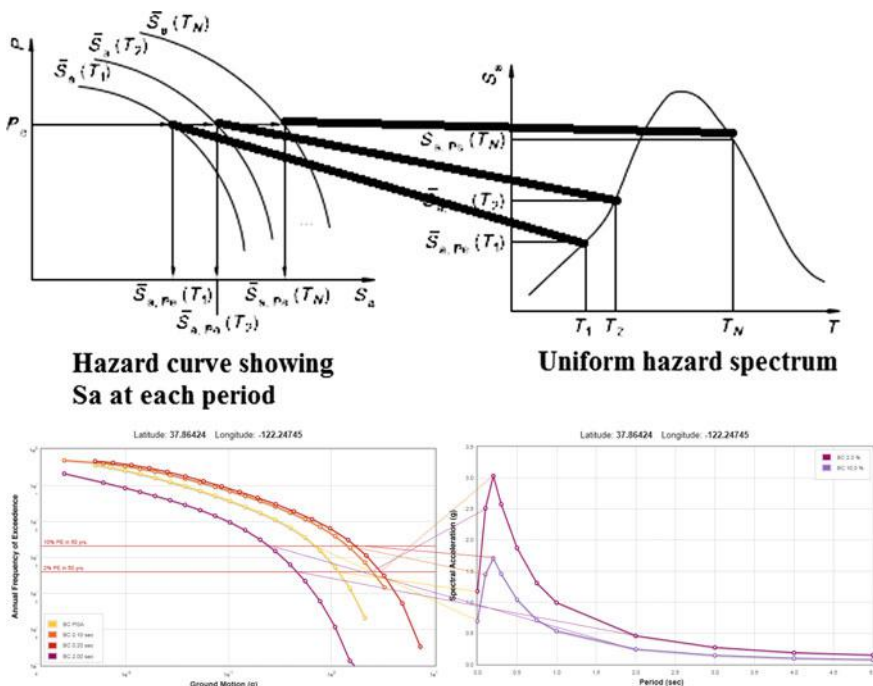


Fig. 9.9 Illustrations of generation of spectra acceleration at each individual period from the seismic hazard curve (left) to generate the UHS (right)

example, it is a typical objective for a PSHA to generate design response spectra for structural design. Therefore, one has to first perform the PSHA for spectral accelerations at various periods of interests, and then based on the target probability of exceedance P_e , one can find the spectral value at each individual period (T_1, T_2, \dots, T_N). The uniform hazard spectrum (UHS) used for design can finally be generated, as shown in Fig. 9.9.

Obviously, every ordinate in a UHS has an equal rate of being exceeded (the reason why it is called “uniform hazard”). However, a UHS is an envelope of separate spectral acceleration values at different periods, each of which may have come from a different earthquake event. This mixing of events to create a spectrum has sometimes been used to criticize the entire PSHA procedure: UHS conservatively implies that large amplitude spectral values will occur at all periods within a single ground motion time history. Therefore, it is important to recognize that a UHS is only one way to use the output of PSHA [8], as the concept of a design earthquake is lost, i.e., there is no single event (specified in simplest terms, by a magnitude and source-to-site-distance) that represents a realistic earthquake threat at, for example, a 3000 year return period of ground motion level (so-called “target ground motion”). This disadvantage results directly from the integrative nature of PSHA, and it means that other characteristics of the ground motion (e.g., the

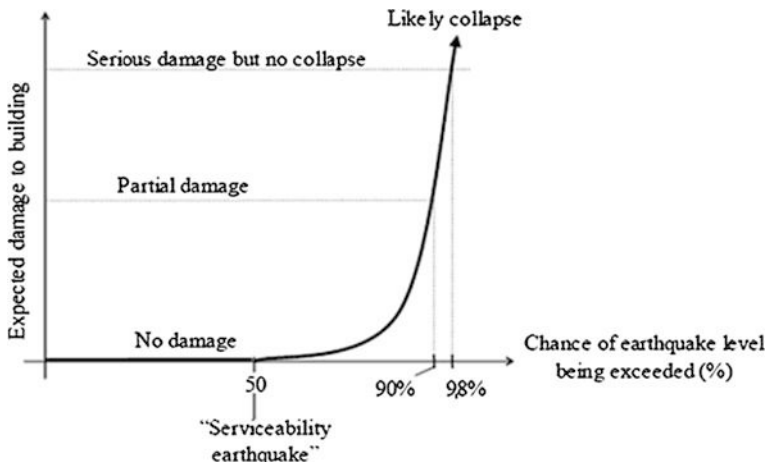


Fig. 9.10 The expected damage of a building versus probability of exceedance [37]

duration or non-stationarity characteristics of motion) must be estimated in an ad hoc fashion if these characteristics are important for analysis or design [32]. It also creates a barrel of utilizing the UHS, which has been stated by AKI committee in 1988 PSHA [33], who recommended a “recursive” PSHA be performed to determine the dominant earthquake at any particular hazard level. The earthquake and attenuation models can then be revised to reasonably reflect the realistic characteristics of this dominant earthquake, and the hazard analysis can be repeated using these more reasonable models. Another method to solve the problem associated with the utilization of the UHS is to replace the UHS with conditional mean spectrum (CMS) for the design, which will be discussed in Sect. 9.4.

Various software are available to perform seismic hazard analysis such as EZ-FRISK [34], Deqas-R [35], or SELENA [36]. With an implementation of various attenuation equations for various regions, those codes can calculate the probability of earthquake ground shaking in the bedrock/rock outcrop based on the location of surrounding faults. Some of these software may even calculate the response spectra at ground surface if a site response analysis package accounting for the local site condition is also implemented, or if site correction factors dependent on site condition are given (which is used to scale the spectral ordinates at the bedrock to the appropriate values corresponding to the spectral values at ground surface, as presented in Sect. 6.2).

In seismic design of infrastructures, the risk involved strongly depends on the ground shaking level of the earthquake. Figure 9.10 shows a typical relationship between the expected damage to building and ground shaking levels. It is obvious that under an earthquake that has only a 50 % chance of being exceeded in a 50 year period, no damage is expected. On the other hand, in an extremely large earthquake, with a chance of only 2 % of being exceeded in a 50 year period, serious damages without structural collapse can be expected.

9.1.4 Deaggregation (Disaggregation) in PSHA for Multiple Sources

During the process of a PSHA, for a site with multiple earthquake sources, it is necessary to assess the probability of occurrence for $Y > y$ from all earthquake sources. As discussed previously, since the annual occurrence rate for all n sources is equal to the sum of annual occurrence rate $\lambda(M_i > m_{min})$ from each individual source i , the relative contribution from each source can be identified. The process for this identification is called deaggregation [32] or disaggregation [38], which is essentially a part of the results obtained from PSHA.

Seismic hazard can be deaggregated to show the contribution by magnitude M , distance R , and ε . Any uncertainties in seismicity parameters can be incorporated and represented in this deaggregation. As an example, we examine the method to characterize the contribution of the earthquake magnitude, given that a ground motion $Y > y$ has occurred, the probability that an earthquake's magnitude equal to m can be expressed as:

$$P(M = m \mid Y > y) = \frac{\lambda(Y > y, M = m)}{\lambda(Y > y)} \quad (9.20)$$

In Sect. 9.1.3.3, we have learned that the annual occurrence rate for all n sources is equal to the sum of annual occurrence rate $\lambda(M_i > m_{min})$ for each source i . This is exactly the solution for the denominator of the equation above. The numerator can also be calculated in a similar manner:

$$\lambda(Y > y, M = m) = \sum_{i=1}^n \lambda(M_i > m_{min}) \sum_{k=1}^{n_{R_i}} P(Y > y \mid m, r_k) P(M_i = m) P(R_i = r_k) \quad (9.21)$$

Figures 9.11, 9.12 and 9.13 show an example of deaggregation for PGA, spectral acceleration at 1.0 and 5.0 s, during a process of PSHA, for a site at the University of California, Berkeley (Fig. 9.14), with return periods of 2475 years (an exceedance probability of 2 % in 50 years) and 475 years (an exceedance probability of 10 % in 50 years). It is clearly shown that for the longer return period of 2475 years with higher acceleration levels, sources nearby (1.5 to 3.5 km from the site) and magnitudes ranging from 5.5 to 7.5 contribute most to the seismic hazard. For the lower return period of 475 years with lower acceleration levels, there is an additional contribution from sources at around 28 km away from the site with magnitudes of more than 8.0. This is more obvious for longer periods of spectral acceleration than that of the shorter period. In addition, even with the same return period, the contribution from various magnitudes and source-to-site distances also depend on which spectral period of the spectral acceleration is under study.

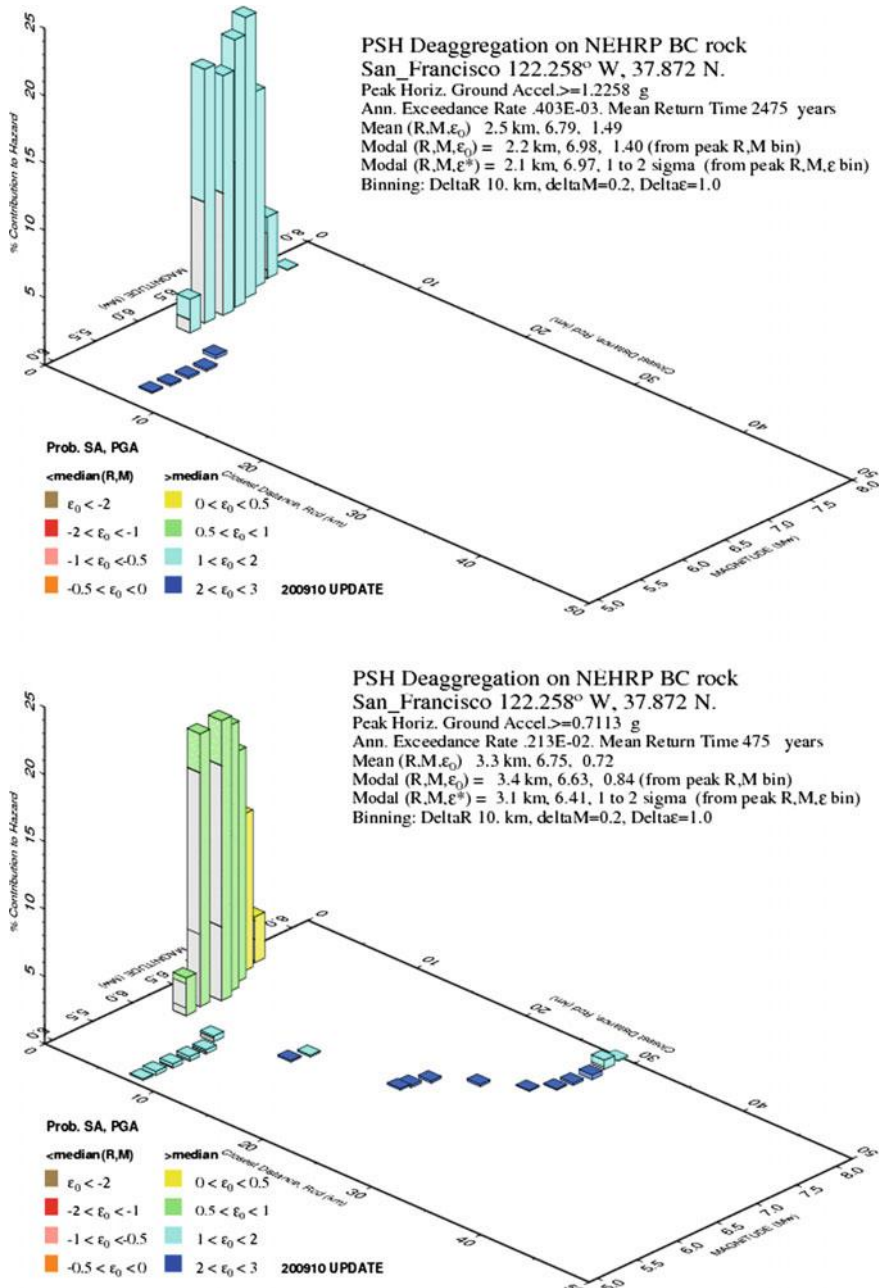


Fig. 9.11 PSHA deaggregation for the PGA at the University of California, Berkeley (courtesy of US Geological Survey 2008 Interactive Deaggregation), with return periods of 2475 years (*upper*) and 475 years (*lower*)

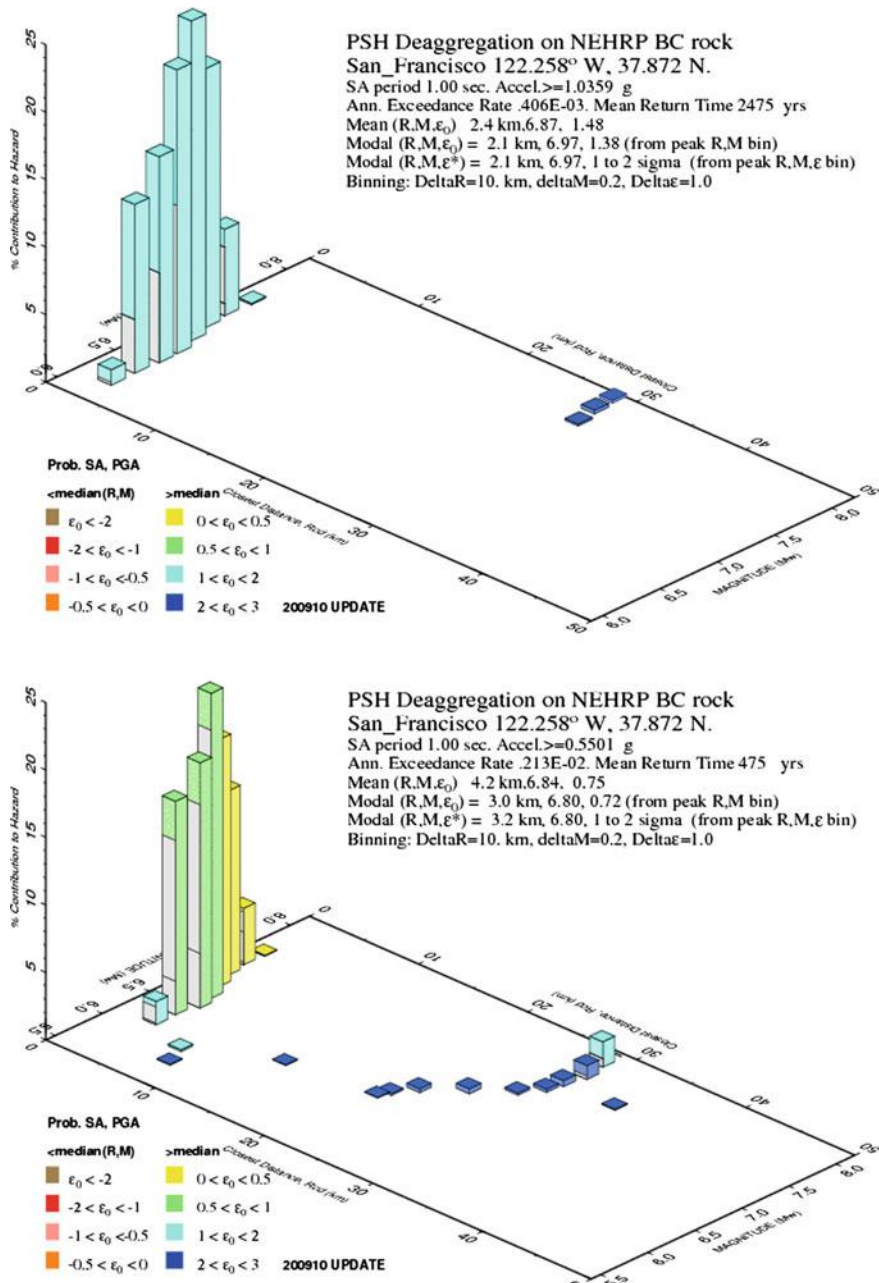


Fig. 9.12 PSHA deaggregation for the spectral acceleration at 1.0 s at the University of California, Berkeley (courtesy of Geological Survey 2008 Interactive Deaggregation), with return periods of 2475 years (*upper*) and 475 years (*lower*)

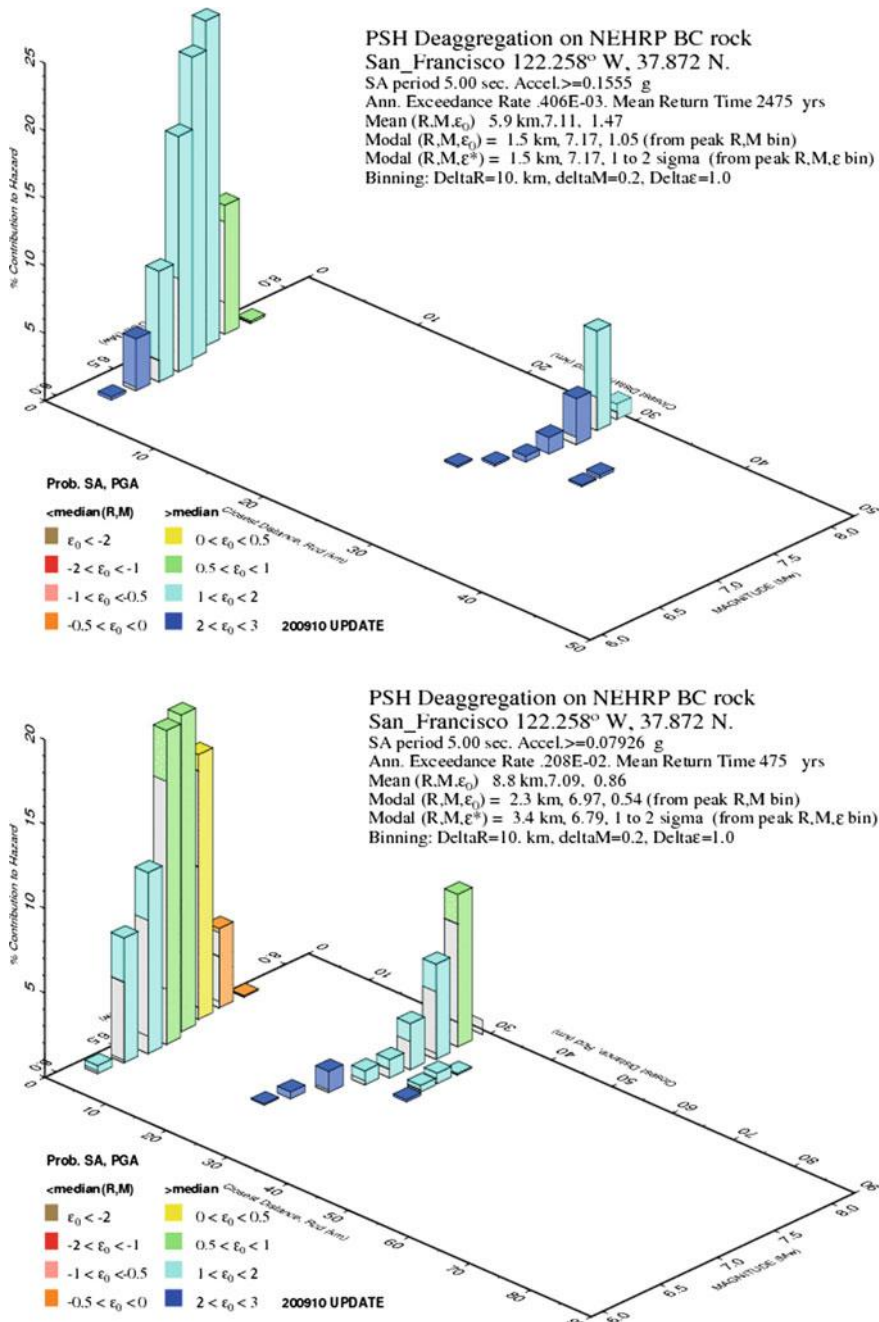


Fig. 9.13 PSHA deaggregation for the spectral acceleration at 5.0 s at the University of California, Berkeley (courtesy of US Geological Survey 2008 Interactive Deaggregation), with return periods of 2475 years (*upper*) and 475 years (*lower*)

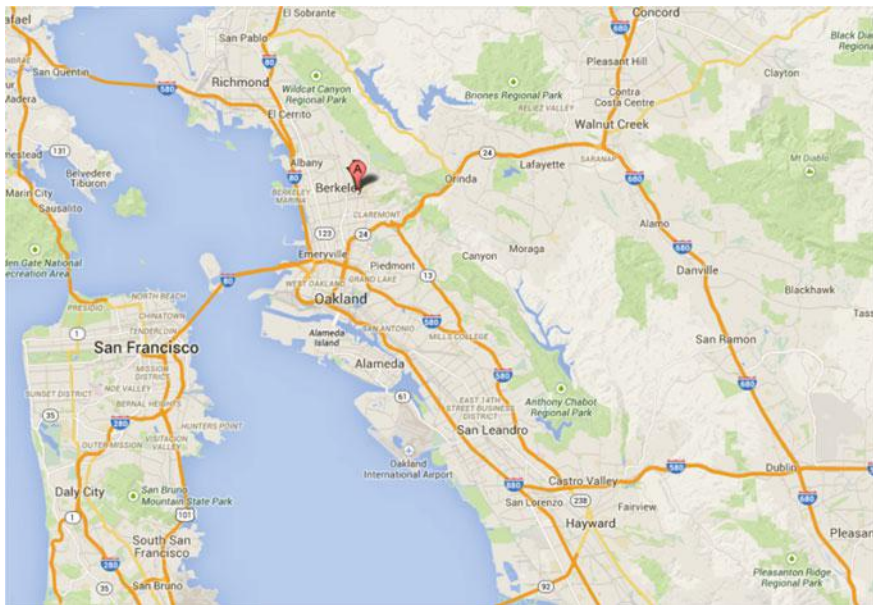


Fig. 9.14 The location of University of California, Berkeley (generated from Google Maps)

Note that compared to UHS, the disaggregation of seismic hazard identifies values of some earthquake characteristics providing the largest contributions to the hazard in terms of exceeding a specified spectral ordinate threshold. These events are essentially the earthquakes dominating the seismic hazard in a probabilistic sense, and may be used as design earthquakes (DEs) as originally introduced by McGuire [39]. In case the contribution from a single seismic source dominates the hazard at all period ranges that are of interest, one may use a single design earthquake to represent the entire response spectrum. However, if the contribution from several seismic sources dominates the hazard at different period ranges, the single design earthquake is not appropriate. Then values of M , R , and ε derived at different periods, for example at $T = 0.1$ and 1 s, by weighting earthquakes for each attenuation equation (Sect. 3.6), can be used to represent design earthquakes for short and long periods, respectively [32].

9.1.5 Logic Tree Method

The PSHA requires, either fully or partially probabilistically, extensive treatments of uncertainties in many aspects in a systematic and rational way. To perform this task, a logic tree [40, 41] is often employed to address the statistical uncertainties in the major elements of seismicity. This is because the best choices for elements of

the seismic hazard model itself may not be clear, where various alternatives for the input parameters can be used, and each is assigned with different weights that is interpreted as the relative likelihood of that particular model being correct and based on expert judgment, etc. [28]. And there is still an ongoing debate on how logic tree should be interpreted [29]. This is more important for earthquakes that occur off known faults and with the magnitudes smaller than a certain magnitude limit, say 6.5, so that they do not need to be modeled on faults. The seismicity may then be assumed as a random seismicity-derived sources accounting for earthquakes that occur off known faults, and for moderate-size earthquakes that are not modeled on faults; the seismicity can also be modeled by gridded seismicity models based on historical earthquakes to account for the observation that larger earthquakes occur at or near clusters of previous smaller earthquakes [42, 43]; or modeled as uniform background zones to account for the future random seismicity in areas without historical seismicity documentation; or as special zones allowing for local variability in seismicity characteristics within a zone (for example, changes in b -value in Gutenberg-Richter relationship as presented in Sect. 9.1.3, changes in maximum magnitude, and variations of uniform seismicity characteristics) [44]. The complexity of the logic tree is a function of several factors such as the scientific knowledge of the causes of earthquakes, the association of seismicity with geologic structure, the understanding of the geologic behavior of individual seismic sources, and the adequacy of the historical seismicity database, etc. [40].

An example of a logic tree is shown in Fig. 9.15. The nodes in the logic trees are sequenced to provide for the conditional aspect or dependencies of the seismic parameters and a logical development to determine the ground motions statistically. A series of branches represent various models. Each of those branches (models or

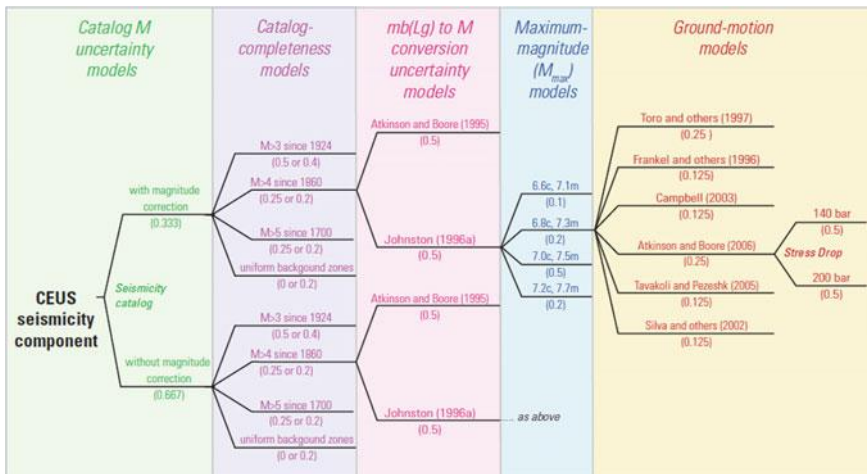


Fig. 9.15 An example of a logic tree for seismicity-derived hazard component in the Central and Eastern United States (courtesy of USGS)

values) is assigned a weighting factor, reflecting relative degree of belief in each model or value. And the weights are in practice treated as (subjective) probabilities. The branches follow a hierarchy from the left to the right, comprising 5 columns for this particular example, each of which represents various model categories to model the uncertainties in the aspects of source, magnitude, maximum magnitude, and attenuation model (ground motion models in Fig. 9.15). The relative likelihood of a combination of models along a complete hierarchy (from left to the right) is the product of the relative likelihood of each model (branch) in this combination, and the sum of the probability of all branches under each column is equal to 100 %. Compared to a convenient PSHA procedure, the logic tree method requires a significantly higher computation effort, and this effort is dramatically increased with an increase in the number of branches.

It should be noted that PSHA is simple in principle, but complex in practice. During the process of performing a PSHA, even experts tend to adopt what is familiar for them, to prefer certain models for unclear reasons, and to have pre-conceived opinions on which results to expect. The results such as seismic hazard curves calculated from PSHA by different experts can be significantly different. This creates a significant problem on the reliability of the entire PSHA and greatly degrades the advantages of PSHA over DSHA. Therefore, in performing a PSHA, people need to be wary of dismissing any data, models or methods [29].

9.2 Seismic Hazard Map

Seismic hazard studies are a common task for an engineering project relevant to seismic design. As discussed previously, based on a reduction (attenuation relationship) in ground motion mainly due to the distance from the fault rupture, and dividing the territory into regions of approximately equal peak ground motion, it uses contour lines to illustrate the ground motion parameters such as PGA or spectral values at specific period(s). Site ground motions are estimated for specific probability of ground motion exceedance within a design time period or for selected values of annual frequency or return period for ground motion exceedance.

A typical hazard map for designing building structures commonly specifies PGA that a site can expect during, for example, the next 50 years with 10 % probability (90 % chance of non-exceedance), corresponding to a return period of 475 years, and this return period is selected rather arbitrarily. Figure 9.16 shows the global seismic hazard map for sites onshore measured with PGA for a return period of 475 years. This map is especially useful for constructing the design spectra for structural analysis as elaborated in Sect. 5.4.2.2. Figure 9.17 shows an example of a rather rough seismic hazard map for offshore areas worldwide with a return period of 475 years. The PGA for return periods other than the one specified in the hazard map can be calculated based on relationship between the ground motion intensities at two different return periods. This is typically reflected in a seismic hazard curve as presented in Fig. 9.8 and Sect. 9.3.

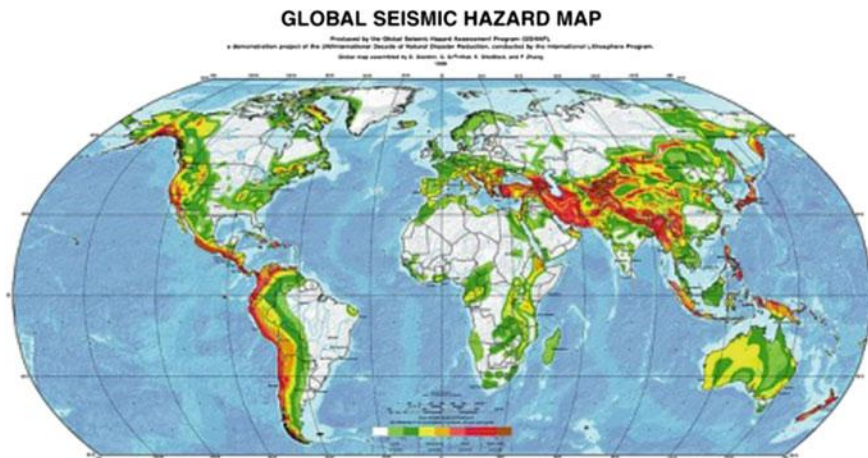


Fig. 9.16 Global seismic hazard map for with a return period of 475 years (courtesy of GSHAP)

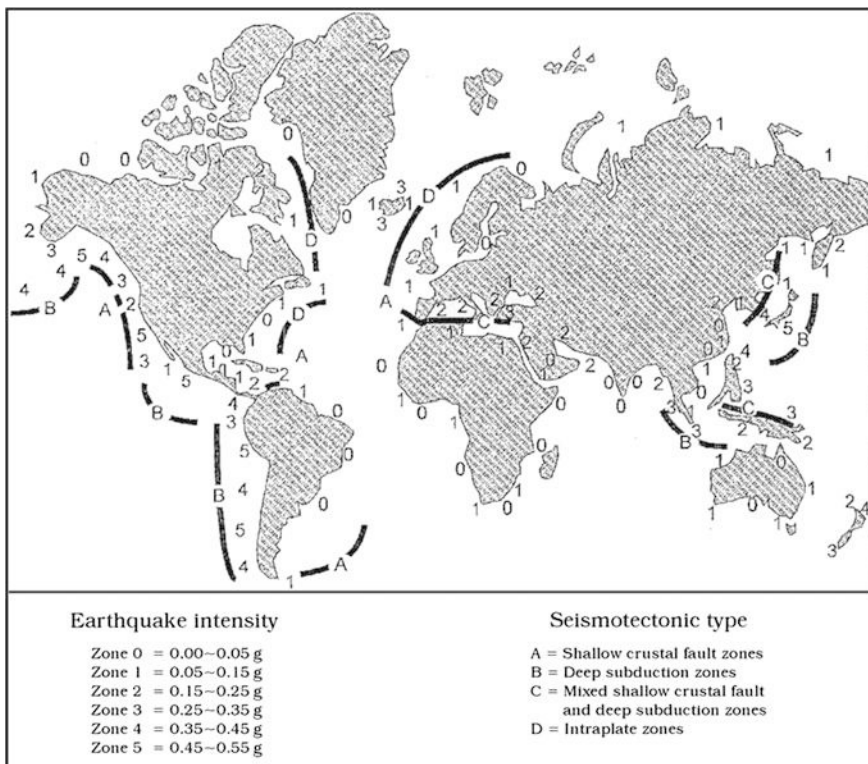


Fig. 9.17 Seismic hazard map for offshore areas worldwide with return period of 475 years [47]

As presented in Sects. 5.4 and 6.2, in many seismic hazard maps, only the PGA at a single period is defined. By using this PGA to scale a normalized response spectral shape for each portion of the spectrum, a design response spectrum can be obtained. However, note that the response spectrum is period/frequency dependent: it is a combination of contributions of various earthquake magnitudes at varying site-to-source distances, the ground motions of which attenuate differently at different period, and this is likely to result in a response spectrum having inconsistent or even unknown probabilities of exceedance at different periods [28]. As mentioned above, to have a constant probability of exceedance with various periods, PSHA at a number of periods/frequencies needs to be performed. Through ground motion attenuation functions, the spectral acceleration varied with period can be obtained. This results in a uniform hazard spectrum (UHS) [45]. For example, for seismic design of offshore structures, ISO 19901-2 [10, 30] presents a coarse seismic hazard map for bedrock outcrop with a return period of 1000 years for each region, at spectral periods of both 0.2 and 1.0 s.

In the uniform hazard map, the short period end typically represents the rock motions attributed to moderate nearby earthquakes, while the long period end reflects the hazard from larger and more distant events. Again, readers need to bear in mind that the map typically does not resemble the response spectrum from any specific earthquake magnitude and distance. This method is already implemented in many seismic design codes. The ground attenuation functions are normally valid only within the period range below 4 s, and occasionally below 10 s. Therefore, for period larger than 4 s, the spectral acceleration is assumed to be inversely proportional to period and anchoring spectral demand at a period of 3 s or 4 s. However, this assumption can be erroneous for near-fault sites as the effects of near-fault can significantly alter the spectral demand in longer period range.

Typically, it is assumed by the mappers that the structure at a site is on solid rock and the ground shaking is relatively fast (e.g. at 0.2 s period). The influence from different soil conditions within 20–50 m below ground surface is important in determining the exact seismic risk for a particular structure, and this can be accounted for in a site response analysis (Sect. 4.3) or simplified selection of site coefficient (Sect. 6.2). Different parts of the world use different techniques to develop seismic hazard maps [46]. Since this subject is more related to the science of seismology, it is not elaborated in the current text.

The US Geological Survey (USGS) National Hazard Mapping Project supported by NEHRP provides the latest peer reviewed and published seismic hazard data for the United States. These data are provided in probabilistic hazard maps and interactive web-based query for certain ground motion parameters. The hazard maps are available at the USGS website for downloading or viewing, which correspond to PGA values, 0.2 and 1.0 s spectral acceleration values for probabilities of exceedance of 10 % in 50 years and 2 % in 50 years, corresponding to approximate return periods of 500 and 2500 years, respectively. Figure 9.18 shows the probabilistic maps for the 0.2 and 1.0 s spectral accelerations corresponding to a probability of exceedance of 2 % in 50 years. The website also provides an interactive menu where the user can obtain the mapped values for a given location

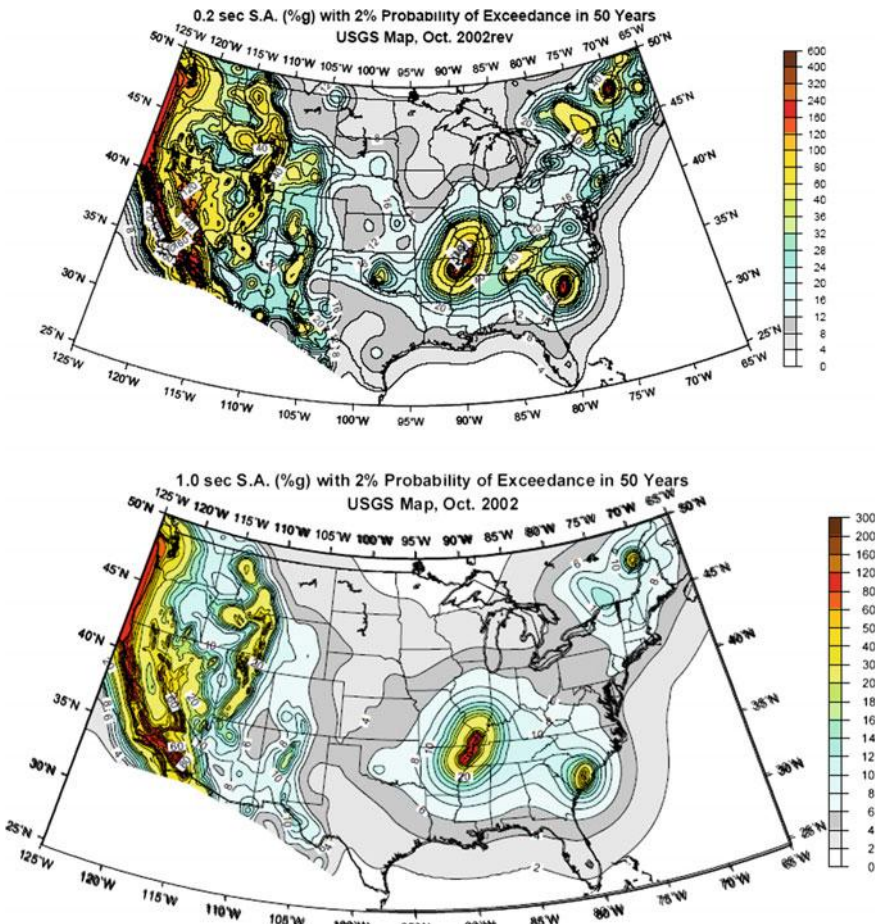


Fig. 9.18 0.2 s (upper) and 1.0 s (lower) spectral accelerations with 2 % probability of exceedance in 50 years [49, 50] (courtesy of USGS)

specified by latitude/longitude. Ground motion values for the 48 states have been calculated for a grid spacing of 0.05° . Interpolated values are typically calculated using the four surrounding corner points. For guidance, 0.1° latitude is about 10.9 km; the 0.1° longitude varies, but for the 48 states is in the order of 9.0 km. It should be mentioned that to develop a global seismic map is a rather challenging task, mostly due to both the inconsistency of the state of knowledge around the world, and the relative social and political sensitivity among various nations [48].

Unlike for areas onland, the seismic hazards in many offshore areas around the world remain unmapped. For example, in California, only approximately 50 % of the coastline is mapped at resolution to permit hazard evaluations, but for the other regions the situation is even worse [51]. For example, in ISO 19901-2 [10, 30], the

seismic hazard maps in offshore areas are given in a rather coarse manner for each region, as mentioned before. Therefore, extensive efforts are required to develop the seismic hazard maps for offshore areas.

Based on a continuously updated knowledge in many aspects, such as the new findings of faults, updated GMPEs/attenuation models (Sect. 3.6) etc., seismic design codes in some countries such as US and Canada regularly update the seismic hazard maps, often at 5 year intervals.

9.3 Apply PSHA for Engineering Design

For practical structural design purposes, there are two approaches to utilize the seismic hazard curve shown in Fig. 9.8.

In the first approach, based on the design ground motions with a specified mean annual frequency of exceedance, e.g., 0.002, a linear analysis is performed to calculate the responses of target structures, which is followed by checks with regard to an allowable stress design (Sect. 14.2.3) process to a set of forces reduced by factors that reflect the implicit member ultimate-strength/allowable-strength ratios, implicit non-linear static overstrength ratios, and implicit non-linear dynamic factors that represent the system's ability to sustain non-linear deformations without life threatening behavior [52, 53]. Based on this method, the net effect of these conventional design criteria is to produce a frequency of collapse that is approximately half that for the design ground motions [54], i.e., a mean annual frequency of exceedance of 0.002 produces a mean annual frequency of collapse of about 0.001.

The second approach is to adopt checks in multiple levels of limit states [55], as will be presented in Sect. 14.2.2. Normally, two limit states are used. One corresponds to a lower linear design (to ensure little or no damage to a target infrastructure), which is associated with ground motion intensity having a minimum return period to ensure economic viability of a design as a function of the exposure level of a target structure, typically in the range of 50–200 years (e.g. 100 years for ultimate limit state required by Norsok N-003 [56] and 50–200 years for extreme level earthquake required by ISO 19901-2 [10, 30]; they mainly aim to perform checks for structures and foundations at component level) for offshore structures. Another, more interestingly, corresponds to a system ductility level check (to ensure that no global failure modes or collapses, which can potentially lead to high consequences such as loss of life or major environmental impact, occur) of an extreme rare event (abnormal level earthquake with a probability of exceedance P_{ALE} depending on the exposure level in ISO 19901-2 [10, 30] or an annual probability of exceedance of 0.0001 in Norsok N-003 [56], which mainly aims to perform checks for structures and foundations at a system level) associated with a target probability of exceedance P_e . The value of the target probability of exceedance depends on the structure exposure level, which is related to the life safety and consequence (which may be determined by the owner prior to the design of a new structure or the assessment of an existing

structure, and must be agreed upon or given by the regulators where applicable), and the randomness and the uncertainties in seismic actions and structural resistance. The ground motion intensity in certain forms of expression (e.g. PGA or spectral acceleration etc.) at the target probability of exceedance P_e is normally given in seismic hazard curves (Fig. 9.8) or seismic hazard maps (Figs. 9.18 and 9.20). It should be noticed that, when selecting a decent exposure level, different from that of the other environmental loading such as ocean wave or wind loading that can be predicted in advance, it is not possible to predict a destructive earthquake with a great certainty (earthquake prediction). Therefore, the relevant exposure level associated with evacuation (such as L2 exposure level in ISO 19900 offshore standard [10, 30]) is not feasible for a seismic event.

It is noted that the randomness and uncertainties in seismic actions and structural resistance are not captured in a seismic hazard curve and invariably increase the probability of failure, but they can affect the reliability of a structure, which is related to the uncertainty in structural resistance to earthquake actions. Therefore, in the second approach, the final annual probability of exceedance P_{ALE} should be lower than the target annual probability of failure P_f as shown in Fig. 9.19. The associated decrease of probability of occurrence (corresponding to an increase in the return period) primarily depends on two factors: the relative importance of these additional uncertainties and the local slope α_R of the seismic hazard curve at P_f [55]. The local slope α_R is defined as the ratio of the spectral accelerations corresponding to two probability levels P_1 and P_3 as shown in Fig. 9.8, one either side of P_f (P_2 in Fig. 9.8), and they are typically one order of magnitude apart, while P_1 should preferably be close to P_f . The local slope (tangent) α_R of the seismic hazard curve

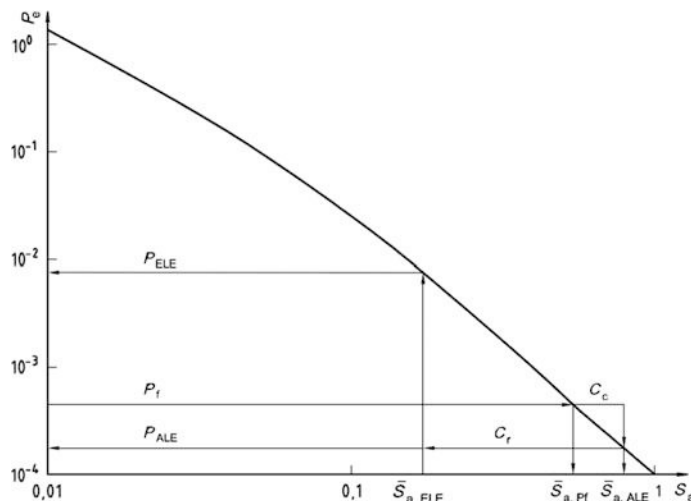


Fig. 9.19 Derivation of the ALE (abnormal level earthquake) and ELE (extreme level earthquake) spectral accelerations with associated probabilities of occurrence [10, 30]

depends on sites, structural period, and the target failure probability P_f (P_2 in Fig. 9.8). Therefore, in practice, an additional factor C_c (Fig. 9.19) can be used to determine the final annual probability of exceedance P_{ALE} , which would guarantee a failure probability P_f for the design of a structure fulfilling the abnormal level earthquake requirement. Table 9.4 lists the value of C_c given in ISO 19901-2 [10, 30], which is a function of the α_R . For example, a target P_f of 1/2500 defined for exposure L1 structures is an upper bound value that structures will survive. In high seismic areas such as Japan and California typical structural failures designed on this basis occur with an equivalent return period of 4000–5300 years, while in areas with less seismicity such as the Gulf of Mexico, the North Sea and the Caspian Sea, these seismic events generally do not control the design and there is consequently no cost penalty for designs to meet a 10,000-year return period seismic event [57].

C_r in Fig. 9.19 is a seismic reserve capacity factor for structural systems that consider the static reserve strength and the ability to sustain large non-linear deformations of each structure type (e.g. steel versus reinforced concrete). The C_r factor represents the ratio of spectral acceleration causing catastrophic system failure of the structure, to the extreme level earthquake (ELE) spectral acceleration. Its value can be estimated prior to the design of a structure in order to achieve an economic design that will resist damage due to an ELE and is at the same time likely to meet the abnormal level earthquake (ALE) performance requirements. Values of C_r may be justified by prior detailed assessment of similar structures [10, 30]. In ISO offshore structural design codes, C_r ranges from 2.0 to 2.8 depending on the exposure level of the target structure, and the higher the exposure level, the higher the C_r factor will be. However, as mentioned before, it should be observed that C_r should lead to a return period for the ELE earthquake that is higher than the minimum ELE return period that is given to ensure economic viability of a design as a function of the exposure level of a target structure (for example, 50 to 200 years depending upon the exposure level of a target structure as required by ISO 19901-2 [10, 30]).

For infrastructures with low seismic risk, rather than performing a complicated PSHA to determine the seismic hazard curve, one may use the seismic hazard maps with one or a few given return periods (e.g., 1000 years in ISO 19901-2 [10, 30]) given by various design codes and standards. The final ground motion intensity (PGA or spectral accelerations at various periods) corresponding to the target probability of failure P_f can simply be derived from the ground motion intensity at the return period of what the given seismic hazard map implies to a return period 1/ P_f . This task can be carried out by multiplying the ground motion intensity given by

Table 9.4 Correction factor C_c (Fig. 9.19) in ISO 19901-2 [10, 30] to cover the randomness and uncertainties in seismic actions and structure resistance, which are not captured in the seismic hazard curve and invariably increase the probability of failure

α_R	1.75	2.0	2.5	3.0	3.5
C_c	1.20	1.15	1.12	1.10	1.10

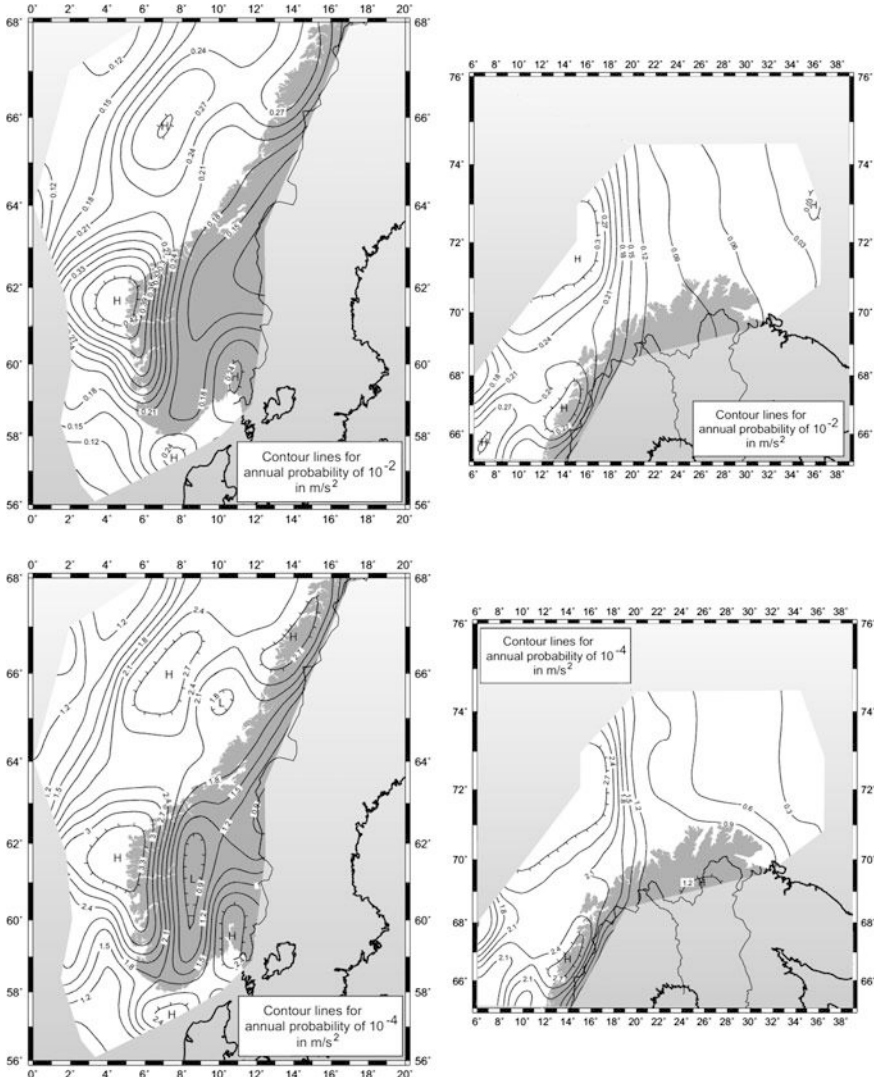


Fig. 9.20 Norwegian seismic zonation maps for 100 year (*upper*) and 10,000 year (*lower*) return period of earthquake events in terms of PGA contour lines [58]

the seismic hazard map with a scale factor, which is the ratio between the ground motion intensity corresponding to the target probability of failure P_f and the one implied by the seismic hazard map. This ratio is dependent on both the exposure level of the target structure and the slope of the seismic hazard curve in the target area (area dependent). If one compares the different seismic hazard curves for various locations in the United States as shown in Fig. 9.5, it is obvious that the slope of the seismic hazard curves for various locations can be quite different.

As mentioned before, with the same P_f , the seismic action in high seismicity areas may be the dominant action for the structural and foundation design, while in low seismic regions other loads rather than the seismic loads are governing loads for the structural and foundation design. This has a great influence on the structural and foundation concept selection and detailing.

9.4 Conditional Mean Spectrum

Ground motion selection is often associated with a target response spectrum. Traditionally, design target spectra for selection are often based on the uniform hazard spectrum (UHS) as discussed in Sect. 9.1. Readers may bear in mind that UHS is a combination of different magnitude of earthquakes with different sources and source-to-site distances. Each portion within UHS may represent a particular earthquake magnitude and a source-to-site distance. Therefore, UHS does not provide the probability of simultaneous occurrence of these parameters, i.e., UHS is hardly able to reproduce any realistic single earthquake ground motion record. As an example, the left figure in Fig. 9.21 shows a smoothed curve being the predicted median spectral acceleration [which equals the exponential of the mean $\ln S_a(T)$]. However, the curve does not represent the response spectrum of any actual (individual) ground motion. Instead, individual response spectrum shows variability in spectral amplitudes over different periods [59].

To solve this dilemma, the conditional mean spectrum (CMS) is proposed by Baker [19], which is essentially intended to calculate the joint distribution of ground motion intensity parameters. The resulting CMS has been gradually recommended

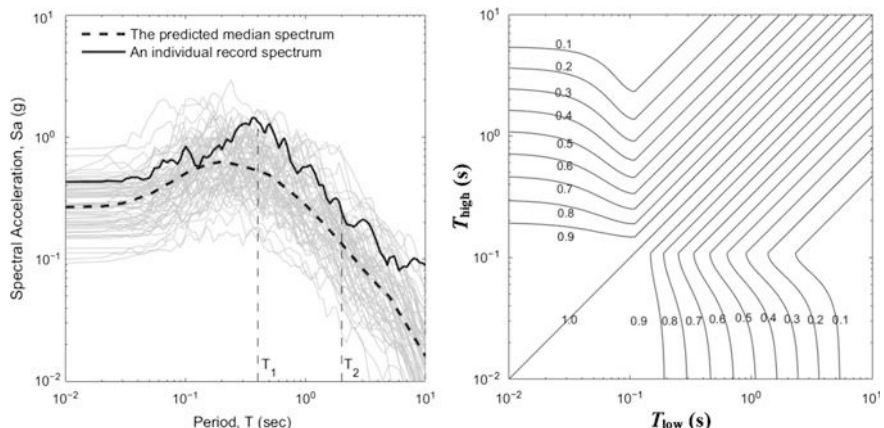


Fig. 9.21 An example of response spectrum variability and correlation with spectral acceleration variability (left) and correlation coefficient of spectral accelerations (right) [59]

by various PSHA tools and seismic design guidelines in the US for land-based structures.

As a starting point to calculate the CMS, one may study the PSHA deaggregation for the spectral acceleration at 1.0 s with a return period of 475 years shown in the lower figure of Fig. 9.12, which indicates that the mean value of causal magnitude (M), source-to-site distance (R) and ε (presented in Sect. 3.6, is the number of standard deviations ($\sigma_{\ln Y}$) measured as the difference relative to the mean predicted ground motion $f(M, R, \theta)$ and represent the observed variability in $\ln Y$) are 4.2 km, 6.84, and 0.75. Note that $\varepsilon(T)$ in this example is used to characterize the difference between the median of spectral acceleration at 1.0 s and 0.55 g amplitude associated with this deaggregation, and also by recognizing that $S_a(T)$ can be well represented by lognormal distribution, $\varepsilon(T)$ can then be expressed in terms of $\ln S_a(T)$:

$$\varepsilon(T) = \frac{\ln S_a(T) - \mu_{\ln S_a}(M, R, T)}{\sigma_{\ln S_a}(T)} \quad (9.22)$$

where $\mu_{\ln S_a}(M, R, T)$ and $\sigma_{\ln S_a}(T)$ are the mean and standard deviation of $\ln S_a(T)$, which can be determined from attenuation models; $\ln S_a(T)$ is the natural-log of the spectral acceleration at period T .

It is obvious that $\varepsilon(T)$ varies at different periods T , i.e., individual spectra are not all equally above the average of the spectral acceleration at all periods.

Here, readers may recall that in Sect. 3.6, it has been presented that the predicted ground motion is typically quantified in terms of a median value in case of non-log of ground motion parameter is used, or mean value in case of natural-log of ground motion parameter $\ln Y$ is used.

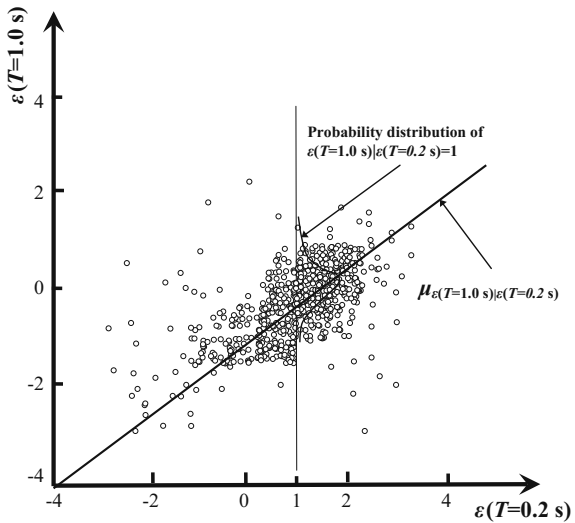
Since the joint distribution follows a normal distribution, conditional distributions of one intensity measure parameter, given the other, are also normally distributed as shown in Fig. 9.22. Therefore, the conditional mean value of $\varepsilon(T)$ at a period T_i : $\varepsilon(T_i)$, given $\varepsilon(T^*)$, can be computed using only a linear correlation coefficient $\rho(T_i, T^*)$ between the two parameters:

$$\mu_{\varepsilon(T_i)|\varepsilon(T^*)} = \rho(T_i, T^*) \cdot \varepsilon(T^*) \quad (9.23)$$

where T^* is often taken to be equal to the most important eigenperiod of a target structure.

The correlation between the spectral values of different periods is found to be an intrinsic property of ground motions [60]. In Fig. 9.22, it is noticed that the slope of the solid line represents the correlation coefficient $\rho(T_i, T^*)$. The coefficient $\rho(T_i, T^*)$ can be determined in a similar manner as what ground motion prediction models are calibrated. One may notice that $\rho(T_i, T^*)$ for different pairs of (T_i, T^*) may have different values, and practically, no $\rho(T_i, T^*)$ is equal to 1.0 (full correlation), even if $\rho(T_i, T^*)$ may be in the range of strong correlation, e.g., $\rho(T_i, T^*) > 0.7$. For a set of response spectra with N seismic ground motion records, the correlation can be calculated as:

Fig. 9.22 A scatter plot of $\varepsilon(T)$ values from a large number of measured ground motions with $\varepsilon(T = 0.2 \text{ s})$ versus $\varepsilon(T = 1.0 \text{ s})$. Each dot represents the $\varepsilon(T = 1.0 \text{ s})$ given $\varepsilon(T = 0.2 \text{ s})$ values observed from a single ground motion measurement



$$\rho(T_i, T^*) = \frac{\sum_{k=1}^N \left[\ln S_a^{(k)}(T_i) - \overline{\ln S_a(T_i)} \right] \left[\ln S_a^{(k)}(T^*) - \overline{\ln S_a(T^*)} \right]}{\sqrt{\sum_{k=1}^N \left[\ln S_a^{(k)}(T_i) - \overline{\ln S_a(T_i)} \right]^2} \sum_{k=1}^N \left[\ln S_a^{(k)}(T^*) - \overline{\ln S_a(T^*)} \right]^2}} \quad (9.24)$$

where $\ln S_a^{(k)}(T_i)$ is the $\ln S_a(T_i)$ obtained from the k th seismic ground motion record, and $\overline{\ln S_a(T_i)}$ is the mean value of $\ln S_a(T_i)$ for all N records.

For spectral period ranging from 0.05 to 5 s, Baker [19] recommended that:

$$\rho(T_{\text{low}}, T_{\text{high}}) = 1 - \cos \left[\frac{\pi}{2} - \left(0.359 + 0.163 I_{(T_{\text{low}} < 0.189)} \ln \frac{T_{\text{low}}}{0.189} \right) \ln \frac{T_{\text{high}}}{T_{\text{low}}} \right] \quad (9.25)$$

where T_{low} and T_{high} are the lower and higher of the two periods of interests, respectively [61]. The indicator function $I_{(T_{\text{low}} < 0.189)}$ is equal to 1 if $T_{\text{low}} < 0.189$ s, and equal to 0 otherwise.

For a wider spectra period ranging from 0.01 to 10 s, a more complicated expression can be adopted as proposed by Baker and Jayaram [62]:

$$\rho(T_{\text{low}}, T_{\text{high}}) = \begin{cases} C_2 & \text{if } T_{\text{high}} < 0.109 \text{ s} \\ C_1 & \text{else if } T_{\text{low}} > 0.109 \text{ s} \\ \min(C_2, C_4) & \text{else if } T_{\text{high}} < 0.2 \text{ s} \\ C_4 & \text{else} \end{cases} \quad (9.26)$$

where

$$\begin{aligned} C_1 &= 1 - \cos\left\{\frac{\pi}{2} - 0.366 \ln\left[\frac{T_{\text{high}}}{\max(T_{\text{low}}, 0.109 \text{ s})}\right]\right\}; \\ C_2 &= \begin{cases} 1 - \left[0.105 \left(1 - \frac{1}{1 + e^{100T_{\text{high}} - 5}}\right) \left(\frac{T_{\text{high}} - T_{\text{low}}}{T_{\text{high}} - 0.0099 \text{ s}}\right)\right] & \text{if } T_{\text{high}} < 0.2 \text{ s} \\ 0 & \text{otherwise} \end{cases}; \\ C_3 &= \begin{cases} C_2 & \text{if } T_{\text{high}} < 0.109 \text{ s} \\ C_1 & \text{otherwise} \end{cases}, \quad C_4 = C_1 - \left\{0.5 \left(\sqrt{C_3} - C_3\right) \left[1 + \cos\left(\frac{\pi T_{\text{low}}}{0.109 \text{ s}}\right)\right]\right\}. \end{aligned}$$

The right figure in Fig. 9.21 graphically shows the equations above. It is observed that the resulting covariance matrix is a symmetric positive definite matrix, allowing for a random sample generation, which is an important property for the proposed ground motion selection procedure [59].

Finally, the CMS can be computed by utilizing correlation across periods to estimate the expected spectral acceleration values at all periods T_i . Given the target spectral acceleration value at the period of interest T^* , i.e., based on the predicted mean $\mu_{\text{InSa}}(M, R, T_i)$, the predicted standard deviation $\sigma_{\text{InSa}}(T_i)$, $\varepsilon(T^*)$, as well as the correlation $\rho(T_i, T^*)$, given $\text{InSa}(T^*)$, the CMS can then be calculated as:

$$\mu_{\text{InSa}(T_i) | \text{InSa}(T^*)} = \mu_{\text{InSa}}(M, R, T_i) + \rho(T_i, T^*) \cdot \varepsilon(T^*) \sigma_{\text{InSa}}(T_i) \quad (9.27)$$

where $\mu_{\text{InSa}}(M, R, T_i)$ and $\sigma_{\text{InSa}}(T_i)$ at period T_i can be calculated from the attenuation models as presented in Sect. 3.6, M , R , and $\varepsilon(T^*)$ can be calculated by performing a PSHA deaggregation as shown in Figs. 9.11, 9.12 and 9.13. Commercial or free software (such as the “Interactive Deaggregation” provided by USGS online) are available to perform such tasks.

The left figure in Fig. 9.23 shows an example of CMS given occurrence of $S_a(0.8 \text{ s})$ values exceeded with 2, 10 and 50 % probabilities in 50 years. The right figure shows the CMS conditioned at 0.2, 0.8 and 2 s together with their corresponding UHS. All have a 10 % probability of exceedance in 50 years. By observing the figure, it is noted that the UHS has spectral accelerations higher than any conditional mean spectra. It has a peak value at the target period and decays toward the median spectrum in other periods. The decreasing process is based on a correlation model between the spectral acceleration values for all periods. This is because UHS is basically an envelope of spectral values associated with multiple earthquake scenarios rather than a single one, while the CMS acceleration values at their respective conditioning periods equal those of the UHS and the CMS provides the information of the mean spectral shape only associated with the $S_a(T^*)$. The characteristics of CMS above remind readers that a single CMS conditional at a period T^* only reflects realistic ground motions being conditioned at this particular spectral period of T^* .

Because under strong ground motions, many structures are designed to have a degraded stiffness due to the development of plasticity, the natural period may be increased significantly. Furthermore, the natural period may not be the only period that dominants the seismic response of a structure. Therefore, to appropriately

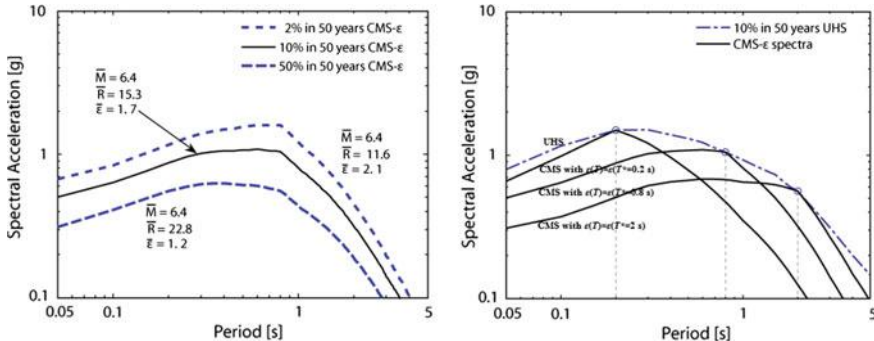


Fig. 9.23 Examples of conditional mean spectra, considering ε , for a site in Los Angeles, given occurrence of $S_a(0.8 \text{ s})$ values exceeded with 2, 10 and 50 % probabilities in 50 years (left) and CMS with S_a values at $T^* = 0.2, 0.8$ and 2 s together with their corresponding UHS, all have a 10 % probability of exceedance in 50 years [63] (courtesy of USGS)

represent the response of the structure across the full period range to which it is sensitive and thoroughly assess the response, it is usually necessary to develop several CMSs at different periods. In such cases it is not necessary that any of the selected periods represent the first mode period of the structure. Moreover, for some structures, there may not be any clearly defined first mode period, but this does not preclude the use of CMS to develop target spectra [64].

As recommended by Baker [19], four steps are necessary to compute a CMS that is likely to represent realistic earthquake records:

1. Determination of the targeted S_a at a given period, and the associated M , R , and ε . T^* is often taken as the most important eigenperiod(s) of the target structure. In practice, several T^* that are of interest should be used to generate several CMS as mentioned above, so that the sensitivity of seismic response of the target structure can be identified.
2. Compute the mean and standard deviation of the response spectrum, M and R are given.
3. Compute ε at other periods, given $\varepsilon(T^*)$.
4. Compute CMS.

Similar to the record selection to match a UHS, the ground motion matching a CMS can be performed by simply scaling the ground motion with a factor of S_c , so that the ground motion spectrum $S_{a\text{-record}}(T^*)$ at the single period T^* is matched to that of the CMS $S_a(T^*)$ [19]:

$$S_c = S_a(T^*) / S_{a\text{-record}}(T^*) \quad (9.28)$$

Alternatively, one may scale each ground motion so that the average response spectrum over the periods ($T_1 \dots T_N$) of interest is equal to the average of the target spectrum over the same periods [19]:

$$S_C = \frac{\sum_{j=1}^N S_a(T_j)}{\sum_{j=1}^N S_{a-record}(T_j)}. \quad (9.29)$$

Structural responses from ground motions matching the CMS may be significantly smaller than the responses from ground motions matching the UHS having the same $Sa(T^*)$ level, even though occasionally the opposite trend may also be the case.

It is obvious that the establishment of a CMS is less demanding regarding the analysis efforts than deriving a UHS, even if the latter is much more widely adopted in earthquake engineering. However, because CMS is a newer concept than UHS—and also because, quite often, seismic criteria are defined before structures/facilities are designed, without the involvement of seismologists—most structural and geotechnical engineers are not capable of calculating a complete series of CMS with varied conditioning periods. This obstacle actually deters the application of CMS despite its obvious advantages over the UHS, and the majority of concurrent seismic design codes do not specify the requirement of using CMS.

In conclusion, it can be summarized that the advantages of using CMS is that it gives a more realistic and normally less conservative spectrum than UHS, and it utilizes deaggregation information such as magnitude, distance, and ε to predict spectral shape, and the spectrum changes in shape as one increases in amplitude. The drawbacks of CMS are that it is less widely available than UHS, and it requires a re-selection of ground motions as each case changes, the spectrum changes with increasing amplitude, requiring multiple ground motion sets.

Based on the concept of CMS, Mousavi et al. [65] proposed an E-CMS by modifying ε with a so-called Eta indicator as a control parameter to determine the spectral shape. They claimed that compared to a traditional CMS, the E-CMS is a more reliable predictor of non-linear response of structures because the correlation of Eta and the structural response is stronger than the correlation between the conventional ε and the structural response [66]. Interested readers may read the references cited above.

9.5 Forecasting “Unpredictable” Extremes—Dragon-Kings

Most physical, natural and social phenomena can be characterized by power law statistics, which is a functional relationship between two quantities, where one quantity varies as a power of another. This is usually used to model data whose frequency of an event varies as a power of some attribute of that event, as illustrated in Fig. 9.24. This is based on the assumption that small, large and extreme events belong to the same population, the same distribution, and reflect the same underlying mechanisms.

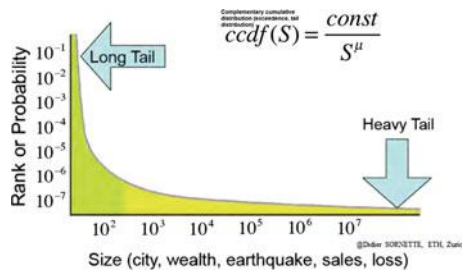


Fig. 9.24 Illustration of power law that assumes that both small and extreme value events follow the power law (courtesy of Didier Sornette, ETH Zurich, Switzerland)

Figure 9.25 shows the earthquake magnitude distribution for the region of Southern California, which is measured as the number of earthquakes per year with magnitude ($M > m$). Two portions of distributions that occurred deviate from the Gutenberg-Richter rule: at low magnitudes and at very high magnitudes range, as shown in the figure. The mismatch at the low magnitude portion is caused by the fact that many small scale earthquakes cannot be detected. However, it is difficult to find a convincing reason to explain the mismatch at large magnitude of earthquakes. The major school of thought considers this mismatch as exceptions (such as “black swans”) that are therefore not predictable, which is often called “self-organized criticality” introduced by Bak [67]. Therefore, major catastrophes are considered unpredictable as they are regarded as events that start small and do not stop growing to develop into large or extreme sizes [67, 68].

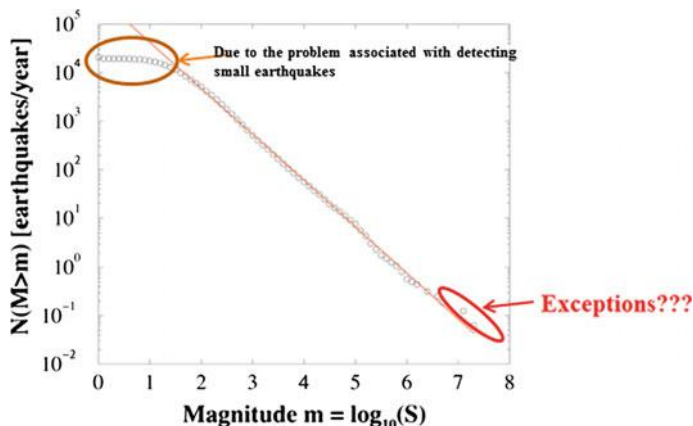


Fig. 9.25 Earthquake magnitude distribution showing a power law behavior over six decades; the solid line in the graph follows the Gutenberg-Richter model: $\log_{10}N_c(M > m) = a - bm$, where the $b = 1$, the dots represent the earthquake statistics based on the actual occurrence (courtesy of Didier Sornette, ETH Zurich, Switzerland)

This view is particularly pessimistic, and alarming if true, as it casts a strong doubt on possibilities of precise hazard prediction, with all the societal consequences of this. As stated by Sornette and Ouillon [68], this view is dangerous as it promotes an attitude of ir-responsibility: in a world where catastrophes (in human-controlled activities, for instance) are pure surprises, no one can be responsible. In response to this challenge, they proposed the concept of dragon-kings, which are defined as extreme events that do not belong to the same population as the other events, in a precise quantitative and mechanistic sense that will be developed. The notion “dragon-king” stems from a combination of the supernatural powers of dragons and the anomaly of a king’s wealth relative to that of his subjects. Essentially, dragon-kings appear as a result of amplifying mechanisms that are not necessarily fully active for the rest of the population [69]. By following this thought, dragon-kings are defined with specific properties and signatures having unique characteristics close to a regime transition, where a system bifurcates through the variation of a single or a few control parameters.

The concept of dragon-kings is widely used in various fields of applications, such as financial economics, geophysics, material science, population geography, hydrodynamics and even brain medicine. While still not a fully developed concept, it has received increasing amounts of research interest worldwide.

In parallel to the development of the concept of dragon-kings, based on the idea of “filling in” a heavy/fat tailed (scaling) distribution, Rundle et al. [70] also proposed the Natural-Time-Weibull (NTW) model to predict extreme earthquake magnitude distribution.

Interested readers may study this subject by reading the references cited above.

9.6 Assessing Earthquake Disaster Assisted by Satellite Remote Sensing

Satellite remote sensing technology has been applied in assessing natural disasters such as in forecasting and controlling of floods, forecasting hurricanes, monitoring landslides and forest fires and so on. It has also been used for earthquake research very early, with the first appearance of satellite images. By collecting the remote sensing data and analyzing them, the seismic data in an area can be identified rapidly. Remote sensing technology can also be used to monitor the crustal movement, which is important for seismic hazard analysis and to forecast future earthquakes, especially when earthquakes are caused by fault ruptures of unknown hidden strike faults [71]. Moreover, timely and accurate detection of change in Earth’s surface features is very important for understanding relationships and interactions between human and natural disasters, especially in supporting better decision making. The availability of images within a short time to manage the crisis is crucial for relevant parties who need a quick and draft overview of the epicentral area, quick information on the extension and distribution of damages, and the

evaluation of infrastructure (roads, bridges) conditions. For example, after a devastating earthquake, emergency assistance must be provided based on damage data, and such information should be provided no later than up to 8 h after the occurrence of the earthquake. No other technologies can be as efficient and fast as the satellite remote sensing technology to assess the earthquake damage. The contribution of space technologies has been demonstrated to be effective for regional/continental damage assessment using low- or medium-resolution remotely sensed data (ranging from 30 m to 1 km). There is also further development in precision of sensing systems with medium spatial resolution and a combination with GPS technique. Nowadays, research has been carried out to assess local or detailed damage using Very-High-Resolution satellite data with a spatial resolution ranging from 0.6 to 1 m. Interested readers may read Ref. [72].

9.7 Seismic Risk

Risk is hereby defined as a combination of the severity and probability of an event. Human beings live on a planet where risk plays an essential role in our life. Great amounts of human effort are directed toward struggling against or mitigating risk.

With respect to the risk in earthquake engineering, it is generally related to the frequency of occurrence, level of hazard or consequence to society, and exposure (time and vulnerability) [17, 18]. While sometimes mixed with seismic hazard, which describes the natural phenomenon or properties of an earthquake as discussed in the previous sections, seismic risk is used to describe the effects of earthquakes on social, economic, and environmental consequences in a given period of time. Understanding risk is important because it gives information on what mitigation measures are most worth taking to protect families, homes, businesses and society.

The concept of seismic risk is broader and more subjective than that of the seismic hazard. Although seismic risk can generally be defined as the probability of occurrence of the adverse consequences to society [39, 73], it has different meanings and contents for different stakeholders [74]. For example, engineers are interested in the probability that a specific level of ground motion at a site of interest could be exceeded in a given period, which is analogous to flood and wind risk [75, 76]. However, insurance companies are more interested in the probability that a specific level of losses in a region or at a specific site could be exceeded in a given period [77].

Within the subject of earthquake engineering, by using the results from a seismic hazard analysis, seismic risk includes not only seismic hazard, but also exposure time and vulnerability as shown in Fig. 9.26. The expression for the seismic risk can be defined by:

Fig. 9.26 Seismic risk is an interaction among seismic hazard, exposure time and vulnerability [79]



$$P(R_i) = \sum_{j=1}^J P(R_i|S_j)P(S_j) \quad (9.30)$$

where $P(R_i)$ is the probability that the system is at state i with a total J states, S_j indicates that the seismic hazard is at level j , $P(S_j)$ is the probability that the seismic hazard is at seismic level j , $P(R_i|S_j)$ is the probability that the system is at the behavior state R_i given that the seismic hazard S_j takes place. From this expression, it is clear that it is important to specify seismic hazard in the calculation of the seismic risk.

As mentioned before, seismic risk is an interaction among seismic hazard (for example: an earthquake of magnitude 8.0 or greater with a recurrence interval of 100 years), exposure (for example: an offshore platform with a service life of 25 years) and consequence (for example: collapse of a particular building has direct and indirect costs of US\$8 million). A high seismic hazard does not necessarily lead to a high seismic risk, and vice versa. For example, due to the lack of preventive measures in low seismicity regions, the vulnerability in those regions is rather high, and this may eventually lead to a high seismic risk [78].

Many seismic provisions are based on the concept of “acceptable risk,” which attempts to balance the cost of seismic-resistant construction against the chance of unacceptable losses in future earthquakes.

A convenient and most widely adopted approach to account for the seismic risk in the evaluation of infrastructure safety is to formulate safety criteria in which the hazard is defined probabilistically as a function of the potential consequences of failure expressed in general terms, which is often called a code based approach. Compared to a complex risk assessment, in the code based approach, the emphasis is placed on the probability of the hazard rather than the probability of the consequence. For example, in ISO 19901-2 [10, 30], based on the three exposure levels by considering the life safety, environmental and economic consequence, a structure can be categorized into level 1, 2 or 3, with the associated probability of failures ranging from 4×10^{-4} to 2.5×10^{-3} . The seismic risk category (in a total of 4 categories) of a particular structure at a specific site can then be determined based on a combination of ground shaking level (in this case it is the spectral acceleration values at bedrock with a fixed spectra period) and exposure level. Similar approaches can be found on many other national and international seismic design codes and guidelines.

Improving emergency response and infrastructure design are two major ways of reducing the seismic risk. For offshore structures, these can be reflected by an efficient evacuation system (after strong ground motion ceases) and a dedicated structural design and modification with regard to seismic resistance, which will be discussed later in this book.

The detailed elaboration of seismic risk analysis is beyond the scope of the current book. For readers who are interested in this subject, more detailed information can be obtained in [80, 81].

Before concluding this chapter, it should be emphasized that risk analysis nowadays is based on various types of probability distribution assumptions, but these assumptions are empirical rather than being based on a solid theoretical background. Therefore, a development in reducing the uncertainties or in increasing accuracy associated with those assumptions are essential in the development of risk analysis.

References

1. Kramer SL (1996) Geotechnical earthquake engineering. Prentice Hall, Upper Saddle River
2. Lin T, Haselton CB, Baker JW (2013) Conditional spectrum-based ground motion selection, part I: hazard consistency for risk-based assessments. *Earthq Eng Struct Dyn* 42(12):1847–1865
3. www.pge.com/diabloseismic
4. US Nuclear Regulatory Commission (2012) Confirmatory analysis of seismic hazard at the Diablo Canyon power plant from the shoreline fault zone
5. DR Baker (2015) PG&E: Diablo Canyon nuclear plant can withstand 10,000-year quake. SFGATE, 12 March 2015
6. Abrahamson NA (2006) Seismic hazard assessment: problems with current practice and future developments. In: Keynote paper, first European conference on earthquake engineering and seismology, Geneva, Switzerland
7. Abrahamson NA (2006) Probabilistic seismic hazard analysis—an overview. Rose School, Pavia
8. Baker JW (2008) An introduction to probabilistic seismic hazard analysis (PSHA). US Nuclear Regulatory Commission
9. Cornell CA (1968) Engineering seismic risk analysis. *Bull Seismol Soc Am* 58(5):1583–1606
10. ISO19901-2 (2004) Petroleum and natural gas industries—specific requirements for offshore structures—part 2: seismic design procedures and criteria
11. Gutenberg B, Richter CF (1954) Seismicity of the earth and associated phenomena. Princeton University Press, Princeton
12. PC Marrow (1992) Seismic monitoring of the North Sea. Prepared by Global Seismology for the Health and Safety Executive, Health & Safety Executive, OTH, vol 90, p 323
13. Schwartz DP, Coppersmith KJ (1984) Fault behavior and characteristic earthquakes: examples from the Wasatch and San Andreas fault zones. *J Geophys Res* 89(B7):5681–5698
14. Youngs RR, Coppersmith KJ (1985) Implications of fault slip rates and earthquake recurrence models to probabilistic seismic hazard analysis. *Bull Seismol Soc Am* 75(4):939–964
15. Der Kiureghian A, Ang AHS (1977) A fault rupture model for seismic risk analysis. *Bull Seismol Soc Am* 67(4):1173–1194
16. Bungum H, Selnes PB (1988) Earthquake loading on the norwegian continental shelf—summary report. NORSAR, NGI and Principia Mechanica Ltd, Oslo

17. Wang Z (2006) Understanding seismic hazard and risk assessments: an example in the New Madrid Seismic Zone of the central United States. In: Proceedings of the eighth national conference on earthquake engineering, San Francisco, Paper 416
18. Wang Z (2007) Seismic hazard and risk assessment in the intraplate environment: the New Madrid Seismic Zone of the central United States. In: Stein S, Mazzotti S (eds) Continental intraplate earthquakes: science, hazard, and policy issues. Geological Society of America Special Paper 425, pp 363–373
19. Baker JW (2011) Conditional mean spectrum: Tool for ground motion selection. *J Struct Eng* 137(3):322–331
20. Srbulov Milutin (2008) Geotechnical earthquake engineering—simplified analyses with case studies and examples. Springer, Heidelberg
21. Ritsema AR (1981) On the assessment of seismic risk in the North Sea area. Koninklijk Nederlands Meterologisch Instituut Report
22. Gumbel EJ (1958) Statistics of extremes. Columbia University Press, New York
23. Marrow PC (1992) Seismic monitoring of the North Sea. Prepared by Global Seismology for the Health and Safety Executive, Health & Safety Executive
24. Ellsworth WL (1999) A physically-based earthquake recurrence model for estimation of long-term earthquake probabilities. In: workshop on earthquake recurrence: state of the art and directions for the future, Institute Nazionale de Geofisica, Rome, Italy
25. Nishenko SP, Buland R (1987) A generic recurrence interval distribution for earthquake forecasting. *Bull Seismol Soc Am* 77:1382–1399
26. Kameda H, Takagi H (1981) Seismic hazard estimation based on non-Poisson earthquake occurrences, Memoirs of the Faculty of Engineering, Kyoto University, v. XLIII, Pt. 3, July, Kyoto
27. Anagnos T, Kiremidjian AS (1984) Temporal dependence in earthquake occurrence. In: Proceedings of the eighth world conference on earthquake engineering, vol 1. Earthquake Engineering Research Institute, Oakland, CA, pp 255–262
28. Chen WF, Lui EM (2006) Earthquake engineering for structural design, 1st edn. CRC Press, Boca Raton
29. Bungum Hilmar (2012) Recent advances in earthquake hazard assessment. NORSRA, Oslo
30. ISO19901-2 (2016) Petroleum and natural gas industries—specific requirements for offshore structures—part 2: seismic design procedures and criteria, 2nd edn
31. Pinto AV (2003) Earthquake performance of structures—behavioural, safety and economical aspects. Special Publication No. I.98.111, EC Joint Research Center, ISPRA, October, 2003
32. McGuire RK (1995) Probabilistic seismic hazard analysis and design earthquakes: closing the loop. *Bull Seismol Soc Am* 85(5):1275–1284
33. National Research Council (1988) Probabilistic seismic hazard analysis, report of the panel on seismic hazard analysis. National Academy Press, Washington DC
34. McGuire RK (1978) FRISK: computer program for seismic risk analysis using faults as earthquake sources. US Geological Survey, Reports, United States Geological Survey Open-file 78-1007, p 71
35. Yule DE, Kala R, Matheu EE (2005) DEQAS-R: standard response spectra and effective peak ground accelerations for seismic design and evaluation (computer program) version 1.0. US Army Engineer Research and Development Center, Vicksburg, MS
36. Molina S, Lang DH, Meslem A, Lindholm CD (2015) User manual for the earthquake loss estimation tool, SELENA v6.5, user and technical manual v6.5
37. Sahin C (2014) Seismic retrofitting of existing structures. Portland State University, Portland
38. Bazzurro P, Cornell CA (1999) Disaggregation of seismic hazard. *Bull Seismol Soc Am* 89 (2):501–520
39. McGuire RK (2004) Seismic hazard and risk analysis, vol 221. Report MNO-10, Earthquake Engineering Research Institute Publication, Oakland, CA
40. Kulkarni RB, Youngs RR, Coppersmith KJ (1984) Assessment of confidence intervals for results of seismic hazard analysis. In: Proceedings of the eighth world conference on earthquake engineering, vol 1. Prentice Hall, Englewood Cliffs, NJ, pp 263–270

41. Coppersmith KJ, Youngs RR (1986) Capturing uncertainty in probabilistic seismic hazard assessments with intraplate tectonic environments. In: Proceedings of the third US national conference on earthquake engineering, Charleston, South Carolina, vol 1, pp. 301–312
42. Frankel A, Mueller C, Barnhard T, Perkins D, Leyendecker E, Dickman N, Hanson S, Hopper M (1996) National seismic hazard maps—documentation June 1996. US Geological Survey Open-File Report 96-532, vol 110
43. Kafka AL (2002) Statistical analysis of the hypothesis that seismicity delineates areas where future large earthquakes are likely to occur in the Central and Eastern United States. *Seismol Res Lett* 73(6):992–1003
44. US Geological Survey (2008) Documentation for the 2008 update of the United States national seismic hazard maps, Open-File Report 2008-1128
45. Anderson JG, Trifunac MD (1977) Uniform risk absolute acceleration spectra, advances in civil engineering through engineering mechanics. In: Proceedings of the second annual engineering mechanics division specialty conference. American Society of Civil Engineers, New York, pp 332–335
46. McGuire RK (1999) Deterministic vs. probabilistic earthquake hazards and risks. *Soil Dyn Earthq Eng* 21:377–384
47. Mutlu Sumer B (2014) Liquefaction around marine structures. World Scientific Press, London
48. Mattheu EE, Yule DE, Kala RV (2005) Determination of standard response spectra and effective peak ground accelerations for seismic design and evaluation. US Army Engineer Research and Development Center Vicksburg, MS
49. Frankel AD, Mueller C, Barnhard T, Perkins D, Leyendecker EV, Hanson S, Hopper M (1996) National seismic hazard maps, June 1996 documentation. Open-File Report 96-532, US Geological Survey, Golden, CO
50. Frankel AD, Petersen MD, Mueller CS, Haller KM, Wheeler RL, Leyendecker EV, Wesson RL, Harmsen SC, Cramer CH, Perkins D, Rukstales S (2002) Documentation for the 2002 update of the national seismic hazard maps. Open-File Report 02-420, US Geological Survey, Golden, CO, 2002
51. Mutlu Sumer B, Ansar A, Onder Cetin K, Damgaard J, Riza Gunbak A, Ottesen Hansen N-E, Sawicki A, Synolakis CE, Yalciner AC, Yuksel Y, Zen K (2007) Earthquake-induced liquefaction around marine structures. *J Waterw Port Coast Ocean Eng ASCE* 133(1):55–82
52. Cornell CA (1996) Reliability-based earthquake-resistant design: the future. In: Proceedings of the 11th world conference on earthquake engineering, Acapulco, Mexico, Paper No. 2166
53. Popov EP, Yang TS, Grigorion CE (1994) New directions in structural seismic designs. *Earthq Spectra* 9(4):845–875
54. US DOE (Department of Energy) (1994) Natural phenomena hazards design and evaluation criteria for DOE facilities. DOE-STD-1020-94, Washington, DC
55. Cornell CA (1996) Calculating building seismic performance reliability: a basis for multi-level design norms. In: Proceedings of 11th world conference on earthquake engineering, Acapulco, Mexico
56. NORSOK Standard N-003 (2004) Actions and action effects, Rev. 2
57. International Association of Oil and Gas Producers (2014) Reliability of offshore structures: current design and potential inconsistencies. OGP Report No. 486
58. NORSAR (1998) Seismic zonation for Norway. Prepared for Norwegian Council for Building Standardization by NORSAR and Norwegian Geotechnical Institute
59. Wang G (2011) A ground motion selection and modification method capturing response spectrum characteristics and variability of scenario earthquakes. *Soil Dyn Earthq Eng* 31:611–625
60. Baker JW, Cornell CA (2006) Spectral shape, epsilon and record selection. *Earthq Eng Struct Dyn* 35(9):1077–1095
61. Baker JW, Cornell CA (2006) Correlation of response spectral values for multi-component ground motions. *Bull Seismol Soc Am* 96(1):215–227
62. Baker JW, Jayaram N (2008) Correlation of spectral acceleration values from NGA ground motion models. *Earthq Spectra* 24(1):299–317

63. Baker JW (2007) Evaluation of ground motion selection and scaling techniques for long period structures. USGS Award No. 07HQAG0129
64. Somerville PG, Thio HK (2011) Development of ground motion time histories for seismic design. In: Proceedings of the ninth Pacific conference on earthquake engineering: building an earthquake-resilient society, Auckland, New Zealand
65. Mousavi M, Ghafory-Ashtiani M, Azarbakht A (2011) A new indicator of elastic spectral shape for the reliable selection of ground motion records. *Earthq Eng Struct Dyn* 40 (12):1403–1416
66. Mousavi M, Shahri M, Azarbakht A (2012) E-CMS: a new design spectrum for nuclear structures in high levels of seismic hazard. *Nucl Eng Des* 252:27–33
67. Bak P (1996) How nature works: the science of self-organized criticality. Copernicus Press, New York
68. Sornette D, Ouillon G (2012) Dragon-kings: mechanisms, statistical methods and empirical evidence. *Eur Phys J Spec Top* 205(1):1–26
69. Sornette D, Woodard R, Zhou WX (2009) The 2006–2008 oil bubble: evidence of speculation, and prediction. *Phys A* 388:1571–1576
70. Rundle JB, Holliday JR, Graves W, Turcotte DL, Tiampo KF, Klein W (2012) Probabilities for large events in driven threshold systems. *Phys Rev E* 86:021106
71. Xie LL (2000) Some challenges to earthquake engineering in new century. In: Proceedings of the China–US millennium symposium of earthquake engineering: earthquake engineering frontiers in the new millennium, Beijing
72. Yang XJ, Li J (2012) Advances in mapping from remote sensor imagery: techniques and applications. CRC Press, Boca Raton, FL
73. Reiter L (1990) Earthquake hazard analysis. Columbia University Press, New York, p 254
74. Smith W (2005) The challenge of earthquake risk assessment. *Seismol Res Lett* 76:415–416
75. Sacks P (1978) Wind forces in engineering, 2nd edn. Pergamon Press, Elmsford, p 400
76. Gupta RS (1989) Hydrology and hydraulic system. Prentice Hall, Englewood Cliffs, p 739
77. Wang Z (2008) Understanding seismic hazard and risk: a gap between engineers and seismologists. In: 14th world conference on earthquake engineering, Beijing
78. Bachmann H (2003) Seismic conceptual design of buildings: basic principles for engineers, architects, building owners, and authorities. Swiss Federal Office for Water and Geology and Swiss Agency for Development and Cooperation, BWG, Bern
79. Solomos G, Pinto A, Dimova S (2008) A review of the seismic hazard zonation in national building codes in the context of Eurocode 8, EUR 23563 EN. European Commission, Luxembourg
80. Ilki A, Karadogan F, Pala S, Yuksel E (2009) Seismic risk assessment and retrofitting: with special emphasis on existing low rise structures (geotechnical, geological and earthquake engineering), 1st edn. Springer, Dordrecht
81. Mulargia F, Geller RJ (eds) (2004) Earthquake science and seismic risk reduction (NATO science series: IV: earth and environmental science)

Chapter 10

Influence of Hydrodynamic Forces and Ice During Earthquakes

10.1 Hydrodynamic Forces

10.1.1 Introduction to Hydrodynamic Force Calculation

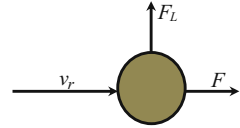
Under strong seismic ground motion, the structure may undergo large motions. Compared to land-based structures, offshore structures cherish unique effects of fluid–structure interactions: the hydrodynamic forces due to the relative velocity and acceleration between structural members and their surrounding waters. This induces drag and inertia forces applied on offshore structures. In addition, the hydrodynamic interaction with the offshore environment, such as waves, current and wind, also gives rise to additional environmental loading applied on structures.

For slender tubular members, the accelerated flow separates from the surface of the submerged structural member, forming a wake (low pressure region) “behind” the member. Subject to ocean wave and current loading, the hydrodynamic forces due to this effect include both the drag and inertia forces as shown in Fig. 10.1. The hydrodynamic forces per unit length on members along the relative motion direction between members and water are calculated by Morison’s equation [1], which is only applicable when the diameter of the structural member d is less than 1/5 of the ocean wave length, as is the case for typical jacket/jackup structures:

$$F = \rho \cdot A \cdot a_w + \rho \cdot C_m \cdot A_r \cdot a_r + \frac{1}{2} \rho \cdot C_D \cdot v_r \cdot |v_r| \cdot d \quad (10.1)$$

where ρ is the density of the fluid; A is the cross-section area of the body; a_w is the component of the water particle acceleration normal to the member axis; C_m is the added mass coefficient, which is defined as the ratio between added mass of fluid and the associated displaced fluid mass, which will be discussed in Sect. 10.1.3; A_r is the reference area normal to the structural member axis; a_r is the relative acceleration between water particle and member normal to member axis; C_D is the

Fig. 10.1 Direction of hydrodynamic drag and inertia force F and lift force F_L relative to motion between structure member and fluid v_r



drag coefficient; v_r is the water particle velocity relative to the member normal to the member axis; d is diameter of the member exposed to the water.

The first item $\rho \cdot A \cdot a_w$ on the right hand side of the equation above is the wave potential related Froude Krylov excitation force, which is the sum of the hydrodynamic pressures acting on the surface of the body, which would exist even in the absence of a structure ($\rho \cdot C_m \cdot A_r \cdot a_r$).

The pressure disturbance due to the presence of the structure modifies the flow, which is taken into account in the second item $\rho \cdot C_m \cdot A_r \cdot a_r$, which is the added mass ($\rho \cdot C_m \cdot A_r$) related force due to the relative acceleration (a_r) between the structure and the fluid. In general, this depends on the flow condition as well as the location of the body. Even if, when a structure is subject to ocean wave loading, the added mass in the vicinity of a free surface is strongly wave frequency dependent (it is sometimes misunderstood by people that the added mass is a finite amount of water that oscillates rigidly connected to structural members), this dependence characteristics may be disregarded for deeply submerged bodies provided that the dimension of the body is smaller than the wave length. For seismic analysis of offshore structures, the added mass may in most cases be simply approximated with a constant value, which will be discussed in Sect. 10.1.3.

Note that both the Froude Krylov force and added mass force are due to the inertia of the structures and the surrounding fluid. The viscous effects are then accounted for in the third item (drag force) $\frac{1}{2}\rho \cdot C_D \cdot v_r |v_r| \cdot d$. This item also indicates a non-linear relationship between the resultant forces on structural members and the wave particle velocity. The effect of drag force is usually to introduce hydrodynamic damping, which can normally be conveniently estimated using Borgman's linearization, in which the expanded series of $v_r |v_r|$ can be approximated as the first term of the series by replacing $|v_r|$ with $(8/\pi)^{0.5} v_{r(rms)}$ for sinusoidal velocity of wave, where $v_{r(rms)}$ is the root mean square of v_r [2]. For the case of a sinusoidal velocity superimposed on a current flow, the drag force induced damping can be approximated based on a minimum average error between $v_r |v_r|$ and the linear approximation [3].

For conditions with a fixed body or in which the acceleration and velocity of structural components are small, one has $a_r = a_w$ and $v_r = v$. By assuming $A_r = A$, the equation above can be rewritten as:

$$F = \rho \cdot C_M \cdot A \cdot a_w + \frac{1}{2} \rho \cdot C_D \cdot v \cdot |v| \cdot d \quad (10.2)$$

in which the inertia coefficient is defined as $C_M = 1 + C_m$, which may be determined based on a root mean square measured average value of inertia coefficients.

For moving structures in still water, the hydrodynamic drag and inertia force can be calculated as:

$$F = -\rho \cdot C_m \cdot A \cdot a_s - \frac{1}{2} \rho \cdot C_D \cdot v_s \cdot |v_s| \cdot d \quad (10.3)$$

where a_s and v_s are acceleration and velocity of structures/members normal to its axis.

Both C_D and C_M can be determined experimentally. They can also be obtained by checking relevant handbooks and diagrams.

For circular members, the drag and inertia coefficients are a function of the following non-dimensional parameters:

Reynolds (Re) number:

$$Re = v_{max}d/\nu \quad (10.4)$$

Keulegan-Carpenter (K_C) number:

$$K_C = v_{max}T/d \quad (10.5)$$

Surface roughness

$$\delta = k/d \quad (10.6)$$

where v_{max} is the maximum velocity between water particle and members; ν is the kinematic viscosity of water, typically taken as $1.1 \times 10^{-6} \text{ m}^2/\text{s}$; T is the period of ocean wave loading; and k is the surface roughness height, typically ranging between 0.004 and 0.06.

Figure 10.2 shows drag coefficients for smooth cylinders and cylinders of various roughnesses varied with Reynolds number (Re) in steady uniform flow. Note that there is a distinct drop in the drag coefficient in a certain Reynolds number range. This is referred to as the critical flow regime and is very pronounced for a smooth circular cylinder. The surface roughness height can be selected based on the material and surface condition, with one recommended by DNV [4] as listed in Table 10.1.

Figure 10.3 shows variations of inertia coefficient with K_C number for smooth and rough cylinders. For intermediate roughness the values can be determined by a linear interpolation between the curves for smooth and rough cylinders. For large K_C number, the drag force is the dominating force compared with the inertia force; asymptotic values of inertia coefficient for smooth and rough cylinders can be taken as 1.6 and 1.2, respectively [4].

As mentioned before, Morison's equation is only applicable when the diameter of structural members is less than 1/5 of the wave length, which is the case for many offshore structures such as jacket or jackup structures. However, for large volume bodies with $\pi d/\lambda > 0.5$ (where D is the dimension of structure body, and λ is the ocean wave length), the incident waves undergo significant scattering or diffraction

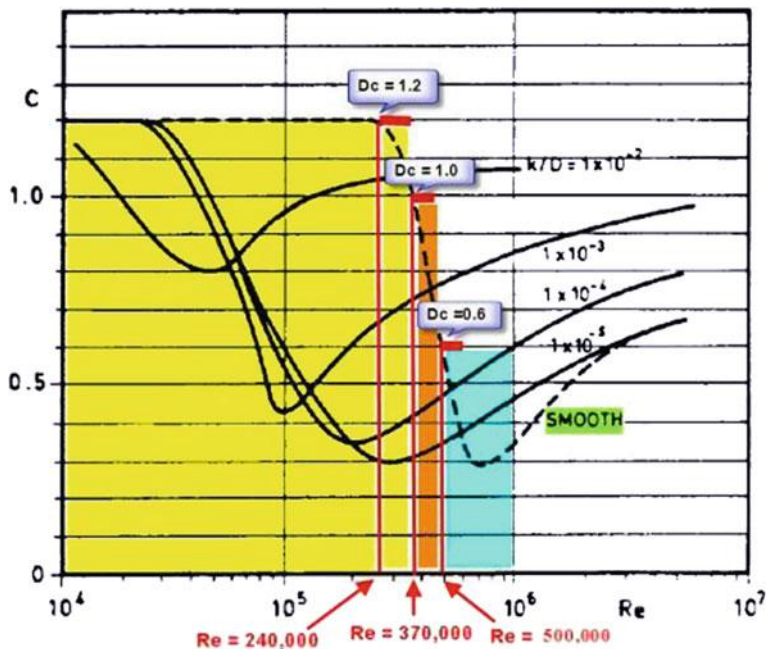
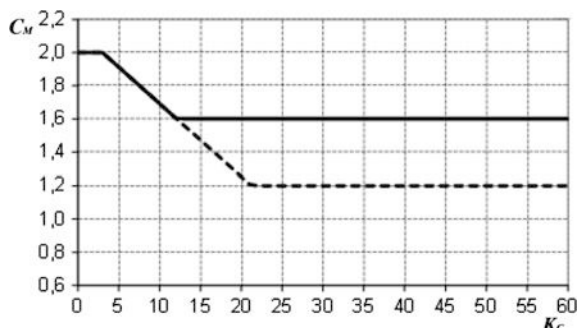


Fig. 10.2 Variation of drag coefficient with Reynolds (Re) number and surface roughness

Table 10.1 Surface roughness recommended by DNV [4]

Structural surface exposed to fluid	k (m)
Steel, new uncoated	5×10^{-5}
Steel, painted	5×10^{-6}
Steel, highly corroded	3×10^{-3}
Concrete	3×10^{-3}
Marine growth (see Sect. 10.1.5)	5×10^{-3} to 5×10^{-2}

Fig. 10.3 Variations of inertia coefficient with K_c number for smooth (solid line) and rough (dashed line) cylinder



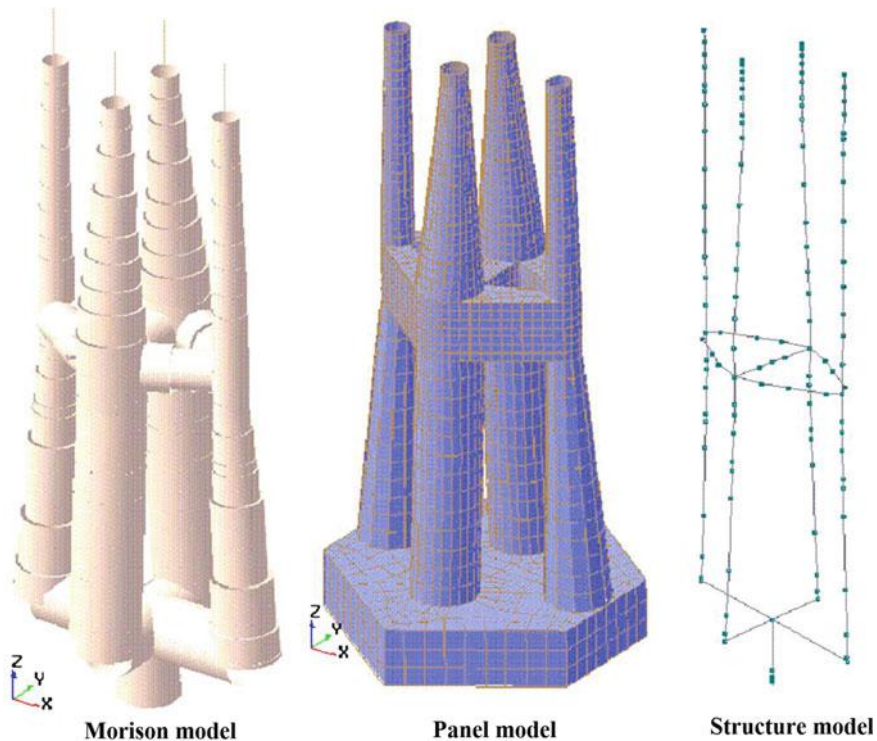


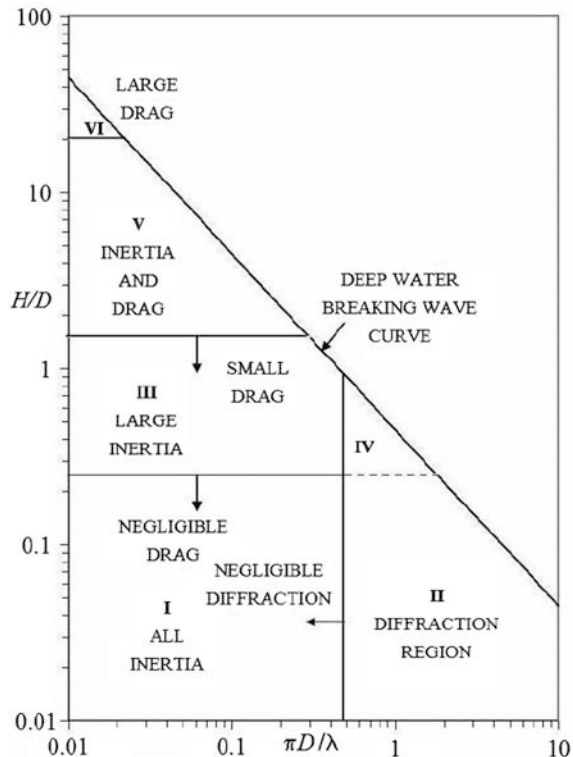
Fig. 10.4 Combining Morison and panel model to calculate the hydrodynamic loads transferred to the structural model (courtesy of Aker Solutions)

surrounding the structure, the drag effects are small while the diffraction of the waves from the surface of the structure plays a dominant role in the calculation of hydrodynamic forces, and the structure is large enough to fall into the diffraction wave force regimes II and IV shown in Fig. 10.5. In engineering practice, the hydrodynamic force due to wave diffraction can be calculated by modeling the structure as a panel model and integrating the panel pressure on each part of the structure, together with the Morison model, the hydrodynamic forces applied on the structure can be determined as shown in Fig. 10.4. For more details, readers may refer to [5, 6].

On the basis of the discussion above, it can be summarized that the calculation of hydrodynamic forces can be handled as two types of problems [5]:

- (1) Forces on a body when the structure is restrained from oscillating and there are incident ocean waves. The forces are referred to as wave excitation loads, comprising Froude-Kriloff and diffraction forces.
- (2) Forces on the body when the structure is forced to oscillate with the excitation frequency in any rigid-body motion mode without interference from incident waves, which include added mass, damping and restoring terms.

Fig. 10.5 Dominant types of wave forces at different regimes (D is the characteristic dimension of structures/members, H is the wave height, and λ is the wave length) [7]



In addition to the hydrodynamic force applied along the direction of relative motion between a structure member and surrounding fluid, the structural member can also receive lift force (Fig. 10.1) perpendicular to direction of the relative motion:

$$F_L = \frac{1}{2} \rho \cdot C_L \cdot v_r \cdot |v_r| \cdot d \quad (10.7)$$

where C_L is the lift coefficient, which is a function of Reynolds number.

In the following sections, the effects of drag and added mass coefficients, buoyance, and marine growth on seismic responses of offshore structures will be briefly discussed.

10.1.2 Effects of Drag Forces

The drag forces applied on structures are caused by the relative velocity between the member and the water flow. Under storm wave condition, they can cause a significant wave loading, which is a dominant environmental load for designing the

majority of offshore structures constructed with slender members. On the other hand, drag loading also introduces a hydrodynamic damping to mitigate the seismic response of offshore structures [8]. This hydrodynamic damping is higher in random seas than in still water and is more significant under sea states with large wave height than under small wave height, even though this effect is generally small [9].

However, under certain circumstances, the combination of seismic and wave loading on offshore structures can even increase the dynamic response. By studying the seismic responses of jacket structures under both earthquake and wave loading, Jin et al. [10], Etemad et al. [11] and Bargi et al. [12] showed that when the ocean waves propagate in different directions from that of seismic loading, the structural response can even be increased.

10.1.3 Effects and Determination of Added Mass

As mentioned before, added mass accounts for the inertia of the fluid entrained by the accelerating structure, i.e., since the structure accelerates, the fluid surrounding the structure must also accelerate. Added mass increases the effective mass and effective mass moment of inertia of the structure. Since the water has a comparable density to that of the body of the marine structures, added mass plays a significant role in the dynamic analysis of marine structures [13]. Table 10.4 shows an example of mass distribution of a jacket among the jacket, added mass, marine growth and the topside. It is found that the value of added mass is in the same order of significance as the jacket's structural mass.

In analysis practice, the added mass can normally be accounted for by a simplified modeling of an additional mass distributed on each submerged structural member or along all surfaces of the structure that interact with surrounding water, and be effective only along direction(s) of fluid–structure relative motion direction. For tubular members with circular cross sections, the contribution to the added mass per unit length can be calculated as:

$$m_a = \left[\rho \frac{\pi d^2}{4} (C_M - 1) \right] + \left[\rho \left(\frac{\pi}{4} (d - 2t_g)^2 - \sigma \right) (1 - I) \right] + \left[\rho_g \pi (dt_g - t_g^2) \right] \quad (10.8)$$

where ρ is the density of the fluid; ρ_g and t_g are the density and thickness of marine growth (Sect. 10.1.5); d is the member diameter including marine growth; C_M is the inertia coefficient; σ is the solid area of member's cross-section; $I = 0$ for fully flooded member (internal water is to be included) and $I = 1$ for non-flooded member (internal water is not to be included).

The first, second and third item on the right hand side of the equation above indicate the added mass contributed from parts outside the members, inside the members, and marine growth, respectively.

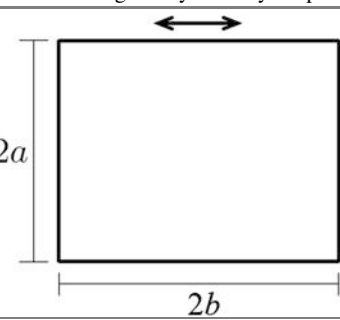
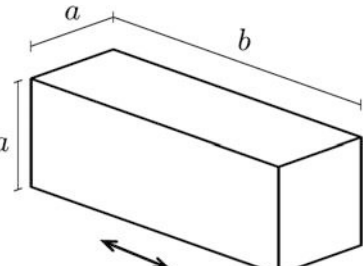
Even though the inertia coefficient C_M in the equation above is frequency dependent (a function K_c or Re) as presented in Sect. 10.1.1, indicating that the finite volume of fluid does not oscillate rigidly connected to the member, for calculating the seismic responses of offshore structure with high frequency vibrations (typically much higher than wave loading frequency), it may roughly be taken as 2.0. As a further simplification, the added mass of non-flooded (buoyant) members can be modeled as the mass of water (along the direction of structure-fluid relative motion direction) with the enclosed volume of the structure members. For flooded members the added mass is modeled as twice the mass of the water with the enclosed volume of the structural members.

For the added mass for various cross sections or body shapes, readers may check the relevant handbooks or guidelines, such as Appendix D in DNV-RP-C205 [4]. For example, depending on the relative direction between structural members and the water particle motions, Table 10.2 shows the added mass coefficient for structural members with square prismatic shape, which can be used to calculate added mass:

$$m_a = \rho C_m V = \rho C_m A l \quad (10.9)$$

where V is reference volume of the structural object in m^3 ; A is reference area of the object in m^2 ; both V and A are given in Table 10.2; and l is the length of the object

Table 10.2 Analytical added mass coefficient C_m for structural objects with square prismatic shape in two- and three-dimensions [4]; the direction of motion for structural objects is indicated by double-end arrow line

Section through body or body shape	a/b	C_m	V or A
	∞	1.0	$A = \pi a^2$
	10	1.14	
	5	1.21	
	2	1.36	
	1	1.51	
	0.5	1.70	
	0.2	1.98	
	0.1	2.23	
	1	0.68	$V = a^2 b$
	1/2	0.36	
	1/3	0.24	
	1/4	0.19	
	1/5	0.15	
	1/6	0.13	
	1/7	0.11	
	1/10	0.08	

affected by added mass effects, which is applicable when two-dimensional geometry is assumed.

Added mass generally gives an increase in natural period of the structure due to its contribution to the inertia of the structure. This normally results in a decrease in spectral acceleration, but may sometimes increase local forces on the submerged part of the structure due to a possible increase in inertia force on that part.

It is noted that in many engineering practices, for simplicity, the effects of added mass are represented-modeled as point masses attached to the submerged part of the offshore structures that are equivalently effective in all three translational degrees-of-freedom in a dynamic analysis. This is likely to give an incorrect representation of the added mass as it is in reality only active along the direction(s) of relative oscillatory motion between the structural object and the water particle. This inappropriate modeling can be non-conservative. For example, when the added masses are modeled as real structural masses that are effective in all three translational degrees-of-freedom, it can cause additional gravity loads applied throughout the structure, which artificially reduces the tensile stresses or increases/induces compressive stresses on concrete shafts' cross sections for a GBS structure, or artificially decreases the uplifting forces on pile foundations for a jacket structure. In addition, the inappropriate modeling of added mass can also induce artificial inertia forces in the vertical direction of the structure, which can be either conservative or non-conservative.

10.1.4 Effects of Buoyancy

The buoyance force applied to non-flooded members or large volume submerged structures can be rather significant. Its effects on structural and foundation capacity can be both positive and negative. For example, for an offshore structure with submerged concrete shafts, the buoyance force along the shafts generally decreases the compressive stress along the longitudinal axis of the shafts. However, when combined with horizontal earthquake or ocean wave loading, it can result in an increase of tensile stress in the tensile side of each concrete shaft. Similarly, for an offshore structure's foundation constructed in the form of a pile group, when combined with seismic or ocean wave loading, the buoyance force on the offshore structure can decrease the compressive forces on some piles, but at the same time it also increases the tensile forces on some other piles.

10.1.5 Effects and Modeling of Marine Growth

After a certain period of installation for an offshore structure, various types of marine fouling organism may be found on the structure's submerged member. They are referred to as marine growth as shown in Fig. 10.6. Their distributions on



Fig. 10.6 Marine growth at water depths of 14 m (*upper*) and 41 m (*lower*) on an offshore jacket structure in the North Sea

structural members vary depending on many factors, such as geographical location, water depth, water temperature and season, ocean current, platform design and operation.

Marine growth can be classified into three main categories, namely hard growth, soft growth and long and flapping weed. Hard growth includes mussels, oysters, barnacles and tubeworms. Soft growth includes seaweeds, soft corals, sponges, anemones, hydroids, sea-squirts and algae. Long flapping weed is kelp, which could also come under soft growth but is singled out because of its much larger size.

The major effects of marine growth can be summarized as [14]: (1) increase in structural diameter and displaced volume; (2) increase in structural weight (normally insignificant); (3) increase in hydrodynamic drag coefficient (Fig. 10.2) and decrease in added mass coefficient due to the surface roughness (Fig. 10.3); (4) possible increase in hydrodynamic forces; (5) increase in natural period due to contributions from the increased added mass and structural weight; (6) coverage of the member's outer surface, causing difficulties for subsea inspection; (7) physical obstruction that restricts functionality.

From the seismic response point of view, as marine growth will cause an increase of a structure's eigenperiod by adding more mass, it may slightly modify frequency content of the seismic response. It may also increase the hydrodynamic forces and modify the static stability of the structure.

It is also worth mentioning that, among different types of marine growth, it is mainly the hard marine growth that contributes to the hydrodynamic forces. Soft marine growth hardly contributes accountable hydrodynamic forces, and can therefore normally be omitted in the hydrodynamic load calculation.

In structural design and analysis, the marine growth is typically assumed to be a function of location. It would be preferable to measure the marine growth on structural members. In the absence of site specific information on the types and thickness of marine growth, various design codes provide recommended values, such as the one recommended by Norsok [15] as listed in Table 10.3. The density of marine growth can typically be taken as 1325 kg/m³.

Table 10.4 shows an example of mass distribution of a jacket platform among the jacket steel, added mass, marine growth and the topside modules. It is found that even though the value of added mass is in the same order of significance as the jacket's structural mass, the mass of marine growth is much less significant.

Instead of using the marine growth thickness provided by codes and standards, such as the one given by Norsok [15] as listed in Table 10.3, it is preferred to

Table 10.3 Marine growth varied with altitude applied for offshore design in Norway [15]

	Latitude 56–59°N	Latitude 59–72°N
Water depth (m)	Thickness (mm)	Thickness (mm)
+2 to -40	100	60
Below -40	50	30

Table 10.4 An example of mass and added mass distribution of a jacket structure with a water depth of 110 m located in the North Sea

Item	Mass (tons)
Structural weight of jacket	8600
Marine growth	700
Added mass	4600
Total jacket mass	13,900
Topsides modules	13,000

perform in-site measurement to reduce the uncertainties. The measured thickness is normally below the one given by Table 10.3, thus reducing the hydrodynamic forces and slightly increasing the natural frequency of the structure. Moreover, to reduce the hydrodynamic forces, a cleaning of marine growth can be performed at certain period intervals. It is also a practice in some offshore jacket structures to install metal bands around the legs and conductors that are moving up and down with the ocean wave, which can clean the marine growth in the wave zone.

10.2 Effects of Ice

10.2.1 General

In cold region such as the north Sakhalin or Alaska, sea ice may cover the area for more than half the year. Therefore, it is reasonable to assume that an earthquake can occur while ice is surrounding the offshore structures.

Most of the design codes do not address the combination of earthquake and surrounding ice loads. However, ISO 19906 [16] requires that for abnormal/accidental level earthquakes (with an annual probability of exceedance not greater than 10^{-4}), it is normally sufficient to consider only ice to be present when an earthquake occurs. For extreme level earthquake (with an annual probability of exceedance not greater than 10^{-2}), in addition to the ice load, the wave, wind, and current shall also be considered. A few existing guidelines, such as CSA [17] and API [18] also recommend considering a combination of the various load effects, even though they do not give explicit guidance on it.

Figure 10.7 shows two major types of ice loading on fixed offshore structures: surface ice sheet (upper) and packed ice ridges (lower). The former is characterized by a flat sheet shape ice with maximum thickness of 2 m and a maximum crushing strength of a few MPa (typically 2–5 MPa). It may induce large abrasion effects on legs of offshore structures. For example, an offshore GBS structure off Sakhalin can experience 4000 km of ice passing from same main direction each year. Packed ice ridges are characterized by packed ice forming a solid block around offshore structures, with a higher crushing strength at the sail than that at the keel. It can have a thickness (from sail to keel) of up to 30 m, with a consolidated layer of a few meters. The number and geometry of platform legs are essential for determining the ice ridge induced forces. Compared with the ice sheet induced load, the load due to ice ridges are normally higher. In addition, icebergs may also impact with offshore structures and induces enormous forces. However, since this type of load is irrelevant to the combination with earthquake induced load (the probability of an iceberg impacting an offshore structure and a significant earthquake occurring simultaneously is extremely low), it is not considered in a seismic design of relevant offshore structures.

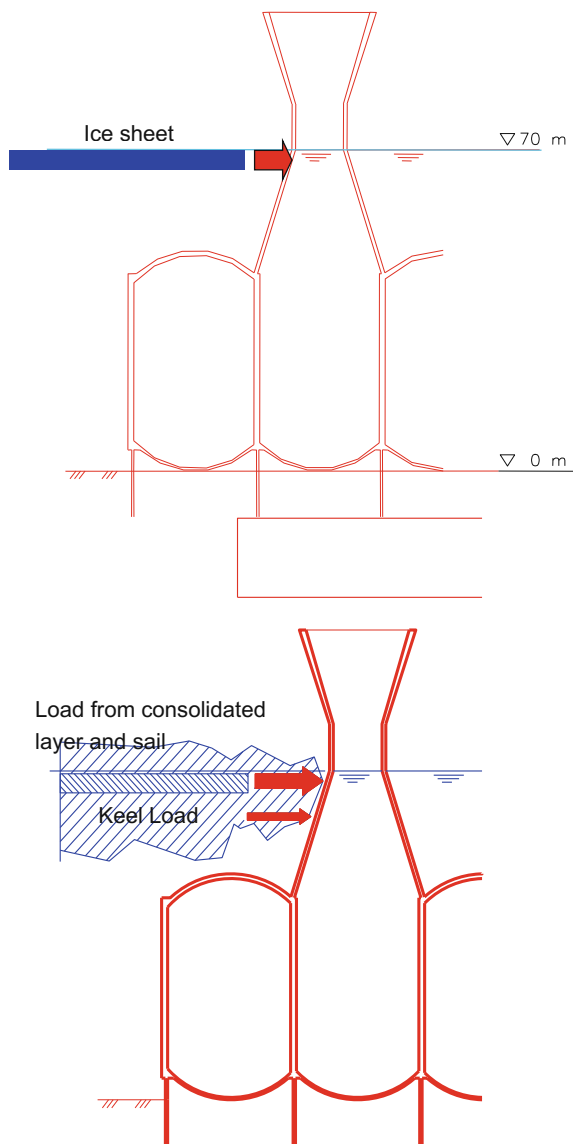


Fig. 10.7 Two major types of ice loading on fixed offshore structures: surface ice sheet (*upper*) and packed ice ridges (*lower*) (courtesy of Aker Solutions)

There are two typical load scenarios for the combination of ice and seismic loading:

1. An earthquake occurs when a structure is surrounded by a stable, uniform ice cover (hereafter, an earthquake load under a stable ice cover condition).

2. An earthquake occurs when a uniform ice cover is impacting with a structure (hereafter, an earthquake load under a drifting ice cover condition).

At low stress states, ice exhibits creeping and ductile characteristics, while brittle properties emerge at high stress states. The mechanical behaviors of ice are also dependent on the rate of deformation and deformation history. The ice loading state differs significantly from static loading to dynamic loading [19]. Regarding dynamic loading, the initial contact conditions are invariably irregular and non-uniform and the duration of the impact is generally determined by kinetic energy of the impacting ice feature, which may come to rest during the impact process.

The ice load on marine structures can be measured by total (global) load and local loads (pressures). The global load affects the overall motion and stability of structures, while local load affects areas from 1 m^2 to as much as 100 m^2 [20]. For both measures, the ice thickness and relative velocity between ice and structures are two essential parameters to determine the load level.

With respect to local load, close observations show that, when ice crushes a structure, local ice pressure on small patches or a narrow line-like area can reach rather high values [16]. Such areas are termed high pressure/critical zones. This pressure may be well beyond the normal uni-axial crushing strength of sea ice [21]. The explanation is that the stress field is in fact multi-axial. The process of ice-structure interaction is characterized by fracture and damage processes, which play a key role in the appearance and disappearance of high pressure zones. Further, the high pressure has an important effect on local ice actions. However, the global ice pressure is significantly lower than the local ice pressure because in local regions of ice the intense pressure occurs over a short time.

Note that the ice loads on offshore structures are generally limited by the failure of the ice itself [22], and the strength of ice due to bending is less than half of that due to crushing (Fig. 10.8). The use of conical or sloping structures will induce the

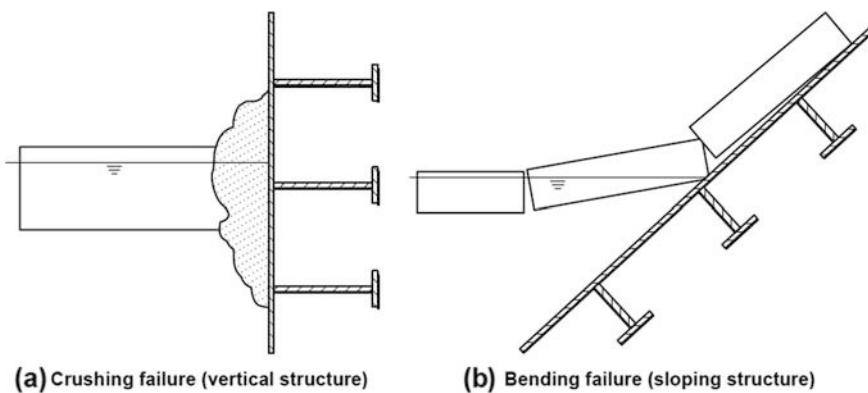


Fig. 10.8 Crushing failure for vertical structures and bending failure for sloping structure [16]

bending failure of the ice sheet when the ice crushes structures. Therefore, conical structures are often a preferred design option for structures located in ice-covered waters. Recently, field measurements have also indicated that the adoption of conical structures can avoid severe steady-state vibrations [23]. Figure 5.1. shows a cone installed on an offshore monopod structure originally with a vertical leg in China Bohai Sea. The ice excitation time history on conical and slope structures is generally narrow banded with a long tail toward higher loads in the probability distribution, while it can be wide banded on vertical leg structures.

Even though the ice loads on offshore structures are normally limited by the failure of the ice, the ice-induced vibrations in offshore structures can be rather severe when the ice is moving driven by winds or current. Dynamic loading scenarios include both transient impact loads and continuous ice failure loads. Resonance of fixed offshore structures due to ice loading may occur.

It should be noted that the knowledge development of ice–structure interaction is far less matured than that of fluid–structure interactions. There is still abundant research that needs to be carried out to increase our knowledge, especially in respect of ice condition data for marine operations and the dynamic interaction mechanism of ice–structure interactions.

10.2.2 Effects of Ice–Structure Interaction on the Seismic Response of Structures

The presence of ice may significantly affect the response of offshore or coastal structures under seismic loading. For example, in the design of the port of Anchorage in Alaska, the horizontal ice load is assumed to be 10 % of the dead and live load, which has the same magnitude as the seismic load. The ice cover can affect a structure's dynamic response with respect to both motions and their frequency content [24]. However, the ice can stiffen a structure by providing lateral supports to it, and can therefore have positive effects in resisting miscellaneous horizontal seismic load. This positive effect was witnessed during the magnitude 9.2 earthquake in Anchorage in March 1964, which caused massive damage on the Anchorage area, but the marine structures at the port of Anchorage survived with only minor damage [25].

The presence of frozen soil, even in a relatively thin layer, can significantly affect the dynamic behavior of piles. Han [26] presented that, when the thickness of the frozen soil layer is about 1/19 of the pile length, its presence increases the horizontal stiffness of the pile by 15 times and its resonant frequency by about 3.5 times. However, this could potentially increase spectral accelerations of the pile-substructure system as well.

Figure 10.9 [27] shows a numerical modeling of a GBS structure subject to earthquake loading in which the structure interacts with both ice and soil.

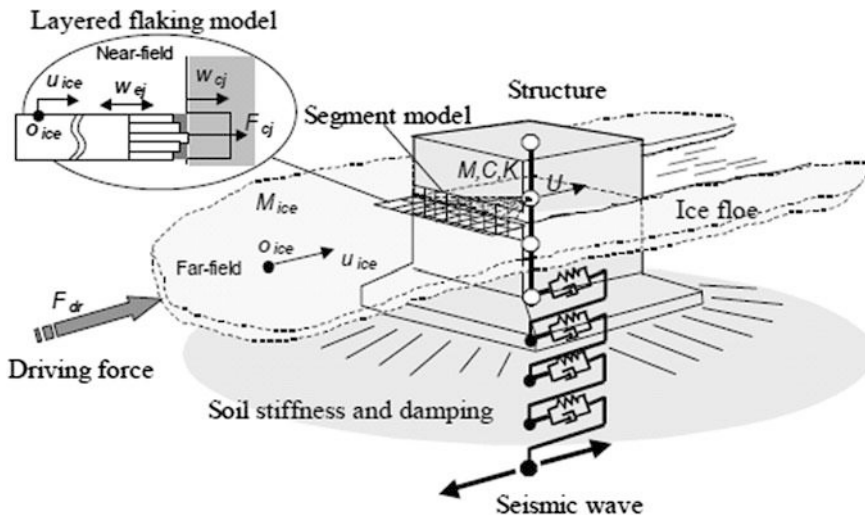


Fig. 10.9 Numerical modeling of ice–structure and soil–structure interaction under seismic excitations [27]

By applying either a sinusoidal seismic excitation or observed seismic motion on the structure with surrounding ice floe less than 1 m thick, the global load due to the combination of ice and seismic load was studied. It shows that ice would slightly (a few percent) increase the global load for an earthquake with a 100 year return period but would not affect the design global load with 1000 year return period in a moderate ice sea area such as the Sea of Okhotsk.

10.2.3 Icing and Its Effects

Icing of structures or structural members can result from wind- and wave-driven seawater spray, rain/snow fall, fog, freezing rain, green water trapped on decks, or tidal variation. Table 10.5 shows the ice accumulation thickness due to sea-spray or rain/snow with annual probability of exceedance of 10^{-2} recommended by Norsok [15].

Similar to the effects of marine growth but with the applied location above the sea level, ice accumulation will also cause a slight increase in a structure's natural period by adding more mass, which may slightly modify the frequency content of the seismic response. Moreover, ice accumulation may also modify the hydrodynamic properties and static stability of the structure.

Table 10.5 Ice accumulation thickness with a return period of 100 years [15]

Height above sea level (mm)	Action case 1			Action case 2	
	Ice caused by sea-spray			Ice caused by rain/snow	
	56°N to 68°N (mm)	North of 68°N (mm)	Density (kg/m ³)	Thickness (mm)	Density (kg/m ³)
5–10	80	150	850	10	900
10–25	Linear reduction from 80 to 0	Linear reduction from 150 to 0	Linear reduction from 850 to 500	10	900
Above 25	0	0	—	10	900

References

- Morison JR, O'Brian MP, Johnson JW, Schaaf SA (1950) The force exerted by surface waves on piles. *J Petrol Technol* 2(5):149–154
- Borgman LE (1967) Spectrum analysis of ocean wave forces on piling. *J Waterw Harb ASCE* 93(2):129–156
- Borgman LE (1969) Ocean wave simulations for engineering design. *J Waterw Harb ASCE* 9 November: 557–583
- Det Norske Veritas (2014) DNV-RP-C205, environmental conditions and environmental loads, Høvik
- Faltinsen OM (1990) Sea loads on ships and offshore structures. Cambridge University Press, Cambridge
- Chakrabarti SK (1993) Hydrodynamics of offshore structures, 2nd edn. Computational Mechanics Publications, Southampton
- Chakrabarti SK (1987) Hydrodynamics of offshore structures. Springer, Heidelberg
- Venkataramana K, Kawano K (1995) Nonlinear dynamics of offshore structures under sea wave and earthquake forces. *Adv Nonlinear Struct Dyn* 20(2):501–512
- Gurpinar A, Gryspeerdt BJ, Cole-Baker JR (1980) Dynamic analysis of offshore platforms under seismic excitation. In: Proceedings of the seventh world conference of earthquake engineering, Istanbul, vol 8
- Jin DY, Matsui T (1997) Stochastic response analysis of jacket-type ocean platforms under simultaneously acting waves and earthquakes. *Am Soc Mech Eng Saf Reliab* 2:297–302
- Etemad AK, Gharabaghi ARM, Chenaghli MR (2004) Nonlinear dynamic behavior of fixed jacket-type offshore platforms subjected to simultaneously acting wave and earthquake loads. In: Proceedings of the 23rd international conference on offshore mechanics and arctic engineering, Vancouver
- Bargi K, Reza Hosseini S, Tadayon MH, Sharifian H (2011) Seismic response of a typical fixed jacket-type offshore platform (SPD1) under sea waves. *Open J Mar Sci* 1:36–42
- Blevins RD (1979) Formulas for natural frequency and mode shape. Robert E. Krieger Publishing, Malabar, USA
- Jusoh I, Wolfram J (1996) Effects of Marine growth and hydrodynamic loading on offshore structures. *Jurnal Mekanikal Jilid* 1:77–98
- NORSOK Standard N-003 (2004) Actions and action effects, Rev. 2, Oct 2004
- ISO 19906: 2010 (2011) Petroleum and natural gas industries—Arctic offshore structures
- Canadian Standards Association (1992) General requirements, design criteria, the environment, and loads, CAN/CSA-S471-92

18. American Petroleum Institute (1995) Recommended practice for planning, designing, and constructing structures and pipelines for arctic conditions, API recommended practice, 2nd edn
19. Sanderson TJO (1988) Ice mechanics—risks to offshore structures. Graham and Trotman Limited, London
20. Naess A, Moan T (2012) Stochastic dynamics of marine structures. Cambridge University Press, Cambridge
21. Johnston ME, Croasdale KR, Jordaan IJ (1998) Localized pressures during ice–structure interaction: relevance to design criteria. *Cold Reg Sci Technol* 27(2):105–117
22. Kärnä T, Kamesaki K, Tsukuda H (1999) A numerical model for dynamic ice structure interaction. *Comput Struct* 72:645–658
23. Xu N, Yue Q, Guo F (2010) Mitigating ice-induced vibration by adding ice-breaking cone. In: Proceedings of the 20th international offshore and polar engineering, Beijing, China
24. Bouaanani N, Paultre P, Proulx J (2002) Two-dimensional modelling of ice cover effects for the dynamic analysis of concrete gravity dams. *Earthq Eng Struct Dyn* 31(12):2083–2102
25. Tsinker GP (1995) Chapter 2: Marine structures in cold regions, marine structures engineering: specialized applications. Chapman & Hall, New York
26. Han Y (1995) Dynamic behavior of pile foundations with soil–pile interactions. Memorial University of Newfoundland, St. John’s Newfoundland, Canada
27. Yamauchi Y, Kamesaki K, Hyodo M (2010) Numerical simulation on ice–structure interaction during earthquakes. In: Proceedings of the 20th international offshore and polar engineering conference, Beijing

Chapter 11

Shock Wave Due to Seaquakes

11.1 Introduction

Note that both seaquakes and tsunamis are caused by the vertical deformation of seafloors. Seaquake induced shock waves are due to the vertical seismic motions at seabed/riverbed/lakebed that propagate through waters and result in vertical shocks (hydrodynamic pressure) applied on ships, submerged structures, submarines, and other floating structures, while tsunamis are essentially tidal waves traveling to shore and they propagate all around as long surface waves and grow into huge waves near coasts.

Floating structures are normally considered to be isolated from horizontal seismic motions. However, the longitudinal (compressive) P-waves (Sect. 3.2.1) due to the vertical seismic motions at seabed/riverbed/lakebed can propagate through waters and result in vertical shocks (hydrodynamic pressure) applied on various types of floating offshore structures [1, 2]. The applied shocks are often referred to as seaquake shocks. Persons on-board the floating structures will feel as if the vessel has been struck by a rock. In offshore regions with high seismicity, extreme displacements and shock waves are often of primary interest in the design of a taut mooring system. The hull structure is designed elastically for the corresponding actions. International offshore standards such as ISO 19901-2 [3] require a consideration of the effects of shock waves on facilities with critical mechanical and electrical systems, e.g., power generation, emergency shutdown, etc.

The response of floating structures due to seaquake depends on the frequency of seismic waves and the depth of water. At water with shallow depth and a flat seabed of an open sea area, a floating structure makes almost the same movements as that of the seabed motions. In areas with deep water or where the seismic motions are dominated by high frequency components in relation to the compressibility of the water, the seaquake responses are not close to the seismic motion at seabed. Moreover, since seaquakes are caused by the resonance of longitudinal waves, the effect of compressibility of fluid cannot be ignored. The resonance frequencies of

the vertical exciting forces acting on floating structures are affected by their breadth: the resonance occurs between the free surface and the seabed when the floating structure is small; and it occurs between both ends of the structure when the floating structure is large [4].

The seaquake response of TLPs is higher than those without the tension leg system [5]. For submerged floating tunnels with anchor bars fixed to the seabed, the effects of seaquake (water transfers the seabed motion to the tunnel structure with hydrodynamic pressures on it) can be more significant than that of the seabed seismic motions (anchor bars transfer seabed motions to the tunnel structure) [6].

11.2 Simplified Model for Simulating Seaquakes

During an oceanic earthquake, the fault rupture generates both shear wave (S-wave) and compressional wave (P-wave). However, as mentioned earlier, the shear wave cannot travel through fluid. Therefore, only compressional wave (P-wave) can travel from seabed through waters. Therefore, by assuming that the seaquake waves can be regarded as P-wave propagating in water due to the vertical vibrations, the boundary value problem around the floating structure can be represented using the form of Helmholtz equation as a governing equation in flow field. The compressive wave velocity potential Φ exists and the boundary value problem around a floating body can be solved by solving the wave equation, i.e., the governing equation of wave velocity potential in water can be expressed as a two-dimensional Helmholtz equation in the Cartesian coordinate system:

$$\frac{\partial^2 \Phi}{\partial x^2} + \frac{\partial^2 \Phi}{\partial z^2} + \frac{\omega \Phi}{c^2} = 0 \quad (11.1)$$

where x is the coordinate axis in the horizontal direction; z is the coordinate axis in the vertical direction; ω is the angular frequency; c is the velocity of sound in water, typically around 1500 m/s;

The boundary conditions at the sea surface and the seabed are given by:

$$\frac{\partial \Phi}{\partial z} - \frac{\omega^2}{g} \Phi = 0 \quad \text{at sea free surface} \quad (11.2)$$

$$\frac{\partial \Phi}{\partial z} = 0 \quad \text{at seabed} \quad (11.3)$$

In addition, the continuity condition of the velocity of the seismic motion at seabed and the floating body's surface can be expressed as:

$$\frac{\partial \Phi}{\partial n} = 0 \quad \text{at wetted floating body's surface means the velocity amplitude is zero}$$
(11.4)

$$\frac{\partial \Phi}{\partial n} = v \quad \text{at seabed and seismic wave source}$$
(11.5)

where n is the normal unit vector perpendicular to the sea bottom or surface of the floating body; v is the velocity amplitude of the motion of seabed.

The velocity potential Φ also needs to satisfy the Sommerfeld radiation [7] condition in order to solve uniquely the Helmholtz equation.

The fluid pressure p can also be expressed using the velocity potential Φ :

$$p = -\rho \frac{\partial \Phi}{\partial n} - \rho g z \quad \text{at seabed}$$
(11.6)

where ρ is the density of the water; t is the time; and g is the acceleration of gravity.

By combining all equations above, the fluid pressure load p can be obtained numerically.

The motion of the fluid body can then be calculated by solving the equation of dynamic equilibrium of the floating body by accounting for the interaction between the floating body and the fluid.

Similar to the resonance at site period (Sect. 4.2) in geotechnical earthquake engineering analysis, but because of the water compression, resonance of seaquake can occur, leading to the significant magnification of pressure load when the seismic motion period at seabed coincides with that of the natural period of the compressional wave propagation T_p :

$$T_p = 4H/v_p$$
(11.7)

where v_p is the velocity of sound in water, which is around 1500 m/s; H is the water depth.

Since the peak period of the seismic motions at seabed is normally below 4 s, the water depth that may lead to potential seaquake resonance is below 1500 m.

11.3 Case Study by Kiyokawa

By assuming small amplitude of vessel motions as $\{D\}e^{-i\omega t}$, in which $\{D\}$ is the complex displacement amplitude vector, and substituting the motion expression into a typical dynamic equations of equilibrium, one obtains:

$$\{[c] - i\omega[N] - \omega^2([m] + [M])\}[D] = \{F\} \quad (11.8)$$

where $[c]$ is the restoring force coefficient matrix; $[N]$ is the damping coefficient matrix; $[m]$ is the mass matrix of the floating structure under study; $[M]$ is the added mass matrix for the floating structure; $[N]$ and $[M]$ can be evaluated by various methods such as the convenient strip theory [8] for sea keeping analysis; $\{F\}$ is the hydrodynamic force vector.

By assuming that the heave (vertical) component of the hydrodynamic force vector can be calculated by accounting for the fluid compressibility that may cause a high frequency response motion using Green function, Kiyokawa [9] presented the exact solution of potential function that is derived from the case of a flat wave source on sea bottom. For a rectangular floating structure with width B and draft d , the heave force on the structure for unit amplitude acceleration of the wave source can be calculated as:

$$F_z/\rho = \frac{2i(k_0^2 - v^2) \sin \lambda_0 a \cosh k_0(h-d)}{\lambda_0^2[h(k_0^2 - v^2) + v]} \sin \frac{\lambda_0 B}{2} e^{i\lambda_0 L} + \sum_{n=1}^S \frac{2i(k_n^2 + v^2) \sin \lambda_n a \cos k_n(h-d)}{\lambda_n^2[h(k_n^2 + v^2) - v]} \sin \frac{\lambda_n B}{2} e^{i\lambda_n L} \quad (11.9)$$

where i is the imaginary unit; ω is the angular frequency; $v = \frac{\omega^2}{g}$; $\lambda_n^2 = (\frac{\omega}{c})^2 \pm k_n^2$; c is the velocity of sound in water; h is the water depth; k_0 is the wave number [10]; L is the horizontal distance between the centers of the wave source and the floating structure, from design point of view, the distance may be taken as the maximum value; k_n ($n = 1, 2, \dots$) is the eigenvalues; the wave number and the eigenvalues are obtained as real and positive solutions of the equation:

$$k_0 \tanh k_0 h = -k_n \tan k_n h = v \quad (k_1 < k_2 < k_3 < \dots) \quad (11.10)$$

The frequency response function of motion is obtained using frequency domain analysis, and by using an inverse FFT technique, the time domain simulation can be carried out. The entire procedure is illustrated in Fig. 11.1.

Using the procedure above, Kiyokawa [9] studied the responses of two floating vessels of different sizes, the smaller one representing a middle class ship while the large one represented a large floating structure such as a marine city. Both structures are floated at a water depth of 1000 m, and the wave source of 1000 m width on the seabed as shown in Fig. 11.2.

By inputting a real ground motion recorded during the 1923 Kanto earthquake as the acceleration at wave source (with a peak acceleration of around 200 gal (cm/s^2)), Fig. 11.3 shows the heaving force for both vessels. The maximum values for the small and large floating vessels are 1.48 and 1.87 ton/ m^2 , respectively. The heave acceleration response histories of both the smaller and the larger floating structure are shown in Fig. 11.4. For the small vessel, a significant high frequency

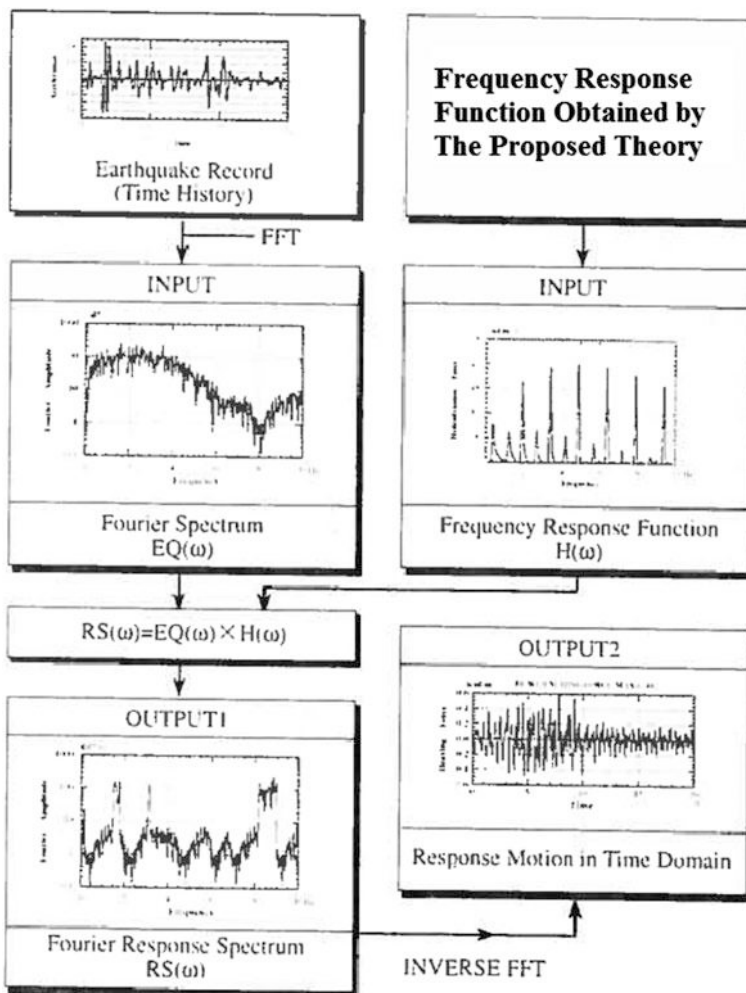


Fig. 11.1 Schematic illustration of a procedure for calculating the shock wave induced responses in time domain using a frequency domain solution [9]

component of response can be identified, which seems to agree well with the fact reported due to ships encountering seaquakes, in which the crew on board feel a very strong shock that is similar to the feeling of a vessel running ashore. Interestingly, the maximum response of the large vessel is only less than half of the small vessel with less high frequency components. Therefore, large floating structures are more reliable to resistance shock wave due to seaquakes than that of the small floating structures.

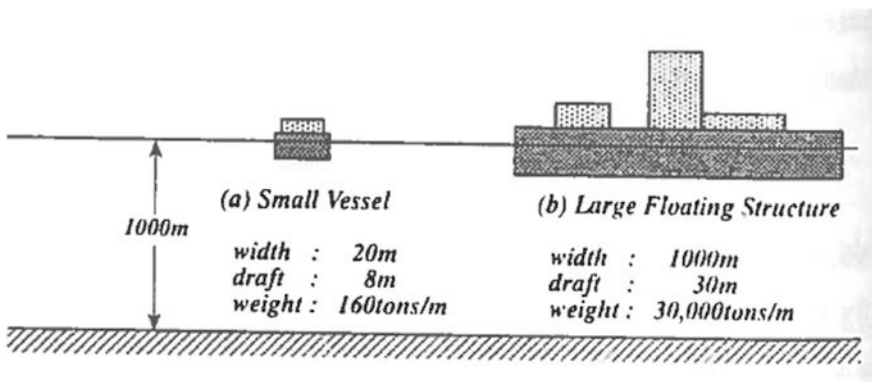


Fig. 11.2 Models for numerical calculation by Kiyokawa [9]

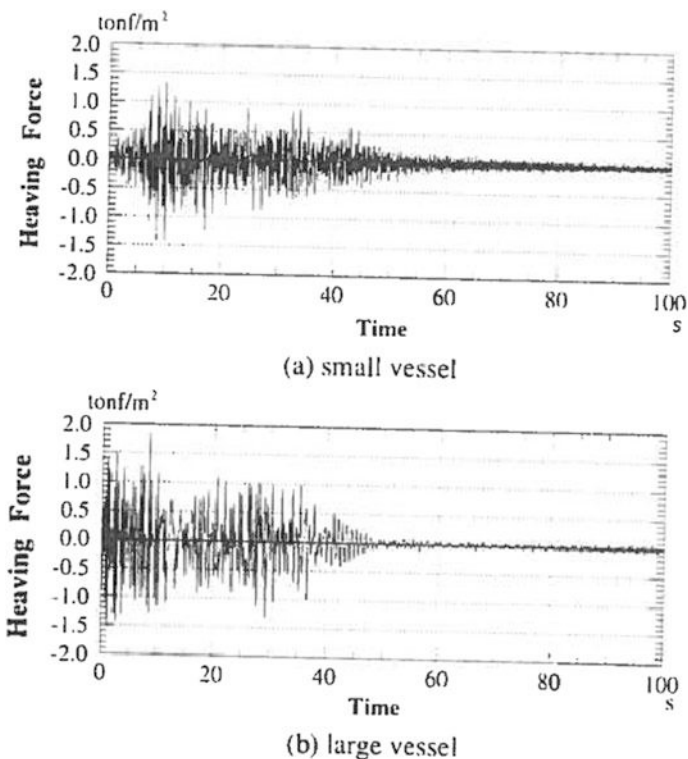


Fig. 11.3 Time history of hydrodynamic heaving force for **a** smaller (*upper*) and **b** larger (*lower*) vessel [9]

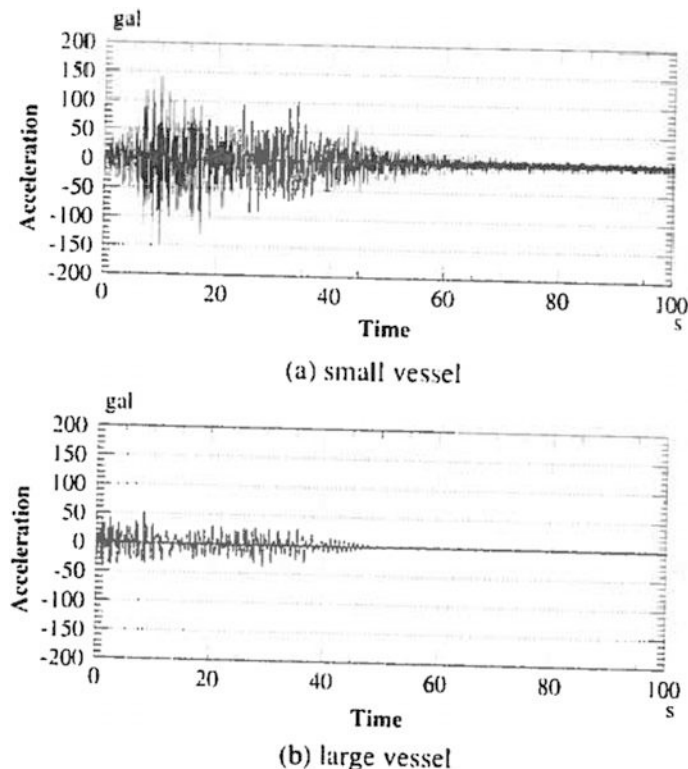


Fig. 11.4 Time history of heave response accelerations for **a** smaller (*upper*) and **b** larger (*lower*) vessel [9]

References

1. Okamoto K, Sakuta M (1993) Effects of seaquakes on floating structures. In: Narendra K, Saxena (eds) Recent advances in marine science and technology. Pacon International, Honolulu
2. Ambraseys N (1985) A damaging seaquake. Earthq Eng Struct Dynam 13:421–424
3. ISO19901-2 (2016) Petroleum and natural gas industries—specific requirements for offshore structures—Part 2: seismic design procedures and criteria, 2nd edn
4. Mochizuki K, Kihara H, Takagi K, Nairo S (1997) Effects of seaquake on offshore floating structure. In: Seventh international offshore and polar engineering conference, Honolulu
5. Yoneyama H, Nozu A (1996) Experimental study on seaquake response characteristics of floating structures. In: Proceedings of the 11th world conference on earthquake engineering, Paper no. 763, Acapulco, Mexico, 23–28 June 1996
6. Perotti F, Shi C, Domaneschi M, Martinelli L (2013) The non-linear dynamic response of submerged floating tunnels to earthquake and seaquake excitation, Strait Crossings, Bergen, Norway, 16th to 19th of June, 2013

7. Sommerfeld A (1949) Partial differential equations in physics. Academic Press, New York, NY
8. Lloyd ARJM (1998) Seakeeping: ship behaviour in rough weather. ARJM Lloyd, Gosport
9. Kiyokawa T (1995) Numerical prediction for response motion of floating structures subject to seaquakes. In: Fifth international offshore and polar engineering conference
10. Faltinsen OM (1990) Sea loads on ships and offshore structures. Cambridge University Press, Cambridge

Chapter 12

Introduction to Tsunamis

Among natural disasters, tsunamis may be the closest to being completely unsurvivable.

Kathryn Schulz, The Really Big One, 2015.

12.1 Cause of Tsunamis

Originally used to describe large amplitude resonance oscillation of waves in a harbor, tsunami is a Japanese word made from two word roots: “tsu” means harbor and “nami” means wave. The term sometimes refers to as tidal waves dominated by long period motions.

It is well recognized that a major earthquake below or near the seafloor, landslide, or volcanic activity not only causes ground shaking, but may also induce tsunami, posing a significant threat to coastal communities and structures. Tsunami is generated by the abrupt deformation of the seafloor and especially the vertical displacement of the overlying water, causing the instantaneous deformation of the water surface. The potential energy suddenly gained is converted into kinetic energy by the gravitational force, which serves as the restoring force of the system.

For earthquake induced tsunami, shallow subduction zone (Chap. 1) earthquakes are one of the most common sources of destructive tsunamis worldwide as shown in Fig. 12.1, in comparison to spreading ridges and transform faults. Therefore, earthquake related tsunamis occur particularly along the costal belts that rim the Pacific and south Asia, and rarely occurs in the North Atlantic and Mediterranean regions, as most of the subduction zones are located along the Pacific and south Asia, as shown in Fig. 12.2. Examples of relevant earthquakes are the 1960 Chile and 1964 Alaska earthquakes, which resulted in large vertical displacements of the seafloor, leading to significant tsunamis. Landslides can also generate significant tsunami. For example, the three most severe landslide generated tsunamis, which occurred in 1905 (Loen) 1936 (Loen) and 1934 (Tafjord), caused a fatality of 174 in total, and the waves reached about 10–15 m above normal sea level several

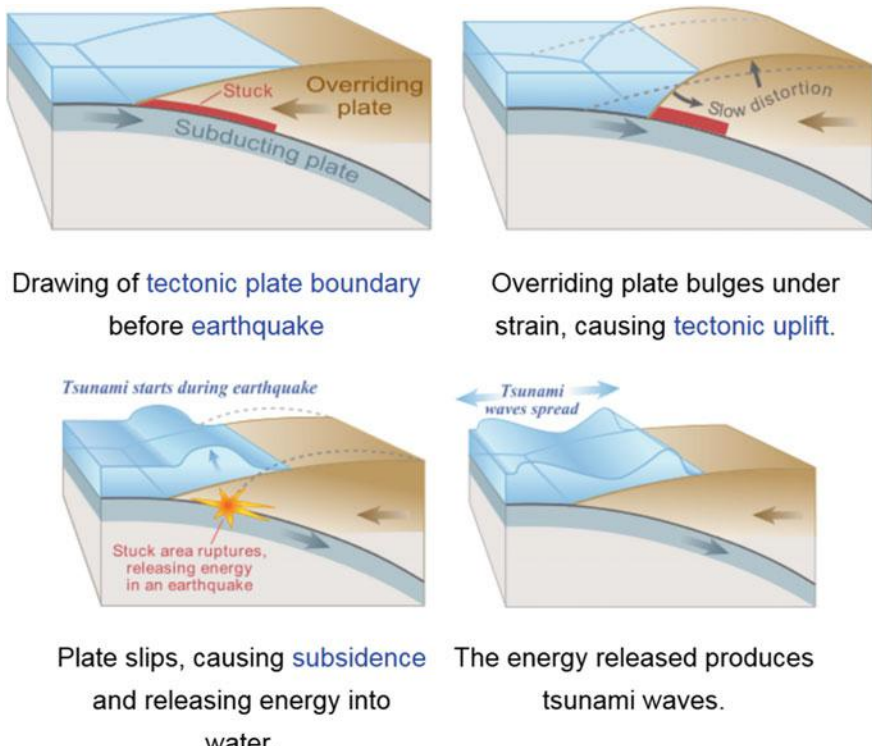
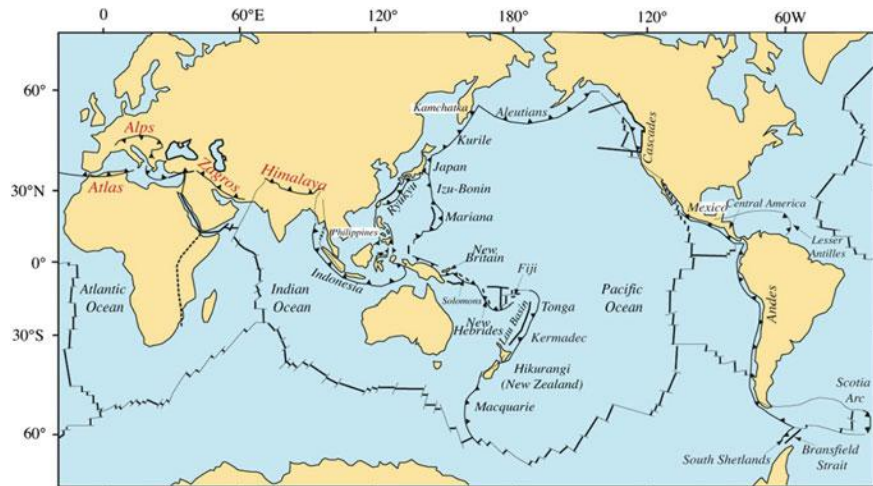


Fig. 12.1 Generation of tsunami due to shallow subduction zone earthquakes (courtesy of USGS)

kilometers away from the slide areas [1]. Figure 12.3 shows the locations of historical tsunamis.

The generated tsunami waves contain both long and short wave components. The leading wave of a tsunami has a wavelength proportional to the longitudinal dimension of its earthquake source region, which could be in the order of several hundred or a thousand kilometers for a major earthquake. Compared to wind induced waves, tsunami waves cherish characteristics of significant longer wave length and wave period, and velocities ten or a hundred times larger, so that even when traveling in deep ocean, they are considered shallow water waves. For tsunami waves in shallow water, the depth and the topology of the seabed strongly influence how the waves propagate as will be discussed in Sect. 12.4.2. The height of tsunami waves is generally not higher than a storm wave (15–30 m), but they are much more powerful in their damage to structures.

At the source, the seabed can move up to 5 m vertically within the duration of earthquake tremors. Since the long wave components propagate faster than the short ones, at deep ocean, a tsunami travels with rather high wave length and speed. This can also be explained with the group velocity (the propagating velocity of leading



Global convergent plate margins, ~55,000 km long, shown as barbed lines. These are connected to subduction ones at depth. Convergent margins include continental *collision zones* as well as normal subduction zones.

Fig. 12.2 Global distribution of subduction zone (courtesy of USGS)

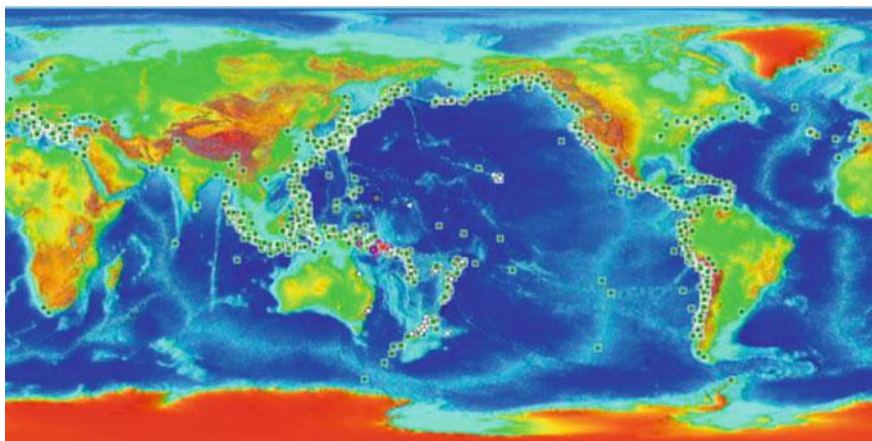


Fig. 12.3 Historical tsunami occurrence worldwide (courtesy of NOAA, NGDC database)

edge of the first full amplitude wave) c of wave propagating in deep water with a depth of h , which is the speed of wave energy propagation as expressed by:

$$c = \sqrt{gh} \quad (12.1)$$

From the equation above, it is noticed that, at deep ocean with a water depth of 3000–4000 m, which is a typical depth of the Pacific Ocean, the group velocity ranges from 713 to 618 km/h. This is the speed of a jet airplane. With this velocity range, it only takes around 15 h for the tsunami wave to propagate for 10,000 km.

At deep ocean, even though sailors may feel a trembling short period vibration (slight “seaquake”) due to the elastic vibration of the water caused by the short period component of the sea bottom ground motions [2], the tsunami is rather insignificant (approximately 0.1–2 m in height) and is almost unnoticeable. The corresponding orbital velocity and the associated momentum fluxes are also small. The wave period of a tsunami is typically within the range of 10 min to up to a few hours. This is also why it generally passes unnoticed at deep sea. During this process, because the rate at which a wave loses its energy is inversely related to its wave length, the tsunami can propagate more than several thousand kilometers without significantly losing energy [3].

When tsunami wave approaches shallow water coast, its speed reduces dramatically due to the reduced water depth and the friction between the seafloor and the front of the wave. In addition, its wave length also reduces significantly.

When propagated to coastal lines, tsunami waves get closer to each other. According to conservation of energy, a decrease in distance between individual waves leads to an increase of amplitude of waves as shown in Fig. 12.4, a phenomenon known as shoaling. Figure 12.5 shows a picture of shoaling of tsunami waves. When it reaches the shallow water offshore and approaches the beach, it slows down and at the beach it travels at around 10 m/s (36 km/h)—about the speed of a slow car. The top of the wave moves faster than the bottom, the wave then rises dramatically and can be as high as 20 m. Unlike wind generated large sea waves in the ocean, which in general have a period of between 8 and 20 s, tsunami

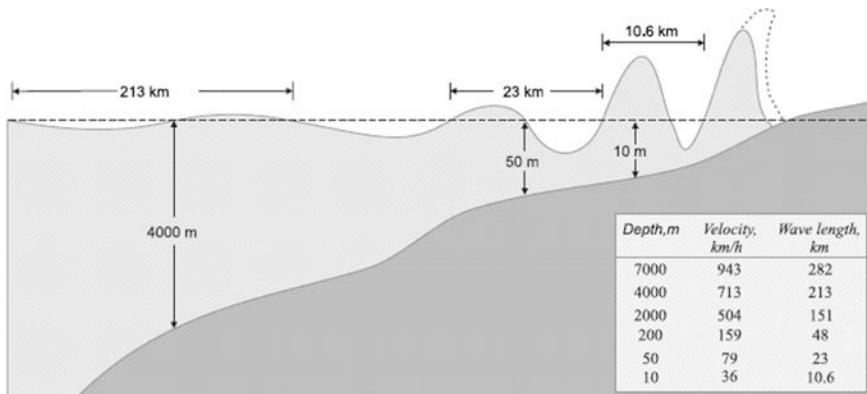


Fig. 12.4 Tsunami travels at different water depth with various wave length and velocity [5]



Fig. 12.5 Shoaling effects of tsunami at coast

waves can have a wave periods from a few minutes to a few hours [4]. This time-scale indicates the potential for wave reflection, amplification or resonance within coast areas [3].

12.2 History and Consequences of Tsunamis

Although tsunamis occur much less frequently than earthquakes, they still happen on a regular basis. Between 1900 and 2001, 796 tsunamis were recorded in the Pacific Ocean [6], with around 20 % of these events strong enough to generate damaging tsunami waves.

Tsunamis can cause extensive damage on coastal and offshore structures. Tsunami waves can move entire structures off their foundations and carry them inland; they can damage buildings through impact with vessels carried from offshore and other debris accumulated as the wave advances inland, undercut foundations and pilings with erosion caused by receding waves, overturn structures by suction of receding or thrust of advancing waves, and lead to impacts of large ships with docks during oil or cargo transfer operations, often causing fires [7].



Fig. 12.6 A ship is carried to shore by tsunami waves with a height of up to 15 m after the moment magnitude 9.0 Sendai earthquake, Japan, 11 March, 2011 (*photo source China News*)

Tsunami poses a great threat to human life and infrastructure. The 10 strongest tsunamis of the 1990s took more than 4000 lives [3]. On 26 December 2004, a great earthquake of magnitude 9.3 occurred 150 km off the west coast of the Indonesian island of Sumatra. The quake generated the most destructive tsunami ever in Southeast Asia, causing a loss of 225,000 lives and US\$13 billion, and affecting 11 countries bordering the Indian Ocean. In seismically active regions such as Sakhalin in Russia, Alaska in the USA, and the east coast of Japan, where increasing numbers of offshore infrastructures are being constructed, the potential threat from tsunami and earthquake is also high. For example, the powerful earthquake and tsunami in North Kurilsk of Sakhalin in 1952 damaged the region and caused a significant number of fatalities. More recently, a magnitude 9.0 earthquake hit the offshore area near Sendai, in the north-east of Japan, on 11 March, 2011, triggering a tsunami with a maximum height of more than 15 m, causing a loss of more than 20,000 lives and US\$200 billion. Figure 12.6 shows a ship pushed to shore by tsunami waves ore after the Sendai earthquake of 2011.

Even though many damaging tsunami events occurred in the Asia-Pacific region in recent years, their occurrence is rather infrequent in the European-Africa regions. The most noticeable tsunami in the European region occurred in the northern North Atlantic region around 8000 calendar years ago, caused by one of the world's

largest underwater landslides known as the Storegga slide. It caused large scale flooding along parts of the Norwegian coastline and the Shetland Isles, up to levels 20–35 m above sea level, while along the UK mainland coastline the highest flood levels reached up to around 6 m above sea level [8–10]. During historical times, several large tsunamis took place in Europe. In 1755 AD, immediately after the large Great Lisbon earthquake, a tsunami occurred on the seabed west of Portugal. Maximum tsunami flood levels along parts of the coastline of Portugal were in the order of 20 m above sea level. Another well-known tsunami is claimed by several authors to have taken place in the eastern Mediterranean ca. 3600 year BP (Before Present), caused by the eruption of the Santorini (Thera) volcano [8].

From a review of previous tsunami events [3], the structural damages due to tsunamis are (1) hydrostatic and hydrodynamic forces from water inundation (flooding); (2) impact forces from water-borne debris; (3) fire spread by floating debris and combustible liquids; (4) scour and foundation failure; and (5) wind forces induced by wave motion.

12.3 Characterizing Tsunami Size

Similar to those for earthquake magnitudes, two tsunami scales are used for comparison, namely the Imamura-Iida magnitude scale m and the Soloviev-Go intensity scale i .

The Imamura-Iida magnitude scale m [11, 12] is defined based on the maximum tsunami height h_{max} :

$$m = \log_2 h_{max} \quad (12.2)$$

On the other hand, the Soloviev-Go intensity scale i [13] is based on the mean tsunami height h_m :

$$i = \log_2(\sqrt{2}h_m) \quad (12.3)$$

Figure 12.7 shows tsunami magnitude (using only local tsunami measurements) versus moment magnitude (M_w) for circum-Pacific subduction zone earthquakes occurred from 1896 to 1996. Considerable variability in tsunami run-up as a function of seismic moment (for the most frequent tsunamigenic earthquakes with $7.0 < M_w < 8.5$) can be observed.

Since the tsunami amplitude is strongly influenced by the energy release of relevant earthquakes, the tsunami amplitude is roughly correlated to the earthquake magnitude. Abe [14, 15] established the far-field (tsunamis far from the source) scaling of tsunami amplitude with seismic moment magnitude M_w for subduction zone earthquake:

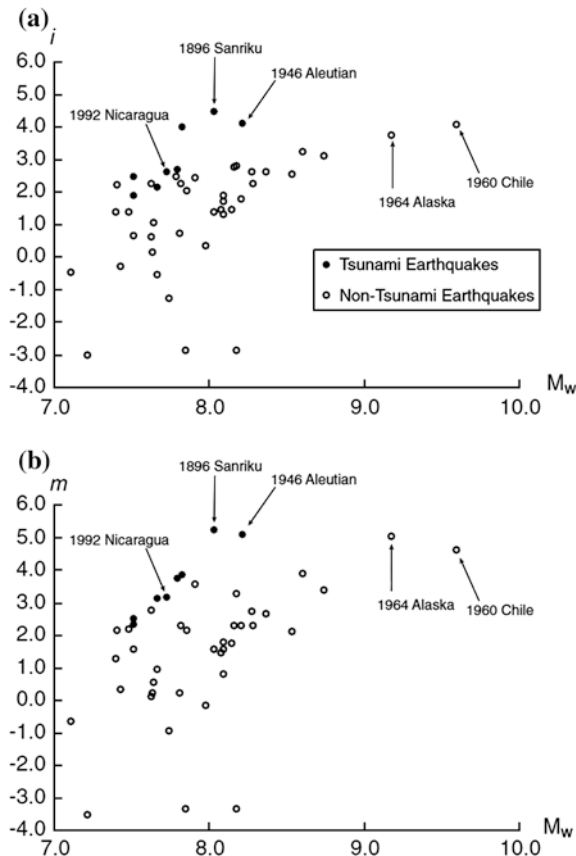


Fig. 12.7 Tsunami magnitude (using only local tsunami measurements) versus moment magnitude (M_w) for circum-Pacific subduction zone earthquakes, with the tsunami magnitude measured with **a** the Soloviev-Go intensity scale and **b** the Imamura-Iida magnitude scale. Solid and open circles represent tsunami and non-tsunami earthquakes, respectively [17]

$$\log_{10} H = M_w - \log_{10} R - 5.55 \quad (12.4)$$

where H is maximum crest-to-trough tsunami amplitude (in meters) and R is the distance along the shortest oceanic path from earthquake epicenter (in kilometers).

For local tsunamis (tsunamis near the source), however, Abe [16] indicated that the far-field relation above overestimates local tsunami heights and proposed the following local limit of tsunami height (H_r):

$$\log_{10} H_r = 0.5M_w - 3.3 + C \quad (12.5)$$

where $C = 0.0$ for fore arc (subduction zone) events and $C = 0.2$ for back-arc events, with the fore arc and back-arc basic illustrated in Fig. 12.8.

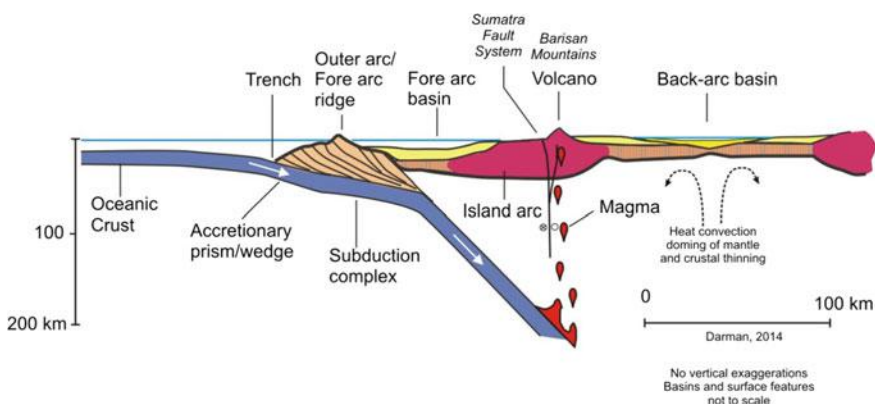


Fig. 12.8 Illustration of fore arc and back-arc basin (under license CC BY-SA 4.0 by Herman Darman)

12.4 Calculation of Tsunami Waves

There are two ways to determine the tsunami wave characteristics at a defined location, namely interpolation or simulation.

Interpolation is based on the interpolation of tsunami survey of historical data at a certain area or region, from which the statistics of parameters related to tsunami are characterized and used to predict a future tsunami. This is often referred to as the geo-statistical approach. This method is relative convenient, and it is especially useful for situations where only limited information such as height of inundation area along coast needs to be determined.

Using simulation to estimate the water level at the epicenter involves creating computer models with a modeling of source containing physical characteristics of the faults and tsunami, and to calculate the height and direction of tsunami waves generated by potential undersea earthquakes of different sizes in high risk areas.

Tsunami simulation considers three stages of tsunami: generation, propagation in open ocean and run-up, and perhaps breaking during the propagation on sloped beach, which are expressed by complicated physical process and mathematical equations. Here the run-up describes a process of a large amount of water being pushed by a tsunami onto the shore above the regular sea level, which is the maximum vertical height onshore above sea level reached by a tsunami. Run-up produces more damaging force than the huge tsunami wave does as it surges inland and powerfully destroys infrastructures built in its path.

The simulation is basically based on the fact that, despite differences in the underlying physics of wave propagation in the ocean and on solid earth, the tsunami wave field emanating from an earthquake source can be thought of as an extension to the seismic wave field [17], and tsunami wave forms can be simulated through the superposition of normal modes in the same way Rayleigh waves are reconstructed [18, 19].

The current book touches on the topic of tsunami generation (Sect. 12.4.1), propagation in open ocean (Sect. 12.4.2) and run-up (Sect. 12.4.3) at coastal areas and beaches. For more details about the calculation of tsunami waves, readers may refer to [20, 21].

12.4.1 Tsunami Generation at Source

For simulating the generation of tsunami, a source model of estimated seabed deformation for each earthquake scenario is required. This source model defines the physical characteristics of the tsunami that serve as input into the tsunami propagation and inundation model, allowing the calculation of the maximum tsunami waves to reach the target location. Earthquake source parameters, includes dip angles, rake angles, strike angles, and focal depth, are essential to estimate the initial displacement field of tsunami numerical simulation by the theory of fault dislocation.

The role of fault mechanism on tsunami generation is not as obvious as the influence of the seismic moment. However, it is obvious that tsunamis are gravity waves excited by a sudden increase in potential energy that arises from vertical displacement of the seabed during an earthquake. Therefore, earthquakes that induce large vertical displacement of seafloor would be more effective than faults that make large horizontal displacement, even though under certain circumstance, horizontal component of the seafloor displacement must also be accounted for in regions of steep slope [22] or under which the horizontal seafloor motion is much larger than the vertical motion, such as strike-slip faulting or dip-slip faulting (Chap. 1) on very shallowly dipping fault. An important assumption in this process is that sea surface normally mimics the deformation of seafloor since an earthquake usually occurs in seconds and water column over the seafloor cannot escape within this short duration. Regarding the focal depth, it is also logical to believe that shallow earthquakes produce more significant tsunami than deep earthquakes do.

On the basis of the discussion above, to calculate the tsunami height at sea surface above the epicenter, let us consider a coordinate system (x , y , z) with positive x toward north, positive y toward east and positive z downward. By assuming that the seafloor has an uplift $u_z^{bot}(r_0)$ at a point r_0 and time $\tau(r_0)$, the surface tsunami wave form $u_z^{surf}(r, t)$ due to the seafloor uplift $u_z^{bot}(r_0)$, in open sea with a uniform depth of h , at an observation point r (x , y) and time t , can be expressed as:

$$u_z^{surf}(r, t) = \text{Re} \int_k dk \frac{e^{i[k \cdot r - \omega(k) \cdot t]}}{4\pi^2 \cosh(kh)} F(k) \quad (12.6)$$

where k is the wave number, which is equal to 2π divided by the wave length λ : $k = 2\pi/\lambda$.

The exponential term in the equation above includes all information regarding the travel time, geometrical spreading, and the frequency dispersion.

$F(k)$ is termed as the wave number spectrum of the seafloor uplift, which is related to the amplitude, spatial and temporal distribution of the uplift:

$$F(k) = \int_{r_0} dr_0 u_z^{bot}(r_0) e^{-i[k \cdot r_0 - \omega(k) \cdot \tau(r_0)]} \quad (12.7)$$

where $\omega(k)$ is the angular frequency of wave depending on the wave number.

The integrals of the two equations above cover all wave number k space and locations r_0 where the seafloor disturbance $u_z^{bot}(r_0) \neq 0$.

Moreover, the $1/\cosh(kh)$ term is a low-pass filter of the source spectrum $F(k)$, i.e., for long wave (long wave length or small wave number), $1/\cosh(kh)$ is smaller but close to 1, indicating that the amplitude of tsunami wave above epicenter is slightly lower than the seafloor uplift $u_z^{bot}(r_0)$; while for short wave, $1/\cosh(kh)$ is close to zero. This essentially means that only wave lengths λ of the uplift source that exceed three times the ocean depth ($kh = 2\pi h/\lambda \leq 2$) dominate the tsunami's wave at the epicenter.

For a simplified estimation, an interpolation method can be adopted. The height of a tsunami at the sea surface above the fault depends on how much up-and-down motion was caused by the earthquake. This height, typically referred to as water level increase (slip) Du , has an obvious relation with fault length L as proposed by Ward [23]:

$$Du = 2 \times 10^{-5} L \quad (12.8)$$

There are several interpolation models for the evaluation of fault length L , see Sect. 3.4.1.4 for details. For evaluation of seafloor slip, Ward [23] recommended:

$$\log_{10}^L = 0.5M_w - 1.8 \quad (12.9)$$

where M_w is the moment magnitude of the associated earthquake.

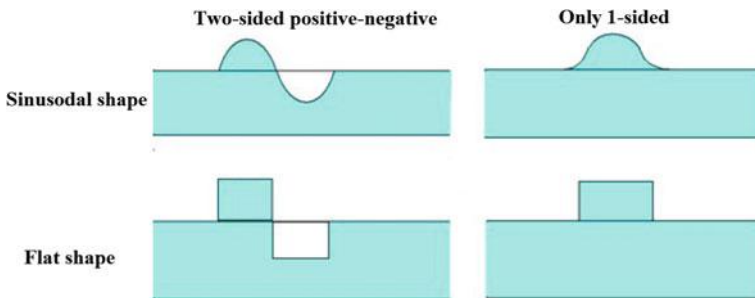
Therefore, above the moment magnitude of around 7, the fault length based on Ward method is lower than the one proposed by Ambrasseys and Jackson [24] as described in Sect. 3.4.1.4, and is higher when the moment magnitude is below 7.

Table 12.1 illustrates the relationship between earthquake moment magnitude and moment with values of fault area, length and mean slip for typical earthquakes that can potentially generate tsunami. From this table, it is seen that a moment magnitude of 8.0 may generate a seafloor slip of more than 3 m.

When the water level is increased at the epicenter, different patterns of water elevation profile can occur. One scenario is that a part of water rises and the other

Table 12.1 Parameters of submarine earthquakes proposed by Ward [23]

Moment magnitude M_w	Moment M_0 (Nm)	Fault Length L (km)	Fault width W (km)	Fault area A (km^2)	Seafloor slip Du (m)
6.5	6.3×10^{18}	28	8	224	0.56
7.0	3.5×10^{19}	50	14	708	1.00
7.5	2.0×10^{20}	89	25	2239	1.78
8.0	1.1×10^{21}	158	45	7079	3.17
8.5	6.3×10^{21}	282	79	22,387	5.66
9.0	3.5×10^{22}	501	141	70,794	10.02
9.5	2.0×10^{23}	891	251	223,872	17.8

**Fig. 12.9** Water rise profiles at epicenter [25]

part decreases. The water increases in all directions of the same quantity (full rise) etc. Figure 12.9 illustrates different water rise profiles.

Note that the far-field tsunami amplitudes are fairly well predicted by the seismic moment of subduction zone earthquake. There is a significant variation in the scaling of local tsunami amplitude with respect to seismic moment. From a global catalog of tsunami run-up observations this variability is greatest for the most frequently occurring subduction zone earthquakes in the magnitude range of $7.0 < M_w < 8.5$. This is primarily because the tsunami source parameters are independent of seismic moment: variations in the water depth in the source region, the combination of higher slip and lower shear modulus at shallow depth, and rupture complexity in the form of heterogeneous slip distribution patterns. Although there are some available models and commercial software for tsunami simulation, such as COMCOT, TUNAMI, CLAWPACK, JRC, etc., complex requirements of many parameters, detailed initial condition and boundary condition should still be treated carefully [26].

12.4.2 Tsunami Propagation in Ocean

After initial seafloor displacement fields are determined as presented in Sect. 12.4.1, it is prescribed as one of the initial conditions for either interpolating or simulating the propagation of each tsunami source.

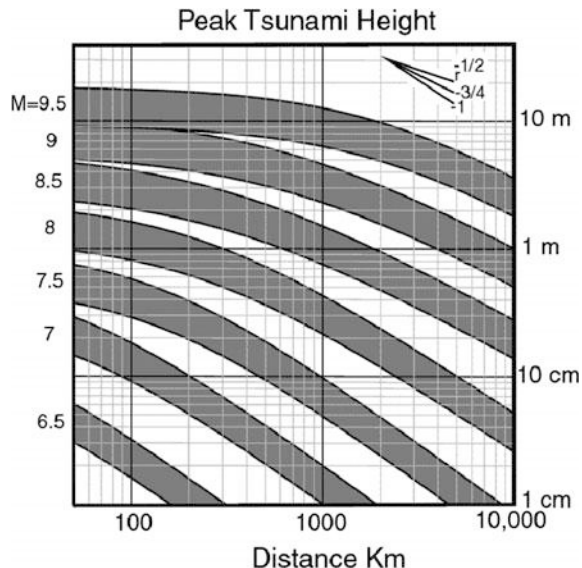
In oceans with approximately uniform depth, tsunamis propagate out from their source in circular rings (with ray paths similar to bicycle wheel spokes) with a constant velocity and amplitude. If a tsunami with an initial water height H_0 propagates from a point source with a constant water depth, the tsunamic wave height H at a distance r from the epicenter is proportional to the inverse of the distance and proportional to the initial water height:

$$H \propto H_0 \cdot r^{-1} \quad (12.10)$$

As a widely used interpolation method, Ward [23] proposed that the maximum open ocean tsunami height is proportional to the distance r with an exponents ranging from -1 to $-1/2$ as shown in Fig. 12.10.

However, in reality, the topology of the ocean bottom varies, the depth of ocean varies from place to place, there are likely to be obstacles such as an isle in the path of the tsunami propagation, and the ray paths then refract and become bent, causing both the velocity and amplitude to vary, even though the wave frequency/period is kept constant. In such a complex situation, to be able to estimate the tsunami wave propagation, a simulation approach has to be adopted. For a distant tsunami, such as

Fig. 12.10 Computed maximum open ocean tsunami height during propagation determined by the earthquake moment magnitude and traveling distance [23]



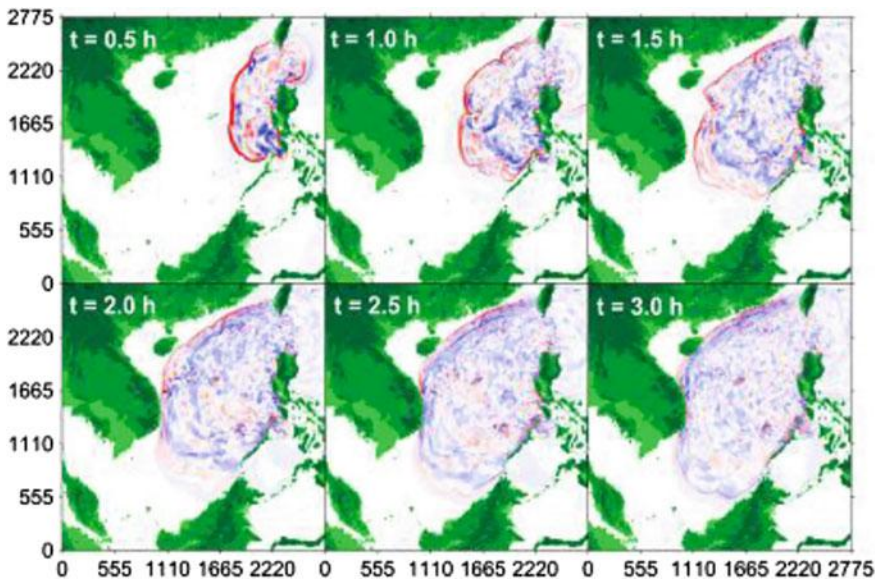


Fig. 12.11 Tsunami propagation from the Manila Trench [27]

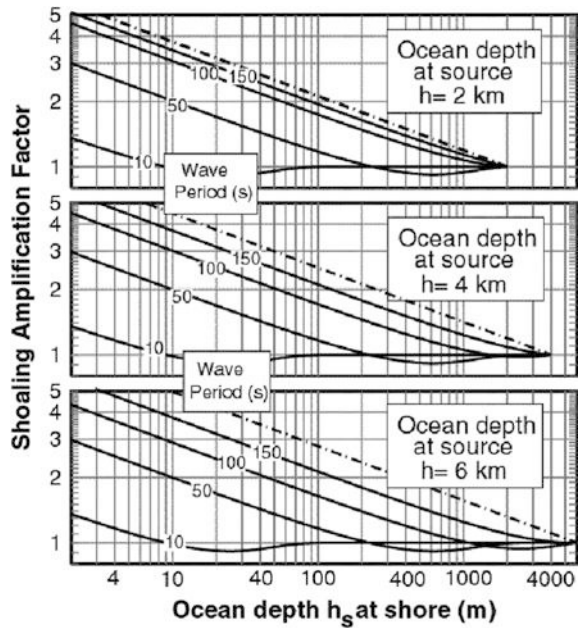
the ones that travel across the Pacific Ocean, both the frequency dispersion and Coriolis force could play important roles. On the other hand, the wave slope of a typical tsunami is rather small. Therefore, the non-linear convective inertia force and bottom friction can normally be neglected, while frequency dispersion effects are dependent on the wave length and may be included in the governing equations of tsunami propagation. The tsunami propagation can be simulated by various models, such as Navier–Stoke equation (or Euler equations for potential flow), the Boussinesq-type equation for weakly dispersive waves, and shallow water wave equations for non-dispersive equation, with both the computation efforts and short wave accuracy from high to low.

Figure 12.11 shows the tsunami propagation originally initiated from the Manila Trench.

12.4.3 Tsunami Run-up (Shoaling) at Coastal Areas and Sloped Beach

As the tsunami propagates over a continental shelf and approaches a coastal area, i.e., in the run-up stage, due to the dramatic decrease of the water depth toward shore, the wave height dramatically increases (shoaling amplification), while the velocity of the wave propagation decreases; this stage is also called shoaling.

Fig. 12.12 Shoaling amplification factors for various combinations of wave period, source depth and shore depth [23]



Comprehension of run-up on beaches is essential for estimating beach erosion and costal impact of both tsunamis and storm surges. It should be noted that a typical wind driven ocean wave (with a period of around 6–16 s) amplifies much less than a tsunami wave (with a much longer period of 100–2000 s) does. The non-linear convective inertia force becomes increasingly important, while the Coriolis force and the frequency dispersion are insignificant. In very shallow water, the bottom frictional effects also become significant. Figure 12.12 shows the shoaling amplification factors at various combinations of wave period, source depth and shore depth. The shoaling amplification factor is based on the linear wave theory:

$$S(\omega, r) = \sqrt{\frac{u_z^{\text{surf}}(\omega, h(r_c))}{u_z^{\text{surf}}(\omega, h(r_s))}} \quad (12.11)$$

where $u_z^{\text{surf}}(\omega, h(r_c))$ and $u_z^{\text{surf}}(\omega, h(r_s))$ are the vertical wave motion of tsunami at the sea surface of coastal (c) areas and source (s), respectively; $h(r_c)$ and $h(r_s)$ are the water depth at coastal area and source, respectively.

For calculating responses of structures in offshore areas, the tsunami wave run-up often does not exhibit a clear wave trough that dips below the sea surface. This allows the use of the solitary wave theory to simulate the wave that is further used to calculate the forces applied on the structures. The solitary wave theory is a special case of conical wave theory in which the wave crest lies completely above the still water, and the water particles move only in the direction of wave

propagation, and there is no return flow, the wave period and length are essentially infinite. For more details, readers may read Sorensen [28].

When tsunami propagates over a sloped beach, for practical reasons, it is important to measure the wave run-up. With slope angle of the beach denoted as θ , the solitary wave amplitude H and a constant depth D just before the tsunami wave begins to propagate over the sloped beach, the maximum run-up height R at the sloped beach can be approximated by various formulas.

For nonbreaking solitary waves, the relative maximum run-up height R is proposed by Synolakis [29]:

$$R = 2.83D\cot(\theta)^{0.5}(H/D)^{1.25} \quad \text{for nonbreaking waves} \quad (12.12)$$

Increasing the wave height changes the flow regime from nonbreaking to breaking waves. Based on the analytical solutions for the non-linear wave, Synolakis [30] suggested that solitary wave first breaks during the run-up will occur when:

$$H/D = 0.479\cot(\theta)^{-10/9} \quad (12.13)$$

And for breaking waves, the relative maximum run-up height R is proposed by Synolakis [29]:

$$R = 1.109D(H/D)^{0.583} \quad \text{for breaking waves} \quad (12.14)$$

where $\cot(\theta) = 1/\tan(\theta)$ is the cotangent of θ .

However, by employing smoothed particle hydrodynamics to simulate tsunami run-up, Shadloo and his coworkers [31] proposed that relative maximum run-up height R for breaking waves (i.e., $H/D > 0.6$) is:

$$R = 3.149D(H/D)^{0.51} \quad (12.15)$$

12.4.4 Shallow Water Wave Theory

As mentioned above, compared to the wind induced waves, tsunami waves have much longer wave length and wave period, and significantly higher velocities (up to 10 or 100 times larger). Even when traveling in deep ocean, they are considered as shallow water waves.

Therefore, we briefly present the shallow water equations including the bottom frictional terms, which are widely accepted for use to calculate the tsunami wave propagation and inundation, and are typically solved by finite difference method. Earthquake induced tsunamis are mainly generated by the movement of sea bottom, in which the vertical acceleration of water particles is negligible compared to the

gravitational acceleration except for an oceanic propagation of tsunami. Therefore, the vertical motion of water particles can also be regarded as insignificant on the pressure distribution.

Based on the assumption above, together with the dynamic and kinetic condition at the water surface and sea bottom, the equation of mass conservation and momentum in the three dimensions, defined by two perpendicular axes in a horizontal plane x and y (related to M and N), and the vertical axis z (related to η), can be expressed as:

$$\frac{\partial \eta}{\partial t} + \frac{\partial M}{\partial x} + \frac{\partial N}{\partial y} = 0 \quad (12.16)$$

$$\frac{\partial M}{\partial t} + \frac{\partial}{\partial x} \left(\frac{M^2}{D} \right) + \frac{\partial}{\partial y} \left(\frac{MN}{D} \right) + gD \frac{\partial \eta}{\partial x} + \frac{\tau_x}{\rho} = A \left(\frac{\partial^2 M}{\partial x^2} + \frac{\partial^2 M}{\partial y^2} \right) \quad (12.17)$$

$$\frac{\partial N}{\partial t} + \frac{\partial}{\partial x} \left(\frac{MN}{D} \right) + \frac{\partial}{\partial y} \left(\frac{N^2}{D} \right) + gD \frac{\partial \eta}{\partial y} + \frac{\tau_y}{\rho} = A \left(\frac{\partial^2 N}{\partial x^2} + \frac{\partial^2 N}{\partial y^2} \right) \quad (12.18)$$

where η is the vertical displacement of water surface; $D = \eta + h$ is the total water depth; g is the acceleration of gravity; $M = u(\eta + h)$ and $N = v(\eta + h)$ are the discharges along x - and y -direction, which are perpendicular to each other in the horizontal plane; u and v are the averaged particle velocity along the x - and y -direction; τ_x and τ_y are the bottom friction along x - and y -direction, which can be expressed as:

$$\tau_x = \frac{gn^2}{D^{\frac{10}{3}}} M \sqrt{M^2 + N^2} \quad (12.19)$$

$$\tau_y = \frac{gn^2}{D^{\frac{10}{3}}} N \sqrt{M^2 + N^2} \quad (12.20)$$

where n is called Manning's roughness, defined as:

$$n = \sqrt{\frac{\mu D^{1/3}}{2g}} \quad (12.21)$$

where μ is the friction coefficient of the sea bottom.

From the equation above, it is noticed that the friction coefficient increases significantly with the decrease of the total depth. In practice, the Manning's roughness n rather than the friction coefficient μ is used and can be conveniently checked from tables of various handbooks with an example shown in Table 12.2.

Table 12.2 Typical values of Manning's roughness n

Channel material	n
Neat cement, smooth metal	0.010
Rubble masonry	0.017
Smooth earth	0.018
Natural channels in good condition	0.025
Natural channels with stones and weeds	0.035
Very poor natural channels	0.060

12.5 Tsunami Induced Load on Structures Located in Shallow Water and Coastal Areas

Due to the short time duration and significant higher flow velocity of tsunami events, and possibilities of upward deck load due to tsunami wave impacting in deck and special scour mechanism [3], the tsunami force applied on structures in shallow water and coastal areas can be enormous. Note that there are well-established codes worldwide for calculating the applied loading on structures due to river floods and storm waves, many codes and guidelines for structural design against tsunami loading are based on extrapolations from flood event design procedures. On the other hand, there is a significant difference between tsunami and non-tsunami events in terms of water velocity as shown in Fig. 12.13, i.e., they underestimate the tsunami forces. Therefore, an experimental validation of the velocity, flow depth and loading expressions is needed. Moreover, applied tsunami

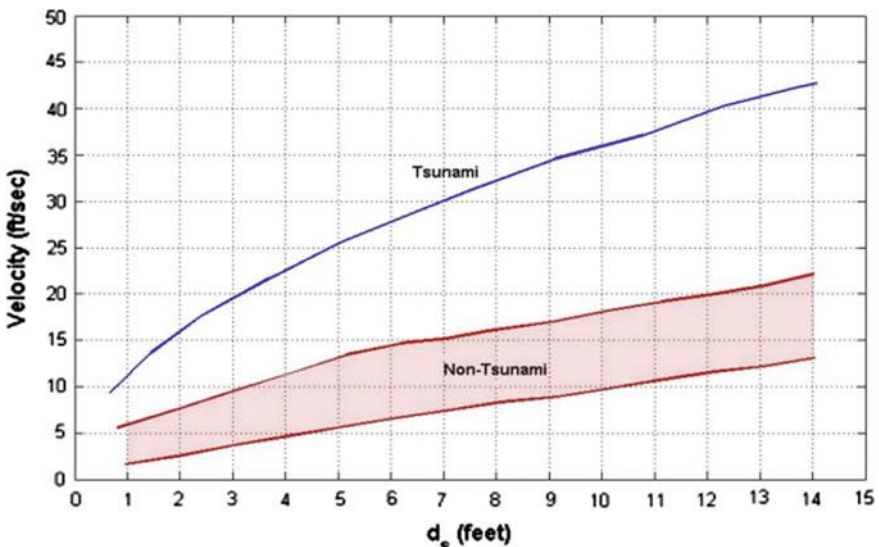


Fig. 12.13 Tsunami design versus stillwater depth design [33, 34]

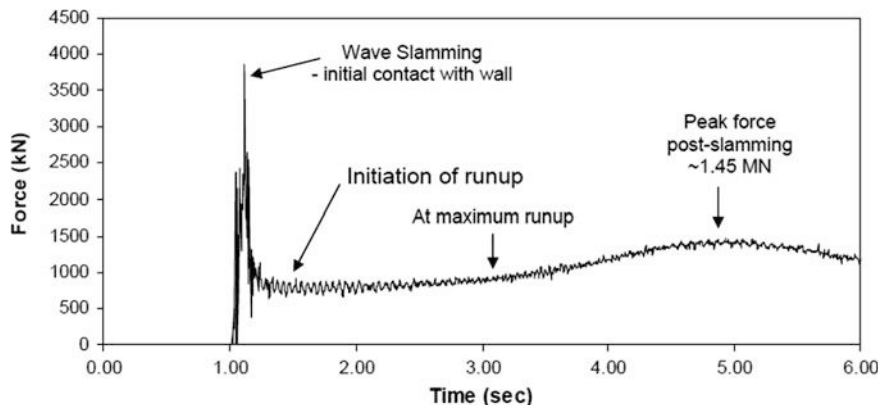


Fig. 12.14 Time history of tsunami force on a rigid wall calculated from CFD simulation [32]

forces often exceed the design forces based on wind and seismic design conditions. The facts above produce a situation in which very little guidance is available for estimating tsunami induced forces, while they are sometimes the dominating actions in cases in which they are relevant for design.

When tsunami waves impact on offshore and coastal structures, the turbulent water flows around the structures generate hydrodynamic forces on them. Figure 12.14 illustrates a typical tsunami induced force history on walls, which is obtained from computational fluid dynamics (CFD) simulations by Haritos and Ngo [32]. It shows that a peak slamming impact occurs immediately after the tsunami wave comes into contact with the structure, which is followed by a sustained but lower pressure force.

It is obvious that not all the tsunami local peak forces occur simultaneously. Nistor et al. [35] summarized the two tsunami wave load scenarios:

1. Initial impact, which includes surge and debris impact forces as the main lateral load components.
2. Post impact, which considers debris impact, hydrodynamic and hydrostatic forces as the lateral loads, and buoyant force as the vertical load.

In addition, the rapidly rising water within flooded structures can also induce significant uplift forces on deck systems.

The Coastal Construction Manual released by FEMA [36] states that “Coastal construction in tsunami hazard zones must consider the effects of tsunami run-up, flooding, erosion, and debris loads. Designers should also be aware that the ‘run-down’ or return of water to the sea can also damage the landward sides of structures that withstood the initial run-up.” The manual also states that the effects of tsunami will be determined by the magnitude of the earthquake, the location of the triggering event, the configuration of the continental shelf and shoreline, and the upland topography.

Tsunami loads can generally be categorized into static and dynamic loads. Static loading includes hydrostatic and buoyancy forces, while dynamic loading involves hydrodynamic (drag), surge, and debris impact loading. From another angle, the forces related to tsunami events include the horizontal hydrostatic and buoyant forces (vertical hydrostatic forces), the hydrodynamic force, surge forces (controlled by the flow velocity of the front of run-up tsunami wave), breaking wave force (tsunami waves generally break offshore and approach the shore as a broken bore), forces due to a water-borne missile/debris (drift object, small boats etc.) impact, uplift forces and additional gravity forces from retained water on decks.

FEMA also specifies the method to perform force combinations due to tsunami, which influence both global structural behavior and local individual member behavior. These combinations are explicitly formulated for flood scenarios and include wave breaking forces.

There is a wide range of literatures on how to calculate the hydrostatic and hydrodynamic force due to tsunamis. Almost all of these approaches model the force effects on continuous infinite vertical walls, but only a few look at the three-dimensional nature of structures such as cylinders. In parallel, CFD modeling to calculate the interaction between structures and tsunami, especially with respect to wave slamming effects, has attracted certain research efforts and application interests. In addition, there is also research work focusing on model testing. Haritos and Ngo [32] presented a review evaluating tsunami wave forces applied on structures. Commercial CFD software, such as FEMLAB, LS-DYNA and ANSYS CFX etc., is available for modeling of water propagation and fluid–structure interactions. They can be used for simulating the tsunami run-up and calculating the tsunami force applied on structures. Figure 12.15 shows an example of a typical grid layout for simulating tsunami [32]. In this modeling, both water bore and air are modeled and a decent mesh grid is adopted, thus enabling water to expand into the air (and soil).

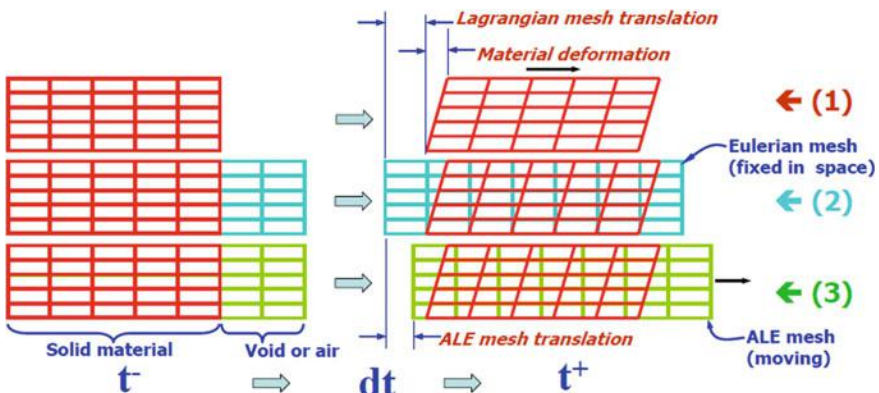


Fig. 12.15 Grid used for modeling of solid and air for tsunami simulation [32]

Wave tank experiments are a direct tool for estimating tsunami forces. Dimensional analysis by Thusyanthan and Madabhushi [37, 38] showed that the tsunami force mainly comprises three types of drag: the skin friction drag (associated to Reynolds number), wave drag (associated to Froude number) and pressure drag (independent of the two). As it is not possible to cope with the requirement due to a compatibility to both the Reynolds and Froude numbers, therefore, the scaling may be based on the Froude number alone, as the wave drag force is normally larger than the skin friction drag load.

12.6 Structural Resistance Due to Tsunami

The design forces due to tsunami often exceed the levels of design load associated with wind and seismic loads. Therefore, generally, for a normal residential structure, its design capacity is not sufficient to withstand extreme tsunami loads. However, for important structures, such as offshore platform and infrastructures for emergency purposes in coastal areas, they should be designed with sufficient capacity to resist tsunami loads.

After a review of historic tsunami data, FEMA [3] summarizes the following implications for tsunami resistant design.

On the load estimation aspects:

1. If the tsunami is generated due to an earthquake close to shore, it is likely that the structures first experience seismic ground motions immediately prior to the tsunami; sufficient reserve capacity after the earthquake should thus be provided to resist the tsunami wave loads.
2. In some cases, the wind load can also contribute to the damage of the structures.
3. Impact forces caused by water-borne debris and damming effects are significant and should be considered. Due to uncertainties involved in the prediction of those forces, progressive collapse concepts should be adopted in the design of tsunami resistant structures.
4. For floors subject to inundation, uplift force due to vertical hydrodynamic forces, buoyancy and trapped air should be considered.
5. Scour and soil liquefaction around the structural foundation should be taken into account.

On the structural design and performance aspects:

1. Structures should have an open system that allows water to flow through.
2. The structures should have sufficient ductility and redundancy, normally constructed with well-engineered reinforced concrete or steel frames.
3. The vertical evacuation structures must be outside the wave breaking zones.

12.7 Mitigation of Tsunami Hazard

Designs to mitigate tsunami hazard still need significant improvement as many infrastructures were damaged during large historic tsunami events. One well-known example is the accident at Fukushima Dai-Ichi nuclear power plant due to the tsunami induced by the moment magnitude 9.0 Sendai earthquake, Japan, 11 March 2011, caused core-melting of three units and a release of a large amount of radioactive material.

An efficient and economical means of tsunami hazard mitigation planning is to construct inundation maps along coastlines that are potentially vulnerable to tsunami flooding.

Efficient tsunami warning system and tsunami resistant structures and shelters are important measures to resist threats from tsunami. Many ancient and current reports state that the first obvious warning of a tsunami is when the sea recedes dramatically, leaving fish flapping on the former seabed. People go down to investigate and profit, and then the real tsunami comes. Moreover, it has been reported in Japan that a fierce wind often blew just before a tsunami arrived. All these phenomena are not fully understood so far. However, because the seismic waves containing information about earthquake fault travel 20 or 30 times faster than the tsunami waves, with the aid of computer models that are widely available, this gives scientists enough time to analyze seismograms, to estimate earthquake source parameters, and to forecast the expected tsunami propagation and wave height.

There are two major tsunami warning centers: the Pacific Tsunami Warning Center (PTWC) at Ewa Beach near Honolulu, Hawaii, and West Coast/Alaska Tsunami Warning Center (WC/ATWC) at Palmer, Alaska. When an earthquake of greater than magnitude 7.0 occurs and it is located offshore or beneath seafloor at open ocean, tsunami warnings, watches and information bulletins will be issued by these two warning centers. Warnings of a damaging tsunami are issued for the location within a 3 h travel time from epicenter. All communities within 3–6 h travel time from the epicenter are put on tsunami watch, meaning that an earthquake that has a potential to induce a tsunami has occurred and local bodies should be on the alert for further information. Tsunami information bulletins are issued to locations farther than 6 h travel time from the epicenter. This also works as an alert for the local authorities. On the other hand, tsunami information bulletin is also issued when there is no tsunami threat posed by a particular significant earthquake [39]. As an example of the efficiency of a warning system, during the tsunami triggered by the magnitude 9.0 Sendai earthquake, the length of warning time residents at Sendai had before the tsunami hit was around 8–10 min. It is worth mentioning that a similar warning system did not exist in the Indian Ocean at the time when the 2004 Indian Ocean tsunami occurred, otherwise there might have been a dramatic reduction in the number of fatalities.

Furthermore, earthquakes may occur just near-shore, and then a local tsunami may follow within as little as 20 min. This time is likely to be insufficient for an

office warning system to work well. In such cases, the best warning for the occurrence of tsunami is the earthquake itself that people can feel at the coast.

Even though the early warning systems can be used for evacuating people and saving lives, better designs for offshore and coastal structures are required in the event of a tsunami and to reduce the social and economic losses. The main failure modes of relevant infrastructures due to tsunamis are sliding, overturning and scouring.

As mentioned before, generally tsunami poses no destructive threats to offshore structures in the open ocean, but it does pose significant threats to both fixed and floating offshore structures in shallow water. This conclusion has led to the development of floating nuclear power station/plant, which is essentially a floating structure used as small scale nuclear power plant. This concept found its first application in the World War II Liberty Ship, in which a small nuclear power station was built in the 1960s. This application received more attention after the 2011 Sendai earthquake and the subsequent tsunami in which the serious accident at Fukushima nuclear power plant occurred mainly due to the shutdown of cooling systems, causing the reactor cores to melt down. This is because coastal locations tend to be the areas of maximum tsunami damage, requiring a protective design and a minimized risk of catastrophic failure. A floating facility, near a coast but not in shallow water, can avoid the worst problems due to earthquakes and tsunamis. In waters of sufficient depth, tsunamis have minimal effect on floating structures. In the event of an accident, terrorist attack, or other calamity, it is essential to keep the core cooled, usually by covering it with water. An emergency measure can be



Fig. 12.16 An artist's rendition of the first Russian floating nuclear power station barge Akademik Lomonosov (courtesy of Ministry for Atomic Energy of the Russian Federation)

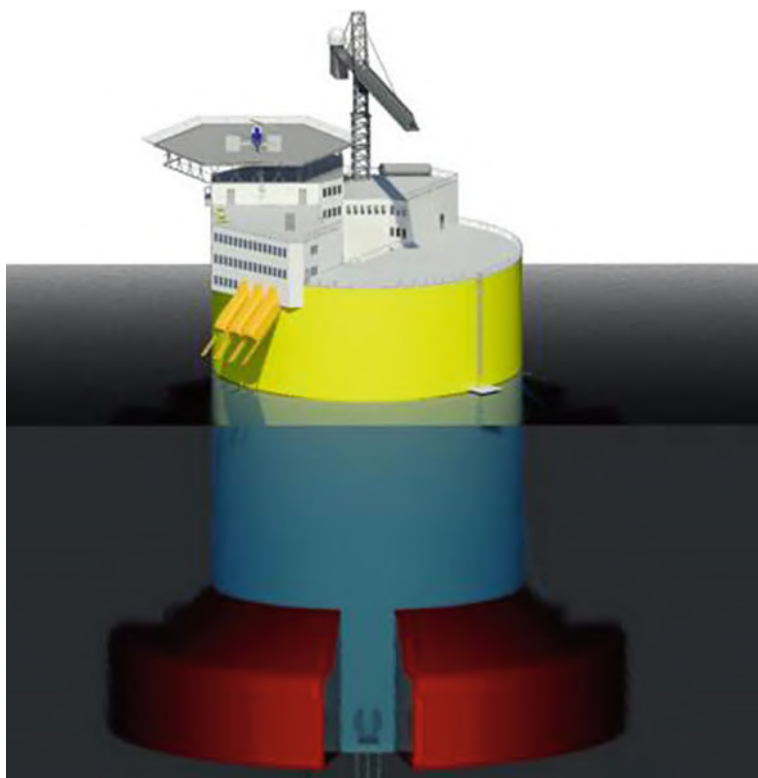


Fig. 12.17 A concept design of spar type floating nuclear plant, which has a skirt with a diameter of 75 m, a waterline diameter of 45 m, an operational draft of 48.5 m, and a total weight of about 38,200 tons when the skirt is empty. This can provide the most stable environment for a 200–300 MW reactor to operate in (courtesy of Jacopo Buongiorno, Massachusetts Institute of Technology)

performed to lower the core into the sea to arrange underwater compartments that allow the sea to act as an automatic coolant. In the worst case, accidental sinking or intentional scuttling will keep sea water on the core and prevent atmospheric release. Moreover, retired land-based nuclear power plants can be difficult and expensive to clean up, including safety hazards of contamination. A floating plant is towed to a remote location that handles multiple such tasks. Finally, the floating nuclear plant can also be used in remote locations such as Polar Regions or deep sea for the need of offshore energy development, or places to provide power in an emergency situation. The engineering realization of this concept is the Rosatom project initiated by the Ministry for Atomic Energy of the Russian Federation in the early 2000s. The project plans to build at least seven such vessels. The first vessel Akademik Lomonosov [40], a non-self-propelled vessel as shown Fig. 12.16, has a length of 144 m and a width of 30 m, and has two modified naval propulsion reactors together providing up to 70 MW of electricity or 300 MW of heat. The

vessel was constructed from April 2007 at a cost of US\$232 million. Akademik Lomonosov was planned to supply power at remote regions of Kamchatka in Russia's Far East from 2016, and to potentially support operations to the Arctic.

Another design concept of floating nuclear plants is a spar type nuclear power plant shown in Fig. 12.17, which could be built in a shipyard, and then be towed to destinations offshore, where it can be moored to the seafloor and connected to land by an underwater electric transmission line. A key design characteristic of the spar type floating nuclear plant is a large chamber flooded with seawater at the bottom of the spar. The flooded chamber freely exchanges water with the ocean through dedicated inlet and outlet ports [41].

References

1. NORSAR (1998) Seismic zonation for Norway, prepared for Norwegian Council for Building Standardization by NORSAR and Norwegian Geotechnical Institute
2. Murata S, Imamura F, Katoh K, Kawata Y, Takahashi S, Takayama T (2009) TSUNAMI: to survive from tsunami, advanced series on ocean engineering, vol 32. World Scientific, Hong Kong
3. FEMA 646 (2008) Guidelines for design of structures for vertical evacuation from tsunamis, Federal Emergency Management Agency (FEMA)
4. FEMA (2005) Coastal Construction Manual, FEMA 55 Report, 3rd ed. Federal Emergency Management Agency, Washington, DC
5. <http://www.prh.noaa.gov/itc>
6. “About Tsunamis” at www.prh.noaa.gov/ptwc/abouttsunamis.htm
7. Sumer BM, Ansal A, Cetin KO, Damgaard J, Gunbak AR, Ottesen Hansen N-E, Sawicki A, Synolakis CE, Yalciner AC, Yuksel Y, Zen K (2007) Earthquake-induced liquefaction around marine structures. *J Waterway Port Coastal Ocean Eng* 133(1):55–82
8. Dawson AG, Lockett P, Shi S (2004) Tsunami hazards in Europe. *Environ Int* 30(4):577–585
9. Dawson AG, Long D, Smith DE (1988) The Storegga slides: evidence from eastern Scotland for a possible tsunami. *Mar Geol* 82:271–276
10. Bondevik S, Svendsen JI, Johnsen G, Mangerud J, Kaland PE (1997) The Storegga tsunami along the Norwegian coast, its age and run-up. *Boreas* 26(1):29–54
11. Iida K (1963) Magnitude, energy, and generation mechanisms of tsunamis and a catalogue of earthquakes associated with tsunamis. In: Proceedings: tsunami meetings associated with the 10th Pacific science congress, International Union of Geodesy and Geophysics, Paris, pp 7–18
12. Iida K, Cox DC, Pararas-Carayannis G (1967) Preliminary catalog of tsunamis occurring in the Pacific Ocean. Data Rep. 5, HIG-67-10, University of Hawaii, Honolulu, pp 274
13. Soloviev SL (1970) Recurrence of tsunamis in the Pacific. In: Adams WM (ed) *Tsunamis in the Pacific Ocean*. East-West Cent. Honolulu, Hawaii, pp 149–163
14. Abe K (1979) Size of great earthquakes of 1837–1974 inferred from tsunami data. *J Geophys Res* 84:1561–1568
15. Abe K (1981) Physical size of tsunamigenic earthquakes of the northwestern Pacific. *Phys Earth Planet Inter* 27:194–205
16. Abe K (1995) Estimate of tsunami run-up (the process of wave propagation from the initial shoreline to the maximum run-up) heights from earthquake magnitudes. In: Tsuchiya Y, Shuto N (eds) *Tsunami: progress in prediction, disaster prevention and warning, advanced national technological hazards resolution*, vol 4. Kluwer, Norwell, pp 21–35
17. Geist EL (2002) Complex earthquake rupture and local tsunamis. *J Geophys Res* 107(B5)

18. Ward SN (1980) Relationships of tsunami generation and an earthquake source. *J Phys Earth* 28:441–474
19. Okal EA (1982) Mode-wave equivalence and other asymptotic problems in tsunami theory. *Phys Earth Planet Inter* 30:1–11
20. Liu PLF, Woo SB, Cho YS (1998) Computer programs for tsunami propagation and inundation. Department of Civil Engineering and the Institute of Waterway Industry, Sejoing University, Seoul, Korea, October
21. Liu PLF, Yeh H, Synolakis C (2008) Advanced numerical models for simulating tsunami waves and runup. World Scientific, Singapore
22. Tadepalli S, Synolakis CE (1996) Model for the leading waves of tsunamis. *Phys Rev Lett* 77:2141–2144
23. Ward SN (2002) Tsunamis. In: Meyers RA (ed) Encyclopedia of physical science and technology, vol 17. Academic Press, Amsterdam, pp 175–191
24. Ambrasseys NN, Jackson JA (1998) Faulting associated with historical and recent earthquake in Eastern Mediterranean region. *Geophys J Int* 133:390–406
25. Alessandro A (2007) The tsunami assessment modeling system by The Joint Research Centre. *Sci Tsunami Hazards* 26(2):70–92
26. Jiang X, Tatano H, Kajitani Y (2012) Geo-statistical approach for interpolation of tsunami height: a case study on Tohoku tsunami event. In: The annual international conference organized by the International Institute for Infrastructure, Renewal and Reconstruction (IIIRR)
27. Teh SY, Koh HL (2011) Tsunami simulation for capacity development. In: Proceedings of international multiconference of engineers and computer scientists, II
28. Sorensen RM (1993) Basic wave mechanics for coastal and ocean engineers. Wiley, New York
29. Synolakis CE (1987) The runup of solitary waves. *J Fluid Mech* 185:523–545
30. Synolakis CE (1986) The run-up of long waves. PhD thesis. California Institute of Technology, CA
31. Shadloo MS, Weiss R, Yildiz M, Dalrymple RA (2015) Numerical simulation of long wave runup for breaking and nonbreaking waves. *Int J Offshore Polar Eng* 25(1):1–7
32. Haritos N, Ngo T (2005) Evaluating tsunami wave forces on structures, international symposium: disaster reduction on coasts. Scientific-sustainable-holistic-accessible, Melbourne, Australia
33. Como A, Mahmoud H (2013) Numerical evaluation of tsunami debris impact loading on wooden structural walls. *Eng Struct* 56:1249–1261
34. Kong L, Robertson I, Yeh H (2006) Structural response to tsunami loading (lecture notes)
35. Nistor I, Palermo D, Nouri Y, Murty T, Saatcioglu M (2008) Chapter 11: Tsunami forces on structures. In: Young K (ed) Handbook of coastal and ocean engineering. World Scientific, Singapore
36. FEMA (2005) 55 Coastal Construction Manual, FEMA
37. Thusyanthan NI, Madabhushi SPG (2006) Model testing of tsunami safe(r) house design. In: Proceedings of the first European conference on earthquake engineering and seismology, Sep 2006, Geneva, paper 1526
38. Thusyanthan NI, Madabhushi SPG (2008) Tsunami wave loading on coastal houses: a model approach. *Proc ICE Civil Eng* 161(2):77–86
39. Bryant E (2008) Tsunami: the underrated hazard, 2nd edn. Springer, Heidelberg
40. <https://www.youtube.com/watch?v=YpZohKz5GKE>
41. Jurewicz J, Buongiorno J, Todreas N, Golay M (2014) Spar-type platform design for the offshore floating nuclear power plant. In: The 10th international topical meeting on nuclear thermal-hydraulics, operation and safety, Okinawa, Japan, 14–18 Dec 2014

Chapter 13

Earthquake Damages

The frame and huge foundation of the earth shake like a coward.

William Shakespeare
Henry IV, Part 1.

13.1 General

Earthquakes can lead to various types of damages, including foundation damage, structural damage, non-structural component damage, and contents and furniture damage. In addition, extensive loss can be caused by the so-called induced hazards such as landslides, soil liquefaction, fire, retaining structure failures, critical lifeline failures, tsunamis and seiches (global sloshing behavior of lakes or semi-enclosed sea), etc. [1]. Those damages can cause the loss of human life or injury, or financial losses, and can negatively affect normal business of the society. Table 13.1 lists various types of sources and consequences of earthquake damages.

13.2 Structural and Foundation Damage

Except for structural failure of coastal structures due to tsunami, no significant structural damages of offshore structures due to earthquakes have been reported so far. This is, to a great extent, due to the fact that no offshore structures have been exposed to strong earthquakes. The absence of earthquake impact can be an obstacle to recognize earthquake hazards and initiating consequence mitigation [3]. On the other hand, structures may have more than sufficient safety, leading to an uneconomic and over-redundant design. Abundant significant earthquake accidents have occurred on land, which provide valuable knowledge for the seismic design

Table 13.1 Sources and consequences of earthquake damages [2]

Potential losses	Sources of damage			
	Structures and foundations	Non-structural components	Contents and furnishings	Externalities
Death or injury	• Collapse-prone structure types	• Brick chimneys	• Tall or heavy furnitures	• Adjacent collapse-prone structures
	• Unreinforced brick parapets	• Exterior falling hazards: ornament, roofing, etc.	• Storage racks	• Adjacent falling hazards
	• Collapse induced by ground failure	• Interior falling hazards: Ceilings, light fixtures, equipment • Gas-fired equipment or hazardous materials	• Trade furnishings and equipment • Contents that fall or slide to block exits	• Adjacent or nearby hazardous material release or fire hazard
Repair costs and direct losses	• Collapse or damage-prone structure types • Damage from structural foundation or ground failure	• Damageable finishes • Unbraced ceilings, lights, equipment, etc. • Sprinkler or piping leaks	• Unbraced office equipment or trade furnishings • Fragile or perishable inventory • Vulnerable electronic records and data	• Damage from adjacent fire, collapse, etc.
Business disruption	• Damage causing restricted use	• Loss of water, wastewater, power • Loss of data/telecom • Damage requiring extensive cleanup • Damage causing restricted use	• Damage requiring extensive cleanup • Damage causing restricted use • Damage interfering with business records or transactions	• Loss of customer or client base • Loss of vendor or supplier support • Loss of key staff • Loss of utilities, data/internet, infrastructure, or city services

for offshore structures, even if the two have a few essential differences as discussed in Chap. 2.

Most of the damages during strong earthquakes appear as global or local failures of the structures, foundations, and/or the surrounding soil. Figure 13.1 shows the collapse of a five story building during a strong earthquake with a magnitude of 8.0. The strong ground motion induces rather high inertia force transferred to the foundation, causing the failure of the connection between the foundation and the

upper structure. If the foundation is stronger, the failure may be shifted to the upper structure if the building structure does not have a sound seismic resistance. Therefore, structures and foundations should be regarded as an integrated system during seismic designs, so that critical damages and system failures can be avoided even if the system is subject to extremely large ground motions. Figure 13.2 shows typical types of structural failures during a strong earthquake, which are due to the failure of upper structures, foundations, and soil.



Fig. 13.1 The collapse of a five story concrete building on land during the magnitude 8.0 Wenchuan earthquake in China, 12 May 2008 (courtesy of *ChinaDaily*)

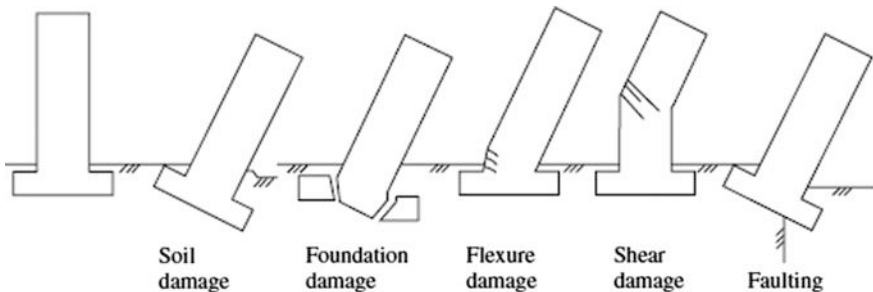


Fig. 13.2 Typical structural failures during an strong earthquake [4]

Moreover, critical facilities necessary for a community's response and recovery from seismic or other hazards, such as pipelines, can also be rather vulnerable structures during major earthquakes. For example, a review of earthquake damage of both land-based and subsea pipelines shows that permanent deformations due to soil failure have a severe influence on the integrity of both buried and unburied pipelines, whereas seismic ground motions only have a significant influence on the damage of unburied pipelines [5].

13.3 Soil Liquefaction

13.3.1 General

During earthquakes, the loose sandy soils may lose grain to grain contact, causing the material to flow and a loss in both strength and stiffness, which makes the soil behave more like a liquid than a solid. This process is called soil liquefaction, as shown in Fig. 13.3. To get an idea of the process, imagine a person standing still on a layer of wet sand. The sand can normally support the person, but if this person starts to jump or shakes his/her body, the sand will flow as a result of liquefaction. Eventually, the person's feet will sink into the sand. The soil liquefaction is essentially due to a reduction of effective stress under repeated loading, causing particles to pack together more tightly, leaving the water inside sand to take the entire weight. Therefore, direct normal stress between sand particles no longer exists, leading to a complete loss of friction resistance to shear deformation of the soil.

Soil liquefaction is particularly a concern for sandy sites subject to seismic loading. Due to the transmission of the seismic shear wave, the excitation accelerations go along with horizontal shear stresses induced by an upward propagation



Fig. 13.3 Appearance of soil liquefaction after the Loma Prieta earthquake of 1989 (courtesy of Department of Civil Engineering, University of Washington)

of the shear wave. Similar to the variation of vertical stress with depth, the shear stress in the upper sand layers is roughly proportional to the depth below the soil surface, indicating a gradual change in relative shear stress that does not strongly vary with depth [6]. Cyclic excitations induce cyclic shear stress in the soil, causing the soil to undergo cyclic shear deformation, a pore water pressure build-up, as well as a reduction in the effective stress and the shear strength of the soil, and eventually leading to a possible liquefaction in case the soil is undrained for silt, fine sand, and even medium sand [7]. Here, the pore pressure is defined as the difference between the actual pore pressure and the hydrostatic pressure for still water level. Figure 13.4 illustrates the process of seismic wave transmission to trigger soil liquefaction.

Liquefaction can cause ground surface settlement, loss of foundation bearing capacities, and lateral movement of slopes. It is responsible for damages during many earthquakes. For example, during the Loma Prieta earthquake of 17 October 1989, 18,306 houses were damaged, with the most intense damage among occurring in areas where infrastructures were built on loosely consolidated and saturated soils, which are susceptible to damage due to liquefaction. During the Kobe earthquake of 1995, on artificial islands off Kobe, significant ground shaking caused liquefaction of reclaimed lands, and the quay wall built by the caisson method suffered serious damages. During the Tangshan earthquake of 1976, 15 out

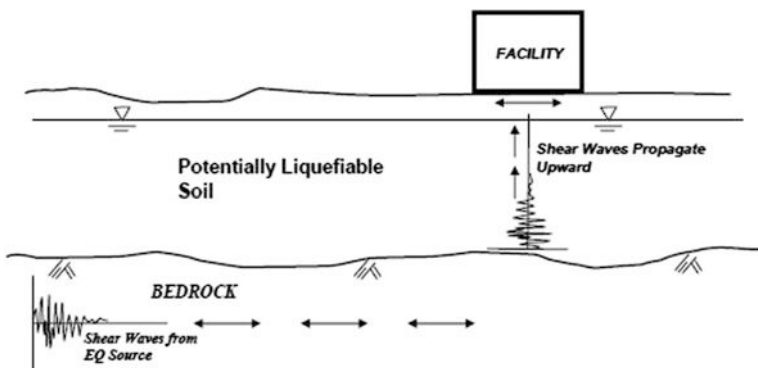


Fig. 13.4 The potential of liquefaction due to the transmission of shear wave through soils (courtesy of FEMA)

of 18 collapsed bridges were caused by liquefaction, leading to the failure of foundations and bridge piers. The magnitude 7.4 Niigata earthquake of 1964 caused damage of more than US\$1 billion and most of those damages were related to soil liquefaction of loose sand deposits in low-lying areas [8]. Figure 13.5 shows the collapsed buildings due to bearing capacity failure in the liquefied ground during the Niigata earthquake, in which the building in the middle tilted about 80° . All buildings shown in this figure tilt to some extent, with some tilting more adversely



Fig. 13.5 Appearance of soil liquefaction after the magnitude 7.4 Niigata earthquake, Japan, 16 June 1964

than others. Interestingly, almost all buildings tilt in the direction of the eccentricity of gravity force caused by the eccentricity of the roof, indicating an effect due to a rotational moment generated by gravity and buoyancy on these buildings [9], resulting in the actual direction of tilting. Liquefied sand has a density 1.7–2.1 times that of the water. Therefore, when the weight of a supported structure is not larger than the buoyancy force provided by the liquefied sand, the structure will float. An exception is the building on the upper right of Fig. 13.5, which was the only structure built with pile foundations instead of gravity-based foundations. Furthermore, even for the building that entirely collapsed in the middle of Fig. 13.5, the entire process took a few minutes, thus providing sufficient alarm time for the people inside the building to escape. This is also the reason why not all buildings exhibit significant structural damage due to liquefaction. During the Niigata earthquake, underground structures such as storage tanks, septic tanks, sewage conduits and manholes floated upwards out of the ground. Sand flows and mud volcanoes ejected water shortly after the earthquake and were reported to continue for as much as 20 min after shaking had stopped. Sand deposits 20–30 cm thick covered much of the city [8].

For offshore and coastal infrastructures, as their foundations often rest on sand soil, the liquefaction (potentially caused by ocean wave or earthquake loading) can cause an immediate drop of the structures and lateral spreading, resulting in significant settlement (for all types of foundations) and loss of lateral support (for pile foundations). If the settlement is uneven, the structures and/or pipelines may be damaged. Buried pipelines may float up through the liquefied sand. In addition, soil liquefaction can also cause slope failures.

It should be noted that soil liquefaction is traditionally believed to occur at sites with soils having low plasticity index, such as sand and occasionally silt soils as mentioned before. For soils with high plasticity index such as clay, even if high pore water pressure can be built up for those soils, liquefaction rarely occurs. However, evidences have shown that liquefaction can also occur in cohesive soils, such as the ejection of gravel and some cohesive soil observed at Port Island after the 1995 Kobe earthquake [10]. The liquefaction can even occur at sites with substantial gravel content [11], even though observational data are as yet insufficient for establishing a reliable evaluation method.

13.3.2 Assessment of Liquefaction

A typical assessment of liquefaction potential requires a screening of liquefaction potential and detailed site response analysis.

1. Screening the liquefaction potential

The screening of liquefaction is normally carried out by studying the site geology, soil types and density, depth to water table, ground surface slope, as well as potential for lateral and vertical differential displacement, etc. [12].

FEMA-356 presents a simple but quantified evaluation for liquefaction potential: if the granular sandy soils with $(N_1)_{60} > 30$ blows/ft ($(N_1)_{60}$ is obtained from standard penetration test (SPT) [13], as will be briefly explained in the text below), stiff clay or clayey silt with plasticity index (a measure of the ability of soils to retain water, it provides an indication of how much clay can shrink or swell [13]) over 20 and ground water table of 10 m below foundation level or 15 m below ground surface, they are not vulnerable to liquefaction.

2. Site response analysis

For sites susceptible to liquefaction potential in the screening stage, a detailed site response analysis may be performed. Various approaches have been used to evaluate the potential of liquefaction, and the majority of them are focused on the evaluation of initiation of liquefaction. The most commonly used ones are the cyclic stress approach and cyclic strain approach [13].

In the cyclic stress approach, by comparing the induced cyclic shear stresses from the site response analysis to the cyclic soil resistances, the likelihood of the liquefaction can be identified.

Cyclic soil resistance could be determined based upon SPT “N-values” from soil borings, tip resistance (q_c) from cone penetration test (CPT), and shear wave velocity (v_s) from down-hole seismic test. Field SPT blow counts (“N-values”) should be adjusted to account for various correction factors, i.e., overburden, delivered energy, rod length, borehole diameter, and liners corrections to obtain the normalized, standardized $(N_1)_{60}$. Similarly, q_c and v_s should be corrected against overburden pressure to obtain the normalized q_{c1} and v_{s1} values. Using charts found from relevant handbooks and guidelines, the cyclic soil resistances of soil deposits can be determined based on the value of normalized $(N_1)_{60}$, q_{c1} and v_{s1} [13]. For more details, readers may read the NCEER chart [14].

In addition to the SPT, CPT and shear wave velocity measurement methods, other in situ testing methods are also used for the exploration of subsurface soils, which have been utilized in the evaluation of liquefaction potential. For example, as SPT and CPT are not adequate for assessing the liquefaction potential for sites with gravel deposits, especially if the sites contains mainly coarse to very coarse grained soils, Becker penetration test (BPT) [15] can then be employed. This is because the diameter of the BPT penetrometer tip is much larger than that of the SPT sampler or the cone penetrometer: gravel-sized particles have much less effect on the BPT, whereas results obtained from SPT for sites with gravel contents greater than as low as 15–20 % can be erroneous. BPT is quite similar to a small pile driving test, and consists of driving a plugged steel casing into the ground using a diesel pile driving hammer. The number of blows per unit length (usually fet) of penetration is recorded and adjusted for driving conditions, and has been designed to be correlated with the SPT N-values so that the procedure for liquefaction potential analysis using SPT can also be used by BPT. Two methods [15, 16] are widely adopted for this correlation. However, another BPT method, called iBPT [17], emerged in 2014 and is currently regarded as state-of-the art for BPT interpretation. For more details, readers may read the references cited above.

The induced cyclic shear stresses could be calculated either from a simplified Seed–Idriss equation [14] or from a more detailed dynamic site response analysis (Sect. 4.3). The latter analysis method is recommended because site response analysis has a more dedicated accounting for the frequency content of ground motion, the variation of soil layer and shear wave velocity with depth, and the depth to bedrock. Therefore it gives more reliable results than that of the simplified See-Idriss equation. If the ground motion is not strong, the site response analysis can be performed by the equivalent linear site response analysis (Sect. 4.3.9). Otherwise, a non-linear site response analysis may be performed.

As liquefaction potential can not be expressed in one simple equation, many semi-empirical equations were presented during the period from the 1970s to 1990s by researchers worldwide [18]. Among them, Seed and Idriss [19–25] made significant contributions. For more details on this, readers may refer to [13, 26].

13.3.3 *Mitigation Measures of Soil Liquefaction*

The general strategy to mitigate the liquefaction hazard can be reached through the following measures:

1. Improve the strength, density, and/or drainage characteristics of relevant soils.
This can be fulfilled by using a variety of soil improvement techniques
2. Design foundation elements to resist liquefaction
3. Avoid liquefaction susceptible soils

For more detailed practice to mitigate liquefaction potential, ref. [26] is recommended.

13.4 Landslides

13.4.1 *General*

Damages from triggered landslides and other ground failures have sometimes exceeded damages directly related to strong ground shaking and fault rupture such as structural collapses.

As shown in Fig. 13.6, landslides can occur with five types of geology appearances:

- Fall: also shown in Fig. 13.7, is a detachment of soil or rock from steep slopes along surface, with little or no shear displacement
- Topple: a forward rotation of soil or rock about a point

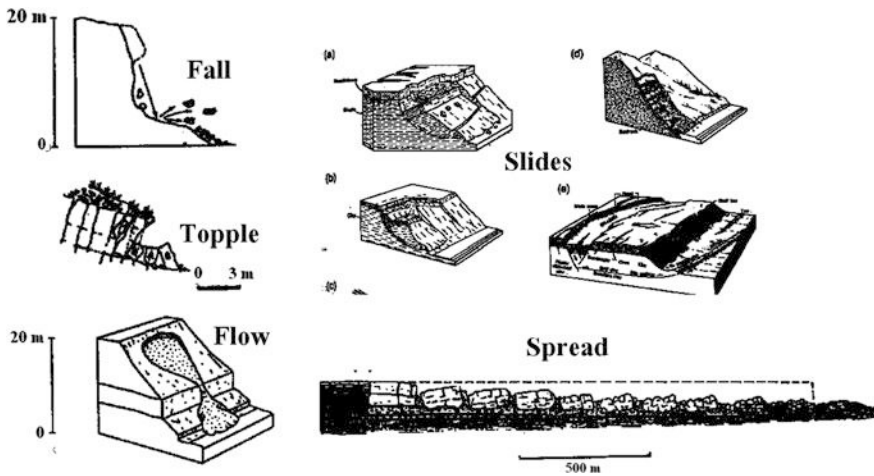


Fig. 13.6 Landslides appearances [27]



Fig. 13.7 The fall of a stone from the steep slope after the Wenchuan earthquake, 12 May 2008, China [28]



Fig. 13.8 Appearance of slides after the Wenchuan earthquake, 12 May 2008, China [28]

- Slides, also shown in Fig. 13.8, are a down-slope displacement of soil or rock masses. They include: rotational, translational, and debris slide
- Flow: a continuous movement of soil masses where shear surfaces are short lived
- Spread: is a sudden movement of water bearing rock masses

Several sources can trigger landslides: earthquake ground shaking, volcanic eruption, intense rain-fall, change of water level, ground water flow, rapid snow-melt, and human activities.

13.4.2 Assessment of Regional Landslide Potential by Arias Intensity

Landslides triggered by earthquakes can roughly be classified into three types [30]: (1) type I is rock falls and disrupted soil slides, which are mainly found in closely jointed or weakly cemented rocks (rock falls) or on steep slopes in loose, residual or colluvial materials with low cohesion (disrupted soil slides); (2) type II is coherent deep-seated slumps, which are often found in relatively flat zones in deposits with significant cohesion; (3) type III is lateral spreads, which are sometimes formed as a consequence of liquefaction.

To characterize landslide potential on a regional scale with landslide hazard zonation, the Arias Intensity (I_A), which is a measure of the strength of a ground motion as presented in Sect. 3.7.2.2, can be used to identify possible occurrence of landslide and the associated type. It has been found to be a fairly reliable parameter to describe earthquake shaking necessary to trigger landslides [31]. As mentioned before, it is typically defined as the sum of all the squared acceleration values from seismic ground motion records. Wilson and Keefer [33] presented a calculation of the spatial distribution of Arias Intensity as a function of earthquake moment magnitude M_w , distance to the closest point on the surface projection of the fault rupture R_{JB} (Fig. 3.31), focal depth h , and probability of exceedance P_e :

$$\log_{10} I_A = -4.1 + M_w - 2 \log_{10} \sqrt{R_{JB}^2 + h^2} - 0.5 P_e (\text{m/s}) \quad (13.1)$$

Based on this definition of Arias Intensity, Harp and Wilson [34] found a minimum Arias Intensity of 0.11 m/s to initiate landslides of type I. The same authors reported a minimum Arias Intensity of 0.32 m/s to be required for the initiation of landslides of type II. Larger Arias Intensities indicate that stronger and longer duration shaking is required to trigger type II landslides. The knowledge above can lead to a creation of seismic landslide hazard zonation map.

For more details of evaluating landslide potential and seismic landslide hazard zonation, readers may read the references cited above and [31].

For assessing slope stability locally due to the cyclic seismic loading, four methods, namely, pseudostatic analysis approach, dynamic stress-deformation analysis approach, Newmark sliding block approach, and testing method, have been extensively used. For a presentation of the methods, readers may refer to [13].

13.5 Human Body Safety and Motion Induced Interruptions

13.5.1 General

As described in Table 13.1, under strong ground motions, the collapse of structural and non-structural elements and the falling down of contents, furnishings and externalities can cause the death or injury of people. It is therefore of great importance to protect the human body from impacts by falling objects, which will be introduced in Sect. 13.5.2.

In addition, ground motions may also cause a sliding and toppling over (tipping) of the human body. During a strong earthquake, people may have difficulty to move and stand, known as motion induced interruptions. This is normally governed by the sliding or tipping of a human body, as will be discussed in Sect. 13.5.3. With regard to consequences, special concern is placed on the human's ability to carry

out proper emergency activities, such as evacuations, first aid assistance, keeping control of important production facilities and machinery in a safe condition, etc.

13.5.2 Remedial Measures with Regard to Human Body Safety

During a strong earthquake, people inside an infrastructure are much more vulnerable to falling or flying objects than to the collapses of structures (less likely). Therefore, it is often not possible to escape (evacuate people) from buildings or offshore platforms during the process of a strong shaking, because the objects may fall off and potentially cause serious injuries or even fatalities.

Official rescue teams around the world advocate a use of the internationally recognized “*Drop, Cover and Hold On*” protocol (Fig. 13.9) to protect lives during earthquakes. It states that when one feels strong motions on the ground, the following actions should immediately be taken:

1. *Drop* to the ground (before the earthquake drops you)
2. Take *Cover* by getting under a sturdy table or other piece of furniture; if there is no table or desk besides you, cover your face and head with your arms and crouch in an inside corner of the building
3. *Hold On* until the shaking stops

It is worth mentioning that in many countries with a large number of old and poorly constructed buildings, it is recommended that, during an earthquake, the safest place to be indoors is on the floor next to a large object that cannot collapse, like a sofa or a bed, which is often referred to as the “Triangle of Life.” This claim is based on the assumption that, if the ceiling collapses, a person can avoid being crushed if he/she is in the space under a piece of the ceiling that falls to rest leaning against a non-collapsible object. However, in many regions with buildings designed



Fig. 13.9 Illustration of “*Drop, Cover and Hold On*” process during an earthquake [32]

and constructed based on modern building codes, they are constructed to prevent floor collapse. Extensive research has indicated that the method of “*Drop, Cover and Hold On*” has saved lives in various devastating earthquakes.

13.5.3 Motion Induced Interruptions

13.5.3.1 Sliding/Slipping

Consider a person who stands on the ground surface as shown in Fig. 13.10. When an earthquake occurs, motions with ground accelerations a_X , a_Y , and a_Z along three directions X , Y and Z will be transmitted from ground to the person's feet, hands and body. The maximum friction force of the person to resist ground surface sliding is μmg , where μ is the friction coefficient between the feet (shoe bottoms) and ground surface, m is the mass of the person, and g is the acceleration of gravity. By assuming that the ground surface is horizontal, the person stands vertically, and his/her body is rigid. Sliding will then occur if the following equation is fulfilled:

$$\sqrt{F_X^2 + F_Y^2} \geq \mu m(g \pm ma_z) \quad (13.2)$$

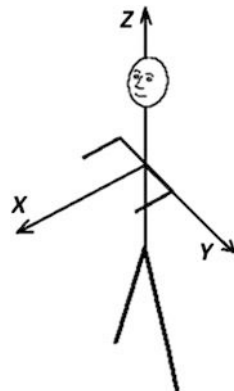
where F_X and F_Y is the human body's inertia force due to the seismic ground motions.

By neglecting the vertical acceleration a_z of the human body, the sliding condition measured with the horizontal resultant ground accelerations a_{XY} can be expressed as:

$$a_{XY} \geq \mu g \quad (13.3)$$

where $a_{XY} = \sqrt{a_X^2 + a_Y^2}$.

Fig. 13.10 The human body fixed coordinate system and the body forces due to motions



Typical friction coefficient between a shoe bottom and floor or ground surface ranges from 0.3 to 0.7. Therefore, the resultant horizontal ground acceleration needs to be larger than 0.3–0.7 g to induce a sliding. This can occur during a strong earthquake event.

13.5.3.2 Tipping

Side tipping can also occur if the following equation can be fulfilled:

$$F_Y h \geq mgb \quad (13.4)$$

where $F_Y = ma_y$; h is the height of center of gravity of a person measured from the ground surface; b is the half stance width of the person.

By assuming that $\frac{h}{b} \approx 4$ [35], one then reaches the condition for inducing side tipping expressed as:

$$a_y \geq 0.25 \text{ g} \quad (13.5)$$

For front-back (X direction in Fig. 13.10) tipping, by assuming the similar center of gravity height to stance width ratio of 4, one also reaches the condition for front-back tipping:

$$a_x \geq 0.25 \text{ g} \quad (13.6)$$

It is also noted that the ground/floor accelerations a_x or $a_y \geq 0.25 \text{ g}$ are likely to occur during a strong earthquake events. Therefore, due to the high ratio between the center of gravity to the half stance width of a person, tipping is more likely to occur than sliding under strong ground motions. However, for some other objects such as a car, sliding is more likely to occur than tipping.

It should be noticed that the sliding and tipping control discussed in this book is based on a quasi-static analysis with a standing rigid human body assumption. In reality, when a person feels strong floor/ground motions, he/she is likely to react to the motions by sitting down, crouching or changing the stance. This can mitigate the likelihood of sliding and tipping.

13.6 Structural Damage Measures

13.6.1 Basic Parameters for Damage Measures

One of the most important issues in seismic design is to estimate the damage amount of designed structures at different levels of risk.

Two major mechanisms cause earthquake damages: seismic accelerations and displacements/inter-story drift. A particular type of component, either structural or non-structural, can be sensitive to either acceleration or displacement, or both.

Structural components with high inertia characteristics, non-structural and equipment sensitive to accelerations are potentially vulnerable to strong accelerations. Examples of these conditions are: seismic inertial forces on the structural components inducing yielding; cracking in a masonry shear wall; out-of-plane failure of a free-standing wall or heavy partition; shear failure of anchored bolts at the base of heavy equipment; and pipe rupture at an anchor point for a long, unbraced section of heavy pipe. Furthermore, for equipment sensitive to motions, the accelerations imparted to the equipment are to be checked.

The displacements of a structure, and structural or non-structural component provide information about the separation of the adjacent structures or components. Light items with low inertia forces can still potentially be damaged by large imposed deformations. Examples of such situations are: a beam of a frame structure may collide with adjacent pipe lines during earthquakes, in which the deformation of the beam may far exceed the serviceability limits of the structure; non-structural components attached to adjacent floors can be damaged by the relative displacement between two adjacent floors; non-structural components such as glazing, precast cladding, rigid full-height partitions, piping, ductwork, elevators, and exterior veneer or ornamentation may be damaged by large inter-story drifts caused by the seismic displacements of the building frame; items that cross seismic joints between adjacent buildings are also vulnerable to displacement damage [36].

Along with the two measures above, velocity (with mass m and velocity v , the strain energy stored in the system can be calculated as $\frac{1}{2} mv^2$) is a measure of kinematic energy level in structures. Forces applied on the foundations and structural members during the ground motion are also important measures for capacity control. It is directly related to the mass and acceleration of the structure or structural components. Similarly, stress, strain and energy dissipation are also sometimes used as a measure to perform damage control.

It is noted that damage is eventually affected by an accumulation and distribution of several parameters, such as structural damage, the failure mode of elements, the number of cycles, and the duration of ground motions [37].

13.6.2 Damage Indices

In a performance-based design (Sect. 14.2.9), which is to introduce design checks at various limit states to the probability that the seismic action can reach the intensity required to induce the corresponding failure modes, it is important to quantify the performance level from, for example, operational, immediate occupancy, damage control, life safety, to collapse prevention [38]. Damage indices are acceptable measures with which to define the performance levels.

Many damage indices have been proposed to quantify the extent of structural damage, and are generally categorized into two types: non-cumulative and cumulative measures [39]. In a non-cumulative measure, damage is calculated by a maximum value of an inelastic response parameter, usually displacement, while in an accumulated measure, damage is typically measured by hysteretic energy or plastic strain for the entire response duration [40]. Damage in cumulative indices has commonly been considered as a function of cumulative plastic deformation, which can be divided into four classes [41]: (1) force based cumulative indices; (2) displacement-based cumulative indices; (3) hysteretic energy-based cumulative indices; and (4) combined cumulative indices (defined as a combinations of the indices above [42, 43]).

As an example of utilizing damage indices for performance-based design, it is noted that for different extents of damages, in order to fulfill the performance requirement, energy dissipated by the target structure E_d must be equal to or larger than a portion of seismic input energy contributing to damage (αE_I):

$$E_d \geq \alpha E_I \quad (13.7)$$

where α is a factor representing the portion of input energy; it varies between 0 and 1.0, and it is typically dependent on the force-deformation characteristics and the ductility of structures [44].

By substituting values for all parameters into the equation above, the inequality equation can be established and solved for each combination of natural period of the structures, ductility factors and damage extents.

References

1. Bachmann H (2003) Seismic conceptual design of buildings—basic principles for engineers, architects, building owners, and authorities. Swiss Federal Office for Water and Geology and Swiss Agency for Development and Cooperation, BWG, Bern
2. QUAKE SMART. www.quakesmart.org, FEMA
3. Visser RC (1997) Seismic considerations in design and assessment of platform topside facilities. SPE western regional meeting, Long Beach, California
4. Chen WF, Lui EM (2006) Earthquake engineering for structural design, 1st edn. CRC Press, London
5. Bai Y, Bai Q (2005) Subsea pipelines and risers, 2nd edn. Elsevier Science, Amsterdam
6. de Groot MB, Bolton MD, Foray P, Meijers P, Palmer AC, Sandven R, Sawicki A, Teh TC (2006) Physics of liquefaction phenomena around marine structures. J Waterw Port Coast Ocean Eng 132(4):227–243
7. Sumer BM (2014) Liquefaction around marine structures. World Scientific Press, London, p 472
8. Jefferies M, Been K (2015) Soil liquefaction: a critical state approach, 2nd edn. CRC Press, Boca Raton
9. Towhata I (2008) Geotechnical earthquake engineering. Springer, Heidelberg
10. Ishihara K, Yasuda S, Nagase H (1996) Soil characteristics and ground damage, special issue of soils and foundations on Kobe earthquake. Jpn Geotech Soc 109–118

11. Kuwabara F, Yoshimi Y (1973) Effect of subsurface liquefaction on strength of surface soil. ASCE JGE 19(2)
12. FEMA (2000) Prestandard and commentary for the seismic rehabilitation of buildings, FEMA 356/Nov 2000
13. Jia J (2016) Soil dynamics and foundation modeling: offshore and earthquake engineering. Springer, Heidelberg
14. Youd TL, Idriss IM et al (2001) Liquefaction resistance of soils, summary report from the 1996 NCEER and 1998 NCEER/NSF workshops on evaluation of liquefaction resistance of soils. J Geotech Geoenvir Eng ASCE 127(10):817–833
15. Harder Jr LF, Seed HB (1986) Determination of penetration resistance for coarse-grained soils using the becker hammer drill. Report No. UCB/EERC-86-06, NTIS PB87 124210, Earthquake Engineering Research Center, College of Engineering, University of California, Berkeley, California, May 1986
16. Sy A, Campanella RG (1994) Becker and standard penetration tests (BPT-SPT) correlations with consideration of casing friction. Can Geotech J 31(3):343–356
17. Ghafghazi M, Thururajah A, DeJong JT, Wilson DW, Armstrong R (2014) Instrumented Becker penetration test for improved characterization of gravelly deposits. In: Proceedings of GeoCongress 2014, American society of civil engineers geotechnical special publication No. 234, Atlanta, Georgia, pp 37–46
18. NCEER (2001) Liquefaction resistance of soils, 1996 NCEER and 1998 NCEER/NSF workshop on evaluation of liquefaction resistance of soils. ASCE J Geotech Geoenvir Eng 127(10)
19. Seed HB (1987) Design problems in soil liquefaction. J Geotech Eng Div ASCE 112(8):827–845
20. Seed HB (1968) The fourth Terzaghi Lecture: Landslides during earthquake due to liquefaction. J Soil Mech Found Div ASCE 94(5):1053–1122
21. Seed HB, Lee KL (1966) Liquefaction of saturated sands during cyclic loading. J Soil Mech Found Div ASCE 92(6):105–134
22. Mitchell JK (1995) Harry Bolton Seed 1922–1989, A Biographical Memoir, National Academy of Sciences, National Academies Press, Washington, DC, 1995
23. Seed HB, Idriss IM (1971) Simplified procedure for evaluating soil liquefaction potential. J Soil Mech Found Div ASCE 97(9):1249–1273
24. Seed HB, Idriss IM (1967) Analysis of soil liquefaction: Niigata earthquake. J Soil Mech Found Div ASCE 93(3):83–108
25. Seed HB, Arango I, Idriss IM (1983) Evaluation of liquefaction potential using field performance data. J Geotech Eng Div ASCE 109(3):458–482
26. Kramer SL (1996) Geotechnical earthquake engineering. Prentice Hall, Upper Saddle River, NJ
27. Turner AK, Shuster RL (1996) Landslides: investigation and mitigation, transport research board, rep no. 247
28. <http://blog.sina.com.cn/u/1222264142>
29. Keefer DK (1984) Landslides caused by earthquakes. Geol Soc Am Bull 95:406–421
30. van Westen J, Terlien MTJ (2007) Seismic landslide hazard zonation. <http://www.itc.nl/ilwis/applications/application07.asp>
31. <http://www.dropcoverholdon.org/>
32. Wilson RC, Keefer DK (1985) Predicting aerial limits of earthquake-induced landsliding. In: Zimor JI (ed) Evaluating earthquake hazards in the Los Angeles region: an earth-science perspective. USGS professional paper 1360, pp 316–345
33. Harp EL, Wilson RC (1995) Shaking intensity thresholds for rock falls and slides: evidence from the 1987 Whittier Narrows and Superstition Hills earthquake strong motion records. Bull Seismol Soc Am 85(6):1739–1757
34. Lloyd ARJM (1998) Seakeeping: ship behavior in rough weather. ARJM Lloyd, Hampshire, UK
35. <http://www.hnd.usace.army.mil>

36. Ghobarah A (2004) On drift limits associated with different damage levels. Performance-based seismic design: concepts and implementation. In: Fajfar P, Krawinkler H (eds) Proceedings: international workshop, Bled, Slovenia
37. Priestley MJN (2000) Performance based seismic design. In: Proceedings of the 12th world conference on earthquake engineering, Auckland, New Zealand, paper no. 2831
38. Williams MS, Sexsmith RG (1995) Seismic damage indices for concrete structures: a state-of-the-art review. *Earthq Spectra* 11(2):319–349
39. Sucuoğlu H, Yücemén S, Gezer A, Erberik A (1998) Statistical evaluation of the damage potential of earthquake ground motions. *Struct Saf* 20(4):357–378
40. Mihai M (2013) A theoretical review of the damage indices used to model the dynamic nonlinear behavior of reinforced concrete structures. *Bull Polytech Inst IASI Constr Archit Sect* 63(2):109–120
41. Banon H, Veneziano D (1982) Seismic damage in reinforced concrete frames. *Earthq Eng Struct Dyn* 10:179–193
42. Park YJ, Ang AHS (1985) Mechanistic seismic damage model for reinforced concrete. *J Struct Eng ASCE* 111(4):722–739
43. Fajfar P, Vidic T (1994) Consistent inelastic design spectra: hysteretic and input energy. *Earthq Eng Struct Dyn* 23(5):523–537

Chapter 14

Design Philosophy

Since the earthquake phenomenon itself is substantially the same as nature displays it worldwide, that eventually we may see more uniform expression of the principles needed to be applied to resist earthquake motions in man-made structures.

John Rinne (former president of the International Association for Earthquake Engineering)

14.1 General

Design is a mixed decision made from an environment of partial truth, partial knowledge, and partial uncertainty. A structure subjected to seismic loads is required to have a certain amount of safety related to strength, ductility, deformation and energy absorption. The design of seismic-resistant structures evolved from originally stiff to more recent flexible and ductile concepts, which is due to increased knowledge on earthquake engineering and development of modern engineering structures with various forms. This is certainly beneficial to reduce a great amount of seismic load transferred to structures due to more flexible characteristics of newly designed structures, and is also beneficial to utilize the capacity reserve and energy dissipation due to plasticity development of structural members. Moreover, in the last few decades, various artificial mitigation measures such as viscous damper, base isolation system etc., have been extensively used to more efficiently minimize the seismic response of structures, which will be discussed later in this book. All the developments above have also positively motivated engineers to introduce design checks at various limit states to the probability that the seismic action can reach the intensity required to induce the corresponding failure modes, which is called performance-based design, as will be presented in Sect. 14.3.

It is noted that both loads and the resistance of structures are highly variable and dependent on many factors, such as the seismicity at sites, the randomness of ground motions, and variations of different characteristics of structures, etc. For example, the ground motion due to earthquake can be greater than the design

accelerations used in pseudostatic analysis. This concern had been factored in by the nuclear industry, resulting in two levels of earthquakes, the design basis earthquake and the maximum credible earthquake. Research also shows that the dynamic strength of massive concrete is dependent on size effect, decreasing with an increase in dimensions. All these factors bring difficulties to assess the structural performance in a purely deterministic way. Instead, reliability based design, which aims to design a structure that is fit for use with an acceptable target reliability, is therefore promoted in many codes to cope with the difficulties above.

Every year, 100,000 or more earthquakes that can be felt by people occur worldwide [1]. Among them, only around 18 strong earthquakes on average occur with an amplitude above 7.0, but around 800 moderate earthquakes occur with a magnitude ranging from 5.0 to 5.9. From a risk assessment point of view, engineers need to find a trade-off between safety and cost. Extremely strong earthquakes can cause serious consequences, but their probability of occurrence is fairly low; mild earthquakes cause much less damage but they happen more frequently. It is therefore not economical to design a structure that can withstand any extremely strong earthquake without any damage. On the other hand, the consequence of those strong earthquakes should not be ignored in the design process. With these considerations, the objective of designing an earthquake resistant structure is to control the damage and manage the risk at an acceptable level with a reasonable cost. In practice, it is common to design a structure for which, during a minor or moderate earthquake, the load carrying members should not be damaged or should sustain only repairable ductile damage; while under strong and rare earthquake shaking, even the load bearing members may sustain damage, but the system integrity of the structure will be maintained such that the structure will not collapse.

Note that a similar design philosophy is also adopted for design of offshore structures subject to ocean environmental loading. For example, subject to cyclic loading such as seismic or ocean wave loading, the plastic failure mechanism of a structure can cause a local low-cycle fatigue failure (alternating plasticity) of critical components as shown in the left figure of Fig. 14.1. This may in turn trigger a global instability and a subsequent failure of the entire structure. Alternatively, ratchetting may occur with excessive deformation (incremental plasticity), in that the global deformation in each loading cycle increases until they are no longer tolerable, as shown in the mid figure of Fig. 14.1. To avoid repeated plasticity development and incremental plastic collapse is important in many structural design associated with the actions effects due to cyclic loading. However, limiting the behavior of the structure or components to the elastic range is not an economical way to design a structure, because this leads to over-conservative and expensive design as mentioned before. Therefore, in many applications, it is acceptable to allow limited plastic deformation to occur provided it can be shown that the structure shakes down to elastic action, i.e., the increment of structure deformation ceases after the first few loading cycles, after which the whole structure will respond in a purely elastic manner as shown in the right figure of Fig. 14.1. The structure's response can be shown to be well controlled below the elastic shake-down load. This is because if the structure continues to be subject to the load above

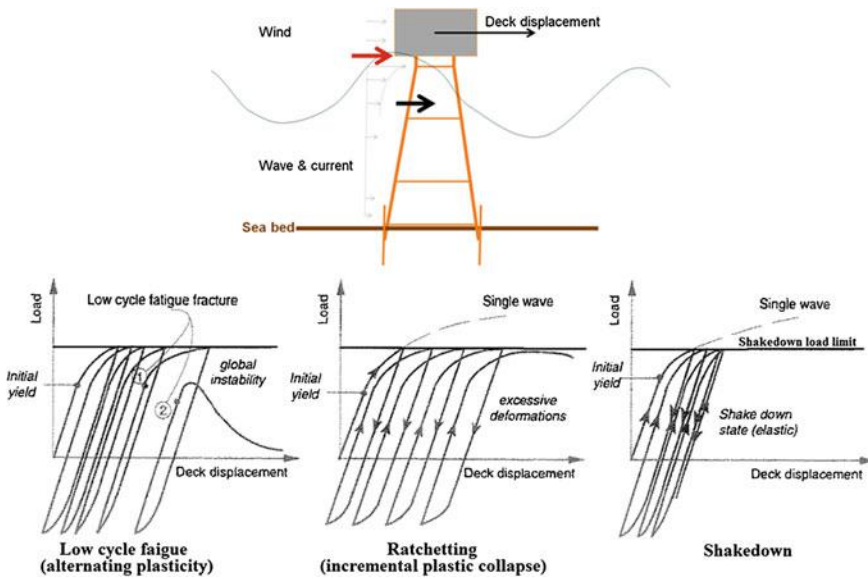


Fig. 14.1 Three different response scenarios (*lower*) of an offshore steel structure subject to cyclic ocean wave loading

the shakedown load, ratchetting or local low-cycle fatigue failure will occur under repeated loading. Therefore, for structures subject to significant cyclic loading, the shakedown load limits provides a rational criterion for structural design. In order to check the cyclic behavior of a structure during a shakedown analysis, the material behavior and associated material modeling need to account for the kinematic hardening [2].

On the basis of the discussion above, it is realized that the effectiveness of system ductility is essential in the design of earthquake resistant structures. These have also been reflected in various seismic design codes, for example, many seismic design codes for both offshore and land-based structures account for ductility by a reduction of elastic forces (response spectral acceleration), using response modification factor, behavior factor or ductility factor, as presented in Sect. 5.4.3. The level of the design force corresponding to inelastic behaviors is generally lower than that for elastic behavior and it is a function of the structure's ability to dissipate energy during earthquakes. As different structural systems and different materials have different energy absorption capacity, this implies an adoption of different values of behavior factor. However, if the structure was expected to respond elastically during a major earthquake event, no reduction would be allowed in the level of applied seismic forces [3]. On the other hand, rather than making a reduction on loads, the ductility or plasticity can be directly accounted for by a decent inclusion/modeling of plasticity for materials, leading to the so-called plastic design, as will be presented in Sect. 14.2.4.

From another angle, seismic damage can be controlled by one or a combination of the following four approaches:

1. Deflection/deformation control: limit the inter-story and global deflection under prescribed loads
2. Importance factor: prescribe a factor, normally above 1.0, to the expected seismic loads
3. Ductile details: special detailing to avoid brittle failures
4. Dynamic response mitigation: with external damping apparatus, base isolation or dynamic absorber etc., the seismic energy can be dissipated and the response of primary structure can be effectively reduced

It is noticed that none of the measures above can be applied to all types of structures. The selection of the methods must be carried out based on detailed characteristics of structures, foundations, and site specific seismic motion characteristics, etc. Moreover, a decent selection of corresponding seismic analysis methods is essential in order to provide a reliable assessment of structural damage, which will be discussed in Chap. 15 presenting the seismic analysis methods.

The following sections present an introduction on the seismic design philosophy with an evolutionary order: the allowable stress design (Sect. 14.2.3) with one safety factor to define the limit states (Sect. 14.2.2); plastic design (Sect. 14.2.4) that utilizes capacity reserve of structures beyond the yielding with a consideration of failure conditions rather than the working load condition; load and resistance factor design (Sect. 14.2.5) that accounts for uncertainties involved in both loads and resistance separately; and the state of the art design philosophy-performance-based design (Sect. 14.3), which is promoted by many professionals to be adopted for future structural and geotechnical design.

14.2 Prescriptive Code Design

14.2.1 Introduction

With the development of structural and geotechnical design and analysis, especially in the fields of strength of material, structural mechanics, and soil mechanics, seismic design codes have been extensively evolved over time to insure the safety of infrastructures. The codes have also been continuously revised based on the observations of the performance of structures during past earthquakes, and on the updated knowledge in aspects of seismology, new material performance, and structural analysis methods etc.

Uncertainties exist in every stage of engineering design, as they do in the development of seismic design. In seismic design codes, the uncertainties can be accounted for by various factors. Today, several design approaches coexist: allowable stress design, which is sometimes also referred to as working stress

design or elastic design as will be presented in Sect. 14.2.3; its extended version, namely plastic design, which is also called ultimate strength design or limit design, as will be presented in Sect. 14.2.4; and more evolved load and resistance factor design, which is also called load factor design, as will be presented in Sect. 14.2.5.

In the allowable stress design, uncertainties are handled by one factor of safety. In contrast, in the load and resistance factor design, uncertainties are handled through a determination of nominal capacity, an application of resistance factor (to account for uncertainties due to material properties, dimensions, type of structures, and construction tolerances, etc.) and load factors (to account for uncertainties in variable loads etc.), which reflects a more dedicated determination on both load and resistance. This slight modification in the format of load and resistance from allowable stress design to load and resistance factor design, however, implies a significant advancement with regard to reliability calibration, which will be discussed in Sects. 14.2.6 and 14.2.7. However, it should be emphasized that even with the adoption of load and resistance factor design, the performance level specified by the codes and regulations still includes an implied risk, mainly due to uncertainties involved in estimating earthquake loading. In addition, performance-based design (Sect. 14.3) has recently emerged, with its unique advantages as well as associated challenges. All those approaches are associated with various limit states (Sect. 14.2.2) beyond which the structure no longer satisfies the performance requirements.

Design codes and standards for earthquake resistance are essential for the safety of human life and properties, as well as the soundness of structures. For example, as mentioned in Chap. 1, the 7.0 magnitude Haiti earthquake that occurred in 2010 caused a loss 92,000 lives and massive destruction, primarily due to the lack of implementation of earthquake resistant building codes. Therefore, Sect. 14.2.8 briefly reviews the development of seismic design codes. Moreover, as it is not unusual for several codes and standards to aim to address the same design issues, it is of great importance to know the priority of them. To enable engineers to have an explicit understanding of the priority for the adoption of relevant codes and standards, Sect. 14.2.9 briefly discusses the hierarchy of codes and standards.

14.2.2 Limit States Design

Limit states are the acceptable limits for the safety and serviceability requirements before failure occurs. They are the states beyond which the structure no longer satisfies the performance requirements specified, which can be defined as

$$S_{upper} \leq R_{lower} \quad (14.1)$$

where S_{upper} and R_{lower} are the upper limit of load (or load induced response) and lower limit of resistance.

Previously, both S_{upper} and R_{lower} were obtained deterministically. A typical method related to this type of determination of load and resistance is the allowable stress method (Sect. 14.2.3), which involves the use of factor of safety to establish the equation above, but it cannot be used to calculate the probability of failure. With the extensive development and application of reliability in recent decades, especially motivated by the design of costly and important structures such as long bridges, large dams, nuclear power plants, offshore platforms etc., design methods by accounting for the uncertainties in loads and resistance and their joint probability of occurrence have been extensively promoted. The method can be used to explicitly calculate the probability of failure of structures. A representative method of this is the load and resistance factor design, as will be presented in Sect. 14.2.5.

Limit state design aims to achieve a structural design that will not become unfit for use with an acceptable target reliability, i.e., the probability of a limit state being reached during its lifetime should be very low. Since the definition of return period is more sensible for engineers, which is an average time in years between exceeding an event of specified magnitude of loading, and is determined based on the acceptable level of risk for relevant parties and/or on a calibration of performances of existing structures, the limit states are often associated with a certain level of return period, which has a relationship with the target reliability, as has been presented in Sect. 9.1.3.

Nowadays, all engineering structures are required to be designed to safely withstand all loads likely to act on them throughout their service lives. Moreover, they shall also satisfy the serviceability requirements, such as limitations of deflection and vibrations, and shall not collapse under accidental loads. Usually, a structure is designed on the basis of the most critical limit state(s) and is also checked for other limit states.

In the limit state design, explicit conditions under which the structure may cease to fulfill its intended function are specified. For these conditions, the applicable capacity or strength is estimated and used in design as a limit for such behavior [4].

The conventional structural design codes normally require a life safety check for a few limit states, i.e., a structure must resist minor earthquake without damage; moderate earthquake without structural damage (or with repairable structural damage) but with non-structural damage; and large earthquake without collapse but with structural and non-structural damage. These provisions are intended to avoid major failures and loss of life, but not to limit damage, maintain functions, or provide for easy repairs. For example, in ISO 19901-2 [5], the ground motion levels are primarily categorized as extreme level earthquake (ELE) and Abnormal Level Earthquake (ALE), of which limited yielding without major structural damage is allowed for the ELE, and significant component damage without a complete loss of structural integrity is acceptable for the ALE condition. To meet a higher requirement than the life safety requirement, checks with several load levels and their corresponding design objectives (performance) can be defined. For example, to ensure a proper post-earthquake functionality, the seismic demands on structural

elements and non-structural elements (such as ceiling, cladding, stairs, utilities, equipment, etc.) may be reviewed for a number of stated levels of seismic hazard from minor/frequent to larger/rare earthquakes. This is the basic philosophy of performance-based design (PBD), as will be discussed in Sect. 14.3, i.e. more limit state checks with different detailed performances/objectives and the corresponding load levels. This can eventually lead to an economical design with lower life-cycle costs than that of the conventional design.

The objective of any seismic code is to provide collapse prevention and an acceptable minimum life safety, to increase the expected structural performance depending on the occupancy or use, and to maintain the continuity of service of essential facilities to function after earthquakes. The prescriptive codes such as Eurocode 8 [6] or IBC [7] require a structure to satisfy a number of checks (limit states) to ensure its integrity for occupancy. Among all those checks, the safety check against the ultimate limit state and accidental limit state are the most important ones. They require that structures have a proper combination of strength and energy dissipation capacity subject to loading at levels corresponding to required return periods. This is fulfilled in the design codes by means of provisions to assure a minimum level of strength and by means of designing and detailing rules for obtaining the required energy dissipation capacity. The minimum strength level is strongly dependent on the energy dissipation capacity of the structure, which is sometimes expressed through the reduction factor (q-factor) [8] as mentioned before. Table 14.1 presents definitions of basic terms used in limit state design.

14.2.3 Allowable Stress Design

Allowable stress design (ASD), also called permissible stress design or elastic working stressdesign, is a design method to ensure that the stress developed in a structure or structural members due to working/service loads (loads at their actual levels) does not exceed the elastic limit. In an ASD, the allowable stress is defined by dividing the resistance (in the elastic range) with a factor of safety (resistance factor) FS . The margin of safety is introduced by considering structural behavior under working/service load conditions and comparing the responses under these conditions with allowable strength, which is normally determined using elastic analysis method:

$$S_n \leq R_n/FS \quad (14.2)$$

where S_n is applied load effects, which can be the load effects due to a single load or a combination of different types of loads by considering the probability of their simultaneous occurrence; R_n is the nominal strength/capacity.

Table 14.1 Definition of basic terms used in limit state designs

Term	Definition
Limit state	State beyond which the structure no longer fulfills the relevant design criteria
Ultimate limit state (ULS)	Conditions that correspond to the resistance to maximum applied actions, which is measured by strength and stability, and it is related to excessive yielding and buckling, brittle fracture, loss of static equilibrium of the structure, or of a part of the structure, considered as a rigid body, e.g. overturning or capsizing, failure of critical components of the structure caused by exceeding the ultimate resistance (in some cases it is reduced due to repeated loads) or the ultimate deformation of the components, and transformation of the structure into a mechanism (collapse or excessive deformation) [9]
Serviceability limit state (SLS)	Conditions that correspond to the criteria governing normal functional use, which is measured by stress, deformation, and cracking, and it is related to deflections that may alter the effect of the acting forces, deformations that may change the distribution of loads between supported rigid objects and the supporting structure, excessive vibrations producing discomfort or affecting non-structural components, motion that exceeds the limitation of equipment, and temperature induced deformations
Fatigue limit state (FLS)	Conditions that correspond to the accumulated effect of repetitive actions, which is measured by stress range and crack growth under repetitive loads, and material toughness
Accidental limit state (ALS)	Conditions that correspond to situations of accidental or abnormal events, which are measured by strength and stability, and are related to structural damage caused by accidental loads, ultimate resistance of damaged structures, maintaining structural integrity after local damage or flooding, and loss of station keeping (free drifting)
Characteristic load	Load with a defined probability of not being exceeded in a given year of return period, see Sect. 14.2.5
Return period	Average time in years between exceeding an event of specified magnitude, see Sect. 9.1.3

ASD was the norm before the promotion of load resistance factor design (LRFD), as will be presented in Sect. 14.2.5. And actually some codes and standards used today are still based on the ASD. It is convenient and shares many common characteristics with LRFD. However, one of the greatest problems with the use of ASD is that it commonly misleads engineers into believing the factor of safety used in the design is a true measure of the safety of the structure [10], and the variability in both loads and resistance is not fully realized, which will be discussed in Sects. 14.2.5 and 14.2.7. Therefore, in many codes and standards, it is specified that if ASD has any conflict with LRFD provision, LRFD should be prioritized to resolve the conflict.

Note that different failure modes or collapse mechanisms are likely to have different safety margin. For example plate yielding can normally be better controlled/understood than the plate buckling. Therefore, different failure modes can have different values of factor of safety.

14.2.4 Plastic Design

Note that in the allowable stress design, an initial yielding in most cases does not represent the capacity of a structure, implying that the structure has a certain amount of capacity reserve beyond the yielding. To realize this capacity reserve, as an extension of allowable stress design in the plasticity regime, plastic design is introduced based on a consideration of failure conditions rather than the working load condition. In plastic design, a structure or a structural member is selected and dimensioned by using the criterion that the structure will fail (collapse or exhibit extremely high deformation) at a load substantially higher than the working load.

By adopting plastic design, the structures can be further optimized to avoid over-design, and the plastic design also allows for a detection of certain critical structural responses due to the development of plasticity and the subsequent variation in stiffness. This is more important for highly redundant structures, as a variation in local stiffness due to plasticity development can significantly modify the load transmission path.

As some background knowledge to plastic design, Fig. 14.2 shows the stress-strain diagram obtained from uni-axial tensile tests for a specimen made from typical structural steel. Below the proportional point, strain and stress have a linear (proportional) relationship, and the slope of the curve is constant and referred to as modulus of elasticity E . For typical low carbon steel, this point ranges from 200 to 300 MPa. With a load increase from the proportional point, the linear stress-strain relationship no longer exists. Instead, the slope of stress-strain curve becomes smaller and smaller until the yielding point is reached. After passing the yielding point, the curve becomes flat with a significant elongation, i.e., strain increases without noticeable change in stress. This flat part of the curve indicates a process of yielding. This is followed by strain hardening in which the stress level rises again with a declined slope (compared with the slope during the linear elastic range) of the curve until the ultimate strength (maximum load value) is reached. The strain level corresponding to the ultimate strength is many times that at yielding point. After passing the ultimate strength point, the increase of strain is actually accompanied by a reduction in stress (load), and the fracture finally occurs.

For a beam subject to bending moment, by neglecting strain hardening (which is normally conservative) and assuming that the entire cross-section of the beam can be fully utilized when it reaches plasticity, the stress distribution along the beam's cross-section can be divided into three stages: elasticity, partial plasticity and full plasticity, as shown in Fig. 14.3. It can be shown that compared to initial yielding (ii), the development of plasticity can increase the resistance of the beam significantly, which shows a significant benefit of plastic design.

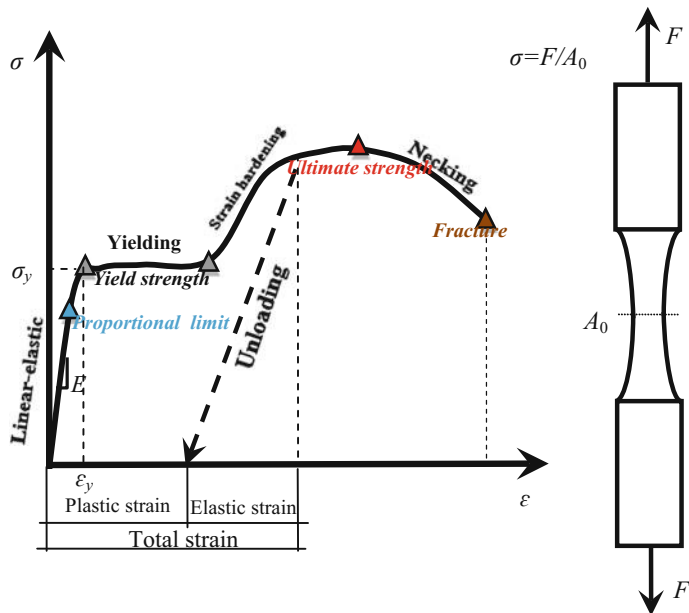


Fig. 14.2 Engineering stress (σ)–strain (ε) curve for a typical ductile steel material that has an obvious yield strength (not to scale), A_0 is undeformed cross-section area

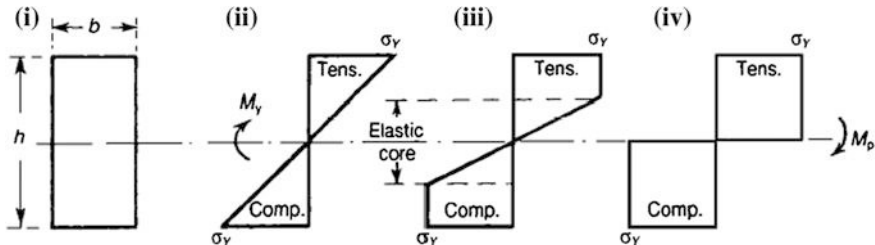


Fig. 14.3 Process of elasticity-initial yielding (ii), partial plasticity (iii) and full plasticity (iv) for a rectangular cross-section beam under pure bending [11]

14.2.5 Load and Resistance Factor Design

14.2.5.1 Probability of Failure

Since the probability distribution between the load and resistance items is different, the major difference between allowable stress design (ASD) and load resistance factor design (LRFD) is the expression of the safety factor. In ASD, uncertainties are generally lumped into a single safety factor and applied to the stress that defines the allowable limits (in the traditional stress based terminology of ASD). While in

LRFD, load factors are applied to various types of loads and a resistance factor is applied to the strength [12]. Therefore, LRFD is essentially meant to consider the uncertainties in both loading and resistance, and to ensure a prescribed safety margin by using procedures from probability theory. By splitting the factor of safety into the independent load and resistance factors, LRFD can result in safer (in a reliability sense) and probably less expensive structures, depending on the predictability of the load types being used.

As shown in Fig. 14.4, the LRFD design can be described as:

$$\gamma_{F1}S_{k1} + \gamma_{F2}S_{k2} + \cdots + \gamma_{FN}S_{kN} \leq R_k/\gamma_M \quad (14.3)$$

where S_{k1}, \dots, S_{kN} are the characteristic values of N types of load effects acting on a structure. They typically represent load effects corresponding to a specific annual probability of occurrence (or return period). For example, for design of offshore structures, the characteristic load at ULS load combination normally cherishes an annual probability of exceedance equal to, or less than, 10^{-2} (100 years), and the characteristic load effects at ALS load combination for damaged structure may correspond to load effects with the most probable annual maximum value or an annual probability of exceedance equal to, or less than around 10^{-4} (10,000 years). The characteristic load effects at FLS condition normally correspond to a load with expected load history, and the characteristic load effects at SLS condition correspond to a load effect with a specified value depending on operational requirements; $\gamma_{F1}, \dots, \gamma_{FN}$ are the load factors (partial safety factors) for N types of loads. They are used to account for the possibility of unfavorable deviations of the action values from the representative values (fundamental variability in environmental loads), the uncertainties in the modeling of load effects (such as the computational model and statistical uncertainty due to a lack of knowledge), and the uncertainties in the

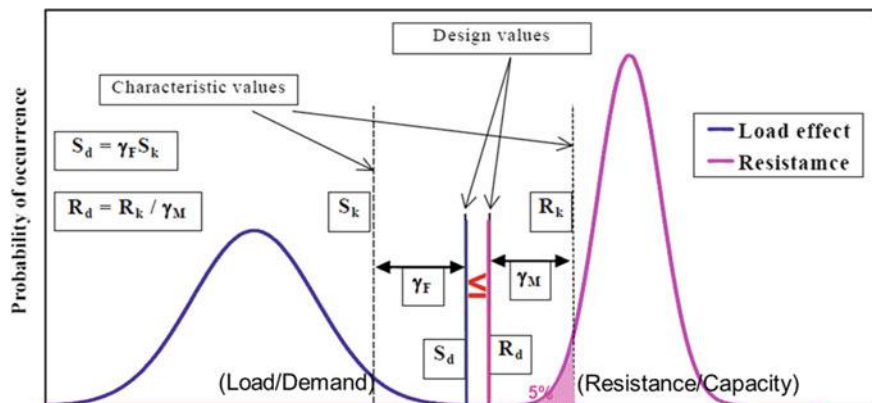


Fig. 14.4 An illustration of LRFD design (courtesy of John Michael Rotter, University of Edinburgh)

assessment of the limit states being considered; R_k is the characteristic value of the particular resistance of the structure or resistance of materials of the structure, which typically corresponds to characteristic or nominal ($=R_n$) values for the material properties and dimensions, it is usually determined by a 5 %-fractile material strength (a lower bound or 95 % exceedence value) from tests; γ_M is the partial factor (resistance factor or partial safety factor) for particular resistance, which accounts for the uncertainties due to material properties, dimensions and type of structures, and the capacity of the structure (related to corrosion, quality of the construction, method considered for the determination of the capacity, etc.), it is based on past experience, but is in principle meant to provide an acceptable level of safety or performance, its value also depends on the limit states and the material (indicating different degrees of control in the manufacturing process of structural materials, e.g., steel, concrete, composites, timber, mortar and bricks) applied; $R_d = R_k/\gamma_M$ is the corresponding design resistance of the structural element.

Readers should notice that, in LRFD, both the applied loads (left hand side of the equation above) and the strength/resistance (right hand side in the equation above) are fictitious due to the factors applied. Moreover, as the partial safety factors for both load and resistance represent the uncertainties in the characteristic values, while due to a lack of detailed statistical data on all the parameters considered in design and also the complexity of the statistical analysis, there is a compromise to use a more subjective assessment of the partial safety factors than is mathematically consistent with the design philosophy.

Furthermore, readers need to be reminded that even though uncertainties due to design errors and construction errors are also important, they are normally not accounted for by design codes but are addressed through proper quality assurance (QA) such as third party verification and/or QA by engineers who are not involved in the same design project before the QA.

In cases where a high resistance is unfavorable for design, the characteristic resistance may be determined as an upper characteristic resistance. The corresponding probability may be of the same level as the probability of a lower value, e.g. 5 % versus 95 % fractile. For geotechnical analyses “low probability” will in most cases mean a conservatively estimated mean value. As discussed in Sect. 7.4, for performing site response analysis, it is recommended that a sensitivity analysis be performed by accounting for the variation of soil properties from lower bound, average (best-estimate) to upper bound value. If the ground motions are not sensitive to the variation in soil properties, typically, the best-estimate value of soil properties can be used to compute the ground motion time histories. It is consequently expected that designers involved consider the relevant cases. When the action effect is increased with the material resistance, the design may also be based on an upper characteristic resistance, e.g. based on 95 % fractile. An example of this is an analysis of pile driving or lifting, in which the upper bound soil resistance is normally used. Design against fatigue failure in steel, aluminum and concrete may adopt S-N curves with characteristic resistance based on 2.3 % fractile. Fracture mechanics analyses of crack propagation can be used in special cases.

Design actions and resistances may be calculated by using deterministic computational models.

In Eurocodes [13, 14], for concrete or timber structures, characteristic strength and design strength given by the corresponding failure probability are used in the design procedures, implying a partial safety factor of material $\gamma_M > 1.0$. However, in the case of steel structures, the nominal values instead of characteristic values of steel yield strength are utilized for the structural design, with a partial safety factor for material $\gamma_M = 1.0$. This is because manufacturers of steel structural components present strength of steel with different evaluation and determination methods, which are not the characteristic value any more. These values have been derived based on the statistical and probabilistic evaluation of the data sets of actual material properties obtained from various steel producers.

The equation above can be simply expressed as:

$$S \leq R \quad (14.4)$$

where S and R represent the factored loads and factored resistance (strength), respectively.

Note that both the load and resistance factor vary significantly depending on the applications. For example, in structural engineering problems, the determination of loads are usually less certain than that of resistances/materials. Therefore, S typically has a larger variability than R , implying that S has a higher coefficient of variation, hence a wider PDF. The opposite trend can typically be found in geotechnical design problems.

It is important to build the equation above in connection with probabilistic measures. Therefore, the probability of failure, which is the probability that the factored loads exceed the factored resistance, can be expressed as:

$$P_f = P(R \geq S) \quad (14.5)$$

Given that the load effects s and resistance r are varying randomly in a statistically known manner, a safety margin can then be established as:

$$m = r - s \quad (14.6)$$

For all combinations of r and s that satisfy the condition $m > 0$, the design is the on safe side, and for those combinations giving a safety margin $m \leq 0$, the structure is suspected to fail. Therefore, the equation above can be utilized as a measure of failure probability. By observing Fig. 14.4, it is noticed that the failure probability depends on both the difference between the load and resistance and the variability of them.

With the construction of the equation above, one has moved from deterministic design to probabilistic design, in which the material properties, structural member dimensions, and loads are interpreted as random variables x , uncertainties can be described if the probability density function of the random variables are known.

Therefore, if their probability density functions $f_R(x)$ and $f_S(x)$, with the corresponding probability distribution functions or cumulative distribution functions (CDFs), $F_R(x)$ and $F_S(x)$, are known, the safety margin m can be defined as a random variable M , with a probability density function $f_M(x)$ and a probability distribution function $F_M(x)$. The equation to determine the probability of failure can then be rewritten as:

$$P_f = P[M \leq 0] = F_M(0) = \int_{-\infty}^0 f_M(x)dx \quad (14.7)$$

Since it is not possible to define $f_M(x)$ and $F_M(x)$ analytically except for a few special cases, the equation above can be written in terms of load and resistance effects:

$$P_f = P[R - S \leq 0] = \int_{-\infty}^{+\infty} F_R(x)f_S(x)dx = F_M(0) \quad (14.8)$$

The equation above indicates that when the load effects lie in the interval $(x, x + dx)$ and the resistance is smaller than x , the probability of failure is $F_R(x)f_S(x)dx$. The total probability of failure is equal to the integral above when the load effect is in the interval $(-\infty, +\infty)$.

Alternatively, the probability of failure expressed in the equation above can also be written as:

$$P_f = \int_{-\infty}^{+\infty} (1 - F_S(x))f_R(x)dx = F_M(0) \quad (14.9)$$

Since the resistance cannot be negative, the lower boundary for the integrals in the two equations above may be changed into 0. Moreover, the integral of the three equations above usually does not have a closed form solution. It can be solved numerically by either numerical integration or Monte-Carlo methods [15].

The reliability can then be calculated as:

$$P_r = P[R - S > 0] = 1 - P_f = 1 - \int_{-\infty}^{+\infty} F_R(x)f_S(x)dx = 1 - F_M(0) \quad (14.10)$$

Due to a lack of statistical data that defines probability density functions of load and resistance variables, as well as the fact that the expression of probability density functions are complicated, the load and resistance variables can normally be defined by their mean values and variance. It is then convenient to present a less complicated probabilistic measure for the reliability of the structure, namely safety index or reliability index β originally proposed by CA Cornell [16] in 1969, which is the number of standard deviations of the derived probability density function m , separating the mean safety margin from the nominal failure value of m being zero:

$$\beta = \mu_M / \sigma_M \quad (14.11)$$

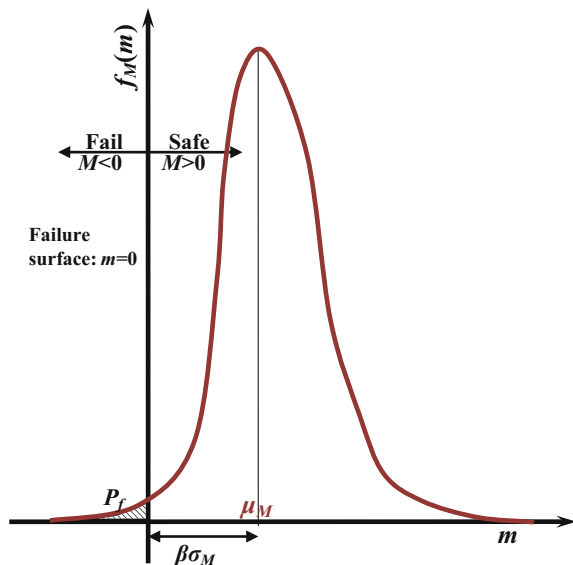
where μ_M and σ_M are the mean value and standard deviation (square root of the variance) of safety margin M .

Provided the safety margin can be described by only one normally distributed random variable, where the failure surface is a point $m = 0$, the exact safety index β can be defined as the distance between the expected value μ_M of the safety margin and the boundary for failure $m = 0$ as shown in Fig. 14.5. And the distance is usually measured in terms of σ_M .

When both R and S are independent and normally or lognormally distributed variables, the exact safety index is directly related to the failure probability through the standard normal distribution function:

$$\begin{aligned} P_f &= P[M \leq 0] = \Phi[(0 - \mu_M)/\sigma_M] = \Phi(-\beta) \\ &= 1 - \Phi(\beta) \leftrightarrow \beta = -\Phi^{-1}(P_f) \end{aligned} \quad (14.12)$$

Fig. 14.5 Illustration of safety index β



where $\Phi()$ is the standard normal distribution function, defined as:

$$\Phi(x) = \int_{-\infty}^x \frac{1}{\sqrt{2\pi}} e^{-t^2/2} dt \quad (14.13)$$

The values of the standard normal distribution function can also be obtained by a spreadsheet (e.g., NORMSDIST in Excel) or from various mathematical handbooks. Table 14.2 shows a few correspondences between β and P_f .

For a quick estimation, the failure probability can also be approximated as:

$$P_f \approx 0.475 \exp(-\beta^{1.6}) \quad (14.14)$$

or be more roughly estimated as:

$$P_f \approx 10^{-\beta} \quad (14.15)$$

Therefore, by assuming that both R and S are independent and normally distributed variables (as shown in Fig. 14.4), the safety margin m , which is a linear combination of R and S , also follows a normal distribution. Their mean value μ_M and variance σ_M^2 can be calculated as:

$$\mu_M = E_M = \mu_R - \mu_S \quad (14.16)$$

$$\sigma_M^2 = V_M = \sigma_R^2 + \sigma_S^2 \quad (14.17)$$

where $E[]$ and $V[]$ are the expected value and variance, respectively.

Therefore, the safety index can be calculated as:

$$\beta_N = \frac{\mu_R - \mu_S}{\sqrt{\sigma_R^2 + \sigma_S^2}} = \frac{\mu_R/\mu_S - 1}{\sqrt{(\mu_R/\mu_S)^2 V_R^2 + V_S^2}} \quad (14.18)$$

As the performance of the physical behavior of engineering systems usually cannot obtain negative values (load and resistance), it is better described by a lognormal distribution [17]. The safety margin can then be expressed as:

$$m = \ln R - \ln S = \ln(R/S) \quad (14.19)$$

Table 14.2 Correspondences between β and P_f

β	1.0	1.2	1.28	1.4	1.6	1.8	2.0	2.2
P_f (%)	16	12	10	8.1	5.5	3.6	2.3	1.4
β	2.33	2.7	3.09	3.3	3.7	4.0	4.4	4.9
P_f (%)	1.0	0.35	0.1	0.048	0.011	0.0032	0.00054	0.000048

In case both R and S are independent and lognormally distributed variables, even though $R-S$ is not lognormally distributed, $\ln R$ and $\ln S$ follow normal distributions, and thus the safety margin, $m = \ln R - \ln S$ follows a normal distribution. As such, the relationship obtained in Eq. (14.12) is still valid to calculate the probability of failure. One can show that the safety index can be calculated as [18]:

$$\beta_{LN} = \frac{\ln\left[\left(\mu_R/\mu_S\right)\sqrt{(1+V_S^2)/(1+V_R^2)}\right]}{\sqrt{\ln[(1+V_R^2)(1+V_S^2)]}} \approx \frac{\ln(\mu_R/\mu_S)}{(V_R^2 + V_S^2)} \quad (14.20)$$

Upon the presentation above, it is known that in LRFD, it is important to perform a calibration process to determine the load factor and the resistance factor so that the distributions of R and S can answer the requirements of a specified safety index. In other words, the γ_F and γ_M described in Fig. 14.4 need to answer to the prescribed target reliability (i.e., a predetermined probability of failure) in the two equations above. Several solutions are available for this calibration purpose, such as first order reliability method (FORM) and Monte-Carlo simulation etc., as will be presented in Sects. 14.2.5.2 and 14.2.5.3. References [15, 19] also give an elaboration of this topic.

The definition of safety index in Eq. (14.11) and one-to-one relation between the failure probability and the safety index calculated in Eq. (14.12) are also valid when R and S are correlated, but the variance σ_M^2 must be calculated to account for the correlation between R and S :

$$\sigma_M^2 = \sigma_R^2 + \sigma_S^2 - 2\rho_{R,S} \cdot \sigma_R \cdot \sigma_S \quad (14.21)$$

where $\rho_{R,S}$ is the correlation coefficient between R and S , ranging from -1.0 to 1.0 , as defined by:

$$\rho_{R,S} = \text{Cov}[R, S]/(\sigma_R \cdot \sigma_S) \quad (14.122)$$

where $\text{Cov}[R, S]$ is the covariance of R and S , defined by:

$$\text{Cov}[R, S] = \sigma_{R,S} = E[(R - \mu_R)(S - \mu_S)] = \int_{-\infty}^{+\infty} \int_{-\infty}^{+\infty} (r - \mu_R)(s - \mu_S)p(r, s)drds \quad (14.23)$$

where $p(r, s)$ is the probability density function, which can be represented as a surface above a horizontal plane, and the cumulative probability ($P(r, s)$) of r lying in the range between r and $r + dr$ as well as s lying between s and $s + ds$ is $p(r, s)drds$.

The load and resistance factor design can normally be used with a few limit states: serviceability limit state (deflection), ultimate limit state (yielding, fracture

and buckling), fatigue limit state, and accidental limit state (progressive collapse limit state) as presented in Sect. 14.2.2.

If the safety margin $m = f(x)$ is a linear combination of n basic variable x_i , and the random variation of all basic variables can be described by normally distributed independent random variables X_i , the resulted safety margin can then be described by a normally distributed random variable M :

$$M = f(X) = a_0 + a_1 X_1 + a_2 X_2 + \cdots + a_n X_n \quad (14.24)$$

where $i = 1, \dots, n$.

And the mean value and variance of the safety margin function above are:

$$\mu_M = a_0 + a_1 \mu_{X_1} + a_2 \mu_{X_2} + \cdots + a_n \mu_{X_n} \quad (14.25)$$

$$\sigma_M^2 = a_1^2 \sigma_{X_1}^2 + a_2^2 \sigma_{X_2}^2 + \cdots + a_n^2 \sigma_{X_n}^2 \quad (14.26)$$

As a special case of the three equations above, if the safety margin is defined by two independent random variables that give $M = f(X) = a_0 + a_1 X_1 + a_2 X_2$, the failure surface is a curve $f(x) = 0$. If X_1 and X_2 are normally distributed random variables, their probability density functions are then symmetrical with respect to their mean values, and the curves for each constant level of the probability density function are in a form of ellipses, which is shown in Fig. 14.6. While since the variance $\sigma_{X_1}^2$ and $\sigma_{X_2}^2$ are different in x_1 and x_2 axis, it is difficult to find a simple measurement of the distance between point (μ_{X_1}, μ_{X_2}) and the failure surface $f(x) = 0$. Therefore, a linear variable transformation must be made to replace the two independent normally distributed random variables X_1 and X_2 by two standardized normally distributed random variables Z_1 and Z_2 with $\mu_{Z_1} = \mu_{Z_2} = 0$ and $\sigma_{Z_1} = \sigma_{Z_2} = 1$, which is essentially to transform the linear failure surface $f(x) = 0$ in x -space to linear failure surface $f_Z(z)$ in z -space:

$$z_1 = (x_1 - \mu_{X_1}) / \sigma_{X_1} \quad (14.27)$$

$$z_2 = (x_2 - \mu_{X_2}) / \sigma_{X_2} \quad (14.28)$$

Therefore, the contours with ellipsed shape shown in Fig. 14.6 in x -space can now be transformed into concentric circles with their center at the origin in z -space as shown in Fig. 14.7. Cornell's reliability β_C can be defined as the shortest distance from the origin to the failure surface as shown in Fig. 14.7. The point z^* shown in Fig. 14.7 is called the design point.

Obviously, a high value of safety index indicates a lower possibility of failure, but a more expensive design. Therefore, the design must account for the cost and consequence, so that a target safety index acceptable to various parties can be reached. In reality, consequences and risk acceptance in society are also implicitly considered in structural design codes, leading to required levels of reliability in various situations. Examples of possible classes of consequences include [20]:

Fig. 14.6 Contours of the joint probability density function for normally distributed X_1 and X_2

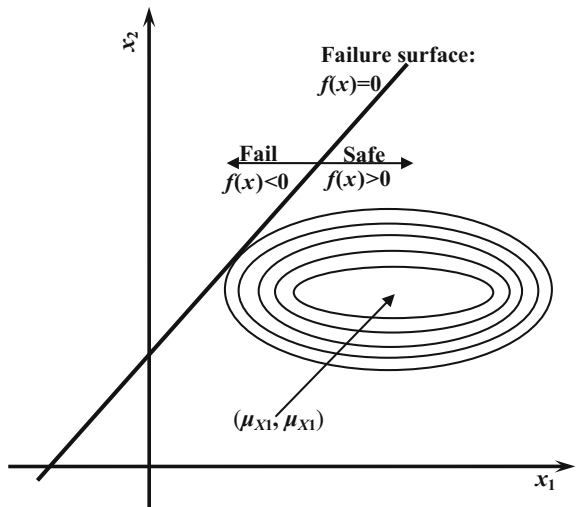
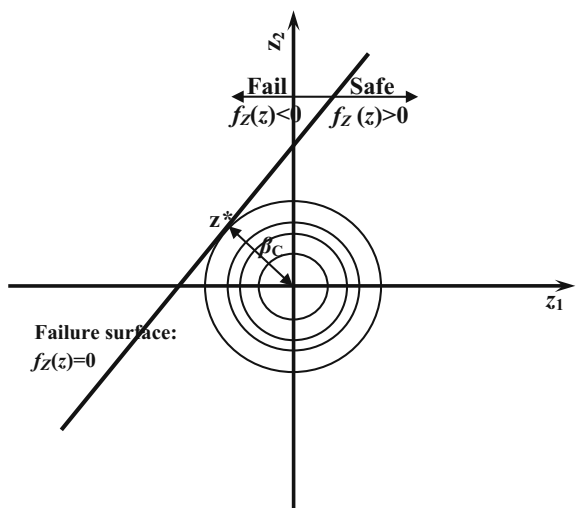


Fig. 14.7 Contours of the probability density function for the standardized normally distributed Z_1 and Z_2 and an explanation of Cornell's reliability index β_C



1. Minor consequences: risk to life, given a failure, is small to negligible, and economic consequences are small or negligible (e.g. agricultural structures, silos, masts).
2. Moderate consequences: risk to life, given a failure, is medium, or economic consequences are considerable (e.g. office buildings, industrial buildings, apartment buildings).

3. Large consequences: risk to life, given a failure, is high, or economic consequences are significant (e.g. main bridges, theaters, hospitals, high-rise buildings, offshore platforms).

Example [15] A column fixed at its bottom is subject to two lateral forces F_1 and F_2 at 4 and 8 m above the fixed end, as shown in Fig. 14.8. The bending moment capacity of the column at the fixed end is B , the means and variations of the basic variables (B, F_1, F_2) are: $\mu_B = 250 \text{ kN m}$, $\sigma_B^2 = 900 (\text{kN m})^2$, $\mu_{F1} = \mu_{F2} = 10 \text{ kN}$, $\sigma_{F1}^2 = \sigma_{F2}^2 = 9 (\text{kN})^2$. Calculate the safety index and the failure probability when: (1) the two lateral forces F_1 and F_2 are statistically independent; (2) the two forces are dependent with a correlation coefficient of $\rho = 2/3$.

Solution As the largest bending moment is at the column's bottom end, the safety margin can be calculated as:

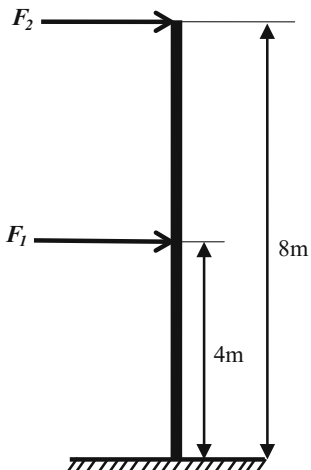
$$m = r - s = B - 4F_1 - 8F_2$$

Establish the safety index: $\beta = \mu_M/\sigma_M$

where $\mu_M = \mu_B - \mu(4F_1) - \mu(8F_2) = 130 \text{ kN m}$

$$\sigma_M^2 = \sigma_r^2 + \sigma_s^2 = \begin{cases} \sigma_B^2 + (4\sigma_{F1})^2 + (8\sigma_{F2})^2 = 1620 (\text{kN m})^2 & \text{for } \rho_{F1F2} = 0 \\ \sigma_B^2 + (4\sigma_{F1})^2 + (8\sigma_{F2})^2 + 2\rho(4\sigma_{F1})(8\sigma_{F2}) = 2000 (\text{kN m})^2 & \text{for } \rho_{F1F2} \neq 0 \end{cases}$$

Fig. 14.8 A column fixed at the *bottom* is subject to two lateral forces F_1 and F_2



Therefore, when

- (1) when the two forces are statistically independent: $\beta = \mu_M / \sigma_M = \frac{130}{\sqrt{1620}} = 3.23$, $\Phi(-\beta) = P_f = 0.0006$.
- (2) when the two forces are statistically dependent: $\beta = \mu_M / \sigma_M = \frac{130}{\sqrt{2000}} = 2.90$, $\Phi(-\beta) = P_f = 0.0019$.

By comparing the results above, it is noted that the failure probability is larger when the random load variable F_1 and F_2 are statistically dependent.

14.2.5.2 Probability of Failure for Non-linear Safety Margin Functions

It is noted that in Sect. 14.2.5.1, the safety margin function $m = f(x)$ is a linear function of basic variables, the resultant safety index is Cornell's reliability index. However, many safety margin functions are non-linear, which can be expressed by Taylor series expansion. In case a safety margin function is only approximated by its first order (linear) Taylor series terms, the resultant safety index is called first-order-reliability-index. In case both the first and second-order terms are retained, the resultant safety index is called second-order-reliability-index. The corresponding methods are first order reliability method (FORM) and second-order reliability method (SORM), respectively. Below a brief introduction of the two methods is given.

By generating Taylor series of the safety margin $m = f(x)$ around point $q(q_1, q_2, q_3, \dots, q_n)$, and retaining only the first order terms, one obtains a linearized safety margin:

$$m = f(x) \approx f(q) + \sum_{i=1}^n \frac{\partial f}{\partial x_i}(q)(x_i - q_i) \quad (14.29)$$

If x_i can be described by normally distributed random variables X_i , the safety margin m can then be approximately described by a normally distributed random variable:

$$M \approx M_{FO} = f(q) + \sum_{i=1}^n \frac{\partial f}{\partial x_i}(q)(X_i - q_i) \quad (14.30)$$

Based on the equation above, a first-order-reliability-index β_{FO} can be calculated as:

$$\beta_{FO} = \frac{f(\mathbf{q}) + \sum_{i=1}^n \frac{\partial f}{\partial x_i}(\mathbf{q})(E[X_i] - q_i)}{\sqrt{\sum_{i=1}^n \left(\frac{\partial f}{\partial x_i}(\mathbf{q}) \sigma_{X_i} \right)^2}} \quad (14.31)$$

If the linearized point \mathbf{q} is chosen such that $\mathbf{q} = (\mu_1, \mu_2, \mu_3, \dots, \mu_n)$, the first-order-reliability-index can be determined by:

$$\beta_{FO} = \frac{f(\mathbf{q})}{\sum_{i=1}^n \left(\frac{\partial f}{\partial x_i}(\mathbf{q}) \sigma_{X_i} \right)^2} \quad (14.32)$$

It should be noticed that the first-order-reliability-index β_{FO} is not a unique measure of the reliability since the determination of its value depends on the choice of the linearization point and the approximation made for the safety margin (which is not unique either), a structure can have more than one reliability index. However, the failure surface for a structure is always unique because regardless how the safety margin function is calculated, it is always the same combination of $x_1, x_2, x_3, \dots, x_n$ that gives failure. Therefore, it is desirable to have a safety index defined based on the failure surface rather than safety margin, so that the resulting safety index is unique (i.e., a failure function invariant) since all equivalent failure functions result in the same failure surface in the x -space and therefore also in z -space. This is exactly what Hasofer and Lind proposed [21], which results in Hasofer-Lind safety index β_{HL} to determine the realibity of a structure. Similar to what Cornell's reliability is defined in z -space, β_{HL} is defined as the shortest distance from the origin to the point \mathbf{z}^* on the failure surface ($f_Z(z) = 0$) as shown in Fig. 14.9, such that:

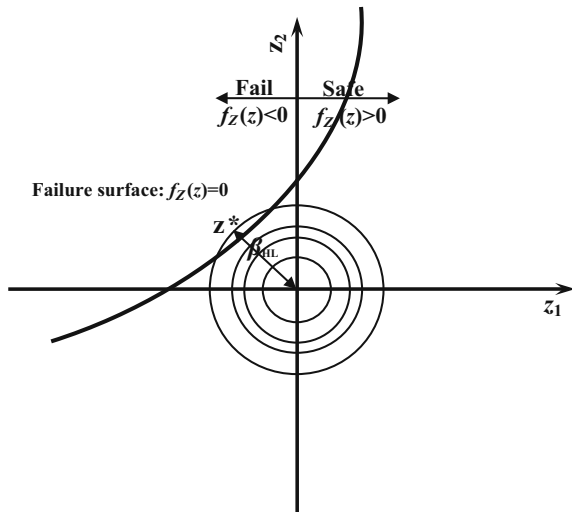
$$\beta_{HL} = |\mathbf{z}^*| = \min |\mathbf{z}^*| = \min \sqrt{\sum_{i=1}^n z_i^2} \quad (14.33)$$

From the definition above, the reliability index for a non-linear failure surface is equal to the reliability index for the linear tangent hyperplane in the design point \mathbf{z}^* . In order to calculate β_{HL} , various types of optimization method can be used to determine point \mathbf{z}^* on the failure surface.

A second-order-reliability-index can be solved with an exact analytical expression. For a detailed solution, readers may refer to [22].

Note that the transformed probability density function $f_Z(z)$ in z -space decreases rather quickly with an increasing $|Z|$. The largest contribution to the probability of failure comes from the area around the design point \mathbf{z}^* shown in Fig. 14.9. Therefore, to calculate reliability of many structures, β_{HL} is a close approximation of the exact value of safety index β defined in Eq. (14.12).

Fig. 14.9 Illustrations of contours of the probability density function for non-linear failure surface, normalized coordinates, an explanation of Hasofer-Lind safety index β_{HL} and design point z^*



Moreover, it is obvious that for linear failure surface and normally distributed basic variables X_i , the definition in Eq. (14.11) and the Hasofer-Lind safety index result in the same β -value. Therefore, Hasofer-Lind safety index β_{HL} and Cornell's reliability index β_C equal the exact safety index β :

$$\beta_{HL} = \beta_C = \beta \quad (14.34)$$

On the other hand, if the safety margin function is non-linear, it cannot be described by a normally distributed random variable. Even though Eq. (14.12) is still valid to calculate the exact failure probability β , it is approximate:

$$\beta_{HL} \approx \beta = -\Phi^{-1}(P_f) \quad (14.35)$$

In summary, the probability of failure with FORM/SORM can be determined in four steps [15]:

1. Transform the random vector X in x-space to a standardized normal random vector Z in z-space
2. Determine the design point z^*
3. Approximate the failure surface in z-space with respect to z^*
4. Determine the β_{FO} , β_{HL} or β_{SO} as an approximation of the reliability index β .

For more details about FORM and SORM, Refs. [19, 23, 24, 25] are recommended.

14.2.5.3 Monte-Carlo Method for Calculating Probability of Failure

Instead of calculating the reliability index, the reliability can also be directly calculated using the Monte-Carlo method, which essentially involves performing a simulation (virtual experiments) based on repeated random sampling to obtain numerical results. In this method, for each variable, the random values are generated using, for example, a Gaussian random number generator and are scaled with the specified standard deviation. If a two standard deviation is assumed, it means a 95 % confidence estimate. Figure 14.10 shows an example of random number

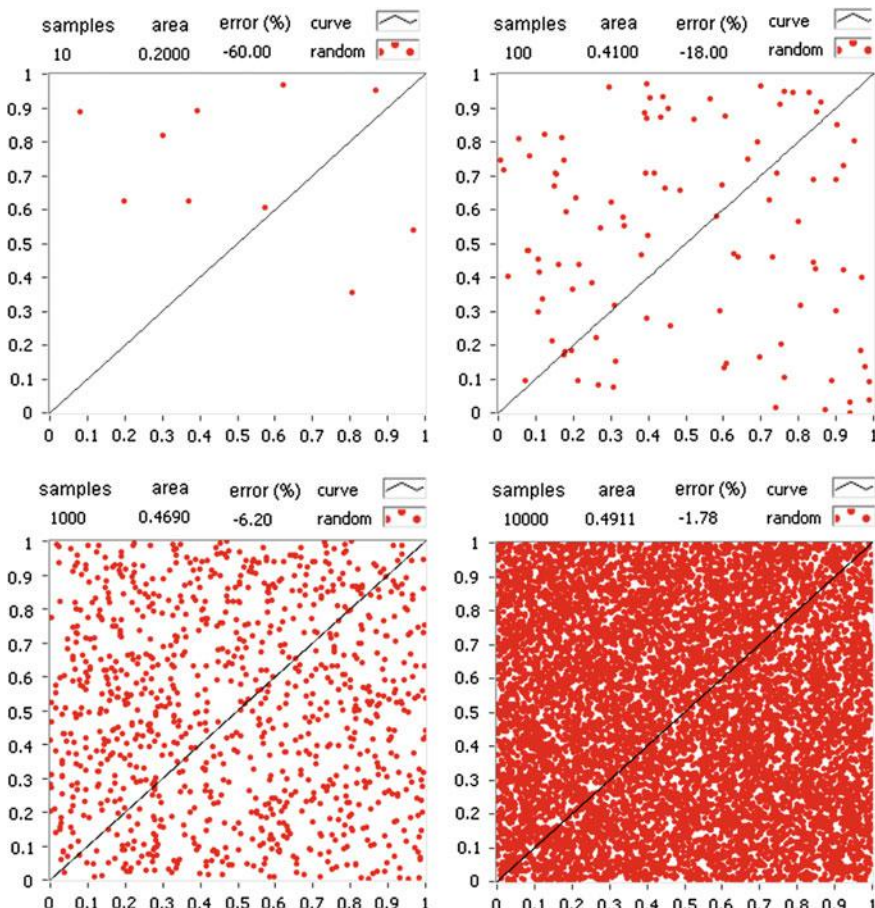


Fig. 14.10 Random value generation in a Monte-Carlo simulation and a comparison of random value points with the value of the variable function (*line*) for different number of samplings; the coordinates of random values in *horizontal* and *vertical* axis are randomly varied and compared to the value of the variable function for each coordinate; it is obvious that with an increase in the number of samples, the percentage of error decreases

generator in a Monte-Carlo simulation. The individual error values are then summed and added to the true value of a variable to obtain a calculated value (“measured” from a “sampling”) of that variable with errors from the specified error populations. After obtaining the measured values of the variables, result(s) of an objective test are calculated. The 95 % confidence uncertainty of each result is obtained by multiplying the calculated standard deviation by a factor of 2. The procedure above corresponds to running the test once, and it should be repeated many times (thousands or even more depending on the problem considered), and the means and standard deviations of the distribution of the results can then be determined. The Monte-Carlo method is a relatively convenient way to incorporate assumed non-Gaussian error distributions for the variables or to specify any degree of confidence level. Moreover, this method is straightforward for investigating complex cases, especially when the number of variables are large [26]. Obviously, the major drawback of this method is its relatively high computation cost as mentioned above.

Both FORM and SORM are analytical and approximate methods that can be conveniently used in numerical solution. They generally apply when the probability of failure is small, e.g., 10^{-3} – 10^{-8} . When such low probability of failure is concerned, the computation time by using FORM or SORM is much less than other numerical methods such as Monte-Carlo method. Further, the difference between FORM and SORM is small for cases with large safety index (small probability of failure). However, for higher probability of failure the error in the FORM approximation can be significant. Moreover, the CPU-time for FORM increases linearly with the number of the basic variables, where the CPU-time for SORM increases approximately with the square of the number of basic variables.

14.2.6 *Levels of Reliability Method*

In case only mean values, variance and correlation of load and resistance variables are used to calculate a nominal probability of failure, usually expressed in terms of a reliability or safety index, as presented in Sect. 14.2.5, the evaluation method is referred to as semi-probabilistic method (level 2), which is sometimes also called the second moment reliability method.

In contrast, a direct calculation of failure probability is referred to as a full-probabilistic method (level 3). This method makes use of a full-probabilistic description of joint occurrence of various quantities that affect the response of structures and take the true nature of the failure domain into account, which can determine the “exact” probability of failure, and be used to calibrate the semi-probabilistic approach. In some design codes, they are also recommended for particular situations. It is noted that the results based on a full-probabilistic method strongly depend on the modeling of the tails in the probability distribution involved. This makes the use of full-probabilistic method rather difficult or not attainable in practice, as for instance the tail in the load (and response, e.g., seismic loading and

response) and/or resistance (e.g., soil strength) is rather uncertain (i.e. “fat tail” in the probability distribution).

On the other hand, in ASD (level 1), the failure probability cannot be defined (an essential reason why LRFD is preferred over the ASD). Instead, factors for resistance and/or load are used separately, and engineers work with random resistance and/or load variables that are represented only by their mean value (lowest statistical moments of load and resistance), or any other characteristic value, while the variation in both load and resistance cannot be reflected, which will be further explained in Sect. 14.2.7.

In addition to the 3 levels of methods introduced above, in some literatures, there is further a level 4 method, which is essentially an extension of the level 3 (full-probabilistic) method by introducing consequences of a failure with respect to economical and environmental terms. This can be regarded as a decision support tool, as it can be used to compare the overall (life-cycle) cost of various alternative designs [27].

14.2.7 ASD Versus LRFD

In ASD, the focus is on keeping the stresses resulting from the design load effects (actual stress) under a certain working stress level (allowable stress) that is usually based on material strength or successful similar past experience. For example, the allowable stress can be defined as a certain fraction of the mechanical properties of materials (e.g., uni-axial yield or ultimate tensile strength). On the other hand, LRFD compares required strength to actual strength. However, the difference between measuring strengths versus stresses does not present any essential difference as it is normally just a matter of multiplying or dividing both sides of the limit state inequalities by a factor, depending on which way is chosen. In fact, in some codes, the specification of ASD has been switched from the traditional stress based terminology to a strength based terminology, virtually eliminating this difference between the two methods.

However, it is almost impossible to incorporate the uncertainties associated with either load or resistance in ASD. This is because in ASD, engineers work with random load and resistance variables that are represented only by their mean value, or any other characteristic value, but the variation in both load and resistance cannot be accounted for. This can be explained by observing Fig. 14.11, which shows probability distribution for load effects and resistance. Here we define two safety factors: one is the central safety factor $FS_\mu = \mu_R/\mu_S$, and the other is the nominal factor of safety $FS_k = \mu_k/\mu_k$. In case uncertainties in the resistance R are increased, the probability density function curve changes from a solid line into a dashed line, which is more broad, as shown in Fig. 14.11. It is likely that the mean resistance μ_R of the curve does not change, indicating an increase in the variation (uncertainties). Therefore, even though the central safety factor FS_μ (associated with ASD) remains unchanged, utilizing the distribution with the higher variation in resistance will

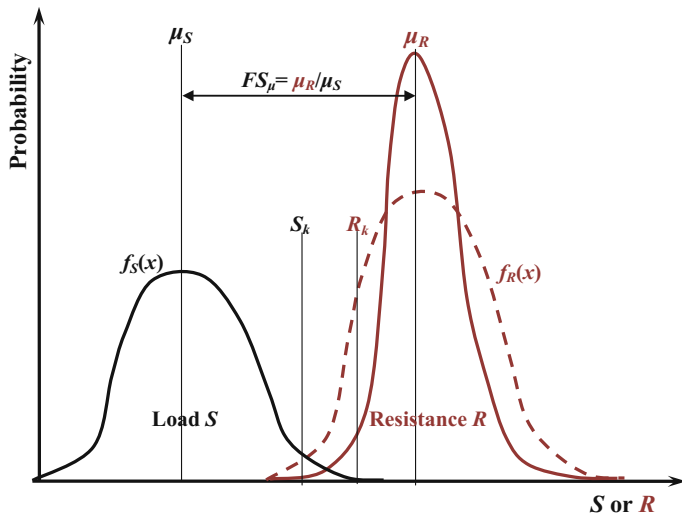


Fig. 14.11 A schematic illustration of probability density distribution for both loads (S) and resistance (R) with smaller uncertainties (solid curve) and larger uncertainties (dashed curve) for the resistance

require the application of a higher partial safety factor (resistance factor) γ_M (associated with LRFD), so that the same prescribed probability of failure can be achieved.

Upon the explanation above, it is known that LRFD and ASD loads are not directly comparable because they are used differently by design codes, and are normally not allowed to be mixed in the same design project. For example, the service load in ASD is unfactored while the load defined in LRFD is factored. Moreover, LRFD loads are normally compared to member or component strength, whereas ASD loads are compared to member or component allowable values that are less than the full strength of the member or component.

14.2.8 Development of Seismic Design Codes

Nowadays, all structures must be designed and constructed in accordance with the design requirements of the applicable codes in order to get permission from local jurisdictions.

The first construction code can be traced back to early 1800 BC. The Babylonian emperor Hammurabi enforced what was known as the Code of Hammurabi. This code strictly stated that “if a builder build a house for someone, and does not construct it properly, and the house which he/she built fall in and kills its owner, then that builder shall be sentenced to death.” However, the real development of

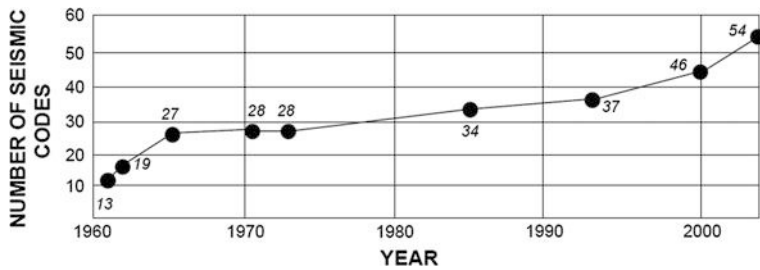


Fig. 14.12 Development of seismic codes worldwide by quantity [29, 30]

seismic design code has its origins in the paper “Statics of Anti-seismic Construction” [28] by Danusso, a professor of structural engineering from Milan, who first elaborated the equivalent static approach, also called the static coefficient method. This method was then gradually spread to countries with high seismicity and finally adopted by building codes in each of these countries. After the 1923 Great Kanto earthquake, the Japanese Building Ordinance published the first official seismic design code, which stipulated that building should be designed to resist a force equivalent to 10 % of their weight. The US used a similar coefficient of 8 % of the weight, regardless of earthquake or building characteristics. The 1933 Long Beach earthquake, which gave nearly 6 times the 8 % coefficient in terms of response, resulted in a few buildings collapsing, the ductile behavior and energy absorption then attracted attention from researchers and design code developers.

From the early 1970s until now, extensive activities have been carried out for developing seismic codes as shown in Fig. 14.12. Today, more than 70 codes specially dedicated for seismic design have been issued worldwide. Examples of those codes are ISO 19901-2, Eurocode 8, Uniform Building Code in US, Building Code for Seismic Design in China, Uniform Building Code in Japan, and the New Zealand Seismic Design Code, etc.

It is noted that developments or revisions of design codes are mainly due to the updated knowledge or lessons learned from significant structural and foundation failures. For example, every time a strong earthquake occurred and caused disasters, the relevant design codes were pushed to be upgraded. In addition, based on continuously updated knowledge such as the new findings of faults, updated GMPEs/attenuation models (Sect. 3.6) etc., seismic design codes in some countries such as the US and Canada regularly update seismic hazard maps, often at 5 year intervals.

14.2.9 Hierarchy of Codes and Standards

In the design and upgrading of structures, it is important to perform relevant design and analysis in accordance with pertinent codes and standards. In this process,

engineers need to have an explicit understanding of the contents for each relevant codes. As it is not unusual that several codes and standards aim to address the same design issues, it is of great importance to know the priority of them.

Generally, there are five levels (1–5) in the hierarchy of codes and standards, with the lower level having higher priority:

- Level 1: international or national regulations. They are released by national (governmental) authorities in the forms of regulations, guidelines, interpretations (examples, answers to certain engineering projects), etc. They contain functional requirements (regulations), i.e., what to be achieved, and recommendations (guidelines) on how to comply with the requirements by referring to technical standards such as Eurocodes [13], ISO, etc. They also provide responses to questions raised on a case by case basis. For example, in Norway, the Petroleum Safety Authority Norway (PSA) is responsible for developing and enforcing regulations that govern safety and working environment related to petroleum activities on the Norwegian continental shelf and associated land facilities. Table 14.3 provides a list of such national regulators.
- Level 2: referred standards. As the level 1 regulations are typically general, they normally refer to a number of codes and standards that elaborate technical requirements. For example, for design of structures in Europe, most of the national authorities require a use of Eurocodes [6], with minor modifications (typically in the form of national annex) in specifications of certain items such as national resistance factor (Sect. 14.2.5), etc. For offshore structural design in Norway, the principal referred standards are Norsok N-001 [31] and ISO 19900 (e.g., ISO 19901-2 [5] for seismic design), which define overall safety level of offshore structures in terms of load and resistance factors, and load combinations, etc.

Table 14.3 National regulators that govern safety and working environment in the petroleum activities in representative countries

Country	Regulators
Brazil	Agência Nacional do Petróleo, Gás Natural e Biocombustíveis (ANP) http://www.anp.gov.br
Canada	National Energy Board http://www.neb-one.gc.ca
Denmark	Danish Energy Authority (Energistyrelsen) http://www.energistyrelsen.dk
India	Oil Industry Safety Directorate (OISD) http://www.oisd.gov.in/
Italy	Ministry of the Economic Development (Ministero dello Sviluppo Economico) http://www.sviluppoeconomico.gov.it/
Netherland	State Supervision of Mines (SSM) www.sodm.nl
Newzeland	Department of Labour http://www.dol.govt.nz/
Norway	Petroleum Safety Authority (PSA) http://www.ptil.no
UK	Health and Safety Executive (HSE) www.hse.gov.uk
USA	Minerals Management Service, US Department of the Interior www.mms.gov and Coast Guard (USCG), US Department of Homeland Security www.uscg.mil

- Level 3: standards referred to by level 2 standards. Examples of level 3 standards are other standards referred to by PSA for the design of offshore structures in Norway, such as the rest of standards associated with Norsok (developed by Norwegian petroleum industry) and ISO 19900 (international standards).
- Level 4: other commercial standards, such as DNV-GL rules, standards and guidelines [32] for the design of offshore structures in Norway.
- Level 5: other client and design specifications, such as project design basis (specific multidiscipline document with overall design requirements such as design lifetime, material requirement, ambient conditions, accidental scenarios, re-use or removal criteria, fabrication and traceability requirements), design specifications in addition to level 3 and level 4 standards, technical requirements such as clients' specification on method and functionality, recommended design and engineering practices, specification by designers, and technical papers. Level 5 is typically associated with additional performance requirements that are not included in or beyond requirements of the current codes and standards, which are associated with performance-based design (Sect. 14.3). For example, clients may specify a higher resistance factor for pile foundation design, or require a special check on the consequence of sudden subsidence of offshore platforms.

It is worth mentioning that in various codes and standards, users should be clear about what is a requirement and what is a recommendation or other statement. ISO and many other national and international standardization bodies use the following words to clarify this:

1. Requirements: shall, shall not
2. Recommendations: should, should not
3. Permission: may, need not
4. Possibility and capability: can, cannot

14.3 Introduction to Performance-Based Design

14.3.1 *Limitations of Traditional Prescriptive Code Design*

It is noted that prescriptive codes cannot explicitly provide acceptable levels of life-cycle performance. This is because they include a great number of provisions, which are designed to ensure adequate strength of structural members and implications of the overall structural response [33]. As prescriptive codes mainly aim to provide life safety and damage control (safety check), serviceability performance is, unfortunately, not receiving enough attention. For example, in many cases, the smaller but more frequent earthquakes contribute more to the cumulative damage of a structure than the larger earthquakes on which structural design is traditionally based [34]. Therefore, it is important to evaluate the damage sustained by a

structure over its lifetime in a seismic environment beyond what the codes require for life safety. Furthermore, the cost of structural parts of a building is typically around 15–40 % of the total building cost. Therefore, for structures with high value contents, such as mechanical and electronic equipment, non-structural elements, luxury decorations etc., the value of these contents may be well above that of the structures. The design criteria with regard to ground motions can then be much more stringent than those of the structural strength requirement.

Moreover, prescriptive codes were formulated partially based on experience and partially based on science. It is difficult to specify rules for new technology. For a structure with new structural form or material, and large structures such as an offshore platform or a high-rise building, the design of those structures may not meet the prescriptive definitions, and requirements of the codes may not be sufficient for detailed individual situations. For example, the challenges from the discrepancy between the structural parameters and the corresponding optimal values for satisfactory static and dynamic performance, as often encountered by engineers, can lead to a considerable cost with regard to construction and maintenance. Therefore, one needs to make an efficient design from a seismic resistance point of view, such as designing innovative separate structural systems and their optimal parameters [35]; the performance of the structure corresponding to each individual demand is then optimized, resulting in a reduction in total cost.

Furthermore, it is realized by more and more engineers, property owners, insurance companies, researchers and authorities etc. that, although structures designed to comply with current code requirements performed well during a strong earthquake from a life safety perspective, the level of damage to structures, equipment etc., economic loss due to the loss of use, and cost of repair etc. has been unexpectedly high [36].

Finally, but not the least relevant, global warming effects nowadays have a great impact on construction activities. This requires the production of cement and steel materials with more environmental concern, especially with a focus on a significant decrease of CO₂ emission. An increase of the structure's service life and utilization of environmentally friendly new materials are, among others, two ideal solutions to relieve this concern. This further poses challenges on the structural design and analysis, which cannot be easily or directly handled by traditional prescriptive code design.

14.3.2 Introduction to Performance-Based Design

To overcome all the limitations and challenges derived from the traditional prescriptive code design as discussed in Sect. 14.3.1, it is possible to override the standards or codes by introducing project specific criteria developed by experienced professionals [37]. By introducing design checks at various limit states to the probability that the seismic action can reach the intensity required to induce the corresponding failure modes, engineers are therefore allowed to explicitly

determine the load demands at present performance levels associated with earthquake hazard, i.e., a combination of a performance level with a specific level of ground motion provides a performance design objective. This design process is called performance-based design (PBD) or Performance-Based Seismic Design (PBS). It can be generalized as a design philosophy in which the design criteria are expressed in terms of achieving stated performance objectives under the stated levels of seismic hazard. It provides the designers with the criteria for selecting a decent structural and foundation system and its layout and for proportioning and detailing both the structural and non-structural components, so that at specified levels of earthquake intensity the structural damage will be constrained within certain limits [8]. PBD can result in a structure that is cost effective, easy to build, stronger and allows more design freedom for other engineering disciplines.

The original prototype of PBD is actually the limit state design (Sect. 14.2.2) that was used since the early 1970 and is now widely applied in structural design for both land-based and offshore structures. However, because the level of damage that has to be prevented for a given magnitude of strong ground motions is not quantitatively defined, the current limit state design based codes fall short in realizing their objectives. Therefore, a more detailed definition of limit states and of the corresponding magnitude of ground motions are desired. Table 14.4 illustrates an example of a recommended three-level format for limit states of structural system. It is noted that in this table, the three limit states, namely serviceability, damage control and collapse prevention, are intrinsically related to structures' stiffness, strength and ductility, respectively [38]. The performance levels are then determined by correlating them with the performance objective and the probability of occurrence, which are shown in Fig. 14.13. Therefore, PBD not only ensures that structures will not be destroyed (as all prescriptive design codes do), but also controls desired level of damage (and safety) at a specified level of seismic intensity, this desired level of damage can normally be chosen by designers and clients.

As mentioned before, PBD may not only check the performance of primary structures, but also the integrity of non-structural systems, contents and soil-foundation-structural systems. Due to the difference in various characteristics between offshore and onshore structures as discussed in Chap. 2, specific design procedures need to be proposed for two types of structures, especially on the definition of multiple performance objectives. Appropriate computation tools for structural analysis are needed, and these should be more engineering design oriented instead of research oriented.

Even though PBD has been considered in a number of seismic design codes applied to land-based structures, it has not yet been adopted in design codes for offshore structures. It is therefore an important task of researchers and engineers to promote its application in offshore industry.

Table 14.4 Example of a typical three-performance level format limit states for a structural system [38]

Performance level		Performance objectives			Performance criteria			Seismic hazard	
Limit state	Structural characteristics	Engineering	Socio-economic	Type	Prob. exceedance (in %)	Type	Prob. event (in %)		
Serviceability	Stiffness	Non-structural damage	Operational	Near elastic response	P_{e1} in N_{s1} years	Frequent	P_{s1} in N_{s1} years		
	Strength	Moderate structural damage	Limited economic loss	Limited inelastic response	P_{e2} in N_{s2} years	Occasional	P_{s2} in N_{s2} years		
Collapse prevention	Ductility	Severe structural damage	Life loss prevention	Large inelastic response	P_{e3} in N_{s3} years	Rare	P_{s3} in N_{s3} years		

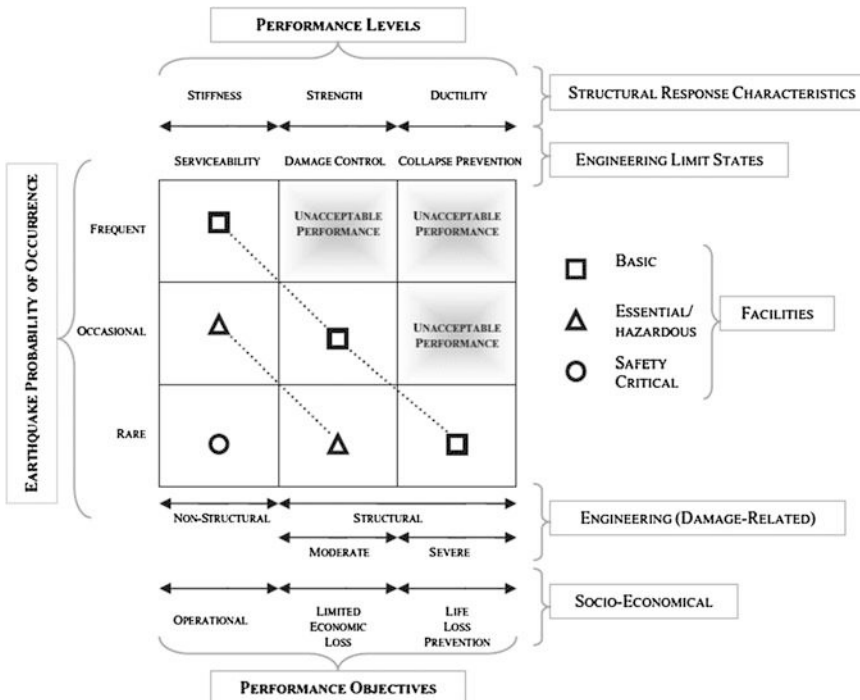


Fig. 14.13 A performance objective correlated to the a certain level of seismic action with various limit states [38]

14.3.3 Performance-Based Design for Structures

As mentioned above, the reliability of performance-based design certainly depends on the scientific rationality for both structural design and ground motion calculations. Therefore, the application of performance-based design procedures requires a higher level of analysis and design skills; a clear understanding of the relation between performance and non-linear response; a selection and manipulation of ground motions appropriate to the seismic hazard; a selection of decent non-linear models and analysis procedures; an interpretation of results to determine design quantities based on non-linear dynamic analysis procedures; and appropriate structural details. Peer review by independent qualified experts is acceptable [39].

Recently, by applying the concept of earthquake hazard, several codes such as International Building Code [7] and ASCE/SEI 41-06 [40] have elaborated performance-based design, which links the inherent risk of human life to the return period of earthquake event. The PBD is stated as performance goals in the form of recommended minimum confidence levels. For example, in ASCE/SEI 41-06 Seismic Rehabilitation of Existing Buildings, the seismic objective is defined by the links between performance levels (Collapse, Collapse Prevention, Life Safety,

Immediate Occupancy and Operational) and earthquake design levels (Frequent, Design Earthquake and Maximum Considered Earthquake for immediate occupancy with corresponding return period of earthquakes), with a category for essential facilities and standard occupancy buildings.

Even though intensive research efforts have been made, the implementation of PBD on design codes is not smooth and efficient. One important obstacle is that authorities are cautious about the reliability of the PBD because it requires much higher levels of engineering skills. In addition, the implementation of PBD in engineering design requires that not only the research and intellectual sources, but also the authority agencies, infrastructure owners and operators, engineering, insurance, and lawyer companies work together to promote the application of PBD.

One of the most important issues in PBD is to estimate the damage amount of designed structure at different levels of risk. To perform this task, various damage indices (Sect. 13.6.2) have been introduced in order to quantify the level of damage. While the seismic design codes generally define damage/performance levels based on the inter-story drift of structures, some project specific designs define damage based on accumulation and distribution of structural damage, the failure mode of elements, the number of cycles, and the duration of ground motion. They include two types: non-cumulative and cumulative type [41]. The former is calculated by a maximum value of an inelastic response parameter, such as displacement, whereas the latter uses an accumulated parameter, such as hysteretic energy or plastic strain through the entire response duration [42].

During the past decade, the PBD approach has radically changed the design methodology and trends in the seismic codes and practices for designs of land-based structures. However, the offshore industry appears not to have kept up with the pace of PBD. Unlike the guideline developed for onshore structures such as FEMA 356 [43], no generally accepted structural performance criteria, such as the Continued Operation (CO), Immediate Occupancy (IO), Life Safety (LS) or Collapse Prevention (CP) criteria have yet been developed for seismic design of offshore structures, as mentioned before.

14.3.4 Introduction to Practical Methods for PBD

The performance of a structure itself can normally be assessed by the physical quantities of force, displacement, strain, and energy etc.

During strong ground motions, the energy input into a structure can be dissipated through the inherent structural damping, plasticity development and additional installation of damper (damper apparatus or dynamic absorbers). In addition, one can also decrease the energy input to structures through cutting the load transfer from ground to the superstructure using base isolation, as will be presented later in this book.

The performance objective can be related to the level of damage of a structure, which is related to the cross-section deformation and ultimate strain of the structure,

which is, in turn, related to the displacement and drift [44]. Therefore, by investigating structural displacement, the level of damage can normally be identified. Note that the level of damage is also influenced by other parameters such as the accumulation and distribution of structural damage, the number of cycles and duration of the ground motions, and the acceleration level, etc.; as a single design/response parameters such as displacement may not sufficiently control all performance objectives [45], the assumption of sole relationship between the displacement and the level of damage is therefore an over-simplification [46]. However, in most engineering applications, this assumption is still accepted and is a recommended practice.

Various methods have been developed for PBD, such as capacity spectrum method (Sect. 15.2.5) [47] that was introduced in US provisions [48–50], the N-2 method [51] that was implemented in Eurocode [6], and direct displacement-based design [52, 53]. Based on a more systematic category, two methods dominate displacement-based design, namely indirect- and direct-performance design. In indirect performance-based design, a traditional force based analysis is first performed, and an indirect control using ductility coefficients rather than a direct control of displacements may be performed as a control of displacements. This is then followed by displacement check (normally using a pushover analysis) against established displacement limit obtained from the seismic response spectrum analysis. If the displacement limit requirement cannot be fulfilled, a redesign still using the traditional force based analysis and the procedures above is repeated until the displacement limit requirement is fulfilled. This approach has the merit of being simple and consistent with the traditional design approach (more understandable by structural engineers) and therefore becomes the most popular approach for the execution of performance-based design. Direct performance design, however, starts by establishing the displacement with a certain performance, by assuming a deformation shape and proportion the structural displacement with the deformation and strength of each individual structural component, the individual member is then designed. This is followed by the displacement check with certain performance requirements [54]. Since the direct approach needs extensive efforts on the step of “proportion the structural displacement with the deformation and strength of each individual structural component” and its procedure also deviates far from the traditional design approach, it is not widely adopted in engineering practice.

References

1. FEMA P-749 (2010) Earthquake-resistant design concepts, Washington, DC
2. Jia J (2014) Essentials of applied dynamic analysis. Springer, Heidelberg
3. Sahin C (2014) Seismic retrofitting of existing structures. Portland State University
4. Paik JK, Thayamballi AK (2003) Ultimate limit state design of steel-plated structures. Wiley, Hoboken, NJ
5. ISO19901-2 (2014) Petroleum and natural gas industries—specific requirements for offshore structures—part 2: seismic design procedures and criteria

6. Eurocode 8 (2004) Design of structures for earthquake resistance—part 1: general rules, seismic actions and rules for buildings
7. International Building Code, International Code Council, 2015
8. Faella C, Piluso V, Rizzano G (2000) Structural steel semirigid connections: theory, design and software. CRC Press LLC, Boca Raton, FL
9. Veritas DN (2011) DNV-OS-C101, design of offshore steel structures, general (LRFD method), April, Høvik
10. Roeder CW (1990) Comparison of LRFD and allowable stress design methods for steel structures. Fifth Seminario de Ingenieria Estructural, San Jose, Costa Rica
11. Case J, Chilver L, Ross CTF (1999) Strength of materials and structures. Elsevier, Oxford
12. Segui WT (1994) LRFD steel design, 2nd edn. PWS Publishing Company, Boston
13. EN 1990 (2004) Basis of structural design, CEN, Brussels
14. EN 1993-1-1 (2008) Design of steel structures, part 1-1: general rules and rules for buildings, CEN, Brussels
15. Björkenstam U (1998) Reliability based design, 1st edn. Chalmers University of Technology, Göteborg
16. Cornell C (1969) A probability-based structural code. *J Am Concr Inst* 66(12):974–985
17. Transportation Research Board of the National Academies, National Cooperative Highway Research Program, LRFD Design and Construction of Shallow Foundations for Highway Bridge Structures, NCHRP Report 651, Washington, DC, 2010
18. Phoon K, Kulhawy F, Grigoriu M (1995) Reliability-based design of foundations for transmission line structures, report TR-105000. Electrical Power Research Institute, Palo Alto, CA
19. Thoft-Christensen P, Murotsu Y (1986) Application of structural systems reliability theory. Springer, Berlin
20. Ryden J (2011) Failure probabilities and safety index (lecture notes). Uppsala University, Spring 2011
21. Hasofer AM, Lind NC (1974) Exact and invariant first order second-moment code format. *ASCE J Eng Mech Div* 100(EM1):111–121
22. Tvedt L (1989) Second order reliability by an exact integral. In: Thoft-Christensen P (ed) Reliability and optimization of structural systems, proceedings of the second IFIP WG7.5 conference (1988). Springer, London
23. Björkenstam U (2002) Exercise in ship structures basic course. Department of Naval Architecture and Ocean Engineering, Chalmers University of Technology, Göteborg
24. Ditlevsen O, Madsen HO (2007) Structural reliability methods. Wiley, Chichester, UK
25. Melchers RE (1999) Structural reliability analysis and prediction, 2nd edn. Wiley, New York
26. Coleman HW, Steele WG (1999) Experimentation and uncertainty analysis for engineers, 2nd edn. Wiley, New York
27. Jensen JJ (2001) Load and global response of ships. Elsevier Science Ltd., Oxford
28. Danusso A (1909) Statics of anti-seismic construction, Milan
29. Reitherman R (2008) International aspects of the history of earthquake engineering. Earthquake Engineering Research Institute, Oakland, CA, USA
30. International Association for Earthquake Engineering (2004) Regulations for seismic design—a world list 2004, IAEE
31. NORSOOK N-001 (2012) Integrity of offshore structures, 8th edn, Sept 2012
32. <https://www.dnvgi.com/rules-standards/>
33. Papadakakis M, Lagaros ND, Fragiadakis M (2006) Seismic design procedures in the framework of evolutionary based structural optimization, computational mechanics—solids, structures and coupled problems. Springer, Heidelberg
34. Ghisbain P (2015) Damage-based earthquake engineering. WII Press, Southampton
35. Lee D, Ng M (2010) Application of tuned liquid dampers for the efficient structural design of slender tall buildings. *CTBUH J* 4:30–36
36. Ghobarah A (2001) Review article: performance-based design in earthquake engineering: state of development. *Eng Struct* 23:878–884

37. Galambos TV (2006) Structural design codes, the bridge between research and practice. International association for bridge and structural engineering, Budapest, Hungary, Sept 2006
38. Elnashai AS, Di Sarno L (2008) Fundamentals of earthquake engineering. Wiley, London, UK
39. Moehle JP (2008) Performance-based seismic design of tall buildings in the US. In: The 14th world conference on earthquake engineering, Beijing, Oct 2008
40. ASCE/SEI 41-06 (2007) Seismic rehabilitation of existing buildings, ASCE
41. Williams MS, Sexsmith RG (1995) Seismic damage indices for concrete structures: a state-of-the-art review. *Earthq Spectra* 11(2):319–349
42. Sucuoğlu H, Yüçemen S, Gezer A, Erberik A (1998) Statistical evaluation of the damage potential of earthquake ground motions. *Struct Saf* 20(4):357–378
43. FEMA (2000) Prestandard and commentary for the seismic rehabilitation of buildings, FEMA 356/Nov 2000
44. Priestley MJN (1997) Displacement-based seismic assessment of reinforced concrete buildings. *J Earthq Eng* 1(1):157–192
45. Krawinkler H (1996) A few basic concepts for performance based seismic design. In: Proceedings of eleventh world conference on earthquake engineering, Acapulco, Mexico. Paper no. 1133, Pergamon, Oxford
46. Ghobarah A (2001) Review article: performance-based design in earthquake engineering: state of development. *Eng Struct* 23:878–884
47. Freeman SA (1998) The capacity spectrum method as a tool for seismic design. In: Proceedings of the 11th European conference on earthquake engineering, 6–11 Sept, Paris
48. Federal Emergency Management Agency (FEMA) (2000) Pre standard and commentary for the seismic rehabilitation of buildings—FEMA 356, Washington, DC
49. Federal Emergency Management Agency (FEMA) (2005) Improvement of nonlinear static seismic analysis procedures—FEMA-440, Washington, DC
50. ATC 40 (1996) Seismic evaluation and retrofit of concrete buildings, vol 1. Applied Technology Council, USA
51. Fajfar P (2000) A nonlinear analysis method for performance based seismic design. *Earthq Spectra* 16(3):573–592
52. Chopra AK, Goel RK (2001) Direct displacement-based design: use of inelastic vs. elastic design spectra. *Earthq Spectra EERI* 17(1):47–64
53. Sullivan TJ, Priestley MJN, Calvi GM (2004) Displacement shapes of framed wall structures for direct displacement based design. In: Proceedings of Japan–Europe fifth workshop on implications of recent earthquakes on seismic risk, Bristol
54. Bachmann H, Dazio A (1997) A deformation-based seismic design procedure for structural wall buildings. In: Fajfar P, Krawinkler H (eds) Seismic design methodologies for the next generation of codes. AA Balkema, Rotterdam, pp 159–170

Chapter 15

Seismic Analysis and Response of Structures

15.1 General

The major objective of seismic analysis is to develop a quantitative measure or a transfer function that can convert the strong ground motions at a structure's foundation to loading and displacement demands of the structure, which provide essential input for a reliable assessment of structural capacity.

Traditional methods exist by accounting for various aspects of structural effects due to non-linearity and dynamics. With respect to ground motion characteristics, a few methods can also account for effects due to spatial variation, non-Gaussian and non-stationary properties. The five traditional seismic analysis methods are as follows:

- Simplified static coefficient method
- Response spectrum analysis
- Non-linear static pushover analysis
- Random vibration analysis
- Non-linear dynamic time domain analysis

It should be emphasized that the engineering intention behind earthquake resistant design is not to make earthquake-proof structures that will not get damaged even during a rare and extremely strong earthquake, as such structures will be too robust and expensive to build. Instead, engineers should design structures to resist the effects of strong ground motions in such a way that damages on structures can be significant in case the earthquake ground motions are significant (associated with an extremely high return period), but the system integrity of the structures shall be maintained and structural collapse will not occur. While under minor earthquakes, infrastructure should remain intact. Subject to ground motions at the intermediate level (between strong and minor), local damages of infrastructures are allowable but should be repairable, which is in many senses difficult for engineers to manage because the definition of "repairable" is not explicit.

With the advent of performance based design (PBD) [1] for land based structures, which is a design philosophy for engineers to manage the cost of construction as well as maintaining the safety and functionality performance of structures in an efficient manner, as discussed in Chap. 14, various seismic analysis methods are emerging. Note that the traditional seismic analysis methods aim for pursuing accuracy of the calculated responses, while the recently developed methods place more focus on the compatibility between the structural response calculation and the evaluation of detailed performance demand, on revealing a structure's intrinsic seismic response and essential performance characteristics, and on improving the robustness of seismic load estimation and analysis results. This is because the random nature of seismic loading makes the satisfactory prediction of seismic response an extremely difficult task. Therefore, it would be unwise to place too strong a focus on the accuracy of calculated seismic response. To cope with the requirements above, the most widely presented or researched methods are:

- Incremental dynamic analysis (IDA), also named as dynamic pushover analysis
- Endurance time analysis (ETA)
- Hybrid method
- Probability-based seismic design (PBSD)
- Critical excitation analysis
- Wavelet analysis

However, it is noticed that the offshore industry appears not to have kept pace with the newly developed methods. This is mainly due to the difficulties of implementing PBD into offshore structural design. It is therefore a strong intention by many earthquake professionals to promote PBD for facilitating modern seismic design of both offshore and land based structures.

Furthermore, readers need to bear in mind that regardless of the sophistication of the numerical methods, it is not exact. Many uncertainties still exist. Therefore, in the development new methods for the future seismic analysis, even more attentions should be paid on their robustness performance.

15.2 Traditional Seismic Analysis Methods

15.2.1 Introduction

Note that Earthquakes are by their very nature dynamic events, and can exhibit significant material and geometric nonlinearities. However, engineering analysis tools often ignore (or implicitly account for) either non-linearity (linear response spectrum analysis) or dynamic effects (pushover analysis), or both (equivalent static analysis), even though these effects may be critical in evaluating the performance of a structure under earthquake loads [2].

The non-linear effects due to strong ground motions can be summarized as follows [3]:

1. Yielding and plasticity development on structural components can occur, which show a non-linear stress-strain relationship (material non-linearity).
2. Under large deformation, the stiffness and damping of structures may change significantly, which present geometric and damping nonlinearities.
3. The geometric non-linearity may also be derived from P-Delta ($P-\Delta$) effects, which is due to a variation in a structure's lateral deformation in the horizontal plane [4]. This changes the action point of the structure's resultant vertical force, and consequently induces additional actions on the structure and a change in its stiffness. Such change in stiffness further alters the force distribution on the structure. The P-Delta effects play an important role in increasing the effective load on a structural bay.
4. The foundation and its surrounding soil can also exhibit non-linear stiffness characteristics and experience cyclic degradation of strength to a certain extent.
5. For offshore structures, the hydrodynamic drag force due to the movement of a structure surrounded by water and the hydrodynamic damping (both viscous effects and radiation) enhance the non-linear characteristics of loading and responses. However, these effects are generally small during an earthquake event and can normally be neglected.

In addition, the spatial variation of ground motion, as well as the non-Gaussian and non-stationary effects may also be significant in a seismic analysis.

Table 15.1 illustrates the applicability and performance of each traditional analysis method with respect to the dynamic effects, the relevant nonlinearities, non-stationary effects, spatial variation effects, and computation cost.

Figure 15.1 illustrates a typical sequence of traditional seismic analysis methods used in different stages of structural analysis and design. By representing the dynamic seismic loading with statically equivalent forces, analysis using the static coefficient method (Sect. 15.2.2) provides general information on the structural capacity. However, the use of this method may only be valid for a preliminary design. Response spectrum analysis method (Sect. 15.2.4) can provide more insight into why a certain type of structure performs in a certain way, thus highlighting patterns of seismic response [1]. If the structural capacity is significantly lower than what is required, for a detailed control of structural capacity and also to reduce the uncertainties derived from the seismic load and structural response, non-linear dynamic analysis method (Sect. 15.2.6) is preferred. The complex non-linear dynamic analysis is regarded as the “ultimate” solution compared to other methods, mainly because it can incorporate almost all sources of non-linear, dynamic and time-dependent-sequence effects. However, one needs to realize the drawbacks of this method (Sect. 15.2.6) primarily due to its high computational demand, because in order to consider the variation of seismic ground motion in both frequency contents and duration, a number of analyses need to be performed and computational efforts spent on each such time series analysis is normally much higher than a

Table 15.1 Major seismic analysis methods and their applicability

Analysis type	Analysis method	Dynamic effects	Geometric non-linearity	Material non-linearity	Non-stationary effects	Spatial variation of ground motion	Computation cost
Deterministic	Simplified static coefficient method	NO/YES (implicitly)	NO	YES	NO	NO	VERY LOW
	Non-linear static pushover analysis	NO/YES (implicitly)	YES	YES	NO	NO	HIGH
	Response spectrum analysis	YES	NO	NO (elastic spectrum)/YES (ductile spectrum)	NO/YES (implicitly)	YES (multisport excitations)	LOW
	Non-linear dynamic time domain analysis	YES	YES	YES	YES	YES	VERY HIGH
	Random vibration analysis	YES	NO	NO	NO	YES	LOW to HIGH

response spectrum analysis. On the other hand, from an engineering point of view, it is acceptable and preferable to use a relatively simple method that can capture essential features of the seismic responses significantly affecting the performance objective. In this respect, the accuracy of demand prediction may not be essential. This is because neither seismic input nor capacities are known with accuracy [5]. A postulated greater accuracy of sophisticated methods is not an advantage if the input parameters can only be determined approximately.

Even though the non-linear static pushover analysis does not appear in the sequence list of Fig. 15.1, it is especially suitable for the PBD, which is different from the traditional prescriptive code design as has been introduced in Chap. 14.

For seismic analysis of offshore structures, among all analysis methods, the predominant method in industry practice has shifted from the response spectrum method to the non-linear dynamic time domain analysis.

In the calculation of seismic response, the rotational ground motions are not accounted for because they are normally regarded as having little influence on the seismic response of structures and foundations. However, for sites close to faults,

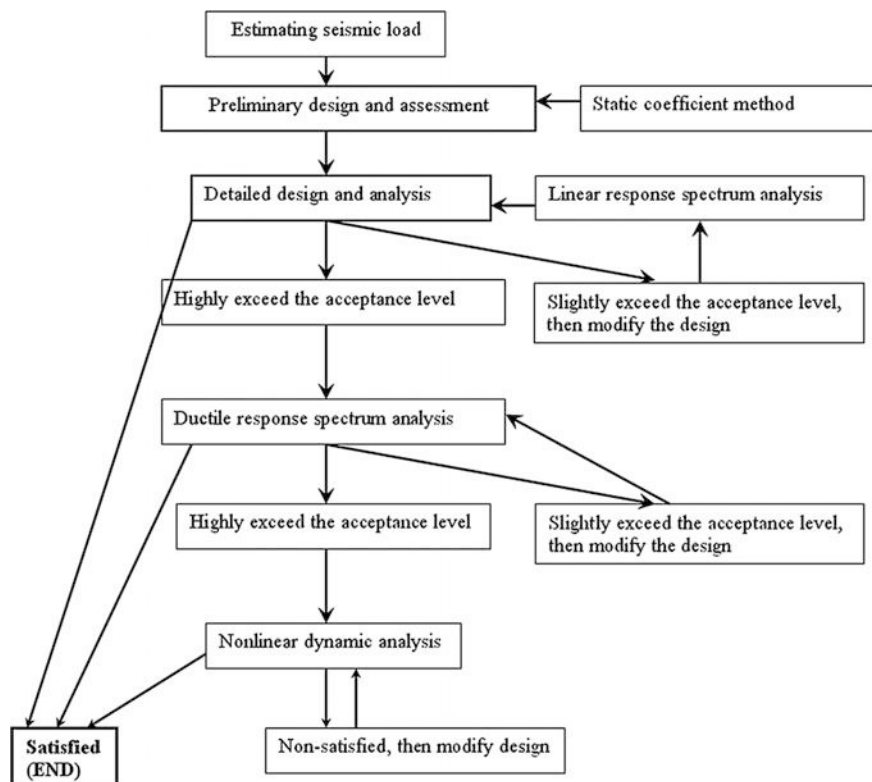


Fig. 15.1 A typical sequence of various traditional seismic analysis methods adopted in different stages of structural design and analysis

rotational excitations may reach a few degrees; and the vertical motion can be twice as much as the horizontal motion and may exceed 2g level in the proximity of fault rupture; coupling of different components of ground excitation may then significantly amplify the seismic demand by introducing additional lateral forces and enhanced P-Δ effects [6].

15.2.2 Simplified Static Seismic Coefficient Method

15.2.2.1 Method Description

As a first approximation, by assuming that a structure is subject to acceleration with the value of the peak in a response spectrum, the static seismic resulting forces applied on the structure can then be roughly approximated by multiplying the mass of the structure by its acceleration. The acceleration level depends on the level of ground motions.

For a realization of the method above, by taking different parameters related to structures and ground motions into account, for a single-degree-of-freedom system, the equivalent static load or the horizontal seismic shear force acting at the base of the structure or a structural part, in the direction being considered, can be calculated as:

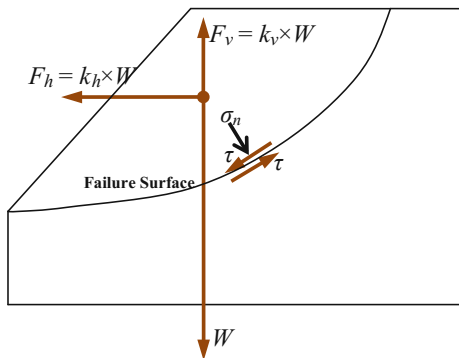
$$F_{eqs} = M \cdot C_s \cdot I \cdot S_{a(max)} \quad (15.1)$$

where M is the mass of the structure or a structural part; C_s is a coefficient depending on the characteristics of the structure, which especially depends on the structure's energy dissipation performance and plasticity development, it ranges from 1/8 to 1; I is a coefficient depending on the importance of the structure; and $S_{a(max)}$ is the peak/maximum acceleration of the response spectrum at the ground surface, or more preferably taken as the spectra acceleration at the natural period of the structure, as described below.

If more dynamic characteristics of the structure can be obtained, the uncertainties can be further reduced. For example, if the natural period of the global structure vibration is significantly below the period of response spectrum peak, and the seismic response is not significantly affected by vibration modes with orders higher than that of the one associated with the natural period, the spectral acceleration at the ground surface with the period equal to the natural period of the structure can replace $S_{a(max)}$ in the equation above. It is even possible to further reduce the base shear force if the natural period of the global lateral structural vibration is well below twice the upper limit period of constant spectral acceleration branch.

Based on the calculated base shear expressed in the equation above, the base shear force can be distributed into each height level of a structure based on the height and the modal mass distribution along the height of the structure (for vertical

Fig. 15.2 Illustration of pseudo-static analysis approach, k_h and k_v are horizontal and vertical pseudo-static (seismic) coefficients, respectively; W is the weight of the potential sliding soil mass



extended structures such as a tower or a building), so that the response of the structure can be calculated using a static analysis.

As an extension of static seismic coefficient method based on the calculation of base shear force, the accelerations at each height level or each location can first be calculated using response spectrum analysis (Sect. 15.2.4), which can then be applied on each corresponding location of the structure as equivalent to a quasi-static acceleration to represent the earthquake effects, so that the structural response can be obtained using a static analysis. This procedure is described in Sect. 15.2.4.5.

It is worth mentioning that the static coefficient method is also widely used in the assessment of slope stability, such as the pseudo-static analysis approach, which simplifies earthquake loading as static horizontal forces and in many cases also vertical forces applied to the potential sliding soil mass, typically represented by horizontal and vertical pseudo-static (seismic) coefficients as shown in Fig. 15.2. Typical horizontal pseudo-static coefficients range from 0.05 to 0.5 as given by various seismic design codes.

15.2.2.2 Limitations of the Static Coefficient Analysis Approach

Even though the static coefficient analysis approach has the merit of being simple, it may only apply to very regular structures (such as a monopile structure with a concentrated mass at its top) with dynamic responses dominated by a fundamental eigenmode vibration exhibiting global bending. Therefore, several disadvantages deter its application:

- (1) In situations with complex geometry and local vibration characteristics of the structural components on the top of the structure (e.g., an offshore topside frame structure at the top of structure), the irregularity of supporting structures, a static coefficient analysis approach cannot predict a reasonably accurate response.

- (2) For only a limited number of structures, the fundamental eigenmode is the only governing mode with a mass participation factor above 90 %. The seismic responses of structures may involve significant contribution from higher order vibration modes.
- (3) For structures with significant dynamic torsional effects, the simple static coefficient analysis gives rather unreliable results.

15.2.3 Random Vibration Analysis

In Chap. 8, it is elaborated that, for extended structures covering a large area of at least a few hundred meters long, long pipelines, and for structures with significant torsional eccentricity (low torsional stiffness, such as an L shape structure), spatial variation of strong ground motions may be relevant to the structural response. Under these situations, the random vibration analysis may be adopted for calculating the seismic response.

The random vibration approach has the merit of being consistent with probabilistic modeling since the input is specified directly by cross spectral density functions. It has attracted a significant amount of research efforts during the last two decades. However, because this approach is limited in its ability to reliably predict non-stationary response, and also due to its complexity, which is not fully compatible with the specifications from the various seismic design codes, it is not widely used in engineering practice.

15.2.4 Response Spectrum Analysis

15.2.4.1 Method Description

Structural design for earthquake is preferably performed on a probabilistic basis considering the stochastic nature of the ground motion. Rather than depending on particular ground motion record, the calculated response may be expressed in a form that can represent an envelope response of various possible ground motions. In this aspect, response spectrum analysis is the recommended method with regard to both reliability and computation efficiency, even though it is sometimes regarded as over-conservative [7]. It involves less computational cost than that from a time history analysis, and it also inherently includes the non-stationary effects of the earthquake excitation because the spectra acceleration at each period is obtained from time domain analysis of SDOF subject to realistic ground motion excitations. Unlike the simplified static coefficient method as presented in Sect. 15.2.2, the response spectrum analysis can account for the response of both lower and higher order vibration modes in frequency domain, i.e. for each direction of seismic

excitations, the response of a structure is calculated as a combination of multiple vibration modes. In addition, by using the ductile design spectrum (Sect. 5.4.3), it can also account for the plasticity development on structures.

In a response spectrum analysis, by simplifying a structure with one or a few degrees of freedoms, eigen-analysis is first performed to obtain various orders of eigenfrequencies, and the associated mode shapes and modal masses. For more complex structures for which a simplification of structure is not possible, finite element analysis can be used to model the structure and to determine the eigen-modes. For each mode, a response is read from the design spectrum at the corresponding modal frequency/period. The number of the eigenmodes used for modal combination later on is normally decided based on the criterion that sufficient (summed) modal mass should be included [4]. As a rule of thumb, along each principal direction (Sect. 15.2.4.3) of a structure, the summed modal mass (participating mass) of the included eigenmodes may account for at least 85–90 % of the all modal masses. To calculate the peak value of the dynamic response of the structure, the included modes are then combined using a decent modal combination rule, as will be discussed in Sect. 15.2.4.2. To obtain the total structural response due to the seismic excitations from all three translational directions, spatial combination of response are required as will be presented in Sect. 15.2.4.3.

15.2.4.2 Modal Combination Techniques for Response Spectrum Analysis

Readers may recall that a design spectrum is roughly divided into three regions: acceleration sensitive region, velocity sensitive region and displacement sensitive region. The structural responses in three regions are different:

- In the low period or acceleration sensitive region, little or no amplification of peak acceleration of the input ground motions can be observed. An SDOF oscillator having a natural period in this region is almost accelerated in-phase with the input ground accelerations in time. A system with natural period in this region can be simplified as a static problem, which is subject to loading equal to its mass times the spectral acceleration at the system's natural period. This concept can be extended to low period modal responses of multi-modal systems. To obtain the response contribution from all modes with periods in the low period region, one can treat the system as quasi-static. Therefore, the load applied on the system equals to the mass not participating in the amplified modal responses (i.e., “missing mass”) multiplied by the acceleration in the response spectrum at the system's natural period [8].
- In the high period or displacement sensitive region, an SDOF oscillator having a natural period in this region is neither accelerated in-phase with the input ground accelerations, nor accelerated in-phase with each modal response at different periods (out-of-phase modal response).

- In the middle period or velocity sensitive region, the vibration of an SDOF oscillator having a natural period in this region composes both out-of-phase and in-phase components. In addition, there is a transition from out-of-phase to in-phase response. In engineering practice, it is normally assumed that the individual modal responses in this period region are out-of-phase with each other. Normally, the modal combination method applicable to high period region above is also adoptable for the velocity sensitive period region [8].

The design response spectrum contains no phasing information, i.e. each individual modal response reaches peak value at different time and the combined response attains its peak at yet a different times. Therefore, in order to obtain the peak modal responses for a multi-modal period structural system and calculate the response such as force and displacement, reliable methods for combining the modal response at each individual period must be adopted. Three popular methods used by engineers to perform modal combination are summarized as follows:

- (1) Sum of absolute value: by assuming that the maximum modal values for all modes occur at the same time and their algebraic sign can be neglected, a straightforward but most conservative method is to sum the absolute modal response value together as written by:

$$R = R_1 + R_2 + \cdots + R_n \quad (15.2)$$

where $R_1, R_2 \dots R_n$ are peak modal response, i.e., peak response in each mode. They can be a displacement, force, stress, etc.

It is obvious that this method is over-conservative, and is therefore not popular in engineering applications.

- (2) Square root of the sum squares (SRSS) method [9]: by assuming that the maximum modal values in each individual mode are statistically independent and randomly phased, the peak response can then be calculated as the Square Root of the Sum Squares (SRSS) expressed as:

$$R = \sqrt{R_1^2 + R_2^2 + \cdots + R_n^2} \quad (15.3)$$

where R_n is the peak modal response of n th mode.

This combination rule provides excellent response estimates for a system with well separated natural periods. However, for a structure with large degrees-of-freedom or high redundancy, such as the complex frame structures, complex piping systems, and multistory buildings with unsymmetric plan etc., a large number of modes appear at close or even nearly identical frequencies, and the use of SRSS method is thus limited [10]. Moreover, the SRSS method can be non-conservative when the eigenfrequencies of two modes are closely spaced, i.e. the two modes are coupled and the responses due to the two modes are dependent. In this case the method can be modified by using absolute

summation of all modes whose eigenperiods are less than 10 % apart and the SRSS of all other modes [11], expressed as:

$$R = \sqrt{(R_1^2 + R_2^2 + \dots + R_n^2)} \quad (15.4)$$

where R_1 and R_2 are peak modal responses of closely spaced modes, R_n is the peak modal response of n th mode.

- (3) Complete quadratic combination (CQC) method: in order to account for potential phase correlation when modal frequencies are close, as a replacement of SRSS method, the most popular method used nowadays is the complete quadratic combination (CQC) method [12]. It overcomes the limitations of SRSS methods by including cross modal contributions, which are calculated as:

$$R = \sqrt{\sum_{i=1}^N \sum_{n=1}^N \rho_{in} R_i R_n} \quad (15.5)$$

where ρ_{in} is cross modal coefficient, which indicates the correlation coefficient of mode i and mode n . It varies between 0 and 1, and $\rho_{in} = 1$ for $i = n$, as calculated by:

$$\rho_{in} = \frac{8\xi^2(1+r)r^{3/2}}{(1-r^2)^2 + 4\xi^2 r(1+r^2)} \quad (15.6)$$

where $r = \omega_i/\omega_n$ is the ratio of angular frequency corresponding to i th and n th eigenmode; ξ is the damping ratio.

R_i and R_n are the peak modal response of mode i and mode n , respectively.

Therefore, the peak response according to CQC method can then be calculated as:

$$R = \sqrt{\sum_{n=1}^N R_n^2 + \sum_{i=1}^N \sum_{n=1}^N \rho_{in} R_i R_n} \quad \text{for } i \neq n \quad (15.7)$$

If the eigenfrequencies of structures are well separated, i.e., the modal responses are uncorrelated, the off-diagonal terms of ρ_{in} tend to be zero ($\rho_{in} = 0$ for $i \neq n$), the CQC method then approaches the SRSS method.

The SRSS and CQC methods would be most accurate for ground motions with wide-banded frequencies and long duration of strong ground motions several times longer than the natural period of structures not having too light damping (>0.5 %). If the ground motions are of short duration impulsive or contain many cycles of

essentially harmonic excitations, the two modal combination methods will become less accurate [10].

Furthermore, based on the random vibration assumption, the peak response R can be interpreted as the mean of the peak values of responses to a combination of ground motions. Therefore, the two modal combination methods are well applicable by using a smoothed design response spectrum, which is calculated from the mean or median or even more conservative spectra (e.g. mean plus one standard deviation spectrum), obtained from many individual ground motion histories. The calculated peak response may be either conservative or non-conservative, but is generally within a few percent. However, if the two combination methods are used for calculating peak response due to a single ground motion time history characterized by a jagged response spectrum, the errors are larger in the range of possibly 10–30 %, depending on the natural period of the target structure [10].

It should be noted that the response parameters must always be calculated directly by summing the response parameter of interest, and cannot be calculated from other response parameters [11]. For example, the peak response at the bottom of a building structure must be calculated by combining peak modal response at the same location; and it would be theoretically wrong to sum up the peak forces at each elevation/height of the building. This is because the modal combination does not contain sign information. However, in case the summing up of the peak forces at each elevation/height must be performed in special circumstances, the combined response must be calculated by summing up the forces with signs that lead to the most conservative evaluation with regard to structural capacity control.

Other modal combination rules are also available, such as Wilson et al. [12], Der Kiureghian [13] method or Rosenblueth and Elorduy [14] methods. Interested readers may read the literatures cited above.

15.2.4.3 Spatial/Directional Combination of the Ground Motion Excitations and Structural Response

When responses due to each directional component of ground motions are calculated separately, to obtain the seismic response of a structure, the response due to all three translational directions needs to be combined by considering their correlation among various modes of vibrations. Therefore, when responses due to each directional component of ground motions are calculated separately, the spatial combination of the responses due to the three translational directional ground motion excitations can be performed. Several combination methods are available, such as SRSS, CQC, or adjusted SRSS method.

Even though the three translational directions of ground motions are in reality a correlated process, for a simplification in a response spectrum analysis, the correlation in ground motion excitations can often be implicitly accounted for or even omitted. By following this approach, as an alternative of the directional combination method introduced above, seismic design codes and engineering practice normally require that structures under assessment be subject to 100 % seismic

excitations in one translational direction (the first principal direction, typically corresponding to the vibration direction of the first global vibration mode) and 30–80 % in its perpendicular direction in the horizontal plane. For example, Norsok N-003 [15] requires that “the motion components are assumed to be statistically independent. One of the horizontal excitations should be parallel to a main structural axis, with the major component directed to obtain the maximum value for the response quantity considered. Orthogonal bedrock horizontal component may be set equal to 2/3 of the major component and the vertical component equal to 2/3 of the major component”. In the ISO 19901-2 [16], 2/3 is replaced by 40 %, and the sign of each response parameter shall be selected such that the response combination is maximized. It should be emphasized that, in this method, the sign of each response parameter should be conservatively selected such that the response combination is maximized.

It is noted that the representation of the vertical excitation using a constant V/H ratio (30–80 %), such as the ones adopted in Norsok N-003 [15] and the first edition of ISO 19901-2 [16], cannot be justified, as discussed in Sect. 5.4.4. Therefore, a varied V/H ratio with frequency to represent more realistic vertical excitation response spectra (for the majority of offshore and land based infrastructures) or dedicated vertical response spectra directly given by seismic design codes are increasingly adopted by design codes. Note that the vertical/axial stiffness of a structure is generally much higher than that of the horizontal stiffness, even if the vertical ground motions are generally lower (but not always, such as the one on a near-source site as discussed in Sect. 5.4.4) than the dominant horizontal ground motions, the vertical ones can induce significant axial forces on the structure’s vertical components such as columns at short vibration period range, causing damage to those components and their connections. An important collapse scenario is that a weak intermediate single story would separate the stiffness continuity of its upper and lower parts. Horizontally, this can cause separate seismic response between these two parts with different dominant vibration period and phase. Vertically, when the structure is under strong vertical ground motions, the two parts may collide with each other at the intermediate story, causing serious damages. This has been proved to have been the cause of collapses of 16 building structures during the magnitude 7.2 Kobe earthquakes in 1995.

It is noticed that, in order to explicitly account for the phase between ground motion excitations and responses, a dynamic time domain analysis can be used, which will be presented in Sect. 15.2.6.

The rotational components of ground motion can normally be neglected as they are regarded as non-significant on most of the structures’ response and also because they have never been recorded properly during previous earthquake events. However, as discussed in Sect. 3.3.2, various recorded structural damage may be potentially caused by rotational ground motions or a combination of translational and rotational ground motions.

15.2.4.4 Limitations of the Response Spectrum Analysis

In spite of its computation efficiency and representativeness, one needs to apply spectrum analysis with caution.

The damping properties can only be estimated with a low degree of confidence. Moreover, even though the adoption of ductility-modified (inelastic) design spectrum as presented in Sect. 5.4.3 can take certain aspects of inelasticity into account, its theoretical background is still in question, especially for the analysis of complex three dimensional structures.

The P- Δ effect cannot be explicitly accounted for in any linear method such as response spectrum method. However, it is rather important if the lateral displacement of the structure is large.

It is noted that a smooth design spectrum is an average of a number of ground motions, and the spectrum analysis only calculates the maximum displacement and member forces in each mode without sign information. However, in reality, the members are not necessarily designed for this maximum peak values. Therefore, the response spectrum analysis may lead to an over-conservative design. This limitation has been emphasized by Dr. Ed Wilson [17], one of the initial promoters of the response spectrum method. In his technical notes published in 2015, it is clearly stated that "*The use of the Response Spectrum Method in Earthquake Engineering must be terminated. It is not a dynamic analysis method—the results are not a function of time.*" He also explained that the reason why the design response spectrum method was developed initially and verified (in the mid-1900s) was based on the limited number of seismic motion records accessible at that time.

As the structural response may be quite sensitive to ground motions at certain frequencies, compared to a specific jagged spectrum with ups and downs, the artificially smoothed response spectrum may significantly lose the information of the structural response's sensitivity to loading frequencies, which may miss important characteristics of dynamic structural responses.

Even though the response spectrum analysis is a deterministic method and it implicitly takes the ground motion duration into account, the information regarding the explicit duration of ground motions, and number and sequence of damaging cycles are not included in a spectrum analysis, this limitations can significantly influence the accuracy of damage assessment.

The basis for creating a design spectrum is the maximum response of an SDOF with only one concentrated mass. For many complex structures with irregular shapes, high rise slender structures, and structures having rather large degrees-of-freedom, structures with various types of distribution in mass and stiffness, and structures with significant local vibrations, however, the use of the response spectrum method may no longer be appropriate, i.e. it may not capture the response in an accurate manner and may not reproduce a similar response as dynamic time domain analysis does.

Furthermore, any modal combination rule to sum each individual modal response also involves uncertainties and approximations, as discussed in Sect. 15.2.4.2.

Finally, the utilization of the traditional spectrum analysis implies that the entire structure would be subject to the same uniform acceleration, which cannot be justified if the spatial variation of the ground motion is important, such as the case for extended structures as discussed previously.

15.2.4.5 Determination the Equivalent Quasi-Static Acceleration for Offshore Platform Structures

The following procedure describes how to determine the equivalent quasi-static acceleration:

- (1) Make a rather simplified FE model with a single mass for each part of a structure, e.g., for fixed offshore platforms, its supporting structure, and topside structures with various modules including module support frame, drilling modules, living quarters etc., may be modeled with a “tent” like structure with lumped masses at the top of each “tent.”
- (2) Replace each part of the structure with a refined model with major beams, columns and braces, each time any part of the structure is replaced, and apply a system of mass to each part of the structure to simulate the mass distribution. Foundation stiffness can be modeled using ground springs in all six degrees-of-freedom.
- (3) For each structure’s modeling with a replaced refined modeling part, calculate the eigenfrequency and mode shapes. And then, by performing response spectrum analysis, calculate the accelerations in each translational degree-of-freedom at each representative height level and at each representative location in the horizontal plane of the refined modeling part.
- (4) For each direction (x-, y-, or z-) and each single part of the structure, calculate their accelerations. From the acceleration versus height relationship, determine the equivalent quasi-static acceleration. Each part of the structure may be divided into several height levels; at each height level, the accelerations at several (n) selected points, $a_1, a_2, a_3, \dots, a_n$, should be calculated. The representative acceleration along each direction (x-, y-, or z-) at each height level may then be calculated as the root-of-mean-square (RMS, also known as quadratic mean) values of the accelerations at the n selected points:

$$a = \sqrt{\frac{(a_1^2 + a_2^2 + a_3^2 + \dots + a_n^2)}{n}} \quad (15.8)$$

It should be noted that by using the RMS values of accelerations to calculate the resultant acceleration at each height level, the equation above implies an assumption that the accelerations at n selected points follow a normal distribution.

Fig. 15.3 An example of the distribution of horizontal accelerations along different height levels of a topside structure for an offshore platform

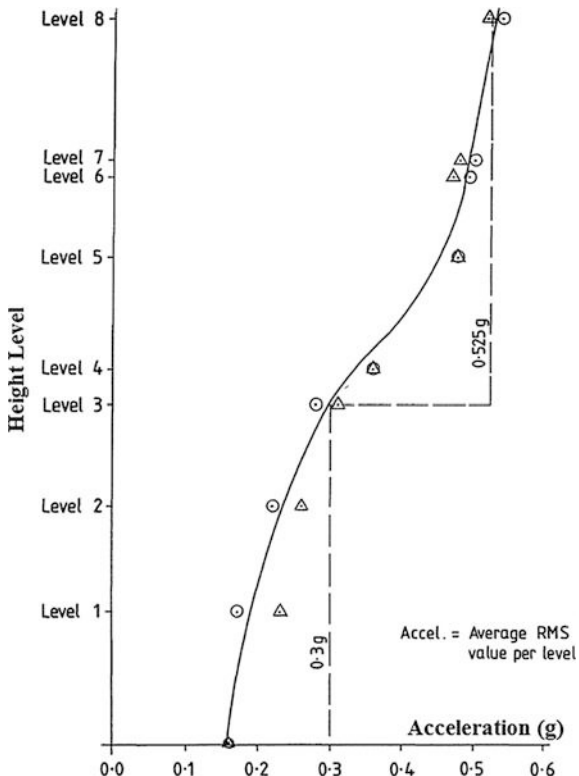


Figure 15.3 shows the distribution of horizontal accelerations along different height levels of a topside structure, the acceleration at each height level is calculated using the equation above.

- (5) If significant local vibrations (often at locations with attached mass) are identified and those vibrations are realistic, one needs to calculate the displacement at those particular locations in the response spectrum analysis described in step (3).
- (6) In order to calculate seismic response of each individual part of the structure, apply the acceleration level (typically using acceleration field) on each part of the structure obtained in step (4). Moreover, the high local vibration responses can be accounted for by applying prescribed displacements at those particular locations (typically with attached mass modeling) obtained in step (5).

Due to the characteristics and limitations of response spectrum analysis, as will be discussed in Sect. 15.2.4.4, the applied accelerations on each structural part along each direction (x -, y -, or z -) do not have sign information. Therefore, the applied accelerations along all three directions should be combined in a conservative manner such that the most unfavorable structural response with regard to capacity control should be obtained.

It is noted that the procedure above is complicated. With the development of computer technology and inexpensive digital computers, for the seismic analysis of offshore structure, the static seismic coefficient method has almost been phased out, while for land based building structures with regular geometry and of less importance, it is still used in certain circumstances.

15.2.5 Non-linear Static Pushover Analysis

15.2.5.1 Method Description

Since the knowledge on seismic design is continuously developing, many existing structures have been shown to be highly seismically deficient during earthquakes. One important aspect is the seismic performance of a structure after the first yielding. Static pushover analysis can provide an insight into the seismic structural demand imposed by the design ground motion, and can indicate the weak links, failure modes as well as the post-yield performance of the structure.

First proposed by Freeman et al. [18], pushover analysis is a two-step method, in which the permanent load is applied first, followed by a monotonically gradually increasing lateral seismic loading in two opposite directions to induce member yielding and/or buckling. The seismic loading is scaled until a predefined limit state or collapse (sometimes, the computation fails due to convergence, which does not indicate a real collapse of the structure) occurs. Note that the seismic loading can be either forces (force controlled) or displacements (displacement controlled).

During this process, the sudden slope change in the plot of global load (base shear)-displacement relationship indicates a weakness and a premature failure of the structure, and the termination or sudden drop (stiffness degrading) of curve would indicate the collapse of the structure system. To allow sufficient ductility and energy dissipation, a rule of thumb for ensuring structural integrity due to seismic loading is that the energy absorbed by the structure at collapse should be at least four times the energy at the first yield or buckling [11].

Compared to the non-linear dynamic time domain analysis (Sect. 15.2.6), static pushover analysis requires less computation efforts and is therefore efficient [19, 20]. It is especially suitable for the purpose of the PBD.

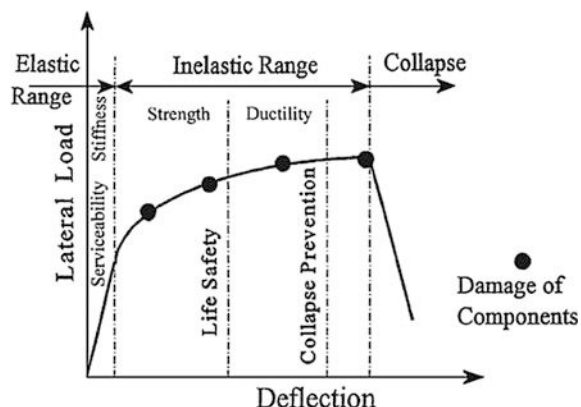
Static pushover analysis has been applied since the 1970s and it has gained increasing popularity since the 1990s. Many national and international seismic design codes or guidelines such as Eurocode 8 [21], ATC40 [22] and FEMA356 [23] have introduced this analysis.

15.2.5.2 Procedure for Executing a Pushover Analysis

The following procedure gives a general description of how a typical pushover analysis can be performed in practice:

- (1) Define a target displacement that is the maximum displacement likely to be experienced during a design earthquake. The target displacement can be defined as the seismic demand derived from a smoothed elastic/inelastic response spectrum (demand curve) instead of individual ground motion records. It can also be calculated based on a mathematical model directly incorporating the non-linear load-deformation characteristics of individual components and elements, i.e. a degraded stiffness after member yielding, and a spectral displacement from the design response spectrum at a structure's natural period with a degraded stiffness. Another more complicated alternative is to apply lateral load patterns as described in Sect. 15.2.5.3. The target displacement is then determined at the collapse of the structure. Note that pushover analysis is used as a design evaluation tool, therefore, the inelastic displacement demand cannot be explicitly computed directly, but needs to be deduced from spectral data and auxiliary information that account for differences between the elastic and inelastic displacement demand. For more details of how to estimate the inelastic demand, readers may read references by Krawinkler and Seneviratna [5] and Seneviratna [24].
- (2) Apply the gravity load that is typically force controlled.
- (3) Apply lateral load as described in Sect. 15.2.5.3. In practice, it is convenient to use the inverse triangle shape (category one (1) in Sect. 15.2.5.3.) and uniform shape (category two (1) in Sect. 15.2.5.3.) as shown in Fig. 15.6. It should also be noticed that lateral load should be applied in both positive and negative directions. For unsymmetrical structures, depending on the degree of asymmetry, the lateral load may be applied in various directions.
- (4) Draw a capacity curve: the global lateral load varies with the displacement at a reference point. The analysis results are rather sensitive to the selection of the reference point. Normally, it is the global maximum displacement at the center of mass (e.g. on top of a cantilever structure) and along the direction of a global shear force considered. Figure 15.4 shows a typical performance curve obtained from a non-linear pushover analysis. The performance in this figure

Fig. 15.4 Schematic illustration of a typical performance curve for a structure obtained from a pushover analysis



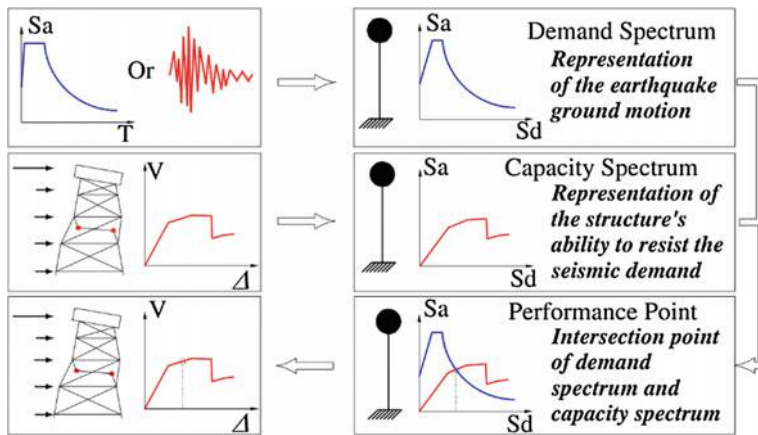


Fig. 15.5 The capacity-spectrum method, S_a and S_d , are spectral acceleration and spectral displacement, respectively [89]

is divided into four levels: serviceability, life safety, collapse prevention, and collapse, with the first three corresponding structural characteristics in stiffness, strength and deformation/ductility capacity, respectively [5, 25].

Various guidelines and codes provide detailed procedures to determine the structural performance based on non-linear pushover analysis. For example, in ATC40 [22], a capacity-spectrum method is proposed to determine the performance of a structure. As illustrated in Fig. 15.5, in capacity-spectrum method, the base shear versus displacement (capacity) and seismic ground motion (demand) are plotted in an acceleration-displacement response spectrum. The maximum inelastic displacement can be obtained from the intersection of the demand and capacity, which is regarded as the performance point.

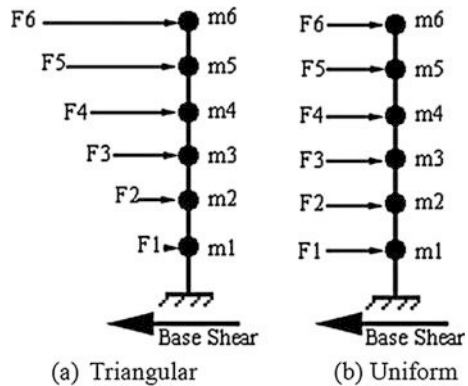
15.2.5.3 Lateral Load Patterns

The pushover analysis has no rigorous theoretical foundation. The analysis results are rather sensitive to the lateral load patterns. The distribution of lateral load determines relative magnitudes of shears, moments, and deformations within the target structure, and it can be based on a uniform acceleration in specified directions, a specified mode shape, or a user-defined static load pattern, etc.

1. Conventional pushover analysis load pattern

Based on the assumption that the structural response of a multi-degrees-of-freedom system can be represented as an equivalent single degree-of-freedom system, implying that the response can be calculated by a single vibration mode, and the shape (ϕ_n) of this mode remains constant throughout the

Fig. 15.6 Two typical lateral load pattern used in a traditional static pushover analysis [20]



time history responses, regardless of the deformation level, the structure is loaded with a predefined lateral load pattern as either force or displacement. This predefined load pattern should deform the structure in a similar manner as experienced in corresponding earthquake events. Figure 15.6 shows two typical lateral load patterns used in the traditional pushover analysis.

The static lateral load F_n ($n = 1, 2, 3, \dots$) can be calculated and applied on structural nodes from response spectrum analysis, in which the static loads at nodes would give the correct linear dynamic behavior for mode n [11], as expressed by:

$$F_n = K_n \cdot X_{n\max} = \phi_n \cdot L_{nr} \cdot S_{an} \quad (15.9)$$

where L_{nr} is the modal participation factor for mode n and along direction r , and S_{an} is the spectra acceleration at the frequency corresponding to mode ϕ_n .

2. Multiple mode pushover analysis

When the seismic response is dominated by more than a single mode vibration, higher order mode effects should be accounted for in the load pattern. Recent studies have extended the modal pushover analysis from a single mode pushover analysis to multi-mode response, and the corresponding method is normally referred to as multiple mode pushover analysis or modal pushover analysis (MPA). This is achieved by including the pertinent vibration modes in the seismic response calculation, which was proposed by Paret et al. [26] and Sasaki et al. [27], and was further developed by many researchers such as Chopra and Goel [28]. In this process, a decent modal combination method such as SRSS method should be used to combine the modal responses.

3. Adaptive pushover analysis

Note that the stiffness of a structure varies with its deformation level due to plasticity development and/or geometric non-linearity [4]. A constant mode shape assumed by either the traditional pushover analysis or MPA cannot account for the influence due to this change. Based on the mode shapes and modal participation

factors in each loading step of a pushover analysis, a more recent pushover analysis method proposes updating the load pattern in each loading step, leading to adaptive pushover analysis [29, 30]. The load pattern can be defined either by displacement or force vector. In adaptive pushover analysis, after defining an initial load vector, a looping is performed to compute the updated load pattern vector shape in each step of load or displacement increment. This implies that in each step of the increment, it is required to perform an eigenvalue analysis to obtain the mode shape(s) and the modal participation factor(s) based on the stiffness of the target structure at that load or displacement increment level.

4. FEMA-356 method

For building structures, FEMA-356 [23] suggests that two types of lateral load pattern should be used, one from each of the two following categories to perform the pushover analysis.

- Category one (first eigenmode modal pattern):
 - (1) Height and mass related lateral load pattern: the lateral load applied on floor i is determined by:

$$F_i = \frac{w_i h_i^k}{\sum_{j=1}^n w_j h_j^k} BS_b \quad (15.10)$$

where $k = 2.0$ when the natural period of the structure in the direction under consideration is not less than 2.5 s and $k = 1.0$ for natural periods not larger than 0.5 s. For intermediate natural periods between 0.5 and 2.5 s, linear interpolation shall be used to obtain the value of k . w_i and w_j are the masses associated with floor i and j , respectively. BS_b is the total pseudo-lateral load of the structure at its bottom. It is noted that when $k = 1.0$ the lateral load exhibits an inverse triangle shape distribution as shown in the left figure of Fig. 15.6.

FEM 356 further specifies that this distribution pattern shall be used only when more than 75 % of the total mass participates in the fundamental eigenmode vibrations in the direction under consideration, and the uniform distribution in category two (1) is also used.

- (2) First mode shape related lateral load pattern: the lateral load distribution is proportional to the shape of the fundamental mode in the direction under consideration, which can be expressed as:

$$F_i = \phi_{1i} BS_b \quad (15.11)$$

where ϕ_{1i} is the relative displacement of the fundamental mode shape at floor i . This distribution pattern shall also be used only when more than 75 % of the total mass participates in the fundamental mode vibrations.

- (3) Combined lateral load pattern: the lateral load distribution is proportional to the shear force distribution for each story, which is obtained from a response spectrum analysis (Sect. 15.2.4), using appropriate ground motion spectrum and modal combination such as the SRSS or CQC method. This distribution pattern shall be used only when more than 90 % of the total mass participates in the fundamental mode vibrations and the structure's fundamental period is more than 1.0 s. For example, the forces at each node expressed in the equation above can be summed up for more modes using CQC or SRSS method. It should be noted that the lateral load obtained by the CQC method will not equal the base shear calculated from the CQC method. The lateral load should therefore be adjusted to obtain a base shear value equal to the base shear from the CQC rule.

- Category two:

- (1) Mass related lateral load pattern: the lateral load applied on floor i is determined by:

$$F_i = \frac{w_i}{\sum_{j=1}^n w_j} BS_b \quad (15.12)$$

It is noted that if the mass on each floor w_i is equal, the lateral load has a uniform shape distribution as shown in the right figure of Fig. 15.6.

- (2) Self-adaptive lateral load pattern: the load pattern changes as the structure is displaced. This is generally performed by modifying the original load distribution using a procedure to account for yielding and/or higher order vibration modes for long period structures. This is a more realistic pattern if the plasticity is developed on the structure, even though this load pattern in practice has different implementations [31–34]. However, in order to identify the target displacement of each mode, repetitive runs of single-degree-of-freedom response history analysis for a given ground motion are required. In addition, the analysis is based on the individual analysis for each mode without accounting for the influence from other modes. This may lead to inaccurate estimations/errors of plastic hinge rotations [35, 36], which are an important parameter for comparing acceptance criteria in a PBD. Therefore, this method does not have significant merit compared to its counterparts described above.

15.2.5.4 Advantage of Non-linear Static Pushover Analysis

Pushover analysis is capable of providing the non-linear structural characteristics that a linear elastic static or dynamic analysis cannot predict [20, 37]. Based on the

evaluation of the performance parameters including global drift, inter-story drift, inelastic element deformations (either absolute or normalized with respect to a yield value), deformations between elements, and element and connection forces (for elements and connections that cannot sustain inelastic deformations), pushover analysis gives clear and essential information on the seismic force and deformation demands [5].

Their general merits are as follows:

- (1) Presents relatively realistic force demands on potentially brittle elements.
- (2) Can estimate deformation demands on inelastically deformed elements, in order to dissipate energy.
- (3) Can identify the effects of strength deterioration of an individual member on the overall structural capacity.
- (4) Can identify crucial regions with considerable plastic deformations.
- (5) Can account for plan or elevation strength irregularities.
- (6) Can estimate the global inter-story drifts that account for strength or stiffness discontinuities, which identify damages on both structural and non-structural elements.
- (7) Can identify and verify the load path, considering both structural and non-structural elements of the system.
- (8) Can identify the sequence of the member's yielding and hinge formation and the progress of the overall structural capacity curve.
- (9) Compared to a non-linear dynamic analysis, static pushover or elastic analysis requires less computational cost: it does not need to include contribution of hydrodynamic masses for offshore structures, and this simplifies the analysis modeling; while buoyancy effects may still be included.

15.2.5.5 Limitations of Conventional Pushover Analysis

Despite the indicative performance and simplicity of a conventional pushover analysis, one must realize that the theoretical background of this method is not strictly correct. The analysis is based on a static structural response calculation. Its drawbacks mainly lie in the fact that the dynamic effects cannot be explicitly included:

- (1) A conventional pushover analysis cannot properly account for the contribution from higher order vibration modes. This is because it is based on the assumption that the seismic response of the target structure is dominated by the fundamental eigenmode vibrations. However, the higher order of eigenmodes can also have a significant influence on the structural member forces. Furthermore, if one or two of the eigenmodes are dominated by torsion in the first few eigenmodes, the analysis results can be questionable. Therefore, it is recommended to include the load patterns due to the contribution from a higher order of mode shapes. For example, topsides of fixed offshore platforms generally show significant vibrations at a higher frequency than their

supporting structures' (jackets or GBSSs etc.) natural frequency. This implies that the conventional pushover analysis method cannot be applied for the topside analysis. This limitation may be mitigated by applying more than one load pattern, including load patterns that account for elastic higher mode effects. However, in engineering practice, this is difficult to attain. Moreover, research [24] has shown that for frame and wall structures with a natural period of less than 2 s, the accuracy of the response from a pushover analysis is normally reliable. However, abundant fixed offshore structures have a natural period close to or higher than 2 s. Numerous studies [10, 38, 39] have reported that neither a predefined load pattern shown in Fig. 15.6 nor a single mode load pattern is capable of representing the dynamic response of structures. The omission of the higher order modes can result in either a decrease or an increase in member and joint forces. Therefore, for structures with complex geometry, such as an offshore platform or a high rise structure with irregular geometry, pushover analysis should be adopted with caution.

- (2) Some important dynamic structural behaviors may not be explicitly accounted for or detected by static pushover analysis, such as dynamic amplification, and dynamic torsional effects due to mass, stiffness and strength irregularities. In some cases, a static pushover analysis can lead to a non-conservative estimation compared to that of the non-linear dynamic time domain analysis (Sect. 15.2.6). For example, to account for the dynamic effects, one may apply a single factor on the static seismic loading. However, this cannot be justified because it cannot account for the stiffness degradation with time, and also because, for complex structures, different parts of structures may cherish different values of factors for loading.
- (3) The method cannot explicitly account for the effects of time duration, structures' system damping or additional damping introduced by dynamic absorber or damping apparatus (as will be presented later in this book), the subsequent response decay as well as energy dissipation.
- (4) The load reversal cyclic effects cannot be explicitly or properly accounted for.
- (5) Based on the constant mode shape assumption, the conventional pushover analysis may only detect the first local plasticity mechanism under strong ground motions, after which the dynamic characteristics may change due to the changed stiffness.
- (6) Under the same load pattern, the load path from a pushover analysis is unique. This hinders the possibility of other collapse mechanisms [40]. This is especially significant for structures with large degrees of redundancy.
- (7) The errors induced from the assumption of lateral load pattern may magnify the response errors from the pushover analysis.
- (8) The stiffness degradation during the plasticity development may pose special challenges for numerical computation, largely due to the convergence problem.

15.2.6 Non-linear Dynamic Time Domain Analysis

15.2.6.1 Method Description

Compared to other analysis methods presented previously, non-linear dynamic time domain analysis is generally regarded as the “ultimate” solution with sufficient reliability. It can be applied to almost every type of structure. The method requires a set of deterministic excitation time histories to be used as input, which account for uncertainties and differences in frequency characteristics, ground motion duration and severity. Each time history takes the non-stationary characteristics of ground motions into account. The information regarding the phase lag of the ground motions among three translational directions and signs (compression or tension) of structural member forces are also explicitly included in the analysis. Regarding the adoption of ground motion time histories, various codes have different specifications. Eurocode 8 [21] generally permits using natural ground motions, artificial accelerograms, and simulated ground motion time histories. Furthermore, the non-linear dynamic time history analysis method accounts for the nonlinearities (plasticity, cyclic load-deformation characteristics and large deformation) in the response calculations. Therefore, the time domain analysis is essentially a type of Monte-Carlo simulation with a small number of ground motion samples, where a realization of a stochastic input (the ground motion) is analyzed with a certain system (the structural model) to provide a realization of an output random variable (the demand parameters) [41].

The effects of a future earthquake on a structure may differ substantially from those of previous earthquakes. Thus, using a previously recorded time history in design may have serious implications for the safety of the structure. Since the calculated time history responses are very sensitive to the characteristics of the individual ground motion used as seismic input, several analyses with different ground motion time histories are required using different ground motion records, i.e. the load effect should be calculated for a number of sets of time histories. The time series shall be selected in such a way that they are representative of earthquakes for the specific sites at a given probability of exceedance. Artificial, recorded, or simulated accelerograms may be adopted. Here simulated accelerograms indicate the ones generated through a physical simulation of source and travel path mechanisms. Most of the codes such as Eurocode 8 [21], Norsok N-003 [15], and China Building Code [42] require that at least three sets of ground motion time histories be used. All time histories should match the elastic design response spectra at the target sites. Furthermore, for artificial accelerograms, Eurocode 8 specifies that in the range of periods between 0, $2T_1$ and $2T_1$, where T_1 is the fundamental period of the structure in the direction of the applied accelerogram, no value of the mean 5 % damping elastic spectrum, calculated from all time histories, should be less than 90 % of the corresponding value of the 5 % damping elastic response spectrum. The mean value of the maximum values of the calculated action effects or the maximum value of the action effects from the time history analyses

may be taken as a basis for design. ISO 19901-2 [16] requires a minimum of four and recommends seven time histories to be used to capture the randomness in ground motions. If seven or more time history records are used, global structure survival shall be demonstrated in half or more of the time history analyses. If fewer than seven time history records are used, global survival shall be demonstrated in at least four time history analyses.

Note that the variation in the ground motion intensity and frequency content are considerable. Depending on the nature of the application and on the information actually available, the ground motion time histories may be represented using artificial, recorded, or simulated accelerograms that are consistent with the relevant design spectra. They can be obtained through three ways: (1) measured data: those measured at relevant sites or those calculated by scaling the earthquake records to a required intensity level; (2) site response analysis: by modeling the excitation time history or the earthquake design spectrum at the seismic source and propagation of the seismic waves through soil medium, the topology effects on the seismic wave propagation may also need to be considered; (3) artificial time history from a predefined design spectrum: by calculating time histories to match the relevant earthquake design spectrum at all or a certain period range. For more details on how to calculate the ground motion histories, readers may read Chaps. 4–7.

Note that engineers often assume that the response spectrum method can provide all the information representing structural response. However, due to the limitation of linear and stochastic characteristics of response spectrum method, this assumption cannot be justified: when the ground motions with similar response spectrum are converted into the time histories for a non-linear dynamic time domain analysis, the structural response among the various ground motions can vary widely. This is especially important when assessing irregular structures. The recent PBD also promotes the application of non-linear dynamic time domain analysis.

With respect to minimizing prediction uncertainty, non-linear dynamic analysis is so far the most rigorous analyzing method utilizing a combination of ground motion records with a detailed structural model. Non-linear dynamic analysis can more precisely determine the safety factor of the structure. This can, for example, be helpful for the modeling of seismic protection system (damper apparatus, base isolation, or dynamic absorber) with an explicit modeling of damping.

15.2.6.2 Limitations of the Non-linear Dynamic Time Domain Analysis

In spite of its obvious merits, the non-linear dynamic time domain analysis also has the following drawbacks:

1. The computational efforts are higher than for any other type of analysis. Non-linear dynamic time domain analysis requires significantly higher computational cost than the response spectrum method.

2. The response can be quite sensitive to a slight variation of the numerical parameters in the time integration (such as time step length, numerical damping, etc.) of the dynamic analysis.
3. The calculated responses are highly dependent on the characteristics of the selected ground motion records. Therefore, a number of ground records, typically 2–10 records, must be selected as the input for structural analysis.

15.2.7 Case Studies

15.2.7.1 Case Study 1—Spectrum Analysis of a Jacket Structure

- Structural modeling

The structure under investigation is a typical jacket structure with its topside located in the North Sea, as shown in Fig. 15.7. The jacket comprises five horizontal frames

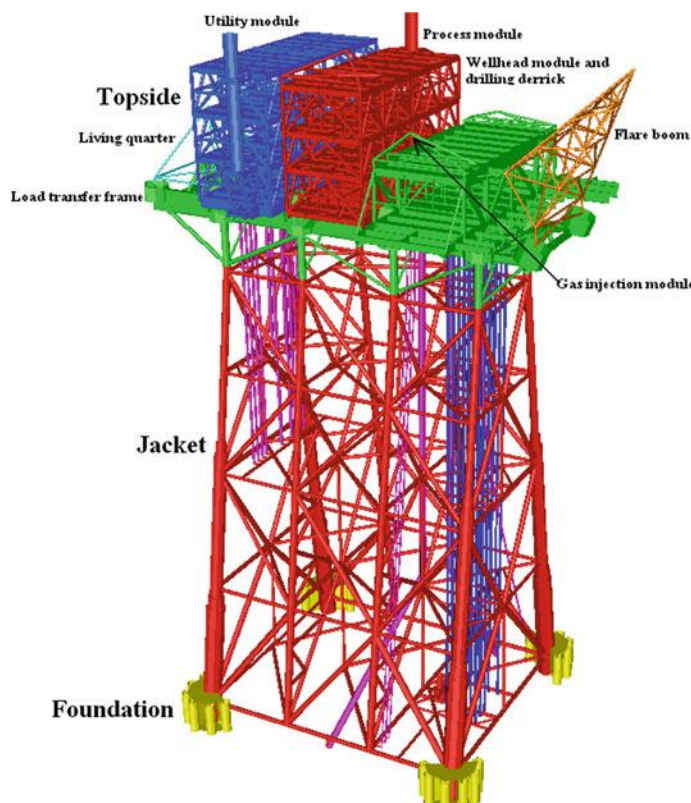


Fig. 15.7 Geometry modeling of the jacket-topside structure and notation of each module

and has a water depth of 110 m. The dimension of the jacket at the top elevation is 27×66 m. The legs are battered outward from top elevation, resulting in corner legs being double battered. Plan dimension at seabed is 70 m by 60 m. The weight of topside and jacket (including J-tubes and riser) is 29,000 and 13,000 tons, respectively. The foundation is modeled as springs with six degrees-of-freedom connected to the ground. In addition, added mass is also accounted for.

The objective of this case study is, by performing linear response spectrum analyses, to evaluate if the load transfer frame and the jacket structure comply with the current regulations regarding accidental limit state design for seismic intensity level corresponding to a return period of 10,000 years.

- Eigen-analysis

Figure 15.8 shows the first three eigenpairs with global bending in two principal directions and global torsion. The fourth eigenmode shows that the topside participates in the global vibration with the eigenfrequency of 1.390 Hz as shown in Fig. 15.9.

Contrary to a simple structure, for an offshore platform with a complex structural system, the determination of the number of eigenmodes must be carefully chosen. From a parametric study, it is found that the inclusion of more eigenmodes (50 eigenmodes) for calculating the dynamic response produces no difference in the capacity control results. Therefore, a total of 50 eigenmodes ranging from 0.402 to 5.209 Hz have been included in the dynamic analysis. These eigenmodes cover all the important global and local vibration modes of the jacket-topside structures. Furthermore, they cover more than 90 % of the total effective modal mass in three directions.

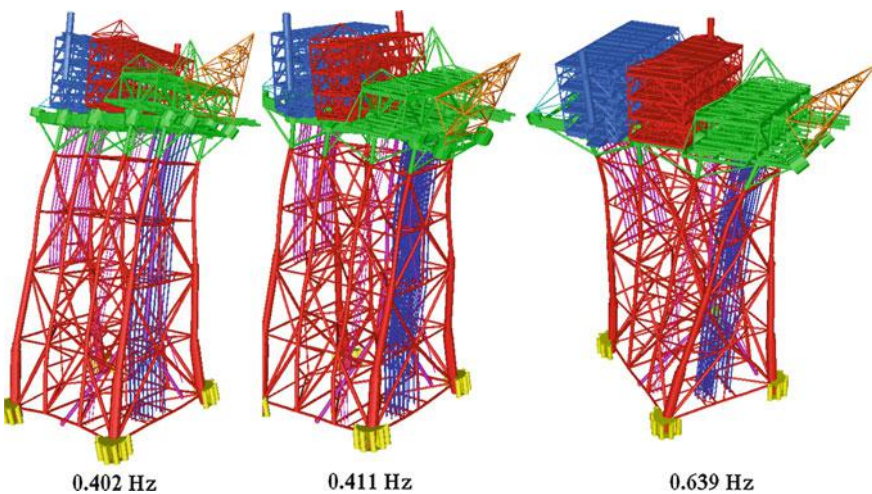
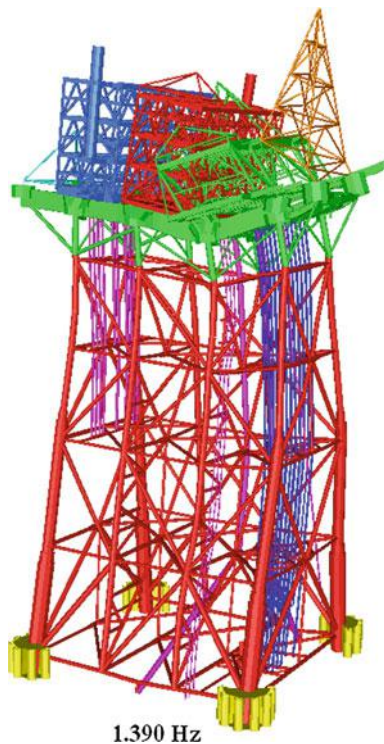


Fig. 15.8 First three global vibration modes of the jacket-topside structure

Fig. 15.9 The fourth global vibration modes showing the topside bending vibration



- Calculation of ground motions

The earthquake ground motion's determination criteria used in this study are those established by NORSAR and NGI [43].

The horizontal peak ground acceleration (PGA) for the bedrock site of the target platform, with the 10,000 years (ALS) return period of 0.26 g, is used for performing the site response analysis.

In line with the linear response spectrum analysis, before using the acceleration time histories in the site response analyses (by using SHAKE [44]), a frequency domain scaling was applied to them to obtain a better match with the specified bedrock spectra. For example, the east-west component of the Friuli earthquake (1976) record was scaled to match the bedrock outcrop spectrum. The site response analysis is then performed by using SHAKE [44]. Revised design accelerations response spectra at seabed have been finally made available as shown in Fig. 15.10.

- Load combinations for response spectrum analysis

Three different combinations and load factors of the acceleration spectra together with permanent loads are given in Table 15.2. Note that the phase difference between each direction of ground motion has been implicitly included in the load factors.

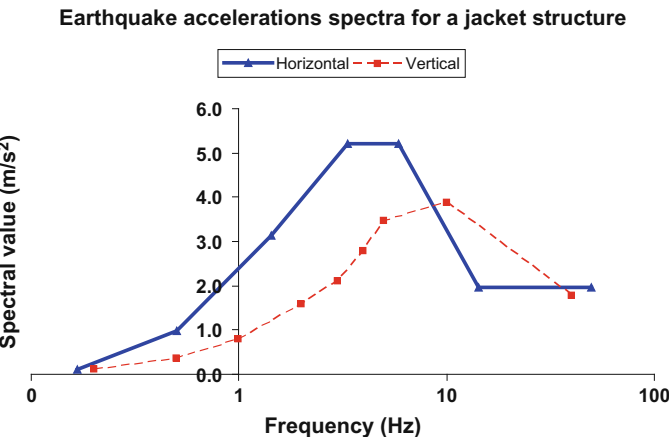


Fig. 15.10 Earthquake accelerations spectra with 10,000 years of return period for the target jacket structure

Table 15.2 Load combinations and load factors for response spectrum analysis

Load case	Factors for accelerations			Permanent load (dead weight)
	East-west	North-south	Vertical	
1	1	2/3	2/3	1
2	2/3	1	2/3	1
3	2/3	2/3	1	1

- Analysis

At first a static run is carried out to only obtain the member forces under the permanent load without hydrodynamic added mass being involved. A dynamic analysis (with added mass) with mode-superposition technique is performed. The purpose is to obtain member forces under dynamic earthquake excitations with the acceleration spectrum. The CQC method is adopted to carry out the modal combinations. The member forces obtained from the static run are then added to the member forces in the dynamic earthquake analysis for capacity control (code check).

- Results

All structural members (for both jacket and the load transfer frame) and jacket joints are checked by Eurocode [45].

For the jacket structure, the maximum utilization with the value of 0.8 (for capacity control of members, also referred to as member check) occurs on a horizontal brace member at the lower part of the jacket, and six joints have the utilization above 1.0 through joint punch check. For the load transfer frame, two horizontal members have utilization factors above 1.0 through capacity control of members (member check) [3].

15.2.7.2 Case Study 2—Spectrum Versus Time Domain Analysis of a Gravity Based Structure (GBS) Structure and Its Topside

- Structural modeling

The structure under investigation is a typical gravity based structure (GBS) located in the North Sea. It has a water depth of 146 m. The weights of topside and GBS are 55,000 and 1100,000 tons, respectively. In addition, added mass is also accounted for.

The objective of the study is to evaluate if the module support frame (MSF), drilling modules, living quarter connections and flare boom comply with the current regulations associated with accidental limit state design for ground motion level corresponding to a return period of 10,000 years. In addition, the potential foundation failure and soil liquefaction are also evaluated.

Both linear response spectrum and non-linear time history seismic analyses were performed.

For the GBS structure, compared to ultimate limit state (ULS), the accidental limit state (ALS) is normally the governing one. Therefore, the structure assessment has been performed upon the ALS, with a material factor of 1.0.

- Eigen-analysis

Before carrying out the response spectrum analysis, an eigen-analysis has been performed to obtain the eigenfrequency and mode shapes. Figure 15.11 shows the first three eigenpairs with global bending in two principal directions and global torsion. In addition, the flare boom shows a vertical bending vibration at 1.259 Hz.

A total of 50 eigenmodes ranging from 0.434 to 4.108 Hz have been included in the dynamic analysis. These eigenmodes cover all important global and local vibration modes of the GBS-topside structures. Furthermore, they cover a rather high fraction (X: 98.06 %, Y: 98.30 %, Z: 98.82 %) of the total effective modal mass in three translational directions as shown in Fig. 15.12. The figure shows that the mass participation in global X and Y reaches more than 90 % when only the first five eigenmodes are included. However, the mass participation in Z direction

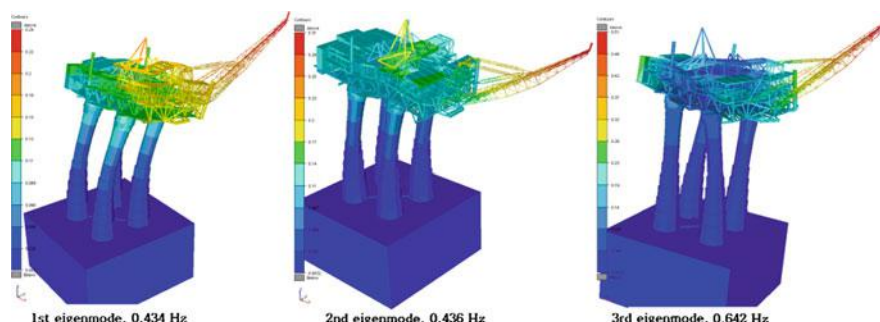


Fig. 15.11 First three global vibration modes of the GBS-topside structure

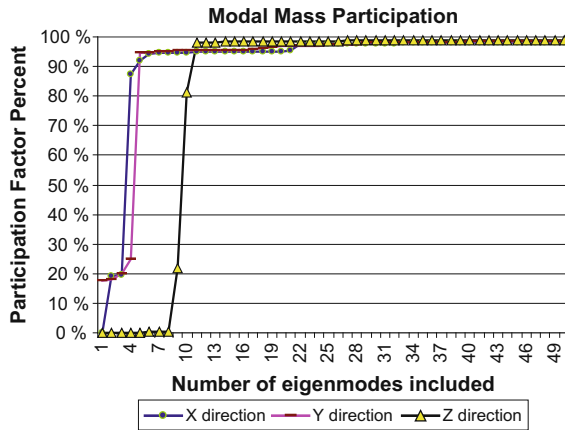


Fig. 15.12 Modal mass participation influenced by the number of the eigenmodes selected

converges to more than 90 % after 11 eigenmodes have been included. This is due to the fact that the horizontal stiffness is much lower than vertical stiffness of the structure, resulting in the lower order of eigenmodes dominated by vibrations along horizontal directions.

- Calculation of ground motions

For the site of the target platform, the horizontal peak ground acceleration (PGA) of 0.27 g, with the 10,000 years (ALS) return period, is used for performing the site response analysis.

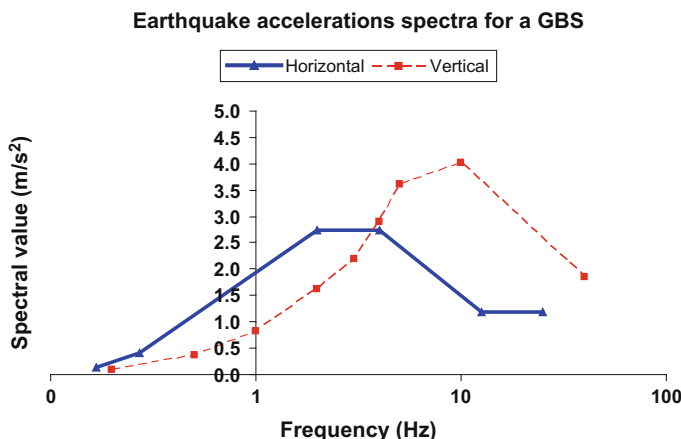


Fig. 15.13 Earthquake accelerations spectra with 10,000 years of return period for the target GBS structure

For linear analysis, Fig. 15.13 shows an example of the horizontal acceleration spectrum. This is obtained by scaling the east-west component of Friuli earthquake (1976) ground motions to match the design spectrum at bedrock outcrop according to Norsok N-003 [15], followed by performing a series of site response analyses using SHAKE [44].

For non-linear time history analysis, in order to generate the ground motion history at seabed, the following earthquake time histories have been selected and scaled to match the bedrock outcrop spectrum and used as the bedrock excitations:

1. Nahanni, Canada, 1985
2. Friuli, St. Tarcento, Italy, 1976
3. Imperial Valley, Mt. Superstition, USA, 1979

Before using the acceleration time histories in the site response analysis (using SHAKE), a frequency domain scaling was applied to them to obtain a better match with the specified bedrock spectra. Through the site response analysis by using SHAKE [44], three sets of ground motion time histories at seabed have been made available as shown in Figs. 15.14, 15.15, and 15.16.

For both linear spectrum and non-linear analysis, in addition to a site response analysis (kinematic interaction), a soil–structure interaction analysis should also be performed, with outputs of equivalent (directional) mass, stiffness and damping properties [46], which are modeled at the base of the structure to account for the effects of the interaction between the GBS foundation and its surrounding soil.

- Load combinations

For linear spectrum analysis, three different combinations and associated load factors together with permanent load are given in Table 15.2.

For non-linear time history analysis, the time histories calculated from the site response analysis can be directly used for analysis with a load factor of 1.0.

- Analysis

For linear spectrum analysis, at first a static run is carried out to only obtain the member forces under the permanent load without hydrodynamic added mass being involved. Subsequently, a dynamic analysis (with added mass) with mode-superposition technique is performed. The hydrodynamic damping due to structure–water interaction is neglected. The purpose is to obtain member forces under dynamic earthquake excitations with the acceleration spectrum. CQC method is adopted to carry out the modal combinations. The member forces obtained from the static run are then added to the member forces in the dynamic analysis for the code check.

For non-linear analysis, the ground motion time histories at seabed, in all translational degrees-of-freedom, are applied on the foundation point of the GBS structure. The dynamic responses at three locations are investigated from the bottom of the shaft, shaft-topside connection to the center of MSF at topside as shown in Fig. 15.17. The dynamic acceleration responses under the artificial ground

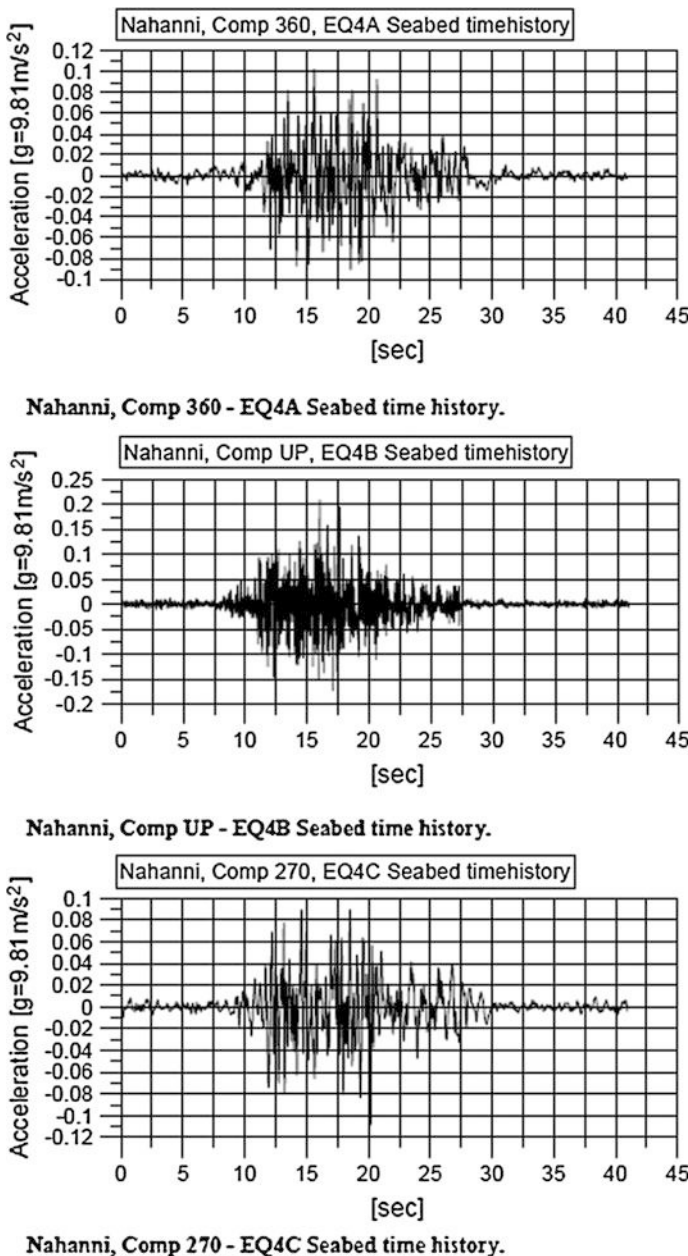


Fig. 15.14 Calculated seismic acceleration time history at seabed/ground surface based on the Nahanni earthquake record applied on bedrock

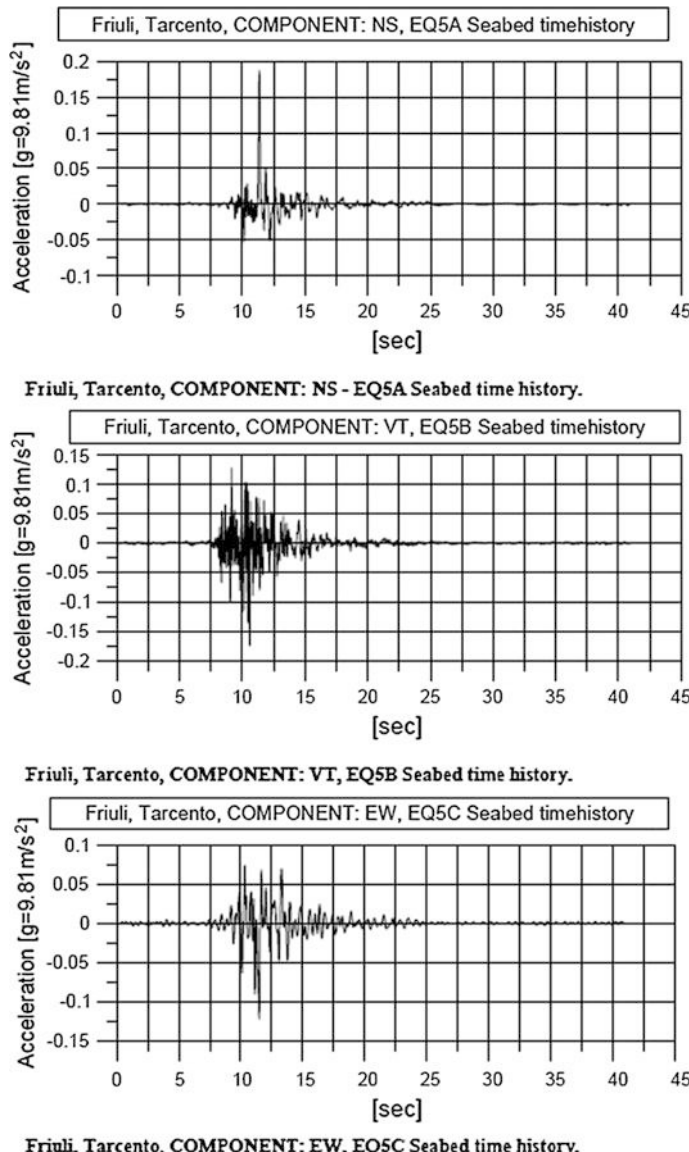


Fig. 15.15 Calculated seismic acceleration time history at seabed/ground surface based on the Friuli earthquake record applied on bedrock

motion time history generated based on the Nahanni earthquake are illustrated in Fig. 15.18. It is clearly shown that the responses reach their peaks at around 1 s, and then begin to decrease. The responses at the MSF and shaft-topside have a significant amplification compared with the excitation at the bottom of the shaft.

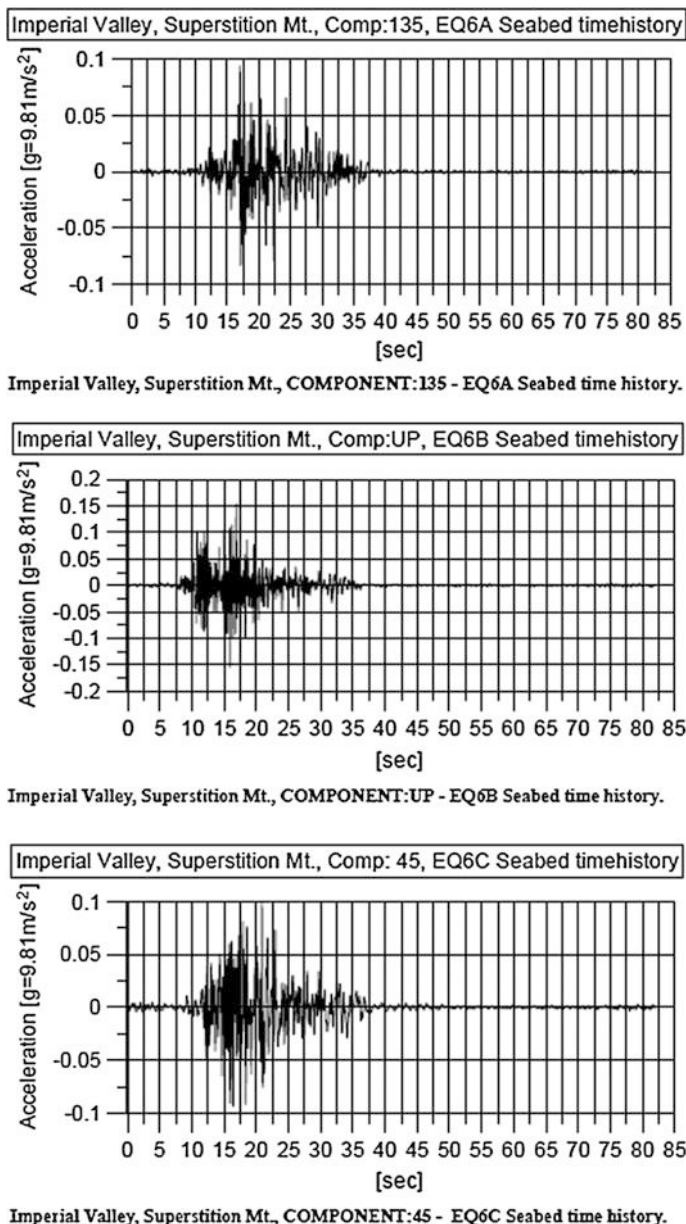


Fig. 15.16 Calculated seismic acceleration time history at seabed/ground surface based on the Imperial Valley earthquake record applied on bedrock

This is especially obvious for the response along the vertical direction, in which the eigenperiod of vibration on MSF is closer (than that of the horizontal direction) to that of the earthquake excitation (Fig. 15.13).

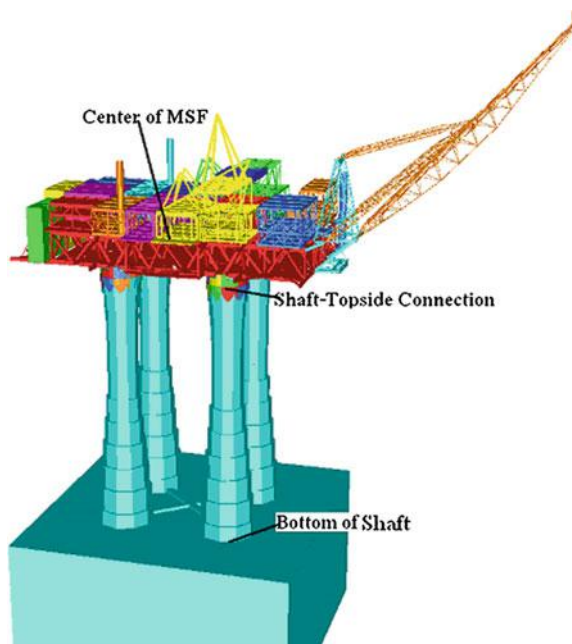
- Results

All structural members are checked by Eurocode 3 [45]. For linear spectrum analysis, in total 46 members have the utilization above 1.0. The most highly utilized members are illustrated in Fig. 15.19. No members on the flare boom are highly utilized. For non-linear analysis, only 16 members have a utilization above 1.0. It is clearly shown that the seismic response using time history analysis method is greatly reduced. This is mainly due to the fact that, compared to the linear response spectrum analysis, dynamic time history analysis explicitly accounts for the phase information among three translational ground motions and phase (sign) of structural responses. Furthermore, dynamic time history analysis can also model the structural and material nonlinearities as well as damping in a more rational manner [3]. Note that the work associated with structural reinforcement for offshore structures is normally very costly compared to that of the land based structures, the decrease of number of structural members requiring reinforcement directly leads to an attractive cost saving.

- Foundation capacity check

By assuming that the foundation remains linearly elastic during the earthquake, the combination of maximum base shear and overturning moment from the non-linear

Fig. 15.17 Locations of reading points for dynamic acceleration response



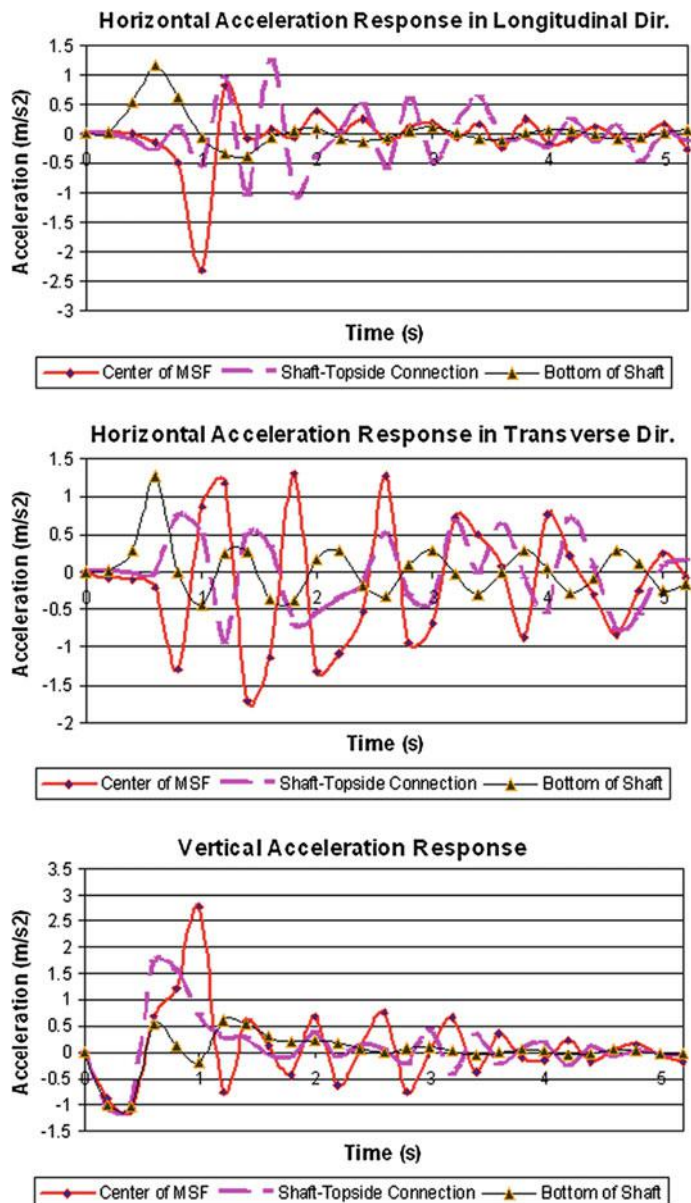


Fig. 15.18 Dynamic acceleration responses at different parts of the structure under the earthquake acceleration of Nahanni

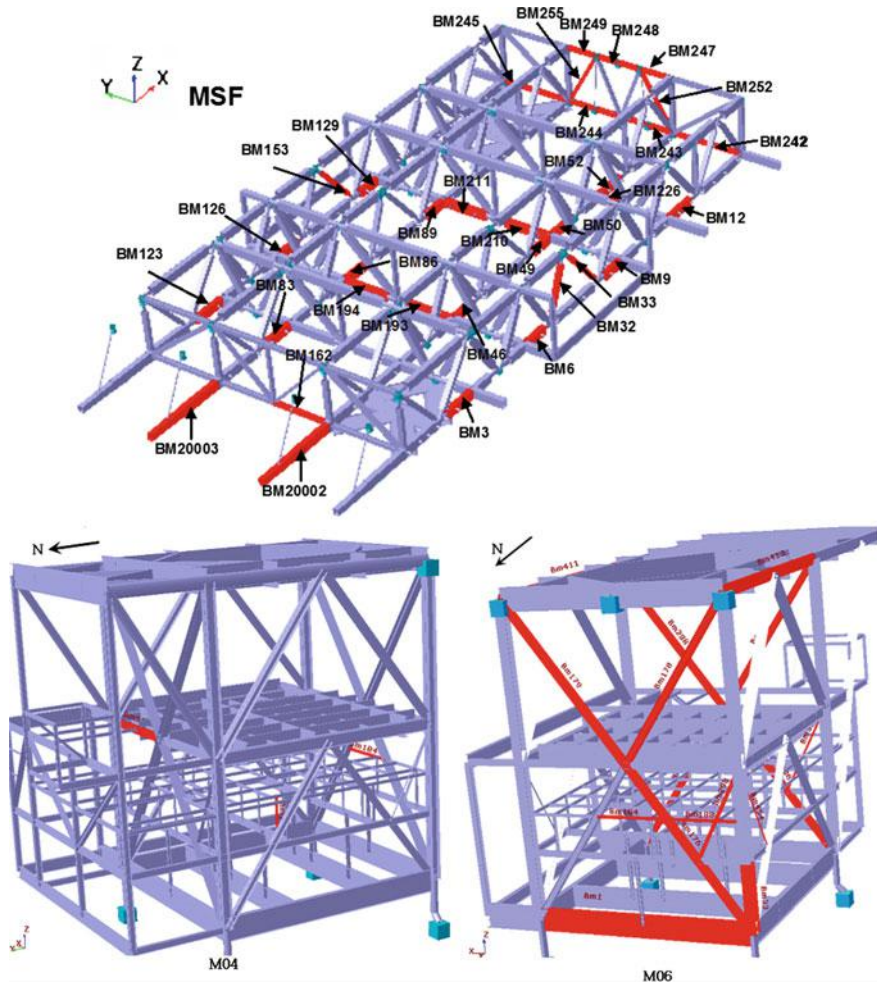


Fig. 15.19 MSF and drilling module members (*marked*) with utilization factor above 1.0 from the linear response spectrum analysis [3]

dynamic analysis are used for evaluating soil failure. The capacities were checked using the limit equilibrium methods by CAP and CARL [47]. The results show that the foundation capacity is sufficient to resist the maximum earthquake load (the combination with the maximum horizontal base shear) with a factor of 3.6.

Based on the ground acceleration calculated from SHAKE, it is also concluded that the potential of soil liquefaction due to seismic excitations is not a concern for the site. For the method for evaluating liquefaction potential, readers may read reference [46].

Table 15.3 The influence of soil stiffness on the natural frequency and number of members with utilization above 1.0

Soil stiffness	Natural frequency (Hz)	Numbers of MSF failure members	Numbers of M06 failure members
0.7 Reference value	0.414	26	18
Reference value	0.434	22	24
1.3 Reference value	0.438	30	23
1.6 Reference value	0.442	38	21

- Influence from soil stiffness

A parametric study has been carried out to identify the influence from the variation in the soil stiffness through linear spectrum analysis. The results are shown in Table 15.3. It is found that the variation in the soil stiffness in this range only slightly influences the eigenfrequency, but has a clear influence on the number of beams with the utilization above 1.0.

15.2.8 *Response Difference Between Response Spectrum and Non-linear Dynamic Time Domain Analysis*

The calculated responses based on the two methods should generally be similar to each other, and the response spectrum analysis normally results in more conservative evaluation. However, for flexible systems with large numbers of degrees-of-freedom, the results begin to differ. For non-linear systems, particularly those with elements that undergo stress or stiffness degradation or have elements with dramatically different strengths, the agreement ranges from excellent to very poor. This is also dependent on the number of degrees-of-freedom the structure possesses.

Generally, since time histories analysis method can reduce the uncertainties induced from the nonlinearities as well as the phase among three components of ground motion input, it provides more reliable results than the response spectrum method. Furthermore, through a reduction of uncertainties, the calculated structural responses can be reduced to a certain extent, which can be illustrated in the case study presented in Sect. 15.2.7.2.

15.3 Selection of Principal Directions in Seismic Analysis

During an earthquake event, at any location and any time instant, three ground motions, which are perpendicular and uncorrelated with each, generally exist. If these three directions remain constant during an earthquake event, they are of

special engineering interest in that the ground motions can be simplified as the translational motions along these three directions. Several pieces of research work have concluded that these three orthogonal directions exist [48–50]. On the other hand, there are also studies showing that the perpendicular uncorrelated directions only exist in the horizontal plane [51].

It is then reasonable to assume that the ground excitation has a principal direction during an earthquake event, or when the maximum ground acceleration occurs. However, this principal direction is almost impossible to determine. Therefore, one has to assume that the structure can resist an earthquake of given ground motions from any direction. This complicates the seismic assessment task.

However, in engineering practice, by carefully observing the eigenmode shape and the associated modal mass for each individual eigenmode, one can normally identify principal directions as the two along the vibration directions of eigenmodes with the two highest modal mass values. These two directions are often perpendicular to each other in horizontal plane. For regular structures, the principal directions are normally the longitudinal and transverse directions of structures. For a four or more leg supporting offshore structure, in addition to the longitudinal and transverse directions, diagonal directions at the leg bottom may also be relevant for critical leg and pile capacity control.

For irregular structures in the horizontal plane, the principal direction may not be unique or may be difficult to identify. Therefore, a large number of analyses with a repeated variation of principal direction may be used for analysis of the irregular structures.

15.4 Recently Developed Methods

15.4.1 Incremental Dynamic Analysis

First proposed by Bertero [52], incremental dynamic analysis (IDA), also named dynamic pushover analysis, is used to perform non-linear dynamic structural analysis under a suite of ground motion records. Each is progressively scaled to several intensity measures (IM, e.g. PGA) levels to cover the entire range of structural response from elasticity to yielding and finally to global dynamic instability (collapse) [53, 54]. This analysis method can provide useful information regarding dynamic characteristics of a structure as well as useful inputs for applications of PBD [55], and it gives a clear and precise indication of the relationship between concerned damage measure (response parameters) and the IMs. Limit state for a given IM can then be specified on the relationship curve. Combined with probabilistic seismic hazard analysis as elaborated in Chap. 9, the results can be conveniently integrated with a conventional seismic hazard curve, facilitating the calculation of mean annual frequency of exceeding a certain damage limit state capacity (designated performance goals) [56].

15.4.1.1 Method Description

To perform an IDA for a target structure, the following steps are required:

1. Choose a suite of ground motion records representative of the site (soil condition), earthquake magnitude and epicenter distance etc. The number of ground motions records is normally greater than 10.
2. Scale the selected ground motion time history records to the same IM through either a scaling of time history (i.e. the measure of IM is usually a target PGA), a single period spectrum matching (i.e. the measure of IM is a target spectral acceleration at the dominated period of the structure), or multiple-period spectrum matching for a range of periods (i.e. the measure of IM is the mean of target spectral acceleration at several periods of interests). The motivation for performing the spectrum matching is that it can efficiently minimize the bias of damage estimation [57]. The response spectra from all the scaled ground motions records normally cherish a significant degree of variability. However, the lognormal standard deviation should be small (low dispersion) within and below the period range of interests (e.g. 2–4 s).
3. Perform dynamic time history analysis by applying the scaled seismic ground motion histories obtained in step 2 with an elastic load factor. The value of the elastic load factor is determined so that time history analysis would result in a response that would produce incipient yielding in the structure. Then document the structural response, measured by engineering demand parameters (EDP) at the elastic load factor. The EDP can be drift, acceleration, rotations at relevant locations, etc. On a graph with an abscissa consisting of EDP and an ordinate axis of the load factor, plot the point consisting of the maximum calculated EDP from the analysis and the scaled value of load factor. Draw a straight line from the origin of the axes to this point. The slope of this line is referred to as the elastic slope K [58].
4. Perform non-linear dynamic time history analysis by further increasing load factor larger than the elastic one such that mild non-linear behavior will be introduced on the structure. Again document the EDP at the corresponding load factor and plot it in the graph.
5. Perform non-linear dynamic time history analysis by further slightly increasing load factor larger than the one used in the previous step. Document the EDP at the corresponding load factor and plot them in the graph.
6. Repeat step 5 until the graph shows a flat line, where the structure response displays disproportionately large EDP increase for a rather small increment of the load factor as shown in Fig. 15.20, i.e. global stability limit (collapse) is reached. In FEMA 350 [58], this point can be identified as the point when the slope of the straight line in the graph connecting two adjacent load factors is less than 20 % of the elastic slope K defined in step 3.
7. For each original ground motion time history obtained in step 2 and used for scaling, perform the dynamic analysis with gradual increases in load factor, and

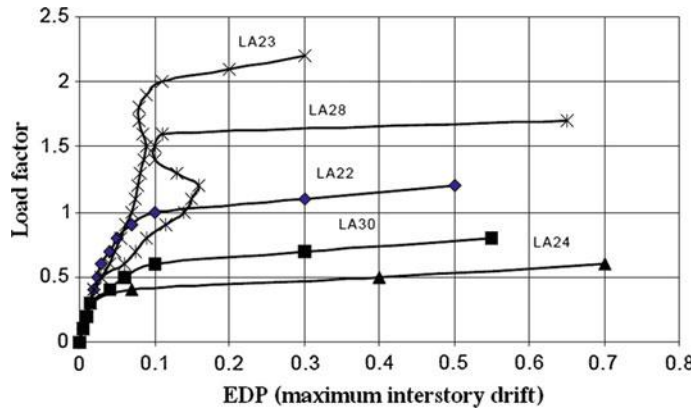


Fig. 15.20 An illustration of an incremental dynamic analysis plot [58]

construct the IDA graph described from step 2 to step 6. Figure 15.20 shows an example of graph used for IDA.

It is noted that due to the significant variability among each ground motion record generated in step 2, for all the records, the determination of load factor at the incipient yielding, mild plasticity and final global instability requires substantial computational efforts, and may lead to a large waste of runs [59]. However, certain tracing algorithm and parallel processing can be rather efficient ways to relieve these efforts [60].

15.4.1.2 Assign Limit States by Using IDA Curves

In Fig. 15.20, the load factor in the ordinate axis can be converted into a more direct IM measure to quantify the effect of the ground motions, such as PGA, spectral acceleration at the natural period of the target structure or a variety of vector-valued IMs. Shome and Cornell [61] presented that, compared to the PGA measure that is entirely site specific, the elastic 5 % damped first mode spectral acceleration $S_a(T_1, 5\%)$ is more effective due to its structure-specific characteristic, $S_a(T_1, 5\%)$ is therefore widely used for performing IDA.

For assigning limit states quantitatively, a model to represent the IDA curves is desired. Several models exist, such as the multiple-interpolation-spline-function [62], the Ramberg-Osgood model (originally used for describing non-linear stress-strain relationship) [63] etc. The latter is less comprehensive and can be applied more conveniently for risk analysis. The Ramberg-Osgood model is expressed as:

$$\frac{EDP}{EDP_c} = \frac{IM}{IM_c} + \left(\frac{IM}{IM_c} \right)^n = \frac{IM}{K \cdot EDP_c} + \left(1 + \left| \frac{IM}{IM_c} \right|^{n-1} \right) \quad (15.13)$$

where K is the elastic slope of the IDA curve; IM_c is the “critical” intensity measure that occurs at the onset of large EDPs that subsequently lead to collapse; $EDP_c = IM_c/K$ is the “critical” EDP; and n is a constant that varies little among various IDA curves [56].

By fitting the model into the actual IDA data using certain curve fitting methods (e.g. least square) for 10th, 50th and 90th percentile curves, the constant n (for all percentile), K and IM_c can be obtained for each percentile curve.

With the value of K and IM_c , it is possible to determine the expected EDP for a given level of IM. Different limit states based on various performance levels can then be assigned to the model.

15.4.2 Endurance Time Analysis

Whereas the IDA and non-linear dynamic analysis require considerable computation efforts, because a large number of time history analyses need to be performed in addition to the computation of each site specific ground motion history prior to each time history analysis, significant reduction of the analysis efforts can be achieved by performing endurance time analysis (ETA). It is carried out by applying a single pre-designed/artificial intensifying ground motion history to the structure for dynamic analysis. Variations in relevant response parameters and damage indexes are then monitored as the ground motion is increased, and structural performance is assessed based on its response at various excitation levels [64–66]. For alternative designs, based on the order in which these alternative structures fail, one can evaluate and compare their seismic performance, as illustrated in Fig. 15.21. Since the ETA acceleration increases with time, the load consequence is in a sense accounted for, i.e. structures gradually experience the entire process from elastic deformation to yielding and non-linear plasticity, and finally reach global instability.

The essential issue for performing the ETA is to determine the ETA ground motion time histories so that the results from ETA can be correlated reliably with the response of structures subject to seismic excitations, i.e. decent IMs at various time instants [67]. This is carried out by generating ground motion histories that would produce a response spectrum matching the code design spectrum at a particular time t_{Target} , which is also called the target time.

In practice, the target spectrum $S_{aETA}(T, t)$ corresponding to a time t is a scaled version of the same spectrum (normally a standard design spectrum at a vibration period T) $S_{aD}(T)$ [67]:

$$S_{aETA}(T, t) = \frac{t}{t_{Target}} S_{aD}(T) \quad (15.14)$$

With the equation above, it is possible to consider different target spectra at different times pertaining different hazard levels.

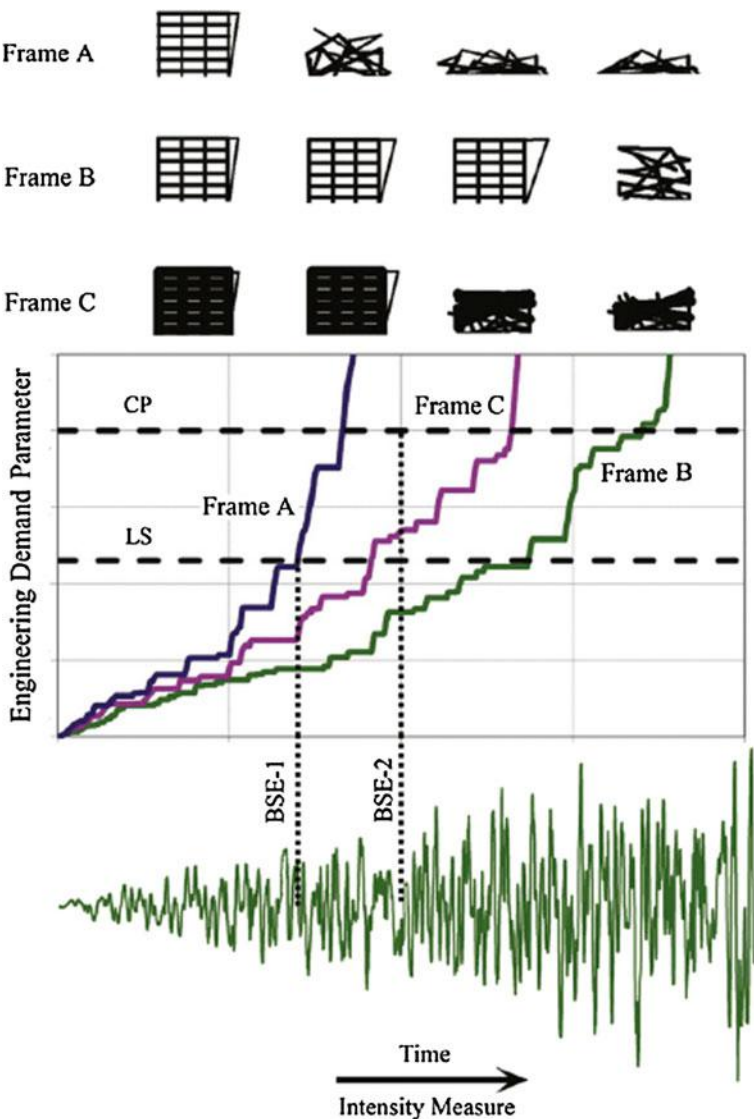


Fig. 15.21 Schematic representation of ETA and its application in PBD (*CP* and *LS* stand for collapse prevention and life safety in a PBD, respectively) [68, 70]

The target spectrum can also be expressed with a target displacement spectrum $S_{dETA}(T, t)$:

$$S_{dETA}(T, t) = \frac{t}{t_{Target}} S_{aD}(T) \times \frac{T^2}{4\pi^2} \quad (15.15)$$

Optimization techniques can be used in order to establish ETA ground motion histories with the property of having response spectra that proportionally intensify with time while remaining compatible to a pre-specified design spectra $S_{aD}(T)$ curve as much as possible. To obtain proper ground motion histories is rather challenging. Estekanchi et al. [67] proposed to treat the problem numerically with unconstrained optimization formulation:

Minimize:

$$F(a_g) = \int_0^{T_{\max}} \int_0^{t_{\max}} \left\{ [S_a(T, t) - S_{aT}(T, t)]^2 + \alpha [S_d(T, t) - S_{dT}(T, t)]^2 \right\} dt dT \quad (15.16)$$

where a_g is the ETA acceleration function being sought; $S_{aT}(T, t)$ and $S_{dT}(T, t)$ are the target acceleration response and displacement response at time t , respectively; $S_a(T, t)$ and $S_d(T, t)$ are the acceleration response and displacement response of acceleration function at time t , respectively; α is a weight parameter (can be assumed as 1.0); and T is the vibration period.

The equation above can be numerically satisfied by performing optimization at a rather fine time step Δt (e.g. 0.01 s) and the period interval ΔT (e.g. 0.02 s for vibration periods equal and lower than maximum period of interests, and 2 s for periods above). Figure 15.22 shows the generated spectrum for ETA at four time instants.

For simplicity, by using the ground motions that only match the same first mode spectral acceleration from the design spectrum, Riahi and Estekanchi [68] compared the results obtained from ETA, a traditional non-linear dynamic time history analysis, and a static non-linear pushover analysis accounting for only a single vibration mode. They found that the responses calculated by ETA and time history analysis are mostly close to each other. However, due to the fact that the load pattern in traditional pushover analysis is only based on a single period of mode and it does not account for the modification of dynamic characteristics with time, it gives quite different results to those of the other two methods.

Although the results of ETA are not exactly consistent with the results of non-linear dynamic analysis with real ground motions, the ETA can identify a structure with better performance even in the case of complex structures. Therefore, ETA can be a useful tool for PBD [67, 69]. Estekanchil and his co-workers presented a procedure for the utilization of ETA in the performance based seismic design as shown in Fig. 15.23.

In summary, the major benefits of using ETA include a significant reduction in computational demand, simplicity and sensibility for engineering applications, and applicability to a wide range of structures regardless of their complexity [69]. The procedure can also be beneficial to greatly reduce the practical test cases in experimental studies. For an elaborated description of the ETA and its applications, readers may read Refs. [64–71].

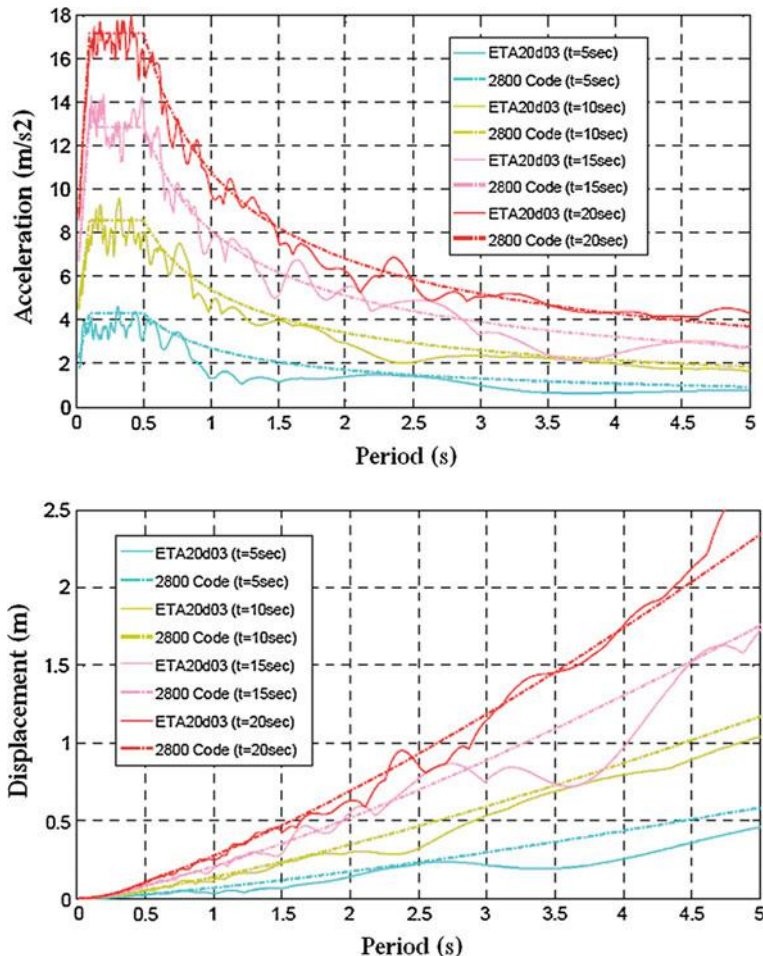


Fig. 15.22 Matched response spectra of ETA at 5th, 10th, 15th and 20th s: measured with acceleration (*upper*) and displacement (*lower*) [69]

It is worth mentioning that the basic methodology of ETA has also been extended to simulate the ocean wave loading on marine structures, in which the structures are exposed to artificial wave functions. The wave functions are used to provide increasing excitation wave load levels rather than the increasing IMs with time in earthquake engineering applications. For this purpose, the sea states (significant wave heights) are increased continuously by time in a wave function, and each time instant represents a specific sea state, i.e., at each time instant, the result of the endurance time analysis can be compared with the results of a typical 3-h time history record obtained from the wave energy spectrum of the same sea state (represented by a significant wave height and wave period). Hence, ETA results

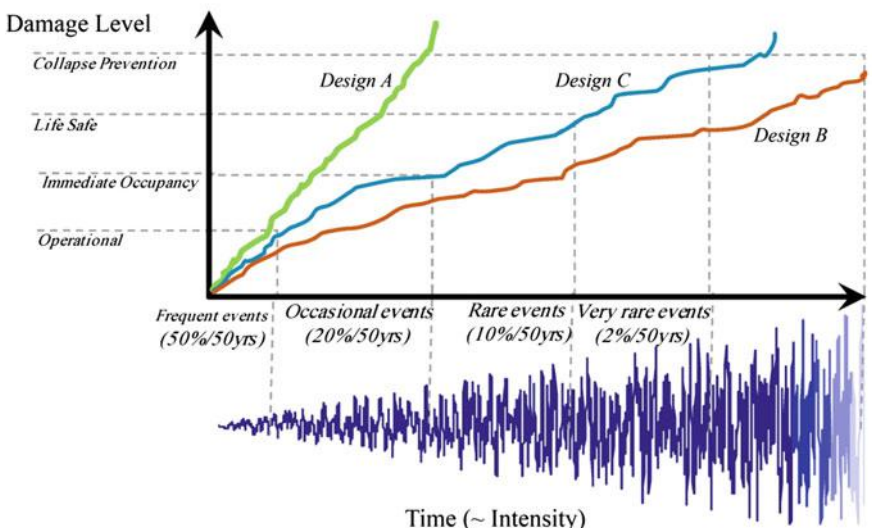
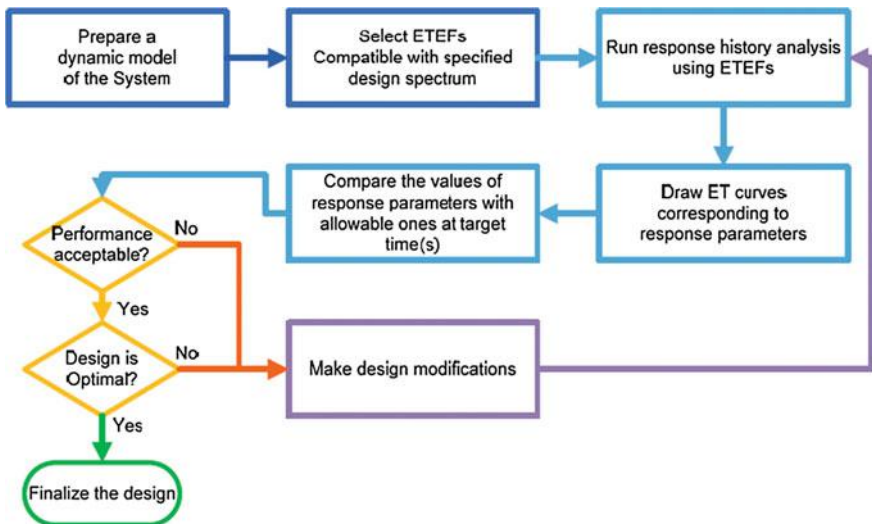


Fig. 15.23 General methodology of ETA design procedure (*upper figure*, ETEFs stand for endurance time excitation functions) and an example of performance comparison for different alternative designs (*lower figure*) [69]

include an estimate of the response under different levels of wave excitations in each single analysis. Figure 15.24 shows a typical artificial wave function and response of an offshore structure presented by Jahanmard et al. [72]. Since all the desired significant wave heights are swept by a single time history analysis, and the time is representative of the sea states in ETA, both the wave function and response

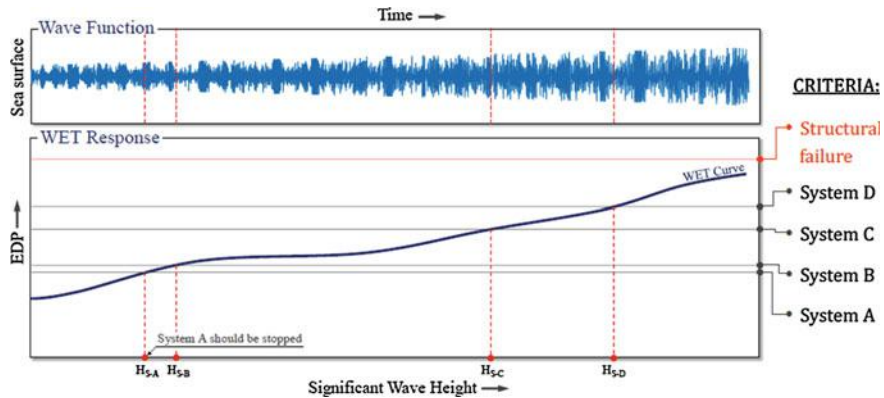


Fig. 15.24 An example of an artificial wave function to simulate various ocean wave sea states [72]

show a continuous increase. In the lower figure, the operating limits of the systems A, B, C and D correspond to four sea states with four different significant wave height levels.

15.4.3 Critical Excitation Method

Every time a devastating earthquake occurs, there are always unexpected structural damages requiring an update of relevant seismic design codes. However, this repetition never resolves all the issues and new damages have occurred even recently [73]. This is mainly due to the variability of ground motions, which was witnessed by several recent earthquakes such as Loma Prieta earthquake that occurred in 1989, Northridge earthquake of 1994, Kobe earthquake of 1995, and Chi-chi earthquake of 1999, implying that the frequency contents of ground motions is difficult to estimate [74]. Therefore, it is essential but rather difficult to completely include a complete coverage in ground motion variability by the code specified design, which is usually constructed by using past observations and probabilistic insights. However, uncertainties in the occurrence of earthquakes (or ground motions), the fault rupture mechanisms, the wave propagation mechanisms, the ground properties, etc., cause more difficulties in defining reliable design ground motions, especially for important structures in which severe damage or collapse must be avoided [75–79].

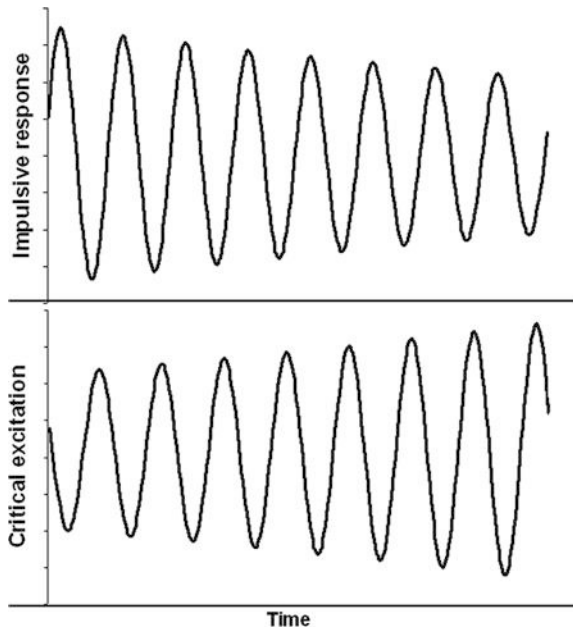
This circumstance motivates the emergence of the critical excitation method. Rather than attempting to model the range of ground motions that a given structure may experience over its lifetime, based on reliable physical data, the critical excitation method aims to find the most unfavorable ground motions that produce the maximum structural responses for a robust structural design (a tailor made

“worst case”). To fulfil this objective, one can account for the ground motion uncertainties by including the variability in the acceleration or velocity power spectrum, and using the input energy and the energy input rate, or response acceleration, as measures (objective) of criticality.

The critical excitation models can be developed within the frameworks of response spectra, time histories or random process modeling. By assuming that energies of all seismic excitations have a known upper limit and the magnitude of the response peak is the critical measure of the response of a structure, Drenick [80] first presented that, for a linear elastic viscously damped SDOF system, the critical excitation is its impulse response function reversed in time, i.e. mirror image excitation, which is shown in Fig. 15.25. This implies that the critical envelope function for the system in deterministic problems can be given by an increasing exponential function, and the critical excitation has to be defined from the time of minus infinity. Due to the conservativeness of Drenick’s method, Shinozuka [81, 82] further developed the critical excitation problem by specifying an envelope of Fourier amplitude spectra in frequency domain, resulting in a nearer upper bound of the maximum response. Other researchers [83, 84] also sought to solve the critical excitation problem by specifying an envelope function of ground motions in the time domain, which is less efficient than their frequency domain counterpart.

The core process of performing a critical excitation is to maximize the measures of criticality as an objective subject to restraints on response and input parameters. The restraints can be, for example, a power limit or PSD amplitude limit etc. In

Fig. 15.25 Critical excitation (lower) is the mirror image of impulse response (upper)



many cases, the critical excitation has a frequency very close to the fundamental natural frequency of the structural model. For an elaboration of this method, readers may read references [73–85] by various authors.

15.5 Characteristics of Seismic Responses

Different from dynamic loads due to wind, wave and ice impact on structures, the loads generated on a structure during an earthquake are in a sense purely due to the inertia of the structure, which is caused by the acceleration of the structural masses. The acceleration is the sum of the ground acceleration and the acceleration of the structural masses relative to the ground. Similarly, the dynamic structural responses measured with different units (acceleration, velocity or displacement) under seismic excitations are hereby quantitatively discussed by categorizing the dynamic characteristics of both structures and seismic ground motions.

When a structure is stiff (such as a low rise building) with a natural period below 0.5 s, it is more sensitive to acceleration than displacement, and the structure tends to move in the same acceleration amplitude as the ground, the acceleration of the structural masses relative to the ground is negligible, and the resultant earthquake loading is then purely proportional to the structure's mass.

However, when a structure is more flexible with a natural period above 2 s (such as high rise buildings, fixed offshore structures, some fluid tanks, and base-isolated buildings), by observing an earthquake design spectrum, it is found that the structure is more sensitive to ground displacement than acceleration, i.e., the structure undergoes large relative horizontal displacement, which may result in damage to non-structural elements, equipment etc. The acceleration of the structural masses tends to oppose the acceleration motions, and the sum of the acceleration is therefore low. For a preliminary design for those more flexible structures, the resultant acceleration responses are approximately proportional to the square root of the sum of structure masses. Figure 15.26 shows a comparison between the excitations at the bottom and the responses at a location on the topside (the frame structures above the concrete shaft shown in Fig. 15.17) for a fixed gravity based offshore structure. The natural period of the structure corresponding to the first global bending vibration mode is 2.3 s. It shows that the acceleration responses at the topside in all three directions are much lower than the excitations, indicating that this structure may work as a filter to decrease accelerations due to the earthquake excitations transferred from the foundation.

For a very flexible structure, such as a compliant offshore tower structure with a natural period above 10 s, the structural masses tend to remain motionless, which does not generate any significant loading, and the structure subjected to seismic ground motions is free from damage.

Furthermore, if a structure's natural period is close to the period of earthquake ground motions, the energy is then effectively fed into the structure and the structural responses are amplified. In this case, the damping in the structure will

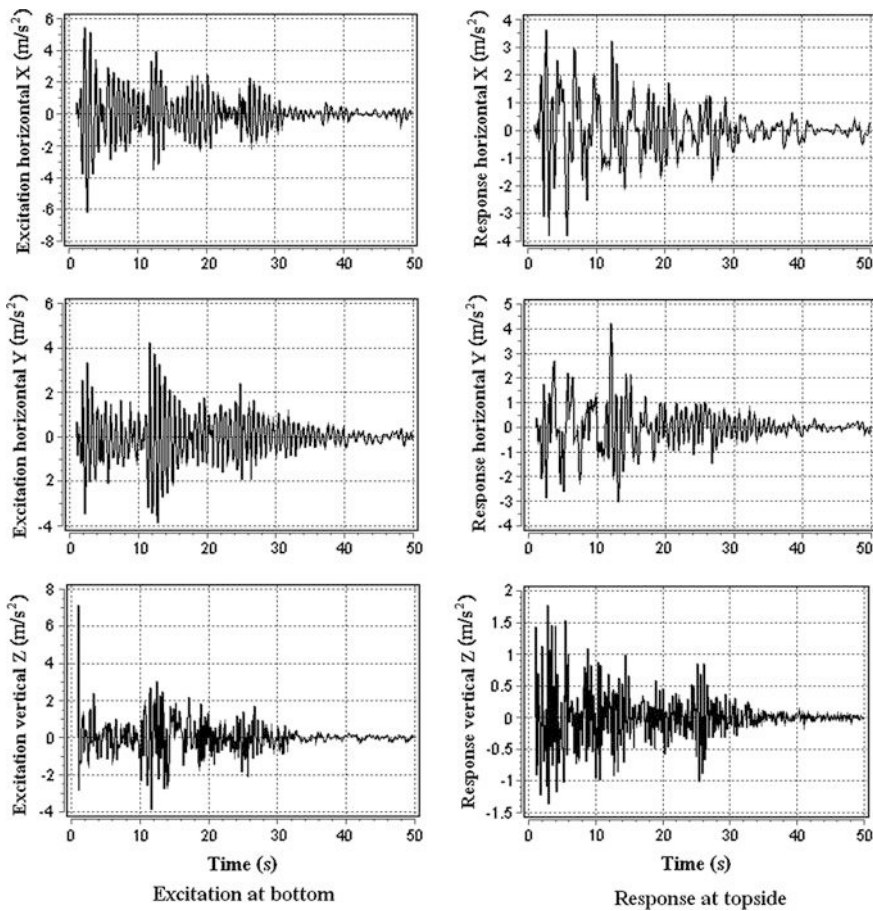


Fig. 15.26 Comparison between the seabed ground excitations (*left*) and responses (*right*) at topside of a fixed offshore structure with a natural period of 2.3 s

absorb the energy from the structural response and dissipate it, then mitigate the build-up of the resonant responses and reduce the response amplitudes.

Except for inertia forces due to ground accelerations transferred to structures, for offshore structures, the relative motions between the submerged structural members and their surrounding fluids also create hydrodynamic damping forces. Furthermore, the surrounding fluids will also enhance the inertia effects of the submerged structural members, which are normally referred to as the effects of added mass. The hydrodynamic damping in a seismic analysis can normally be neglected. However, when a strong earthquake occurs together with a significant storm (i.e., large wave height), the hydrodynamic damping forces can dramatically increase. Note that the joint probability of occurrence of both events is practically extremely low, and the simultaneous occurrence of both events is therefore not

considered by typical offshore structural design codes. Section 10.1 presents more details regarding the modeling and effects of hydrodynamic damping/drag forces and added mass.

In addition, large earthquakes generate strong ground motions in three dimensions and with multiple frequencies. The horizontal motions directly excite the vertical and oblique structures, and the vertical excitations directly excite the horizontal and oblique structures. Both the horizontal motions and vertical motions may not only induce the bending of the structures, but also exert large torsional moments. If little or no bracing is used to resist the torsion moments, a large torsional deformation, especially on corners of the structure, may be significantly increased, which poses a threat to the safety of the structure.

In special cases, for asymmetric structures or symmetric/anti-symmetric structures subject to asymmetric excitations, vertical ground motion excitations can also induce the horizontal response of the structures. Therefore, when the frequency of a dynamic vertical excitation is close to the natural frequency of a horizontal vibration mode, the resonance of horizontal response may also occur. In a similar manner, horizontal ground motions can also induce the resonance response of a structure along the vertical direction.

15.6 Seismic Transient Excited Vibrations

Even if the seismic loading itself may not cause structural collapse or damage, it can excite vibrations of different parts of a structure so that the vibration of one part of a structure can induce a significant transient loading on other parts of the structure, posing potential threats to the structural integrity.

Here we take a GBS platform as an example, its structural modeling is shown in Fig. 15.27. The natural period corresponding to global bending vibrations of the entire platform is 2.56 s, while the natural period for the vibration of the flare boom is 1.36 s (0.74 Hz).

As shown in Fig. 15.28, under the selfweight loading of the structure, all structural members have stresses far below yielding. However, subject to seismic excitations, the support braces under the flare boom show a significant increase in stress close to yielding.

To investigate the cause of the high plasticity utilization of the four critical braces, a Fourier analysis of the seismic response of four brace members is performed as shown in Fig. 15.29, which shows a peak at the natural frequency (0.74 Hz) corresponding to the flare boom's self-vibration. This indicates that the seismic loading works as a transient loading to excite the vibrations of the entire GBS platform at its natural period of 2.6 s, which further excites the flare boom to vibrate at its own natural frequency of 0.74 Hz as shown in Fig. 15.30. Because of the vibration of the flare boom, it then exerts the dynamic forces on its support

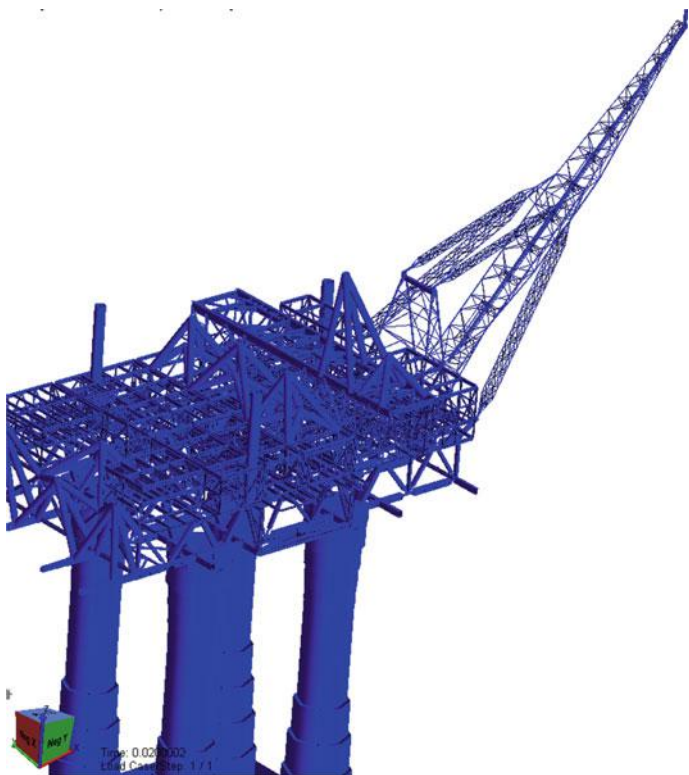


Fig. 15.27 The modeling of a GBS platform (courtesy of Aker Solutions)

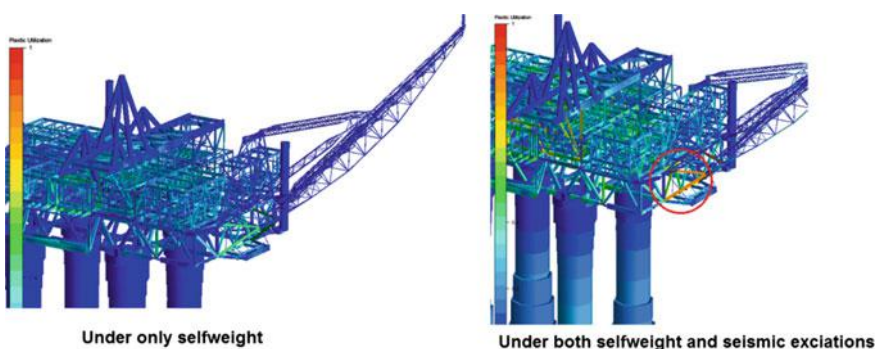


Fig. 15.28 Plastic utilization of structural members under only the static selfweight (left) and under both selfweight and seismic excitations (right) (courtesy of Aker Solutions)

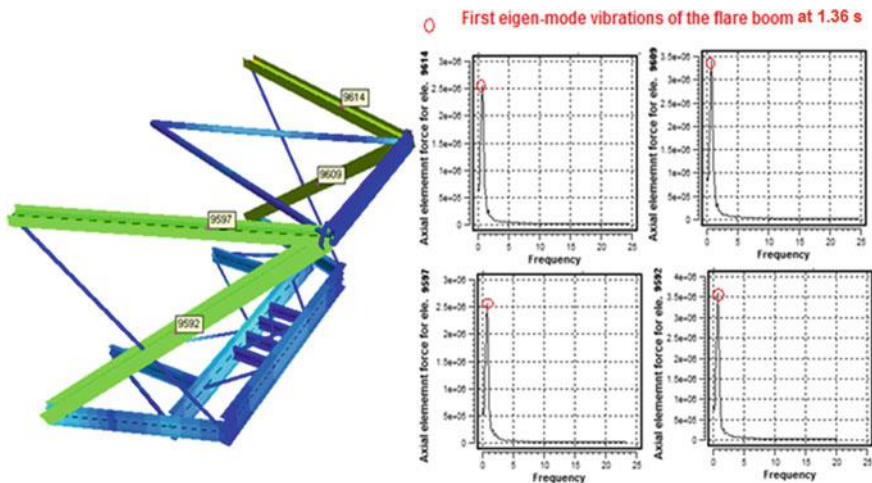


Fig. 15.29 Fourier analysis of the response for four critical brace members showing that the dynamic forces applied on them are mainly due to the vibrations of the flare boom (corresponding to a period of 1.36 s or a frequency of 0.74 Hz as shown in the *right figure*) supported by the four braces (courtesy of Aker Solutions)

braces, causing the high utilization of those braces. On the other hand, for members far from the flare boom, the dynamic structural response is strongly influenced by the vibration of the entire structure corresponding to the global bending vibration period of 2.56 s, as shown in Fig. 15.31.

15.7 Whipping Effect

15.7.1 Introduction

To control the global dynamic response of the structure, it is desirable to design a structure with a pyramid-shape, so that the vertically propagating shear wave energy on the structure can be dispersed within a broad range of frequencies, even under resonance. This is because the modal mass of the pyramid-shaped structure is not concentrated in one single vibration mode, and the global seismic force and the response of the structure are thus limited. This design strategy is referred to as elevation control as will be discussed in Chap. 19. However, as the elevation control often results in a rather slender tip, the seismic responses at this tip may be greatly amplified without significant interaction with the vibrations at other parts of the structure. This phenomenon is called the whipping effect, and it is mainly due to the decrease of lateral stiffness at the tip compared to the rest of the structure.

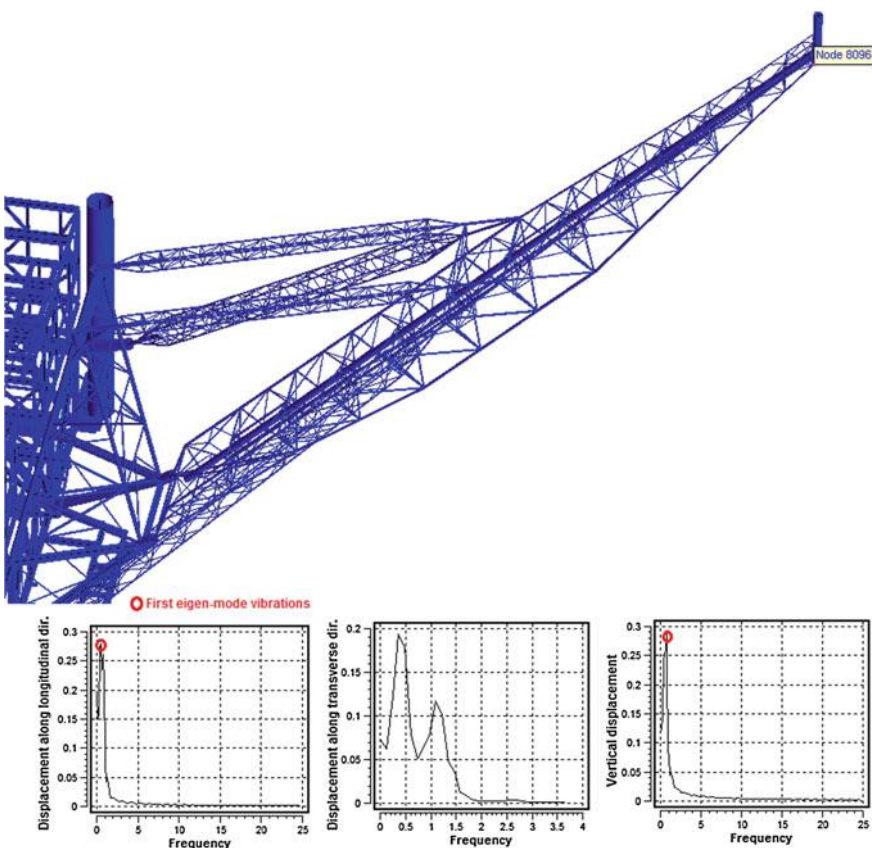


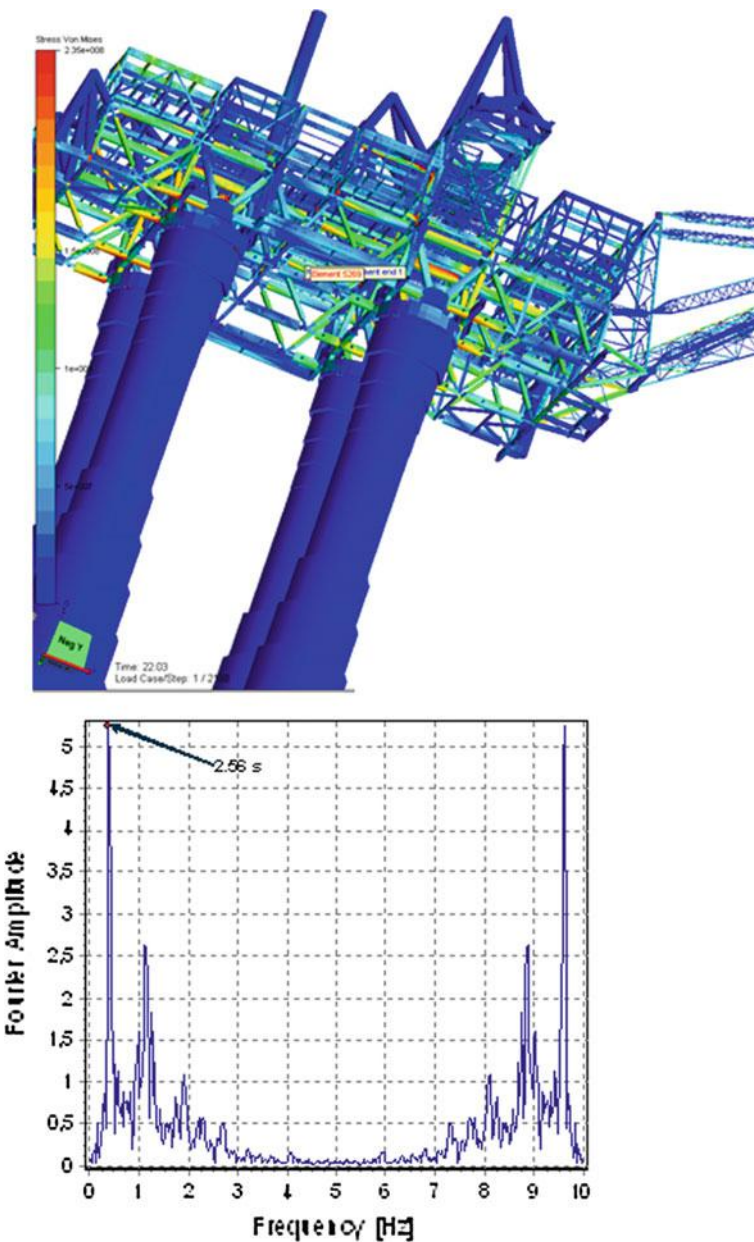
Fig. 15.30 Fourier analysis of the response at the top of the flare boom subject to seismic loading (courtesy of Aker Solutions)

15.7.2 Investigation of the Whipping Effect for a Jacket and Topside Structure

To study the whipping effect, the structure model (Fig. 15.7) described in the case study 1 of Sect. 15.2.7.1 is further refined by a more detailed modeling of the flare boom, drilling derrick and by adding a new installed pump module, which is shown in Fig. 15.32.

The objective of the study is to calculate the accelerations at different levels and parts of the topside for the assessment of equipment operability and structural integrity, and these data will also be used as acceleration input for performing an equivalent quasi-static acceleration analysis.

The earthquake design spectrum (Fig. 15.10) and load combination (Table 15.2) described for case study 1 are adopted for this study.



Fourier spectrum of Node 3916 for accelerations along X dir.

Fig. 15.31 Fourier analysis of the response for a structural member at the module support frame that is far from the flare boom (courtesy of Aker Solutions)

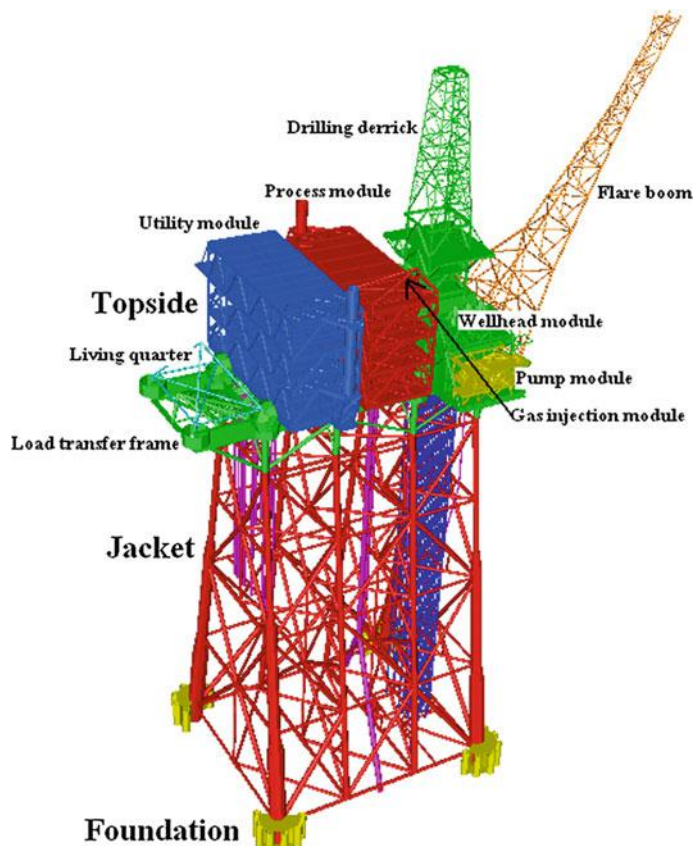


Fig. 15.32 Geometric modeling of jacket-topside structure and notation of each module (courtesy of Aker Solutions)

The first eight eigenmode shapes of the detailed modeling, with eigenperiods ranging from 2.47 to 0.66 s, are illustrated in Fig. 15.33. The first three eigenmodes show typical mode shapes for a fixed offshore structure, including global bending along weak and strong axis and the global torsional vibration mode. They are the most important ones in that they contain the majority of the total modal mass participating in the vibrations. Their corresponding periods are marked in the acceleration spectra input shown in Fig. 15.34. It is shown that the spectral accelerations at these three periods are well below the peak value of spectral acceleration. Furthermore, by comparing the eigenperiods and mode shapes between the simplified structure model in case study 1 and the current more dedicated structure model, it is found that they agree well. However, the fourth eigenperiod (with topside bending concentrated at the load transfer frame below the wellhead module and drilling module) for the dedicated model has a noticeable

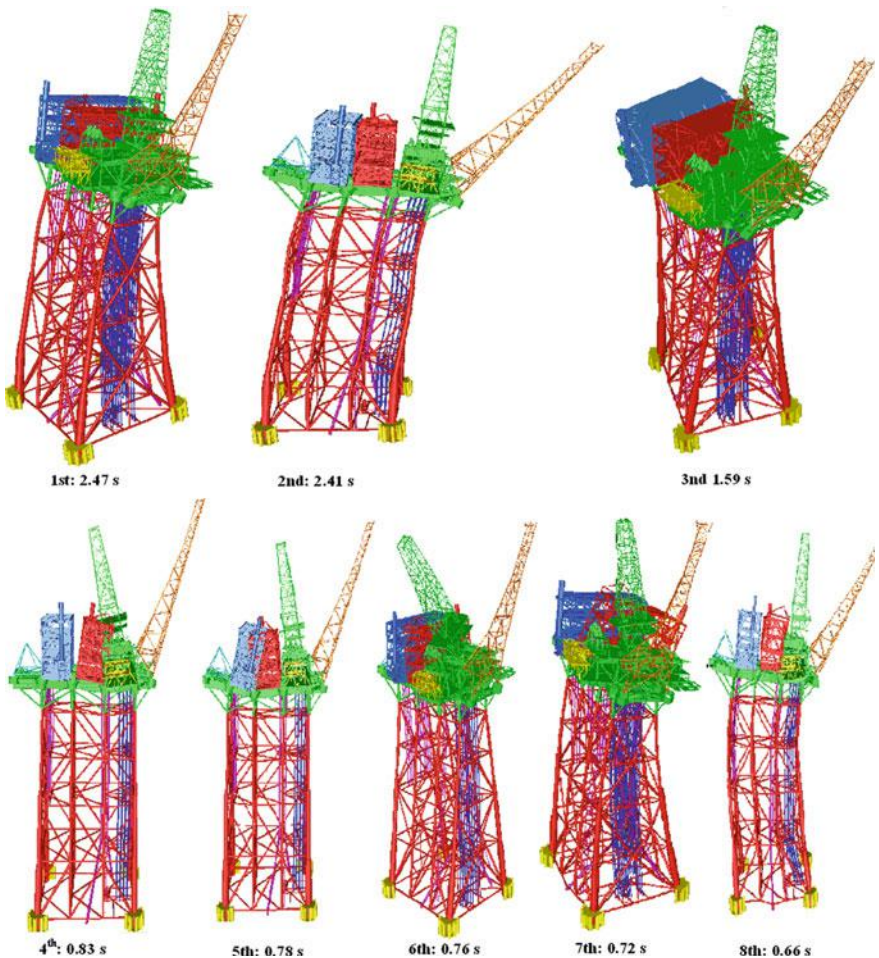


Fig. 15.33 First eight eigenperiods and mode shapes of the target jacket-topside structure (courtesy of Aker Solutions)

increase compared with the simplified modeling. This is mainly due to influence from the added weight of the pump module.

Accelerations and the relative displacements to the ground motions at 13 representative locations (Fig. 15.35) all over the platform topside are calculated, and are listed in Table 15.4.

It is clearly shown that the responses at the tip of the derrick (location 10) and the tip of the flare boom (location 13) have significantly higher acceleration and displacement than the rest of the topside and jacket. This is because the lateral stiffness of the modules supporting the derrick and flare boom are much stiffer than the derrick and the flare boom themselves, and they also become slender with an

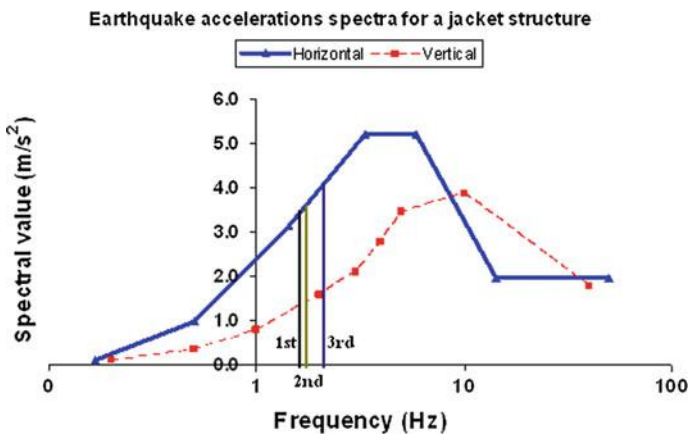


Fig. 15.34 First three eigenperiods marked on the accelerations spectra with 10,000 years return period for the target jacket structure

Fig. 15.35 Thirteen representative locations on the jacket structure under investigation (courtesy of Aker Solutions)

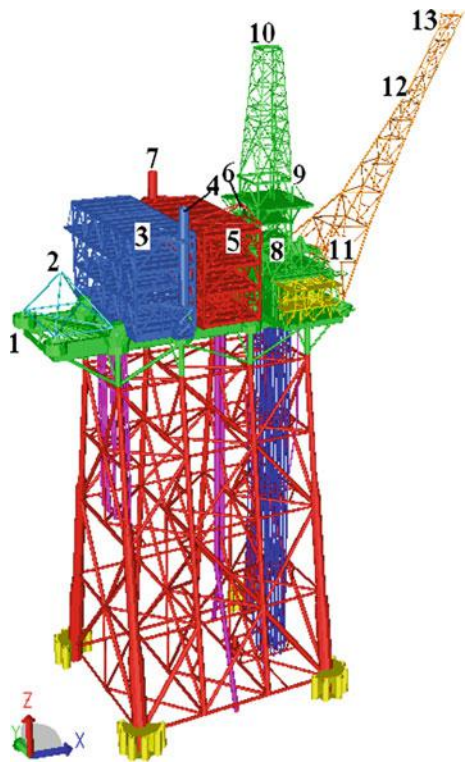


Table 15.4 Maximum seismic accelerations and relative displacements in all three directions (X, Y and Z, shown in Fig. 15.35) on various locations of the topside of the jacket structure shown in Fig. 15.35

Location	a_x (m/s ²)	a_y (m/s ²)	a_z (m/s ²)	d_x (cm)	d_y (cm)	d_z (cm)
1	1.0	1.5	2.1	9.7	8.9	4.0
2	1.3	1.2	1.7	11.5	10.3	3.0
3	1.4	2.3	1.4	12.4	12.0	1.9
4	1.9	2.1	2.2	13.3	12.7	3.2
5	1.6	2.1	1.5	12.7	11.5	1.7
6	2.0	2.6	1.6	13.7	12.0	2.4
7	1.9	2.7	2.0	13.8	11.5	3.1
8	1.0	1.0	1.4	10.8	11.5	1.8
9	1.8	2.6	1.7	14.0	13.2	1.4
10	5.2	9.1	1.7	20.5	16.6	1.7
11	1.1	1.5	1.5	9.8	9.1	3.1
12	3.7	2.9	3.2	16.3	13.5	6.5
13	5.3	3.7	4.0	18.9	15.2	7.9
Jacket top (EL + 119 m)	1.4	1.7	1.1	8.2	7.1	1.7

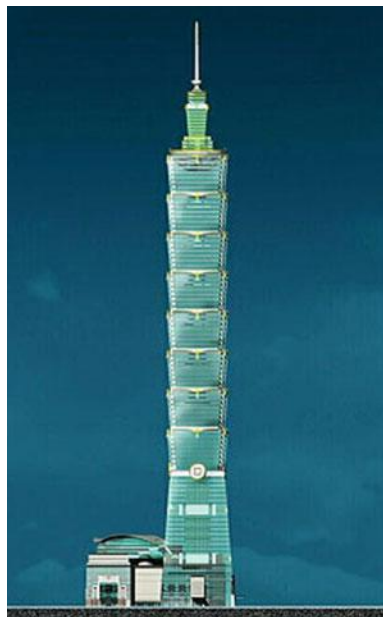
increase of height. Consequently, it is expected that the seismic response at their tips will be significantly amplified without significant interaction with vibrations from other parts of the structure.

For building structures that may have a higher lateral stiffness than a tower, the sudden significant change in the lateral stiffness at the top of the structure (Fig. 15.36) may lead to an even higher increase of seismic response on the top part of the structure. It is almost impossible to avoid this problem by using the conventional structural modification or a slight change in structural configuration. In addition, the complexity in plan configuration due to the podium structure as an appendix of the tower possibly leads to an increase of torsional response due to an accountable deviation of stiffness center from mass center for the whole structural system [86].

15.7.3 Investigation of the Whipping Effect for a GBS and Topside Structure

A seismic analysis is carried out for a GBS structure (Fig. 15.37) subject to seismic excitations represented by accelerations spectra (Fig. 15.38) with a return period of 10,000 years. As shown in Fig. 15.39, the first two eigenmodes of the GBS structure show the sway (global bending) motions in two principal directions, and the associated eigenperiods are 2.23 and 2.22 s, respectively. It is noticed that the

Fig. 15.36 Taipei 101 building with a sudden change in lateral stiffness at the top due to the presence of a slender pinnacle at its top



spectral accelerations shown in Fig. 15.38 at these two eigenperiods are rather low. Translational and rotational accelerations at 18 representative locations (Fig. 15.37) on the GBS and its topside structure are calculated, which are shown in Table 15.5. The effect due to whipping can be clearly identified as the tip of the flare boom (location 18) has a much higher motion than the other parts of the GBS and the topside structure.

15.7.4 Investigation of the Whipping Effect for a Tower-Podium System

By modeling a high tower-podium structure with a standardized 3D model of two stories surrounded by a 3D one-story model, Yang et al. [86] studied the whipping effects and torsional responses of the tower-podium structure. A series of parametric studies have been carried out to check the response sensitivity due to the variation in ratio of story number, stiffness and mass ratio between upper and lower parts of the tower, translational stiffness ratio and torsional stiffness ratio of the tower to its podium, lateral stiffness eccentricities for the podium, the upper part and the lower part of the tower, supplemental damping resulting from linking fluid dampers, and plan distribution of the fluid dampers etc. The analytical results show that the whipping effects are mainly attributed to the first vibration mode rather than the second one. Compared with rigid connection case, the vibration performance of a

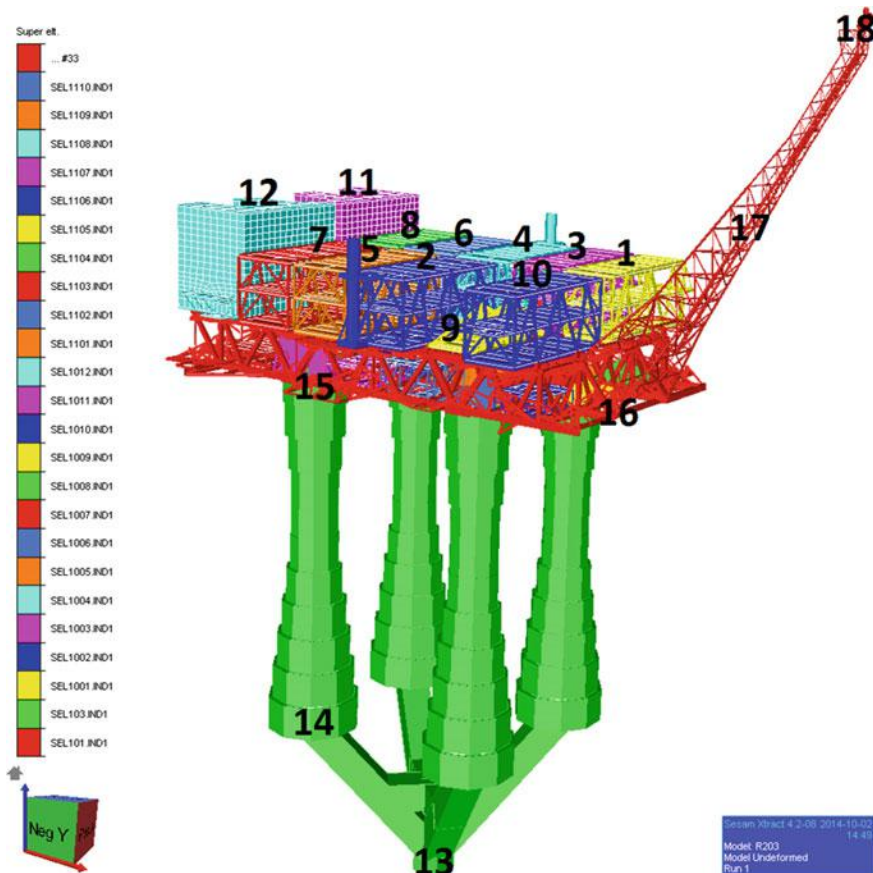
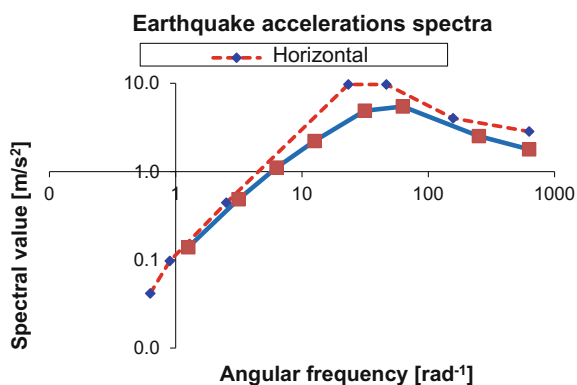


Fig. 15.37 Eighteen representative locations on the GBS and topside structure under investigation (courtesy of Aker Solutions)

Fig. 15.38 Accelerations spectra with 10,000 year return period for the target GBS structure



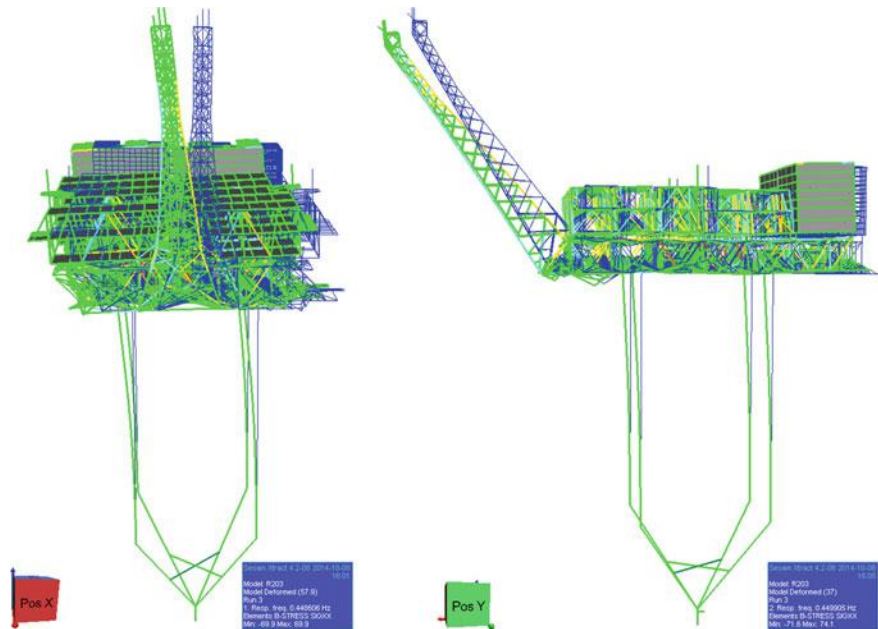


Fig. 15.39 The first two eigenmodes of the GBS and the topside structure showing the sway motions in two principal directions with the corresponding eigenperiods of 2.23 and 2.22 s (courtesy of Aker Solutions)

tower can usually be improved by installing fluid dampers (Sect. 24.6) between tower and podium, and accordingly whipping effects can be significantly reduced, even though this may be compromised by an increase in the seismic response of the podium, which is due to the limited energy-dissipating capability of the damper and the effect of direct interaction between tower and podium predominating over the energy dissipation of dampers. In addition, most seismic responses can be reduced for the tower and podium if the damper parameters are selected appropriately.

15.7.5 Documented Observations of Whipping Responses

The whipping effect has actually been observed during many earthquake events, mainly on land based structures but also on offshore platforms. For example, an earthquake with a moment magnitude of 5.7 occurred in south-eastern Sicily on 13 December 1990, with its epicenter in Augusta Bay. During the earthquake, large displacements were observed on the top of a derrick tower installed on Vega platform (Fig. 15.40) [87], which is located 25 km offshore and 80 km from the epicenter, and the site has a water depth of 122.3 m. In addition, note that the derrick and flare boom with their supporting module structure as an integrated part

Table 15.5 Maximum translational (m/s^2) and torsional (rad/s^2) seismic accelerations for all three directions (X, Y and Z, shown in Fig. 15.37) on various locations of the GBS and topside structure shown in Fig. 15.37

Location	Module	a_x	a_y	a_z	R_x	R_y	R_z
1	M01	7.4	3.4	3.4	0.1	0.6	0.1
2	M02	4.8	3.4	2.5	0.2	0.2	0.1
3	M03	5.1	3.0	2.2	0.1	0.2	0.0
4	M04	3.2	2.4	2.3	0.1	0.1	0.0
5	M05	4.4	3.1	2.5	0.2	0.1	0.1
6	M06	5.3	2.1	2.4	0.1	0.3	0.2
7	M07	5.0	2.6	2.2	0.1	0.1	0.1
8	M08	16.8	2.9	2.6	0.3	1.2	0.6
9	M09	1.5	1.5	1.9	0.1	0.1	0.0
10	M10	7.0	4.9	4.0	0.2	0.2	0.2
11	L01	4.6	3.8	3.5	0.2	0.2	0.1
12	L02	5.8	3.8	3.9	0.2	0.2	0.1
13	Caisson at seabed	1.6	1.7	1.1	0.0	0.0	0.0
14	GBS top caisson, leg 1	1.4	1.5	1.3	0.0	0.0	0.0
15	Leg 1, top	1.0	0.8	1.6	0.1	0.1	0.0
16	Flare boom, base	1.1	1.9	4.8	0.1	0.8	0.1
17	Flare boom, mid	13.3	5.3	12.8	0.1	0.2	0.3
18	Flare boom, tip	34.5	10.3	13.0	1.3	2.2	1.5

may also introduce a deviation between the shear (stiffness) center and center of mass, which may further induce significant torsional vibrations. Similarly, Fig. 15.41 shows that during the Loma Prieta earthquake that occurred in 1989, the recorded horizontal movement on the 49th floor of San Francisco's Transamerica Pyramid building was five times greater than that measured in the basement of the building.

It is worth mentioning that for many slender light-weight structures such as guyed steel stacks (Fig. 15.42) and chimneys, tips of elevated structures etc., the structural design is governed by the wind loading rather than the seismic loading because wind loading increases with the height from ground surface and the structure is normally sufficiently soft to exhibit large deflections due to wind loading. However, partially due to the whipping effect, the design of slender structures may be governed by seismic loading and therefore requires a dedicated consideration of their seismic resistance.

Despite a significant de-amplification or amplification of the horizontal response on the structure, it is noticed that, among different parts of structures, the responses along the vertical direction do not differ significantly. This is because the vertical stiffness on typical engineering structures is significantly higher than that of the horizontal, which makes the entire structure follow the ground motions more or less rigidly. However, this does not apply to structures with inclined orientations or cantilevers, such as an oblique flare boom shown in Figs. 15.27 and 15.44, i.e. the



Fig. 15.40 Vega jacket platform

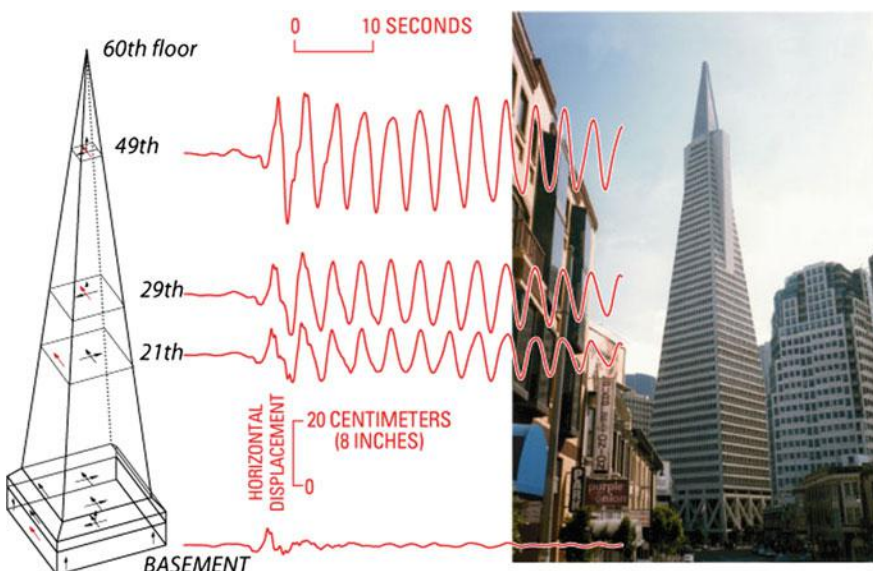


Fig. 15.41 Measured sway motions at various heights along San Francisco's Transamerica Pyramid during the moment magnitude 6.9 Loma Prieta earthquake that occurred in 1989 (courtesy of USGS)

Fig. 15.42 Designs of slender light-weight structures may be governed by the wind or seismic loading at their tops



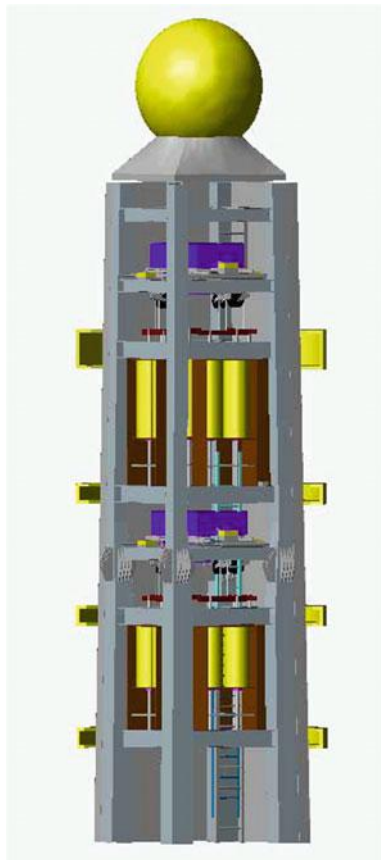
stiffness along the vertical direction on those structures is not as high as other parts of the platform structure. This results in a significant amplification of vertical response at the flare tip as indicated in Tables 15.4 and 15.5.

15.7.6 *Mitigation of Whipping Response*

Adding mass or a tuned mass damper (TMD) to the structural tip, linking adjacent structures or connecting podium structures to main structures using passive dampers, semi-active dampers, or active dampers are efficient ways to mitigate whipping responses. The technical descriptions of those mitigation measures will be presented in Chaps. 19–28.

For example, in order to mitigate the dynamic response (mainly to reduce wind induced response) of the pinnacle on the top of Taipei 101 between 450 and 509 m above the ground level, two compact TMDs, each weighing 6 tons and designed to mitigate vibration at one single period [88], are installed at the tip of the spire as

Fig. 15.43 Two TMDs, each weighing 6 tons, are installed to mitigate two tip vibration modes at the periods 1.16 and 0.93 s



shown in Fig. 15.43. The two TMDs are designed to mitigate the vibration responses at the two most contributing vibration modes with periods of 1.16 and 0.93 s, respectively. These two modes of vibration can also trigger vortex induced vibrations contributing to the metal fatigue damage (they oscillate up to 180,000 times a year). Therefore, the two TMDs essentially prevent damage to the structure due to strong wind loads, seismic loading and wind induced fatigue damage.

15.8 Influences from Structures' Orientations

It is obvious that the orientation of the structure also influences seismic responses. For horizontally-oriented structures such as a horizontal cantilever, its seismic responses can be more sensitive to the vertical excitations at its base. However, for vertically-oriented structures such as a tower structure or a building, the horizontal acceleration is more dominant. For oblique structures such as a flare boom shown in



Fig. 15.44 A flare boom (marked with a *circle*) installed on a gravity based offshore structure in the North Sea

Fig. 15.44, the responses are sensitive to both vertical and horizontal accelerations at the base. Moreover, for a frame structure, if the structure or the applied vertical seismic loading is not symmetric, the vertical seismic loading can also induce horizontal movements of the structure.

15.9 Remarks on Modeling of Material Properties for Seismic Analysis

It should be pointed out that partial safety factors for loads and resistance/materials extensively used in current structural design codes essentially serve for structural designs based on linear analysis and are in many cases not suitable for non-linear analysis, either in the structural analysis or in the verification of strength. For example, as presented in Sect. 14.2, it is a normal practice to perform non-linear structural response calculation for steel structures based on a modeling of structures with characteristic material strengths (Which typically implies that there is less than

5 % probability that the resistance is less than this value). Because the material in reality may reach yielding far above the characteristic value, by modeling a structure with characteristic yield strength, the yielding and the subsequent plasticity redistribution in the structure will occur earlier, which will influence not only the calculated resistance of the structure but also the distribution of sectional forces and internal stresses on relevant structural components, thus possibly changing the failure modes compared with a scenario where more realistic material properties are modeled. This is even more obvious for structures with a high degree of redundancy. This normally gives conservative results, but it may also lead to an un-conservative assessment and design. To solve this problem, mean strength rather than characteristic strength of the structural material may be used for modeling and design, as it normally results in a more probable responses, and has been implemented in many seismic assessment projects. However, this can also introduce large uncertainties toward safety as sometimes the manufacturers may over-specify the mean strength of the material.

Furthermore, in a non-linear analysis, to more realistically represent the yielding initiation and the subsequent plasticity development, the material/resistance factor is recommended to be applied on the load scaling side together (multiplied with) with load factors rather than on the material strength side. Similarly, choices of

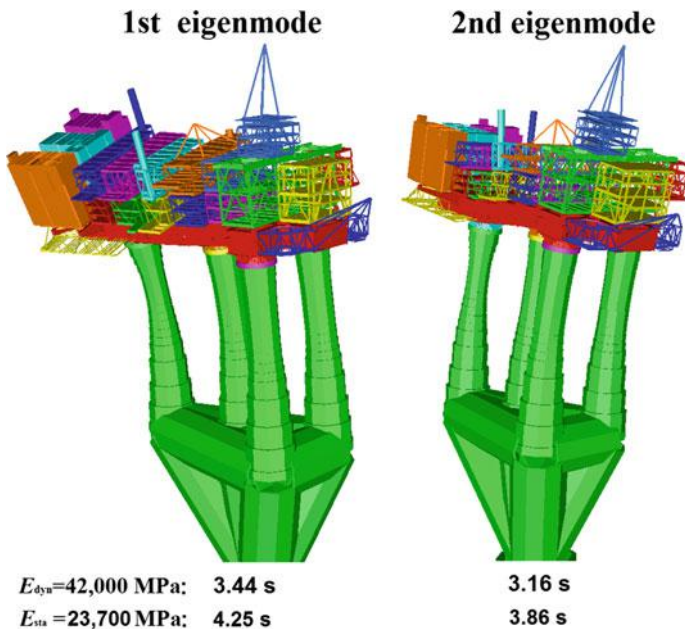


Fig. 15.45 Comparison of the first two eigenperiods of a GBS structure due to the modeling of dynamic (E_{dyn}) and static (E_{sto}) Young's modulus of concrete

modeling in non-linear constitutive relationship of structural materials such as strain hardening can also significantly influence the calculated responses and their closeness to the reality.

Moreover, the dynamic strength of some materials such as concrete is dependent on the strain rate and size effect. For example, the strength of concrete decreases with an increase in dimensions and a decrease in strain rate. Similarly, the Young's modulus of concrete under dynamic loading is also higher than that under static loading. All of these must be accounted for in seismic design and analysis. By modeling a concrete shaft and caisson for a GBS with dynamic (E_{dyn}) and static (E_{sta}) Young's modulus of concrete, respectively, Fig. 15.45 shows a comparison of the first two eigenperiods of the GBS due to the two sets of modeling for Young's modulus. When using dynamic Young's modulus (higher than the static Young's modulus) for modeling, a significant decrease of the first two eigenperiods can be observed. Subject to earthquake excitations represented by a particular design response spectrum at a location in the North Sea, the use of dynamic Young's modulus leads to an increase in calculated maximum accelerations on the top of the concrete shafts by up to 27 %.

References

1. Ghobarah A (2001) Performance-based design in earthquake engineering: state of development. *Eng Struct* 23(8):878–884
2. Kelly TE (2004) Analysis paralysis: a 2003 state-of-the-art report on seismic analysis. *Bull NZ Soc Earthq Eng* 37(1):23–34
3. Jia J (2012) Seismic analysis for offshore industry: promoting state of the practice toward state of the art. In: Proceedings of the 22nd international ocean and polar engineering conference (ISOPE), Rhodes, Greece
4. Jia J (2014) Essentials of applied dynamic analysis. Springer, Heidelberg
5. Krawinkler H, Seneviratne GDK (1998) Pros and cons of a pushover analysis of seismic performance evaluation. *Eng Struct* 20(4–6):452–464
6. Kalkan E, Graizer V (2007) Multi-component ground motion response spectra for coupled horizontal, vertical, angular accelerations, and tilt. *ISET J Earthq Technol* 44(1):259–284
7. Wilson Ed (2013) Comments on the response spectrum analysis method. In: Presentation at SAB Meeting, 28 August, 2013
8. Moran R, Wang Y, Chokslhi N, Kenneally R, Norris W (1999) Evaluation of modal combination methods for seismic response spectrum analysis, Paper ID K4-A4-US, United States Nuclear Regulatory Commission
9. Rosenblueth E (1951) A basis for aseismic design. PhD thesis, University of Illinois, Urbana
10. Chopra AK (2000) Dynamics of structures: theory and application to earthquake engineering, 2nd edn. Prentice Hall, Upper Saddle River
11. Barltrop NDP, Adams AJ (1991) Dynamics of fixed marine structures, 3rd edn. MTD Ltd., London
12. Wilson EL, Der Kiureghian A, Bayo ER (1981) A replacement for SRSS method in seismic analysis. *Earthq Eng Struct Dyn* 9:187–192
13. Der Kiureghian A (1981) A response spectrum method for random vibration analysis of MDF systems. *Earthq Eng Struct Dyn* 9:419–435

14. Rosenblueth E, Elorduy J (1969) Responses of linear systems to certain transient disturbances. In: Proceedings of the fourth world conference on earthquake engineering, Santiago, Chile, vol I, pp 185–196
15. NORSO N-003 (2007) Actions and action effects, 2nd edn. Standards Norway, Lysaker, Norway
16. ISO19901-2 (2004) Petroleum and natural gas industries—specific requirements for offshore structures—part 2: seismic design procedures and criteria, 1st edn. International Organization for Standardization, Geneva
17. Wilson Ed (2015) Termination of the response spectrum method (RSM)
18. Freeman SA, Nicoletti JP, Tyrdl JV (1975) Evaluations of existing buildings for seismic risk: a case study of Puget Sound Naval Shipyard, Bremerton, Washington. In: Proceedings of US national conference on earthquake engineering, Berkeley, pp 113–122
19. Bozorgnia Y, Bertero V (2004) Non-linear dynamic analysis, in earthquake engineering: from engineering seismology to performance-based design. CRC Press, Boca Raton, pp 1–17
20. Seifi M, Noorzaei J, Jaafar MS, Yazdan Panah E (2008) Non-linear static pushover analysis in earthquake engineering: state of development. In: International conference on construction and building technology, ICCBT 2008, Kuala Lumpur, pp 69–80
21. Eurocode 8 (2004) Design of structures for earthquake resistance, part 1: general rules, seismic actions and rules for buildings. European Committee for Standardization (CEN), Brussels
22. ATC 40 (1996) Seismic evaluation and retrofit of concrete buildings, vol 1. Applied Technology Council, Redwood City, USA
23. FEMA-356 (2000) Prestandard and commentary for the seismic rehabilitation of buildings. FEMA, Washington DC
24. GDPK Seneviratna (1995) Evaluation of inelastic MDOF effects for seismic design. PhD dissertation, Department of Civil Engineering, Stanford University
25. Ghobarah A (2001) Review article: performance-based design in earthquake engineering: state of development. Eng Struct 23:878–884
26. Paret TF, Sasaki KK, Eilbeck DH, Freeman SA (1996) Approximate inelastic procedures to identify failure mechanisms from higher mode effects. In: Proceedings of the 11th world conference on earthquake engineering, Disc 2, Paper No. 966
27. Sasaki KK, Freeman SA, Paret TF (1998) Multi-mode pushover procedure (MMP): a method to identify the effects of higher modes in a pushover analysis. In: Proceedings of the sixth US national conference on earthquake engineering
28. Chopra AK, Goel RK (2002) A modal pushover analysis procedure for estimating seismic demands for buildings. Earthq Eng Struct Dyn 31(3):561–582
29. Antoniou S, Pinho R (2004) Advantages and limitations of adaptive and non-adaptive force-based pushover procedures. J Earthq Eng 8(4):497–522
30. Antoniou S, Pinho R (2004) Development and verification of a displacement-based adaptive pushover procedure. J Earthq Eng 8(5):643–661
31. Chopra AK, Goel RK (2004) A modal pushover analysis procedure to estimate seismic demands for unsymmetric-plan buildings. Earthq Eng Struct Dyn 33(8):903–927
32. FEMA-273 (1997) NEHRP guidelines for the seismic rehabilitation of buildings. FEMA, Washington DC
33. FEMA-274 (1997) NEHRP commentary on the guidelines for the seismic rehabilitation of buildings. FEMA, Washington, DC
34. FEMA-450 (2004) NEHRP recommended provisions and commentary for seismic regulations for new buildings and other structures. FEMA, Washington DC
35. Lu X, Ye L, Miu Z (2009) Elastic-plastic analysis for earthquake resistant building structures: theory, modeling and applications. In: ABAQUS, MSC.MARC, and SAP2000 (In Chinese), China Architecture and Building Press
36. Kalkan E, Kunmath SK (2004) Method of modal combinations for pushover analysis of buildings. In: 13th world conference on earthquake engineering, Vancouver, BC, Canada

37. Habibullah A, Pyle S (1998) Practical three dimensional non-linear static pushover analyses. *Structure Magazine*, Berkley
38. Elnashai AS (2001) Advanced inelastic static (pushover) analysis for earthquake applications. *Struct Eng Mech* 12(1):51–69
39. Mwafy AA, Elnashai AS (2001) Static pushover versus dynamic collapse analysis of RC frames. *Eng Struct* 23:407–424
40. Gupta B, Kunnath SK (2000) Adaptive spectra-based pushover procedure for seismic evaluation of structures. *Earthq Spectra* 20(4–6):452–464
41. Seifried AE (2013) Response spectrum compatibilization and its impact on structural response assessment. PhD thesis, Stanford University
42. China Net for Engineering Construction Standardization (2010) Code for seismic design of buildings, GB 50011-2010. China Building Industry Press, Beijing
43. NORSAR, NGI (1998) Seismic zonation for Norway. Report for the Norwegian Council for Building Standardization
44. SHAKE 2000 (2008) A computer program for the 1-D analysis of geotechnical earthquake engineering problem. University of California, Berkeley 2008
45. Eurocode 3 (2005) Design of steel structures—part 1-1: general rules and rules for buildings. European Committee for Standardization (CEN), Brussels
46. Jia J (2016) Soil dynamics and foundation modeling: offshore and earthquake engineering. Springer, Heidelberg
47. Lauritsen R, Kvitrud A, To P (1985) User manual for computer program CAP, NGI, Report No. 52406
48. Kubo T, Penzien J (1979) Analysis of three-dimensional strong ground motions along principal axes, San Fernando earthquake. *Earthq Eng Struct Dyn* 7:265–278
49. Kubo T, Penzien J (1979) Simulation of three-dimensional strong ground motions along principal axes, San Fernando Earthquake. *Earthq Eng Struct Dyn* 7:279–294
50. Penzien J, Watabe M (1975) Characteristics of 3-dimensional earthquake ground motion. *Earthq Eng Struct Dyn* 3:365–374
51. Hadjian AH (1978) On the correlation of the components of strong ground motion. In: Proceedings of second international conference on microzonation, vol. III, San Francisco
52. Bertero VV (1977) Strength and deformation capacities of buildings under extreme environments. *Struct Eng Struct Mech* 53(1):29–79
53. Vamvatsikos D, Cornell CA (2000) Seismic performance, capacity and reliability of structures as seen through incremental dynamic analysis, Report No. RMS-55, RMS Program, Stanford University, Stanford
54. Vamvatsikos D (2002) Seismic performance, capacity and reliability of structures as seen through incremental dynamic analysis. PhD thesis, Stanford University, Stanford, CA
55. Asgarian B, Aghakouchak AA, Alanjari P, Assareh MA (2008) Incremental dynamic analysis of jacket type offshore platforms considering soil–pile interaction. In: Proceedings of the 14th world conference on earthquake engineering, Beijing
56. Mander JB, Dhakal RP, Mashiko N, Solberg KM (2007) Incremental dynamic analysis applied to seismic financial risk assessment of bridges. *Eng Struct* 29(10):2662–2672
57. Shome N, Cornell CA, Bazzuro P, Carballo JE (1998) Earthquakes, records, and non-linear responses. *Earthq Spectra* 14:469–500
58. FMA 350 (2000) Recommended seismic design criteria for new steel moment-frame buildings. FEMA 350, Washington DC
59. Vamvatsikos D, Cornell CA (2004) Applied incremental dynamic analysis. *Earthq Spectra* 20 (2):523–553
60. Vamvatsikos D (2011) Performing incremental dynamic analysis in parallel. *Comput Struct* 89(1–2):170–180
61. Shome N, Cornell CA (1999) Probabilistic seismic demand analysis of non-linear structures, Report No. RMS-35, RMS Program, Stanford University, Stanford
62. Vamvatsikos D, Cornell CA (2002) Incremental dynamic analysis. *Earthq Eng Struct Dyn* 31 (3):491–514

63. Ramberg W, Osgood WR (1943) Description of stress-strain curves by three parameters, Technical Note No. 902, National Advisory Committee for Aeronautics, Washington, DC
64. Estekanchi HE, Vafai A, Sadeghazar M (2004) Endurance time method for seismic analysis and design of structures. *Sci Iran* 11:361–370
65. Razavi M (2007) Evaluation of endurance time method compared to spectral dynamic analysis method in seismic analysis of steel frames. Department of Civil Engineering, Sharif University of Technology, Tehran, Iran
66. Mirzai A (2007) Usage of ET method in performance-based design of steel frames. Department of Civil Engineering, Sharif University of Technology, Tehran, Iran
67. Estekanchi HE, Riahi HT, Vafai A (2008) Endurance time method: exercise test for seismic assessment of structures. In: Proceedings of the 14th world conference on earthquake engineering, Beijing
68. Riahi HT, Estekanchi HE (2010) Seismic assessment of steel frames with the endurance time method. *J Constr Steel Res* 66(6):780–792
69. Estekanchi HE, Vafai A, Valamanesh V, Mirzaee A, Nozari A, Bazmuneh A (2011) Recent advances in seismic assessment of structures by endurance time method. In: Proceedings of a US–Iran–Turkey seismic workshop: seismic risk management in urban areas; PEER report 2011/07, 14–16 December 2010, pp 289–301, Istanbul, Turkey
70. Estekanchi HE, Riahi HT, Vafai A (2011) Application of endurance time method in seismic assessment of steel frames. *Eng Struct* 33(9):2535–2546
71. Estekanchi HE, Alembagheri M (2012) Seismic analysis of steel liquid storage tanks by endurance time method. *Thin Walled Struct* 50(1):14–23
72. Jahanmard V, Diznab MAD, Mehdiyoli H, Tabeshpour MR, Seif MS (2015) Performance-based assessment of steel jacket platforms by wave endurance time method. *J Ships Offshore Struct*, articles in press
73. Takewaki I (2007) Critical excitation methods in earthquake engineering. Elsevier, Oxford
74. Takewaki I (2004) Critical envelope functions for non-stationary random earthquake input. *Comput Struct* 82(20–21):1671–1683
75. Singh JP (1984) Characteristics of near-field ground motion and their importance in building design, ATC-10-1 critical aspects of earthquake ground motion and building damage potential, ATC, 23–42
76. Anderson JC, Bertero VV (1987) Uncertainties in establishing design earthquakes. *J Struct Eng* 113(8):1709–1724
77. Geller RJ, Jackson DD, Kagan YY, Mulargia F (1997) Earthquakes cannot be predicted. *Science* 275:1616
78. Takewaki I (2002) Critical excitation method for robust design: a review. *J Struct Eng* 128 (5):665–672
79. Stein RS (2003) Earthquake conversations. *Sci Am* 288(1):72–79
80. Drenick RF (1970) Model-free design of aseismic structures. *J Eng Mech Div* 96(4):483–493
81. Shinozuka M (1970) Maximum structural response to seismic excitations. *J Eng Mech Div* 96 (EM5):729–738
82. Shinozuka M (1970) Chapter 5: maximum structural response to earthquake accelerations. In: Lind NC (ed) Structural reliability and codified design. University of Waterloo, Waterloo, pp 73–85
83. Iyengar RN (1970) Matched inputs, Report No. 47, Series J, Center for Applied Stochastics, Purdue University, West Lafayette, IN
84. Yang JN, Heer E (1971) Maximum dynamic response and proof testing. *J Eng Mech Div* 97 (4):1307–1313
85. Takewaki I (2007) Critical excitation methods in earthquake engineering, 1st edn. Elsevier, Oxford
86. Yang Z, Lu X, Hwu T-H, Xu Y (2004) Effect of linking fluid dampers on whipping effect and torsional response of tower-podium system. In: 13th world conference on earthquake engineering, Vancouver

87. Gusella V, Spadaccini O, Vignoli A (1996) In-service dynamic behavior of a drilling derrick on a jacket platform. *Int J Offshore Polar Eng*, 6(3):184–194
88. Joseph LM, Poon D, Shieh S (2006) Ingredients of high rise design, Taipei 101 the world's tallest building. *Structure Magazine*, 6
89. Tabeshpour MR, Komachi Y, Golafshani AA (2012) Assessment and rehabilitation of jacket platforms. In: Moustafa A (ed) *Earthquake-resistant structures: design, assessment and rehabilitation*. Intech, Rijeka, Croatia

Chapter 16

Sudden Subsidence and Its Assessment

16.1 General

On 7 May, 2001, a minor earthquake occurred in the vicinity of the Ekofisk oil-field (Fig. 1.23) in the North Sea, which comprises several offshore jackets and tripod structures connected by bridges. During this earthquake, a permanent vertical movement of platforms occurred. The people on board the platforms and the platform connecting bridges felt a strong sudden vertical drop, which is often referred to as sudden subsidence or sudden drop. The vertical movement is estimated to have been approximately 80 mm. Assuming that the vertical displacement took place in a single motion with the acceleration of gravity (free drop), the duration of the sudden subsidence is estimated to have been 0.13 s. This is the only reported sudden subsidence event to have occurred offshore thus far. Such events can cause failures of structural members or even a collapse of topside and supporting structures, and may also influence the capacity of the foundation and grout connection of pile clusters, etc.

A sudden subsidence of offshore installations can be induced by several sources, such as earthquakes, hydrocarbon extraction, gas bubbles under the offshore foundation, fluid injection, offshore installations and drilling operations. All these phenomena can lead to the disturbance of foundation soil, which is the direct cause of a sudden subsidence. For example, the planning and execution of conductor installation and shallow well drilling can cause a disturbance to foundation soils, which can lead to a consequent risk of a reduction in stability and sudden subsidence accident of the fixed structure or adjacent conductors. During drilling operations, soil disturbances may result from hydraulic fracture, wash-out or from encountering shallow gas pockets. If pile foundations are installed within the zone of soil disturbance, reduction in axial and lateral capacity as well as foundation stiffness can occur. Similarly, the stability of shallow foundations can be reduced and settlements can be increased. When the foundation capacity is insufficient to resist the loads applied on offshore structures, the sudden subsidence and even

collapse of offshore installations will eventually occur. Sudden subsidence is more relevant for oil fields with large reservoirs, due to the extraction of oil, gas and water injection. The central area of these large reservoirs are more vulnerable to sudden subsidence than the boundaries.

16.2 Structural Assessment

Regarding the structural integrity of offshore platforms, cantilever areas at topside (e.g. living quarters, cantilever beams, flare booms, etc.) or connecting bridges are the most vulnerable parts with regard to structural integrity due to sudden subsidence.

So far no design codes have been published to specify an explicit requirement for sudden subsidence assessment. However, more and more energy companies realize the risk associated with potential sudden subsidence, and therefore set up their internal requirements for the assessment of consequences due to sudden subsidence. This assessment is normally based on the evaluation of an accidental limit state event.

Two assessment approaches can be adopted in sudden subsidence analysis, namely simplified static approach and time series dynamic approach, as will be presented in Sects. 16.2.1 and 16.2.2.

16.2.1 Simplified Static Approach

By applying a vertical acceleration field downward ranging from 1.2 to 3.0 g on an offshore structure, where g is the acceleration of gravity, the structural integrity may be assessed by studying the static response of the structure. The only obvious advantages of this approach is its simplicity, its accuracy and the correctness of its theoretical background. However, it does need to be justified.

16.2.2 Dynamic Time History Approach

To increase the accuracy of assessment, a non-linear dynamic time history analysis is recommended. It generally comprises two steps as follows:

1. First, gradually apply gravity load statically (no inertia effects) for a period of 0.2–2.0 s.
2. The sudden subsidence is then simulated by applying a prescribed vertical displacement to the bottom of the foundation. The prescribed displacement w may be calculated by assuming a single step and free drop (-1.0 g) process:

$$w = gt^2/2 \quad (16.1)$$

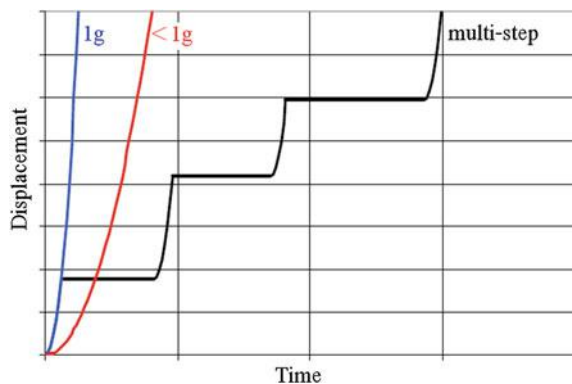
where g is the acceleration of gravity (9.81 m/s^2), t is the duration of the drop process, a typical drop process last for $0.05\text{--}0.3 \text{ s}$, corresponding to a drop distance of $12\text{--}441 \text{ mm}$. If the drop displacement is below 10 mm , there is normally no risk associated with the structural integrity.

In reality, due to the soil–foundation interaction and other environmental and structural factors, the sudden subsidence may follow a single step drop but with significantly less free drop acceleration than g . It may also follow a multi-step drop equal to or less than the free drop acceleration. Those processes are summarized in Fig. 16.1.

Furthermore, a more dedicated and realistic approach is to adopt linear or non-linear springs on the pile foundation with varied vertical spring stiffness. The vertical stiffness should be zero when sudden subsidence has just begun at $t = 0 \text{ s}$, and then be gradually increased to simulate the soil–foundation interaction. By applying the acceleration of gravity, the more realistic sudden subsidence process can be simulated.

However, the free drop assumption is the simplest method and is likely to be conservative. Therefore, it is normally adopted as the starting point of the assessment.

Fig. 16.1 Sudden subsidence process used in time series dynamic approach



16.3 Case Studies

16.3.1 Case Study 1: Response of Topside Bridges and Modules Due to Sudden Subsidence

Figure 16.2 shows a finite element model of a structural system with two bridges supported by a tripod structure at one end and two jacket platforms at the other two ends. On both tripod and jackets, by applying a prescribed displacement of 0.1 m under free drop condition (free drop lasts for 0.14 s under the acceleration of gravity) on the foundations, the sudden subsidence process is simulated. The time history of the accelerations on the two bridges is then studied as shown in Fig. 16.3. It shows that after the prescribed displacement (which can be taken as a sudden excitation) terminated at time $t = 0.14$ s, the acceleration response reaches its maximum at time 1–1.5 s, and is then decreased dramatically. The free damped vibration characteristics can be clearly observed and the vibration period follows the natural period of vertical bending vibrations of two individual bridges without significant coupling with each other.

The structural response is checked for:

1. Repeated yielding
2. Cross section plasticity
3. Joint failure
4. Buckling
5. Maximum displacements and permanent displacements

No yielding, buckling or joint failure has been detected on the bridges, the two jackets, and the tripod structure. The maximum displacement is within acceptable limits.

Furthermore, by applying the acceleration time history (calculated from the global modeling in Fig. 16.2) at the jacket-topside interface to the supports of the each detailed modeling of topside modules, the responses of the topside modules are studied in detail. Figure 16.4 shows an example of three checked locations (P1, P2 and P3) on a module structure modeling resting on the jacket 2, P1 is located on a cantilever of a module, P2 is located at the middle of top deck level, and P3 is located on the top of a hanging module. The vertical displacement time histories of these three locations are illustrated in Fig. 16.5, which exhibit almost harmonic vibrations. The responses at the three locations have phase lags with each other. The cantilever location P1 shows higher displacement than the other two locations. The maximum vertical displacement at P1 occurs at time $t = 3.2$ s, which lags significantly behind the time with maximum excitations at the module support, i.e., $t = 1.4$ s. It is also noted that the displacement peaks occur at different time instants. No yielding or buckling has been detected on the module structure.

Fig. 16.2 Location (*upper*) corresponding to calculated acceleration histories at two platform connecting bridges and their actual installation on site (*lower*) (courtesy of Aker Solutions)

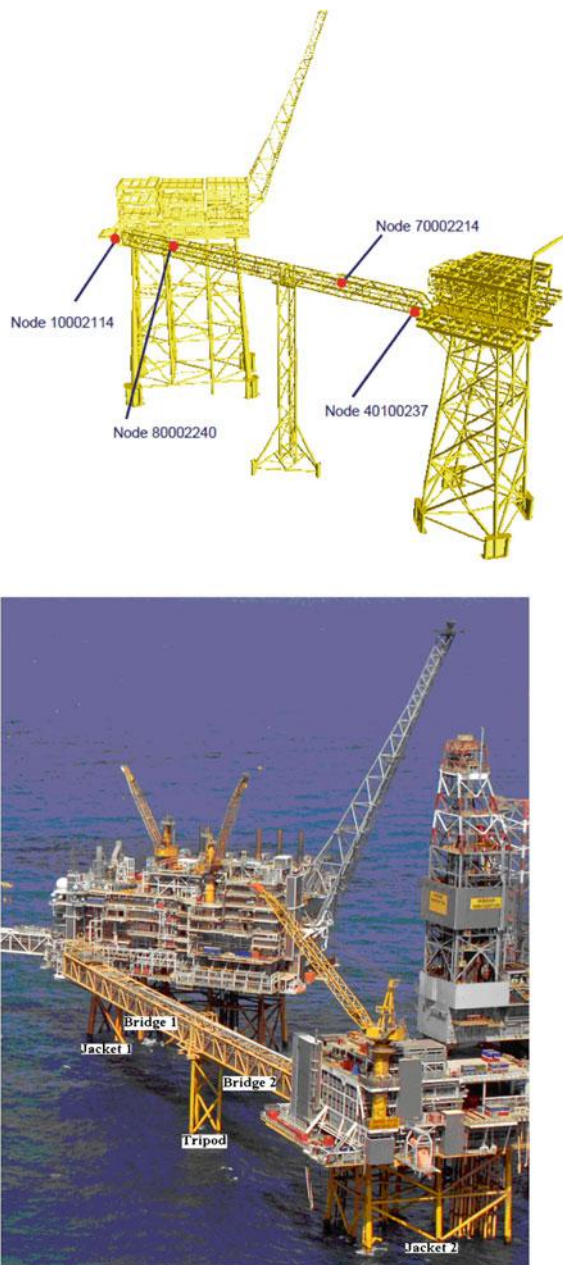


Fig. 16.3 Vertical accelerations of bridges' midspan (*upper figure*) and bridges' supports (*lower figure*) (courtesy of Aker Solutions)

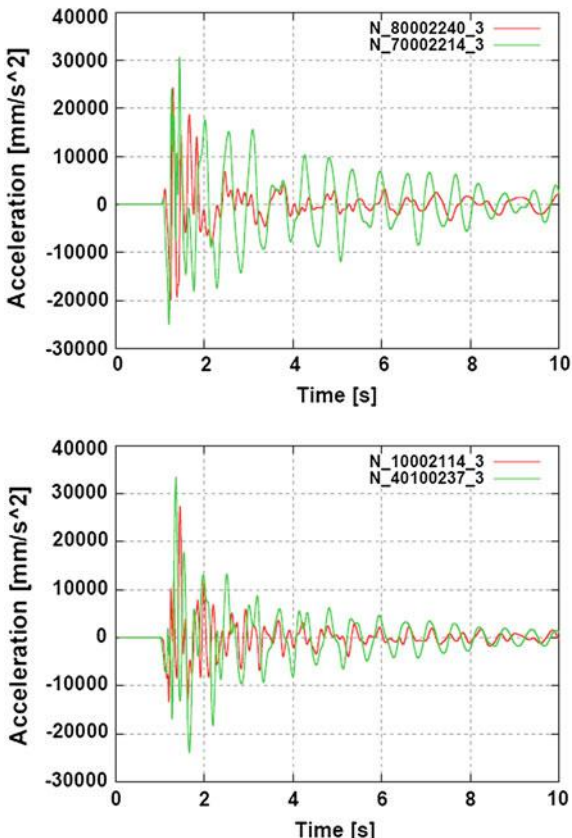


Fig. 16.4 Checked locations of a detailed topside module modeling of the south platform (jacket 2) shown in Fig. 16.2

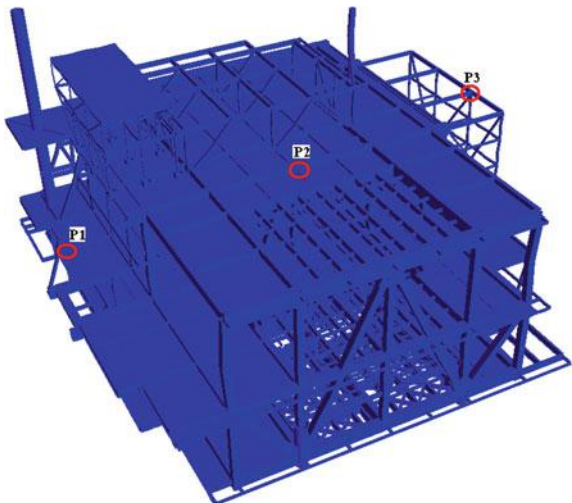
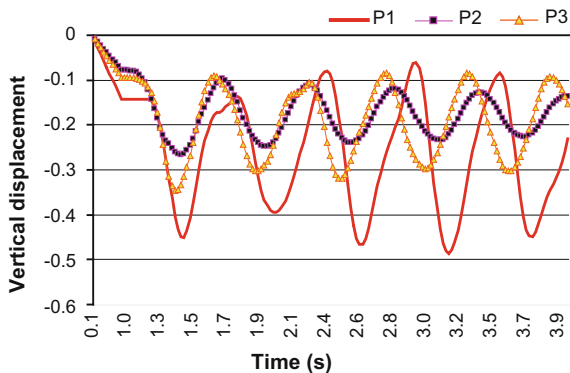


Fig. 16.5 Vertical displacement time histories for three checked locations at a topside module of the south platform (jacket 2)



16.3.2 Case Study 2: Response of a Topside Flare Boom Due to Sudden Subsidence

A flare boom structure is installed on the topside of a jacket structure located in the North Sea.

By realizing that the vertical stiffness of the platform is rather high, and in order to perform the capacity check of the flare boom subject to sudden subsidence, the sudden subsidence of the flare boom is calculated as vertical displacement time history with a constant acceleration of 9.81 m/s^2 downward. The drop is realized by prescribing nodal displacements on the supports of the flare boom with the drop time history shown in Fig. 16.6. The gravity load is first applied, the sudden subsidence is then activated at time $t = 10 \text{ s}$, assuring no interference to the gradual transfer of the gravity load. The time step during the drop is set to 0.001 s.

Figure 16.7 shows the vertical displacement of the flare boom. It is obvious that the vertical displacement at the top of the flare boom is most adverse with a maximum value of 0.27 m, compared to a vertical static deflection of 0.13 m under only the influence of the flare boom's selfweight. Figure 16.8 shows a time history of the vertical displacement at the tip of the flare. After the sudden subsidence

Fig. 16.6 Prescribed nodal vertical displacement of the supports for the flare boom to simulate a sudden subsidence

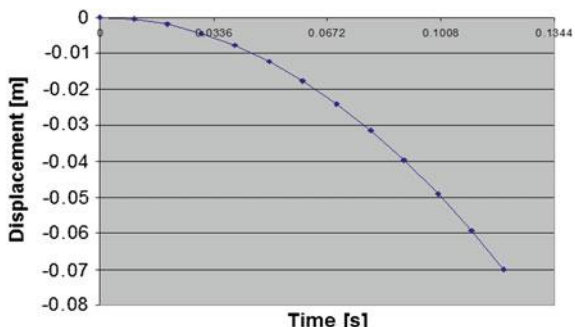


Fig. 16.7 Vertical displacement at time 11.4 s (courtesy of Aker Solutions)

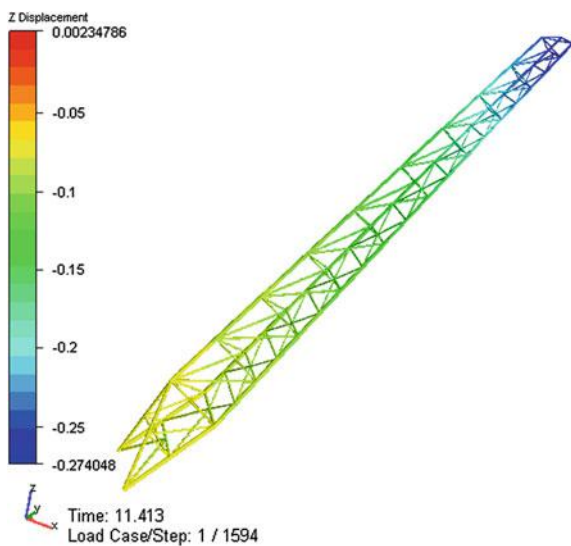
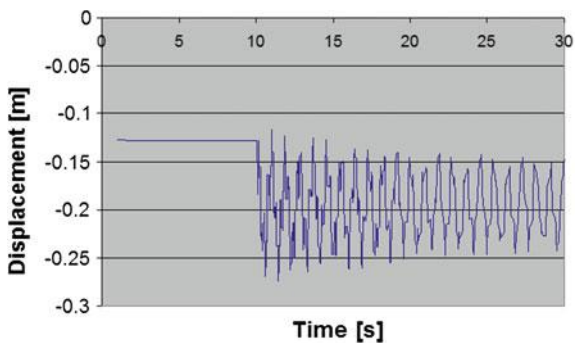


Fig. 16.8 Vertical displacement time history at the tip of the flare boom (courtesy of Aker Solutions)



terminates at $t = 10.2$ s, the flare boom reaches a maximum vertical displacement of 0.27 m at around 11.4 s, which is followed by a damped vibration with a gradual decrease of the vertical displacement.

By observing calculated response results, it is concluded that only local yielding on a few members occurs, while no failures of joints and buckling are detected. The vertical displacement is within the acceptable limit. And the permanent plastic deformation is negligible.

Chapter 17

Tank Liquid Impact

17.1 General

Tanks are used in water distribution systems and in industrial plants for the storage and/or processing of a variety of liquids and liquid-like materials, such as oil, liquefied natural gas, chemical fluids and wastes of different forms, tanks are used and often constructed with thin shells due to efficiency of load carrying capacity, i.e. the strength properties of all materials can be used completely in tension or compression. This is because, with a properly designed curvature of shells, all fibers over the shell cross section are equally strained due to membrane stress, and load carrying capacity may simultaneously reach the limit for the whole shell section [1]. However, contrary to ordinary structures, the stiffness of the tanks cannot be increased considerably [2]. Due to the low ductility and unstable nature of shell buckling (implying a low behavior factor), as well as low redundancy of tanks, the lateral seismic design forces are generally higher than those for normal structures such as offshore structures or building structures with “equivalent” dynamic responses as that of the tanks. And due to the higher utility and damage consequences, the importance factor associated with reliability requirement for liquid tanker is high, which depends on the potential loss of life due to the failure of the particular tank and on the economic and social consequences of failure. However, present codes such as API 650 [3] do not provide fully satisfactory procedures for an earthquake resistance design of tanks [4]. This can lead to an un-conservative tank design. Furthermore, unlike beam or frame design, the knowledge regarding the design of thin-walled structures is not well developed among engineers. This can cause either an unsafe or “more than sufficiently” safe tank design.

Moreover, typical storage tanks have natural periods above 1.0 s and are therefore similar to structures with a soft first story. During a strong earthquake and soft soil condition, resonance of tank structure with ground motions at lower order of eigenperiod may occur.



Fig. 17.1 Tank damage during the 7.4 moment magnitude of Kocaeli earthquake on 17 August 1999, in Turkey

Tanks can be categorized into two types: ground-supported tanks (Fig. 17.1) and elevated tanks (right figure in Fig. 17.2). Elevated tanks normally have significant masses concentrated at the top of slender supporting structures, thus they may be especially vulnerable to the earthquake loading.

As an important consideration in the seismic design of tanks, the liquids' sloshing motions inside tanks can exert significant impact on tanks, causing structural damages. For elevated tanks installed on a platform or a supporting structure, it can also alter both the natural frequency and the damping of the platform and the supporting structure.

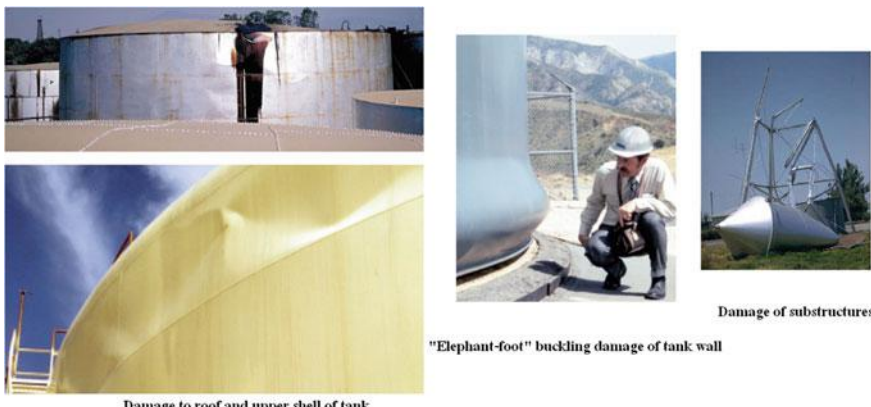


Fig. 17.2 Examples of tank sloshing damage scenarios (courtesy of University of California, Berkeley)

17.2 Tank Damages Due to Earthquakes

Earthquake induced liquid motions can cause tank damage in several scenarios, such as structural damage of tank walls and roof, base-anchorage failures, tank support-system failures, differential settlements, partial uplifting and pipe failures, and the subsequent leakage and spillage combined with fire etc.

Extensive damages have been found for tanks that were not properly designed or detailed [5–10]. A well-known severe accident due to earthquake induced sloshing damage occurred during Tokachi-oki earthquake in 2003, leading to the damage of seven large oil storage tanks with floating roof structures. This is because the seismic ground motions at the tanks' sites had a long peak period of 4–8 s, which is in the range of the tanks' sloshing period of 5–12 s [11]. During the 1906 San Francisco earthquake, due to damages of water tanks, the lack of water supply after the earthquake caused a major fire that resulted in more damage than the earthquake itself. Other relevant accidents due to liquid tank damages have also occurred in Alaska (1964), Japan (Nigata 1964, Kobe 1995), San Juan in Argentina (1977), California (San Fernando 1971, Imperial Valley 1979, Loma Prieta 1989, Northridge 1994), Maule in Chile (2010), Kocaeli Turkey (1999) (Fig. 17.1) and Emilia-Romagna in Italy (2012).

With regard to structural damage of tanks, a number of damage scenarios can be observed through historical accidents of tanks: (1) “elephant foot” buckling damage (Fig. 17.2) due to the large axial compressive stresses induced by the beam like bending of the tank wall, causing an outward bulge just above the base of the tank. The formation of the bulge is caused by buckling under large circumferential tensile stresses due to the internal pressures (hydrostatic and hydrodynamic due to vertical excitation), in combination with the axial compression stresses due to the overturning moment caused by horizontal earthquake excitation. This is normally associated with the elastic-plastic behavior of the material; (2) “diamond shape” buckling is less common than, and contrary to “elephant foot” buckling which is essentially a type of elastic-plastic buckling. The “diamond shape” is normally induced primarily by elastic shell buckling at the base of the tank as shown in Fig. 17.3. Both failure scenarios above are a type of shell buckling that appears at a short distance above the base and usually extends around most or all of the circumference, and have been addressed in relevant codes and standards such as Eurocode 8 [12] and New Zealand guidelines [13, 14]; (3) shear buckling occurs on the side wall of a tank. Figure 17.5 shows the occurrence of shear buckling and bending buckling of cylindrical tanks based on the ratio of height to radius and radius to wall thickness. It is noticed that shear buckling is more likely to occur at a small height to radius ratio, while “elephant foot” buckling predominantly occurs for large ratios of height to radius; (4) secondary buckling, as shown Fig. 17.4, is due to external pressure and cavitation [15], and it is an elastic type of buckling mode influenced by the plasticity development on other parts of the tank wall. However, this type of damage is not covered by the majority of the design codes, and until now, no empirical formula for it has been provided in the literatures. Very



Fig. 17.3 Diamond shape buckling during Emilia earthquake, Italy, 2012 [17]



Fig. 17.4 Secondary buckling during Emilia earthquake, Italy, 20 and 29 May 2012 [17]

few studies have shed light on this topic by performing numerical studies of secondary buckling, such as the ones performed by Virella et al. [16] and Buratti and Tavano [17]; (5) failure of tank roof may occur due to sloshing wave impact of the upper part of the contained liquid when there is insufficient freeboard between the liquid surface and the roof [18], as shown in Fig. 17.2; (6) failure of attached

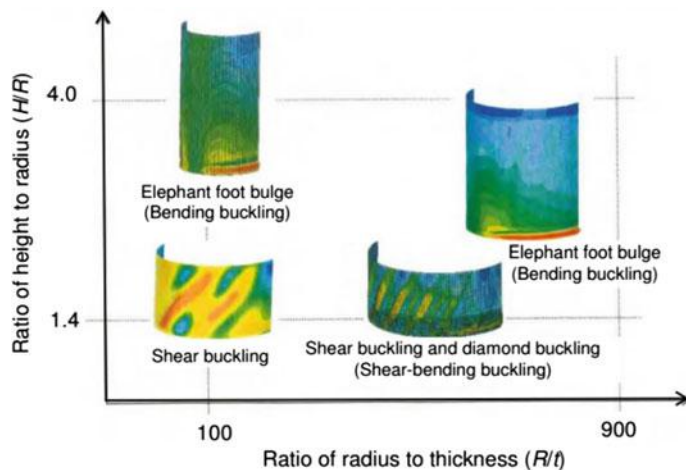


Fig. 17.5 Occurrence of shear buckling and elephant foot bending buckling of cylindrical tanks based on the ratio of height to radius and ratio of height to radius and wall thickness [79]

piping and other accessories, due to the inability of these elements to accommodate the deformations of the flexible shell [19].

However, the damage phenomenon should be considered in its entirety and a unique criterion is required to identify the possible buckling loads, including all types of possible buckling modes and to use such a criterion to build fragility curves [17]. Therefore, more efforts need to be devoted to the relevant studies.

In addition, the sloshing may also induce large base shear and overturning moments, causing the rupture of base anchors, pipe connections to the tank, tank sliding or uplifting [20–22], or the collapse of the support structure of the tank (Fig. 17.2).

From the discussion above, it can be concluded, as also specified in various design codes for tanks, that it is required to verify the following failure scenarios of liquid subjected to seismic loading:

1. Development of “elephant foot” buckling at the lower course of the tank
2. Buckling at the top of the tank due to the alternating sign of the hydrostatic and hydrodynamic pressures
3. Rupture or leakage because of the increased induced hoop hydrodynamic stresses
4. Plasticification of the base plate in unanchored tanks due to uplifting
5. Failure of the anchor bolts
6. Failure at the nozzles and piping system, especially in the case of unanchored tanks
7. Sliding of the tank.

By accounting for the sloshing effects of tanks, Fischer and Rammerstorfer [23] presented that land based tank structures may be exposed to sloshing during strong ground motions. By studying the sloshing damage of oil storage tanks (with floating roof) during Tokachi-oki earthquake of 2003, which induced a maximum sloshed oil height of more than 3 m in 30,000–40,000 m³ tanks, Ken Hatayama [11] concluded that not only the fundamental mode, but also higher modes of sloshing can cause damages to the floating roofs of the tanks. Furthermore, they also confirmed that it is the long period (4–8 s) strong ground motions, with a broad period range covering both fundamental and higher order sloshing modes, which contribute to the oil sloshing. By using a finite difference model, Chen et al. [24] investigated the sloshing motions in two-dimensional tanks excited by the horizontal component of four seismic events, and the occurrence of significant sloshing motions was presented. In addition, they also demonstrated that non-linear effects of non-overturning waves during certain earthquakes could be sufficiently strong to damage tanks.

Experiments and engineering practices indicate that the sloshing problem can be greatly mitigated by using spherical tanks as shown in Fig. 17.6, regardless of the levels to which the tanks are filled. Spherical tank (Fig. 17.7) in LNG carriers have operated in service from near empty to full load, and the sloshing damages have never occurred [25]. Earthquakes have been major tests for verifying the appropriateness of their seismic designs [26]. During the Kobe earthquake of 1995, which was Japan's second worst earthquake in the 20th century after the Great Kanto earthquake of 1923, it created intense motion in the spherical gas tanks near the epicenter. This was the first serious earthquake to occur since the construction of spherical gas tanks began in Japan. However, there was no damage in these spherical gas tanks.

As will be elaborated in Sect. 24.6 on tuned liquid damper, on one hand, the tank fluid causing sloshing vibration can damage and induce significant lateral



Fig. 17.6 Spherical gas (compressed gas) tank farm in the petroleum refinery in Karlsruhe (photo courtesy of Karlsruhe: Raffinerie)



Fig. 17.7 Liquefied natural gas (LNG) carrier with spherical shape of tanks (photo courtesy of Wolfgang Meinhart)

forces applied on the tank and supporting structures. On the other hand, it can also be used, in the case of an elevated tank or a tank installed on a structure, as a dynamic absorber [27] to suppress the dynamic response of supporting structures.

17.3 Calculation of Hydrodynamic Forces Due to Tank Impact

Mechanical systems consisting of tanks with fluid and soils are essentially multi-phase systems. The comprehensive and accurate analysis of multi-phase structural systems in dynamic environments has a substantial impact on the structural design procedures, especially whenever relative motion among the phases is expected. Such cases can be classified into problems with large relative motion governed by flow characteristics, problems of short duration, and problems of long duration with limited fluid displacement. The latter includes typical fluid–structure–soil interaction phenomena such as the ones encountered in calculating dynamic responses of offshore structures, liquid filled tanks, dams, and nuclear reactor components, subjected to waves or earthquakes [28].

The current book briefly presents simplified methods for modeling the fluid in tank, for calculating the forces applied on tank structure due to fluid motion under earthquakes, and for modeling of fluid in tanks using FEM.

For a comprehensive coverage of the topic on sloshing and fluid-structure-soil-interaction of tank structures, readers may read Refs. [18, 29–32].

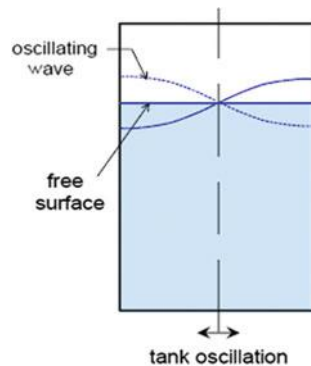
17.3.1 Fluid–Tank Interaction in Horizontal Direction

For a partially filled tank, when the period of tank motion is close to a period of fluid motion, the free surface of liquid inside the tanks can have an alarming propensity to undergo rather large excursions and induce considerable hydrodynamic forces, causing high local pressures and large forces on tank structures, the violent fluid motion is hereby referred to as sloshing. This indicates that, different from load scenarios of typical engineering structures such as buildings, not only seismic excitation but also the hydrodynamic force induced by liquid must be included for evaluating the structural integrity of the tanks. Two major sources enhance the sloshing response of liquids: when the tank motion due to seismic excitation has a period close to the period of liquid sloshing in the tank, or if the damping connected to the fluid is rather low [33]. For offshore structures, a worst scenario is when the lowest sloshing mode frequency and the natural frequency of the tank installed on a platform are both close to that of the platform's first global vibration mode. Moreover, in this scenario, for higher sloshing modes but with less extent [34], a splitting of the peak response of tanks will occur and the nature of splitting peak will vary with small changes in the liquid-depth. Since structures of liquid storage tanks generally have low redundancy, less ductility and possess lower energy-dissipating capacity during the seismic excitation, they are more vulnerable to dynamic loading than conventional structures, as previously mentioned.

When a liquid tank is under motion, in addition to the hydrostatic pressure, the liquid exerts hydrodynamic pressure, including both impulsive and oscillating pressures on tanks and tank base. They can be separated into impulsive and convective parts: the part of the liquid in the upper region of the tank, known as convective/sloshing liquid, undergoes long period sloshing motion and vibrates relative to the tank wall. While the rest in the lower region of the tank, known as impulsive/rigid liquid, moves rigidly with the tank and vibrates along/in union with the tank wall. The convective/sloshing liquid determines the height of the free surface waves, and hence the freeboard requirements, and it also contributes to the base shear and overturning moment of the tank. The impulsive/rigid liquid, which experiences the same acceleration of the tank, only contributes to the base shear and overturning moment of the tank. The hydrodynamic response of the tank-liquid system is characterized by the superposition of contributions from both convective/sloshing liquid and impulsive/rigid liquid. It is noted that since the associated period of the two parts differ significantly, the loadings caused by two parts can be assumed to be uncoupled. Furthermore, even though the liquid sloshing can exert a significant impact on the upper part of the tank wall and tank roof, because the sloshing motion is associated with long periods, it makes a relatively small contribution to the total hydrodynamic pressure on the tank walls. Therefore, the global tank response is primarily influenced by the impulsive/rigid liquid motions (Fig. 17.8).

By utilizing the potential flow theory and assuming a zero damping, the n th order of eigenfrequencies of the anti-symmetric mode of sloshing wave in rad/s are then calculated by [34, 35]:

Fig. 17.8 Oscillating rectangular tank with a sloshing wave (courtesy of Dodge [35])



$$\omega_n^2 = g(2n - 1) \frac{\pi}{a} \tanh\left(\frac{2n - 1}{a} \pi h\right) \quad (17.1)$$

where $n = 1, 2, 3\dots$; g is the acceleration of gravity in m/s^2 ; a is the tank length (m) in the direction of tank oscillation; h is the mean depth (m) of tank liquid.

It is noted that only the anti-symmetric mode of sloshing wave produces lateral force due to a shift of the center of mass (c.m.) of the liquids, as shown in Fig. 17.9. This is because the oscillation of center of mass for liquid is the source of sloshing induced forces. The first ($n = 1$) anti-symmetric mode has the largest shift of c.m., therefore it produces much larger lateral forces than any other higher modes.

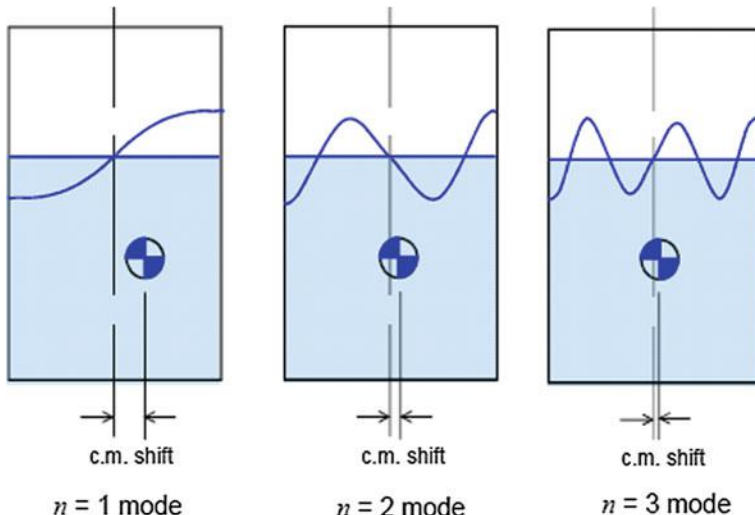


Fig. 17.9 First three anti-symmetric modes of sloshing wave with a shift of liquid c.m. (courtesy of Dodge [35])

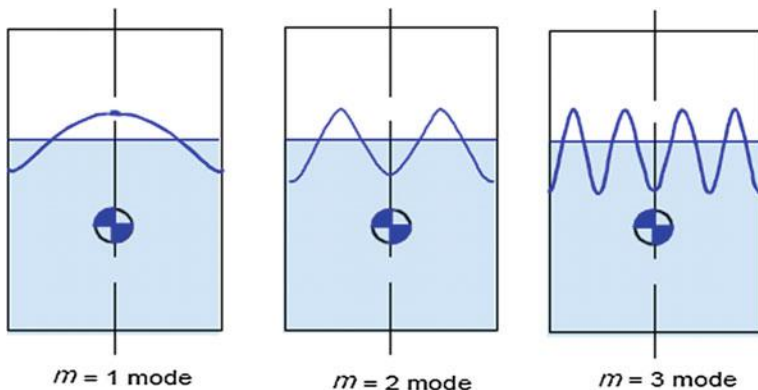


Fig. 17.10 First three symmetric modes of slosh wave with no shift of liquid c.m. (courtesy of Dodge [35])

The symmetric sloshing modes do not have any horizontal shift of center of mass, as shown in Fig. 17.10, thus producing no lateral forces. The m th order of eigenfrequency of the symmetric mode of sloshing wave in rad/s is then calculated by:

$$\omega_m^2 = g(2m) \frac{\pi}{a} \tanh\left(\frac{2m}{a}\pi h\right) \quad (17.2)$$

For three dimensional sloshing waves, the eigenfrequencies of the sloshing modes vary in both longitudinal and transverse direction, as expressed by:

$$\omega_{m,n}^2 = \left\{ \left[\gamma_n^2 + \eta_m^2 \left(\frac{a}{b} \right)^2 \right] \frac{g}{a} \right\} \tanh \left\{ \left[\gamma_n^2 + \eta_m^2 \left(\frac{a}{b} \right)^2 \right] \frac{h}{a} \right\} \quad (17.3)$$

where $n = 1, 2, 3\dots$; $m = 1, 2, 3\dots$; a and b are the tank length and width in meters; γ_n is either $2\pi n$ or $2\pi(n - 0.5)$ depending on whether the three dimensional wave is symmetrical or anti-symmetrical in the x direction; and η_m is likewise $2\pi m$ or $2\pi(m - 0.5)$; the wave shapes are a combination of the two-dimensional x - and y -mode shapes [35].

A tank with the hydrodynamic effects can generally be idealized by an equivalent spring mass model, which was originally developed by Westergaard [36] in a seminal study concerning the dynamic interaction between dams and reservoir systems. As a milestone in its further development, Housner [37–39] developed a simple two-degrees-of-freedom mechanical model to simulate the tank-liquid system response. In this model, the contained fluid is assumed to be incompressible, inviscid and irrotational, and is replaced by two masses, one of which is rigidly attached to the tank wall and the other of which is connected to the tank wall by springs. The method includes effects of tank wall–liquid interaction, and the parameters of this model depend on the geometry and flexibility of the tank wall. This concept constitutes the basis for the API 650 [40] standard provisions

(Appendix E) for vertical cylindrical tanks. The horizontal oscillation of the tank can be expressed as:

$$X(t) = Ae^{i\omega t} \quad (17.4)$$

where A and ω are the amplitude and angular frequency of the oscillation of the tank, respectively.

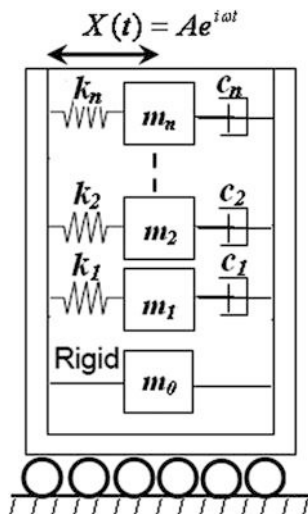
And the resultant horizontal force exerted on the walls of a rectangular tank can be expressed as [34]:

$$F(t) = A\omega^2 e^{i\omega t} \left[M_l + \sum_{n=1}^{\infty} \frac{8M_l \tanh[(2n-1)\frac{\pi h}{a}]}{\frac{h}{a}(2n-1)^3 \pi^3 \left[\frac{\omega_n^2}{\omega^2} - 1 \right]} \right] \quad (17.5)$$

where M_l is the total liquid mass in kg; a is the tank length in meter; h is the mean depth of tank liquid in m.

To incorporate the viscous damping of liquids, a more useful method is to model the tank liquid system using a mechanical model. The total liquid mass M_l is divided into impulsive/rigid (m_0) masses (which act as a rigid body attached to the tank) and convective/sloshing masses (m_n), as shown in Fig. 17.11. Each m_n represents a convective mass associated with the n th sloshing frequency. The damping for convective and impulsive motion can normally be taken as 0.5 and 5 % of the critical damping ($2 \times \text{mass} \times \text{angular natural frequency}$), respectively [19, 41]. As described previously, liquid in the lower portion mostly contributes to impulsive/rigid mass and liquid in the upper portion mostly contributes to convective/sloshing mass. Generally, the broader (the lower the ratio of vertical to horizontal planes) a tank is, the more liquid contributes to the sloshing related convective mass

Fig. 17.11 The equivalent mechanical spring-damping-mass model of tank fluid dynamics



compared to the impulsive/rigid mass, and vice versa. For the case of zero viscous damping ($c_n = 0$), the resultant horizontal force in the equation above can then be rewritten as:

$$F(t) = A\omega^2 e^{i\omega t} \left[m_0 + \sum_{n=1}^{\infty} m_n + \sum_{n=1}^{\infty} \frac{m_n}{\frac{\omega_n^2}{\omega^2} - 1} \right] \quad (17.6)$$

From the equation above, it is obvious that, if the tank is regarded as rigid, the impulsive mass experiences the same acceleration as the ground. The convective masses are subjected to the pseudo-accelerations that are function of the sloshing frequencies.

By matching the two equations above, one obtains:

$$\frac{m_n}{M_l} = \frac{8 \tanh[(2n-1)\pi r]}{\pi^3 r (2n-1)^3} \quad (17.7)$$

$$m_0 + \sum_{n=1}^{\infty} m_n = M_l \quad (17.8)$$

It is not necessary to explicitly evaluate k_n because it is required that:

$$\omega_n^2 = \frac{k_n}{m_n} = g(2n-1) \frac{\pi}{a} \tanh\left(\frac{2n-1}{a} \pi h\right) \quad (17.9)$$

If one accounts for the weight of the tank structure m_s , the total horizontal base shear caused by the tank motion can be expressed as:

$$Q(t) = (m_s + m_0) \ddot{X}(t) + \sum_{n=1}^{\infty} m_n \ddot{x}_n(t) \quad (17.10)$$

where $\ddot{x}_n(t)$ is the acceleration of sloshing liquid associated with n th sloshing frequency and at time t .

In the case of rigid tank walls, the impulsive motion exactly follows the ground motion. In such a case the impulsive frequency has an infinite value. However, most tank walls have a certain degree of flexibility. This normally causes an increase in the impulsive hydrodynamic effects compared with those of tanks with rigid walls. On the other hand, the convective forces and response are normally insensitive to variations in wall flexibility, because they are associated with natural periods of vibration that are significantly longer than the dominant periods of the ground motion or pipe wall vibrations. Therefore, in practice, the convective components of seismic action can be considered the same as those obtained for rigid tanks [19].

In a response spectrum design expression, for tanks fixed to the foundation, by disregarding the phase between the impulsive/rigid liquid and the sloshing/convective liquid at each eigenmode, the maximum total base shear caused by the

tank motion can be calculated using the Square Root of the Sum Squares (SRSS) method to combine the modal contribution, as given by:

$$Q = \sqrt{\sum_{i=1}^{\infty} [(m_{\tan k} + m_0)S_e(\omega_{0i})]^2} + \sqrt{\sum_{n=1}^{\infty} [m_n S_e(\omega_n)]^2} \quad (17.11)$$

where $m_{\tan k}$ is the mass of the tank structure; $S_e(\omega_{0i})$ is the spectrum acceleration (in m/s^2) at the i th impulsive/rigid liquid frequency ω_{0i} ; $S_e(\omega_n)$ is the spectrum acceleration (in m/s^2) at the n th sloshing frequency ω_n .

For elevated tanks, the maximum total base shear caused by the tank motion is given by:

$$Q_{elevated} = \sqrt{\sum_{i=1}^{\infty} [(m_{\tan k} + m_s + m_0)S_e(\omega_{(\tan k+s+0)i})]^2} + \sqrt{\sum_{n=1}^{\infty} [m_n S_e(\omega_n)]^2} \quad (17.12)$$

where $S_e(\omega_{(\tan k+s+0)i})$ is the spectrum acceleration (in m/s^2) at the i th eigenfrequency of the system when accounting for the mass of the tank, the supporting structure and the impulsive/rigid liquid as a whole, i.e. $\omega_{\tan k+s+0} = \sqrt{\frac{k_s}{m_{\tan k} + m_s + m_0}}$; k_s is the global flexural stiffness of the supporting structure; $S_e(\omega_n)$ is the spectrum acceleration at the n th sloshing frequency ω_n .

It is obvious that both the impulsive and convective pressure are applied not only horizontally on the tank wall, but also vertically on the tank bottom, as is shown in Fig. 17.12. The horizontal shear force and the overturning moment above the tank base plate are only caused by the horizontal pressure, while the overturning moments at and below the tank plate are determined by both horizontal and vertical pressures.

For most storage tanks, the mass corresponding to the first impulsive/rigid (m_{01}) and first convective/sloshing (m_{n1}) mode together account for 85–98 % of the total liquid mass [42]. Therefore, it is practical to only consider the mass of the first impulsive (m_{01}) and convective (m_{n1}) mode. By assuming that the mass of the structure can be represented as an equivalent concentrated mass m_s at the top of the tank, the two equations above are then written as the three equations below:

$$Q = (m_{\tan k} + m_s + m_{01})S_e(\omega_{01}) + m_{n1}S_e(\omega_{n1}) \quad (17.13)$$

for tanks directly attached to the foundation

$$Q_{elevated_tankbottom} = (m_{\tan k} + m_{01})S_e(\omega_{(\tan k+s+0)_1}) + m_{n1}S_e(\omega_{n1}) \quad (17.14)$$

for elevated tanks at the bottom of the tank

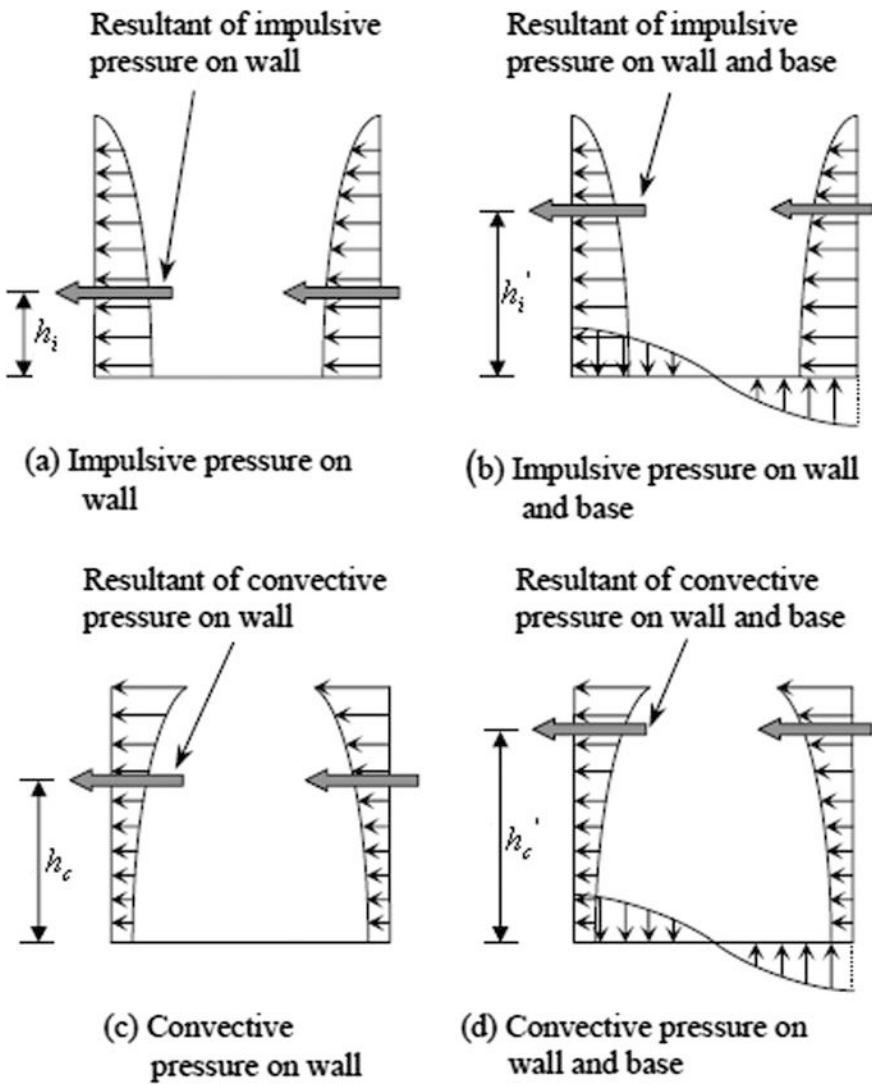


Fig. 17.12 The distribution of impulsive and convective pressure applied on the tank wall and bottom [80]; hydrostatic pressure is not accounted for in this figure

$$Q_{elevated_structurebottom} = (m_{tan k} + m_s + m_{01})S_e(\omega_{(tan k + s + 0)1}) + m_{n1}S_e(\omega_{n1})$$

for elevated tanks at the bottom of the supporting structure

(17.15)

Since only the hydrodynamic pressure on the tank wall contributes to the overturning moment immediately above the base plate of the tank, the overturning moment immediately *above* the base plate is then calculated by the two equations as

$$M = (m_{\text{tank}} h_{\text{tank}} + m_{01} h_i) S_e(\omega_{01}) + m_{n1} h_c S_e(\omega_{n1}) \quad (17.16)$$

for tanks directly attached to the foundation

$$M_{\text{elevated_tan k bottom}} = (m_{\text{tan k}} h_{\text{tan k}} + m_{01} h_i) S_e(\omega_{(\text{tan k} + s + 0)_1}) + m_{n1} h'_c S_e(\omega_{n1}) \quad (17.17)$$

for elevated tanks

where $h_{\text{tan k}}$, h_i and h_c are the heights of the centroids of tank mass, of the impulsive and convective hydrodynamic wall pressures to the base plate, in which h_i and h_c are defined in Fig. 17.12 and can be obtained in Table 17.1.

Both the hydrodynamic pressures on the tank wall and on the base plate contribute to the overturning moment immediately below the base place of the tank. Therefore, the overturning moment immediately *below* the base plate is calculated by the two equations as follows:

$$M' = (m_{\text{tan k}} h_{\text{tan k}} + m_{01} h'_i) S_e(\omega_{01}) + m_{n1} h'_c S_e(\omega_{n1}) \quad (17.18)$$

for tanks directly attached to the foundation

$$M'_{\text{elevated_tan k bottom}} = (m_{\text{tan k}} h_{\text{tan k}} + m_{01} h'_i) S_e(\omega_{(\text{tan k} + s + 0)_1}) + m_{n1} h'_c S_e(\omega_{n1}) \quad (17.19)$$

for elevated tanks

where h'_i and h'_c are the heights of the centroids of the impulsive and convective hydrodynamic wall pressures to the base plate by accounting for both the hydrodynamic pressure on the tank wall and that on the base plate. They are defined in Fig. 17.12 and can be obtained from Table 17.1.

Based on the equation above, the overturning moment at the bottom of the supporting structures is rewritten as:

Table 17.1 Recommended design values [44, 81, 82] for the first impulsive/rigid and convective/sloshing modes of vibration as a function of liquid-height-to-tank-radius ratio H/r for vertical circular tanks

H/r	m_{01}/M_l	m_{n1}/M_l	C_i	$C_c(\text{s}/\sqrt{\text{m}})$	h_i/H	h_c/H	h'_i/H	h'_c/H
0.3	0.176	0.824	9.28	2.09	0.4	0.521	2.64	3.414
0.5	0.3	0.7	7.74	1.74	0.4	0.543	1.46	1.517
0.7	0.414	0.586	6.97	1.6	0.401	0.571	1.009	1.011
1	0.548	0.452	6.36	1.52	0.419	0.616	0.721	0.785
1.5	0.686	0.314	6.06	1.48	0.439	0.69	0.555	0.734
2	0.763	0.237	6.21	1.48	0.448	0.751	0.5	0.764
2.5	0.81	0.19	6.56	1.48	0.452	0.794	0.48	0.796

$$\begin{aligned} M'_{elevated_structurebottom} &= (m_s h_s + m_{tan\ k}(h_{tan\ k} + h_{tb-sb}) + m_{01}(h'_i + h_{tb-sb}))S_e(\omega_{(tan\ k+s+0)_1}) \\ &\quad + m_{n1}(h'_c + h_{tb-sb})S_e(\omega_{n1}) \end{aligned} \quad (17.20)$$

where h_s is the height of structure, from top to bottom; h_{tb-sb} is the height of the bottom of the tank to the structure's bottom. If the tank-structure interface is located at the top of the structure, $h_{tb-sb} = h_s$.

For vertical circular cylinder tank, the first impulsive mass m_{01} and the first convective mass m_{n1} can be obtained from Table 17.1. The corresponding frequencies ω_{01} and ω_{n1} can be calculated by the two equations below:

$$\omega_{01} = \frac{2\pi}{C_i H} \sqrt{\frac{Et}{\rho r}} \quad (17.21)$$

$$\omega_{n1} = \frac{2\pi}{C_c \sqrt{r}} \quad (17.22)$$

where C_i and C_c are coefficient of impulsive and convective mode frequency, respectively. They can also be obtained from Table 17.1; t and E are the equivalent thickness and Young's modulus of the tank wall, respectively, if the tank wall's thickness varies with height, the equivalent uniform thickness t of the tank wall is calculated by weighting the thickness of each part of wall with respect to the distance from that part to the free surface of the liquid, see the first example below for its calculation; H and r are the liquid height and radius of the vertical circular tank.

Since the sloshing wave height is mainly contributed by the first sloshing mode [12], the maximum sloshing wave height d can be conservatively approximated as:

$$d = \frac{r S_e(\omega_{n1})}{g} \quad (17.23)$$

The spectral acceleration $S_e(\omega_{n1})$ in the equation above has a unit of m/s^2 .

For rectangular tanks, the first convective/sloshing mass m_{n1} and the corresponding sloshing frequencies ω_{n1} can be calculated by:

$$m_{n1} = \frac{8\rho b L^2}{\pi^3} \tanh\left(\frac{\pi h}{L}\right) \quad (17.24)$$

$$\omega_{n1} = \frac{\pi g}{L} \tanh\left(\frac{\pi h}{L}\right) \quad (17.25)$$

where L is the tank length in the direction of base excitation; b is the tank width; h is the depth of the liquid inside tank; and ρ is the density of the liquid.

And the maximum vertical sloshing wave height d for rectangular tank can be approximated as:

$$d = \frac{L}{2g} S_e(\omega_{n1}) \quad (17.26)$$

The spectrum acceleration $S_e(\omega_{n1})$ in the equations above has a unit of m/s^2 .

For more in-depth information on sloshing dynamics and their calculations, readers may refer to Faltinsen and Timokha [18].

Example A water tank has been designed with a vertical circular shape. It has an inner diameter of 20 m and a height of 9.6 m including a designed freeboard of 1.0 m. The thickness of the tank wall is 10 mm for the lower 4.8 and 8 mm for the upper 4.8 m. The density and the Young's modulus of the tank wall are 7850 kg/m^3 and 210 GPa, respectively. The water has a density of 1000 kg/m^3 . The weight of the designed tank roof is 12 t at the top of the tank wall. The weight of the designed tank bottom is 21 t. The horizontal earthquake acceleration design spectrum along E-W direction, with a return period of 475 years, has been given in Fig. 17.13. The importance factor is assumed to be 1.0. Using the information above, give an estimation of the corresponding maximum base shear and overturning moment on the tank bottom; assess whether the freeboard is sufficient.

Solution according to Eurocode 8 [12], linear elastic behavior of the structure is assumed, allowing only for localized non-linear phenomena without affecting the global response. The hydrodynamic response of the fluid needs to be included. Particularly, the convective and impulsive components of fluid

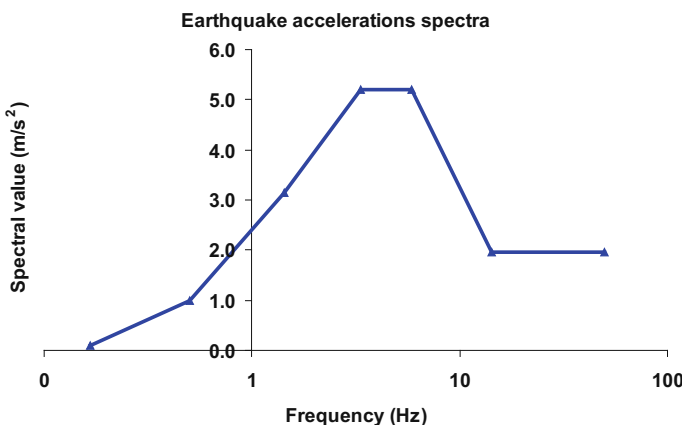


Fig. 17.13 The earthquake acceleration design spectrum—horizontal component with 0.5 % damping

motion as well as the tank shell deformation due to hydrodynamic pressure and interaction effects with the impulsive component should be taken into account. The proposed procedure satisfies these principles in a simple and efficient way for the design of fixed-base cylindrical tanks [42].

1. Calculation of weight

The maximum water depth H of the tank is $9.6 \text{ m} - 1.0 \text{ m} = 8.6 \text{ m}$

The mass of water inside tank is $M_l = \pi \times (20 \text{ m}/2)^2 \times 8.6 \text{ m} \times 1000 \text{ kg/m}^3 = 2,700,400 \text{ kg}$

The mass of the tank wall is $[(2 \times \pi \times 10 \text{ m} \times 0.01 \text{ m} \times 4.8 \text{ m}) + (2 \times \pi \times 10 \text{ m} \times 0.008 \text{ m} \times 4.8 \text{ m})] \times 7850 \text{ kg/m}^3 = 42,615 \text{ kg}$

The total mass of the tank structure including tank wall, 12 t of roof and 21 t of tank bottom plate: $m_{\text{tank}} = 42,615 \text{ kg} + 12,000 \text{ kg} + 21,000 \text{ kg} = 75,615 \text{ kg}$

2. Estimation of impulsive/rigid and convective/sloshing mass

With $H/r = 0.86$, by checking Table 17.1, one obtains:

$$\frac{m_i}{M_l} = 0.414 + \frac{(0.548 - 0.414) \times (0.86 - 0.7)}{(1.0 - 0.7)} = 0.4855$$

The rigid/impulsive mass is:

$$m_{01} = 0.4855 \times M_l = 0.4587 \times 2,700,400 \text{ kg} = 1311,044 \text{ kg}$$

The convective/sloshing mass is:

$$m_{n1} = (1 - 0.4855) \times M_l = 0.5413 \times 2,700,400 \text{ kg} = 1389,356 \text{ kg}$$

3. Estimation of natural frequency for impulsive and convective masses

With $H/r = 0.86$, by checking Table 17.1, one obtains:

$$C_i = 6.97 - \frac{(6.97 - 6.36) \times (0.86 - 0.7)}{(1.0 - 0.7)} = 6.64$$

$$C_c = 1.6 - \frac{(1.6 - 1.52) \times (0.86 - 0.7)}{(1.0 - 0.7)} = 1.56 \text{ s}/\sqrt{\text{m}}$$

The equivalent uniform thickness of the tank wall is calculated by weighting the thickness of each part of wall with the distance from each part to the free surface of the liquid:

$$t = \frac{4.8 \text{ m} \times 0.01 \times (8.6 \text{ m} - \frac{4.8 \text{ m}}{2}) + [(8.6 \text{ m} - 4.8 \text{ m}) \times 0.008 \times \frac{8.6 \text{ m} - 4.8 \text{ m}}{2}]}{4.8 \text{ m} \times (8.6 \text{ m} - 2.4 \text{ m}) + (8.6 \text{ m} - 4.8 \text{ m}) \times \frac{8.6 \text{ m} - 4.8 \text{ m}}{2}}$$

$$= 0.00961 \text{ m} = 9.61 \text{ mm}$$

The natural frequency due to impulsive/rigid mass is:

$$\omega_{01} = \frac{2\pi}{C_i H} \sqrt{\frac{Et}{\rho r}} = \frac{2\pi}{6.64 \times 8.6 \text{ m}} \sqrt{\frac{210 \times 10^9 \text{ Pa} \times 0.00961 \text{ m}}{7850 \text{ kg/m}^3 \times 10 \text{ m}}} = 17.63/\text{rad}$$

$$= 2.81 \text{ Hz}$$

The natural frequency due to sloshing/convective mass is:

$$\omega_{n1} = \frac{2\pi}{C_c \sqrt{r}} = \frac{2\pi}{(1.56 \text{ s}/\sqrt{\text{m}}) \sqrt{10 \text{ m}}} = 1.274/\text{rad} = 0.203 \text{ Hz}$$

4. Estimation of base shear

By reading Fig. 17.13, the maximum horizontal/lateral acceleration of the sloshing/convective mass is: $S_e(\omega_{n1}) = S_e(0.203 \text{ Hz}) = 0.2 \text{ m/s}^2$.

And the maximum horizontal acceleration of the impulsive/rigid mass is: $S_e(\omega_{01}) = S_e(2.81 \text{ Hz}) = 4.63 \text{ m/s}^2$.

Therefore, the base shear at the tank bottom is:

$$Q = (m_{\text{tank}} + m_{01})S_e(\omega_{01}) + m_{n1}S_e(\omega_{n1})$$

$$= (75,615 \text{ kg} + 1,311,044 \text{ kg}) \times 4.63 \text{ m/s}^2 + 1,389,356 \text{ kg} \times 0.2 \text{ m/s}^2$$

$$= 6698 \text{ kN}$$

It is noted that the base shear at the tank bottom is 25 % of the total weight (27,233 kN) of the tank–fluid system.

5. Estimation of heights of the centroid's impulsive and convective mass to the tank bottom plate

With $H/r = 0.86$, by checking Table 17.1, the height of the centroid's impulsive/rigid mass to the tank bottom plate is:

$$h_i = \left[0.401 + \frac{(0.419 - 0.401) \times (0.86 - 0.7)}{(1.0 - 0.7)} \right] \times 8.6 \text{ m} = 3.5 \text{ m}$$

The height of the centroid of the convective/sloshing mass to the tank bottom plate is:

$$h_c = \left[0.571 + \frac{(0.616 - 0.571) \times (0.86 - 0.7)}{(1.0 - 0.7)} \right] \times 8.6 \text{ m} = 5.1 \text{ m}$$

The height of the centroid of the impulsive/rigid mass to the tank bottom plate by accounting for both the hydrodynamic pressure on the tank wall and that on the base plate is:

$$h'_i = \left[1.009 - \frac{(1.009 - 0.721) \times (0.86 - 0.7)}{(1.0 - 0.7)} \right] \times 8.6 \text{ m} = 7.4 \text{ m}$$

The height of the centroid of the convective/sloshing mass to the tank bottom plate by accounting for both the hydrodynamic pressure on the tank wall and that on the base plate is:

$$h'_c = \left[1.011 - \frac{(1.011 - 0.785) \times (0.86 - 0.7)}{(1.0 - 0.7)} \right] \times 8.6 \text{ m} = 7.7 \text{ m}$$

6. Estimation of overturning moment

The vertical center of gravity of the tank (tank wall + roof + bottom) to the tank bottom plate is:

$$\begin{aligned} h_{\text{tank}} &= \frac{\{[(2 \times \pi \times 10 \text{ m} \times 0.01 \text{ m} \times 4.8 \text{ m}) \times 2.4 \text{ m} + (2 \times \pi \times 10 \text{ m} \times 0.008 \text{ m} \times 4.8 \text{ m}) \times 7.2 \text{ m}] \times 7850 \text{ kg/m}^3\} + [12,000 \text{ kg} \times 9.6 \text{ m}] + [21,000 \text{ kg} \times 0 \text{ m}]}{75,615 \text{ kg}} \\ &= 4.1 \text{ m} \end{aligned}$$

The overturning moment immediately above the base plate is calculated as:

$$\begin{aligned} M &= (m_{\text{tank}} h_{\text{tank}} + m_{01} h_i) S_e(\omega_{01}) + m_{n1} h_c S_e(\omega_{n1}) \\ &= [(75,615 \text{ kg} \times 4.1 \text{ m}) + (1,311,044 \text{ kg} \times 3.5 \text{ m})] \times 4.63 \text{ m/s}^2 \\ &\quad + (1,389,356 \text{ kg} \times 5.1 \text{ m}) \times 0.2 \text{ m/s}^2 \\ &= 24,098,011 \text{ Nm} = 24,098 \text{ kN m} \end{aligned}$$

The overturning moment immediately below the base plate is calculated as:

$$\begin{aligned}
 M' &= (m_{tan} h_{tan} + m_{01} h_i') S_e(\omega_{01}) + m_{n1} h_c' S_e(\omega_{n1}) \\
 &= [(75,615 \text{ kg} \times 4.1 \text{ m}) + (1,311,044 \text{ kg} \times 7.4 \text{ m})] \times 4.63 \text{ m/s}^2 \\
 &\quad + (1,389,356 \text{ kg} \times 7.7 \text{ m}) \times 0.2 \text{ m/s}^2 \\
 &= 48,493,997 \text{ Nm} = 48,494 \text{ kN m}
 \end{aligned}$$

7. Check the freeboard requirement

The maximum vertical sloshing wave height can be roughly estimated as:

$$d = \frac{rS_e(\omega_{n1})}{g} = \frac{10 \text{ m} \times 0.2 \text{ m/s}^2}{9.81 \text{ m/s}^2} = 0.21 \text{ m}, \text{ which is less than the freeboard of } 1.0 \text{ m.}$$

Example in this example, the tank in the example above is installed on a four leg offshore jacket structure. The layout of the jacket's piles and legs is shown in Fig. 17.14. The un-factored single pile capacity due to pile–soil interaction is 4 MN in tension and 12 MN in compression. The weight of the jacket is 1905 t (including added mass by assuming the legs are flooded). The height of the jacket-tank bottom interface to the seabed mudline is 56 m. The overall

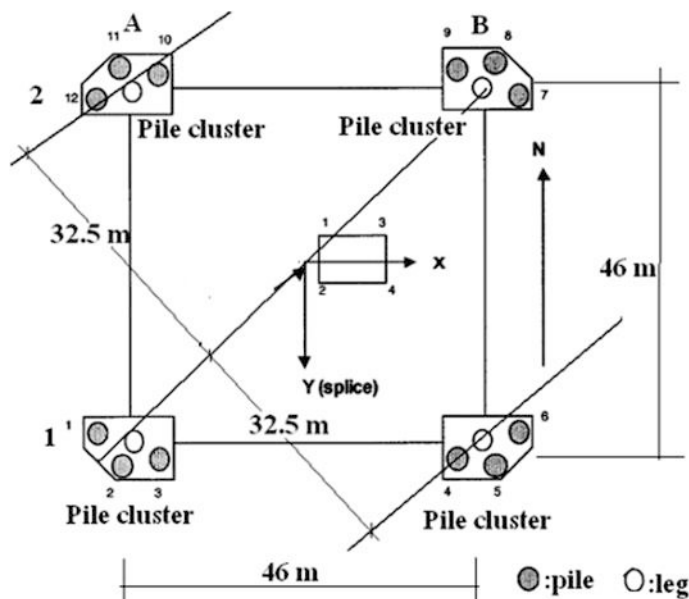
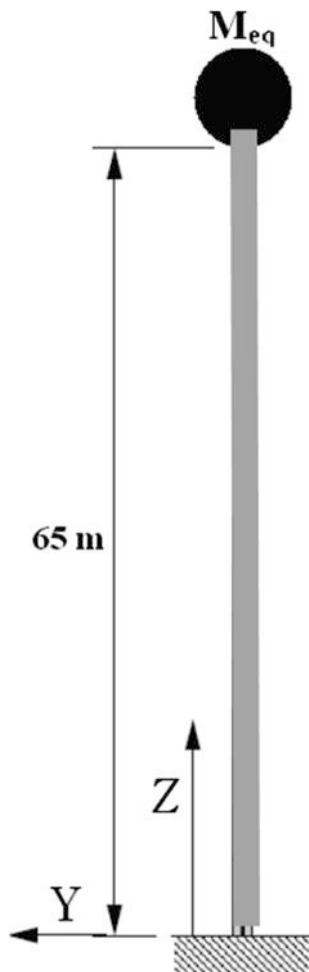


Fig. 17.14 The layout and overall dimensions of a jacket's pile foundation with 12 piles; each leg is supported by three piles connected by a pile cluster

bending stiffness of the jacket along E-W direction is designed as 20,060 kN m. The horizontal earthquake acceleration design spectrum along E-W direction is the same as the example above (Fig. 17.13). Give an estimation of the corresponding maximum base shear and overturning moment on the tank bottom and the tip of jacket pile foundation at the mudline. Calculate the axial pile forces due to the earthquake excitation. Assess if the freeboard is sufficient.

Fig. 17.15 An SDOF system representing a tank-liquid-jacket system



Solution

1. Estimation of the natural frequencies for impulsive and convective masses

By assuming the tower structure's weight is uniformly distributed along its height, the equivalent mass contributed by the tower structure to the tip mass (shown in Fig. 17.15) is around 1/3 of the tower's total mass: 1,905,000 kg/3.

By simplifying the tank-liquid-jacket system as a single-degree-of-freedom as shown in Fig. 17.15, the mass of the jacket structure can be represented as an equivalent concentrated mass m_s at the top of the structure. The equivalent mass at the top of the jacket can be calculated as:

$$\begin{aligned} M_{eq} &= m_{tan k} + m_s + m_{01} = 75,615 \text{ kg} + (1,905,000/3)\text{kg} + 1,311,044 \text{ kg} \\ &= 2,021,659 \text{ kg} \end{aligned}$$

The natural frequency of a single-degree-of-freedom (the tank-structure-impulsive/rigid liquid mass) system is:

$$\omega_{(tan k + s + 0)_1} = \sqrt{\frac{K_s}{M_{eq}}} = \sqrt{\frac{20,060 \times 10^3 \text{ Nm}}{2,021,659 \text{ kg}}} = 3.15/\text{rad} = 0.5 \text{ Hz}$$

The natural frequency due to sloshing/convective mass is:

$$\omega_{n1} = \frac{2\pi}{C_c \sqrt{r}} = \frac{2\pi}{(1.56 \text{ s}/\sqrt{\text{m}}) \sqrt{10 \text{ m}}} = 1.274/\text{rad} = 0.203 \text{ Hz}$$

2. Calculation of the base shear force

By looking at Fig. 17.13, the maximum horizontal/lateral acceleration of the sloshing/convective mass is: $S_e(\omega_{n1}) = S_e(0.203 \text{ Hz}) = 0.2 \text{ m/s}^2$.

And the maximum horizontal acceleration of the elevated tank is: $S_e(\omega_{(tan k + s + 0)_1}) = S_e(0.5 \text{ Hz}) = 0.98 \text{ m/s}^2$.

Therefore, the base shear at the tank bottom is:

$$\begin{aligned} Q_{elevated_tan k bottom} &= (m_{tan k} + m_{01})S_e(\omega_{(tan k + s + 0)_1}) + m_{n1}S_e(\omega_{n1}) \\ &= (75,615 \text{ kg} + 1,311,044 \text{ kg}) \times 0.98 \text{ m/s}^2 + 1,389,356 \text{ kg} \times 0.2 \text{ m/s}^2 \\ &= 1636,797 \text{ N} = 1637 \text{ kN} \end{aligned}$$

Note that if the tank is installed on the jacket, the tank-structure-impulsive/rigid liquid mass system has a much lower frequency (0.5 Hz) than that of the tank-impulsive/rigid liquid mass system (2.81 Hz) when the tank is directly attached to the ground in the first example above. Therefore, by checking the

acceleration response spectrum shown in Fig. 17.13, it is observed that the horizontal acceleration of the tank-structure-impulsive/rigid liquid mass (0.98 m/s^2) is much lower than that (4.63 m/s^2) without the jacket structure, causing a significant reduction in the estimated base shear from 6698 kN in the first example above to 1637 kN in the current example. Therefore, the effects of the supporting structure on the tank are similar to those of a base isolation system as will be presented later in this book.

The base shear at the bottom of the jacket is:

$$\begin{aligned} Q_{elevated_structurebottom} &= (m_{tan\ k} + m_s + m_{01})S_e(\omega_{(tan\ k + s + 0)_1}) + m_{n1}S_e(\omega_{n1}) \\ &= (75,615 \text{ kg} + 635,000 \text{ kg} + 1,311,044 \text{ kg}) \times 0.98 \text{ m/s}^2 \\ &\quad + 1,389,356 \text{ kg} \times 0.2 \text{ m/s}^2 \\ &= 2,259,097 \text{ N} = 2259 \text{ kN} \end{aligned}$$

It is noticed that the base shear at the bottom of the jacket is 8 % of the total weight (29,102 kN) of tank–fluid-structure system.

3. Calculation of overturning moment

The overturning moment immediately above the base plate is calculated as:

$$\begin{aligned} M_{elevated_tan\ kbottom} &= (m_{tan\ k}h_{tan\ k} + m_{01}h_i)S_e(\omega_{(tan\ k + s + 0)_1}) + m_{n1}h_cS_e(\omega_{n1}) \\ &= [(75,615 \text{ kg} \times 4.1 \text{ m}) + (1,311,044 \text{ kg} \times 3.5 \text{ m})] \\ &\quad \times 0.98 \text{ m/s}^2 + (1,389,356 \text{ kg} \times 5.1 \text{ m}) \times 0.2 \text{ m/s}^2 \\ &= 6,217,845 \text{ Nm} = 6218 \text{ kN m} \end{aligned}$$

The overturning moment immediately below the base plate is calculated as:

$$\begin{aligned} M'_{elevated_tan\ kbottom} &= (m_{tan\ k}h_{tan\ k} + m_{01}h'_i)S_e(\omega_{(tan\ k + s + 0)_1}) + m_{n1}h'_cS_e(\omega_{n1}) \\ &= [(75,615 \text{ kg} \times 4.1 \text{ m}) + (1,311,044 \text{ kg} \times 7.4 \text{ m})] \\ &\quad \times 0.98 \text{ m/s}^2 + (1,389,356 \text{ kg} \times 7.7 \text{ m}) \times 0.2 \text{ m/s}^2 \\ &= 138,591,191 \text{ Nm} + 20,201,236 \text{ Nm} = 158,792,427 \text{ Nm} \\ &= 158,792 \text{ kN m} \end{aligned}$$

The overturning moment at the structure's bottom is:

$$\begin{aligned}
 M'_{elevated_structurebottom} &= (m_s h_s + m_{tan\ k}(h_{tan\ k} + h_{tb-sb}) + m_{01}(h'_i + h_{tb-sb})) \\
 &\quad S_e(\omega_{(tan\ k+s+0)1}) + m_{n1}(h'_c + h_{tb-sb})S_e(\omega_{n1})[635,000\text{kg} \\
 &\quad \times 65\text{m} + (75615\text{ kg} \times (4.1\text{ m} + 65\text{ m}) \\
 &\quad + 1311044\text{ kg} \times (7.4\text{m} + 65\text{m})) \times 0.98\text{ m/s}^2 \\
 &\quad + (1389356\text{ kg} \times (7.7\text{m} + 65\text{ m})) \times 0.2\text{ m/s}^2 \\
 &= 158,792,426\text{ Nm} = 158,792\text{ kNm}
 \end{aligned}$$

4. Check the single pile capacity

By neglecting the influence from the selfweight of the jacket and the tank, the tension or compression forces applied on six piles in either column A or B, due to the earthquake induced vibrations of the tank-jacket system, can then be approximated as:

$$F = \frac{158,792\text{ kN m}}{46\text{ m}} = 3452\text{ kN} = 3.45\text{ MN}$$

The single pile tension or compression force can be approximated as: $N = \frac{3.45\text{ MN}}{6} = 0.575\text{ MN}$, which is much less than either the tension or compression capacity of the single pile. Therefore, the wave induced load may be the governing load for pile design in this jacket structure.

5. Check the freeboard requirement

The maximum vertical sloshing wave height can be roughly estimated as:

$$d = \frac{rS_e(\omega_{n1})}{g} = \frac{10\text{ m} \times 0.2\text{ m/s}^2}{9.81\text{ m/s}^2} = 0.21\text{ m}, \text{ which is less than the freeboard of } 1\text{ m.}$$

17.3.2 Effects of Flexibility of Tank Walls

It should be noted that the flexibility of tank walls (which are a relevant factor for most steel and aluminium tanks) are likely to cause a significant magnification of the impulsive/rigid liquid acceleration that is several times peak ground acceleration. Therefore, the impulsive hydrodynamic effects for flexible tanks are generally significantly larger than those for rigid tanks. On the other hand, convective/sloshing liquid is insensitive to the variations in flexibility of tank wall, because they are associated with natural periods of vibration that are significantly longer

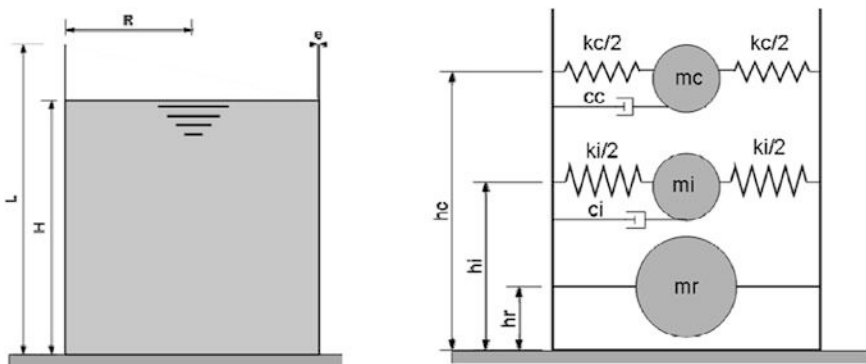


Fig. 17.16 A three-mass mechanical model of tank fluid dynamics, accounting for the impulsive mass's vibrations along with the tank wall [48]

than the dominant periods of the ground motion or pipe wall vibration motions. Therefore, the convective/sloshing components of seismic action for tanks can be considered to have the same values as those obtained based on a rigid tank assumption.

By realizing that the impulsive mass also vibrates along with the tank wall due to the flexibility of the tank wall, Haroun and Housner [43] modeled the liquid inside the tank with at least three masses (Fig. 17.16): (1) the convective/sloshing mass at the top of the tank; (2) the impulsive mass representation at the intermediate level of liquid vibrating along with the tank wall; and (3) the rigid mass that rigidly moves with the base of the tank and corresponds to the portion of liquid mass at the bottom of the container.

The equivalent mechanical spring-damping-mass model has the merits of being convenient for application using either analytical or finite element analysis. However, readers may bear in mind that this model assumes that the mass values are constant during different time instants, which cannot be fully justified as the tank-fluid interaction is influenced by the time varying deflection of the tank wall, even though the studies by Veleiros and Yang [44] and Haroun and Housner [45] have shown that the pressure distribution due to the liquid impulsive component in rigid and flexible tanks is similar, in particular for broad tanks with radii larger than the tank height. Malhotra [46] further developed the models for flexible tanks proposed by Haroun and Housner [45] by combining the effects of the higher impulsive and convective modes with those corresponding to the first modes.

From a review of the mechanical model developed as presented in Sect. 17.3.1, and a discussion of influences due to tank walls' flexibility given in Sect. 17.3.2, it can be concluded that the main aspects considered in the development of these equivalent mechanical models were:

- A subdivision of the fluid mass into two components corresponding to the impulsive and the convective behavior.

- The identification of the vibration frequencies of these two dynamic components.
- The identification of the tank wall flexibility on the dynamic response of the system.

17.3.3 Fluid–Tank Interaction in the Vertical Direction

According to Ref. [41], the hydrodynamic pressure on the walls of a rigid tank due to vertical ground acceleration can be computed by the following equation:

$$f_v(\xi, t) = \rho h(1 - \xi)\ddot{x}_v(t) \quad (17.27)$$

where $\ddot{x}_v(t)$ is the vertical ground acceleration input; ξ is the damping; ρ is the density of the liquid; h is the mean depth of liquid in m.

The corresponding hydrodynamic pressure distribution is axisymmetric and does not produce a shear force or moment resultant at any horizontal level of the tank, or immediately above or below the base.

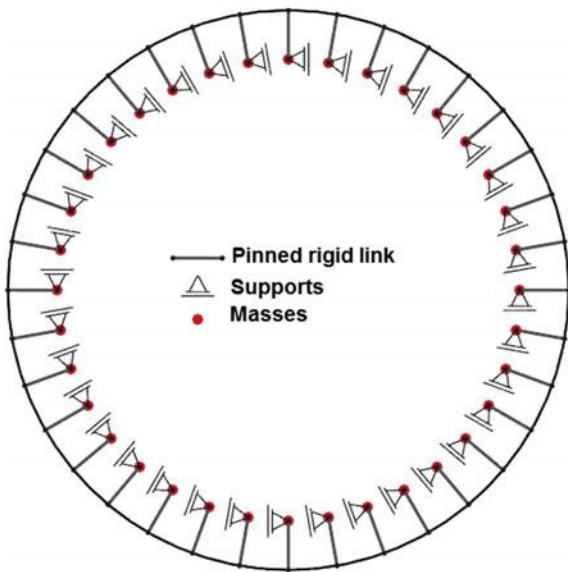
By using the method of response spectral analysis as presented in Sect. 15.2.4, $f_v(\xi, t)$ in the equation above can be calculated by replacing $\ddot{x}_v(t)$ with the peak vertical ground acceleration a_{gv} .

17.3.4 Implementation of Fluid Modeling in Finite Element Analysis

For implementing the equivalent mechanical spring-damping-mass model into a dynamic analysis using finite element method, the masses derived at each elevation based on the pressure distributions can be attached to element nodes of tank walls (normally modeled by shell elements) by means of one-direction elements normal to the shell surface, and each support is restricted in global tangential and vertical direction so that it can only move freely in the radial direction, as illustrated in Fig. 17.17. For a detailed procedure of this implementation, Refs. [17, 47] are recommended.

Moreover, the hydrostatic pressure and selfweight of a tank will introduce a pre-stressing on the tank wall, which can strongly affect the natural periods of the tank–fluid system by reducing the natural periods. Therefore, it can significantly influence the response of the tank wall. However, since the mass participation along horizontal directions is normally small for the tank structure, the pre-stress state can be neglected when investigating the global base shear force or the overturning bending moment at the tank base.

Fig. 17.17 An implementation of the equivalent mechanical spring-damping-mass model into a dynamic analysis using finite element method [47]



Furthermore, readers need to bear in mind that, by implementing the equivalent mechanical spring-damping-mass model, only two types of damage scenarios can be predicted: “elephant foot” buckling damage and secondary buckling presented in Sect. 17.2.

Moreover, the fluid can also be directly modeled by finite element, using for example the solid elements typically with eight nodes with incompressible and inviscid liquid material. Similar to the equivalent mechanical spring-damping-mass model, the continuity conditions between the fluid and the tank wall (typically modeled by shell elements) must be satisfied, which can normally be treated in a way that the coincident nodes of the fluid and shell elements are coupled along the direction normal to the tank wall, while along tangential directions of the tank wall surface, a free movement between the fluid and tank wall is allowed.

By performing the tank impact analysis subject to various seismic excitations, with the tank–fluid problems addressed by the simplified three-mass model as originally proposed by Haroun and Housner [43], finite element modeling using ANSYS, and experimental study separately, Compagnoni et al. [48] compared the obtained sloshing frequency and wave height (Fig. 17.18), sloshing force and global tank forces for a cylindrical tank with the aspect ratios (liquid height/radius of the tank) of 0.5, 1.0, and 1.5, respectively. They concluded that the frequency of the fundamental mode of the tank-liquid system obtained from the three models is virtually identical, while the three-mass mechanical model underestimates the vertical displacement of the free surface of the liquid. Finite element analysis gives results closer to those of the experimental study than of the three-mass model. Moreover, the three-mass mechanical model also leads to a conservative design with respect to the calculated tank’s base shear force and overturning moments.

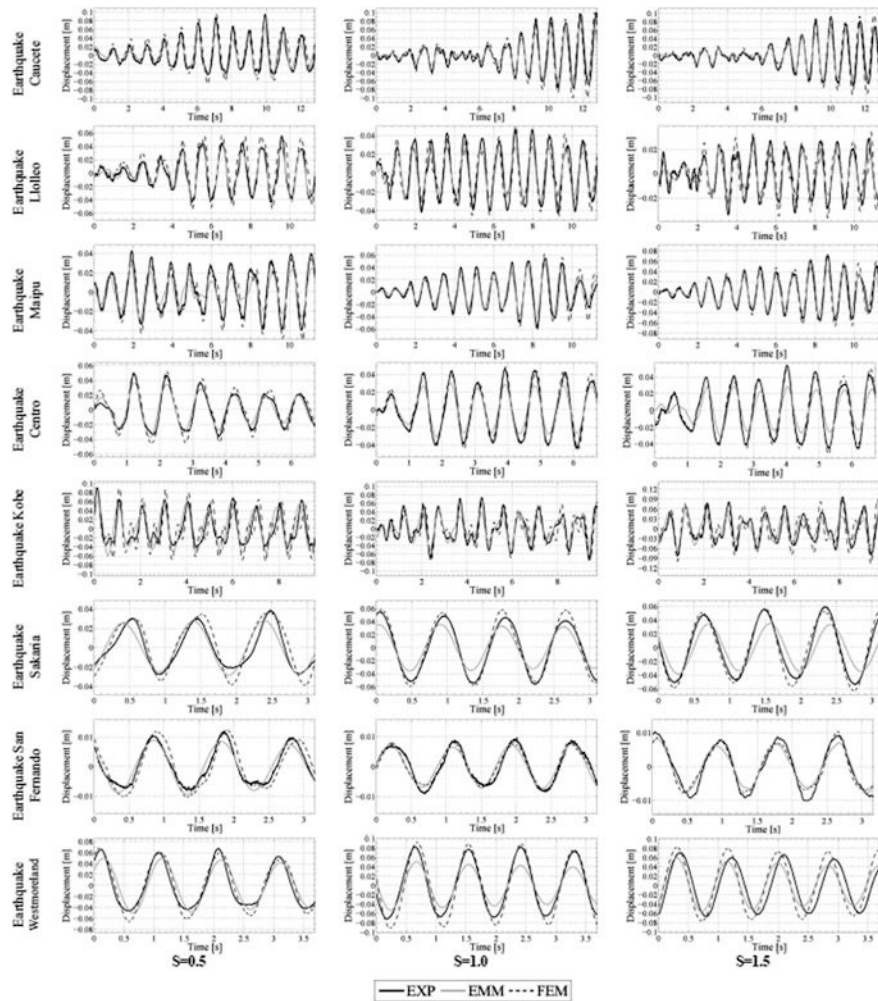


Fig. 17.18 A comparison of sloshing wave height obtained among three-mass model (*EMM*), finite element analysis (*FEM*), and experimental study (*EXP*) with various aspect ratios (S) [48]

Complex analyses to account for fluid–structure interactions have also been investigated by various researchers [49–54]. Numerical methods to perform fluid–tank interaction analyses include explicit finite element [55], implicit Lagrangian-Eulerian [56], and volume of fluid [57]. Rebouillat and Liksonov [58] presented a complete list of two-dimensional and three-dimensional models. For more details of the methods, readers may read the references cited above.

17.4 Soil-Tank Interaction

According to Ref. [41], for tanks on relatively soft ground, the base motion can be significantly different from the free-field motion. In general the translational component is modified and there is also a rocking component. Furthermore, for the same input motion, as the flexibility of the ground increases, both the fundamental period of the tank–fluid system and the total damping increase, thus reducing the peak seismic force. The increase in the fundamental period is more pronounced for tall, slender tanks, because the contribution of the rocking component is greater. The reduction in the peak seismic force, however, is less pronounced for tall tanks, since the damping associated with rocking is smaller than that associated with horizontal translations.

The vibration periods and the applied pressure associated with convective mass are generally assumed not to be affected by soil–structure interaction. A simple procedure, initially proposed for buildings [59] and consisting of an increase in the fundamental period and of the damping of structures on a rigid soil, has been extended to the impulsive (rigid and flexible) components of the response of tanks [60–62]. A good approximation can be obtained through the use of an equivalent simple oscillator with parameters adjusted to match the frequency and peak response of the actual system. The properties of this “substitute oscillator” are given in the form of graphs, as functions of the ratio between fluid depth and tank diameter described in the references cited above.

An alternative procedure to account for soil flexibility has been proposed by Priestley et al. [63]. The procedure suggests a modification of the frequency and the damping of the impulsive motion, based on the work by Gazetas [64], and the corresponding equations for the modified natural periods and damping values can be found in Annex A (Sect. A.7.2.2) of Eurocode 8 E 1998-4 [65].

17.5 Codes and Standards for Seismic Tank Design

With the theoretical background presented in Sect. 17.3, readers should be able to calculate the seismic forces on tanks by referring to various design codes and standards, such as API [66, 67], Eurocode 8 [12], NZSEE [13], ACI [68, 69], 2006IBC/ASCE7 [70], AWWA [71–73], and AIG design recommendation [74], etc. However, with regard to the impulsive and convective base shear coefficients, significant differences exist between different codes and standards [75]. American codes and standards generally provide a detailed classification of tanks and are assigned a different value of the response modification factor. In contrast, the current Eurocode 8 and NZSEE do not have such a detailed classification.

Note that the sloshing component of liquid mass undergoes vertical displacement, which can reach the roof of a tank. Therefore, it is important to provide sufficient free board to prevent the roof impact and spill of the liquid. Most of the

codes provide explicit expressions to evaluate the maximum sloshing wave height, ranging between $0.84A_cR_c$ (AWWA D-100 & D103, NZSEE) and A_cR_c (ACI 350.3, Eurocode 8), where A_c is convective acceleration and R_c is the radius in the horizontal plane or half of the width of a tank. In addition, the NZSEE also considers the contribution of higher orders of sloshing modes.

While detailed and specific seismic design rules for cylindrical tanks are provided by several codes, such rules are missing for spherical tanks (Fig. 17.6), especially regarding the calculation and consideration of sloshing effects in spherical tanks.

Performance based design (PBD) applied in the seismic design of tanks has been researched by several researchers [76, 77]. In order to perform PBD, it is necessary to quantify all possible failure modes (presented in Sect. 17.2) in terms of seismic response parameters, which are referred to as engineering demand parameters (EDPs), and to define appropriate performance levels that classify the severity of damage [78].

References

- Ventsel E, Krauthammer T (2001) Thin plates and shells: theory, analysis, and applications. Marcel Dekker, New York
- Heuer R, Irschik H, Ziegler F (1991) Earthquake resistance of deep-pile foundations for liquid storage tanks. In: Schueler GI (ed) Structural dynamics: recent advances. Springer, Berlin
- API Standard 650 (1988) Welded steel tanks for oil storage, 8th edn. American Petroleum Institute, Washington, DC
- Fischer FD, Rammerstorfer FG, Scharf K (1991) Earthquake resistance of anchored and unanchored liquid storage tanks under three-dimensional earthquake excitation. In: Schueler GI (ed) Structural dynamics: recent advances. Springer, Berlin
- Manos GC, Clough RW (1985) Tank damage during the May 1983 Coalinga earthquake. J Earthq Eng Struct Dyn 1(4):449–466
- Brown KJ, Rugar PJ, Davis CA, Rulla TA (1995) Seismic performance of Los Angeles water tanks. In: O'Rourke MJ (ed) Proceedings of the fourth US conference on lifeline earthquake engineering. ASCE, New York, pp 668–675
- Hanson RD (1973) Behavior of liquid-storage tanks, the Great Alaska earthquake of 1964. Proc Natl Acad Sci Wash 7:331–339
- Gates WE (1980) Elevated and ground-supported steel storage tanks. Reconnaissance report, Imperial County, California Earthquake of October 15, 1979. Earthquake Engineering Research Institute, Oakland
- US Department of Commerce (1973) Earthquake damage to water and sewage facilities, San Fernando Earthquake of February 9, 1971. Proc Natl Ocean Atmos Adm Wash 2:135–138
- Hall JF (ed) (1995) Northridge earthquake of January 17, 1994, reconnaissance report, vol 1. Earthquake Engineering Research Institute, Oakland
- Hatayama K (2008) Lessons from the 2003 Tokachi-oki, Japan, earthquake for prediction of long period strong ground motions and sloshing damage to oil storage tanks. J Seismol 12:255–263
- European Committee for Standardization (1998) Design provisions for earthquake resistance of structures, part 1: general rules and part 4: silos, tanks and pipelines, Eurocode 8, Brussels, Belgium
- NZSEE (1986) Seismic design of storage tanks. Recommendations of a Study Group of the New Zealand National Society for Earthquake Engineering, Wellington, New Zealand

14. Priestley MJN et al (1986) Seismic design of storage tanks. Recommendations of a Study Group of the New Zealand National Society for Earthquake Engineering
15. Rammerstorfer FG, Scharf K, Fisher FD (1990) Storage tanks under earthquake loading. *Appl Mech Rev* 43(11):261–282
16. Virella JC, Godoy LA, Suárez LE (2006) Dynamic buckling of anchored steel tanks subjected to horizontal earthquake excitation. *J Constr Steel Res* 62:521–531
17. Buratti N, Tavano M (2014) Dynamic buckling and seismic fragility of anchored steel tanks by the added mass method. *J Earthq Eng Struct Dyn* 43:1–21
18. Faltinsen AN, Timokha OM (2009) *Sloshing*. Cambridge University Press, Cambridge
19. Nascimbene R (2015) Cylindrical storage containers under seismic loading, technical notes prepared for European shell buckling recommendations, 6th edn
20. Malhotra PK, Veletsos AS (1995) Seismic response of unanchored and partially anchored liquid-storage tanks, Report TR-105809. Electric power res inst, Palo Alto
21. Malhotra PK (1995) Base uplifting analysis of flexibly supported liquid-storage tanks. *J Earthq Eng Struct Dyn* 24(12):1591–1607
22. Malhotra PK (1997) Seismic response of soil-supported unanchored liquid-storage tanks. *J Struct Eng ASCE NY* 123(4):440–450
23. Fischer DF, Rammerstorfer FG (1999) A refined analysis of sloshing effects in seismically excited tanks. *Int J Press Vessel Pip* 76(10):693–709
24. Chen W, Haroun MA, Liu F (1996) Large amplitude liquid sloshing in seismically excited tanks. *Earthq Eng Struct Dyn* 25:653–669
25. Tor Skogan (2015) Safety contained. *LNG Industry*
26. Takiguchi A (2000) The seismic design margins for spherical gas tanks. In: The 12th world conference on earthquake engineering, Auckland, New Zealand
27. Den Hartog JP (1947) *Mechanical vibrations*, 3rd edn. McGraw-Hill, New York
28. Karavasilis TL, Rizos DC, Karabalis DL (2004) Seismic analysis of spherical tanks including fluid–structure–soil interaction. In: The 13th world conference on earthquake engineering, Vancouver, Canada
29. Rizos DC, Karabalis DL (1999) Soil–fluid–structure interaction. In: Kausel E, Manolis GD (eds) *Wave motion problems in earthquake engineering*. WIT Press, Southampton
30. Beskos DE (1997) Boundary element methods in dynamic analysis: part II 1986–1996. *ASME Appl Mech Rev* 50(3):149–197
31. Beskos DE (1987) Boundary element methods in dynamic analysis. *Appl Mech Rev* 40(1)
32. Markerle J (1996) FEM and BEM in geomechanics: foundations and soil–structure interaction: a bibliography (1992–1994). *Finite Elem Anal Des* 22(3):249–263
33. Faltinsen OM (1990) *Sea loads on ships and offshore structures*. Cambridge University Press, Cambridge
34. Kirk CL (1982) Dynamic analysis of offshore structures. CML Publications, East Sussex, pp 25–32
35. Dodge FT (2000) The new “dynamic behaviour of liquids in moving containers”. Southwest Research Institute, San Antonio
36. Westergaard HM (1933) Water pressures on dams during earthquakes. *Trans Am Soc Civ Eng* 98:418–433
37. Housner GW (1954) Earthquake pressures on fluid containers. In: 8th technical report under office of naval research. Project Designation No. 081-095, California Institute of Technology, Pasadena, California
38. Housner GW (1957) Dynamic pressures on accelerated fluid containers. *Bull Seismol Soc Am* 47:313–346
39. Housner GW (1963) Dynamic behavior of water tanks. *Bull Seismol Soc Am* 53:381–387
40. API 650 (2007) *Seismic design of storage tanks*, Appendix E: welded steel tanks for oil storage, 11th edn. Washington, DC
41. ECCS (2016) European shell buckling recommendations, 6th edn, Chapter 17. In: cylindrical storage containers under seismic loading

42. Malhotra PK, Wenk T, Wieland M (2000) Simple procedure for seismic analysis of liquid-storage tanks. *Struct Eng Int* 3:197–201
43. Haroun MA, Housner GW (1981) Seismic design of liquid storage tanks. *J Tech Councils ASCE* 107(1):191–207
44. Veletsos AS, Yang JY (1977) Earthquake response of liquid storage tanks. In: Advances in civil engineering through engineering mechanics: second annual engineering mechanics division specialty conference, ASCE. North Carolina State University, Raleigh, North Carolina, pp 1–24
45. Haroun MA, Housner GW (1981) Earthquake response of deformable liquid storage tanks. *J Appl Mech* 48(2):411–417
46. Malhotra PK (2000) Practical non-linear seismic analysis of tanks. *Earthq Spectra* 16(2):473–492
47. Virella JC, Suárez LE, Godoy LA (2005) Effect of pre-stress states on the impulsive modes of vibration of cylindrical tank liquid systems under horizontal motions. *J Vib Control* 11 (9):1195–1220
48. Compagnoni ME, Curadelli O, Martínez CA (2016) Experimental and numerical study of the dynamic response of cylindrical steel tanks under seismic excitation. *J Constr Steel Res*, article in press
49. Wu GX, Ma QW, Taylor RE (1998) Numerical simulation of sloshing waves in a 3D tank based on a finite element method. *Appl Ocean Res* 20:337–355
50. Frandsen JB (2004) Sloshing motions in excited tanks. *J Comput Phys* 196(1):53–87
51. Pal NC, Bhattacharyya SK, Sinha PK (2003) Non-linear coupled slosh dynamics of liquid filled laminated composite containers: a two dimensional finite element approach. *J Sound Vib* 261(4):729–749
52. Alembagheri M, Estekanchi HE (2011) Non-linear analysis of aboveground anchored steel tanks using endurance time method. *Asian J Civ Eng* 12(6):731–750
53. Alembagheri M, Estekanchi HE (2011) Seismic assessment of unanchored steel storage tanks by endurance time method. *Earthq Eng Eng Vib* 10(4):591–604
54. Alembagheri M, Estekanchi HE (2012) Seismic analysis of steel liquid storage tanks by endurance time method. *Thin Wall Struct* 50(1):14–23
55. Maekawa A, Fujita K (2009) Dynamic buckling analysis of cylindrical water storage tanks: a new simulation method considering coupled vibration between fluid and structure. In: Proceedings of ASME pressure vessels and piping conference, PVP2009-77083, Prague, Czech Republic
56. Haroun MA, Tayel MA (1985) Axi-symmetric vibrations of tanks-numerical. *J Eng Mech Div ASCE* 111(3):329–345
57. Vesenjak M, Mullerschon H, Hummel A, Ren Z (2004) Simulation of fuel sloshing: comparative study. LS-DYNA Answenderforum, Bamberg
58. Rebouillat S, Liksonov D (2010) Fluid–structure interaction in partially filled liquid containers: a comparative review of numerical approaches. *Comput Fluids* 39:739–746
59. Veletsos AS (1977) Dynamics of structure—foundation systems—structural and geotechnical mechanics. In: Hall WJ (ed). Prentice Hall, Englewood Cliffs, pp 333–361
60. Veletsos AS, Tang Y (1990) Soil–structure interaction effects for laterally excited liquid storage tanks. *Earthq Eng Struct Dyn* 19:473–496
61. Veletsos AS, Tang Yu, Tang HT (1992) Dynamic response of flexibly supported liquid storage tanks. *J Struct Eng ASCE* 118(1):264–283
62. Habenberger J, Schwarz J (2002) Seismic response of flexibly supported anchored liquid storage tanks. In: Proceedings of the 13th European conference on earthquake engineering, London
63. Priestley MJN, Davidson BJ, Honey GD, Hopkins DC, Martin RJ, Ramsey G, Vessey JV, Wood JH (1986) Seismic design of storage tanks. Recommendations of a Study Group of the New Zealand National Society for Earthquake Engineering
64. Gazetas G (1983) Analysis of machine foundation vibrations: state-of-the-art. *Soil Dyn Earthq Eng* 2(1):2–43

65. Eurocode 8 (2006) EN 1998-4: design of structures for earthquake resistance—part 4: silos, tanks and pipelines
66. American Petroleum Institute (API) (2009) 620: design and construction of large, welded, low-pressure storage tanks, 11th edn. American Petroleum Institute, Washington, DC
67. American Petroleum Institute (API) (1998) Welded storage tanks for oil storage. API 650, American Petroleum Institute Standard, Washington, DC
68. American Concrete Institute (2001) Seismic design of liquid containing concrete structures. ACI 350.3, Farmington Hills
69. American Concrete Institute (1998) Guide for the analysis, design and construction of concrete pedestal water towers. ACI 371, Farmington Hills
70. American Society of Civil Engineers ASCE (2005) Minimum design loads for buildings and other structures
71. American Water Works Association (AWWA) D-100 (2005) Welded steel tanks for water storage. Denver
72. AWWA D-110 (1995) Wire-and strand-wound circular, pre-stressed concrete water tanks. Denver
73. AWWAD-115 (1995) Circular prestressed concrete water tanks with circumferential tendons. Denver
74. Architectural Institute of Japan (2010) Design recommendation for storage tanks and their supports with emphasis on seismic design
75. Jaiswal OR, Rai Meeri DC, Jain SK (2007) Review of seismic codes on liquid-containing tanks. Earthq Spectra 23(1):239–260
76. Reza MS, Bursi OS, Paolacci F, Kumar A (2014) Enhanced seismic performance of non-standard bolted flange joints for petrochemical piping systems. J Loss Prev Process Ind 30(1):124–136
77. Bursi OS, Reza MS, Abbiati G, Paolacci F (2015) Performance-based earthquake evaluation of a full-scale petrochemical piping system. J Loss Prev Process Ind 33:10–22
78. Vathi M, Karamanos SA, Kapogiannis IA, Spiliopoulos KV (2015) Performance criteria for liquid storage tanks and piping systems subjected to seismic loading. In: Proceedings of the ASME 2015 pressure vessels and piping division conference, vol 8, Massachusetts
79. Maekawa A (2012) Recent advances in seismic response analysis of cylindrical liquid storage tanks. In: Moustafa A (ed) Earthquake-resistant structures: design, assessment and rehabilitation. Intech, Rijeka
80. Indian Institute of Technology Kanpur and Gujarat State (2007) Disaster management authority, IITK-GSDMA guidelines for seismic design of liquid storage tanks—provisions with commentary and explanatory examples. National Information Center of Earthquake Engineering, Kanpur
81. Veletsos AS (1984) Seismic response and design of liquid storage tanks. Guidelines for the seismic design of oil and gas pipeline systems. ASCE, New York, pp 255–370
82. Veletsos AS et al (1990) Seismic response of anchored steel tanks. In: Gupta AK (ed) Proceedings of the third symposium on current issues related to nuclear power plant structures, equipment and piping. North Carolina State University, pp 2–15

Chapter 18

Selection of Computer System and Computation Precision

18.1 General

Advances in computer technology allow engineers to solve problems of increasing complexity in two aspects: first, it allows for the calculation of results based on classical solutions but with numerical evaluation of certain terms that cannot be expressed in a closed form; second, it also allows for the modelling of complex systems (structures, foundations, soils, or faults) using approximation methods such as finite element method and to perform numerical calculations to obtain the system's response.

Modern earthquake engineering requires a large amount of numerical and analytical analysis associated with various issues such as site response analysis, non-linear dynamic structural analysis, etc. Many of those analyses involve sophisticated numerical algorithms and require significant computation efforts. An optimized computer system makes those demanding analyses feasible and efficient. Therefore, Sect. 18.2 will briefly discuss general methods for selecting an optimized computer system for improving numerical analysis efficiency. Moreover, during either the analytical or computer based analysis, computation precision is often ignored by engineers and researchers. This ignorance can result in unnecessary labor (without increasing computation accuracy) and even more errors. Section 18.3 discusses the general methods to ensure computation precision associated with computation accuracy.

18.2 Computer System for Improving Numerical Analysis Efficiency

It is noticed that, with the development of computer technology, users are allowed to solve numerical problems of increasing complexity.

For numerical analysis such as a finite element analysis for large scale structures (with a large number of degrees-of-freedom) and with the involvement of various types of nonlinearities, sufficient CPU speed, Random Access Memory (RAM, also called computer memory or working memory) size and number, and the performance of operating system are important for an efficient calculation with respect to both computational capability and time. The specification for some of these parameters is described in the user manual of typical finite element analysis software.

The CPU performs the basic arithmetical, logical and input/output operations of the computer system. The speed of the CPU depends on the clock rate (generally given in multiples of Hz) and the instructions per clock (IPC), which are the two factors for the instructions per second (IPS) that the CPU can perform. Computers' processing performance can be increased by using multi-core processors, which is essentially plugging two or more individual processors (cores) into one integrated circuit [1]. Theoretically, a dual core processor would be nearly twice as powerful as a single core processor. In practice, however, the performance gain is far less, of only about 50 %, due to imperfect software algorithms and implementation [2]. Based on the FE simulation to obtain the time series response for two structural models with different numbers of degrees-of-freedoms, both of which represent an offshore structure subject to dynamic ocean wave loading, Fig. 18.1 shows the time required for computation (elapsed time). It is clearly shown that the elapsed time is dramatically decreased with the increase of CPU speed. Over the last four decades, computer speed has been increased astonishingly, as illustrated in Fig. 18.2, which shows a dramatic increase in transistor count number, the most common measure of integrated circuit complexity. According to Moore's Law, the transistor count of the integrated circuits doubles approximately every two years. This also brings the

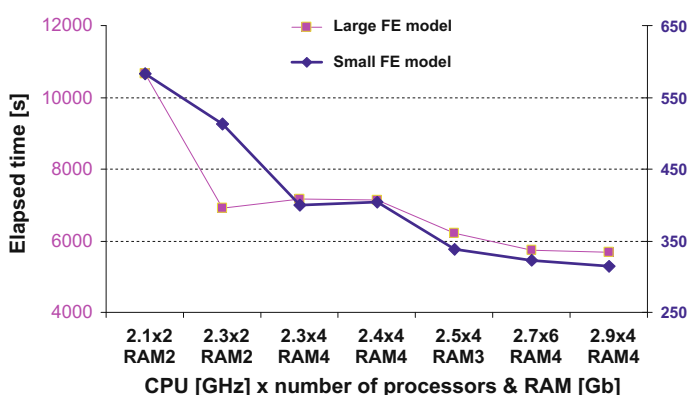


Fig. 18.1 Elapsed time due to different CPU speed, RAM number and size for calculating structural response time history for a small and a large FE model, respectively (courtesy of Aker Solutions)

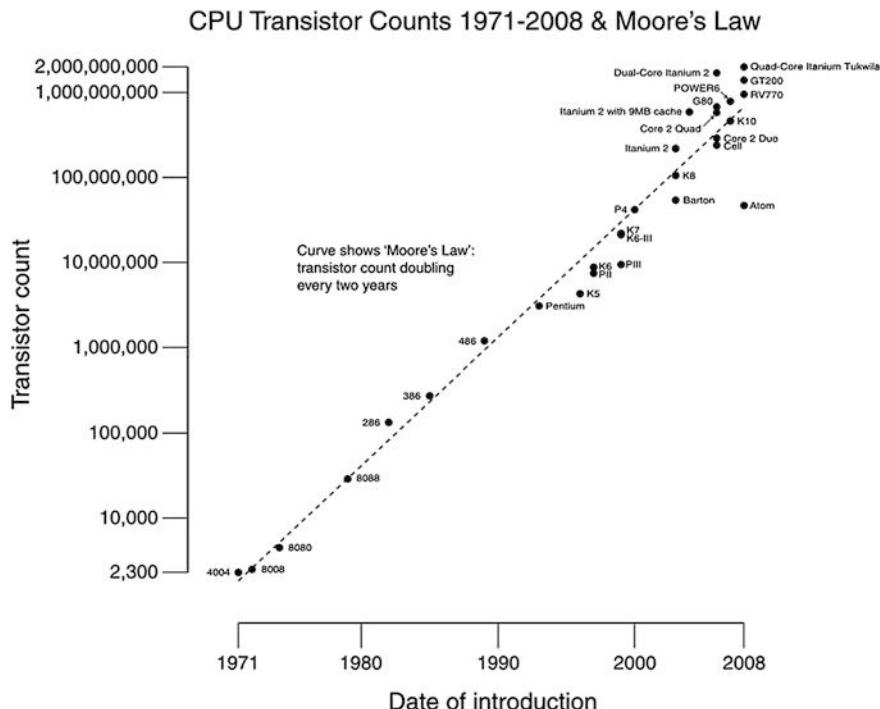


Fig. 18.2 Trend of computer calculation speed (figure by Oleg Alexandrov)

possibility of performing a large numerical analysis task that is computationally demanding and would originally have been difficult to perform.

Since multiple CPUs/processors allow for parallel computing, it is especially favored by FE models with large degrees-of-freedom. This is because, generally, element matrices and load vectors for all elements can be performed in parallel, since the computation of each element quantity is independent from other elements. Moreover, after solving the system equations, the recovery of element's strain and stress based on the computed nodal displacements is also independent of other elements. Furthermore, the solution of the system equations governing the behavior of the structure can begin as soon as all contributions to a node have been assembled [3]. In addition, it is quite usual that multiple analyses are required to perform simultaneously in a single computer. All these reasons promote the adoption of parallel computing. The varying processor allocation scheme was also recommended within the parallel computing technique because it is more effective than the fixed processor allocation.

RAM provides space for the computer to read and write data to be accessed by the CPU, i.e., more installed RAM on a computer can reduce the number of times the CPU must read data from the hard disk. This usually enables a computer to work significantly faster, as RAM is many times faster than a hard disk. For this

reason, for running large FE simulations, engineers often switch from Windows to Unix/Linux operating system, since the Microsoft Windows system requires more occupied RAM, which sometimes forced the computer to use virtual memory or even go out-of-core.

In recent years, the computers used by engineers and FE codes have been drastically changed from the traditional 32-bit operating systems to the 64-bit ones. Regardless of how large a capacity of RAM is installed on a computer, the addressable RAM memory for a computer is limited to the size of the operating system to the power of two. Theoretically, this means that the change from a 32-bit operating system to 64-bit one can increase this memory limit from 4 GB to 128 GB. For a typical Microsoft Windows operating system, the system itself normally reserves 2 GB memory use (in many cases, it is only 1 GB since Microsoft addresses this to a small extent with a 3 GB switch that can be set up in the boot.ini file.), leaving the rest for external programs. With this significant increase of memory, engineers normally do not need to shift from Windows to Unix/Linux for running large FE models [4].

In addition to the three essential factors (CPU speed, RAM, and operating system) described above, the memory capacity of hard disk should be sufficient for saving the resulting data from FE calculation. It is noted that if the calculated results are simultaneously stored in an external or a remote hard disk, the calculation process will normally be slowed down compared to a direct saving of the results into the computer's internal hard disk. In addition, a regular freeing up of disk space, disk fragmentation and disk error, etc., also helps to improve the computer performance.

Well maintained computer hardware can guarantee the FE simulation performance with respect to speed. For example, if hardware is subject to heavy dust, the computational speed may decrease dramatically due to the hardware's temperature increasing during numerical simulation. Therefore, a computer should preferably not be placed on the ground where more accumulated dusts may be sucked into the computer hardware. Figure 18.3 shows a badly maintained computer, with little space between the computer and other objects to allow sufficient air circulation (to decrease the temperature of the hardware), as well as dusts all over the computer and on the ground. Moreover, the computer is not far from a room heater, which can increase the hardware's temperature significantly.

It is worth mentioning that information security is becoming more and more important for any type of business. This strongly depends on every user to maintain information security when using a computer. A typical security incident requires an average of 55 man hours to remediate, involving substantial extra costs for affected organizations or persons. It may be surprising to know that, nowadays, for a typical international engineering company, 60–90 % of all emails received by the company's accounts are spam, some of which contain viruses. Therefore, it is important to have well performing virus protection software installed. In addition, one needs to be very careful to open e-mail attachments or follow web links of unknown content. All those measures above help to maintain computers for numerical calculations.

Fig. 18.3 A badly maintained computer with dust on the ground and all over the computer and paper box for air circulation; the computer is also close to a heater



18.3 Computation Precision

During either the analytical or computer based analysis, computation precision is often ignored by engineers and researchers. This oversight can result in an unnecessary labor (without increasing any computation accuracy) and even accumulated errors. A typical problem within this topic is the use of significant figures (also known as significant digits), which are those digits that carry meaning contributing to precision. For example, 3713, 65.25 and 0.0003785 each have four significant figures. However, the accuracy of a number such as 98,000 is not apparent: it may have two significant figures, with the three zeros serving only to locate the decimal point, or it may have three, four or five significant figures. Under this situation, it is recommended to use powers of ten to clearly indicate the significant figures, i.e., 98×10^3 for two significant digits; 980×10^2 or 98.0×10^3 for three significant digits;

As a general rule, the precision of a number is plus or minus one-half of the unit corresponding to the last significant digit [5]. For example, the number 3713 has a precision of ± 0.5 , and 65.25 has a precision of ± 0.005 .

During mathematical calculation, the accuracy of a calculated number depends upon the accuracy of the numbers used in performing the calculation. The general rule [6] for maintaining computation precision is that:

- For addition and subtraction, the result should have as many decimal places as the measured number with the smallest number of decimal places (for example, $106.3 + 1232.7461 = 1339.0$).
- For multiplication and division, the result should have as many significant figures as the measured number with the least number of significant figures (for example, multiplying 6.3 by 3.14, the results should only have two significant numbers, i.e. 20).
- In a logarithm, the number of significant figures must be the same as the number of digits in the mantissa (for example, $\log_{10}^{(30000)} = 4.47712125472$, should be rounded to 4.4771).
- When taking anti-logarithms, the resulting number should have as many significant figures as the mantissa in the logarithm.

In calculations performed by computers or calculators, the number of significant figures kept are normally 10–12, while many data provided in the design documentation only give an “approximate” value, for example, the yield stress of a steel member is often given with a value such as 355 MPa, the weight of the material is 7850 kg/m^3 , a uniform load with 20 kN/m^2 , etc. However, the precision for those data are not very much in the mind of a design engineer. Therefore, to avoid the results that are even less precise in the subsequent calculation, one can assume that the data are correct.

To avoid rounding errors and to preserve numerical accuracy, during the calculation of intermediate results, it is recommended to keep as many digits as is practical (without clearing the intermediate value from either the computer or the calculator if it can be used in the next computation) until the end of calculation to avoid rounding errors [7, 8]. When reporting final results, the number of digits should be limited to those that are significant.

References

1. What is (a) multi-core processor? Data center definitions. www.searchdatacenter.com, 27 Mar 2007
2. Central processing unit, Wikipedia, 2012
3. Rehak DR, Keirouz WT, Cendes ZJ (1984) Evaluation of finite element system architectures. Department of Civil and Environmental Engineering, Carnegie Institute of Technology, Pittsburgh
4. Dalidd J (2007) Should you migrate to 64-bit FEA programs, Design World
5. Gere JM, Timoshenko SP (1991) Mechanics of materials, 3rd edn. Chapman & Hall, London
6. Significant figures, Wikipedia, 2012
7. Freshman Physics Laboratory (2001) Measurements and significant figures. California Institute of Technology, Pasadena
8. Segui WT (1994) LRFD steel design. PWS Publishing Company, Boston

Chapter 19

Avoid Dynamic Amplifications

Life is pretty simple: You do some stuff, most fails, some works. You do more of what works. If it works big, others quickly copy it. Then you do something else. The trick is the doing something else.

Leonardo da Vinci (1452–1519)

19.1 Seismic Design Principles

The design of modern structures allows them to sustain loads (such as a structure's self-weight and its relevant content loads) in the vertical direction. The lateral loads along the horizontal direction, such as the ocean wave loading or typically the horizontal (major) components of seismic loading on structures etc., receive less attention, even though those lateral loads can be dominating for structural design. Furthermore, when those time varying lateral loads are applied on dynamic sensitive structures, problems with regard to structural integrity and serviceability may be even worse than those under static loads.

The form of structures should allow both vertical and horizontal loads to be transferred with explicit/clear load paths (structural simplicity) and have sufficient redundancy and capacity reserve. It is noted that a structure design with a clear and direct path for the transmission of seismic forces is more preferred than a structure even optimized with less material cost but without a clear load transmission path. This is because the modeling, analysis, dimensioning, detailing and construction of simple structures are subject to the influence of uncertainties, and thus the prediction of their seismic behaviors is much more reliable. Moreover, structural redundancy is also essential for seismic resistance. For example, design of evenly distributed structural elements usually helps to increase redundancy and allows a more favorable redistribution of action effects and widespread energy dissipation across the entire structure [1].

As discussed in Sect. 14.1, in order to reach an optimized design with regard to both construction cost and economy, engineers should design structures to resist the effects of strong ground motions in such a way that damages on structures can occur in case the earthquake ground motions are significant (associated with an extremely high return period) but the integrity of structures will be maintained and the structural collapse will not occur (system ductility). It is worth mentioning that a similar design philosophy is also adopted for design of offshore structural subject to ocean environmental loading.

In the design phase, one of the most critical problems for dynamic design arises from resonance. To avoid this problem, engineers attempt to keep the frequency between a structure and its loading far away from each other. Frequency here does only not refer to the fundamental frequency of the structure, but more precisely the eigenfrequencies that are dominating to contribute to the seismic response. This is because, in many cases, the second or higher orders of eigenmodes are significant or even more influential on the seismic response than the fundamental eigenfrequency. From the seismic loading point of view, note that the seismic loading can be either narrow-banded or wide banded in frequency domain. Avoiding resonance essentially means that the frequency range of important vibration modes of a target structure should not overlap with (or more preferably be distant from) frequency range of the majority of the seismic loading energy. Moreover, different measures of structural response may be sensitive to different frequency ranges of loading. For example, peak floor accelerations (maximum acceleration observed over all floors over the duration of shaking) are usually observed at upper stories of a building and sensitive to excitation of higher vibration modes of the building, but they are not highly correlated with peak story drift ratios (which are often more closely related to fundamental eigenmode response) [2].

Moreover, it is also noted that the seismic motions can in many cases introduce critical excitations at or close to the natural frequency of structures and/or soil layers (site period) as discussed in Sect. 4.2, which can introduce damaging seismic loading. While due to various uncertainties involved in predicting ground motion characteristics, the ground motions specified by seismic design codes may not be capable of predicting all the possible critical excitations, as illustrated in Fig. 19.1. This problem requires a special consideration of calculation methods for seismic loading in a more reliable manner.

In practice, in order to mitigate seismic response, it is sometimes rather efficient to tune a structure's stiffness, weight (both in magnitude and distributions), and redundancy (increase or decrease), so that an optimized structural configuration can be achieved to efficiently mitigate seismic response. This often results in a design with a continuous distribution of mass, stiffness, strength, and ductility. Furthermore, a dedicated consideration with respect to elevation control (Sect. 19.3) can induce wide banded frequency vibrations of a structure, thus eliminating the likelihood of structural resonance, which is typically dominated by a significant single modal mass vibration. Moreover, for existing structures, seismic rehabilitation is also a rather typical and efficient manner to recover or upgrade

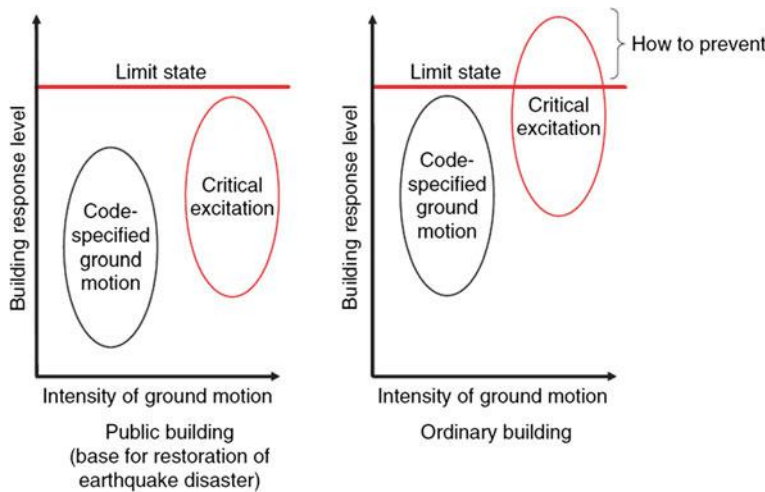


Fig. 19.1 The critical seismic excitations that may not be predicted by the code specified ground motions [3]

original structural performance and to mitigate seismic response, which will be discussed in Chap. 29.

It is also important to avoid significant coupling between torsional and flexural vibration of structures as the torsional resistance (both in stiffness and strength) in a typical engineering structure is generally much lower than that of flexural/bending vibrations. This often requires that the structure plan be simple, symmetric, regular, and be symmetrically loaded, which will be discussed in Sect. 19.4.

A dedicated seismic resistant structural design involves a combination of redundancy, strength, deformability, and energy absorption. For each type of structures, one or a few factors are more important than other factors to govern the design. While strength criteria are usually a dominant factor in the design of low rise structures, stiffness and stability may often govern the design process when structures' height increases. Moreover, traditional seismic design often aims for increasing the capacity, such as strengthening and reinforcement, as will be discussed in Chap. 29, but this often results in an additional cost and a heavy structure. Modern designs devote more efforts to reducing demand rather than increasing capacity. This requires a ductile structural system to minimize the seismic load transferred to the structure and to maximize the energy dissipation, which can be accounted for in the selection of structural configuration and in the design of local detailing. For example, it is important that column-beam should be aligned coaxially, and beams should always fail first before connected columns. These issues will be discussed in Chap. 20.

To decrease the demand, the seismic energy transmitted to structures can be dissipated through both structural damping and external damping devices. This emphasizes the importance of increased damping through various measures as will

be discussed in Chaps. 21 and 22. Broadly speaking, the damping can also be contributed by using base isolation techniques or hanging isolation system, which aim to cut the seismic load transmission path between the supporting structure and the superstructure, to increase the relevant eigenperiod of structural vibrations and thus decreasing the seismic accelerations on structures, as will be discussed in Chap. 23. Furthermore, dynamic absorber, as will be elaborated in Chap. 24, uses a mechanism that vibrates in resonance condition while attached to the main structure, so that the vibration energy of the main structure can be efficiently transferred into the absorber mechanism, thus efficiently mitigating dynamic response of structures.

It is also possible to design a load and energy sharing mechanism that enables the distribution of the ground motion energy among more structures or designated resisting structural elements. This can be realized with structural designs by connecting a structure with adjacent structure(s) (Sect. 25.2), or by installing lock-up and shock transmission unit (Sect. 25.3) to connect various resisting structural elements together.

Failure of non-structural elements leads to the majority of earthquake damage in many earthquakes caused either by excessive accelerations or excessive movements and distortion in the structural components that support the non-structural components. Therefore, to reduce their response through dedicated connection, detailing or dynamic mitigation measures are important. Chapter 26 will briefly discuss this topic.

In relation to the issues above, this book will present a discussion on special considerations for mitigating dynamic responses with a special focus on seismic responses. However, depending on their applicabilities and limitations, the methods discussed can also be extended as mitigation measures to resist other types of dynamic loading, such as wind, ocean wave, and pipe and machinery vibrations.

It should be noted that the mitigation measures are also related to the issues associated with geotechnical engineering for ensuring adequate foundation, such as compatibility of superstructures with supporting foundations, a dedicated design of foundations to ensure that the whole structure is subject to a uniform seismic action, soil improvement using for example densification, reinforcement, grouting, drainage, etc., a selection of ground topology and site conditions. As they are not within the scope of the current book, readers may read more relevant references on geotechnical earthquake engineering. Reference [4] gives essential coverage on this topic.

19.2 Stiffness and Mass Distribution

The magnitude and distribution of dynamic loads applied on structures strongly depend on the stiffness and mass of the structures and their distribution. The stiffness in a structure is mainly related to the following factors: material (elastic modulus and yield stress etc.), geometric (cross section area, moment of inertia etc.)

and dimensional (e.g. length, width and height etc.) properties of structural members; characteristics and magnitude of variation of the properties above; capacities of each structural members (yielding and buckling etc.); loading and support conditions of structural members. In addition, characteristics of connections and joints are strongly relevant to the global and local structural deformations. Considerations of stiffness and mass distribution along the vertical direction can be realized through a dedicated elevation control, as will be discussed in Sect. 19.3. Similarly, a rational distribution of stiffness and mass in the horizontal plane is also essential, which is especially necessary to mitigate torsional vibrations, as will be discussed in Sect. 19.4.

19.3 Elevation Control

Resonance can, for example, be avoided through properly designed elevation control. This is because a properly configured structure disperses the vertical propagating shear wave energy within a broad range of frequencies. This requires that the stiffness and mass reduce gradually towards the structure's top. And an abrupt change in stiffness, mass and strength between vertically adjacent parts of the structure (the so-called soft floor with respect to stiffness or weak floor with respect to strength for land-based structure) should be avoided. No significant masses are allowed to be located on the top of the structure [5], even though this situation cannot be avoided for offshore platforms that have relatively heavy topsides resting on the top of the supporting structures. As specified by FEMA, typically, a building structure is regarded as vertically irregular or lacking elevation control if the effective modal mass of any story is more than 150 % of the effective mass of an adjacent story (vertical mass irregularity), or if the dimension of the lateral force resisting system at any story is more than 130 % of that for any adjacent story (vertical geometric irregularity), or if stiffness of any story is less than 70 % of the stiffness of the story above or less than 80 % of the average stiffness of the three stories above (stiffness irregularity or soft story), or if the lateral strength of any story is less than 80 % of the strength of the story above (strength irregularity or weak story).

A special case of elevation controlled structures is the pyramid-shaped structure as shown Fig. 19.2. It is traditionally regarded as an unfavorable structural shape due to structural irregularity over height. However, it can be utilized to efficiently prevent structural resonance and to enhance structural stability against lateral seismic and wind loading. Moreover, in many cases, a structural configuration with pyramid-shape is attractive from both aesthetic/architecture and functionality points of view. Figure 19.2 shows the pyramid-shaped elevation control of Transamerica Tower in San Francisco. In practice, the elevation control can be performed by a proper tapering of profile, mass or stiffness or a combination of these items.

Fig. 19.2 Elevation control of Transamerica Tower in San Francisco with a pyramid-shaped elevation control



Examples of structures having good elevation controls are tower structures (Fig. 19.3) and super-high rise buildings (Fig. 19.2). They have pyramid-shapes for attracting less wind load (below a certain height, the wind speed increases dramatically with the increase of height from ground surface) and stability. However, as pyramid-shaped structures often have rather slender tips, the seismic responses at these tips may be significantly amplified, which is often referred to as the whipping effect [6] as discussed in Sect. 15.7. This is the potential drawback of designing a pyramid-shape structure. On the other hand, the amplification normally occurs only at the local tip of the structure without significant interaction with other parts of the structure. This is because the modal mass of an elevation controlled structure is not concentrated in one single vibration mode, and consequently modal vibrations at each

Fig. 19.3 An elevated truss tower



eigenperiod are not significant. As an example, Fig. 19.4 shows a flare boom tower weighing 450 tons installed on an offshore platform. By observing the modal mass distribution in each eigenmode shown in Table 19.1, it is noted that maximum modal mass is only 132 tons associated with the second eigenmode shown in Fig. 19.5, i.e. the total mass is not concentrated in one single mode. This means that even if structural resonance/amplification occurs at one or a few vibration modes, its effects on the global response are not very significant since the modal mass participation factors within those modes are limited.

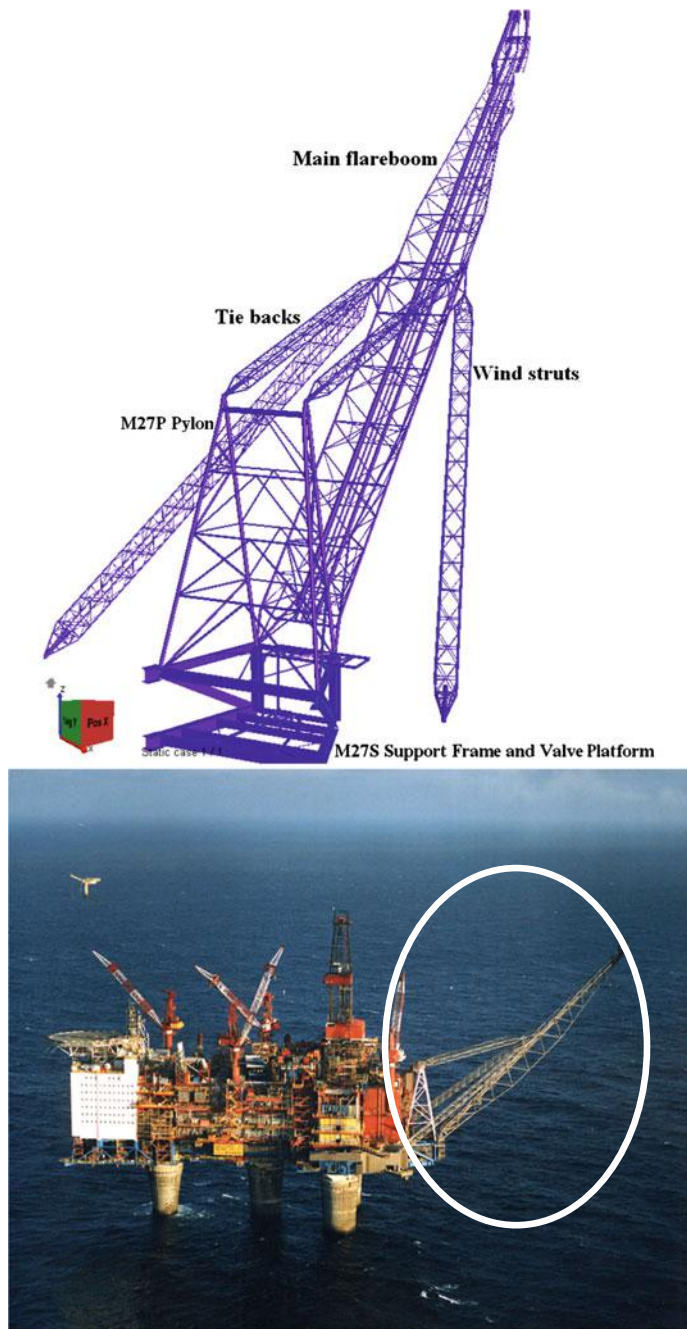


Fig. 19.4 A flare boom (*upper*) installed on a gravity based offshore structure (*lower*) at North Sea (courtesy of Aker Solutions)

Table 19.1 The eigenfrequencies, mode shapes and the corresponding modal masses for a flare boom shown in Fig. 19.4 (courtesy of Aker Solutions)

Mode number	Eigenperiod (s)	Remarks	Modal mass (tons)		
			Longitudinal direction	Transverse direction	Vertical direction
1	1.462	Local sway vibration at the tip of the original high and lower pressure pipes	0.0	10.8	0.0
2	1.424	1st bending eigenmode of the main flareboom	132.0	0.0	158.0
3	1.070	Local coupled sway vibration at the tip of all pipes and flare boom	0.0	32.3	0.0
4	0.810	Global torsional vibration of the flare boom coupled with the sway vibration at the tip of all pipes and flare boom	0.0	103.0	0.0
5	0.751	2nd bending eigenmode of the main flare boom	51.7	0.0	78.5
6	0.734	1st torsional vibration of the wind struts coupled with the sway vibration at the tip of all pipes and flare boom	0.5	1.0	0.6
7	0.710	1st torsional vibration of the wind struts coupled with bending vibration at the top flare boom	0.1	0.0	0.0
8	0.693	2nd torsional vibration of the wind struts coupled with the sway vibration at the tip of all pipes and flare boom	0.0	16.6	0.0
9	0.657	Bending vibration of the wind struts coupled with the sway vibration at the tip of the ventilation pipe	0.0	72.2	0.0
10	0.644	Pure bending vibration of the wind struts	2.4	0.0	2.9

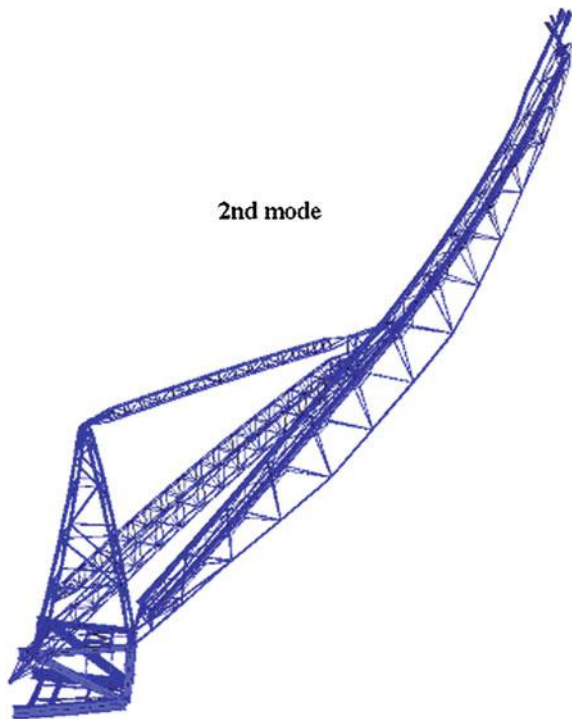


Fig. 19.5 The second eigenmode of the flare boom shown in Fig. 19.4



Fig. 19.6 Partial failure due to inadequate shear strength of the building at garage level, damage in San Francisco due to the Loma Prieta earthquake (courtesy of USGS)



Fig. 19.7 Collapse of top stories of Hotel Continental in Mexico City during the 8.1 magnitude Mexico City earthquake in 1985

As mentioned above, elevation control also includes a gradual change of strength along structures' height. Figure 19.6 shows the damage of a building due to the presence of a weak story with inadequate shear strength at the garage level. The damage of the weak story can also occur at an upper story rather than at the bottom, as shown in Fig. 19.7.

19.4 Dynamic Magnification Due to Torsional Effects

19.4.1 Introduction

The torsional resistance of engineering structures or structural members is normally much weaker than the bending and axial resistance. Therefore, the dynamic structural response (especially at the corner area) is rather sensitive to torsional vibrations, and the torsional response also complicates calculation and assessment of seismic response.

The sources of torsion in a structure can usually be divided into two groups: inherent (natural) torsion and accidental torsion. The inherent torsion accounts for the coupling between translational and torsional response due to lack of symmetry in the horizontal plane, which leads to non-uniform displacement demands on the lateral resisting plane of the structure. Such displacement demands are of principal interest in sizing and detailing of structural elements for earthquake resistance [7]. The accidental torsion accounts for uncertainties in the location of the center of

mass, differences between the theoretical and real stiffness, excitation at the base of a structure due to rotational component of ground motions, and other sources of accidental torsion not included in the analysis [8].

Damages due to torsional motion were reported in various past earthquakes such as 1971 San Fernando earthquake [9], 1985 Mexico earthquake [10], 1985 Loma Prieta earthquake [11], 1990 Philippines earthquake [12], 1994 Northridge earthquake [13], and 1995 Kobe earthquake [14].

19.4.2 Mitigation Measures

Mass and stiffness eccentricity of structures (Fig. 19.8) may give rise to significant torsional vibrations due to deviation of stiffness center (resistance center) from the mass (inertia load) center and vice versa, as illustrated in Figs. 19.9 and 19.10. Therefore, by arranging the structural stiffness center (shear center or resistance center) close to the center of gravity in the horizontal plane, the dynamic seismic response associated with torsion can be minimized.

Uniformity in plane is important to mitigate torsional response. It is characterized by an even distribution of the structural elements that allows short and direct transmission of the inertia forces created in the distributed masses of the structure. If necessary, uniformity may be realized by subdividing the entire structure by seismic joints into dynamically independent units, provided that these joints are designed against pounding of the individual units [1].

It should be noticed that the measures above are based on the assumption that supporting structures subject to ground motions remain linearly elastic. When significant plasticity is developed in the supporting structure, for example, one leg in an offshore jacket structure develops a plasticity hinge, and the stiffness center

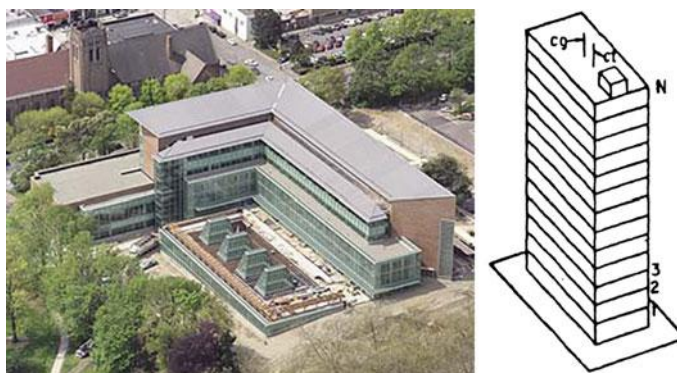
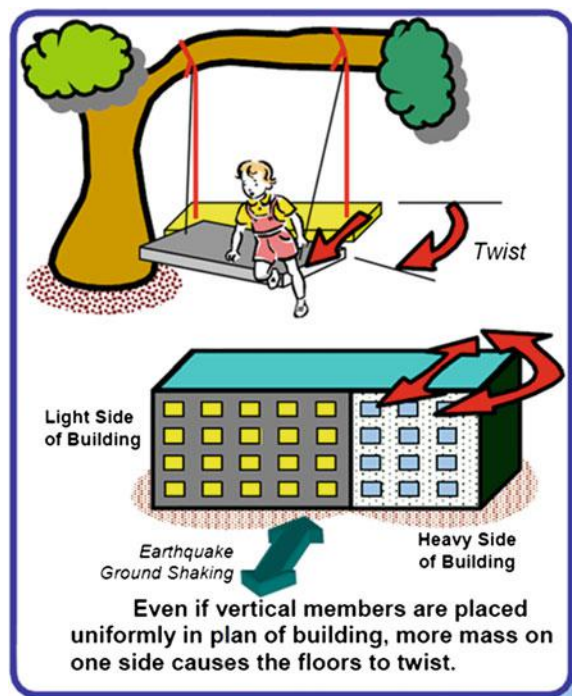


Fig. 19.8 Buildings with mass and stiffness eccentricity in the horizontal plane that may potentially excite torsional responses (*cg* and *ct* in the *right figure* are the center of the gravity and shear in the horizontal plane, respectively)

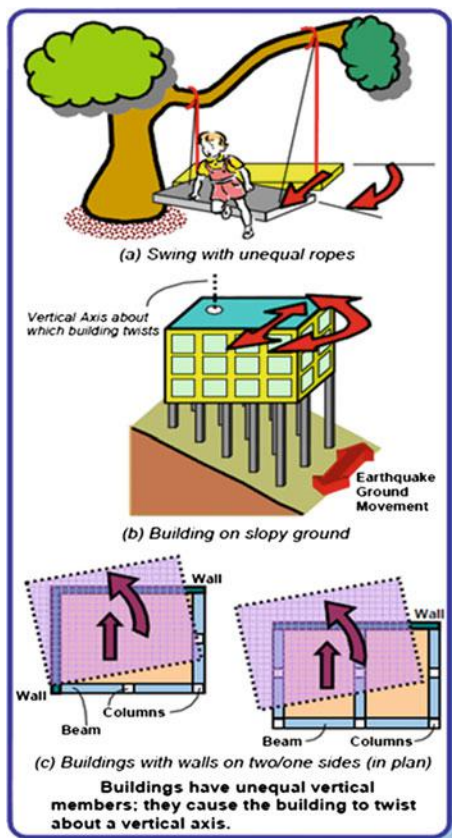
Fig. 19.9 Deviation of inertia load center from stiffness center in the horizontal plane (courtesy of CVR Murty)



will also change, which may alter the load transfer and complicate the assessment of structural integrity. This indicates that, from an earthquake resistance point of view, the supporting structure should not be designed to develop significant plasticity.

In the design phase, it is essential to fully understand the dynamic characteristics of a structure. A good way to reach this goal is to carefully check the first few eigenmode shapes and associated frequency and modal mass participations, as this provides clues on which mode(s) give a significant contribution to global structural response such as base shear or global deflection due to dynamic loading. If those important modes show significant torsional vibrations, it is recommended to redesign the structure so the torsional vibration can be minimized in those important eigenmodes. Furthermore, since the dynamic response of coupled global flexural and torsional vibration increase with an increase in the ratio between the global torsional vibration period and the global bending vibration period, it is recommended to increase the torsional stiffness (decrease the global torsional vibration period) so that the ratio between the global torsional vibration period and the global bending vibration period is as low as possible. By doing this, more energy due to strong ground motions will contribute to the flexural (bending) vibration instead of torsional vibration of structures, which are easier to control. For example, wind induced flutter response is of a serious concern for suspension bridges and cable-stayed bridges due to dynamic wind loading. This is due to the coupled bending and torsional vibration under wind loading. An important accident due to

Fig. 19.10 Deviation of stiffness center from inertial load center (courtesy of CVR Murty)



wind flutter is the collapse of Tacoma Bridge as shown in Fig. 19.11. The composed system (bridge-fluid) enables the excitation energy to be inserted into the bridge during each cycle so that it neutralizes the natural damping of the structure. Therefore the system behaves as if it has an effective negative damping. For design of bridges, efforts are made to increase the vibration frequency of torsion much higher than that of vertical bending. An efficient measure is to use deck-stiffening trusses as shown in Fig. 19.12, so that, as in the case of beam bridges, the torsional vibration can be minimized if it cannot be completely eliminated. However, for large span suspension or cable stay bridges, the deck truss alone is not sufficient to prevent torsional vibrations. Wind tunnel tests on models may be performed to determine the bridge's resistance to torsional movements. For other types of bridges such as arch bridges, the truss structure supporting the bridge deck greatly protects the structures from excessive torsional vibrations.

Moreover, the vertical load bearing elements should run continuously between the foundation and the structure top. However, if a column ends at a horizontal beam or slab at a certain story level, it is also necessary to consider the torsional effects around the vertical axis [5].

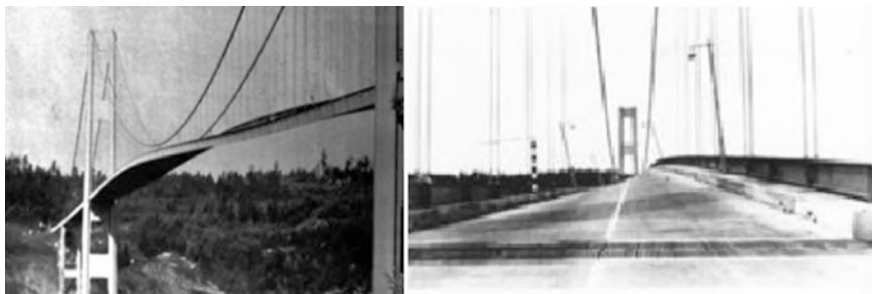


Fig. 19.11 Excessive coupled torsional and bending vibrations before the collapse of the Tacoma Bridge

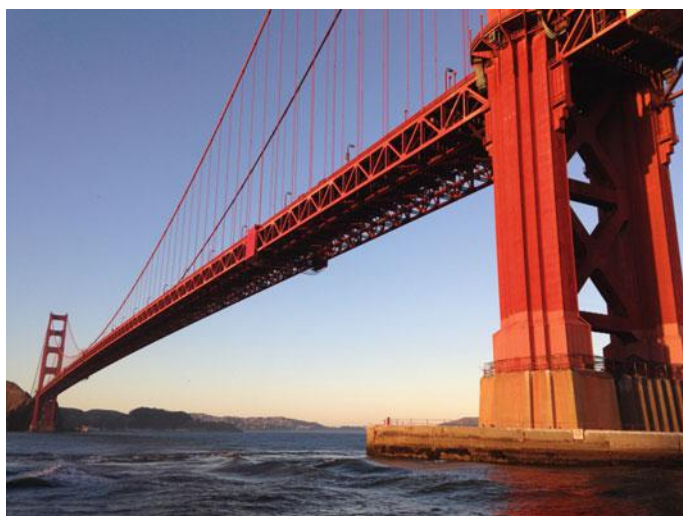


Fig. 19.12 Deck-stiffening trusses used for the Golden Gate Bridge (photo by Wa17gs under the license of CC BY-SA 4.0)

19.4.3 Accounting for Torsional Effects

As mentioned above, torsional response can even be observed in symmetrical structures if the rotational components (around vertical axis) of the ground motions are significant. This torsional component is an important type of accidental torsion and can be derived from the translational components of seismic motion records, and is proportional to the spatial derivatives of the ground motion velocities with respect to orthogonal horizontal directions. Angular displacements, velocities and accelerations depend on the site conditions, which are characterized by the shear wave velocity. The resulting values are in acceptable error limits if the ground

motions are recorded in dense networks. However, the spatial derivatives cannot always be used because the recording devices are often not so close to each other and the differences between the records during the same seismic event also involve the local geological conditions [15].

When using the equivalent static force procedure, most of the building codes account for torsional effects by computing the torsional moments at each floor as the product of design story shear and a quantity termed design eccentricity e_d . In many codes, the design eccentricity consists of two components. The first one is a function of the distance between center of mass and center of stiffness of each floor, called static eccentricity e_s , which accounts for the unsymmetrical distribution of the mass and/or lateral load resisting elements in the plane of the structure. The second component is the accidental eccentricity, which accounts for the torsional component of ground motions, non-uniform ground motion along the foundation of the structure, and possible difference between actual and computed eccentricities due to the uncertainties in workmanship and distribution of non-structural component [16]:

$$e_d = \alpha e_s + \beta b \quad (19.1)$$

$$e_d = \gamma e_s + \beta b \quad (19.2)$$

where α , β , and γ are parameters that vary with different seismic design codes; α and γ usually range from 1.0 up to 1.5 with 1.0 being more typical, if they are different from 1.0, the design eccentricities require an explicit calculation of the location of the center of stiffness of each floor; β usually ranges between 0.05 and 0.1; b is the maximum dimension in the direction perpendicular to the applied load.

For a comparison of specification for various codes regarding the calculation of design eccentricity, readers may read reference [17]. It should be noticed that the level of coupling between lateral and torsional response in a structure can be larger than that implied by the code based equivalent static force procedure due to the dynamic amplification and the inelastic deformation, potentially leading to an increase in the lateral-torsional coupling than that predicted by a linear-elastic analysis [16].

References

- EN 1998-1-1, European Committee for Standardization (2004) Eurocode 8: design of structures for earthquake resistance—Part 1: general rules, seismic actions and rules for buildings
- Lin T, Haselton CB, Baker JW (2013) Conditional spectrum-based ground motion selection. Part I: hazard consistency for risk-based assessments. *Earthq Eng Struct Dyn* 42(12):1847–1865
- Takewaki I (2007) Critical excitation methods in earthquake engineering, 1st edn. Elsevier Science Ltd, Oxford

4. Kramer SL (1996) Geotechnical earthquake engineering. Prentice Hall, Upper Saddle River
5. Flesch R (2012) Fundamental rules for earthquake resistant design. SAMCO (Structural Assessment, Monitoring and Control) report, Arsenal research, Vienna
6. Jia J (2014) Essentials of applied dynamic analysis. Springer, Heidelberg
7. Chopra AK, De la Llera JC (1996) Accidental and natural torsion in earthquake response and design of buildings. In: 11th world conference on earthquake engineering
8. De la Llera JC, Chopra AK (1994) Accidental and natural torsion in earthquake response and design of buildings. University of California at Berkeley, College of Engineering, Berkeley
9. Hart GC et al (1975) Torsional response of high rise buildings. *J Struct Div ASCE* 101:397–416
10. Esteve L (1987) Earthquake engineering research and practice in Mexico after 1985 earthquake. *Bull N Z Natl Soc Earthq Eng* 20:159–200
11. Mitchell D, Tinawi R, Redwood RG (1990) Damage to buildings due to 1989 Loma Prieta earthquake: a Canadian code perspective. *Can J Civ Eng* 17(5):813–834
12. Booth ED, Chandler AM, Wong P, Coburn AW (1991) The central Luzon, Philippines earthquake of 16th July 1990. Report of the earthquake engineering field investigation team. Institute of Structural Engineers, London
13. Mitchell D, DeVall RH, Saatcioglu M, Simpson R, Tinawi R, Tremblay R (1995) Damage to concrete structures due to the 1994 Northridge Earthquake. *Can J Civ Eng* 22(2):361–377
14. Mitchell D, DeVall RH, Kobayashi K, Tinawi R, Tso WK (1996) Damage to concrete structures due to the Jan 17, 1995 Hyogo-ken Nanbu (Kobe) Earthquake. *Can J Civ Eng* 23 (3):757–770
15. Enache R, Demetriu S, Albota E (2009) Rotational components of the ground motion for Vrancea earthquakes. In: Proceedings of the 11th WSEAS international conference on sustainability in science engineering, pp 305–309
16. Sedarat H, Gupta S, Werner SD (1994) Torsional response characteristics of regular buildings under different seismic excitation levels. Report CSMIP/94-01, California Department of Conservation
17. Tola A (2010) Development of a comprehensive linear response history analysis procedure for seismic load analysis. Virginia Polytechnic Institute and State University, Blacksburg

Chapter 20

Ductility Through Structural Configuration and Local Detailing

20.1 Steel Brace Frames

The conventional approach requires that structures can passively resist seismic loading through a combination of redundancy, strength, deformability, and energy absorption. In an earthquake prone area, a ductile structural system with minimal weight is preferred and is often the governing design principle. Therefore, it is normally easier to satisfy the associated criteria with steel structures, although carefully detailed concrete structure can also fulfil the criteria. Figures 20.1, 20.2, 20.3, and 20.4 show engineering realizations of steel brace frames, which are economical with high lateral stiffness.

Figure 20.5 presents the basic configurations of brace frames. Braces buckle in compression and yield in tension. The initial compressive buckling capacity is smaller than the tensile yield force, and for subsequent buckling cycles, the buckling capacity is further reduced due to prior tensile yielding (inelastic excursion). Therefore, bracing systems must be balanced so that the lateral resistance in tension and compression is similar in both directions. This means that in case diagonal bracing is designed, it must be used in matched tensile and compressive pairs, i.e., they should be designed in opposing pairs to achieve this required balance as shown in Fig. 20.6.

It is noted that K-braces can introduce bending into columns following buckling of compression brace, and the bending moments and inelastic deformation occurred in the column may cause frame collapse. Therefore, generally, a design with K-braces should be avoided. V-braces and inverted V-braces (chevron braces) require a continuity of beams. They have the same unbalanced force problem as the K-braces, but are only introduced into the beams, and are therefore less dangerous. X-braces are widely used in both offshore and land-based structures. For example, for offshore jacket structures, it is recommended to use vertical frame configurations as shown Fig. 20.7. These configurations enables vertical framing to transmit the shear force between two adjacent horizontals consisting of X-braces or leg to leg

Fig. 20.1 A building constructed with steel braced frames



Fig. 20.2 John Hancock Tower in Chicago constructed with steel braced frame design concept



diagonals, so that those braces can carry shear between the adjacent horizontals in both tension and compression. Moreover, the horizontal members shall also have sufficient capacity in compression to support a redistribution of actions resulting from buckling of diagonal braces. Similar configuration can also be found in many land-based structures, with an example shown in Fig. 20.8. In addition, tension-only bracing has shown relatively poor performance during past

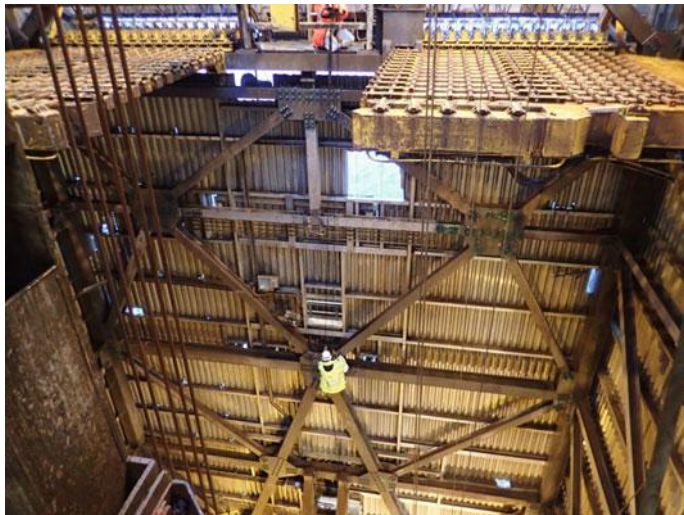
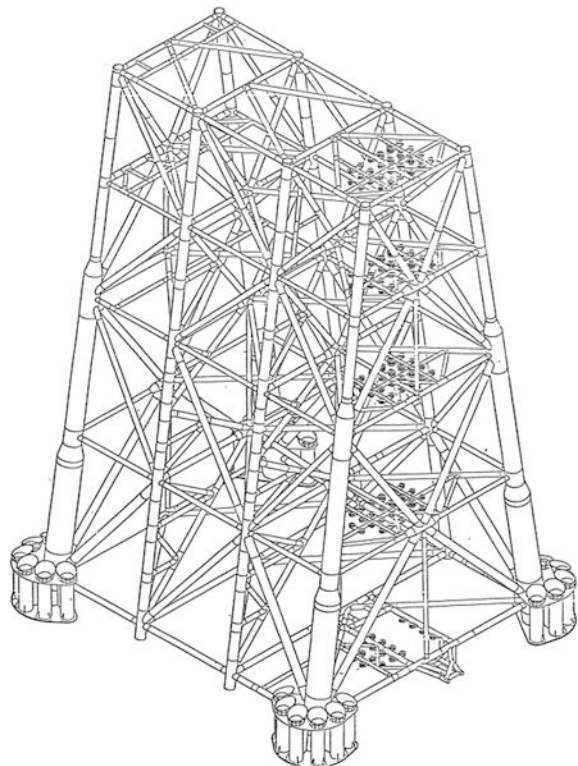


Fig. 20.3 A part of a typical drilling derrick structure on a North Sea offshore platform constructed by steel braced frame (courtesy of Aker Solutions)

Fig. 20.4 A typical offshore jacket structure with braces and legs connected at joints (courtesy of Aker Solutions)



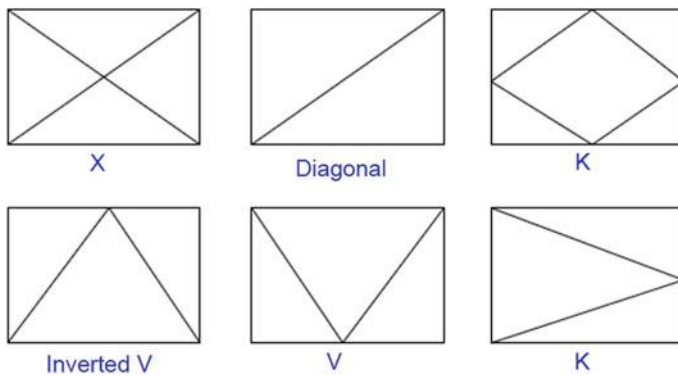


Fig. 20.5 Basic configurations of brace frames (courtesy of FEMA)

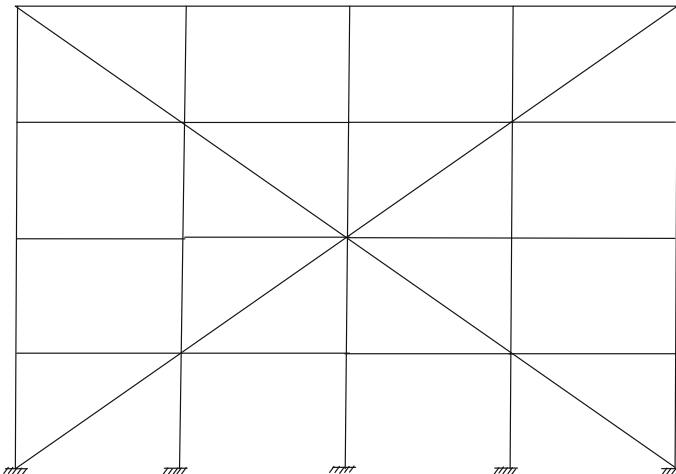


Fig. 20.6 Diagonal bracing designed in opposing pairs so that the lateral resistance in tension and compression is similar in both directions

earthquakes because of a lack of compressive brace resistance leads to an inelastic behavior with slack braces that have no stiffness until the slack is taken up. The slack braces may lead to progressively increasing deflections and impact loading on the brace, and early brace fracture may occur. Therefore, tension-only braces should also be avoided [1].

However, X-braces may introduce a serious failure under cyclic loading: when a diagonal bracing is under tension due to strong ground motion excitations, it may reach yielding under tension, be gradually lengthened with each load cycle, and then buckle under compression. Under repeated cyclic movements, the stiffness of the truss may be degraded and becomes very small at the zero deformation point. This, combined with dynamic effects, can contribute to a failure or even collapse of

Fig. 20.7 Vertical frame configurations with X-braces or leg to leg diagonals for resistance to horizontal ocean wave, wind and earthquake loading [2]

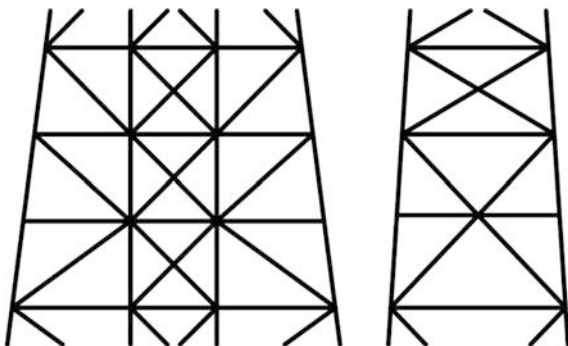


Fig. 20.8 A three story garage building with X-braces to resist horizontal wind and earthquake loading



the structure. Therefore, X-brace system is preferred only for elastic behavior, or if necessary very low ductility. Moreover, if more stiff bracing or other bracing systems (e.g. walls) may be needed, a thorough check of the compatibility between the brace deformations and those of the other structural and non-structural elements is required. Steel truss systems with eccentric connections and compact members perform better than trusses with center connections and slender members [2], as will be discussed in Sect. 20.5.

For high rise buildings, most of the structural systems deployed were steel frames with diagonal bracings of various configurations. However, while the structural importance of diagonals was well recognized, their aesthetic potential was not explicitly appreciated. Thus, diagonals were generally embedded within the building cores, which were usually located in the interior of the building. The 100-story high John Hancock Building (Fig. 20.2) in Chicago was among the first group of high rise buildings utilizing the diagonals along the entire exterior perimeter surfaces of the building in order to maximize their structural effectiveness and capitalize on the aesthetic innovation [3]. Moreover, note that the traditional diagonal braced frame structures are constructed to mainly carry horizontal load,

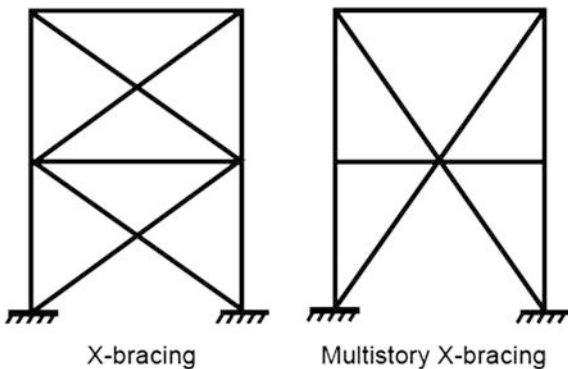
Fig. 20.9 China Central Television Headquarter Tower



and the emerging diagrid (perimeter diagonals) structures are designed to carry both horizontal and vertical load. They use exclusive exterior frames comprised entirely of diagonal members, thus eliminating or greatly reducing the use of vertical columns. Figure 20.9 shows that China Central Television Headquarter Tower was constructed with diagrid/triangulated bracings, forming a network of diagrids in an extremely strong closed braced tube structure. This external diagrid structure is also expressed boldly in the building's façade. It reinforces the transparency between structure and architecture, a central concept for the building's design. The unique diagrid pattern in the external structure was arrived at after extensive iteration and optimization, in close collaboration with the architect [4].

It is noted that, with the utilization of the brace frame configuration, concentration of inelastic deformation in a limited number of stories occurs. Experiments suggest that multi-story X bracing (right figure in Fig. 20.10) offers a slightly better performance in that it provides a somewhat more robust path for transferring story shear to adjacent stories even after brace buckling and/or fracture, this is because

Fig. 20.10 X bracing and multistory X-bracing [1]



the remaining tension brace may directly transfer its force to the next story. Chevron or inverted-chevron bracing (inverted V-bracing or V-bracing) has intersecting brace connections at mid-span of the beam. Large unbalanced forces and bending moments on the beam occur because the buckling load is smaller than the tensile yield resistance and decreases with increasing damage. The bending moment increases as the compressive resistance deteriorates, and it is therefore required that the beam be designed for these bending moments [1].

Brace buckling induces large inelastic demands often at the middle of the brace, typically resulting in a plastic hinge at mid-span (Fig. 20.11a). Brace buckling also places significant demands on the end of the brace, typically on gusset plate connections (Fig. 20.11b) and adjacent framing members (Fig. 20.11c). Limited cracking of the welds joining the gusset plate to the beams and columns is generally expected because of gusset plate deformation [1]. For land-based frame structures, these cracks normally initiate at story drifts in the range of 1.5–2.0 %, but the cracks normally remain stable if the design follows concurrent design code requirements such as AISC 341 [6].

As discussed previously, the steel brace frames have rather high lateral stiffness and are thus effective in controlling lateral deflections due to small seismic ground motions or wind, but may perform sub-optimally during a strong earthquake due to their relatively high stiffness (attracting higher seismic forces and exhibiting higher accelerations) and limited energy dissipation capacity. These higher accelerations affect the structure as well as the equipment and contents. Several failures of braced buildings occurred during the 1995 Kobe earthquake. However, as the brace steel frames are stiff, they tend to protect built-in non-structural components such as partitions from drift-induced damage. Note that in the design, a brace buckling of beams and columns are not preferred means of dissipating seismic energy, as such response would endanger the gravity load carrying capacity of the structure. Therefore, inelastic action under earthquakes must only take place in the diagonal bracing members and adequate detailing is important to ensure that the braces can go through the expected inelastic demand. The diagonal braces should share the lateral load exerted in a given direction by having certain level of resistance in tension while others take compression. The non-ductile braced frame behavior must be avoided by following the following recommendations [8]:

1. The diagonal should not transfer significant seismic force to beam-column joint.
2. A repeated yielding in tension under cyclic load should be avoided as this can cause a slack in the system.

Design of the bracing system is usually performed by considering only the diagonals in tension and neglecting the contribution of the compressed diagonals in the pre-buckling phase but with a requirement on the range of the brace slenderness ratio $\bar{\lambda}$. For example, in Eurocode [7], $\bar{\lambda}$ is required to be within the range below:

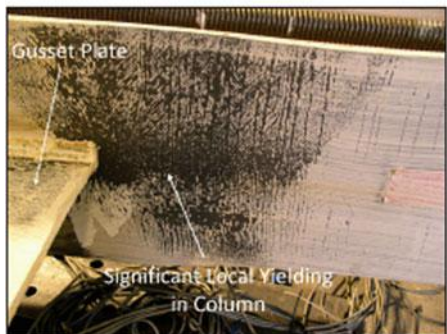
Fig. 20.11 Brace frame behavior [1]



(a) Brace buckling deformation



(b) Deformation of gusset plate



(c) Local yielding in beam and column

$$1.3 \leq \bar{\lambda} \leq 2.0 \quad (20.1)$$

where $\bar{\lambda}$ is the ratio between the diagonal slenderness λ and the elastic limit slenderness $\lambda_y = \pi\sqrt{E/f_y}$; E and f_y are the elastic modulus and the yielding strength of the brace material, respectively.

Moreover, a homogeneous dissipative behavior of the diagonals should be achieved by ensuring that the ratio between the maximum over-strength Ω_{\max} and the minimum one Ω_{\min} is less than a limiting value Φ (1.25 required by Eurocode [7]):

$$\Omega_{\max}/\Omega_{\min} \leq \Phi \quad (20.2)$$

where:

$$\Omega_{\max} = \max(\Omega_i) \quad (20.3)$$

$$\Omega_{\min} = \min(\Omega_i) \quad (20.4)$$

$$\Omega_i = N_{pl,Rd,i}/N_{Ed,i} \quad (20.5)$$

in which $N_{pl,Rd,i}$ is the design resistance of diagonal i , which should be less than the design ultimate resistance of the net section at the end joints to avoid brittle fracture; $N_{Ed,i} = N_{Ed,i,G} + 1.1\gamma_{ov}\Omega_i N_{Ed,i,E}$; $N_{Ed,i,G}$ and $N_{Ed,i,E}$ are the axial force due to nonseismic and seismic actions, respectively; γ_{ov} is the over-strength factor, and can be taken as 1.25 recommended by Eurocode [7].

Moreover, connections in dissipative zones should be designed to have sufficient over-strength to allow yielding of the connected parts. In Eurocode [7], it is required that the resistance of a connection $R_{j,d}$ should fulfil the condition below:

$$R_{j,d} \geq 1.1\gamma_{ov}R_{pl,Rd} = R_{U,Rd} \quad (20.6)$$

where $R_{pl,Rd}$ is the plastic resistance of connected dissipative member; $R_{U,Rd}$ is the upper limit of the plastic resistance of connected dissipative member.

It is important to prevent brittle fracture at the welds under cyclic seismic loading, which is a common cause of failure modes in connections, as observed after many destructive earthquakes such as the 1994 Northridge earthquake.

20.2 Buckling-Restrained Brace Frame

Note that the traditional steel brace system provides limited ductility by post-buckling resistance to compressive loads. The brace members can be designed through a de-coupling of axial strength from buckling resistance by providing transverse restraint to the brace, thus allowing an equal plasticity development of

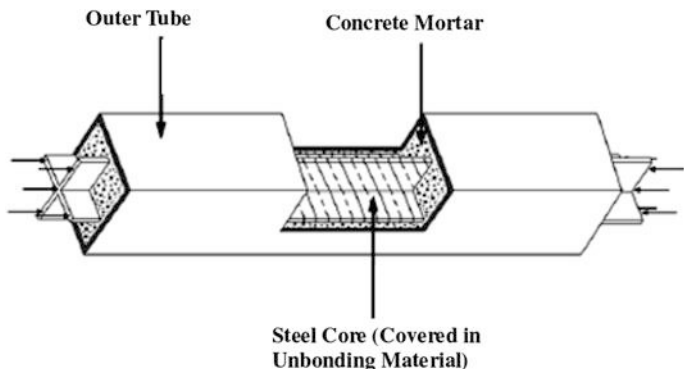


Fig. 20.12 An illustration of a buckling-restrained brace frame (BRBF) design [7]

the brace in tension and compression, leading to a so-called buckling-restrained brace frame (BRBF) design, as shown in Fig. 20.12. A typical design of BRBF is to install a steel core element confined in concrete mortar filled steel outer tube. The steel core is designed to axially resist the lateral forces and the concrete confinement prevents buckling of the core while the outer steel tube encases concrete mortar and restrains buckling [8]. To allow an independence of movements along axial direction between the two parts, the friction in the axial direction between the yielding core element and the confining material are minimized by using a de-bonding layer between the two parts. Figure 20.13 shows an example of



Fig. 20.13 Buckling-restrained braces installed on Los Angeles Tower's 26th floor to support the transition from hotel to condo tower (courtesy of Southern California Public Radio)

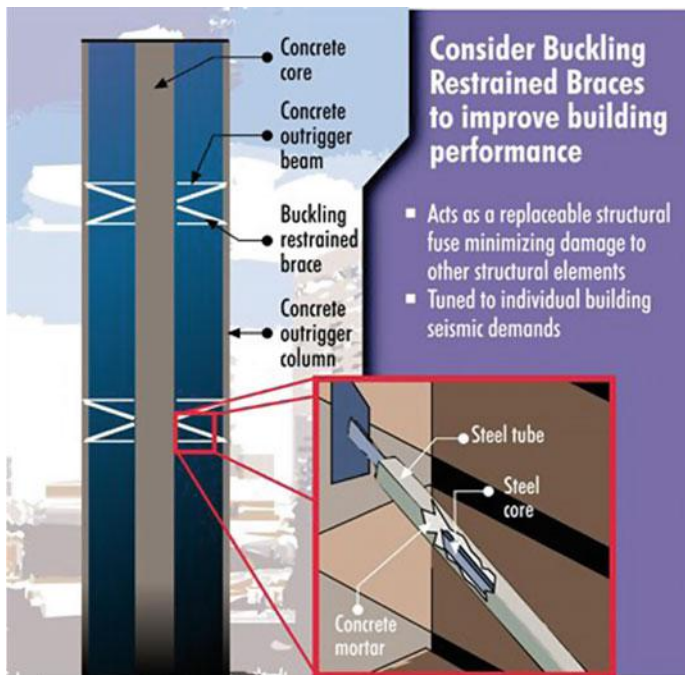


Fig. 20.14 Buckling-restrained braces installed on the One Rincon Hill residential towers (courtesy of Don Davies, Magnusson Klemencic Associates, USA)

buckling-restrained braces installed on Los Angeles Live's 54-story hotel and condo tower. Each has a capacity of 10,000 kN. Figure 20.14 shows another example of buckling-restrained braces installed on the One Rincon Hill residential towers in San Francisco.

20.3 Moment Resisting Frame

Different from steel brace frames, moment resisting frames (Fig. 20.15) perform better during significant earthquakes due to their stable ductile behavior under cyclic loading. This has been realized by engineering communities in that various seismic codes allow a lower design seismic loading applied on the moment resisting frames. Note that the moment resisting frame is very flexible due to a reduction in lateral stiffness compared to that of the steel brace frames, and it attracts less seismic force and exhibits lower accelerations. However, it is difficult to control the story drifts and deflections to prevent non-structural damage. During the 1995 Northridge earthquake, various welded beam-column connections of moment resisting frames were found to be susceptible to damage. In order to avoid



Fig. 20.15 An illustration of a moment resisting frame (courtesy of EERI)

development of structural instability due to P- Δ effects, the lateral drift over the structure's height should be as uniform as possible. To achieve this, it is important to avoid early formation of single story mechanisms in which inelastic response is dominated by formation of plastic hinges at the tops and bottoms of columns within a single story, with an example shown in the left figure of Fig. 20.16. Therefore, seismic design codes promote the formation of multi-story sideway mechanisms dominated by plastic hinge formation on beams rather than on columns as shown in the right figure of Fig. 20.16. Moreover, moment resisting frames are generally preferred as the seismic force resisting system when architectural space planning flexibility is desired.

Controlling drift, avoiding instabilities due to P- Δ effects, and proportioning structures to comply with the strong-column/weak-beam are the primary factors affecting steel moment resisting frame member size [8].

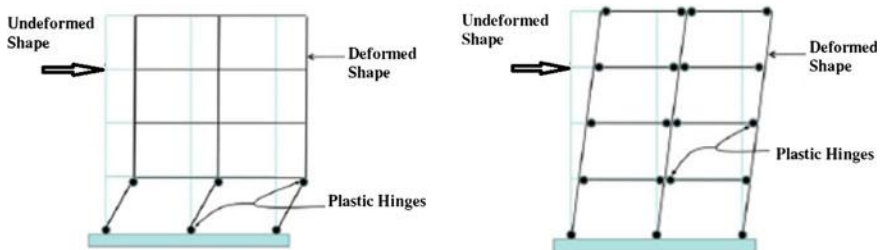


Fig. 20.16 Illustration of single story frame mechanism and idealized sideway mechanism [7]

20.4 Shear Walls

Shear walls are vertical elements of the horizontal load resisting system. They can be made with reinforced concrete (most typically used due to its high stiffness to cost ratio) shown in Fig. 20.17, or steel shown in Fig. 20.18, or timber frames, or masonry. Shear walls generally start at the foundation and are continuous throughout the building height. The walls provide large strength and stiffness to buildings in the direction of their orientation, mostly due to their large cross section area that provide a great moment of inertia, which significantly reduces lateral sway of the structure. The shear wall can also work as a sound isolator and fire protection system [9]. To stabilize a structure against lateral loads from different directions, at least three shear walls should be placed, not intersecting at the same point or being parallel to each other [10].

If reinforced concrete shear walls are constructed, due to the added stiffness from the shear wall, the entire structure attracts higher seismic forces and exhibits higher acceleration, and the ductility in a reinforced concrete shear wall is rather sensitive to detailing and quality control. Any advantages gained by added stiffness may be negated by the increased amount of seismic energy input, which thus places higher requirements on strength and ductility [11].

Damage to structural walls in recent significant earthquakes in Chile (2010) and New Zealand (2011) demonstrated that modern reinforced concrete walls may not achieve the expected ductile response but could possibly be triggered by out-of-plane displacements of the wall [12]. Figure 20.19 shows an example of the collapse of a building constructed with thin concrete wall during the 2010 Chile earthquake.



Fig. 20.17 Reinforced concrete shear wall



Fig. 20.18 Coupled steel plate shear wall (Image credit: Mehdi Kharrazi under a CC BY-SA 3.0 license)



Fig. 20.19 Building made of thin concrete walls destroyed during the 2010 Chile earthquake (Image credit: Claudio Núñez under a CC BY-SA 2.0 license)

20.5 Eccentrically Braced Frame

The eccentrically braced frame (EBF), as shown in Fig. 20.20, combines the advantages of ductility in moment frames (Sect. 20.3) and the high lateral stiffness associated with concentrically braced frames (Sect. 20.1).

The EBF is intentionally designed with an element called a “link” beam, and the location of inelastic behavior is strategically and explicitly designed to occur typically in the middle of the beam, so that the integrity of gravity-load-resisting system is ensured. The diagonal brace, at least at one end, is connected to the end of the link rather than to the beam-column joint. All plasticity should be developed in those links, which work as structural fuses and can dissipate applied seismic energy without a degradation of strength and stiffness. Due to eccentric connection of the braces to beams, the lateral stiffness of the system depends upon the flexural stiffness of the beams and columns, thus reducing the lateral stiffness of the frame. The vertical component of the bracing forces due to earthquake causes lateral concentrated load on the beams at the point of connection of the eccentric-braces.

The excellent ductility and energy dissipation capacity is obtained by two factors. First, inelastic activity under severe seismic loading is restricted mainly to the links that are detailed to sustain large inelastic deformations. Second, braces are designed not to buckle regardless of lateral loading. Note that the strength of the link can be accurately estimated, and the designer can easily avoid the buckling of the brace by making the brace stronger than the link [13]. EBF also allows larger spaces for doors, windows, and hallways, providing access through the frame, while braces in typical concentric configurations get in the way of such features (Fig. 20.21).

Although eccentric bracing was originally introduced to be designed as wind bracing, and this was followed by its application on the seismic design of structures, the excellent performance of EBFs under severe earthquake loading was demonstrated on one-third scale model frames at the University of California in 1977. Soon after this study, several major buildings were constructed incorporating EBFs as part of their lateral seismic resisting systems, including the 19 story Bank of America building in San Diego [15] and the 47 story 174 m high Four Embarcadero Center building in San Francisco [16] (constructed in 1981, the first building in the

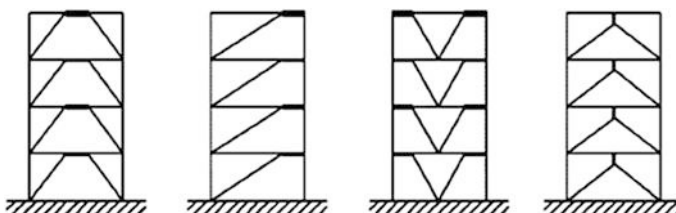


Fig. 20.20 Illustration of various configurations of the eccentrically braced frame

Fig. 20.21 An example of an eccentrically braced frame [14]



US constructed with eccentric bracings). Since that time, numerous applications of eccentric bracing systems have been adopted in practice [17].

As will be introduced in Sect. 22.7.2.1, eccentrically braced frames can also be designed as an energy dissipation mechanism by intentionally introducing localized damage concentrated at specifically detailed shear links of eccentrically braced frames during severe earthquakes.

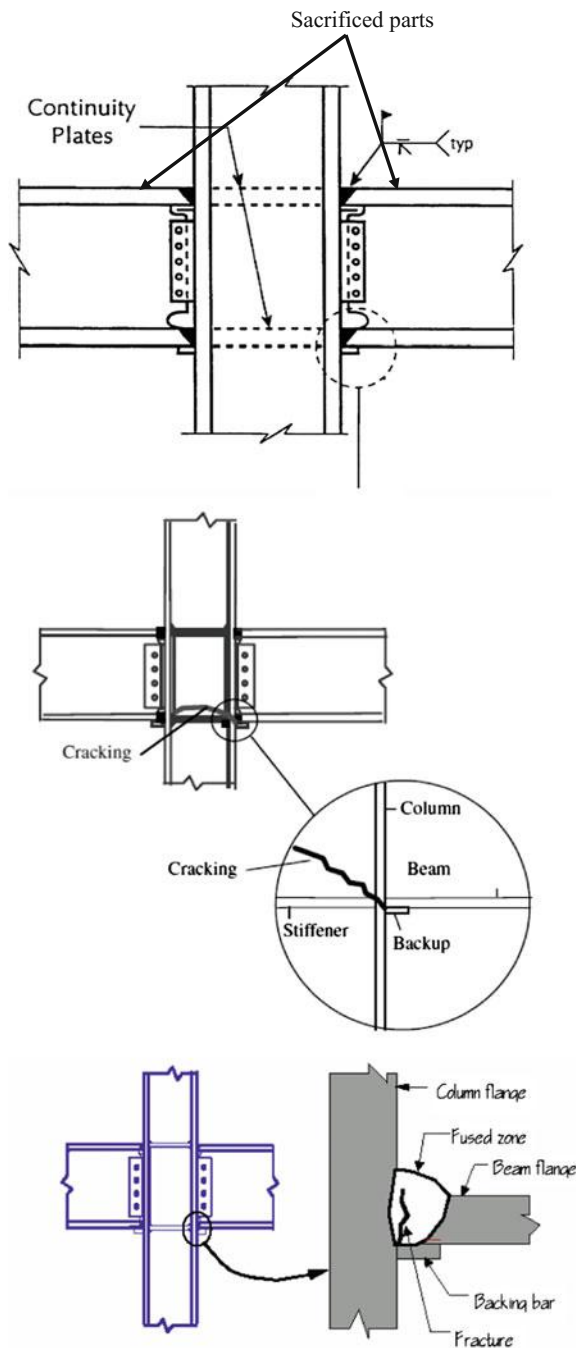
20.6 Local Structural Detailing

It is noted that damping of a structure within elastic limit is normally rather low. Under significant dynamic loading such as strong seismic loading, the local plasticity developed on the structure dramatically increases the damping. Therefore, much of the energy is absorbed by localized plasticity/damage [18], and the local plasticity should thus be developed in members far from joints to avoid substantial collapse.

In reality, during strong ground motions, plasticity may only be developed at a localized beam flange-column connection as shown in Fig. 20.22, i.e. little energy is dissipated, cracking then typically initiates at the lower beam flange location and propagates upward into the shear panel. This type of connection failure has been observed during several earthquakes such as 1994 Northridge and 1995 Kobe earthquakes.

According to the design philosophy of strong-column-weak-beam, the highest plasticity demand should be shifted from beam-column connection to its adjacent interior in the beam itself. The use of a beam strengthening concept can be adopted. This concept includes a dedicated connection design with welded haunch, bolted bracket, beam ribs, flange-welded beam cover plates, side plates (proprietary), and

Fig. 20.22 Developments of plasticity and cracking at localized beam flange-column connections during past earthquakes [19–21]



bolted flange plate etc. [19], as shown in Fig. 20.23, so that the plastic hinges are shifted from the connection to the beam member.

A dog bone profile with a narrow flange outside the weld details/beam-column connection as shown in Fig. 20.24 can introduce an overloading at the reduced flange cross section, leading to the first yield and increased plastic deformations within this part, and an increase in ductility performance of the entire structure.

Note that, for beams, yielding in shear dissipates more energy than in bending. Researchers [23, 24] proposed concept design to perforate the beam web (typically close to the two ends of the beam) so that the desirable yielding in shear of the beam web will be reached prior to yielding in bending.

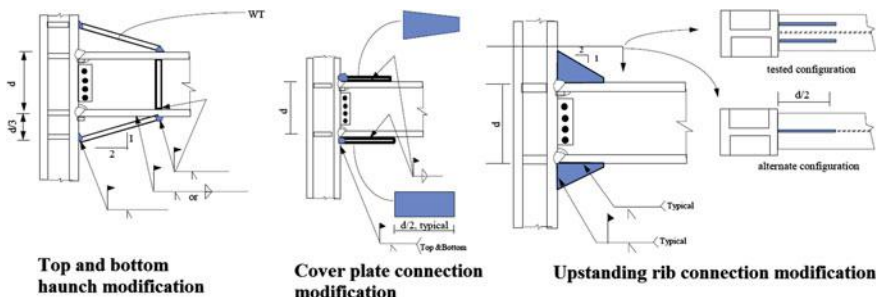
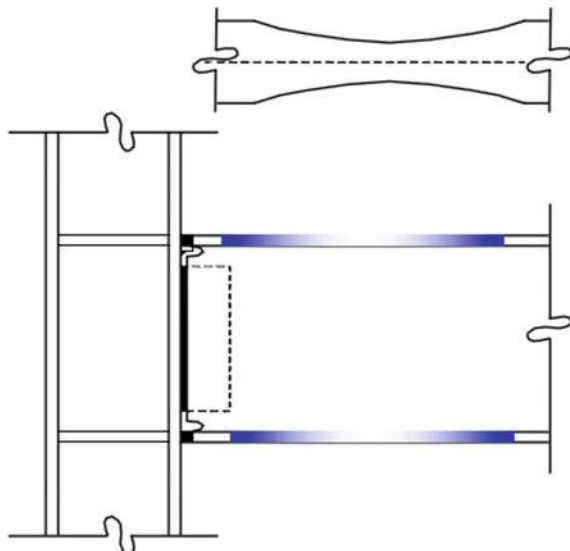


Fig. 20.23 Illustration of post-earthquake modification of steel column connections (courtesy of FEMA) [22]

Fig. 20.24 Reduced beam section circular cut in flange with a dog bone design (courtesy of FEMA)



However, it is noticed that for real world engineering structures, many factors may influence the location and proper development of plastic hinges. For example, under a strong earthquake, the foundations of a bridge could fail before plastic hinges can develop. With the assumption that the foundations are strengthened, a plastic hinge would develop at an unexpected location of the tallest pier of bridge due to the curtailment of the longitudinal reinforcement [25]. Therefore, the use of external damping devices (Chaps. 21 and 22) is promoted as a more efficient tool to reduce the seismic response, even though many structural engineers are conservative and reluctant in adopting mechanical devices, especially for devices based on friction or comprising many “moving parts” [25].

References

1. Sabelli R, Roeder CW, Hajjar JF (2013) NEHRP seismic design technical Brief No. 8 seismic design of steel special systems—a guide for practicing engineers. National Institute of Standards and Technology, US Department of Commerce
2. ISO 19902 (2007) Petroleum and natural gas industries—fixed steel offshore structures
3. Bachmann H (2003) Seismic conceptual design of buildings: basic principles for engineers, architects, building owners, and authorities. Swiss Federal Office for Water and Geology and Swiss Agency for Development and Cooperation, BWG, Bern
4. Moon K, Connor JJ, Fernandez JE (2007) Diagrid structural systems for tall buildings: characteristics and methodology for preliminary design. Struct Design Tall Spec 16:205–230
5. Carroll C, Duan X, Gibbons C, Lawson R, Lee A, Luong A, McGowan R, Pope C (2006) China Central Television Headquarters: structural design. Steel Struct 6:387–391
6. American Institute of Steel Construction (2011) Seismic provisions for structural steel buildings, Chicago
7. Sahin C (2014) Seismic retrofitting of existing structures. Portland State University, Portland
8. EN 1998-1-1, European Committee for Standardization (2004) Eurocode 8: design of structures for earthquake resistance—Part 1: general rules, seismic actions and rules for buildings
9. Sandelin C, Budajev E (2014) The stabilization of high-rise buildings. Uppsala University, ISRN UTH-INGUTB-EX-B-2013/38-SE
10. Severin P, Sekic H (2012) Jämförelse och utvärdering för stabilisering av väggar av armerad betong i höga hus (in Swedish). Royal Institute of Technology, Stockholm
11. Pall AS, Pall R (1996) Friction-dampers for seismic control of buildings: a Canadian experience. In: 11th world conference on earthquake engineering
12. Rosso A, Almeida JP, Beyer K (2016) Stability of thin reinforced concrete walls under cyclic loads: state-of-the-art and new experimental findings. Bull Earthq Eng 14(2):455–484
13. Popov EP, Engerhardt MD (1988) Seismic eccentrically braced frames. Constr Steel Res
14. Azmoodeh BM (2011) Optimum seismic retrofitting technique for buildings. J Civil Eng Environ Syst 28(1):61–74
15. Libby JR (1981) Eccentrically braced frame construction: a case history. Eng J, AISC
16. Merovich AT, Nicoletti JP, Hartle E (1982) Eccentric bracing in tall buildings, ASCE 108, No. 9
17. Mekonnen Y (2015) Comparative evaluation of concentrically bracing system for lateral loads on medium rise steel building structures. Addis Ababa University, Addis Ababa
18. Wada A (2005) Damage-controlled structures for strong earthquake. In: Ninth world seminar on seismic isolation, energy dissipation and active vibration control of structures, Kobe, Japan

19. FEMA 350 (2000) Recommended seismic design criteria for new steel moment-frame buildings, Washington DC
20. Kaufmann EJ, Fisher JW, DiJulio RM, Gross JL (1997) Failure analysis of welded steel moment frames damaged in the Northridge earthquake. National Technical Information Service (NTIS), Technology Administration, US Department of Commerce, Springfield VA, 22161
21. Hamburger RO, Scawthorn C (2006) Seismic design of buildings. In: Chen WF, Lui EM (eds) Earthquake engineering for structural design. Taylor & Francis, New York
22. FEMA-267 (2014) Interim guidelines evaluation, repair, modification, and design of welded steel moment frame structures
23. Williams M (2004) Seismic performance of dissipative devices. In: Japan-Europe workshop on seismic risk, Bristol
24. Halterman A, Aschheim M (2000) Analytical studies of shear-yielding moment-resistant steel frame. In: Proceedings of 12th world conference on earthquake engineering, New Zealand
25. Flesch R (2012) Earthquake engineering: mechanical devices for energy dissipation versus capacity design, Arsenal Research

Chapter 21

Damping

21.1 General

A few thousand years ago, human beings began to use damping to control the motions of structures. For example, the columns in ancient Greece and the Roman Empire were typically composed of numerous masonry blocks of varying size and shape. The friction at the column segment connections (Fig. 21.1) and between the column and the foundation can provide significant damping, which is beneficial to dissipate seismic energy and to prevent structural collapse, at the cost of permanent displacement of the column.

From the point of view of efficiency for mitigating dynamic response, damping plays a significant role to dissipating seismic energy and reduce structural responses as follows:

All structures have a certain level of inherent damping. Within elastic limits, the damping level for a typical structure is generally low. However, when the structure deforms above the elastic limit and develops plasticity, it can absorb a large amount of energy through the localized plastic deformation (e.g. forming plastic hinges). This also results in an increased flexibility, ductility and energy dissipation. The ductility not only benefits the earthquake resistance of the structure, but also contributes to the damage mitigation due to action effects of other environmental loading such as ocean wave, wind and ice excitations. For example, for an offshore platform, in order to keep its integrity so that it does not collapse during, for example, a storm wave event with 10,000 years of return period, it needs to have a good structural redundancy, ductility and capacity reserve through a well-engineered ductile design.

For dynamic sensitive structures, the structural dynamic performance may depend extensively on the initial assumption of damping, which is essential to decrease the dynamic response through energy absorption and dissipation. As an indication of importance of the initial assumption of damping, assuming a structure

Fig. 21.1 The remaining columns of the Temple of Ithomis at Delphi, Greece (photo by Patar knight)



has an initial inherent damping of 1 %, the rate of acceleration reduction expected from the equivalent damping ratio of $x\%$ can then be estimated by:

$$\lambda = \frac{1}{\sqrt{1+x}} \quad (21.1)$$

The dynamic loadings can not only be handled by the structures' own stiffness, mass and damping (normally less than a few percent), but also be more effectively resisted by introducing artificial dampers or installing base isolation etc., to reduce the excitations. The amount of inherent damping cannot be estimated with certainty. However, a known level of damping may be introduced through artificial dampers (damping apparatus) or isolation systems, as will be discussed in Chaps. 22 and 23.

The mitigation of the dynamic response not only decreases the demand associated with the ultimate limit strength, but also improves the structural performance associated with structural fatigue (both high cycle and low cycle fatigue) due to dynamic response and comfortability due to human perception. Both benefit from decreased acceleration responses. As an example, for a typical jacket comprising abundant tubular members and joints, the negative inverse slope of the S-N curve (Fig. 21.2) for tubular joints normally ranges from 3.0 to 5.0. This indicates that a reduction of dynamic stress amplitude of 15 % can extend the high cycle fatigue service life to 150–200 % of the original one. For offshore structures, the cost of inspection and repair under water is substantial. Therefore, the mitigation of dynamic response leads to significant economic benefits from both construction and maintenance points of view.

Figure 21.3 illustrates the possible measures to mitigate seismic dynamic response, which will be elaborated in subsequent chapters.

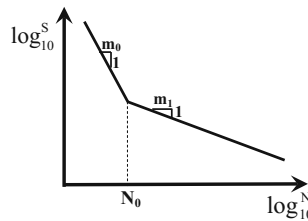


Fig. 21.2 An illustration of an S–N curve (m_1 is the inverse slope for the first and second segment of the S–N curves; N is the predicted number of cycles to failure under stress range S) used in the high cycle fatigue assessment in stress-based approach [5]

Fig. 21.3 Measures to mitigate seismic response

Response Mitigation	Ductile/plastic design Direct damping apparatus Base and hanging isolation systems Dynamic absorber Load and energy sharing mechanism Seismic rehabilitation and reinforcement
---------------------	---

21.2 Damping Apparatus

Instead of relying on increased structural ductility to increase the damping of a structure, devices are also available to increase damping by dissipating energy and/or partially cutting the transmission path of loading when the structure moves [1–3]. These devices are designed to act as energy dissipating systems, to isolate the structure from ground motion, to mitigate dynamic response through the momentum exchange, or to include a combination of effects above.

Therefore, if tuning the weight and stiffness or utilizing the structural ductility is not efficient and feasible, adding damping apparatus to dissipate energy and control undesired structural vibrations of the primary structure is then an alternative and more efficient tool for engineers. In engineering practice, a common technique is to add direct damping, such as a friction or a viscous damper (as will be discussed in Chap. 22), to the joints of the primary structure to stabilize the structural vibration. A large number of dampers may be needed in order to achieve an effective damping effect when the movements of the joints are not sufficient to contribute to energy absorption. Another alternative is to add indirect damping to the structure. For example, by installing base isolation systems (Chap. 23) or dynamic absorbers (Chap. 24), a large amount of damping is then introduced and the dynamic response of the structure can be effectively reduced.

21.3 Equivalent Viscous Damping

Even though viscous damping modeling has obvious advantages, the energy dissipation for an actual structure is more prone to be displacement proportional rather than velocity proportional, and is sometimes a combination of the two. This leads to the concept of equivalent viscous damping [4], which is to define the damping of a system using viscous damping based on the equivalent energy dissipation between the viscous damping and that of the actual system [5]. In case of relatively low damping (less than 15 %), viscous, friction and hysteretic damping can be conveniently expressed by equivalent viscous damping.

Consider an SDOF system with viscous or hysteretic damper subjected to harmonic loading $F(t) = F_0 \sin(\Omega t)$. It is noted that the work done by conservative forces such as elastic, inertia and gravitational forces in a complete loading cycle will be zero. Therefore, the net work will be dissipated by damping only. When the motions reach steady-state, the energy dissipation (E_d) during a complete cycle by viscous damping is illustrated in the left figure of Fig. 21.4, which can be expressed as:

$$E_d = \int F_d d\delta = \int_0^{2\pi/\omega} (c \dot{\delta}) \dot{\delta} dt = c \int_0^{2\pi/\omega} [\Omega X_{0d} \cos(\Omega t - \phi)]^2 dt = \pi \Omega c X_{0d}^2 \quad (21.2)$$

From the equation above, it is found that, rather than being a constant value, the energy dissipation is proportional to the excitation frequency Ω or the square of the motion amplitude X_{0d} .

The equation above is only valid with the presence of spring stiffness k , as shown in the middle figure of Fig. 21.4 which gives:

$$E_d = \pi \Omega c X_{0d}^2 = 2\pi\zeta \frac{\Omega}{\omega_n} k X_{0d}^2 \quad (21.3)$$

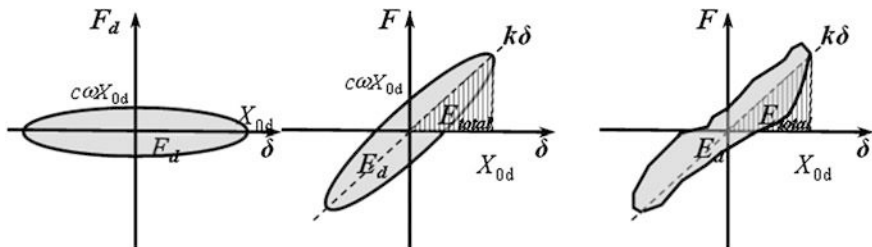


Fig. 21.4 Energy dissipation and strain energy by a viscous damper (left, strain energy is zero), hysteretic damper (middle) and measurement from real structures (right)

With total energy expressed as either the maximum potential/strain energy ($\frac{1}{2}kX_{0d}^2$) or the maximum kinetic energy ($\frac{1}{2}m\Omega^2X_{0d}^2$), one can measure the dissipation as the fraction of the total energy, which is called specific damping capacity:

$$\frac{E_d}{E_{total}} = \frac{2\pi\zeta \frac{\Omega}{\omega_n} kX_{0d}^2}{\frac{1}{2}kX_{0d}^2} = 4\pi\zeta \frac{\Omega}{\omega_n} \quad (21.4)$$

Realistic measurement of force response diagram (right figure Fig. 21.4) does not show a perfectly ellipse shape. However, damping level can be conveniently calculated by measuring the total energy (E_{total}) and energy dissipation (E_d) as shown in the right figure of Fig. 21.4.

The most convenient determination of equivalent damping ζ_{eq} is by measuring the harmonic force and harmonic responses at $\Omega = \omega_n$:

$$E_d = E_{total}4\pi\zeta_{eq} \frac{\Omega}{\omega_n} = E_{total}4\pi\zeta_{eq} \quad (21.5)$$

This gives:

$$\zeta_{eq} = \frac{E_d}{4\pi E_{total}} \quad (21.6)$$

The concept and calculation procedure of equivalent viscous damping can be extended to MDOF systems, in which each eigenmode has an individual equivalent viscous damping so that the dissipated energy in viscous damping matches the energy loss when the system vibrates at that eigenfrequency and corresponding mode shape. This is assumed by dynamic analysis using the modal superposition method. In many engineering structures, the damping level increases with the increase of eigenmode orders.

It should also be noted that, strictly speaking, equivalent viscous damping modeling is only valid for frequency domain analysis where the excitation is harmonic. However, practically, the use of this concept has been extended to model the damping in the form of modal damping, Rayleigh damping, and even non-proportional damping, for both time and frequency domain analysis.

21.4 Relationship Among Various Expressions of Damping

Damping can be represented by various parameters. The relationship of damping expressed by the different parameters is summarized as [5]:

$$\eta = 2\zeta = \frac{2c}{c_n} = \frac{2c}{2\omega_n m} = \frac{1}{Q} = \tan \varphi = \frac{\delta}{\pi} = \frac{D}{2\pi U} = \frac{\Delta\omega}{\omega_n} \quad (21.7)$$

where η is the loss factor; ζ is the ratio of critical damping; c is the viscous damping coefficient; c_n is the critical viscous damping; ω_n is the resonant frequency; Q is the amplification factor; $\varphi = \Delta t \cdot \omega$ is the phase angle between cyclic stress and strain; δ is the logarithm decrement of transient responses; D is the energy dissipation per cycle; U is the stored energy during loading; and $\Delta\omega$ is the frequency space determined from the half-power bandwidth point down from the resonance peak.

21.5 Practical Damping Modeling for Dynamic Analysis ...

It is rather difficult to explicitly implement and formulate detailed damping forces for an entire structure. Therefore, for the sake of both mathematical convenience and the representativeness of energy dissipation, practical damping models have to be adopted for a dynamic analysis. This mainly includes proportional (modal damping and Rayleigh damping) and nonproportional damping.

21.5.1 Modal Damping

Physically, an actual structure comprises abundant damping mechanisms all along it. However, even with the most convenient viscous damping modeling, it is still impossible to model all those mechanisms. Therefore, in most cases, modal damping is widely adopted in computer modeling to approximate the energy dissipation within the structure. In order for the modal equations to be uncoupled, the damping must fulfill the condition:

$$2\omega_i \zeta_i = \phi_i^T c_i \phi_i \quad (21.8)$$

where ζ_i is the viscous modal damping at i th eigenmode.

Damping ratios typically used in seismic analysis range between 1 and 10 % of critical damping [6]. Damping values depend on the construction materials, vibration amplitude, fundamental period and mode shapes, type of connections and the building configuration.

21.5.2 Rayleigh Damping

Damping effects can be conveniently accounted for in modal superposition analysis with the fulfillment of the equation above. However, in nonlinear dynamic analysis for which the mode shapes are changing with stiffness changes (especially for dynamic analysis with direct time integration methods), and with more realistic damping that is varied with frequency, Rayleigh damping is commonly used. It is a linear combination of the system's mass and stiffness as shown in Fig. 21.5 and the damping at frequency ω_i is:

$$c_i = \alpha m_i + \beta k_i \quad (21.9)$$

where α with the unit of s^{-1} and β with the unit of s are two coefficients to be determined from two given damping ratios at two specific frequencies of vibrations.

αm_i and βk_i , namely mass proportional and stiffness proportional damping, respectively, are the simplest way to formulate a proportional damping matrix because the undamped mode shapes are orthogonal with respect to each of these.

α and β can be evaluated by the solution of a pair of simultaneous equations at two separate frequencies as follows:

With the orthogonality properties of mass and stiffness matrix, the equation above can be rewritten by inserting it into Eq. (21.8) as:

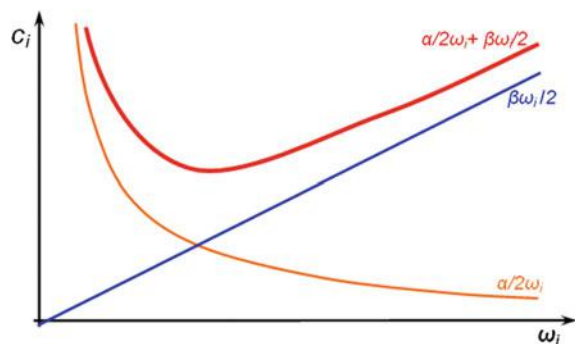
$$2\omega_i \zeta_i = \alpha + \beta \omega_i^2 \quad (21.10)$$

Rearranging the equation above, the relationship between modal damping (ζ_i) and Rayleigh damping is finally expressed as (Fig. 21.5):

$$\zeta_i = \frac{\alpha}{2\omega_i} + \frac{\beta\omega_i}{2} \quad (21.11)$$

It is normally recommended that the two specific frequencies for determining Rayleigh damping should ensure reasonable damping values in all the modes

Fig. 21.5 Rayleigh damping as a function of frequency



significantly contributing to the vibrations. At the frequency outside the range of these two frequencies, the damping will dramatically increase and the modal responses at the corresponding frequency range will almost be eliminated. Practically, this can be used to damp out the high and low frequency vibrations/noises that are outside the frequency range of interests. In many cases, the variation of damping ratio with frequency is not available, and one can then assume the damping at the two specific frequencies to be identical.

Even though Rayleigh damping is very convenient for modeling, it cannot be physically justified: the mass proportional damping introduces externally supported dampers, which do not exist for a fixed structure. As illustrated in Fig. 21.5, the stiffness proportional damping increases the damping dramatically at a higher order of eigenmodes, which is not physically true either, even if it is numerically efficient.

Example In a modal testing for an offshore structure, the two important eigenfrequencies are 0.12 and 0.23 Hz with the corresponding modal damping of 3 and 5 %. Establish the Rayleigh damping that will be used in a dynamic analysis using direct time integration methods.

Solution Using Eq. (21.11): $\zeta_i = \frac{\alpha}{2\omega_i} + \frac{\beta\omega_i}{2}$

$$3 \% = \frac{\alpha}{2(2\pi \times 0.12 \text{ Hz})} + \frac{\beta(2\pi \times 0.12 \text{ Hz})}{2} = 0.66\alpha + 0.38\beta$$

$$5 \% = \frac{\alpha}{2(2\pi \times 0.23 \text{ Hz})} + \frac{\beta(2\pi \times 0.23 \text{ Hz})}{2} = 0.35\alpha + 0.72\beta$$

Therefore, we obtain $\alpha = 0.0076$ and $\beta = 0.0658$.

21.5.3 Caughey Damping

If one needs to specify damping ratios at more than two eigenmodes, instead of Rayleigh damping, an extended or more generalized form of Rayleigh damping called Caughey damping can be used:

$$c = m_i \sum_{i=0}^{\eta-1} \gamma_i (m_i^{-1} k_i)^i \quad (21.12)$$

where γ_i is a constant, and η is the number of modes one wants to specify damping.

The modal damping ratio ζ_r at modes r higher than η can then be expressed as:

$$\zeta_r = \frac{1}{2} \sum_{i=0}^{\eta-1} \gamma_i \omega_r^{2i-1} \quad (21.13)$$

Similar to modal damping, the mass and stiffness matrices adopted in formulating Caughey damping also satisfy the mode shape orthogonality condition. However, Caughey damping normally results in a full matrix, which is computationally demanding for solving the equations of motions. Therefore, it is generally not practical to use this type of damping.

21.5.4 Non-proportional Damping

Both modal and Rayleigh damping are proportional damping, the corresponding damping matrices can be diagonalized in the modal matrix of the undamped system [7]. This provides computational convenience, but only applies for lightly damped structures with uniformly distributed damping mechanism, where off-diagonal terms in the damping matrix can be neglected. However, for many types of structures such as an offshore jacket structure shown in Fig. 20.4, the majority of the structural damping (Sect. 21.6.2) is concentrated at the joints between structural members, which in many cases does not result in a proportional distribution in damping [8]. Moreover, with the advent of external artificial dampers to mitigate the dynamic structural responses, the damping force values may be in the same levels as that of stiffness or inertia forces. The locally-installed dampers will also make the distribution of damping disproportional to that of mass or stiffness, and the equations of motions will then be coupled by means of undamped mode shapes. Furthermore, if various parts of a structure are constructed with different materials, the energy dissipation mechanisms in the different parts also vary, and the distribution of inertia and elastic forces will differ from one part to another. In addition, many structures have locally concentrated defects that also exhibit a non-uniformly distributed damping through the structures. All the factors above emphasize the significance of off-diagonal terms in the damping matrix and result in nonproportional damping matrices. In those conditions, both analytical and computer model must account for this effect in a more detailed and exact manner.

Similar to proportional damping matrices, nonproportional damping matrices can be obtained by a direct assembly of viscous damping matrices from different parts of a structure. This introduces a coupling between the undamped modal coordinate equations of motions. Note that the resulted modal coordinate damping matrix is a full matrix; therefore, the superposition method cannot be employed for structures/systems with nonproportional damping.

Generally, the equations of motions with non-proportional damping can be solved by using either a step-by-step integration of the geometric coordinate system or normal coordinates [9]. In addition, a so-called pseudo-force iteration method, developed by Claret and Vinancio-Filho [10], can also be used to solve the

equations by moving the off-diagonal coefficients to the right side (external force) of the equations of motions.

In case simplifications are applied to the system [11] or the total damping after the installation of the dampers is still not significant [12], the non-proportional damping may be simply modeled with proportional damping, typically with modal and Rayleigh damping, where the corresponding damping matrices can be diagonalized in the modal matrix of the undamped system [7], yielding uncoupled equations that can finally be solved by linear methods such as modal superposition. In all other cases, it was proven that if not considered, the analyses of real structures could lead to unrealistic results [12].

For computer modeling, the majority of commercial finite element analysis codes do not have the capability to solve the equations of motions with nonproportional damping. In order to overcome this challenge, user programd scripts have to be added to the codes. This also adds the physical requirement of data storage space for finite element based damping matrices and the combined system damping matrix.

21.6 Damping Levels for Engineering Structures

In the dynamic analysis of engineering structures, damping is one of the most difficult parameters to model with sufficient accuracy. It is contributed by various sources, typically from materials and the structural joints, of which the former is typically of hysteretic type and the latter is of friction type. As discussed previously, based on the equivalent energy loss, an equivalent viscous damping can be obtained. Even if the major contribution of damping is, in most cases, not of a viscous type, for a convenient modeling and the subsequent mathematical treatment, viscous damping is still the most widely used damping measure.

21.6.1 Material Damping

Material damping occurs due to energy dissipation in a volume of macro-continuous media. Hysteretic damping modeling is normally used to represent material damping. Detailed study of material damping is a task of solid physics and thus beyond the scope of the current book.

Table 21.1 illustrates typical values of material damping, expressed as a percentage of critical damping ($2m\omega_n$), for use with the modeling of viscous damping. It is noted that the damping for an un-cracked concrete structure is lower than for a cracked one, which is due to the damping mechanism of concrete: in the un-cracked state only viscous damping presents; in the cracked state, both viscous damping in the un-cracked compression zone and friction damping between the concrete and the reinforcing steel in the cracked tension zone contribute to the damping [13].

Table 21.1 Typical values of material damping [15]

Material	Damping of the critical (%)
Reinforced concrete	0.5 (uncracked)–3 (cracked)
Steel	0.05–0.4
Cast iron	0.15–1.5
Pure aluminum	0.001–0.1
Dural aluminum alloy	0.02–0.05
Manganese copper alloy	2.5–5
Lead	0.4–0.7
Natural rubber	5–15
Hard rubber	50
Glass	0.03–0.1
Wood	0.25–0.5

Generally, high damping materials usually exhibit low strength accompanied with high cost, and are therefore not suitable for structures with load carrying functions. An exception is manganese copper, which has high damping at a large strain level together with high strength.

21.6.2 Structural/Slip Damping

From Table 21.1, it is noticed that, for most of the engineering structures made of steel or concrete, the material damping is rather small. For example, with a damping of 0.0005 for steel, the amplification factor Q is 1000 (Eq. 21.7), which is not realistic. Therefore, there must be other damping sources to limit the dynamic responses.

The damping generated by structural joints is typically such a type of damping, which is called structural damping, or slip damping. Rather than generating damping in a volume of macro-continuous media as material damping does, slip damping arises from the boundary shear effects at joints between distinguishable parts or at mating surfaces. It can be a type of viscous in case of lubricated sliding, Coulomb friction or hysteretic. For Coulomb friction type of joint interface, efficient energy dissipation can be achieved with optimum interface pressure and geometry. However, a small deviation from this optimum condition may lead to a significant damping reduction. In addition, the optimum condition may result in serious corrosion due to wear. This leads to the development of other types of interface treatment, such as lubrication or adhesive separator at interface [14].

21.6.3 System Damping

System damping arises due to the energy dissipation from materials, joints, fasteners and interfaces. It is basically the sum of material and structural damping and in some cases also accounts for the radiation damping due to the radiation of waves in a continuous medium away from the area of excitations. This type of damping is usually what is actually used for modeling in a typical structural dynamic analysis.

21.6.4 Hydro- and Aerodynamic Damping

The relative velocity between the fluid and the encountering objects produces either hydrodynamic or aerodynamic damping, depending on the type of media. Both possess viscous characteristics and are categorized as fluid damping. See Sect. 10.1 for details of effects of hydrodynamic damping.

21.6.5 Typical Damping Levels

Table 21.2 shows the typical system damping value for land-based structures without accounting for the soil damping.

Table 21.3 illustrates typical values used for the modeling of offshore structures, which include the damping due to structures' energy dissipation, fluid-structure interactions (drag), and soil damping. It is noticed that, under extreme loading conditions such as significant seismic excitations or ocean wave load during a major

Table 21.2 Typical system damping for land-based structures and non-structural elements under seismic excitations [16, 17]

Structure type	System damping without soil damping (%)
Reinforced concrete	4 (uncracked)–7 (cracked)
Prestressed concrete	2–5
Reinforced masonry	4–7
Natural stone	5–7
Welded or bolted steel with friction connections	2–4
Bolted steel with friction connections	4–7
Large diameter (>304.8 mm) piping	2–5
Small diameter (\leq 304.8 mm) piping	1–3
Mechanical or electronic components	2–3
Storage tank (sloshing mode)	0.3–0.7
Storage tank (impulsive mode)	2–3
Transmission lines (aluminum or steel)	4–6

Table 21.3 Typical damping level for modeling of offshore structures [18, 19]

Structure type	Damping		
Jacket fatigue loading ^a	1–3 % for fundamental global bending mode and 2–3 % for higher-order mode		
Jacket extreme wave loading ^a	2–3 % for fundamental global bending mode and 3–4 % for higher-order mode		
Welded pile in soil ^a	0.6 (land-based)–1.4 % (offshore)		
Welded brace ^a	0.3 (land-based)–0.8 % (offshore)		
Welded mast (in air) ^a	0.8 %		
Bolted mast (in air) ^a	0.3–3 %		
Piled support structure (e.g. offshore wind turbine supporting structures) under extreme wave [19]	Radiation damping from wave creation due to structural vibrations	0.1–0.3 %	
	Hydrodynamic damping	0.1–0.2 %	
	Steel material damping (without ground connections)	0.15–0.3 %	
	Soil damping	Internal friction	2–7 %
		Geometric damping	0.6 (elastic)–0.8 % (plastic)
Jacket under seismic loading	Structural damping	0.5 (elastic)–2 % (plastic)	
	Hydrodynamic damping	0.5 (elastic)–1.5 % (plastic)	
	Soil damping	1 (elastic structure)–5 % (significant soil inelasticity)	
GBS under seismic loading	Structural damping	1 (elastic)–3 % (plastic)	
	Hydrodynamic damping	0.5 %	
	Soil damping	Under calculation	

^aSee Ref. [18], the damping includes both structural and hydrodynamic damping, but the soil damping is not accounted for

storm, a higher damping value due to structures' energy dissipation shall be used. This is because, under significant loading, the strain level is higher than that under a normal loading such as the one associated with high-cycle fatigue, leading to a higher damping level.

References

1. Oh SH, Kim YJ, Ryu HS (2009) Seismic performance of steel structures with slit dampers. *Int J Eng Struct* 31(9):1997–2008
2. Soong TT, Dargush GF (1997) Passive energy dissipation systems in structural engineering. Wiley, Chichester
3. Chen WF, Lui EM (2005) Structural engineering. CRC Press, Boca Raton
4. Jennings PC (1968) Equivalent viscous damping for yielding structures. *J Eng Mech Div ASCE* 94:131–165
5. Jia J (2014) Essentials of applied dynamic analysis. Springer, Heidelberg
6. Taranath BS (2005) Wind and earthquake resistant buildings: structural analysis and design. Marcel Dekker, New York
7. Caughey TK (1960) Classical normal modes in damped linear dynamic systems. *J Appl Mech* 27:269–271
8. Ewins DJ (2000) Modal testing: theory, practice and application, 2nd edn. Research Studies Press, New York
9. Qin Q, Lou L (2000) Effects of nonproportional damping on the seismic responses of suspension bridges. In: World conference on earthquake engineering, Auckland
10. Claret AM, Venancio-Filho F (1991) A model superposition pseudo-forces method for dynamic analysis of structural systems with non-proportional damping. *EESD* 20(4):303–315
11. Hwang JS, Wang SJ, Huang YN, Chen JF (2007) A seismic retrofit method by connecting viscous dampers for microelectronic factories. *Earthq Eng Struct Dyn* 36(11):1461–1480
12. Liang Z, Lee GC, Dargush GF, Song J (2012) Structural damping: application in seismic response modification. CRC Press, Boca Raton
13. Bachmann H, Ammann WJ, Deischl F, Eisenmann J, Floegl I, Hirsch GH, Klein GK, Lande GJ, Mahrenholz O, Natke HG, Nussbaumer H, Pretlove AJ, Rainer JH, Saemann EU, Steinbeisser L (1995) Vibration problems in structures—practical guidelines. Springer, Heidelberg
14. Harris CM, Piersol AG (2002) Harris' shock and vibration handbook, 5th edn. McGraw-Hill, New York
15. Benjamin Joseph Lazan (1968) Damping of materials and members in structural mechanisms, 1st edn. Pergamon Press, Oxford
16. Recommendations for revision of seismic damping values in regulatory guide 1.61 (2006) Brookhaven National Laboratory, US Nuclear Regulatory Commission Office of Nuclear Regulatory Research, Washington DC
17. ASME, BPVC Section III—rules for construction of nuclear facility components-division 1-appendices, 2007
18. Barltrop NDP, Adams AJ (1991) Dynamics of fixed marine structures, 3rd edn. MTD, London
19. Overall Damping for Piled Offshore Support Structures, Germanischer Lloyd Industrial Services GmbH, Hamburg, 2005

Chapter 22

Direct Damping Apparatus

22.1 Introduction

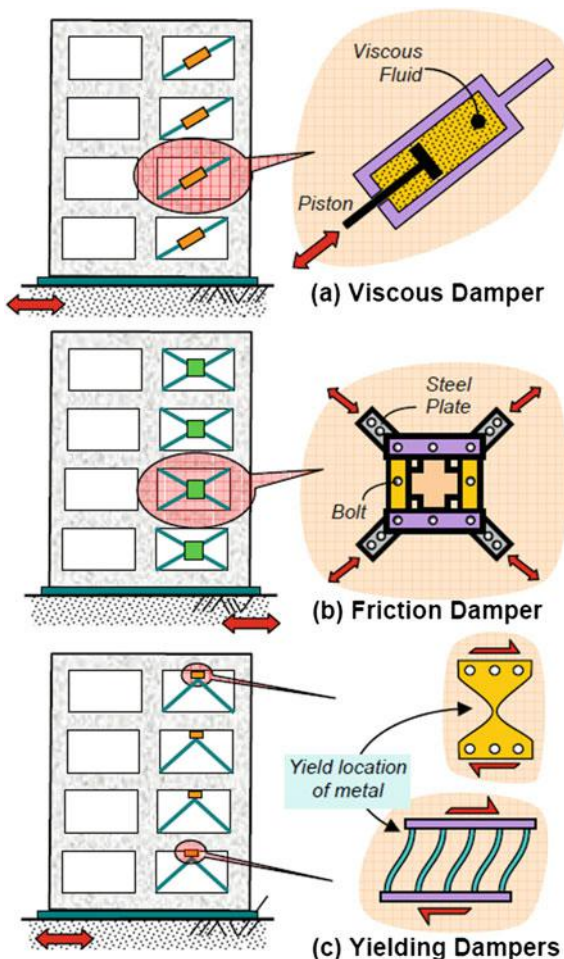
Originally used in the automobile industry to decrease the dynamic response and fatigue loading on vehicles, damping apparatuses have also been recognized as an effective technique to mitigate dynamic seismic (from 1990s) and wind induced (from 1960s) response for structures. They can sometimes decrease the seismic response by 60 % [1, 2]. It should be noted that damping apparatuses are normally not designed as static load bearing members but as a part of structural elements subjected to dynamic loading. Under low amplitude of dynamic loading, they have sufficient stiffness to behave elastically. However, dampers deform significantly when they are subject to large amplitude of dynamic loading, and in the meantime, absorb the seismic (or other types of dynamic loading) energy transmitted from other parts of the structure. Through the energy absorption, the loads applied on primary load bearing structural members can be dramatically decreased, and the safety of the structure is therefore ensured.

A wide range of damping apparatuses are commercially available. These may rely on viscous, dry friction, hysteretic effects or a combination of the effects above.

Figure 22.1 shows typical types of damper, namely viscous (sometimes viscoelastic) damper, frictional damper, and yielding damper, which will be elaborated later from Sects. 22.2 to 22.7. The load-displacement relationship for those types of dampers is shown in Fig. 22.2. Obviously, for all those types of dampers, the amount of energy dissipation or equivalent viscous damping increases with an increase in structural deformation. Therefore, to account for the time variation of structural deformation, it is recommended to use a dynamic time history analysis to assess the effectiveness of the damper design. Table 22.1 presents a comparison of important advantages and drawbacks of the four types of dampers, which will be further elaborated in the subsequent sections.

Most seismic design codes allow for the adoption of non-traditional energy dissipating devices, but require a dedicated analysis. In many cases, prototype

Fig. 22.1 Typical damping apparatus to mitigate seismic and other types of dynamic responses (courtesy of CVR Murty, Indian Institute of Technology, Kanpur, India)



testing is also required to demonstrate the performance of the damper when subjected to a number of load cycles expected during the maximum credible earthquake or design seismic ground motions.

The effectiveness of the energy dissipation by direct damping apparatus is strongly dependent on the deformation capacity of the structure. Therefore, for structures that suffer from inadequate seismic detailing, which translates into insufficient deformation capacity, the use of direct damping apparatus for mitigating seismic response may not be effective. To solve this problem, deformation enhancement measures may be taken to ensure the effectiveness of direct damping apparatus.

A review of these energy dissipation devices is presented by Hanson et al. [3].

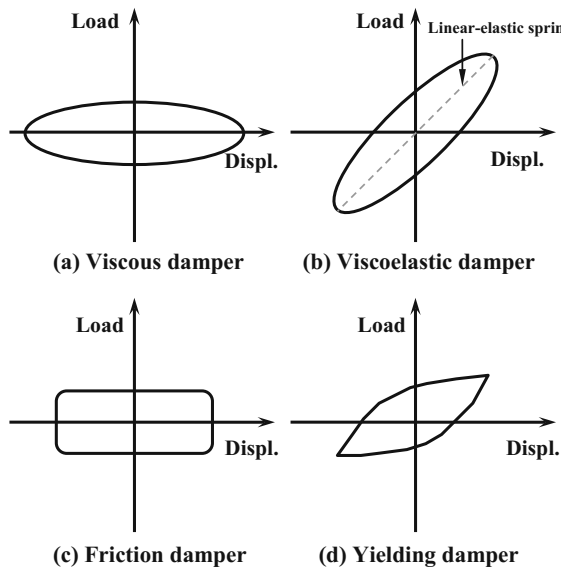


Fig. 22.2 Force-displacement curve for different types of dampers

Table 22.1 A comparison of important advantages and drawbacks of the four types of dampers [97]

	Viscous damper	Viscoelastic damper	Friction damper	Yielding damper
Advantages	Activated at low displacements	Activated at low displacements	A significant amount of energy dissipation per load cycle	Stable hysteretic behavior
	Minimal restoring force	Provides restoring force	Insensitive to ambient temperature	Long term reliability
	For linear damper, modeling of the damper is simplified	Linear behavior allows for simplified modeling of the damper		Insensitive to ambient temperature
	Properties are largely independent of frequency and temperature			Materials and mechanical behavior are familiar to engineers
	Proven design in military applications			

(continued)

Table 22.1 (continued)

	Viscous damper	Viscoelastic damper	Friction damper	Yielding damper
Drawbacks	Possible fluid seal leakage (reliability concern)	Limited deformation capacity	Sliding interface conditions may change with time (reliability concern)	Dampers damaged after an earthquake may require a replacement
		Properties are frequency and temperature dependent	Strongly non-linear behavior may excite higher modes of vibrations	Non-linear plastic behavior may require non-linear analysis
		Possible debonding and tearing of viscoelastic material (reliability concern)	May require non-linear analysis Can induce permanent displacement if no restoring force mechanism is available	

22.2 Viscous Damper

22.2.1 Introduction

Viscous dampers, as shown in Fig. 22.3, absorb energy via fluid (typically silicone fluid) flow through orifices. They are extensively used in automotive and aerospace industries. Their applications can also be found on many new engineering structures and retrofits in seismic zones or areas where potentially significant dynamic loads exist for bridge and building structures, nuclear power plants, offshore oil rigs, aerospace and military hardware, canal lock buffers, etc. They are one of the most widely used damping apparatuses for mitigating dynamic structural responses.

Viscous dampers are connected to the structure in three typical ways:

1. Damper installation in the floor (deck) or foundation.
2. Connecting dampers in stern pericardial braces.
3. Damper installation in diagonal braces.

Figure 22.4 shows the construction of a Taylor viscous damper, which comprises a stainless steel piston with a bronze orifice head and an accumulator. The flow through the orifice with high velocity is compensated by a passive bi-metallic thermostat that allows the operation of the damper over a wide range of temperature, from -40 to 70 °C. The force in the damper is generated by a pressure differential across the piston head. This process generates heat that is radiated into the surrounding air, thus dissipating energy. Note that since the fluid is



Fig. 22.3 Viscous dampers installed on a steel frame structure

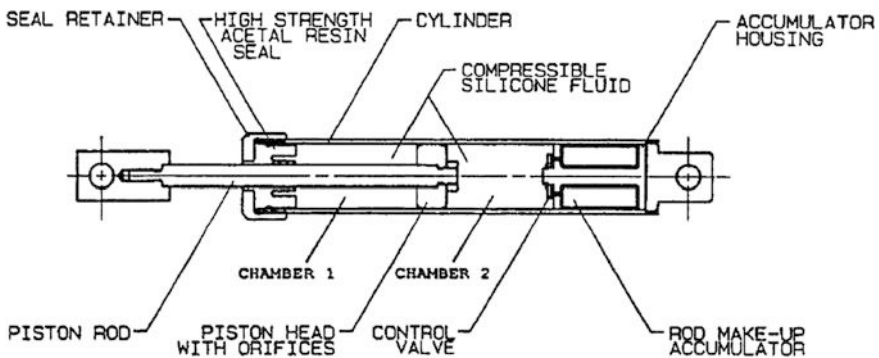


Fig. 22.4 Construction of a Taylor viscous damper [87]

compressible, the viscous fluid volume can be reduced by the product of the travel distance and the piston rod area, which causes a restoring force prevented by the accumulator [4]. The damping force produced by this type of damper can be calculated as:

$$F_d = c \cdot |v|^{\alpha} \operatorname{sgn}(v) \quad (22.1)$$

where c is the damping constant; v is the piston velocity; $\operatorname{sgn}(\cdot) = \text{signum function}$; and α is velocity exponent (orifice coefficient) determined by the piston head orifice design, and it is typically obtained from experiments, ranging from 0.3 to 2.0.

The physical model corresponding to the equation above is a viscous dashpot as shown in Fig. 22.12b.

An α value of less than 2.0 can be achieved through specially shaped orifices to alter the flow characteristics with the fluid speed. Depending on the design requirement, viscous damper can be designed to have damping force with either a linear ($\alpha = 1$) or a non-linear relationship with the speed of piston velocity.

For mitigating seismic response, it is normally required that $\alpha \approx 1$, because in this condition the viscous device can develop excessive damper forces in structures with long periods of vibrations subject to intense ground motions, which induce large structural velocities.

However, for applications with extremely high velocity shocks similar to those encountered in the near fault seismic ground motions, α may be tuned to 0.5. This can be controlled by the piston head, which utilizes specially shaped passages to alter the flow characteristics with fluid speed, as previously described. It is noted that a viscous damper cherishes this characteristic only for motions below a cut-off frequency determined by the design of the accumulator valve. Above this cut-off frequency, both the stiffness and energy dissipation capacity of the viscous damper dramatically increase [5]. This helps to significantly mitigate the dynamic response at high frequency range through both damping and stiffening, while still effectively damping out lower frequency vibration response.

$\alpha = 2.0$ is achieved using cylindrical orifices, but such a high α value is not desirable when the seismic excitations comprises significantly high velocity components.

Under steady-state harmonic motions, the viscous damper's force-displacement loop for the linear case ($\alpha = 1$) is elliptical as shown in Fig. 22.2a. By observing Fig. 22.12b, it is clearly shown that the response of the viscous dampers is out-of-phase (a 90° phase angle) with the response on primary structures, i.e. the peak of damper force occurs when the displacement is zero, and vice versa. Therefore, the damper generates zero force to the structural system at maximum displacement while delivering maximum force to the structure when the structure passes through a zero displacement state.

When α approaches zero, the hysteresis loop is a rectangular. The energy dissipated per cycle of steady-state harmonic motion can be calculated by integrating the equation above over the displacement [6]:

$$E_d = 4F_0u_02^\alpha \left[\frac{\Gamma^2(1 + \alpha/2)}{\Gamma(2 + \alpha)} \right] = \lambda F_0 u_0 \quad (22.2)$$

where F_0 is the peak force developed by the viscous damper; u_0 is the peak displacement across the damper; Γ is the gamma function; and λ is a parameter whose value depends exclusively on the velocity exponent α .

For a given force and displacement amplitude, the energy dissipated per cycle for a non-linear fluid damper is larger, by a factor λ/π , than that for the linear case

and increases monotonically with an decrease in velocity exponent α (up to a theoretical limit of $4/\pi \approx 1.27$, which corresponds to a zero α value) [7].

When a viscous damper moves at a given frequency ω , and a displacement amplitude u_0 , to dissipate the same amount of energy per cycle, the damping coefficient of the non-linear damper c_{nl} is larger than that of the linear damper c_l [8]:

$$c_{nl} = c_l \frac{\pi}{\lambda} (\omega u_0)^{1-\alpha} \quad (22.3)$$

22.2.2 Advantages and Drawbacks of Viscous Dampers

The obvious advantages of the viscous dampers can be summarized as follows:

1. Does not alter the stiffness and eigenperiod of a structure: note that if a structure's natural period is altered, its seismic response can be increased especially when the natural period is decreased due to an increase in stiffness. This is because viscous dampers do not contribute to the stiffness of the primary structure. Therefore, this type of damper is especially suitable for retrofitting existing infrastructures. However, the lack of change in the eigenperiod may also occasionally cause a resonance of a structure, which should be accounted for in the design of viscous dampers.
2. Substantial response reduction: can increase the structural damping by 20–50 % of the critical damping without introducing localized stiffness increase. Note that a typical structural damping without damper's installation ranges from 0.1 to 3 %. Viscous dampers can then significantly decrease the deflection and stress responses of structures, allowing the structure to remain elastic during strong earthquakes.
3. Decrease stress and deflection of primary structures simultaneously: this is because the response of the dampers has a 90° phase with the response on primary structure, as the forces on the dampers vary with the piston's velocity. For example, if a viscous damper is installed in such a way that it has an inclined force (such as a damper arranged along the diagonal brace orientation as shown in Fig. 22.3), the horizontal component of the damper force is out-of-phase with the displacement. Therefore, the induced peak column moments are less than those when the maximum damper force occurs at peak displacement. Note that, due to the hysteretic behavior for friction dampers (Sect. 22.6) and yielding dampers (Sect. 22.7), and strong viscoelastic behavior of viscoelastic dampers (Sect. 22.5), the damping forces for those types of dampers are developed in-phase with the maximum bending moments in columns, which can introduce substantial force on structures while reducing deflection. Therefore, even though they can effectively reduce the deflection, at the same time, the stress levels on the primary structures can also be elevated.

4. Proven design: viscous dampers have been successfully applied in abundant numbers of engineering projects. In addition, viscous dampers are also used by vehicle, military and aerospace industries. They can work under rather severe environments.
5. A viscous damper is small, compact and easy to install. It does not need auxiliary equipment or power.
6. With low or no maintenance cost, it can have a proven durability and effectiveness of more than 100 years [9].
7. Does not prevent a structure from returning to its original position after the earthquakes, which is a typical problem for plastic hinges, yielding dampers or friction dampers.
8. Insensitive to temperature changes [5] compared to viscoelastic dampers.
9. Can work as an isolation system to further increase the energy dissipation capacity of base isolators (Chap. 23). Experiments by Constantinou et al. [10] demonstrated that the installation of viscous dampers could decrease the deformation of base isolator and force transmitted to the superstructure. At sites with extremely strong ground motions, viscous dampers can be used together with base isolation systems to limit the displacements at isolation bearings.

However, the disadvantages of viscous dampers mainly lie in the fact that even small motions in a structure may cause seals to wear and fluid inside dampers to leak out. Moreover, it is challenging to maintain seals over the lifetime of a structure.

22.2.3 Engineering Applications of Viscous Dampers

Engineering applications using viscous dampers can be found on many infrastructures, such as the West Seattle Bridge, Woodland Hotel (Woodland, CA), CSUS Science II Building (Sacramento, CA), Bell Emergency Communications Building (Sacramento, CA) etc.

A very early application of viscous damper for mitigating seismic response was for the earthquake-resistant design of the San Bernardino County Medical Center in Colton, California (Fig. 22.5), located in a high seismicity zone. It was built in 1995

Fig. 22.5 San Bernardino County Medical Center



Fig. 22.6 Viscous dampers installed in San Bernardino County Medical Center. Each has an output force of 1456 kN and a maximum energy dissipation rate of 2.17 MWs [11]



and comprises five buildings with a total floor area of 84,000 m². The buildings were designed to remain occupied and in service during and after seismic transients of up to 1.52 m/s peak translational velocity. To mitigate the seismic response, in the initial concept design, base isolation using rubber bearing (Sect. 23.3) technique was chosen by the design team. However, the calculated deflection by installing rubber bearings was as high as ± 1.5 m, which was not acceptable. Therefore, 186 viscous dampers with non-linear damping ($F_d = c \cdot |v|^a \text{sgn}(v)$) were added to the buildings. Each has a ± 600 mm stroke, and a maximum output force of 1456 kN (at the maximum velocity level of 1.5 m/s), and a maximum energy dissipation rate of 2.17 MWs [11], for which the design was based on the experience from a previous US Military program used to attenuate weapons' ground attack motions on the MX Intercontinental Ballistic Missile. The added damping is around 45–50 % of the critical and the deflections are finally kept within ± 0.56 m [12]. This also enables the rubber bearing to re-center when strong ground motion ceases. Figure 22.6 shows the viscous damper for installation. It is noted that other types of dampers that were hysteretic or of yielding material type would cause a large offset due to their essentially hysteretic response.

BC Place Stadium was built in 1983 as the world's largest air-supported stadium. In 2010, the stadium was closed for a major renovation and reconfiguration. During the renovation, Taylor Devices Inc. USA in conjunction with Teratec Inc. Canada was responsible for the design and installation of viscous dampers for seismic protection. In total 96 dampers were installed on the frames of the primary structure, they have a maximum output force of either 2000 kN with 60 mm stroke or 1500 kN with 50 mm stroke. After the renovation, the stadium was reopened in 2011 as the world's largest cable supported retractable roof stadium (Fig. 22.7). In addition, it can also be used as an emergency regional shelter.

Due to the excessive lateral vibrations of the bridge caused by people walking across the London Millennium Footbridge, a total of 37 viscous dampers were installed on this pedestrian bridge to mitigate the vibrations. The majority of these



Fig. 22.7 BC Place Stadium in Vancouver with new roof (photo credit: Yvrphoto)



Fig. 22.8 Viscous dampers were installed on the London Millennium Footbridge [88]

dampers are situated beneath the bridge deck supported by transverse members as shown in the left figure of Fig. 22.8. Viscous dampers were also installed in the planes between the cables and the deck at the piers to increase the damping of the vertical bending vibration and coupled vertical-torsional modes of vibration (right figure in Fig. 22.8).

It is worth mentioning that the viscous dampers were even designed to mitigate the response to nuclear attack. During the Cold War, they were used by the military as a cost effective method to protect missiles against both conventional and nuclear weapon detonation. For large structures, extreme high damping is desired to

decrease the transient shock. The shock from a near missile weapons detonation can contain free field velocity of 3–12 m/s, displacement up to 2 m and accelerations up to 1000 times of gravity [11]. As an example, viscous dampers were installed in North American Air Defence Command (built in 1984) in Wyoming to mitigate structural responses due to weapon attack.

The well-known manufacturers of the viscous dampers are Taylor (<http://www.taylordevices.com>) and Enidine (<http://www.enidine.eu/>).

22.3 Viscous Damping Walls

Viscous dampers can also be constructed in the form of viscous damping walls. The left figure in Fig. 22.9 shows the arrangement of a viscous damping wall in the main frame [13, 14] developed by Sumitomo Construction Co. Ltd. in Japan. It consists of an outer steel casing (with two vertical walls facing each other with a small gap) attached to the lower floor and filled with a highly viscous fluid (the viscosity ranges from 3000 to 100,000 at a temperature of 30 °C). An inner moving steel plate hanging from the upper floor is contained within the steel casing. The viscous damping force is introduced by the relative velocity between the two floors. The viscous damping wall is installed in a pattern so that the accumulation of axial force in the columns caused by the viscous damping wall and the rotation of the viscous damping wall can be avoided, thus keeping the movement in a horizontal shear mode.

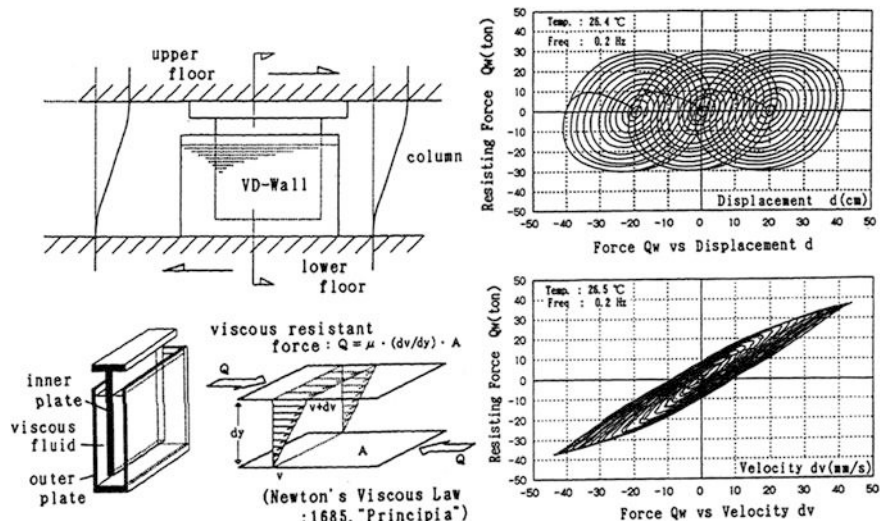


Fig. 22.9 Diagram of viscous damping wall mechanism (left), its force-displacement relationship (upper right) and force-velocity relationship (lower right) [14]

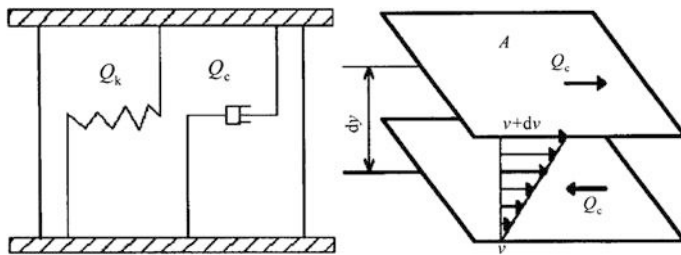


Fig. 22.10 Physical modeling of a viscous damping wall [89]

The upper right and lower right figure in Fig. 22.9 show typical hysteresis loops and force-velocity relationship of the system. By observing the hysteresis loop, it can be found that the viscous damping wall can efficiently dissipate energy. Furthermore, it can be seen that when the viscous damping wall works together with elastic frames, they exhibit a viscoelastic behavior, which can be expressed by the Voigt model shown in the left figure of Fig. 22.10. The total resistance force Q_w can then be calculated as the summation of the viscoelastic restoring force Q_k and the viscous damper force Q_c (Fig. 22.10):

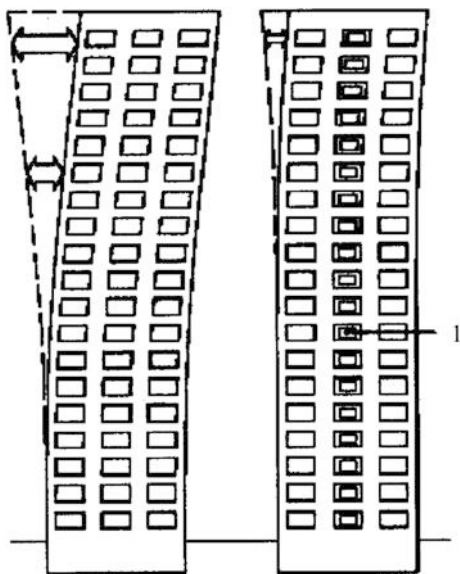
$$Q_w = Q_k + Q_c = cA \frac{\delta^{1+\beta}}{dy^2} + cA \left(\frac{dv}{dy} \right)^\alpha \quad (22.4)$$

where c is the damping constant; A is the area of inner plate that is submerged in the viscous fluid; δ is the relative displacement between the inner plate and the outer casing walls; β is a constant obtained from experiments; dy is the distance between the inner plate and the outer casing walls; v is the relative velocity between the inner moving plate and outer casing walls; and α is a velocity exponent typically obtained from experiments.

Figure 22.11 illustrates that the dynamic displacement response of a building can be significantly decreased when a number of viscous damping walls are installed from the top to the bottom of the building. Actually, the viscous damping wall has been utilized in mitigating seismic response of more than 30 building structures, mainly located in Japan. For example, in the 78 m high steel framed SUT-building (construction finished in October 1994) with a total construction area of 11,521 m² in Shizouka, 170 viscous damping walls were installed in all 14 stories above the ground (they are not installed in the two stories underground). Of these, 80 viscous damping walls are orientated in one horizontal direction, and the other 90 are orientated in the perpendicular direction horizontally. They provide around 20–35 % of damping (27 % in a 20 °C environment) for the building, which can reduce the seismic response up to 80 % based on the non-linear dynamic response analysis [14].

Viscous fluid in the casing is normally a polymer at room temperature but begins to decompose when the temperature exceeds 200 °C. Therefore, in the majority of

Fig. 22.11 Illustration of maximum deformation of a building subject to seismic motions for the case without (left) and with (right) the installation of viscous damping walls from the top to the bottom of the building [89]



engineering applications, fire protection for the viscous damping walls are constructed typically using steel reinforcement or calcium silicate insulation board.

It is worth mentioning that the viscous damping walls can also be applied to mitigate wind induced structural response. Through wind tunnel test of a 1:12 scale four story steel frame structures installed with viscous damping walls, Yeung [15] presented that the dampers can lead to a maximum 70 % reduction in dynamic response in terms of acceleration or displacement. They are most effective under mild wind conditions.

22.4 Cyclic Responses Among Structural Members Made of Elastic, Viscous and Hysteretic (Viscoelastic) Materials

When a structural member made of elastic material is subject to cyclic loading, all the energy stored during loading is returned when the loading is removed. As a result, there is no time lag between the responses and loading, i.e., the displacement of the structural member responds immediately (in-phase) to the cyclic load. The stress and strain time histories are also completely in phase (Fig. 22.12a). Furthermore, for linear-elastic materials, Hooke's law applies, where the stress is proportional to the strain.

Conversely, for structural members made of a purely viscous material, no energy is conserved after the loading is removed. The input stress disappears due to "pure

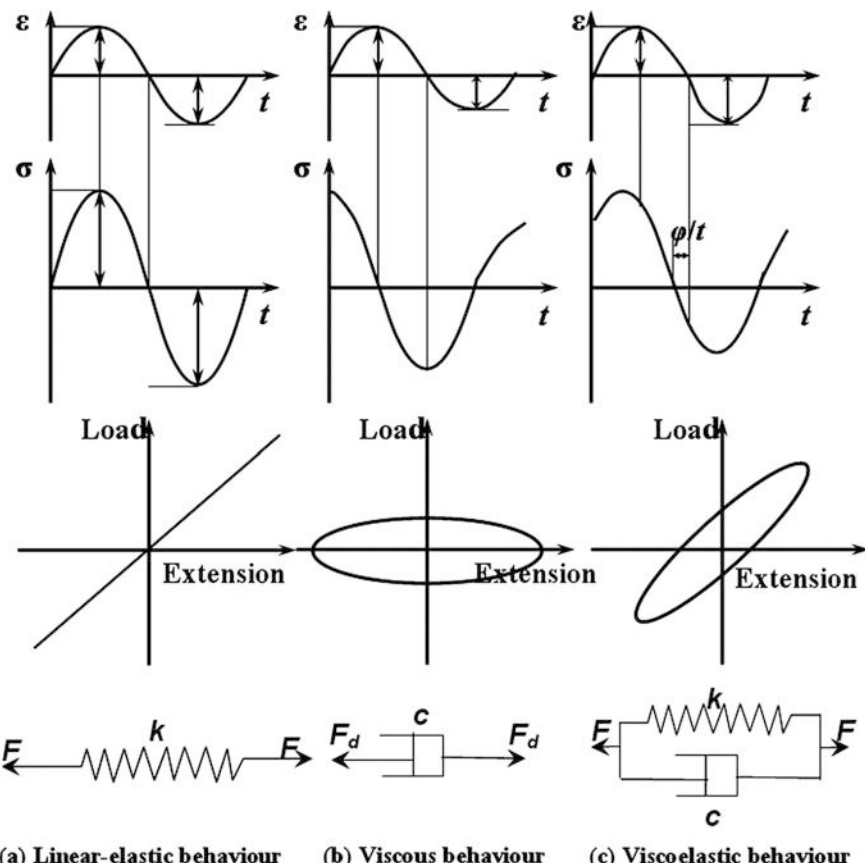


Fig. 22.12 Cyclic stress and strain time histories and load extension behavior for **a** linear-elastic, **b** viscous, and **c** viscoelastic materials; the stress denoted as σ can be either normal stress σ or shear stress τ , and the strain denoted as ε can be either normal strain ε or shear strain γ [90]

damping” as the vibratory energy is transferred into internal heat energy. The stress and strain time histories have a 90° phase difference as shown in Fig. 22.12b.

For damping that does not fall into one of the two categories above, the assumption of viscoelasticity may be used for modeling, which has both elastic and viscous properties as shown in Fig. 22.12c.

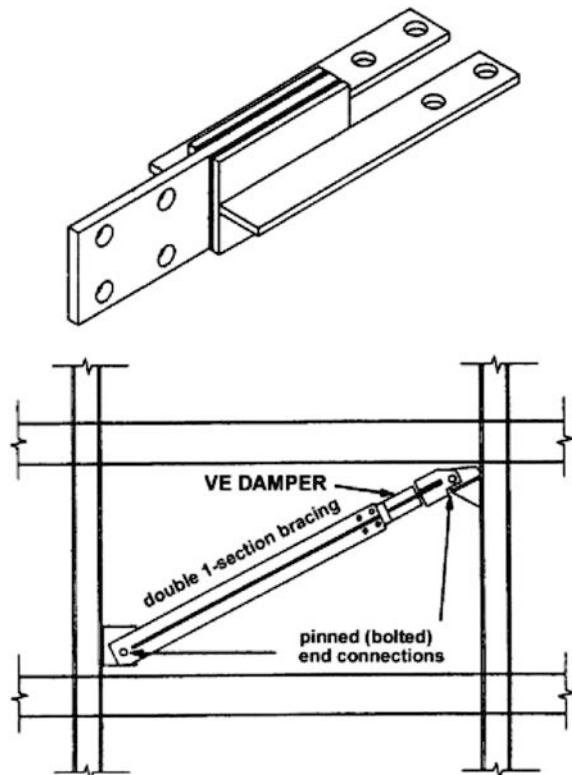
22.5 Viscoelastic Damper

22.5.1 General

Viscoelastic dampers served as one of the earliest types dampsers successfully applied to engineering structures [16], and are now widely used as an efficient measure to mitigate dynamic response on structures and mechanical components. They are usually made of two viscoelastic layers (acrylic polymers) bonded between three parallel rigid surfaces as shown in Fig. 22.13. Through the shear action of the viscoelastic layers, their damping behavior is controlled.

As their name suggests, viscoelastic dampers have an output that is somewhere between that of a viscous damper and an elastic spring, and they return to their original shape after each cycle of deformation and dissipate a certain amount of energy as heat. Figure 22.2b shows the force-displacement loop for a typical viscoelastic damper. It is clearly shown that a major portion of force is in-phase with the displacement. Under high level seismic inputs, the spring response dominates, producing a response that increases column stresses at any given deflection. Viscoelastic dampers not only directly add damping to a primary structure, but also

Fig. 22.13 An illustration of a viscoelastic damper and installation details [17]



contribute to an increase in stiffness and therefore alter the eigenfrequency of the primary structure to a certain extent. It is noted that the latter effect does not exist for viscous dampers as discussed in Sect. 22.2.2.

Viscoelastic damper can be used either at the beam-column connections or as a part of diagonal braces. Their performance on mitigating dynamic response is satisfactory for both steel and concrete structures. The lower figure in Fig. 22.13 shows an example of viscoelastic damper and its installation as a part of a frame brace.

Through experimental tests, Aiken and Kelly [17] showed that the performance of viscoelastic dampers measured with inter-story drift reductions is slightly better than that of friction dampers (Sect. 22.6). The ratio of inter-story drift between the viscoelastically damped structure to the traditional moment resisting frame ranges from 0.5 to 0.9. However, due to the limited stiffness contribution of the dampers, the base shear forces of the two are about the same.

Due to the development of tensile stresses in the damper, several delamination failures of viscoelastic dampers have been reported [17]. To prevent delamination, bolts may be used to clamp the damper [18].

The material of viscoelastic layers generally exhibits viscoelastic solid behavior with both its storage and loss of moduli being dependent on frequency, temperature as well as the shear strain level [18]: with an increase in temperature or shear strain, both the storage and loss of shear moduli decrease. Both moduli increase with an increase of frequency. Experiments have also showed that the damper properties remain more or less constant when the strain level is below 20 % for a given temperature and frequency [19, 20]. Among these effects, the temperature dependency is a major concern for designing viscoelastic dampers. This can be the most serious problem with viscoelastic devices: an unacceptable increase in force at low temperatures coupled with an accompanying overloading of the bonding agent used to “glue” the viscoelastic material to its steel attachments. At high temperatures, unacceptable softening or reduction of output occurs. This thermal variance from high to low temperature can be in the range of 50–1 [21].

Viscoelastic dampers can also be used at the beam-column connection in braced frames [22, 23], such as the one developed by the Lorant Group. As shown in Fig. 22.14, the connection consists of two steel plates interlocked by a single tooth. The shear force is transferred through a shear pin resulting in an energy dissipating device being subject to axial force only. If properly designed, this type of damper can lead to a reduction in the lateral displacements of around 30–60 %. This type of damper has been installed in a two-story steel structure in Arizona, US [22].

Since viscoelastic dampers do not cherish a threshold or activation force level, they dissipate energy for all levels of earthquake excitation. This makes them a suitable candidate for dissipating wind induced vibration as well.

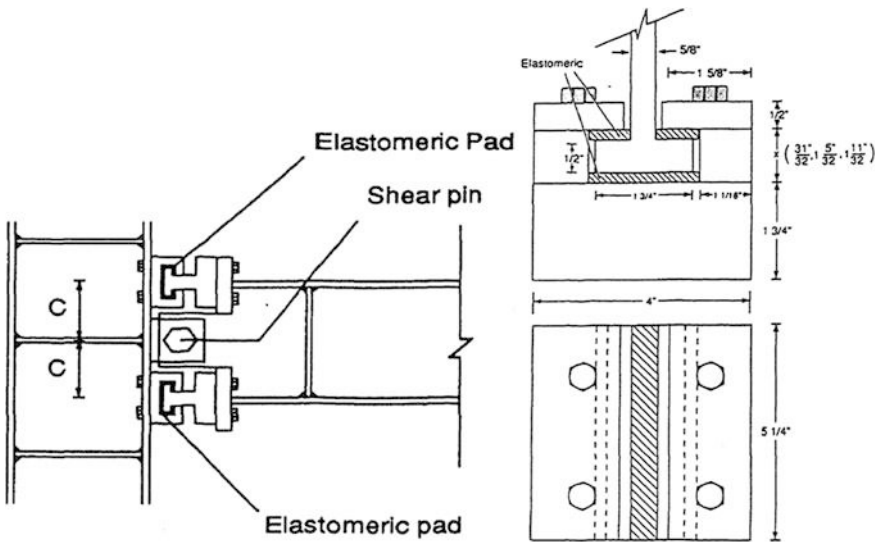


Fig. 22.14 Single tooth beam-column connection using viscoelastic dampers [23]

22.5.2 Design of Viscoelastic Dampers

The viscoelastic damper has both elastic and viscous properties as shown in Fig. 22.12c. When it is subject to a cyclic sinusoidal loading with a frequency of Ω , the shear stress history $\tau(t)$ generated between the viscoelastic layers in terms of the peak shear strain γ_0 and peak shear stress τ_0 can be expressed as:

$$\tau(t) = [G'(\Omega) \sin \Omega t + G''(\Omega) \cos \Omega t] \gamma_0 \quad (22.5)$$

where $G'(\Omega) = \tau_0 \cos \phi / \gamma_0$; $G''(\Omega) = \tau_0 \sin \phi / \gamma_0$; ϕ is the phase angle between the shear stress and shear strain as shown in Fig. 22.12c.

The equation above can be expressed as the summation of an in-phase elastic stiffness component in terms of $G'(\Omega)$, and an out-of-phase (not anti-phase) damping component in terms of $G''(\Omega)$:

$$\tau(t) = G'(\Omega) \gamma(t) \pm G''(\Omega) [\gamma_0^2 - \gamma(t)]^{1/2} \quad (22.6)$$

The equation above indicates that the viscoelastic damper works partially as an elastic spring and partially as a viscous damper. It specifies an elliptical stress-strain relationship shown in Fig. 22.12c. Within each cycle of loading, the dissipated energy per unit volume by the damper is equivalent to the enveloped area of the ellipse.

The equation above can be rewritten as:

$$\tau(t) = G'(\Omega)\gamma(t) + \frac{G''(\Omega)}{\Omega}\dot{\gamma}(t) \quad (22.7)$$

where the dot above a symbol indicates a derivative taken with respect to time t .

From the equation above, the damping ratio can be calculated as:

$$\xi = \frac{G''(\Omega)}{\Omega} \left(\frac{\Omega}{2G'(\Omega)} \right) = \frac{G''(\Omega)}{2G'(\Omega)} \quad (22.8)$$

In the equation above, $G'(\Omega)$ and $G''(\Omega)$ are typically referred to as shear storage modulus and shear loss modulus, respectively. They are generally functions of excitation frequency, shear strain, ambient temperature, and material temperature. They increase with an increase in excitation frequency, and decrease with an increase in temperature. For example, when the temperature varies from 21 to 38 °C, a change of 300 % in $G'(\Omega)$ and $G''(\Omega)$ can be expected [24]. However, experimental results presented by Chang et al. [20] have shown that a variation in the damper temperature due to dynamic excitation becomes negligible after several loading cycles as an equilibrium temperature is reached between the surroundings and the damper. Moreover, the damping is relatively insensitive to changes in excitation frequency and temperature.

Abbas and Kelly [25] proposed the following two equations to calculate the shear storage modulus and shear loss modulus for viscoelastic dampers:

$$G' = 16.0\Omega^{0.51}\gamma^{-0.23}e^{(72.46/T)} \quad (22.9)$$

$$G'' = 18.5\Omega^{0.51}\gamma^{-0.20}e^{(73.89/T)} \quad (22.10)$$

where γ is the shear strain of the damper material; and T is material temperature (in °C) of the viscoelastic dampers.

The relationship between $G'(\Omega)$ and $G''(\Omega)$ is also related to damping, which can be investigated through a calculation of loss factor (Sect. 21.4) η :

$$\eta = G''(\Omega)/G'(\Omega) = \tan \varphi \quad (22.11)$$

The equilibrium equation in terms of force on viscoelastic damper can be expressed as the summation of in-phase elastic stiffness component in terms of $k'(\Omega)$, and an out-of-phase damping component in terms of $c'(\Omega)$:

$$F(t) = k'(\Omega)\delta(t) + c'(\Omega)\dot{\delta}(t) \quad (22.12)$$

where $k'(\Omega) = AG'(\Omega)/h$; $c'(\Omega) = AG''(\Omega)/(\Omega h)$; A and h are the shear area and thickness of viscoelastic damper.

For framed structures, the damping ratio in case of horizontal viscoelastic dampers can be expressed:

$$\xi = \frac{\eta}{2} \frac{k_c}{k_s + k_c} \quad (22.13)$$

where k_c is the lateral stiffness of the dampers; and k_s is the lateral stiffness of the primary frame without viscoelastic dampers.

From the equation above, the added lateral stiffness of the dampers k_c can be calculated as:

$$k_c = \frac{2\xi k_s}{\eta - 2\xi} \quad (22.14)$$

If the dampers are located in the diagonal braces with an angle θ with the floor, the stiffness of the damper is $k_d/\cos^2\theta$.

The lateral base shear, which is proportional to the lateral stiffness of the structure, can be expressed as:

$$BS = BS_c + BS_s = 2 \frac{\xi}{\eta - 2\xi} BS_s + BS_s \quad (22.15)$$

where BS_c is the base shear shared by the viscoelastic dampers, and BS_s is the design base shear of the primary frame without dampers.

Therefore, the base shear taken by the primary frame can be expressed as:

$$BS_s = \frac{\eta - 2\xi}{\eta} BS \quad (22.16)$$

Based on the discussion above, Zhang and Soong [26] and Chang et al. [27] presented a practical procedure for the design of viscous elastic damper:

1. Determine the force demand/capacity ratios of the structural members for the original structure without dampers installed.
2. Determine the required damping ratio ξ to ensure that the response of the target structure remains elastic.
3. Determine the added stiffness k_c due to the installation of viscoelastic damper.
4. Determine the required damper area $A = k'(\Omega)h/G'(\Omega)$, in which the thickness of viscoelastic damper h can be determined such that the shear strain in the damper is lower than the ultimate design strain value.
5. Determine the quantity, size and location of the dampers.
6. Check the capacity of the structural members that are a part of the damper bay assembly using a force slightly higher than the damper force (with a scaling factor between 1.1 and 1.3).

7. Perform a seismic analysis using response spectrum method and carry out capacity control check; if the structural capacity is not sufficient, add more dampers.
8. Check the deflections of the structure and the inter-story drifts (if applicable) to ensure that they fulfil the requirement.
9. Perform non-linear dynamic seismic analyses, make a capacity control with a focus on the global structural stability and strains in the dampers.

Other methods to design viscoelastic dampers are also available, such as the one presented by Shen and Soong [28], using the concept of damage index introduced by Park and Ang [29]. Interested readers may read the references cited above.

22.5.3 Engineering Applications of Viscoelastic Dampers

In order to improve occupant comfort due to wind loading, viscoelastic dampers have been applied in many infrastructures worldwide, such as the previous 110 story World Trade Center in New York, and the 73 story Columbia SeaFirst Building in Seattle, Two Union Square Building in Seattle, Torishima Riverside Hill Symbol Tower, and Seavans South Tower in Japan etc. For example, the World Trade Center used thousands of viscoelastic dampers, attaching the lower truss chords to columns with rubber materials that can dissipate heat under building motion. These dampers were mostly designed for human comfort rather than for damage prevention or life safety.

Apart from their wide applications for reducing wind induced structural response, the applications of viscoelastic dampers on reducing seismic response have also begun to become common [30]. These are mainly related to the projects with retrofitting purposes. The first engineering project to use viscoelastic dampers for seismic applications was the retrofitting of the Santa Clara Civic Center Building in San Jose, California. After the Loma Prieta earthquake of 1989, the East Wing building of Santa Clara Civic Center was partially damaged. Viscoelastic dampers were then installed in a single diagonal bracing system.

Many companies such as 3M (<http://www.3m.com>) or Taylor Devices, Inc. (<http://www.taylordevices.com>) manufacture viscoelastic dampers.

22.6 Friction Damper

22.6.1 Introduction to Friction Dampers

Friction dampers absorb energy by the friction between surfaces rubbing against each other. The mechanism of friction damper is similar to the brake to stop the motion of equipment, vehicles, railway trains, airplanes etc. The friction damper

starts to dissipate energy when the friction force exerted on the friction interface exceeds the limiting frictional force. The damping induced by this type of damper is independent of loading velocity and ambient temperature, and they are typically installed in parallel to bracing members.

Figure 22.2c shows the force-displacement loop for friction dampers. It is shown that the loop possesses large rectangular hysteresis loops with negligible fade, similar to ideal elasto-plastic behavior, thus providing effective energy dissipation capacity. Moreover, friction dampers have a rather large initial stiffness and a nearly rectangular angular hysteretic behavior, i.e. the peak force of the friction dampers is almost constant with the change of displacement.

By carrying out experimental studies, Filiatrault and Cherry [31] and Aiken and Kelly [32] confirmed that friction devices could enhance the seismic performance of structures. Compared to conventional moment resisting structures, friction dampers can provide a substantial increase in energy dissipation capacity and reduced drift. By performing non-linear time domain analysis, Hakimi et al. [33] suggested that a decrease in higher story strength provides friction dampers with higher potential of energy dissipation. An optimum arrangement of story strengths provides the structure with an almost uniform relative drift and energy dissipation demands in the stories of the structure.

22.6.2 Pall Friction Damper

Pall friction damper is the most widely used type of friction damper. It was originally designed by PALL [34, 35] based upon the automotive brake, and can be installed either as a part of braces or as joints. As shown in Figs. 22.15 and 22.16, hinged links are arranged to form a quadrilateral shape, and two diagonal links are also hinged at the joints of the horizontal diagonal braces. Inside the quadrilateral region each of the diagonal links is made up of two separate parts that are partially superimposed by means of a friction brake joint located at the center of the damper

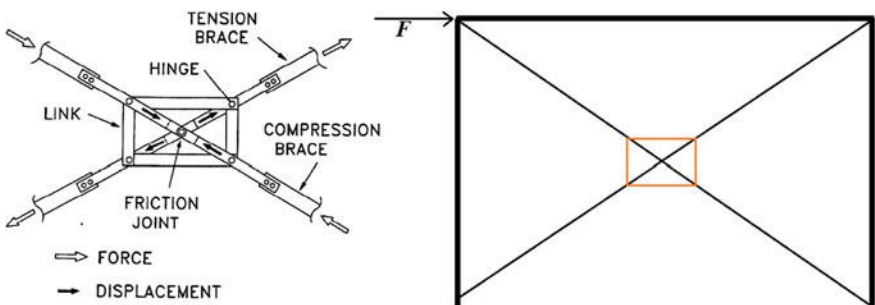
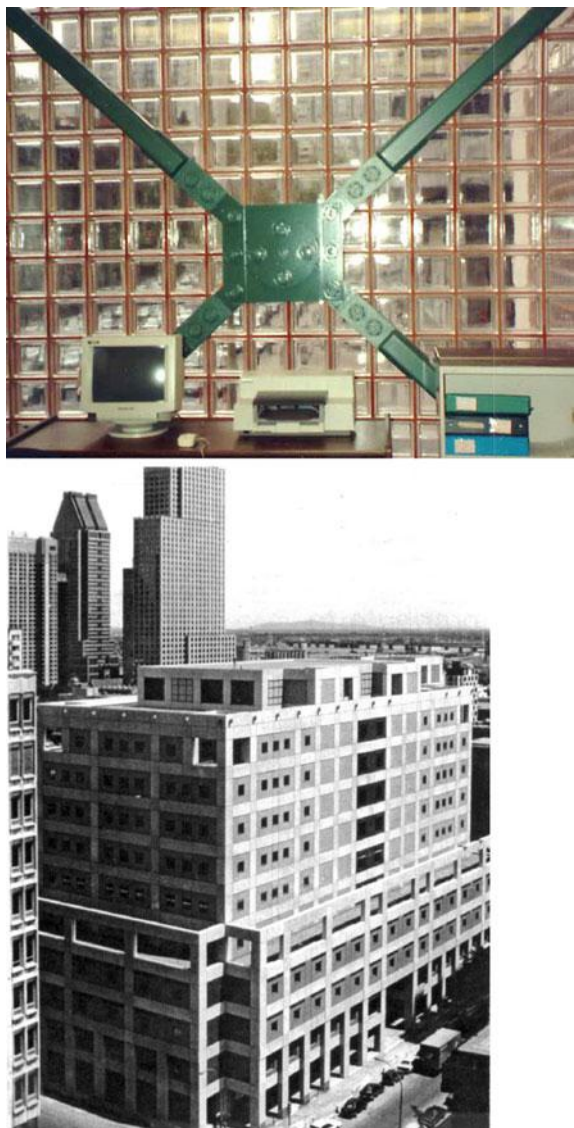


Fig. 22.15 Pall friction damper (left) [34] and its location (the *rectangle* in the middle of the right figure) in braced system

Fig. 22.16 Pall friction damper (*upper*) installed in the office at Concordia University Library Building (*lower*) [55]



[36]. Pall friction dampers are essentially formed by steel plates tightened together by means of high strength bolts with either axial or rotational deformation mechanism leading to a transformation of kinetic energy to thermal energy. Therefore, the maximum magnitude of friction force can be controlled by adjusting the friction coefficient of the sliding surfaces and the compression force of the tightened bolts, and is independent of the sliding velocity and the contact area of the sliding surface.

Pall friction based bracing has utilized the lever mechanism wisely, to transform relatively low global displacements of braced frames to local high deformations of dampers [33]. Before the friction damper works, both braces are active and behave elastically in tension and compression. When the seismic load begins to apply on the structure, the damper slips at a predetermined optimum load [37] before the yielding of the primary structure, the compression braces buckle and undergo large out-of-plane deflections, while the tension braces remain elastic within certain seismic load levels. With a further increase of seismic load, the external buckled braces remain subject to the same critical buckling load, while the tension brace begins to induce slippage at the friction joint [36], the related friction force is determined by tuning the clamp force and friction coefficient of the dampers. This, in turn, activates the four links that force the compression brace to slip. When the load is reversed, the brace originally in compression can absorb energy in tension. At the completion of a loading cycle, the resulting areas of the loops are identical for both braces.

It is interesting to mention that the first building with seismic dampers in North America was built with Pall friction dampers installed. They have successfully gone through sophisticated studies based on shake table tests [31, 38].

As shown in Figs. 22.15, 22.16 and 22.17, a friction damper is typically placed at the intersection point of X bracing, chevron bracing or one end of a single diagonal brace.

Pasquin et al. [39] carried out a series of non-linear dynamic analyses of frame structures based on two retrofitting concepts of Eaton's Building in Montreal, which is a ten story building originally built in 1925, comprising both concrete and steel frames with concrete slabs. One concept design is frame structures with friction dampers installed (FDF), and the other is concentrically braced moment frames (BMF, which are frames with concentric rigid bracing in moment frames). Both structures have the same member properties, except that the braced moment frames have twice the cross section area of brace members than those in friction damped frames. The damper slip loads are 700 kN at ground story, 600 kN for the next five stories, and 300 kN at upper stories. They found that FDF has a dual advantage over the BMF. Firstly, FDF attracts only 50 % of the seismic energy input of the stiffer BMF. Secondly, the friction dampers in the FDF dissipate about 50 % of the input energy. So the remaining energy left in the FDF is approximately



Fig. 22.17 A friction damper is typically placed at the intersection point of X bracing (left), chevron bracing (middle) or one end of a single diagonal brace (right) [55]

25 % of the energy in the BMF. The peak amplitude at the building roof in FDF is only 54 % of that in BMF. The base shear for buildings with FDF design is less than half of that in BMF. Moreover, while the forces in braces for FDF remain constant for all earthquake records, the forces in BMF are different for different earthquakes. Therefore, the use of friction dampers provides an engineered solution, i.e., the design engineers rather than ground motions control the maximum seismic forces.

A three story frame equipped with friction dampers was tested on a shake table at the University of British Columbia. It was shown that while the conventional frames were severely damaged at lower seismic ground motion levels, the braced frame with the friction dampers installed sustained ground motions with a peak acceleration of 0.9 g [40]. Similarly, a nine story three bay frame, equipped with friction dampers, was tested on a shake table at University of California at Berkeley. All members of the friction damped frame remained elastic subject to ground motions with a peak acceleration of 0.84 g, while the moment resisting frame would have yielded at about 0.3 g acceleration [38].

22.6.3 Other Types of Friction Dampers

Sumitomo Metal Industries in Japan developed another type of friction damper as shown in Fig. 22.18. This type of damper was originally adopted as a shock absorber for railway cars. The damper consists of copper pads impregnated with graphite in contact with the steel casing of the damper. The load on the contact surface is developed by a series of wedges that act under the compressive force of the Belleville washer springs (cup springs). The graphite serves as a lubricant between the contact surfaces and ensures a stable coefficient of friction and silent operation.

As shown in the lower figure in Fig. 22.18, Sumitomo dampers can be installed in frame structures by placing them parallel to the floor beams with one end attached to the floor beam above and the other end connected to a stiff chevron brace arrangement attached to the floor beam below.

Through an experimental study, Aiken and Kelly [17] presented Sumitomo dampers' efficiency to mitigate seismic responses, which is outstanding compared to that of a bare moment resisting frame. Furthermore, the energy dissipation was concentrated in the friction dampers rather than due to the inelastic action of the structural members.

Sumitomo dampers were installed in the 31 story Sonic City Office Building in Omiya and the 22 story Asahi Beer Azumabashi Building in Tokyo, Japan.

The low-cost slotted bolted dampers [41] are also used as a type of friction damper typically installed at one end of bracing members. It comprises a series of steel plates (a gusset plate, two back to back channels, and cover plates) bolted together with a specified clamping force as shown Fig. 22.19.

Cylindrical frictio

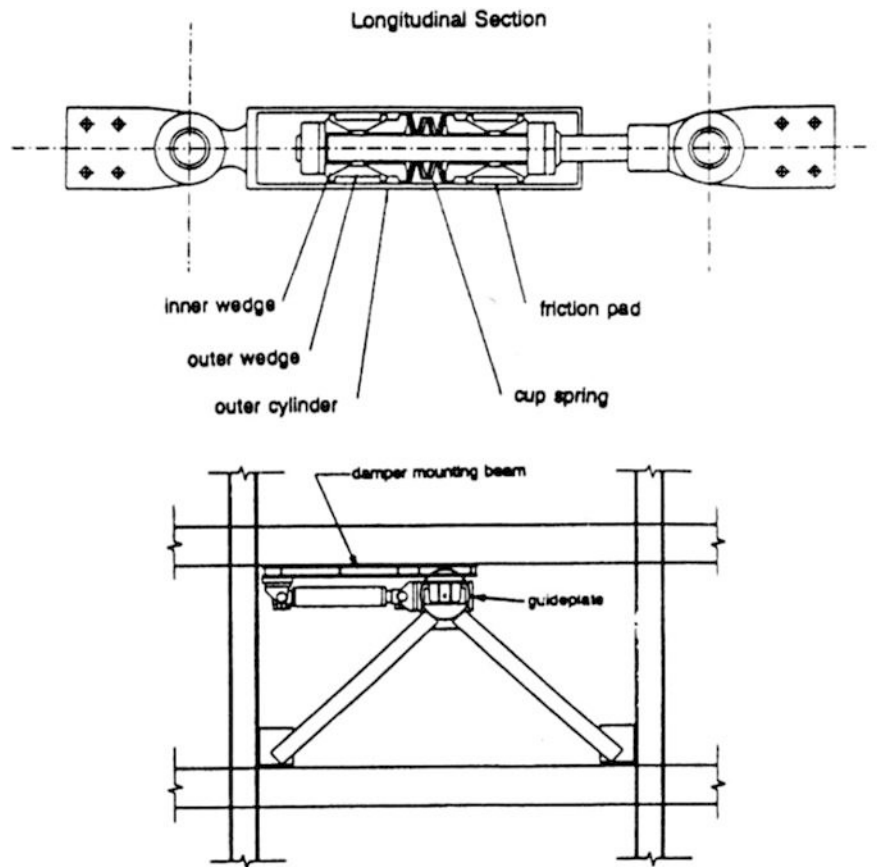


Fig. 22.18 An illustration of Sumitomo friction damper (*upper*) and its installation detail (*lower*) [17]

```
$getvar 01530,"c_page"<>
$^c_page+1<>
$tpgoto ^c_page^<>
$trun -1<>
$'*****<>
```

n dampers dissipate energy via sliding friction between internal solid shaft and the external hollow cylinder [42]. As shown in Fig. 22.20, the inner diameter of the solid shaft is slightly smaller than the diameter of the cylindrical element at the contact length L_0 . By heating the cylindrical part, its diameter will increase due to thermal expansion and the unheated shaft can easily be placed in the cylinder. This type of damper does not use bolts or any other pre-tension element to induce friction between contact surfaces.

Fig. 22.19 Slotted bolted connection [91]

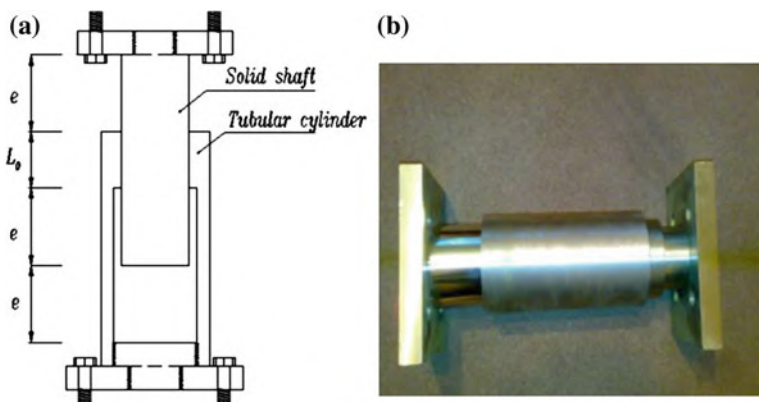
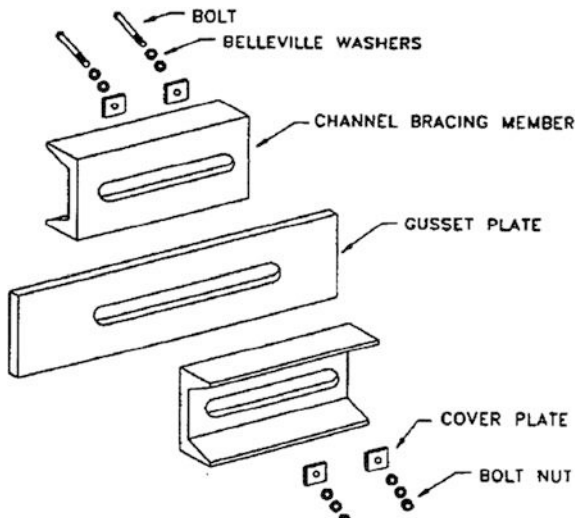


Fig. 22.20 An example of cylindrical friction damper [92]

Originally developed as a seismic restraint device to support piping systems in nuclear power plants, Energy Dissipating Restraint (EDR) [43], as shown in Fig. 22.21, is the only frictional device that generates non-rectangular hysteresis loops and a slip load proportional to displacement. In contrast to other friction dampers exhibiting rectangular hysteresis loops, EDRs are activated even by small excitations. They consist of sliding friction through a range of motions with a stop at the ends. The design of this friction damper is similar to the Sumitomo friction damper since this device also includes an internal spring and wedges encased in a

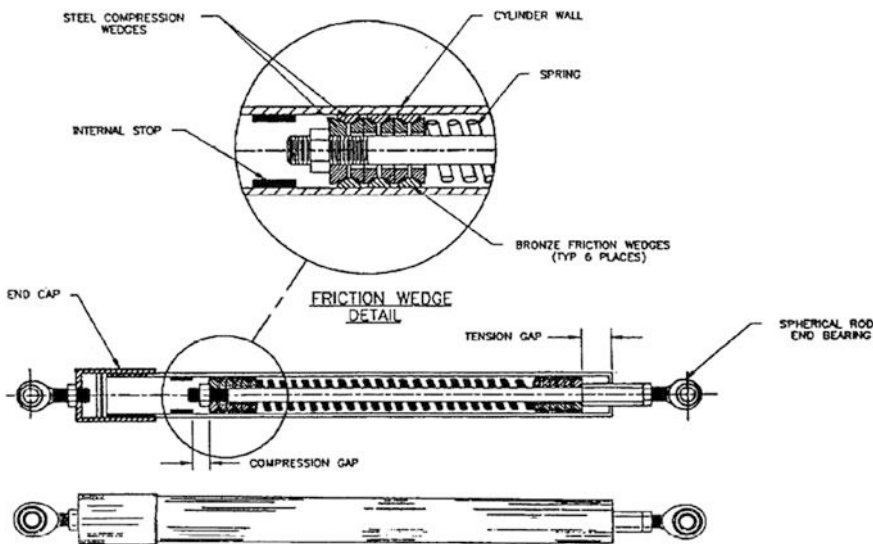
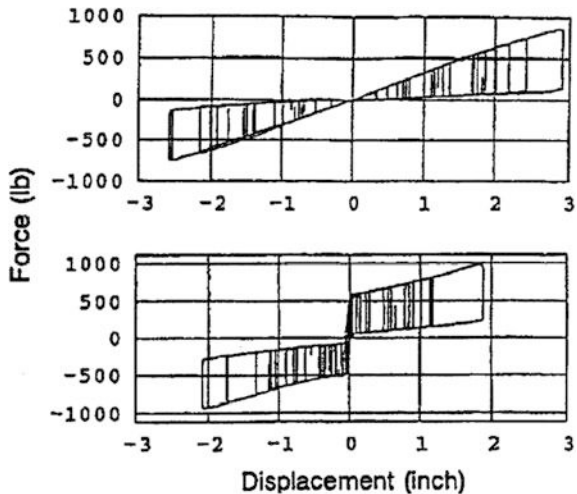


Fig. 22.21 External and internal views of energy dissipating restraint [43]

Fig. 22.22 Typical hysteresis loops for EDRs [93]



steel cylinder. The EDR utilizes steel and bronze friction wedges to convert the axial spring force into normal pressure on the cylinder, i.e., the compression force in the spring, acting on the compression and friction wedges, causes a normal force on the cylinder wall, and the normal force is proportional to the force in the spring. Different hysteresis behaviors, as shown in Fig. 22.22, can be reached by tuning the spring constant, configuration of the core, initial slip load, and gap size.

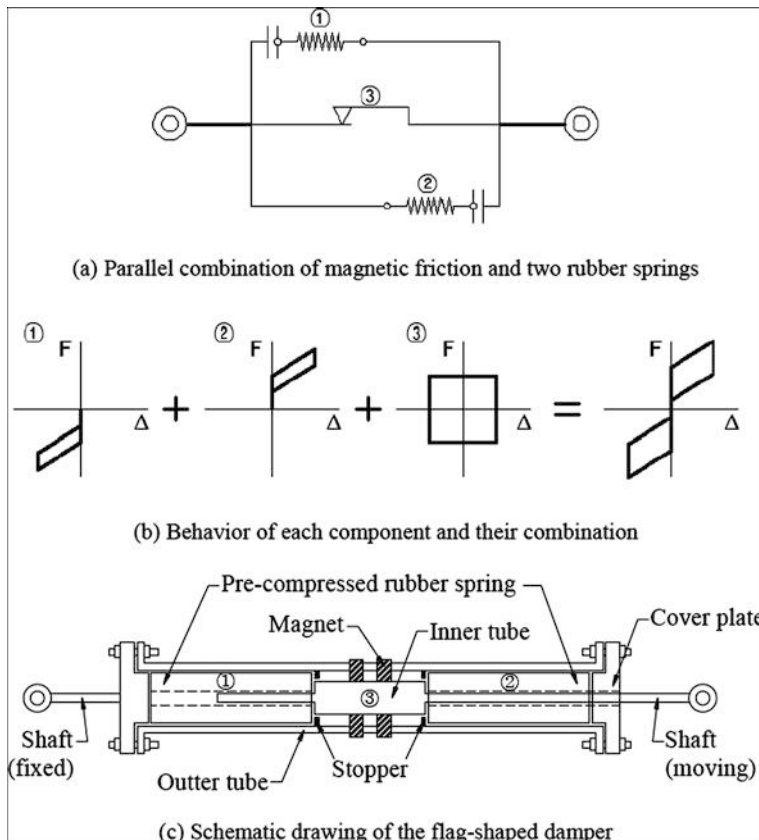


Fig. 22.23 Smart damper by combining magnets and rubber springs proposed by Choi [45]

Choi et al. [44, 45] proposed the concept of a smart damper by combining a magnetic friction damper and pre-compressed rubber springs separately as shown in Fig. 22.23. Two pre-compressed rubber springs and magnetic friction are arranged in parallel as shown in the upper figure of Fig. 22.23. The rubber springs work only in one direction, while the magnetic friction resists sliding in both directions. Thus, in moving to the left, spring ① and friction ③ are activated, and, in the reverse direction, spring ② and friction ③ are involved. The force-deformation behavior for each separate damper and the combined one is shown in the middle figure of Fig. 22.23. The lower figure in Fig. 22.23 shows design of the smart damper. Magnets are attached to the inner tube through holes in the outer tube. The rubber springs penetrate into the outer tube and are compressed by clamping of the cover plate; the stoppers provide resistance against compression. This procedure introduces pre-compression on the rubber springs. The rubber springs have a hole at the

Fig. 22.24 A design of friction damper devices (FDD) proposed by Mualla and Nielsen [46]

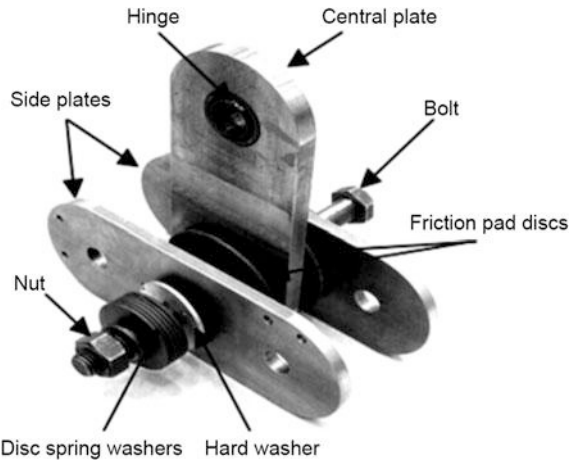
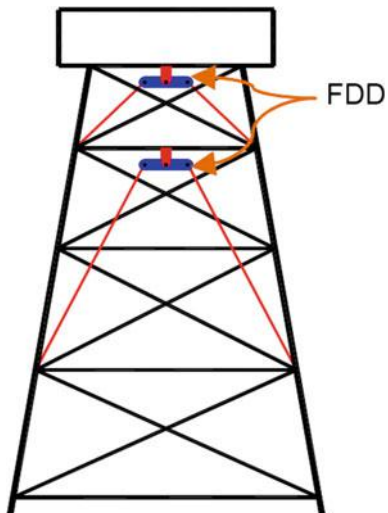


Fig. 22.25 Typical arrangement of FDD installed on an offshore jacket structure [47]



center; thus, the shaft moves through the hole. When the inner tube is moving, the magnets' sliding is restricted by the outer tube and friction occurs. When the moving shaft and inner tube move to the left, rubber spring ① is compressed by the inner tube, while spring ② remains uncompressed because of the stoppers. For movement in the reverse direction, spring ① recovers deformation up to the stopper, and spring ② is compressed when the inner tube comes into contact with spring ②. The pre-compressive force can be controlled by the bolt's torque at the cover plate, and the frictional force is proportional to the number of magnets.

Mualla and Nielsen [46] proposed a friction damper design as shown in Fig. 22.24, in which the main parts of the damper are the central (vertical) plate, two side (horizontal) plates, two circular friction pads placed in between the steel plates and bracing members. Komachi [47] also investigated the potential application of this type of damper in offshore jacket structures as shown in Fig. 22.25.

22.6.4 Pros and Cons of Friction Dampers

22.6.4.1 Advantages

The advantages of using the friction dampers are:

1. Subject to the dynamic loading, the natural period of structures installed with friction dampers varies with the amplitude of vibration, leading to wide-band frequency vibrations, thus avoiding resonance to a great extent.
2. Greater energy dissipation for a given force as shown in Fig. 22.2c. As stated by Pall [48], a much greater quantity of energy can be dissipated in friction than any other method involving the yielding damper, viscous or viscoelastic dampers. Hence, fewer Pall friction dampers are needed. Conversely, this requires less strength demand (exerts less force) for a given damping.
3. Simple mechanism and fool-proof in construction.
4. Easy to install, compact and narrow enough to be hidden in partitions.
5. Provides supplemental damping and supporting force for added stability.
6. Low manufacture cost.
7. Low maintenance cost because there is nothing to yield and damage, or leak. Therefore, they do not need regular inspection, maintenance, repair or replacement before (and perhaps after) earthquakes, but wearing of friction surface may be a concern [49].
8. Performance is independent of loading velocity and temperature.
9. Friction dampers' performance is not affected seriously by the amplitude, the frequency contents or the number of loading cycles.
10. The maximum force on a friction damper is constant and known, the maximum seismic force in the braces and connections is also known. Therefore, the design of these members is straightforward and economical [50].
11. They are not active subject to mild loading condition, such as service loads and mild wind or ocean wave loading. Hence, there is no possibility of failure due to fatigue before a significant loading.
12. After an earthquake, the building returns to its near original alignment due to spring action of an elastic structure.
13. Available for all types of bracing, including tension cross-bracing and expansion joints.
14. Can be incorporated in new or existing buildings of the appropriate type with little modification to the system.

15. Custom made, easily adaptable to any site condition, can be welded or bolted.
16. Even though friction dampers are painted to provide an additional seal in order to maintain the performance of the original installation, sliding surfaces are normally immune to corrosive attack, except in very aggressive environments, where corrosion may pose a problem.

22.6.4.2 Drawbacks

In order to dissipate a significant amount of energy, the slipping displacement needs to be high (dampers do not slip and dissipate energy for forces less than the slip force), and in the meantime, friction dampers do not have re-centering capacity. They must be incorporated into elastic systems that form a necessary restraint as the joints slip. Therefore, they can only be installed on structures mainly exhibiting elastic responses subject to dynamic loading. Examples of such type of structures include coupled shear walls, braced steel or concrete frames that are designed on the basis of strong-column-weak-beam when acting as a rigid frame under lateral loads. As masonry enclosures and concrete shear walls are rigid in shear, and do not permit the distortion needed, friction dampers are normally not suitable to be used to mitigate dynamic response for these types of structures. Moreover, low rise framed buildings with metal cladding or panel walls will be expected to suffer some damage to the enclosure unless the attachment system is designed to permit the required movement. The wind loading applied on high rise buildings is in many cases more dominant to control the structural design than seismic loading, which makes friction dampers unsuitable. This is because if friction dampers are designed to exhibit slip for seismic forces, they would also slip under wind action [51]. Furthermore, due to the frequent and sudden change in the sticking-sliding conditions, high frequency impulse may be introduced in the structural response. In addition, as the dissipated energy of friction dampers are proportional to the slipping displacement, this can limit their use in cases where sudden impulses occur, and the resonance peaks cannot be properly mitigated in many cases. Finally, durability may be an important issue with a major concern of friction surface wearing. This is because the energy dissipation is quite sensitive to the coefficient of friction of the contact surfaces in friction.

As friction dampers have a constant friction force, they may not cope well with various intensities of ground motions.

During the service life of the friction damper, the normal pressure applied on the friction plate will be released due to the relaxation of tightening of force on the friction bolts. This may significantly influence the performance of the friction dampers.

During significant slippage, the generated heating may alter the frictional response by causing material softening or by promoting oxidation, even though this is not a concern if the slippage is relatively small.

22.6.5 Modeling of Friction Dampers

For a design of friction dampers, it is required that non-linear analysis must show that a structure installed with friction dampers performs equally well in seismic events as the same structure designed following seismic requirement designed by relevant codes.

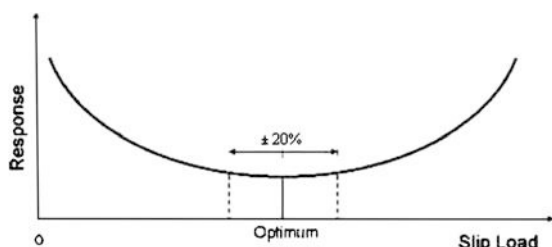
Since the hysteretic loop of the friction dampers is perfectly rectangular (Fig. 22.2c), similar to perfectly elasto-plastic material, the friction dampers can be modeled as fictitious plasticity element having an axial yield force equal to slip load and a member stiffness equal to brace stiffness. Friction dampers installed in chevron braces can be modeled as braces plus dampers. These dampers have non-linear yield force in shear equal to the slip load.

Moreover, for friction dampers installed in X-braced frames shown in Fig. 22.28, when tension in one of the braces forces the damper to slip, the mechanism shortens the other brace, thus preventing buckling. Therefore, in the next half cycle, the other brace is ready to force the damper to slip in tension. The analysis requires that each brace be modeled to slip (yield) in tension and slip in compression at almost zero load without buckling. Therefore, it is desirable to model the non-linear link element with different yielding forces for tension and compression. However, in FE analysis, it is preferred to input only one value of yielding regardless the sign for axial forces (tension or compression). As a simplification for analysis, the hysteretic loop of each tension brace can be modeled to be equal to the hysteretic loop of one single diagonal tension-compression brace having half of the slip load, even though the brace and the connections should be designed considering the full slip load.

22.6.6 Design of Friction Dampers

For an optimal design, a series of analyses should be performed to determine an optimum slip load of friction dampers to achieve minimum response [52]. Figure 22.26 shows a typical response-slip-load relationship for framed structure installed with friction dampers. As discussed in Sect. 22.6.4, selection of slip load should also ensure that after an earthquake, the structure returns to near its original

Fig. 22.26 An illustration of response-slip-load relationship [48]



alignment under the elastic action of the structure. Studies have also shown that variations of up to $\pm 25\%$ of the optimum slip load do not affect the response significantly. Therefore, small variations in slip load (8–10 %) over the service life of the structure do not warrant any adjustments or replacement of friction damper [53].

For a preliminary simple and rough estimation, as a structure and the installed friction dampers act in parallel, therefore they can be regarded as a dual system. By modeling the dual system as an SDOF frame with stiffness k_s and a damping device with stiffness k_d attached to the brace with stiffness k_b , the resultant stiffness of the entire system can be calculated as:

$$k_{bd} = k_b k_d / (k_b + k_d) \quad (22.17)$$

By assuming that the system behaves elastically, the equivalent viscous damping ratio, as elaborated in Sect. 21.3, can be calculated as:

$$\zeta_{eq} = \frac{E_d}{4\pi E_{total}} = \frac{2FR(SR - FR)}{\pi(SR + FR^2)} \quad \text{for } FR < SR \quad (22.18)$$

where FR is the ratio between slip loads and the total force exerted by the structure; $SR = k_{bd}/k_s$ is the ratio between the damper stiffness to the total structural stiffness.

According to the equation above, Fig. 22.27 shows a family of equivalent viscous damping ratio curves for a dual system varied with both FR and SR . By observing this figure, it is found that the higher the stiffness of the damper relative to the structure, SR , the higher the damping and the energy dissipation capability.

Fig. 22.27 Equivalent viscous damping ratio for a dual system [54]

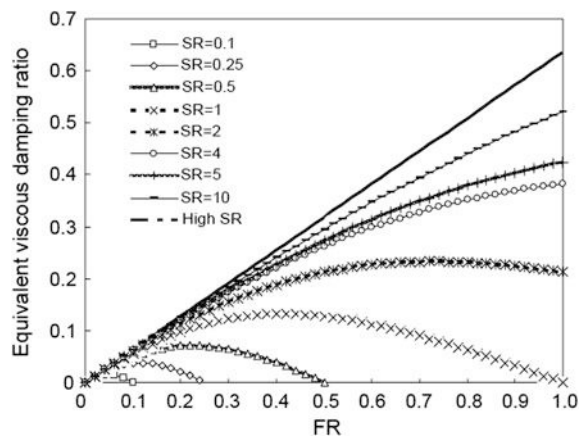
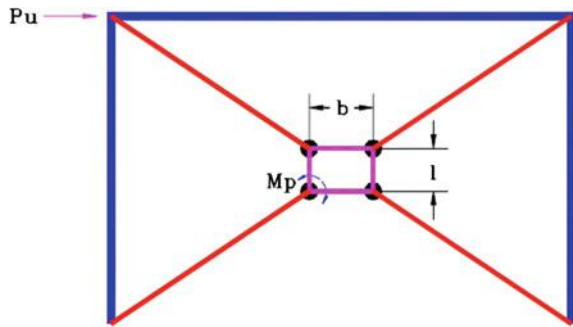


Fig. 22.28 Configuration of friction braced frames and related parameters [33]



Even though SR larger than two is a recommended value for design, in many cases, it is difficult to achieve values of SR well above unity and so damping of the order of 10–15 % is a reasonable target. Moreover, for a realistic value of the stiffness ratio, SR , there is an optimum value of the brace strength to the elastic structure force. An increase of SR causes an increase in stiffness [54].

Based on the analysis, the design of friction dampers and yielding dampers (Sect. 22.7) may follow the procedures below:

1. Perform a dynamic or response spectrum analysis for the structure without dampers to determine the target damping ratio for which the structure response remains elastic.
2. Determine the stiffness of braces and the dampers as presented above.
3. Estimate the value of FR from Fig. 22.27 or the equation above using the target damping ratio determined in step 1.
4. Calculate the slip load (for friction dampers) or yield load (for yielding dampers) based on the FR value calculated in step 3.
5. Perform non-linear analysis and structural capacity control based on parameters determined above.

As shown in Fig. 22.28, for Pall friction damper installed in X-braced frames, the plastic resisting moment of each friction connections M_p due to the external frame lateral force P_u can be calculated as:

$$M_p = P_u b^2 l / 4(b^2 + l^2) \quad (22.19)$$

It should be noted that in case the friction dampers are added to the compression diagonals, the assembly is required to possess bending rigidity comparable to that of the member. When damped braces are added to existing rigid frames, connection details need careful attention, as does the revised distribution of forces in the structural system [54].

It is worth mentioning that before delivery to site, each friction damper is recommended to be load tested to ensure proper slip load, and variations in slip load from design value should not be greater than $\pm 15\%$.

22.6.7 Engineering Applications of Friction Dampers

The utilization of the friction dampers can be found in more than 100 structures worldwide, for both concrete and steel buildings, elevated water towers, and for new construction and retrofit of existing structures. Examples include the Boeing Commercial Airplane Factory in Everett, WA, Sonic City Office Tower in Omiya, Asahi Beer Tower in Tokyo, and Moscone West Convention Center in San Francisco. Significant savings of construction cost have been achieved due to the installation of friction dampers. For example, friction dampers have been used for the seismic protection of more than 80 major building projects, including the Boeing Commercial Airplane Factory at Everett, WA—the world's largest building in volume, in which the use of friction dampers led to a saving of more than US\$30 million. The City and County of San Francisco chose Pall friction dampers for the seismic control of Moscone West Convention Center and saved US\$2.25 million, compared to the case using viscous dampers.

Figure 22.16 shows an example of Pall friction damper installed at the Concordia University Library, which consists of a ten story and a six story building interconnected with an atrium, with a total floor area $50,000 \text{ m}^2$. Instead of using concrete shear walls, steel braces are installed. To ensure the ductility of the building, 143 Pall friction dampers with 600–700 kN slip load were installed at the junction of each steel cross-bracing in the concrete frame, which minimize the dependence on the member ductility and provide more flexibility in space. Moreover, since bracing was mainly installed to carry horizontal seismic loading rather than vertical gravity load, they do not need to be installed all the way down to the basement, thus allowing more flexibility and space for the underground parking in the basement. The utilization of friction dampers resulted in a net saving of 6.5 % of the structural cost, or 1.5 % of the total building cost of US\$65 million [55].

St. Vincent Hospital comprises five blocks of five story concrete frame construction, of which four were built between the 1890s and 1950s and one is a new construction. For the four old blocks, the demand of earthquake resistance is significantly higher than the existing structural capacity. Due to the tight budget and time schedule, instead of reinforcing the structures with concrete shear walls or rigid steel bracing, Pall friction dampers are installed in the steel bracing system. Different from constructing shear walls, the friction damper bracing system does not need to be vertically continuous as aforesaid. This gives flexibility in space planning and time schedule, which was particularly appealing. The design slip load of the friction dampers was 300 kN, and in total 183 friction dampers were used in all blocks [50].

Various manufacturers around the world produce friction viscous dampers, such as Enidine (<http://www.enidine.eu/>) and Pall Dynamics Limited (PDL) (<http://www.palldynamics.com/>).

22.7 Yielding Damper

22.7.1 General

Yielding dampers absorb energy through hysteretic behavior during plastic deformation of metallic components, and were originally proposed and tested by Kelly et al. [56]. Yielding dampers are relatively inexpensive, and are able to utilize flexural, shear or axial deformations. Through the installation of this type of damper, not only energy dissipation, but also the stiffness and strength of the primary structure can be increased.

Figure 22.2d shows the force-displacement loop for yielding dampers. It is clearly shown that the response of the yielding dampers is in-phase with the response on primary structures, i.e. the peak of damper force occurs when the displacement is at peak, and vice versa. This is different from that of the viscous damper, in which the viscous damper force is out-of-phase with the displacement.

The post-yield deformation range of the yielding dampers is a major concern that should be considered to ensure that the dampers can sustain a sufficient number of loading cycles without premature fatigue. Moreover, another concern is the stable hysteretic behavior of the yielding dampers under repeated inelastic deformation [4].

Similar to friction dampers presented in Sect. 22.6, yielding dampers are also force limited, highly non-linear, and their response is velocity independent. The design method and procedure for a dual system are almost identical as that of friction dampers, which has been presented in Sect. 22.6.6.

22.7.2 Types of Yielding Dampers

22.7.2.1 Eccentrically Braced Frame

Eccentrically braced frame presented in Sect. 20.5 is one of the most popular types of yielding dampers and has long been recognized and used to improve the seismic performance of structures [57]. In this type of damper, energy dissipation is primarily concentrated at specifically detailed shear links of eccentrically braced frames. These links represent part of the structural system that is likely to suffer localized damage in severe earthquakes [5]. However, the ability of braced frames to dissipate energy over extended periods is questionable because the repeated buckling and yielding of the braces may cause degradations in both stiffness and strength.

22.7.2.2 Yielding Steel Cross-Braced System

Tyler [58] from New Zealand proposed a yielding steel damper fabricated from round steel bars for cross-braced system as shown in Fig. 22.29. The compression brace disconnects from the rectangular steel frame to prevent buckling and pinched hysteretic behavior. Energy is dissipated through plastic deformation of the rectangular steel frame in the diagonal direction of the tension brace. Several modified designs using the form of cross-braced system have been utilized to enhance the seismic resistance of structures in Italy, such as a 29 story suspended steel building built in Naples, with floors hung from a central core with tapered steel yielding dampers acting as energy dissipaters between the core and the suspended floors.

22.7.2.3 Added Damping and Stiffness (ADAS) Dampers

Originally introduced by Bechtel Power Corporation, Added Damping And Stiffness (ADAS) dampers utilize a series of steel plates [with either hourglass (X-shape) as shown in Fig. 22.30, or a triangular form as shown in Fig. 22.31], which undergo distributed flexural yielding. By using rigid boundary members, so that the dampers will deform due to the movement of these two rigid plates located at the top and bottom, the steel plates intentionally designed to sacrifice deform in double curvature, and yielding takes place over the entire plate surface. The device can sustain repeated inelastic deformation by avoiding concentrations of yielding and premature failure. Even though the installation of ADAS can even increase the base shear force [5] as has been observed during a few shake table tests, ADAS dampers yield in a controlled and predetermined manner and also decrease the ductility demands of the primary moment resisting frame.

Figure 22.30 shows an ADAS damper consisting of multiple X-shaped steel plates. The plates are narrow at the middle and wide at the top and bottom. This leads to a situation in which the stress and strain along the plate height are almost uniformly distributed. Therefore, different parts of plate yield at almost the same

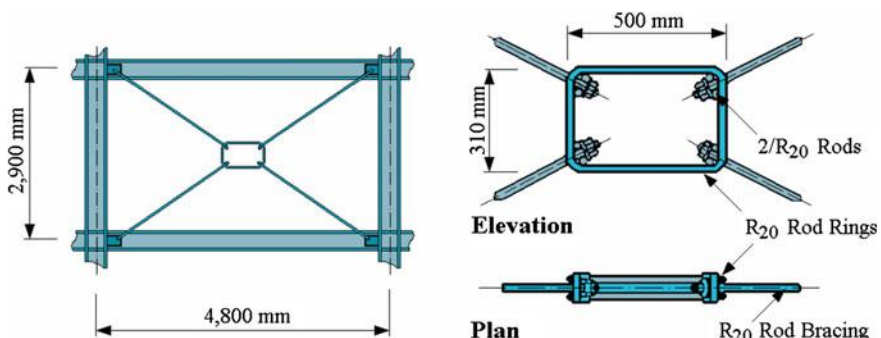


Fig. 22.29 Yielding steel cross-braced system [58]

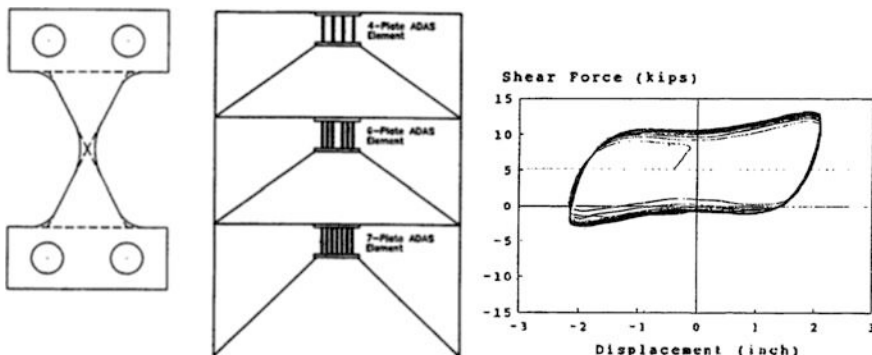


Fig. 22.30 X-shape added damping and stiffness (XADAS) damper installations (*middle*) on Chevron braces with X-shaped steel plate (*left*) [94] and their hysteresis loops (*right*) [95]

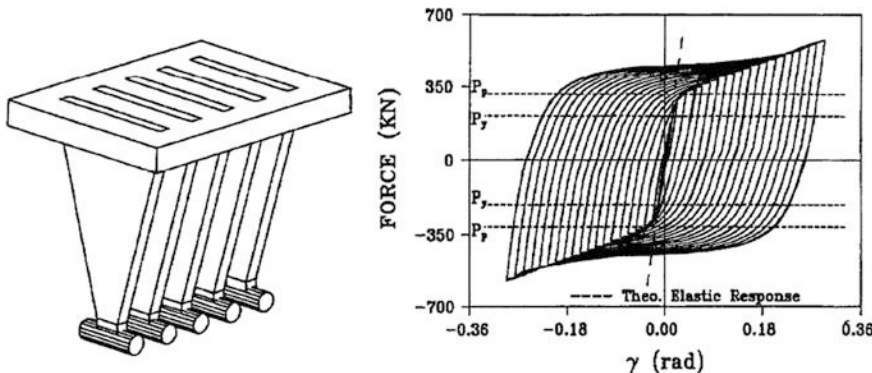


Fig. 22.31 Triangular added damping and stiffness (TADAS) damper and its hysteresis loops

time, and the energy dissipation capacity is therefore maximized. Actually, the stress at the middle of the plate is normally a little bit lower than that at other parts of a plate, i.e. when other parts of the plate yield, the middle of the plate is slightly below yielding, and this is helpful for re-centering structures after strong ground motions cease. Shake table tests of a three story moment resisting steel frame demonstrated that the installation of ADAS elements improved the performance of the frame by increasing its stiffness, strength, and ability to dissipate energy. The inter-story drift in the frame was reduced by 30–70 %. However, the ratios of base shears in the structure with ADAS installed to that without ADAS installed ranged from 0.6 to 1.25 because the shear forces are primarily resisted by the ADAS and their supporting braces [4]. The ADAS elements yield in a predetermined/controlled manner and relieve the frame from excessive deformation and plasticity development.

As mentioned previously, in addition to XADAS shown in Fig. 22.30, triangular plate yielding dampers (TADAS), as shown in the left figure of Fig. 22.31, were also used in building structures in the form of tapered or triangular ADAS elements [59], with typical hysteresis loops shown in the right figure of Fig. 22.31.

22.7.2.4 Seesaw Energy Dissipation System

Recently, Tagawa and Gao [60] proposed a seesaw energy dissipation system, in which the rotatable member moves similarly to a seesaw as shown in Fig. 22.32, thus converting horizontal displacement of the structure into rotational movement of seesaw mechanism. It utilizes a quasi-linear motion mechanism of three link members called a Chebyshev linkage. Dampers are installed underneath the seesaw to mitigate the structural vibrations. An important advantage of this system is that it enables the usage of steel rods or cables as bracing because the bracing members with pre-tension retain their tension during vibrations [61], thus avoiding compression buckling of the brace members, which allows a design of braces with a relatively small cross section area. A combination of steel yielding (slit) dampers with a seesaw damper is proposed by Tagawa et al. [62], which is shown in Figs. 22.33 and 22.34. Subject to lateral force F applied on the frame, the brace's tensile force acts on the seesaw member edge. The rotation of seesaw member around the pin forces the yielding dampers to deform, as shown in the right figure Fig. 22.33. The yielding dampers exhibit plastic deformation and dissipate energy. As mentioned previously, by providing pre-tension force to the bracing members, it is expected that both bracing members are in axial tension during the frame

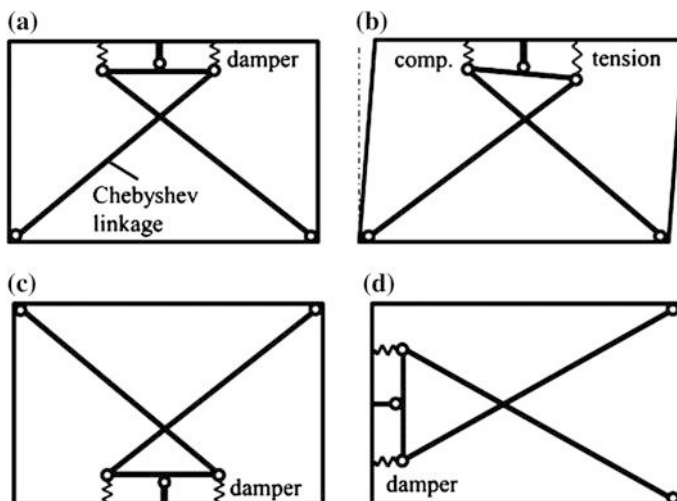


Fig. 22.32 Concept of seesaw energy dissipation system: **a** initial configuration, **b** deformed configuration, **c** bottom installation type, **d** vertical installation type [62]

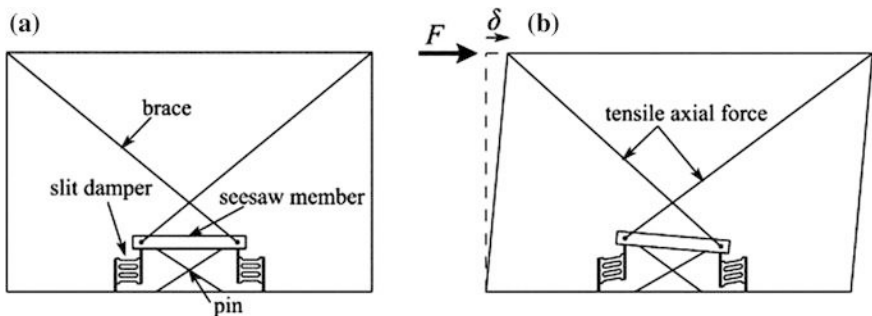
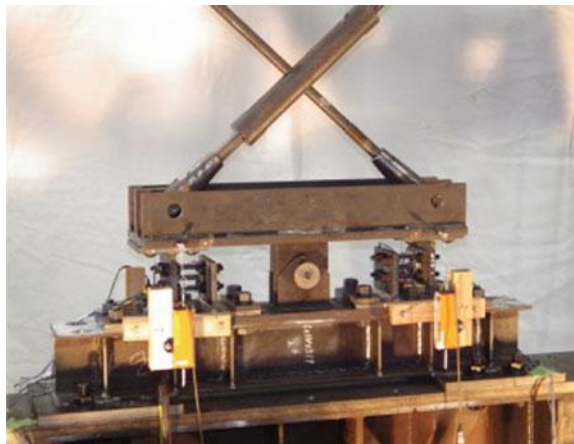


Fig. 22.33 Seesaw system with steel slit dampers: **a** initial configuration and **b** deformed configuration, the frame exhibits a lateral displacement δ subject to a lateral force of F [62]

Fig. 22.34 An example of seesaw system with steel slit damper [62]



deformation [60]. As an alternative, friction dampers rather than yielding dampers can also be used as dampers in a seesaw energy dissipation system [63].

22.7.2.5 Replaceable Shear Link Beams

As a type of yielding damper, shear link beams [64] were developed with an example shown in Fig. 22.35. Before or subjected to medium scaled seismic excitations, the shear link beams maintain a certain amount of stiffness and strength and are integrated as a part of the main structure to resist the external loading. However, subject to significant seismic motions, they exhibit significant plastic bending deformation in their middle or “fuses” section, so that a significant amount of seismic energy can be absorbed due to the metal yielding and subsequent hysteresis behavior. This will minimize the damage on the main structure with a

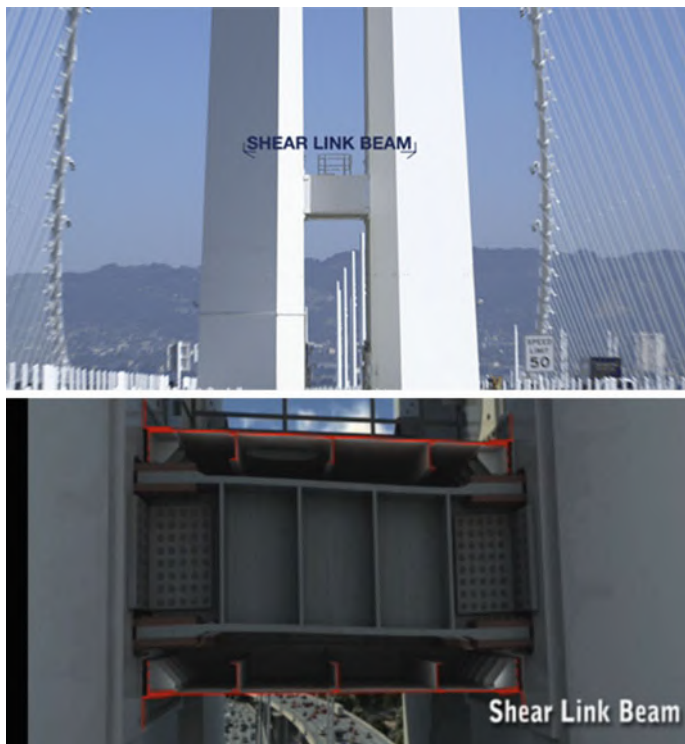


Fig. 22.35 Shear link beams installed in the Eastern San Francisco Bay Bridge (courtesy of California Department of Transportation) to absorb the seismic energy through their own plastic deformation

sacrifice of the “fuses” damages. The damaged “fuses” can then be removed and replaced.

Figure 22.35 shows that the shear link beams were installed to connect tower legs of Eastern San Francisco Bay Bridge, allowing the legs to move independently and be flexible, thus releasing even more seismic energy, and the flexibility of tower legs can also reduce the seismic forces transmitted to the bridge and towers.

Replaceable coupling beams, as shown in Fig. 22.36, can also be installed to connect the adjacent frames or shear walls. Under strong seismic loading, the “fuses” will absorb significant transmitted seismic energy, leaving the main structures (frames or shear walls) intact or experiencing minor damage. The “fuses” are normally made of steel or aluminum with a weak cross section and/or low yield strength. Figure 22.37 shows the failure mechanism of four kinds of coupling beam: (1) CSW: conventional RC coupling beams; (2) F1SW: a steel I-beam, whose web has a diamond-shaped hole; (3) F2SW: two webs of the steel I-beam, filled with lead between the webs; (4) F3SW: two round steel tubes, filling with lead inside the tube. In CSW, vertical cracks start to develop at the coupling beam’s end, and

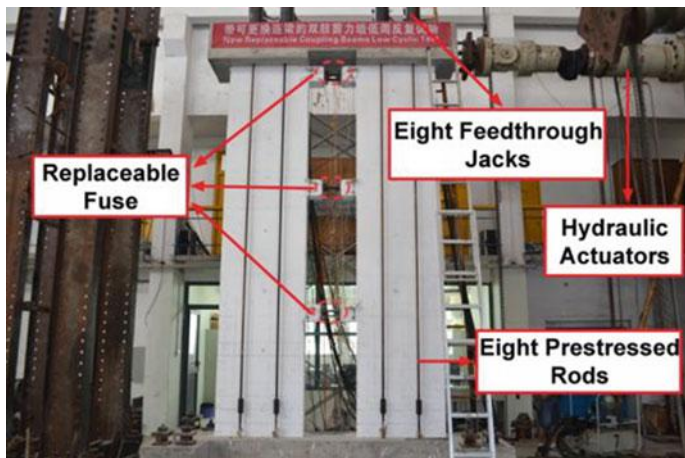


Fig. 22.36 Coupled shear wall with replaceable coupling beams (fuses) (courtesy of Xilin Lu, Tongji University)

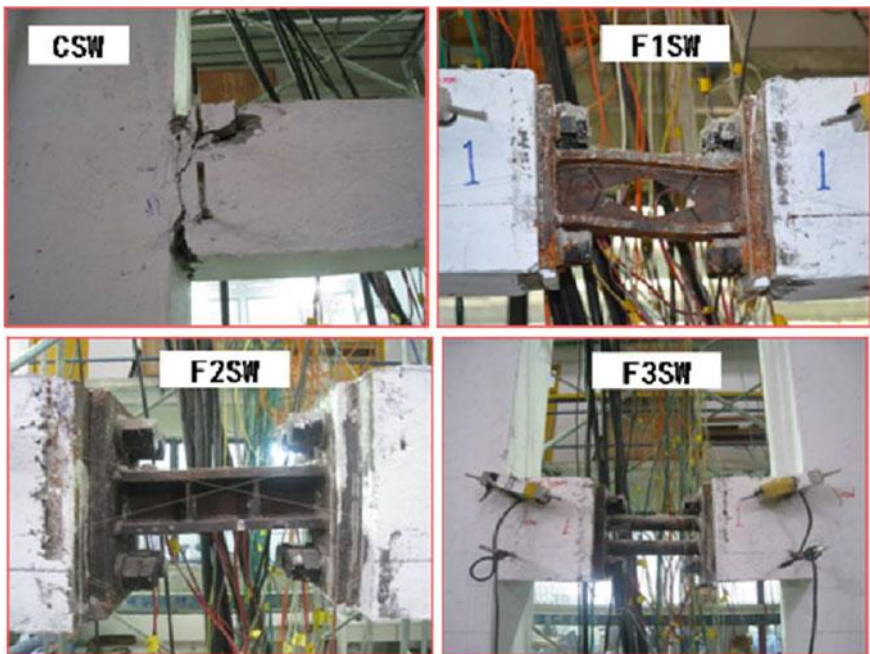


Fig. 22.37 Failure mechanism of four types of coupling beams (courtesy of Xilin Lu, Tongji University)

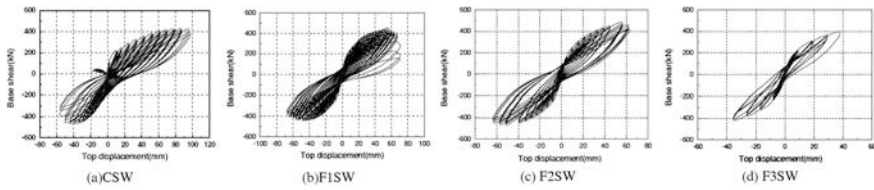


Fig. 22.38 Measured displacement-base shear hysteretic loops of four types of coupling beams [65]

ultimately extend to the entire part of the coupling beam end. In F1SW/F2SW/F3SW, microscopic cracks in the beam first appear at the non-yield segment of coupling beams. However, these cracks do not develop further. Moreover, the size of these cracks is very small during the entire process of the seismic loading. The replaceable coupling beams finally fail because of the failure of “fuse” while the non-yield segment is kept nearly intact [65]. Figure 22.38 shows the measured top displacement-base shear hysteretic loops of the four types of coupling beams. By observing this figure, it is clearly shown that the hysteretic response for all four types of coupling beams are rather stable.

Another similar concept is to adopt a replaceable weak shear wall to connect frames with pin supports, which is often referred to as a pin-supported wall-frame structure [66, 67].

Yet other replaceable devices have also been proposed to dissipate seismic energy through utilizations of friction damper [68] or viscoelastic damper [69].

In summary, all concepts introduced above allow a quick replacement or repair of the “fuses,” allowing a quick recovery of the structure’s functionality.

22.7.2.6 Other Types of Dampers Utilizing Yielding Mechanism

Mitsubishi Heavy Industries, Ltd. [70] has developed a yielding damper brace with additional buckling restraint pipe constraining the energy dissipating yielding elements to avoid buckling of the energy dissipating elements (similar to the concept of buckling-restrained brace frame as discussed in Sect. 20.2).

Other concepts of yielding dampers also include lead extrusion dampers. As will be discussed in Sect. 22.8, this type of damper utilizes a piston to extrude lead through a constricted orifice within a confined cylinder to give a fairly stable hysteretic behavior over cyclic yield cycles. The application of this type of damper can be found in Japan and New Zealand.

Researches also reported the development of “yielding” dampers by using shape memory alloys such as the nickel-titanium alloy, Nitinol. Those materials have the ability to undergo a reversible phase transformation under stress. One of the advantages of using shape memory alloys is that the dampers can dissipate energy in a similar way as other types of yielding metal dampers, but without permanent plastic damage [37]. The shape memory alloy dampers will be discussed in Sect. 22.9.

22.7.3 Engineering Applications of Yielding Dampers

Engineering applications of yielding dampers can be found in many structural designs such as Fujita Corp. Main Office, KI building, Hitachi Main office, Ohjiseishi Building in Tokyo, and Wells Fargo Bank in San Francisco, etc.

The Art Hotel in Sapporo, Japan is a 96 m high moment resisting steel frame structure with 26 stories above ground. It was constructed in 1996 by Kumagai Corporation. To cope with the earthquake induced lateral loads, 2020 steel yielding dampers with a yielding strength of 325 MPa were installed in the building. Among them, 952 steel yielding dampers are installed for mitigating response in the principle X direction and the other 1068 dampers are for Y directions. It is estimated that around 20 % of steel in weight was saved due to the installation of yielding dampers in this structure [71].

As shown in Fig. 22.39, in order to reduce the seismic response of inter-story drift concentrated at the first story with a height of 7.5 m, single round-hole and double X-shaped metallic dampers were installed in a 5-story building in Dalian, China. The dampers were named “dual functions” metallic dampers (DFMD) by the designers [72] because they not only increase the stiffness of the building, but also function as seismic energy dissipaters. Each DFMD damper comprises three DFMD plates placed together, as shown in Fig. 22.39. For the single round-hole damper,

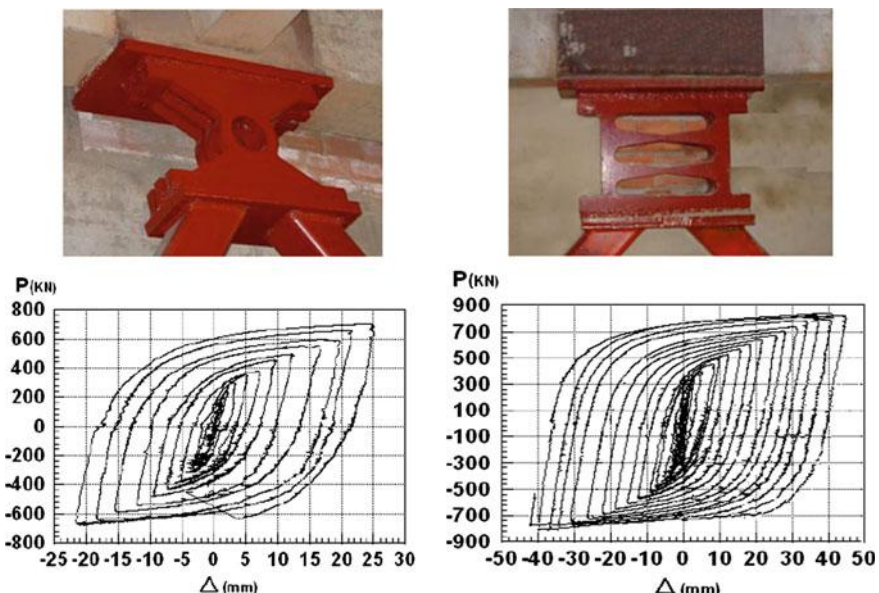


Fig. 22.39 Single round-hole (*upper-left*) and double X-shaped yielding dampers (*upper right*) with their hysteretic curves (*lower*) from testing (courtesy of Hongnan Li, Dalian University of Technology)

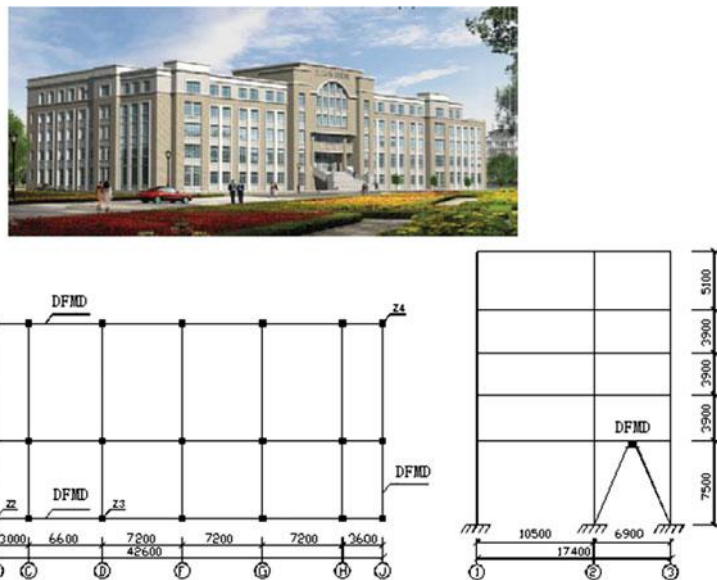


Fig. 22.40 Arrangement (*lower figures*) of the single round-hole and double X-shaped metallic dampers (DFMD) in a reinforced concrete building (*upper*) (courtesy of Hongnan Li, Dalian University of Technology)

the elastic lateral stiffness is 170.5 kN/mm, the plastic yielding force is 375 kN, and the displacement at yielding point is 2.2 mm. For the X-shaped metallic damper, the elastic lateral stiffness is 102.5 kN/mm, the plastic yielding force is 410 kN, and the displacement at yielding is 4 mm. All these data are obtained from testing. By observing Fig. 22.39, the substantial hysteretic loops for both dampers can be identified, indicating a sound energy dissipation performance. As shown in Fig. 22.40, the single round-hole metallic dampers are installed between the C and D axes along the ① and ③ axes, and the double X-shaped metallic dampers are arranged between the ② and ③ axes along the A and J axes. From a modal analysis, it is noticed that the fundamental eigenperiod of the building is decreased by 20 % (decreased from 1.06 to 0.86 s) due to the added stiffness contributed by the yielding dampers together with their supporting braces. By performing a non-linear dynamic analysis of the structure subject to ground excitations with a peak acceleration of 2.2 m/s^2 , the maximum displacement in the building with the installation of the yielding dampers is reduced by more than 50 % [72].

22.8 Lead Dampers

Similar to friction and yielding dampers, lead dampers also utilize the mechanism of hysteretic energy dissipation properties. The most typical type of lead damper are lead extrusion dampers, as shown in Fig. 22.41, which were first proposed by Robinson and Cousins [73]. During dynamic loading, the lead inside the damper is under process extrusion through a hole or an orifice, thereby altering its shape. The hysteretic behavior of lead extrusion dampers essentially shows a rectangular hysteretic shape (similar to friction dampers).

As shown in the upper figure of Fig. 22.41, the device consists of a thick-walled tube and a co-axial shaft with a piston. The lead is separated from the tube by a thin layer of lubrication materials kept in place by hydraulic seals around the piston heads. Subject to excitation, the piston moves along the tube and the lead is forced to extrude back and forth through the orifice formed by the constriction of the tube. The lower figure in Fig. 22.41 shows another formation of lead extrusion dampers similar to the constricted-tube type, except that the extrusion orifice is formed by a bulge on the central shaft rather than by a constriction in the tube. The shaft is supported by bearings that also serve to hold the lead in place. Along with the movement of the shaft, the lead must extrude through the orifice formed by the bulge and tube [4].

The lead extrusion dampers have a stable load-deformation relationship, they are unaffected by the number of loading cycles and resistant to ageing, and they do not need to be replaced or repaired after an earthquake because the lead in the damper returns to its undeformed state after the unloading process. Moreover, the yield

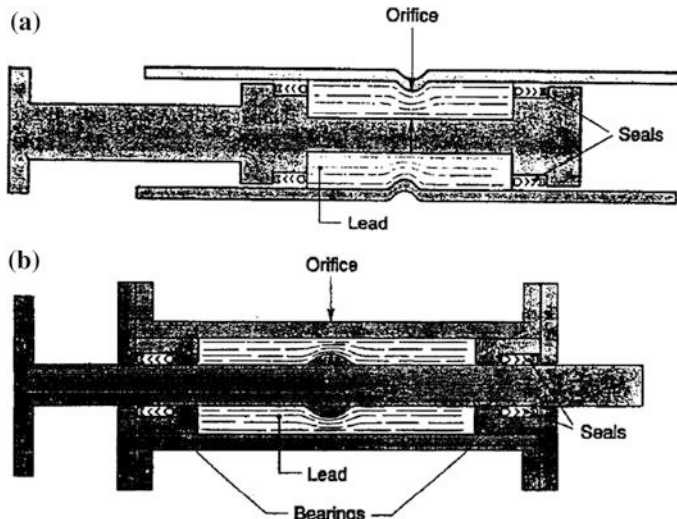


Fig. 22.41 Longitudinal section of lead extrusion dampers with constricted-tube type (*upper*) and bulge-shaft type (*lower*) [96]

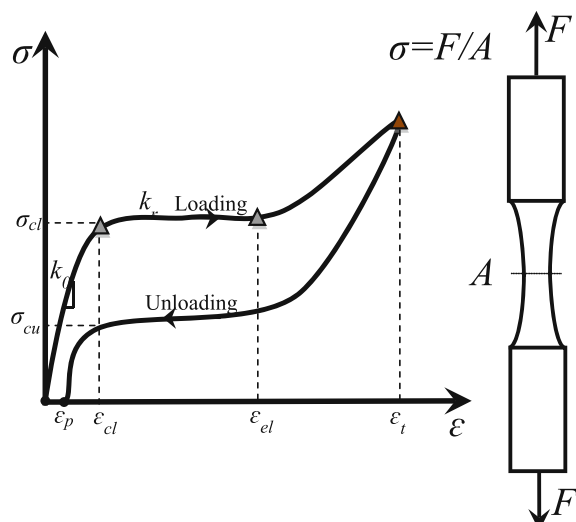
strength of the extrusion dampers can be tuned, but once the yielding strength is determined, it cannot be changed easily. Therefore, this type of damper cannot cope well with the capacity requirement with different ground motion intensities, i.e., in case the yield strength is set to a rather low value, the dampers will exhibit rather large deformation subject to high seismic motions; on the other hand, when the yielding strength of the damper is high, it may not dissipate energy during a mild earthquake.

Lead extrusion dampers have been applied to mitigate seismic responses in various structures. For example, it has been applied in a 10 story base-isolated cross-brace concrete building with sleeved piles and lead extrusion dampers in Wellington, and they are used on several seismically isolated bridges [74].

22.9 Shape Memory Alloy Dampers

Different from yielding damper or friction damper, the shape memory alloy dampers, often made from Nitinol (nickel-titanium) [75], undergo a sort of super-elastic deformation that can be more or less recovered (minor permanent deformation with a recovery strain less than 10 %) after unloading. This behavior is referred to as shape memory effect. The physical explanation for this behavior is that when the shape memory alloy materials exhibit large deformations, even if the crystal phase transformation is induced with a non-linear load-deformation relationship and a reduced modulus of elasticity, the deformation is elastic and can be reversed during the unloading as the material undergoes a reverse transformation at a stress level lower than that for the loading process. The behavior above is illustrated in Fig. 22.42.

Fig. 22.42 Stress (σ)-strain (ϵ) curve for typical shape memory alloy materials, A is cross section area; F is the external axial force on the specimen; ϵ_p , ϵ_{cl} , ϵ_{el} , and ϵ_t are the permanent, critical loading, elastic limit, and total strain, respectively; σ_{cl} and σ_{cu} are the critical loading and unloading stress, respectively; k_0 and k_r are the initial and reduced stiffness, respectively



This indicates that shape memory alloy dampers can have a self-centering capacity due to their elastic behavior. Moreover, shape memory alloy is rather suitable to be used for base isolation purpose because it is insensitive to temperature changes and can sustain significant loading. However, because shape memory alloy such as Nitinol is rather expensive, its application in mitigating dynamic response of engineering structures is limited.

Even though the applications of shape memory alloys in civil engineering are challenged by the high material cost, they have been implemented for field applications with positive results [76–79]. On the other hand, shape memory alloys have been applied in many other areas due to their high power density, solid state actuation, high damping capacity, durability and fatigue resistance,

Several types of shape memory alloy dampers have been proposed. MANSIDE (Memory Alloys for New Seismic Isolation Devices) damper, shown in Fig. 22.43, is the outcome of a European research project with the aim to investigate the possibilities of making use of shape memory alloys in passive control of buildings [80]. This damper consists of two concentric steel pipes attached to two separate parts of a structure (e.g. between two floors in a building). Two bolts are inserted transversely in the two pipes and into oval-shaped holes. An adequate number of shape memory alloy wires are wound around the bolts, configured as a re-centering group. The special arrangements of bolts and holes are such that, for any positive or negative mutual movements of the pipes, the wires are always subject to elongation,

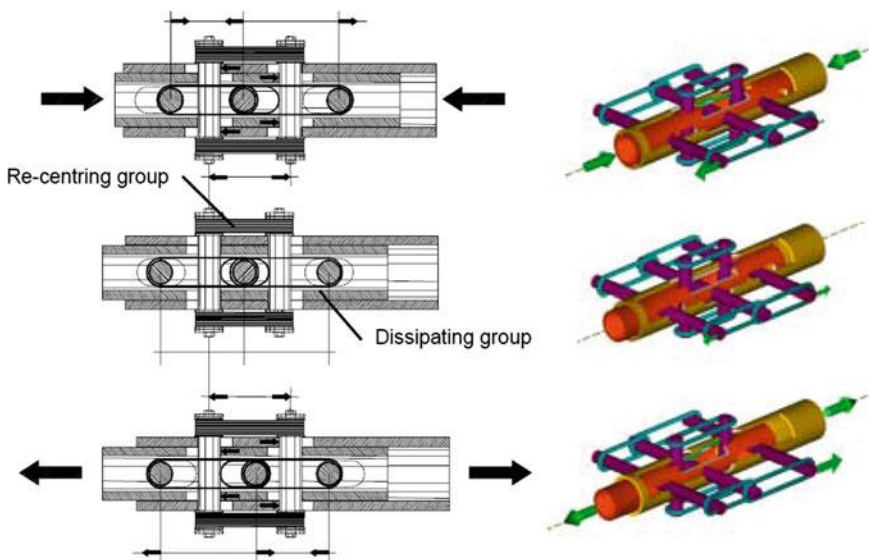


Fig. 22.43 Seismic damper with two groups of shape memory alloy wires [81]

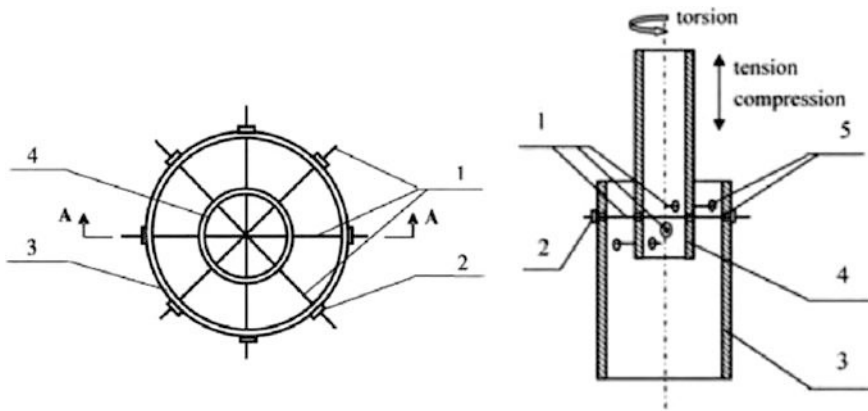


Fig. 22.44 A damper made of shape memory alloys: 1 NiTi wires, 2 chuck, 3 outer tube, 4 inner tube [83]

thus increasing the tensile strains. Similarly, three bolts, two of which move with the internal pipe and the other with the external pipe (or vice versa), as well as the wire looped around the bolts and the mechanism to apply and to calibrate specific pre-tension load, are configured as an energy dissipating group. When the two tubes move reciprocally, one loop elongates and the other shortens, thus acting as a double counteracting system of springs and exploiting the austenitic wires to dissipate energy in an optimal way [81]. Dolce et al. [82] presented that the cost of damping devices using the MANSIDE (with NiTi wires) is comparable to cost of other energy dissipating devices, e.g., the cost is around about 3.5 % of the cost of construction if MANSIDE is used as an isolation system. This is based on the assumption that the cost of shape memory alloy (NiTi) wires is as follows: (1) devices based on shape memory alloy (NiTi) wires working in tension with a stress of 0.5 kN/mm^2 for the maximum strain of 8 %; (2) cost of shape memory alloy equal to 200 €/kg ; (3) weight density of SMA equal to $7 \cdot 10^{-6} \text{ kg/mm}^3$; (4) cost of construction equal to 600 €/m^2 ; (5) weight of construction equal to 10 KN/m^2 .

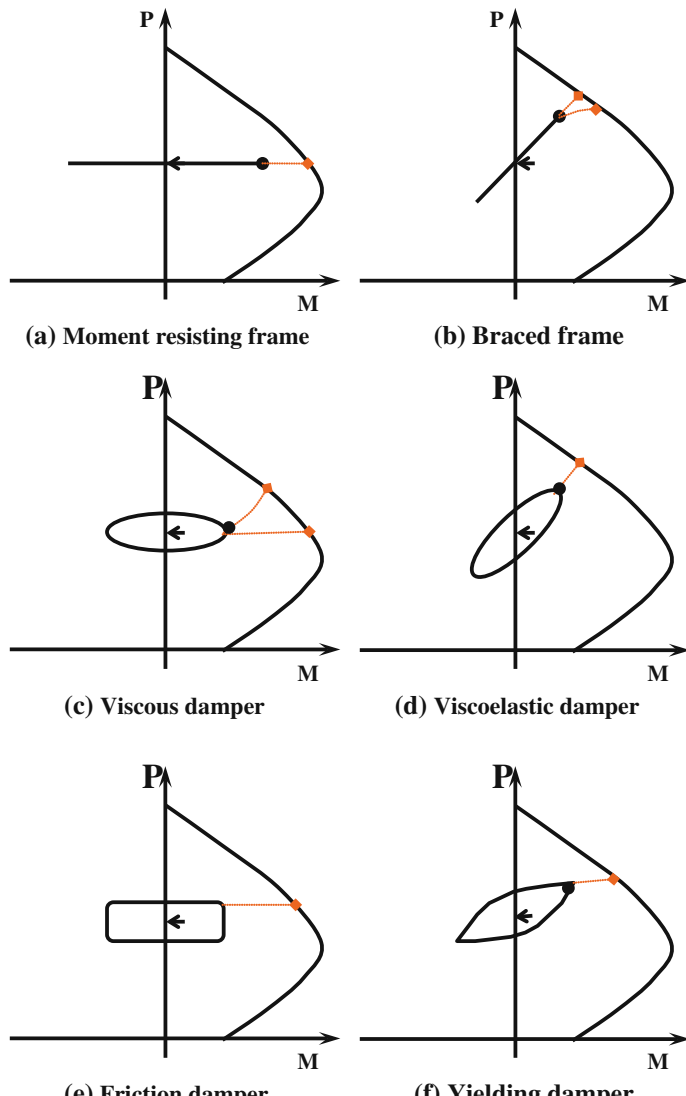
To mitigate the response in tension, compression and torsion simultaneously, Han et al. [83] developed a damper device with two concentric pipes and NiTi wires that run through the pipes as shown in Fig. 22.44. Through the deformation of NiTi wires independent of load type, the energy is dissipated. Moreover, the same amount of energy can be dissipated independent of the size-ratio between inner and outer pipes.

Other types of shape memory alloy dampers have also been researched, such as the one proposed by Clark et al. [84] with multiple NiTi-wires, and Olsen [85]. For an introduction to those types of damping devices, readers may read reference [86].

22.10 Comparison of Structural Behavior Among Conventional Structures and Structures with Different Damping Apparatus Installed

Figure 22.45 shows the axial force–moment behavior of a column for conventional moment resisting or steel brace frames and frames with damping apparatus installed on the column. It is plotted in a nominal axial force–moment interaction diagram for columns. Under base excitations, for conventional moment resisting framed structure (Fig. 22.45a), the deformation of the frame dramatically increases, as does the column moment, while the axial force does not change. For braced frame (Fig. 22.45b), the deformation and moment are lower than that of the moment resisting frame, but the column’s axial force is higher. This can lead to a deterioration of the hysteresis cycles following the first loading cycle, because of the simultaneous presence of tensile plastic deformations and flexural deformations due to buckling, which can eventually make the structural system have a rather low stiffness. When combined with dynamic loading effects, the failure of the structure can occur. For example, for a cross-bracing system, during the first loading phase, the compression braces buckle, undergoing large out-of-plane deflection, while during the unloading stage, the system can exhibit a significant loss of stiffness before the compression brace recovers the straightened shape.

For framed structures with damping apparatus installed (Fig. 22.45c–f), the deformation and moment are lower than that of the moment resisting frames, and may be higher or lower than that of the braced frames. For viscous dampers, due to the damping force being out-of-phase with the motion velocity, the distance between the P-M curve and the nominal force–moment interaction diagram is significantly longer than that of conventional moment resisting or braced frames, indicating an increase in the capacity reserve of the column. However, for other types of dampers, the distance may be longer or shorter than that of conventional moment resisting or braced frames. This means that, along with viscous dampers, other types of dampers may significantly increase a column’s axial force, which can eventually lead to a column failing in compression. This concern is particularly important for slender columns or those damaged due to previous accidental loading. Reinforcing the column can be a measure to fully or partially solve this problem as will be presented in Chap. 29.

**Notation:**

P: axial force on a column of beam–column frame

M: bending moment on a column of beam–column frame

←: axial force due to gravity load

→: failure path and failure point

Fig. 22.45 Comparison of a column's axial force–moment behavior for conventional moment resisting or braced frames and frames with installed damping apparatus on the column

References

1. Soong TT (1990) Active structural control: theory and practice. Longman Scientific & Sons Inc, New York
2. Kelly JM (1990) Base isolation: linear theory and design. *Earthq Spectra* 6(2):223–244
3. Hanson RD, Aiken ID, Nims DK, Richter PJ, Bachman RE (1993) State-of-the-art and state-of-the-practice in seismic energy dissipation. Technical papers on passive energy dissipation, ATC-17-1, ATC, pp 449–471, March, 1993
4. Sadek F, Mohraz B, Taylor AW, Chung RM (1996) Passive energy dissipation devices for seismic applications, NISTIR 5923, National Institute of Standards and Technology, US Department of Commerce, Gaithersburg, Maryland
5. Constantinou MC, Symans MD, Tsopelas P (1993) Fluid viscous dampers in applications of seismic energy dissipation and dissipation and seismic isolation. In: Proceedings of the ATC-17-1 seminar on seismic isolation, passive energy dissipation, and active control, San Francisco, March, 1993
6. Symans MD, Constantinou MC (1998) Passive fluid viscous damping systems for seismic energy dissipation. *J Earthq Technol* 35(4):185–206
7. Symans MD, Charney FA, Whittaker AS, Constantinou MC, Kircher CA, Johnson MW, McNamara RJ (2008) Energy dissipation systems for seismic applications: current practice and recent developments. *J Struct Eng ASCE* 134(1):3–21
8. Filiatrault A, Tremblay R, Wanitkorkul A (2001) Performance evaluation of passive damping systems for the seismic retrofit of steel moment resisting frames subjected to near field ground motions. *Earthq Spectra* 17(3):427–456
9. Taylor DP, Constantinou MC (1996) Fluid dampers for applications of seismic energy dissipation and seismic isolation. Taylor Devices Inc, North Tonawanda
10. Constantinou MC, Fujii S, Tsopelas P, Okamoto S (1992) University at Buffalo–Taisei Corporation research project on bridge seismic isolation system. In: Proceedings of the third NSF workshop on bridge engineering research in progress, La Jolla, CA, p 235
11. Taylor DP (1996) Fluid dampers for applications of seismic energy dissipation and seismic isolation. In: Proceedings of 11th world conference on earthquake engineering, paper no. 798. Elsevier Science Ltd
12. Asher J, Young R, Ewing R (1994) Seismically damping—the San Bernardino County Medical Center, Structural Engineering Forum, pp 39–43
13. Arima F, Tanaka H (1988) A study on buildings with large damping using viscous damping walls. In: Proceedings of the ninth world conference on earthquake engineering, vol 5. Tokyo-Kyoto, Japan
14. Miyazaki M, Mitsusaka Y (1992) Design of a building with 20 % or greater damping. In: Proceedings of the 10th World conference on earthquake engineering, Madrid, pp 4143–4148
15. Yeung N (2000) Viscous-damping walls for controlling wind-induced vibrations in buildings. PhD thesis, University of Hong Kong
16. Mahmoodi P, Robertson LE, Yontar M, Moy C, Feld L (1987) Performance of viscoelastic structural dampers in World Trade Center towers. *Dynamics of Structures, Structures Congress '87*. Orlando, FL
17. Aiken ID, Kelly JM (1990) Earthquake simulator testing and analytical studies of two energy absorbing systems for multistory structures. Report no. UCB/EERC-90/03, University of California, Berkeley
18. Constantinou MC, Symans MD (1993) Seismic response of structures with supplemental damping. *Struct Des Tall Build* 2:77–92
19. Oh ST, Chang KC, Lai ML, Nielsen EJ (1992) Seismic response of viscoelastically damped structure under strong earthquake ground motions. In: Proceedings of the 10th world conference on earthquake engineering, Madrid, Spain
20. Chang KC, Soong TT, Oh ST, Lai ML (1992) Effect of ambient temperature on a viscoelastically damped structure. *J Struct Eng ASCE* 118(7):1955–1973

21. <http://www.taylordevices.com>
22. Hsu SY, Fafitis A (1992) Seismic analysis and design of frames with viscoelastic connections. *J Struct Eng ASCE* 118(9):2459–2474
23. Hsu SY, Fafitis A (1992) Seismic analysis of frames with viscoelastic beam-column connections. In: Proceedings of 10th world conference on earthquake engineering, Balkema, Rotterdam
24. Shen KL, Soong TT (1995) Modeling of viscoelastic dampers for structural applications. *J Eng Mech ASCE* 121(6):694–701
25. Abbas H, Kelly JM (1993) A methodology for design of viscoelastic dampers in earthquake-resistant structures. Report no. UCB/EERC 93/09, Earthquake Engineering Research Center, University of California at Berkeley, Berkeley, CA
26. Zhang RH, Soong TT (1992) Seismic design of viscoelastic dampers for structural applications. *J Struct Eng ASCE* 118(5):1375–1392
27. Chang KC, Lai ML, Soong TT, Hao DD, Yeh YC (1993) Seismic behavior and design guidelines for steel frame structures with added viscoelastic dampers, NCEER 93-009. National Center for Earthquake Engineering Research, Buffalo, NY
28. Shen KL, Soong TT (1996) Design of energy dissipation devices based on concept of damage control. *J Struct Eng ASCE* 122(1):76–82
29. Park YJ, Ang AHS (1985) Mechanistic seismic damage model for reinforced concrete. *J Struct Eng ASCE* 111(4):722–739
30. Samali B, Kwok KCS (1995) Use of viscoelastic dampers in reducing wind- and earthquake-induced motion of building structures. *Eng Struct* 17(9):639–654
31. Filiatrault A, Cherry S (1987) Performance evaluation of friction damped braced steel frames under simulated earthquake loads. *Earthq Spectra* 3(1)
32. Aiken ID, Kelly JM (1988) Experimental study of friction damping for steel frame structures. In: Proceedings of the PVP conference, vol 133, ASME, Pittsburgh, Pennsylvania, pp 95–100
33. Hakimi BE, Rahnavard A, Honarbakhsh T (2004) Seismic design of structures using friction damper bracings. In: 13th world conference on earthquake engineering, Vancouver
34. Pall AS, Marsh C (1982) Response of friction damped braced frames. *J Struct Eng ASCE* 108 (6):1313–1323
35. Pall AS, Verganelakis V, Marsh C (1987) Friction dampers for seismic control of Concordia University library building. In: Proceedings of the fifth Canadian conference on earthquake engineering, Ottawa, Canada, pp 191–200
36. Colajanni P, Papia M (1995) Seismic response of braced frames with and without friction dampers. *Eng Struct* 17(2):129–140
37. Kareem A, Kijewski T, Tamura Y (1999) Mitigation of motions of tall buildings with specific examples of recent applications. *Perception* 2(3):48
38. Aiken ID, Kelly JM, Pall AS (1988) Seismic response of a nine-story steel frame with friction damped cross-bracing, report no. UCB/EERC-88/17, EERC, University of California Berkeley
39. Pasquin C, Leboeuf N, Pall RT, Pall A (2004) Friction dampers for seismic rehabilitation of Eaton's Building, Montreal. In: 13th world conference on earthquake engineering, Vancouver
40. Filiatrault A, Cherry S (1986) Seismic tests of friction-damped steel frames. In: Third conference on dynamic response of structures. ASCE, Los Angeles
41. Grigorian CE, Yang TS, Popov EP (1993) Slotted bolted connection energy dissipaters. *Earthq Spectra* 9(3):491–504
42. Soong TT, Dargush GF (1997) Passive energy dissipation systems in structural engineering. Wiley, Chichester
43. Nims DK, Inaudi JA, Richter PJ, Kelly JM (1993) Application of the energy dissipating restraint to buildings. In: Proceedings of the ATC 17-1 on seismic isolation, energy dissipation, and active control, pp 627–638
44. Choi E, Choi G, Kim TH, Youn H (2015) Smart damper using the combination of magnetic friction and precompressed rubber springs. *J Sound Vib* 351:68–89

45. Choi E, Kim T, Youn H, Jeon J-S (2016) Vibration tests of precompressed rubber springs and a flag-shaped smart damper. *Eng Struct*
46. Mualla IH, Nielsen LO (2002) A friction damping system low order behavior and design. Department of Civil Engineering, Danmarks Tekniske University, Bygning
47. Komachi Y, Tabeshpour MR, Golafshani AA, Mualla I (2011) Retrofit of Ressalat jacket platform (Persina Gulf) using friction damper device. *J Zhejiang Univ Sci A* 12(9):680–691
48. Pall A, Pall RT (2004) Performance-based design using Pall friction dampers—an economical design solution. In: Proceedings of the 13th world conference on earthquake engineering, Vancouver
49. <http://www.palldynamics.com>
50. Malhotra A, Carson D, Gopal P, Braimah A, Giovanni GD, Pall R (2004) Friction dampers for seismic upgrade of St. Vincent Hospital, Ottawa. In: Proceedings of the 13th world conference on earthquake engineering, Vancouver, BC, Canada
51. Nikam SG, Wagholarikar SK, Patil GR (2014) Seismic energy dissipation of a building using friction damper. *Int J Innov Technol Explor Eng* 3(10)
52. Pasquin C, Leboeuf N, Pall RT, Pall A (2004) Friction dampers for seismic rehabilitation of Eaton's Building, Montreal. In: 13th world conference on earthquake engineering, Vancouver, paper no. 1949
53. <http://www.palldynamics.com/DesignWithFrictionDampers.htm>
54. Tabeshpour MR, Ebrahimian H (2010) Seismic retrofit of existing structures using friction. *Asian J Civil Eng* 11(4):509–520
55. Pall AS, Pall R (1996) Friction-dampers for seismic control of buildings: a Canadian experience. In: 11th world conference on earthquake engineering
56. Kelly JM, Skinner RI, Heine AJ (1972) Mechanisms of energy absorption in special devices for use in earthquake-resistant structures. *Bull N Z Natl Soc Earthq Eng* 5(3):63–88
57. Roeder CW, Popov EP (1978) Eccentrically braced steel frames for earthquakes. *J Struct Div ASCE* 104(3):391–412
58. Tyler RG (1985) Further notes on a steel energy absorbing element for braced frameworks. *Bull N Z Natl Soc Earthq Eng* 18(3):270–279
59. Tsai KC, Hong CP (1992) Steel triangular plate energy absorber for earthquake-resistant buildings. In: Proceedings of the first world congress on constructional steel design, Mexico
60. Tagawa H, Gao J (2012) Evaluation of vibration control system with U-dampers based on quasi-linear motion mechanism. *J Constr Steel Res* 70:213–225
61. Kang JD, Tagawa H (2013) Seismic response of steel structures with seesaw systems using viscoelastic dampers. *Earthq Eng Struct Dyn* 42(5):779–794
62. Tagawa H, Yamanishi T, Takaki A, Chan RWK (2016) Cyclic behavior of seesaw energy dissipation system with steel slit dampers. *J Constr Steel Res* 117:24–34
63. Chan R, Wong PSP (2014) A passive rotary system for seismic risk mitigation of steel structures. *Australas J Constr Econ Build Conf Ser* 2(2):72–79
64. Fortney PJ, Shahrooz BM, Rassati GA (2007) Large-scale testing of a replaceable “fuse” steel coupling beam. *J Struct Eng* 133(12):1801–1807
65. Lu X, Mao Y, Chen Y, Zhou Y (2014) Earthquake resilience of tall buildings using replaceable energy dissipation members. In: 10th US national conference on earthquake engineering, Anchorage, Alaska
66. Holden T, Restrepo JI, Mander JB (2003) Seismic performance of precast reinforced and pre-stressed concrete walls. *J Struct Eng ASCE* 129(3):286–296
67. Restrepo JI, Rahman A (2007) Seismic performance of self-centering structural walls incorporating energy dissipators. *J Struct Eng ASCE* 133(11):1560–1570
68. Chung HS, Moon BW, Lee SK, Park JJ, Min KW (2009) Seismic performance of friction dampers using flexure of RC shear wall system. *Struct Des Tall Spec Build* 18(7):807–822
69. Lyons RM, Christopoulos C, Montgomery MS (2012) Enhancing the seismic performance of RC coupled wall high-rise buildings with viscoelastic coupling dampers. In: Proceedings of 15th world conference on earthquake engineering, Lisbon

70. Ishii M, Uehira S, Ogi Y, Morishita K (2005) Hysteresis dampers for controlling seismic response of bridges and structures, Mitsubishi Heavy Industries, Ltd. Technical review, vol 42, no 1
71. Nikkei Architecture (1997) Art Hotel Sapporo, two thousand hysteretic dampers reduce 20 % steel weight, no. 588, pp 202–205 (in Japanese)
72. Li G, Li H (2008) Earthquake-resistant design of RC frame with “dual function” metallic dampers. In: Proceedings of the 14th world conference on earthquake engineering, Beijing
73. Robinson WH, Consins WJ (1982) Recent developments in lead dampers for base isolation. In: Pacific conference on earthquake engineering, vol 2, pp 2279–2283, New Zealand
74. Charleson AW, Wright PD, Skinner RI (1987) Wellington Central Police Station, based isolation of an essential facility. In: Proceedings of the Pacific conference on earthquake engineering, vol 2, NX
75. Duerig TW (ed) (1990) Engineering aspect of shape memory alloys. Butterworth-Heinemann Ltd, London
76. Dolce M, Cardone D (2001) Mechanical behaviour of shape memory alloys for seismic applications; austenite NiTi wires subjected to tension. *Int J Mech Sci* 43(11):2657–2677
77. Saadat S, Salichs J, Noori M, Hou Z, Davoodi H, Bar-on I, Suzuki Y, Masuda A (2002) An overview of vibration and seismic application of NiTi shape memory alloy. *Smart Mater Struct* 11:218–229
78. Van der Eijk C, Zhang ZL, Akselsen OM (2004) Seismic dampers based on shape memory alloys: metallurgical background and modeling. In: Proceedings of the third European conference on structural control, 3ECSC, Vienna, Austria, 12–15 July, pp M1–5
79. Song G, Ma N, Li HN (2006) Applications of shape memory alloys in civil structures. *Eng Struct* 28(9):1266–1274
80. Dolce M, Cardone D, Nigro D (2000) Experimental tests on seismic devices based on shape memory alloys. In: Proceedings of the 12th world conference on earthquake engineering, Auckland, New Zealand, p 8
81. Dolce M, Marnetto R (2000) Passive seismic devices based on shape memory alloys. In: Proceedings of the 12th world conference on earthquake engineering, Auckland, New Zealand
82. Dolce M, Marnetto R (1999) Seismic devices based on shape memory alloys. In: Proceedings of the final workshop of the BRITE-MANSIDE (memory alloys for new seismic isolation devices) project, Rome, Italy, p 28
83. Han YL, Xing DJ, Xiao ET, Li AQ (2005) NiTi-wire shape memory alloy dampers to simultaneously damp tension, compression, and torsion. *J Vib Control* 11(8):1067–1084
84. Clark PW, Aiken ID, Kelly JM, Higashino M, Krumme R (1995) Experimental and analytical studies of shape-memory alloy dampers for structural control. *Proc SPIE* 2445:241
85. Olsen JS (2006) Seismic dampers with composite NiTi wires: a new damper system. MSc thesis, Norwegian University of Science and Technology
86. van der Eijk C, Olsen JS, Zhang Z (2007) Applications of NiTi shape memory alloy dampers in civil structures. In: Proceedings of the first international conference on self healing materials, Noordwijk aan Zee, Netherland
87. Constantinou MC, Symans MD (1992) Experimental and analytical investigation of seismic response of structures with supplemental fluid viscous dampers, NCEER 92-0032. National Center for Earthquake Engineering Research, Buffalo, NY
88. Ji T, Bell a (2008) Seeing and touching structural concepts. Taylor & Francis, New York
89. Meiliang W, Qian J (2003) Research and application of viscous damping walls. *Ind Constr* 33 (5):61–65
90. Jia Junbo (2014) Essentials of applied dynamic analysis. Springer, Heidelberg
91. Fitzgerald TF, Anagnos T, Goodson M, Zsutty T (1989) Slotted bolted connections in aseismic design of concentrically braced connections. *Earthq Spectra* 5(2):383–391
92. Mirtaheri M, Zandi AP, Samadi SS, Samani HR (2011) Numerical and experimental study of hysteretic behavior of cylindrical friction dampers. *Eng Struct* 33:3647–3656

93. Richter PJ, Nims DK, Kelly JM, Kallenbach RM (1990) The DER energy dissipating restraint, a new device for mitigation of seismic effects. In: Proceedings of the SEAOC 59th annual convention, Lake Tahoe
94. Whittaker AS, Bertero VV, Alonso JL, Thompson CL (1989) Earthquake simulator testing of steel plate added damping and stiffness elements. Report no. UCB/EERC-89/02, University of California, Berkeley
95. Whittaker AS, Bertero VV, Thompson CL, Alonso LJ (1991) Seismic testing of steel plate energy dissipation devices. *Earthq Spectra* 7(4):563–604
96. Skinner RI, Robinson WH, McVerry GH (1993) An introduction to seismic isolation. Wiley, New York
97. Symans MD, Charney FA, Whittaker AS, Constantinou MC, Kircher CA, Johnson MW, McNamara RJ (2008) Energy dissipation systems for seismic applications: current practice and recent developments. *J Struct Eng ASCE* 134(1):3–21

Chapter 23

Base and Hanging Isolation System

23.1 General

The base isolator was scientifically proposed by Skinner et al. [1] as shown in Fig. 23.1. It possesses the following essential elements [2]: (1) a flexible mounting so that the period of vibration of the total system is lengthened sufficiently to reduce the force response; (2) a damper or energy dissipater so that the relative deflections between the building and ground can be controlled to a practical design level; (3) a means of providing rigidity under low (service) load levels due to mild wind and minor seismic ground motions.

Nowadays, in earthquake prone areas, infrastructures are sometimes found on base isolators that allow the ground to move laterally back and forth beneath the structures while the accelerations of the superstructure are rather limited and free from damage [3]; the structure then remains almost still. This requires the base isolators to not only provide the vertical load transmission, but also, if possible, active re-centering of the superstructure during and after an earthquake.

In engineering practice, base isolators are widely used. They have low horizontal stiffness between the structures and the foundation, leading to a decrease in the structure's natural frequency, thus effectively reducing the spectral excitation demands (except for very soft soil condition) and increasing the damping during their deformations, while increasing the horizontal translational displacement, as shown in Figs. 23.2 and 23.3. However, this displacement is concentrated in the isolation system itself (Fig. 23.3) with a relatively small deformation in the primary structure, i.e., the relative displacement between the bottom and the top of the primary structure is rather low. Generally, there are two types of base isolators: elastomeric bearings (Sect. 23.3) or sliding isolation systems (Sect. 23.4).

The effectiveness of the base isolation system makes it a popular candidate among all the seismic protective systems. It is particularly regarded as an effective measure if the superstructure is massive and stiff in the horizontal plane. Examples of this type of superstructure are topside modules of offshore platforms, and

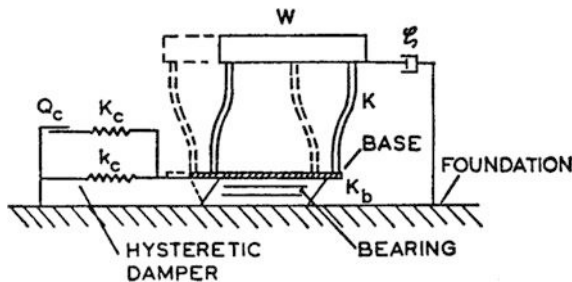


Fig. 23.1 Illustration of a structure with base isolation [1]

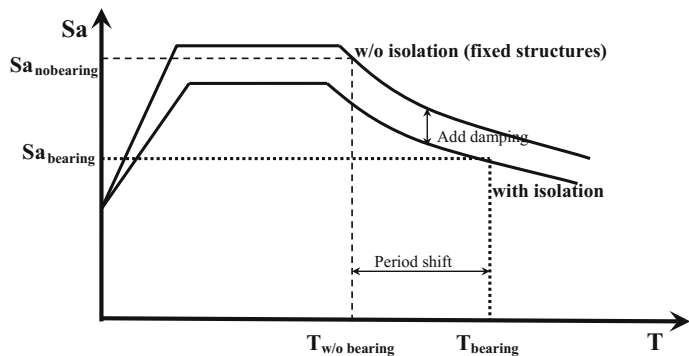
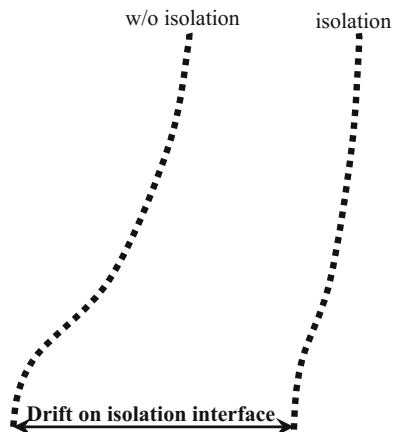


Fig. 23.2 The response spectrum showing decreased spectral demands due to the installation of the isolation system

Fig. 23.3 The seismic displacement response of a structure without (left) and with (right) base isolation system



buildings with low height to width ratio. It has been widely applied in land-based structures such as buildings, bridges, etc., especially in earthquake prone regions such as Japan, China, and USA. It is also used as a mitigation measure on offshore structures, such as sliding isolation systems installed on two GBS platforms offshore of Sakhalin, which will be presented in Sect. 23.4.5.

Attention should be paid to the applicability of base isolators: they are used to separate the response of an original fixed structure from the site period of the underlying soil. Therefore, they are most effective when the natural period of the original structure coincides with or is close to that of the site period. In cases where the natural period of the original structure is significantly different from the site period, the base isolation may even increase the response of the structure. Possible examples of this condition are: very soft structures on rather stiff soil, or very stiff structures on rather soft soil. For an initial screening, engineers may use a design spectrum at the ground surface or seabed, and then compare the spectral acceleration at the natural period of the original target structure with that of the isolated structure. The effectiveness of the designed isolator can then be estimated.

Rather than isolate structures from their bases as introduced above, the objective of isolating structures from seismic motions can also be reached using a pendulum isolation mechanism by hanging the structures through strings with extremely low bending and torsional stiffness but high axial strength, such as the suspended high rise structures as shown in Fig. 23.27, in which the occupied structure is suspended using cables or rods from the top of a very stiff core structure. This will be introduced in Sect. 23.7.

It should be emphasized that, in the design stage, engineers should always keep in mind that the isolation system should not only work during seismic strong ground motions, but also be designed to carry other loads during the service life of the structure, such as loads due to wind, ocean wave, self-weight, and ice load, etc. Therefore, isolation systems must provide sufficient stiffness at small displacements for daily service-level environmental loading, and have reasonable capability to dissipate energy, thus limiting the displacement of the isolator itself.

23.2 Dynamic Analysis of Base Isolation System

Because a typical superstructure is much stiffer than its base isolation system, the deformation is mainly concentrated on the isolation system. One may thus assume that the superstructure can be modeled with a single degree-of-freedom in the horizontal direction with negligible damping. The equation of motion for the entire structure-isolation system is then given by the equation below:

$$M \ddot{x}_s(t) + C \dot{x}_s(t) + K \ddot{x}_s(t) = C \ddot{x}_g(t) + K x_g(t) \quad (23.1)$$

where M , C , and K are the matrices associated with mass of the superstructure, equivalent damping, and horizontal stiffness of the isolation system, respectively. \ddot{x}_s

and \ddot{x}_g are the horizontal acceleration at the superstructure and on the ground, respectively.

By assuming that the ground motion can be represented as a harmonic motion with the site frequency ω , i.e. $\dot{x}_g = e^{i\omega t}$, and only accounting the fundamental eigenmode vibration of the structure, and also implementing the expressions for fundamental eigenfrequency of the structure $\omega_n = \sqrt{\frac{K}{M}}$ and the damping ratio $\zeta = \frac{C}{2M\omega_n}$, the transfer function of the frequency response between the superstructure's and ground acceleration can then be calculated as [4]:

$$H_X(\omega) = \frac{\ddot{x}_s(\omega)}{\ddot{x}_g(\omega)} = \sqrt{\frac{1 + (2\zeta\omega/\omega_n)^2}{[1 - (\omega/\omega_n)^2]^2 + (2\zeta\omega/\omega_n)^2}} \quad (23.2)$$

The above equation can be used as an important measure of the effectiveness of a base isolation system, when the ratio between the superstructure's and ground acceleration is prescribed at the site frequency ω . Based on the equation above, the damping ratio can be expressed as the equation below, which can be used to determine the damping level of the isolation system:

$$\zeta(\omega) = \frac{1}{2(\omega/\omega_0)} \sqrt{\frac{1 - H_X^2(\omega)[1 - (\omega/\omega_0)^2]^2}{H_X^2(\omega) - 1}} \quad (23.3)$$

The transfer function of the frequency response between the superstructure's displacement and ground acceleration can then be expressed as:

$$G_X(\omega) = \frac{x_s(\omega)}{\ddot{x}_g(\omega)} = \frac{H_X(\omega)}{\omega_n^2} = \frac{1}{\omega_n^2} \sqrt{\frac{1 + (2\zeta\omega/\omega_n)^2}{[1 - (\omega/\omega_n)^2]^2 + (2\zeta\omega/\omega_n)^2}} \quad (23.4)$$

The ratio of the maximum absolute value of displacement between the superstructure-base isolation system and that of the ground motion can then be calculated as [5]:

$$\frac{\max(|x_s|)}{\max(|x_g|)} = \frac{\max(|\ddot{x}_g|)}{\omega^2} = \frac{(\omega/\omega_n)^2}{\sqrt{[1 - (\omega/\omega_n)^2]^2 + (2\zeta\omega/\omega_n)^2}} \quad (23.5)$$

From the equation above, it is clearly shown that the maximum displacement at the superstructure-base isolation system is related to ω , ω_n and ζ . In practice, the displacement of the isolation system is mainly controlled by tuning the damping ratio ζ .

23.3 Elastomeric Bearings

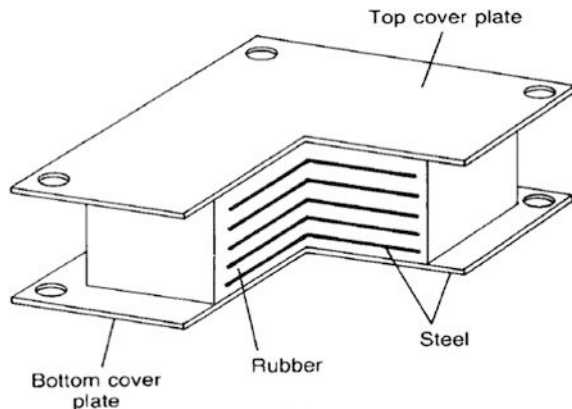
23.3.1 General

The most commonly used base isolation method is to use rubber bearings on the foundations of structures. As shear deformation is known to provide the maximum energy dissipation per unit volume of elastomeric materials such as rubber, which also performs well in resistance to creep [6], the rubber layers in the bearings can be designed to deform in shear to allow the isolator to become a parallelogram in cross section in response to relative motion between the ground and the structure. By placing the steel and rubber plates in alternate layers, as shown in Fig. 23.4, it was first applied in the construction of a primary school in Skopje, Macedonia [7, 8]. However, these isolators had no steel reinforcing plates as are used nowadays, so they were soft in the vertical direction. The layered rubber system was also promoted by the US National Research Center [9] decades ago.

Essentially, the elastomeric bearings work to smooth out or damp earthquake shock impulse, and convert kinetic energy to another form of energy (mainly thermal energy/heat, which can be easily dissipated).

Figure 23.4 shows the steel reinforced layer rubber isolation system, often referred to as laminated rubber bearings. The rubber bearing consists of a standard elastomeric laminated rubber bearing, with steel plates vulcanized with the rubber to increase the vertical compressive stiffness of the isolator while maintaining the shear stiffness similar to that of a rubber block, which is illustrated in Fig. 23.5. The rubber layers can be made of natural rubber or chloroprene rubber, and be either round or rectangular in shape. They are generally made with low damping (unfilled) elastomers with shear moduli of 0.6–1.4 MPa. Standards such as ASSHTO, BS, SETRA DIN, and Eurocode provide design specifications for rubber bearings. The maximum design shear strain value ranges from 125 to 200 % [11]. The left figure in Fig. 23.7 shows the force-displacement relationship of elastomeric bearings.

Fig. 23.4 The steel reinforced layered rubber isolation system [10]



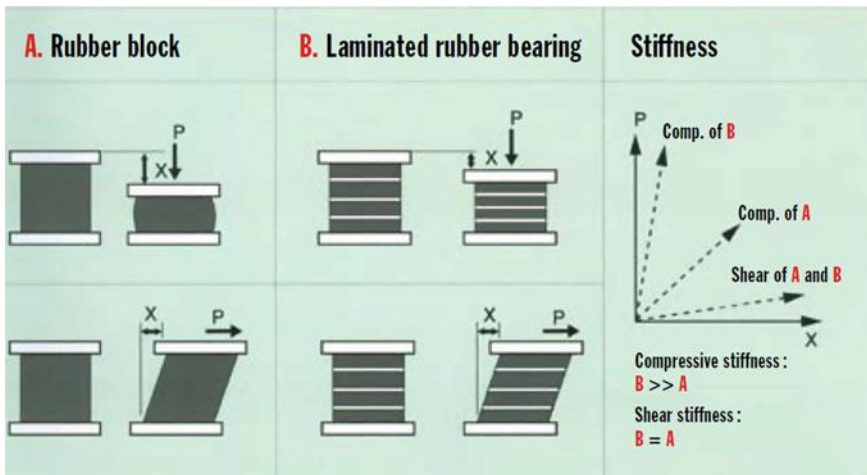


Fig. 23.5 Principles of laminated rubber bearing [12]

The rubber layers have the function of supporting vertical load, shifting the natural period of the superstructure-rubber bearing system to a less adverse motion period in the response spectrum, self-recentering due to the elasticity of the rubber, and also providing damping by means of passive energy dissipation (converting seismic energy into heat). However, it should be noticed that an increase in damping/energy dissipation is usually accompanied by a decrease of self-recentering capacity, and vice versa. Therefore, one needs to optimize the design based on the relative importance of these two functions. Elastomeric bearings sometimes show almost linear behavior and need additional devices to provide damping such as viscous and/or frictional dampers.

Another type of rubber bearing, namely lead rubber bearing (LRB), as shown in Fig. 23.6, is manufactured by making a lead hole with 15–33 % of the bearing diameter/width in the center of the steel reinforced layered rubber isolation system,

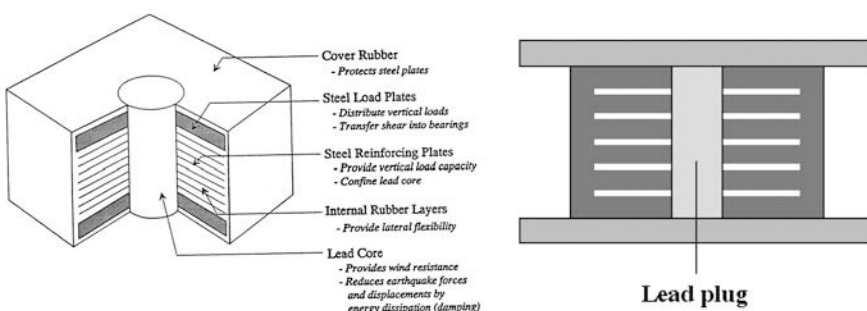


Fig. 23.6 Perspective and side view of lead rubber bearing systems [14]

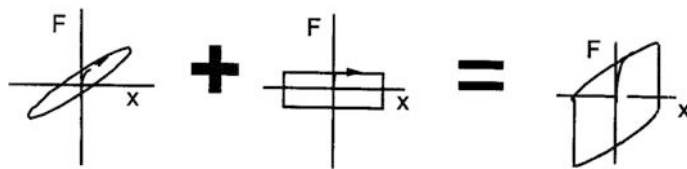


Fig. 23.7 Force-displacement relationship of LRB (*right*) due to the contribution from both laminated elastomeric (*rubber*) bearing (*left*) and lead (*middle*) [15]

and by inserting a lead plug into the hole. Subject to cyclic loading, due to dynamic and meta-dynamic recrystallization of lead [13], the lead will yield in shear at low stress level but dissipate a large amount of energy, while maintaining its mechanical properties. Therefore, lead can introduce a significant damping, typically in the range of 10–30 %, depending on the size of the lead core. However, it is only used to reduce horizontal displacements, and should be not designed to transmit any vertical loads. Moreover, subject to cyclic loading, lead has good fatigue properties. Figure 23.7 shows that the force-displacement relationship of LRB is due to the contribution from both elastomeric bearings and lead.

By using lead rubber as the isolator without additional damper as shown in Fig. 23.8, Monir and Nomani [16] studied the efficiency of the system. Through numerical analysis of a jacket structure with the total weight of 3295 tons and a natural frequency and damping ratio of 0.725 Hz and 5 %, and by applying the strong ground motions recorded during El-Centro (1940), Kobe (1995) and Tabas (1979) earthquakes to the jacket structure, they presented that the lead rubber

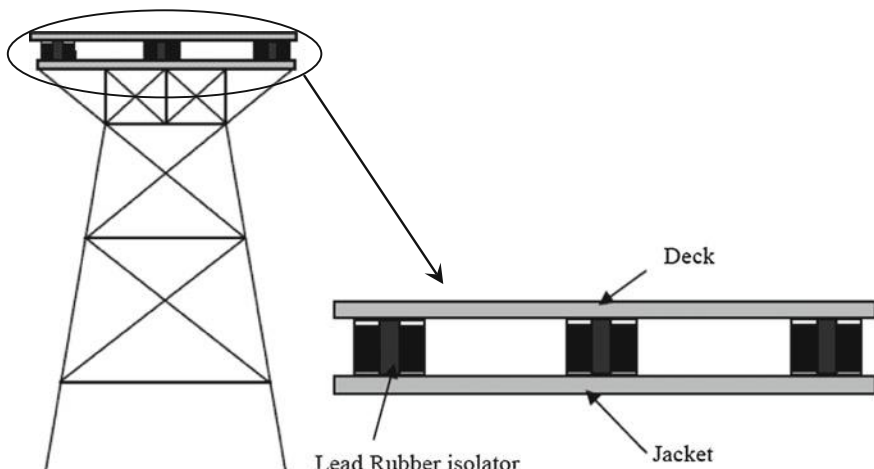


Fig. 23.8 Isolation system with lead rubber bearings proposed by Monir and Nomani [16]

isolation system can reduce the maximum deck acceleration by 79 % on average and jacket displacement by 44 % on average, with the mild inter-story drift of 33.6 mm on average at the isolation level.

Besides shifting the natural frequency of the structure away from the dominant frequencies of seismic response, Ou et al. [17] proposed a damping isolation system aiming at dissipating vibration energy. As shown in Fig. 23.9, the isolation system comprises low stiffness rubber isolators mainly for the purpose of increasing lateral deformation and viscous dampers to dissipate energy. It is placed between the bottom of the modules and the jacket supports. Through both numerical and experimental study of a jacket structure installed with this isolation system, with the mass values of the superstructure and of the jacket and pile of 2576.8 and 550 tons, respectively; the natural frequency and damping ratio being 0.87 Hz and 4 %, respectively, and by applying excitation records of El-Centro, Taft, Bobe and Tianjin earthquakes on the structure foundation, they showed that both the deck's maximum acceleration and the jacket cap's maximum relative displacement were reduced by 55 % on average, indicating a high effectiveness of the system. However, by realizing the practical limitations on the placement positions of the dampers and relatively low vibration amplitude of the platforms due to other types of environmental load (e.g., ice load) than those caused by the seismic loading, they concluded that the damping ratios added by the dampers are relatively small to mitigate dynamic responses of other types of loading, and practically, the effectiveness of adding the damping isolation system on offshore structures, for the purpose of reducing structural vibration responses, is not significant.

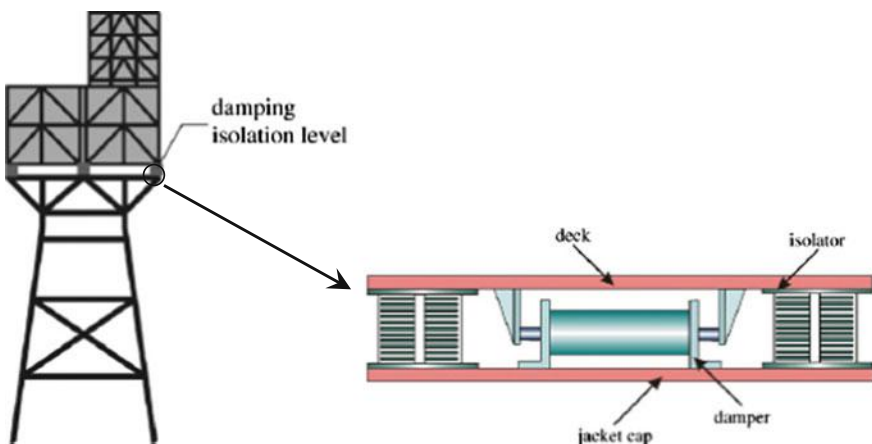


Fig. 23.9 Damping isolation system with both elastomeric bearings and a viscous damper proposed by Ou et al. [17]

23.3.2 Simplified Calculation of Rubber Bearings' Properties

23.3.2.1 Horizontal Stiffness of Rubber Bearings

Based on the assumption that only shear force exists in the bearing without bending moment, the horizontal stiffness of the rubber bearings with n layers of rubbers can be calculated as:

$$K_H = \frac{GA}{\sum_{i=1}^n t_i} \quad (23.6)$$

where G is the shear module of the rubber layer, typically in the range of 0.6–1.4 MPa; A is the effective cross section area of the bearing in shear (rubber area of plan view); t_i is the thickness of the rubber for layer i , thus $\sum_{i=1}^n t_i$ is the total thickness of all the rubber layers.

The equation above is normally valid with the condition that the primary shape factors S , defined as aspect ratio of loaded/contact surface area over force free area (side surface area of a single layer of rubber); $S_1 \geq 15$ and secondary shape factor (ratio of diameter of rubber layers to their total thickness) $S_2 \geq 5$.

It should be noted that the horizontal stiffness varies with a change in horizontal shear strain. When the shear strain is small, the horizontal stiffness is rather high. When the shear strain increases to 50 % or more, the horizontal stiffness begins to decrease. However, when the shear strain further increases to above 300 %, the horizontal stiffness increases again. This behavior is beneficial to the design requirement of base isolation: under normal conditions, the isolated superstructures are subject to dynamic loading such as wind and ocean wave load in horizontal direction and minor earthquake ground motions, and they remain still together with the rubber bearing. When they are subjected to strong ground motions, the decrease in horizontal bearing stiffness leads to the local deformation concentrated in only the rubber bearing. In addition, the decrease in stiffness also further increases the natural period of the bearing-superstructure systems and the spectral acceleration for the superstructure is then decreased. When the deformation of the bearing is too large, the increase in bearing stiffness effectively limits the superstructure from excessive vibrations [18].

It should also be noted that, under large axial vertical compression load P , due to the “stress softening” effects [19], the horizontal stiffness of the bearing will degrade. By applying Galef's formula [20–23], the effective horizontal stiffness depending on the vertical load P can be calculated as:

$$K_{Heff} = K_H \left[1 - \left(\frac{P}{P_{crit}} \right)^2 \right] \quad (23.7)$$

where P_{crit} is the critical Euler buckling load of the isolator, which can be expressed as:

$$P_{crit} = \frac{\pi^2 E_c}{\lambda^2} A \quad (23.8)$$

where λ is the slenderness of the isolator (by taking it as a column), defined as $\lambda = \frac{\mu h}{i}$; μ is the factor depending on the support condition of the column ($\mu = 1$ for simply supported condition at two ends, 0.5 for fixed condition at two ends, 0.7 for fixed-simply supported condition); h is the height of the isolator; and i is the radius of gyration, defined as $i = \sqrt{\frac{I}{A}}$; I is second moment of inertia of the bearing plan section with respect to the axis perpendicular to the horizontal load direction.

By assuming that the rubber behaves elastically and the lead plug does not yield, the resultant horizontal force on a bearing can then be calculated as:

$$F = K_{Heff} \cdot d + \tau_{lead} \cdot A_{lead} \quad (23.9)$$

where d is the horizontal displacement of the bearing; τ_{lead} is shear stress on the lead plug; and A_{lead} is cross section area in shear on the lead plug.

23.3.2.2 Vertical Stiffness of Rubber Bearings

The vertical stiffness of the rubber bearings with n layers of rubbers can be calculated as:

$$K_V = \frac{E_c A}{\sum_{i=1}^n t_i} \quad (23.10)$$

where E_c is the instantaneous compression modulus at the corresponding vertical load level acting on the isolator, which can be taken as compression modulus of a single layer rubber isolator [24].

By assuming that rubber is incompressible material, i.e. the Poisson's ratio is equal to 0.5 or $E = 3G$, the compression module can then be calculated as:

$$E_c = 3G(1 + 2S^2) \quad (23.11)$$

where S is the primary shape factor. S indicates the level of restraint from the steel plate (inside rubber) on the rubber layer. The higher the primary shape factor, the higher the axial vertical compression capacity and vertical stiffness the bearing will have. For a square elastomer isolator with the plan dimension (width and length) of a and a single layer with a thickness of t , S is calculated as follows:

$$S = \frac{A}{4ta} = \frac{a^2}{4ta} = \frac{a}{4t} \quad (23.12)$$

For a circular isolator with the radius of r , S is calculated as:

$$S = \frac{A}{2\pi rt} = \frac{\pi r^2}{2\pi rt} = \frac{r}{2t} \quad (23.13)$$

Naeim and Kelly [25] presented another two equations for calculating the compression module E_c for square and circular shape bearings:

$$E_c = 6.73GS^2 \quad \text{for square shape bearings} \quad (23.14)$$

$$E_c = 6GS^2 \quad \text{for circular shape bearings.} \quad (23.15)$$

Note that the vertical stiffness of the elastomeric bearing is rather high and can reach up to 6000 kN/mm. The eigenfrequency of the rubber bearing's vertical vibration is less than 0.1 s, which is much lower than site periods (associated with horizontal ground motions due to SH wave propagation, see Sect. 4.2) typically above 0.4 s, it may coincide with the frequency of the vertical ground motions. Moreover, the vertical strength of rubber bearings is normally sufficient even if they are subject to strong vertical seismic motions. For example, during the 1994 Northridge earthquake and 1995 Kobe earthquake, even if the vertical ground motions are rather high in many sites and can reach up to 3 m/s^2 , there was no reported damage on the rubber bearings.

It is worth mentioning that the rubber bearings are also widely used for mitigating the vertical excitations transmitted from running trains to rails. For example, they have been installed in the rail structure in the Japanese JR high speed train, London Tube (underground), and Guangzhou Metro, etc. In the rail design of the Guangzhou Metro, the eigenperiod of the rubber bearings' vertical vibrations is set as around 0.1 s, which is far from that of the vertical excitations of the passing trains on the rails, typically ranging from 0.03 to 0.05 s. This provides a reduction in excitation acceleration on the rails by 70–90 %, and effectively mitigates the vibrations and sound transmission to the surroundings [5].

23.3.3 *Compression and Tension Capacity of Rubber Bearings*

Under axial vertical compression, due to the restraints from the steel plate, the rubber layers have rather higher capacity, the failure of steel plates then dominates the bearing failure mechanism. The maximum stress on the steel plate can be estimated based on the following equation, provided the secondary shape factor S_2 (ratio of diameter of rubber layers to their total thickness) is not less than 3, and the hardness is between 40 and 60 [26]:

$$\sigma_{V_S_{max}} = \frac{P}{A_P} \leq \sigma_y \left[0.3(t_s/t_r)^3 - 0.69(t_s/t_r)^2 + 0.83(t_s/t_r) \right] \sqrt[3]{S/15}. \quad (23.16)$$

where A_P is the effective load area of rubber layers under compression; σ_y is the yielding strength of the steel plates; t_s and t_r are the thickness of a single steel plate and a single rubber layer, respectively. It can be observed from the equation above that an increase in σ_y , t_s or S leads to an increase of axial capacity of the bearing. In the initial dimensioning of a bearing, the design stress of steel plates σ_{V_S} can be taken as around 10 MPa to 15 MPa. However, to obtain a high vertical capacity with $\sigma_{V_S} \geq 90$ MPa, the ratio of t_s/t_r may be chosen between 0.4 and 0.5.

In cases in which the vertical ground motion is significant, the bearing may be subjected to axial tension, provided that the bonding between the steel plates and the rubber layers are strong enough, the failure of bearing is dominated by local or global failure of rubber layers, the design capacity for the rubber layers normally ranges between 2 MPa to 6 MPa.

23.3.4 *Determination of Damping in Rubber Bearings*

In addition to a shift of natural period, added damping is also a very important function of rubber bearings as aforesaid. It is produced due to the internal friction and energy dissipation during the rubber deformation. Because during strong earthquakes, the isolated superstructure is intended to behave elastically, i.e. no plastic deformation or relevant energy dissipation, the energy dissipation mainly relies on the damping provided by the rubber bearings.

The damping can be determined from experiments. In general, two methods are valid to obtain the damping: static mechanical test and dynamic testing.

The former one requires mechanical tests to obtain the lateral force-bearing displacement relationship curve. The damping can then be calculated based on the enveloped area of the curve. Figure 23.10 illustrates a lateral force-bearing displacement relationship curve from a test of a rubber bearing, and its idealization with a viscoelastic modeling. By equating the measured energy dissipated per cycle

Fig. 23.10 Modeling of idealized viscoelastic behavior and its comparison with actual hysteretic behavior for rubber isolation systems

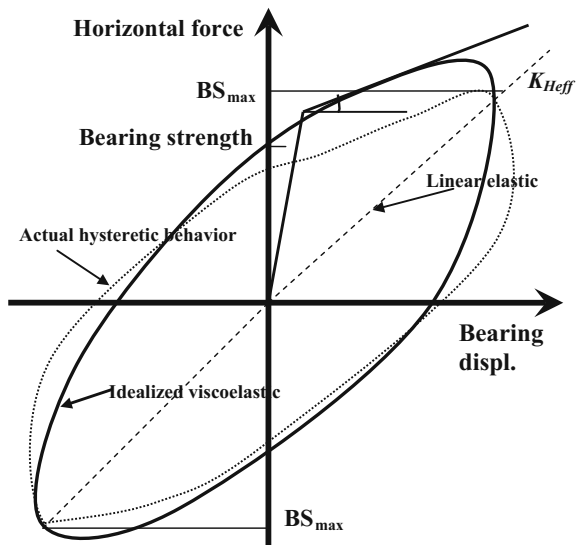
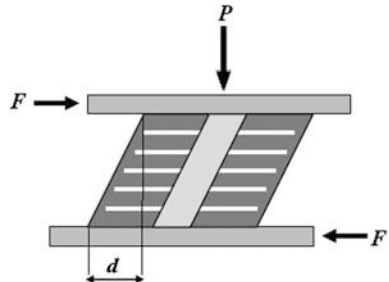


Fig. 23.11 Deformation of a lead rubber bearing under lateral and vertical load



to that of a viscous damper as discussed in Sect. 21.3, the damping ratio can be calculated as:

$$\zeta = \frac{\omega_A}{2\pi K_{\text{eff}} d} \quad (23.17)$$

where ω_A is the envelope area of the curve under a quasi-horizontal static load to reach a shear strain of 100 %; d is the relative horizontal displacement between the top and bottom plate of the rubber bearing as shown in Fig. 23.11.

23.3.5 Design of Elastomeric Bearings

The stiffness and displacement limits are the two most important parameters for designing optimized rubber bearings. Based on the determination or assessment of

vertical load capacity, target period, required horizontal stiffness and displacement limits, and the stability of the elastomeric bearings, the following steps describe a simplified procedure for an initial design of elastomeric bearing system:

1. The structural designer presents a preliminary conceptual requirements of the elastomeric bearings; the main requirements are load capacity, damping, and stiffness, etc.
2. First assume a target natural frequency ω_H of the structure-isolator system corresponding to horizontal vibrations.
3. Based on the target natural frequency ω_H assumed in step 2 and the damping value given by the structural designer in step 1, check the design displacement spectra, the spectral displacement in the horizontal direction can then be determined.
4. The preliminary horizontal stiffness is then calculated as $K_H = \omega_H^2 M$, where M is the total mass of the superstructure.
5. The total thickness of the rubber is then designed as:

$$\sum_{i=1}^n t_i = \frac{\text{maximum spectral horizontal displacement}}{\text{design shear strain of the rubber layer}} \quad (23.18)$$

6. As presented in Sect. 23.3.2.1, the required effective cross section area of the bearing in shear can then be calculated as:

$$A = \frac{(\sum_{i=1}^n t_i)^2 K_H}{G} \quad (23.19)$$

7. From the calculated area A , design the plan dimension (width and length) a for square bearings or r for circular bearings.
8. Calculate the vertical vibration frequency dominated by vertical stiffness of structure-isolator system $\omega_V = \sqrt{\frac{K_V}{M}}$, where K_V is vertical stiffness as presented in 23.3.2.2.
9. In order to prevent a rocking motion of the superstructure, the vertical vibration frequency ω_V should be significantly larger than its horizontal counterpart ω_H . If this requirement is not fulfilled, one may go back to re-dimension the bearing.
10. If the requirement in step 9 is fulfilled, check if the vertical buckling load P_{crit} (Sect. 23.3.2.1) is greater than the vertical axial load P . If this requirement is not fulfilled, re-dimension the bearing by decreasing the height of the isolator or increasing the second moment of inertia of the plan section. During the process of re-dimensioning, design requirement or space restrictions must be respected.
11. Calculate the effective horizontal stiffness described in Sect. 23.3.2.1:

$$K_{Heff} = K_H \left[1 + \left(\frac{P}{P_{crit}} \right)^2 \right]$$

12. Recalculate the natural frequency ω_{Heff} of the structure-isolator system in the horizontal direction $\omega_{Heff} = \sqrt{\frac{K_{Heff}}{M}}$, obtain spectral displacement at ω_{Heff} by checking the design displacement spectra. If the spectral displacement at ω_{Heff} is higher than what is originally obtained based on the target frequency ω_H , set the new target frequency ω_H with the value of ω_{Heff} and go back to step 2.

It should be noted that several national and international design codes provide guidelines for the design of seismic base-isolation, such as International Building Code 2000 [27] and Uniform Building Code 1997 [28], etc. Recent revisions to international codes for the design of base-isolation systems also set more stringent requirement compared to the previous ones, and this potentially leads to a complexity and increased cost for constructing base-isolated structures.

The location of the base isolator plays an important role for the performance of the isolator. When the center of the isolator coincides with the stiffness center of the isolated structure in the horizontal plane, it is best for accommodating the torsional effects in the base isolator system [29–32], and this is also recommended by various seismic design codes.

For irregular structures or soft isolated structures with effective natural periods of more than 3.0 s at the maximum displacement, or the isolation system is not capable of producing restoring forces, or the force-deflection properties are dependent on the rate of loading or vertical load, a time history analysis should be performed for the design assessment. In addition, the influence of environmental temperature and fluid exposure should be considered in design.

23.3.6 Advantages and Drawbacks

The elastomeric isolation system behaves as a parallel linear spring and damper, and exhibits high damping capacity and high vertical stiffness with horizontal flexibility. Due to the horizontal flexibility between the structures and the foundations, the system works by decoupling the structures (and the response of the structures) from the horizontal components of seismic ground motion. For structures supported by several elastomeric bearings, load distribution on all bearings is allowed. Note that even if isolation effects of the system are not produced by absorbing the earthquake energy [33], the system can absorb a certain amount of energy, thus providing additional damping and also reducing the fatigue damage of the structural material under repeated loading.

The drawback of the system also comes from the horizontal flexibility of the system, meaning that, after a strong ground motions, the system may not provide enough restoring force to push the structure back to its initial location. Furthermore,

the maximum vertical load taken by a single elastomeric bearing is generally limited. Because the dimensions of an elastomeric bearing are determined by the parameters associated with vertical load, displacement and possibly rotation, the horizontal stiffness depends on these input parameters and therefore cannot be freely selected in order to achieve an optimum distribution of the horizontal loading [34]. In addition, the stiffness also varies due to the ageing of bearing material and temperature change. Those challenges can be well overcome by the sliding isolation system as elaborated in Sect. 23.4. However, note that the seismic motions at a near fault site are likely to have significant and long period pulses that do not normally exist in ground motions recorded at locations at some distance from the near fault region. This can reduce the effectiveness of base isolations (elastomeric isolation system either or sliding isolation system) for structures located in such areas.

It is also worth pointing out that elastomeric bearings are especially suitable for base isolations of relatively rigid structures. If the superstructure without isolation has a natural period of more than 3.0 s, other mitigation measures such as dynamic absorber (Chap. 24) may be better alternatives.

23.3.7 *Engineering Applications*

Because the elastomeric bearing technology is relatively matured and regarded as approved design, many building and bridge structures in earthquake prone areas such as Italy, China, USA, Japan, New Zealand, Canada, Mexico, France, Iran, Chile, South Africa, England, Russia and Iceland etc. use elastomeric bearings to mitigate the earthquake induced response. Priestley and his co-workers [35] reported that, by 1996, elastomeric bearings had been applied in a total of 255 bridges worldwide. Of them, lead rubber bearing were used in 69 bridges mainly in Japan, USA and New Zealand. In the USA and Japan, among all bridges utilizing base isolation techniques, more than 90 % used lead rubber bearings. For buildings using base isolation systems in those two countries, the relative use of high damping rubber and lead rubber bearing systems was more or less equal with a small number of other systems such as rubber isolation plus steel dampers, sliding isolation systems. In Japan, more than 2000 base-isolated buildings were constructed. Many of them have been constructed since the Kobe earthquake. In China, more than 700 buildings are base-isolated [12].

The 18 story, 98 m high Oakland City Hall (Fig. 23.12), located in Oakland, California, was the first high rise government building in USA. It was constructed in 1914 using a riveted steel frame with infill masonry walls of brick, granite, and terracotta, after its predecessor was destroyed in the 1906 San Francisco earthquake. During the Loma Prieta earthquake of 1989, major structural damages on the building occurred and the Oakland City Hall was immediately closed. Since the building is listed on the historic register, retrofit had to preserve the interior architecture and the historic fabric of the building. During a feasibility study, both the conventional fixed base and base isolation techniques were investigated. As



Fig. 23.12 The 18 story, 98 m high Oakland City Hall (photo credit: Sanfranman59)

shown in Fig. 23.13, the seismic response with the base isolation system is significantly lower than that with conventional retrofitting approach, and the overall cost with the base isolation system is also lower. During the installation phase, part of the steel columns just above the concrete mat foundation were cut and replaced with 42 lead rubber bearings and 69 natural rubber bearings, as shown in Fig. 23.14. During the installation of the bearings, a jacking system was applied to limit the vertical column displacement to less than 25 mm. A temporary lateral bracing system is also applied to prevent the structural damage against possible earthquake occurrence. The cutting and bearing installation also follow a symmetric work sequence to reduce the torsional response in case an earthquake occurs during the installation of bearings. Together with added steel beams, the repaired city hall can withstand more than half a meter of horizontal displacement. The repair cost for the building was US\$85 million.

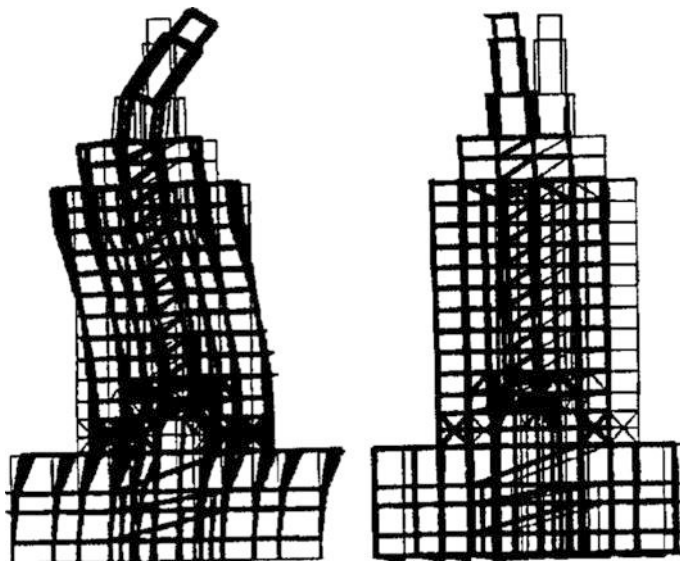


Fig. 23.13 The dynamic response of Oakland City Hall under mitigation measures of fixed based retrofit approach (*left*) or with rubber bearings (*right*) (courtesy of University of South California)



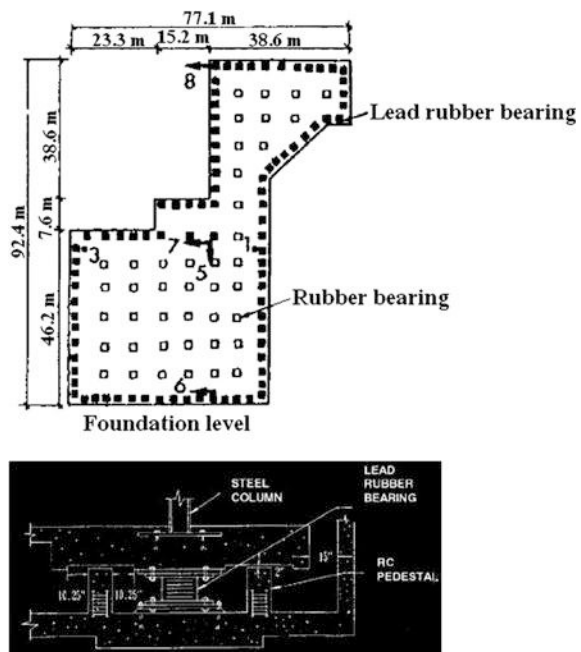
Fig. 23.14 A rubber bearing isolator installed between the steel column and the concrete mat foundation of Oakland City Hall [36]

The seven story high University of Southern California Hospital Building (Fig. 23.15) comprises a steel braced superstructure above a reinforced concrete base slab supported by reinforced concrete beams. It has a length of 92 m and a width of 77 m as shown in the upper figure of Fig. 23.16. The total area of the hospital is 33,000 m². The isolation system consists of 149 isolation bearings: 59



Fig. 23.15 University of Southern California Hospital Building

Fig. 23.16 Plan (upper) and details (lower) of isolators at the foundation level of University of Southern California Hospital Building



lead rubber bearings with a plane dimension of 55.88 cm in square and the diameter of the lead core is 13.97 cm, 9 lead rubber bearings with 66.04 cm in square and 13.97 cm diameter lead core, 8 rubber bearings with 55.88 cm in square, and 73 rubber (elastomeric) bearings, with 66.04 cm in square. The shear module of the rubber layer at a strain level of 50 % strain is 0.69 MPa. The nominal thickness of the steel shim plates is 0.31 cm. Top and bottom cover plates are 2.54 cm thick. With 14 layers of rubber and 13 steel shim plates, the total height of the bearings is 34.61 cm. As shown in the upper figure of Fig. 23.16, the lead rubber bearings were installed under the exterior columns and the rubber bearings were installed under the interior columns. The lower figure of Fig. 23.16 shows details of a typical isolation bearing welded into the end plates of concrete pedestals. The bearing connects the drop panels and footings, and the footing further supports the reinforced concrete pedestal for backup safety (fail-safe). The isolators are designed for a maximum displacement of 26 cm [37]. During the 1994 Northridge earthquake, the free field acceleration was 0.49 g and peak foundation/ground acceleration at the building site was 0.37 g. The building structure performed well and deflected only elastically. During this earthquake, measurements on different locations of the building were documented. It was indicated that the maximum accelerations at the first, fourth, sixth floor and roof were 0.13, 0.1, 0.15 and 0.21 g, respectively. They were much lower than the peak ground acceleration, and they are only around 1/6 that of the Southern California Hospital Building, which is 20 km away and has no isolators installed [5]. The bearing displacement during the earthquake was only 14 % of the design displacement (26 cm). It is estimated that all bearings together contribute to a damping ratio of 20 % for the structure. It is also noted that the horizontal ground motions of the Northridge earthquake have significant energy in the higher frequency range, while due to the presence of isolators, the energy cannot be transmitted to the higher modes of building vibrations [37].

23.3.8 *Performance of Elastomeric Bearings During Real Earthquake Events*

During the 2004 Chuetsu earthquake in Japan, instrument records from the Hokuriku Gakuen College, mounted on 17 high-dampening rubber isolators, indicated that the acceleration at the first floor, just above the isolation system, was reduced to 50 % of the ground acceleration. In China, during the 2008 Sichuan earthquake, the performance of buildings with base isolation implemented verified the efficiency of the base isolation technique: three base-isolated six story apartment blocks with brick wall construction, located in southern Gansu Province 200 km from the earthquake's epicenter, were well protected, and equipment and furniture inside the building were left intact. On the other hand, a fixed base building in the same area experienced significant damage to both the structure and the equipment inside [12].



Fig. 23.17 Rupture of an elastomeric bearing (*right*) of the Tobu Viaduct during the 1995 Kobe earthquake, causing a 0.5 m transverse offset of the bridge deck (*left*) [38]

During the 1995 Kobe earthquake, bridges installed with elastomeric bearing were not damaged or experienced minor damage. However, some bridges suffered severe damage to their elastomeric bearings, such as the Tobu Viaduct in Sendai, where elastomeric bearings ruptured with the rubber layers detached from the steel plates as shown in Fig. 23.17, possibly due to a design flaw or the possibility that the interaction of adjacent decks was not properly considered. This caused the bridge deck to offset in the transverse direction by 0.5 m.

However, during several earthquakes, there has also been evidence showing that the performance of elastomeric bearings during real earthquake events is not as positive as what was concluded by numerical analysis or experimental testing. Table 23.1 shows a comparison of the measured maximum acceleration on structures and ground underneath each of the structures. In almost all six structures, the

Table 23.1 The measured maximum acceleration between structures and grounds during four earthquake events (data provided by Valentin Shustov, California State University, Northridge)

Structure	Earthquake	Maximum structure/ground acceleration	Isolation type
Santa Ana River Bridge	Whittier Narrows Oct. 1, 1987	0.18 g/0.05 g	Lead rubber
Sierra Point Overpass	Loma Prieta Oct. 17, 1989	0.41 g/0.09 g	Lead rubber
LA County Fire Command Facility	Northridge, 17th of January, 1994	0.35 g/0.19 g	High damping rubber
USC Teaching Hospital		0.19 g/0.17 g 0.21 g/0.37 g	Rubber/lead rubber
Rockwell International Headquarters		0.15 g/0.08 g	Lead rubber
Three story Residential Building		0.63 g/0.44 g	Spring and viscodamper

maximum measured accelerations are higher than those on the ground. This means that the performance of these particular isolated structures was worse than their non-isolated counterparts. The possible reasons may be that the resonance amplification of structures above the isolators occurred in a higher or wide frequency range rather than their fundamental frequencies. The design of base isolators is based on calculation of rigid body rocking vibration of structures on the isolators. This ignores the vibration of structures at higher order modes, which sometimes show significant local vibrations. In addition, designers might ignore the effects of the heavy damping of the isolators, which can generate short pulses with high intensity, leading to high structural accelerations [39].

The findings above cast serious doubt on the functionality of base isolators. Further, they also push engineers to abandon the expectation of “five-ten-fold” mitigation effects for isolators [40] and to put more efforts into investigating the successful case of using base isolators.

23.4 Sliding Isolation Systems

23.4.1 General

Sliding base isolation systems utilize the frictional sliding mechanism between the structure and foundation. On one hand, the mechanism requires a low friction to partially cut the load transmission path. The forces transmitted to the superstructure are limited by the maximum friction forces, regardless of amplitude of ground motions. Therefore, the transfer of ground motions to the structure can be significantly reduced. On the other hand, the mechanism also provides friction to dissipate energy independent of frequency. The displacements of sliding are controlled by high tension spring or by making the sliding surface curved, thus providing a restoring force, otherwise unavailable, to return the structure to the equilibrium position [41].

Originally invented in US [42], sliding isolation systems have been installed as bearings between structures and their foundations/supports. The bearings reduce lateral loads and horizontal movements transmitted to the structure, thus protecting the primary structures from damage due to strong ground motions.

A typical type of sliding isolation system is a combination of friction pendulum and spherical bearing. As the slider travels across the concave surface, causing the gravity mass to rise, some of the kinetic energy is transformed into potential energy. The gravity load and potential energy stored by the superstructure will induce restoring force (shear force) parallel to the surface, provides stiffness during the sliding, and also enabling the structural mass return back to its original location after the strong motions cease. As shown in Fig. 23.18, three basic types of sliding isolation systems are used for reducing vibrations: rocker, ball and roller pendulum bearings, respectively. Among these, the ball pendulum is widely used in real world

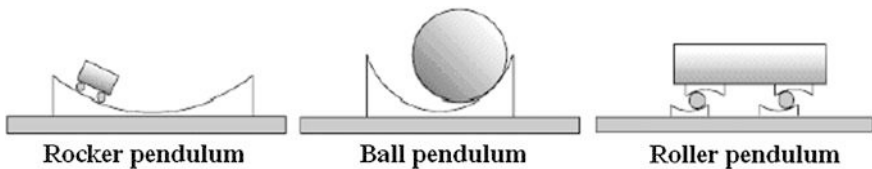


Fig. 23.18 Three types of sliding isolation system [43]

engineering structures. Note that the seismic force transferred from the bearing to the supported structure above depends not only on the friction force of the bearing, but also on the curvature of the sliding surface. These two parameters are essential in the design of a sliding isolation system.

Damping in a typical single ball pendulum sliding isolation system is selected by choosing a decent friction coefficient. When the seismic induced forces on the system are below the friction generated forces, the sliding isolation system stands still as a conventional structural support, with the structure's non-isolated vibration period. However, if the earthquake induced force on the system is just above the friction generated force, the structure supported on the bearing begins to slide at its isolated period, but its response and damping are controlled by the isolation system. Generally, with an increase in friction coefficient of the bearing, the global base shear increases while the structure's displacement decreases, and vice versa. The effective damping of the sliding isolation system generally ranges from a few percent to up to 25 %.

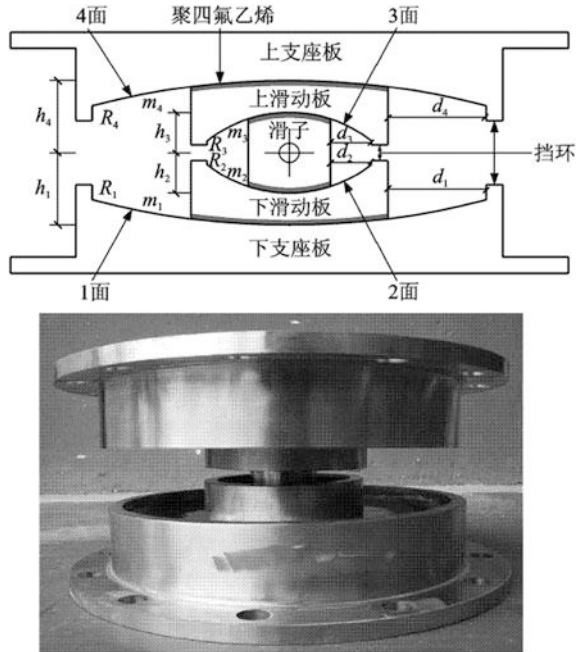
Abundant experimental tests have proved the reliability and effectiveness of the dynamic and sliding properties of ball pendulum bearings [44–55]. For example, shake table test has been performed on a seven story steel framed structure with a friction pendulum isolator. The results show a reduction of lateral base shear, story shears and story drifts by factors between 4 and 6 [56].

Under repeated cyclic loadings, the ball sliding system exhibits a consistent bilinear response without noticeable degradation. The specified effective stiffness and damping values are accurately delivered for either unscratched or scratched bearings, new or aged bearings, and for temperatures ranging from -1 to 38 °C. Full-size bearing tests also showed that they retain their full strength and stability throughout their displacement range, with high strength factors of safety [56].

Based on the number of sliding surfaces, the sliding isolation system can be classified as single-spherical-friction pendulum bearing (FPS) and multiple-spherical-friction pendulum bearing [57–65].

Note that a challenge in the design of isolation systems is that, to withstand very severe seismic motions, bearings often become so large, stiff and strong that they provide little isolation during moderate seismic events. This problem can be solved by using a multiple-spherical-friction pendulum isolation bearing, which is capable of progressively exhibiting different hysteretic properties at various levels of displacement demand. Through the selection of geometric quantities such as spherical surface radii and slider height, combined with specification of friction coefficients for each sliding interface, pendulum stages can be set to address specific response

Fig. 23.19 A triple-friction-pendulum bearing [66] (courtesy of Xiuli Du, Beijing University of Technology)



criteria for moderate, severe and very severe events [65]. Figure 23.19 shows a design of a triple-friction-pendulum bearing, which incorporates four concave surfaces and three independent pendulum mechanisms. Note that for each sliding surface, the associated surface curvature, friction coefficient and excursion capability can be tuned independently of that of other surfaces (adaptive), so that the level of damping and stiffness of the bearing can be controlled to meet the design requirement. In this design, the sequence of the sliding for each part is dependent on the friction coefficient, the stiffness of the bearing is dependent on the curvature of the sliding surfaces, and the lateral seismic force transmitted to the superstructure is dependent on both the friction coefficient and the curvature of the sliding surfaces [66]. As for the triple-friction-pendulum bearings, three effective radii and three friction coefficients are selected to optimize performance for different strengths and frequencies of earthquake shaking. This allows for a maximum design flexibility to accommodate both moderate and extreme motions.

23.4.2 Determination of Basic Properties for Sliding Isolation Systems

The natural frequency of the sliding isolation bearing is independent of the mass of the supported structure, and can be selected by only choosing the radius of curvature of the concave surface expressed as:

$$\omega = \sqrt{\frac{g}{R}} \quad (23.20)$$

where g is the acceleration of gravity and R is the radius of curvature of the sliding surface.

The constant lateral stiffness K of the sliding isolation system providing the restoring capacity is calculated as:

$$K = G/R \quad (23.21)$$

where G is the self-weight of the structure.

When the bearing slides with a distance of l away from the neutral position, the lateral load (the base shear) BS transmitted to the structure causing the sliding can be expressed as:

$$BS = Kl + \mu G \quad (23.22)$$

where μ is the friction coefficient, which depends on the material of contacting surfaces (typically Teflon-coated), as well as the contact pressure between the slider and the stainless steel surface, for an effective sliding system design, μ is normally required to range between 3 and 10 % [67].

From the two equations above, it is noted that the stiffness only depends on the curvature of the bearing concave surface. A more realistic effective stiffness K_{eff} is defined as the lateral force expressed divided by the lateral displacement l , which gives:

$$K_{eff} = \frac{BS}{l} = \frac{Kl + \mu G}{l} = K + \frac{\mu G}{l} \quad (23.23)$$

From the equation above, it is clearly seen that friction of the isolation bearing contributes to the effective stiffness with a value of $\frac{\mu G}{l}$, which can be illustrated in the hysteresis modeling of the sliding bearing system as shown in Fig. 23.20.

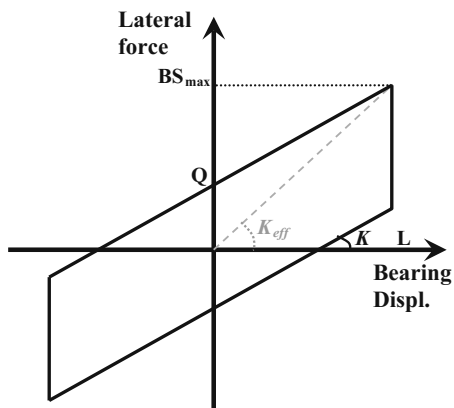
Based on the effective stiffness, the corresponding equivalent natural frequency of the sliding isolation system can be estimated as:

$$\omega_{eff} = \sqrt{\frac{K_{eff}}{G/g}} \quad (23.24)$$

The energy dissipated per cycle of sliding with an amplitude of L is calculated as:

$$E_L = 4\mu GL \quad (23.25)$$

Fig. 23.20 Simplified modeling of hysteresis for sliding bearing system



From the equations above it is noted that a sliding isolation bearing with higher natural frequency will generally result in a bearing with dimension higher (R) vertically but smaller horizontally, and the restoring force/re-centering capacity is also higher. Generally, with an increase of natural frequency of the sliding isolation bearing, the global base shear increases while the structure's displacement decreases, and vice versa. The sliding isolation bearing is normally designed to decrease the natural frequency of the isolated structure, so that the highest lateral forces due to strong ground motion can be significantly decreased. The force is independent of the mass of the supported structure.

This section presents a calculation to determine the basic properties for sliding isolators. For a more comprehensive coverage of this topic and also its application for both single-spherical-friction pendulum bearings and multiple-spherical-friction pendulum bearings, readers may read relevant references cited in Sect. 23.4.1.

23.4.3 Design of Sliding Isolation Systems

The design of a sliding isolation system essentially involves choosing a decent damping value, which is mainly determined by the properties of bearing friction coefficient μ and the radius of curvature of the sliding surface R . A simplified general procedure for an initial design of a sliding isolation system is described as follows:

1. Based on the support dimensions of the target superstructure and engineering experience, choose a decent size sliding bearing; especially important is the value of the radius of curvature of the sliding surface and friction coefficient, of which the friction coefficient can be assumed to be a value at a range of 3–10 %.
2. Choose a total damping value ξ (the percent of critical damping) required for the structure-bearing system, which comprises an inherent structural damping ξ_s

(from 0.5 to 5 %) and the damping contributed by the sliding isolation system ξ_d : $\xi = \xi_s + \xi_d$.

3. The damping of the sliding isolation system ξ_d is calculated by $\xi_d = \frac{E_L}{2\pi K_{eff} L^2}$; here it is important to choose a decent value of L , which is the value used for the iteration procedure to reach a convergence, as will be described in the later steps.
4. With total damping calculated above, determine the horizontal acceleration design spectrum.
5. Based on the natural frequency of the sliding isolation bearing (Sect. 23.4.2) and the design spectrum determined in step 4, the spectral acceleration can be calculated as $S_a = \omega_{eff}^2 L$, where L is the amplitude of the sliding system or spectra displacement.
6. From the previous steps, it is noticed that the amplitude of the sliding system L is a function of ω_{eff} and ξ_d . Note that ω_{eff} and ξ_d are again functions of the L ; an iterative procedure by repeating all the steps above is needed until the convergence of L is reached.

23.4.4 Advantages and Drawbacks of Sliding Isolation Systems

Compared to the traditional elastomeric isolation method, the sliding isolation systems have the following advantages:

1. Since the friction force is almost independent of the motion frequency, sliding isolation systems are effective for a wide range of frequency excitations.
2. Because the frictional force is developed at the base of the structure, it is proportional to the mass of the structure. The center of mass and center of resistance of the sliding support coincide. Therefore, the torsional effects produced by the asymmetric characteristics are avoided or at least minimized.
3. The restoring force is independent of the structural mass, but is dependent on the displacement of the pendulum.
4. The bearing's period, vertical load capacity, damping, displacement capacity, and tension capacity can all be selected independently.
5. The compressional stiffness of a typical ball sliding system is more than 5–10 times higher than its rubber bearing counterparts. This enables the ball bearing to resist much higher vertical loading and overturning moment (normally more than 10 times).
6. The high compressional stiffness also results in a higher vertical vibration frequency (generally higher than 20 Hz), which is less vulnerable to dynamic amplification of vertical motions, thus mitigating the vertical bearing loads due to vertical ground motions.

7. Due to the curvature of the sliding surface, the ball bearing can normally be restored to its original place after strong seismic motions are ceased.
8. The bearing is less sensitive to extremes in temperature, and more compact.

However, similar to those with elastomeric bearings, sliding isolation systems may not be effective in reducing the seismic response of structures at a near fault site in which the seismic motions may contain significant and long period pulses. Moreover, since sliding isolation systems have rather high vertical stiffness, even though they are used to cut the transmission path of horizontal seismic motion from foundations to upper-structures, they cannot be used to decrease the seismic motion transmission along the vertical direction, which can be significant and comparable to that of the horizontal ones in the near fault regions as discussed in Sect. 5.4.4.

23.4.5 Engineering Applications

To develop the reserves of 1.2 billion barrels of oil and 17 trillion cubic feet of gas in the Piltun-Astokhskoye and Lunskoye fields off Sakhalin Island, US\$10 billion was invested on Sakhalin II project, making it the largest single foreign investment in Russia and one of the largest offshore engineering projects in the world.

As shown in Figs. 23.21 and 23.22, two four leg GBS offshore platforms PA-B and LUN-A have been designed and constructed at water depths of 48.2 and 30.8 m, respectively. The topside (structures above the concrete shafts' top) weight for the PA-B and LUN-A platforms is around 26,000 and 33,000 tons, respectively.

During the front end engineering phase, in addition to loadings conventionally experienced in most of the offshore environments, significant seismicity and the harsh Arctic climate make earthquake and ice loading two detrimental loads

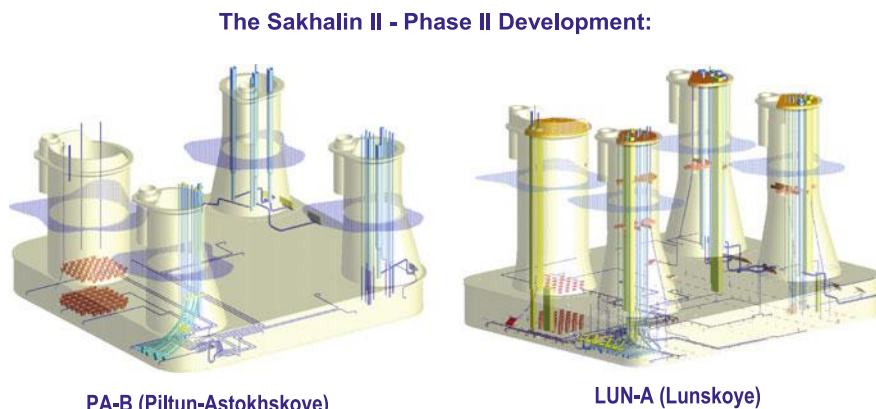


Fig. 23.21 Designs of PA-B and LUN-A GBS structures located offshore of Sakhalin (courtesy of Aker Solutions)



Fig. 23.22 The construction site of PA-B and LUN-A GBS structures (courtesy of Aker Solutions)

challenging the structural design. The design criteria are defined as: during a 200 year (strength level earthquake) return period seismic event, the platforms are expected to remain elastic, and during a 3000 year (ductility level earthquake) return period event, only limited structural damage is expected, with facilities to evacuate the platform without major environmental consequence. The design load due to horizontal ice crushing on the GBS shafts are 269, 324 and 405 MN for return periods of 1, 100 and 10,000 years, respectively. Moreover, it is noted that the exposed shafts experience higher ice loads than downstream legs. This causes applied load on the topside both differentially and multi-directionally. The differential loads for the shafts are in the order of 103, 124 and 155 MN, respectively. Around 20 % of the differential load will be transferred to the topside if it is rigidly connected to the GBS, requiring a large amount of steel work to be added to the topside. Furthermore, the atmospheric temperature induced thermal contraction load and wave load are also important loadings for the structural design. In addition, dynamic ice crushing load can also induce topside vibrations, which influences the comfortability of personnel on board the platform.

At the end of the front end engineering design stage, it was estimated that the seismic risk comprised almost 50 % of the total risk [68].

To overcome these challenges, Friction Pendulum Bearing (FPB) is proposed and interposed between the topside and GBS shafts (Fig. 23.23) with a maximum excursion capacity of 0.7 m, which reduced the seismic risk to 26 % of all risks with an associated seismic return period of 6000 years. Figure 23.24 shows the FPB used in the two GBSs, which make the topside–GBS shaft interface a floating deck during strong seismic motions. Based on the optimization with regard to cost

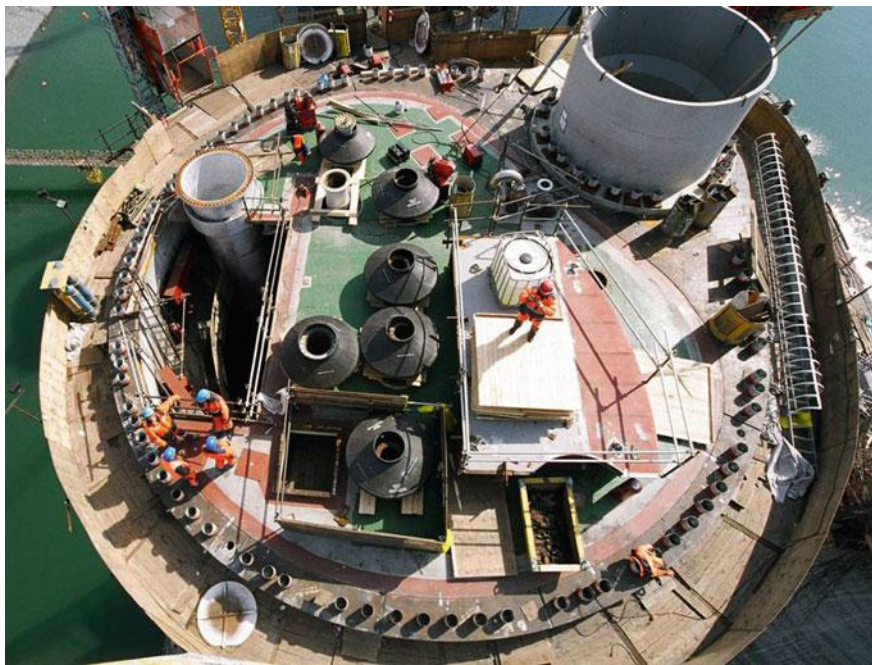


Fig. 23.23 The top view of GBS top above which the FPB are installed, allowing large relative movement between the topside and GBS during earthquake (courtesy of Aker Solutions)

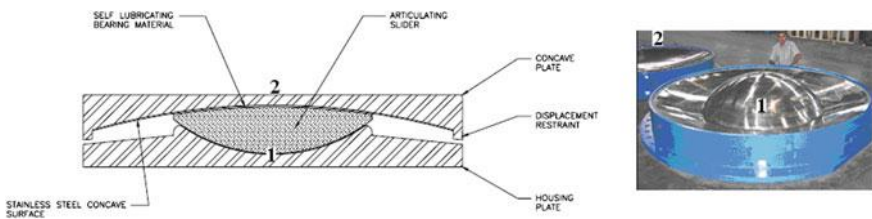


Fig. 23.24 The concave and slider of FPB in PA-B and LUN-A platforms (courtesy of Earthquake Protection System, Inc.)

and effectiveness, the FPB system is selected with a natural frequency of 0.25 Hz and a 5 % damping. Through non-linear dynamic analyses, it shows that, during a 100 years return period of earthquake, accelerations on decks, flare tower and cranes are decreased to less than half of that without installing the FPB. The maximum deck shear force drops from 195 to 29 MN, which is within an acceptable level with regard to safety. Figure 23.25 shows the response spectrum at the underside of the deck (immediately above FPB) [69], for which a significant reduction in acceleration can be observed.

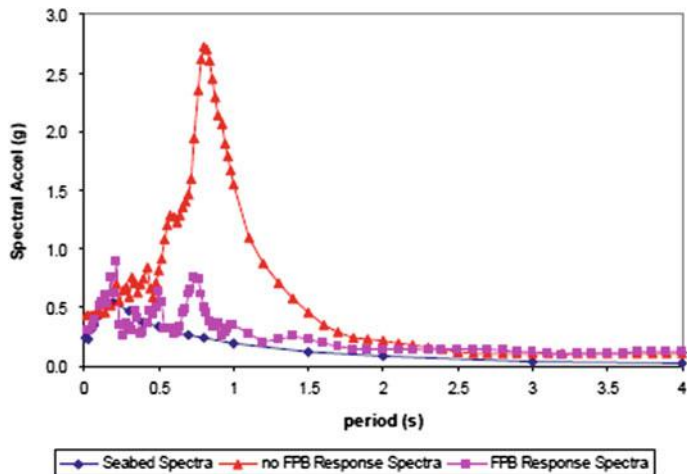


Fig. 23.25 The response spectrum at the underside of the deck, under a 100 years return period of earthquake excitations [69]

Since friction forces on FPB are relatively low with a kinematic friction coefficient ranging from 0.04 to 0.06 in normal temperature conditions, in addition to isolating the seismic load and ice load, wave and thermal contraction loads were also decoupled from the topsides, thus effectively removing these loadings from the topsides' structural design [69].

It is estimated that by using FPB, US\$300 million of construction costs were saved for the two platforms.

23.5 Testing of Base Isolation System

Since the base isolation systems are used to function during extreme load conditions under large deformation or movement, testing is essential and normally compulsory to confirm the reliability and performance of the system. In general three types of testing programs may be required during different phases of a project:

Basic property test: this test is to obtain the fundamental characteristics of a new isolation system or a substantially revised version of an existing system, such as the effects of load frequency, virgin loading, vertical load or pressure, load direction, velocity, etc. It is only performed once for a new or revised version of system.

Prototype test: this test is, prior to production of all isolators for a specific project, to confirm the mechanical properties of the isolators. The test is normally conducted on at least two isolator specimens of each type and size of isolator to be manufactured.

Production test: this test is, for the quality control/assurance, to confirm the quality of manufacture and as-built properties of isolators before they are installed on a structure. The test is normally carried out along with the material test. Because the mechanisms and materials used for elastomeric or sliding isolation system are different, separate production test requirements are specified for each type of system.

For more detailed information regarding testing for base isolation systems, the reference by Taylor [70] is recommended.

23.6 Selection and System Comparison Among Conventional Design, Base Isolation and Damping Apparatus

Generally, base isolation systems are most effective if an isolated structure has a period significantly higher than that of the original structure. Different from base isolation systems, damping apparatuses are most effective in reducing damage to flexible structures, and much less effective in reducing damage to rigid structures [71]. This is because in order for a damping apparatus to dissipate energy, a large structural deflection is desirable, as previously mentioned. Table 23.2 illustrates the system comparison among conventional design, base isolation or damping apparatus. It is shown that the selection of the system depends on the primary structures' characteristics and design objectives (acceleration or displacement).

Furthermore, to avoid resonance, the natural period associated with the horizontal vibration mode of a base isolator, typically ranging from 2.0 to 3.0 s, should not coincide with the site period.

It should also be noticed that both base isolation and damping apparatus are rarely designed for structures located in unmapped areas with regard to seismic hazard, or close to active faults. In the latter, the ground motions can be extremely high and the majority of the seismic energy may be contained in an initial large and long period pulse. Historic records show that near fault ground motions may have one or more displacement pulses ranging from 0.5 m to more than 1.5 m, with peak velocities in the order of 0.5 m/s or higher. The duration is normally in the range of 1–3 s, but can extend up to 6 s [72]. Therefore, near fault seismic motions can introduce significantly large deformation demands on flexible structures such as high rise buildings, long span bridges [73], and heavy and high rise offshore platforms. This is more obvious for base-isolated structures [74], and previous studies and recent in-field observations have raised serious concerns about the safety of flexible structures located in potential near fault regions and in particular on the effectiveness of base isolations for structures located in such areas. However, such significant and long period pulses do not normally exist in ground motions recorded at locations at some distance from the near fault region.

Table 23.2 System comparison among conventional design, base isolation or damping apparatus [71]

Structure characteristics	Conventional design		Structures with seismic isolators		Structures with damping apparatus		Recommended system
	Seismic displ.	Seismic accel.	Seismic displ.	Seismic accel.	Seismic displ.	Seismic accel.	
Rigid (e.g., shear wall, masonry)	Low	High	Low	Low	Low	High	Seismic isolators
Semi-rigid or semi-flexible (e.g., braced frames, stiff moment frames, tall shear walls)	Moderate	Moderate	Low	Low	Low	Low	Seismic isolators or damping apparatus
Very flexible structures (e.g., steel or concrete frame)	High	Normally high ^a	Normally moderate ^a	Normally low ^a	Normally moderate ^{a,b}	Normally low ^a	Damping apparatus ^b

^aFlexible structures cover a broad range of structural types and wide period range. Selection of an appropriate system to reduce earthquake damage depends on the dynamic characteristics of the structure in question. Energy dissipation schemes are more likely to be effective for very flexible structures, but either system might be used for semi-rigid and semi-flexible structures.

^bSpecial detailing may be required to protect elements vulnerable to displacement damage as a result of the moderate inter-story displacements

23.7 Hanging Isolation System

Rather than isolate the structure from the base, Fig. 23.26 illustrates the principles of a pendulum isolation mechanism by hanging the weight through strings. Because the flexural stiffness of the suspension strings is rather low, basically any movement from the bearing frame cannot be transmitted to the bob/weight through the strings.

The engineering realization of the pendulum isolation mechanism are the so-called suspended high rise structures as shown in Fig. 23.27, in which the

Fig. 23.26 Principles of pendulum isolation mechanism

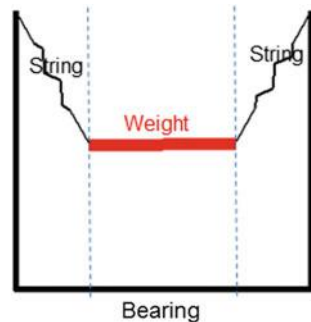
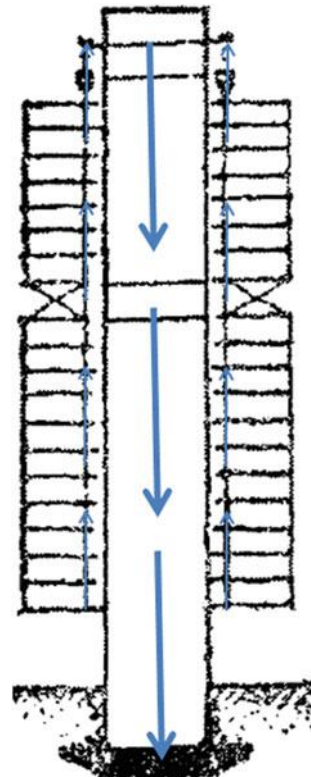


Fig. 23.27 Mechanism of suspended high rise structures



occupied structure is suspended using cables or rods from the top of a very stiff core structure. Therefore, there are fewer columns inside the buildings because the load is taken by the hanger, and this allows flexibilities to arrange space and also reduces the potential for column buckling because the high strength hangers in tension replace the large compression columns. Therefore, the suspended high rise structures can attain a high level of earthquake resistance along with architecturally desirable form. The suspended high rise structures also optimize the utilization of structural material for the right function: steel for tension and concrete for compression. Regarding the load path, the vertical load path of the hanged structure travels up to the top, and then further travels down to the foundation. However, the uses of fewer columns require that the rigid core columns need to have a large root foundation to resist the overturning moment.

Figure 23.28 shows BMW Tower built between 1968 and 1972. The tower's exterior is supposed to mimic the shape of four cylinders in a car engine. The four

Fig. 23.28 The BMW tower using a pendulum isolation mechanism



“cylinders” are suspended from an assembly of four semi-cylindrical concrete cores by means of hangers. The stairs and elevator are inside the concrete cores. Each floor is supported by a high strength hanger at its center and stabilized horizontally by the core. To keep differential deflection within acceptable limits, the tower is partitioned into an upper part with seven floors and lower part with 11 floors. Apart from the four hangers, the office space is free from columns, which provides great flexibility.

References

1. Skinner RI, Beck JL, Bycroft GN (1975) A practical system for isolating structures from earthquake attack. *Earthq Eng Struct Dyn* 3(3):161–201
2. Buckle I, Mayes R (1990) Seismic isolation: history, application, and performance—a world view. *Earthq Spectra* 6(2):161–201
3. Allen E (1999) Fundamentals of building construction materials and methods, 3rd edn. Wiley, New York
4. Zhou F (1983) Experimental investigations of solid state steel energy absorbers for earthquake resistant structures. University of British Columbia, Vancouver
5. Zhou F (1997) Anti-seismic control of engineering structures. China Seismological Press, Beijing (in Chinese)
6. Piersol A, Paez T (2009) Shock and vibration handbook, 6th edn. McGraw-Hill Education, New York
7. Stanton J, Scroggins G (1990) Stability of laminated elastomeric bearings. *J Struct Eng ASCE* 116:1351–1371
8. Jangid R, Datta T (1985) Seismic behavior of base isolated buildings: a state of art review. *Proc Civ Eng Struct Build* 110:186–203
9. Kelly JM (1990) Base isolation: linear theory and design. *Earthq Spectra* 6(2):223–244
10. Kunde MC, Jangid RS (2003) Seismic behaviour of isolated bridges: a-state-of-the-art review. *Electron J Struct Eng* 3:140–170
11. Product and Technical Information (2008) MAURER Seismic Isolation Systems with Lead Rubber Bearings (MLRB)
12. Nishi T, Kelly JM, Zhou F (2009) Rubber structural mounts save lives during earthquakes. ISO Focus, Geneva, pp 26–28
13. Monti MD, Ferguson WG, Robinson WH (1995) Lead as a cyclic motion damper. *NZNSEE Pac Conf Earthq Eng* 3:323–330
14. Zhang R (2000) Seismic isolation and supplemental energy dissipation. In: Chen W-F, Duan L (eds) Bridge engineering handbook. CRC Press, Boca Raton
15. Robinson WH (1998) Passive control of structures, the New Zealand experience. *ISET J Earthq Technol* 375(4):63–75
16. Monir HS, Nomani H (2011) Application of lead rubber isolation systems in the offshore structures. In: Proceedings of the international multi conference of engineers and computer scientists, vol 2, Hong Kong
17. Ou JP, Xu L, Li QS, Xiao YQ (2007) Vibration control of steel jacket offshore platform structures with damping isolation systems. *Eng Struct* 29(7):1525–1538
18. Zhou F (1997) Seismic response control of engineering structures. China Seismological Press, Beijing (in Chinese)
19. Jia J (2014) Essentials of applied dynamic analysis. Springer, Heidelberg
20. Galef AE (1968) Bending frequencies of compressed beams. *J Acoust Soc Am* 44(8):643

21. Bokaiyan A (1988) Natural frequency of beams under compressive axial loads. *J Sound Vib* 126(1):49–65
22. Amba-Rao CL (1967) Effect of end conditions on the lateral frequencies of uniform straight columns. *J Acoust Soc Am* 42:900–901
23. Rivin EI (1999) Stiffness and damping in mechanical design. Marcel Dekker Inc., New York
24. Hsiang-Chuan T (2004) Compression stiffness of infinite-strip bearings of laminated elastic material interleaving with flexible reinforcements. *Int J Solids Struct* 41:6647–6660
25. Naeim F, Kelly JM (1999) Design of seismic isolated structures. Wiley, New York
26. Jiao Z, Zhou F, Li X (1995) Finite element analysis of ultimate capacity for layered rubber bearings. Research Report of Huanan Construction Institute, Beijing (in Chinese)
27. International Building Code, International Code Council, 2015
28. International Conference of Buildings Officials (1997) Earthquake regulations for seismic-isolated structures. Uniform Building Code, Appendix Chapter 16, Whittier, CA
29. Yang YB, Huang WH (1998) Equipment–structure interaction considering the effect of torsion and base isolation. *Earthq Eng Struct Dyn* 27:155–171
30. Kilar V, Koren D (2009) Seismic behavior of asymmetric base-isolated structures with various distributions of isolators. *Eng Struct* 31:910–921
31. Narasimhan S, Nagarajaiah S, Johnson EA, Gavin HP (2006) Smart base isolated building part I: problem definition. *Struct Control Health Monit* 13:573–588
32. Erkus B, Johnson EA (2006) Smart base-isolated benchmark building part III: a sample controller for bilinear isolation. *Struct Control Health Monit* 13:605–625
33. Kelly JM (1997) Earthquake design with rubber. Springer, Heidelberg
34. Braun C (2009) The sliding isolation pendulum: an improved re-centering bridge bearing. *Steel Constr* 2(3):203–206
35. Priestley MJN, Seible F, Calvi GM (1996) Seismic design and retrofit of bridges. Wiley, New York
36. Steiner F, Elsesser E (2004) Oakland City Hall repair and upgrades. Publication No. 4, series on applied seismic design of buildings, EERI, Oakland, CA
37. Nagarajaiah S, Sun X (2000) Response of base-isolated USC Hospital Building in Northridge earthquake. *J Struct Eng ASCE* 1177–1186
38. Kawashima K (2012) Damage of bridges due to the 2011 Great East Japan earthquake. In: Proceedings of the international symposium on engineering lessons learned from the 2011 Great East Japan Earthquake, Tokyo
39. Shustov V (1994) Briefing on the 1994 Northridge earthquake experience: seismic isolation. California State University Northridge
40. PEER (2001) KRON 4 News broadcast from March 1, 2001 on the current Pacific Earthquake Engineering Research Center/UC Berkeley shaking table experiments, Project, no. 5051999, San Francisco, CA. [http://www ecs csun.edu/~ shustov/KRON_broadcast_Peer mpg](http://www ecs csun edu/~ shustov/KRON_broadcast_Peer mpg)
41. Chopra AK, De la Llera JC (1996) Accidental and natural torsion in earthquake response and design of buildings. In: 11th World conference on earthquake engineering
42. Zayas VA, Low S, Mahin S (1990) A simple pendulum technique for achieving seismic isolation. *Earthq Spectra* 6:317–334
43. Matta E, De Stefano A (2009) Robust design of mass-uncertain rolling pendulum TMDs for the seismic protection of buildings. *Mech Syst Signal Process* 23:127–147
44. Al-Hussaini TM, Zayas VA, Constantinou MC (1994) Seismic isolation of multi-story frame structures with friction pendulum isolators. Technical report 94-007. National Center for Earthquake Engineering Research, State University of New York at Buffalo
45. Zayas VA, Constantinou MC, Tsopelas P, Kartoum A (1996) Testing of friction pendulum seismic isolation bearings for bridges. In: Proceedings of the fourth world congress on joint sealing and bearing systems for concrete structures, Sacramento, California, Sept 1996
46. Constantinou MC, Tsopelas P, Kim YS, Okamoto S (1993) NCEER-Taisei corporation research program on sliding isolation systems for bridges: experimental and analytical study of friction pendulum system. Report no. 93-0020, National Center for Earthquake Engineering, State University of New York at Buffalo, Nov 1993

47. Mokha AS, Constantinou MC, Reinhorn AM (1990) Experimental study and analytical prediction of earthquake response of a sliding isolation system with a spherical surface. Report no. NCEER 90-0020, National Center for Earthquake Engineering Research, State University of New York at Buffalo, Oct 1990
48. Zayas VA, Low S (1993) Seismic isolation retrofit of a historic building. In: Proceedings of national earthquake conference, Central United States Earthquake Consortium, Memphis, Tennessee
49. Zayas V, Low S, Bozzo L, Mahin S (1989) Feasibility and performance studies on improving the earthquake resistance of new and existing buildings using the friction pendulum system, UCB/EERC-89/09, Earthquake Engineering Research Center, University of California, Berkeley
50. Zayas VA, Low SS, Mahin SA (1987) The FPS earthquake resisting system, experimental report. Report No. UCB/EERC 87/01, Earthquake Engineering Research Center, University of California, Berkeley, June 1987
51. Zayas V, Piepenbrock T, Al-Hussaini T (1993) Summary of testing of the friction pendulum seismic isolation system: 1986–1993. In: Proceedings of the ATC-17-1 seminar on seismic isolation, passive energy dissipation and active control, Applied Technology Council, San Francisco, Mar 1993
52. Zayas VA, Low SS, Mahin SA (1989) Shake table testing of a friction pendulum seismic isolation system, seismic engineering: research and practice. The American Society of Civil Engineering, Structural Congress, San Francisco
53. Lambrou V, Constantinou MC (1994) Study of seismic isolation systems for computer floors. Technical report NCEER-94-0020, National Center for Earthquake Engineering Research, State University of New York at Buffalo, July 1994
54. Constantinou MC (1996) Research on longevity and reliability of sliding seismic isolation systems. NCEER highway project technical report, National Center for Earthquake Engineering Research, State University of New York at Buffalo
55. CERF Report: HIITEC 98-07 #40370 Evaluation findings for Earthquake Protection Systems, Inc. Friction pendulum bearings, Sept 1998
56. Earthquake Protection Systems (2003) Technical characteristics of friction pendulum bearing. Earthquake Protection Systems Inc., Vallejo
57. Constantinou MC, Mokha AS, Reinhorn AM (1990) Teflon bearings in base isolation: modeling. *J Struct Eng* 116:455–473
58. Tsopelas P, Constantinou MC, Okamoto S, Fujii S, Ozaki D (1996) Experimental study of bridge seismic sliding isolation systems. *Eng Struct* 18(4):301–310
59. Constantinou MC (2004) Friction pendulum double concave bearing. NEES report
60. Tsai C, Chiang T, Chen B (2005) Experimental evaluation of piecewise exact solution for predicting seismic responses of spherical sliding type isolated structures. *Earthq Eng Struct Dyn* 34:1027–1046
61. Kim YS, Yun CB (2007) Seismic response characteristics of bridges using double concave friction pendulum bearings with tri-linear behaviour. *Eng Struct* 29(11):3082–3093
62. Fenz DM, Constantinou MC (2008) Spherical sliding isolation bearings with adaptive behavior: theory. *Earthq Eng Struct Dyn* 37:163–183
63. Du XL, Han Q, Qi LK et al (2010) Multi-spherical sliding isolation bearing with adaptive behavior. Chinese Patent ZL2009201783677
64. Fadi F, Constantinou MC (2010) Evaluation of simplified methods of analysis for structures with triple friction pendulum isolators. *Earthq Eng Struct Dyn* 39:5–22
65. Morgan TA, Mahin SA The optimization of multi-stage friction pendulum isolators for loss mitigation considering a range of seismic hazard. In: The 14th world conference on earthquake engineering, Beijing, China
66. Liu W, Han Q, Du X, Qi L (2012) Design principle and theoretical model of multi-spherical sliding isolation bearing. *J Disaster Prev Mitig Eng* 32(4):417–422 (in Chinese)
67. Wang YP (2002) Fundamentals of seismic base isolation. In: International training programs for seismic design of building structures, Taipei, pp 139–148

68. International Association of Oil and Gas Producers (2014) Reliability of offshore structure—current design and potential inconsistencies. OGP report no. 486
69. Clarke CSJ, Buchanan R, Efthymiou M (2005) Structural platform solutions for seismic arctic environments—Sakhalin II offshore facilities, offshore technology conference, Houston
70. Taylor AW (2004) Primer on seismic isolation. ASCE, Virginia
71. <http://www.hnd.usace.army.mil>
72. Sharma A, Jangid RS (2011) Influence of high initial isolator stiffness on the seismic response of a base-isolated benchmark building. *Int J Struct Stab Dyn* 11(6):1201–1228
73. Malhotra PK (1999) Response of buildings to near-field pulse-like ground motions. *Earthq Eng Struct Dyn* 28:1309–1326
74. Jangid RS, Kelly JM (2001) Base isolation for near fault ground motion. *Earthq Eng Struct Dyn* 30:691–707

Chapter 24

Dynamic Absorber

24.1 General

To absorb the kinetic energy produced by dynamic loading such as by wave, wind, earthquake and ice loading on a structure, one can install a mechanism called a dynamic absorber [1] at an anti-node location (where the maximum vibration amplitude occurs) of a dominating eigenmode of the main structure, but with a much smaller mass than the mass of the main structure, and tune the natural frequency of the mechanism to be equal to the frequency of the disturbing force applied by the main structure on the mechanism. Therefore, the resonance of the mechanism with the vibration of the main structure facilitates the vibration energy of the main structure to be efficiently transferred into the absorber, and the main structure's dynamic response is reduced in an optimized manner.

The mechanism essentially imparts indirect damping to the structure by modifying its frequency response [2]. Theoretically, this can cause the primary structure mass to almost stand still. In addition, the energy dissipated during the movement of the smaller mass also introduces damping to the primary structure-smaller mass system, which is beneficial in attenuating the excessive vibration amplitudes of the primary structure as well as the smaller mass. The smaller mass can be in the form of solid mass or liquid. In engineering practice, this mechanism design is realized as a tuned mass damper (TMD) (Sect. 24.5) and tuned liquid damper (TLD) (Sect. 24.6). From another angle, the dynamic absorber can be viewed as an energy sink, where excess energy that is built up in a structure is transferred to the mass of an absorber. The absorber indirectly imparts additional damping to the structural system by modifying the frequency response function of the primary structure [3], thereby reducing the response. The energy is then dissipated by a form of viscous damping device that is connected between the structures and the absorber itself [4].

The concept of dynamic absorber was originally proposed by Frahm in 1909, who invented a vibration control device without any accountable inherent damping

called a dynamic vibration absorber. Note that the positive effect of the absorber diminishes when the excitation frequency is far from the absorber's self-vibration frequency. This drawback was eliminated by introducing a certain amount of damping in the absorber as proposed by Ormondroyd and Den Hartog [5]. Bishop and Welbourn [6] developed analytical solutions of absorbers with damping. Unlike Den Hartog who considered the absorber damping to be purely viscous, Snowdown [7] developed analytical solutions by considering the damping with various types. An optimization procedure was developed by Falcon and his coworkers [8] by implementing a restricted amount of damping applied to the main system. Several researchers [9, 10] introduced correction factors for the absorber parameters as functions of the main mass and damping. All their efforts contributed to the major feature of modern TMD and TLD design.

A Dynamic absorber can dramatically reduce the resonance response in a narrow frequency band, thus the dynamic absorber is most effective for periodic excitations and structures under dominated self-vibrations (e.g. a tower vibrating due to wind buffeting). For mitigating earthquake induced structural vibrations, the frequency of a dynamic absorber is ideally tuned close to the frequencies of both the natural frequency of the structure and the dominant frequency of strong ground motions. The displacement response will generally be multi-peaks (Fig. 24.4), corresponding to the vibrations at the structure's higher order of eigenfrequencies rather than the structure's natural frequency, which are mitigated by the TMD. There might still also be some other peaks corresponding to the dynamic loading frequency. In addition, readers should be aware of the following facts.

As illustrated in Fig. 24.1, the resonance vibrations of the dynamic absorber are out-of-phase (with a phase lag up to 90°) with the excitation from the structure, i.e., if a viscous damper is used as a connection between the absorber and the primary structure, the phase angle will be 90° [11]; if a viscoelastic damper is used as the

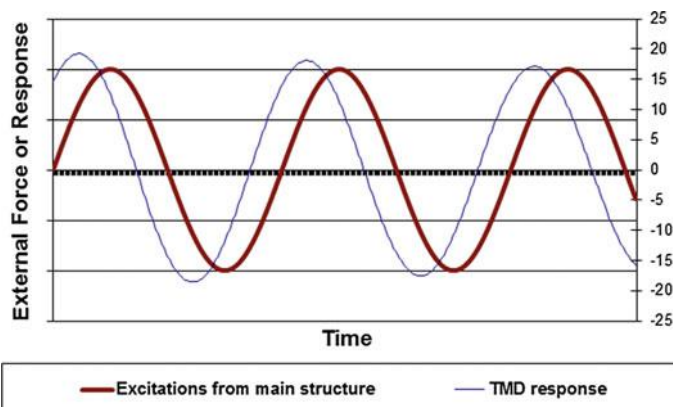


Fig. 24.1 The response of a TMD and the excitation from the main structure has a phase angle difference of up to 90°

connection, the phase angle will be less than 90° , see Fig. 22.12b, c for an illustration. However, it is noted that some literatures wrongly describe that the response is at all instants opposite/counter to the main structure's response, i.e., a 180° phase difference between the absorber response and the excitation.

The frequency content of the ground motion is complicated and may be rather wide banded.

The lower order eigenfrequencies of structures are normally separated well apart. In this frequency range, with small damping, the modal series will generally be dominated by a single mode with eigenfrequency close to the loading frequency and a single mode with natural frequency of the structure.

The higher order eigenfrequencies are more closely spaced. With a dynamic loading in this frequency region, multiple eigenmodes contribute in a similar extent to the modal expansion. Modes above the loading frequency will be out-of-phase with those below the loading frequency, causing dynamic cancellation, i.e., the net vibration is potentially less than any of the single mode vibrations in this frequency range [12].

Due to the reasons above, damping will be most influential in decreasing the dynamic response only at a frequency range very close to the natural frequency of the structure, and sometimes at the lower order eigenfrequencies of structures as well.

Dynamic absorber is most effective when installed at an anti-node location corresponding to the vibration modes most significantly contributing to structural dynamic responses, such as the top of a high rise building/tower or the middle of a bridge span.

Therefore, it is practical to adjust the dynamic absorber to the natural frequency of a structure. By doing this, rather than influencing the loading controlled response region (in most cases this region is quasi-static), the presence of the dynamic absorber may only mitigate the dynamic response due to the vibration of a structure close to its natural frequency.

Dynamic absorbers are relatively convenient to implement in both new structures and in the retrofit of existing structures. They normally do not require an external power source to operate and do not interfere with vertical and horizontal load paths. Moreover, dynamic absorbers can also be combined with active control systems (Sect. 28.3) to function as hybrid systems, or serve as a backup in the case of failure of active device [13].

Compared to high rise buildings that have modal masses distributed in various eigenmodes, the dynamic response of offshore structures is typically dominated by a single or double mode vibration (typically the first bending mode or first two bending modes) due to the concentrated weight on topside modules. Therefore, dynamic absorbers can be very efficient to mitigate offshore structural response when absorbers are installed on the anti-node (topside) of structures.

24.2 Dynamic Responses Due to the Installation of Dynamic Absorbers

Consider a physical modeling of a platform with a dynamic absorber shown in Fig. 24.2. The equation of motion for the entire primary structure-absorber system including the fundamental vibration mode is given by:

$$\ddot{F}(t) = \overline{M} \ddot{\overline{X}}(t) + \overline{C} \dot{\overline{X}}(t) + \overline{K} \overline{X}(t) \quad (24.1)$$

where $F(t) = \begin{bmatrix} M_s \\ m_a \end{bmatrix} \ddot{x}_g$; and \ddot{x}_g are the ground accelerations; $\overline{M} = \begin{bmatrix} M_s & 0 \\ 0 & m_a \end{bmatrix}$; $\overline{C} = \begin{bmatrix} C_s & c_a \\ c_a & 0 \end{bmatrix}$; $\overline{K} = \begin{bmatrix} M_s \omega_s^2 + m_a \omega_a^2 & -m_a \omega_a^2 \\ -m_a \omega_a^2 & m_a \omega_a^2 \end{bmatrix}$.

The displacement response spectrum of the primary structure M_s to a modal seismic spectral density ($S_g(\omega)$) of ground motions is given by:

$$S_X(\omega) = S_g(\omega) |H_x(\omega)|^2 \quad (24.2)$$

The mean square displacement response of the primary structure can then be calculated as:

$$E[X(t)^2] = \int_{-\infty}^{\infty} S_X(\omega) d\omega \quad (24.3)$$

By only accounting for the first eigenmode vibration of the absorber and assuming that the absorber's vibration near and below the natural frequency of the structure can be neglected, and the higher order modal mass of the absorber is added to the mass of the primary structure M_s , the transfer function of the complex

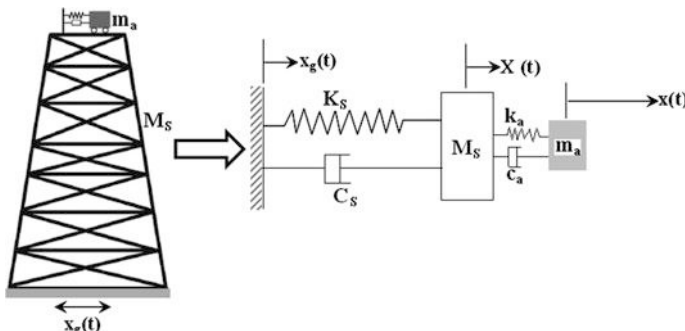


Fig. 24.2 Physical modeling of a primary structure installed with a dynamic absorber (K_s , C_s , M_s and k_a , c_a , m_a are the equivalent stiffness, damping and mass of the primary structure and the dynamic absorber, respectively; x_g is the ground translation motions)

frequency response for the structure-absorber system can then be derived from the equation of motion, resulting in an expression as below:

$$H_X(\omega) = \frac{X(\omega)}{F(\omega)} = \frac{M_s + Y(\omega)}{\omega_s M_s - \omega^2 M_s + i\omega C_s - \omega^2 Y(\omega)} \quad (24.4)$$

where $Y(\omega) = \frac{i\omega c_a + \omega_a^2 m_a}{\omega_a^2 - \omega^2 + (i\omega c_a / m_a)}$.

The equation above can also be expressed in term of spring stiffness of both the primary structure and the dynamic absorber:

$$\begin{aligned} H_X(\omega) &= \frac{X(\omega)}{F(\omega)} \\ &= \frac{-\omega^2 m_a + i\omega c_a + k_a}{2[(-\omega^2 M_s + i\omega C_s + K_s)(-\omega^2 m_a + i\omega c_a + k_a) - \omega^2(i\omega c_a + k_a)m_a]} \end{aligned} \quad (24.5)$$

where m_a is the modal mass corresponding to the first eigenmode of the absorber.

If the expression above is used in the equation that calculates the displacement response spectrum of the primary structure, one may solve for the structure's displacement response spectrum directly. The additional spectral peaks, and the shift in the peak of the fundamental eigenmode vibration will be explicitly calculated. If this expression is integrated into the equation that calculates the mean square displacement response of the primary structure, the effect of the dynamic absorber on the total mean square response can then be evaluated.

One drawback of the equation above is that it only considers the structure's first eigenmode vibration at the structure's natural frequency. This means that, under no circumstances should natural frequency of the absorber ω_a be close to or larger than the second eigenfrequency of the structure. This is fortunately the case for most dynamic absorber designs. Also, in most cases, the characteristics of the dynamic responses are dominated by the first mode vibration. However, for wide banded loading such as earthquake ground motions, the influence from many vibration modes may need to be accounted for in the design of dynamic absorbers.

An optimized dynamic absorber with respect to a structure's dynamic response can normally be reached by minimizing equation that calculates the mean square displacement response of the primary structure.

A simplification of the equations above is that the calculation of the fundamental frequency of the structure ω_s does not account for the contribution from the absorber and vice versa. This simplification can be justified if the natural frequency and the mode shape are not altered greatly by the presence of the absorber [14].

It should be noted that dynamic absorber may have both negative and positive influences on the structural response: the displacement of the structure may have a noticeable peak near the natural frequency of the dynamic absorber ω_a . This additional peak may increase the dynamic response (in the form of total mean square response of the primary structure). However, if the absorber is designed such

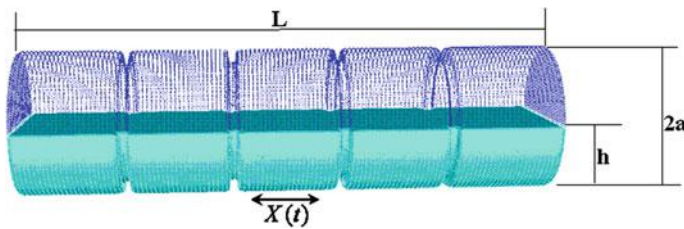


Fig. 24.3 Notations of dimensions for a horizontal cylindrical shaped tank

that ω_a is very close to the natural frequency of the primary structure ω_s , then the mean square displacement of the primary structure can be reduced.

For a rough estimation of the natural frequency of the dynamic absorber in the preliminary concept design stage, the following formula can be used:

For tuned mass damper (Sect. 24.5)

- (1) For tuned mass damper spring-mass system: $\omega_a = \sqrt{\frac{k_a}{m_a}}$.
- (2) For tuned mass damper simple pendulum system: $\omega_a = \sqrt{\frac{g}{L}}$, where L is the length of the hanging rope in m.

For tuned liquid damper (Sect. 24.6)

- (1) For tuned liquid damper system with a rectangular shaped tank: $\omega_a = \frac{2\pi}{L} \sqrt{gh}$, where L is the length of tank in direction of tank oscillation, h is the mean depth of liquid in m.
- (2) For tuned liquid damper system with a horizontal cylindrical shaped tank, with the length of the tank (in direction of tank oscillation) is larger than the diameter ($2a$) of the tank (Fig. 24.3): $\omega_a = 1.3 \sqrt{\frac{g}{a}}$ [15], where a is the radius of the tank in m.
- (3) For tuned liquid damper system with a vertical cylindrical shaped tank: $\omega_a = 1.36 \sqrt{\frac{g}{R} \tanh(\frac{1.84h}{R})}$, where R is the inner radius of tank, and h is the water depth in m.
- (4) For tuned liquid column damper system with U-tube tank: $\omega_a = \sqrt{\frac{2g}{L}}$, where L is mean fluid-filled length of the tube (measured along the center line of the tube) in m.

24.3 Design Procedure for an Optimized Dynamic Absorber

To effectively mitigate vibration responses of structures, one needs to first determine the mass and the frequency ratio between the primary structure and the absorber. The following procedure can be followed:

1. Estimate how much reduction of dynamic response is needed based on the acceptable response limits.
2. Based on the amount the reduction calculated in the step above, determine the damping (c_a or ζ_a) needed from the absorber in addition to the damping (c_s or ζ_s) of the primary structure.
3. Based on the damping determined in the step above, calculate the mass ratio μ between the absorber and the primary structure with the formula: $\zeta_a = \sqrt{\frac{3\mu}{8(1+\mu)}}$ under harmonic excitation [16] and $\zeta_a = 0.25\sqrt{\frac{\mu+\mu^2}{1+0.75\mu}}$ under white noise excitation; μ is the mass ratio of the damper and the primary structure.
4. Based on the optimized mass ratio μ calculated in the step above, calculate the ratio of natural frequencies between the dynamic absorber and the primary structure with the formula below and then determine the natural frequency of the optimized absorber ω_a .
 - (1) $\Omega = \frac{\omega_a}{\omega_s} = \frac{1}{1+\mu}$ under harmonic excitation
 - (2) $\Omega = \frac{\omega_a}{\omega_s} = \frac{1+\mu}{\sqrt{2\mu + \frac{3\mu^2}{2}}}$ under white noise excitation
5. Based on the step above, determine the stiffness needed for the dynamic absorber as: $\omega_a = \sqrt{\frac{k_a}{m_a}}$.

Note that in third step above, the optimized damping ratio is normally specified based on the assumption that the damping ratios at two peaks (above and below the natural frequency of the structure-absorber system, shown in Fig. 24.4) in the frequency response of the primary structure are identical.

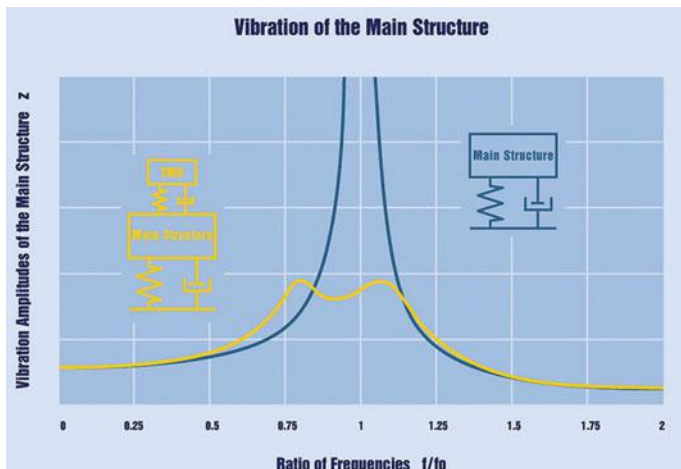


Fig. 24.4 Amplitude–frequency response of a low damped system without (blue) and with (yellow) TMD (courtesy of GERB vibration control system)

24.4 Practical Considerations for Designing a Dynamic Absorber

Due to the unique mechanism of dynamic absorbers, several issues need to be considered during the design:

1. A dynamic absorber is normally designed for decreasing only one single mode of vibration. To mitigate dynamic response due to contribution of several significant modes of vibrations, it is recommended to increase either the absorber's damping or to install several dynamic absorbers on the primary structure.
2. Because the frequency of the ground motions may vary from one earthquake to another, it is not recommended to design an absorber with a target ground motion frequency.
3. For offshore structures, their eigenfrequencies vary slightly due to the changes of marine growth thickness with season (Sect. 10.1.5) and of fluid tank levels. The design of an absorber should account for these variation effects.
4. The most optimized location with regard to its efficiency is the location with the maximum modal response (anti-node). For most vertical engineering structures (buildings, towers etc.), the first mode dominates the response. It is therefore desirable to locate the damper at the top of these structures. Similarly, for an offshore platform structure, this location is normally at the topside structure. For a bridge structure, this can be a location in the middle of a span.
5. For stiff structures built on sites with soft soil, the effectiveness of an absorber may be greatly degraded. This is because the absorber works more effectively if the ground motion frequency is higher than the natural frequency of the target structure, which leads to a condition in which the structure will exhibit significant vibrations at its natural frequency, which further excites the dynamic absorber and causes the resonance or close to resonance of the absorber, thus enabling the absorber to effectively dissipating seismic energy.
6. An absorber can only be used to effectively mitigate the structural response at its target frequency. It can also decrease responses at frequencies higher than the absorber's target frequency, but with a degraded efficiency. The structural responses at frequencies lower than the absorber's target frequency may be decreased or even increased [17].

24.5 Tuned Mass Damper (TMD)

24.5.1 General

A TMD is a passive damping system that utilizes a secondary mass attached to a vibrating structure (primary). The secondary mass has dynamic characteristics that relate closely to that of the primary structure. By varying the mass ratio of the

secondary mass to the primary body, the frequency ratio between the two masses, and the damping ratio of the secondary mass, the vibration energy will be efficiently transferred to the secondary mass (the secondary mass usually experiences large displacements/stroke lengths), the maximum displacement of the primary structure can then be minimized. The response of the tuned mass damper and its phase lag with that of the primary structure is illustrated in Fig. 24.1. In addition, a certain amount of damping can be produced through energy dissipation [4].

Due to its merits of being inherently stable and reliable during major earthquakes, together with its efficiency to dissipate a substantial amount of vibration energy of the main structure, and without requiring any connection to ground, tuned mass dampers have been successfully adopted to mitigate the dynamic response of many high rise structures due to wind and earthquake loading.

A TMD is generally designed as an auxiliary device of a relatively small mass, typically in the order of a few percent of that of the primary structure. The performance of a TMD installed on a structure can be evaluated based on an evaluation of the mean square displacement response of the primary structure as described in Sect. 24.2. An alternative evaluation is to observe the frequency response of the primary structure, as illustrated in Fig. 24.4. It is clearly shown that, with the utilization of a TMD, frequency response at the structure's natural frequency is greatly mitigated and the response peaks have been shifted from the natural frequency of the primary structure to another two frequencies with much lower vibration amplitude.

Figure 24.5 shows an example of TMDs installed on London Millennium Footbridge to mitigate vibrations along both vertical and horizontal directions. The TMDs have a type of spring-viscous-damper-mass mechanism with the following characteristics [18]:

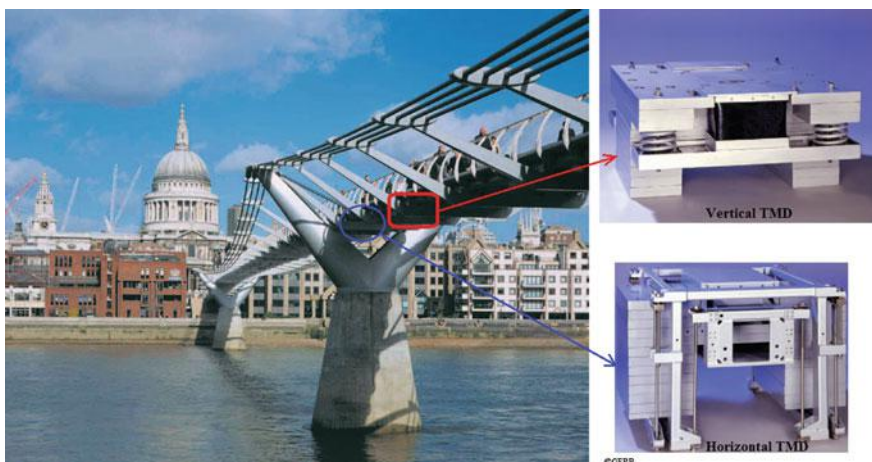


Fig. 24.5 TMDs installed on London Millennium Footbridge to mitigate vibrations along both vertical and horizontal directions (courtesy of GERB vibration control system)

- Every TMD is exactly tuned to the main natural frequency of the structure.
- TMD's dynamic properties must not change over time, even when exposed to variable weather conditions.
- TMDs can mitigate horizontal, vertical and torsional vibrations. For this particular design by GERB, to protect against vertical vibrations, TMDs can be equipped with helical compression springs and viscous dampers, as shown in the upper right figure in Fig. 24.5. To mitigate horizontal (and torsional) vibrations, TMDs can be equipped with leaf springs or pendulums, and viscous dampers, as shown in the lower right figure in Fig. 24.5.

Figure 24.6 shows various types of TMD system, of which the spring and damper system is the most popular.

By performing dynamic analysis of various structures installed with TMDs, Murudi and Mane [20] investigated the effectiveness of TMD in controlling the seismic response of structures and the influence of various ground motion parameters on the seismic effectiveness of TMD. They concluded that the effectiveness of TMD for a given structure depends on the frequency content, bandwidth and duration of strong seismic motion. A TMD's performance is more significant for lightly damped structures, long duration of ground motions, and for structures with natural frequencies close to that of the central frequency of ground motions. It is effective for controlling structural response to harmonic base excitation and is more effective for long duration earthquake ground motions. TMD is most effective for lightly damped structures, and its effectiveness decreases with an increase in structural damping. However, the TMD's performance is theoretically not affected by the magnitude of intensity of ground motion. Moreover, it is also reasonably effective for broad banded motions across the spectrum of structural frequencies.

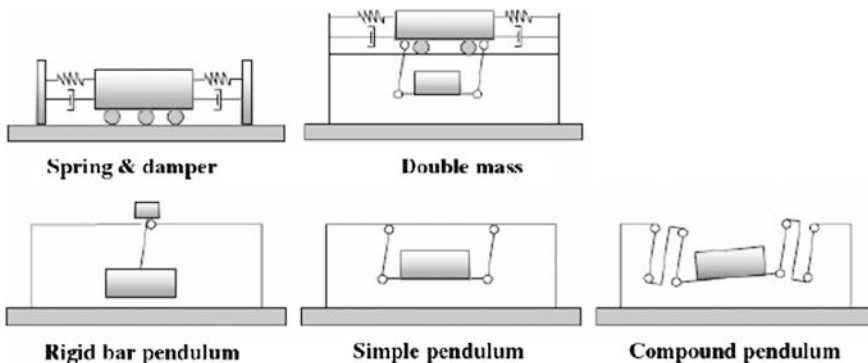


Fig. 24.6 Various types of TMDs [19]

24.5.2 Advantages and Drawbacks of TMDs

24.5.2.1 Advantages

Due to its compactness of the concentrated mass made by the material with high density, the mass can effectively contribute to the modal mass. In addition to mitigating seismic response, a TMD can also work to decrease dynamic responses due to other types of dynamic loads, such as ocean wave, wind, impact loads, and mechanical vibrations. Furthermore, the application of a TMD is flexible, and it does not require any significant modification of the primary structure. Therefore, compared to a base isolation system, a TMD can be easily implemented in an existing structure. Finally, the cost of TMD is relatively low.

Abundant research and engineering applications have also indicated the competence of TMD for enhancing the vibration control due to both wind and earthquake loading.

24.5.2.2 Drawbacks

Since TMD is built for the sole purpose of mitigating dynamic response and adds the weight of the structure, in addition to its maintenance cost, a TMD may induce certain amount of cost with regard to construction and maintenance. Furthermore, if a TMD is supported by mechanical bearings, in some cases, friction can stop the movement of the tuned mass completely. In addition, it is noticed that, compared to direct damping apparatuses presented in Chap. 22, a TMD is normally tuning-sensitive and will not provide highly reliable control when a structure's dynamic characteristics suddenly change, e.g., the structure develops significant plasticity during strong seismic excitations and its natural period is therefore increased. Therefore, there is no consensus regarding the effectiveness of the TMD system to reduce the dynamic structural response [21, 22].

24.5.3 Engineering Applications

Many TMDs are installed on high rise buildings and bridge structures. Representative examples are Taipei World Financial Center (Taiwan, China), Washington National Airport Tower (USA), Sydney Tower (Australia), Citicorp Center (New York), John Hancock Building (Boston), the Crystal Tower (Osaka, Japan), and Infinity Bridge (UK), etc.

The Infinity Bridge, shown in Fig. 24.7, is a public pedestrian and cycle footbridge across the River Tees in the north east of England. It has a total length of 240 m with two arches with a length of 120 m (weighting 300 tons) and 60 ms, respectively. These two arches together with their mirror images on the river form



Fig. 24.7 The Infinity Bridge comprising two arches

the mathematical symbol for infinity, and it is from this that the bridge derives its name. It has an estimated daily traffic of 4000 people and a design life of 120 years. The total construction cost was £ 15 million. Four exposed, high strength post-tensioned locked coil steel tie cables run alongside the deck and tie the bases of the arches together, providing pre-stressing for the concrete deck sections [23, 24]. Each piece of concrete deck has a width of 5 m, a length of 7.5 m and a small thickness down to 0.125 m. To mitigate the dynamic responses due to traffic and environmental load in both horizontal and vertical directions, seven TMDs are installed immediately below the bridge deck. Figure 24.8 shows a single TMD fitted to the underside of the concrete deck under the 60 m arch. It is planned to install additional TMDs when the issue of maintenance arises.



Fig. 24.8 TMDs installed under the bridge deck of the Infinity Bridge (photo by John Yeadon)

Taipei World Financial Center (Taipei 101) is one of the world's tallest (with a height of 509.2 m and 101 stories) and most expensive buildings (with a total cost of around US\$ 2 billion). It also features challenges in respect of difficult foundation conditions, unusual building shapes, demanding lateral stiffness requirements, mixed structural materials, seismic demands, special ductility details, wind/building interaction, fatigue life concerns, and human comfort criteria. To increase lateral stiffness mainly due to the requirement to resist dynamic wind loading, simply adding steel area was impractical due to a significant cost increase. Therefore, the building utilizes 36 steel super-columns (with a maximum column cross section size of $2.4 \text{ m} \times 3 \text{ m}$) that contain 70 MPa high strength concrete below story 62, and the steel column extends to story 90, built up from steel plates with a thickness from 50 to 80 mm. This results in a global natural vibration period of 6.8 s, which would be significantly higher if the structural concept with steel super-columns filled with high strength concrete were not adopted. With such a height and high natural period, the seismic response can be mitigated to a certain extent and is insignificant during a 100 year return period of earthquake, because the natural period is much higher than the period range of the majority of the seismic motion energy. However, dynamic response due to the wind can be significant and may cause damage to the structure. To mitigate the dynamic response of the building, a 660 ton (728 short ton, which is only 0.26 % of the building weight) pendulum TMD, designed, manufactured and constructed by RWDI, Motioneer Division, with a cost of US\$ 4 million, was installed at the top of the building. As shown in Figs. 24.9 and 24.10, the TMD mass is suspended from the tuning frame at the 92nd floor to the 88th floor, by eight (four pairs) of steel cables



Fig. 24.9 660 metric ton simple pendulum TMD system (*left*) installed in Taipei World Financial Center (*right*) with a height of 509.2 m to mitigate the seismic and wind induced response of the building. The TMD is suspended from the 92nd to the 88th floor and costs US\$ 4 million

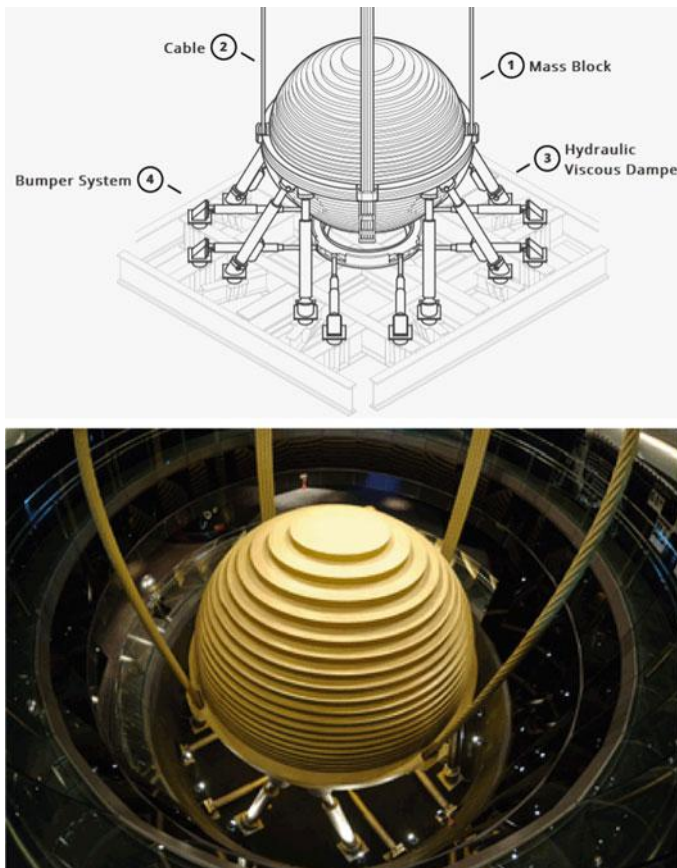


Fig. 24.10 The mechanism of TMD used in Taipei 101

42 m in length and 9 cm in width, each comprising over 2000 smaller cables to ensure flexibility and durability. The cables attain a security parameters index score of around 9, i.e. each individual cable can support the entire weight of the TMD. By carefully adjusting the free cable length, the TMD is tuned to move/swing with the building at the natural period of the building. Its sphere, with a diameter of 5.5 m, is the largest damper sphere in the world. It consists of 41 circular steel plates, each with a height of 125 mm, welded together to form a 5.5 m diameter sphere. A bumper ring fixed to the TMD is connected to eight horizontal snubber hydraulic viscous dampers situated beneath the TMD, to limit the sway motion of the TMD by absorbing dissipated energy from vibration impacts, particularly in major typhoons or earthquakes where movement exceeds 150 cm [25]. For a 100 year return period of earthquake, the TMD is designed to move relatively calmly, as does the building in which it has been installed. However, for a 1000–2500 years return period of strong earthquake, the TMD will be effective to greatly mitigate the

dynamic response of the structure, and to remain in place and intact after strong ground motions cease and the vibrations of the structure terminate. As aforementioned, the TMD on Taipei 101 is also designed to mitigate wind induced structural response. During a strong wind storm with a return period of half year, the TMD will reduce the peak acceleration of the top occupied floor from 7.9 to 5.0 mg.

In addition, due to the discontinuities at the structural tip (the pinnacle between 450 and 509 m), two tip vibration modes at periods of 1.16 and 0.93 s can trigger vortex induced vibrations, which significantly contribute to metal fatigue damage (they oscillate up to 180,000 cycles a year). Therefore, another two compact TMDs, each weighing 6 tons and designed to mitigate vibration at one single period [26, 27], are installed at the tip of the spire. These prevent damage to the structure due to strong wind loads and also mitigate the wind induced fatigue damage.

To mitigate the dynamic response of cables in transmission lines, a special type of TMD, called a Stockbridge damper (Fig. 24.11) is used. This comprises two metal bell-shaped weights at the end of a flexible shaft that can be tuned to a frequency close to the natural frequency of the cable vibrations. The Stockbridge dampers are usually installed close to the end of an insulator string where the vibration amplitude is large. To provide for greater freedom of motion, the weights of the damper may be partially slotted in the vertical plane, allowing the cable to

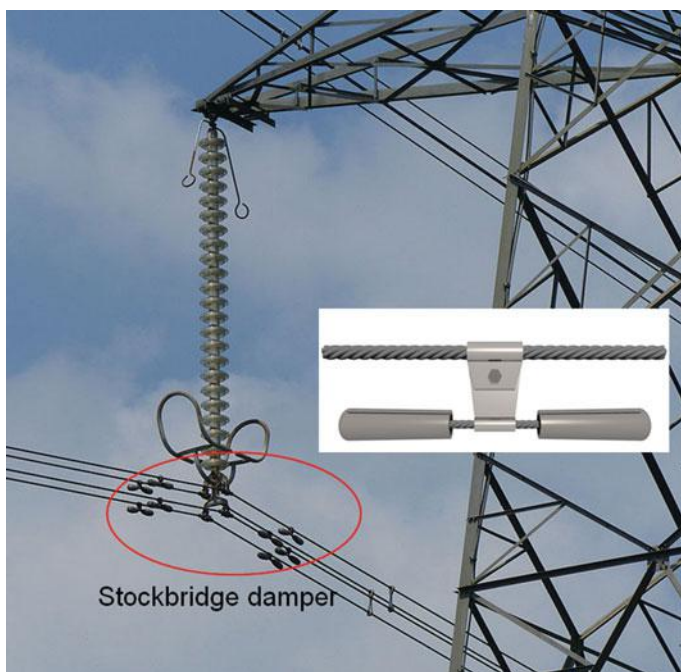


Fig. 24.11 Stockbridge damper installed on transmission lines

travel outside the confines of the bell. In some installations, the weights are unequal, allowing damping over a greater frequency range. A more dedicated design of Stockbridge damper is to arrange weights with asymmetric mass distribution, thus enabling the damper to oscillate in several different frequency modes of vibrations.

24.5.4 Research of TMD Systems

By performing numerical analysis to calculate seismic time history responses of a 120 m high jacket structure at a water depth of 110 m, with a natural period of 2.06 s, Kawano and Venkataramana [28] showed the effectiveness of the TMD installed on the topside of the jacket structure, which is most effective when the mass of the TMD is only 0.6 % of the total mass of the superstructure including the added mass due to the presence of sea water. They also discovered that the TMD system has different effects on the response evaluation due to the characteristics of the input seismic motions. By calculating the response of an offshore jacket structure with a height of 43 m, a total mass of 400 tons, and a natural frequency of 1.31 Hz (with associated modal mass of 256 tons), Zhang and Yue [29] studied the efficiency of TMD when the jacket is subject to dynamic ice loading measured from a site in China Bohai Sea. They found out that when the mass ratio between the TMD and the jacket is increased from 0.3 to 1.0 %, the efficiency of the TMD to mitigate ice induced dynamic response is significantly increased.

By carrying out a parametric study of the seismic response of SDOF structures with a TMD attached, and utilizing the Kanai-Tajimi spectrum [30] defined by the ground frequency and the ground damping ratio with a derived transfer function of a structure, Hoang et al. [31] presented that a TMD becomes very effective in minimizing the structural response at its natural frequency, while it generates a fairly small stroke length. TMDs' performance is robust with respect to uncertainty in the system parameters (mass ratio and ground frequency ratio) as well as the excitation frequency range. In general, the characteristic ground frequency has a stronger influence on the optimal tuning frequency than the optimal damping ratio of TMD. When the ratio of the characteristic ground frequency to the structural frequency is equal or larger than three, the ground motion can be practically assumed as a white noise for designing TMD.

However, the effectiveness of TMD control is reduced when the soil-structure interaction is taken into account. Furthermore, for high rise structures with large modal damping (higher than 5 %) or with foundations on soft soil, the implementation of TMD technique is almost ineffective in reducing the seismic response [32].

To mitigate large deformations of a base isolation system on the bearings, a method to combine TMDs and base isolation systems together was proposed, which was found to be most effective at reducing the structural response when the damping in the bearings was low [33, 34]. For example, by simulating a TMD-base

isolation hybrid system subjected to white noise, as well as near- and far field earthquake ground motions, Taniguchi et al. [35] presented that the displacement demand was reduced by up to 25 % for white noise and far field excitations. For near field ground motions, the reduction in displacement demand was found to be approximately 10 %.

24.6 Tuned Liquid Damper (TLD)

24.6.1 General

Similar to a TMD, a TLD is also a passive damping system while the damping effects are provided by liquid motions in tanks. It consists of rigid tanks filled with liquid. The moving of liquid has a similar function as the moving mass of a TMD: gravity acts as a restoring force and energy is mainly dissipated by using a damping screen or mesh to create turbulence in the liquid, viscous action of the liquid, and also through the wave breaking and the impact of liquid on the tank wall. The geometry of the tank that holds the water is determined by theory of hydrodynamics to give the desired natural frequency of water motion and also by the requirement of existing space where the tank can be located. Typical geometry of liquid tanks used as a TLD is rectangular or circular, of which the former can be tuned to two different frequencies in two perpendicular directions.

TLDs are extensively used in space satellites and marine vessels (Fig. 24.12) to control motions. The basic principal of a TLD to mitigate the structural response is illustrated in Fig. 24.13 [36]:

1. Before loads are applied on a structure, liquids inside a tank remain still.
2. When loads due to earthquake, wind or ocean wave begin to excite the structure, causing vibrations of the structure, the dynamic vibrations will immediately be transmitted to the liquid tank. Due to the fluid inertia from gravity, the motions of the tank will cause the fluid to move, thus absorbing the energy due to the structural vibrations. Together with the associated momentum exchange, the dynamic response of the structure will be reduced.
3. Energy dissipation: fluid motion is damped to some extent due to the turbulence caused by flow restrictions or damping facility such as baffles or screens (Fig. 24.16) inside the tank. In engineering practice, this damping induced by baffles or screens is generally significantly higher than the damping induced by the viscous effects of fluid itself.
4. The phenomenon depicted in steps 2 and 3 repeats until the loads cease and the structure's vibrations stop.

TLDs can be categorized as either tuned sloshing dampers (TSDs) or tuned liquid column dampers (TLCDs), with their geometries shown in Fig. 24.14. TSDs utilize sloshing of the liquid in a container/tank. However, only a fraction of the

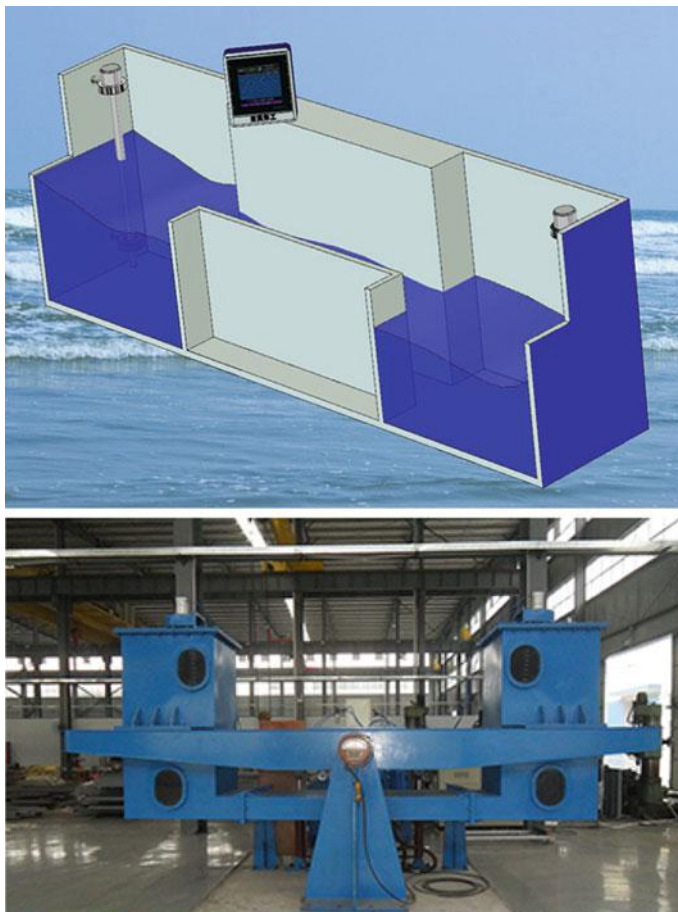
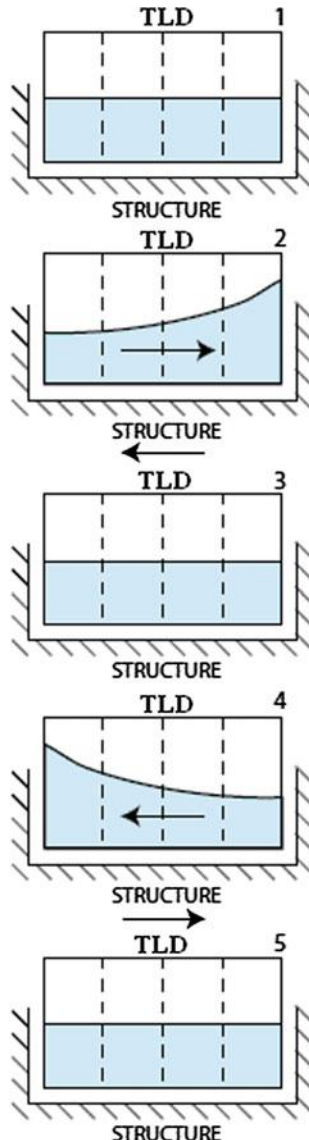


Fig. 24.12 Anti-roll tanks used for marine vessels to control ships' roll motions (courtesy of Yoyeah Marine, Shanghai)

liquid mass, namely sloshing/convective mass (described in Chap. 17), participates in the sloshing motion, and is therefore tuned to the dominant vibration frequency of the primary structure. To increase the effective mass of the sloshing liquid, a U- or V-shaped TLCD, originally proposed by Sakai et al. [37], can be adopted [38–42]. An engineering realization of this period tuning technique is the development of TLCD with Period Adjustment Equipment (LCD-PA) [43]. Such a system has been installed in the top floor of the 26 story Hotel Cosima (Hotel Sofitel in Tokyo) [44]. As mentioned before, TLCDs have for a long time been installed on ships as efficient anti-rolling measures (Fig. 24.12).

Fig. 24.13 Basic principle of a simple TLD (courtesy of RWDI, Motioneerig Division)



24.6.2 Calculation of Structural Response with TSDs Installed

Even at higher orders of sloshing modes, significant forces induced by sloshing can occur. However, these forces do not generally vibrate out-of-phase with the base excitation, and therefore do not contribute to the mitigation of dynamic responses.

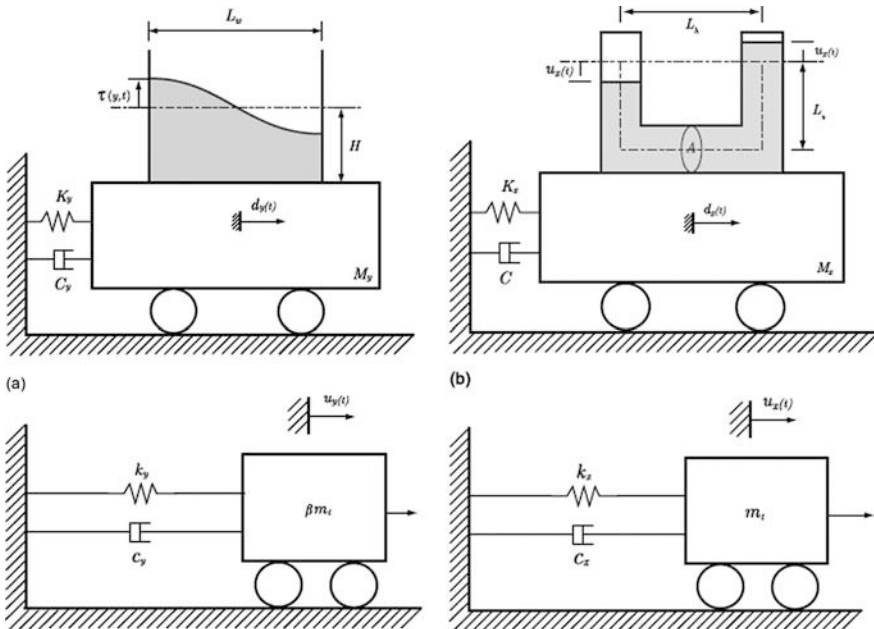


Fig. 24.14 The basic geometry and physical modeling of a TSD (left) and a TLCD (right) [38]

By neglecting influence from the higher order sloshing modes, the performance of a TLD installed on a structure can be evaluated based on the evaluation of the mean square displacement response of the primary structure presented in Sect. 24.2.

For a rectangular tank, the first sloshing mass m_{n1} , the corresponding sloshing frequencies ω_{n1} and the equivalent stiffness k_{n1} can be calculated by the following equations:

$$m_{n1} = \frac{8\rho b L^2}{\pi^3} \tanh\left(\frac{\pi h}{L}\right) \quad (24.6)$$

$$\omega_{n1} = \frac{\pi g}{L} \tanh\left(\frac{\pi h}{L}\right) \quad (24.7)$$

$$k_{n1} = \frac{8\rho b L g}{\pi^2} \tanh^2\left(\frac{\pi h}{L}\right) \quad (24.8)$$

where L is the tank length in the direction of base excitation; b is the tank width; h is the still water depth of the liquid inside tank; and ρ is the density of the liquid.

From the first equation of the three equations above, it is noted that in order to maintain a high ratio of equivalent sloshing mass to the total liquid mass, a TLD should be designed with a low h/L ratio. From the second equation, it is found that as h/L is increased, the natural frequency of sloshing becomes independent of the

water depth. This situation brings great challenges with regard to tuning operation, and should therefore be avoided.

For vertical circular tank, for optimization purposes, the first sloshing/convective mass m_{n1} , the corresponding frequencies ω_{n1} and the equivalent stiffness k_{n1} can be approximated with the equations as follows:

$$m_{n1} = 0.77\rho\pi r^2 \tanh\left(\frac{1.837h}{r}\right) \quad (24.9)$$

$$\omega_{n1} = \sqrt{\frac{g\sigma_1}{r} \tanh\left(\frac{\sigma_1 h}{r}\right)} \quad (24.10)$$

$$k_{n1} = 5.4 \frac{m_{n1}^2 gh}{M_l r^2} \quad (24.11)$$

where ρ is the density of the liquid inside the tank; h and r are the height and radius of the vertical circular tank; σ_1 is the coefficient of Bessel function, equal to 1.84 for the current condition [45], and M_l is the total mass of the tank liquid.

If the higher order of the sloshing mode must be accounted for, the natural (first) and higher order frequency of sloshing motions can be calculated based on the formula presented in Chap. 17. Then the transfer function can be adjusted to:

$$H_X(\omega) = \frac{X(\omega)}{F(\omega)} = \frac{1}{2 \left[(-\omega^2 M_s + i\omega C_s + K_s) - \omega^2 \sum_{n=1}^j m_n \frac{i\omega c_n + k_n}{-\omega^2 m_n + i\omega c_n + k_n} \right]} \quad (24.12)$$

For a rectangular tank, $k_n = M_l \left\{ 8 \left(\frac{g}{h} \right) \frac{\tanh^2[(2n-1)\pi h/L]}{(2n-1)^2 \pi^2} \right\}$.

The notations in the equation above are described in Chap. 17.

24.6.3 Research Progress of TLDs

24.6.3.1 Effects of TLDs on Mitigating Earthquake and Ocean Wave Induced Responses

To investigate the effectiveness of TLDs, Jin et al. [46] carried out both experimental and numerical study (with lumped mass model) on controlling earthquake response of an offshore jacket platform. They found a good match between the experimental and numerical results, and they confirmed that the ratio of the fundamental sloshing frequency of liquid to the natural frequency of platform is the most important factor to control platform response due to seismic excitations. Even though a larger ratio of liquid-mass to platform-mass is more effective to reduce

vibration, practically, it is economic to mitigate the structural vibrations with liquid-mass to platform-mass ratios ranging between 1 and 5 %. From the shaking table tests of TLDs carried out at Kyoto University, Soong and Constantinou [65] investigated the performance of TLDs for seismic applications. Subject to seismic motions of 1940 Imperial Valley Earthquake scaled to a peak ground acceleration of 0.25 m/s^2 , the results indicate that the TLD mainly reduces the first mode of vibration response, but it is not effective to mitigate total dynamic response.

It is noted that TLDs installed on a structure can function to mitigate responses not only due to earthquake, but also due to waves and wind. Vandiver and Mitome [14] utilized storage tanks on a fixed offshore platform as tuned liquid dampers (TLD) to suppress wave induced structural vibration response. They confirmed that if the frequency of the lowest sloshing mode of tank liquid is close to the natural frequency of an offshore structure, the sloshing will split the response peak and the nature of the split peak will vary with small changes of the liquid depth in the tank. They also presented that the sloshing motions of tank liquids can alter both the measured natural frequency and damping of the structure. Dong et al. [47] studied the effectiveness of a TLD both numerically and experimentally, from which they concluded that a reduction in wave induced dynamic response could be significant if the dimensions and liquid depth of TLD are properly selected. Furthermore, they confirmed that the effectiveness of a TLD is increased if the liquid sloshing frequency is close to that of a structure's natural frequency. In addition, they also presented that, even if the TLD was slightly mistuned to the natural frequency of a structure, no adverse effect was observed. However, when the height of incident sloshing wave of the liquid is higher than a certain value, the TLD becomes saturated, and its effectiveness will not be further increased. Ideally, if the incident wave is close to one-half of a structure's natural frequency, and the TLD has a first sloshing frequency close to the natural frequency of the structure, the maximum reduction in dynamic response can be achieved. However, a properly designed TLD can mitigate dynamic responses even if the frequency content of the load is broad banded.

Abundant studies indicate the high effectiveness of TLCD dampers [37, 48]. Kareem [49, 50], Yalla et al. [51], Abe et al. [52], and Haroun and Pires [53] extended the research of passively-controlled TLCD dampers to semi-active-controlled and active-controlled ones. They found a significant increase in dampers' effectiveness to mitigate dynamic structural response compared to their passive-controlled counterparts. Chapter 28 gives a description of those types of control techniques.

Under larger base accelerations, a TLD is more effective through more significant sloshing. It can be connected to a secondary mass attached to the primary structure. By tuning the stiffness of connecting spring(s) of the secondary mass to make it move in resonance with the primary mass, the TLD is therefore subjected to higher amplitude of excitation than it would be if rigidly connected to the primary structure. Researchers [54] investigated the effectiveness of the hybrid TLD-secondary mass system shown in Fig. 24.15 and found that if the stiffness of the secondary mass was optimal, the hybrid system was rather effective as a

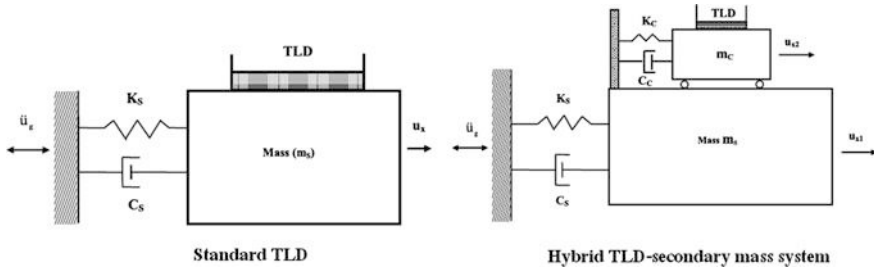


Fig. 24.15 Physical modeling representation of a standard TLD (*left*) and a hybrid TLD-secondary mass system [54]

structural control device; and, under broad-band seismic ground motions, it can mitigate 20–30 % more responses than that when a TLD is rigidly connected to a primary structure. Similar to this system, researchers [55] also proposed a design with softer springs connecting TLD and the primary structure. The spring with low stiffness induces significant excitations to the TLD due to resonance. However, the applicability of this system is limited due to its complexity.

24.6.3.2 Effects of TLDs' Baffles or Screens

The presence of baffles or screens for deep water tanks, and surface contamination such as PVC or lip along the tank wall for the shallow water tanks, can further increase the damping [44] and as an alternative to the adjustment of water depth to tune the sloshing frequency. Figure 24.16 shows an example of screens installed on a TLD tank.



Fig. 24.16 Damping screen used in a TLD tank (courtesy of RWDI, Motioneer Division)

A number of studies have indicated the effectiveness of installation of baffle screen inside the tank [56]. Based on the derivation of equivalent damping provided by a device located at the center of a tank that is subjected to sinusoidal excitations, Warnitchai and Pinkaew [57] conducted both analytical study and experimental test of a TLD with wire-mesh screen installed. In addition, they also showed that the damping due to screen–tank fluid interaction also caused a slight reduction in the sloshing frequency. By developing an equivalent mechanical model, Tait [58] expanded the work by Warnitchai and Pinkaew to the case with random excitation. He also discussed and verified analytical models for simulating TLDs equipped with baffle screens. Tait et al. [59, 60] developed both linear and non-linear numerical modeling of a TLD with slat screens and the modeling is further verified by a comprehensive experimental study. A procedure to calculate the theoretical value of the force coefficient of a slat-type screen is presented and verified by experimental study. They also concluded that even though the linear model was capable of providing a first estimate of the energy dissipating characteristics of a TLD, it could not provide realistic evaluation of the free surface response with amplitudes experimentally investigated. The non-linear model can accurately describe the free surface motion, the resulting base shear forces, and the energy dissipated over a range of excitation amplitudes. Furthermore, the non-linear model is capable of modeling a TLD equipped with multiple screens at various screen locations inside the tank, which is also verified over a range of practical fluid depth to tank length ratio values. Vassolato et al. [61] also developed an amplitude-dependent mechanical model to calculate the steady-state response of a TLD tank, and this model is validated by experiments. Their study shows that the damping ratio of a TLD is decreased with an increase in the screen angle. Through the experimental tests, Fediw et al. [62] confirmed the effectiveness of TLDs and the installation of screens, which is illustrated in the left figure of Fig. 24.17. They

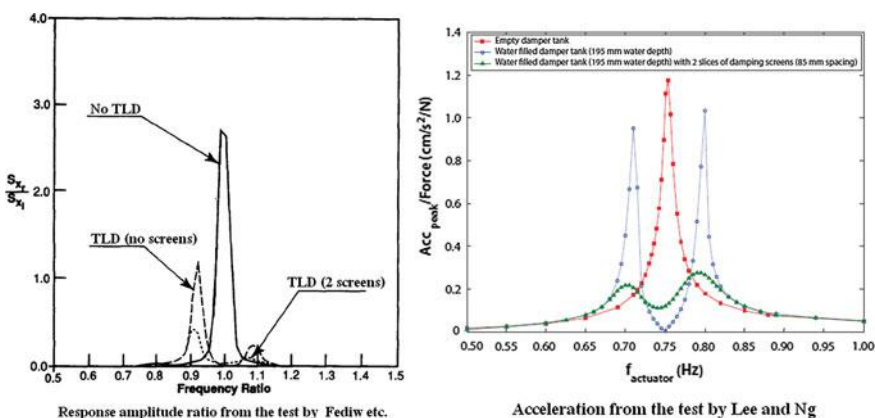


Fig. 24.17 Effects of TLD and screens from the tests by Fediw et al. [62] (left) and Lee and Ng [63] (right)

also demonstrated that, because the increased damping acts to suppress the wave amplitude and to reduce the higher harmonic response, as the number of screens and/or the solidity ratio (the ratio of the area of the shadow projected by the screen on a plane parallel to the screen to the total area contained within the frame of the screen) is increased, both the dynamic structural response and the nonlinearities decrease. As shown in the right figure of Fig. 24.17, through both the numerical calculation and a 1:10 scale model test of a structure-TLD system with two TLDs to control the first and the second modes of vibration, the conclusion given by Fediw and his co-workers is also confirmed by Lee and Ng [63]. In the study, baffle screens are selected with a solidity ratio of 40 %. Their study also shows that the performance of the TLD under test is only slightly affected by the orientation variation in the horizontal plane provided that the variation is within 24°. This indicates a robust performance of TLD to the coupled structural motions, which is in reality helpful for structures with unsymmetrical layout. In addition to the introduction of significant damping during fluid sloshing, baffles or screens also lead to a decrease in fluid sloshing response as mentioned before, and may strongly change resonant sloshing frequencies and add an extra non-linear damping due to cross-flow resulting in either flow separation or jet flow [64]. To obtain the highest damping without changing the lowest sloshing frequency, the solidity ratio of screens is normally chosen as a value close to 0.5.

By neglecting the local flow at the screen edges and adopting the linear sloshing theory and domain decomposition method, Faltinsen and Timokha [64] presented a more accurate analytical calculation of the natural sloshing modes in a rectangular tank with a slat-type screen at the tank middle. They presented that the natural sloshing frequency depends on solidity ratio, the number of screen gaps (slots and screen openings) between each adjacent slat, the position of these gaps relative to the mean free surface, and the liquid depth. They found that when the solidity ratio is lower than 0.5, the eigenvalues can already vary with a non-negligible magnitude with the varying position of screen openings relative to the mean free surface, needless to say designs with a solidity ratio larger than 0.5. The positions of gaps may also have a significant influence on the sloshing frequency.

24.6.4 Advantages and Drawbacks of TLDs

24.6.4.1 Advantages

The main advantages of TLDs are:

1. Compared to the mechanical parts of TMDs, TLDs are a comparatively simple system.
2. Relatively low manufacturing and installation costs.
3. Relatively low or zero maintenance requirements.

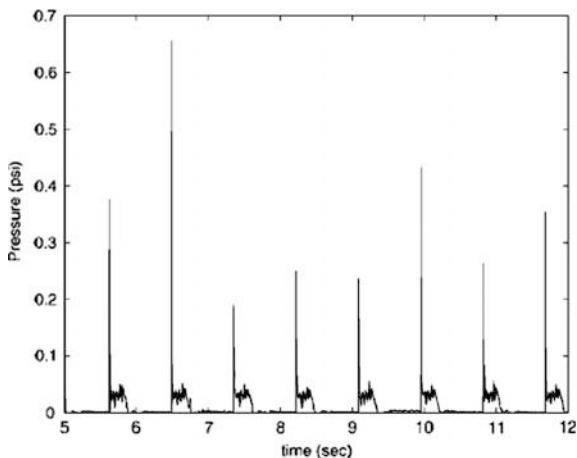
4. Practical and versatile functionality, high flexibility to be incorporated during the design stage of a structure, or to be retrofitted to serve a remedial role. They normally serve the purpose of liquid (fuel, crude oil, mud, etc.) storage [63] as necessary contents for emergency purposes, industry production, or for everyday function if fresh water is used [66]. TMDs, in contrast, apart from mitigating structural response, have no other functional uses.
5. Without adversely affecting the functional use of a TLD tank, it can be designed with proper dimensions or reconfigured with internal partitions of existing tanks. This can be useful to cope with physical and architect requirements.
6. Can reduce structural vibrations in two directions simultaneously and does not require large stroke lengths.
7. Note that the natural frequency of a structure calculated during the design stage may not represent the realistic one after the structure has been constructed, and also, during the service life of a structure, its natural frequency may vary due to the changes in both stiffness (e.g., due to additional reinforcement) and weight (e.g., due to a variation of storage weight). It is therefore much easier to tune the TLD's natural frequency by adjusting the water depth of TLD tanks.
8. From the tank strength point of view, if it is designed with the assumption that possible sloshing can occur, the reliability with regard to the tank's structural integrity can also be improved, which further increases overall safety level for the entire structure.

24.6.4.2 Drawbacks

Compared to TMDs, the drawbacks of TLDs are:

1. The sloshing waves can induce significant slamming force on tank walls. This is especially obvious for high amplitudes of sloshing waves, forming a well-developed breaking wave, and the impulsive slamming can also exert a mean peak pressure caused by short duration impulsive slamming of 5–10 times higher than the regular sloshing pressure [67, 68]. Figure 24.18 shows a sample history of pressure pulses at the mean liquid height of a TLD, and the slamming induced load peaks with short time duration can be clearly identified. This calls for additional consideration with regard to the structural reinforcement of the tank and its supports.
2. If the moving mass serves as a criterion for comparison, TLDs are not as efficient as TMDs. This is due to the compactness of TMD mass, which is more effective than the active sloshing/convective mass of the liquid in a TLD.
3. Due to the relatively lower density of the liquid and the less active sloshing/convective mass utilization than that of a TMD, a TLD requires larger space for installation in order to achieve the same damping effect.

Fig. 24.18 Time history of the resonant pressures at the mean liquid height of a tuned liquid damper [68]



24.6.5 Engineering Applications of TLDs

As elaborated in previous sections, TLDs are utilized as a means to mitigate structural dynamic response due to earthquake, wind and ocean wave loading. Since their first application in the 1980s [69, 70], TLDs have become a popular form of inertial damping device due to their effectiveness and practicality [2, 3, 37, 44, 50, 71, 72]. Their application can be found in high rise buildings and chimney structures worldwide. They have been proven to be economical, and can be easily adjusted to physical and architectural requirements. Representative examples are One Rincon Hill skyscraper (US), Shin Yokohama Prince Hotel (Japan), Comcast Center (Japan), Hobart Tower (Australia), Gold Tower in Kagawa (Japan), Shanghai Financial Trade Center (China), The Summit (China), Harbourfront Landmark (China), and Nagasaki airport tower (Japan), etc.

In the 150 m high Shin Yokohama Prince Hotel (Fig. 24.19), 30 TLDs units were attached to the top floor as shown in Fig. 24.20. Each TLD comprises a multi-layer stack of nine circular containers each 2 m in diameter and 22 cm high, giving a total height of 2 m. By installing the TLDs, the root of mean square (RMS) accelerations in each direction were reduced to 50–70 % of the original without installing TLDs. For example, at a wind speed of 20 m/s, the RMS acceleration without TLDs was over 0.01 m/s, and it was reduced to less than 0.006 m/s^2 , taken as the minimum perception level at 0.31 Hz according to ISO 6897 [73, 74]. Similar installations are reported for Nagasaki airport tower, Tokyo international airport tower and Yokohama marine tower [75].

One Rincon Hill is a 180 m (60 stories) high residential skyscraper built in San Francisco, which is located in a high seismicity region. The skyscraper is located on a hill with no shielding from wind, and the strong ground motion is also an important loading to govern the design. Four concrete water tanks equipped with baffles, which can hold up to 190 tons of water, are installed on the top of the

Fig. 24.19 Shin Yokohama Prince Hotel (photo credit: U-Kane under the license of CC-BY-SA-4.0)



skyscraper, as shown in Fig. 24.21. The water tanks are built not only for fire-fighters, but also as a TLD to mitigate the wind and earthquake induced response. Therefore, the water level in tanks is adjusted to have a sloshing natural frequency close to that of the building structure. Together with other measures to increase the performance of the building, US\$ 54 is saved per square meter.

Two residential buildings of 55 and 65 stories were built in New York City. Due to the estimated environmental wind load and vibration characteristics of the structures, the buildings had a tip vibration response higher than what is required in serviceability limit design. Therefore, more effective damping was required than the conventional method to reduce building motions to an acceptable level. RWDI, Motioneer Division was engaged to design two dynamic absorbers, one for each building. In the initial design stage, construction of TLD was identified as the most suitable way to fulfil the mitigation task. Based on weighting the relative importance among dynamic response reduction, space availability, and the short and long term cost benefits, the optimized geometry and size of TLD are designed as bi-directional TLD tanks with two directional sloshing modes, i.e. the tank liquids are tuned to slosh and provide damping in two perpendicular directions. In addition, to generate liquid wave turbulence so that an increase in energy dissipation and damping can be reached, static screen elements are anchored to the tank roof and

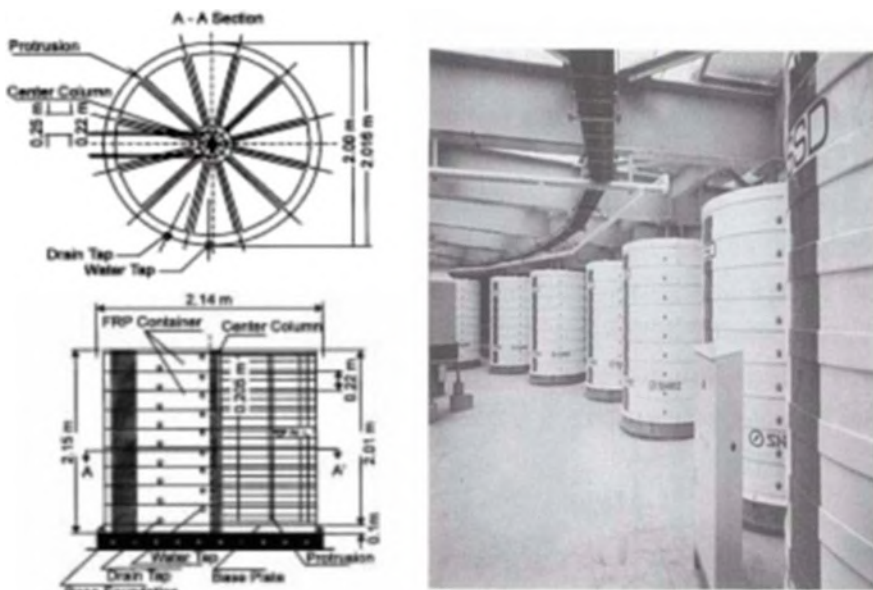


Fig. 24.20 Illustration of TLDs installed in Shin Yokohama Prince Hotel [62]



Fig. 24.21 A TLD installed on the top of One Rincon Hill in San Francisco, USA (courtesy of John Hooper, Magnusson Klemencic Associates, USA)

suspended into the water in the TLD tanks as shown in Fig. 24.16. Automatic water level monitoring was provided using a standard float-type sensor and water supply make-up solenoid valve. Both experimental model tests and time domain simulations were carried out to calculate the structural response and to determine the effectiveness of the bi-directional TLD tanks. After the construction work of the two buildings was completed, modal tests were performed to obtain the first two eigenfrequencies of the buildings, which provided guidance for the final adjustment of the water level in the TLD tanks. As with any building system, periodic visual inspections are recommended as part of a routine maintenance plan [36].

24.7 Multifrequency Dynamic Absorber

Sections 24.5 and 24.6 describe the dynamic absorbers to mitigate dynamic response at a single frequency (except rectangular TLD tanks, which have two different tank liquid sloshing frequencies along two perpendicular directions in the horizontal plane). However, if the frequency of a structure's dominating dynamic loading is also known, and the frequency content of the dynamic loading is narrow-banded and constant, it is possible to mitigate the dynamic responses at both the natural frequency of the structure and the frequency of the dynamic loading. To do that, in addition to the dynamic absorber with a natural frequency close to that of the structure (k_a , c_a , and m_a), a second dynamic absorber with a natural frequency close to the loading frequency can also be attached to the primary structure, which is referred to as a multifrequency dynamic absorber, as illustrated in Fig. 24.22. This technique can also be extended to suppress multiple modal responses at different eigenfrequencies by equalizing the damping ratios of the system's main vibration modes.

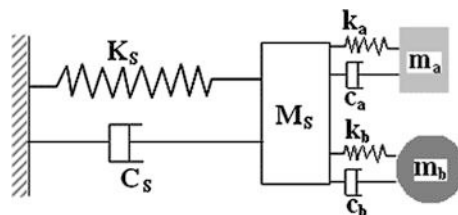


Fig. 24.22 Physical modeling of multifrequency dynamic absorbers attached to a primary structure (K_s , C_s , M_s , k_a , c_a , m_a , and k_b , c_b , m_b are the equivalent stiffness, damping and mass of the primary structure, the dynamic absorber to mitigate the dynamic response at a structure's natural frequency, and the dynamic absorber to mitigate the dynamic response at loadings' frequency, respectively)

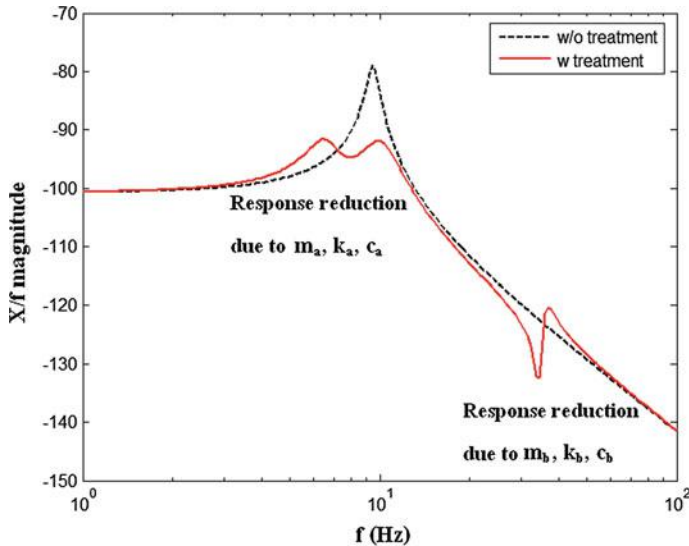


Fig. 24.23 Frequency response functions of the structure without and with vibration treatment (installation of two dynamic absorbers) (courtesy of Deicon dynamics and control)

Figure 24.23 shows a comparison of frequency response function of a structure without and with the installation of two dynamic absorbers. The structure with K_s , C_s , M_s has a natural frequency of 9.5 Hz and the frequency of loading excitation is 35 Hz [76]. The mitigation effects can be clearly observed at both frequencies.

To mitigate both the fundamental and second eigenfrequency modes of response, Yalla and Kareem [77] calculated the response and examined the effectiveness of a multiple TLCD system installed on the top of a five story building. They found that the total dynamic response is even increased compared to a single TLCD. This is because the presence of a TLCD tuned to the second mode decreases the effective damping in the first mode, leading to an increase in the response. To solve this problem, it is recommended to have different fluid masses for each single TLCD of the multiple TLCD system. This can give a better performance than a single TLCD system. A similar problem is also discussed by Rana and Soong [78].

Kitada and Park [79] proposed a method to replace each individual mass damper with a mass-damping-floor-diaphragm-substructure system consisting of a multitude of differently tuned mass dampers. As shown in Fig. 24.24, each tuned mass is designed in the form of a vertical cantilever that vibrates at a relevant eigenfrequency of the structure. Therefore, they can mitigate the lateral displacement response to certain extent.

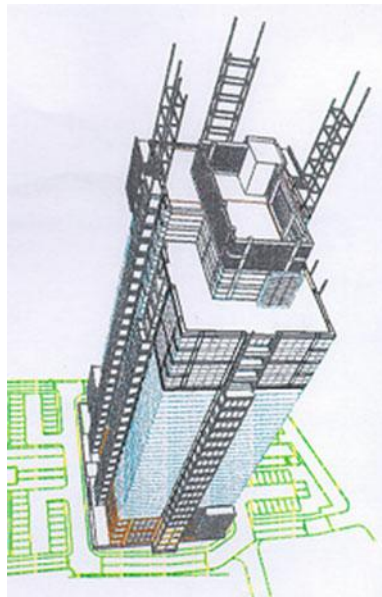


Fig. 24.24 Illustration of mass-damping-floor-diaphragm-substructure system [80]

24.8 Impact Dampers

24.8.1 General

Originally developed by Lieber and Jensen [81] in 1944 to control vibrations, an impact damper [82, 83] comprises a small rigid mass placed inside a container mounted on the side of the structure. The small mass has a small optimal clearance to the container wall, thus allowing collisions between the mass and the container wall to occur when the displacement along the clearance direction exceeds the clearance. The collision introduces both momentum exchange and energy dissipation, the latter of which is mainly produced in the contact surface between the mass and the wall. A schematic diagram of an impact damper is shown in Fig. 24.25. The value of the clearance ($d/2$ in Fig. 24.25) is the most important design parameter. In addition, the mass ratio between the small mass m and the mass of the primary structure M also serves as an important parameter for the design. By neglecting the friction forces, the impact interface between the impact wall and the small mass can be modeled using a contact spring (k_1) and a viscous damper (c_1) as shown in Fig. 24.25. The container can be either mounted directly to the primary structure or designed as a part of the structure.

Detailed analysis of impact dampers has been carried out by Cheng and Xu [84]. From a parametric study of an inner mass impact damper shown in Fig. 24.26, they

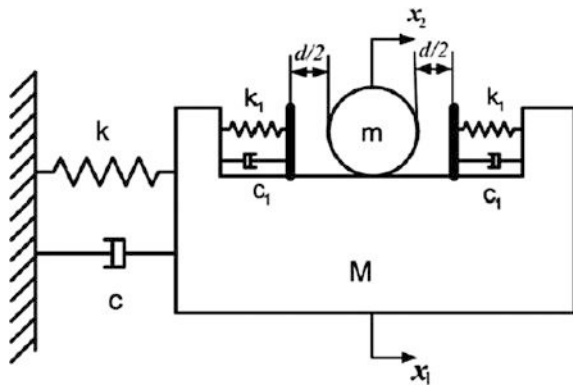


Fig. 24.25 Schematic diagram of an impact damper model [84]

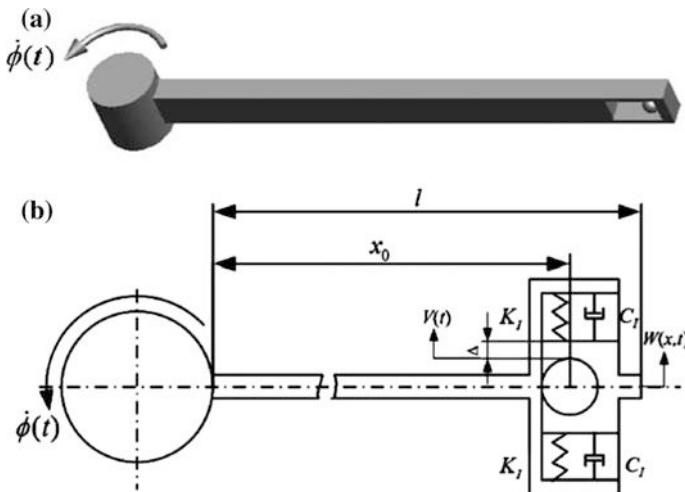


Fig. 24.26 Schematic diagram (a) and top view (b) of an impact damper model by Cheng and Xu [84]

found that, if the initial displacement of the structure is optimally selected, or if the ratio between the clearance d and the root of mean square amplitude without the impact damper is 10, the vibration attenuation can be extremely effective. They also found that the damping ratio can be significantly increased through filling liquid into the clearance, and the high frequency resonance is then greatly eliminated, as shown in Fig. 24.27. By observing this figure, it is found that, compared to water, silicone oil is more effective to increase the damping, but a greater reduction in displacement response from the adding of the oil may not be obtained.

Through the study of a resilient impact damper in free damped vibrations, researchers [85–89] recommended that the clearance between two masses in an

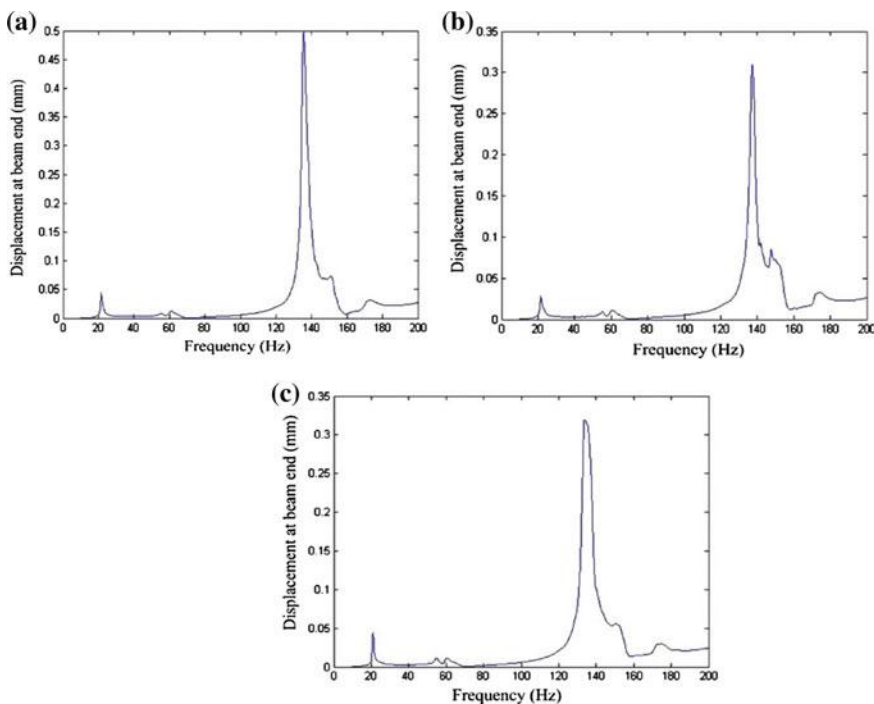


Fig. 24.27 The frequency responses of the displacement at beam end for the mass damper with different liquid filled in clearance: **a** w/o liquid, **b** with water, **c** with silicone oil [84]

impact damper ought to be smaller than twice the initial displacement of the main mass in a vibration system, provided that the system is stimulated by an initial displacement only.

24.8.2 Advantages and Drawbacks of Impact Dampers

Compare to a tuned mass damper, an impact damper cherishes a simple design and is inexpensive. It can operate in harsh environments where traditional TMDs or TLDs cannot.

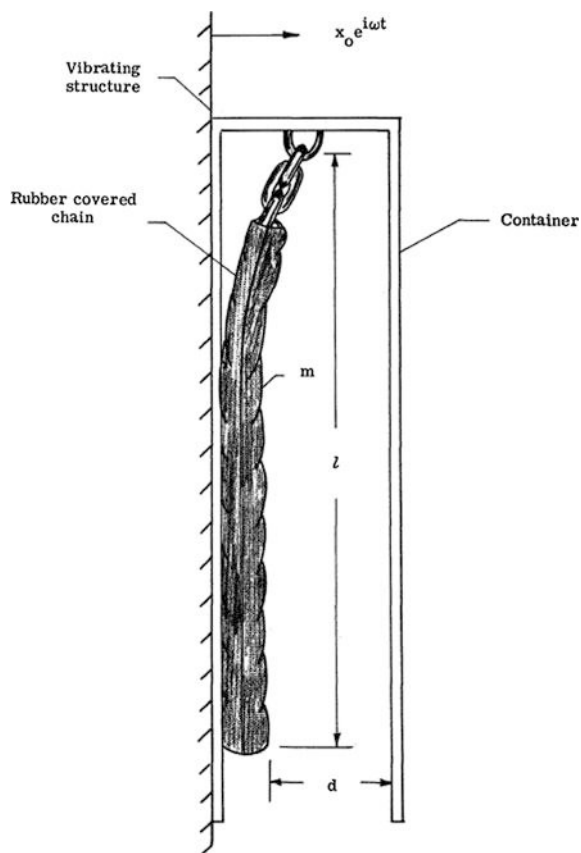
However, the impact damper's effectiveness is reduced when it is subjected to non-harmonic excitation.

24.8.3 Engineering Applications of Impact Dampers

Even though impact dampers have been extensively used in mechanical equipment such as robot arms, turbine blades, propeller blades, printed circuit boards, and

machine tools etc., their engineering applications on structures are rather limited [90]. They are mainly installed in the form of chains encased in plastic or rubber sleeve and suspended with freedom to impact against a vertical channel, which is termed a hanging chain damper as shown in Fig. 24.28. It is capable of absorbing significant energy associated with transverse oscillations of the channel. Even though this design looks quite different from what is shown in Fig. 24.25, their essential mechanism and principles are rather similar. Reed [83] reported that the dynamic response of structures can be significantly reduced via the impact of rubber coated chains housed in cylinders. It combines the benefits of the inelastic impacts with the added internal friction of the chain links rubbing against each other. The engineering applications of hanging chain damper can be found in towers, light poles and masts in Australia and Japan to control wind induced vibrations [44]. Figure 24.29 shows a hanging chain damper installed on a 21 m high erected launch vehicle, which increased the damping of the structure by a factor of up to 3 [83].

Fig. 24.28 Illustration of a hanging chain damper [83]



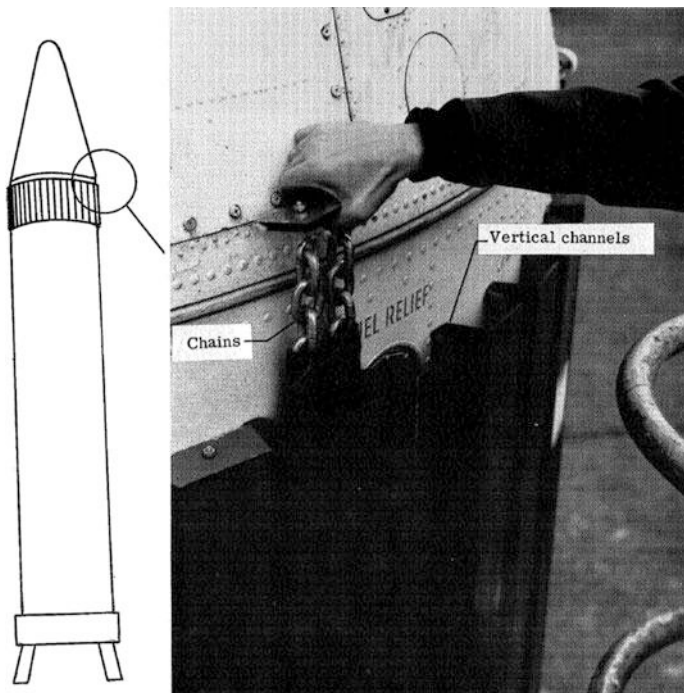


Fig. 24.29 Hanging chain damper installed on erected Jupiter launch vehicle [83]

For smaller diameter conductors or overhead shield wires on transmission lines, spiral vibration dampers can also be used, as shown in Fig. 24.30. They are made of a rugged non-metallic material that has a tight helix on one end that grips the conductor or wire. The remaining part rests loosely on the conductors or the overhead shield wires, and the vortex induced vibrations can then be mitigated by slapping or impacting against conductors/wires.



Fig. 24.30 Spiral vibration dampers (courtesy of Zhuang Huaneng Electric Power Fitting Co., Ltd.)

References

1. Den Hartog JP (1947) Mechanical vibrations, 3rd edn. McGraw-Hill, New York
2. Kareem A (1983) Mitigation of wind induced motion of tall buildings. *J Wind Eng Ind Aerodyn* 11(1–3):273–284
3. Kareem A (1990) Reduction of wind induced motion utilizing a tuned sloshing damper. *J Wind Eng Ind Aerodyn* 36:725–737
4. RWDI (2001) Technical notes—damping systems, Iss. 10. Rowan Williams Davies & Irwin Inc., Guelph
5. Ormondroyd J, Den Harog JP (1928) The theory of dynamic vibration absorber. *Trans. ASME* 50(7):9–22
6. Bishop RED, Welbourn DB (1952) The problem of the dynamic vibration absorber, engineering, London, pp 174–769
7. Snowdown JC (1960) Steady-state behaviour of the dynamic absorber. *J Acoust Soc Am* 31 (8):1096–1103
8. Falcon KC, Stone BJ, Simcock WD, Andrew C (1967) Optimization of vibration absorbers: a graphical method for use on idealized systems with restricted damping. *J Mech Eng Soc* 9:374–381
9. Ioi T, Ikeda K (1978) On the dynamic vibration damped absorber of the vibration system. *Bull Jpn Soc Mech Eng* 21(151):64–71
10. Zahrai SM, Ghannadi-Asl M (2006) Effectiveness of TMDs in mitigating seismic vibration of multi-story buildings. In: Seventh international congress on civil engineering, Tehran, Iran, 8–10 May 2006
11. Jia J (2014) Essentials of applied dynamic analysis. Springer, Heidelberg
12. Mansour AE, Ertekin RC (2003) Proceedings of the 15th international ship and offshore structures congress, San Diego, USA
13. Sadek F, Mohraz B, Taylor AW, Chung RM (1996) Passive energy dissipation devices for seismic applications, NISTIR 5923, National Institute of Standards and Technology, US Department of Commerce, Gaithersburg, Maryland
14. Vandiver JK, Mitome S (1982) Effect of liquid storage tanks on the dynamic response of offshore platforms. In: Kirk CL (ed) Dynamic analysis of offshore structures. CML, Heidelberg, pp 25–32
15. Dodge FT (2000) The new “dynamic behaviour of liquids in moving containers. Southwest Research Institute, San Antonio, Texas
16. Warburton GB, Ayorinde EO (1980) Optimum absorber parameters for simple systems. *Earthq Eng Struct Dyn* 8:197–217
17. Zhou F (1997) Anti-seismic control of engineering structures. China Seismological Press, Beijing (in Chinese)
18. GERB (2015) Tuned mass dampers for bridges, buildings and other tall structures. GERB Schwingungisolierungen GmbH & Co.KG, Berlin
19. Matta E, Stefano AD (2009) Robust design of mass-uncertain rolling pendulum TMDs for the seismic protection of buildings. *Mech Syst Signal Process* 23:127–147
20. Murudi MM, Mane SM (2004) Seismic effectiveness of tuned mass damper (TMD) for different ground motion parameters. In: Proceedings of 13th world conference on earthquake engineering, Vancouver, No. 2325
21. Gupta YP, Chandrasekaren AR (1969) Absorber system for earthquake excitation. In: Proceedings of the fourth world conference on earthquake engineering, Santiago, Chile, vol II, pp 139–148
22. Kaynia AM, Veneziano D, Biggs JM (1981) Seismic effectiveness of tuned mass dampers. *J Struct Div ASCE* 107:1465–1484
23. Infinity Bridge (2009) www.flintneill.com, Flint & Neill
24. Infinity Bridge (2011) <http://en.wikipedia.org>
25. www.taipei-101.com.tw

26. Haskett T, Breukelman B, Robinson J, Kottelenberg J (2003) Tuned mass dampers under excessive structural excitation. Motioneer Inc., Guelph
27. Joseph LM, Poon D, Shieh S (2006) Ingredients of high-rise design. Taipei 101 the world's tallest building. *Structure Magazine*, 6, 2006
28. Kawano K, Venkataramana K (1992) Seismic response of offshore platform with TMD. In: 10th World conference on earthquake engineering
29. Zhang L, Yue Q (2016) Experimental study on mitigation of ice induced offshore structure vibration with TMD. In: Proceeding of fourth China-Japan-US symposium on structural control and monitoring, Hangzhou
30. Kanai K (1967) Semi-empirical formula for the seismic characteristics of the ground. *Bulletin of the Earthquake Research Institute*, vol 35. University of Tokyo, pp 309–25
31. Hoang N, Fujino Y, Warnitchai P (2008) Optimal tuned mass damper for seismic applications and practical design formulas. *Eng Struct* 30(3):707–715
32. Lou M, Jingning W (1998) Effects of soil–structure interaction on structural vibration control. *Dev Geotech Eng* 83:189–202
33. Palazzo B, Petti L (1997) Aspects of passive control of structural vibrations. *Meccanica* 32:529–544
34. Palazzo B, Petti L (1999) Combined control strategy: base isolation and tuned mass damping. *ISET J Earthq Technol* 36:121–123
35. Taniguchi T, Der Kiureghian A, Melkumyan M (2008) Effect of tuned mass damper on displacement demand of base-isolated structures. *Eng Struct* 30:3478–3488
36. Robinson JK, Gamble SL, Myslimaj BM (2007) Supplemental damping and using tuned sloshing dampers. *Struct Mag* 6:14–18
37. Sakai F, Takaeda S (1989) Tuned liquid column damper: new type device for suppression of building vibrations. In: Proceedings of international conference on high rise buildings, Nanjing, China
38. Lee S-K, Min K-W, Lee H-R (2011) Parameter identification of new bidirectional tuned liquid column and sloshing dampers. *J Sound Vib* 330:1312–1327
39. Hitchcock PA, Kwok KCS, Watkins RD, Samali B (1997) Characteristic of liquid column vibrations absorbers (LCVA)—I. *Eng Struct* 19:126–134
40. Hitchcock A, Kwok KCS, Watkins RD, Samali B (1997) Characteristic of liquid column vibrations absorbers (LCVA)—II. *Eng Struct* 19:135–144
41. Hochrainer MJ, Ziegler F (2006) Control of tall building vibrations by sealed tuned liquid column dampers. *Struct Control Health Monit* 13:980–1002
42. Reiterer M, Ziegler F (2006) Control of pedestrian-induced vibrations of long-span bridges. *Struct Control Health Monit* 13:1003–1027
43. Shimizu K, Teramura A (1994) Development of vibration control system using Ushaped tank. In: Proceedings of the first international workshop and seminar on behavior of steel structures in seismic areas, Timisoara, Romania, 7.25–7.34
44. Kareem A, Kijewski T, Tamura Yukio (1999) Mitigation of motions of tall buildings with specific examples of recent applications. *J Wind Struct* 2(3):201–251
45. Faltinsen OM, Rognebakke OF, Lukovsky IA, Timokha AN (2000) Multidimensional modal analysis of non-linear sloshing in a rectangular tank with finite water depth. *J Fluid Mech* 407:201–234
46. Jin Q, Li X, Sun N, Zhou J, Guan J (2007) Experimental and numerical study on tuned liquid dampers for controlling earthquake response of jacket offshore platform. *Mar Struct* 20 (4):238–254
47. Dong S, Li H, Takayama T (2001) Characteristics of tuned liquid damper for suppressing wave induced vibration. In: Proceedings of the 11th international offshore and polar engineering conference, Stavanger, Norway, pp 79–83
48. Xu YL, Samali B, Kwok KCS (1992) Control of along-wind response of structures by mass and liquid dampers. *J Eng Mech* 118(1):20–39
49. Yalla SK, Kareem A, Kantor JC (2001) Semi-active tuned liquid column dampers for vibration control of structures. *Eng Struct* 23:1469–1479

50. Kareem A (1994) The next generation of tuned liquid dampers. In: Proceedings of the first world conference on structural control, vol I, Los Angeles, FB5. USA: IASC, pp 19–28
51. Yalla SK, Kareem A, Kantor JC (1998) Semi-active control strategies for tuned liquid column dampers to reduce wind and seismic response of structures. In: Proceedings of the second world conference on structural control, Kyoto, Japan, John Wiley, UK, pp 559–568
52. Abe M, Kimura S, Fujino Y (1996) Control laws for semi-active tuned liquid column damper with variable orifice opening. Paper presented at the second international workshop on structural control, Hong Kong, December, 1996
53. Haroun MA, Pires JA (1994) Active orifice control in hybrid liquid column dampers. In: Proceedings of the first world conference on structural control, vol I, Los Angeles, FA1. USA: IASC, pp 69–78
54. Banerji P, Samanta A (2011) Earthquake vibration control of structures using hybrid mass liquid damper. Eng Struct 33(4):1291–1301
55. Love JS, Tait MJ, Toopchi-Nezhad H (2011) A hybrid structural control system using a tuned liquid damper to reduce the wind induced motion of a base isolated structure. Eng Struct 33 (3):738–746
56. Kaneko S, Ishikawa M (1999) Modeling of tuned liquid damper with submerged nets. ASME J Press Vessel Technol 121:334–343
57. Warnitchai P, Pinkaew T (1998) Modeling of liquid sloshing in rectangular tanks with flow-dampening devices. Eng Struct 20(2):593–600
58. Tait MJ (2008) Modeling and preliminary design of a structure-TLD system. Eng Struct 30 (10):2644–2655
59. Tait MJ, El Damatty AA, Isyumov N, Siddique MR (2005) Numerical flow models to simulate tuned liquid dampers (TLD) with slat screens. J Fluids Struct 20:1007–1023
60. Tait MJ, El Damatty AA, Isyumov N (2004) Testing of tuned liquid damper with screens and development of equivalent TMD model. Wind Struct 7(4):215–234
61. Cassolato MR, Love JS, Tait MJ (2010) Modelling of a tuned liquid damper with inclined damping screens. J Struct Control Health Monit 18(6):674–681
62. Fediw AA, Isyumov N, Vickery BJ (1995) Performance of a tuned sloshing water damper. J Wind Eng Ind Aerodyn 57:237–247
63. Lee D, Ng M (2010) Application of tuned liquid dampers for the efficient structural design of slender tall buildings. CTBUH J 4:30–36
64. Faltinsen OM, Timokha AN (2011) Natural sloshing frequencies and modes in a rectangular tank with a slat-type screen. J Sound Vib 330:1490–1503
65. Soong TT, Constantinou MC (1994) Passive and active structural vibration control in civil engineering. Springer, Heidelberg
66. Hitchcock PA, Kwok KCS, Watkins RD (1997) Characteristics of liquid column vibration absorbers (LCVA)-I. Eng Struct 19(2):126–134
67. Yalla SK, Kareem A (2002) Discussion of paper: tuned liquid dampers for controlling earthquake response of structures by P. Banerji *et al.*, Earthquake Engng Struct. Dyn., 2000; 29(5):587–602. Earthq Eng Struct Dyn 31:1037–1039
68. Yalla SK (2001) Liquid dampers for mitigation of structural response: theoretical development and experimental validation. PhD thesis, University of Notre Dame, August, 2001
69. Modi VJ, Welt F (1987) Vibration control using nutation dampers. In: International conference on flow induced vibrations, London, England, pp 369–376
70. Tamura Y, Fuji K, Sato T, Wakahara T, Kosugi M (1988) Wind induced vibration of tall towers and practical applications of tuned sloshing dampers. In: Proceedings of symposium/workshop on serviceability of buildings, Ottawa, Canada, vol 1, pp 228–241
71. Kareem A (1993) Tuned liquid dampers: past, present, and future. In: Proceedings of the seventh US national conference on wind engineering
72. Fujino Y, Sun L, Pacheco BM, Chaiseri P (1992) Tuned liquid damper (TLD) for suppressing horizontal motion of structures. J Eng Mech 118(10):2017–2030

73. International Organization for Standardization (1984) Guidelines for the evaluation of the response of occupants of fixed structures, especially buildings and offshore structures, to low-frequency horizontal motion (0.063 to 1.0 Hz) ISO 6897-1984. International Organization for Standardization, Geneva, Switzerland
74. Wakahara T, Shimada K, Tamura Y (1994) Practical application of tuned liquid damper for tall buildings. In: ASCE structures congress and IASS international symposium, Atlanta
75. Tamura Y, Fujii K, Ohtsuki T, Wakahara T, Kohsaka R (1995) Effectiveness of tuned liquid dampers under wind excitation. *Eng Struct* 17(9):609–621
76. www.deicon.com
77. Yalla S, Kareem A (2000) Optimum absorber parameters for tuned liquid column dampers. *J Struct Eng ASCE* 126(8):906–915
78. Rana R, Soong TT (1998) Parametric study and simplified design of tuned mass dampers. *Eng Struct* 20(3):193–204
79. Kitada Y, Park KC (1994) A comparative study of distributed vs. concentrated hybrid mass damper systems in high-rise buildings. In: Proceedings of the first world conference on structural control, FA2-23, vol. 3, Pasadena, CA
80. <http://www.ecs.csun.edu/~shustov/Topic9.htm>
81. Lieber P, Jensen DP (1945) An acceleration damper: development, design, and some applications. *Trans ASME* 67:523–530
82. Masri SF, Caughey TK (1966) On the stability of the impact damper. *Transactions of the ASME*, pp 586–592
83. Reed III WH (1967) Hanging-chain impact dampers: a simple method for damping tall flexible structures. In: International research seminar—wind effects on buildings and structures, Ottawa, Canada, pp 284–321
84. Cheng J, Hui X (2006) Inner mass impact damper for attenuating structure vibration. *Int J Solids Struct* 43:5355–5369
85. Carotti A, Turci E (1999) A tuning criterion for the inertial tuned damper: design using phasors in the Argand–Gauss plane. *Appl Math Model* 23:199–217
86. Ema S, Marui E (1996) A fundamental study on impact dampers. *Int J Mach Tools Manuf* 36 (3):293–306
87. Cheng CC, Shiu JS (2001) Transient vibration analysis of a high speed feed drive system. *J Sound Vib* 239(3):489–504
88. Dlmentberg MF, Iourtchenko DV (2004) Random vibrations with impacts: a review. *Non-linear Dyn* 36:229–254
89. Zhang D, Angeles J (2005) Impact dynamics of flexible-joint robots. *Comput Struct* 83:25–33
90. Ying Z, Semercigil SE (1991) Response of a new tuned vibration absorber to an earthquake-like random excitation. *J Sound Vib* 150(3):520–530

Chapter 25

Load and Energy Sharing Mechanism

25.1 General

Load and energy sharing mechanisms aim to distribute seismic energy and load among more designated resisting structures or structural elements. Typical such mechanisms include the measures to connect a structure to adjacent structure(s) (Sect. 25.2), and lock-up and shock transmission units (Sect. 25.3).

It is interesting to mention that similar mechanisms also exist in nature. For example, researchers [1] revealed that the woodpecker's brain (a vulnerable part for most animals) can withstand repeated collisions and deceleration of more than a few hundreds of acceleration of gravity (more than 20 times the deceleration the human brain can withstand) during rapid pecking, which is due to the anti-shock biomechanical structure of woodpeckers: 99.7 % of impact energy in the pecking is spread out to the body and converted into the strain energy stored in the bulk of body, and only a small fraction (0.3 %) of the energy is stored in the head after three successive peckings but is dissipated in form of heat, causing a rapid temperature increment in the brain while alleviating the mechanical injury to brain. Figure 25.1 shows stress distributions on a woodpecker during a pecking process.

25.2 Connecting to Adjacent Structures

For improving the structural seismic performance, various studies have indicated the effectiveness of using dampers to link a structure to adjacent structure(s) or lateral resistant walls (middle and right figure in Fig. 25.2) or to link two adjacent stories (left figure in Fig. 25.2) with passive dampers [2–4] and active actuators [5, 6]. These solutions, firstly studied in the early 1970s to reduce the wind-induced response of high rise buildings, were applied 20 years later to prevent the problem of mutual pounding between adjacent structures, which have been observed during

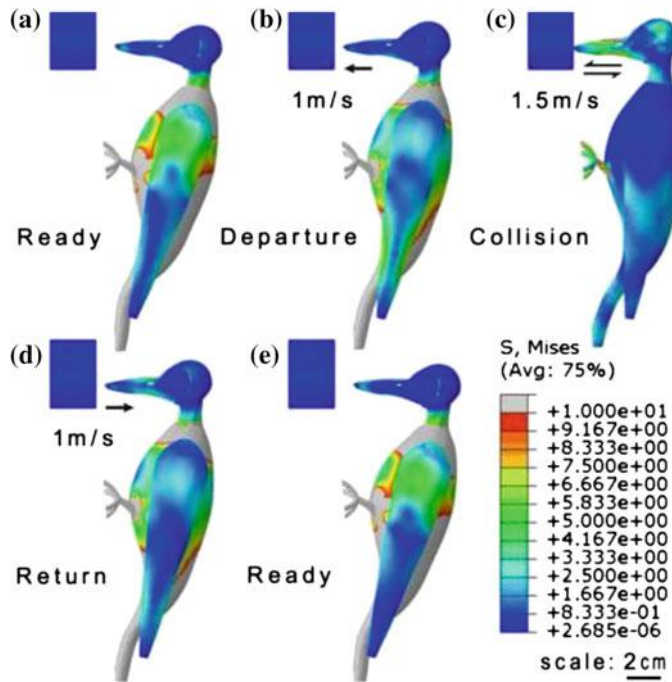


Fig. 25.1 Illustration of pecking process of a woodpecker and the von-Mises stress at different times: **a, e** are moments of readiness to peck; **b, d** are the moments of departure and return, respectively; **c** is the moment of collision; arrows on the beaks show velocity direction [1]

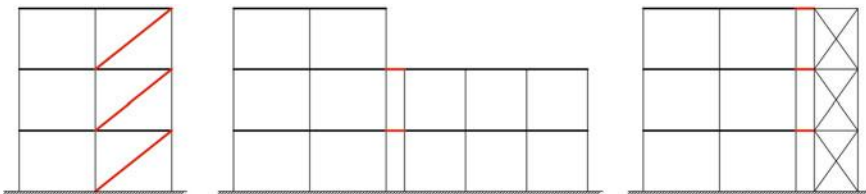


Fig. 25.2 Methods for implementing dissipative devices in the retrofit of existing buildings: between two adjacent stories (*left*), connecting adjacent buildings (*middle*), and connecting a building with lateral resistant walls (*right*) [7]

strong earthquakes [3]. The way to connect a structure to the adjacent structure(s) is essentially a coupling between the two structures, so that the load critical to one structure can be transferred to and shared with the adjacent structure(s) that is less critical with regard to seismic resistance. It has been shown that coupling two structures with dissipative connections is much more efficient than using a rigid connection [7].

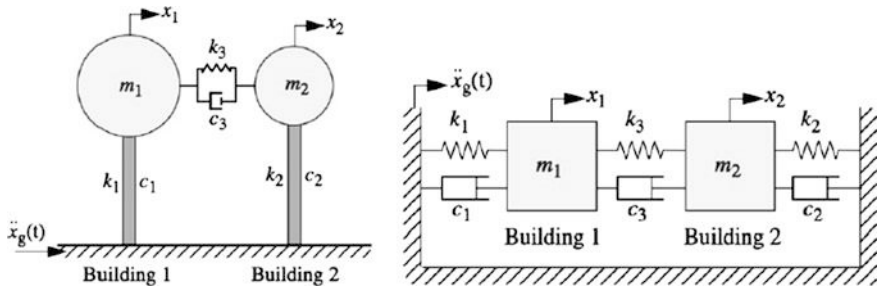


Fig. 25.3 Simplified modeling of two structures (buildings) connected by a passive link, each structure is modeled as a single-degree-of-freedom system [10]

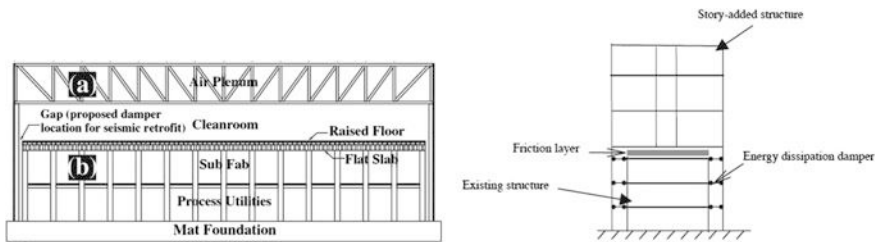


Fig. 25.4 An existing structure is connected to a newly designed resistant structure for seismic retrofit purpose [13, 14]

Structures together with connections can be modeled in various ways. The most convenient way to represent the coupled structure is to model both structures with two single-degree-of-freedom structures as shown in Fig. 25.3. The structures can also be modeled with multiple-degrees-of-freedom [8, 9].

As an extension of the method of connecting adjacent structures to mitigate seismic response, an existing structure can also be connected to a newly designed resistant structure as shown in the right figure of Fig. 25.4. This provides the possibility to design a complementing structure with desired geometry and dynamic properties, and could lead to a more focused and efficient strategy [7]. For example, this could be used to create a new elevator core [11], to add spaces to a building through lateral expansion or elevation [12], or to design a new resistant structure as an external cladding [7].

25.3 Lock-up and Shock Transmission Unit

Instead of cutting the load transfer between foundation and superstructure as a base isolation system does, the lock-up and shock transmission unit is a load and energy sharing mechanism, which enables the distribution of the ground motion energy

among more designated resisting structural elements, thus avoiding energy accumulation in localized part(s) of the structure, making the violently vibrating part(s) calm down. This technique has certain similarities with the method to connect adjacent structures discussed in Sect. 25.2.

Figure 25.5 shows a typical type of shock transmission unit. It works similarly to that of a car's safety seat-belt. In normal condition, when structural parts A and B stand still or move slowly in relation to each other, the fluid inside the piston can flow through the narrow orifices. Therefore, the interaction force between part A and part B is almost zero. When one part of the structure exhibits more violent vibrations than the other part or both parts vibrate violently with a phase such as the case during a strong earthquake, the fluid inside the piston tends to move much faster, but the increase in shear causes the viscosity of the fluid to rise, thus reducing flow of the liquid past the piston. The narrow orifices then block the fluid, and the piston is therefore locked. As shown in Fig. 25.6, this type of mechanism is already applied in bridge type structures. Essentially, the device locks up and transmits the load into the expansion abutment or pier, and the inertia forces from the superstructure can be transmitted to the designated supporting structures.

The lock-up and shock transmission unit is especially suitable for mitigating responses of multi-span bridge decks under seismic loading. The longitudinal forces generated in a bridge deck during large earthquakes are normally far greater than those forces caused by traffic acceleration and braking. The seismic forces would normally only be resisted at the location of the fixed bearings. But with the installation of lock-up devices to the bridge structure, these forces can be shared between all supports where the devices are installed. During a significant seismic

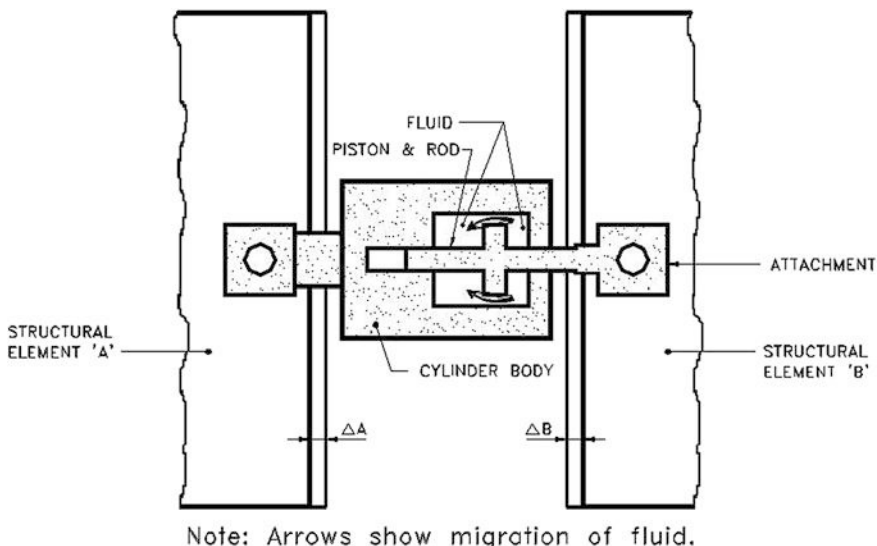


Fig. 25.5 The mechanism of shock transmission system [16]

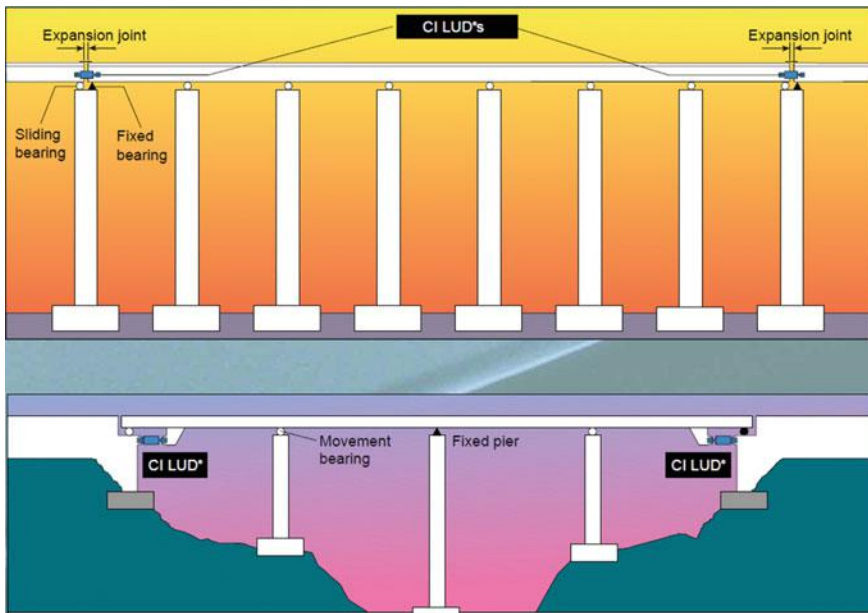


Fig. 25.6 The arrangement of lock-up devices (CI LUD) on multiple multi-span bridges (courtesy of Colebrand International Limited, CI LUD[®])



Fig. 25.7 The installation of lock-up devices on Neath railway bridge in Wales (courtesy of Colebrand International Limited, CI LUD[®])

event, the devices are temporarily locked. But after the shock ceases, they revert to their passive state [15] thus permitting the structure to expand or contract during its service life. Figure 25.7 shows an installation of lock-up devices on Neath railway bridge in Wales.

References

1. Zhu ZD, Zhang W, Wu CW (2014) Energy conversion in woodpecker on successive peckings and its role on anti-shock protection of brain. *Sci China Technol Sci* 57(7):1269–1275
2. Kobori T, Yamada T, Takenaka Y, Maeda Y, Nishimura I (1988) Effect of dynamic tuned connector on reduction of seismic response: application to adjacent office buildings. In: Proceedings of the ninth world conference on earthquake engineering, Tokyo-Kyoto, Japan, vol 5, pp 773–778
3. Luco JE, De Barros FCP (1998) Optimal damping between two adjacent elastic structures. *Earthq Eng Struct Dyn* 27:649–659
4. Xu YL, Yang Z, Lu XL (2003) Inelastic seismic response of adjacent buildings linked by fluid dampers. *Struct Eng Mech* 15(5):513–534
5. Yamada Y, Ikawa N, Yokoyama H, Tachibana E (1994) Active control of structures using the joint member with negative stiffness. In: Proceedings of the first world conference on structural control, Los Angeles, California, USA, vol 2, TP2, pp 41–49
6. Seto T, Matsumoto Y (1996) A structural vibration control method of flexible buildings in response to large earthquakes and strong winds. In: Proceedings of the second international workshop on structural control, Hong Kong, pp 490–496
7. Passon C, Beller A, Marin A, Riva P (2014) Existing structures connected with dampers: state of the art and future development. In: Second European conference on earthquake engineering and seismology, Istanbul
8. Xu YL, He Q, Ko JM (1999) Dynamic response of damper-connected adjacent buildings under earthquake excitation. *Eng Struct* 21(2):135–148
9. Huang X, Zhu HP (2013) Optimal arrangement of viscoelastic dampers for seismic control of adjacent shear-type structures. *J Zhejiang Univ Sci A* 14(1):47–60
10. Christenson RE (2001) Semiactive control of civil structures for natural hazard mitigation: analytical and experimental studies. Ph.D. thesis, University of Notre Dame, Indiana
11. Trombetti T, Silvestri S (2007) Novel schemes for inserting dampers in shear-type systems based upon the mass proportional component of the Rayleigh damping matrix. *J Sound Vib* 302(3):486–526
12. Li H, Wang SY, Song G, Liu G (2004) Reduction of seismic forces on existing buildings with newly constructed additional stories including friction layers and dampers. *J Sound Vib* 269:653–667
13. Hwang JS, Wang SJ, Huang YN, Chen JF (2007) A seismic retrofit method by connecting viscous dampers for microelectronic factories. *Earthq Eng Struct Dyn* 36(11):1461–1480
14. Li H, Wang SY, Song G, Liu G (2004) Reduction of seismic forces on existing buildings with newly constructed additional stories including friction layers and dampers. *J Sound Vib* 269:653–667
15. CI Lock-up device, Colebrand International Limited, London, 2011
16. Tandon M (2005) Economical design of earthquake-resistant bridges. *J Earthq Technol* 42(1):13–20

Chapter 26

Resistance of Non-structural Components

Non-structural components are physically connected to primary structures by various connections. They are normally not taken into account as a stiffness and/or damping contributor in a holistic structural analysis even though they increase a certain amount of damping and stiffness. However, they may behave unintentionally as structural elements by participating in the load path to transfer inertia forces and contributing accountable stiffness, strength and damping to structural elements. In this case, their contribution should be considered in the relevant seismic structural design.

Non-structural components can be divided into three broad categories [1]:

1. Architecture components, such as partitions, ceilings, storefronts, glazing, cladding, veneers, chimneys, fences, and architectural ornamentation.
2. Mechanical, electrical, and plumbing components, such as pumps, chillers, fans, air handling units, motor control centers, distribution panels, transformers, and distribution systems including piping, ductwork and conduit.
3. Furniture, fixtures, and equipment, such as shelving and book cases, industrial storage racks, retail merchandise, books, medical records, computers and desktop equipment, wall and ceiling mounted TVs and monitors, file cabinets, kitchen, machine shop or other specialty equipment, industrial chemicals or hazardous materials, museum artifacts, and collectibles.

Failures associated with non-structural components led to the majority of earthquake damage in many earthquakes. Their damages can generally be caused by either excessive accelerations or excessive movements and distortion in the structural components that support the non-structural components. Of these two causes, non-structural components can be classified as either deformation sensitive or acceleration sensitive.

If the performance of a component is controlled by the supporting structure's deformation (typically measured by inter-story drift), it is deformation sensitive. Examples of deformation sensitive components include partitions, curtain walls, doors, and piping systems running between adjacent stories. These components are

often rigidly connected to the structure and are vulnerable to racking and damage due to story drift (deformation sensitive). Their integrity and proper performance can normally be ensured by limiting inter-story drift of the supporting structure, and by designing elements to accommodate the expected lateral displacement without damage [2]. For example, a recurring problem in past earthquakes has been the jamming of large overhead doors in fire stations, causing delay in dispatching fire apparatus. Excessive structural drift causes the support and guide rails to distort and the door to bind. Excessive drift has also caused doors opening onto exit corridors to jam, trapping the occupants. This problem can be solved by limiting the drift rather than by non-structural design measures [3].

On the other hand, when non-structural components are not vulnerable to damages from inter-story displacements, or there is no negative interaction between structural and non-structural components, and such non-structural components are fixed to the structure, the components are normally regarded as acceleration sensitive. In case the anchorages or bracings for acceleration sensitive components are inadequate, they are vulnerable to shifting or overturning. Examples of acceleration sensitive components are electrical and mechanical equipment, parapets, appendages, HVAC equipment, boilers, furnaces and piping systems (except for parts of air distribution system or piping run between adjacent stories, under which they are deformation sensitive). Since they are vulnerable to shifting and overturning, their integrity and proper performance can be ensured by designing proper connections and bracing systems. Among them, light and flexible equipment generally exhibits higher amplification of acceleration responses than that for heavy and rugged equipment. Since they are vulnerable to shifting and overturning, their integrity and proper performance can be ensured by designing proper connections and bracing systems. Large non-structural elements such as storage tanks, are not only acceleration sensitive, they can also influence the seismic response of the entire structure where the tanks are supported by. Furthermore, the seismic performance of mechanical or electronic components inside the equipment also needs to be considered by limiting their motions.

Figure 26.1 shows the response sensitivity of various non-structural components given by FEMA [3]. It is noticed that many components are both deformation and acceleration sensitive, although a primary mode of behavior can generally be identified [2]. Engineers must use judgment in evaluating the need for rehabilitation and appropriate design solutions [3].

In a few seismic design guidelines such as FEMA 274 [3], non-structural elements are also categorized based on the loss incurred after their failure during earthquake shaking. The failure can be represented as a life hazard, economic loss, and loss of function [4].

The causes of damages to non-structural elements are mainly due to [1]: (1) structural deformation damage interconnected with non-structural elements; (2) acceleration and inertia effects, leading to sliding, rocking or overturning; (3) separation or pounding between separate structures damages non-structural components crossing between them; (4) interaction between adjacent non-structural components.

Nonstructural Components: Response Sensitivity					
COMPONENT	Sensitivity		COMPONENT	Sensitivity	
	Acc.	Def.		Acc.	Def.
A. ARCHITECTURAL				B. MECHANICAL EQUIPMENT	
1. Exterior Skin			1. Mechanical Equipment		
Adhered Veneer	S	P	Boilers and Furnaces	P	
Anchored Veneer	S	P	General Mfg. and Process Machinery	P	
Glass Blocks	S	P	HVAC Equipment, Vibration Isolated	P	
Prefabricated Panels	S	P	HVAC Equipment, Nonvibration Isolated	P	
Glazing Systems	S	P	HVAC Equipment, Mounted In-line with Ductwork	P	
2. Partitions			2. Storage Vessels and Water Heaters		
Heavy	S	P	Structurally Supported Vessels (Category 1)	P	
Light	S	P	Flat Bottom Vessels (Category 2)	P	
3. Interior Veneers			3. Pressure Piping	P	S
Stone, Including Marble	S	P	4. Fire Suppression Piping	P	S
Ceramic Tile	S	P	5. Fluid Piping, not Fire Suppression		
4. Ceilings			Hazardous Materials	P	S
a. Directly Applied to Structure	P		Nonhazardous Materials	P	S
b. Dropped, Furred, Gypsum Board	P		6. Ductwork	P	S
c. Suspended Lath and Plaster	S	P			
d. Suspended Integrated Ceiling	S	P			
5. Parapets and Appendages	P				
6. Canopies and Marquees	P				
7. Chimneys and Stacks	P				
8. Stairs	P	S			

Acc = Acceleration-Sensitive
Def = Deformation-Sensitive

P = Primary Response
S = Secondary Response

Fig. 26.1 Assumed sensitivity of various non-structural components (an excerpt from [3])

The seismic design codes generally produce design forces high enough to prevent sliding, toppling, or collapse of acceleration sensitive components. Demands on non-structural components should generally be less than the limiting values established by designers for sound collapse prevention performance. Moreover, it is important to carefully consider the following items during the design of non-structural elements [1]:

1. Interaction of non-structural components: because many non-structural systems are interconnected or interdependent, they can impact one another, and dropped objects can damage items below them. It is noticed that lights, ceilings, diffusers, ducts, piping, sprinkler heads, and variable air volume boxes may all share the plenum space above the ceiling and it may be challenging to find ways to keep them separated and to provide independent support for all of them.
2. Interaction of non-structural and structural components: non-structural components may be damaged by the deformations of structural components. Items that cross seismic separations between buildings, connect at adjacent story levels, or are located in base isolated structures deserve special design considerations based on the expected deformations of the structural system.

3. Strength of structural components: since non-structural components are typically fixed to structural components such as slabs/decks, walls, and framing, it is important that those structural components have sufficient capacity especially when tall and heavy non-structural items are being anchored to them.
4. Location: accelerations are typically higher for items located in mid- and high rise buildings and on roofs. The location of the items in the building can have a significant influence on the design of non-structural elements.
5. Primary versus secondary effects of failure: if failure of an item may result in a release of water or hazardous materials such as toxins, chemicals, or asbestos, it may warrant additional attention to address these failures.
6. System performance: fire protection systems, emergency power generation systems, and computer and communication networks are systems that depend on the functionality of multiple components; the failure of any part might compromise the functionality of the system. All related components must be checked if the system is required for functionality.
7. Emergency egress: items located over exits, in stairways, and along exit corridors may warrant special attention in order to ensure a safe exit of building occupants.

The non-structural components normally account for more than 70 % of the total value of an infrastructure and their damages can also be relevant to life safety. Improved protection at the non-structural component level can also produce significant benefits. In a study carried out by Kircher [5], economic losses for non-residential buildings were re-calculated for the region influenced by the 1994 Northridge earthquake under hypothetical improvement of building performance with a viscous damping system or a base-isolation system. By studying Table 26.1, which shows direct saving in economic loss through improved building performance of non-residential buildings, it is clearly indicated that 51 % savings can be reached by using the damping system technology. This number is further increased to 63 % in case isolation technology is utilized. Increased recognition of the benefits of reducing non-structural damage will also lead to an increased appreciation that this is an additional cost and service worth paying for. The relevant mitigation methods should be based on dedicated studies on the relevant failure modes [6]. This will also promote an implementation of performance based design because different damage control limit states need to be defined.

Table 26.1 Reductions in direct economic loss through improved building performance of non-residential buildings [5]

Non-structural system	Economic loss (in millions US\$)				
	As-built	With damping system	Benefit (%)	With isolation system	Benefit (%)
Drift-related	1086	407	63	303	72
Acceleration-related	1952	1013	48	777	60
Contents/inventory	2162	1124	48	862	60
Sum	5200	2544	51	1942	63

For offshore platforms, through both quantitative and qualitative analyses, Visser [7] presented that the risk of damage to non-structural elements due to earthquake is low, provided all equipment and piping are adequately restrained and the drilling rigs are designed for the appropriate earthquake loading.

For a detailed elaboration of seismic design for non-structural components, references [2, 3, 8] are recommended to read.

References

1. Federal Emergency Management Agency (FEMA) (2011) Reducing the risks of nonstructural earthquake damage—a practical guide. FEMA, Washington
2. Gillengerten JD (2003) Design of nonstructural systems and components. In: Naeim F (ed) The seismic design handbook, 2nd edn. Kluwer Academic Publishers, Berlin, pp 682–721
3. FEMA 274 (1997) NEHRP commentary on the guidelines for the seismic rehabilitation of buildings. FEMA, Washington
4. Mondal G, Jain SK (2005) Design of non-structural elements for buildings: a review of codal provisions. Indian Concr J 78(8):22–28
5. Kircher CA (2003) It makes dollars and sense to improve nonstructural system performance. In: Proceedings of the ATC 29-2 seminar on seismic design, performance, and retrofit of nonstructural components in critical facilities, Newport Beach, CA, October 23–24, 2003
6. Arnold C (1991) The seismic response of non elements in buildings. Bull N Z Natl Soc Earthq Eng 24(4):306–316
7. Visser RC (1997) Seismic considerations in design and assessment of platform topside facilities. In: Conference paper, Society of Petroleum Engineers, SPE Western Regional Meeting Long Beach, California
8. FEMA 74-FM (2005) Earthquake hazard mitigation for nonstructural elements. Federal Emergency Management Agency (FEMA), Washington

Chapter 27

Structural Health Monitoring and Earthquake Insurance

27.1 Introduction

Structural Health Monitoring (SHM) or Structural Health Assessment (SHA) is the inspection of the structural soundness (conditions) and detection of damages at every stage during the service life of a structure. SHM carries out a diagnosis of the state of the constituent materials, of the different parts, and of the full assembly of these parts constituting the structure as a whole. It is an emerging engineering field that is led by two main objectives [1]:

1. Safety and improving performance
2. Commercial motivation and basis for condition-based maintenance

It is required that the state of the structure must remain in the domain specified in the design, although this can be altered by normal ageing due to usage, by the action of the environment, and by accidental events. Therefore, SHM are basically associated for fault detection, fault identification, fault assessment, fault monitoring, and remaining lifetime evaluation or failure prediction.

SHM is nowadays widely applied to various types of infrastructures. Especially when damages to structures are concerned, it is important to note that detecting damages at stages with increasing details and difficulty require the knowledge of previous stages:

1. Detecting the existence of the damage on the structure.
2. Locating the damage.
3. Identifying the types of damage.
4. Quantifying the severity of the damage.

In light of the ageing structures and recent structural failures of important infrastructures, long term monitoring techniques are being increasing investigated and adopted.

In SHM, it is usually necessary to employ signal processing and statistical classification to convert sensor data on the infrastructural health status into damage information for assessment.

Various methods are available for detecting important damage indicators, such as strain, temperature effect, moisture and overall risk zone, flaw/faults on the structure. Different types of structural health monitoring techniques have their own advantages and limitations.

Depending on whether sensors are physically in contact with the structure/body or not for damage detection, the SHM can be categorized as either wired or wireless. Wired techniques with tethered monitoring systems are widely used from past and come into present situation uses of smart sensors and fiber optics sensors, etc. Sensors and sensor characteristics depend on the location, material, and methods applying to detect the flaws or faults. Wireless SHM is suitable for conditions where sensors are distributed over a large area, such as the case for long span bridges or for monitoring machinery vibrations at different locations in an offshore platform [1]. Wireless structural monitoring systems have been shown to provide equivalent data acquisition performance compared to traditional wired monitoring systems at substantially reduced costs [2]. The recent development of the smart sensors with embedded microprocessors, wireless communication, and information technologies has made SHM with a dense array of sensors possible [3, 4]. The wireless structural monitoring has also been extended to actuate and control the monitored structure as will be introduced in Chap. 28, so that tasks of both the damage detection and mitigation measures can be carried out within the same system.

Moreover, it is of great importance to adopt decent SHM algorithms, which can take advantage of the distributed computing environment offered by smart sensor technologies, even though these aspects of technology are currently limited. Therefore, development of the SHM methods that match well with the smart sensor technology is highly desired [5].

Section 27.2 will present an introduction to vibration-based SHM. For a brief presentation of all those techniques, reads may read Ref. [1].

Similar to the control techniques of external dampers as will be presented in Chap. 28, SHM can be passive or active. If SHM is carried out on a structure equipped with both sensors and actuators, and the person carrying out SHM can generate perturbations in the structure, and can use sensors to monitor the response of the structure, the SHM is then categorized as an active monitoring. If only sensors are used without involvement of actuators, the SHM is a passive monitoring.

For more details on SHM, readers can refer to [6, 7].

Moreover, because drones or unmanned aerial vehicles (UAVs) are more convenient, more efficient, safer, cheaper, and more environmentally friendly (much less pollution and noise than inspection using a full sized aircraft/helicopter) to observe and collect data, drone based SHM has been emerging and has attracted great commercial interest in recent years, which will be briefly discussed in Sect. 27.3.

27.2 Vibration-Based SHM

Traditionally, structural damages are often detected through periodic visual inspection. Visual inspection can impose high cost. For example, for offshore structures, since they are surrounded by water, inspections such as subsea inspection involves certain risks for inspection divers and significant cost, and the application may require a lengthy approval process from the regularity authorities. Furthermore, even though periodical visual inspections are mandatory for important infrastructures, the reliability of this method is questionable and strongly depends on the inspection condition, and how experienced and dedicated the participating inspectors and engineers are. A survey by Moore et al. [8] from the US Federal Highway Administration revealed that, at most, only 68 % of the condition ratings were correct and in-depth inspections could not find interior deficiencies given that visual examinations are very seldom carried out by inspectors. In some cases, termination of normal operation activities on structures may be required solely for the sake of allowing an inspection to be carried out, such as the possible production shutdown if one wants to inspect a tip of a flare tower for an offshore platform.

All the drawbacks above motivate the technology of SHM for assessing the state of health (e.g., damage) of instrumented structures from measurements. It can be either short term (e.g., reparation) or a long term (monitoring parameters continuously or periodically) process. The safety and reliability of structures can be improved by detecting damage before it reaches a critical state [9], thus minimizing the probability of catastrophic failures and allowing reduced efforts on inspection services and maintenance, the reduction of down time and improvement in reliability enhances the productivity of the structure. The cost of SHM is relatively low, which only accounts for 2–5 % of total structure's cost for a period of 10 years [10]. In case the value of equipment and contents in a structure is also accounted for, this percentage is even much lower. Furthermore, it can also provide quick assessment after a major accident such as an earthquake, hurricane, explosion, or ship collision etc., which is essential for property owner, operators and relevant insurance companies etc. In addition, the immediacy and sensitivity of SHM also allows for the short term verification of new designs, for which there is no or limited service experiences, which needs a more rigorous monitoring and inspection, until adequate confidence is gained. This is because new designs often involve a high utilization of strength, new structural details (possibly with high stress concentration), as well as large uncertainty in the responses [11]. SHM also serves to confirm the design parameters and perform quality assurance through the detection of damages that caused any changes in properties than expected by original design, and in the meantime, it can sometimes approve a better structural performance than expected by the design, which provide flexibility for the structure capacity.

The most fundamental vibration-based SHM detects structural damage when noticeable changes in measured eigenfrequencies and mode shapes occur. Moreover, more detailed assessment can be performed by studying the peak responses (accelerations, velocity and displacement) and drift. More advanced

vibration-based SHM involves a determination of the model that best fits data taken from, identification of certain structural characteristics of a monitored structure. The changes in structural characteristics are then used as a measure to predict damage severity and location of damages. The focus of model parameter identification to achieve SHM is usually on local loss of stiffness as a proxy for local damage [12].

With respect to earthquake damages, SHM is especially important for aftershock inspection, simply because after a major earthquake, the local resources will be overwhelmed. Therefore, it is difficult to allocate inspection staffs to physically inspect all infrastructure sites that are potentially at risk, and SHM can give a fast assessment for the conditions of the infrastructures. As aforementioned, SHM not only applies to inspections associated with earthquake damages, but also can be used to inspect the structural conditions due to accidental loading such as ship collisions, explosions, fires, fatal structural fatigue failure, etc.

The physical diagnostic tool of a SHM system is the integration of various sensing devices and ancillary systems including sensors, data acquisition and processing system, communication system and damage detection and modeling system [13] as shown in Fig. 27.1.

Sensors are used to measure various mechanical and physical parameters. Typical sensors include accelerometers, gyroscopes, inclinometer, strain gauges, fiber optic gauges, deflection transducers, curvature sensor, etc. For vibration-based SHM, accelerometers are typically used sensors. Important specifications of accelerometers are measurable acceleration range and resolutions, size, noise level, stability over time and temperature, frequency response and filters, and power consumption. As a general rule, more sensors with an appropriate data processing can secure a more reliable assessment.

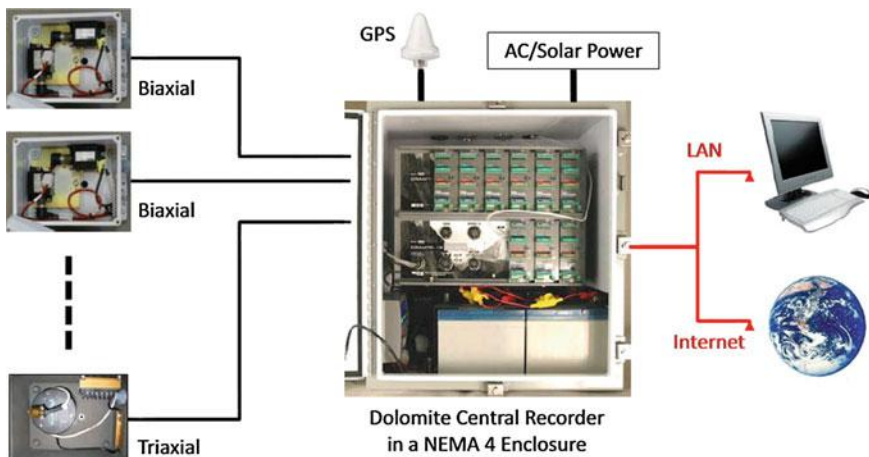


Fig. 27.1 SHM system including sensors (*left*, accelerometers in the current case), connection system, data acquisition (*middle*, the GPS is used for precise timing), communication system (*LAN* or *Internet*), data process system (computer in this case), and damage detection and modeling system (computer) (courtesy of Kinematics Inc.)

The transfer of measurement data from sensors to the data acquisition system is important. Lead wires are usually used to transfer data. Note that long wires may have a negative influence due to the noise collected with the measured data; therefore, one needs to pay attention to the allowable length of the wire corresponding with the data acquisition system. As an alternative to wires, wireless communication between the sensors and data acquisition can be used in cases when a large number of sensors are used. In addition, for underwater monitoring, acoustic transmissions, which are subject to underwater noise but are relatively easy to install and operate, are also used.

The data acquisition system can accommodate many channels (typically with 12, 24, and 36 channels). It is also the most expensive single piece of equipment in a vibration-based SHM task.

The communication system transmits the data from the acquisition system to the location where the data is processed (data process system). This can be a telephone lines, internet, transmitting devices, electric wires etc.

The processing of data is of great importance. It is basically a computer that processes the data from the sensor-acquisition system's input. The data from different sensor inputs will be related to each other. Typically, process tasks include the post-processing of inter-story drift, drift hysteresis loop, accelerations, velocity and displacement, calculation of transfer functions, etc. Ideally, the processing should be performed prior to the data storage. In some cases for onsite measurement with duration of less than a few days, the data acquisition system and process system are integrated together as one equipment package.

Despite the appealing advantages of SHM over traditional visual inspection, significant uncertainties involved in the modal testing and its interpretation still pose major challenges to a reliable vibration-based SHM. This is more obvious for offshore structures, in which environmental conditions (temperature, humidity, and wind etc.) and prevailing excitations from waves and wind impart the uncertainties into ambient or forced vibration testing. The change of weight (mainly topside content weight) and marine growth varying with the season also add further uncertainties. In addition, measurement noise and bias errors arising from sensors, cables and the data acquisition system is an important source of uncertainty [14]. On top of this uncertainty, vibration-based SHM is sometimes unable to detect the local damages of structures simply because it measures the global vibration eigenfrequencies and mode shapes, and is thus insensitive to local stiffness changes. This is especially the case for rather redundant structures.

27.3 Drone Based Structural Inspections

Because, as mentioned before, the use of drones or unmanned aerial vehicles (UAVs) is more convenient, more efficient, safer, cheaper, and more environmentally friendly to observe and collect data, they have been used in missions where the risks to human life and safety are deemed too high. For example, in the

aftermath of the Fukushima incident in 2011, drones were used to assess the damage and radiation hazard at the plant. Drones can also be used for search and rescue operations in the Arctic and in remote seas. By using drones, one can obtain high definition photography and videos of damage, corrosion, or rust for maintenance and reparation purposes without shutting down systems or facilities, or collect asset data for certification purposes. In addition, without the requirements imposed by human safety, the design of drones is much more flexible. Larger drones have the capacity to fly continuously for days, while smaller ones can operate at ground level, indoors and in other areas inaccessible to manned aircrafts for a typical time of 10 min to a few hours. Drones thereby reduce both the financial and the technological resources required to operate in the air, and have opened the airspace to new users and purposes [15].

Drones come in many shapes and sizes. Each of these has their own unique advantages and limitations. These characteristics ultimately lead to the operator's decision in which platform will best fit the application. Drones can be manufactured with either fixed wing (Fig. 27.2) or rotary wing (Fig. 27.3).

Fixed wing UAVs consist of a rigid wing that has a predetermined airfoil so that sufficient lift force is generated during the fly with certain airspeed or above. This airspeed is generated by forward thrust usually by means of a propeller being turned by an internal combustion engine or electric motor. The main advantage of a fixed wing UAV is that it consists of a much simpler structure in comparison to one with rotary wing(s). The simpler structure provides a less complicated maintenance and repair process thus providing more operational time at a lower cost. More importantly, the simple structure of the fixed wing ensures more efficient aerodynamics that provide the advantage of higher flight range at higher flight speeds as well as longer flight time, thus enabling larger survey areas during each flight.



Fig. 27.2 Fixed wing UAVs



Fig. 27.3 UAV with rotary wing used to inspect power lines. *Source* CSIRO

Rotary wing UAVs consist of two or three rotor blades that revolve around a fixed mast, typically referred to as a rotor. Rotary wing UAVs can be categorized as one rotor (helicopter), three rotors (tricopter), four rotors (quadcopter), six rotors (hexacopter), eight rotors (octocopter) and more unusual set-ups like 12 and 16 rotors. The major advantage of UAVs with rotary wings is reflected in their capability to take off and land vertically. This allows the user to operate those UAVs within smaller vicinity that has no substantial landing/take off area required. Since they can hover and perform agile maneuvering, the rotary wing UAVs can be used to inspect structures with a high precision maneuvering and have the ability to maintain a visual/inspection position on a single target for extended periods of time. However, since rotary wing UAVs involve a higher complexity related to mechanical and electronic components, which generally requires more complicated maintenance and repair processes, higher cost, and a decrease in operational time. Moreover, rotary wing UAVs operate at lower speed and shorter flight range than their fixed wing counterparts, which further increase the inspection time and cost [16].

In civil engineering, by using micro drones to carry high resolution cameras to capture video data, an increasing number of inspections have been carried out for bridges and their associated pylons and stay cables, power lines, high rise towers and mast light poles, and offshore structures (flares, bottom of topside, offshore wind turbines), etc. Figures 27.3 and 27.4 show two examples of using UAVs to inspect power lines and wind turbine blades. In recent years, multi-axis (rotors) UAVs, as shown in Fig. 27.4, have become popular for carrying out inspection tasks, primarily due to their high performance for wind stability and carrying capacity compared to the single axis helicopter drone (Fig. 27.3). The relevant types of drones can be operated in a wind speed up to 16 m/s and can have an auto-pilot function that can return to a designated location (“going home”) in case it is required by the controller or the control signal is lost. By modifying a drone to



Fig. 27.4 A hexacopter used to inspect wind turbine blades (courtesy of Aibotix)

make it waterproof, it is also possible to operate the drone to fly close to water surface in case it can potentially be hit by water waves. In addition, since occasionally visual inspections are accompanied by some form of hands-on (tactile) information such as sounding for loose or delaminated concrete, with a dedicated drone flitting-sensor, it is possible to come into contact with a structure with centimeter accuracy, without damaging the structure in the least or putting oneself in danger [17].

Moreover, higher power storage and longer battery life-span also facilitate the operation of UAV for inspection. The use of drones to inspect a structure allows for a close-up view of areas (on height and distance from the inspector) that are of interest without physical contact with the area (eliminate the possibility to damage the structure by inspectors); increases the inspection efficiency especially for areas (such as stay cables of bridges or high rise towers) that are difficult for the inspector to reach; avoids or minimizes the required physical skills and high risk associated with inspectors that would otherwise be required in a traditional visual inspections; it also avoids a termination of operation and requirement of specialized types of access equipment if the operation is dangerous for the inspector. As an extension of drone based inspection, by adding a thermal infrared imagery camera or an acoustic coupling to gauge steel (to estimate the metal wall thickness through the measured acoustic velocity) on the drone, it is technically feasible to detect the delamination and subsurface cracks in the concrete or the defect (and/or the loss of material) of an inspected structure.

Drone based SHM have attracted an increasing commercial interest worldwide. Within just the wind turbine inspection business, it is estimated [18] that a cumulative global revenue for UAV sales and inspection services for wind turbines can reach nearly US\$6 billion by 2024. The emerging wind turbine UAV market is driven by the massive number of blades that need to be inspected for normal

deterioration and for pre-end-of-warranty inspections. If uninspected, deterioration caused by the elements to the more than 800,000 blades in operation can result in reduced energy production and blade collapse.

Drones have also been used for interventions in emergency situations due to destructive disasters (such as an earthquake or hurricane disaster) in order to bring support to the local authorities regarding surveillance of areas or targets.

It is worth mentioning that the cost for the inspection equipment (typically including a drone, visual inspection facilities (e.g., camera), data collection and analysis software) has been reducing dramatically in recent years, and is expected to further reduce in the coming years. This paves the way for an increasing number and a wider scope of structural inspection applications using drones.

27.4 Inspections by Remotely Unmanned Underwater Vehicles

Rather than using divers for subsea inspections that can introduce high risk and usually require applying for permissions a few months before the diver inspection, other types of techniques are also developed for inspecting the underwater part of offshore structures and bridges, and for studying sea floors and river beds, etc. Among them, unmanned underwater vehicles are widely used, which can be categorized as remotely operated vehicles (ROVs) and autonomous underwater vehicles (AUVs). They are characterized with a lack of pilot onboard.

Mainly motivated by the demand of offshore industry, ROVs (Fig. 27.5) are essentially unoccupied and tethered underwater robots, connected to an operator/crew via a series of cables. ROVs carry all relevant sensors. The



Fig. 27.5 A ROV being retrieved by an offshore vessel



Fig. 27.6 A crack developed in an underwater tank detected through a regular inspection by a ROV

connecting cables transmit command and control signals to and from the underwater vehicle and the operator aboard a vessel, allowing a remote navigation of the ROVs and performing relevant inspection tasks. ROVs are highly maneuverable and can meet various types of needs of the offshore industry (for applications with a water depth up to 3000 m) as well as scientific and military community. For example, they are widely used for inspecting structures underwater and sea/river bottom conditions and scour. Figure 27.6 shows a long crack developed in a subsea steel tank located at 60 m below sea surface, which was detected by a ROV during



Fig. 27.7 A Bluefin-12 AUV with a Buried Object Scanning Sonar (BOSS) integrated in two wings

a regular inspection. Recently, portable (weighting only a few kilograms) and affordable ROVs were also developed to carry out inspection work at shallow waters (typically less than 100 m). In aquaculture industry, this special type of ROVs has been applied for inspecting cage net, moorings, and monitoring fish farm.

As shown in Fig. 27.7, AUVs are unmanned submersible vehicles and they travel underwater without requiring input from an operator. Therefore, they can fulfill missions without the help of operators. Current applications of AUVs include: subsea inspection, subsea survey, pipeline inspection, cable inspection, oceanographic sampling, environmental monitoring, iceberg profiling, under-ice surveys, mine detection and countermeasures, diver delivery/supply vehicles, downed airplane/shipwreck searches, and underwater photography [19].

27.5 Earthquake Insurance

From the business insurance point of view, earthquakes represent the worst kind of risk: the one that everyone “knows” is going to happen “someday,” but which cannot be predicted or prevented. According to the US Geological Survey, among natural disasters, earthquakes are the most costly from which to recover. In addition, a strong earthquake is likely to cause significant disaster in an area, i.e. a devastating earthquake destroying one property is likely to destroy many properties in the same area. Therefore, insurance companies are very careful when assigning earthquake related insurance, and this is normally based on a detailed study from seismic experts to develop a model for predicting the probability of future earthquakes and put it into a risk assessment. The Swiss Re Group [19] presented that seismic events caused economic losses of over US\$276 billion in 2010–2011 around the world. Therefore, standard property insurance does not cover losses from earthquakes without a specific earthquake rider.

Nevertheless, earthquake insurance, where available, should be considered an important measure to mitigate risk [20]. Many insurance companies in USA, New Zealand, and Japan offer earthquake coverage. The cost of the insurance depends on the coverage amount, age of a particular property, proximity to relevant faults, deductible (typically 10–15 % of the losses) and types of property etc. It is noticed that rehabilitation (Chap. 29) or mitigation measures (Chaps. 19–28) may significantly decrease the insurance cost for the property owner.

Many earthquake prone areas remain under-insured. This is especially the case for the earthquake areas in USA and Japan, where only around 12 and 17 % of property owners in the relevant areas bought the earthquake insurance. After the 1994 Northridge earthquakes in California, 12 % of the homeowners in the affected areas (California) who had bought earthquake insurance claimed US\$12 billion. Following this earthquake, 30 % of homeowners in California purchased earthquake insurance. However, since there were no destructive earthquakes in California after that, this number has fallen to less than 12 %, even though the

seismic risk remains at the same level. By contrast, earthquake insurance penetration is highest in New Zealand among all countries, with 90 % of homeowners having earthquake insurance. As a consequence, the insurance industry will pay an estimated 80 % of the overall cost of the February 2011 earthquake in New Zealand, but no more than 17 % for the disastrous event in Japan in March 2011.

Earthquake insurance for offshore industry receives less attention. This may be related to the fact that no earthquake damages have been reported for offshore platforms as described in Chap 1. However, it would be more relevant from a risk point of view and also because an increasing number of offshore activities have been carried out in earthquake prone areas and the value of many offshore platforms is increased after each time of upgrading.

References

1. Dhakal DR, Neupane K, Thapa C, Ramanjaneyulu GV (2013) Different techniques of structural health monitoring. *Int J Civil Struct Environ Infrastruct Eng* 3(2):55–66
2. Lynch JP, Law KH, Kiremidjian AS, Carrier E, Farrar CR, Sohn H, Allen DW, Wait JR (2004) Design and performance validation of a wireless sensing unit for structural monitoring applications. *Struct Eng Mech* 17(3–4):393–408
3. Kurata N, Spencer BF, Ruiz-Sandoval M (2005) Risk monitoring of buildings with wireless sensor networks. *Struct Control Health Monit* 12(3–4):315–327
4. Glaser SD, Li H, Wang ML, Ou J, Lynch J (2007) Sensor technology innovation for the advancement of structural health monitoring: a strategic program of US–China research for the next decade. *Smart Struct Syst* 3(2):221–244
5. Nagarajaiah Satish, Dyke Shirley, Lynch Jerome, Smyth Andrew, Agrawal Anil, Symans Michael, Johnson Erik (2008) Current directions of structural health monitoring and control in USA. *Adv Sci Technol* 56:277–286
6. Balageas D, Fritzen CP, Güemes A (2006) Structural Health Monitoring (ISTE). Wiley-ISTE, London
7. Gopalakrishnan S, Ruzzene M, Hanagud S (2011) Computational techniques for structural health monitoring. Springer, London
8. Moore M, Phares B, Graybeal B, Rolander D, Washer G (2001) Reliability of visual inspection for highway bridges, Federal Highway Administration Report, No FHWA-RD-01-020 and FHWA-RD-01-021
9. Kinematics, system for SHM. Pasadena, CA (2001)
10. Glisic B, Inaudi D (2007) Fibre optic methods for structural health monitoring. Wiley, Chichester
11. Moan T (2005) Safety of offshore structures. Centre for Offshore Research & Engineering, National University of Singapore, Singapore
12. Beck JL, Vanik MW, Katafygiotis LS (1994) Determination of stiffness changes from modal parameter changes for structural health monitoring. In: First world conference on structural control, Los Angeles, CA
13. Guidelines for structural health monitoring. ISIS Canada (2001)
14. Zhang J, Prader J, Grimmelmann KA, Moon F, Aktan AE, Shama A (2009) Challenges in experimental vibration analysis for structural identification and corresponding engineering strategies. In: Third experimental vibration analysis for civil engineering structures conference, Wroclaw, Poland
15. Moe ÅR (2013) Take-off for civilian drones, Teknologirådet, 19 June, 2013

16. <http://www.questuav.com>
17. <http://www.civicdrone.com>
18. Navigant Research (2015) Drones for wind turbine inspection
19. www.swissre.com
20. National Earthquake Technical Assistance Program (2012) New earthquake basics training course (lecture notes). Emergency Management Institute, The Federal Emergency Management Agency (FEMA), Emmitsburg, MD, US

Chapter 28

Control Techniques for External Damping Devices

28.1 Introduction

For direct damping apparatuses, base isolation, hanging isolation, dynamic absorber and lock-up and shock transmission devices, three types of techniques are available for vibration control: passive, semi-active and active, which are illustrated in Fig. 28.1. Moreover, hybrid technique takes the advantages of both passive and active control technique.

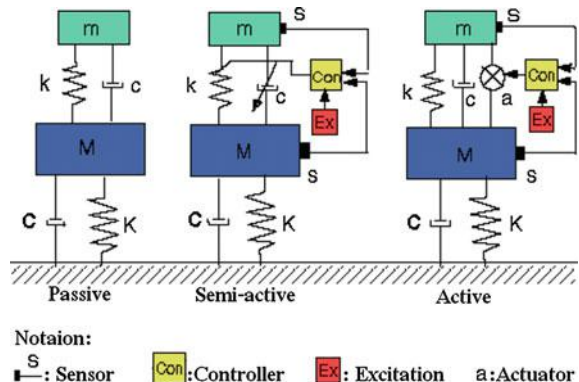
Vibration control has been widely applied in many types of structures. For example, after 2000, around 80 % of the high rise buildings in Japan with heights more than 60 m were designed with the concept of vibration and damage control. There is a report showing that 20 % of steel in weight can be saved for steel buildings if they are designed with this concept [2].

Moreover, with the concept of vibration control, it is possible, in many cases, to re-center the primary structures or to replace the damaged energy dissipation components after a major earthquake.

28.2 Passive Control Devices

Passive control devices utilize the dynamics of the structure itself to dissipate energy. Passive vibration control has the merit of being reliable, simple, and cost effective, i.e. no requirement for controlling electronics or powered drive mechanisms. They can immediately respond to structural responses with great reliability, even during extreme conditions when the power supply is shut down. Therefore, in today's engineering practice, most of the vibration reduction control measures use passive control technique, even with a sacrifice to its effectiveness, i.e. without the use of control mechanisms, a passive damper is incapable of adjusting itself to a variation in any parameters of the system.

Fig. 28.1 Three basic types of vibration control techniques [1]



The passive control devices include many dynamic mitigating apparatuses described in previous chapters (Chaps. 22–25). Table 28.1 categorizes a few of them based on their behavior to absorb energy from main structures. Velocity-activated devices absorb energy through the relative velocity between their connection points. The behavior of these dampers is usually dependent on the frequency of the motion, and is out-of-phase with the maximum internal forces generated at the end of each vibration cycle corresponding to the peak deformations of the structure, leading to decreased forces on structural members. Displacement-activated devices absorb energy through the relative displacement between the points they connect to the structure. Their behavior is usually independent of the frequency of the motion and is in-phase with the maximum internal forces generated at the end of each vibration cycle corresponding to the peak deformations of the structure. Motion-activated dampers are secondary masses that absorb structures' vibration energy through structures' motion. They are tuned to resonate with the main structure, but out-of-phase from it. These dampers absorb the input energy of a structure and dissipate it by introducing extra forces to the structure, therefore, less amount of energy is stored in the main structure [3, 4].

Based on whether or not a damping or base isolation device is linear, Table 28.2 lists flexibility and damping of typical passive control systems.

Table 28.1 Types of dampers as passive control devices

Velocity activated	Displacement activated	Motion activated (Sect. 23.7)
<ul style="list-style-type: none"> • Viscous damper (Sect. 22.2) • Viscous damping wall (Sect. 22.3) • Lock-up and shock transmission unit (Sect. 25.3) 	<ul style="list-style-type: none"> • Viscoelastic damper (Sect. 22.5) • Friction damper (Sect. 22.6) • Yielding damper (Sect. 22.7) 	<ul style="list-style-type: none"> • Tuned mass damper (Sect. 24.5) • Tuned liquid damper (Sect. 24.6) • Impact damper (Sect. 24.8)

Table 28.2 Flexibility and damping of typical seismic isolation and damping devices [5]

Property	Linearity	Nonlinearity
• Restoring force (providing spring constant and flexibility)	<ul style="list-style-type: none"> • Laminated rubber bearings • Flexible piles or columns • Springs • Viscoelastic dampers • Sliding isolation systems 	<ul style="list-style-type: none"> • High damping rubber bearings • Lead rubber bearings • Sliding isolation systems (gravity) • Hanging isolation systems (gravity and inertia)
• Damping	<ul style="list-style-type: none"> • Laminated rubber bearings • Viscous dampers (when velocity exponent $\alpha = 1$, see Sect. 22.2.1) 	<ul style="list-style-type: none"> • High-damping rubber bearings • Lead rubber bearings • Lead extrusion dampers • Yielding dampers • Sliding isolation systems (friction)

Passive control is relatively well-understood and widely accepted by the engineering community as a means for mitigating the damages from unfavorable dynamic loads. However, it cannot adapt to the changes in structural characteristics and environment. Therefore, active, hybrid and semi-active control systems, as will be introduced in Sects. 28.3 and 28.4, are a natural evolution of passive technologies. The devices integrate with real-time controllers and sensors within the structure. They act simultaneously with the dynamic excitation and structural responses to provide enhanced behavior for improved service and safety [6].

28.3 Semi-active and Active Control Devices

To increase the damping efficiency, a control mechanism can be introduced in the damper with the ability to respond to the changes in the vibration system. This leads to the application of semi-active and active dampers, which can control vibration systems with a smaller size of damper. Compared to the use of passive control devices, the use of semi-active and active control devices can further facilitate advancements toward PBD of structures. Semi-active and active dampers usually utilize hydraulic or electro-mechanical actuator systems driven by an appropriate control algorithm, such as: (1) closed loop or feedback, in which the control forces are determined by the feedback response of the structure; (2) open loop or feed-forward, in which the control forces are determined by measured external excitations; or (3) closed-open loop or feedforward-feedback, in which the control forces are determined by both measured response of the structure and measured external excitations.

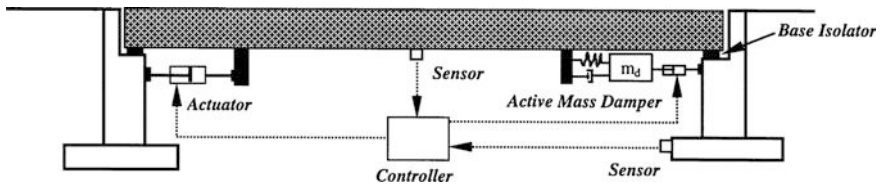


Fig. 28.2 Hybrid control system with base isolator and added active control system [9]

The major difference between semi-active and active dampers is that the semi-active damper only changes the damping level, and does not add any other external mechanical energy (through actuator) to the structural system. Active systems include active mass drivers, active variable stiffness systems (AVS), active tendon control systems, active gyro stabilizers (AGS), active aerodynamic appendages, and active pulse control systems [1].

Since the active systems require a large amount of energy to operate, semi-active systems are more energy efficient in this aspect since they may only store and dissipate energy [7]. They require little power for operation, being able to run on battery power. Furthermore, they offer highly reliable operation at a modest cost and are regarded as fail-safe as they default to passive devices should the control hardware malfunction [8]. Semi-active dampers include variable stiffness system, magnetorheological dampers, and variable orifice dampers.

28.4 Hybrid Control Devices

As aforementioned, control systems can also include a combination of active and passive control system. The combined system is called hybrid control system. For example, base isolators (passive control system) can be combined with active mass dampers, and be installed on a bridge, forming a hybrid control system, as shown in Fig. 28.2.

References

1. A. Kareem, T Kijewski, Y Tamura (1999) Mitigation of motions of tall buildings with specific examples of recent applications. Perception 2(3):1–48 (Techno-Press, South Korea)
2. Nikkei Architecture (1997) Art Hotel Sapporo, two thousand hysteretic dampers reduce 20 % steel weight, No. 588, pp 202–205 (in Japanese)
3. Christopoulos C, Filiatrault A (2006) Principles of passive supplemental damping and seismic isolation. IUSS Press, Pavia
4. Venkateswara Rao K (2013) Experimental and numerical studies on tuned liquid damper. Department of Civil Engineering, National Institute of Technology, Rourkela

5. Robinson WH (1998) Passive control of structures, the New Zealand experience. *ISET J Earthq Technol* 35(4):63–75
6. Nagarajaiah S, Dyke S, Lynch J, Smyth A, Agrawal A, Symans M, Johnson E (2008) Current directions of structural health monitoring and control in USA. *Adv Sci Technol* 56:277–286
7. Wilson CMD, Abdullah MM (2005) Structural vibration reduction using fuzzy control of magnetorheological dampers. In: Proceedings of the structures congress and the forensic engineering symposium, ASCE
8. Dyke SJ, Spencer BF, Sain MK, Carlson JD (1996) Modeling and control of magnetorheological dampers for seismic response reduction. *Smart Mater Struct* 5:567–575
9. Wu Z (2000) Active control in bridge engineering. In: Chen W-F, Lian D (eds) *Bridge engineering handbook*. CRC Press, Boca Raton

Chapter 29

Seismic Rehabilitation for Structures

29.1 General

Seismic rehabilitation includes all concepts associated with reparation, upgrading, retrofitting, and strengthening. They contribute to a reduction in the vulnerability of structures due to various reasons and motivations, such as a revision of design codes or earthquake damages, etc.

It is noticed that significant efforts have been placed on the improvement of earthquake resistance design of new structures. However, existing structures pose a greater threat with regard to loss of human lives and properties. Therefore, assessments of the seismic capacity of existing structures and prioritization for rehabilitation are essential tasks to ensure seismic performance of infrastructures [1].

29.2 Seismic Rehabilitation Measures

Seismic rehabilitation generally aims to recover or upgrade original structural performance, to mitigate seismic response [2], and sometimes to reach a combination of the aims above.

Recovery of original performance can be reached by repairing damage and deterioration; upgrading original performance can be fulfilled by various measures to stiffen or strengthen existing structures, or to improve structural irregularity and/or discontinuity as shown in Fig. 29.1; mitigating seismic responses requires a dedicated design related to the structural configuration, ductility design, addition of structural damping or damping apparatus, base isolation, loading sharing and energy transfer system, etc., which has been discussed from Chaps. 19–25.



Fig. 29.1 Corner joint steel reinforcement and high tensile strength rods with grouted anti-burst jacket below (photo under license CC SA 1.0)

29.3 Strengthening of Structures

Deterioration of structural members are widely confronted for almost all types of infrastructures. They can be caused by ageing, environmentally induced degradation, poor initial design and/or construction, lack of maintenance, and by accidental events such as wind storm or earthquakes [3]. The infrastructure's increasing decay is often accompanied by more demanding design requirements (e.g. increased equipment weight of offshore structures, increased traffic volumes in bridges exceeding the initial design loads, etc.). Therefore, the strengthening of structures is important to ensure the structures' integrity and functionality.

In order to strengthen existing or new structures, several methods exist for enhancing the seismic resistance of infrastructures. Conventional retrofitting methods include strengthening existing structures (Figs. 29.2, 29.3 and 29.4), addition of new structural elements to the system, and enlarging the existing members. Addition of shear walls and bracings is a rather popular strengthening method due to its effectiveness, relative ease, and low overall project cost compared to column and beam jacketing. It is used to provide longitudinal and lateral reinforcements with steel or concrete encasement, as shown in Figs. 29.5 and 29.6. Outrigger systems (Fig. 29.7), which are to improve the efficiency of the core system by simply engaging the exterior columns to aid in resisting part of the overturning moment resulting from lateral loads [4]. The jacking increases the shear

Fig. 29.2 Reinforcement of a dormitory building at the University of California, Berkeley using infill shear trusses (photo under license CC SA 1.0)



capacity and the ductility. In Fig. 29.6, the original unmodified column (left) is strengthened (right) with a jacket of steel plates welded into a single cylinder. The space between the jacket and the column is then filled with concrete, a process called grouting. Moreover, recently, carbon fiber reinforced polymer (Sect. 29.4.4) has been extensively used for increasing the strength and ductility of beams (Fig. 29.19), columns (Fig. 29.8), and floor decks (Fig. 29.20).

Figure 29.9 shows typical load-displacement relationships of strengthened frames with various construction techniques. This graph is used to compare the strength and ductility performance among all strengthening techniques. By observing this figure, it is found that when adequate connections were provided, post-cast walls (infill walls) exhibit almost the same strength as monolithic wall. Steel framed braces cherish high strength and ductility. Figure 29.10 shows typical load-displacement relationships of columns reinforced with various techniques. It is

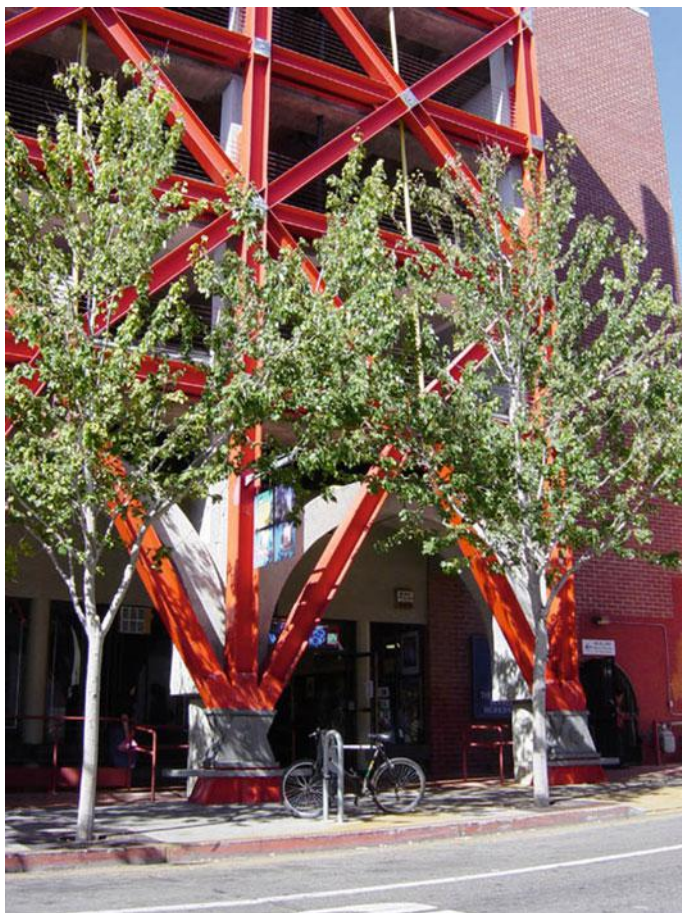


Fig. 29.3 Exterior general reinforcement of an existing garage structure with street level shops, located in Berkeley near the Hayward Fault (photo credit: Leonard G, under license CC SA 1.0)

noticed that concrete jacking can significantly increase the strength and ductility of columns, while steel jacket can provide a significant increase in strength but a decrease in ductility.

The adoption of improved construction materials that show high ductility and ultimate strength can effectively enhance the seismic performance. In the maintenance phase, the first and most economic measure is usually to tune the structure's stiffness or mass to reduce the excessive vibrations due to dynamic loading during normal service, such as adding a column or reinforcing structural members, changing the stiffness distribution of the structure, or changing the structural deck material into the one with a higher strength and/or lower weight, etc. The



Fig. 29.4 The San Francisco-Oakland Bay Bridge deck is reinforced by installing additional diagonals under the deck (photo under license CC SA 1.0)

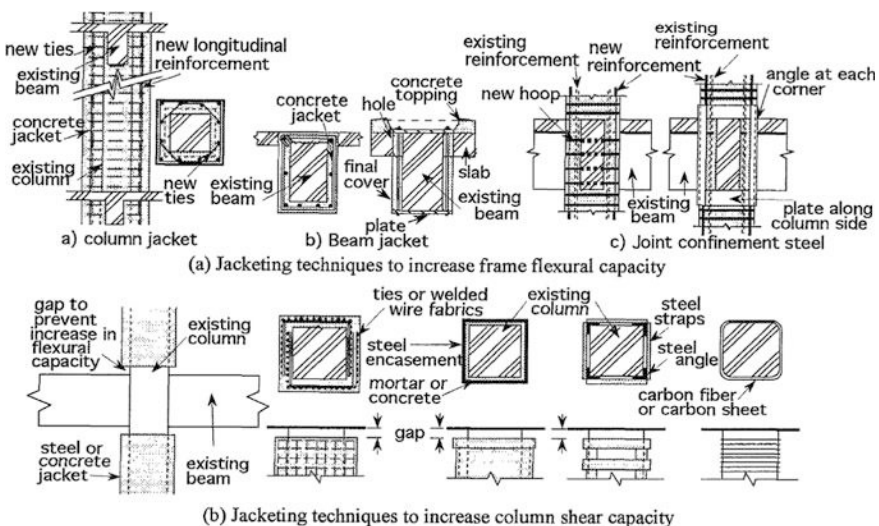


Fig. 29.5 Jacking of structural members [2]



Fig. 29.6 An example of jacketed and grouted column (*right*), compare to the unmodified column (*left*) (photo under license CC SA 1.0)

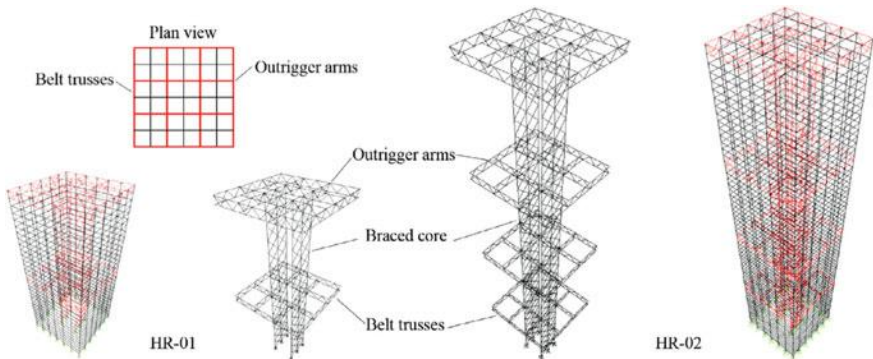
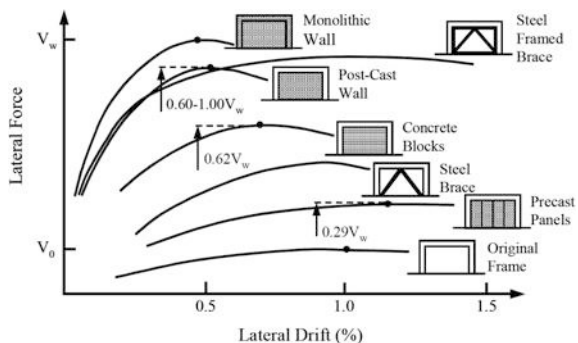


Fig. 29.7 Schematic illustration of a high rise building design with concentrically-braced-frame-core and outriggers/belt trusses to limit the inter-story drift and second order effects [5]



Fig. 29.8 Reinforcement of columns using carbon fiber reinforced polymer (CFRP) to increase their seismic capacity

Fig. 29.9 Typical load-displacement relationship of framed structures strengthened by various structural walls and bracings [2]



retrofitting of existing structures to resist lateral force due to earthquakes and wind and to increase the load bearing capacity is widely adopted in civil engineering practice, which will be introduced in Sect. 29.4. In addition, dampers, base isolators, dynamic absorbers and lock-up and shock transmission units, etc., are commercially available for mitigating dynamic response due to earthquake and other types of dynamic loading, as has been discussed in previous chapters.

It should be noted that an increase in structural stiffness by reinforcing the target structure may lead to a decrease in the structure's natural period. This is likely to increase spectral accelerations on the structure, causing an increase in member forces. This is somewhat of a paradox, since even if the structure's strength and stiffness are increased, this increase may be compromised by an increase in seismic loading. Furthermore, structural rehabilitation practice may also be limited by constraints in space, work-abilities, and cost etc. Therefore, it may be more

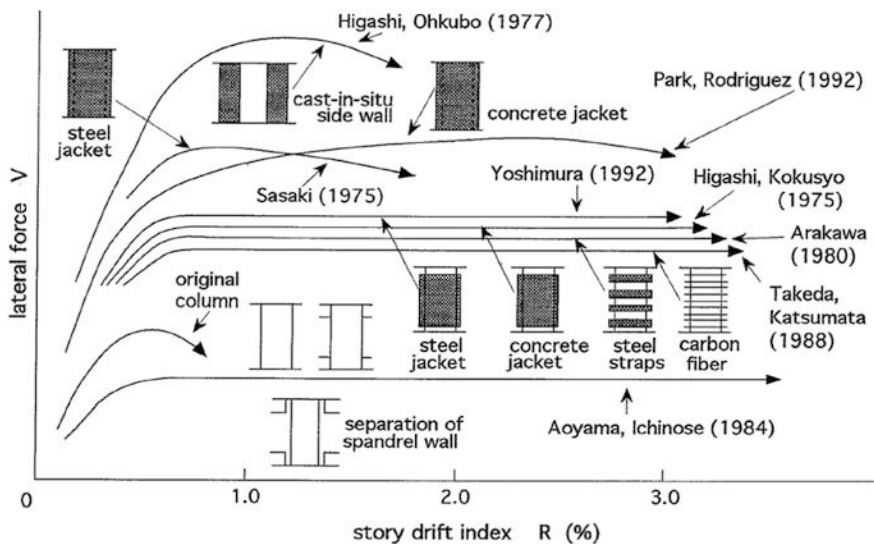


Fig. 29.10 Typical load-displacement relationships of columns reinforced with various techniques [2]

advisable to reduce the structural dynamic response rather than increasing the stiffness and strength. Furthermore, different measures may be taken during different stages of a structure in service.

29.4 Reinforcement of Structural Members

The current section introduces a few widely used techniques to reinforce structural members. For more details, readers may read references cited in the text.

29.4.1 Local Joint Reinforcement for Tubular Structures

Tubular structures are mainly fabricated from tubular members by welding, forming the so-called tubular joints, which are critical structural components playing a key role in transferring loads in a tubular structure [6]. During the fabrication of tubular structures, several methods are available to increase the strength of tubular joints, such as joint can, doubler plate, ring, and rack/rib. However, only a few methods can be adopted for both fabrication and operation phase, such as collar plate (Fig. 29.11) and fiber-reinforced-polymer (FRP) reinforcement (Fig. 29.12).

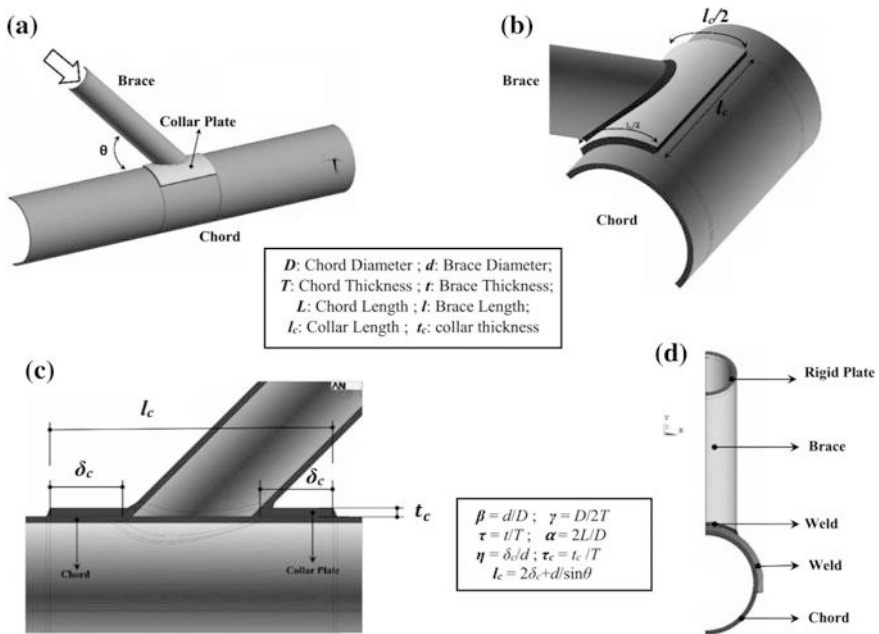


Fig. 29.11 Use of collar plates for reinforcement [7]



Fig. 29.12 Reparation of aluminum truss members using FRP (courtesy of Federal Highway Administration)

29.4.2 Sticking Steel Reinforcement

Sticking steel reinforcement is used to retrofit structures through sticking steel plates to the structural members for both retrofitting and reparation purposes. For example, pasting a steel plate in the tensile region of a concrete beam can efficiently improve the tensile and flexural strength of the beam. Sticking a steel plate to a corroded part of the structural steel members is a widely used method to repair the structural members for both offshore and onshore structures. Pasting a steel plate to the web of a beam can significantly increase the buckling strength of the beam.

Sticking steel reinforcement has appealing advantages, such as short construction period, little or no downtime due to the fast hardening of adhesive, convenient process without open flame, requiring little space and seldom increasing the section dimension and the weight of reinforced members [8].

29.4.3 Adding Members, Enlarging Cross Sections and Shortening Spans

Adding members, enlarging cross sections of members and shortening beam spans can all significantly increase the stiffness of reinforced structures and structural members, leading to a decrease in deformation and stress. The former two measures are also sometimes used to increase beam spans with less pillar supports, so that a better space flexibility can be achieved. However, those measures can also increase the seismic loading due to the increased stiffness.

Adding members includes additions of lateral supports, welding beam(s) to decks or providing extra bridging, additional beam(s) running in parallel to existing beams (essentially to decrease the deck span as shown in Fig. 29.13), etc.

Enlarging cross sections of members can be an effective method to increase the load bearing capacity for both steel and concrete structures. For example, to prevent the buckling due to weak axis bending and axial force of an I-cross section beam, two plates can be welded to the original I section as shown in Fig. 29.14, forming a closed cross section beam. Figure 29.15 shows reinforcements welded to the original beam to increase the cross section area and section modulus, so that the stress on the beam cross section due to both axial and bending loads can be mitigated. Moreover, the material of reinforcement can be different from that of the original structural members. Figure 29.13 shows steel beams are added underneath the original concrete beams. Sections 29.4.4 and 29.4.6 will introduce utilizations of fiber-reinforced-polymer material to reinforce original structural members made of concrete, steel, masonry or timber.

If a beam cross section is limited because of architectural or other considerations, it may happen that the concrete cannot develop the compression force required to resist the bending moment. Steel reinforcement can then be added in the compression zone, resulting in a so-called doubly reinforced beam with both

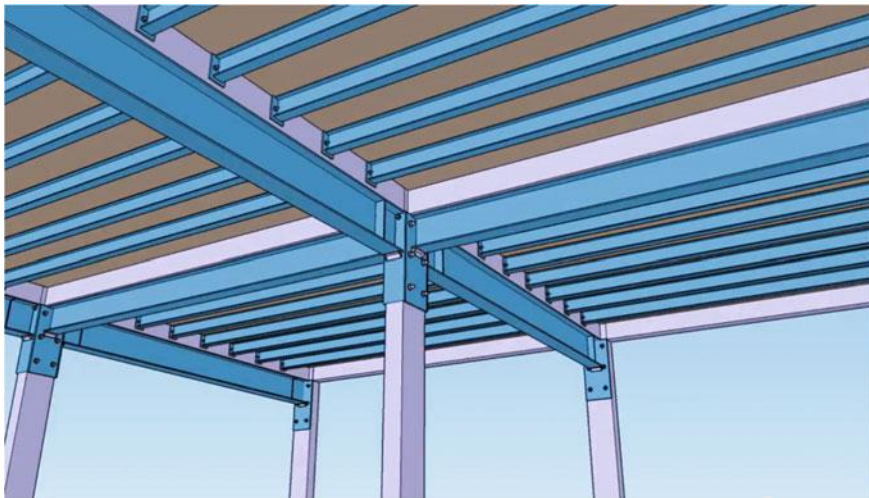
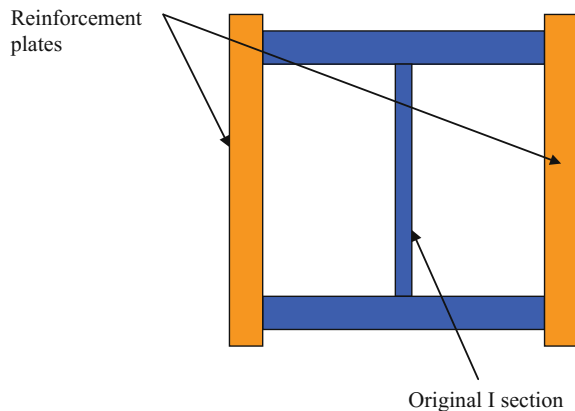


Fig. 29.13 Steel beams running in parallel to existing beams (image courtesy of Antonio Ortiz) [9]

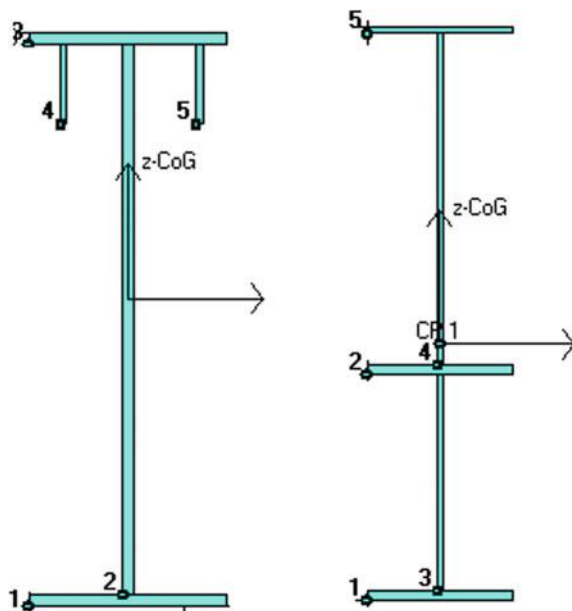
Fig. 29.14 Reinforcements with I section boxed-in (in practice, the welding can only be performed at the outside of the box) [10]



compression and tension reinforcement. This method is also adopted to improve serviceability and long term deflections, and to provide support for stirrups throughout reinforced concrete beams.

Shortening span can also be effective to significantly decrease the bending moment and associated stresses. In engineering practice, this can be realized by adding columns, girders, diagonal braces (not knee-braces) or additional walls on existing structures. Depending on how significantly the span is decreased, those measures can sometimes dramatically increase the structural stiffness and decrease the natural period of the structure. For example, by performing a modal analysis of a ship deck with various middle beam span distance, Jia and Ulfvarson [11] studied the natural frequency of a ship deck. By modeling the middle beam span (supported

Fig. 29.15 Reinforcements (parts 4 and 5 for both figures) welded to the original beam to increase the cross section area and section modulus



by pillars) distance with fully supported condition, 9.6 m distance case, and no pillar supports case, the natural frequencies exhibiting global bending vibration mode of the deck are 11.66, 10.6, and 3.4 Hz, respectively. This indicates a high sensitivity of natural frequency to the middle beam span. As previously mentioned, for land-based structures, a significant increase in structures' natural frequency can potentially lead to a significant increase in seismic loading.

29.4.4 Retrofitting Using Fiber-Reinforced-Polymer (FRP)

Fiber-reinforced-polymer (FRP) utilizes composite material consisting of polymeric resin reinforced with high strength fibers (carbon fibers, glass fibers, or aramid fibers) as shown in Fig. 29.16. It can be used to reinforce both steel and concrete structural members (with reinforcing concrete structure being more usual). Using FRP to retrofit structural members may not significantly alter the stiffness and dynamic properties of reinforced structures. However, it can significantly increase the deformation capacity of an infrastructure, and can increase its load capacity to certain extent. This technique is most appropriate for the retrofitting of structures with slightly insufficient seismic resistance. For structures with large seismic deficiencies, a combination of conventional and FRP strengthening techniques may be an effective retrofitting solution. FRP is available in forms of laminates plates (thin unidirectional strips with thickness in the order of 1 mm and made by pultrusion), sheet (fabrics), and bars.

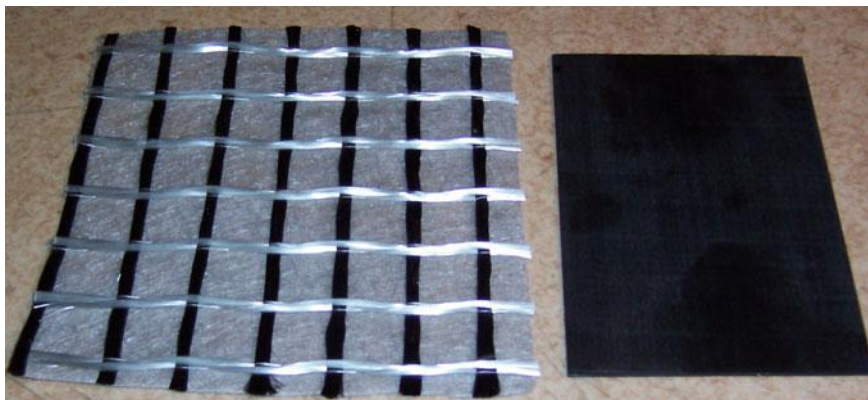


Fig. 29.16 Fiber-reinforced-polymer (FRP) with the arrangement of fibers along two perpendicular directions (*left*) and a plate-shaped FRP element (*right*)

FRP composites using glass fibers and carbon fibers are usually denoted as glass-fiber-reinforced-polymer (GFRP) and carbon fiber reinforced polymer (CFRP), respectively. Glass fibers are used in structural applications requiring medium high performance but requiring relatively low elastic modulus (70–80 GPa for E-glass). Moreover, glass fibers are prone to creep and have relatively low fatigue strength. On the other hand, carbon fibers cherish high modulus of elasticity and strength (much higher than steel). They have an intrinsically brittle failure behavior with a relatively low energy absorption capacity. Nevertheless, their failure strength is higher than their glass or aramid counterparts. Carbon fibers are less sensitive to creep rupture and fatigue and show a slight reduction in the long term tensile strength. FRP composites using aramid fibers are organic fibers made of aromatic polyamides in an extremely orientated form, which are denoted as AFRP. Their modulus of elasticity and tensile strength are in between that of the glass and carbon fibers. Their compressive strength is typically around 1/8 of their tensile strength. Due to the anisotropy of the fiber structure, compression loads can induce a localized yielding of fibers resulting in fiber instability and formation of kinks. Aramid fibers may degrade after extensive exposure to sunlight, losing up to 50 % of their tensile strength. In addition, they may be sensitive to moisture. The creep behavior of aramid fibers is similar to that of glass fibers, even though their failure strength and fatigue behavior are higher than that of GFRP [12]. Figure 29.17 shows uniaxial tension stress–strain diagrams of FRPs and mild steel.

Along with fibers, FRP composites also comprise a matrix to protect the fibers from negative impacts from the environment and to transfer forces between the fibers and the matrix. The thermosetting resins are most exclusive in the application of structural engineering. Of the thermosets, vinylester and epoxy are the most common matrices, with epoxy being more widely utilized because it has a good performance regarding strength, bond, creep properties, and chemical resistance, even though it is more expensive than vinylester.

Fig. 29.17 Comparisons of uniaxial tension stress-strain diagrams between different unidirectional FRPs and mild steel under short term monotonic loading [3]

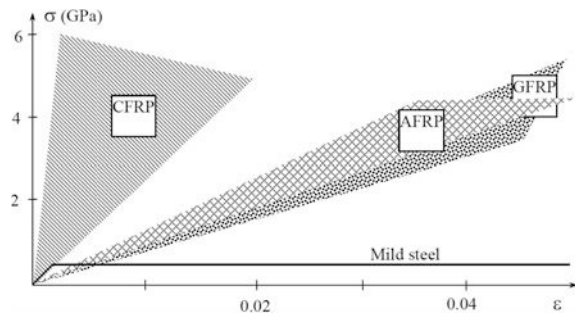


Figure 29.18 shows stress–strain relationships and strength for fibers, matrix and FRP. It can be observed that, at strain levels above the yielding strain of the mild steel, fibers generally cherish high tensile strength and stiffness, while their strain at failure is lower than that of the matrix. This design intentionally makes the fibers fail prior to the occurrence of cracks on matrix so that the integrity and stiffness of the FRP (fiber-matrix system) can be controlled by fibers rather than the matrix. The resulting FRP has lower stiffness than the fibers but fails at the same strain level as the fibers, which is shown in Fig. 29.18. However, this also indicates that the ductility for FRP at high stress levels is very limited and should be treated with care. Table 29.1 shows a comparison of mechanical properties among fibers, matrix materials and steel.

In addition to the material properties of the fibers and matrix, the amount of fibers used, fiber orientations as well as stack sequence are important factors influencing the bearing capacity and failure mechanisms and failure modes of FRPs.

Among all types of FRPs, CFRP has been most extensively used in repairing and strengthening of structures due to their higher strength than GFRP. Apart from the stiffness and strength of CFRP, the bonding between the CFRP and reinforced structural members is essential and in many cases governs the reinforcement design [13]. Significant research efforts have been placed on the issues related to bond strength, bond length, and fatigue performance of CFRP reinforced structures.

Fig. 29.18 A schematic illustration of stress–strain relationships and strength for fibers, matrix and FRP

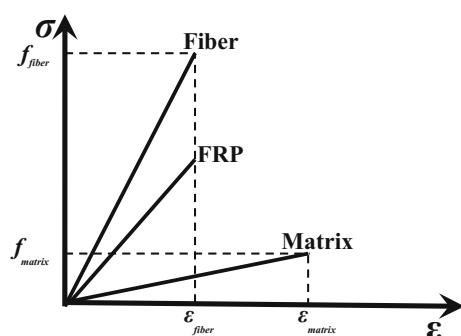


Table 29.1 Mechanical properties of fibers, matrix materials and steel

	Elastic modulus (GPa)	Tensile strength (MPa)	Strain at failure (%)	Coefficient of thermal expansion ($10^{-6} \text{ }^{\circ}\text{C}^{-1}$)	Density (g/cm ³)
E-glass	70–80	2000–3500	3.5–4.5	5.0 to 5.4	2.5–2.6
S-glass	85–90	3500–4800	4.5–5.5	1.6 to 2.9	2.46–2.49
Carbon	240–760	2400–5100	0.5–1.8	−1.45 to −0.6	1.75–1.90
Aramid	62–180	3600–3800	1.9–5.5	−2	1.44–1.47
Polymeric matrix	2.7–3.6	40–82	1.4–5.2	30–54	1.10–1.25
Steel	205–210	250–800	15–30	10.4	7.8

The advantages of utilizing FRPs in engineering over conventional materials can be summarized as: high strength to weight ratio; good resistance to corrosion and fatigue [14]; short curing time; ease of installation (similar to putting up wall papers); and great dimensional and thermal stability [15]; stiffness that can be tailored to design requirements; large deformation capacity; and practically unlimited availability in sizes and geometry and dimensions; high impact resistance (experimental studies show that beams strengthened with CFRP laminates performed well under impact loading, although they could not provide the same energy absorption as the beams strengthened with steel plates [16]).

On the other hand, using FRPs for strengthening engineering structures also has a few important drawbacks: it normally must be used in the linear-elastic range (low ductility) without significant yielding or plastic deformation even though it can fail at large strain levels (Fig. 29.18), in contrast to the mild steel which can develop significant plasticity before rupture (Fig. 29.17). Moreover, the cost for FRP materials on a weight basis is several times higher than that for steel. Moreover, some FRP materials, e.g. carbon and aramid, have incompatible thermal expansion coefficients with concrete. Finally, their exposure to high temperatures, such as the case of fire, may cause premature degradation and collapse (some epoxy resins start softening at about 45–70 °C). Hence FRP materials should not be blindly taken as a replacement of steel (or other materials) in structural intervention applications [3].

When a concrete structure is reinforced with FRP as shown in Figs. 29.19 and 29.20, its ultimate strength and ductility increase, leading to a decrease in both the extending and width of the concrete.

The use of FRP laminate plates and fabric for the reparation and strengthening of reinforced concrete structures is well established, and various relevant design guidelines are available in different countries, such as ACI 440-02 [17] and European Fib Bulletin 14 [3]. In addition, FRP bars and tendons are also widely used to strengthen existing structural members (constructed with concrete, wood, stone, or masonry) subject to bending moments and shear force.



Fig. 29.19 Laboratory test of beams reinforced by CFRP



Fig. 29.20 Floor deck reinforced by CFRP

Many metal structures are structurally deficient due to various reasons. For example, more than 52 % of the 72,524 structurally deficient bridges listed in American National Bridge Inventory (NBI) for 2007 by the Federal Highway Administration (FHWA) have steel superstructures (FHWA 2007). However, the application of FRP to metal structures has been limited. Figure 29.12 shows an

example of utilizing FRP to repair an aluminum sign truss bridge. During inspection it was found that the welds connecting the diagonals to the chord had cracked over a significant portion of their length, and FRP was then used for reparation. The application included member cleaning and application of the FRP material using strips wrapped around the members. These types of repairs, initially thought to be just temporary for 1 year or less, are now being considered as a permanent repair solution [18].

CFRP itself does not creep, the creep of GFRP is negligible, but the creep of AFRP cannot be neglected. Therefore, creep is seldom a controlling factor in the dimensioning of FRP-strengthened concrete structures, unless the structures are newly-built, in which case the concrete can still be expected to develop substantial creep deformations. Glass fibers exhibit premature tensile rupture under sustained stress, a phenomenon called stress rupture. Hence the tensile strength of GFRP drops to very low values (as low as 20 %) when the material carries permanent tension [3].

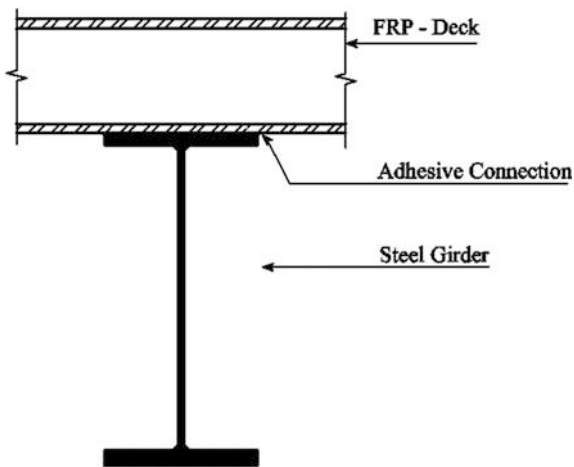
In order to avoid potential galvanic corrosion of steel reinforcement, CFRP should not come in direct contact with steel. Furthermore, in case CFRPs are subject to lightning striking, they should be protected using for example metal grids, as this is a well proven technique in the aircraft industry that lightning will not strike an object placed in a grounded metal cage [3].

The wide range in mechanical properties of FRP materials means that one traditional method used for modeling steel structures can hardly be generalized to predict load bearing capacities of FRP or FRP reinforced structures, since these methods normally are suited only for an extremely brittle case or for ductile cases. For any case in between, such as a quasi-brittle case, however, models that include fracture softening may be involved. Moreover, a change in the temperature can cause both a dimensional change and a change in its creep and relaxation characteristics. Consequently, these have an important influence on the mechanical and structural behavior of FRP and FRP reinforced structures, which are also important for the design and construction applications.

Figure 29.21 shows a design using GFRP deck to replace the original deteriorated steel deck of a pedestrian bridge, which can significantly reduce the weight of the deck. In the meantime, because the elastic modulus of GFRP is much lower than that of the steel as shown in Fig. 29.17, it is convenient to dimension the FRP deck to have a higher natural period so that seismic spectral acceleration of the bridge can be decreased compared with that of the original steel deck bridge. However, this often results in a soft deck design. Therefore, the serviceability limit state must also be fully accounted for in the design to limit the deflection of the deck.

For a more detailed elaboration of retrofitting using FRPs, Ref. [3] is recommended to read.

Fig. 29.21 The original concrete deck is replaced by a FRP deck, the deck is connected with steel girder by adhesive connections



29.4.5 Load Sequence Effects Due to the Reinforcement

When the reinforcements or structural members are installed without pre-stressing them to the original structure, the reinforcements or the members should be considered to only carry future changed (added or deducted) loads together with the existing structural members.

In order to practically account for the load sequence effects, Jia [10] presented a method for specifying the consequent analysis phases that depend on factors such as whether the loads are acting at the time the structure is altered, whether only the final state of the structure is of analysis interest or intermediate states are as well, etc. In general, the occurrence of stiffness changes should be considered as the “boundary” between analysis phases. In each phase, the pertinent loads and support conditions should be applied on the structure model corresponding to the condition in that phase. In addition, two types of loads should be applied with care: (1) the environmental loads varying with time, especially for the ocean wave and wind loads, which always exist and vary during the entire lifetime of the offshore installations: they are recommended to be applied in the final phase/time of the analysis. (2) The operating loads (e.g. drilling machinery loads, moving crane loads) moved in different locations within structures in different analysis phase: they should be applied in the way that the relevant loads being applied in the current analysis phase should first include the operating loads with the same location and magnitude but in the opposite direction (negative sign) as the previous analysis phase; by doing this, the operating load effects from the previous analysis phase on the current analysis phase are “cancelled.” Then the new operating loads corresponding to the current analysis phase can be applied.

By performing a series of linear-elastic analyses for an offshore topside frame structure shown in Fig. 29.22, which is subjected to various permanent and environmental loads, and both the support condition changes and the reinforcements are

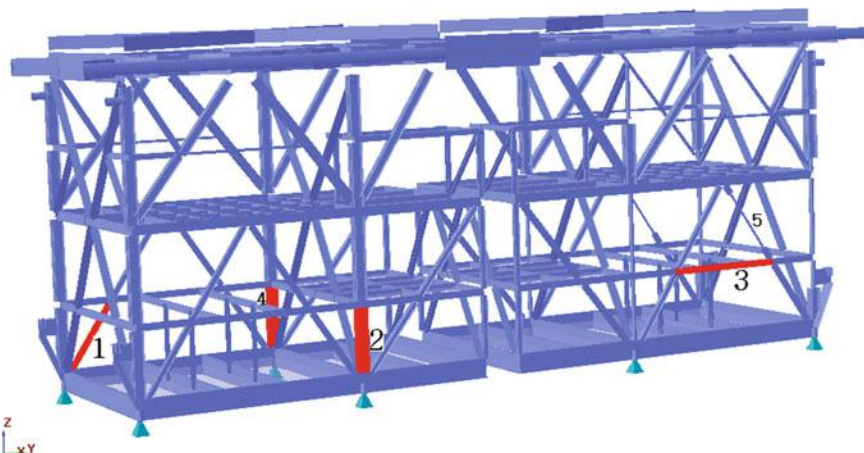


Fig. 29.22 A topside frame structure under investigation (courtesy of Aker Solutions)

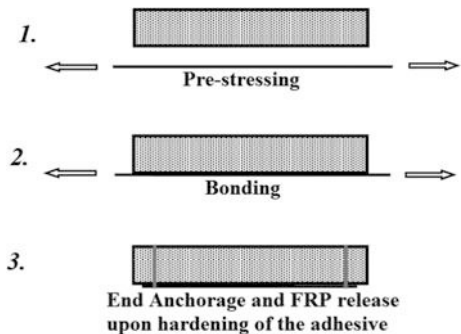
applied at different stages of the structure's service life, Jia [10] investigated the ultimate strength of the frame structure influenced by the sensitivities of the support condition changes and the reinforcements installations. It is found that the changes in support conditions and the added stiffness from the reinforcements only slightly change the global stiffness of the structure, while they do influence the local stiffness and reaction forces on reinforced members and members close to the supports and reinforced members. The load and support condition sequence effects may have a significant influence on the utilizations of those members. For this particular structure, the load sequence effects are more significant from the change of the support conditions than that from the installation of the reinforcements.

29.4.6 External Pre-stressing Using FRP

Most common deficiencies, i.e. failure, found in ageing reinforced concrete columns are due to lack of confinement, insufficient lateral reinforcement and inadequate reinforcement splicing. It may then be advantageous to apply external pre-stressing. Both laboratory and analytical research [19, 20] show that pre-stressing can significantly increase the efficiency of FRP strengthening technique.

Various methods have been developed to pre-stress the FRP composites under real life conditions [21]. The traditional reinforcement method such as steel or concrete jacketing, with an example shown in Fig. 29.6, may significantly increase the stiffness of a structure, thus increasing the seismic loading on the structure. Therefore, the use of pre-stressed FRP reinforcement by bonding the external FRP reinforcement (laminates or tendons) onto the concrete surface in a pre-stressed state, represents a significant contribution to the advancement of the FRP

Fig. 29.23 Schematic illustrations of strengthening with external pre-stressing FRP strips [3]



strengthening technique. Several methods have been developed to pre-stress the FRP composites under real life conditions. The main advantage of pre-stressing is that the same amount of strengthening can be achieved with smaller areas of pre-stressed FRP compared with unstressed FRPs. And, in case FRP strips are used, if adequate anchorage is provided, pre-stressing may increase the ultimate resisting moment by avoiding failure modes associated with peeling-off, both at cracks and at the ends of the strips. Figure 29.23 schematically illustrates basic procedures to strengthening structures with external pre-stressing FRP strips.

Two major methods of pre-stressing the external strengthening are available: indirect or direct pre-stressing. Indirect pre-stressing applies pre-stressing to the FRP strip or sheet by cambering the flexural member using hydraulic jacks to induce negative curvature [22] before the strengthening application. The direct pre-stressing applies the tension directly on the FRP strip or sheet either by jacking against an external reaction frame [19, 20] or by reacting on the beam itself [23, 24].

The concept of pre-stressing FRP fabrics applications is a relatively recent development. The major technological challenge of pre-stressing FRP fabrics consists in seizing the fabric itself. This is typically solved by pre-stressing and wrapping fabrics several times around a resin-impregnated steel rod, or restraining it with rounded brackets. The fabric can also be bonded to the bottom of the beam in order to gain the effects of a full interaction between the beam itself and the external strengthening. Several layers can be subsequently applied with the same method, with a partial loss of the pre-stressing force in the layers previously applied, as if they are bonded—no additional tension can be applied to them [25]. Similarly, an important problem with external FRP tendons is the anchorage. Due to its anisotropy as a material, perpendicular forces might crush the tendon, which is a problem for some wedge systems.

Similar to pre-stressing technique, post-tensioning using tendons eccentrically placed at the tension side of beam's cross section is widely used to reinforce beam members so that both the stress and deflection of the beams can be decreased. The pre-stressed concrete structures as extensively used for large span beams use a similar mechanism while the pre-stressing steel bars are embedded into the concrete as an integrated part of the beam's cross section.

References

1. Flesch R (2012) Short information on recent initiatives in earthquake engineering—assessment of seismic risk of important civil structures. *Arsenal Res*, Vienna
2. Sugano S (1996) State-of-the-art in techniques for rehabilitation of buildings. In: Proceedings of 11th world conference on earthquake engineering, Elsevier Science Ltd.
3. FIB Bulletin 14 (2001) Externally bonded FRP reinforcement for RC structures, task group 9.3. International Federation of Structural Concrete (FIB)
4. Kareem A, Kijewski T, Tamura Y (1999) Mitigation of motions of tall buildings with specific examples of recent applications, *Perception*, 2(3), Techno-Press, South Korea, pp 1–48
5. Brunesi E, Nascimbene R, Casagrande L (2016) Seismic analysis of high-rise mega-braced frame-core buildings. *Eng Struct* 115:1–17
6. Qu H, Huo J, Xu C, Fu F (2014) Numerical studies on dynamic behavior of tubular T-joint subjected to impact loading. *Int J Impact Eng* 67:12–26
7. Nassiraei H, Lotfollahi-Yaghin MA, Ahmadi H (2016) Static strength of axially loaded offshore tubular T/Y-joints reinforced with collar plates. *J Constr Steel Res* (article in press)
8. Xilin Lu (2005) Retrofitting design of building structures. CRC Press, Boca Raton
9. <https://www.youtube/Xoh8N70tvbo>
10. Jia J (2011) The load sequence effects on structures' ultimate limit strength evaluation. *J Constr Steel Res* 67(2):255–260
11. Jia J, Ulfvarson A (2005) A systematic approach toward the structural behavior of a lightweight deck-side shell system. *J Thin Walled Struct* 43(1):83–105
12. An The Vinh (2009) Flexural Strengthening of reinforced concrete beams with prestressed FRP laminates. Master Thesis, University of Padova
13. Zhou T, Li Z, Jia J (2001) The study and design method of FRP in the reinforcement of structures. In: Proceedings of FRP composites in civil engineering, Hong Kong
14. Busel JP, Lockwood JD (eds) (2000) Product selection guide: FRP composite products for bridge applications, 1st edn. The Market Development Alliance of the Composites Industry, New York
15. Jia J, Lu L, Jia Z (2001) The application study in the reinforcement of CFRP. Building technique development (in Chinese)
16. Erki MA, Meier U (1999) Impact loading of concrete beams externally strengthened with CFRP laminates. *ASCE J Compos Constr* 3(3):117–124
17. ACI Committee 440 (2002) Guide to the design and construction of externally bonded FRP systems for strengthening concrete structures, ACI 440.2R-02. American Concrete Institute, Farmington Hills, MI
18. Federal Highway Administration (2015) Guidelines for the installation, inspection, maintenance and repair of structural supports for highway signs, luminaries, and traffic signals, Federal Highway Administration, Washington
19. Triantafillou TC, Deskovic N, Deuring M (1992) Strengthening of concrete structures with prestressed fiber reinforced plastic sheets. *ACI Struct J* 89(3):235–244
20. Deuring M (1993) Verstärken von Stahlbeton mit gespannten Faserverbundwerkstoffen (Strengthening of RC with prestressed fiber reinforced plastic sheets). EMAP research report 224, Dübendorf, Switzerland (in German)
21. Luke PS, Leeming MB, Skwarski AJ (1998) ROBUST results for carbon fibre. *Concr Eng Int* 2(2):19–21
22. Saadtmanesh H, Ehsani MR (1991) RC beams strengthened with GFRP plates. I: experimental study. *J Struct Eng ASCE* 117(11):3417–3433

23. Andrä HP, Maier M (1999) Poststrengthening of RC structures by pre-stressed externally bonded CFRP strips. In: Forde MC (ed) Proceedings of structural faults and repair, London
24. Wight RG, Green MF, Erki MA (2001) Prestressed FRP sheets for post-strengthening reinforced concrete beams. *J Compos Constr* 5:215–220
25. Monti G, Liotta MA (2007) Pretension of externally bonded FRP fabrics for flexural reinforcement of RC beams: methods and design equations. In: Asia-Pacific conference on FRP in structures, international institute for FRP in construction

Appendix

Unit conversions

Quantity	Unit	\times	Unit	\times	Unit
Length	in.	25.4	mm	0.03937	in
	ft	0.3048	m	3.281	ft
Area	in. ²	645.16	mm ²	1550×10^{-3}	in. ²
	ft ²	0.0929	m ²	10.76	ft ²
	ft ²	2.3×10^{-5}	Acre	43,500	ft ²
Volume	yard ³	21.7	Bushels	1.244	ft ³
	in. ³	1.639×10^{-4}	mm ³	6.102×10^{-5}	in. ³
Mass	slug	14.594	kg	2.205	lb _m
	slug	32.2	lb _m	0.454	kg
Pressure	lb/in. ²	6.895	kPa	0.1450	lb/in. ²
	lb/ft ²	0.0479	kPa	20.89	lb/ft ²
	psi	6.895	kPa	0.1450	psi
	ksi	6.895	MPa	0.1450	ksi
	psi	6.895×10^{-6}	GPa	1.450×10^{-5}	psi
	ksi	6.895×10^{-3}	GPa	145	ksi
	lb _m /ft ³	16.02	kg/m ³	0.0624	lb _m /ft ³
Force	lb _f	4.448	N	0.2248	lb _f
Moment	lb in.	0.1130	N m	8.851	lb in.
	lb ft	1.356	N m	0.7376	lb ft
Energy	in. lb	0.113	Joule	8.85	in. lb
	kW h	2655.18	klbs ft	3.766×10^{-4}	kW h
Velocity	m/s	2.237	mph	0.447	m/s
	mph	1.467	ft/s	0.682	mph
	mph	17.6	in./s	5.68×10^{-2}	mph
	knot	0.514	m/s	1.944	knot
Power	W	0.73755	ft lb/s	1.356	W
	W	1.341×10^{-3}	hp	745.7	W

Acceleration of gravity (1 g) = 9.81 m/s² = 32.2 ft/s² (at latitude 45°)

Index

A

Acceleration sensitive, 479, 787–789
Acceleration sensitive region, 479
Accelerograph, 54, 250
Accidental limit state (ALS), 439, 450, 498, 501, 546
Accidental torsion, 603, 607
Active aerodynamic appendage, 810
Active gyro stabilizers (AGS), 810
Active mass driver, 810
Active pulse control system, 810
Active tendon control systems, 810
Active variable stiffness systems (AVS), 810
Actuators, 781, 794, 809
Adaptive pushover analysis, 490
Added damping and stiffness (ADAS) dampers, 681
Added mass coefficient, 361, 366, 368, 371
Adding members, 822
Aleatory uncertainties, 316
Allowable stress design (ASD), 342, 436, 437, 439, 441, 442
Amplification, 99, 103, 151, 175, 180, 189, 192, 194, 217, 232, 238, 270, 494, 593, 722, 788
Amplification factor, 191, 235, 243, 277, 641
Anisotropy, 825, 832
Anti-symmetric mode, 560
Apparent velocity, 302
Aramid fibers, 824, 825
Architecture component, 787
Arias Intensity, 145, 155, 156, 423, 424
Aromatic polyamides, 825
Attenuation models, 142, 148, 151, 152, 279, 331, 347, 349, 460
Attenuation relations, 142, 312
Attenuation relationship, 142, 147, 148, 151, 162, 293, 321, 322, 338

B

Ball, 119, 722, 723, 727, 728
Base-anchorage failure, 555
Base isolation, 433, 436, 467, 596, 633, 653, 701, 703, 705, 716, 720, 731, 732, 756, 807
Basic property test, 731
Beam-column connection, 621, 626, 628, 660
Becker penetration test (BPT), 420
Bedrock, 170, 171, 175, 176, 184, 194, 245, 277, 282, 283, 288, 499
Behavior factor, 242, 243, 276, 435, 553
Behavior state, 355
Body wave magnitude, 129, 130, 132, 134
Body waves, 107, 108, 113, 118, 190, 192
Braced frames, 625, 626, 660, 680, 694, 695 chevron braces, 611, 676, 682 diagrid/triangulated bracing, 616 K-braces, 611 X-braces, 611, 614, 615
Bracketed duration, 153–158
Broad-banded, 209, 218
Buckling-restrained brace frame (BRBF), 619, 620, 687
Buoyance, 366, 369
Business interruptions, 13

C

Capacity reserve, 433, 436, 441, 694
Capacity-spectrum method, 489
Caughey damping, 638, 639
Central safety factor, 458
Channel wave, 117
Characteristic ground frequency, 216, 756
Characteristic load, 443
Characteristic material strength, 250, 539
Characteristic values, 443–445
Clock rate, 588
Code based design, 173, 282

- Coherence function, 297–301, 304
 Coherency, 296, 300–302, 304, 307
 Collar plate, 820
 Combined cumulative indices, 429
 Combined lateral load pattern, 492
 Communication system, 796, 797
 Complementary solution, 93
 Complete quadratic combination (CQC), 481
 Compliant structure, 77, 78, 81, 96
 - articulated towers, 78
 - buoyant towers, 78, 79
 - compliant tower, 78
 - flexible towers, 78
 - guyed towers, 78
 - hybrid compliant platform, 78
 Compressional wave. *See* P-wave
 Computation cost, 204, 457, 473
 Computation precision, 587, 591, 592
 Concentrically braced frame, 625
 CONDEEP, 76
 Conditional mean spectrum (CMS), 287, 331, 346
 Cone penetration test (CPT), 420
 Connection system, 796
 Constant acceleration, 187, 225, 232, 233, 236, 551
 Constant displacement, 232, 233, 271, 272
 Contents and furniture damage, 413
 Continental drift, 20, 21, 23, 43
 Convective/sloshing liquid, 560, 577
 Convective/sloshing mass, 563, 568, 570, 571, 577
 Conventional RC coupling beam, 685
 Convergent boundary, 40, 44
 - continent-continent collision zone, 44, 46, 48
 - ocean-oceanic subduction zone, 44, 46
 - oceanic-continent subduction zone, 44, 46
 Core processor, 588
 Cornell's reliability index, 451, 455
 Corner frequency, 159, 208, 210
 Correlation coefficient, 318, 346, 347, 449, 452, 481
 Corrosion, 62, 67, 118, 444, 641, 674, 798, 827, 829
 CPU, 457, 588–590
 CQC. *See* Complete quadratic combination
 Creep, 705, 825, 829
 Critical damping, 92, 220, 228, 235, 277, 563, 636, 651
 Critical Euler buckling load, 710
 Critical excitation analysis, 472
 Cross-covariance, 297, 298, 300
 Cross-modal coefficient, 481
 Cross-spectra density, 297, 298
 Crust, 12, 18, 21, 33, 35, 36, 43, 44, 46, 57, 117
 Cryoseism, 33, 50
 Cumulative distribution function (CDF), 319, 322, 446
 Cutoff frequency, 208, 210
 Cyclic effects, 152, 494
 Cyclic shear, 158, 195, 417, 420, 421
 Cylindrical friction damper, 669, 670
- D**
- Damage control, 174, 428, 462, 790
 Damage detection and modeling system, 796
 Damage indices, 428, 467
 Damping apparatus, 436, 494, 633, 646, 694, 695, 807
 Damping ratio, 92, 182, 216, 228, 235, 237, 247, 481, 636–638, 662, 663, 704, 707, 708, 713, 720, 747, 773
 Damping screen, 757, 763
 Data acquisition, 796, 797
 Data process system, 796
 Deaggregation, 246, 281, 332, 347, 351
 De-amplification, 176, 193, 536
 Deflection amplification factor, 242
 Deflection/deformation control, 436
 Deformability, 595, 611
 Deformation sensitive, 787, 788
 Degrees-of-freedom, 480, 510
 Design ground motions, 173, 315, 342
 Design resistance, 444
 Design spectrum, 137, 138, 231, 232, 236, 248, 250, 254, 267, 269, 272, 273, 282, 283, 323, 479, 484, 503, 514, 516, 703, 727
 Deterministic seismic hazard analysis, 312, 313, 315
 Diamond shape buckling, 555
 Differential settlement, 555
 Direct analysis approach, 182, 183
 Direct displacement-based design, 468
 Direct scaling, 283, 287
 Disaggregation. *See* deaggregation
 Discrete Wavelet Transform (DWT), 258
 Displacement-activated, 808
 Displacement-based cumulative indices, 429
 Displacement sensitive region, 479
 Divergent boundary, 40, 41
 Dog bone, 628
 Doubler plate, 820

- Drag coefficient, 362, 363, 371
Drag force, 362, 363, 366
Dragon-kings, 353
Drift, 250, 253, 468, 512, 622, 665, 788
Drone based structural inspections, 797
Ductile details, 436
Ductility design, 813
Ductility factor, 240, 242, 244, 245, 429, 435
Ductility-modified (inelastic) design spectrum, 239, 243, 484
Dynamic absorber, 436, 467, 494, 496, 559, 596, 633, 716, 741–745, 747, 748, 768, 770, 807, 819
Dynamic cancelation, 97
Dynamic pushover analysis. *See* Incremental dynamic analysis
Dynamic response mitigation, 436
Dynamic strength, 434, 540
- E**
- Earthquake forecast, 52, 59
Earthquake induced liquid motions, 555
Earthquake insurance, 793, 803
Earthquake prediction, 52, 56–59, 343
Eccentrically braced frame (EBF), 625, 626, 680
Effective horizontal stiffness, 709, 714
Effective shear strain, 195
Eigenfrequency, 87, 97, 485, 498, 501, 510, 562, 565, 594, 635, 660, 704, 711, 745, 771
Eigen-mode, 97, 170, 284, 306, 478, 479, 491, 493, 498, 501, 511, 528, 564, 594, 599, 605, 635, 636, 638, 704, 741, 743, 745
Eigenmode. *See* Eigen-mode
Eigenperiod, 175, 220, 245, 254, 284, 347, 350, 371, 481, 505, 528, 531, 540, 541, 596, 599, 711
Elastic limit slenderness, 619
Elastic rebound, 20–23, 57, 131
Elastic response spectrum, 218, 220, 243, 270, 272, 488, 495
Elastomeric bearing, 705–707, 711, 713, 715, 716, 720, 721, 728
Elasto-plastic, 665, 676
Elephant foot buckling, 555, 580
Elevated tank, 554, 559, 565, 575
Elevation control, 103, 104, 525, 594, 597, 598, 603
Emergency response, 356
Energy absorption, 243, 433, 435, 460, 595, 611, 633, 645, 825
Energy Dissipating Restraint (EDR), 669
Energy dissipation, 140, 276, 428, 433, 593, 631, 634, 636, 642, 646, 665, 675, 682, 683, 690, 705, 733, 772
Energy dissipation per cycle, 636, 650, 712, 725
Enlarging cross section, 822
Epicenter, 22, 29, 107, 121, 130, 158, 321, 397, 408, 720
Epistemic uncertainties, 316
Epoxy, 825, 827
Equivalent linear model, 195
Equivalent mechanical spring-damping-mass model, 563, 577, 579, 580
Equivalent viscous damping, 634, 635, 640, 645, 677
Extended source effects, 296
External damping devices, 54, 595, 629, 807
External pre-stressing, 831, 832
- F**
- Factor of safety, 438, 440, 443, 458
Fast Fourier Transformation (FFT), 214
Fatigue, 62, 90, 97, 100, 445, 537, 633, 643, 645, 680, 692, 707, 715, 753, 755, 825, 826
Fault geometry, 312, 318
Fault length, 132, 148, 314, 397
Fault rupture, 22, 24, 50, 51, 53, 107, 125, 131, 142–144, 151, 160, 169, 171, 176, 317, 322, 380, 476, 519
Faults
 dip-slip fault, 34, 396
 listric faults, 39
 normal faults, 34–36, 39
 oblique-slip fault, 35, 37, 40
 reverse faults, 36
 strike-slip (lateral) faults, 34, 37, 49, 396
Fiber-reinforced-polymer (FRP)
 carbon fiber reinforced polymer (CFRP), 815, 819, 825
 glass fiber reinforced polymer (GFRP), 825
Firm soil, 197
First-order-reliability-index, 453, 454
Flexural/bending vibrations, 595
Floating production, storage, and offloading facility (FPSO), 73, 74, 79
Focal depth, 29, 48, 107, 116, 129, 396, 424
Focal distance. *See* Hypocentral distance
Force based cumulative indices, 429
Force-displacement loop, 650, 659, 665, 680
Force reduction factor (FRF), 242
Foreshock, 24, 52, 57
Foundation damage, 9, 14, 413

- Foundation filter effects, 296
 Fourier amplitude spectrum, 185, 208–210, 212
 Fourier series, 195, 207, 208, 212
 Fourier spectrum, 159, 203, 207, 208, 212, 225, 254
 Fourier spectrum. *See* Fourier amplitude spectrum
 Fourier transform, 207, 208, 255, 258, 298
 Freeboard, 557, 560, 569, 573, 577
 Free-field motion, 183, 185, 581
 Friction damper, 651, 660, 664, 665, 667–669, 673–676, 678, 679, 684, 691
 Friction pendulum, 722, 723, 726
 Froude-Krylov excitation force, 362
 Full-probabilistic method, 457
 Fundamental variability, 444
- G**
 Galef's formula, 709
 Geometric nonlinearity, 79
 Geothermal energy, 18, 19, 30
 Gravity based platform, 77
 Gravity foundation, 81
 Green function, 382
 Ground motion intensity, 139, 142, 145, 268, 280, 312, 315, 321, 323, 342, 344, 346, 496
 Ground motion parameter, 145, 154, 227, 312, 315, 322, 329, 340, 347, 750
 Ground motion prediction equations (GMPEs).
See Attenuation relations
 Guided wave, 108, 117, 118
 Gumbel model, 326
 Gutenberg-Richter relationship, 318, 319, 328, 337
- H**
 Half-power bandwidth point, 636
 Hanging chain damper, 775, 776
 Hanging isolation, 596, 734, 807
 Hard growth, 370
 Hardness, 131, 712
 Hasofer-Lind safety index, 454, 455
 High-rise building, 463
 Homogenous zone model, 318
 Horizontal amplification factor, 188
 Horizontal shear wave propagation, 185
 Human engineered earthquakes, 24, 52
 Human induced earthquakes, 52
 Human perception, 632
 Hybrid control device, 810
- Hybrid control system. *See* Hybrid control device
 Hybrid method, 472
 Hydrostatic pressure, 417, 560, 566, 579
 Hypocenter, 107, 108, 143, 322
 Hypocentral depth. *See* Focal depth
 Hypocentral distance, 107, 126, 318, 322
 Hysteretic behavior, 152, 651, 665, 680, 681, 687, 690
 Hysteretic energy-based cumulative indices, 429
- I**
 Ice induced earthquakes, 19, 33
 Ice sheet, 33, 372, 373, 375
 Icing, 376
 Imamura-Iida magnitude scale, 393, 394
 Immersed tube, 66, 67
 Impact damper, 772–774
 Importance factor, 270, 436, 553, 569
 Improve structural irregularity, 813
 Impulsive force, 221
 Impulsive/rigid liquid, 560, 564, 565, 575, 577
 Impulsive/rigid mass, 563, 571, 572
 Incremental dynamic analysis (IDA), 472, 511, 513
 Indirect performance-based design, 468
 Induced hazards, 413
 Inelastic excursion. *See* Tensile yielding
 Inertia coefficient, 362, 363, 367, 368
 Inertia force, 78, 87, 96, 103, 104, 232, 241, 242, 361, 363, 369, 414, 639, 787
 Inertial interaction, 173, 186, 296
 Inertia load center, 605
 Inertial seismometers. *See* Seismograph
 Inherent damping, 237, 631, 632, 741
 Initial impact, 405
 Initial strain, 195
 Initial water height, 399
 In-phase, 479, 651, 657, 659, 661, 662, 680, 808
 Instructions per clock (IPC), 588
 Instructions per second (IPS), 588
 Intraplate earthquake, 23, 49, 50
- J**
 Jacket, 73, 75, 77, 84, 90, 91, 97, 367, 371, 372, 497, 500, 529, 530, 545, 548, 551, 576, 611, 707, 756, 815, 816
 Jacket pile, 75, 573
 Jacking, 717, 814, 816, 817, 832

- Jackups, 73, 103
Joint can, 820
Joint Reinforcement, 820
Joyner-Boore distance, 144, 147
- K**
Kanai-Tajimi model, 215, 217
Keulegan-Carpenter (KC) number, 363
Kinematic interaction, 173, 182, 184–186, 296, 503
Kinetic energy, 96, 374, 387, 635, 666, 705, 722, 741
- L**
Landslides, 14, 124, 153, 155, 353, 393, 421, 422, 424
Lateral load patterns, 488, 489
Lead dampers, 690
Lead extrusion dampers, 687, 690, 691
Life-cycle performance, 175, 462
Life safety, 174, 342, 355, 438, 462, 463, 467, 515, 790
Lift force, 362, 366, 798
Limit states, 175, 342, 428, 433, 436, 437, 439, 444, 450, 463, 513, 790
Linear (areal) source, 318
Linear failure surface, 450, 454, 455
Liquefaction, 66, 141, 152, 157, 259, 413, 416, 417, 419–421, 423, 509
Liquid impact, 554, 557, 559, 560
Lithosphere, 21, 48
Load and energy sharing mechanism, 596, 781, 783
Load and resistance factor design, 436–438, 450
Load factors, 437, 443, 499, 503, 512, 540
Load sequence effect, 830, 831
Load transmission path, 441, 593, 596, 722
Local soil/site effects, 296, 301
Local structural detailing, 626
Lock-up and shock transmission unit, 596, 781, 783, 784, 819
Logarithm decrement of transient responses, 636
Logic tree, 279, 316, 336, 337
Long flapping weed, 370
Longitudinal wave. *See* P-wave
Loss factor, 636, 662
Love wave, 113, 114, 116, 117
Lower limit of resistance, 437
Luco and Wong coherency function, 301, 307
- M**
Magneto-rheological damper, 810
Maintenance cost, 652, 674, 751
Manning's roughness, 403
Mantle, 21, 24, 44, 117
Mantle convection, 24, 41
Margin of safety. *See* Safety margin
Marine growth, 104, 366, 367, 369–372, 748
Mass and stiffness eccentricity, 604
Mass-damping-floor-diaphragm-substructure system, 771, 772
Mass proportional, 637, 638
Mass related lateral load pattern, 491, 492
Material damping, 142, 144, 170, 640, 641
Material nonlinearity, 507
Matrix, 300, 302, 382, 637, 639, 640, 825
Maximum Considered Earthquake, 315, 467
Maximum Credible/Capable Earthquake (MCE), 314, 315, 434, 646
Maximum crest-to-trough tsunami amplitude, 394
Maximum shear strain, 195, 196
Mechanical, electrical, and plumbing component, 787
Memory alloys, 687, 692
Memory capacity, 590
Mid-Atlantic ridge. *See* Mid-oceanic ridge
Mid-oceanic ridge, 41
Mitigation measures, 12, 13, 17, 52, 354, 433, 596, 604, 718
Modal combination, 479, 480, 482, 490, 503
Modal participation factor, 490, 491
Modal pushover analysis (MPA), 490
Modified mercalli intensity (MMI), 135, 145, 322
Modified/matched recordings, 288
Modified the Kanai-Tajimi model, 217
Moment magnitude, 23, 27, 49, 50, 55, 130, 134, 158, 392, 397, 407, 536
Moment resisting frame, 621, 660, 668, 681, 694
Momentum fluxes, 390
Monopile, 81, 84, 85, 477
Monte-Carlo method, 446, 456, 457
Moore's Law, 588
Morison's equation, 361, 363
Mother wavelet function, 257, 258
Motion-activated, 808
Motion induced interruptions, 424
Moving resonance, 96, 141, 259
Multiple mode pushover analysis, 490

Multiple-spherical-friction pendulum isolation bearing, 723, 726

N

N-2 method, 468

Narrow-banded, 208, 594, 770

Net work, 634

Nominal values, 445

Nonbreaking waves, 402

Non-flooded member, 367, 369

Nonlinear dynamic, 637

Non-linear dynamic time domain analysis, 471, 475, 487, 495, 496, 510

Non-linearity, 471, 472, 490

Non-linear static pushover analysis, 471, 487, 492

Non-proportional damping, 635, 639, 639, 640

Non-stationarity. *See* Non-stationary

Non-stationary, 124, 137, 140, 141, 205, 217, 254, 256, 300, 303, 473, 478

Non-structural component, 62, 245, 428, 464, 596, 617, 787, 788, 790

Non-structural component damage, 413, 788

Non-structural damages, 16

Non-structural elements. *See* Non-structural component

Non-traditional energy dissipating devices, 645

Normal distribution, 145, 347, 448, 449

Normalized Arias Intensity, 156

Nyquist frequency, 212

Nyquist sampling theorem, 213

O

Offshore bridges, 66, 67

Offshore platforms, 13, 17, 61, 67, 73, 73, 106, 248, 326, 438, 485, 493, 546, 701, 791

Offshore structures, 16, 17, 62, 73, 74, 80, 102, 105, 272, 342, 363, 375, 391, 493, 553, 708, 799

Offshore wind turbine substructures, 81

One-dimensional, 184, 191, 192, 194, 267, 296

Operating system, 588, 590

Orbital velocity, 390

Orientation, 27, 85, 91, 536, 538, 623, 765

Orifice coefficient. *See* Velocity exponent

Out-of-phase, 96, 97, 306, 480, 651, 680, 742, 759

Out-of-plane displacement, 623

P

Packed ice ridge, 372, 373

Pall friction damper, 665, 667, 679

Panel model, 365

Pangaea, 20

Parallel computing, 589

Partial safety factors, 444, 539

Partial uplifting, 555

Particular solution, 93

Passive control device, 807, 809

Path effects, 144, 169

P-Delta effect, 473

Peak ground acceleration (PGA), 111, 137, 142, 147, 150, 154, 157, 176, 233, 235, 246, 277, 326, 502

Peak ground displacement (PGD), 113, 138, 233, 234

Peak ground responses, 185

Peak ground velocity (PGV), 113, 138, 147, 152, 233, 234

Peak response, 228, 301, 480, 482, 582, 795

Performance-based design, 175, 428, 433, 436, 439, 462, 463, 466, 468

Phase angle between cyclic stress and strain, 636

Pipe failure, 555

Piston velocity, 649, 650

Plastic design, 435–437, 441

Point source, 318, 320, 399

Poisson model, 324

Post-buckling, 619

Post impact, 405

Potential/strain energy, 635

Power spectra, 204, 216, 217, 298

Power spectrum density, 211, 214–216

Prescriptive code design, 436, 462, 463, 475

Primary shape factor, 709, 711

Probabilistic seismic hazard analysis (PSHA), 146, 247, 315, 511

Probabilities of exceedance, 340

Probability-based seismic design (PBSD), 472

Probability density function (PDF), 319, 320, 322, 446, 447, 450, 454, 458

Probability of failure, 276, 343, 355, 442, 445, 446, 449, 454, 457

Production test, 732

Prototype test, 646, 731

Pseudo-acceleration spectrum, 224

Pseudo-relative-velocity spectrum, 224

Pseudostatic analysis, 424, 434

P-wave, 57, 63, 108, 109, 111, 115, 121, 129, 245, 380

Q

Quality assurance (QA), 444, 795

Quasi-linear solution, 185

Q-wave. *See* Love wave

R

Rack/rib, 820
Radiation damping, 142, 170, 642
Radius of gyration, 710
Random Access Memory (RAM), 588
Random number generator, 456
Random vibration analysis, 471, 478
Rayleigh damping, 635–640
Rayleigh wave, 113, 114, 116, 117, 129, 192, 395
Redundancy, 54, 85, 407, 480, 494, 540, 553, 560, 593, 594, 611, 631
Referred standards, 461
Reinforcement, 8, 507, 595, 596, 629, 657, 766, 814, 820, 822, 826, 830, 831
Relative maximum run-up height, 402
Repeated yielding, 548, 617
Replaceable shear link beam, 684
Replaceable weak shear wall, 687
Reserve capacity factor, 276, 277, 344
Residual deformation, 197
Resonance, 79, 90, 94, 96, 103, 175, 208, 254, 375, 387, 594, 674, 748, 773
Response modification factor, 435, 582
Response-slip-load relationship, 676
Response spectrum, 150, 189, 204, 218, 220, 224, 228, 229, 247, 268, 272, 275, 282, 288, 315, 340, 346, 473, 477, 479, 480, 484, 485, 488, 496, 501, 509, 510, 564, 730, 745
Response spectrum analysis, 204, 228, 468, 471, 472, 478, 479, 484, 492, 501, 510
Return period, 100, 146, 246, 277, 279, 314, 323, 325, 326, 330, 338, 340, 344, 347, 439, 471, 531, 729, 754
Reynolds (*Re*) number, 363, 364, 366, 406
Richter magnitude, 40, 50, 125, 127, 130, 132, 137, 157
Richter scale, 30, 120, 158
Risk category, 355
Rocker, 722
Rock outcrop, 170, 172, 175, 184, 185, 188, 197, 273, 275, 282, 283, 288, 331, 340, 499, 503
Roller pendulum, 722
Rounding error, 592
Run-up, 393, 395, 398, 400–402, 405, 406
Rupture mechanism, 145, 169, 170, 322

S

Safety criteria, 355
Safety margin, 440, 443, 445, 447–450, 453–455
San Andreas Fault, 22, 39, 49, 50, 52, 131

Satellite remote sensing, 353
Saturation, 29, 129, 130, 132, 134
Seafloor uplift, 396, 397
Seaquakes, 63, 65, 67, 379, 380, 383
Secondary buckling, 555, 556, 580
Secondary shape factor, 709, 712
Second moment of inertia, 710, 714
Second moment reliability method. *See* Semi-probabilistic method
Second-order-reliability-index, 453, 454
Sedimentary basin, 151, 194
Seesaw energy dissipation system, 683, 684
Seiche, 14, 15, 413
Seismic gap, 23, 50, 57
Seismic hazard analysis, 23, 54, 142, 146, 151, 171, 228, 231, 247, 279, 311–313, 315, 320, 331, 353, 354, 511
Seismic hazard curve, 277, 322, 323, 329, 330, 338, 342–344, 511
Seismic hazard map, 162, 338–340, 342, 344, 460
Seismic rehabilitation, 466, 594, 813
Seismic risk, 12, 13, 53, 123, 323, 340, 344, 354–356, 729, 804
Seismic sources, 117, 169, 336, 337
Seismic vulnerability, 13
Seismology, 53, 340, 436
Self-adaptive lateral load pattern, 492
Self-centering capacity, 692
Semi-active and active control device, 809
Semi-probabilistic method, 457
Sensor, 251, 770, 794, 796, 800, 809
Separation distance, 301, 302
Serviceability limit state, 440, 450, 829
Shallow bedrock, 238
Shallow crustal earthquakes, 147, 148, 150, 248
Shannon sampling theorem. *See* Nyquist sampling theorem
Shape function, 217, 300, 303
Shape memory alloys, 687, 692, 693
Shear buckling, 555, 557
Shear link beams. *See* Replaceable shear link beam
Shear walls, 623, 675, 679, 685, 733, 814
Shear wave. *See* S-wave
Shear wave velocity, 115, 147, 176, 180, 181, 238, 268–270, 273, 274, 302, 307, 420, 421, 607
Shear wave velocity measurement, 420
Shelters, 68, 408, 653
Shoaling amplification factor, 401
Shock wave, 65, 110, 383
Shortening span, 822, 823

- Short Time Fourier Transform (STFT), 255
 SH wave, 112, 114, 191, 562, 711
 Significant digits. *See* Significant figures
 Significant duration, 153, 155, 156, 159, 160
 Significant figures, 591
 Single point anchor reservoir platform (SPAR), 73, 74, 79, 81, 410
 Single story mechanism, 622
 Site amplification, 147, 175, 176, 180, 238, 270
 Site effects, 169, 171, 194, 210, 267, 282, 296, 301
 Site period, 96, 117, 170, 175–179, 181, 238, 381, 594, 703, 711, 732
 Site response analysis, 111, 150, 171, 176, 177, 180, 182, 184, 185, 188, 190, 192–194, 196, 267, 268, 281, 282, 288, 296, 301, 331, 340, 419, 421, 444, 496, 499, 502, 503, 587
 Site-specific response analysis. *See* Site response analysis
 Slenderness, 617, 710
 Sliding/Slipping, 426
 Sliding isolation systems, 701, 703, 716, 722, 724, 726–728, 809
 Slip rate, 131
 Sloshing, 413, 554, 555, 557, 558, 560–565, 567, 568, 570, 571, 573, 575, 577, 580–582, 642, 757, 759–763, 765, 766, 768, 770
 Sloshing wave height, 568, 582
 Slotted bolted damper, 668
 Smart damper, 671
 Soft growth, 370
 Soft-soft design, 86, 87
 Soft-stiff design, 86
 Soft story, 597
 Soil depth, 179, 238
 Soil particle friction, 142
 Soil–structure interactions (SSI), 169, 173, 182, 183, 187, 270, 503, 581
 Soil-tank interaction, 581
 Solitary wave amplitude, 402
 Soloviev-Go intensity scale, 393, 394
 Sommerfeld radiation, 381
 Source-to-site distance, 113, 142, 144, 145, 147, 148, 157, 158, 160, 170, 246, 284, 312, 313, 315, 316, 318, 320, 346, 347
 Spatial/directional combination, 482
 Spatial varied (asynchronous) ground motion, 293
 Spectral displacement, 223–225, 228, 271, 277, 488, 489, 714, 715
 Spectral matching. *See* Spectrum matching
 Spectral shape, 227, 283, 284, 287, 340, 349, 351
 Spectral velocity, 151, 224, 225, 230
 Spectrum matching, 259, 283–285, 287, 512, 514
 Spherical bearing, 722
 Spiral vibration damper, 776
 Spreading ridge. *See* Divergent boundary
 Spreading zones, 41, 44
 SRSS. *See* Square root of the sum squares
 Stable continental region, 145, 148, 151
 Standard penetration test, 270, 420
 Static coefficient method, 460, 471, 473, 477, 478
 Static eccentricity, 608
 Stationary process, 203, 204, 254, 256
 Steady-state, 93, 94, 96, 218, 375, 634, 650, 764
 Sticking steel reinforcement, 822
 Stiffness, 54, 87, 90, 103, 152, 173, 181, 183, 189, 245, 349, 464, 483, 488, 494, 502, 510, 532, 535, 547, 594, 596, 597, 605, 623, 633, 639, 662, 677, 682, 709, 710, 728, 753, 796, 816, 826, 831
 Stiffness proportional, 637, 638
 Stiff-stiff design, 86
 Stockbridge damper, 755
 S-to-P-wave conversion, 137, 245
 Strengthening, 595, 626, 813–815, 824, 826, 827, 831, 832
 Structural configuration, 531, 594, 595, 597, 611, 813
 Structural damage, 105, 117, 124, 127, 176, 281, 413, 419, 428, 438, 464, 554, 716, 729, 795
 Structural Health Assessment (SHA). *See* Structural health monitoring (SHM)
 Structural health monitoring, 105, 261, 793, 794
 Subduction zones, 41, 44, 46, 49, 51, 117, 387
 Subgrade impedances, 173, 184, 186
 Submerged floating tunnel, 65, 66, 380
 Substructure approach, 173, 182–184, 186
 Subsurface irregularity, 173, 192
 Suction bucket, 81
 Sudden drop. *See* Sudden subsidence
 Sudden subsidence, 17, 102, 545–548, 551
 Sumitomo friction damper, 669, 670
 Sum of absolute value, 480
 Superposition, 223, 243, 296, 395, 560, 635, 637, 639, 640
 Surface roughness, 213, 363, 371

- Surface wave, 64, 96, 107, 109, 111, 113, 115–117, 123, 124, 127, 129, 130, 134, 140, 151, 192, 302, 379, 560
Surface wave magnitude, 129, 130, 132, 230, 247, 269, 271
SV wave, 111, 114, 124, 190, 245
Swarm, 60
S-wave, 108–111, 114, 118, 121, 123, 140, 192, 380
System performance, 790
- T**
Tank support-system failure, 555
Taylor series, 453
Taylor viscous damper, 648, 649
Tectonic boundaries, 34
Tectonic plates, 21, 23–25, 38, 40, 41, 44, 49, 51, 320
Tectonic-related earthquakes, 19, 24, 34
Tensile yielding, 611
Theory of plate tectonics, 22, 23
Three-dimensional, 174, 184, 187, 190, 193, 194, 267, 281, 317, 406, 581
Time-located information, 204, 254, 255
Time-scale domain, 256
Tipping, 424, 427
TLP, 63, 65, 74, 79–81, 83, 380
Topographic irregularity, 173
Torsional resistance, 595, 603
Torsional seismic motions, 124
Transform boundary. *See* Transform faults
Transform faults, 48, 51, 387
Transient excited vibrations, 523
Translation/shifting parameter, 257
Transverse wave. *See* S-wave
Tripile, 81
Triple-friction-pendulum bearing, 724
Tripod-pile, 81
Tsunami, 5, 14, 62, 65, 66, 387, 390, 392, 393, 395–400, 402, 404–408, 413
Tsunamic wave height, 399
Tsunami resistant structures, 407, 408
Tsunamis, 14, 27, 67, 68, 379, 387, 391–394, 399, 406, 409, 413
Tsunami warning system, 408
Tuned liquid column damper, 746, 757
Tuned liquid damper, 558, 741, 746, 757, 762
Tuned mass damper (TMD), 100, 217, 537, 741, 749, 771, 774
Tuned mass damper simple pendulum system, 746
Tuned mass damper spring-mass system, 746
- Tuned sloshing dampers (TSDs), 757
Two-dimensional, 173, 192, 194, 267, 281, 369, 380, 558, 562, 581
- U**
Ultimate limit state, 342, 439, 450, 501
Uncertainty, 62, 145, 316, 320–322, 343, 433, 444, 457, 496, 756, 795, 797
Unconstrained optimization formulation, 516
Undersea tunnel, 66
Uniform hazard spectrum, 282, 324, 330, 340, 346
- Unit impulse, 220, 221
Unmanned aerial vehicles, 794, 797
Upper limit of load, 437
- V**
V/a ratio, 152
V/H, 189, 198, 246, 247, 483
Variable orifice damper, 810
Variable stiffness system, 810
Velocity-activated, 808
Velocity exponent, 649–651, 656
Velocity potential, 380, 381
Velocity sensitive region, 237, 479
Vibration-based SHM, 794–797
Vinylester, 825
Viscoelastic damper, 651, 659–664, 674
Viscous damper, 433, 633, 648, 650–654, 656, 679, 694, 713, 750, 754
Viscous damping coefficient, 636
Viscous damping walls, 655–657
Viscous effects, 362, 473, 757
Volcanoes, 19, 25, 27, 41, 44–46, 419
Volcanoes induced earthquakes, 26
Volumetric source, 318
Vulnerability, 12, 354, 355, 813
- W**
Water-borne debris, 393, 407
Water column, 105, 197, 275, 396
Water level increase, 28, 397
Water particle velocity, 362
Wave length, 116, 117, 176, 179, 207, 238, 361–363, 366, 388, 390, 397, 400, 402
Wavelet analysis, 256, 260, 472
Wavelet function, 256, 258
Wavelet transform, 141, 204, 255, 256, 258, 261
Wave number spectrum, 397
Wave passage effects, 296, 301, 307
Wave potential, 362

- Wave propagation, 111, 114, 139, 151, 169, 173, 175, 190, 194, 217, 267, 296, 297, 316, 399, 496
Wave scattering, 137, 139, 169, 245, 296
Wave tank, 406
Weak story, 597, 603
Wegner's theory. *See* Continental drift
Weight, 28, 75, 78, 103, 337, 371, 416, 501, 529, 564, 592, 611, 688, 707, 734, 751, 754, 766, 797, 822
Whipping effect, 101, 525, 526, 531, 532, 536, 598
White noise input, 215
Windowed filter, 253
Wood-Anderson seismograph, 120, 126, 127, 129
X
X-shape added damping and stiffness (XADAS) damper, 682
Y
Yielding damper, 645, 651, 678, 680, 683, 687, 688, 690
Yielding steel cross-braced system, 681